

Lecture Schedule and Associated Preparatory Readings

Dear ISSCG-17 Attendee,

Welcome to the 17th International Summer School on Crystal Growth! We are continuing a tradition which began on 1971 with ISSCG-1 associated with the conference ICCG-3 in Marseille France. The purpose of the school is to provide a forum and information to those entering the crystal growth field, as well as others, which can for the basis of understanding the fundamentals of crystal growth and provide entry to understanding the literature crystal growth. This 'book' contains selected literature articles and tutorials meant to prepare you for the lectures at the school and provide reference materials for the years to come. ***These articles are meant for your personal use and should not be reproduced or disseminated without the authors' or publishers' explicit permission.***

The organizers of ISSCG-17 and ICCGE-19 would like to thank all the lecturers and organizers for their help and participation.

Joan M. Redwing
Pennsylvania State University

Thomas F Kuech
University of Wisconsin -Madison

Chapters and Presentations

1.	Introduction and History of Crystal Growth	Robert Feigelson	Stanford University, Stanford, CA, USA
2.	Thermodynamics of Crystal Growth	Detlef Klimm	Leibniz Institute for Crystal Growth, Berlin, Germany
3.	Transport Phenomenon in Crystal Growth	Jeffrey Derby	University of Minnesota, Minneapolis, MN, USA
4.	Nucleation and Growth Kinetics	Elias Vlieg	Radboud University, Nijmegen, The Netherlands
5.	Bulk Crystal Growth from the Melt	Chung-wen Lan	National Taiwan University, Taipei, Taiwan
6.	Defects and Impurities	Mark Goorsky	University of California-Los Angeles, Los Angeles, CA, USA
7.	Characterization and in situ Observation	Sarah Kurtz	University of California-Merced, Merced, CA, USA
8.	Solution Growth	Peter Vekilov	University of Houston, Houston, TX, USA
9.	Epitaxial and Vapor Growth	Tania Paskova	North Carolina State University, Raleigh, NC, USA
10.	Bulk Growth of Oxide Materials	Satoshi Uda	Tohoku University, Sendai, Japan
11.	Growth of advanced complex oxides	Darrell Schom	Cornell University, Ithaca, NY, USA
12.	Crystal Growth of Materials for Energy	Roberto Fornari	Università di Parma, Parma, Italy
13.	Crystal Growth of 0, 1 and 2D Materials	Zakaria Al Balushi	University of California, Berkeley
14.	Crystal Growth of Organic Materials	Kevin Roberts	University of Leeds, Leeds, UK

ISSCG 2019																						
			Location TBD			Location (TBD)			Location (TBD)			Location (TBD)			Location (TBD)			Location (TBD)				
	Sunday		MONDAY			TUESDAY			WEDNESDAY			THURSDAY			FRIDAY			SATURDAY				
7:00-7:30			Breakfast			Breakfast			Breakfast			Breakfast			Breakfast			Breakfast				
7:30-800																						
8:00-8:30			Opening Remarks			Transport Phenom in Crystal Growth (J. Derby)			Defects and Impurities (M. Goorsky)			Solution Growth (P. Vekilov)			Crystal Growth of Materials for Energy (R. Fornari)							
8:30-9:00			Intro to Crystal Growth (R. Feigelson)															Check-Out by 10AM				
9:00-9:30																						
9:30-10:00			coffee break			coffee break			coffee break			coffee break			coffee break							
10:00-10:30			History of Crystal Growth (R. Feigelson)			Transport Phenom in Crystal Growth (J. Derby)			Characterizatio n and In Situ Observation (S. Kurtz)			Epitaxial and Vapor Growth (T. Paskova)			Crystal Growth of Low Dimensional Materials (Z. Al Balushi)			Shuttle Transportati on to Keystone				
10:30-11:00																						
11:00-11:30	Arrival																					
11:30-12:00			Lunch			Lunch			Lunch			Lunch			Lunch							
12:00-12:30																						
12:30-1:00																						
1:00-1:30			Thermo of Crystal Growth (D. Klimm)			Nucleation and Growth Kinetics (E. Vlieg)			Free Time			Bulk Growth of Oxide Materials (S. Uda)			Bulk Growth of Organic Materials (K. Roberts)							
1:30-2:00																						
2:00-2:30																						
2:30-3:00																						
3:00-3:30			coffee break			coffee break						coffee break			Concluding Remarks							
3:30-4:00	Registration and Welcome Reception		Thermo of Crystal Growth (D. Klimm)			Bulk Crystal Griowth from Melt (C.W. Lan)						Growth of Advanced Complex Oxides (D. Schlom)			Free Time							
4:00-4:30																						
4:30-5:00																						
5:00-5:30			Dinner			Dinner						Dinner			Dinner							
5:30-6:00	Dinner																					
6:00-6:30									Reception and Barbeque													
6:30-7:00																						
7:00-7:30			Poster Session I			Poster Session II						Poster Session III										
7:30-8:00																						
8:00-8:30																						
8:30-9:00																						
9:00-9:30																						

1. Introduction and History of Crystal Growth



Handbook of Crystal Growth

Fundamentals: Thermodynamics and Kinetics

VOLUME I, Part A

Crystal Growth through the Ages: A Historical Perspective

Robert S. Feigelson
Geballe Laboratory for Advanced Materials
Stanford University, Stanford, CA, USA

Reprinted from The Handbook of Crystal Growth, Vol 1A, 2nd Edition, Robert S. Feigelson, Crystal Growth through the Ages, 1-83, Copyright 2015, with permission from Elsevier .

Elsevier
Radarweg 29, PO Box 211, 1000 AE Amsterdam, The Netherlands
The Boulevard, Langford Lane, Kidlington, Oxford OX5 1GB, UK
225 Wyman Street, Waltham, MA 02451, USA

First edition 1993

Second edition 2015

Copyright © 2015, 1993 Elsevier B.V. All rights reserved.

The crystals on the front cover are high-quality synthetic diamond crystals grown by Sumitomo Electric Industries, LTD by a temperature gradient method under high pressure and high temperature. The yellowish crystals are ordinarily synthetic diamonds containing nitrogen impurity of several tens of ppm (type Ib). The colorless ones are high-purity synthetic diamonds free of impurities (type IIa). The size of the largest high-purity crystal (lower left) is about 12 mm in diagonal length. The photo was provided by Dr. Hitoshi Sumiya.

No part of this publication may be reproduced or transmitted in any form or by any means, electronic or mechanical, including photocopying, recording, or any information storage and retrieval system, without permission in writing from the publisher. Details on how to seek permission, further information about the Publisher's permissions policies and our arrangements with organizations such as the Copyright Clearance Center and the Copyright Licensing Agency, can be found at our website: www.elsevier.com/permissions.

This book and the individual contributions contained in it are protected under copyright by the Publisher (other than as may be noted herein).

Notices
Knowledge and best practice in this field are constantly changing. As new research and experience broaden our understanding, changes in research methods, professional practices, or medical treatment may become necessary.

Practitioners and researchers must always rely on their own experience and knowledge in evaluating and using any information, methods, compounds, or experiments described herein. In using such information or methods they should be mindful of their own safety and the safety of others, including parties for whom they have a professional responsibility.

To the fullest extent of the law, neither the Publisher nor the authors, contributors, or editors, assume any liability for any injury and/or damage to persons or property as a matter of products liability, negligence or otherwise, or from any use or operation of any methods, products, instructions, or ideas contained in the material herein.

British Library Cataloguing in Publication Data
A catalogue record for this book is available from the British Library

Library of Congress Cataloging-in-Publication Data
A catalog record for this book is available from the Library of Congress

SET Volume ISBN: 978-0-444-56369-9
Volume 1, Part A–978-0-444-63322-4
Volume 1, Part B–978-0-444-63323-1

For information on all Elsevier publications
visit our website at www.store.elsevier.com

Printed and bound in the UK.



1 Crystal Growth through the Ages: A Historical Perspective

Robert S. Feigelson

GEBALLE LABORATORY FOR ADVANCED MATERIALS, STANFORD UNIVERSITY, STANFORD, CA, USA

Excerpt from Pliny the Elder's, *Natural History*, AD 77, "*… I have prefaced these volumes with the names of my authorities. I have done so because it is, in my opinion, a pleasant thing and one that shows an honourable modesty, to own up to those who were the means of one's achievements…*"

Trans. H. Rackham

CHAPTER OUTLINE

1.1 Introduction **2**
1.2 Evolution of Crystal Growth Theories **4**
1.2.1 Early Developments (Before the Nineteenth Century) 4
1.2.2 The Nineteenth Century 5
1.2.3 The Twentieth Century 6
1.3 Crystal Growth Methods **16**
1.3.1 Melt Growth 17
1.3.1.1 The Nineteenth Century and the Verneuil Process 18
1.3.1.2 The Twentieth Century 20
1.3.1.3 The Czochralski Crystal Pulling Method 20
1.3.1.4 Bridgman–Stockbarger/Gradient Freeze Methods 25
1.3.1.5 Nacken–Kyropoulos Methods 28
1.3.1.6 Stöber/Heat Exchanger Methods 30
1.3.1.7 Kapitza's Method 30
1.3.1.8 Zone Melting 31
1.3.1.9 Shaped Growth 33
1.3.1.10 Skull Melting 37
1.3.2 Solution Growth **38**
1.3.2.1 Introduction 38

Handbook of Crystal Growth. http://dx.doi.org/10.1016/B978-0-444-56369-9.00001-0
Copyright © 2015 Elsevier B.V. All rights reserved.

1.3.2.2 Aqueous Solution Growth 38
1.3.2.3 Growth of Biological Macromolecules 41
1.3.2.4 Growth from Gels 43
1.3.2.5 Nonaqueous Solution Growth 44
1.3.2.6 High Temperature Solution (Flux) Growth 44
1.3.2.7 Hydrothermal Growth 49
1.3.2.8 Electrochemical Crystal Growth 52
1.3.3 Vapor Growth 53
1.3.3.1 Introduction 53
1.3.3.2 Bulk Growth 55
1.3.3.3 Vapor Phase Epitaxy 58
1.3.3.4 The VLS Method 63
1.3.3.5 Artificial Epitaxy (Graphoepitaxy) 64
1.3.4 Synthetic Diamond Crystals 65
1.3.5 Solid State Recrystallization 70
1.4 Epilogue **72**
Acknowledgments **72**
References **73**

1.1 Introduction

Most scientists and engineers are aware that the basic tools they use in their daily research activities were developed by groups of researchers working in series or parallel over decades, in some cases centuries. It was often in an incremental way, one study building on another. As time went on, these earlier ideas became more refined and practical, providing future workers with a more through understanding of the physics and chemistry involved in different materials systems and leading to innovative new processes for making materials and devices that have affected everyone's lives. They helped define the world we live in and used their newly gained knowledge to stoke the technological revolution.

The crystal growth field (a branch of materials science, physics, chemistry and crystallography) has a rich historical background that goes back at least several millennia. It basically deals with understanding the underlying mechanisms involved in the crystallization process and the technology to produce a single crystal from some medium in a controlled fashion. One of the earliest written accounts documenting work on methods for preparing crystals was given by the Roman Pliny the Elder in 77–79 AD [1]. His collected work was a summary of knowledge going back to even more ancient times. It is probable that even prehistoric man engaged in the recrystallization of materials like salt. Among other topics, Pliny discussed the preparation of Vitriol (iron,

copper and zinc sulfate hydrates). The process involved evaporating mine or spring waters obtained from the Mediterranean region. About 1500 years later, in medieval times, Pliny's work was referred to by both Biringuccio [3] and Agricola [2]. They concentrated on preparing crystals of these compounds for medicines, dyes, fluxes and acids. The various methods employed generally began with the purification of mineral deposits, followed by recrystallization of the remaining solutions by evaporation.

The field of crystal growth encompasses a wide spectrum of scientific disciplines and includes (1) experimental and theoretical studies of crystallization processes, (2) the growth of crystals under controlled conditions for both scientific purposes and industrial applications and (3) crystal characterization. It also covers almost all classes of materials, i.e., inorganic and organic compounds, elemental materials as well as biological macromolecules. Many methods have been developed over the years for producing single crystals, the size range for which varies from the nanometer to meter scale. These crystals have in common an atomic ordering that persists throughout their bulk and without the presence of grain boundaries. The two principal scientific pillars upon which the field of crystal growth depends are thermodynamics and kinetics. The thermodynamic properties of a system describe how solid, liquid and gaseous phases behave with respect to state variables such as temperature, pressure and composition. They provide a road map, so to speak, which crystal growers use to plan growth strategies. For the preparation of crystals of a size, purity and composition required for a specific application, one needs to know what material phases will exist under various conditions of temperature, T, and pressure, P, etc., and how these phases will form under dynamic solidification processing conditions. Kinetic factors, on the other hand, influence our ability to produce a crystal at a desired growth rate and with a degree of perfection and uniformity suited to the intended application. We will explore below how interface stability and segregation behavior are influenced both by thermodynamic and kinetic factors.

In the beginning, crystal growth was not the well-defined field it is today. Work was carried out by chemists, physicists, etc., and research results were reported in various conferences and journals of these societies. The first conference to concentrate on the topic was at a Faraday Society meeting in 1949, held in Bristol, England. In spite of the growing importance of crystals for solid-state electronic applications in the early 1950s, it was almost a decade later before a second meeting concerning issues in crystal growth arose. That conference, held in Cooperstown, New York in 1958 [4], gathered together some of the most eminent crystal growth researchers to discuss a wide range of topics of interest to the crystal growth community. Conferences were also started in the Soviet Union (Moscow) as early as 1956. However, the major consolidation of the field into a viable entity was the formation in 1966 of the International Organization of Crystal Growth (IOCG) and under their aegis, the subsequent International Conferences on Crystal Growth (ICCG). These conferences have been held every three years since 1966.

The local organizers of the first ICCG conference held in Boston, Massachusetts immediately founded the American Association for Crystal Growth (AACG) under the joint chairmanship of Doctor Robert (Bob) Laudise and Doctor Kenneth (Ken) Jackson.

The AACG held their own national conferences soon afterward and other national groups formed around the world. The *Journal of Crystal* was established in 1967 under the leadership of Professor Michael Schieber, along with Sir Charles Frank and Dr Nicholas Cabrera as co-editors. Although papers on crystal growth topics are published elsewhere as well, the *Journal of Crystal Growth* has remained the major venue for papers on crystal growth theory, practice and characterization and has published related proceedings of conferences focused on various aspects of the field.

Many of the topics discussed in this introductory history are covered in much more detail in various chapters in this comprehensive, updated version of the *Handbook of Crystal Growth*. This treatment is designed to focus mainly on their historical context.

1.2 Evolution of Crystal Growth Theories

Although crystals can be grown by purely empirical means, control of their rate of growth, perfection, dimensions, composition and physical properties is greatly facilitated by having a good grasp of the fundamentals underlying crystal growth processes. Over the past century, a sound theoretical foundation has been built up through the efforts of many different scientists and engineers working in materials-related fields such as chemistry, physics and crystallography. The approach is generally two-fold: first to understand the nature of material systems (crystal structure and morphology, phase equilibrium, etc.), and second, to determine the factors that affect the crystallization process (nucleation, growth kinetics, segregation behavior, interface stability, heat and mass transport, etc.). Although remarkable progress has been made, the complex nature of the field and its changing emphasis on newer materials and structures keeps providing a constant source of challenges to our understanding of crystallization processes.

1.2.1 Early Developments (Before the Nineteenth Century)

The earliest scientific studies important to the field of crystal growth were made by natural scientists trying to understand the morphologies of mineral crystals. One of these early pioneers was the Swiss naturalist Conrad Gesner (1516–1565) who in 1564, after studying different crystals, reported that one crystal differs from another by its angles and form [5]. Later in the sixteenth century, Andreus Caesalpinus (1519–1603) wrote in "De Metallicis" [6] that the shape of crystals grown from water solution (e.g., salt, sugar and alum) were a characteristic of the material. Ichiro Sunagawa [7] proposed, however, that the science of crystal growth started with the treatise of N. Steno. Nicolas Steno, also known as Niels Stensen, (1638–1686) was a well-known Danish scientist specializing in the fields of geology and anatomy. He was also one of the founders of crystallography. In his treatise, published in 1669 [8], he observed that, although quartz crystals differ in appearance from one to another, the angles between corresponding faces are always the same. In addition, he noted that they grew by an inorganic hydrothermal process rather than through the action of bacteria [7]. Years later, Steno's law of *constant interfacial*

angles in crystals was confirmed, first by the Italian Domenico Guglielmini (1665–1710) [9] who asserted, like Casealpinus, that every salt has it own particular shape. A century later, the Frenchman Jean Baptiste Romé de l'Isle (1736–1790) [10], concluded from his study of many hundreds of different crystals that every crystalline substance with a specific composition had a similar and particular crystal shape (1772) See Figure 1.1(A)). He found six different fundamental forms from which all others could be derived. Although the above work, and that of other researchers not mentioned, set the stage for our improved understanding of the nature of crystals, it was not until much later that attention turned seriously to the question of how crystals grew and which mechanisms were involved. Figure 1.1(B) shows the internal structure of a lithium niobate crystal revealed by partial melting.

1.2.2 The Nineteenth Century

French physicist Auguste Bravais (1811–1853), building on l'Isle's previous work, determined in 1848 that there are 14 unique "Bravais" lattices comprising three-dimensional crystalline systems [11]. This work provided the basis for understanding symmetry, crystal morphology and crystalline anisotropy. The morphology of a crystal is influenced by (1) external factors, e.g., the surrounding nutrient phase and (2) internal features, e.g., cell dimensions, atom sizes, positions, and bond energies.

Contemporary quantitative crystal growth science originated with the thermodynamic studies of the American scientist J. Willard Gibbs (1839–1903). Gibbs studied how various phases behaved in heterogeneous systems under the influence of state variables such as temperature and pressure. His seminal work, *On the Equilibrium of*

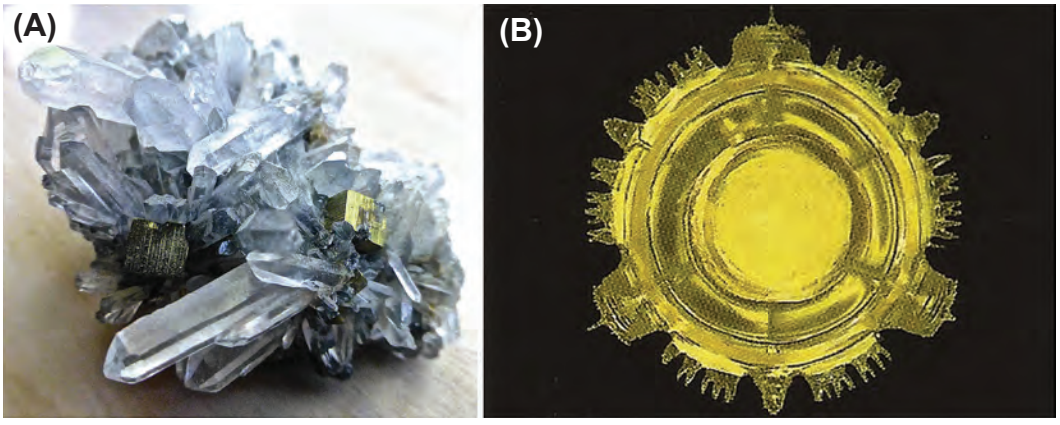


FIGURE 1.1 (A) Naturally occurring crystals of quartz (SiO_2) interspersed with pyrite (FeS_2) crystals. Their different morphologies reflect their internal crystal structures, trigonal and cubic respectfully. (B) The bottom side of a c-axis Czochralski grown lithium niobate crystal that was rapidly heated to cause it to separate from the melt surface. The resulting dendritic-like structure reveals the internal three-fold symmetry along the axis of this rhombohedral crystal.

Heterogeneous Substances (1876 and 1878) [12], included both the first and second laws of thermodynamics and thermodynamic reaction tendencies in any thermodynamic system. His graphical representations, the earliest phase diagrams, have been expanded through the years to include numerous chemical systems of both academic and industrial interest. These were derived largely by experimental studies but also in recent years by numerical simulations. These "phase diagrams" are vital data sources for the crystal grower, enabling him or her to select the most appropriate growth method and produce a crystal with the desired composition and properties.

To form a crystal, a nutrient phase (i.e., liquid, gas or solid) must be in a metastable state. In other words, the free energy (at constant volume) or the Gibbs potential (at constant pressure) of this phases must exceed that of the crystal. This excess is the driving force for crystallization. This metastability is accomplished by either supercooling a melt or supersaturating a solution or vapor phase. During crystallization, latent heat is evolved. Among other remarkable contributions made by Gibbs was that nucleation phenomena resulted from heterophase fluctuations in metastable homogeneous phases. Nucleation can be either homogeneous (from within the pure matrix phase) or heterogeneous (on a foreign substance such as particles or substrates within the matrix phase or the container walls). The maximal amount of supercooling or supersaturation required depends on the thermodynamic properties of the material system, various external forces such as mechanical vibrations, and of course, the nature of the crystal surface, etc. In practice, the initial nucleation stage is often bypassed by using oriented seed crystals.

1.2.3 The Twentieth Century

In the opinion of K. Jackson [13], our modern understanding of crystal growth processes began with the research work of Harold Wilson (1874–1964) [14] and Martin Knudsen (1871–1949) [15]. Wilson's work in 1900 concerned the velocity of solidification and viscosity of supercooled liquids, whereas Knudsen's work involved kinetic molecular theory that much later played an important role in molecular beam epitaxy. One of the most important early growth theories was proposed in 1921 by the German physical chemist Max Volmer (1885–1965) and his student Immanuel Estermann (1900–1973) [16]. Their adsorption-layer theory (i.e., layer-by-layer growth) was deduced from measuring the tangential growth rate of plate-like mercury crystals from the vapor state at low temperatures. The proposed adsorption-layer lies between the crystal and nutrient phase, with the crystallizing species losing only part of their latent heat, while maintaining some surface mobility in the layer parallel to the crystal surface. The species are incorporated into the crystal lattice at the edges of the incomplete atomic layers (steps on the growing crystal face). Volmer was also the first to consider the role of ad-atoms (or molecules) and holes on the crystal surface under equilibrium and nonequilibrium conditions.

Walther Kossel (1888–1956) [17], a German physicist known for his theory of chemical bonding, proposed in 1928 an atomistic view of crystal growth (kinetic theory), as

opposed to a "continuum" thermodynamic interpretation. It was similar to that independently proposed by Iwan N. Stranski (1897–1979), [18] a Bulgarian physical chemist, and was based on earlier diffusion theories concerning mass transport of the crystallizing species to the growth interface with the distinction that what went on in the interface region (how the species found an appropriate lattice site) was *not* a negligible effect. Their work is often linked together as the Kossel–Stranski model. They both concluded from early work on the rock salt structure that no other planes but the cubic ones are possible and that other planes (110, 111, etc.) are not present on the surface as complete planes but are made up of alternating (001) and (100) faces several atoms thick (kinetic roughening). This work led to what is commonly referred to as the TLK (terrace-ledge-kink) model where Kossel [19] suggested that incorporation of an atom required that the steps spread laterally across the surface. Somewhat later came the work of Stranski's younger colleague Rostislav Kaishev (1908–2002) linking the equilibrium crystal shape, i.e., the facets making this shape, with the average work required to detach a molecule from that facet, and thereby accounting for different structural positions on that facet and its edge. Stranski and Kaishev founded the famous Bulgarian school of nucleation and crystal growth (see Ref. [20]). Much of their work was on low-temperature aqueous solution growth and the crystallization of metals at room temperature in electrolyte solutions. An extensive discussion of Kossel and Stranski's work, together with other contemporaries, is given in Buckley's book *Crystal Growth* [21] and numerous other more recent publications.

The goal of scientific studies is the development of effective models that can explain observable physical phenomena and direct practical crystal growing via generalized predictive relationships. These activities were both based on scientific inquisitiveness and to provide guidelines for practitioners to produce material for the benefit of mankind. Basic studies on nucleation and crystal growth have greatly expanded over the years. Older theories and concepts have been refined and new concepts proposed and tested. Basic understanding has greatly benefited from important advances in crystal characterization technologies. They have provided direct evidence of crystal perfection and growth behavior down to the atomic scale. Two examples are the transmission electron microscope and in situ atomic force microscopy. The former technology makes possible the imaging of atomic structures of real crystals, allowing a study of their perfection and the nature of their imperfection. Atomic force microscopy can be used, to great effect, both to study the formation and kinetics of growth layers during solution growth (particularly biological macromolecules) and how they change upon post-growth heat treatments (surface reconstruction). Reflected beam electron microscopy has also been very useful.

The discovery of crystalline imperfections such as edge and screw dislocations, stacking faults, point defects and inclusions in an otherwise uniform crystal lattice, has had a strong impact on our understanding of crystal properties, on the one hand, and crystal growth mechanisms on the other. They are also of great technological importance for the influence they have on the electronic and mechanical properties of a material.

In 1934, Sir Geoffrey Taylor (1886–1975), a noted British physicist and mathematician, proposed that the *plastic* deformation of ductile materials could be explained in terms of the theory of dislocations developed by Vito Volterra in 1905. Some years later, the subject of dislocations occupied the thoughts of Sir Charles Frank (1911–1998), an eminent British crystallographer who spent much of his career at Bristol University. His fundamental contributions to the field of crystal growth include the laws governing dislocation branching, the existence and properties of dislocation networks, and in 1950, the Frank-Read mechanism for the generation of dislocations. In a well-documented account, the idea for this latter mechanism occurred to both Sir Charles and to W.T. Read (an American working at the General Electric Co.) independently and at the same time. Frank had shown the year before [22] that two-dimensional nucleation theory failed significantly to explain observed high crystal growth rates at low supersaturation. This discrepancy could, however, be readily reconciled if the growth face contained a screw dislocation outcrop. That this dislocation should lead to continuous step generation in the form of a "growth spiral" step on the growth face was immediately validated by experimentally observed growth spirals formed on actual crystals (i.e., Refs [23,24]).

Some of the important work on crystal symmetry in modern times was done by Donnay and Harker in 1937 [25] and later by Hartman and Perdok [26]. Hartman and Perdok's theory [26] classified different types of faces, with only one type forming crystal facets. For ionic crystals, they defined the energy released during growth of a layer as E(hkl) and were able to generate growth forms by assuming that E(hkl) was proportional to the growth rate. These calculated forms were similar to natural or manmade crystals such as zircon, garnets, etc. Many researchers before and since have also observed variations from predicted or expected crystal morphologies due to impurity adsorption on a growth face. That led to methods to alter the morphologies for a specific application, one example being the purposeful poisoning of a fast-growing needle axis to make a more equiaxed crystal. Other notable contributions to our understanding of growth shapes include those of Sunagawa (1960) [7] and Bennema (1980) [27].

A major effort to control the purity and dopant uniformity in Si and Ge electronic devices was begun at Bell Laboratories in the early 1950s. The research team of Burton, Prim and Slichter came up with a relationship that described how impurities and dopants are distributed along an as-grown boule (the now well-known BPS equation). Their work was first reported in 1952, but not openly published until 1953 [28]. Measuring solute concentrations, solid–liquid distribution coefficients, diffusion coefficients and solute distributions in actual crystals, they derived equations describing what the concentration of a dopant or impurity would be in an as-grown crystal as a function of its initial melt concentration and growth rate R.

$$K_e = K_o/K_i + (1 - K_o)\exp(-R\delta_D/D) \tag{1.1}$$

where K_e is the effective segregation coefficient, K_o is the interface or equilibrium segregation coefficient, R the growth rate, δ_D is the diffusion boundary layer thickness and

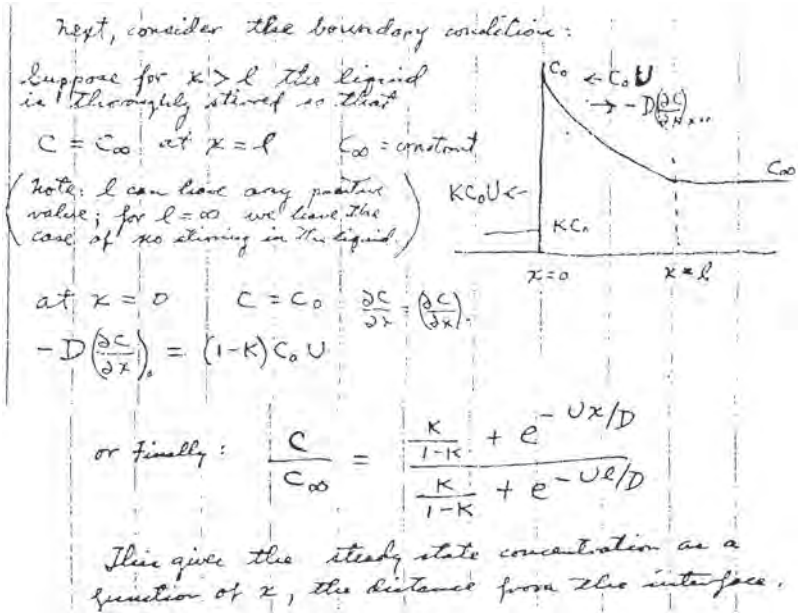


FIGURE 1.2 One of the diagrams in J.A. Burton's laboratory notebook (1951) explaining the concept of the BPS theory. The plot shows the variation of solute concentration in the solid and melt during unidirectional solification. The $x = 0$ position is the growth interface while $x = l$ defines the width of the solute boundary layer [29].

D is the solute diffusion coefficient. Figure 1.2 shows a sketch and notes from Burton's laboratory notebook illustrating the features of the now famous segregation relationship.

This research was part of a larger effort amongst various semiconductor scientists and engineers at Bell Laboratories [29,30]. Since then, BPS segregation theory has become a particularly valuable tool for crystal growth practitioners, allowing them to control the compositional uniformity in single- and multi-component material systems via control of growth velocity, melt composition, fluid convection, etc. While BPS theory is useful for well-behaved systems, it does not work in all cases. A critical analysis of the limitations of the BPS theory and later modifications by various scientists was given by Carruthers [31] (from the standpoint of the mother liquor hydrodynamics) and by Chernov [32] (from the standpoint of equilibrium and nonequilibrium processes at the growing interface). See also Handbook chapter "Segregation and Component Distribution" for a description of the limitations of BPS segregation theory.

As mentioned in the introduction, the Faraday Society in 1949 convened one of its meetings for the sole purpose of presenting and discussing papers on crystal growth. This was the first scientific conference devoted to this topic as a separate subject. Subsequently, the proceedings of this conference, entitled *Crystal Growth*, were published in the Discussions of the Faraday Society. During that meeting, Burton and Cabrera [33] presented their research on the influence of surface structure on the rate of

growth of a perfect crystal. They considered two types of surface structures, one ordered (atomically flat) and the other disordered (stepped, containing terraces, ledges and kinks with ledge heights of atomic dimensions). Burton and Cabrera made use of the analogy between the existence of these two surface structure types and two possible states in two-dimensional systems-ordered and disordered *phases*, transferring from one to another as the temperature/binding energy ratio changes. This concept followed the 1945 suggestion by Yakov I. Frenkel that the step should be disordered and possess a kink configuration at nearly each atomic site. As a result, these steps should grow much faster than a step-free terrace. Indeed, only at the kink configuration can an atom join the crystal lattice, and thereby reduce its Gibbs potential to that of any of the bulk atoms in the crystal. In the simple cubic system, for example, only the (110) and (111) faces are flat, all others are stepped [17]. The growth proceeds by the attachment of atoms at Kossel–Stranski kinks along the step ledges [34], but not on the terraces, which do not participate in the growth phenomena. Therefore, on the flat, ordered surface of a perfect crystal, growth will not proceed until a small island or cluster nucleates on the surface, thus producing a step loop that is kinked by thermal fluctuations. The stability of such a cluster is given by the Gibbs–Thomson relationship that describes the cluster's solubility. If the cluster reaches the critical size, it may expand, generating a new lattice layer. Thus the nucleation frequency (very low at low supersaturations) determines the ordered face propagation rate. If one considers a nonperfect lattice, where the surface contains defects, such as screw dislocations [22], twins, etc., growth can proceed without the necessity for surface nucleation due to the defect providing growth steps.

Burton and Cabrera also examined the kinetics of vapor phase growth on these surfaces, considering the diffusion of the adsorbed atoms across the close-packed crystal surfaces (terraces), where secondary nucleation is required. This was a refinement of the earlier two-dimenstional nucleation model proposed by Becker and Döring in which surface diffusion [35] was not taken into account. Combining their results with Frank's theory concerning the presence of spiral dislocations that can act as growth steps on otherwise atomically flat surfaces, they published together a seminal paper from which the well-known BCF theory derives [36]. In this theory, developed for vapor growth but later extended to solution growth, the boundary between the crystal and nutrient phase was considered to be sharp (interface of zero thickness), i.e., as proposed by Kossel-Stranski, rather than by Gibbs's finite layer thickness model. In this case, atoms or molecules belonged to only one or the other phase. The BCF theory of layer-by-layer growth of the crystal lattice on smooth surfaces was quantitatively confirmed in numerous studies of growth from solutions, including electrocrystallization.

In the ensuing years, interface structure and surface kinetics models have been refined to include more complex interfaces, including material systems such as biological macromolecules [37]. These and other crystals with large lattice spacings grown from room-temperature solutions have made it possible for in situ atomic force microscopy to capture spiral dislocation sources generating new layers during solution growth, as well as the important phenomena of step bunching, low kink density at steps,

etc. Nevertheless, this theory provided the crystal growth field with a more sound theoretical foundation together with a better understanding of experimental results. It formed an important base from which future studies could be built upon.

The roughening concept was employed in 1958 by Jackson [38] to consider the problem of why many melt-grown crystals of nonmetals had specific faceted, euhedral shapes, whereas metal crystals did not. He derived an elegantly simple theory for the solid–liquid interface structure that could successfully explain and predict experimental results. Jackson used a two-layer Bragg-Williams statistical model (rather than the BCF Onsager model) taking into account nearest neighbor bonds into the solid and lateral bonds within the solid–melt interface. The free energy for adding atoms to a singular (or atomically smooth) interface is calculated until a complete monolayer is formed. Starting with the change in excess free energy associated with randomly adding atoms to such a surface, Jackson found the following relationship for solid–liquid transitions.

$$\alpha = (L/KT_e)(\eta/\nu) \tag{1.2}$$

where L is the change in internal energy associated with the transfer of one atom from the bulk liquid to the bulk solid (latent heat), η is the maximum number of adatom nearest neighbors on the surface, ν is the total number of nearest neighbors of an atom in the crystal, and T_e is the equilibrium temperature for the phase change. This so-called Jackson "α factor" consists of two terms: the first is essentially the entropy of melting divided by the gas constant and is a materials parameter, and the second depends on the crystal structure and specific surface under consideration. The crystallographic term is maximum for close-packed planes, and always <1. It has values of 2/3 for a (100) simple cubic, structure and $^1/_2$ for (111) fcc and (110) bcc structures. Materials with $\alpha < 2$ grow with nonsingular interfaces, whereas materials with $\alpha > 2$ exhibit facets on the growing interface. The former are often metals, with simple centro-symmetric crystal structures, whereas the latter are materials with more complex crystal structures. Using transparent systems having different values of α, Jackson and Hunt [39] were able to demonstrate experimentally the efficacy of their model. Figure 1.3 shows the crystalline morphologies observed for high and low α factor materials. A comparison of the BCF and Jackson models was given by Woodruff [40]. In 2004, Chernov [37] discussed how interface growth kinetics has advanced during the past 50 years.

In the years following, interface structure and surface kinetics models were refined to include more realistic interfaces where each interfacial atom cannot be ascribed to one or the other phase. Instead, this disordered interface is viewed as a layer several atomic spacings thick, where all atoms move randomly and, on average over time, realizes continuous transition between the fully ordered crystal bulk and the disordered melt. This approach allowed for the prediction of a kinetic coefficient linearly connecting the supercooling ΔT at the rough crystal–melt interface to its growth rate V for simple liquids, like metals.

$$V = A\sqrt{kT/m}\Delta T/T_e. \tag{1.3}$$

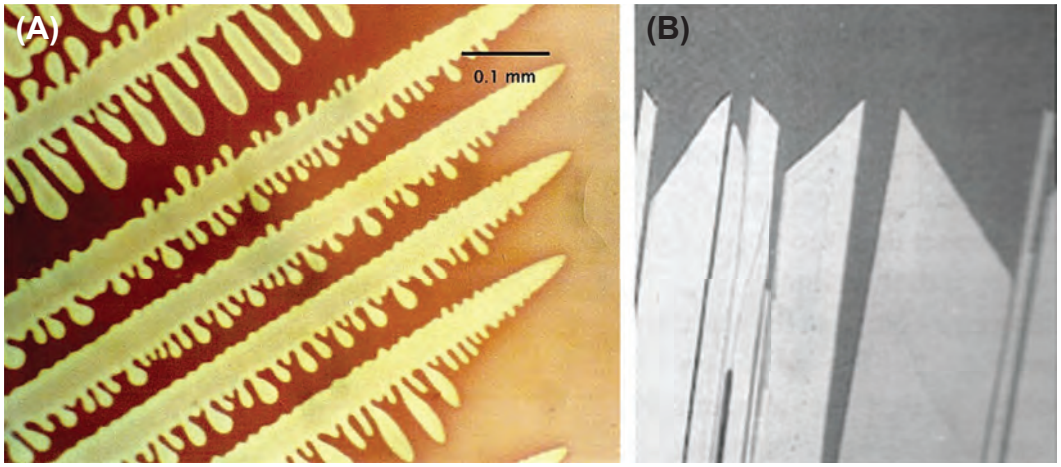


FIGURE 1.3 Comparison of crystal morphologies for (A) a transparent metal analog with an α-factor less than 2. This material grows with a dendritic structure and (B) a benzyl crystal with an α-factor greater than two showing well-developed facets.

Here m is the mass of the atom while the numerical coefficient A is determined by the structure of the liquid and is close to unity. All in all, the BCF theory and its further development provided the crystal growth field with a more stable theoretical foundation together with a better understanding of experimental results. It formed an important base from which future studies could be built upon.

In 1953, research to elucidate and quantify the nature of interface instabilities during crystal growth began with the work of Canadian metallurgists Rutter and Chalmers [41]. They postulated that the cellular (honeycomb-like) substructure that formed in solidifying metals containing a small concentration of impurities (as revealed by rapid melt decanting) was due to some type of instability at the growth interface. This led to the idea that a boundary layer containing rejected impurities develops at a growing solid–liquid interface, depressing the melting point of the liquid in that region so that it became supercooled, but at a higher temperature than the interface. The now well-known term "constitutional supercooling" was derived from Chalmers studies.[1] Shortly thereafter, William Tiller, observed banding in lead crystals arising from unintentional variations in the translation rate (hence growth rate). The structural banding was also found to be associated with the boundary layer composition. Professor Chalmers charged his group to develop a mathematical expression for what was happening at the interface to cause these interesting interfacial instabilities. Their discovery was published later the same year [42]. Their simple

[1]G.P. Ivantsov working independently in Russia in the late 1940s postulated the same concept, calling it "concentrational" supercooling (Dokl. Akad.Nauk. SSSR 81 (1951) 179).

relationship for constitutional supercooling provides one of the most useful tools in the crystal grower's arsenal. The relationship, Eqn (1.4) below, shows how the ratio of temperature gradient in the liquid (G) to the growth velocity (R) must remain above some critical value to achieve stable growth. That value depends upon the material properties of the growth system, i.e., the initial melt concentration C_o (far away from the interface), the slope of the liquidus curve (m), the segregation coefficient (k_o) and the diffusion coefficient. To maintain stable growth and avoid constitutional supercooling one requires that

$$G/R > mC_o(1/k_o - 1)/D \tag{1.4}$$

For the crystal grower this means that to produce a crystal without second phases and cellular structure one *must* either decrease the growth rate for a given temperature gradient or increase the temperature gradient. Faster growth rates are typically very desirable, and so many efforts were undertaken to build special furnaces, sometimes incorporating baffling, localized cooling, etc., to achieve steep thermal gradients.

The early roughening transitions models were two-dimensional models based on the Onsager (BCF) or Bragg-Williams (Jackson) models. It was found that computer modeling was needed to study the problem in more complex three-dimensional systems. Leamy and Gilmer [43] were the first to produce simulated computer images both above and below the surface roughening transition. They also determined the free energy (F) of a growth step for various values of Jackson's α-factor [44]. They showed that F for the step goes to zero at the roughening transition and therefore does not require an energy barrier for new layer formation.

Molecular dynamic simulations have provided detailed information about the process of crystal growth at the atomic level. Its use in morphological stability problems was taken up by numerous groups over the ensuing years which, coupled with experimental work, has led to a significantly greater understanding of the crystallization process (see Figure 1.4).

Modern concepts of interfacial and morphological stability are largely based on the 1963 work of Mullins and Sekerka [45]. Whereas previous researchers knew that various perturbations during growth such as mechanical vibrations, temperature fluctuations, etc., could lead to interface instabilities such as cells and dendrites, they were unable to explain the dynamic mechanisms that were responsible. Mullins and Sekerka developed a mathematical theory of linear morphological interface stability. This was based on small perturbations (sinusoidal ripples) on the growth plane in an unstirred melt that either decay or grow with time. Their analysis led to a more refined relationship that considered the destabilizing effect of the diffusion field and the influence of surface free energy on the boundary conditions. Their results extend the constitutional supercooling criterion described in Eqn (1.3), with several extra terms affecting interface stability [42]. Linear stability theory proves that constitutional supercooling is the correct criterion in the limit of disturbances with small wavenumbers (long wavelengths). The important

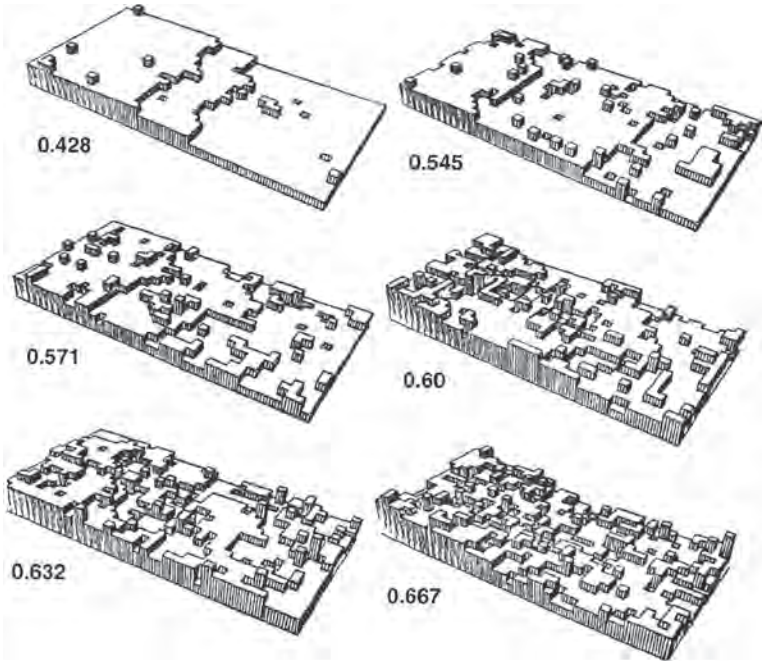


FIGURE 1.4 Monte Carlo simulations of equilibrium surface structures (microstates) for a simple cubic crystal as a function of temperature (as KT/ε) [44]. The surface orientation is the (20,1,0) and at the lowest temperature, $KT/\varepsilon = 0.428$, the step edge is clearly rough. As the temperature increases, the roughness increases. At a critical value, the thermal roughening transition, the steps become indistinguishable.

crystal growth/materials parameters affecting interface stability are the temperature gradient normal to the growing interface, the slope of the liquidus from the phase diagram, the growth velocity, latent heat, mass and interfacial energy densities and the thermal conductivities of the liquid and solid. It was also found that stability depends on whether the thermal conductivity of the melt is greater or less than that of the solid. Other researchers expanded on this research to include molecular attachment kinetic effects, interface energy anisotropy, nonlinear effects, etc., among them V. Voronkov [46] whose independent investigation on mosaic and cellular structures actually predated that of Mullins & Sekerka. John Cahn [47] was the first to treat anisotropic surface tension and interface attachment kinetics (for a spherical geometry). Coriell and Serkeka [48] studied the same types of anisotropies for a planar interface. Chernov [49] treated the case of strong anisotropies and Hurle [50] analyzed the influence of melt convection.

Historically, understanding crystal morphology has provided much of the impetus driving theoretical crystal growth studies. Aside from the regular crystalline forms found in nature (e.g., quartz) or produced during solution or vapor growth in the laboratory, other more complex crystalline morphologies such as dendrites and multiphase eutectic systems have stimulated researchers to uncover the underlying mechanisms involved in their creation.

Dendrites are "tree-like" branched crystal structures that grow in various media under unstable growth conditions. The earliest humans were sure to have noticed and pondered the reason behind the large variety and symmetry of the beautiful snowflake. Snowflakes form when microscopic supercooled cloud droplets freeze and their morphology is dependent on the ambient conditions during their growth. Dendrites also can form during the crystallization of metals, inorganic and organic compounds and even biological macromolecules from melts and solutions. They are common in metals and alloys grown from the melt in shallow temperature gradients.

Dendrites typically contain a stem terminating in a tip and side branches along the stem (see Fig 1.3a). Growth proceeds by steady-state propagation of the tip and a time-dependent crystallization of secondary and tertiary side branches. In 1947, G.P. Ivantsov [357] was the first to identify these self-reproducing crystal shapes—like paraboloids, the basis of the dendrite tip. In pure materials, growth is controlled by diffusion of latent heat away from the advancing growth interface, and in impure systems and alloys it is driven by solute buildup at the interface and where chemical diffusion dominates over thermal transport. In 1960, Temkin [51], and shortly afterward Bolling and Tiller [52], described the role of thermodynamic and kinetic driving forces in the dendritic growth of pure materials. From that time onward, theoretical and experimental dendritic growth studies have proceeded, relying on newer mathematical and computational approaches. Hamilton and Seidensticker [53] examined the role of twin planes in the rapid dendritic propagation of germanium crystals on the basis of re-entrant corner nucleation. In 2004, Glicksman and Lupulescu [54] reviewed 40 years of progress toward understanding the mechanisms involved in the dendritic growth of pure materials including low gravity experiments. An update on this subject is provided in the Handbook chapter "Dendritic Growth."

Growth of polyphase alloys or compounds by unidirectional solidification has also been the subject of much interest to crystal growth researchers. These structures can be produced from eutectic ($L \rightarrow \alpha + \beta$), monotectic ($L_1 \rightarrow \alpha + L_2$) and peritectic ($L + \alpha \rightarrow \beta$) three-phase melt systems. A eutectic crystal can contain four types of structures within a matrix phase (1) parallel lamellar, (2) parallel rods, (3) globular particles of regular shape and (4) irregularly shaped particles. Researchers were interested in the relationship between growth velocity on lamellar spacing and interface undercooling. R. Vogel [55], in 1912, was the first to postulate that growth occurred by both phases growing simultaneously. Eutectic growth theory, however, remained largely qualitative until 1957 when Tiller [56] introduced his diffusion model of eutectic growth. This development was based on the earlier theory on eutectoid growth by Clarence Zener (1905–1993). Tiller's work was used as a basis for Jackson and Hunt's model of 1966 [57], a well-known model and one often used as the basis for later papers. Readers interested in this topic are directed to Glicksman's book [58] that provides, among other crystal growth topics, an excellent review on progress in eutectic solidification.

The transport of heat and mass during crystal growth is of great importance in the design of a growth process and in understanding the resulting features found in the

crystals produced. In melt growth, the dominant factor is often heat transport, whereas in solution and vapor growth, mass transport normally dominates. As to which transport mechanism dominates, it is a matter of degree and an important consideration is what happens in the boundary layer near the interface. As a crystal grows, latent heat is evolved and the allowable growth speed depends on its removal. Therefore, the geometry of the system, the thermal properties of the crystal, the ambient atmosphere and the growth rate all comprise important factors. In addition, the growing crystal needs fresh nutrient to sustain its growth and the rates at which various species reach the interface will partly determine the maximum allowable growth rate and crystal perfection. The concentration of dopant and/or impurity species are often different in the interface region than in the bulk medium, thus influencing mass transport. Instabilities in heat and mass flow can lead to defects such as striations and interface breakdown. The degree and nature of melt convection will strongly affect both the growth process itself and the crystal produced. Many processes, for example Czochralski growth, use forced convection (crystal rotation) to enhance the growth rate and improve thermal and crystal homogeneity, whereas in other methods, for example, vertical and horizontal Bridgman growth, natural buoyant convection occurs from thermally and solutally induced density gradients. In Czochralski growth, the crystal is rotated and sometimes the crucible as well. W. Wilcox [59] and J. Carruthers and K. Nassau [60] studied the fluid dynamic behavior of such systems, as did many other researchers. The effect of fluid flow and flow instabilities are also important in other melt growth processes such as unidirectional solidification, vapor deposition and solution growth. See also Handbook chapter "Segregation and Component Distribution."

Defects, inhomogeneities, segregation, and interface effects during crystal growth have all been the subject of numerous studies. Some useful reviews have been provided by D. Hurle and P. Rudolph [61] and C. Wang et al. [62].

1.3 Crystal Growth Methods

Crystal growth technology is mainly an applications-driven field. In the last 60 years or so, the major applications have been in the fields of electronic and optical materials. Crystals, however, can be prepared from all types of materials including elements, alloys and inorganic, organic and biological compounds. The compounds can vary from simple binary mixtures to multicomponent systems having numerous components and complex molecular or crystal structures. As a result, crystal growth methods vary widely depending on the thermodynamic and kinetic properties of the system of interest. The starting point for developing a viable crystal growth process begins with a thorough knowledge of the phase relations of the system under investigation. For example, we need to know whether the compound melts congruently, has a phase transformation below its melting temperature, has a high vapor pressure, etc. The most appropriate strategy for producing a crystal depends on the size required, purity and an ability to

control its defect structure (either by elimination, neutralization or incorporation). Crystal dimension requirements (size and shape) are a very important issue in determining the methodology. Single crystals can be grown in bulk, thin film, particulate and fiber form and from the nanometer scale up to meter dimensions. During the last decade, nanoscale wires, whiskers and quantum dots have been found to have unique properties, and this has opened up the possibility for new and improved devices for advanced applications. Classical single crystal growth methods and newer techniques have been used to create a variety of desired nanostructures.

The number of crystal growth methods available to the crystal grower is quite large and varied. The simplest approach to categorizing them is by the nutrient phase from which the crystal is grown. Single crystals can be grown from (1) a liquid phase (melt or solution), (2) from a vapor phase (condensation, sublimation or reaction) or (3) from within a strained solid. Each method has certain advantages and disadvantages that depend on both the properties of the material system involved and the application requirements. Melt growth methods are generally preferred to other methods wherever possible, while solid-state growth methods are the least useful from a commercial point of view.

The growth of a crystal from any nutrient phase requires either a seed crystal or the creation of a solid interface within the growth medium by homogeneous or heterogeneous nucleation. Homogeneous nucleation requires additional energy in the form of supercooling in melt growth or supersaturation in solution and vapor growth methods. Wherever possible, however, the use of a seed crystal or a compatible substrate (as in thin film growth) is desirable. We will explore some of the strategies that have been employed by growers to prepare very high quality, high performance materials.

The theoretical studies mentioned above range from fundamental questions about the mechanisms involved in various crystallization environments to computer simulations of actual growth systems. Issues such as growth rate anisotropy, component segregation, interface faceting, stability and morphology, fluid dynamics, thermal stability and gradient effects, etc., have been extensively studied. During the last decade in particular, computer modeling has helped growers design and modify growth systems in a more systematic way to create thermal and fluid flow environments to enhance interface shape, stability and growth rates.

1.3.1 Melt Growth

When a material melts under nearly congruent conditions and has no low-temperature destructive phase transformations, it is usually desirable to prepare a single crystal of it directly from its melt. Often seed crystals are used to control the orientation and to take advantage of growth rate and thermal anisotropies (heat and expansion). The most useful methods include the Czochralski, Bridgman–Stockbarger, Kyropoulos, Verneuil (flame fusion), and float zone methods. There are innumerable variations to these

general techniques such as the heat exchanger method (an inverted Kyropoulos configuration) and the pedestal growth and micro pull-down techniques to name a few. The discussion of melt growth will begin with the oldest technique for growing large crystals from a melt: Verneuil's flame fusion method.

1.3.1.1 The Nineteenth Century and the Verneuil Process

Alchemists were not only trying to transmute base metals into gold, they were also attempting to grow gemstones in the laboratory. From the beginning of the nineteenth century, various researchers were attempting to grow crystals of diamond, emerald, ruby and sapphire by various techniques, particularly by melting various oxide mixtures. These early methods, however, only produced small crystallites. A really viable commercial process did not appear until the work of Auguste Victor Louis Verneuil (1856–1913) on the growth of large ruby crystals was made public in 1902. Actually, he developed the now well-know flame fusion process a decade earlier and spent the next decade improving the method before making it public knowledge. A very thorough description of the life and work of Verneuil was given by K. and J. Nassau [63]. Verneuil (see Figure 1.5(A) below) was a French "renaissance" man and well-beloved teacher, actively interested in music performance and art and whose accomplishments spanned many different areas of chemistry. He became interested in chemistry working in his father's photography shop (his father changed careers after meeting Mr Deguerre (Louis Jacques Maude, 1787–1851), the inventor of photography. In 1873, at age 17, Verneuil went to study in the chemical laboratory of the distinguished Professor Edmund Frémy

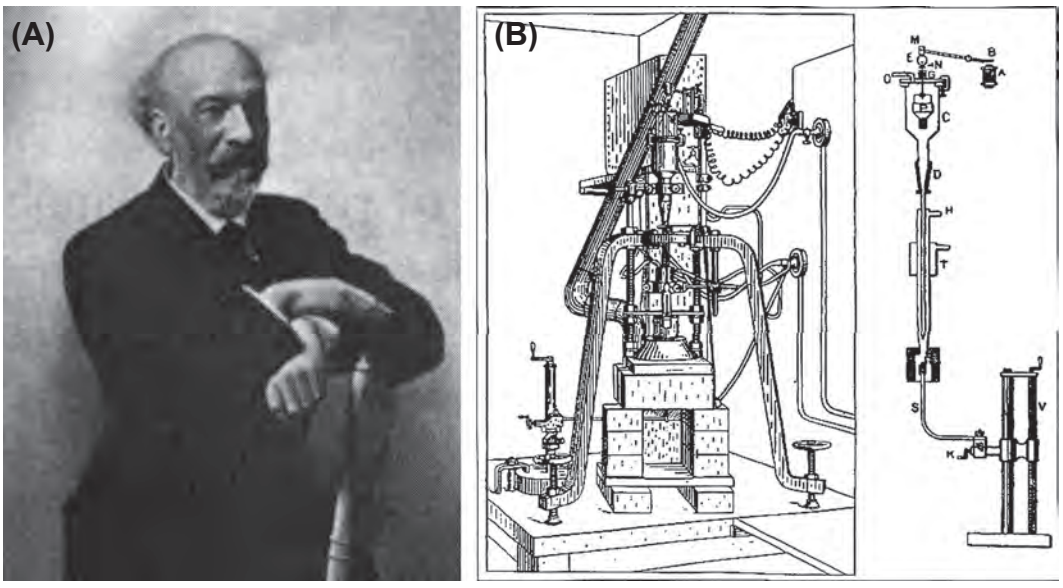


FIGURE 1.5 (A) A photograph of Dr. A.V.L Verneuil, and (B) a schematic diagram of Verneuil's crystal growth apparatus [63].

(1817–1894). He eventually earned his doctoral degree in 1886. In his earlier years in the Frémy laboratory, he participated in research on ruby crystal growth by a melting technique using porous alumina crucibles. He also became friends with Henri Moisson (1852–1902) who worked on diamond crystallization in Frémy's laboratory.

In 1886, an unknown group from Geneva started selling larger synthetic ruby crystals than were available elsewhere. It is now believed that these so-called "Geneva Rubies" were actually grown by an early version of the flame fusion process [63]. Verneuil was intrigued by these samples, and it stimulated him to develop the method for which he became famous. The mysterious group from Geneva ceased operation in 1905, not long after the Verneuil Process had gone into commercial production. Such groups have appeared from time to time trying to pass off synthetic crystals for natural stones that garner much greater value.

The flame fusion method was first developed to produce large, high-quality ruby for the gemstone market and also for watch bearings. The process, which is still in use today, involves passing a powder of the compound through a vertically aligned oxy-hydrogen flame. Molten droplets descend by gravity onto a rotating alumina pedestal containing the growing crystal and the crystal grows upward on the pedestal. The basic apparatus used by Verneuil is shown in Figure 1.5(B). Temperature gradients are steep, boules are prone to cracking and the early powder delivery systems were often unreliable. Important processing refinements were made by Verneuil over his lifetime to improve the process reliability and crystal quality. The first problem he solved was the severe cracking problem. He accomplished this by reducing the contact area of the boule with the pedestal. While preventing cracking, the boules after growth were still highly strained. This strain was relieved naturally when the boules split in half or were split by hand. Powder delivery was done by mechanical tapping mechanism mounted on a hopper containing the charge powder. For ruby growth, the powder Verneuil used was a mixture of ammonium and chrome alums. The chromium oxide concentration in the boules was $\sim$2.5%. The oxygen content in the ambient gas phase was critical for achieving the appropriate oxidation state in the crystal. A flame rich in hydrogen and carbon was necessary to prevent introduction of gas bubbles in the molten ruby melts.

In 1909, Verneuil worked with L. Heller & Son of New York and Paris on developing his process for making blue sapphire. Instead of chromium additions, the sapphire was doped with a mixture of iron and titanium oxides, two impurities found in natural minerals. He suggested that the titanium in the crystal gave the deep blue color by converting the ferrous ions created by the flame back to ferric ions. Another pioneer of the flame fusion growth method was Leon Merker (1917–2007). He also worked with the Heller Co. starting during the early days of World War II, after he escaped fascism in Europe and came to the U.S. to study at the University of Michigan. Based on a friend's recommendation, he met Mr Heller from France. After some fruitful discussions, Heller assigned Merker the task of setting up the Verneuil Process for ruby and sapphire in New Jersey. The venture was successful and the General Synthetics Corporation was formed

in 1941 to provide ruby to the military and for the gem industry [64]. Merker also worked on barium, calcium and strontium titanates; the latter two with greater success.

Since Verneuil dedicated much of his career to the successful development of a commercial process for growing sizable crystals with controllable properties, he might be considered the father of the commercial crystal growth industry.

1.3.1.2 The Twentieth Century

Even while Verneuil was improving on his method, other researchers at the turn of the century were beginning to produce crystals in the laboratory to study both their solidification behavior and physical properties.

One of the earliest was Gustav Tammann (1861–1938). He was born in Russia of Baltic and German parents and spent most of his life in Germany. Among other notable achievements, he established the first Institute of Inorganic Chemistry in Germany at Göttingen University in 1903. Tammann's interests led him to study the solidification of metal alloys and their nucleation behavior. He made important contributions to the fields of heterogeneous equilibria, crystallization and metallurgy. One of his important contributions to crystal growth involved the solidification of metal alloys in long narrow tubes tapered to a point to both confine nucleation and supercooling to a small volume and thereby promoting the propagation of a single crystal along the tube [65]. He was probably one of the first to understand the relationship between grain selection and growth rate anisotropy and the concept of confining the melt to control the number of grains that form. His method would be classified today as the gradient freeze method. He also grew crystals of a number of organic compounds and studied their crystallization behavior.

Within the same time period, Obreimov and Schubnikov from Saint Petersburg, Russia, [66] published a paper describing the growth of metal crystals using a modification of Tammann's method, i.e., in a long glass tube with an imposed temperature gradient along its length. They also briefly discuss the easy to operate Czochralski process (to be discussed below) but rejected it in favor of the Tammann's method because the free-standing Czochralski crystals were not of uniform shape and some of the low-melting metals could deform during growth without being supported. In their experiments, they used a vertical cylindrical tube tapered at the bottom like Tammann. Nucleation was achieved by cooling the tapered tip with cold air and then, after crystallization in this region was accomplished, slowly cooled the furnace to propagate the crystal up the length of the tube. Both these methods distinguish themselves from the Bridgman and Stockbarger methods (also to be discussed later) in that growth is not achieved by moving either the ampoule or furnace to solidify the melt.

1.3.1.3 The Czochralski Crystal Pulling Method

1.3.1.3.1 The Invention

Following Verneuil's pioneering work, a number of other researchers began to grow metal and alkali halide crystals for property studies. In 1918, Jan Czochralski, a well-known young Polish metallurgist (head of AEG's metals laboratory in Berlin), published a

paper [67] that would describe a technique that quickly became one of the most powerful methods for growing crystals in use today. In a story related by Tomaszewski [68], Czochralski, while working late at night in his laboratory, discovered by accident the crystal pulling method for which he because famous. His studies concerned the crystallization rate of metals and while working on his experimental notes, instead of dipping his pen tip into the ink well, dipped it instead into a crucible of molten tin on his desk. When he pulled it out he found a long filament of solidified tin on the end. He subsequently found it to be a single crystal. He then realized the value of studying crystallization rates using such a device. His early apparatus (see Figure 1.6(A)) consisted of a clock-motor-driven lifting mechanism. Replacing the pen tip, a short tapered glass rod with a hook on the end was held on a silk thread connected to the pull mechanism. The rod could be raised or lowered in a continuous fashion. By dipping this rod into the surface of the melt, he was able to solidify metal onto it and pull out crystals of tin, lead and zinc in a continuous and controlled fashion. Czochralski later modified the glass rod, incorporating a capillary at the bottom to draw up the molten metal. This had the effect of restricting nucleation to the limited volume of melt in the capillary. With this apparatus he produced 1 mm thick single crystal wires at maximum crystallization velocities of up to 140 mm/min and in lengths up to 19 cm. Czochralski's life and research accomplishments can be found in Tomaszewski's monograph [68].

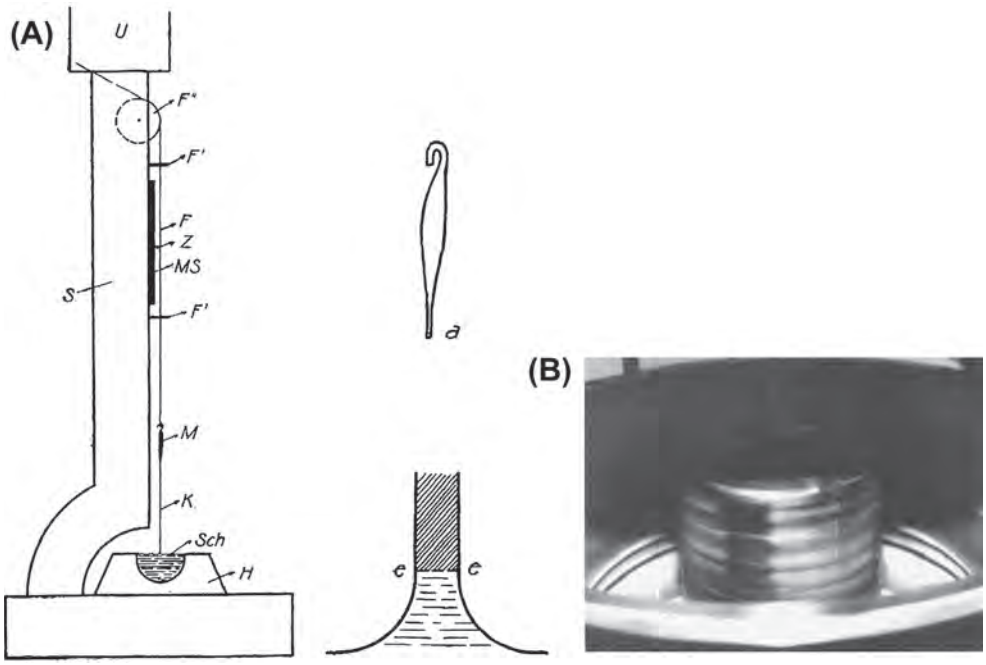


FIGURE 1.6 (A) Czochralski's original experimental setup [67], and (B) a photograph of a five-inch diameter commercial single crystal silicon boule growing by Czochrakski's method. *(From the front cover of the AACG Newsletter 13 (1983)—photo courtesy of the Siltec Corp).*

Czochralski's pulling method was almost immediately put to use by von Wartenberg [69] to grow zinc single crystal wires onto oriented seed crystals. Somewhat later, Von Gomperz [70] pulled single crystal fibers of metals through a hole in a mica plate floating on the surface of the melt. He also used a capillary for seeding. His work was the forerunner of the edge-defined film-fed growth (EFG) and the laser heated pedestal fiber growth methods. In 1928 E.P.T. Tyndall [71] wrote a paper on the *Factors Governing the Growth of Zinc Crystals by the Czochralski-Gomperz Method*. In 1937, Henry Walther of Bell Laboratories published the first paper on the use of Czochralski's method for the growth of nonmetals [72]. He rejected other methods such as the Kyropoulos method because he was intent on growing long, uniform, cylindrical bars of NaCl single crystals for property measurements. He therefore was attracted to the pulling methods that Czochralski and von Gomperz used to grow low-melting metals. He used a quartz crucible to hold the melt and dipped a platinum rod or closed tube into its surface, sometimes with an oriented seed attached. In the beginning, he used Kyropoulos's method of pulling the tube up slightly after the first melt solidified on the rod to reduce melt contact with the crystalline solid that formed. He placed an air-cooled coil containing small holes above the melt to cool the growing crystal and pulled up at rate of 5 cm/hr while rotating the crystal at 10 rpm. He was the first to apply rotation to the Czochralski method and produced the first bulk crystals of a high melting point compound by this method. Walther successfully produced NaCl boules 2 cm in diameter and 30 cm long. It is rather amazing that this paper, although published in a prominent journal and referenced twice a few years after its publication, was only found very recently (by Reinhard Uecker [73]). Strangely, even many Bell Laboratories researchers from that period to the present time seem to have been unaware of Walther's work, and it was not mentioned in the rather extensive review of engineering and science research in the Bell system during the period 1925–1980 [30]. In 1940 Evans [74] used Walther's method to grow single crystals of NaCl, KCl and KBr.

1.3.1.3.2 Semiconductors

Bardeen and Brattain discovered the transistor in 1947 using large-grained Ge samples produced by unidirectional solidification [30]. Shortly afterward, it was demonstrated that single crystals were better, and this led to a dramatic expansion of the crystal growth field in general, and the Czochralski method in particular. This versatile technique has been applied to a wide variety of materials of commercial importance—particularly semiconductors and optical materials.

According to [30] (p. 422), "A single crystal growth technique, first used by J. Czochralski in 1917, was adapted and improved in 1950 by G.K. Teal and J. B. Little for the growth of single crystals of germanium" [75]. They dipped an oriented Ge seed crystal into the melt surface and, while rotating, pulled modest sized crystals (by today's standards) of 2.5 cm diameter and 10 cm in length. The minority carrier lifetimes were significantly better than in polycrystalline materials, and therefore the semiconductor researchers shifted their efforts to producing bigger and better crystals with control of

the dopant concentrations and uniformity. In addition, the single crystal technique allowed for the creation, during growth, of n-p-n junctions by perturbing the growth conditions [76]. While this junction technique was eventually superseded, it was an important step in transistor technology. The importance of homogeneity in semiconductor devices led many researchers to study the thermodynamic and kinetic aspects of impurity and dopant incorporation. One such seminal study, as mentioned earlier, was that of Burton, Prim and Slichter [28,29]. Shortly after the germanium research activities began, the focus shifted to silicon whose properties were deemed to be superior. In 1952, Teal and Buehler [77] reported on the Czochralski growth of silicon crystals—a much higher melting compound (1414 °C compared with 938 °C for Ge) and more difficult to grow due to its reactivity. Over the years, crystal sizes have constantly increased (see Figure 1.6(B) above), and today commercial systems are available to grow Si boules 12 in in diameter and 6 ft long from which substrates can be cut for the preparation of integrated circuits. In situ recharging to grow longer crystals and controlling melt flows using magnetic fields were added over the years to boost production rates and quality. One of the most important factors in producing high quality crystals was not only to control impurities and other point defects but their complex interactions with each other, as well as with dislocations. Removal of one defect can lead to the redistribution of other defects to lower the overall energy of the system.

It was recognized early on that purity of the starting material was critical to semiconductor performance. In 1951, William Pfann [78] invented the zone refining method for ultrapurifying Ge. This very important method, in wide use today, has been successfully adapted to the purification of all classes of materials. Shortly afterward, Theuerer [30] invented the crucible-free float zone process to grow O_2-free silicon. Oxygen incorporation during Czochralski growth was due to the use of SiO_2 crucibles. Theuerer's method is still in commercial use today to produce O_2-free Si for special device applications. It also has been used with other materials for which melt-crucible interactions are problematic. With the use of optical heating systems (such as lasers or xenon lamps), its simplicity makes it very useful for growing crystals of numerous materials for physical property studies. Pfann [79] also invented the zone leveling crystal growth method that is a combination of horizontal Bridgman growth coupled with zone refining. In this case a seed and a dopant are placed at one end of a horizontal tube and by moving a molten zone along the tube, the dopant could be uniformly distributed along the boule. This method was used early on to produce transistors and diodes.

It became apparent that dislocations were affecting the electrical properties of Si single crystals and the need for zero-dislocation material arose. In 1959, William Dash [80] developed a method for doing this during Czochralski growth. Since dislocations propagate mainly from the seed, he used high-quality seeds together with careful control of the initial growth conditions. He was able to produce dislocation-free crystals by "necking" down the growing boule to a very small diameter before widening it back out to the desired size.

Important advances in both purification and control of crystalline perfection has led to the improved performance of Si devices.

When compound semiconductor materials such as GaAs, InP and their alloys became important to the electro-optic field, special Czochralski techniques had to be developed because they have high vapor pressures at elevated temperatures. In 1962, Metz et al. [81] were the first to report the use of molten B_2O_3 as a melt encapsulant for the Czochralski growth of PbTe. Both Pb and Te are volatile at the compounds melting temperature, and they successfully sought to cap the melt to prevent losses. In 1965, Mullins et al. [82] demonstrated that molten B_2O_3 was also a useful encapsulant for the growth of GaAs and InAs. They were able to adapt a commercial low-pressure Czochralski system for the growth of these compounds. This method is now known as the liquid encapsulation Czochralski (LEC) method. A few years later, Mullins et al. [83] extended their work to include the growth of GaP and InP in high-pressure furnace systems. One problem with group V elements was that when the crystal emerges from the encapsulating layer, it starts to lose P or As from its surface. In 1983, Azuma [84] came up with an innovative approach to inhibit these losses. He used a pressure balancing system to control the partial pressure of P in the InP growth chamber. In the upper chamber was extra P_4, maintained at a pressure such as to prevent evaporative losses at the crystal surface.

1.3.1.3.3 Oxide Growth

Following the success of the Czochralski method for growing elemental Si and Ge single crystal boules at Bell Laboratories, they and other laboratories started to use this method extensively for growing bulk single crystals of oxide compounds for laser, nonlinear optical, scintillator and numerous other applications.

The laser was predicted by Arthur L. Schawlow and Charles H. Townes in 1958 [30, 358, 359] but not actually demonstrated until the work of Maiman in 1960 [85] with a single crystal ruby rod prepared at the Union Carbide company. In the same year, Nassau and Van Uitert [86] were the first to use the Czochralski's method to grow a high-quality oxide crystal. They prepared laser crystals of Nd:$CaWO_4$. During the following decade, the Czochralski method was vigorously pursued in many research and industrial laboratories around the World. A wide variety of important optical materials were grown, including $LiNbO_3$ [87,88], $LiTaO_3$ [89], $Bi_{12}Ge$(or Si)O_{20} and $Sr_xBa_{1-x}Nb_2O_6$ [90], YAG ($Y_3Al_5O_{12}$) [91], Nd:YAG [92], Sapphire [93,94], and $Gd_3Ga_5O_{12}$ (GGG) [95]. Many of these materials are still commercially important. A concise history of oxide crystal growth by the Czochralski method was given by C. D. Brandle [96].

Many improvements to the method were made over the succeeding decades. Compositional variations along the length and diameter were of major importance and stimulated the construction and analysis of related phase diagrams. It was found, for example, that the stoichiometric composition was not always the congruent composition [97] and to get uniformity one needed to shift the composition to the off-stoichiometric congruent composition to achieve homogeneity. Another problem often

encountered was that the shape of the phase field boundary of the compound might be curved instead of straight leading to precipitation of a second phase.

During the 1960s, very little was known about how the growth interface shape could influence crystal quality. This was very important in Si growth where zero-dislocation crystals rely on a particular interface shape. Cockayne et al. [98] were the first to show that interface shape could be modified and controlled by crystal rotation. Nominally, crystals growers find that a slightly convex interface toward the melt is most desirable. Another factor of major importance in melt and solution growth is fluid convection. It affects mass and heat transport and therefore interface shape, boundary layer and growth rate instabilities, etc. In Czochralski growth natural convection and crystal rotation can interact to modify both the interface shape and the composition in the melt near the growth interface (boundary layer). Various researchers have achieved significant improvements in crystal quality by controlling these parameters.

The application of computer modeling to help solve crystal growth problems was begun in the 1980s by Robert Brown and his group at MIT. One example is a paper written by Derby and Brown [99] on the dynamics of Czochralski growth. One of the major tasks of computer simulations is to model the flow regimes in a system in which the thermal configurations are adjustable. In recent years, facilitated by the dramatic increase in computing power, almost all types of crystal growth processes (Bridgman, float zone, etc.) have been modeled. Simulations performed have been very successful in helping design and guide refinements to laboratory and commercial crystal growth process.

During Czochralski growth, the melt level in the crucible drops as the crystal grows. This changes a number of factors including the thermal gradients and convection patterns. Often the temperature has to be changed during growth or some other parameters modified. Whiffin and Brice [100] have shown that melt height can affect thermal oscillations in the melt. These thermal fluctuations can lead to growth rate variations and crystalline imperfections such as striations. A striation is a compositional variation parallel to the growth interface, usually caused by poor temperature control and/or melt oscillations. In the 1960s most growth was carried out manually, i.e., the temperature was changed or the crucible position altered by analog temperature and motor controllers. With commercialization came the need for automated diameter control systems. These were based on either crucible or crystal weighing or by controlling the meniscus position optically.

1.3.1.4 Bridgman–Stockbarger/Gradient Freeze Methods

Little did Percy Bridgman (1882–1961) or Donald Stockbarger (1895–1952) know at the time of their respective discoveries that their names would become historically intertwined in describing one of the most popular techniques for growing crystals. Their versatile method(s) made possible the growth of many different types of materials including metals and their alloys, semiconductors, and both inorganic and organic compounds. It was also a method that allowed the preparation of some of the largest manmade crystals ever produced.

Percy Williams Bridgman was a Noble Prize-winning American physicist working at Harvard University, only a few miles away from MIT where Donald C. Stockbarger worked as an Associate Professor of Physics. His prize (1946) was for his work in the field of high pressure physics. The crystal growth method he developed and published in 1925 [101] departed from the work of Tammann [65] and Obreimov and L. Schubnikov [66] in that the vertical tube containing the melt was not stationary during growth. Growth was initiated in a capillary tube at the bottom end of a larger cylindrical ampoule and propagated upward along the tube by lowering it down through a single zone vertical tube furnace and out the bottom. The capillary was used for seed selection and was further enhanced by reducing the capillary diameter at the juncture between the capillary and the larger bore container. His first experiments were done using bismuth melts. Not long afterward, various other researchers used his method or variants of his method to grow other metal crystals, such as copper, and zinc.

In the late 1920s Stockbarger started his work on the growth of large, high-optical-quality crystals of LiF and later CaF. At first, he tried Bridgman's method [101] for CaF but it required more careful atmosphere control to prevent hydrolysis, better starting material purity and temperature stability to produce useful crystals. This led Stockbarger to modify Bridgman's method [102,103]. He used a so-called vertical "elevator furnace" that had two graphite heaters separated by a Mo baffle through which a covered crucible containing the melt could be passed from the upper higher temperature region into a lower temperature section by a motorized translation device. The use of a two-zone furnace led to better control of the thermal gradient at the growth interface. The crucible, support rod and pedestal were graphite. The V-shaped crucible bottom rested in the pedestal. There was no capillary region below the tapered region for seed selectivity, and the included angle was much larger than those used in the Bridgman and other earlier methods. So it is speculated that seed selection was controlled by the locally steep gradient at the tip created by the thermally conducting graphite support rod coupled with the baffle, thereby limiting the volume of supercooled melt that can form.

The Bridgman–Stockbarger method (shown in Figure 1.7 below) has been widely used to grow crystals of varying sizes from its development in the 1920s until the present day. It has also been used extensively in a horizontal configuration. While initially used for metals and then shortly afterward for inorganic optical materials, it has since been used to grow hundreds of other compounds including semiconductors (GaAs, CdTe, HgCdTe, and chalcopyrite compounds such as $CdGeAs_2$, $ZnGeP_2$), organic materials, oxides such as $Pb(Mg_{1/3}Nb_{2/3})O_3$–$PbTiO_3$ (PMNT) and halides such as Tl:CsI and Tl:NaI, and Eu:SrI_2 etc. Process improvements include the use of the accelerated crucible rotation technique to improve melt homogeneity and interface boundary conditions [104], vibroconvective mixing [105], baffles in the melt near the interface, growth under high pressure, etc.

The gradient freeze (GF) method of Tammann [65] differs from the Bridgman–Stockbarger approach in that there are no moving parts. Neither the ampoule nor furnace

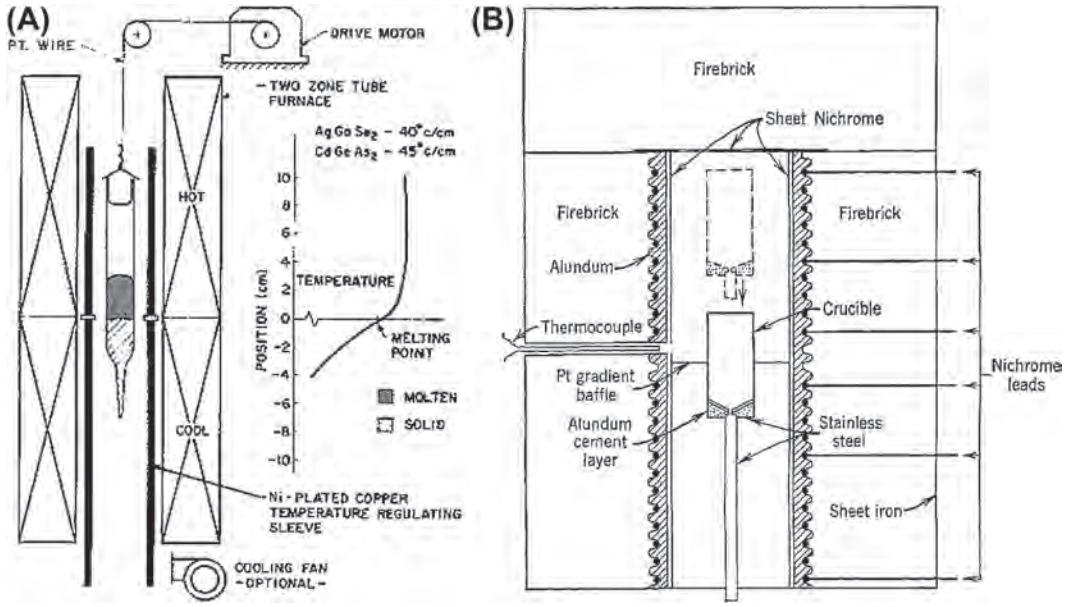


FIGURE 1.7 (A) Drawing of a Bridgman apparatus showing a tapered crucible being lowered through a stationary furnace having a steep gradient at the growth interface. In Bridgman's experiments the crucible is lowered out of the furnace. (B) A schematic diagram of Stockbarger's growth apparatus. Note the platinum baffle that separates the two furnace zones for gradient control and the crucible pedestal.

is translated with respect to the fixed thermal gradient in the furnace. Instead, a temperature gradient is maintained across the melt-containing crucible such that when the temperature of the furnace is lowered, the cool end of the melt solidifies first, and the rest of the melt solidifies layer by layer as the freezing point moves across the melt. This method is simple to implement and was used for the growth of a number of materials. Its big disadvantage was that as the furnace temperature decreased, so did the gradient across the remaining melt. Under constant cooling conditions this change in gradient could lead to changes in growth velocity and thereby variable crystal properties along its length due to component segregation and perhaps interface breakdown. One method used to solve this problem was by continuously changing the furnace-cooling rate to maintain constant freezing rate in the melt. In 1986, Gault et al. [106] successfully applied the vertical gradient freeze method (VGF) to the growth of large diameter GaP, InP, and GaAs crystals.

Attempts to grow some important III–V compounds by the vertical Bridgman and gradient freeze methods were complicated by the fact that these compounds expand on cooling and can aggressively stick to the walls of many crucible materials [107]. These methods both exist in horizontal versions that are applicable to certain important commercial crystals. While many different types of crystals have been grown by the horizontal Bridgman and gradient freeze techniques, their sizes are limited compared their vertical counterparts, and the boules have noncircular cross-sections.

1.3.1.5 Nacken–Kyropoulos Methods

During the early decades of the twentieth century, many new developments in crystal growth technology came out of Germany. During the 1920s in particular, a burst of activity in the field led to numerous growth techniques being developed, many of which are being used today in either their original or modified form.

One of the most important crystal growth pioneers of this period was the German mineralogist Richard Nacken (1884–1971). A few years before Czochralski's discovery, he reported on a process for growing crystals from the surface of a melt using a cooled copper rod with a rounded end and a seed attached [108]. Nacken's apparatus is illustrated in Figure 1.8(B) below. The general idea was to locally supercool the melt adjacent to the rod and initiate growth under controlled conditions. After growth started, the furnace temperature could be lowered to keep the seed growing. No pulling was involved. As the crystal grows, the melt level drops due to the higher density of the crystal. The method was later used by J. M. Adams and W. Lewis [109] to grow very large ice crystals. Nacken also developed a viable hydrothermal process for growing quartz crystals. His unpublished work was found in secret WW II German reports. E. Buehler and A.C. Walker at Bell Laboratories [110] based their successful hydrothermal quartz growth technology on Nacken's process.

About 10 years later, Spyro Kyropoulos (1887–1967), a student of Tammann and professor of Applied Physics at the Gottingen University (later he taught at the California

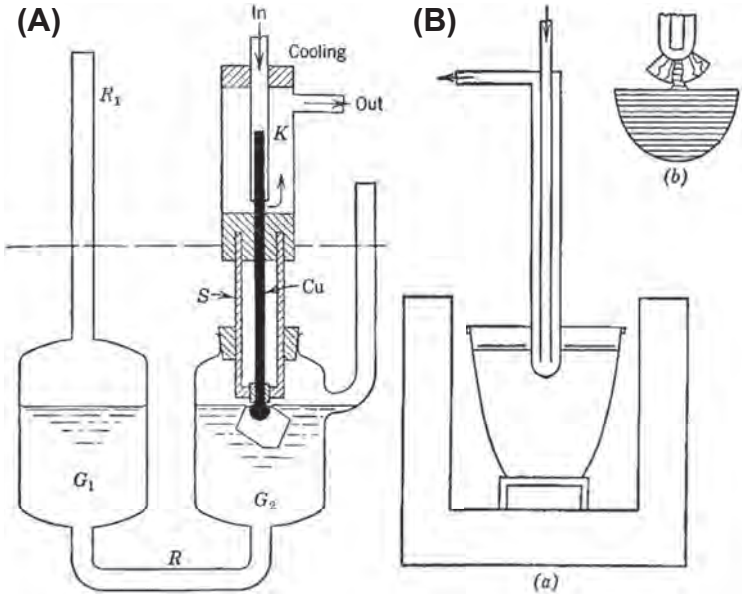


FIGURE 1.8 (A) A drawing of Nacken's apparatus illustrating the growth of a faceted crystal using a seeded cold "finger" inserted into the melt's surface. (B) A schematic diagram of Kyropoulous's experimental setup where, unlike Nacken, a cold rod is place in the melt surface without a seed. The inset shows how seed selection can be accomplished using a rounded seed rod.

Institute of Technology) took up Nacken's melt growth method to grow crack-free alkali halide crystals for precision optics. The advantage of Nacken's method is that the crystal is grown within the melt rather than being confined to a container that can induce strain in the crystal during cooling. Instead of a using a seed, Kyropoulos [111], using an air-cooled platinum tube, nucleated a few crystallites on the end of his tube and then lifted it up slightly so that the melt stayed in contact with only one grain. Kyropoulous's apparatus is shown in Figure 1.8(B) above. This seeding method had to be carefully controlled so that the tube did not break free from the melt surface. After the seeding stage, the furnace is slowly cooled to allow the crystallite with the fastest growing direction of heat flow to grow to cm-size crystals before being pulled out of the melt. The thermal gradients in the melt are generally quite small. As mentioned before, the melt level drops in systems where the density of the solid is greater than the melt density. Kyropoulos used this process for growing many alkali halide crystals [112]. The method is attractive because of its general simplicity, reliability and low operating costs. Two other advantages of the method are (1) the ability to see what was going on and to make adjustments to enhance the crystal quality and (2) its use of lower thermal gradients than in the Czochralski method. On the other hand, the lower gradients lead to faceting at the interface and thus chemical inhomogeneities in the crystals. Several years later, Korth [113] took up this method but used a seed attached to the cooled rod as did Nacken many years earlier. He grew crystals as large as 6×8 cm. A few years later, Katherine Chamberlain in the United States used this method to grow very large KBr crystals up to five inches in diameter and weighing up to seven pounds [114]. Typically Kyropoulos's method does not involve continuous pulling or rotation as in the Czochralski method. Growth rates are of the order of mm's/hr with cooling rates below 1 °C/hr. The crystal diameters usually are up to 90% of the crucible diameter. Bliss [115] gave a detailed review of Kyropoulos's life and method.

The Kyropoulos method has been in commercial use for over 75 years. From its inception until the present time, the method has been used to grow large alkali halide crystals for windows, prisms and scintillators (e.g., Tl:NaI and Tl:CsI) compounds. Due to the development of GaN-based light emitting diodes, there has sprung up a very large industry around the growth of large sapphire crystals for use as substrates. The Kyropoulos method is one of the most widely used methods today for this applications. Up to 12 inch-long crystals have been produced. It is also used in the commercial production of Ti:Sapphire laser crystals. A variety of other materials have been grown by the Kyropoulos method in laboratory settings, including organic materials, semiconductors such as Si, ZnSe, and InP and other types of laser crystals. For the growth of InP crystals [116], liquid encapsulation together with magnetic fields has been applied to the Kyropoulos configuration to improve crystalline perfection. This has been called the MLEK method. Over the years, furnaces have become much more complex. Heat shields are now used to control thermal profiles. Numerical analysis has helped to define the optimal conditions for growth of specific materials through proper baffling and positioning of the crucible in the heater. Other improved capabilities include the ability to weigh the crystal or crucible during growth to control the rate of mass increase with time.

1.3.1.6 Stöber/Heat Exchanger Methods

In 1925, F. Stöber [117] reported on the growth of large crystals of anisotropic materials such as sodium nitrate, zinc and bismuth by removing the latent heat of crystallization from the bottom of a stationary bowl-shaped crucible containing a melt (growth from the bottom upward). A heater plate was placed above the surface of the melt and a water-cooled plate at the bottom creating an axial temperature gradient. The radial heat flow, present in most other growth systems, was minimal. Stöber's method, along with one of Tammann's techniques, were perhaps the first gradient freeze methods (i.e., moving the gradient along the melt rather than by moving the crucible or furnace). Stöber also found that crystal singularity was enhanced when the thermal conductivity in one crystallographic orientation was significantly greater than in other directions. One attractive feature of Stöber's method was that you could produce very large crystals in near-net shape, i.e., in the exact shape of the container. In addition the method is very simple to implement since there are no moving parts, and lower thermal gradients employed help reduce stresses in the final boule. He grew crystals of $NaNO_3$ up to 10 pounds by his method. He also grew ice crystals by inverting the cooler and immersing it into the liquid surface.

In 1970, Frederick Schmid and Dennis Viechnicki [118] from the Army Research Laboratory at the Watertown Arsenal, reported on a new method to produce large-diameter sapphire crystals from the melt. This work was stimulated by the need by the military for very large transparent armor plates. They called their new technique the heat exchanger method (HEM). The method is similar to the Stöber process in that the crystal grows upward from the bottom filling the crucible and taking its shape. Neither the furnace, crucible nor crystal moves during growth. A He-cooled cold finger (similar to the water-cooled bottom plate used by Stöber) extracts heat from the crucible bottom in a controlled manner and independent of the heat input. A furnace that surrounds the crucible replaced the upper pancake heater. In addition, the technique allows for a small-diameter seed to be centered over the cold spot created by the He heat extraction tube. Heat can be removed from the crucible bottom by increasing the He flow rate. Since then (1975), a He recirculation system was developed along with the technology to grow large-diameter, flat-bottom crystals free of light scatter from the small seed centered over the heat exchanger. High-quality sapphire crystals have been grown commercially up to 44 cm in diameter and weighing 160 kg [119]. In situ annealing in shallow gradients is used to relieve stresses. The crystals produced are competitive with commercial Kyropoulos sapphire. The method has also being used to produce single crystal ingots of spinel, ruby, Ti:sapphire, Nd:$Y_3Al_5O_{12}$ and silicon. Commercial growth systems are available.

1.3.1.7 Kapitza's Method

Pyotr Kaptiza (1894–1984) was an important Russian physicist who spent many years in England before returning to Stalinist Russia. He was awarded a Nobel Prize for his work in low-temperature physics. He used the Bridgman method to prepare metal single

crystals for his experiments, but when it came to preparing Bi rods of a specific orientation, he found that its expansion on cooling was sufficient to cause enough strain to prevent the seeded orientation from propagating down the rod. To solve this problem, he developed a method in which the crystal was not completely constrained [120]. He placed a bismuth rod on a copper plate and covered it with loose-fitting glass plates to reduce drafts and then melted the rod. At one end, an oriented seed was attached and by unidirectionally solidifying the rod by cooling he was able to produce an oriented Bi single crystal at rates up to 5 cm per hour. This method was taken up and modified by others, and today it might be considered the forerunner of the horizontal Bridgman method which is widely used today for growing materials like GaAs for LED's [121] and $ZnGeP_2$ and $CdGeAs_2$ [122] for nonlinear optical applications.

1.3.1.8 Zone Melting

Zone melting methods have played an important part in (1) purification of materials for crystal growth and other materials processing (zone refining), (2) for producing crystals with uniform composition (zone leveling) and (3) for growing crystals without crucibles (the float zone method). There are a number of variants to all these methods including different methods of heating, horizontal and vertical arrangements, traveling mechanisms, etc. The first reported use of zone melting was by Kapitza in 1928 [120]. In his experiments, he passed a short resistance heater along a Bi filled tube to produce a single crystal. In 1937, Andrade and Roscoe [123] used zone melting (also a traveling heater) to grow lead and cadmium single crystals having low strain. By far the most important and extensive work on zone melting for purification (zone refining) and zone leveling was that of William Pfann [78]. In 1952, Pfann conceived of the zone refining method when asked by the transistor researchers at Bell Labatories (where he had worked since the late 1930s) to develop a method to produce higher purity Si and Ge for use in growing crystals with better electronic properties. Toward this end, it was used with great success in the early days of semiconductor processing. This very versatile method was found applicable to numerous other materials, including inorganic and organic compounds, metals and semiconductors. Many papers on its adaptation to different materials and operational improvements have been published since then, and it has become an important tool for both research laboratories and industry. Pfann's book on zone melting [124] is the seminal publication on the method, comprehensively covering both the theory and practice involved.

The method consists of moving a molten zone through a bar of material. Two solid interfaces are created. As the zone moves (by moving the heater or furnace), material from one interface dissolves in the zone and is recrystallized at the other interface. Purification occurs for those impurities whose solubility in the liquid is different than that in the solid (segregation coefficients, K, greater or less than one). Materials with $K < 1$ will be rejected at the growth interface and will build up in the last to freeze region. Those with $K > 1$ will tend to congregate at the start of the ingot. It is also a very useful method for growing crystals from materials that melt incongruently.

Various types of heaters have been used with the zone melting method, including resistance, RF, electron beam, plasmas, lasers and xenon lamps. Refining can be done with one zone moved through the ingot many times (passes) or by moving multiple zones simultaneously. The ends of a sample can be removed and the sample zone refined again as many times as needed. More passes are needed when K for a particularly detrimental impurity is close to 1. Volatile species can complicate the process but techniques to control or minimize melt losses have been developed.

Zone leveling is a way to produce material with uniform composition along its length. It has many of the features of zone refining. Once the zone has reached a steady-state composition, the species of interest will transfer from one interface to the other. The composition will be the same on both the melting interface and the solidifying interface. In both zone methods, crystal growth can be carried out during the purification or leveling procedures.

The floating zone technique is a very important variant of the zone melting method. It allows for crucible-free growth and eliminates possible contamination from the crucible material and also stresses due to differential expansion between the crystal and container. The method was invented and patented by H. Theuerer [125], a close colleague of Pfann, to grow ultra pure Si. For better uniformity, the rods can be rotated during growth. As mentioned before, the method is used commercially today for growing low or oxygen-free silicon. In recent years, automated commercial optical lamp heated float zone systems have become available and have permitted researchers from a variety of disciplines to grow crystals of a wide variety of materials for physical property studies [126].

The pedestal growth method is essentially a floating zone process. However, because the pull rate of the crystal (smaller diameter) is different from the push rate of the source rod (larger diameter) it has some characteristics of the Czochralski method. Parenthetically, one might classify the Verneuil method as a pedestal growth method since the crystal is grown on a pedestal and the molten zone is fed by molten powder rather than a solid rod. The first use of a pedestal growth technique was in 1958 by F. Horn [127] at the General Electric Corp. His method was a hybrid technique between the Czochralski and float zone methods. The charge in the crucible was only melted near the top surface and the crystal, of smaller diameter, pulled from this melt. As the crystal grew he changed the heater position to melt some more of the solid below. He grew boules of Sb-doped Ge having a more uniform composition than achievable by the Czochralski technique where the entire charge was melted. Dash [128], and Poplawski and Thomas [129] used this method to grow dislocation-free crystals of Si and Ge.

Two techniques that have been found particularly useful for producing small-diameter crystals for property studies are the *laser-heated* pedestal fiber growth (LHPG) [130] and micro pull-down (μ-PD) [131,132] methods. The LHPG method is a zone melting method in which, rather than a zone traversing a bar of material of uniform diameter, a fiber is grown from a source rod of larger diameter. The pedestal configuration was first used by Horn [127] and Poplawsky [129]. The source rod forms a pedestal

whose upper surface is melted with a small spatially fixed laser beam. A seed crystal is lowered into the melt and is withdrawn at a rate faster than the rate at which the source rod is pushed upward to maintain constant melt volume. It is a crucible-less method, minimizing contamination; the growth rates are much faster than bulk growth (mm/min) because the temperature gradients at the interface are very large (>1000 °C/cm). These high-growth velocities can lead to greater dopant incorporation and to the growth of metastable phases. The method is useful for incongruently as well as congruently melting compounds, although it is limited to systems where the vapor pressures are modest and dissociation is not a problem. The small diameter fibers were often found to have better crystalline perfection than bulk materials. The LHPG method has been used to grow fibers of a vast array of materials including oxides, halides, borides, carbides, and metals. Haggerty [133] was the first to use the pedestal method with laser heating. He grew LaB_6 single crystal fibers. A few years later, it was used to grow single crystal Nd:YAG fiber lasers [134]. One of the big advances in LHPG growth was the replacement of individual laser beams (two or four) with reflaxicon optics [135] giving a circular beam and a much more uniformly heated molten zone. An interesting discovery came about during the growth of $LiNbO_3$ fibers. Lithium niobate is a ferroelectric material whose as-grown bulk crystals contain numerous parallel and antiparallel domains. To be useful in nonlinear and other device applications, these have to be aligned after growth in an electric field at elevated temperatures. During the growth of $LiNbO_3$ fibers using a two-beam laser system, however, the small diameters and steep gradients led to single domain fibers when grown along the c-axis and a bi-domain fiber of opposing 180° domains when grown along the a-axis [136]. The axial gradients were responsible for the single domain c-axis fibers and the radial gradient a-axis fibers. These observations later led to a method to produce fibers with periodically poled domain structures by periodically shuttering one of the laser beams during growth [137]. Later, other periodically poled structures for quasiphase matching applications were produced by other methods.

In 1980, Mimura et al. [131] published a paper on the growth of KRS-5 fiber crystals using an inverted pulling system (modified floating zone technique). They had a crucible filled with melt on the top with a feed rod continuously feeding the melt as the fiber grew. At the bottom of the crucible was a long heated capillary tube with a shaper at the end. The growth interface was below the shaper. The growing crystal was pulled downward. This method was taken up by D. Yoon et al. [132] and called the micro-pull down method. It has been used successfully for many materials, and growth systems are available commercially. This method was reviewed by V. Chani [138].

1.3.1.9 Shaped Growth

Shaped growth generally means a method for producing a crystal with a predetermined cross-sectional configuration. The quest to develop such methods is associated with a need to reduce product cost and/or improve crystal quality. Notable savings can be achieved in device fabrication, such as cutting and polishing, reducing the loss of expensive material and reducing mechanical damage. In addition, the method usually

allows significantly higher than normal growth velocities, thereby increasing production rates. In a very real sense, shaped growth is a hybrid method that borrows from other more established methods. For example, some are simple modifications of the crystal pulling or directional freezing methods.

One might consider the Bridgman–Stockbarger method to be one of the first shaped growth processes because the crystal retains the shape of the ampoule used. It is not quite so obvious since almost all Bridgman crystals are grown from cylindrical ampoules. One of several recent exceptions being a paper by Feigelson and Route [139] on the growth of square cross-section crystals of $AgGaSe_2$ in vacuum-formed quartz crucibles. Using oriented seeds, they grew crystals not only aligned along the c-axis, but also so that the flat crystal side faces would to be normal to the [110] planes in which light propagates during type 1 phase-matched nonlinear interactions. A comprehensive review of the various shaped crystal growth methods is given in Ref. [140] and elsewhere.

Perhaps the earliest attempt at shaped crystal growth is attributed to the 1921 work of von Gomperz [70] at the Institute of Fiber Chemistry in Berlin-Dahlem. He worked in Michael Polyani's group. Polyani [141], reminiscing some 40 years later, recalled "Some metallurgists, interested in my work on the hardening of single crystals, told me of a method invented by Czochralski for producing metal crystals in the form of wires. It consisted in pulling out a thread from a pool of molten metal, so that the thread continued to solidify at the rate at which you were pulling it out. Erwin von Gomperz, who was doing his thesis with me, was put to growing single crystals of tin and zinc in this way. Unfortunately, the metal tended to come out in lumps, and the project was saved only by the intervention of Hermann Mark who covered the liquid metal by a sheet of mica with a hole in the middle, through which the thread came out as a smooth cylindrical wire. But for this ingenious intervention, our subsequent investigations of the plastic flow of metals might not have come about" [142].

In 1938, Stepanov at the Ioffe Institute in St. Petersberg began his extensive studies on shaping crystals during growth using wetted and nonwetted dies [143,144]. These dies have one or more capillaries or slots to transport melt from the crucible to the growth interface. The shape and height of the melt column is dependent on capillary properties such as surface tension, density, melt viscosity, impurities and wetting angle. Over many years, Stepanov's group produced a wide variety of shaped crystals including single and multibore tubes, rectangular bars, sheets, discs, etc. Shaped crystals of a number of different types of materials were grown, including oxides, metals and compound semiconductors.

Shaped growth in the United States began in the late 1960s with the preparation of sapphire filaments (later sapphire tubes for Na-vapor lights) by the edge-defined film-fed growth method (EFG) and single crystal superalloy turbine blades by directional solidification in complex molds [145,146]. The EFG process is in effect one of Stepanov's techniques, but it specifically focused on the advantages of wetted dies. It was discovered independently by LaBelle [147] who made a significant observation during his early attempts to pull sapphire fibers from a die placed in the melt surface. He noticed that the

melt wet the die and instead of being the diameter of the capillary within the die was the shape of the outer rim of the die. This was recognized by Mlavsky [148] as being of significant benefit and thus began extensive work on the EFG method. A sketch of the EFG method is shown in Figure 1.9. In a relatively short time after its discovery, it became a commercially viable technology. This was due to the early recognition that concurrent with experimental work, theoretical studies were needed to thoroughly understand the mechanisms involved in the process and ways to maintain better shape stability and rapid growth rates [149,150]. In 1980, an entire volume of the *Journal of Crystal Growth* was devoted to the subject of shaped growth methods. The EFG method has been successfully used in the commercial production of sapphire single fibers, tubes and ribbons and other materials. Today, the EFG method has gained an increasingly greater market share in the production of sapphire ribbons for GaN substrates used in lighting applications. Automated commercial EFG equipment can now be readily obtained, permitting companies to produce such wafers themselves.

The Stepanov and EFG methods are a meniscus-controlled process like Czochralski growth, and like it, growth is driven by crystal pulling. However, instead of pulling directly off the melt surface, the crystal is pulled from a suitable die face located above the melt surface. It can either float on the surface, like in von Gomperz's early experiments [70], held in a fixed position with respect to the crucible or moved during growth. The die position leaves the growth interface some distance above the hot melt surface and the thermal gradients are much steeper permitting enhanced growth velocities. The die material is chosen on the basis of its wettability with the melt and its reactivity. For sapphire, Mo dies have been used. In commercial systems the die can be moved during growth to maintain constant conditions and be equipped with an automatic monitoring system based on crystal weighing.

During the 1970s, the oil energy crisis led to serious efforts to produce silicon solar cells at a much lower cost than using cut wafers from Czochralski boules. This led to a robust effort to produce Si sheet at high growth rates. One of the most promising methods at the time was the EFG process. Extensive efforts went into adapting it to produce low-cost Si solar cells, but with limited success. Other innovative Si shaped crystal growth methods were studied during this time period, including the dendritic web process [151] in which a silicon dendrite is used a seed. It grows out laterally

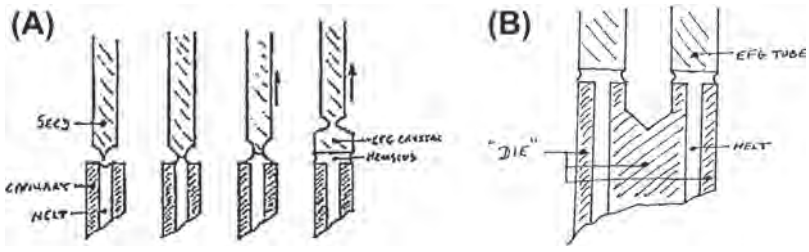


FIGURE 1.9 Illustration of the EFG shaped growth process. (A) the sequential steps involved in seeding and growing a crystal from a cylindrical die. (B) a die used to grow a hollow tubular crystal [148].

forming a thin sheet of silicon bounded by two new dendrites that define the width of the sheet. Some other methods include the ribbon against drop (RAD) method [152], where silicon is deposited as aligned grains on a carbon substrate, and the silicon on ceramic process [153], which is similar to the RAD process except that the substrate is a ceramic material. Two other methods of note are the ribbon to ribbon (RTR) [154] and horizontal ribbon (HRG) [155] growth methods. The former is a laser heated float-zone technique using a poly ribbon as the source and the latter involves pulling a ribbon (cooled from the top) horizontally from a free melt surface. The growth rates achievable in these processes are in the 5–10 cm/min range except for the HRG method where controlled cooling of the upper surface permitted growth rates of 10–40 cm/min. These methods are reviewed in Ref. [140].

The unidirectional casting method used for making single crystal jet engine turbine blades, as mentioned above, has had an important influence on aircraft performance. These blades, made from nickel-based superalloys, were found to have superior creep resistance if they have aligned grains [140] or better yet be one single crystal [156]. The method is like a Bridgman technique with the mold having the shape of the blade and extending down below is a zig-zag-shaped capillary tube mounted on a hollow pedestal that sits on a chill plate (see Figure 1.10). Growth is upward, initiated first from the melt in the pedestal by cooling the chill plate. This produces elongated grains along the mold's vertical axis, one of which will be in line with the capillary to provide seed selection. If by chance more than one grain makes it into the capillary from the pedestal, the crooked capillary will aid in seed selection.

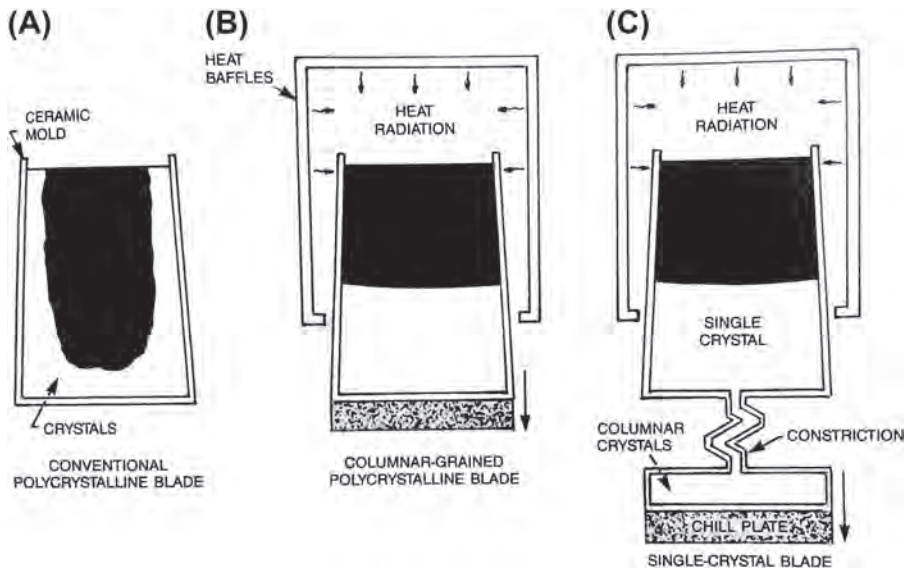


FIGURE 1.10 Schematic diagrams showing various methods for making jet engine turbine blades. (A) original casting method (polycrystalline), (B) single crystal growth by unidirectional solidification and (C) unidirectional growth with grain selection [146].

1.3.1.10 Skull Melting

The skull melting method is a quasi-crucible-less crystal growth method that was developed in the late 1960s in Russia, especially for growing large, high-purity oxide crystals for laser and gemstone production [157]. Since the 1970s it has become an important method for manufacturing cubic zirconia gemstones in a variety of colors (J.F. Wenckus et al. at the Arthur D. Little Company [158]). The method is adaptable to Czochralski and Bridgman growth methods using seed crystals and also in centrifugal casting.

In skull melting, a relatively large powder charge is contained within a water-cooled cylindrical Cu crucible surrounded by an RF heating coil. The RF field generates a magnetic field that in turn generates eddy currents due to ohmic losses in the material within the crucible. The process works for materials whose electrical conductivity increases with temperature, even through the melting stage. Due to the cold crucible wall, a skin (skull) of unmelted materials surrounds the melt and keeps it from coming into direct contact with the crucible, thus preventing contamination. Temperatures of over 3000 °C can be achieved and a wide selection of gas atmospheres are possible. Unless coupled with seeding, it is impossible to grow one single crystal due to the seeding effect of grains in the skull. For the gem industry, large slabs of crystals are retrieved from large-grained poly masses. The nature of the heat flow encourages the grains to grow along the vertical direction.

Cubic zirconia (ZrO_2) is used in the gem industry as a substitute for diamond since its optical properties, hardness, and fracture toughness are similar. Pure zirconia, however, undergoes a number of destructive phase transformations upon cooling. In order to grow single crystals from the melt, therefore, its composition has to be modified (stabilized) by doping to allow the high temperature cubic phase to persist to room temperature. The most common stabilizer is yttrium (YCZ), but CaO and MgO are also used. Concentrations of dopants vary from 10 to 40 mol%. These stabilizers work by creating many vacancies on the oxygen sublattice that prevent the cubic phase from transforming to phases of lower symmetry. Partially stabilized zirconia (PSZ) can be produced by reducing the dopant concentrations to less than 6 mol%. In these materials, part of the material transforms into the tetragonal phase creating a composite structure with excellent mechanical properties, making them attractive for applications such as drilling, threading, medical instruments such as scalpels, etc. [157]. The wide range of colors possible in zirconia gemstones are created using rare earth or transition metal element dopants.

Recently a Ukrainian group [159] developed a technique for growing large Tl:NaI scintillator crystals by a method similar to skull melting. Since the melting temperatures are quite low (~661 °C), they did not need RF heating and reconfigured the system from horizontal heating to vertical resistance heating. Basically, they hold a heater plate about 1 cm over the charge, which is held in a rectangular aluminum tray sitting on the bottom of water-cooled vacuum chamber. Since the heater is smaller in area than the container, only the center part of the charge is melted leaving a skull 5–10 mm thick surrounding

the melt and keeping it out of contact with the aluminum. Growth is achieved by slow cooling from the bottom up by lowering the temperature of the upper heater. It is not clear what the grain structure of the resulting slab is like, since seeding is not used and the plates produced are quite large. However, the scintillator properties are in line with those of single crystals produced by other methods and in a more cost-effective manner.

1.3.2 Solution Growth

1.3.2.1 Introduction

Solution growth methods involve dissolving material in a liquid (or gel) medium and then recrystallizing it under controlled conditions to produce a crystal of a desired size, shape and perfection for a specific application. The control of crystal shape and size can extend from very large crystals for optical applications down to fine powders for pharmaceutical, agricultural, or specialty chemical uses. The solvent media may be a low-temperature solvent like water or a high-temperature flux like PbO. Pressure-enhanced solution growth (the hybrid hydrothermal growth method) has also been a commercial success for the preparation of large crystals of quartz. The most common solvent used is water, and an impressive number of inorganic salts have been converted into single crystals using this technique, some weighing over 50 pounds. Other solvents include organic liquids (for the growth of organic crystals) and liquid ammonia.

Growing crystals from water solutions was undoubtedly the earliest effort by early man to replicate what he observed in nature. Natural salt ponds drying up in the hot summer months and then redissolving during winter rains assuredly piqued his interest and led him to experiment. Since salt became such an important commercial product, it is not surprising that this material and method became one of the first industrial crystal growth activities. Sugar was another material of early commercial interest. Through trial and error, a rudimentary understanding of saturation and supersaturation began to develop and, along with techniques such as seeding and solution homogenization (via stirring), better control of nucleation, crystal size and purity was achieved. Later, the role of additives to enhance growth behavior and tailor crystal properties was incorporated into the growth procedures. The eventual use of solubility diagrams greatly aided crystal growers in choosing appropriate growth conditions, i.e., temperature and composition regions. In these early days, as today, control of purity and size were of great commercial significance. Several basic methodologies are employed in solution growth: (1) controlled evaporation, (2) temperature programing, (3) mass transport in a concentration gradient at constant T and (4) changing the composition of the solution (salting out method).

1.3.2.2 Aqueous Solution Growth

Like all other crystal growth methods, a variety of modifications have been made over the years to facilitate the growth of a specific type of material, and to achieve an appropriate dimension and degree of crystalline perfection (purity, homogeneity, strain,

etc.) required for the application intended. Materials vary so widely in their thermodynamic and kinetic properties that even the growth of related materials of similar composition and structure can require changes in growth procedure or even in overall methodology.

In 1901, G. Wulff [160] published his famous theorem on the influence of surface energy on equilibrium shape of a crystal (morphology). It established a relationship between the crystal habit and the structure of crystals. It was derived from studies on the growth rates on different faces of crystals grown in water solutions. He used a rotating cylindrical crystallizer, in which a seed crystal was placed along the axis of the cylinder at its center-point. This allowed the crystal to grow out of contact with the vessel walls and be exposed to nutrient equally on all faces. Other early pioneers advancing the development of water solution methods during the first half of the twentieth century included Kruger and Finke [161], and Valeton [162]. Kruger and Finke were the first to investigate growth under constant temperature and supersaturation conditions. Their apparatus, shown in Figure 1.11, had in common two vertical chambers connected by upper and lower tubes through which solution passed in a specific way. One chamber contained source material and the other a stirring paddle (growth chamber) to move nutrient and depleted solution from one to the other. After equilibration of the growth chamber in a slightly undersaturated state, a seed crystal was added. Valeton's apparatus had a more precise way to control temperature in each bath. These methods utilized mass transported from the source chamber to the growth chamber to control the growth process. Crystals of potash alum and potassium sulfate were grown in these early experiments. In 1916, Nacken [163] developed a similar but more sophisticated apparatus using a vertical configuration for solute transport. Some 30 years later, Walker and Kohman [164] at Bell Laboratories developed a large-scale commercial crystallizer similar to these earlier methods known as the constant temperature process. Together with Holden's contributions on seed mounting [165], this apparatus was capable of growing four large EDP (ethylene diamine tartrate) piezoelectric crystals at a time. These crystals were used to replace natural quartz in telephone circuits. Crystals weighing up to 40 pounds could be

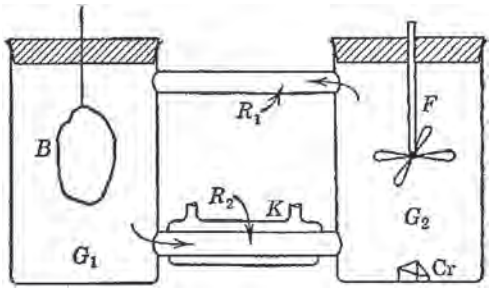


FIGURE 1.11 The aqueous solution crystallizer used by Kruger and Finke [161]. The nutrient was contained in a porous bag in heated beaker G_1. The stirrer in beaker G_2 recirculates saturated from G_1 through a water-cooled tube K, where is becomes supersaturated, into beaker G_2 where the crystals grow. Large potassium sulfate crystals 2 cm in size were produced in this reactor.

grown by this method. The method involved several large chambers with solution in one chamber saturated at one temperature being continuously fed the into the crystallizer chamber being held at a slightly lower temperature, thereby providing the supersaturation conditions necessary for growth.

In 1919, R.W. Moore [166] working at the General Electric Company needed large Rochelle salt crystals for electrical property studies. Since suitable material was not available commercially, he was forced to develop his own method. At first he started with the method of Kruger and Finke [161]. This proved unsuccessful. After thoroughly studying the available literature he came up with a new and simple approach based on the temperature lowering method. First, a saturated solution was formed 10–15 °C above room temperature, the solution decanted to separate it from the excess salt and then filtered. After heating the saturated solution 7–8° above its saturation point, it was poured into a vessel containing small seeds suspended on silk threads or metal wires, covered with a glass plate and then placed in water bath at 0.5 °C above the saturation temperature. From that point onward, the temperature was lowered to cause the seeds to grow. No means of stirring the solution was provided in these early experiments.

Moore's temperature lowering method was eventually modified to supply some fluid movement and distribute nutrient more uniformly to all the faces. The so-called rocking tank method was applied in 1947 by Walker [167] to the growth of large ammonium dihydrogen phosphate (ADP) crystals needed for submarine detection. The tanks were large rectangular trays that were gently rocked to replace depleted solution at the growth interfaces with fresh supersaturated material. Like EDP, crystals as large as $6 \times 6 \times 20$ in were produced by this method. Many crystals could be grown in each tray and for production (Western Electric Co.) rooms were filled with many rocking trays. Evaporation was inhibited and the room temperature had to be carefully controlled. One famous name associated with water solution growth was Alan Holden [165]. Aside from his research at Bell Laboratories, he also wrote a very popular book on the subject [168]. Numerous amateurs have used it to initiate crystal growth experiments. In 1949, he introduced the "rotary crystallizer" originally to grow EDP and then later for ADP crystals. It consisted of a large, one-foot-diameter cylindrical vessel holding the solution. It was heated from the bottom by two concentric heaters, an inner one to keep the bottom center somewhat under saturated. In this way, errant crystallites that have fallen to the bottom would dissolve. The outer heater controlled the overall solution temperature. The important feature introduced by Holden was the rotating seed holder (called a "spider"). The seed crystals were mounted on spokes emanating from the rotation shaft. Several sets of spokes holding the seeds were used along the vertical axis. The seeds were rotated first in one direction for a selected period of time and then in the other direction. The system was sealed and some water condensed on the upper lid forming droplets. When large enough, the droplets fell to the solution surface keeping it under saturated and thus preventing the nucleation of spurious grains.

Most of the growth methods mentioned above have inherently slow growth rates (0.5–1 mm/day) due to low solution supersaturation. The higher supersaturation

needed to yield increased growth rates were hard to achieve and control. In 1983, Loiacono et al. [169], using a three-stage crystallizer (modeled after Walker and Kohman's growth system from 1948 [164]), and under conditions of constant temperature and supersaturation were able to achieve 5 mm/day growth rates for large potassium dihydrogen phosphate (KDP) crystals. KDP is an important nonlinear optical material for modulating lasers. It has been grown commercially for many decades using aqueous methods similar to the ones described above. The need for even larger crystals of KDP for electro-optic switch and frequency converter plates in inertial confinement fusion research led to a big advance in solution growth methodology. It started in 1982 in Rashkovich's group at Moscow University. There they developed a rapid growth process for KDP from water solutions [170]. Over the next several decades, that work was taken up by Zaitseva and colleagues at the Lawrence Livermore National Laboratories in California [171]. They demonstrated that the standard Holden [165] crystallizer with temperature reduction could be used to grow large high-optical-quality KDP and deuterated KDP (DKDP) crystals up to 50 cm on a side at rates 10–100 times faster than older methods and without spontaneous nucleation and macroscopic defects. From their research on growing large crystals under fast growth conditions, they were able to develop a more thorough understanding of the mechanisms involved in solution growth. In addition to the influence of temperature, supersaturation and dislocations on growth rates, they realized the importance of impurities, mass transport (via high solution velocities) and in having a highly stable growth system. It was found imperative to control secondary nucleation. The most important feature of their rapid growth process was using highly supersaturated solutions (70–76 °C) coupled with elaborate techniques for preventing spontaneous nucleation. Toward that end a continuous filtration system and a seed protector were important modifications to the growth system.

1.3.2.3 Growth of Biological Macromolecules

Determining the crystal structure of complex biological molecules such as DNA, proteins, enzymes, etc., is important to both our understanding of animal and plant biology and functionality and our ability to develop pharmaceutical products to combat various illnesses that afflict these species. During the past century, protein crystallographers have slowly worked out the structures of a myriad of important species using X-ray diffraction methods. To accomplish this, researchers needed small, high-quality single crystals of controlled composition.

The first recorded protein crystallization experiments were done by German scientist F.L. Hunfeld in 1840. He prepared acicular crystals of earthworm hemoglobin by pressing blood between glass slides and allowing it to slowly evaporate. Since then, many techniques have been developed to prepare such crystals and the quality and size of the crystals produced were essential to the success of the structural detail obtained. The working out of the structures of myoglobin (1950) and hemoglobin (1955) using heavy metals covalently bonded to the protein led to the Nobel Prize for their researchers.

Another Nobel Prize winner who grew crystals in order to study their crystal structures was crystallographer Dorothy Crowfoot Hodgkin (1910–1994) [172]. As a child, Hodgkin was influenced by books that described how to grow crystals and on the interaction of X-rays with crystals. She won her prize in 1962 for her part in unraveling the crystal structure of the Vitamin B-12 molecule [173]. She also, together with Kathleen Lonsdale, grew crystals of penicillin and potassium and rubidium benzyl-penicillin. One of her major accomplishments was deciphering the structure of insulin.

While the crystal growth of biological macromolecules was primarily the domain of protein crystallographers and biologists during most of the century, in the 1980s the effort expanded to include experts more familiar with the theoretical and practical aspects of crystal growth (albeit small molecule materials). This came about in two ways. First, NASA had received requests from the crystallography community to fund protein crystal growth experiments in the low gravity environment of outer space. It was believed that the quality and size might be enhanced under these conditions. At the same time, NASA had been funding a variety of small molecule crystal growth experiments in low gravity with some promising results. NASA decided to try to engage some of the small molecule crystal growth community in the protein growth field. Several such programs were funded, one of which was my group at Stanford University. I immediately realized that we did not know enough about biological species to carry out his program successfully, and so when I found out that protein crystal growers did not have their own forum to discuss growth problems of mutual interest, I decided to bring them to Stanford basically to teach us about the field. Together with Alex McPherson [174], and with support from the American Association of Crystal Growth and NASA, we organized the first international conference on protein crystal growth at Stanford University in 1985. It not only brought together protein crystal growers for the first time, it also included well-known scientists and engineers from the small molecule crystal community. A total of 140 attendees were present. It was a somewhat contentious meeting at first, but as it proceeded, both sides, who spoke quite a different scientific language, came to understand more clearly the relevant issues, i.e., the physics behind the growth process and the influence of various processing parameters on the size and quality of the crystals produced. This international conference series has been held regularly every since.

Crystals of proteins and other biological species can be grown by a number of techniques including dialysis, sequential extraction, interface diffusion, vapor diffusion (plates, hanging or sitting drops), via pH and temperature changes, evaporation and in thermal (concentration) gradients. McPherson's original book, *Preparation and Analysis of Protein Crystals* [175], gives a comprehensive review of growth methods (see also Ref. [176]). Purification of starting materials and the composition of the growth solutions, like in most small molecule systems, are critically important to produce suitable crystals for X-ray structural analysis. Most of the growths are done in small batches. To establish the correct crystallizing conditions, a matrix approach is often used. Here, small samples with a systematically varied concentration of protein, salting agent,

solvent, etc., are placed within many cells and crystallized under the same conditions. Regions in the matrix that contain crystals are then regrown on a more refined compositional scale to enhance the results. In effect, this is the combinatorial chemistry approach and one that lends itself to automation using robotics to meter out the desired quantities into each cell. This latter approach was pioneered by Ward et al. [177] during the mid-1980s and is in wide use today.

One final comment worthy of mentioning again (see Scientific Study section) is that the large size of the growth units in biological macromolecules gave crystal growth scientists a unique opportunity to dynamically study the morphology and kinetics of step and ledge movement (including step bunching) during growth using the relatively new atomic force microscopy technique. The first such in situ studies were carried out in 1995 by Land et al. [178] and Malkin et al. [179].

1.3.2.4 Growth from Gels

In 1896, the German chemist Raphael E. Liesegang slowly put a drop of silver nitrate-water solution onto a thin gel layer containing potassium dichromate, and in doing so discovered the precipitation ring phenomena named after him [180]. This initial discovery stimulated a strong interest in understanding how the process worked. A gel is a semisolid containing small pores of angstrom dimensions in which a variety of salts can be dissolved. Early efforts on growing crystals in gels include the work of Hatschek [181] in 1911 and Dreaper [182] in 1913. The former grew small crystals of gypsum by letting sulfate ions diffuse in a gelatin containing a dilute solution of calcium chloride and the latter lead chloride crystals in a test-tube-shaped vessel. The idea for growing crystals in a gel media was stimulated by the research work of Fisher and Simons [183] in 1926. They were intrigued by some earlier work with gold and copper crystals produced by the reduction of their metal salts in a silica gel and the coincident occurrence of gold in quartz veins. From their early experiments, they predicted that this method would be "far-reaching" and this enthusiasm caught the attention of later researchers and became an area of vigorous research, particularly from the early 1960s onward. The work by Heinz Henisch's group at Pennsylvania State University stimulated researchers around the world and was summarized in his book *Crystals in Gels* [184].

The gel growth method has been used to prepare an impressively wide range of inorganic and organic crystals, including proteins. Gels provide a medium where mass transport is by the slow diffusion of suitable ions to a region where they can react during crystallization. It is a convection-free method and the crystals, when nucleated under carefully controlled conditions, are suspended from one another. These factors, plus the near room-temperature growth conditions purportedly result in higher crystal quality. Crystal dimensions can vary from micron to centimeter sizes depending on the system under study, but typically they only reach mm sizes. Like other solution growth crystals, they exhibit growth rate anisotropy and faceting. Typical gels used are silica hydrogel (sodium metasilicate), agar (derived from seaweed) and gelatin; however, many other gel compositions have been used as well. Crystals can be grown within gels by a number of

techniques, including (1) chemical reaction, (2) complex dilution, (3) chemical reduction and (4) solubility reduction. An extensive list of crystals grown is given in Ref. [185]. During the last decade or so, interest in gel growth has diminished along with the number of publications.

1.3.2.5 Nonaqueous Solution Growth

Organic crystals are useful for a number of applications including semiconductors and scintillator devices. Organic materials, like other substances, vary widely with respect to their thermodynamic and physical properties. Therefore it is not surprising that a suitable crystal growth method will depend on the specific properties of the material in question. They can be grown by a variety of common crystal growth techniques including vapor, melt and solution methods. Organic materials that melt without dissociation are prime candidates for melt growth methods. Others have been grown in solution or by vapor phase techniques. Solution growth methods usually involve organic solvents such as ethyl alcohol, acetone, hexane, and carbon tetrachloride. The techniques used are similar to water solvent methods and include solvent evaporation, slow cooling or heating, vapor diffusion and liquid–liquid diffusion and are nicely summarized in Ref. [186]. One of the recent examples of solution growth using organic solvents is the work at the Lawrence Livermore Laboratories on the growth of large, high-quality crystals of trans-stilbene ($C_{14}H_{12}$) for fast neutron detectors [187]. The solvents used were toluene or anisole, the latter preferred due to its lower evaporation rate. Melt growth techniques did not yield large, high-quality crystals. Building crystallization systems to withstand the organic solvents and by using the temperature reduction method together with rotation, very high-quality crystals in dimensions up to four inches have been produced.

1.3.2.6 High Temperature Solution (Flux) Growth

1.3.2.6.1 Bulk Crystals

As with other solution growth methods, the high temperature flux growth method also relies on the careful control of the supersaturation and melt composition. Like the low temperature processes, there are three general methods for controlling supersaturation: (1) slow cooling, (2) evaporation and (3) transport in a concentration gradient. In its early incarnations, the method was unseeded and crystals grew on the surface of the melt where supersaturation is usually greatest (due to volatility) or on the crucible walls where heterogeneous nucleation is favored. Later, the use of seeds or cooled probes helps facilitate growth. Generally solvents are classified as common ion or noncommon ion fluxes. An example of the former is the growth of (Ba,Sr)TiO_3 from excess TiO_2 melt [188], and the latter, the growth of $Ye_3Fe_5O_{12}$ from BaO–B_2O_3 based fluxes [189]. The BaO–B_2O_3 flux, while used early on, was not nearly as successful as PbO–B_2O_3 or PbO–PbF_2–B_2O_3 fluxes that form ionic solutions. The 1975 book *Crystal Growth from High Temperature Solutions* by Elwell and Scheel [190] still remains the most thorough, encyclopedic treatment on the history, theory and methodology of flux growth.

Crystal growth from high-temperature solutions probably began during the nineteenth century. One of the earliest documented studies (1823) was by Friedrich Wöhler (1800–1882), a famous German chemist who used a flux-reaction technique to grow sodium tungsten bronze (Na_xWO_3, where x is ≤ 1) crystals by passing H_2 gas over a Na_2WO_4 flux [191]. He is also famous for his synthesis of urea and the codiscovery of Be, Si and silicon nitride. By mid-century, early experiments were of a similar nature and a variety of materials were produced including CdS (using a $CdCl_2$ solvent and H_2S reactant), alkaline earth and transition metal oxides, silicates and sapphire [190]. Later in the century, more traditional flux methods were used to grow a variety of binary, ternary and higher order compounds using chemically compatible solvents. Some examples include Doelter [192], who in 1886 grew Ag_2S by dissolving and recrystallizing it from AgCl or $SbCl_3$ melts. AlB_{12} crystals were grown from B_2O_3 melts by Wöhler and Deville in 1857 [193], and ruby was grown by Fremy and Feil in 1877 [194] using PbO as the flux (which from the 1950s onward became a popular flux for growing oxide crystals for optical applications). The results varied from laboratory to laboratory, and generally the crystal sizes were on the small side. Over 100 flux-grown compounds and their solvent phases are listed in Ref. [190]. In this time period this was probably the most important method used for preparing crystals of non water-soluble materials.

Solvent requirements include (1) a suitable melting temperature and solubility in the temperature range of interest, (2) a temperature coefficient of solubility, (3) low volatilization (an issue with PbO and halide fluxes), (4) compatibility with available crucible materials (reactivity and wettability) and (5) a relatively low viscosity. In the 1950s, the flux growth method again became an important adjunct to other developing crystal growth methods such as the Czochralski and Bridgman methods. It was particularly important for compounds that melt incongruently, have high vapor pressures at their melting temperatures, are refractory with excessive melting temperatures or have destructive phase transformations, etc.

After World War II, the flux growth method gained interest commensurate with device researchers' interests in finding new and better materials for optical, electronic and magnetic applications. The use of this method was very extensive during the 1950s through about 1980 and took place in many laboratories around the world. As a result, it is only possible to cite a few illustrative examples in this brief historical review to give a sense of what growth activities were like during this period. In 1964, Edward Giess [195] successfully prepared $Cr:Al_2O_3$ (ruby) using a PbF_2 flux. Lead fluoride is quite volatile, and so it was often combined with PbO with some added B_2O_3 to stabilize it. At about the same time, Stanley Austerman [196] used the flux growth method to grow BeO crystals. BeO substrates were of interest because of its very high thermal conductivity and therefore its ability to remove heat from electronic devices. This would permit higher power operation. Austerman grew BeO from a Li_2MoO_4-based flux. Later, Newkirk and Smith [197] grew BeO from PbO-based fluxes. In Russia, V.A. Timofeeva's group was very active during this time period, studying the flux growth of many different oxide compounds including Al_2O_3, Cr_2O_3, Fe_2O_3, rare earth oxides and the garnets $Y_3Fe_5O_{12}$, (YIG)

and $Y_3Al_5O_{12}$ (YAG). In the latter case, she investigated how growth defects formed as a function of the flux growth conditions and solvent composition [198].

Single crystal garnets ($A_3B_5O_{12}$) were of great interest for laser, microwave and ultrasonic applications. In 1958, Nielsen and Dearborn at Bell Laboratories were the first to report on the flux growth of $Y_3Fe_5O_{12}$ (YIG) [199]. Major improvements in size and quality were achieved by adding impurities such as CaO to a PbF_2–PbO–B_2O_3 flux. Van Uitert et al. [200] worked on the growth of large, optical-quality $Y_3Al_5O_{12}$ (YAG) crystals in very large platinum crucibles. Remeika, whose extensive crystal growth activities also included the flux growth of YIG, found that pure YIG crystals contained small amounts of Fe^{4+}, which resulted in reduced optical quality [201]. By adding small additions of tetravalent ions such as Si, Sn and Ge to the flux, the problem was eliminated. Some examples of flux grown crystals are shown in Figure 1.12.

Flux growth methods vary from simply slow cooling a melt without seeding (self-nucleation) to more complicated seeded growth techniques. The bottom cooling method helps control nucleation in unseeded melts. A small supersaturated region is created in the melt to limit the volume in which nucleation can take place. This can also be used to prevent a seed from dissolving before it starts to grow (like in the heat exchanger method). In 1955 and 1956, Reisman and Holtzberg were the first to prepare single crystals of potassium niobate $KNbO_3$ (KN) and potassium tantalate $KTaO_3$ (KT). These compounds were of interest for ferroelectric and piezoelectric applications [203]. A K_2O flux was found suitable for this purpose. KN in particular became a very important material for efficient direct diode doubling and other NLO frequency conversion processes, such as generating blue light from a Ti:Sapphire laser via critical phase matching. Over the years, large-scale

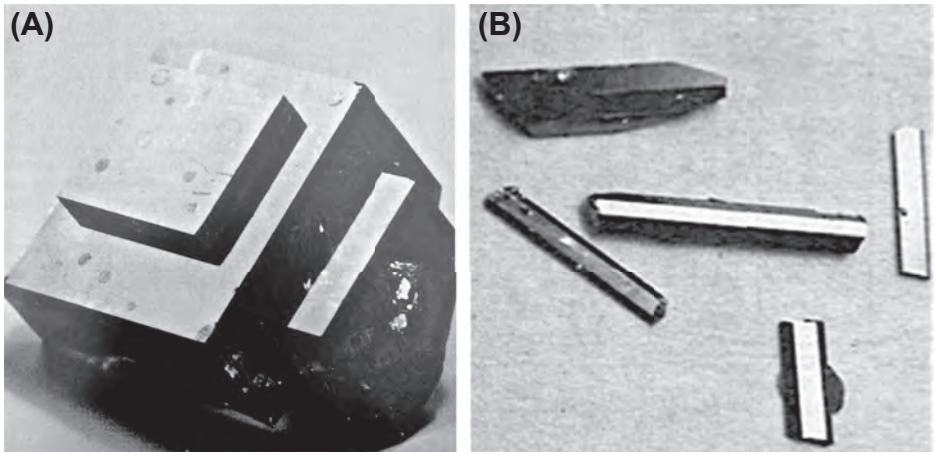


FIGURE 1.12 (A) A photograph of a large ($3.5 \times 3 \times 2.5$ cm), flux-grown crystal of $GdAlO_3$. It contained large inclusion-free regions. A PbO–PbF_2–B_2O_3 flux containing some other minor additives was used. The large size and quality is attributed to ACRT stirring method [202]. (B) Photograph of some highly facetted acicular crystals of $CdGeAs_2$ grown from a Bi flux (author). Some are solid, others contain a core of solidified Bi solvent. Strong growth rate anisotropy is evident.

crystal growth methods capable of producing 100 gm crystals were developed [204,205]. While the K_2O flux was still used, top seeding was added later to control nucleation and growth conditions. This seeding technique, now known as the top-seeded solution growth method (TSSG), became a very important flux growth method. The first description of this method was in a 1958 paper by Miller [206]. He used a seed crystal mounted on a rod that rotated in a reciprocating fashion. Without pulling, he grew KN crystals up to 15 gm from a charge containing K_2CO_3 and Nb_2O_5. He also used an electrical circuit between the crucible and seed to determine the exact moment when the seed touched the melt. The method was used later by Linares for YIG growth [207] and at MIT by Belruss et al. [208] for the growth of $SrTiO_3$ and $BaTiO_3$ crystals from melts containing excess TiO_2 and GeO_2. More recently, the method has been used for growing beta barium borate crystals (β-BaB_2O_4, BBO) from melts containing some Na_2O [209] or other solvents to lower the $\eta\varepsilon$ viscosity and to permit growth at temperatures below the α–β phase transformation temperature. BBO and other similar compounds like LiB_3O_5 (LBO) and $CsLiB_6O_{10}$ (CLBO) are very useful for optical applications in the visible and ultraviolet regions.

As seen with aqueous solution growth, stirring during growth is very beneficial to the enhancement of crystal quality and growth rates. In addition to top seeding with rotation that provides some fluid flow, other methods have been devised. One useful approach is the accelerated crucible rotation technique (ACRT). It was first used by Nelson and Remeika [210] in 1964 for pregrowth stirring. Scheel and Schultz-Dubois first demonstrated its usefulness during growth in 1971 [104]. The method is very helpful with growth from volatile melts that need to be grown in sealed crucibles. No moving parts, like stirring rods, need to be placed in the melt. The method relies on acceleration and deceleration of the crucible, thereby decoupling the fluids movement from the crucible's trajectory in a periodic fashion. Two major flow mechanisms, spiral shearing distortion and Ekman-layer flow, are operative during acceleration and deceleration. It has been found to limit nucleation and to help produce large, inclusion-free crystals. It was first applied to the growth of $GdAlO_3$ crystals from a PbO–PbF_2–B_2O_3 flux and yielded the largest such crystal to date [202].

One other method worth mentioning was that devised by Tolksdorf [211] at the Phillips Central Laboratories in Hamburg. In the past, one of the problems with growing YIG crystals from the volatile PbO–PbF_2 flux was that it redissolves below 950 °C. To prevent this, Nielsen [212] poured off the flux at 1040 °C outside the furnace. Unfortunately, the crystals cracked due to thermal shock. An improvement on this method was by Grodkiewicz, Dearborn and Van Uitert [213]. They punctured the bottom of their large platinum crucibles draining off the melt. This was expensive, as the flux material could not be reused. In Tolksdorf's method he used a sealed crucible that could be rotated on it axis. It was half filled with a PbO/PbF_2/YIG melt and, after the crystals were grown by slow cooling, the crucible was spun 180° separating the crystals from the melt. In a similar way, he could mount a seed on the empty side, and when the melt was saturated, could rotate the seed into the melt, slow cool to initiate growth onto the seed, and when done, rotate the crucible back to its original position to remove the flux from

the crystal. Toldsdorf's method and apparatus was later used to grow $KTiOPO_4$ (KTP) crystals (an important nonlinear optical material) using the flux method.

1.3.2.6.2 Thin Film Liquid Phase Epitaxy

In addition to bulk crystal growth, high-temperature solutions have also been used to grow thin films of semiconductors, oxides (magnetic and electro-optic) and various other compounds. The method is known as liquid phase epitaxy (LPE). The LPE method involves the crystallization of a single crystal or crystallographically oriented layer on a substrate in contact with a liquid phase. The substrate (usually a single crystal wafer) may be either of the same base composition (homoepitaxy) or a different composition (heteroepitaxy). The field of epitaxial growth extends well beyond the LPE method to include numerous vapor phase depositions techniques to be discussed later. While these other methods are very important, the LPE has certain advantages including (1) greater crystalline perfection due to the near equilibrium growth conditions and use of a near perfect substrate template, (2) better stoichiometry control, (3) higher growth rates due to higher solutes concentrations and (4) lower cost compared to other methods. A comprehensive review of LPE field is given in Ref. [214].

Epitaxial deposits have been found in various natural mineral formations. One example is rutile crystals growing on hematite facets [215]. In 1836, Moritz Frankenheim (1801–1869), a German physicist, was the first of many researchers to observe epitaxial growth in the laboratory when he produced oriented crystals of sodium nitrate on a cleaved surface of calcite crystals [216]. In 1906 Baker did some experiments on the orientation of crystals growing from droplets crystallizing on cleaved surfaces [217]. In 1928, Royer followed this line of research [218] and using X-ray diffraction analysis, was the first to describe the requirements for lattice matching between the film and substrate to achieve epitaxy (an orientation relationship between the layer and the substrate).

In the 1960s, attention turned to thin film semiconductor devices. At the RCA Laboratories, H. Nelson [219] was the first to develop an effective LPE method for growing epilayers of GaAs on GaAs substrates (homoepitaxy). He used a horizontal graphite boat system with a GaAs + Sn melt at one end. When the substrate, located at the other end was at 640 °C, the boat was tilted and the melt flowed over the substrate. After cooling for a period of time the melt was poured back off, leaving the substrate covered by a single crystal layer of GaAs. Other LPE techniques involved dipping substrates (either vertically or horizontally) into an appropriate solution and then, after deposition, withdrawing them back out. Substrate rotation has also been used to achieve better uniformity. By using these various methods p-n junctions could be produced using doped layers. These epilayers were used in a number of important device applications including GaAs [220] and $Al_xGa_{(1-x)}As$ [221] lasers and the extensive commercial production of light emitting diodes (LED's). The LPE method has also been used to prepare thin film structures from silicon, germanium and their solid solutions, II–VI compounds such as ZnSe, CdTe, Hg_{1-x} Cd_xTe (MCT), SiC, the III–V nitrides (AlN and GaN) and many other alloy compositions [214]. As with any flux growth method, the solvents have to be tailored to the specific film

composition to be grown and the substrate and its orientation carefully chosen. The requirement for high-quality substrates for both LPE and vapor phase epitaxy have kept the bulk crystal growth industry very active.

In addition to semiconductor research, various applications for magnetic garnet crystals (e.g., $Y_3Fe_5O_{12}$ and $Ca_{2x}Bi_{3-2x}Fe_{5-x}V_xO_{12}$) were developing during this same time period. LPE became an important method for the preparation of various types of microwave, magneto-optic and bubble memory thin film devices. One of the first attempts to use the LPE method for YIG film deposition on garnet substrates was in 1965 by Linares et al. [222]. In 1968 Linares [223] grew high quality YIG films on GGG using the tilting boat method and a lead borate flux. Magnetic bubble memory thin film devices became an important research activity during the 1970s [224]. These thin film structures were once expected to replace Si-based memory chips and various groups extensively studied both their preparation and properties. Magnetic garnet single crystal LPE films were typically grown from PbO-B_2O_3 fluxes. The substrates used were nonmagnetic $Gd_3Ga_5O_{12}$ (GGG). It is a very good lattice match with YIG. Various techniques such as substrate dipping and rotation during growth were studied. Withdrawal after growth could be problematic due to cracking and film pealing. The process gave high growth rates and crystalline perfection, film thickness uniformity, and compositional homogeneity. Over time, ever more complex film compositions evolved to enhance their properties [225,226]. The technology reached its zenith with the growth of bismuth-doped rare earth iron garnet thick films up to one-half mm thick from Bi_2O_3–PbO–B_2O_3 fluxes onto large lattice parameter-matched Ca–Mg–Zr substituted GGG substrates.

In 1986, Bednorz and Müller discovered Hi–Tc superconductivity while working at the IBM research laboratories near Zurich [227]. The ceramic material they produced was an oxygen-deficient Ba-doped Lanthanum cuprate ($La_{2-x}Ba_xCuO_4$), a perovskite-like compound that exhibited zero electrical resistance at 35 K, twice the highest transition temperature achieved to date. This set off a whirlwind of research activities to find other cuprates with even higher Tc's including $YBa_2Cu_3O_{7x}$ (92 K) followed by $Bi_2Sr_2Ca_{n-1}Cu_nO_{4+2n+x}$ ($n = 1$, 2 and 3) with a Tc between 85 and 110 K. Thallium- and mercury-based cuprates had even high Tc's, the latter a record at 134 K. At this point a great effort was made to grow single crystals of these compounds for physical property studies and to enhance their properties. Due to the complex nature of the phase equilibria in these systems, crystal growth was very complicated, making difficult the preparation of large, high-quality single crystals. All manner of bulk and film deposition methods were tried with varying success. In Scheel et al. [228], the LPE method was used to prepare very flat, high quality epitaxial layers of $YBa_2Cu_3O_{7-x}$ on $NdGaO_3$ substrates. Step heights were between 1.2 and 7.2 nm and did not exhibit the spiral islands found using vapor phase deposition techniques.

1.3.2.7 Hydrothermal Growth

Hydrothermal growth is a solution growth method operated at modest temperatures and elevated pressures. Byrappa and Yoshimura [229] authored an exhaustive treatise on the

history and technology behind the hydrothermal growth process. The subject has also been discussed to a lesser extent in numerous other books and journal articles, for example [230]. The process involves the controlled growth of crystals in an autoclave (see Figure 1.13(A)) onto seeds immersed in a water solution containing the nutrient and usually a mineralizing agent. The driving force for growth is the solubility difference generated by a temperature gradient. The method has several advantages. Growth takes place below the material's melting temperature and often below a destructive phase transformation (e.g., α-quartz, the low-temperature polymorph of SiO_2). Since the growth process takes place in a sealed system, the atmosphere can be modified to suit the material being grown (i.e., maintaining an oxidizing or reducing environment). In addition, the method generally produces less stress on the crystal and can lead to an increased crystalline perfection. Another attractive feature of hydrothermal growth is that the growth rates are relatively fast compared to other solution growth methods. High-pressure vessels can be made of various materials depending on the temperature and pressures required.

Hydrothermal growth's principal use has been for the commercial growth of large, highly perfect (dislocation-free) α-quartz crystals for piezoelectric applications. A rack of crystals produced from one large-scale commercial autoclave is shown in Figure 1.13(B). Piezoelectric materials such as quartz generate an electrical polarization when subjected

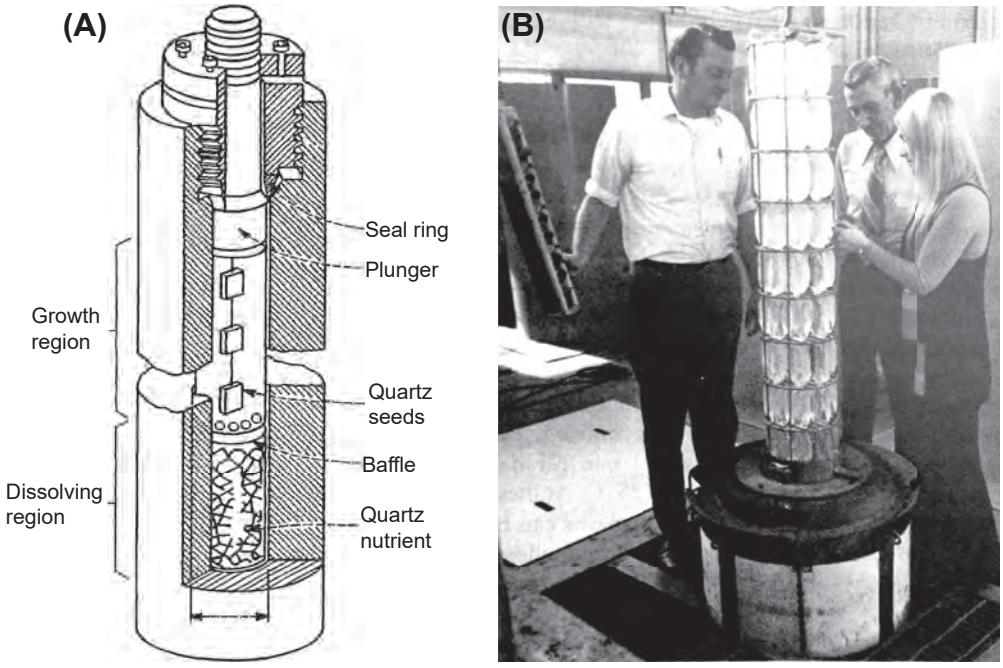


FIGURE 1.13 (A) A schematic diagram of a hydrothermal quartz autoclave. (B) The commercial harvesting of quartz crystals at AT&T's factory in Massachusetts [30].

to a mechanical stress. The hydrothermal method has also been used to successfully grow a variety of crystals of many different classes of compounds from simple binary compounds, such as ZnO, ZnS and GaN, to more complex compounds, such as the phosphates ($AlPO_4$, and $KTiOPO_4$), calcite, hydroxyapatite, zeolites, silicates, metal borates, vanadates, tungstates, and rare earth garnets (e.g., YIG and YAG).

Geologists trying to understand how crystals grew in nature (in an aqueous media under high pressures and temperatures) were the first to carry out hydrothermal phase equilibria studies. Experiments have been traced back to the twelfth century. Their main interest was in phase relationships rather than the growth of large crystals. One of the first published papers on hydrothermal crystallization was by Karl Emil von Schafhäutl in 1845. He prepared microcrystals of quartz. A short time later, in 1848, Robert Bunsen prepared some of the alkaline earth carbonates. The first attempt to grow large crystals hydrothermally was by Henri De Sénarmont in 1851 [231]. He introduced the use of seed plates. It was one of his many studies on the hydrothermal crystallization of minerals. Fifty years later, Giorgi Spezia (1905) published one of the seminal papers on the seeded growth of α-quartz [232]. These early research efforts in Europe eventually formed the basis of the commercial quartz crystal industry.

The modern synthetic quartz crystal growth industry arose during World War II. Supplies of natural Brazilian quartz were not getting to the U.S. due to German submarine attacks on allied shipping. Ironically, one of the applications for quartz crystals was for submarine detection. Piezoelectric materials are needed in single crystal form to take advantage of their anisotropic properties. In oscillators for example, the frequency depends on crystal orientation and devices require precisely oriented parts. Quartz is also used for watches and clocks for precision time management and in signal processing applications.

Major developments in the hydrothermal growth technology were centered on the growth of quartz crystals at the Bell Telephone Laboratories and the Western Electric Company during the 1950s. Walker and Buehler [233] developed a hydrothermal growth method capable of producing very large crystals. They used a welded steel autoclave that was capable of temperatures of 450 $^{\circ}$C and pressures up to 3000 atm. Improvements in autoclave designs were based on some early high pressure studies by Bridgman. Over the following years, improvements were made by the Western Electric Company that led to its successful commercialization. It was in large part due to the efforts of Laudise and Sullivan [234]. Systematic kinetic studies by Laudise [235] led to significant improvements in crystal growth rates. An effort to improve the resonance of quartz oscillators was undertaken by Bell Laboratory scientists and other researchers. Lithium and nitrite ions added to the growth solutions led to improved mechanical Q values [30].

Important hydrothermal growth parameters include (1) operating temperature, (2) temperature gradient, (3) pressure, (4) percent fill, (5) impurity and mineralizer concentration, and (6) seed orientation and surface area. Using quartz as an example, the autoclave is placed in a two-zone furnace with the upper section, containing the oriented seed plates, being cooler than the bottom in which the nutrient, SiO_2, is placed.

A perforated metal disc serves as a baffle between the two zones. The vessel is then filled with solvent to a desired level. The nutrient dissolves in the hot region of the furnace and the upper becomes supersaturated and deposits crystal layers on the seed plates. Convective currents generated by the temperature gradients help move saturated solutions to the seed chamber. For commercial quartz production (see Figure 1.13(B) above), a typical set of conditions might include a hot zone temperature of 400 °C, a seed zone temperature of 360 °C, a fill factor of 80% and a solution containing 1.0 M NaOH, a baffle opening of 5% and a pressure of 21 kpsi (144 MPa) [230].

An important more recent application of hydrothermal growth has been in the preparation of ZnO crystals. ZnO is a transparent, wide bandgap semiconductor (n- or p-type when doped) with a range of useful properties. It is piezoelectric, ferroelectric, exhibits room temperature ferromagnetism, has a large magneto-optic response, etc. It is useful for chemical sensors, catalysis and optoelectronic applications. When doped, its conductivity can vary from insulating to metallic. Bulk crystals, thin films and various nanostructures can be produced using this method. Nanostructures, in the form of platelets, rods, columns, and complex bilayer (column-to-rod), have recently been prepared using hydrothermal methods [236–239].

1.3.2.8 Electrochemical Crystal Growth

Another useful solution growth technology is electrodeposition. It can be carried out in both aqueous and molten salts solutions, and both bulk and thin film single crystals can be grown in this way. The process involves introducing an anode and cathode into either type of solution (of appropriate composition) and applying a suitable voltage across the cell. The driving force for crystallization is the passage of current between the electrodes. The electrode can be a single crystal substrate (wafer or seed), a wire or a more complex structure. Electrodeposition has recently become an attractive method for use in preparing nano-, bio- and micro-structures. It can be used to make functional materials with the aid of three-dimensional masks and scaled up from the deposition of a few atoms to thick deposits.

The first use of electrolysis in chemical processing is attributed to the famous English chemist Sir Humphry Davy (1778–1829). Davy, who was responsible for the discovery of several alkali and alkaline earth metals, separated K from KOH in 1807, the first metal isolated by electrolysis. It has been used since then for the synthesis of a variety of materials. The Hall process, developed in the 1930s for separating Al metal from bauxite (dissolved in a molten salt), is one of its most important industrial applications of electrodeposition. It has also been used to produce many refractory compounds such as borides, phosphides, silicides and carbides. The application of this technology to crystal growth had a late start, surprising since Kunnmann [240] observed that "materials electrochemically precipitated from fused melts can almost always be obtained in the form of reasonably large crystal when sufficiently low current densities are employed."

The potential advantages of electrocrystallization for crystal growth include (1) growth can be accurately controlled solely by electrochemical parameters (current

density and electric potential), (2) the process is isothermal (thermal gradients and temperature ramps are unnecessary, (3) its insensitivity to temperature fluctuations, (4) low growth temperatures minimize thermal decomposition and stresses, as well as vapor losses, (5) purification can be achieved electrochemically and (6) growth features can be studied quantitatively by varying electrochemical parameters [241]. On the other hand, the material to be grown and substrate have to be electrically conducting, and the growth rates are typically slow due to the generally low solute concentrations in the solution. An interesting hybrid method, developed by DeMattei et al. [242], combined molten salt electrodeposition with the Czochralski pulling technique. They demonstrated the method by growing long [110] oriented crystals of sodium tungsten bronze from [110] oriented seed crystals.

Silicon was first electrodeposited in 1854 by Claire-Deville [243]. He used a $NaAlCl_4$–Si molten salt solution. This work was followed a decade later by Ullik [244] who used a K_2SiF_6–KF flux. Cohen and Huggins [245], using a similar flux, were the first to produce coherent epitaxial layers of Si on Si substrates. Metal substrates yielded polycrystalline films. Other semiconductors electrodeposited from molten salt fluxes include the III–V compounds GaP, GaAs and InP. A review of molten salt electrochemical crystal growth was given by Feigelson in 1980 [246].

In the 1990s, an active research area developed around the growth of heteroepitaxial thin films of chalcogenide semiconductors using the low temperature aqueous solution electrodeposition method [247]. Large-scale solar cells were made from electrodeposited polycrystalline CdTe films [248]. Epitaxial films of CdTe can be electroplated from solutions containing cadmium sulfate and TeO_2 onto an InP substrate [249]. In addition, epitaxial films of PbS [250], CdS [251], ZnSe [252] and other related compounds have been electrodeposited. Schlesinger et al. [253] presented a comprehensive review on the subject of semiconductor electrodeposition.

As mentioned above, ZnO is an important and versatile material of great interest to the research and industrial communities. The electrodeposition of ZnO was first demonstrated by Izaki et al. [254] and later Peulon et al. [255]. The growth of oriented rods and flat, disc-shaped crystals were described in Refs. [256–258]. Xu et al. [259] electrodeposited well-defined nano- and micro-structures onto to indium-doped tin oxide substrates using low molecular weight salts in the solutions to control crystal shape. They produced hexagonally shaped tapered ZnO rods and platelets and rhombohedral rods by using amine and other inorganic ions in their solutions.

1.3.3 Vapor Growth

1.3.3.1 Introduction

Vapor phase crystal growth methods have been used extensively for the preparation of both bulk crystals and single crystal thin films. The latter, called vapor-phase epitaxy, are usually deposited on single crystal substrates and have found their greatest utility in the preparation of films and patterned nanostructures for electronic and electro-optic devices.

Important film deposition techniques include OMVPE, MBE, sputtering, etc. In most of these techniques the crystalline lattice of the film needs to be tailored to the substrate upon which it is deposited. Their properties depend not only on their composition, but also on lattice matching between the film and substrate and the crystalline defects that might arise from any misorientation. The substrates are typically thin, crystallographically oriented wafers cut from bulk crystals usually grown by melt growth techniques. The process can be homoepitaxial (growth on a substrate of the same material) or hetero-epitaxial (growth on a different substrate material). Some common examples being Si integrated circuits, GaAs LED devices and more recently GaN on sapphire for lighting applications. Artificial epitaxy, to be discussed later, involves the creation of a geometric pattern (containing some orientational relationship with the film lattice) on a substrate by etching or deposition. The base substrate can be an amorphous material like glass.

Vapor growth technology does not have as long a history as other crystal growth methods. Most research and development work began mainly from 1960 onward. However, it has been traced back a bit further to the German chemist Robert Bunsen (1811–1899) [260]. In 1852, Bunsen observed that Fe_2O_3 crystals formed together with HCl in volcanic gases through a reaction between ferric chloride and water vapor, i.e., a chemical vapor deposition (CVD) process [261]. Not long afterward, in 1861, French chemist Henri Claire-Deville (1818–1881) became the first person to put a CVD process to use preparing artificial oxide minerals of magnesium, titanium and tin [262].

The first commercial CVD process was inaugurated in 1880 for the fabrication of filaments for the new incandescent lamp industry [263]. In 1914, F.C. Brown, studied the crystal habits of Se crystals deposited by sublimation of its vapor in a closed tube under either vacuum or atmospheric pressure [264]. He held the Se at 270 °C for up to a week and the crystals formed along the tube where the temperature was lower. The largest crystals always formed at the higher condensation temperatures (∼210 °C). During the 1920s, Fritz Koref and immediately afterward Anton Eduard Van Arkel used WCl_4 to deposit W on single crystal tungsten wires. Koref [265] used a hydrogen reduction method to dissociate WCl_4 gas near the wire, which was heated to between 110 and 1000 °C. This led to a W deposit containing oriented grains. In Van Arkel's process [266], H_2 was not needed as the process was operated at much higher temperatures (1600–1700 °C). In 1921, research began on growing metal crystals by sublimation. Gross [267] and Gross and Volmer [268] grew leaflet crystals of Zn and Cd by directing vapors onto cool glass plates. This work led Volmer to his adsorption-layer theory discussed earlier. In 1932 Straumanis [269] grew Mg, Zn, and Cd crystals by a similar technique. The metals were held at temperatures somewhat below their melting points.

Three basic techniques have been used to grow crystals from the vapor phase: (1) direct sublimation or evaporation of material followed by condensation, (2) chemical transport reaction and (3) chemical vapor deposition. Chemical thermodynamics (shifts in vapor–solid equilibrium) and mass transport are some basic differentiating features between these methods. The process relies on mass transport of species from the source through the gas phase to its incorporation onto the crystal surface. The sublimation and

chemical vapor deposition methods have been operated in either an open system, using an inert carrier gas, or in a closed growth chamber containing vacuum or higher gas pressures. The chemical vapor deposition method, most often used in thin film epitaxy, involves the decomposition of molecular species (precursors). The chemical transport reaction method, a reversible process, converts nonvolatile species into volatile ones prior to crystallization in closed systems.

Crystals can usually be grown by vapor growth techniques at lower temperatures than from melts of the same composition. Vapor phase methods are especially useful when a compound is difficult to grow because of a high vapor pressure, dissociation prior to melting, etc., or where a thin film is required. While these methods are used more extensively to grow epitaxial thin films, bulk crystals of a wide variety of elements and compounds (inorganic and organic) have also been prepared in useful sizes. Seeds are often used but many studies have involved heterogeneous nucleation on the walls of an ampoule. Vapor grown bulk crystals have been particularly useful for the preparation of small crystals for physical property studies, and in a few cases larger crystals, such as SiC and CdS, have found commercial markets. Crystals prepared by vapor techniques include halides, chalcogenides, oxides, pnictides and organic compounds. Growth rates vary for different materials systems and process details, but generally tend to be slower than melt growth methods. Comprehensive reviews of vapor growth theory and methods have been given by Kaldis [270], Faktor and Garrett [271], and Wilke [272].

1.3.3.2 Bulk Growth

1.3.3.2.1 Physical Vapor Transport

A volatile compound that congruently sublimes (or evaporates from the liquid state) can form crystals when it condenses in a cooler region of a furnace. In its simplest form, a closed glass ampoule containing the source at one end is placed in a temperature gradient. The source sublimes at a selected temperature and condenses at the cooler end either as self-nucleated crystallites or on a seed crystal. When no seed is used, many nuclei usually form and some may outgrow the others due their temperature of deposition or their orientation with respect to the heat flow in the system. In 1954, Pizzarello [273] made an important modification to the method that helped improve crystal size and quality. It involved translating the ampoule in the furnace gradient and has some similarities to zone melting with the source and crystal separated by the gas phase rather than the melt. The amount of vaporization at the source end is balanced by amount deposited on the crystal [274]. This "zonal sublimation method" has been used to grow doped crystals of Cd and Zn chalcogenides (see Ref. [275]). Both vertical and horizontal methods have evolved. By controlling the nutrient flux toward the growth interface, seeded growth is possible. This was demonstrated both by Fochs in 1960 with CdS [276] and by Prior in 1961 with PbSe [277].

Some refractory materials such as SiC and ZnO require high temperatures to achieve useful vapor pressures. SiC and ZnO are important wide bandgap, high-temperature/high-voltage semiconductors. Large crystals are sought-after for the

fabrication of substrates. Since melt growth would require pressures of 100,000 atm and 3200 °C, other growth methods were sought. Various novel growth chambers and heating methods were developed for the vapor growth of these crystals. One of the earliest was by Frisch [278] in 1935. He grew ZnO needles by sublimation of a ZnO pellet heated to very high temperatures. In 1955, Jan Anthony Lely [279] developed a sublimation process for growing SiC single crystals that forms the basis of all commercial processes today. In his method, silicon carbide was placed in a graphite crucible and heated to 2500 °C in an argon atmosphere. Large hexagonal platelets of 6H–SiC formed. The crystals were of different sizes up to 2×2 cm^2 and were of very high quality. In 1978, Tairov and Tsverkov [280] modified the process to include seeding. They placed the source at the bottom of the reactor and the seed at the top. Growth rates of 0.5–1 mm/h were achieved. Further modifications have been made since then, and now crystals greater than 50 cm in diameter can be produced. The formation of defects in these crystals, in particular micro-pipes has been a challenging problem [281]. Much effort has gone into their reduction or elimination.

Large crystals of organic compounds such as urea have also been grown by sublimation techniques [282]. However, the formation of gaseous byproducts such as ammonia during growth were problematic. To remove these unwanted species, which either slowed down or stopped the growth process, a vacuum pumped effusion hole was incorporated into the ampoule. Large cm-size high-optical-quality boules of urea were grown on [001] seeds at rates of 2.5 mm/day (by comparison growth from methanol solutions was 0.3 mm/day). The reactor used for the PVT growth of large urea crystals is shown in Figure 1.14.

1.3.3.2.2 Chemical Transport Reaction

When a material is nonvolatile under convenient processing conditions, it can often be chemically converted into a volatile species. Crystal growth can then proceed in a reversible process. This method is called the chemical transport reaction method (CRT). For example, ZnSe crystals can be grown in a sealed ampoule in the presence of a small amount of I_2 vapor (the transport medium). The ZnSe charge at the hotter end will react to form ZnI_2 (v) + Se (v). These gaseous species will then be transported to the cooler end reforming ZnSe on the growing crystal and thereby releasing I_2. The freed iodine can then react with more ZnSe source material and return to the growth zone. In this case, for deposition at the cold end, the required conditions are that the enthalpy (ΔH) and entropy (ΔS) are <0. For materials where ΔH and ΔS are >0 deposition takes place in the hot zone.

The chemical transport method is based upon the pioneering work of Van Arkel and de Boer [283]. In 1925, they prepared the refractory metals titanium, hafnium and thorium using this iodine transport technique with deposition taking place on a heated wire. By 1963, the field had expanded to encompass many different materials using a variety of transporting agents. Harold Schafer's book entitled *Chemical Transport*

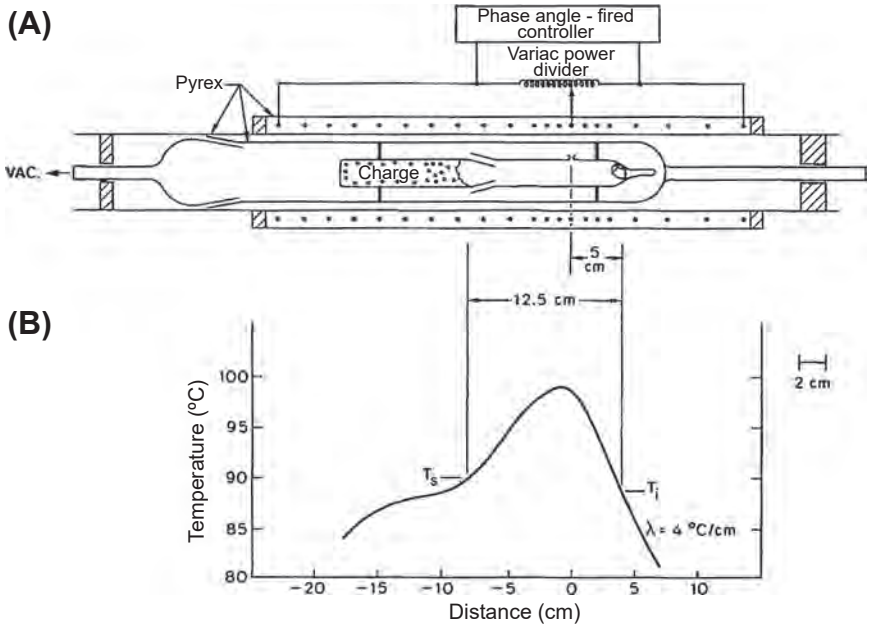


FIGURE 1.14 An example of a physical vapor transport bulk crystal growth apparatus. This growth system was used for growing urea crystals [282].

Reactions [284] has been an invaluable reference source for workers in the field since 1964.

Some important process requirements include (1) a chemical reaction that produces only one stable phase, (2) a free energy close to zero to facilitate reversibility, (3) a non-zero ΔH^o and (4) the ability to control nucleation and the growth kinetics via crystallization zone temperature, temperature gradients, etc. Dopants have been added by incorporating volatile species of the desired element(s) into the growth ampoule. The choice of transporting agent is based on the thermodynamic propensity for the volatile species to form and dissociate in a useful temperature range. Sometimes additional species such as CO are added to the ampoule to facilitate the desired reaction. Sagal showed in 1966 that the growth of Y_2O_3 crystals solely by halogen transport was not favored due to relatively high values of ΔG^o (near 60 kcal/mol for the Cl_2 gas and higher for Br_2 and I_2) [285]. However, by adding CO to Br the ΔG^o value could be shifted closer to zero. The reaction therefore would be:

$$Y_2O_3(s) + 3CO(g) + 3Br_2(g) \rightleftharpoons 2YBr_3(g) + 3CO_2(g) \tag{1.5}$$

During the 1950s and 1960s, considerable research work was in progress using the CTR method. Metals such as iron, cobalt, copper and nickel crystals were produced, as well as classical semiconductors such as silicon, gallium arsenide and gallium phosphide. In addition, various oxide crystals such as alumina, beryllia and silica were grown.

1.3.3.2.3 Chemical Vapor Deposition

The same basic chemical transport process can be use in open systems; however, the process is not reversible. This method is typically known as chemical vapor deposition (CVD). Its most important application by far is the growth of epitaxial thin films to be discussed later. Bulk crystals or thin oriented films are grown by reacting and/or decomposing one or more volatile precursors in the vapor state and depositing them onto the crystal or substrate. These sources can be in many forms; gases, liquids, solutions and aerosols. Any unwanted reaction byproducts can exit the system in the gas stream. Very pure crystals can be produced by this method depending on the type of precursor used. Perhaps the earliest example of this technique was reported by Lorenz in 1891 [286]. He reacted Cd vapor with H_2S gas to form fairly large crystals of CdS. In 1947, Frerichs [287] modified the technique by using a slow stream of H_2 gas to drive the H_2S over Cd metal that was heated to 800–1000 °C. His open tube system produced crystals up to 2 cm^2. An extensive discussion of bulk crystal growth from the vapor phase is given by Schönherr [288]. He provides many useful and practical details including the various methods used, ampoule designs and furnace systems, etc. Bulk growths can be grown in vertical or horizontal configurations or any angle inbetween. Translating the growth chamber or ampoule in a temperature gradient is an often-used procedure. The reactors can be operated at pressures ranging from atmospheric to ultra-high vacuum. Materials produced by the CVD method include refractory metals (such as tungsten), semiconductors (such as silicon and III-V compounds), oxides (such as SiO_2), silicon carbide, nitride and oxynitride, and various carbon structures, including diamond as discussed later. Since the late 1990s, it has found use in the preparation of nanocrystals, one important example being carbon nanotubes and fibers. The nanotubes can be produced by a number of methods including the catalytic decomposition method [289], a CVD technique using metal catalysts together with hydrocarbon precursors. Depending on the details of the process, i.e., the metal catalysts used, etc., aligned single- or multi-walled nanotubes can be produced.

1.3.3.3 Vapor Phase Epitaxy

1.3.3.3.1 Organometallic Vapor Phase Epitaxy

Organometallic vapor phase epitaxy (OMVPE aka MOCVD) is a subset of the more general Chemical Vapor Deposition (CVD) method. It uses at least one organometallic precursor (OM) but may also be combined with other types of volatile species to produce films of many different II-VI and III-V semiconductor compounds and their solid solutions. Like other methods, there are lots of variations in technique. One of the earliest recorded descriptions of the OMVPE process was in Scott et al.'s little known 1957 United Kingdom patent [290]. In it, he describes the deposition of InSb in a cold wall reactor by the pyrolysis of a Group III alkyl (i.e., triethylindium) and a Group V hydride (i.e., stibine-SbH_3). The second, in a 1965 U.S. patent, described the pyrolysis of a Group III alkyl (i.e., triethylindium or trimethylgallium) and a Group V reactant such as arsine to produce a III–V semiconductor [291]. However, the first published work in the

scientific literature was in 1969 in a paper by Harold Manasevit and W. Simpson [292]. They grew single crystal Ga-group V compounds on insulating, GaAs, GaP or Ge single crystal substrates. Either trimethylgallium or triethylgalllium in the presence of arsine, phosphine and arsine-phosphine or arsine-stibine gas phases was used in these experiments. In 2004, Manasevit, now considered one of the founders of OMVPE technology, published his recollections on how the OMVPE field developed [293]. A schematic drawing of his apparatus is shown in Figure 1.15. Along with his colleagues at the Autonetics Division of North American Rockwell, Manasevit published numerous other papers on this topic. In 1975, Seki et al. [294] produced the first important device quality (i.e., very high mobility) GaAs layers. This advancement was due to the enhanced purity and crystalline perfection of the films. Other major technological advancements followed soon afterward.

One of the important virtues of the OMVPE method is that it is can be used to grow epitaxial semiconductor alloy films. In 1977, Dupuis and Dapkus [295] grew low oxygen and carbon films of AlGaAs by the OMVPE method. This material had excellent minority carrier lifetimes making them useful for light-emitting diode devices. In 1978, Gerald Stringfellow, from the Hewlet-Packard Laboratories, both proposed [296] and demonstrated [297] that with OMVPE one could grow very bright LEDs from AlInP and AlGaInP epitaxial films.

In the 1960s, Isamu Akasaki's group at Nagoya University started working on GaN-based LED's devices. In 1989, his work culminated in the invention of a bright gallium nitride p-n junction by using the low temperature OMVPE method with an AlN buffer layer on sapphire [298]. A major step was in creating p-type GaN using magnesium as the dopant and n-type with silicon. In 1994, Nakamura et al. [299] grew the first very bright InGaN/AlGaN double-heterostructure blue-light-emitting diodes also on

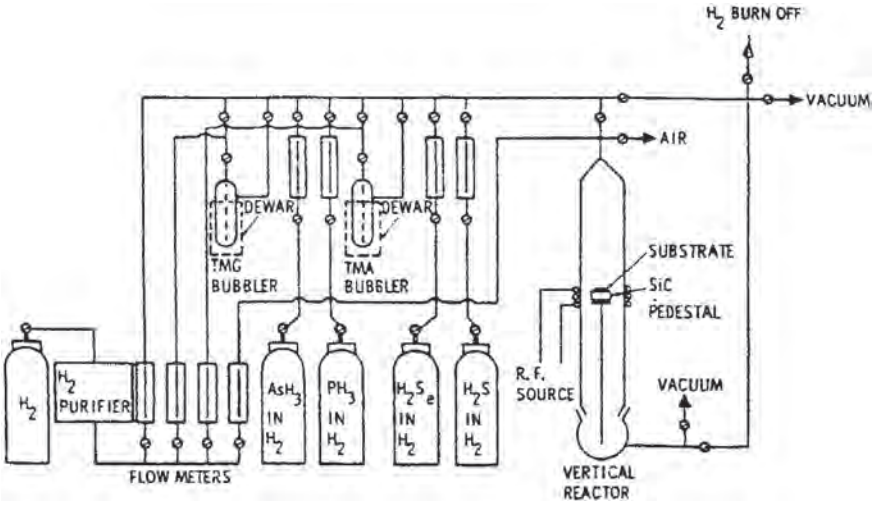


FIGURE 1.15 Schematic drawing of Manasevit's MOCVD deposition system [293].

sapphire substrates using a two-flow OMVPE method. The work of Nakamura's group at the Nichea Chemical Company, as summarized in Ref. [300], was a pivotal step in the development of the now multibillion dollar industry centered on the fabrication of highly efficient GaN-based/sapphire epitaxial films for optoelectronic devices. OMVPE development since then has been continuous with emphasis not only on improving the quality and properties of the epilayers, but also the quality and cost of the sapphire substrates. In an example of a more recent work (2002), Liu et al. [301] grew GaN single crystal epitaxial layers on sapphire in a three-step process using the low-pressure OMVPE method together with an AlN buffer layer and via atomic layer epitaxy (to be discussed later).

Stringfellow reviewed the development and status of the OMVPE method several times (e.g., Refs [297,302]). In the latter, he commented "One reason that OMVPE is so widely used today is that it is the most versatile technique for the growth of materials and structures for a wide range of devices."

1.3.3.3.2 Molecular Beam Epitaxy (MBE)

Molecular beam epitaxy (MBE) is a process in which a thin single crystal layer is deposited on a single crystal substrate using atomic or molecular beams generated in Knudsen cells contained in an ultra-high vacuum chamber. The source beams can be created in a number of ways, including (1) melting and evaporation of solids or liquids contained in crucibles (2) solid sublimation from a crucible, (3) ion beam bombardment, and (4) cracking various chemical species, etc. Its greatest use is for making multilayer semiconductor device structures. Details of the MBE method, as well as other bulk and thin film growth techniques used to prepare compound semiconductors, are given in Ref. [303].

One of the earliest published studies on the use of the MBE method for single crystal film growth was that of Joyce and Bradley [304]. In the mid-1960s they grew homoepitaxial layers of Si from SiH_4. The growth rates were very low comparative to other Si film methods and therefore not competitive in a market that needed 10 um-thick films. A few years later, J. Davey and T. Pankey [305] from the Naval Research Laboratory, and J. Arthur [306] and A. Cho et al. [307] from Bell Laboratories expanded the MBE method for the deposition of GaAs. Arthur focused on surface kinetic studies, Davey and Pankey grew large-area GaAs epitaxial films on GaAs and Ge substrates using the three temperature technique, while Cho focused on device applications. The MBE technique is a powerful method both for film deposition and in situ analysis. It has yielded, in addition to device structures, a wealth of data on the surface atomistic phenomena such as surface reconstruction. It has also been applied to other semiconductor material systems such as the nitrides and has facilitated the construction of novel structures such as periodically poled GaAs for IR nonlinear applications and quantum dots. Today, it is a very important research tool and is used extensively in commercial optoelectronic device processing. A historical review of the MBE method was given by Joyce and Joyce in Ref. [308].

1.3.3.3.3 Sputtering

In 1852, Sir William Robert Grove (1811–1896), a noted Welsh judge, physical scientist and inventor of the fuel cell, was the first to discover the deposition process now known as sputtering [309]. He was able to deposit material from the tip of a wire in a chamber at a pressure of 0.5 Torr onto a polished silver surface when the latter was the positive electrode in an electrical circuit. An interesting factoid is that the first commercial application of the sputtering method may be attributable to Thomas Edison who early in the development of his wax phonograph cylinders using a sputtering methodology for plating them.

The sputtering method, as used to prepare thin films, became popular and of commercial importance from the mid-1960s onward. It has the advantage of not requiring high temperatures to deposit materials, even very refractory ones. The films have compositions similar to the target material and large areas can be deposited. While this physical vapor deposition method is more often used to deposit polycrystalline and amorphous films, single crystal films have been produced by carefully controlling the processing parameters. The method is used for fabricating integrated circuits, antireflection coatings, solar cells and optical waveguides, etc. Typical materials sputtered include metals, semiconductors, oxides, and nitrides, etc.

The simplest sputtering process involves just a temperature-controlled cathode and anode, a source of energetic particles, i.e., ions or atoms, and a vacuum chamber. A DC potential of several thousand volts is usually maintained across the electrodes. Radio frequency sputtering, where the sign of the electrodes is varied at a high rate, has also been found beneficial. The material to be deposited is ejected from the target (at the cathode) by bombarding it with ions or atoms, and the ejected material is transported in the plasma formed to the substrate (at the anode). In addition to the ions released from the target, electrons are also produced and they play an important role in maintaining the plasma. However at the same time they can cause excessive heating of the substrate. The transport mechanism within the gap between the two electrodes is complicated and depends to a great extent on the background gas pressure. For efficient ejection, the sputtering gas should have a similar atomic weight as the target elements. Nonreactive gases such as argon, krypton and neon are often used to eject atoms from the target, but reactive sputtering, using oxygen or nitrogen gas, has been employed to deposit oxide and nitride films (e.g., ZnO and TaN). In the latter process a chemical reaction takes place between the gas and the sputtered ions near the cathode before being transported to the substrate. Higher substrate temperatures encourage the deposition of single crystal films. Williams has given an extensive overview of the sputtering field and sputtered ion emission [310].

Conventional sputtering has some disadvantages including low deposition rates, low ionization efficiencies and substrate heating. One major improvement to this technology was the introduction of magnetron sputtering [311]. In this process a magnetic field is incorporated into the sputtering apparatus with the magnetic field positioned parallel to the target and confining the secondary electron movement close to the target. This

maximizes the probability of electron–atom interactions, increasing ionization efficiency. The result is higher sputtering and deposition rates. It also permits the use of lower operating pressures and voltages. The magnetron was originally conceived by P.M. Penning in 1936 [312]. In 1980, Naoe et al. [313] were the first to use it in a sputtering application. Over the years magnetron sputtering configurations have been modified, and these developments have led to improved film quality and device performance [311].

1.3.3.3.4 Atomic Layer Deposition

In 1977, Dr Tuomo Suntola from Helsinki University in Finland patented a novel technique to prepare highly oriented compound thin films [314]. The method was called atomic layer epitaxy (ALE). More recently, the nomenclature atomic layer deposition (ALD) has been favored. The ALD technique provides precise control of the film thickness and composition and with the proper substrate composition, orientation and temperature, can produce single crystal thin films. It involves the periodic (alternating) pulse deposition of a film's components in a vacuum chamber. In between pulses there is an equilibration period during which the excess components can desorb from the surface and exit the growth chamber. This leaves just one atomic layer on the substrate surface. The next atomic species is then deposited, and a controlled chemical reaction at the surface between these two layers creates the desired film composition or composite structure. By way of example, to produce an epitaxial ZnS film by this technique, a single Zn atomic layer is first deposited on the substrate surface. This layer is then exposed to S_2(g) or H_2S(g), either of which react with the Zn layer to form the compound ZnS. Following equilibration, another Zn layer is deposited and then reacted again with the sulfur-containing gas. The thickness is determined by the number of cycles employed.

Historically, the idea for a sequential layering film deposition process was first mentioned in the 1952 thesis of Professor V. B. Aleskovskii as molecular layering. And years later, (during the 1970s) his group in Russia worked on the developing this concept further [315]. The efficacy and implementation of the method into a commercially viable process derived from the work of Suntola's group during the years prior to their patent application. For a definitive review of all aspects of the methodology, see Suntola [316].

The ALD technique can produce atomically flat films with almost perfect stoichiometry and surface conformity through the self-limiting reaction mechanism. It can be used with many of the chemical vapor deposition methods described above that normally deposit the requisite phases simultaneously. It can be used to produce layered films with abrupt interfaces (e.g., TiO_2/Al_2O_3 films [317]), and M. Ritala and M. Leskela [318] reviewed the method's features and its potential role in nanotechnology. One of the drawbacks of the ALD method is the slow deposition rates. This has been somewhat overcome by increasing the substrate areas during deposition. The use of bias sputtering has given the best stoichiometry to date. Besides oxides and chalcogenides, as mentioned above, the method has also been used for the preparation of various semiconductors, nitrides, and metal films.

1.3.3.4 The VLS Method

Another interesting and useful growth method is the vapor-liquid-solid (VLS) technique. This hybrid method combines chemical vapor deposition with solution growth. Deposition takes place at localized positions on a single crystal substrate to yield a nanostructure, particularly whiskers, rods and nanowires. It starts with a single crystal substrate patterned with an array of small dots made from a solid metal solvent phase (the "catalyst"). The patterning can be done using lithography or by converting a solvent film deposited on the substrate surface to droplets. The growth procedure is simple. When the substrate is heated, the solvent phase melts. The liquid phase rapidly supersaturates by adsorption of nutrient species from the gas phase. Growth subsequently takes place at the substrate–liquid interface and not on the bare substrate surface. The solvent region rises up, as a mass is deposited below it, thus propagating the growth feature. The molten zone remains on the fiber tip during growth. As an example, silicon nanowires have been produced from a Au–Si alloy droplet and with a gas phase containing $SiCl_4$ and H_2 (see Figure 1.16 below). The VLS method has been used in conjunction with CVD, MBE, laser ablation and carbothermic reduction.

The VLS method was first described in 1964 in the pioneering work of Bell Laboratories scientists R. Wagner and W. Ellis [319] (see Figure 1.16). The VLS

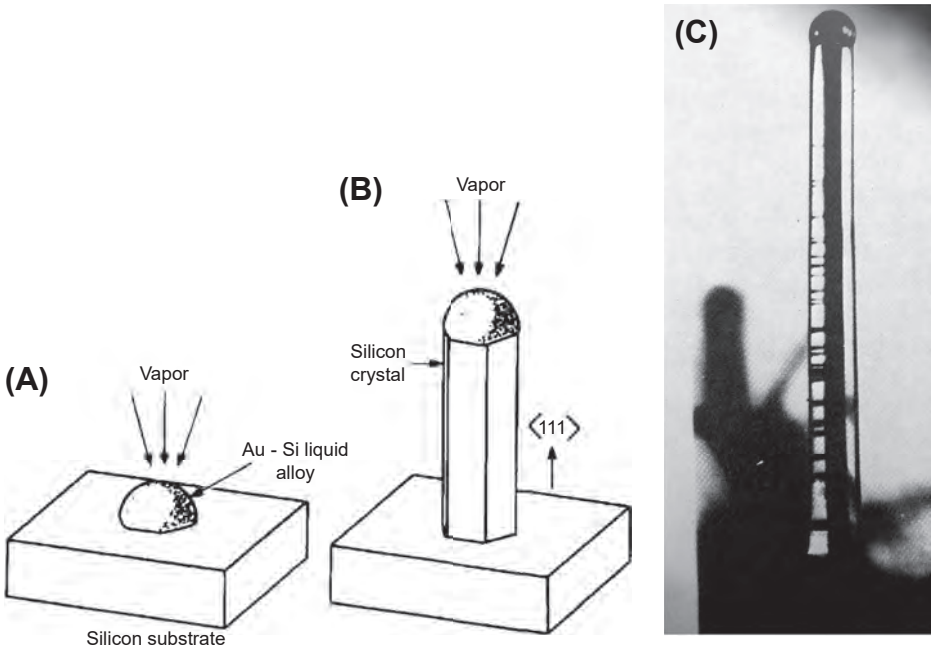


FIGURE 1.16 Original schematic diagram of the VLS process for Si whisker growth on a silicon substrate, (A) Au–Si alloy catalyst droplet on substrate surface before growth. (B) A growing whisker. A photograph of an actual Si whisker (0.5 mm diameter) grown on a {111} Si substrate is shown in (C). It has 12 side facets alternating between the {211} and {110} [318].

mechanism they proposed explained the growth of silicon whiskers on silicon substrates in the absence of the axial screw dislocation growth model described by Frank [22]. Some advantages to the VLS growth process include a lower reaction energy than with regular vapor growth techniques, the structures only grow where the solvent is located, and anisotropic-shaped columns can be produced. Important process parameters include (1) the wettability of the liquid droplet and its reactivity with the substrate, (2) the substrate orientation and surface roughness, (3) the processing temperature, etc. It is also very important and obvious that the solvent phase has to have a low equilibrium vapor pressure.

Some of the popular semiconductor materials grown by VLS include Si, Ge, GaAs, GaN, SiC and ZnO. Gold is most often used as the solvent phase, but other materials such as Ni, Pt have been successfully used. The substrates may be of the same or similar composition as the growth pillars (homoepitaxy) or on different material (heteroepitaxy). One example of the latter is the growth of densely aligned GaN wires grown on sapphire, $LiAlO_2$ or MgO substrates [320]. Schmidt et al. discussed various aspects of the growth of silicon nanowires and their electrical properties, including use of the VLS method [321].

The VLS method has been easily adapted to the growth of nanostructures. This has become a very important active area of research and should lead to exciting new commercial applications in the foreseeable future. One of the leading groups in this area is Lars Samuelson's group at Lund University. They have reviewed the fundamental mechanisms involved in the VLS processing of nanowires and the prognosis for further development of this technology [322]. Many new and unique structures have been created using the VLS process. One example being a decade old study that showed that certain material systems can phase separate into cored nanofibers. In a one-step VLS process, Choi et al. [323] grew GaN cored nanowires with a thick AlGaN skin. Other techniques have also been used to coat the nanowires. An excellent review of the VLS method was given by Choi [324].

1.3.3.5 Artificial Epitaxy (Graphoepitaxy)

Up to now, we have discussed the epitaxial growth of single crystal thin films on substrates made from materials of related composition and/or structure. The usefulness of high-quality single crystal or highly oriented films is well-known and crystalline perfection of the film depends on various attributes of the substrate and its quality. However, it would be highly desirable to be able to grow oriented films on inexpensive amorphous substrates or on substrate layers important to device function. In the early 1970s, Prof. N.N. Sheftal from the Russian Institute of Crystallography first described the concept of growing films on an artificial lattice. The paper, which described the technique as "artificial epitaxy," was translated into English three years later [325]. In 1982, the technique was renamed "graphoepitaxy" [326], and this more catchy term has gained favor in much of the subsequent literature.

Graphoepitaxy involves inscribing a micro-relief pattern onto a flat amorphous substrate surface. The surface patterns consist of only four symmetries, two-, three- four- and

six-fold (i.e., arrays of stripes, triangles, squares and hexagons). The walls of the relief pattern simulate the kinks and ledges associated with a crystal growth surface as described by the Kossel-Stranski model. Rather than atoms or molecules, however, the growth units that attach to these relatively large steps are microcrystallites of nanometer or micron sizes. The pattern chosen is determined by the crystal structure of the material to be deposited. For example, the three-fold relief would be used for the growth of the diamond lattices of Si and Ge. The reliefs can be achieved by a number of techniques including photolithography and etching, etc.

Graphoepitaxy can be accomplished using a variety of gas phase, melt or solution growth techniques, including the VLS method mentioned above. Like other methods described in this chapter many different materials have been prepared by graphoepitaxy, including very large-molecule biological materials [327]. By way of illustration, Figure 1.17 shows two crystals of catalase (an enzyme) that were deposited from an aqueous solution onto a silicon substrate that contained a striated micro-relief [327]. The pattern used here had a 5 μm periodicity and a groove depth of 1–2 μm. The crystals are clearly aligned with the micro-relief. Deposited on an unpatterned substrate, the crystals would have no orientational relationship with one another.

Graphoepitaxy has also been used to prepare oriented single crystal nanowires of semiconductor oxides such as ZnO, SnO_2, In_2O_3. The method has been exhaustively covered in a book by Givargizov [328]. Since this book was written, the technique has become very popular, particularly in the semiconductor field. For example, so-called nano-graphoepitaxy has been used to prepare semiconductors for three-dimensional integration devices [329].

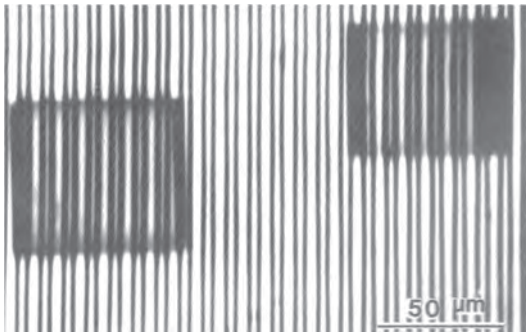


FIGURE 1.17 Two catalase crystals grown from solution onto an oriented Si substrate having an etched micro-relief pattern. The crystals, which are aligned with the pattern, grew by artificial or graphoepitaxy [327].

1.3.4 Synthetic Diamond Crystals

Diamond, while highly sought after as a gemstone, also has a unique combination of properties that make it very useful in industrial applications. Diamond not only has the highest known hardness, it also has a very high thermal conductivity and electron mobility, low thermal expansion coefficient and excellent optical transmission over a

broad spectral range. In addition to its major commercial market, i.e., cutting tools and polishing powders, diamond has a myriad of other uses. Diamond-based devices include high-power electronic devices, high-frequency field effect transistors, LED's, ultraviolet and high-energy particle detectors, substrates and optical windows. The two principal methods used to grow synthetic diamonds are (1) crystallization of bulk crystals from solution at high pressures and temperatures (HPHT) and (2) deposition at low pressures and relatively low temperatures using the chemical vapor deposition (CVD) method. Both were developed during the early 1950s within a few years of each other and are still in use today to manufacture synthetic diamond products.

The earliest known reference to diamond can be found in the Old Testament [330]. It was not until near the end of eighteenth century that it was realized that diamond, while transparent and colorless, was made up solely of carbon atoms like graphite. The discovery came from the French chemist Antoine Lavoiser (1743–1794), who shortly before his death, decomposed a diamond by heating it in oxygen and found CO_2 as the only byproduct. Thereafter, a number of credible researchers tried to synthesize diamond, one of the first being Scottish chemist James Hannay (1855–1931). His attempts in 1879 [331], later questioned, were followed in 1895 by the French Noble Prize-winning chemist Henri Moissan (1852–1907). He tried to synthesize diamond in the laboratory [332] starting with charcoal and iron heated to temperatures as high as 3500 $^{\circ}$C using an electric arc furnace. The heated mixture was then quenched in water to hopefully create the high pressures under which diamond formed in nature. Other researchers who tried to duplicate these studies either failed or had their various claims discredited. Sir Charles Algernon Parsons (1882–1922), the inventor of the steam turbine, spent considerable time and energy over many years trying to duplicate the work of Hannay and Moissan. He also tried to develop his own method to produce diamond. In 1928, as reported by Desch [333], Parsons concluded that synthetic diamonds had not been produced. Kathleen Lonsdale used X-ray diffraction methods to study some of Hannay's "diamonds" held at the British Museum. She concluded in a 1962 paper [334] that they were natural diamonds and doubted that "… neither Hannay, Moisson or Parsons ever, in fact, made diamonds by their respective methods." Percy Bridgman, who as mentioned before won a Nobel Prize for his high pressure work, spent the better part of 50 years (from 1905 to 1955) trying to synthesize diamond. His efforts were apparently unsuccessful as well [330]. In addition to the researchers mentioned above, the nineteenth century was littered with numerous unsuccessful attempts to synthesize diamonds by various means. One particularly engaging and well-researched book on the history and growth of diamond crystals is *The Diamond Makers* by Robert Hazen [335].

In 1941, the General Electric Research Laboratories, in conjunction with the Norton and Carborundum companies, set about to develop a process to synthesize industrial diamonds. The effort was suspended during WW II but started up again in 1951. While GE put together a large staff charged with designing a furnace that could go to both high pressures and high temperatures, it was not until H. Tracy Hall, came

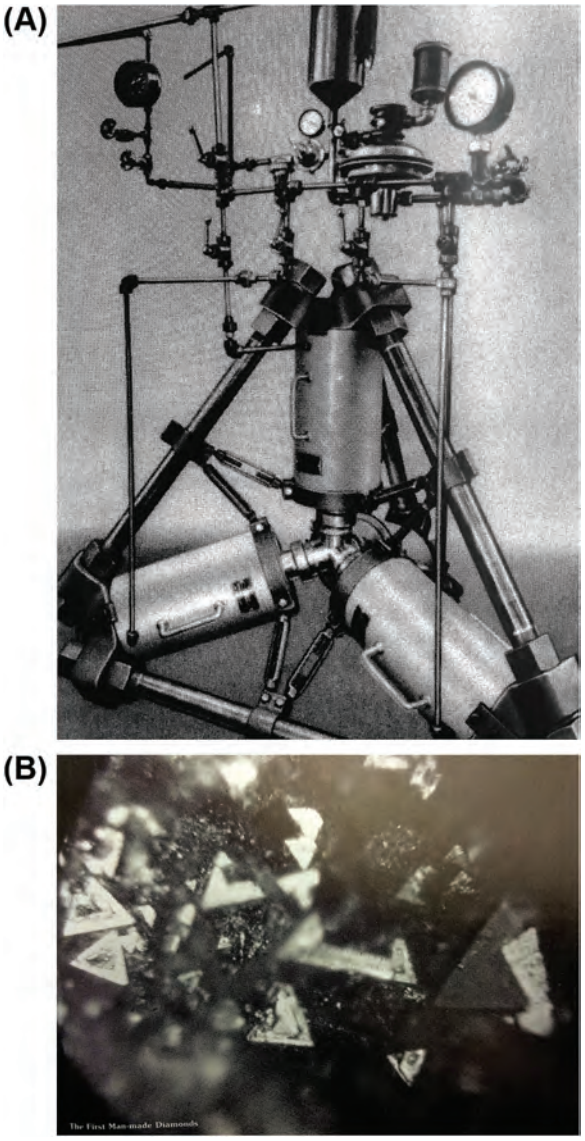


FIGURE 1.18 Early diamond crystal growth (A) Schematic of the belt high-pressure, high-temperature apparatus built at the General Electric Corp., and (B) the first synthetic diamonds produced using this apparatus [330].

up with the "Belt" press (see Figure 1.18(A)) that a breakthrough was imminent. This device exceeded the original specifications of 35,000 atm and 1000 °C to achieve 250,000 atm and 1800 °C [336]. The growth chamber consisted of a graphite tube surrounded by a pyrophyllite container. Inside were placed Ni, Fe, or Co to act as a solvent-catalyst in which the graphite dissolved. The bottom was in contact with a Ta disc. However, even with this capability, diamond was not readily produced. It was

not until the end of 1954, after much experimentation and frustration, that the first small, micron-sized faceted diamond crystals were produced (see Figure 1.18(B)). The addition of FeS to the container did the trick. These were not gem-quality stones but appropriate for abrasive applications. Hall's personal reminiscences, given in Ref. [330], describe how the process was invented and the subsequent events that led to his other important invention—the tetrahedral anvil press shown in Figure 1.19. Oddly, just before the GE success, the Swedish company ASEA, also managed to produce small diamonds in a top-secret project that only went public in 1980 [337].

The first successful preparation of gem-quality diamonds by HPHT was in 1970, again accomplished by GE. The process was similar to that described above with the addition of thin diamond seeds. The first crystals were 5 mm (1 carat) in size and took a week to grow. Longer growth times were required to produce larger crystals. These early crystals were yellow or brown in color due to nitrogen contamination and contained inclusions. By adding nitrogen getters such as Al and Ti, clear colorless crystals could be produced. On the other hand, other dopants have been used to modify the color of synthetic diamonds (e.g., boron gives it a blue color). A variety of colored stones have been produced.

The inherent technological difficulty in preparing diamonds or other materials at high pressures and temperatures and the high cost of equipment led many researchers,

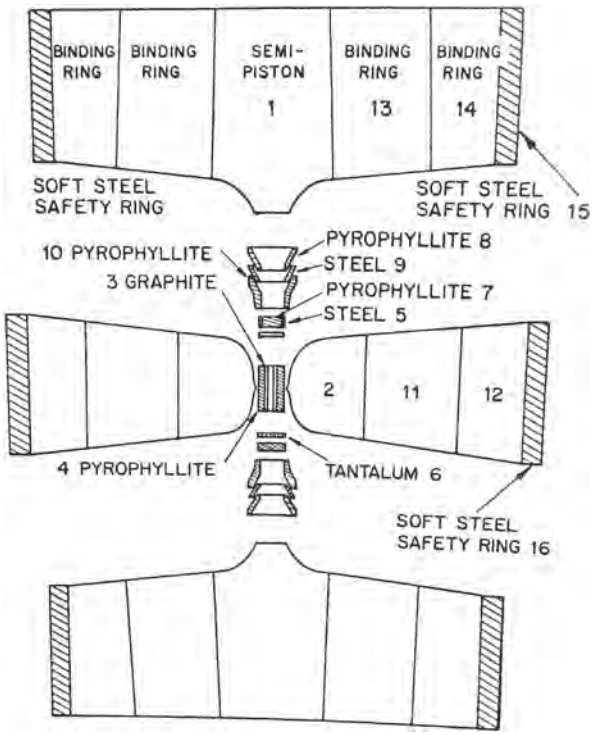


FIGURE 1.19 The original tetrahedral press for producing synthetic diamond [330].

particularly in the U.S. and the Soviet Union, to try to find a low-pressure method. Not many scientists, however, thought this would be possible. Nevertheless, in 1952–1953, William Eversole, at the Union Carbide Corporation, became the first person ever to prepare synthetic diamonds [338] by the chemical vapor deposition technique. It involved slowly depositing carbon atoms on clean diamond particle surfaces (i.e., substrates) in a vacuum at temperatures in the 800 °C range. Carbon monoxide (CO) or methane (CH_4) was used as the source of carbon. Due to the propensity for graphite formation under these conditions, the residual graphite had to be removed after a period of time. This involved removing the crystals from the deposition chamber and cleaning them in an autoclave at 1000 °C and 50 atm of H_2 gas. Numerous such cycles were required. While he accomplished this feat about two years before General Electric and just a few months before ASEA in Sweden [337], his work (described in a patent only) was not published until 1962. In 1968, John Angus [339] independently verified Eversole's work, as did Deryagin and Fedoseev in 1970 [340]. While Angus also deposited diamond on single-crystal diamonds, Deryagin and Fedoseev made epitaxial films on other substrate materials such as Si and metals. From this point onward this very versatile method was aggressively pursued and refined by a number of groups in the USSR (Russia), the U.S. and Japan for the growth of both bulk crystals and homoepitaxial films on diamond substrates and by heteroepitaxial growth on suitably oriented materials like Si. A useful review of diamond growth by the chemical vapor deposition method was written by Garcia et al. [341].

One of the initial problems with the commercialization of CVD bulk diamond was the slow growth rates. In 1969, the former USSR scientists Spitsyn and Dervagin, who had been working on this problem since 1956, were finally able to increase the growth rates reported by Eversole by an order of magnitude. The improvement over their own previous work was due to the use of methane at higher pressures (13–40 Pa), together with an increased deposition temperature (950–1050 °C). Just a year later, a significant breakthrough was made independently by J. Angus (USA) and V. Varnin (USSR) [342]. They found that the use of atomic hydrogen in the growth chamber would remove the graphite co-deposits that form along with diamond due to a large difference in etching rates. A decade later, a group of researchers at Japan's National Institute for Research in Inorganic Materials made a series of important process improvements. They developed the microwave plasma, hot filament, and RF-Plasma CVD methods, new ways to dissociate the carbon-containing gases into reactive species [343–345]. Growth rates up to several μm/hr were achieved. This in turn led to the development of a variety of other processes and process refinements by this and other groups, leading the commercial success of the CVD method for a variety of diamond products including gemstones and coatings for various types of electronic and optical devices.

Two other methods have been employed for growing small-size diamonds. One is the explosive detonation method in which a carbon-based explosive is detonated inside a metal tube containing graphite [346]. The procedure, an HPHT process, produces

nanoscale diamonds. The diamonds are prevented from reconverting to the more stable graphite form due to the quenching effect of a surrounding water-filled chamber. However, they have to be separated from the remaining carbon by dissolution in acid. The second method is the ultrasonic cavitation technique [347]. This more recent process is carried out at room temperature and atmospheric pressure. It involves the application of ultrasonic energy to a suspension of graphite particles in an organic liquid and results in micron-sized diamond crystals.

1.3.5 Solid State Recrystallization

The next to last topic to be covered in this chapter is the growth of sizable single crystals from the solid phase. This technology has a much smaller impact on the crystal growth field than the other methods described above. First, it is mainly limited to metals, and second, there are various processing difficulties associated with controlling nucleation and growth over extended length scales. The mechanisms involved are related to ceramic and powder metallurgy processing, where control of crystallite (grain) size and morphology in polycrystalline structures is a major concern. There are a myriad of important industrial applications for these polycrystalline materials (piezoelectric elements, magnets, etc.) and all aspects from theory to sample preparation are covered in various books on ceramics and powder metallurgy. The use of solid-state methods for crystal growth is covered in the book by R. Laudise [285].

At the heart of solid-state crystal growth (recrystallization) is grain growth. As mentioned before, the method is mainly used with metals such as aluminum, tungsten and iron. The material from which the crystal is grown contains grains of varying sizes and morphologies, plus grain boundaries and dislocations. Single crystals can be formed by controlling the growth of preexisting grains or by nucleating new grains with lower free energies. Wilhelm Ostwald's pioneering work in 1896–1897 explained how crystallites behave at elevated temperatures [348]. He showed that smaller particles adjacent to larger ones would decrease in diameter while the larger grains increased in size (an effect now known as Ostwald ripening). When the more energetic surface atoms on the smaller crystallites redeposit on the larger grains, the total energy of the system decreases. The driving force for grain growth can also be related to orientation differences between grains.

The principal method used to grow large metal crystals involves strain annealing techniques. A suitable polycrystalline sample, a bar, rod, plate, etc., is strained by one of a number of techniques such as rolling, drawing and extrusion. It then may be fabricated into a suitable shape to facilitate growth. The amount of strain induced is usually between 1 and 10% and the amount is critical in controlling the nucleation of strain-free grains. Growth is most often done in a temperature gradient and nucleation control is similar to other growth methods. In some respects, it is related to the Bridgman–Stockbarger method where the sample can be a rod with a tapered

end that is translated through the gradient. The gradients, however, are reversed from melt growth. The polycrystalline charge is heated until the tapered end reaches the recrystallization temperature and strain free grains are created in a localized region at the tip. Further movement propagates the strain-free grain(s) along the axis of the sample consuming the strained grains. If nucleation creates several strain-free grains, the sample can be notched somewhere along the length to permit only one grain to propagate through into the main part of the charge. Seeds can also be used. Suppressing nucleation ahead of the growth front has been a concern, and generally slow translation rates and sharp gradients minimize this problem (e.g., Ref. [348]).

The concept for strain-annealed crystal growth can be traced to Robert Anderson in 1918 [349]. This led, in 1921, to Carpenter and Elam's demonstration of the growth of large aluminum crystals by the strain-anneal method [350]. Over the ensuing years, various other metals have been grown by this method. One technique used to prevent random nucleation ahead of the growth interface during the strain-annealed growth of alpha iron crystals was the incorporation of pulsed heating [351]. Large, 25cm-long oriented single crystal rods and strips could be produced in a few hours using this method.

The solid-state recrystallization method has also been applied to semiconductor fabrication (e.g., Si and Ge). One technique of note is the solid phase epitaxial growth method. In 1968, L. Kulper at IBM, patented a process for the growth of aluminum-doped silicon films by the migration of silicon through an aluminum thin film during a heat treatment process [352]. The solid-state growth process provided doped layers with a maximum amount of aluminum in silicon. Later Mayer et al. [353], from the California Institute of Technology, patented a similar but more general process for doping with other species. In this process, a single crystal substrate is coated with a thin metal film having such properties that it will permit the migration of material through it to form an epitaxial layer without acting as an active dopant itself. Upon this film a dopant layer is deposited followed by an amorphous or polycrystalline layer of the material that will make up the doped epilayer. This sandwich structure is first heated to a temperature that permits the metal layer to dissolve some of the dopant, amorphous film and part of the substrate. After a time, the temperature is raised to allow the transport and epitaxial deposition of the doped layer onto the substrate. For the solid-state epitaxial growth of silicon, for example, the substrate and amorphous or polycrystalline layers would be silicon, the dopant layer might be phosphorous, aluminum, or boron, and the metal film palladium, vanadium, or nickel. A review of this technology is included in the book by Mayer and Lau [354].

Another application for solid-state crystal growth was in the preparation of piezoelectric single crystals, such as lead magnesium niobium-titanate (PMNT) [355]. The principal motivations were its potential cost advantage and enhanced

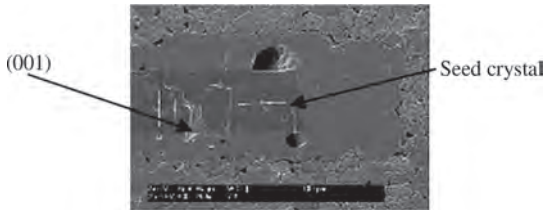


FIGURE 1.20 An example of template growth. Shown is a micrograph of a polished and thermally etched (1080 °C for 30 min) sample of $BiScO_3$–$PbTiO_3$ (BS–PT) that was heat-treated with an embedded barium titanate (BT) seed crystal (5 $mm^2 \times 100$ μm thick). A 5% excess of PbO was used in the mixture to enhance diffusion. An overgrowth of a BS–PT crystal onto the surrounding BT seed can be clearly seen [355].

manufacturing throughput over conventional crystal growth methodologies. Two techniques were explored, conventional grain growth and templated growth in which seed crystals were embedded into a powdered matrix and processed at elevated temperatures. An example of the templated growth of BiScO3-PbTiO3 is shown in Figure 1.20.

1.4 Epilogue

Crystal growth is a field that has had a major impact on modern society. The devices we have come to rely on today were made possible through the contributions of numerous scientists and engineers from a variety of disciplines. These devices are based on single crystals prepared in various ways and in forms and compositions reflecting the application intended. The foundations upon which our understanding of a crystal's structure, thermochemistry, growth mechanisms and methods is based on work from earlier centuries and dramatically expanded on all fronts (theory, growth and characterization) just after World War II. The book by Buckley in 1950 was the first comprehensive treatment (in English) of the prior art and science of crystal growth. Today, there are well over 100 books covering the topic, from surveys of the entire field to various specialized topics. This historical review of the crystal growth field is not comprehensive but was designed to highlight the major achievements. While I have tried to be as inclusive as possible, I apologize in advance if I have left out any major contributors to this field or important theories and growth methods. As a final comment, I must mention that a selection of some pioneering crystal growth papers were collected and reprinted in their original languages by D. Hurle [356].

Acknowledgments

The author is indebted to Alex Chernov, Vince Fratello, Gabe Loiacono, and Jerry Stringfellow for critiquing specific sections of this chapter, and for discussions with Al Ballman, Bill Tiller and others.

References

[1] Pliny the Elder (Gaius Plinius Secundus). Volume 9 (Books 33–35), [H. Rackham, Trans.]. Naturalis Historia circa AD 77–79. Loeb Classical Library/Harvard University Press; 1958. p. 430.

[2] Agricola G. De Re Metallica [L. Hoover and H. Hoover, Trans.]. Dover Publications; 1950.

[3] Biringuccio V. The Pirotechnia [C. Smith and M. Gnudi, Trans.]. Dover Publications; 1990. p. 477.

[4] Doremus RH, Roberts BW, Turnbull D. Proc. int. conf. on crystal growth: growth and perfection of crystals. New York: Wiley; 1958.

[5] Gessner C. De omni rerum fossilium; 1565.

[6] Caesalpinus A. De metallicis libri tres. Rome; 1596.

[7] Sunagawa I. In: Feigelson RS, editor. 50 years progress in crystal growth. Amsterdam: Elsevier; 2004. p. 35.

[8] Steno N. De solido intra solidum naturaliter contento; 1669.

[9] Guglielmini D. Philosophical reflections deducted from figures of salts from Doctor Domenico Guglielmini expressed in a speech recited in academy philosophical experimental affirmations. Archdeacon Marsigli; the evening of March 21, 1688. Bologna.

[10] Romé de l'Isle JB. Essay of crystallography or description of geometric figures. L'Academie Electorale des Sciences Utiles de Mayence; 1772.

[11] Bravais A. Mémoire sur les systèmes formés par des points distribués regulièrement sur un plan ou dans l'espace. J De l'Ecole Polytech 1848;19:1.

[12] Gibbs JW. The collected works of J. Willard gibbs, in two volumes. In: Longley WR, Van Name RG, editors. New Haven: Yale University Press; 1993. 1957 (1928).

[13] Jackson KA. In: Feigelson RS, editor. 50 years progress in crystal growth. Amsterdam: Elsevier; 2004. p. 35.

[14] Wilson HA. Phil Mag 1900;50:238.

[15] Knudsen M. Ann Phys 1909;29:179.

[16] Volmer M, Estermann I. Z Phys 1921;7:13.

[17] Kossel W, Nachr. Gesell. Wiss. Gottingen. Math-Phys. K1 1927;135.

[18] Stranski IN. Phys Chem 1928;136:259.

[19] Kossel W. In: Falkenhagen H, editor. Quantentheorie und Chemie, Leipzig; 1928. p. 46.

[20] Stranski IN, Kaishev R. Z Krist 1931;78:373.

[21] Buckley HE. Crystal growth. New York: John Wiley; 1951.

[22] Frank FC. The influence of dislocations on crystal growth. Discuss Faraday Soc 1949;5:48.

[23] Heck CM. Phys. Rev 1937;51:686.

[24] G.G. Lemmlein, Vestn. Akad. Nauk SSSR 4, 119 (1945)

[25] Donnay JDH, Harker D. Am Mineral 1937;22:44.

[26] Hartman P, Perdok W. Acta Cryst 1955;8:495.

[27] Bennema P. Growth and morphology of crystals. In: Hurle DTJ. Handbook of crystal growth, Parat 1a. North Holland (Amsterdam); 482.

[28] Burton JA, Prim RC, Slichter WP. J Chem Phys 1953;21:1987.

[29] Burton JA, Slichter WP. In: Feigelson Robert S, editor. 50 years progress in crystal growth. Amsterdam: Elsevier; 2004. p. 43.

[30] Millman S, editor. A history and of engineering and science in the Bell system, physical sciences (1925–1980). AT&T Bell Laboratories; 1983.

[31] Carruthers JR. In: Bardsley W, Hurle DTJ, Mullin JB, editors. Crystal growth: a tutorial approach. Amsterdam: North Holland; 1979. p. 157.

[32] Chernov AA. In: Feigelson Robert S, editor. 50 years progress in crystal growth. Amsterdam: Elsevier; 2004. 47 and Sov. Phys. Uspekhi 4 (1961) 116.

[33] Burton WK, Cabrera N. Discuss Faraday Soc 1949;5:33.

[34] Frenkel J. Phys J USSR 1932;1:498.

[35] Becker R, Döring W. Ann Phys 1935;24:719.

[36] Burton WK, Cabrera N, Frank FC. Philos Trans R Soc London Ser A 1951;243:299.

[37] Chernov AA. J Cryst Growth 2004;264:499.

[38] Jackson KA. Interface structure. In: Doremus RH, Roberts BW, Turnbull D, editors. Growth and perfection of crystals. London: Chapman and Hill; 1958. p. 319.

[39] Jackson KA, Hunt JD. Acta Met 1965;13:1212.

[40] Woodruff DP. The solid-liquid interface. Cambridge solid state science series. London: Cambridge University Press; 1973.

[41] Rutter JW, Chalmers B. Can J Phys 1953;31:15.

[42] Tiller WA, Jackson KA, Rutter JW, Chalmers B. Acta Met 1953;I:428.

[43] Leamy HJ, Gilmer GH, Jackson KA. In: Blakely JM, editor. Surface physics on materials, vol. 1. New York: Academic Press; 1975. p. 121.

[44] Leamy HJ, Gilmer GH. J Cryst Growth 1974;24/25:499.

[45] Mullins WW, Sekerka RF. J Appl Phys 1963;34:323; 35 (1964):444.

[46] Voronkov VV. Siev Phys Solid State 1965;6:2378.

[47] Cahn JW. Crystal growth. In: Steffen Peiser H, editor. Proceedings of the international conference on crystal growth. Oxford: Pergamon Press; 1967. p. 681.

[48] Coriell SR, Sekerka RF. J Cryst Growth 1976;34:157.

[49] Chernov AA. J Cryst Growth 1974;24/25:11.

[50] Hurle DTJ. J Cryst Growth 1969;5:162.

[51] Temkin DE. Dokl Akad SSR 1960;132:1307.

[52] Bolling GF, Tiller WA. J Appl Phys 1961;32:2587.

[53] Hamilton DR, Seidensticker RG. J Appl Phys 1960;31:1165.

[54] Glicksman ME, Lupulescu A. In: Feigelson Robert S, editor. 50 years progress in crystal growth. Amsterdam: Elsevier; 2004. p. 97.

[55] Vogel R. Z Anorg Chem 1912;76:425.

[56] Tiller WA. Liquid metals and solidification. Cleveland (OH): ASM; 1958. p. 276.

[57] Jackson KA, Hunt JD. Trans Metall Soc AIME 1966;236:1129.

[58] Glicksman ME. Principles of solidification. New York: Springer; 2010.

[59] Wilcox WR. J Appl Phys 1964;35:636.

[60] Carruthers JR, Nassau K. J Appl Phys 1968;39:5205.

[61] Hurle DTJ, Rudolph P. In: Feigelson Robert S, editor. 50 years progress in crystal growth. Amsterdam: Elsevier; 2004. p. 109.

[62] Wang CA, Carlsen D, Motakef S, Wiegel M, Wargo MJ, for Witt AW. In: Feigelson Robert S, editor. 50 years progress in crystal growth. Amsterdam: Elsevier; 2004. p. 125.

[63] Nassau K, Nassau J. In: Feigelson Robert S, editor. 50 years of progress in crystal growth. Amsterdam: Elsevier; 2004. p. 9.

[64] Merker L. In: Feigelson Robert S, editor. 50 years of progress in crystal growth. Amsterdam: Elsevier; 2004. p. 23.

[65] Tammann G. Metallography [Dean and Swenson, New York, Trans.]. N.Y: The Chemical Catalog Co.; 1925. p. 26.

[66] Obreimov J, Schubnikov L. Z Phys 1924;25:31.

[67] Czochralski J. Z Phys Chem 1918;92:219.

[68] Tomaszewski P. Jan czochralski and his method. Wroclas-Keynia; 2003.

[69] von Wartenberg H. Verh Dtsch Phys Ges 1918;20:113.

[70] von Gomperz E. Z Phys 1921;8:184.

[71] Tyndall EPT. Phys Rev 1928;31:313.

[72] Walther H. Rev Sci Insts 1937;8:406.

[73] Uecker R. JCG 2014;401:7–24.

[74] Evans J. Phys Rev 1940;57:47.

[75] Teal GK, Little JB. Phys Rev 1950;78:647.

[76] Shockley W, Sparks M, Teal GK. Phys Rev 1951;83:139.

[77] Teal GK, Buehler E. Phys Rev 1952;87:190.

[78] Pfann WG. J Met 4, Trans AIME 194 (1952):747.

[79] Pfann WG, Olsen KM. Phys Rev 1953;89:322.

[80] Dash WC. J Appl Phys 1959;30:459.

[81] Metz EPA, Miller RC, Mazelsky R. J Appl Phys 1962;33(6):2016.

[82] Mullins JB, Straughan BW, Bickel WS. J Phys Chem Solids 1965;26:82.

[83] Mullins JB, Heritage RJ, Holiday CH, Straughan BW. J Cryst Growth 1968;3–4:261.

[84] Azuma K. Japanese Patent 60–111299, Furukawa Ind.; 1983.

[85] Maiman. Nature 1960;187:493.

[86] Nassau K, Van Uitert LG. J Appl Phys 1960;31:1508.

[87] Ballman AA. J Am Ceram Soc 1965;48:112.

[88] Nassau K. In: Feigelson Robert S, editor. 50 years of progress in crystal growth. Amsterdam: Elsevier; 2004. p. 155.

[89] Fedulov SA, Shapiro ZI, Ladyshinskii PB. Kristallografia 1965;10(22):268.

[90] Ballman AA. J Cryst Growth 1967;1:109.

[91] Bardsley W, Cockayne B. In: Peiser HS, editor. Crystal growth. Oxford: Pergamon; 1967. p. 109.

[92] Kestigian M, Holloway WW. In: Peiser HS, editor. Crystal growth. Oxford: Pergamon; 1967. p. 451.

[93] Cockayne B, Chesswas M, Gasson DB. J Mater Sci 1967;2:7.

[94] Charvat FR, Smith JC, Nestor OH. In: Peiser HS, editor. Crystal growth. Oxford: Pergamon; 1967. p. 45.

[95] Brandle CD, Valentino AJ. J Cryst Growth 1972;12:3.

[96] Brandle CD. J Cryst Growth 2004;264:593.
[97] Carruthers JR, Peterson GE, Grasso M. J Appl Phys 1971;42:1846.
[98] Cockayne B, Chesswas B, Gasson DB. J Mater Sci 1968;3:224.
[99] Derby JJ, Brown RA. J Cryst Growth 1987;83:137.
[100] Wiffen PAC, Brice JC. J Cryst Growth 1976;13:13.
[101] Bridgman PW. Proc Am Acad Arts Sci 1914;49:625.
[102] Stockbarger DC. Am Mineral 1927;12:26.
[103] Stockbarger DC. Rev Sci Inst 1936;7:133.
[104] Scheel HJ, Schultz-Dubois EO. J Cryst Growth 1971;8:304.
[105] Zawilski KT, Custodio MCC, DeMattei RC, Feigelson RS. J Cryst Growth 2005;282:236.
[106] Gault WA, Monberg EM, Clemens JE. J Cryst Growth 1986;74:491.
[107] Mullins JB. In: Feigelson Robert S, editor. 50 years of progress in crystal growth. Amsterdam: Elsevier; 2004. p. 141.
[108] Nacken R. Neues Jahrab Mineral Geol 1915;2:133.
[109] Adams JM, Lewis W. Rev Sci Instrum 1935;5:400.
[110] Buehler E, Walker AC. Growing quartz. Bell Telephone Publication; 1949.
[111] Kyropoulos S. Z Anorg Chem 1926;154:308.
[112] Kyropoulos S. Z Phys 1930;63:849.
[113] Korth K. Z fur Phys 1933;8:677.
[114] Chamberlain K. Rev Sci Instrum 1938;9:322.
[115] Bliss D. In: Feigelson Robert S, editor. 50 years of progress in crystal growth. Amsterdam: Elsevier; 2004. p. 29.
[116] Bryant GG, Bliss DF, Gabbe DR, Zach FX, Iseler GW. Photonic device engineering for dual-use applications, 2481. SPIE; June 30, 1995. 232.
[117] Stober F. Z Krist 1925;61:299.
[118] Schmid F, Viechnicki D. J Am Ceram Soc 1970;53(9):528.
[119] Kattik C, Schmid F. J Cryst Growth 2001;225:572.
[120] Kapitza P. Proc R Soc London 1928;A 119:358–442.
[121] Mullin JB. In: Miller LS, Mullin JB, editors. Electronic materials: from silicon to organics. New York: Plenum Press; 1991. p. 118.
[122] Schunemann PG, Pollak TM. MRS Bull 1998;23(7):23.
[123] da C. Andrade EN, Roscoe R. Proc Phys Soc London 1937;49:152.
[124] Pfann William G. Zone melting. Wiley series on the science. New York (NY): John Wiley & Sons; 1958.
[125] Theuerer HC. J Met 8, Trans AIME 206(1956):1316.
[126] Poplawsky RP. J Appl Phys 1962;33:1616.
[127] Horn FH. J Electrochem Soc 1958;105:393.
[128] Dash WC. J Appl Phys 1960;31:736.
[129] Poplawski RP, Thomas Jr JE. Rev Sci Inst 1960;31:1303.
[130] Feigelson RS. Mater Sci Eng 1988;B1:67.

[131] Mimura Y, Okamura Y, Komazawa Y, Ota C. Jpn J Appl Phys 1980;19:269.

[132] Yoon DH, Yonenaga I, Fukuda T, Ohnishi N. J Cryst Growth 1994;144:339.

[133] Haggerty JS, Menashi P. Prod fibers by floating zone fiber drawing technique. Final Rep. NASA-CR-120948; 1971.

[134] Burris CA, Stone J. Appl Phys Lett 1975;26:318.

[135] Fejer MM, Nightingale JL, Magid GA, Byer RL. Rev Sci Inst 1984;55:1791.

[136] Luh Y, Feigelson RS, Fejer MM. J Cryst Growth 1986;78:135.

[137] Magel GA, Fejer MM, Byer RL. Appl Phys Lett 1990;56:108.

[138] Chani VI. In: Fukuda T, Chani VI, editors. Advances in materials research-shaped crystals, vol. 8. Berlin: Springer; 2007. p. 3.

[139] Feigelson RS, Route RK. J Cryst Growth 1990;104:789.

[140] Feigelson RS. Growth of shaped crystals. In: Arend H, Hulliger J, editors. Crystal growth in science and technology. Plenum Publishing Corp; 1989. p. 275.

[141] Polanyi M. My time with X-rays and crystals. In: Ewald PP, editor. 50 years of X-ray diffraction. Utrecht: International Union of Crystallography; 1962. p. 629.

[142] Mark H, Polanyi M, Schmid E. Z Phys 1923;12:58.

[143] Stepanov AV. Zh Tech Fiz 1959;29:382.

[144] Antonov PI, Nikandrov SP. J Cryst Growth 1980;50:3.

[145] LaBelle Jr HE, Mlavsky AI. Mater Res Bull 1971;6:581.

[146] VerSnyder FL, Shank ME. Mater Sci Eng 1970;6:231.

[147] LaBelle HE. In: Feigelson Robert S, editor. 50 years of progress in crystal growth. Amsterdam: Elsevier; 2004. p. 179.

[148] Mlavsky AI. In: Feigelson Robert S, editor. 50 years of progress in crystal growth. Amsterdam: Elsevier; 2004. p. 177.

[149] Surek T, Coriell SR, Chalmers B. J Cryst Growth 1980;50:21.

[150] Tatarchenko VA, Brener EA. J Cryst Growth 1980;50:126.

[151] Seidensticker RG. J Cryst Growth 1977;39:17.

[152] Belouet C, Brissot JJ, Martres R, Ngo-Tich Phuoc. In: Proc. photovoltaic solar energy conf. Luxembourg; 1977. p. 164.

[153] Zook J, Koepke BG, Grung BL, Leipold MH. J Cryst Growth 1980;50:260.

[154] Baghdadi A, Gurtler RW. J Cryst Growth 1980;50:236.

[155] Bleil CE. J Cryst Growth 1969;5:99.

[156] Kear BH, Piearcey BJ. Trans AIME 1967;238:1209.

[157] Leomonova EE, Osiko VV. Growth of zirconia crystal by skull-melting technique. In: Scheel HJ, Fukuda T, editors. Crystal growth technology. John Wiley & Sons, Ltd; 2003. p. 461.

[158] Castonguay RA, Menashi WF, Wenckus JF, Arthur D. Little, Inc., U.S. Patent 4049384, (September 20, 1977).

[159] Kisil II, Taranyuk VI, Yaroslavkin SV. Funct Mater 2008;15:600.

[160] Wulff G. Z Krist 1901;34:449.

[161] Kruger F, Finke W. Dtsch Reich Patent. 228, 246, K1, 120, Gr2 (November 5, 1910).

[162] Valeton JJP, Sachs K. Math-physik Klasse, 67. Leipzig: Ges. Wiss; 1915. p. 1.

[163] Nacken R. Z Instrumentenk 1916;36:12.

[164] Walker AC, Kohman GT. Trans Am Inst Elec Engrs 1949;68:222.

[165] Holden AN. Discuss Faraday Soc 1949;5:312.

[166] Moore RW. J Am Chem Soc 1919;41:1060.

[167] Walker AC. Bell Lab Rec 1947;25:35.

[168] Holden AN, Singer Phylis. Crystals and crystal growing. New York: Anchor Press/MIT Press; January 1, 1982. p. 318.

[169] Loiacono GM, Zola JJ, Kostescky G. J Cryst Growth 1983;62:545.

[170] Rashkovich LN. Rapid growth of large crystals for nonlinear optics from solution. Bull Acad Sci USSR 1984;9:15.

[171] Zaitseva N, Carmen L. Rapid growth of KDP-type crystals, progress in crystal growth and characterization of materials. Pergammon 2001;1.

[172] Glusker JP, Dorothy crowfoot hodgkin (1910–1994). Protein Sci 1994;3:2465.

[173] Brink C, Hodgkin DC, Lindsey J, Pickworth J, Robertson JH, White JG. Nature 1954;174:1169.

[174] Protein crystal growth. In: Feigelson RS, editor. Proc. first int. conf. on crystal growth. Stanford (CA): Stanford University; August 1985. North Holland, Amsterdam (1986).

[175] McPherson A. Preparation and analysis of protein crystals. New York: John Wiley and Sons; 1982.

[176] McPherson A. Crystallization of biological macromolecules. NY: Cold Spring Harbor Lab. Press, Cold Spring Harbor Press; 1999.

[177] Ward KB, Perozzo MA, Zuk WM. J Cryst Growth 1988;90:325.

[178] Land TA, Malkin AJ, Kuznesov YG, McPherson A, DeYoreo JJ. Pus Rev Lett 1995;75:2774.

[179] Malkin AJ, Land TA, Kuznetsov YG, McPherson A, DeYoreo JJ. Phys Rev Lett 1995;75:2778.

[180] Liesegang RE. Nat Wochschr 1896;11:221.

[181] Hatschek E. J Soc Chem Ind 1911;30:276.

[182] Dreaper WP. J Soc Chem Ind 1913;32:678.

[183] Fisher LW, Simons FL. Am Mineral 1926;11:124 and 200.

[184] Henisch HK. Crystal growth in gels. University Park (PA): The Pennsylvania State University Press; 1970.

[185] Patel AR, Verikateswara Rao A. Bull Mat Sci 1982;4:527.

[186] Jiang H, Kloc C. MRS Bull 2013;38:28.

[187] Carman L, Zaitseva N, Martinez HP, Rupert B, Pawelczak I, Glenn A, et al. J Cryst Growth 2013; 368:56.

[188] Bethe K, Weltz F. Mat Res Bull 1971;6:209.

[189] Linares RC. J Am Ceram Soc 1962;45:307.

[190] Elwell D, Scheel HJ. Crystal growth from high temperature solutions. London: Academic Press; 1975.

[191] Wöhler F. Ann Chim Phys 1823;29(2):43.

[192] Doelter C. Z Krist 1886;11(29):40.

[193] Wöhler F, St Claire Deville H. Ann Chem Pharm 1857;101(113):347.

[194] Fremy E, Feil C. Compt Rend 1877;85:1029.

[195] Giess EA. J Am Ceram Soc 1964;47:388.

[196] Austerman SB. J Am Ceram Soc 1963;46:6.

[197] Newkirk HW, Smith DK. Am Min 1965;50:44.

[198] Timofeeva VA. J Cryst Growth 1968;3/4:496.

[199] Nielsen JW, Dearborn EF. Phys Chem Solids 1958;5:202.

[200] Van Uitert LG, Grodkiewicz WH, Dearborn EF. J Am Ceram Soc 1965;48:105.

[201] Wood DL, Remeika JP. J Appl Phys 1966;37:1232.

[202] Scheel HJ. In: Feigelson Robert S, editor. 50 years progress in crystal growth. Amsterdam: Elsevier; 2004. p. 173.

[203] Reisman A, Holtzberg F. J Am Chem Soc 1955;77:2115.

[204] Mizell GJ, Fay WR, Alekel III T, Rytz D, Garrett M. Visible and UV lasers, 2115. SPIE; 1994.

[205] Fluckiger U, Arend H. J Cryst Growth 1978;43:406.

[206] Miller CE. J Appl Phys 1958;29:233.

[207] Linares RC. J Appl Phys 1964;35:433.

[208] Belruss V, Kalnajs J, Linz A, Foweiler R. Mat Res Bull 1971;6:899.

[209] Chen CT, Wu B, Jiang A, You G. Sci Sin Ser B 1985;28:235.

[210] Nelson DF, Remeika JP. J Appl Phys 1964;35:522.

[211] Tolksdorf W. J Cryst Growth 1968;3/4:463.

[212] Nielsen JW. Electronics 1964;37:44.

[213] Grodkiewicz WH, Dearborn EP, Van Uitert LG. In: Steffen Peiser H, editor. Crystal growth, proceedings of the international conference on crystal growth. Oxford: Pergamon Press; 1967. p. 441.

[214] Capper P, Mauk M, editors. Liquid phase epitaxy of electronic, optical, and optoelectronic materials. Chicester (England): John Wiley; 2007.

[215] Rakovan J. Rocks Miner 2006;81:317.

[216] Frankenheim ML. Ann Phys 1836;3(7):516.

[217] Baker TV. J Chem Soc Trans 1906;89:1120.

[218] Royer L. Bull Soc Franc Mineral 1928;51:7.

[219] Nelson H. RCA Rev 1963;24:603.

[220] Rupprecht H. Symposium on GaAs, Reading (England). (1966) 57.

[221] Panish MB, Sumski S, Hayashi I. Metall Trans 1971;2:795.

[222] Linares RC, McGraw RB, Schroeder JB. J Appl Phys 1965;36:2884.

[223] C. Linares R. J Cryst Growth 1968;3/4:443.

[224] Bobeck AH, Della Torre E. Magnetic bubbles. Amsterdam: North-Holland; 1975.

[225] Hibiya T. J Cryst Growth 1983;64:400.

[226] Fratello VJ, Wolfe R. In: Francombe MH, Adam JD, editors. Magnetic film devices. Academic Press; 2000.

[227] Bednorz JG, Müller KA. Z Phys-Condensed Matter 1986;64:189.

[228] Scheel HJ, Klemenz C, Reinhart FK, Lang HP, Güntherodt HJ. Appl Phys Lett 1994;65(7):901.

[229] Byrappa K, Yoshimura M. Handbook of hydrothermal technology. Norwich (NY): Noyce Publications; 2000.

[230] Ballman AA, Laudise RA. In: Gilman JJ, editor. The art and science of growing crystals. New York: Wiley; 1963. p. 231.

[231] Senarmont H. Ann chem phys 1851;32:129.

[232] Spezia G. Acad Sci Torino Atti 1905;40:254.

[233] Walker AC, Buehler E. Indust Eng Chem 1950;42:1369.

[234] Laudise RA, Sullivan RA. Chem Eng Prog 1959;55:55.

[235] Laudise RA. J Am Chem Soc 1959;81:562.

[236] Tian ZR, Voigt JA, Liu J, Mckenzie B, Mcdermott MJ. J Am Chem Soc 2002;124:12954.

[237] Vayssieres L, Keis K, Lindquist SE, Hagfeldt AJ. Phys Chem B 2001;105:3350.

[238] E Greene L, Law M, Goldberger J, Kim F, Johnson JC, F Zhang Y, et al. Angew Chem Int Ed 2003;42:3021.

[239] Zhang J, Sun LD, Liao CS, Yan CH. Chem Commun 2002:262.

[240] Kunnmann W. In: Lefever RA, editor. Preparation and properties of solid state materials. New York: Dekker; 1971. p. 1.

[241] Bostanov V. J Cryst Growth 1977;42:194.

[242] DeMattei RC, Huggins RA, Feigelson RS. J Cryst Growth 1976;34:1.

[243] St Claire-Deville H. Compt Rend 1854;39:323.

[244] Ullik F. Ber Akad Wien 1865;52:115.

[245] Cohen U, Huggins RA. J Electrochem Soc 1976;123:381.

[246] Feigelson RS. In: Holt SL, Milstein JB, Robbins M, editors. Solid state chemistry, a contemporary overview; 1980. p. 243. Am. Chem. Soc. Washington, DC.

[247] Hodes G. In: Rubinstein I, editor. Electrodeposition of II–VI semiconductors, physical electrochemistry. New York: M. Dekker Inc.; 1995. p. 515.

[248] Turner AK, Woodcock JM, Ozsan E, Summers JG. In: Luque A, Sala A, Palz W, Dos Santos A, Helm P, editors. Proceedings of the 10th European Solar Energy Conference, held at Lisbon Portugal: Springer [Netherlands]; April, 1991 8–12, p.791.

[249] Isshiki M, Endo T, Masumoto K, Usui Y. J Electrochem Soc 1990;137:2697.

[250] Lincot D, Ortega-Borges R, Froment M. Appl Phys Lett 1994;64:569.

[251] Chaudary GN, Sardesai SN, Sathaye SD, Rao VJ. J Mat Sci 1992;27:4647.

[252] Lincot D, Furlong MJ, Froment M, Cortes R, Bernard MC. Mat Res Soc Symp Proc 1997;451:223.

[253] Schlesinger TE, Rajeshwar K, De Tacconi NR. Electrodeposition of semiconductors. In: Schlesinger M, Paunovic M, editors. Modern electroplating. New York: John Wiley & Sons; 2010.

[254] Izaki M, Omi T. Appl Phys Lett 1996;68:2439.

[255] Peulon S, Lincot DJ. J Electrohem Soc 1998;145:864.

[256] Liu R, Vertegel AA, Bohannan EW, Sorenson TA, Switzer JA. Chem Mater 2001;13:508.

[257] Vanheusden K, Warren WL, Seager CH, Tallant DR, Voigt JA, Gnade BE. J Appl Phys 1996;79:7983.

[258] Yshida T, Tochimoto M, Schlettwein D, Wöhrle D, Sugiura T, Minoura H. Chem Mater 1999;11:2657.

[259] Xu L, Guo Y, Liao Q, Zhang J, Xu D. J Phys Chem B 2005;109:13519.

[260] Allendorf M. From Bunsen to VLSI. Electrochem Soc Interface 1998. Spring.

[261] Bunsen R. J Prakt Chem 1852;56:53.

[262] St Claire-Deville H. Annals 1861;120:176.

[263] Tietjen JJ. Ann Rev Mater Sci 1973;3:317.

[264] Brown FC. Phys Revs 1914;4:85.

[265] Koref F. Z Electrochem 1922;28:511.

[266] Van Arkel AE. Physica 1923;3:76.

[267] Gross R. Z Krist 1921;56:421.

[268] Gross R, Volmer M. Z Phys 1921;5:188.

[269] Straumanis M. Z Phys Chem 1932;B19:63.

[270] Kaldis E. In: Goodman CHL, editor. Crystal growth, theory, and techniques, vol. 1. England: Plenum Press; 1974.

[271] Faktor MM, Garrett J. Growth of crystals from the vapor. London: Chapman and Hall; 1974.

[272] Wilke KT. Kristsall-zuchtung. Berlin: VEB Deutscher Verlag d. Weissenschaften; 1973.

[273] Pizzarello F. J Appl Phys 1954;25:804.

[274] Avinor M. Philips Res Rep 1959;14:211.

[275] Piper WW, Polich SJ. J Appl Phys 1961;32:1278.

[276] Fochs PD. J Appl Phys 1960;31:1733.

[277] Prior AC. J Electrochem Soc 1961;108:82.

[278] Frisch O. Ann Phys 1935;22:375.

[279] Lely JA. Ber Dtsch Keram Ges 1955;32:229.

[280] Tairov TM, Tsvetkov VF. Neorg Mater (USSR) 1977;13:448.

[281] Heindl J, Strunk PH, Heydemann VD, Pensl G. Phys Stat Sol (A) 1997;167:251.

[282] Feigelson RS, Route RK, Kao TM. J Cryst Growth 1985;72:585.

[283] Van Arkel AE, de Boer JH. Zeit anorg Allgem chem 1925;148:345.

[284] Schäfer H. Chemical transport reactions. New York: Academic Press; 1963.

[285] Laudise RA. The growth of single crystals. New Jersey: Prentice-Hall; 1970. 234.

[286] Lorenz R. Chem Ber 1891;24:1509.

[287] Frerichs R. (1996) 1701. Phys Rev 72 (1947) 594.

[288] Schönherr H. The growth of large crystals from the vapor state. In: Crystals, growth, properties and applications. Berlin: Springer-Verlag; 1980. p. 51.

[289] WZ Li, SS Xie, LX Qian, BH Chang, BS Zhou, WY Zhou, et al. Science;274.

[290] Scott TR, King G, Wilson JM. UK Patent 778,383 (1957).

[291] Miederer W, Ziegler G, Dotzer R. US Patent 3,226,270 (1965).

[292] Manasevit HM, Simpson WJ. J Electrochem Soc 1969;12:1725.

[293] Manasevit HM. In: Feigelson Robert S, editor. 50 years progress in crystal growth. Amsterdam: Elsevier; 2004. p. 217.

[294] Seki Y, Tanno K, Iida K, Ichiki E. J Electrochem Soc 1975;122:1108.

[295] Dupuis RD, Dapkis PD. Appl Phys Lett 1978;32:40.

[296] Stringfellow GB. Annu Rev Mater Sci 1978;8:73.

[297] Stringfellow GB. Organometallic vapor phase epitaxy: theory and practice. 2nd ed. Boston: Academic Press; 1999.

[298] Akasaki I, Amano H. Jpn J Appl Phys 2006;45:9001.

[299] Nakamura S, Mukai T, Senoh M. Appl Phys Lett 1994;64:1687.

[300] Nakamura S, Fasol G. The blue laser diode. Berlin: Springer; 1997.

[301] Liu BL, Lachab M, Jia A, Yoshikawa A, Takahashi K. J Cryst Growth 2002;234:637.

[302] Stringfellow GB. J Cryst Growth 2004;264(4):620–30.

[303] Holloway PH, McGuire GE. Handbook of compound semiconductors; growth, processing, characterization and devices. Noyes Publications; 1995.

[304] Joyce BA, Bradley RR. Phils Mag 1966;14:289.

[305] Davey JE, Pankey T. J Appl Phys 1968;39:1941.

[306] Arthur JR. J Appl Phys 1968;39:4032.

[307] Cho AY, Panish MB, Hayashi J. In: Proceedings of the symposium on GaAs and related compounds. Inst. of physics, vol. 2. Germany: Aachen; 1970. p. 118.

[308] Joyce BA, Joyce TB. In: Feigelson Robert S, editor. 50 years progress in crystal growth. Amsterdam: Elsevier; 2004. p. 203.

[309] Grove WR. Trans R Soc 1852;142:87.

[310] Williams P. Surf Sci 1979;90:588.

[311] Kelly PJ, Arnell RD. Vacuum 2000;56:159.

[312] Penning PM. Physica 1936;3:873.

[313] Naoe M, Yamanaka S, Hoshi Y. IEEE Trans Magn 1980;Mag-16:646.

[314] Suntola T. US Patent 4058430 (1977).

[315] Aleskovskii VB. J Appl Chem USSR 1974;47:2207.

[316] Suntola T. Mater Sci Rep 1989;4:261.

[317] Triani G, Evans PJ, Mitchell DRG, Attard DJ, Finnie KS, James M, et al. Proc SPIE 2005;5870:9.

[318] Ritala M, Leskela M. Nanotechnology 1999;10:19.

[319] Wagner RS, Ellis WC. Appl Phys Lett 1964;4:89.

[320] Kuykendall T, Pauzauskie PJ, Zhang Y, Goldberger J, Sirbuly D, Denlinger J, et al. Nat Mater 2004;3:524.

[321] Schmidt V, Wittemann JV, Senz S, Gösele U. Adv Mater 2009;21:2681.

[322] Wacaser BA, Dick KA, Johansson J, Borgstrom MT, Deppert K, Samuelson L. Adv Mater 2009;21:153.

[323] Choi HJ, Johnson JC, He R, Lee SK, Kim F, Pauzauskie P, et al. Chem B 2003;107:8721.

[324] Choi HJ. Vapor-liquid-solid growth of semiconductor nanowires. In: Yi GC, editor. Semiconductor nanostructures for optoelectronic applications, vol. 1. Berlin: Springer-Verlag; 2012.

[325] Sheftal NN. Trends in real crystal formation and some principles for single crystal growth. In: Growth of crystals, vol. 10. New York: Consultants Bureau; 1976. p. 185.

[326] Geis MW, Tsaur BY, Flanders DC. Appl Phys Lett 1982;41:526.

[327] Givargizov EI, Kliya MO, Melik-Adamyan VR, Grebenko AI, DeMattei RC, Feigelson RS. J Cryst Growth 1991;112:758.

[328] Givargizov EI. Oriented crystallization on amorphous substrates. New York: Plenum Oress; 1991.

[329] Crnogorac F, Witte DJ, Pease RFW. J Vac Sci Technol B 2008;26:2520.

[330] Tracy Hall H. In: Feigelson Robert S, editor. 50 years progress in crystal growth. Amsterdam: Elsevier; 2004. p. 193.

[331] Hannay JB. Proc R Soc London 1879;30:450.

[332] Moissan H. Comptes Rendus 1894;118:320.

[333] Desch CH. Nature 1928;121:799.

[334] Lonsdale K. Nature 1962;196:104.

[335] Hazen RM. The diamond makers. Cambridge: Cambridge University Press; 1999.

[336] Tracy Hall H. Rev Sci Instrum 1960;31:125.

[337] Barnard AS. The diamond formula: diamond synthesis: a gemological perspective. Oxford: Butterworth-Heinemann; 2000.

[338] Eversole WG. Synthesis of diamond, US Patent 3,030,188, (April 17, 1962).

[339] Angus JC. J Appl Phys 1968;39:2915.

[340] Deryagin BV, Fedoseev DV. Rus Chem Rev 1970;39:783.

[341] Gracio JJ, Fan QH, Madaleno JC. J Phys D Appl Phys 2010;43:1.

[342] Angus JC. A short history of diamond synthesis. In: Asmussen J, Reinhard DK, editors. Diamond films handbook. New York: Marcel Dekker Inc.; 2002.

[343] Matsumoto S, Sato Y, Kamo M, Setaka N. Jpn J Appl Phys 1982;21L:183.

[344] Kamo M, Sato Y, Matsumoto S, Setaka N. J Cryst Growth 1983;62:642.

[345] Matsui Y, Matsumoto S, Setaka N. J Mater Sci 1983;2:532.

[346] Decarli P, Jamieson J. Science 1961;133:1821.

[347] Galimov ÉM, Kudin AM, Skorobogatskii VN, Plotnichenko VG, Bondarev OL, Zarubin BG, et al. Dokl Phys 2004;49:150.

[348] Ostwald W. Zeit Phys Chem 1897;22:289.

[349] Anderson RJ. J Frankl Inst 1919;187:1.

[350] Carpenter HCH, Elam CF. Proc R Soc London 1921;100:329.

[351] Bailey DJ, Brewer EG. Metal Trans A 1975;6A:403.

[352] Kulper LL. U. S. Patent 3413157, November 26, 1968.

[353] Mayer JK, Nicolet MA, Lau SS. U. S. Patent 4012235, March 17, 1977.

[354] Mayer JK, Lau SS. Electronic materials science: for integrated circuits in Si and GaAs. New Jersey: Prentice Hall; 1989.

[355] Kwon S, Hackenberger WS, Rehrig PW, Lee J-B, Heo T-M, Kim D-H, Lee H-Y. In: Proceedings 2004 IEEE international ultrasonics, ferroelectrics and frequency control conference; 2004. p. 153.

[356] Hurle DTJ, editor. A perspective on crystal growth: a historical collection in celebration of 25 years of the journal of crystal growth. Elsevier Science Publishers; 1992.

[357] Ivantsov GP. Dokl Akad Nauk SSSR 1947;58:567.

[358] Schawlow AL, Townes CH. Phys Rev 1958;112:1940.

[359] Dunn CG, Nonken GC. Metal Prog 1953;71:71.

2. Thermodynamics of Crystal Growth

Thermodynamics of Crystal Growth

Detlef Klimm
Leibniz-Institut für Kristallzüchtung, Max-Born-Str. 2, 12489 Berlin, Germany
detlef.klimm@ikz-berlin.de

Contents

1 Condensed phases **2**

1.1 The basics . . . 2

1.1.1 Some definitions . . . 2

1.1.2 Miscibility . . . 6

1.1.3 Daltonides and berthollides . . . 8

1.1.4 Independent variables for phase diagrams . . . 9

1.2 Systems with 2 components . . . 12

1.2.1 Eutectics and eutectoids . . . 12

1.2.2 Mixed crystals . . . 16

1.2.3 Segregation and lever rule . . . 19

1.2.4 Peritectics and peritectoids . . . 22

1.2.5 Monotectics and synthectics . . . 25

1.3 Systems with 3 components . . . 27

1.3.1 Rectangular concentration coordinates . . . 27

1.3.2 Concentration triangles . . . 28

1.3.3 Reciprocal salt pairs . . . 31

2 Gas phase and kinetic aspects **33**

2.1 Volatile components . . . 33

2.2 Ellingham type diagrams . . . 34

2.3 Kinetic and surface effects . . . 37

2.3.1 Partitioning coefficients . . . 37

2.3.2 Constitutional supercooling . . . 39

2.3.3 Growth shapes . . . 40

1 Condensed phases

1.1 The basics

1.1.1 Some definitions

Phase: Is a region that is homogeneous on scales that are significantly larger than interatomic distances. Examples: diamond C, a solution of sugar in water, air, a "solid solution" = "mixed crystal" between Si and Ge = (Si,Ge) = Si:Ge = $Si_{1-x}Ge_x$ (x – germanium concentration). In Fig. 1, CaF_2 and LiF are solid phases with a fixed composition that is given by the chemical formula. The gray main phase is a solid solution Li:NaCl with variable composition. Every crystal is a phase, but not vice versa!

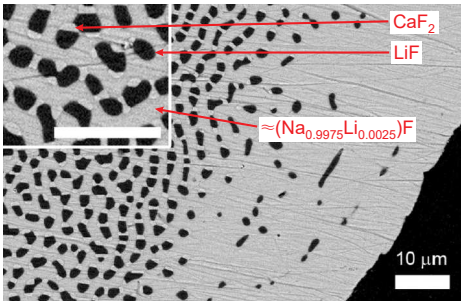


Figure 1: SEM micrograph of a NaCl–LiF–CaF_2 eutectic. Dark phase = LiF, bright phase = CaF_2, main phase = Li:NaCl solid solution. Reproduced with permission from Springer Nature®, reference [2].

Component: Is a chemical building block that can be used to compose the phases in the given system. With a complete set of components it must be possible to compose all phases. Consequently, the entity of all chemical elements that are present can always be used as components. In a system such as NaF–LiF, however, it is not necessary to use Na–Li–F (3 components), because (unless under extreme conditions) no other compounds than NaF and LiF will be formed. Counterexample (1): NaCl–LiF, because also NaF and LiCl could be formed: hence the Na^+, Li^+, Cl^-, F^- are correct components. Counterexample (2): If a metal occurs under the given conditions under different oxidation states, a single compound of that metal can usually not be used as component. Pictures like Fig. 2 [33] are not real phase diagrams, because a transformation between Fe_2O_3 and Fe_3O_4 requires free oxygen. "FeO_x" has no specific chemical composition and is not a component (see also question 1).

Question 1. *Give at least 3 valid sets of components that could describe phase relation of Fig. 2.*

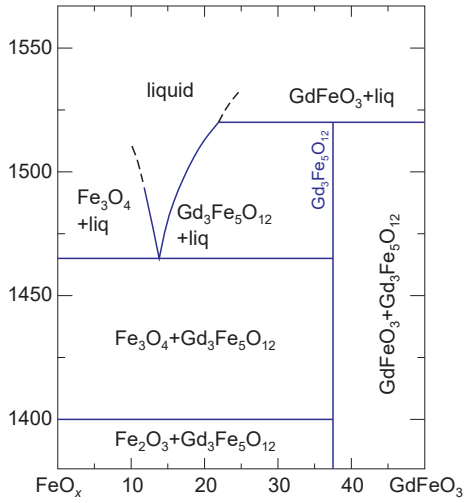


Figure 2: Phase relations of the system Gd_2O_3–Fe_2O_3 in air [33]. Note that neither Fe_2O_3 nor Fe_3O_4 allone are components of the system, because they can be converted only under release/absorption of oxygen.

Answer. *(1): Fe_3O_4–Fe_2O_3–$GdFeO_3$; (2) Fe–Gd–O; (3) Fe_3O_4–Fe_2O_3–Gd_2O_3 (even if Gd_2O_3 does not occur, it gives together with Fe_2O_3 the $GdFeO_3$ phase).*

Phase diagram: Is a representation where for a given choice of axes with independent variables (e.g. temperature T, total pressure p, composition = molar fraction x, fugacity ≈ vapor pressure of species (XY) $p_{(XY)}$, elastic strain $\overset{2\rightarrow}{\varepsilon}$, ...) areas (for $2\mathbb{D}$ representation → phase fields) or volumes (for $3\mathbb{D}$ representation → phase spaces) are shown. Inside one phase field, only a fixed combination of one or more phase(s) is stable. Because experimental conditions x and T can be controlled conveniently, $x-T$ phase diagrams are the most common type, at least in melt growth. For the construction of valid phase diagrams, the consideration of Gibbs phase rule

$$P + F = C + 2 \tag{1}$$

is important (P – number of phases, F – degrees of freedom, C – number of (independent) components). The "2" holds if T and p can be varied independently. For $p =$ const. it has to be replaced by 1, but for additional independent variables (e.g. $\overset{2\rightarrow}{\varepsilon}$) this number can be even higher, as indicated already by J. W. Gibbs 140 years ago [12].

Gibbs free energy: Is defined as

$$G = H - TS = U + pV - TS \tag{2}$$

where H is the enthalpy and S is the entropy of the corresponding phase. H is a state function that is closely related to the internal energy U, which can hardly be measured directly. But from eq. (2) follows, that under isobar conditions ($p =$ const.) the

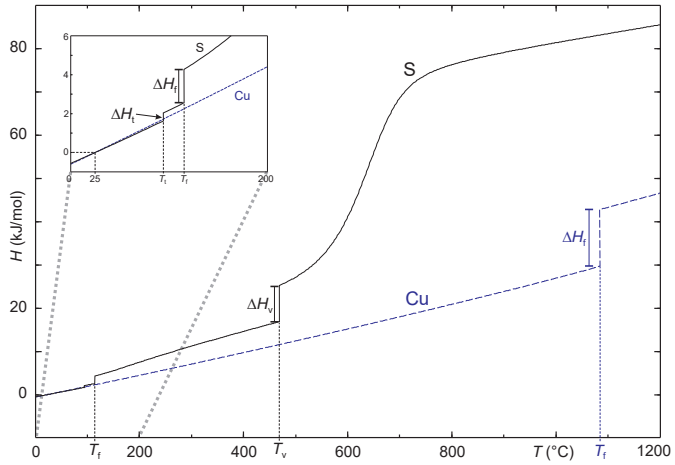


Figure 3: Enthalpy H for copper (blue dashed curves) and sulfur for $0 \leq T \leq 1200\,^{\circ}\mathrm{C}$ ($p = 1\,\mathrm{bar}$). At the temperatures T_t, T_f, T_v first order phase transitions take place: transition between solid phases (t), fusion (f), or vaporization (v), respectively. Copper: $T_\mathrm{f} = 1085\,^{\circ}\mathrm{C}$, $\Delta H_\mathrm{f} = 13.1\,\mathrm{kJ/mol}$, sulfur: $T_\mathrm{t} = 95\,^{\circ}\mathrm{C}$, $\Delta H_\mathrm{t} = 0.4\,\mathrm{kJ/mol}$, $T_\mathrm{f} = 115\,^{\circ}\mathrm{C}$, $\Delta H_\mathrm{f} = 1.7\,\mathrm{kJ/mol}$, $T_\mathrm{v} \approx 469\,^{\circ}\mathrm{C}$, $\Delta H_\mathrm{f} \approx 8.4\,\mathrm{kJ/mol}$.

change of U (e.g. by chemical reactions) equals the change of H. Then $\Delta H = Q_\mathrm{rev}$ is the heat energy that is exchanged reversibly with the environment during this reaction, where $\Delta H > 0$ stands for endothermal processes. Because the measurement of absolute H values is difficult (and often not necessary), for all chemical elements under standard conditions (25 °C, 1 bar) $H = 0$ is defined. Fig. 3 shows this for the chemical elements copper and sulfur. From $H = 0$ at 25 °C it grows monotonously and almost linear with T for both substances. Steps occur there, where first order phase transitions take place. For copper this is only the melting at $T_\mathrm{f} = 1085\,^{\circ}\mathrm{C}$. For sulfur, besides melting, a transition between a monoclinic and an orthorhombic solid phase and vaporization occur in the T range that is shown in the diagram. The strong deviation from linearity of $H(T)$ for sulfur in the gas phase results from significant changes of molecular structure from mainly S_8 molecules (at low T) to mainly S_2 molecules (at high T), leading to significant changes of U.

The rise of H at 1st order transitions is connected with an increase of structural disorder (e.g. from the ordered solid to the less ordered liquid), leading to a growth of entropy

$$\Delta S = \frac{Q_\mathrm{rev}}{T} \tag{3}$$

where Q_rev is the heat that is exchanged during the corresponding transition (e.g. ΔH_f for melting) and T is the temperature where the transition occurs. From (3) follows, that the Gibbs free energy $G(T)$ (2) is a smooth function. For the 4 phases of sulfur this is shown in Fig. 4. The negative slope of the $G(T)$ functions is the entropy S of the corresponding phase. It is obvious that a gas has the lowest degree of order. Molecules in liquids (melts) show already some adhesion, and hence ordering, to nearest neighbors. Solids, which are typically crystals, represent the highest degree of order. For sulfur, this order is in the orthorhombic phase (stable at low T)

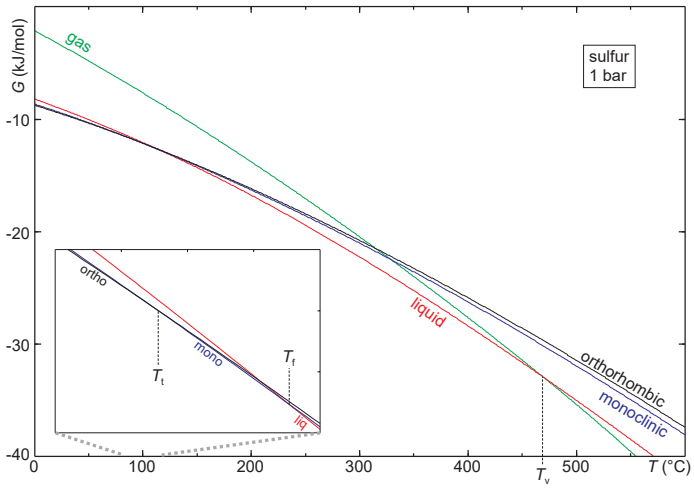


Figure 4: Functions $G(T)$ for the orthorhombic, monoclinic, liquid, and gaseous phase of sulfur. Always the phase with lowest $G(T)$ will be stable.

slightly higher than in the monoclinic phase (stable at high T up to T_f). By the way, sulfur is here an exception: typically the phase with higher crystal symmetry (here orthorhombic) is stable at higher T.

Thermodynamic equilibrium is obtained if the Gibbs free energy for a system for given external conditions, such as T and x, is in a minimum. If the system contains P phases, then $G(T,x)$ of the whole system is the sum

$$G(T,x) = \sum_{i=1}^{P} G^{\Phi_i}(T,x) \tag{4}$$

of the Gibbs free energies G^{Φ_i} of these P phases. In systems with $C > 1$, the minimization of $G(T,x)$ can lead to equilibria where the concentrations x_j of component C^j ($j = 1 \ldots C$) is different in the phases Φ_i ($i = 1 \ldots P$). This phenomenon is called segregation and will be discussed later in sections 1.2 and 1.2.

Question 2. *Prove that in general only one or two phases can coexist in systems with 1 component under isobar conditions!*

Answer. *Gibbs phase rule (1) for $C = 1$ and $p = const.$: $P + F = 2$. Either $F = 0$ (no degree of freedom = fixed point) $\rightarrow P = 2$ or $F = 1$ (T can be varied) $\rightarrow P = 1$.*

For 1-component systems under isobar conditions it follows that only one or two phases may coexist. This is demonstrated for sulfur in Fig. 4. Here the concentration is fixed to $x = 1$, and $G(T)$ in eq. (4) is minized in such a way that always the phase with the smallest G is formed. With rising T this is the orthorhombic, monoclinic, liquid, or gaseous phase, respectively. Only at the intersection points of two $G(T)$ functions one has $P = 2$, which is the case at T_t, T_f, and T_v.

1.1.2 Miscibility

It was mentioned in the definition of the term "phase" (section 1.1.1) that phases can have a fixed composition, or can have variable composition. Experience shows that gases can be mixed nearly always in arbitrary ratio. Besides, ideal mixing ($G^{\mathrm{ex}} = 0$) can often be assumed.

Liquids, this means melts or solutions of different components, are only miscible if they are chemically similar. The term "similar" is somewhat vague, but usually one can assume that components belonging exclusively to one group of substances like metals, oxides, halides, sulfides, hydrocarbons, alcohols show miscibility in arbitrary ratio. Ionic inorganic liquids and nonpolar organic liquids, such as water and mineral oil, are almost completely immiscible. The list above indicates that for inorganics the anion is often more relevant than the cation, because the space that is filled by the anions in a crystal structure is often larger than the space that is filled by cations. Because practically often systems with chemically similar components are investigated, phenomena that are connected with immiscibility of the liquid are not very often investigated. A few examples will be discussed in section 1.2.5 (Figs. 21 and 22).

The conditions for mutual solubility that apply for liquids apply for solid substances too. Besides, two additional conditions that are significantly harder must be fulfilled:

- Both substances must have identical crystal structure. This requires, however, that at least the space symmetry groups must be identical, which is a hard requirement because as much as 230 space groups are existing in total [18]. The number of crystal structures amounts to several thousand!

- The lattice parameters, this means the edge lengths of the unit cell a, b, c should be not too different. Here the acceptable difference is typically in the order of 10% to 15%. For instance: LiCl ($a = 5.14\,\text{Å}$), NaCl ($a = 5.64\,\text{Å}$) and KCl ($a = 6.29\,\text{Å}$) have identical crystal structures ("halite"), but only the combinations LiCl–NaCl and NaCl–KCl show complete mutual miscibility, at least above room temperature up to the melting points. Such mixed crystal systems will be described in section 1.2.2. The solid phases of LiCl and KCl, in contrast, are immiscible and both substances form a eutectic system that is described in section 1.2.1.

Data for the Gibbs free energy of "pure substances" $G^0(T)$, which means chemical compounds of fixed composition in the solid, liquid, or gaseous state, can often be found in printed or electronic data compilations such as Barin [3] or FactSage [13]. For "mixture phases" with variable composition the Gibbs free energy can be expressed as a sum

$$G^{\Phi} = G^0 + G^{\mathrm{id}} + G^{\mathrm{ex}} \tag{5}$$

where the contributions G^0 represents the scaled contribution of the pure components. In systems with 2 components this is a straight line

$$G^0 = xG^{\mathrm{Si}} + (1 - x)G^{\mathrm{Ge}} \tag{6}$$

connecting the $G(T)$ values for the pure components, which is shown for Si ($x = 1$) and Ge ($x = 0$) in Fig. 5. Si and Ge, however, can form solid solutions for arbitrary concentrations $0 \leq x \leq 1$. The possibility to intermix both components on an atomistic level increases disorder of the corresponding phase, and enhances its entropy S. This is basically a statistic effect which is independent on the chemical nature of the corresponding atoms! Nevertheless, increasing S results in a reduction of G (2) for $T > 0$, and hence in a stabilization of the phase. As just mentioned, this contribution

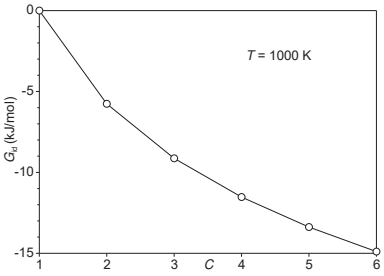
$$G^{\mathrm{id}} = RT \sum_{i}^{C} x_i \ln x_i \qquad (C \text{ components}) \tag{7}$$

$$= RT\,[x \ln x + (1-x)\ln(1-x)] \quad (2 \text{ components}) \tag{8}$$

to G^{Φ} (5) lowers the Gibbs energy of the phase for intermediate compositions; the effect is maximum if the concentrations of all components are equal ($x = 0.5$ for systems with 2 components).

Question 3. *Create a graph where G^{id} for $T = 1000\,\mathrm{K}$ is plotted versus the number of components C for systems with 1 to 6 components, if the concentration of all components is identical.*

Answer.



(Answer to Question 3): For a system with C components all concentrations are $x_i = x = \frac{1}{C}$. (7) gives $G^{\mathrm{id}} = R \cdot T \cdot C \cdot x \cdot \ln x = R \cdot T \cdot \ln x$. For $T = 1000\,K$ one obtains this diagram, showing that the Gibbs energy gain rises significantly with C up to ca. 15 kJ/mol at this temperature.

Especially at very high $T \gg 1000\,^{\circ}\mathrm{C}$ the sum $G^0 + G^{\mathrm{id}}$ gives sometimes a reasonable approximation, because then the excess Gibbs free energy G^{ex} of equation (5) is often small. The contribution G^{ex} summarizes deviations from the ideal behavior that results e.g. from attraction or repulsion of species, or from complicated shapes of the interacting species. Fig. 5 demonstrates this for the solid solution $\mathrm{Si}_x\mathrm{Ge}_{1-x}$ at $1200\,\mathrm{K} = 927\,^{\circ}\mathrm{C}$, which is 10 K below the melting point of pure germanium and 485 K below that of pure silicon. Here (like in most other solid solutions) the contribution G^{ex} results in a somewhat smaller Gibbs energy gain due to solution formation, compared to the ideal case $G^0 + G^{\mathrm{id}}$. One can assume that the statistical arrangement of Si and Ge atoms with different size is energetically slightly less beneficial than the arrangement of atoms with identical size would be.

It is obvious that not only G^{id} but also G^{ex} must vanish for the pure components, because there no interaction is possible (Fig. 5). Indeed, the definition of the ideal Gibbs free energy of mixing (7) results in $G^{\mathrm{id}} = 0$ because for pure components one has either

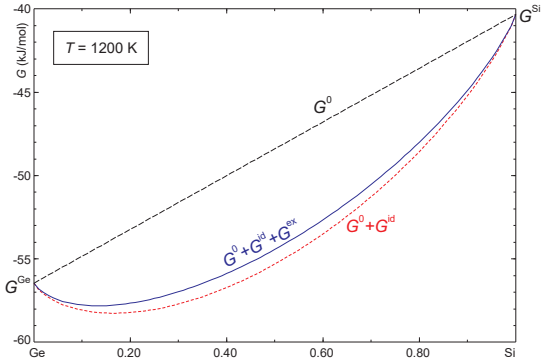


Figure 5: Functions $G(x)$ at $T = 1200\,\mathrm{K}$ for a mechanical mixture of silicon and germanium (G^0) compared to an ideal ($G^0 + G^{\mathrm{id}}$) and a real ($G^0 + G^{\mathrm{id}} + G^{\mathrm{ex}}$) mixture (= solid solution).

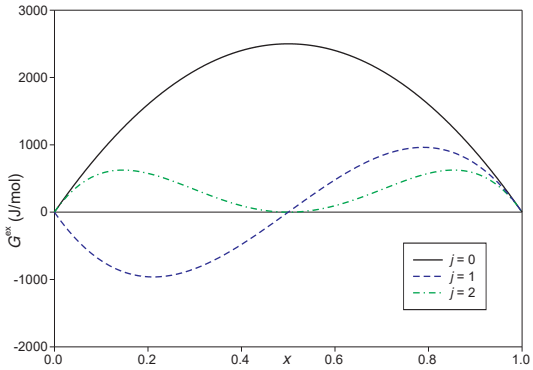


Figure 6: Contributions from Redlich-Kister polynoms (9) to G^{ex} for the degree $j = 0$, $j = 1$, and $j = 2$. $L_j = 10,000$ was set for all j.

$x_i = 0$ or $\ln x_i = 0$. Analytical expressions for the excess Gibbs free energy must also fulfill the condition $G^{\mathrm{ex}} = 0$ for $x_i = 0$ and $x_i = 1$, respectively. A useful model are Redlich-Kister polynoms [37] which are expressed for two components A and B as

$$G^{\mathrm{ex}} = x_{\mathrm{A}} x_{\mathrm{B}} \sum_{j=0}^{N} L_j \left(x_{\mathrm{A}} - x_{\mathrm{B}}\right)^j \tag{9}$$

with interaction coefficients L_j up to the degree N. The degree $j = 0$ results in a G^{ex} contribution that is either always positiv (like shown in Fig. 6 for $L_0 = 10,000$) or always negative. L_1 is positive on one side, and negative on the other side, allowing asymmetric interactions. Usually the sum from several L_j is necessary to describe specific solid or liquid mixtures [17].

1.1.3 Daltonides and berthollides

The slope of the G^{id} function (8) is infinite if it approaches the rims $x = 0$ and $x = 1$, which means that $G^{\Phi}(x)$ drops significantly already if minor additions of another component are added. With other words: everything dissolves at least in very small concentrations (ppm, ppb, or even less) in everything. This is sometimes used if very small concentrations of

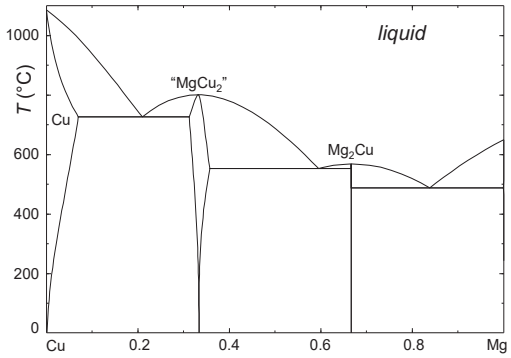


Figure 7: Calculated phase diagram Mg–Cu [13] with two intermediate compounds. Mg_2Cu is a daltonide, "$MgCu_2$" is a berthollide, better to be written as $Mg_{1\pm\delta}Cu_2$ ($\delta \approx 0.11$).

dopants are added to semiconductor crystals for the control of amount and type (electrons of holes) of charge carriers. The same holds for intermediate compounds that are formed in some systems: Some of them have an almost fixed composition that can vary only so insignificantly that it cannot be displayed in the typical scaling of a $x - T$ phase diagram. Mg_2Cu in Fig. 7 is an example; sometimes also called a "line compound", because they are represented as a line perpendicular to the concentration axis. Another example is $Gd_3Fe_5O_{12}$ in Fig. 2.

Other compounds, in contrast, allow significant variations of their composition e.g. by mutual replacements of the component atoms or by other point defects (interstitial atoms, vacancies) in the crystal structure. In Fig. 7 this is "$MgCu_2$" which is also called the Laves phase L15. Compounds with variable composition are sometimes called berthollides; the variation parameter (δ in the caption of Fig. 7) is the "phase width" of the berthollide. δ is a function of T and vanishes at the melting point where the berthollides is in equilibrium with the melt.

It is obvious that the thermodynamic description of daltonids is simpler than for bertollides: for the first $G(T)$ data are sufficient, whereas for the latter $G(T, x)$ data are required. (Assuming that other independent parameters such as p are not relevant, see the following section 1.1.4.)

Question 4. *Why do berthollides have at the melting point no phase width?*

Answer. *Gibbs phase rule (1) for isobar conditions and 2 components would give $P + F = 3$; but the concentration of the liquid must be identical the the concentration of the solid, because no substance is added or removed. (One remains at the same x position.) This restriction means that another degree of freedom is lost (like already for $p = const.$), and one has $P + F = 2$, and hence maximum 2 phases, with no degree of freedom left. Hence, also the composition of the solid (berthollide) must be fixed at one point.*

1.1.4 Independent variables for phase diagrams

Thermodynamic systems aspire towards minimum Gibbs free energy, and in its common definition (2) G is a function of the independent variables pressure p and temperature T

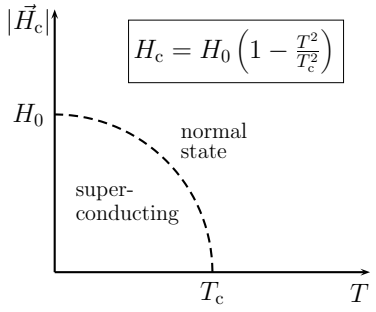


Figure 8: Superconductivity disappears above the critical temperature T_c (for $H = 0$) and above the critical magnetic field H_c (for $T = 0$). The $T-H$ diagram shows a $H(T)$ phase field where superconductivity exists.

only. The restriction to these 2 variables is useful, because both can be most easily varied, influencing this way the system. For constant pressure, or if only condensed phases with negligible compressibility

$$\overset{2\rightarrow}{\chi} = -\frac{\overset{2\rightarrow}{\varepsilon}}{p} \tag{10}$$

are considered, G depends practically only on T. ($\overset{2\rightarrow}{\varepsilon}$ is the second rank tensor of elastic strain, which expresses the elastic distortion in different directions. It can be represented by a 3×3 matrix, where the relative elastic strains in the directions $\vec{e_1}, \vec{e_2}, \vec{e_3}$ of a Cartesian coordinate system are found on the main diagonal [19].)

In strong external fields (which means here other independent variables, or "generalized fields") such as electric $\vec{E}$, magnetic $\vec{H}$, or under elastic stress $\overset{2\rightarrow}{\sigma}$, the Gibbs free energy of a phase can be influenced as a result of the corresponding "generalized fluxes" $\vec{D}$ (dielectric displacement), $\vec{B}$ (magnetic flux), or the above mentioned elastic strain $\overset{2\rightarrow}{\varepsilon}$. Then contributions like

$$\frac{1}{2}\,V_m\,\vec{E}\cdot\vec{D} \qquad \text{(electric)} \tag{11}$$

$$\frac{1}{2}\,V_m\,\vec{B}\cdot\vec{H} \qquad \text{(magnetic)} \tag{12}$$

$$\frac{1}{2}\,V_m\,\overset{2\rightarrow}{\varepsilon}:\overset{2\rightarrow}{\sigma} \tag{13}$$

$$\approx \frac{1}{2}\,V_m\,E\,\varepsilon^2 \qquad \text{(elastic)} \tag{14}$$

(V_m – molar volume, E – Young's modulus) may result in significant shifts of phase boundaries [29, 19]. As an example, Fig. 8 shows the critical magnetic field H_c (which is actually a circular vector $\vec{\overset{\circ}{H}}_c$) where the superconducting state of superconductors disappears as a function of temperature T. The dashed line is the phase boundary between both states.

Mechanical energy (13) can be introduced into epitaxial layers by *strain engineering*. This is typically done by depositing the layer onto a substrate crystal with almost, but not perfectly matched lattice parameters. Fig. 9 (taken from Ref. [16]) shows as an

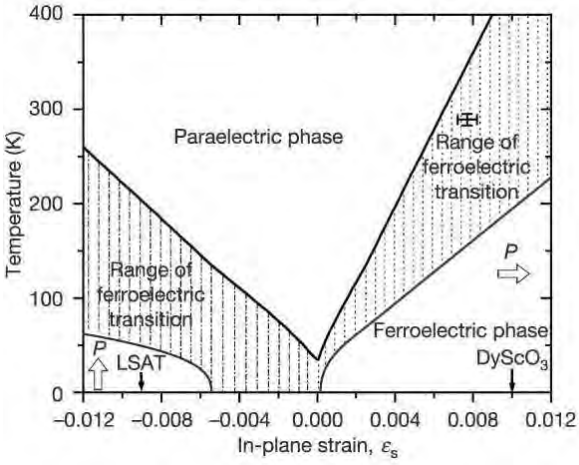


Figure 9: Expected shift in T_c of (100) $SrTiO_3$ with biaxial in-plane strain, based on thermodynamic analysis. The arrows indicate the predicted direction of the polarization for strained $SrTiO_3$: in-plane for biaxial tensile strain and out-of-plane for biaxial compressive strain. The ε_s values for $SrTiO_3$ fully constrained (commensurate) to the lattice constants of LSAT and (110) $DyScO_3$ substrates are indicated by the positions of the corresponding arrows. The cross shows the observed T_c shift of a 500-Å-thick $SrTiO_3$ film epitaxially grown on (110) $DyScO_3$. Reprinted by permission from Haeni et al., Room-temperature ferroelectricity in strained $SrTiO_3$, Nature 430 © 2004 [16].

example the epitaxy of perovskite type $SrTiO_3$ layers on several other substrates belonging to the same crystal structure. The $SrTiO_3$ unit cell shows at ambient temperature no distortions and belongs to the cubic system (space group $Pm\bar{3}m$). The high symmetry prevents ferroelectricity, and this phase is called "paraelectric". If, however, a thin $SrTiO_3$ layer is grown epitaxially on a suitable substrate, the unit cell is elastically stretched or compressed. The product of stress tensor $\overset{2\rightarrow}{\sigma}$ and strain tensor $\overset{2\rightarrow}{\varepsilon}$ (13) or in a scalar form (14) is the elastic energy that raises the temperature of the paraelectric/ferroelectric phase transition of $SrTiO_3$ significantly.

Question 5. *For the perovskite $BaTiO_3$ one finds in the literature the following data: mass density $\varrho = 5800\,kg\,m^{-3}$, molar mass $M = 233.2\,g\,mol^{-1}$, Young's modulus $E \approx 67\,GPa$. The transformation heat from the paraelectric $Pm\bar{3}m$ to the ferroelectric $P4mm$ phase is $\Delta H_t \approx 200\,J\,mol^{-1}$. Show that 1% strain should influence this transition considerably!*

Answer. $V_m = M/\varrho \approx 40\,cm^3\,mol^{-1}$. *With (14):* $E_{elast} = \frac{1}{2}V_m E\varepsilon^2 \approx \frac{1}{2} \cdot 40 \cdot 10^{-6} m^3 mol^{-1} \cdot 67 \cdot 10^9\,N\,m^{-2} \cdot 10^{-4} \approx 134\,J\,mol^{-1}$. *($\varepsilon = 10^{-2}$ has no unit.) Hence, E_{elast} reaches the order of magnitude of ΔH_t, and influence has to be expected.*

For most practical applications, besides the temperature T, the chemical composition is the most relevant independent property of a thermodynamic system. This composition is best expressed by the molar fractions

$$x_i = \frac{n_i}{\sum_{i=1}^{C} n_i} \tag{15}$$

of the components. (The n_i in equation (15) are the numbers of moles of the corresponding component.) For systems with $C = 2$ components, one has $x_2 = 1 - x_1$, and one concen-

tration value x is sufficient to describe the composition. Then $x-T$ phase diagrams are a useful tool to describe systems with two components. In the next section 1.2 we will focus on several typical features of such systems.

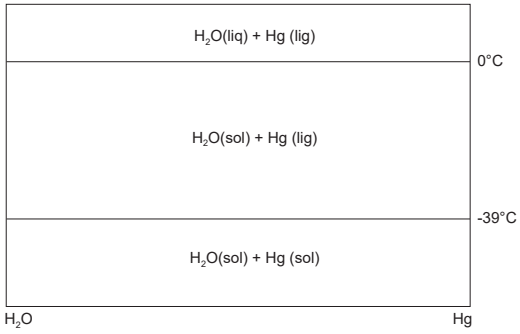
1.2 Systems with 2 components

In the following paragraphs several phenomena leading to typical topographies of phase diagrams with two components will be presented. Whenever possible, such presentations are preferred because such systems have only one independent concentration parameter x, and often the temperature T is used as the second independent parameter – allowing the presentation as $x-T$ diagrams. It will be shown that the topology of such phase diagrams depends mainly on three points:

1. Are both components A and B intermixing in the high-T phase (typically the liquid, or melt)?
2. Are both components intermixing in the low-T phase(s), which is (are) typically solid(s)?
3. Do intermediate compounds exist? This is often the case if the atomic radii of the components are so different, that the smaller atoms can enter voids between the larger atoms.

Question 6. *Draw a phase diagram of two components that are not mixable in the low-T and in the high-T phase, e.g. for water ($T_{\mathrm{f}}^{\mathrm{H_2O}} = 0\,^\circ C$) and mercury ($T_{\mathrm{f}}^{\mathrm{Hg}} = -39\,^\circ C$). Add labels to the phase fields!*

Answer.



(Answer to Question 6): The phase diagram consists of 3 rectangles that are separated by horizontal lines on the level of the 2 melting points.

1.2.1 Eutectics and eutectoids

Function (2) defines the Gibbs free energy of an arbitrary phase; $G(T)$ depends on the enthalpy H and the entropy S. H results from the energy balance during the formation of this phase. For instance, for solid KCl it represents the energy gain of the chemical reaction $\mathrm{K} + \frac{1}{2}\mathrm{Cl_2} \rightarrow \mathrm{KCl}$ at 1 bar and 25 °C (= "normal conditions"). S is a measure

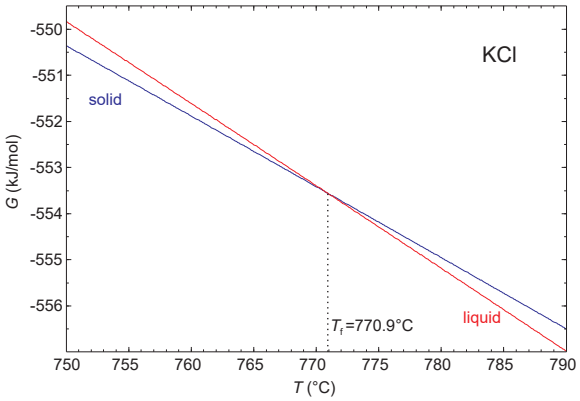


Figure 10: The $G(T)$ functions for KCl(sol, liq) intersect at the melting point $T_\mathrm{f} = 770.9\,^\circ\mathrm{C}$.

of the disorder (on an atomistic scale) of this phase. Of course, this disorder is larger in a liquid than in the well-ordered crystal – consequently liquid phases have usually higher entropy than solids of the same composition. For H it is vice versa: The energy gain during the formation of solid KCl, where every Cl^- is closely coordinated to 6 K^+, is higher than the energy gain during the formation of a KCl melt where interionic distances are larger. For KCl under normal conditions the data are as follows: solid: $\Delta H = -436.684\,\mathrm{kJ/mol}$, $S = 82.5503\,\mathrm{J\,mol^{-1}\,K^{-1}}$; liquid: $\Delta H = -421.825\,\mathrm{kJ/mol}$, $S = 86.5225\,\mathrm{J\,mol^{-1}\,K^{-1}}$.

Fig. 10 shows both $G(T)$ functions for the range $750\,^\circ\mathrm{C} \le T \le 790\,^\circ\mathrm{C}$. Obviously H and S of the phases do not change very much with temperature, and consequently (2) results in almost linear curves. The liquid phase starts at "less negative" values but is steeper, resulting from larger S. The point where both functions are intersecting is the melting temperature $T_\mathrm{f}^\mathrm{KCl} = 770.9\,^\circ\mathrm{C}$. For pure KI a similar diagram could be drawn with $T_\mathrm{f}^\mathrm{KI} = 680.9\,^\circ\mathrm{C}$.

KCl and KI have identical (rocksalt) crystal structure, but the ionic radii of the anions (Cl^-: 167 pm; I^-: 206 pm [41]) are so different, that mixed crystals cannot be formed. The melts, in contrast, are miscible in arbitrary ratio. As a result of this, only Gibbs free energy of the melt can be lowered by admixing the second component to the first one, because a Gibbs free energy of mixing (8) occurs. This holds not for the solid phases of KCl and KI that remain constant. If the red curve (for the liquid phase) in Fig. 10, however, is lowered, the intersection point T_f moves to smaller T – with other words, the "melting temperature" where the whole system becomes liquid is lowered.

Fig. 11 demonstrates this, outgoing from both components or "end members". The red curve shows the lowering T_f, starting from the value that holds for pure KCl, and the blue curves in analogy with a start at pure KI. Both lines represent the lower boundary of the "liquid" phase field. Below these lines KCl(sol) or KI(sol), respectively, starts to crystallize from the melt and 2 phases are in equilibrium. The intersection of both curves is the eutectic point and represents the lowest temperature T_eut where the whole system can be liquid. A mixture of KCl(sol)+KI(sol) with composition x_eut melts exactly at T_eut. Below

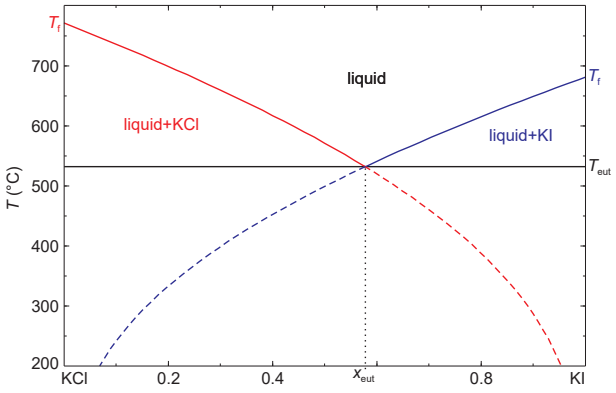


Figure 11: The eutectic system KI–KCl assuming ideal mixing for the liquid. The Gibbs free energy gain (8) results in a depression of the liquidus temperature that start at T_f for both components. Their intersection determines $T_\mathrm{eut} = 531.6\,^\circ\mathrm{C}$. (Considering realistic $G^\mathrm{ex}(x,T)$ contributions (9) one finds the accurate value $T_\mathrm{eut} = 542.9\,^\circ\mathrm{C}$.)

T_eut the whole system is solid and consists of a mixture of KCl(sol) + KI(sol). The dashed lines in Fig. 11 are metastable prolongations of the liquidus curves that can be relevant under non-equilibrium conditions: If e.g. from a KI-rich melt KI(sol) does not crystallize at the corresponding liquidus temperature (blue solid curve), then KCl(sol) can crystallize at the metastable prolongation of the KCl liquidus, which is the red dashed curve below T_eut. In the region between the two dashed lines around x_eut coupled crystallization of both components can occur, leading sometimes to ordered eutectic structures with specific properties [2, 35].

Fig. 12 shows as an example some DTA measurements (heating curves with $10\,\mathrm{K\,min^{-1}}$ of x $BaCl_2$+$(1-x)$ LiCl mixtures, which is another eutectic system. The top curve shows that pure LiCl melts quite sharply at its melting point $T_\mathrm{f} \approx 610\,^\circ\mathrm{C}$. Already a small addition of $BaCl_2$ ($x = 0.01$) leads to another small peak at $T_\mathrm{eut} \approx 520\,^\circ\mathrm{C}$; besides the high temperature peak (liquidus temperature) moves downwards. This process continues: the eutectic peak becomes larger and the liquidus temperature moves towards T_eut. Finally both effects cannot be separated and the whole mixture melts in one single event, almost like a pure substance. It should be pronounced that the melting process of a eutectic system is for compositions outside of the pure components and outside x_eut a continuous process that starts at T_eut and ends at the liquidus.

Under the assumption of ideal mixing in the liquid phase, the bent phase boundaries ("liquidus" of A or B, respectively) in a eutectic system can be described analytically by the expressions

$$x^\mathrm{liq} = 1 - \exp\left[-\frac{Q_\mathrm{A}}{R}\left(\frac{1}{T} - \frac{1}{T_\mathrm{A}}\right)\right] \tag{16}$$

$$x^\mathrm{liq'} = \exp\left[-\frac{Q_\mathrm{B}}{R}\left(\frac{1}{T} - \frac{1}{T_\mathrm{B}}\right)\right] \tag{17}$$

where Q_A, Q_B and T_A, T_B are the heats of fusion and melting temperatures of both pure components. (16) and (17) are called Schröder-van-Laar equations [39, 46].

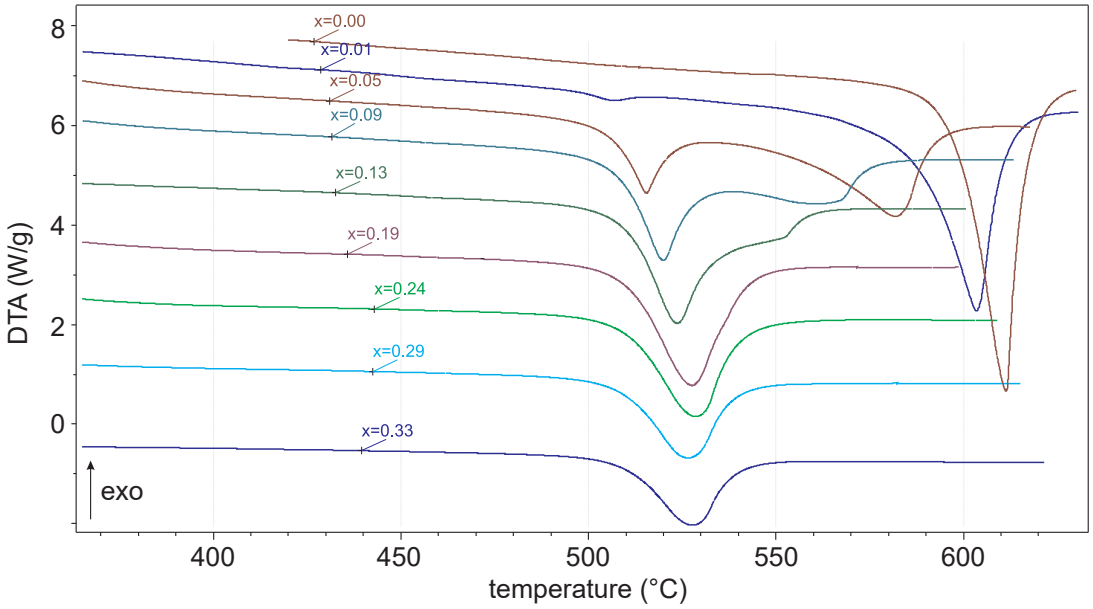


Figure 12: DTA (= *differential thermal analysis*) curves from different mixtures of the eutectic system LiCl–$BaCl_2$. $x = 0$ corresponds to pure LiCl that melts around 610 °C (top curve).

In a eutectic system at x_{eut} and T_{eut} one (homogeneous) high-T phase (the melt, or liquid) decomposes to two solid phases; this process is called the eutectic reaction. From the thermodynamic point of view it is not necessary that the high-T phase is liquid. If instead a (homogeneous) solid high-T phase decomposes to two other phases, the reaction is called eutectoid. The decomposition of γ-iron with ca. 3 mol% carbon at point B in Fig. 13 is an example. γ-Fe "austenite" has a face centered cubic (fcc) structure and can dissolve nearly 9 mol% C. Below 911 °C (pure Fe) or below 738 °C (Fe with ca. 3 mol% C) iron undergoes a phase transition to α-Fe "ferrite" which has body centered cubic (bcc) structure and can dissolve only minor quantities $\ll 1\%$ C. Accordingly, the excess carbon forms in a eutectoid reaction a separate phase (graphite).

The diagram that is shown in Fig. 13 is an equilibrium phase diagram. Under experimental (and especially technical) conditions often the intermediate phase Fe_3C ("cementite") is formed at $x = 0.25$, exactly at the right rim of the diagram. This phase decomposes peritectically (see section 1.2.4) at 1250 °C to graphite and liquid. If the non-equilibrium phase Fe_3C occurs, the eutectic and eutectoid temperatures from Fig. 13 are lowered by a few degrees, but the general topology of the diagram is not changed.

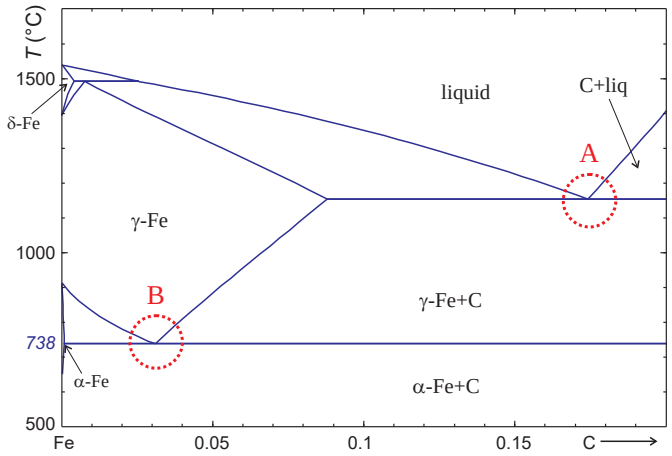


Figure 13: The iron-rich part of the iron-carbon phase diagram shows a eutectic reaction liquid $\rightarrow$ γ-Fe+C at point A and a eutectoid reaction γ-Fe $\rightarrow$ α-Fe+C at point B.

1.2.2 Mixed crystals

In section 1.1.2 several conditions were mentioned that have to be fulfilled for complete mixing of components. These conditions are especially hard for solids, because there identical crystal structure and similar atomic or ionic sizes are required. This is not very often given. If it is the case, not only the high-T (typically liquid) but also the low-T (typically solid) phase are stabilized by a Gibbs free energy of mixing (5). As an example, we will discuss the upper part ($> 1800\,^{\circ}$C, above the dashed blue line) of Fig. 14 which shows the $x - T$ phase diagram Zr–Hf.

At these conditions both pure components exist in their identical high-T β-phase which is body centered cubic. As a result of lanthanide contraction, the atomic radii of Zr and Hf are almost identical, and complete mixing is observed in this phase. The result is a "mixed crystal or "solid solution", with the result that a lense-shaped 2-phase region between the upper bend phase boundary (liquidus) and the lower bend phase boundary (solidus) is formed. In this 2-phase region liquid and solid phase are coexisting, both with variable composition. Liquidus and solidus are meeting at the melting points of the components $T_{\mathrm{f}}^{\mathrm{Zr}}$ and $T_{\mathrm{f}}^{\mathrm{Hf}}$.

If one assumes again ideal behavior of both (liquid and solid) mixed phases, both curves can be expressed analytically

$$x^{\mathrm{sol}} = \frac{\exp\left[-\frac{Q_{\mathrm{A}}}{R}\left(\frac{1}{T}-\frac{1}{T_{\mathrm{A}}}\right)\right]-1}{\exp\left[-\frac{Q_{\mathrm{A}}}{R}\left(\frac{1}{T}-\frac{1}{T_{\mathrm{A}}}\right)\right]-\exp\left[-\frac{Q_{\mathrm{B}}}{R}\left(\frac{1}{T}-\frac{1}{T_{\mathrm{B}}}\right)\right]} \tag{18}$$

$$x^{\mathrm{liq}} = \exp\left[-\frac{Q_{\mathrm{B}}}{R}\left(\frac{1}{T}-\frac{1}{T_{\mathrm{B}}}\right)\right] \times x^{\mathrm{sol}} \qquad \left(T_{\mathrm{A}} \lessgtr T \lessgtr T_{\mathrm{B}}\right) \tag{19}$$

in analogy to (16) and (17) if heat Q and temperature T of the phase transformation are

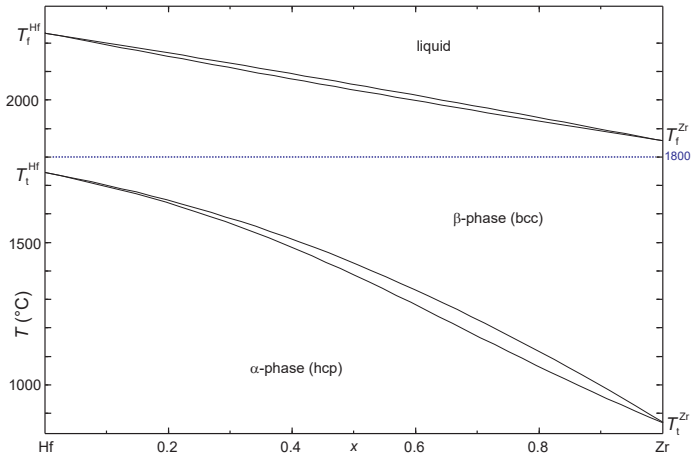


Figure 14: Zirconium and hafnium have identical hexagonal close packed crystal structures (α-phase, Mg type) at low T and form solid solutions for arbitrary concentration x. At temperatures T_t^Zr or T_t^Hf, respectively, they transform to the β-phase which also forms solid solutions for $0 < x < 1$ (isotyp with α-Fe, Fig. 13). The pure components melt at T_f^Zr or T_f^Hf, respectively.

known for both pure substances. The functions (18) and (19) are monotonous rising or falling between the end members – which does not exclude that both curves can be bend slightly up- or downwards – even for ideal mixtures. This is demonstrated at the lower transition $\alpha \rightleftarrows \beta$ in Fig. 14. This is a transition between two solid phases; but because it is of the first order, in can be described thermodynamically in the same way like melting, e.g. with (18) and (19).

Fig. 15 shows the phase diagram KCl–NaCl, and also here both components form a solid solution (K,Na)Cl. In contrast to the phase boundaries in Fig. 14, however, liquidus and solidus have a local minimum. This is only possible if $G^\mathrm{ex} \neq 0$ occurs for at least one of the neighboring solutions. Typically it is so that one has $G^\mathrm{ex} > 0$ in the solid, because there local strain occurs around the different solute atoms in the crystal structure, which destabilizes the solid phase. If such minimum exists, is occurs at one "azeotropic point" for both liquidus and solidus. This is interesting for crystal growth, because melts of an azeotropic composition x_az crystallize without segregation (see section 1.2.3), allowing the growth of bulk single crystals with good quality. This was demonstrated e.g. for the azeotrop mixed crystal system CaF_2–SrF_2 with $Ca_{0.582}Sr_{0.418}F_2$ [23].

The Gibbs free energy of a mixture phase G^Φ is lowered, compared to the contribution of the pure components G^0, mainly by the contributions G^id which scales with the temperature T (8). Consequently the resulting energy gain of mixing decreases for small T. In the final consequence this means that for $T \to 0\,\mathrm{K}$ all solutions, including mixed crystal, become unstable. The resulting process of unmixing in the solid is often not observed experimentally, because upon cooling it requires diffusion steps over significant distances of at least micron scales. Fig. 15 shows below 505 °C a calculated phase boundary that separates the field where one solid solution (K,Na)Cl(ss) is thermodynamically stable from a lower field where such solid solutions are stable only outside a central region. If a solid solution with an intermediate (e.g. the azeotrop) composition is held sufficiently long at a temperature inside the miscibility gap, demixing can occur. In Fig. 15 this means for a

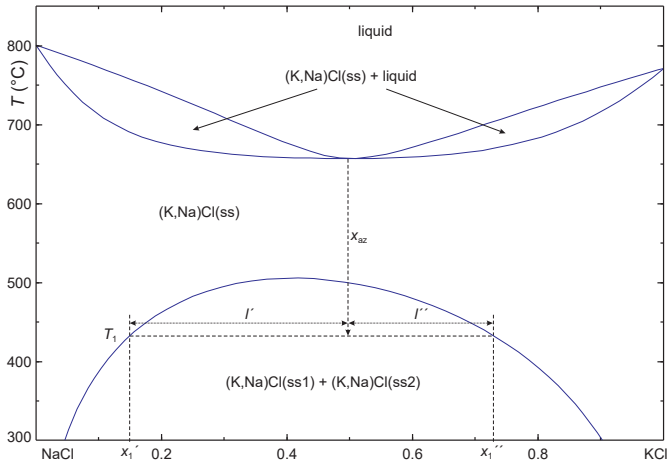


Figure 15: The phase diagram KCl–NaCl shows unlimited mutual solubility in the solid phase, and a mixed crystal = solid solution (K,Na)Cl(ss) = $K_xNa_{1-x}Cl$ ($0 \leq x \leq 1$) is formed. The system is azeotrop. At $T < 505\,^{\circ}C$ a miscibility gap of the solid exists.

annealing temperature T_1 that the solid phase demixes to a mixture of two solid solutions with compositions x_1' and x_1''. It should be noted that the miscibility gaps that are shown in phase diagrams represent typically the thermodynamic equilibrium limit. Like for real gases with the van der Waals equation of state, also a line of spinodal decomposition can be observed inside the miscibility gap. Then the solid solution is stable outside the miscibility gap, unstable inside the spinodal, and metastable between both lines. Some examples can be found in the literature for $Cd_{1-x}Zn_xO$ [31], $A^{III}B^{V}$ semiconductors [43], Au–Pt [51] and $Sn_xTi_{1-x}O_2$ [30].

Crossovers between unlimited solubility in the solid phase (mixed crystals) and no mutual solubility in the solid phases of the components (eutectics, section 1.2.1) do exist. Principally, a vanishing solubility should not be expected at $T > 0\,K$ because the slope $\partial G/\partial x$ of the Gibbs free energy (8) is infinite approaching the pure components ($x = 0$ or $x = 1$, respectively). Nevertheless, if the solubility of one component in the solid phase of another component is so small, that it cannot be reproduced reasonably on the concentration scale of a given phase diagram, the corresponding "almost pure" solid phase is usually called a line compound or daltonide (see section 1.1.3).

Fig. 16, in contrast, shows the phase diagram lead–tin. Both metals belong to the fourth group of the periodic system but show nevertheless different crystal structures, which excludes unlimited mutual solubility. However, the (large) Pb atoms can to ca. 27% be replaced by the smaller Sn atoms, and the resulting mixed crystal $Pb_{0.73}Sn_{0.27}$ is still cubic. Otherwise, ca. 2% of the (small) Sn atoms can be replaced by the larger Pb atoms, and up to $Sn_{0.98}Pb_{0.02}$ the tetragonal β-Sn structure is maintained. From Fig. 16 one can read that the solubility limits become smaller for $T \neq T_{eut}$ and vanishes at the melting points.

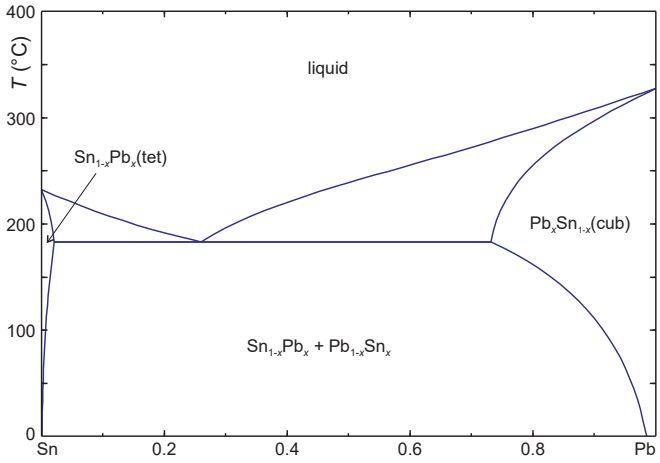


Figure 16: The phase diagram Pb–Sn. Pure Pb crystallizes in a fcc structure, Sn crystallizes at ambient conditions in a tetragonal body centered structure (β-Sn); another (α-Sn) phase with diamond structure that is stable $\lesssim 20\,^{\circ}\mathrm{C}$ is not shown in the diagram. The system is eutectic, with significant mutual solubility at both rims.

1.2.3 Segregation and lever rule

Tie lines In the context of Fig. 15 it was mentioned that a KCl/NaCl melt with azeotropic composition x_{az} crystallizes without segregation. This term stands for processes where from an initially homogeneous phase other phases with different compositions are formed. An example for segregation is given in the same phase diagram if the mixed crystal is cooled below the miscibility gap. If cooling is performed e.g. down to T_1, segregation of the initially homogeneous solid in two solid solutions with compositions x_1' and x_1'' occurs. The isotherm at level T_1 connects the two equilibrium states and is called a "tie line". Because equilibrium thermodynamics describes isotherm states, tie lines in $x - T$ phase diagrams are always horizontal. The stepwise (towards lower T) construction of tie lines is a useful tool for the qualitative and quantitative construction of crystallization paths.

The lever rule In Fig. 15 the tie line at T_1 connects two phase states that are in equilibrium, in this case (K,Na)Cl solid solutions with compositions x_1' and x_1''. From the phase diagram not only this qualitative information can be read, but also the quantities of both phases. The ratio of the phases with both concentrations is given by the inverse ratio of the "levers" l', l''

$$\frac{[x']}{[x'']} = \frac{l''}{l'} = \frac{x'' - x_0}{x_0 - x'} \tag{20}$$

if x_0 is the initial composition (in Fig. 15 $x_0 = x_{\mathrm{az}}$). The lever rule (20) is valid also for equilibria of different phases in other systems.

Crystallization of mixed crystals Lens-shaped fields with 2 phases are typical for systems with mixed crystals. Sometimes these 2-phase fields are almost symmetrical, like in the upper part $> 1800\,^{\circ}\mathrm{C}$ of Fig. 14 for the Zr–Hf system. In other cases the 2-phase field is asymmetric or shows even an azeotrop point, which is shown for KCl–NaCl in Fig. 15.

Such 2-phase fields represent mixtures of a solid solution phase (ss) and a liquid (liq) that are in thermodynamic equilibrium for a given temperature T. In $x-T$ phase diagrams a crystallization process by cooling corresponds to a slow downwards movement of isotherms.

Fig. 17a) shows the high-T part of the KCl–NaCl system from Fig. 15, disregarding the solid miscibility gap that occurs upon further cooling. If a melt, e.g. with a KCl molar fraction $x^{\mathrm{liq}} = 0.9$ (green arrow) is cooled, crystallization of $\mathrm{K}_x\mathrm{Na}_{1-x}\mathrm{Cl}$(ss) starts at the liquidus line, for this composition at $T_{\mathrm{liq}} = 747\,^{\circ}\mathrm{C}$. The composition of the initially formed solid is described by the position of the solidus line at this temperature, $x^{\mathrm{sol}} \approx 0.96$. If the temperature is lowered further e.g. to T_2, a larger fraction of the system is crystallized, and again the compositions of the liquid and the solid solution are described by the corresponding positions of liquidus and solidus at that temperature. It is obvious that at T_2 the solid solution contains less KCl ($x < 0.96$). To reach this equilibrium state, the whole solid crystallized so far had to be converted by solid state diffusion to the new solid solution. This process must be continued until (at the initial composition of the melt $x = 0.9$) the solidus is reached at $T_{\mathrm{sol}} = 716\,^{\circ}\mathrm{C}$. Below that temperature only a solid solution with the initial composition $\mathrm{K}_{0.9}\mathrm{Na}_{0.1}\mathrm{Cl}$ exists.

These diffusion processes in the solid that are necessary to maintain thermodynamic equilibrium consume much time and it is unlikely that in real experiments equilibrium can be obtained. Especially it is almost impossible that equilibrium can be reached at all, if the first crystallized solid is not in close contact with the rest of the melt, e.g. during a crystal pulling process (Czochralski). In such cases it is realistic to assume that solidified parts of the system remain as they are formed, and only the remaining melt is equilibrated with continuously formed fresh solid. This means for Fig. 17a) that the initially crystallized $\mathrm{K}_{0.96}\mathrm{Na}_{0.04}\mathrm{Cl}$(ss) remains as it is, which results in a lower KCl concentration in the melt. Actually, the melt composition moves downwards along the liquidus line, and the continuously crystallizing solid has the composition that is given by a corresponding tie line. This process is continued until a local minimum is reached, which is the case here at the azeotrop point $x_{\mathrm{az}} \approx 0.50, T_{\mathrm{az}} \approx 657\,^{\circ}\mathrm{C}$.

Such kind of crystallization process is called Gulliver-Scheil cooling [5, 15] and the result is shown in Fig. 17b), which should be read from the high-T (right hand) side: The red and blue curves represent the molar amounts of KCl and NaCl in the melt of a system that contains 1 mole substance in total. Both amounts are constant until $T_{\mathrm{liq}} = 747\,^{\circ}\mathrm{C}$ is reached. Because the whole system is liquid, no solid KCl (green) and NaCl (pink) are found at $T > T_{\mathrm{liq}}$. At T_{liq} crystallization begins and the amounts of KCl(ss) as well as NaCl(ss) start to rise. The crystallization process continues down to T_{az} where the liquid phase disappears and a solid solution $\mathrm{K}_{0.9}\mathrm{Na}_{0.1}\mathrm{Cl}$(ss) is formed.

Fig. 17c) shows the case of equilibrium crystallization where the solid phase remains continuously in thermodynamic equilibrium with the melt. The crystallization process starts again at T_{liq}, but proceeds in a significantly narrower range down to $T_{\mathrm{sol}} > T_{\mathrm{az}}$. It should be repeated that segregation can be avoided in mixed crystal systems for melt with the composition x_{az}, which was demonstrated for $(\mathrm{Ca,Sr})\mathrm{F}_2$ mixed crystals [23].

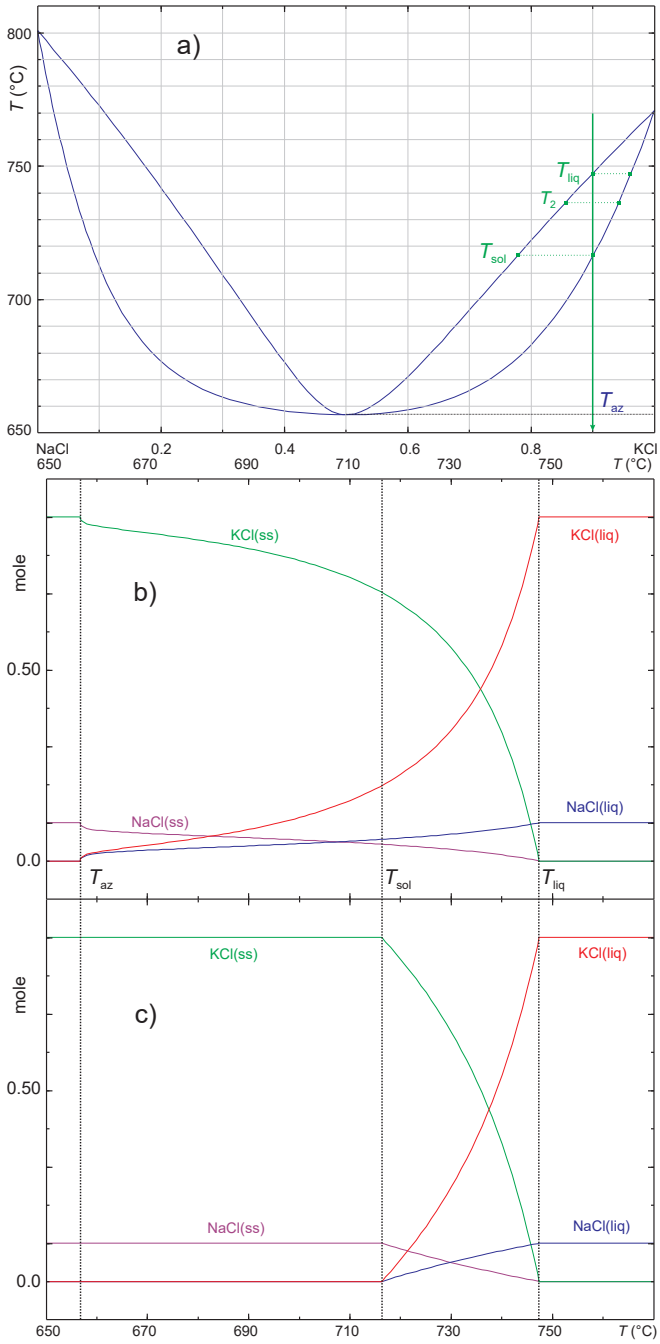


Figure 17: a) Detail of the system KCl–NaCl (see also Fig. 15). Below crystallization of a mixture 90% KCl + 10% NaCl (green arrow): b) Gulliver-Scheil conditions; c) equilibrium conditions.

Crystallization in eutectic systems The lever rule holds also in eutectic systems and can be used for the construction of the crystallization path. This is very straightforward in simple systems with negligible mutual solubility of the components in their solid phases, such as $BaCl_2$–NaCl that is shown in Fig. 18. On both sides of x_{eut} just one pure component crystallizes, and the remaining melt is depleted by this component. Actually this process describes crystal growth from solutions (including melt solutions). Solution growth may be the method of choice in cases where the growth temperature must be lowered for several reasons, e.g.:

- If the substance cannot be molten without decomposition. This is often the case for organics, such as pharmaceuticals. Compounds with peritectic melting (see section 1.2.4) are another example.
- If the fugacity of components is so large, that severe evaporation impedes a stable growth process. This is the case e.g. for ZnO that melts at 1975 °C under evaporation, but could be grown from phosphate and vanadate fluxes [20, 47].
- If the substance undergoes upon cooling from the melting point to room temperature a disruptive transition from a high-T to a low-T phase. The nonlinear optical crystal β-BaB_2O_4 is an example that crystallizes from stoichiometric melts in the high-T α-phase but can be grown from melt solutions with an excess of B_2O_3 and Na_2O in the β-phase [8]. Another example is $Tb_3Al_5O_{12}$, one of the materials which can be used as Faraday rotator [10]. See also question 7!
- If smaller thermal gradients can improve crystalline quality, which was demonstrated for $SrTiO_3$ [14].

In eutectic systems with rim solubility, like Pb–Sn in Fig. 16, one has to discriminate again between equilibrium and Gulliver-Scheil cooling, in analogy to the mixed-crystal systems that were described in the previous paragraph.

Question 7. *What happens if a liquid mixture of 90% $BaCl_2$ and 10% NaCl (see Fig. 18) is cooled from $T_0 = 1000\,°C$? Give a quantitative description!*

Answer. *At $T_1 \approx 903\,°C$ crystallization of the low-T phase $BaCl_2$(s1) begins and continues until the eutectic line is reached at $T_{\text{eut}} = 651\,°C$. There a fraction of $(0.9 - 0.4)/(1 - 0.4) \approx 83\%$ of the initial melt is crystallized as $BaCl_2$(s1). The rest $(1 - 0.9)/(1 - 0.4) \approx 17\%$ is a melt with eutectic composition $x_{\text{eut}} = 0.40$, which crystallizes then together.*

1.2.4 Peritectics and peritectoids

The components of a phase diagram can form intermediate compounds, like $MgCu_2$ and Mg_2Cu in the system Mg–Cu that is shown in Fig. 7. If these two phases are heated of to their melting points, they melt under the formation of a liquid that has the same

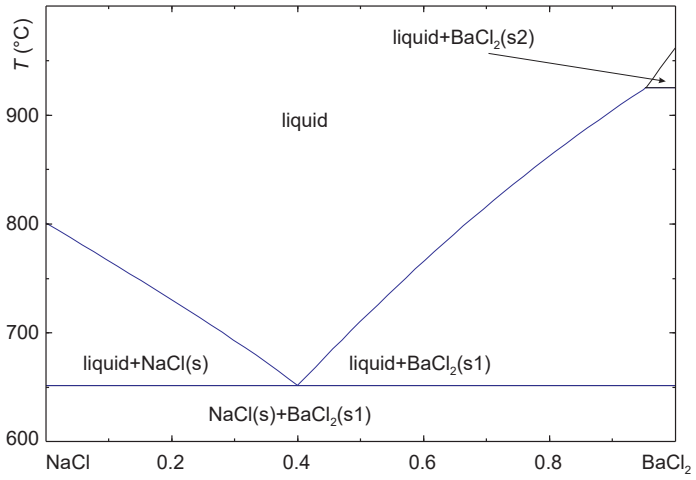


Figure 18: The phase diagram $BaCl_2$–NaCl. $BaCl_2$ undergoes at 925 °C a transition from an orthorhombic phase (s1, cotunnite structure type) to the cubic s2 phase (fluorite type). $T_{\text{eut}} = 651\,^{\circ}\text{C}$, $x_{\text{eut}} = 0.40$.

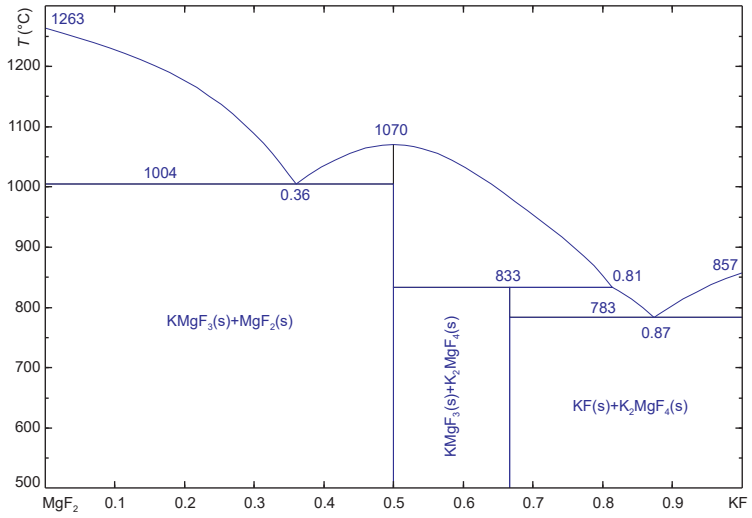


Figure 19: The phase diagram KF–MgF_2 with two intermediate compounds. $KMgF_3$ melts congruently, K_2MgF_4 melts peritectically under the formation of $KMgF_3$.

chemical composition like the initial solid. For Fig. 7 this means that melting $MgCu_2$ is in equilibrium with a melt $x = \frac{1}{3}$, and Mg_2Cu is in equilibrium with a melt $x = \frac{2}{3}$ (x = molar fraction of Mg).

The intermediate compound $KMgF_3$ in the system KF–MgF_2 (Fig. 19) shows the same behavior; at 1070 °C it melts to a liquid with $x = 0.5$. Because the solid and the liquid that are in equilibrium have identical compositions, this melting behavior is called congruent; often one speaks of a "congruent compound". K_2MgF_4 in the same system behaves differently: If this crystalline solid is heated to 833 °C it melts peritectically (or undergoes peritectic decomposition) to a melt with $x = 0.81$ and solid $KMgF_3$. The tie line at 833 °C is the peritectic line of this compound that connects the equilibrium phases K_2MgF_4, $KMgF_3$, and melt. Under isobar conditions the phase rule (1) allows for 2-component systems maximum $C + 1 = 3$ phases in equilibrium, with $F = 0$ then. The point $x = \frac{2}{3}, T_{\text{per}} = 833\,^\circ\text{C}$ is invariant. Consequently even for peritectically melting compounds with variable composition (berthollides) the phase width must vanish at T_{per}.

The equilibrium

$$K_2MgF_4 \rightleftarrows KMgF_3 + \text{melt} \tag{21}$$

is called peritectic reaction. A compound with peritectic melting behavior melts always incongruently because the melt that is in equilibrium has a different composition than the solid. But not vice versa, because incongruent melting is shown not only by peritectics but also by most solid solutions (except at azeotrop points).

Crystal growth of compounds with peritectic melting behavior is a challenge. If one starts with a melt that has the same composition as the desired crystal, the higher melting compound from the right hand side of the peritectic reaction (21) crystallizes first. This can easily be seen from Fig. 19 if a tie line is constructed for a melt $x = \frac{2}{3}$ (which corresponds to K_2MgF_4) below the liquidus. Solid K_2MgF_4 is only in equilibrium with melts $0.81 < x < 0.87$ for temperatures between 833 and 783 °C.

Question 8. *Define a growth process for K_2MgF_4 crystals! What is the maximum yield?*

Answer. *A melt $x = 0.81$ should be cooled slowly, starting from 833 °C down to 783 °C. The crystallized fraction is K_2MgF_4, the rest melt should be removed (e.g. by pulling from the melt). The maximum yield can be calculated using the lever rule: $Y = \frac{\text{share of crystal}}{\text{total charge}} = \frac{0.87-0.81}{0.87-0.67} \approx 0.3 = 30\%$.*

In the peritectic reaction (21) the reaction product "melt" is a phase with variable composition. It is possible that this liquid phase is replaced by a third solid phase with variable composition. Then the reaction is peritectoid, in analogy to a eutectoid like the γ-Fe phase in Fig. 13. In the system Mo–Ni (Fig. 20) three intermediate phases $MoNi_4$, $MoNi_3$ and δ-MoNi are found. It is interesting to note that the nominal composition MoNi ($x = 0.5$) is only at elevated T inside the homogeneity field of δ-MoNi. At lower T the phase is stable only with Mo excess ($x > 0.5$). The end member Ni can incorporate $> 20\%$ Mo into its FCC structure, and the end member Mo can dissolve significantly less ($< 5\%$) Ni into its BCC structure. If $MoNi_4$ is heated it decomposes in a peritectoid reaction

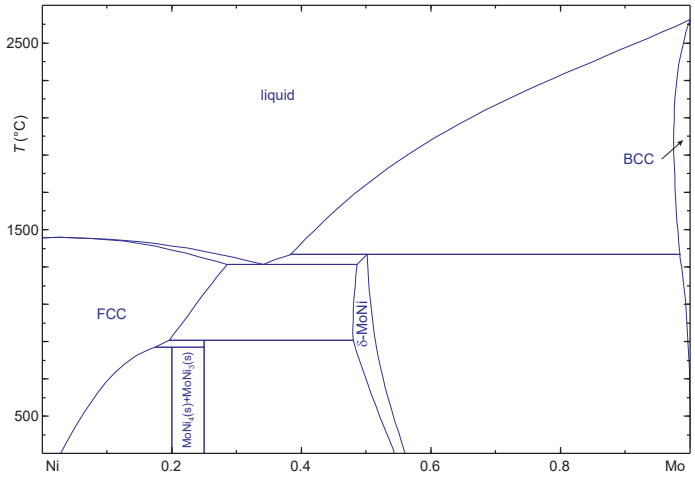


Figure 20: The phase diagram Mo–Ni with two daltonide intermediate compounds $MoNi_4$ ($x = 0.20$) and $MoNi_3$ ($x = 0.25$). These both compounds show peritectoid decomposition. The third intermediate compound δ-MoNi is a berthollide and melts peritectically to a Mo-rich BCC solid solution and melt.

to $MoNi_3$ and the FCC phase. At slightly higher temperature the $MoNi_3$ decomposes in another peritectoid reaction to δ-MoNi and again BCC. The δ-MoNi (which has a finite homogeneity range that shrinks to one point at $T_{\mathrm{per}} \approx 1370\,^{\circ}\mathrm{C}$) melts in a peritectic reaction under the release of the BCC phase, which consists mainly of Mo.

1.2.5 Monotectics and synthectics

Reasons for miscibiliy or nonmiscibility of components were discussed in section 1.1.2, and it was pointed out that miscibility is usually better for less aggregated (liquid) phases. Typically miscibility grows with T, and demixing may occur also in the liquid phase below some threshold, if the components of the liquid (melt) are not sufficiently similar. For metallic alloys such behavior is found quite often if lead is one component, the example Cu–Pb is shown in Fig. 21. Such phenomena are called monotectic. Inorganic chemical compounds show monotectic demixing in the liquid state sometimes if significantly different anions are involved. Fluoride-oxide systems are good examples [7, 52]. Especially CaF_2 (the mineral fluorite or fluorspar) is often used in metallurgy as melter, because demixing of the melt lowers the temperature of the liquidus and enhances slag formation. Also for crystal growth from melt solutions CaF_2 is a popular solvent which allows to lower the growth temperature significantly, which was demonstrated e.g. for $CaTiO_3$ [28].

If below the dome-shaped 2-liquids region a solid compound phase exists, it melts at the lower boundary of the 2-liquids region under the simultaneous formation of two melts with different composition. Such behavior is called syntectic, an example is the intermediate Cd_2As_3I in the system CdI_2–$CdAs_2$ (Fig. 22).

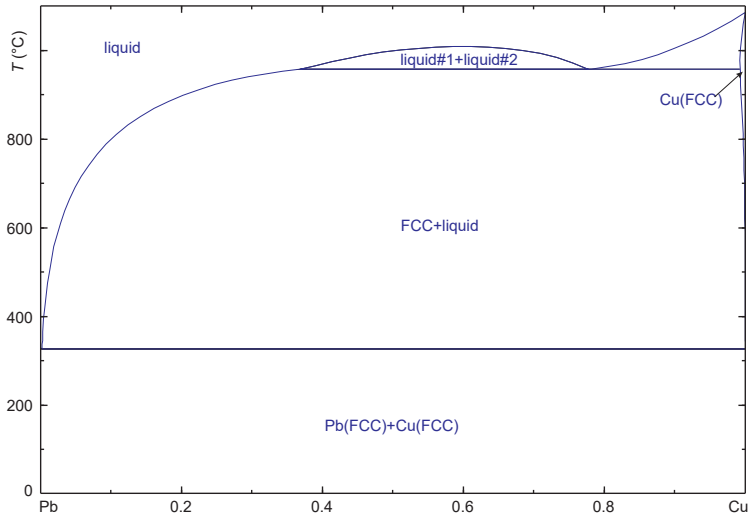


Figure 21: The phase diagram Cu–Pb shows monotectic demixing of the melt. For the isostructural solid phases (FCC) only a small solubility of Pb in Cu is observed at elevated T. The eutectic on the Pb side is degenerate.

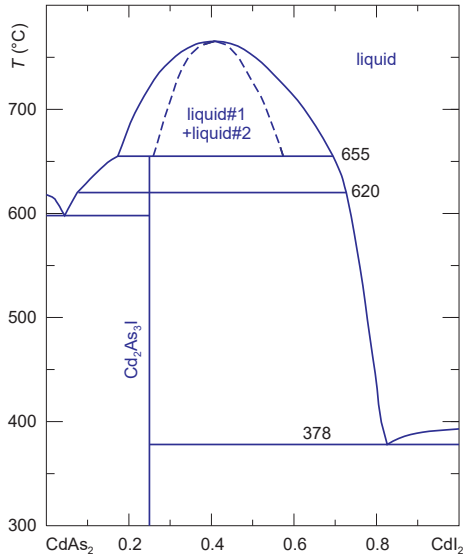


Figure 22: Pseudobinary phase diagram $CdAs_2$–CdI_2 [1]. The intermediate phase Cd_2As_3I shows syntectic melting. The dashed line inside the "liquid#1+liquid#2" region is the spinodal.

1.3 Systems with 3 components

1.3.1 Rectangular concentration coordinates

The introduction of a third component to a thermodynamic system creates one additional degree of freedom. This makes it difficult to present the whole system graphically, even under isobar conditions. One can use the independent concentrations of two components as abscissa and ordinate. For the temperature one of the following two options is used:

1. T is held constant, which is demonstrated in Fig. 23a) and b) for the system Al_2O_3–CaO–BaO. Such diagrams are useful if e.g. the results of annealing experiments have to be evaluated. It can be seen that for the higher temperature ($T = 1900\,°C$) the field where the whole system is liquid is larger than for the lower temperature. Crystallization of one solid phase can be expected from phase fields where the liquid coexists with one solid phase.

2. A polythermal projection is performed, typically onto the liquidus surface which is demonstrated in Fig. 23c) for the same system. For the concentration range that is shown there, $T_f = 2054\,°C$ is the highest temperature. The isotherm contours (in Fig. 23c) every 10 K) show that T_{liq} lowers with increasing x_{CaO} and/or x_{BaO}. The text labels inside the phase fields of Fig. 23c) are the names of the solid phase that crystallizes first in this *field of primary crystallization*, if a corresponding melt is cooled.

Question 9. *Which point in Fig. 23c) is a ternary eutectic? Why?*

Answer. *Point 3 is a ternary eutectic point, because there is a local minimum of the liquidus surface ($T_{eut} = 1718\,°C$). The neighboring phases (Ba,Ca)Al_2O_4(s)/(Ba,Ca)$Al_{12}O_{19}$(s)/$CaAl_4O_7$(s) are its components.*

Rectangular concentration coordinates for 3-component systems can be very useful if one component is clearly prevailing. In Fig. 23 this is Al_2O_3. Other cases are alloys with a well defined main component, like Fe in iron and steel alloys, or for dopants in lasers host and semiconductors. The scaling of the coordinate axes can be chosen from per cents down to parts per million (ppm) in such a way, that useful concentrations are well represented. For too high concentrations of the other components, however, these coordinates are not appropriate: The upper right corner of the diagrams in Fig. 23 corresponds to $x_{CaO} = x_{BaO} = 0.3$, and hence one has just $x_{Al_2O_3} = 0.4$ remaining. For significantly higher x_{CaO} and x_{BaO}, the upper right corner would be meaningless, leaving finally just a rectangular triangle. Unfortunately, in such triangle the 3 components are geometrically not equivalent, and the phase diagram representation is distorted.

In cases with (almost) equivalent components, the presentation of 3-component systems as "concentration triangles", like shown in the next section 1.3.2, is usually more appropriate.

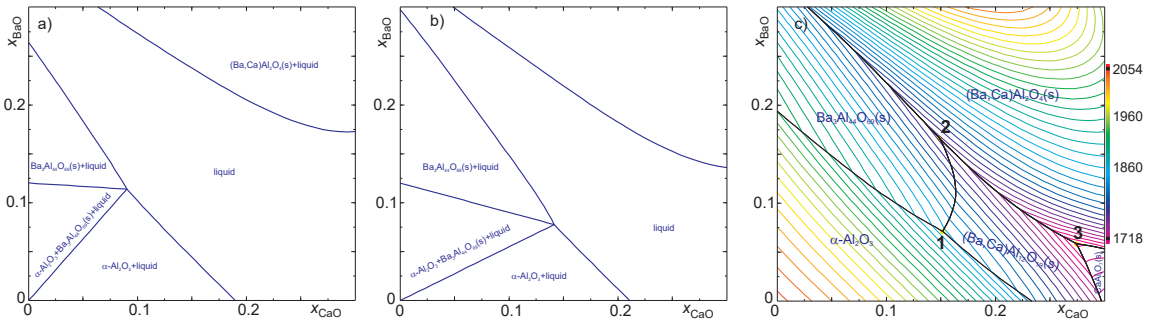


Figure 23: Al_2O_3 rich part of the phase diagram Al_2O_3–CaO–BaO ($x_{CaO}, x_{BaO} \leq 0.3$). a) $T = 1900\,°C$. b) $T = 1870\,°C$. c) Polythermal projection onto the liquidus surface, the maximum temperature 2054 °C (T_f for Al_2O_3) and the minimum temperature 1718 °C are given, isotherms every 10 K. Regions of primary crystallization are labeled. The numbered points of 4-phase equilibria with the liquid phase correspond to the following T: (1) 1863 °C; (2) 1786 °C; (3) 1718 °C.

1.3.2 Concentration triangles

Viviani's theorem says for a regular triangle A–B–C, that for every point inside this triangle the sum of the 3 heights above the opposite sides equals the total height h of the triangle [25].

$$h_A + h_B + h_C = h. \tag{22}$$

If one sets $h = 1$ (=100%), then h_A, h_B, h_C can represent the concentrations x_A, x_B, x_C of the 3-component system A–B–C, because also these concentrations must sum up to unity. Every point of the triangle corresponds one-to-one to a specific chemical composition. The corners i of the regular triangle represent the pure components, because there one has $h_i \equiv x_i = 1$. For lines parallel to the side opposite to corner i the concentration x_i is constant. For a line from corner A towards the opposite side the concentration ratio x_B/x_C is constant (and for lines from corners B and C in analogy).

In contrast to rectangular concentration coordinates (section 1.3.1), the corners in concentration triangles are equivalent. Fig. 24 shows as an example a liquidus projection of the ternary system Al_2O_3–CaO–BaO as concentration triangle. Fields of primary crystallization are labeled. Just some features that are typical for ternary diagrams shall be mentioned here:

- The solubility of Ba in solid CaO and vice versa is limited. In such cases phase names like Ba:CaO(s) are usual. Names like (Ba,Ca)Al_2O_4 hint more on a very wide (if not unlimited) solubility range.

- The phase $CaAl_2O_4$(s) consists of 50% CaO + 50% Al_2O_3. The corresponding point labeled "0.5" on the right side of the triangle lies inside the $CaAl_2O_4$(s) primary crystallization field, which means that at this point a melt and a solid with identical composition are in equilibrium. With other words: $CaAl_2O_4$(s) melts congruently.
- The phase $Ca_3Al_2O_6$(s) (without Ba doping) consists of 75% CaO + 25% Al_2O_3. The point marking this composition is on the right triangle side, 2.5 ticks above the basis line. This point, however, is outside the $Ca_3Al_2O_6$(s) primary crystallization field which begins ca. at 29% Al_2O_3. Consequently $Ca_3Al_2O_6$ melts peritectically under the formation of CaO(s).
- Only $Ba_3CaAl_2O_7$(s) and $BaCa_2Al_8O_{15}$(s) are ternary phases; the other solids are stable already on the rims of the triangle as binary phases.

Question 10. *Where are the concentration boundaries of Fig. 23 in Fig. 24?*

Answer. *Pure Al_2O_3 is the top corner. The bottom right corner $x_{CaO} = 0.3$ of Fig. 23 is on the right triangle side, 3 ticks below the top; accordingly the top left corner is on the same height on the left triangle side. The top right corner $x_{CaO} = x_{BaO} = 0.3, x_{Al_2O_3} = 0.4$ is in the vertical middle, 4 ticks above the bottom of the triangle.*

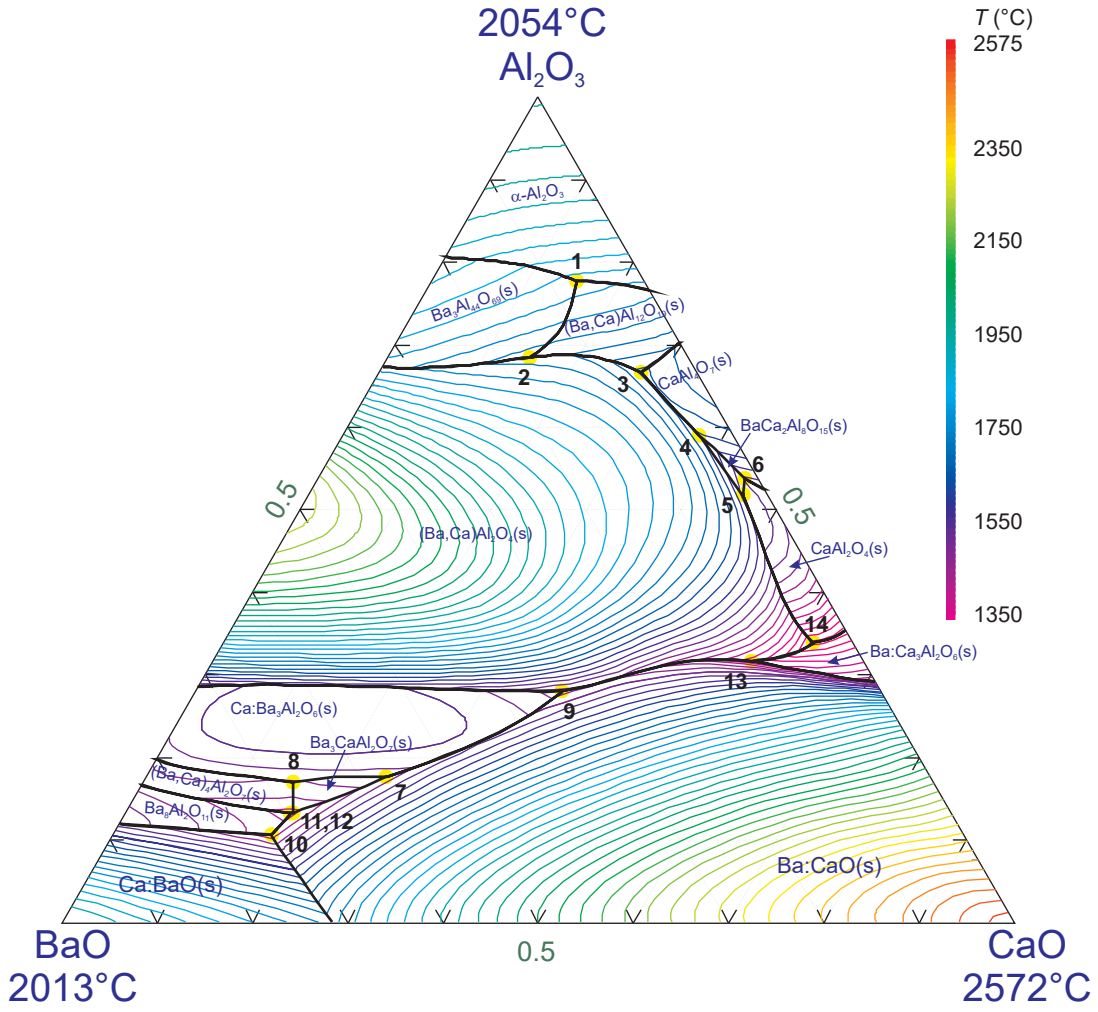


Figure 24: Concentration triangle Al_2O_3–CaO–BaO, projection onto the liquidus surface; isotherms every 25 K. For the region near the top corner see also Fig. 23. T_f for the components given at the corners; T_f^{CaO} is the highest point of the liquidus. The eutectic (14) is the lowest point at 1366 °C.

1.3.3 Reciprocal salt pairs

If two ionic substances with different cations and different anions are mixed, the system behaves often not binary. Fig. 25 shows as an example the sections with components NaF–RbCl, and NaCl–RbF, respectively. Only the first of them, Fig. 25a), can satisfactory be described as a binary system: From a mixture of NaF and RbCl one of these 2 "components" crystallizes first, and at $x_{\text{eut}} \approx 0.07$ a eutectic point occurs. It is clear that in the melt not the species as such, but instead the ions Na^+, Rb^+, F^-, Cl^- will occur, but obviously this does not change the topology of the phase diagram. It should be remarked, however, that at intermediate compositions a significant change of the NaF liquidus slope occurs, which is "suspicious".

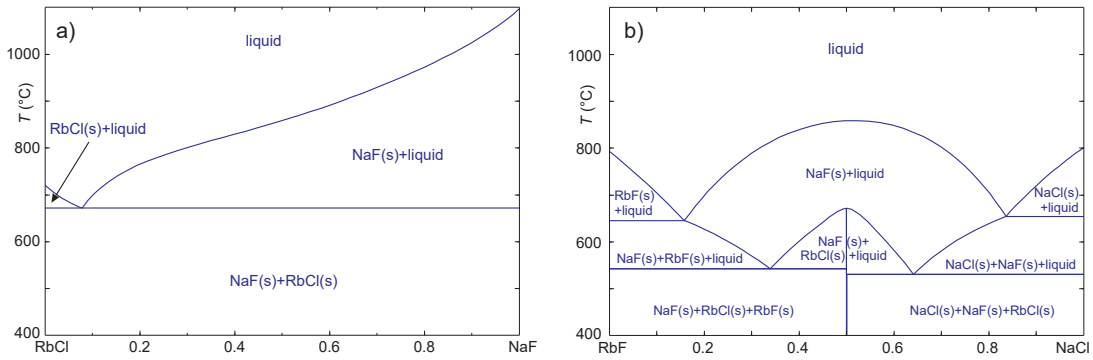


Figure 25: a) The pseudo-binary system NaF–RbCl is eutectic. The untypical change of slope of the liquidus line is remarkable, however. b) The system NaCl–RbF is obviously not binary: It is rather an isopleth section through the reciprocal salt pair Na^+/Rb^+–Cl^-/F^- (Fig. 26).

Obviously the same ions Na^+, Rb^+, F^-, Cl^- occur for mixtures of NaCl and RbF, and the corresponding diagram is shown in Fig. 25b). This diagram is not a binary phase diagram; it contradicts all rules that were treated so far. For instance, from melts with intermediate compositions NaF(s) crystallizes first – a phase that cannot be constructed as a linear combination of NaCl and RbF. It was mentioned already in section 1.1.1 that the corresponding $C = 4$ ions are correct components. Typically such phase diagrams are drawn as "reciprocal salt pairs" in square coordinates, which is shown in Fig. 26 for the current system.

The phase rule (1) can be applied to the current system as follows [2]: One degree of freedom is reduced from isobar conditions. Besides, the sum of cations must be equal to the sum of anions: [Na]+[Rb]=[F]+[Cl]. Hence (1) is reduced to $P + F = C = 4$. With other words, at invariant points $C = 4$ phases are in equilibrium. In Fig. 26 this is the case for the points (1) and (2) where the always 3 neighboring solids are in equilibrium with the melt.

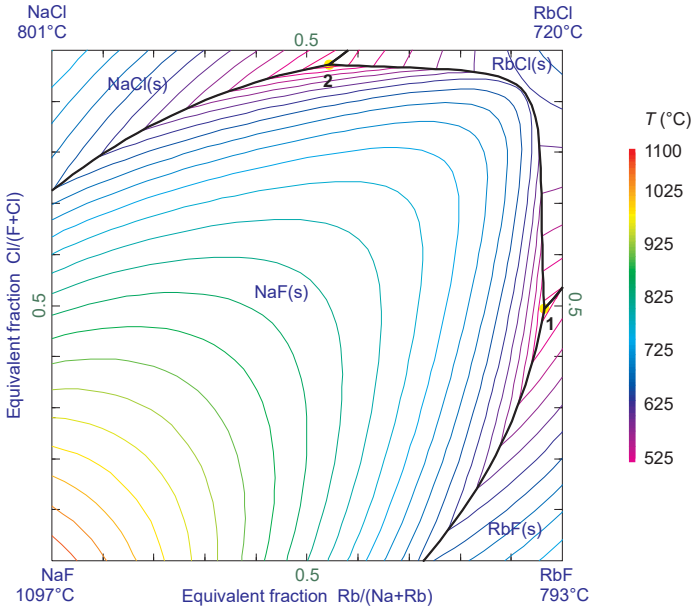


Figure 26: Reciprocal salt system Na/Rb–Cl/F as liquidus projection with 25 K isotherms. All four rim systems are eutectic. The two ternary eutectics are at 542 °C (1) or 530 °C (2), respectively. The two diagrams from Fig. 25 correspond to the diagonals of the reciprocal salt system.

From Fig. 26 it is clear why the two diagrams in Fig. 25 are so different. NaF(s) has by far the highest melting point $T_f = 1097\,°C$, and hence its region of primary crystallization occupies the largest part of Fig. 26. The diagonal from bottom left to top right corresponds to Fig. 25a). At this section the black (eutectic) line between (1) and (2) has a saddle point, and also the isotherms on the liquidus surfaces of NaF(s) and RbCl(s) have saddle points there. Hence, every composition in Fig. 26 that lies exactly on the NaF–RbCl diagonal will remain there during the crystallization process; this subsystem can be regarded as 2-component.

Not so the diagonal from bottom right to top left (RbF–NaCl, Fig. 25b). It crosses primary crystallization fields of RbF(s), NaF(s), and NaCl(s); and all these phases must appear in this isopleth section. Besides, the liquidus surfaces have inclinations to different sides, which is especially obvious for the NaF(s) field. Hence, crystallization is accompanied with segregation away from the line – this is not a binary system.

2 Gas phase and kinetic aspects

2.1 Volatile components

For the phase diagrams that were discussed so far (section 1), mainly equilibria between liquid and solid phase(s) were discussed, which is often sufficient. It turned out, however, that for some crystalline materials of high technical relevance (e.g. GaAs, GaP, GaN, InP, and other $A^{III}B^{V}$ semiconductors) the vapor pressure of the volatile pnictide component (As, P, N) plays a significant role. The crystals that are mentioned above can only be grown from the melt if an overpressure is applied. Not only the melt composition but also the pnictide vapor pressure ($\approx$ its fugacity) in the gas phase influences the III/V ratio of the crystals that can deviate from the ideal value 0.5 [48].

Fig. 27a) shows the concentration–temperature ($x - T$) phase diagram Ga–As which contains one intermediate compound GaAs. Under ambient pressure pure arsenic evaporates before melting, but at elevated pressures of several bars the $G(T)$ function of As(gas) can be raised in such a way, that As(liq) becomes stable (see for the example sulfur Fig. 4). Then a eutectic appears between As and GaAs. The eutectic on the other side, towards Ga, is degenerate because the melting point of Ga is very low (303 K).

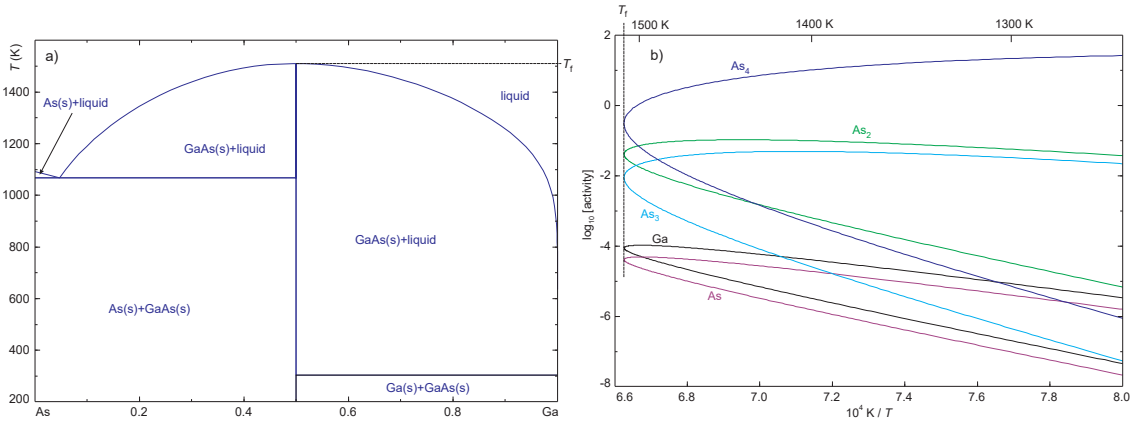


Figure 27: a) Binary $x - T$ phase diagram Ga–As with the intermediate phase GaAs (T in Kelvin!). A total pressure $p = 50$ bar was assumed to stabilize the liquid phase up to the congruent melting point $T_f = 1509$ K. b) Fugacity ($\approx$ vapor pressure) of several species along the GaAs liquidus. For As_i the upper branch is valid for the As-rich part of the liquidus in Fig. a), for Ga vice versa.

From melts between both eutectics GaAs(s) crystallizes first at the corresponding liquidus temperature T_{liq} which is a function of the Ga concentration x. At every point of the liquidus $T_{liq}(x)$, gallium (occurs only as monomer Ga(gas)) and arsenic (occurs as As_i(gas), $i = 1 \ldots 4$) show some degree of volatility which can be expressed as the activity

(fugacity, vapor pressure) of their species in the gas phase. One can expect that

- activity becomes larger for higher T
- activity of Ga(gas) becomes larger for larger x, and vice versa activity of As_i(gas) becomes larger for smaller x.

It is convenient to plot the log[activity] as functions of the reciprocal temperature, as shown in Fig. 27b). For some $A^{III}B^{V}$ [38] and $A^{II}B^{VI}$ [49] semiconductors similar plots were developed already in the 1960s, however often without separate consideration of the single species. The left apex of the $\log_{10}[\text{activity}](T^{-1})$ functions in Fig. 27b) is always at the inverse melting point T_{f}^{-1}, and the upper branch of the As_i curves describes the corresponding fugacities along the liquidus on the As-rich ($x < 0.5$) side of the phase diagram in Fig. 27a). Accordingly, the lower branch gives the logarithmic activities on the Ga-rich side. Vice versa, the fugacity of Ga is higher for $x > 0.5$, and lower for $x < 0.5$.

2.2 Ellingham type diagrams

Most transition metals Me (and some metals from the main groups of the periodic system of elements too) can form with oxygen different oxides $MeO_{m/2}$ (m – valency). Oxidation reactions

$$2\mathrm{MeO}_{m/2} + \frac{1}{2}\mathrm{O}_2 \rightleftarrows 2\mathrm{MeO}_{(m+1)/2} \tag{23}$$

from m to $m+1$ are usually exothermal. Then the equilibrium (23) shifts to the product side if the oxygen fugacity p_{O_2} is increased or if T is reduced, and vice versa. Often the fugacities of the metal oxides can be neglected with respect to p_{O_2}, and then one can write for equilibrium conditions

$$\Delta G^0 = \Delta H^0 - T\Delta S^0 = RT \ln p_{\mathrm{O}_2} \tag{24}$$

which means that plots of $RT \ln p_{\mathrm{O}_2}$ vs. T ("Ellingham plots") are almost straight lines. If $RT \ln p_{\mathrm{O}_2}(T)$ functions are plotted for different (subsequent) oxidation states $m, m+1, \ldots$ of the metal Me, then the areas between these plots are phase fields where one specific oxidation (valency) state is stable [11, 22, 24, 36].

For the system Mn–O_2 such predominance phase diagram is shown in Fig. 28. The upper limit of the diagram corresponds to $\ln[p_{\mathrm{O}_2}] = 0$, which is pure oxygen under ambient total pressure $p = 1\,\mathrm{bar}$. It is obvious that for low T and high p_{O_2} higher valencies of the metal (here $Mn^{4+}O_2$) are stable; towards the bottom right corner of the diagram Mn^{3+}, Mn^{2+}, and finally the metal Mn^0 become stable. Vertical lines for Mn mark a series of transitions between several solid phases of pure manganese, and finally the melting point at 1519 K. The manganese oxides are mixing in the molten state, forming the MnO_x(liq) phase with variable oxygen content that is found in the top right corner of the diagram.

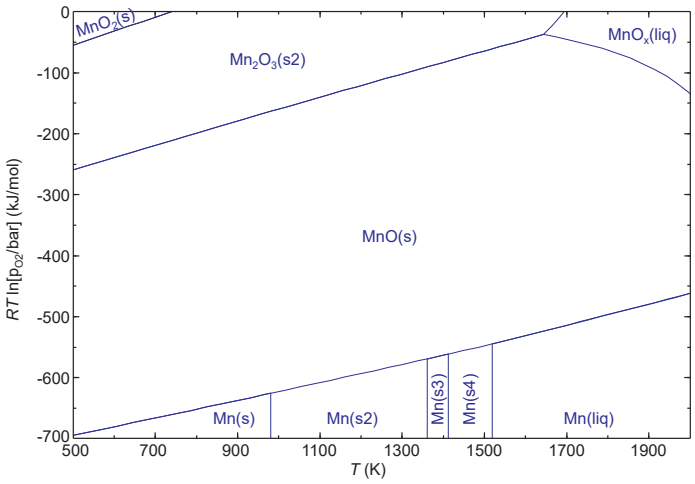


Figure 28: Ellingham type predominance diagram of the system Mn–O_2. The almost linear phase boundaries between the MnO_x describe the Gibbs free energy change of corresponding reactions (23). Other oxides like Mn_3O_4 or Mn_2O_7 were not found in this calculation.

The presentation in Fig. 28 is straightforward from the thermodynamic point of view; certainly the mainly linear phase boundaries are beneficial for calculations. However, the ordinate scaling is for some practical applications not very useful. The blue solid lines in Fig. 29 show the same information with the alternative ordinate scaling $\log[p_{O_2}/\mathrm{bar}]$, where oxygen fugacities can be read directly. Again the upper border of the diagram corresponds to 1 bar of pure oxygen. Air (oxygen concentration 21%) has $\log[p_{O_2}/\mathrm{bar}] = -0.678$. Also an "inert gas", such as argon, has almost some finite oxygen partial pressure: Even a "6N" gas with 99.9999% purity contains 1 ppm unspecified impurities, which are typically air. This results in $\log[p_{O_2}/\mathrm{bar}] \approx -6.7$. Even under high vacuum conditions the logarithmic oxygen partial pressure will be not significantly smaller that -10, but reactive gases such as CO_2, CO, and H_2 can deliver $p_{O_2}(T)$ levels that are partially extremely low [11, 27], see Table 1.

	1000 K	1500 K	2000 K
"pure" CO (see Fig. 29)	6×10^{-22}	1×10^{-17}	1×10^{-15}
CO + 0.1% O_2	6×10^{-22}	9×10^{-17}	7×10^{-12}
H_2 + 0.1% O_2	3×10^{-26}	1×17^{-17}	3×10^{-13}

Table 1: Oxygen fugacities (in bar) of some reactive gas atmospheres for a total pressure $p = 1$ bar. Calculated with FactSage [13].

This is demonstrated by the dashed lines in Fig. 29 which show (as an overlay to the

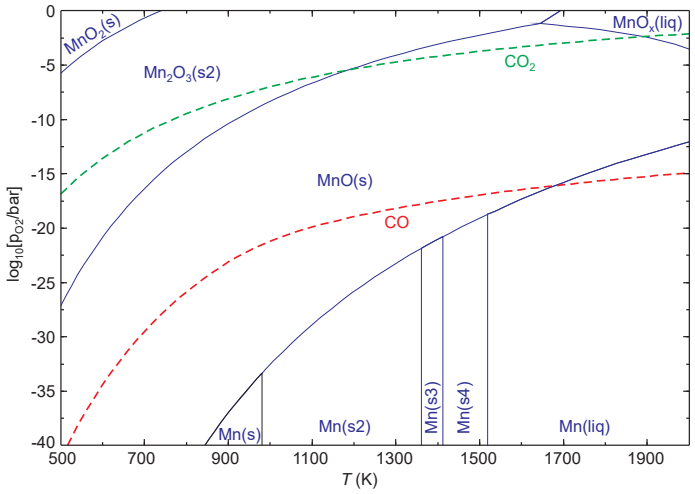


Figure 29: Predominance diagram of the system Mn–O_2 in coordinates $T - \log[p_{O_2}/\mathrm{bar}]$. The blue and red dashed lines describe the $\log[p_{O_2}/\mathrm{bar}](T)$ that is supplied by pure carbon dioxide or carbon monoxide, respectively (total pressure $p = 1\,\mathrm{bar}$).

Mn–O_2 predominance diagram) the temperature dependent oxygen fugacities of carbon dioxide and carbon monoxide which decay according

$$\mathrm{CO_2} \;\rightleftarrows\; \mathrm{CO} + \frac{1}{2}\mathrm{O_2} \tag{25}$$

$$\mathrm{CO} \;\rightleftarrows\; \mathrm{C} + \frac{1}{2}\mathrm{O_2} \tag{26}$$

under the formation of free oxygen. Both reactions (25) and (26) are endothermal and consequently the equilibria shift to the product side for higher T, which means that $p_{O_2}(T)$ grows monotonously.

Fig. 29 shows that pure CO delivers p_{O_2} levels way below that what can be reached in vacuum or in "inert gases" like Ar, N_2. Mixtures of CO_2 and CO can create $p_{O_2}(T)$ levels between the curves of the pure gases. It was demonstrated, e.g., that a mixture of 85% Ar, 10% CO_2 and 5% CO stabilizes Fe^{2+} (FeO, olivine) over a wide temperature range [21].

Carbon monoxide is a rather reducing gas. Alternatively hydrogen as component of the growth atmosphere (often mixed with an excess of nitrogen as "forming gas" 95% N_2 + 5% H_2) can lead with

$$\mathrm{H_2O} \rightleftarrows \mathrm{H_2} + \frac{1}{2}\mathrm{O_2} \tag{27}$$

to low $p_{O_2}(T)$. It is remarkable that accidental oxygen traces in the atmosphere (from impure gases or leaks) can be "buffered away" to a large extend by an excess of H_2 or CO. Table 1 shows that even 0.1% = 1000 ppm oxygen impurity lead only to $p_{O_2}(2000\,\mathrm{K})$ below 10^{-11} bar.

The benefits of convenient abscissa scaling (p_{O_2}, Fig. 29) and almost straight phase boundaries (Fig. 28) are combined if metal–oxygen phase diagrams are plotted in coordinates $T^{-1} - \log[p_{O_2}/\mathrm{bar}]$, which is done again for the Mn–O_2 system in Fig. 30. Similar

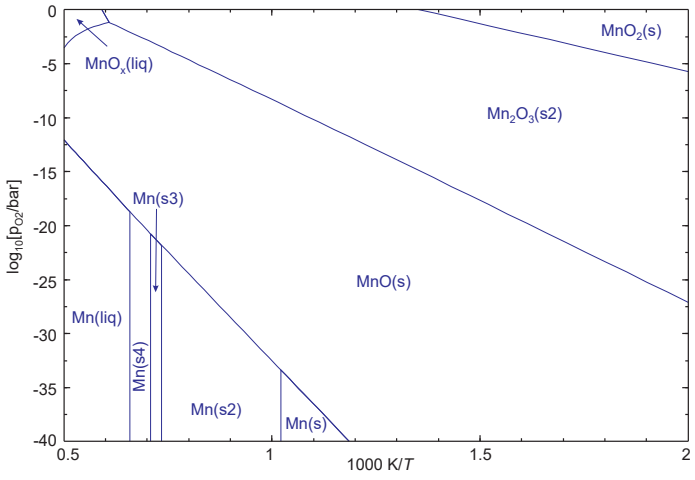


Figure 30: Predominance diagram of the system Mn–O_2 in coordinates $T^{-1}-\log[p_{O_2}/\text{bar}]$ ("TOMBE" diagram [32]).

diagrams were helpful for the description of the crystal growth by physical vapor transport (PVT) of ZnSe [44]. Recently such diagrams were used for the discussion of molecular beam epitaxy (MBE) processes of ruthenate films [32], and Nair et al. named them "TOMBE" (Thermodynamics Of MBE) diagrams.

2.3 Kinetic and surface effects

Already in the context of mixed crystals (section 1.2.2) it was discussed that crystallization processes can lead to significant deviations from thermodynamic equilibrium. If the system is partially crystallized, reaching continuous equilibrium would require permanent diffusion processes between liquid and solid phase, often over distances of millimeters or more. Because such diffusion processes would require time periods which are substantially longer than typical experiments, non-equilibrium cooling as described by Gulliver-Scheil (Fig. 17b) will often occur, rather than equilibrium cooling as described in Fig. 17c).

The uneven distribution of components over different phases and the anisotropy of the surface energy of solid (crystalline) phases leads to several other phenomena that will be discussed in the following sections.

2.3.1 Partitioning coefficients

Only in systems with 1 component and in multicomponent systems at congruently melting compositions solidification does not lead to chemical segregation. In most other cases the composition of the fluid mother phase (often a melt or solution, sometimes a gaseous phase) is different from the composition of a solid that is crystallizing from it.

Often crystals of a specific chemical composition, like a laser host crystal with a defined concentration of the active ion or a semiconductor crystal with a specific doping level, has to be grown from the melt. This process will be described with the help of Fig. 31 which

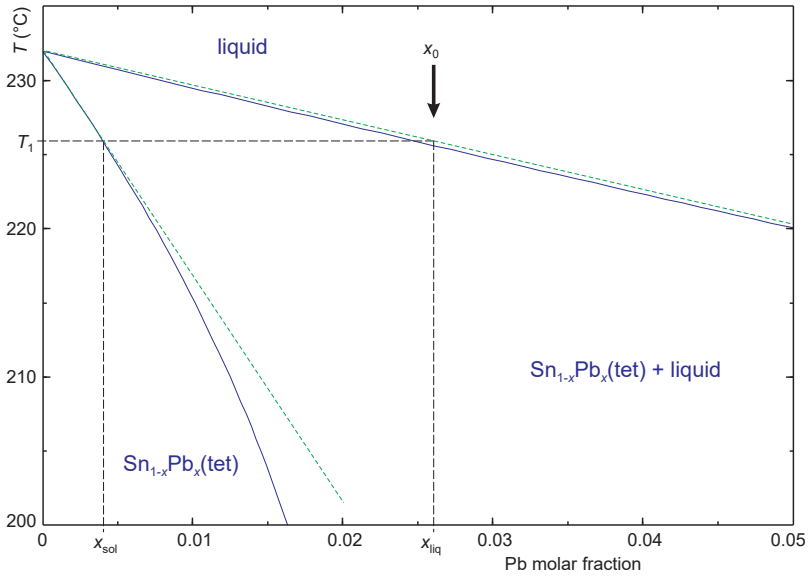


Figure 31: The Sn-rich part of the binary system Pb–Sn that is shown completely in Fig. 16. In the vicinity of $x = 0$ liquidus and solidus (blue full lines) can be approximated by the straight (green, dashed) lines, and the partitioning coefficient is constant.

holds as an example for all similar processes where from a melt with arbitrary composition x_0 a solid with variable composition (here the tin-rich alloy $\mathrm{Sn}_{1-x}\mathrm{Pb}_x$(tet)) crystallizes. For the initial composition $x_0 \approx 0.026$ crystallization starts at $T_1 \approx 226\,^\circ\mathrm{C}$. Then a melt of the initial composition $x_0 = x_{\mathrm{liq}}$ is in equilibrium with a solid of the composition $x_{\mathrm{sol}} \approx 0.004$.

The ratio of the lead concentrations in both phases

$$k = \frac{x_{\mathrm{sol}}}{x_{\mathrm{liq}}} \tag{28}$$

is called equilibrium "partitioning coefficient" or "distribution coefficient" of lead in tin. Often (especially for semiconductors) only small concentrations of the dopant are relevant, and then the originally bent liquidus or solidus curves can be approximated by straight lines (dashed green in Fig. 31). If this holds, k does not depend on x and is usually named k_0. It turns out that often in real systems k does not depend on x over a wide concentration range, at least in the experimental accuracy limits of concentration measurements [42], and k can be replaced by k_0 in equation (28).

If the melt crystallizes, a constituent with $k_0 < 1$ will be enriched in the remaining melt, and in contrast for $k_0 > 1$ the concentration of this constituent in the rest of the melt will drop. This enrichment or depletion, respectively, will take place especially directly near the front of the phase boundary that is continuously moving forward during crystallization. If e.g. for $k_0 < 1$ directly in front of the solid/liquid phases boundary a constituent is

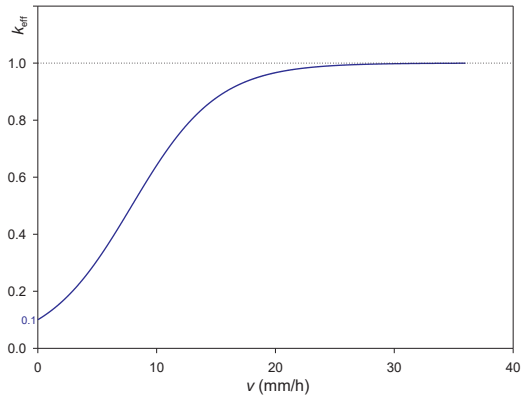
enriched (see bottom curve in Fig. 32). From this locally somewhat higher concentration a larger part will be incorporated into the growing crystal than one would expect if the homogeneous melt volume reaches directly to the interface. The strength of this effect will be a function of the width of the "boundary layer" and of the diffusion coefficient in this layer. Always the resulting effective distribution coefficient [4]

$$k_{\text{eff}} = \frac{k_0}{k_0 + (1 - k_0) \exp\left[-\frac{v\delta}{D}\right]} \tag{29}$$

will be closer to unity than k_0 (v – growth rate; δ – width of the boundary layer; D – diffusion coefficient, see question 11). Alternative concepts for k_{eff} are discussed in the literature [9, 34].

Question 11. *Draw the function (29) for the following parameters: boundary layer width* $\delta = 0.1\,mm$*; diffusion coefficient* $D = 1 \times 10^{-10}\,m^2/s$*; equilibrium distribution coefficient* $k_0 = 0.1$*; growth rate* v *in the range from zero to* $1 \times 10^{-5}\,m/s = 36\,mm/h$*.*

Answer.



(Answer to Question 11): The graph is shown on the left side. It starts for $v = 0$ *at* $k_0 = 0.1$ *and rises then up to* $k_{\text{eff}} = 1$ *at high growth rates, where no segregation occurs.*

2.3.2 Constitutional supercooling

If for $k < 1$ the lower melting component of a mixed crystal system is enriched in the boundary layer at the crystallization front (lowermost curve in Fig. 32), the liquidus temperature T_{liq} of the melt will drop in this region. This is obvious e.g. from Fig. 17a) where the liquidus drops monotonously if the concentration of NaCl in a melt close to KCl grows.

The temperature at the interface is fixed to the melting temperature T_{f}. The melt volume will always be hotter than the interface, resulting in a temperature gradient $\partial T/\partial z = G_T$ in the boundary layer (z – coordinate direction towards the melt volume). If this temperature gradient is very flat (red dashed line $(\partial T/\partial z)'$ in Fig. 32), the temperature in some regions close to the interface may be lower than the local liquidus temperature. This is critical, because a perturbation of the solid surface may reach into melt volumes where the supersaturation is larger. Correspondingly, the perturbation will grow, leading

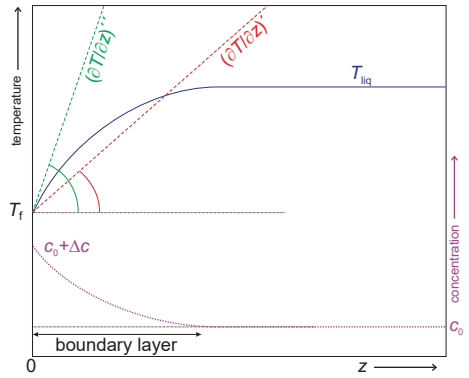


Figure 32: Bottom curve: concentration profile in front of a crystallization front (at $z = 0$) for $k_0 < 1$. Above: the resulting $T_{\mathrm{liq}}(z)$, together with a critical (small) $G_T = (\partial T/\partial z)'$ leading to constitutional supercooling and an uncritical larger $G_T = (\partial T/\partial z)''$.

to growth instabilities or "coarsening". Coarsening can be avoided if the Tiller criterion

$$\frac{G_T}{v} > \frac{m(1-k_0)}{Dk_0} c_0 \tag{30}$$

is fulfilled [40, 45, 26]. $m = \partial T_{\mathrm{liq}}/\partial z$ is the slope of the liquidus curve and c_0 is the concentration of the lower melting component in the melt volume.

2.3.3 Growth shapes

Often the geometrical shape of a growing crystal is determined by external conditions: if a crystal grows from the melt in a temperature field with large gradients, the surface of the crystal will be formed where the temperature reaches the melting point T_{f}. The almost cylindrical shape of most Czochralski boules has its origin in the symmetry of the temperature field of the Czochralski setup where a cylindrical crucible is heated slightly above T_{f} and the heat flows towards the colder center. Remaining asymmetry is typically compensated by rotation of the crystal and/or the crucible.

If crystals are growing in very low temperature gradients, or if crystal spheres are dissoluted slowly in suitable solvents, the crystal can reach its "equilibrium shape" or growth shape, which represents the state where the surface energy of the crystal is minimum for a given volume. This surface energy is the sum

$$W_{\mathrm{sf}} = \sum_i \sigma_{\mathrm{sf}_i} A_i \tag{31}$$

of all free surface areas A_i of the crystal times the specific surface energies σ_{sf_i} of these faces. σ_{sf} is a function of the orientation (hence of the Millers indices $\{hkl\}$ of the corresponding surface) and varies usually not abrupt. Besides, the symmetry elements of the crystal itself must be represented in the symmetry of the σ_{sf} – this is the reason why curly braces, which mark equivalent lattice planes, are used for the $\{hkl\}$.

A geometrical construction of the equilibrium shape that dates back to Gibbs [12] and Wulff [50] is shown in Fig. 33. The drawing is performed perpendicular to a 4-fold axis of a

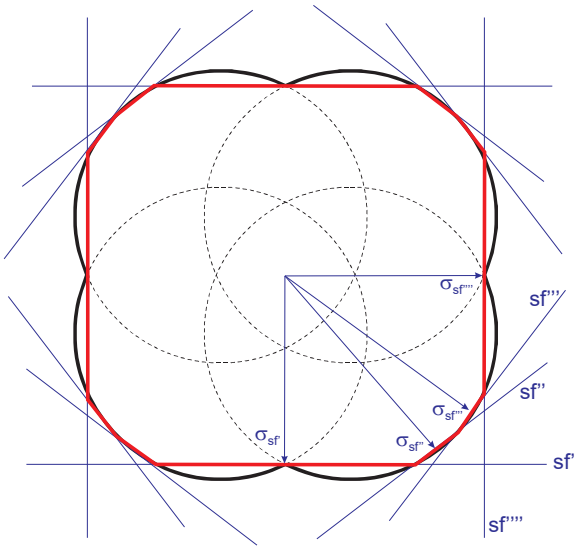


Figure 33: Wulff's construction [50] of an equilibrium polyeder in $2\mathbb{D}$: the angular dependent specific surface energies $f_{\mathrm{sf}'}$, $f_{\mathrm{sf}''}$, ... are plotted in their corresponding directions (blue arrows), and normal planes are constructed at their ends (blue lines sf', sf", ...). The polyhedron with minimum area that is surrounded by these normal planes is the equilibrium growth shape (red thick dodecagon).

crystal, without loss of generality one can assume that this is the $[001] = \vec{c}$ axis. The surface energy shall be represented by the thick black line which is actually approximated by four overlapping segments of circles. Obviously σ has minima in the horizontal and vertical $\{100\}$ directions where inward cusps are found. Maxima are in the diagonals $\{110\}$.

Obviously the symmetry of the crystal requires $\sigma_{\mathrm{sf}'} = \sigma_{\mathrm{sf}''''}$ and $\sigma_{\mathrm{sf}''} = \sigma_{\mathrm{sf}'''}$. The blue thin lines that are drawn at the corresponding arrow end represent potential faces of the crystal. Additional arrows along $\{110\}$ are not drawn, because $\sigma_{\{110\}}$ is so large that the arrow end would be outside the Gibbs-Wulff plot. Hence, only the closed area that is formed by the "valid" normals of $\sigma_{\{hkl\}}$ is the equilibrium shape. For a more recent and more detailled treatment the reader is referred to the literature [6].

Acknowledgment

The author expresses his gratitude to D. Siche for carefully reading the manuscript.

References

[1] ACerS/NIST, *Phase diagrams for ceramists, entry 13691*, Version 3.4.0.

[2] María F. Acosta, Rosa I. Merino, Steffen Ganschow, and Detlef Klimm, *Solidification of $NaCl$–LiF–CaF_2 ternary composites*, J. Mat. Sci. **52** (2017), 5520–5530.

[3] Ihsan Barin, *Thermodynamic data of pure substances*, VCH, Weinheim, 1993.

[4] J. A. Burton, R. C. Prim, and W. P. Slichter, *Distribution of solute in crystals grown from the melt*, J. Chem. Phys. **21** (1953), 1987–1991.

[5] Dirk Durinck, Peter Tom Jones, Bart Blanpain, Patrick Wollants, Gilles Mertens, and Jan Elsen, *Slag solidification modeling using the Scheil-Gulliver assumptions*, J. Am. Ceram. Soc. **90** (2007), 1177–1185.

[6] T. L. Einstein, *Equilibrium shape of crystals*, Handbook of Crystal Growth (Second Edition) (Tatau Nishinaga, ed.), Elsevier, Boston, 2015, pp. 215–264.

[7] Marianne Færøyvik, Tor Grande, Stein Julsrud, and Arne Seltveit, *Phase relations in the system NaF–CaF_2–$NaAlSiO_4$–$CaAl_2Si_2O_8$*, J. Amer. Ceram. Soc. **82** (1999), 190–196.

[8] P. P. Fedorov, A. E. Kokh, N. G. Kononova, and T. B. Bekker, *Investigation of phase equilibria and growth of BBO (β-BaB_2O_4) crystals in BaO–B_2O_3–Na_2O ternary system*, J. Crystal Growth **310** (2008), 1943–1949.

[9] S. Ganschow, *Melt growth of oxide single crystals in controlled oxygen fugacity atmosphere*, Ph.D. thesis, Technische Universität Berlin, 2015.

[10] S. Ganschow, D. Klimm, P. Reiche, and R. Uecker, *On the crystallization of terbium aluminium garnet*, Cryst. Res. Technol. **34** (1999), 615–619.

[11] S. Ganschow, D. Schulz, D. Klimm, R. Bertram, and R. Uecker, *Application of predominance diagrams in melt growth of oxides*, Cryst. Res. Technol. **45** (2010), 1219–1224.

[12] J.W. Gibbs, *On the equilibrium of heterogeneous substances*, Transaction of the Connecticut Academy of Arts and Sciences **III** (1878), 108–524.

[13] GTT Technologies, Kaiserstr. 100, 52134 Herzogenrath, Germany, *Factsage 7.2*, 2018, http://www.factsage.com/.

[14] Christo Guguschev, Detlef Klimm, Frank Langhans, Zbigniew Galazka, Dirk Kok, Uta Juda, and Reinhard Uecker, *Top-seeded solution growth of $SrTiO_3$ crystals and phase diagram studies in the SrO–TiO_2 system*, CrystEngComm **16** (2014), 1735–1740.

[15] G. H. Gulliver, *The quantitative effect of rapid cooling upon the constitution of binary alloys*, J. Inst. Met. **9** (1913), 120–157.

[16] J. H. Haeni, P. Irvin, W. Chang, R. Uecker, P. Reiche, Y. L. Li, S. Choudhury, W. Tian, M. E. Hawley, B. Craigo, A. K. Tagantsev, X. Q. Pan, S. K. Streiffer, L. Q. Chen, S. W. Kirchoefer, J. Levy, and D. G. Schlom, *Room-temperature ferroelectricity in strained $SrTiO_3$*, Nature **430** (2004), 758–761.

[17] Tamino Hirsch, Christo Guguschev, Albert Kwasniewski, Steffen Ganschow, and Detlef Klimm, *Investigation of the Nd_2O_3–Lu_2O_3–Sc_2O_3 phase diagram for the preparation of perovskite-type mixed crystals $NdLu_{1-x}Sc_xO_3$*, J. Crystal Growth **505** (2019), 38–43.

[18] International Union of Crystallography, *International Tables for Crystallography Volume A: Space-group symmetry*, 2016, https://it.iucr.org/Ac/contents/.

[19] J. J. Nye, *Physical properties of crystals*, Clarendon, Oxford, 1957.

[20] D. Klimm, *Growth of bulk ZnO*, Reference Module in Materials Science and Materials Engineering (Saleem Hashmi, ed.), Elsevier, Oxford, 2016, pp. 1–18.

[21] D. Klimm and S. Ganschow, *The control of iron oxidation state during FeO and olivine crystal growth*, J. Crystal Growth **275** (2005), e849—-e854.

[22] D. Klimm, S. Ganschow, D. Schulz, R. Bertram, R. Uecker, P. Reiche, and R. Fornari, *Growth of oxide compounds under dynamic atmosphere composition*, J. Crystal Growth **311** (2009), 534–536.

[23] D. Klimm, M. Rabe, R. Bertram, R. Uecker, and L. Parthier, *Phase diagram analysis and crystal growth of solid solutions $Ca_{1-x}Sr_xF_2$*, J. Crystal Growth **310** (2008), 152–155.

[24] D. Klimm and W. Schröder, *The influence of atmosphere on high temperature crystal growth*, J. Korean Assoc. Crystal Growth **9** (1999), 360–364.

[25] Detlef Klimm, *Phase equilibria*, Handbook of Crystal Growth (T. Nishinaga, ed.), Elsevier, second ed., 2014, pp. 85–136.

[26] Detlef Klimm, *Thermodynamic and kinetic aspects of crystal growth*, Handbook of Solid State Chemistry, Wiley-VCH Verlag GmbH & Co. KGaA, Weinheim, Germany, 2017, pp. 375–398.

[27] Detlef Klimm, Steffen Ganschow, Zbigniew Galazka, Rainer Bertram, Detlev Schulz, and Reinhard Uecker, *Reactive atmospheres for oxide crystal growth*, Advances in Solid Oxide Fuel Cells and Electronic Ceramics (Narottam P. Bansal, Mihails Kusnezoff,

and Kiyoshi Shimamura, eds.), Ceramic Engineering and Science Proceedings, John Wiley & Sons, Inc., Hoboken, NJ, USA, 2016, p. 157.

[28] Detlef Klimm, Max Schmidt, Nora Wolff, Christo Guguschev, and Steffen Ganschow, *On melt solutions for the growth of $CaTiO_3$ crystals*, J. Crystal Growth **486** (2018), 117–121.

[29] Zhen-bang Kuang, *Internal energy variational principles and governing equations in electroelastic analysis*, Internat. J. Sol. Struct. **46** (2009), 902–911.

[30] Yuanyuan Ma and Alexandra Navrotsky, *Calorimetric study of heats of mixing in $Sn_x Ti_{1-x} O_2$ rutile solid solutions*, J. Amer. Ceram. Soc. **93** (2010), 3432–3436.

[31] R. Miloua, F. Miloua, A. Arbaoui, Z. Kebbab, and N. Benramdane, *Theoretical study of phase separation in $Cd_{1-x} Zn_x O$ alloys*, Solid State Commun. **144** (2007), 5–9.

[32] Hari P. Nair, Yang Liu, Jacob P. Ruf, Nathaniel J. Schreiber, Shun Li Shang, David J. Baek, Berit H. Goodge, Lena F. Kourkoutis, Zi Kui Liu, Kyle M. Shen, and Darrell G. Schlom, *Synthesis science of $SrRuO_3$ and $CaRuO_3$ epitaxial films with high residual resistivity ratios*, APL Materials **6** (2018), no. 4, 046101.

[33] K. Oka, H. Unoki, and A. Negishi, *Crystal growth and phase diagram of $Gd_{3-x} Y_x Fe_5 O_{12}$ system*, J. Crystal Growth **284** (2005), 440–445, see also Phase Diagrams for Ceramists, entry 11789.

[34] Aleks G. Ostrogorsky and Martin E. Glicksman, *Segregation and component distribution*, Handbook of Crystal Growth (Second Edition) (Tatau Nishinaga, ed.), Elsevier, Boston, 2015, pp. 995–1047.

[35] Dorota A. Pawlak, Sebastian Turczynski, Marcin Gajc, Katarzyna Kolodziejak, Ryszard Diduszko, Krzysztof Rozniatowski, Julita Smalc, and Irina Vendik, *How far are we from making metamaterials by self-organization? The microstructure of highly anisotropic particles with an SRR-like geometry*, Advanced Functional Materials **20** (2010), 1–9.

[36] A. D. Pelton, *Thermodynamics and phase diagrams of materials*, Phase Transformations in Materials (R. W. Cahn, P. Haasen, and E. J. Kramer, eds.), vol. 5, VCH, Weinheim, 1991, pp. 1–73.

[37] Otto Redlich and A. T. Kister, *Algebraic representation of thermodynamic properties and the classification of solutions*, Industrial & Engineering Chemistry **40** (1948), 345–348.

[38] D. Richman, *Dissociation pressures of GaAs, GaP and InP and the nature of III-V melts*, J. Phys. Chem. Solids **24** (1963), 1131–1139.

[39] Iw. Schröder, *Über die Abhängigkeit der Löslichkeit eines festen Körpers von seiner Schmelztemperatur*, Z. Phys. Chem. **11** (1893), no. 4, 449–465.

[40] R. F. Sekerka, S. R. Coriell, and G. B. McFaden, *Morphological stability*, Handbook of Crystal Growth (Second Edition) (Tatau Nishinaga, ed.), Elsevier, Boston, 2015, pp. 595–630.

[41] R. D. Shannon, *Revised effective ionic radii and systematic studies of interatomic distances in halides and chalcogenides*, Acta Cryst. A **32** (1976), 751–767.

[42] A. Sottile, E. Damiano, M. Rabe, R. Bertram, D. Klimm, and M. Tonelli, *Widely tunable, efficient 2 mum laser in monocrystalline Tm^{3+}:SrF_2*, Optics Express **26** (2018), no. 5, 5368.

[43] G. B. Stringfellow, *Thermodynamic considerations for epitaxial growth of III/V alloys*, J. Crystal Growth **468** (2017), 11–16.

[44] Ching-Hua Su, W. Palosz, S. Feth, and S. L. Lehoczky, *Heat treatments of ZnSe starting materials for physical vapor transport*, J. Crystal Growth **192** (1998), 386–394.

[45] W. A. Tiller, K. A. Jackson, J. W. Rutter, and B. Chalmers, *The redistribution of solute atoms during the solidification of metals*, Acta Metallurgica **1** (1953), 428–437.

[46] J. J. van Laar, *Die Schmelz- oder Erstarrungskurven bei binären Systemen, wenn die feste Phase ein Gemisch (amorphe feste Lösung oder Mischkristalle) der beiden Komponenten ist.*, Z. Phys. Chem. **63** (1908), no. 2, 216–253.

[47] B. M. Wanklyn, *The growth of ZnO crystals from phosphate and vanadate fluxes*, J. Crystal Growth **7** (1970), 107–108.

[48] H. Wenzl, W. A. Oates, and K. Mika, *Defect thermodynamics and phase diagrams in compound crystal growth processes*, Handbook of Crystal Growth 1, Vol. A (D. T. J. Hurle, ed.), Elsevier, Amsterdam, 1993, pp. 103–186.

[49] W. J. Wösten and M. G. Geers, *The vapor pressure of zinc selenide*, J. Phys. Chem. **66** (1962), 1252–1253.

[50] G. Wulff, *Zur Frage der Geschwindigkeit des Wachstums und der Auflösung der Krystallflächen*, Zeitschrift für Krystallographie und Mineralogie **34** (1901), 449–530.

[51] X. N. Xu, G. W. Qin, Y. P. Ren, B. Shen, and W. L. Pei, *Experimental study of the miscibility gap and calculation of the spinodal curves of the Au–Pt system*, Scripta Materialia **61** (2009), no. 9, 859–862.

[52] A. I. Zaitsev, N. V. Korolyov, and B. M. Mogutnov, *Phase equilibria in the CaF_2–Al_2O_3–CaO system*, J. Mat. Sci. **26** (1991), 1588–1600.

3. Transport Phenomenon in Crystal Growth

Transport Phenomena in Crystal Growth

Jeffrey J. Derby

Department of Chemical Engineering and Materials Science,
University of Minnesota, Minneapolis, MN, USA

Abstract

All crystal growth processes are controlled via the interplay among thermodynamics, transport, and kinetic phenomena. This chapter focusses on transport phenomena in various crystal growth systems. The basic concepts of heat, species, and momentum transport are discussed, along with the derivation of conservation equations. Methods are presented by which these conservation equations are analyzed in crystal growth systems. Finally, several examples of transport effects in melt crystal growth are put forth, including heat transfer and interface shape in Bridgman systems, classical analyses of dopant segregation, and morphological instability. The promise of computational modeling for obtaining a deeper understanding of transport in more realistic and complicated crystal growth processes is emphasized.

Contents

1 Introduction **2**

2 Conservation equations **6**
2.1 Heat transfer 8
2.2 Species transfer 10
2.3 Fluid mechanics 11
2.4 Constitutive laws and cross effects 13

3 Analysis approaches **13**
3.1 Scaling 14
3.2 Dimensionless Groups 15
3.3 Dominant Balances 18
3.4 Numerical Methods 20

4 Crystal growth examples **20**
4.1 Interface position and shape during Bridgman crystal growth . . 20
4.2 Classical analyses of segregation 26
4.3 Morphological stability 34
4.4 Growth rate limitations in the traveling heater method 36

5 Final remarks **40**

References **40**

1. Introduction

The synthetic growth of a single crystal of macroscopic size requires the exquisite design and operation of a process that brings atoms or molecules together in a manner that will allow them to self-assemble into a crystalline solid. This process of crystal growth is dependent upon important interactions involving thermodynamics, transport, and kinetics. This chapter addresses transport phenomena in crystal growth, primarily during bulk crystal growth from liquid phases. For the student of crystal growth, we hope to provide a more elementary approach than prior reviews of transport phenomena during melt crystal growth [1–7]. However, we will not discuss some of the interesting complications that arise in gas-phase transport during epitaxial growth of single-crystal films [8], nor will we discuss the many intriguing aspects of solid-state diffusion [9].

At a constant pressure, which is typical for nearly all bulk crystal growth from liquids, the preferred *thermodynamic* state is that with the lowest Gibbs free energy. Thus, bulk crystal growth could be made to occur by simply bringing a finite volume of a fluid to conditions that would favor a stable crystalline state. Namely, this liquid would be thermodynamically unstable with respect to its solid at the same conditions. In a practical sense, simultaneous nucleation events occurring at different points within this volume would likely make the resulting solid an assembly of many crystals, rather than a large, single crystal. So, we need a suitable arrangement of properties through time and space to promote the growth of a single crystal rather than many crystals. This arrangement through space and time is controlled via system design and governed by the principles of *transport phenomena.*

A phase change will thus be driven by thermodynamic state variables, varying in space and time according to the rules of transport. In a crystal growth system, these thermodynamic and transport phenomena are coupled via the *kinetics* associated with phase change from fluid to solid. These ideas are illustrated schematically in Figure 1.

Let us first consider thermodynamics. A crystal growth system must have two phases with a single interface separating them, as shown by the middle image of Figure 1. This is consistent with the profile presented in the upper left diagram, which shows the the local Gibbs free energy of both solid and fluid phases, μ^s and μ^f, respectively, as functions of position. The stable state will be that with the lowest Gibbs free energy, which is indicated in the plot by the solid lines.

Our growth system must provide suitable conditions to bring about the indicated scenario, whereby the solid phase is made to become favorable as we move through space. In melt growth, the Gibbs free energy is determined primarily by the local temperature, so a thermal profile indicated by the upper, middle plot would accomplish this. The engineering of such a thermal profile through space and time is realized by suitably adding and removing heat in a furnace designed with hotter and cooler regions. The Bridgman-Stockbarger method accomplishes this by moving an axial thermal gradient with respect to a sample contained in an ampoule or crucible.

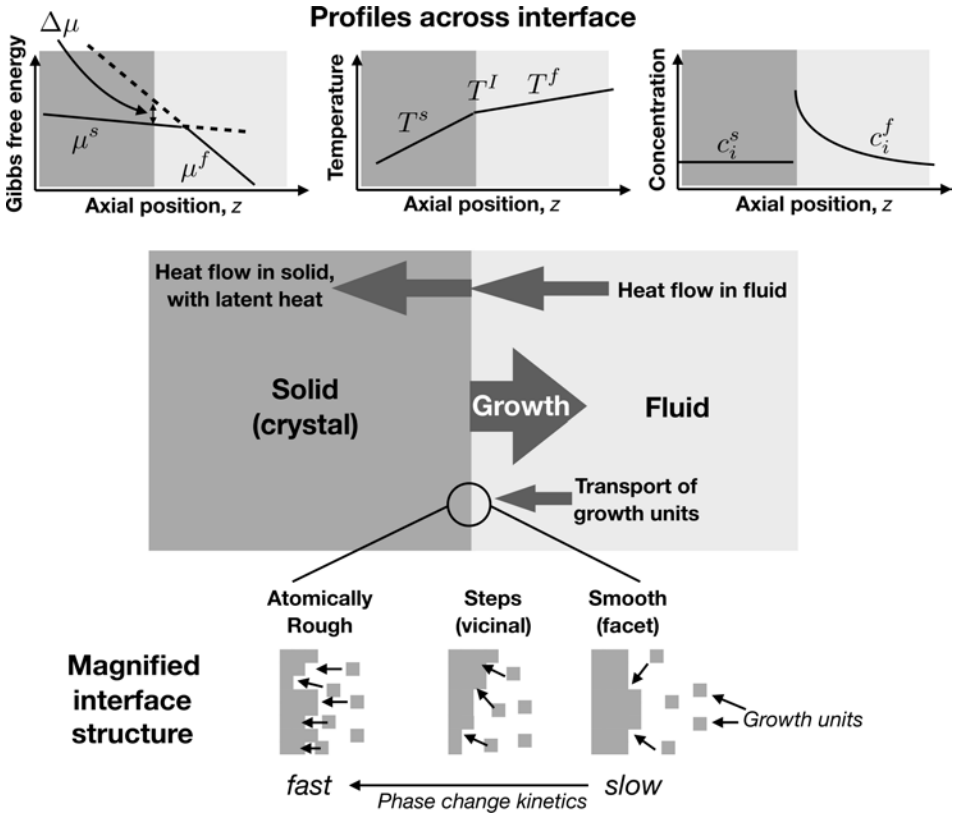


Figure 1: Crystal growth is controlled by interactions among thermodynamics, transport, and kinetics. The middle image depicts macroscopic growth of a bulk crystal with a stable, planar interface at length scales of order cm–m. The upper images show a magnified view near the growth interface at length scales of order mm–cm. The lower images depict phenomena involving growth units at the growth interface, involving atoms, molecules, or atomic complexes at length scales of order nm or smaller.

While all crystal growth processes operate under nearly equilibrium conditions, it is critically important to recognize that *growth* is inherently a non-equilibrium process. There must be a thermodynamic driving force for the phase change to occur. Namely, the fluid phase must be brought to a thermodynamically unstable state so that its elements will add to the the solid phase and advance it, namely to grow the crystal. This is shown in the upper left plot, where a thermodynamic driving force of $\Delta\mu$ exists in a spatial region in front of the interface, where the fluid is undercooled, or, in the case of solution growth, supersaturated.

To maintain the steadily advancing phase-change front, there must be heat and species actively flowing to and from the interface. Thus, growth must simultaneously take place with the transport of heat and species. The transport of heat in a melt growth system is driven by temperature gradients, as indicated in the top middle plot of Figure 1, and associated heat flows, as indicated schematically in the diagram beneath it. The temperature of the interface is indicated as T^I in the plot above. During melt crystal growth, heat must flow from the warmer melt, across the interface, and into the cooler solid. The latent heat of solidification, generated by the phase change, is added to the incoming heat flux at the interface, and the resultant heat flows into the solid.

There is a tremendously important relationship between the amount of thermodynamic undercooling, $\Delta\mu$, and the conditions at the interface, that is dictated by the kinetics associated with the phase change. The classical scenarios near the phase-change interface are represented in the diagrams along the bottom of Figure 1. Many melt growth systems exhibit a melt-solid interface that is atomically rough, as shown by the schematic on the lower left. Jackson [10] was one of the first to describe the thermodynamic conditions that would lead to atomically rough interfaces. Under such conditions, growth units, atoms or molecules, readily attach to the interface, and the kinetics of phase change are very fast compared to transport rates.

However, it may be that the interface prefers to be smooth, again see [10], and to grow layer by layer, in which case growth depends on the existence of one-layer-thick steps on the surface, as would exist on a vicinal surface, i.e., a surface whose orientation is in the vicinity of a singular face (or facet), or as would be nucleated as a two-dimensional island on a facet. Advancing the interface is much slower for these cases than for the rough interface. In fact, the case of growth via two-dimensional nucleation of a new layer long presented a quandary, since actual growth rates of faceted crystals were observed to grow irreconcilably faster than this theory predicted. It was not until the pioneering work of Burton, Cabrera, and Frank [11, 12] that mechanisms were identified that could readily generate steps, such as a screw dislocation intersecting a surface, and advance along the surge-face via the incorporation of growth units at the step ledges. This BCF theory [13, 14] finally predicted growth rates that were consistent with experimental measurements of growth.

The relevance of phase change kinetics can be illustrated by some simple arguments. We denote the rate of growth of a fluid-solid interface in a direction

normal to its shape as,

$$V_n = \beta_\mu \Delta\mu, \tag{1}$$

where β_μ indicates a kinetic coefficient for a thermodynamic driving force of $\Delta\mu$. For a melt growth system, the Gibbs free energy is primarily dependent upon the local temperature, so that the above equation is well approximated by

$$V_n = \beta_T \Delta T = \beta_T (T_m - T^I), \tag{2}$$

where T_m represents the equilibrium temperature between fluid and solid, i.e., the melting point, and T^I is the actual temperature at the melt-solid interface.

Rearranging the above expression and taking the limit of infinitely fast kinetics, we obtain

$$T^I = \lim_{\beta_T \to \infty} \frac{V_n}{\beta_T} + T_m = T_m. \tag{3}$$

Thus, a rough interface, which is characterized by very fast kinetics, results in a phase change interface temperature that is very nearly the equilibrium melting point. If the phase change is not fast, then a significant amount of undercooling, $\Delta T = T_m - T^I$, may be needed to support finite crystal growth rates. For silicon crystal growth, the undercooling at a rough interface in the (100) direction may be on the order of 10^{-4} K or less, whereas a (111) facet may require several degrees K of undercooling for the same growth rate [15].

The rate of the phase change at the interface dominates growth behavior. If very fast, as in the case of a rough interface, growth is controlled almost entirely by transport processes. If very slow, as in the case of faceted interfaces, the growth can depend almost entirely on phase change kinetics, and transport may be relatively unimportant. If intermediate, as for the case depicted by the stepped, vicinal interface, transport and phase change can strongly interact [13, 16–19].

The final element of Figure 1 is shown by the upper right plot, which represent the phenomenon of species segregation at a growth interface. Even though we have argued above that growth requires a departure from equilibrium, it most cases of crystal growth this departure is small enough to describe local conditions at the growth interface as very closely approaching equilibrium. Therefore, equilibrium thermodynamics argues that the Gibbs free energy is continuous across the interface, with $\mu^s = \mu^f$. However, this condition usually requires a discontinuity in chemical composition. For the simplest case of a species i, there is typically a rather simple relationship between its concentration in both phases, with

$$c_i^s = k c_i^f, \tag{4}$$

where k is termed the distribution coefficient. The upper right plot of Figure 1 shows the expected behavior for $k < 1$, in which case the growing solid rejects species i at the interface, resulting in an enriched layer in the liquid in front of the interface. The fate of the rejected species will be determined by transport. Various behaviors caused by segregation during growth are discussed in Section 4.2.

Let's review the elements needed for the growth of a bulk single crystal. First, we desire to bring the growth units that make up the fluid to a thermodynamically unstable state, so that they are ready to form a solid. Next, the growth process is engineered to ensure that this state occurs only very near to an existing crystal, promoting growth of this crystal while avoiding the nucleation of any new crystals. Ideally, the growth units will attach themselves to the fluid-solid interface in a manner that maintains the underlying orientation of the existing crystal. This idea is often put into practice by initiating growth onto a seed crystal, followed by careful growth from that seed. The ensuing growth of a single crystal is usually favored, since any mismatch in the ordering of new material (e.g., to form a different grain) will likely be expensive energetically. Finally, we desire that this process occurs steadily over time, without changing conditions too much, to grow a large volume of high-quality, single-crystal material. The control of all of this is accomplished via appropriate engineering of the system, as dictated by thermodynamics, transport, and kinetics.

2. Conservation equations

As asserted above, transport is needed to support the growth of a crystal, both via the motion of growth units to the interface and also, importantly, the transport of anything that affects the local Gibbs free energy, particularly heat and chemical species. In the following discussion, we will introduce some general ideas of transport, namely conservation laws, and follow with more detailed explanations of heat transfer, species transfer, and fluid mechanics.

The key idea to quantitatively describe transport is a conservation equation. The idea itself is quite simple—that we should be able to account for everything entering and leaving a control volume, defined in space and time, and everything created and destroyed within that control volume. These are the principles of conservation, and we can write mathematical expressions to describe them.

There are very many sources describing the derivation of conservation laws, and I will briefly follow the discussion presented in excellent text by Deen [20]. The most general approach defines a finite volume of space in time, $V(t)$, that is bounded by a surface, $S(t)$. This region is referred to as a time-dependent control volume. Along its bounding surface, we can define an outward-pointing unit normal vector, $\mathbf{n}$, and a velocity vector, $\mathbf{v}$, that represents the flow of material through the surface.

Leaving the details to Deen [20] and the motivated reader, one can show that a conservation law for any quantity b may be written as,

$$\int_{V(t)} \frac{\partial b}{\partial t} dV = -\int_{S(t)} \mathbf{n} \cdot \mathbf{F} dS + \int_{V(t)} B_V dV, \tag{5}$$

where b represents the conserved quantity (per unit volume), t is time, $\cdot$ indicates the vector dot product, $\mathbf{F}$, a vector, is the total flux of b, and B_V represents the rate of formation of b per unit volume.

Don't be put off by the mathematics: the terms in the above equation represent very simple concepts. The term on the left-hand-side of the equation merely represents the time-rate of accumulation within the control volume. This will be balanced by the terms on the right-hand-side of the equation. With respect to the quantity of interest b, the first term on the right represents its net flux across the surface of the control volume, and the second accounts for any generation or depletion within the control volume.

Making use of the divergence and mean value theorems from integral calculus and letting the control volume shrink to zero, the integral equation above is re-expressed in terms of a partial differential equation of the form,

$$\frac{\partial b}{\partial t} = -\nabla \cdot \mathbf{F} + B_V, \tag{6}$$

where ∇ is the gradient operator. In a Cartesian coordinate system,

$$\nabla = \frac{\partial}{\partial x}\mathbf{e}_x + \frac{\partial}{\partial y}\mathbf{e}_y + \frac{\partial}{\partial z}\mathbf{e}_z,$$

where $\mathbf{e}_i$ is a unit vector pointing in the i-coordinate system. Notice that there are still three terms in equation (6), and these terms retain their meaning as in the integral equation (5), now representing accumulation, total flux, and formation rate at any point in the medium of interest.

Deen [20] also derives a general conservation condition across any bounding interface by writing a special, disk-shaped control volume centered on the interface and following a procedure similar to that invoked above. We will not derive this interfacial condition but simply show the end result below.

To make the above equations useful, we need an expression for the total flux, $\mathbf{F}$. First, the total flux is defined as the amount of b that is passing through a surface normal to the direction of the flux (remember that the flux $\mathbf{F}$ is a vector, pointing in a certain direction), so its units are those of b per unit area and time. For example, if we were to consider a specific chemical species, its flux might have units of mole/(cm^{2}s). Second, for most quantities, the total flux is represented by two mechanisms that we refer to as convection and diffusion. Convection is a mechanism of transport whereby the underlying flow of the medium carries b along with it and thus is defined by the product $b\mathbf{v}$. Diffusion arises by molecular mechanisms that act to homogenize a system over time. This phenomenon then will give rise to a flux from an inhomogeneous spatial distribution, namely a distribution having a nonzero gradient. For the moment, we will simply represent the diffusive flux of b using the vector $\mathbf{f}$. Then we have $\mathbf{F} = b\mathbf{v} + \mathbf{f}$.

We use this definition of total flux in equation (6) and in the interfacial balance to write a series of more interesting and useful equations:

$$\frac{\partial b}{\partial t} + \nabla \cdot (b\mathbf{v}) = -\nabla \cdot \mathbf{f} + B_V, \tag{7}$$

which holds within some domain of interest, along with

$$[(\mathbf{f} + b(\mathbf{v} - \mathbf{v}_I))_B - (\mathbf{f} + b(\mathbf{v} - \mathbf{v}_I))_A] \cdot \mathbf{n}_I = B_S, \tag{8}$$

which is the balance across an interface. In equation (8), A and B refer to domains on either side of the interface, $\mathbf{v}_I$ is the velocity of the interface, $\mathbf{n}_I$ is a unit vector normal to the interface pointing toward phase B, and B_S is the rate of formation of b per unit area of interface.

The above conditions are completely general and are almost to the point of being useful to solve problems. What is missing are constitutive laws, namely expressions that relate the diffusive flux to the quantities of interest in the system. We may turn to empirical expressions, such as Fourier's law for heat conduction, Fick's law for species diffusion, and Newton's law of viscosity for the diffusion of momentum, respectively shown below as,

$$\mathbf{q} = -\kappa \nabla T, \tag{9}$$

$$\mathbf{J_i} = -D_i \nabla c_i, \tag{10}$$

$$\boldsymbol{\tau} = \mu[\nabla \mathbf{v} + (\nabla \mathbf{v})^T], \tag{11}$$

where $\mathbf{q}$ is the heat flux vector, κ is the thermal conductivity, and T is temperature; $\mathbf{J_i}$ is the diffusive flux of species i, D_i is a diffusivity, and c_i is the concentration of species i; $\boldsymbol{\tau}$ is the deviatoric stress tensor, μ is viscosity, $\mathbf{v}$ is the mass average velocity, and the superscript T denotes transpose.

We will proceed to derive specific conservation equations using these constitutive laws in the following sections. Of interest also is that the above laws are, strictly speaking, empirical—they were put forth from observation rather than from theory. We will briefly discuss a more fundamental argument for how these laws may arise in Section 2.4.

2.1. Heat transfer

Let's consider defining the conserved quantity to represent a measure of heat, namely enthalpy, $b \equiv \rho C_p T$, with ρC_p representing density and heat capacity, respectively, and T representing absolute temperature. We also define the diffusive flux of heat as $\mathbf{f} = \mathbf{q}$. The the general conservation equation (7) then becomes:

$$\rho C_p \left(\frac{\partial T}{\partial t} + \mathbf{v} \cdot \nabla T \right) = -\nabla \cdot \mathbf{q} + H_V, \tag{12}$$

where we have assumed that the medium is an incompressible fluid, which simplifies the form of the convective term (second term on left side), and have defined H_V as a volumetric heat generation term. Unless there are ongoing chemical reactions involving significant enthalpy effects, which would be unusual in melt or solution crystal growth systems, H_V can typically be ignored.

We further simplify this equation by using a constitutive law to relate the heat flux $\mathbf{q}$ to the underlying temperature field, T. In most cases, this is well represented by Fourier's law, expressed by equation (9) above. We then arrive

at the following equation,

$$\rho C_p \left(\frac{\partial T}{\partial t} + \mathbf{v} \cdot \nabla T \right) = \kappa \nabla^2 T, \tag{13}$$

where we have further assumed that the thermal conductivity, κ, is a constant. While the above partial differential equation may seem quite complicated, it represents straightforward physical reasoning. Namely, the first term on the left corresponds to the accumulation of heat (enthalpy) with time, the second term on the left represents heat transported by convection, and the term on the right side of the equation represents heat conduction.

We similarly follow the general approach of equation (8) above to specify the conservation of heat across a phase-change interface, as depicted in Figure 1. Defining $b \equiv \rho C_p T$ and $\mathbf{f} = \mathbf{q}$, keeping track of mass conservation and the different specific enthalpies of the solid and fluid phases, and ignoring surface heat sources, one ultimately obtains the following condition,

$$\mathbf{n} \cdot (-\kappa_f \nabla T^f + \kappa_s \nabla T^s) = \rho_f \Delta H_f (\mathbf{n} \cdot \mathbf{V}_g), \tag{14}$$

where $\mathbf{n}$ is a unit vector normal to the interface shape and pointing toward the melt, the subscripts and superscripts f and s refer to fluid and solid phases, respectively, ΔH_f is the latent heat of fusion per unit mass, and $\mathbf{V}_g$ is the velocity of the phase-change interface, measured in a frame of reference that is stationary with respect to the solid. Note that we used a simpler notation for the normal growth rate, $V_n = \mathbf{n} \cdot \mathbf{V}_g$ in our discussion in Section 1. In many crystal growth systems, the latent heat of solidification is large enough to significantly affect heat transfer near the interface. We will describe these effects in the Bridgman crystal growth process in Section 4.1.

To complete the specification of conditions across the growth interface, we note that the temperature field must be continuous, as indicated in the top middle plot shown in Figure 1. The temperature along the interface, T^I, will depend upon the kinetics of phase change, as described earlier; however, a common situation for melt growth (with a rough interface) is that the interface is simply located along the melting-point isotherm, so $T^I = T_m$, as discussed previously. To simplify the ensuing discussion, we will typically assume that this melting-point isotherm condition holds for melt growth systems.

In an attempt to keep our discussion relatively brief, we do not discuss other boundary conditions for heat transfer in the system. The motivated reader is referred to [3, 4, 7] for more extensive discussions. However, we will discuss below some complications to heat transfer caused by radiation in high-temperature systems.

Heat transfer in the typically high-temperature environments needed for the melt growth of inorganic crystals is dominated by the exchange of thermal radiation. In an enclosure filled with gas, radiative transport is primarily determined by the emission and absorption of infrared radiation at surfaces. The rate of radiative energy transfer is proportional to a body's absolute tempera-

ture raised to the fourth power, giving rise to strongly nonlinear behavior. In addition, thermal photons travel very long distances through nearly transparent gases and are absorbed, reflected, an re-emitted along all surfaces. Therefore, understanding the details of radiation transport requires analysis of the entire enclosure and can be very challenging. A more extended discussion is provided in [7].

Finally, a phenomenon known as internal radiation is important in high-temperature systems in which the material is partially transparent to infrared radiation. Such media are termed semitransparent, since they are neither opaque nor transparent and both radiative absorption and emission processes are important. Internal radiation is important during the growth of crystalline materials such as yttrium aluminum garnet (YAG), gadolinium gallium garnet (GGG), and sapphire (Al_2O_3). The most straightforward approach to representing internal radiation in an analysis of heat transfer is to modify the heat flux vector as,

$$\mathbf{q} = -\kappa \nabla T + \mathbf{q}_R \tag{15}$$

where $\mathbf{q}_R$ represents the energy flux associated with internal radiation. We refer the interested reader to more specific examples in the early work of Brandon and co-workers [21–24] and the more recent work of Yuferev and co-workers [25, 26].

2.2. Species transfer

Defining a chemical species as the conserved quantity leads to $b \equiv c_i$, where c_i is molar concentration, and to the molar diffusive flux of $\mathbf{f} = \mathbf{J_i}$. Species transport is generally more difficult to formulate than the prior consideration of energy transport, since the diffusive flux is expressed differently, depending on the basis used for defining fluid velocity, whether the fluid density changes, and how many species are present in the fluid. Here, we will consider the simplest form for species transport, where we assume that a mass-average velocity is employed and that the fluid is of constant density. We will also consider that the species i is either present in a binary system or has a relatively small concentration in a multicomponent fluid. The latter case is justification to employ the *pseudobinary* approximation, where we can consider the interactions between molecules of i and all other species to be similar enough to justify a simple application of Fick's law with a pseduobinary diffusion coefficient, D_i. These assumptions are generally quite good for liquids, but they are less accurate for gases, particularly due to the effects of variable density. We will not consider these effects here; the motivated reader will find extended discussions in [20, 27, 28]. We will briefly present complications presented by non-dilute mixtures on diffusion in Section 2.4.

Using Fick's law within the constraints outlined immediately above, the the general conservation equation (7) becomes:

$$\frac{\partial c_i}{\partial t} + \mathbf{v} \cdot \nabla c_i = D_i \nabla^2 c_i, \tag{16}$$

where we have assumed that the diffusion coefficient D_i is constant and that

the net rate of formation of species i per unit volume by chemical reactions is negligible, so $R_{Vi} = 0$.

Following our prior discussion, the terms of this partial differential equation have straightforward meanings. Accumulation in time is represent by the first term on the left side of the equation. The second term on the left represents convective transport of the species, sometimes also referred to as advection. The first term on the right side represent diffusive transport of the species.

Using equation (8) we can specify the conservation of species across a phase change interface, as depicted in Figure 1.

$$\mathbf{n} \cdot (-D_i^f \nabla c_i^f + D_i^s \nabla c_i^s) = (c_i^f - c_i^s)(\mathbf{n} \cdot \mathbf{V}_g), \tag{17}$$

where $\mathbf{n}$ is a unit vector normal to the interface shape and pointing toward the melt, the subscripts f and s refer to fluid and solid phases, respectively, and $\mathbf{V}_g$ is the velocity of the phase-change interface.

A useful approximation is often applied to the above interfacial condition. Typically, the diffusion of a species in the solid is much slower than in a fluid, so that $D_i^s \ll D_i^f$ and only the diffusion in the liquid phase is considered. We may also represent the value of the concentration in the solid via the equilibrium segregation equation (4). Both of these assumptions lead to a simple condition that involves only the fluid phase concentration of species i,

$$\mathbf{n} \cdot (-D_i \nabla c_i) = c_i(1 - k)(\mathbf{n} \cdot \mathbf{V}_g), \tag{18}$$

where the f superscript for the fluid phase has been dropped to simplify notation and k is the distribution coefficient. A more extensive discussion of other boundary conditions for species transport in crystal growth modeling is presented in [3, 4].

2.3. Fluid mechanics

The flow of fluid is governed by a more complicated set of conservation laws. Namely, momentum, a vectorial quantity, must be conserved, as well as overall mass, sometimes referred to as continuity. We could follow an approach similar to that used above, starting with the general conservation equation (7) to derive equations governing fluid dynamics [20]. However, it is conceptually easier to consider how the conservation of momentum follows from enforcing Newton's second law of motion,

$$M \frac{d\mathbf{v}}{dt} = \mathbf{F}_{\text{net}}, \tag{19}$$

to describe a fluid volume element.

For liquids, we typically assume that the fluid is incompressible, namely that its density is constant, and that it obeys Newton's law of viscosity, equation (11). We also often account for small changes in density produced by local variations of temperature and composition using the Boussinesq approximation [20, 27, 29, 30]; these density changes drive buoyant flows and are usually important in melt crystal growth systems.

The equations that describe the motion of the fluid are then the momentum balances:

$$\rho\left(\frac{\partial \mathbf{v}}{\partial t}+\mathbf{v}\cdot\nabla\mathbf{v}\right)=-\nabla p+\mu\nabla^2\mathbf{v}+\rho_0\mathbf{g}[1-\beta_T(T-T_0)-\beta_s(c-c_0)]+\mathbf{F}(\mathbf{v},\mathbf{x},t), \tag{20}$$

where ρ is the density of the fluid, $\mathbf{v}$ is the vectorial velocity field, t is time, ∇ is the gradient operator, p is the pressure field, μ is the fluid viscosity, $\mathbf{g}$ is the gravitational vector, β_T and β_s are the thermal and solutal expansivities, respectively, T is temperature, c is concentration, the subscript zero denotes the reference state about which the linear dependence of the density is approximated, and $\mathbf{F}(\mathbf{v},\mathbf{x},t)$ is an additional body force. This additional body force is needed to represent the application of a magnetic field to a conducting fluid, as is sometimes the case for melt growth systems [31–36].

The requirement for continuity of the fluid phase takes on the following form,

$$\nabla\cdot\mathbf{v}=0, \tag{21}$$

which states the divergence of the velocity field must be everywhere zero. Collectively, equations (20) and (21) constitute the *Navier–Stokes* equations.

Flows driven by buoyancy, referred to as *natural convection*, are important in all bulk crystal growth systems due to thermal or solutal gradients. In addition, temperature or compositional gradients along a liquid-gas interface can drive very strong flows arising from the variation of surface tension along the surface. Often referred to as *Marangoni* flows, these are important in many meniscus-defined melt growth systems, such as the Czochralski and floating zone methods. *Forced convection* flows are driven by applied rotation of crystal or crucible or, in solution growth systems, by pumping or stirring mechanisms.

Also of great importance in many bulk growth systems are time-dependent or turbulent flows, which arise naturally if the driving forces are strong enough. Turbulence arises when the nonlinear effects of inertia dominate over the damping effects of viscosity, and the transition from a laminar flow to a turbulent one is often characterized by a critical threshold in driving forces. However, the detailed spatial and temporal characteristics of the zig-zagging, swirling vortices of a turbulent flow are poorly understood.

In melt crystal growth, turbulence arises in large-scale growth systems, particularly the Czochralski (CZ) growth and directional solidification (DS) of crystalline silicon, processes carried out in crucibles with dimensions on the scale of meters. Important outcomes of these turbulent flows are time-dependent variations in the crystal growth rate and compositional striations in grown crystals. These heterogeneities in composition lead to undesirable variations in material and electronic properties. The application of strong stationary or rotating magnetic fields has been applied to electrically-conductive melts in attempts to control such flows [31–36].

We say little more here on fluid mechanics in crystal growth. Indeed, this topic could have an entire chapter devoted to it. The interested reader is referred

to recent reviews [7, 8, 36–40].

2.4. Constitutive laws and cross effects

Historically, conservation equations have been built upon the empirical, constitutive laws of Fourier and Fick for diffusive heat and species transport, as stated above in equations (9) and (10). However, there is a more fundamental basis for the description of diffusion, originally put forth by Onsager [41] and now known as irreversible thermodynamics [9, 20, 42].

Very briefly, irreversible thermodynamics posits that local departures from equilibrium can generate fluxes to locally move the system toward equilibrium. An important outcome is that all quantities that determine the local production of internal energy, work, and chemical potential are coupled. Through local entropy production, fluxes are driven by conjugate forces represented by thermodynamic potential gradients. In any given system, many pairs of forces and fluxes can be identified to be important, thus fluxes may be expected to be a function of *all* driving forces acting in the system.

Thus, under certain situations, *cross effects* become important for transport. For example, species diffusion can be affected not only by the local concentration gradient, according to Fick's law, but also by the local temperature gradient. This is known as the Soret effect. In addition, heat transport can be driven by species concentration gradients, a phenomenon known as the Dufour effect. Both Soret and Dufour phenomena, outcomes of irreversible thermodynamics, are examples of cross effects. While such cross effects can be important in gas-phase transport, such as occurs in chemical vapor deposition systems, they are rarely significant for transport in liquids.

Another important outcome from irreversible thermodynamics is that the conjugate force responsible for species diffusion is the gradient of chemical potential. Since the chemical potential depends upon composition, the diffusion of individual component will depend upon all other components, a much more complicated situation than represented by Fick's law with a pseudo binary diffusion coefficient. The effects of multiple components on diffusion has also been considered in the Stefan-Maxwell model [9, 20, 27, 28, 43]. Fortunately, these multi-components effects on species diffusion are rarely large and can often be ignored, particularly in liquids.

3. Analysis approaches

The quantitative understanding of transport requires the posing of an appropriate set of conservation equations and boundary conditions, followed by their solution. There are a few, classical analyses describing transport effects in crystal growth, and those addressing segregation phenomena and morphological stability will be discussed in ensuing sections. However, when analytical solutions cannot be found, one must resort to the use of other approaches for insight to transport. In the following brief discussion, we'll demonstrate two approaches that depend upon scaling and dominant balances—approaches that

may give significant insight to a problem without actually obtaining an analytical solution. These approaches have also been put forth in [1, 37, 44].

3.1. Scaling

The art of scaling builds upon a simple premise: A mathematical equation should never have units associated with its terms, namely the equation and all of its associated variables should be *dimensionless*. To illustrate the utility of scaling, let's consider an example. Say we are interested in solute transfer in a system. We start with the original governing equation, equation (16), simplified to consider one spatial dimension,

$$\frac{\partial c}{\partial t} + v\frac{\partial c}{\partial x} = \mathcal{D}\frac{\partial^2 c}{\partial x^2}. \tag{22}$$

Our first objective is to make the variables in this problem span a range in values between zero and one, making these variables to be non-dimensional, $\mathcal{O}(1)$ quantities. This is accomplished by choosing suitable *characteristic* values, i.e., values that we feel are representative of the scale of the problem. This choice is somewhat arbitrary and does depend on some physical insight to the problem. This is one area where the craftsmanship of modeling is invoked. For our mass transfer problem, we may know the maximum possible value of solute concentration and velocity, c_{max} and v_{max}, respectively, and we likely know a characteristic physical dimension of the system of interest, which we'll denote as L.

We now define dimensionless variables,

$$\tilde{c} \equiv \frac{c}{c_{max}}, \quad \text{where} \quad 0 \leq \tilde{c} \leq 1, \tag{23}$$

$$\tilde{v} \equiv \frac{v}{v_{max}}, \quad \text{where} \quad 0 \leq \tilde{v} \leq 1, \tag{24}$$

$$\tilde{x} \equiv \frac{x}{L}, \quad \text{where} \quad 0 \leq \tilde{x} \leq 1. \tag{25}$$

With some algebra applied to our original field equation, equation (22), we write,

$$\frac{\partial(c/c_{max})}{\partial(\mathcal{D}t/L^2)} + \frac{v_{max}L}{\mathcal{D}}(v/v_{max})\frac{\partial(c/c_{max})}{\partial(x/L)} = \mathcal{D}\frac{\partial^2(c/c_{max})}{\partial(x/L)^2}. \tag{26}$$

The above equation is written to directly employ our dimensionless variables, and, furthermore, every term of this new equation is dimensionless. We also find that two new dimensionless quantities arise.

First, we see that a dimensionless variable for time can be defined as,

$$\tau \equiv \frac{\mathcal{D}t}{L^2}. \tag{27}$$

Next, there is an expression that multiplies the second term of the dimensionless equation, equation (26). This is termed a *dimensionless group*, and in this case

this group is termed the *Peclet number,*

$$Pe \equiv \frac{v_{max} L}{\mathcal{D}}. \tag{28}$$

Finally, let's rewrite the field equation of interest using our dimensionless variables and groups:

$$\frac{\partial \tilde{c}}{\partial \tau} + Pe \frac{\partial \tilde{c}}{\partial \tilde{x}} = \frac{\partial^2 \tilde{c}}{\partial \tilde{x}^2}. \tag{29}$$

What have we achieved? First, the act of nondimensionalizing an equation restates it using the fewest number of possible parameters. Obviously, our understanding of something is simplified if it involves fewer parameters. Next, we have chosen scalings to make our variables $\mathcal{O}(1)$, so the terms of the equations involving those scalings, namely the derivatives of concentration in this equation, are also expected to be $\mathcal{O}(1)$ quantities. Thus, the relative importance of each term of the equation can be assessed. Here, we see that the second term of equation (29) is multiplied by the Peclet number, Pe. If $Pe \gg 1$, we know that this term is very important. Conversely, if $Pe \ll 1$, this term is relatively unimportant and might even be discarded from the equation. Finally, we know that there is a physical interpretation of the relative importance of the second term of equation (29). This term represents convective mass transfer. Thus, the Peclet number represents a measure of the importance of convective transport to diffusive transport, and we can understand the relative importance of these two phenomena simply from our scaling of the original equation, without ever actually solving it.

3.2. Dimensionless Groups

The nondimensional scaling of governing equations will naturally lead to dimensionless groups. Some of the most common dimensionless groups encountered in the analysis of crystal growth systems are presented in Table 1. Most symbols used in this table have been defined above or will be clarified in the ensuing discussion. Additional symbols include the following: $\nu = \mu/\rho$ is the kinematic viscosity of a fluid, $d\gamma/dT$ represents the change of surface tension γ with temperature (the comparable measure with respect to composition is $d\gamma/dc$), V is a characteristic velocity scale, and $\alpha = \kappa/\rho C_p$ is the thermal diffusivity. For a other discussions on dimensionless groups in crystal growth, the interested reader is referred to refs. [1, 5].

The most important dimensionless groups in heat and mass transfer scaling are shown in Table 1. The Prandtl number for heat transfer and the Schmidt number for mass transfer are analogous measures of diffusivity ratios. Multiplied by an appropriate Reynolds number that scales then intensity of the flow in a system, they form Peclet numbers for heat and mass transfer, which are useful measures of the importance of convection with respect to conduction or diffusion. If $Pe \gg 1$, then convection is extremely important for transport through the system. This was shown via the scaling analysis of the prior section.

Table 1: Useful dimensionless groups for characterizing bulk crystal growth systems.

Heat Transfer			
Name	Definition	Description	Comments
Prandtl	$Pr \equiv \frac{\nu}{\alpha}$	$\frac{\text{Momentum diffusivity}}{\text{Thermal diffusivity}}$	A physical property of the fluid. Molten metals and most semiconductors have $Pr \approx 10^{-2}$; molten oxides and fluorides have $Pr \approx 1$–10^2; aqueous systems have $Pr \approx 7$.
Peclet	$Pe \equiv \frac{VL}{\alpha}$	$\frac{\text{Convec. heat transport}}{\text{Conduc. heat transport}}$	Importance of convective heat transfer. Characteristic velocity of fluid, V, is estimated or measured. $Pe = RePr$.
Mass Transfer			
Name	Definition	Description	Comments
Schmidt	$Sc \equiv \frac{\nu}{\mathcal{D}}$	$\frac{\text{Momentum diffusivity}}{\text{Solutal diffusivity}}$	A physical property of the fluid. Most liquids have $Sc \approx 10^2$–10^3.
Peclet	$Pe_s \equiv \frac{VL}{\mathcal{D}}$	$\frac{\text{Convec. mass transport}}{\text{Diffusive mass transport}}$	The *solutal* Peclet number represents the importance of convective mass transfer. Characteristic velocity of fluid, V, is estimated or measured. Generally $Pe_s \gg 1$ for crystal growth systems. $Pe_s = ReSc$.
Fluid Mechanics			
Name	Definition	Description	Comments
Grashof	$Gr \equiv \frac{g\beta_T \Delta T L^3}{\nu^2}$	$\frac{\text{Buoyancy force}}{\text{Viscous force}}$	Intensity of buoyancy-driven convection. Solutal Grashof number, $Gr_s \equiv g\beta_s \Delta c L^3/\nu^2$; Rayleigh number, $Ra = PrGr$.
Marangoni	$Ma \equiv \frac{\frac{d\gamma}{dT}\Delta T L}{\mu\nu}$	$\frac{\text{Surface shear stress}}{\text{Viscous force}}$	Intensity of flows driven by surface-tension gradients. Solutal Marangoni number, $Ma_s \equiv \frac{d\gamma}{dc}\Delta c L/\mu\nu$.
Reynolds	$Re \equiv \frac{VL}{\nu}$	$\frac{\text{Inertial force}}{\text{Viscous force}}$	Overall intensity of flow. Characteristic velocity of fluid, V, is estimated or measured. Rotational Reynolds number, $Re_\omega \equiv \omega L^2/\nu$.

Several useful generalizations can be made about heat and mass transfer in bulk crystal growth processes. The Prandtl and Schmidt numbers are ratios of physical properties; their values are constant for any specific system. Generally, molten metals and semiconductors have characteristic Prandtl numbers of $Pr \approx 0.01$, while non-metallic melts and fluxes, such as organic, oxide, and fluoride materials, have $Pr \approx 1 - 100$ or higher. Aqueous systems possess a Prandtl number of very nearly $Pr \approx 7$. Therefore, for *the same flow intensity,* convective heat transfer is much less important in semiconductor melts than in melts of oxides and fluorides. Remember, though, that flows vary dramatically from system to system; in large scale semiconductor growth systems convective heat transfer can be significant, while in small-scale oxide growth systems convective heat transfer can be negligible. In solution growth systems, convective heat transfer can be important, but often the thermal gradients are so small that the system is nearly isothermal and heat transfer is unimportant. The Schmidt number for virtually all liquid systems is $Sc \approx$ 100–1,000. So, unlike heat transfer, where convection may or may not be important, convective mass transfer effects are nearly always important, even for extremely weak flows. This sensitivity of mass transfer to fluid flow explains the complicated effects of convection on segregation in melt growth systems and the significant effects on mass transfer and growth rate in solution growth systems.

Also listed in Table 1 are the three three most common dimensionless groups for characterizing fluid flow in bulk crystal growth systems—the Grashof number, the Marangoni number, and the Reynolds number. The Grashof number represents the strength of buoyant driving forces and the intensity of the resulting flows. One may also encounter the Rayleigh number being used in this capacity; the Rayleigh number is related to the Grashof number by $Ra = PrGr$, where Pr is the Prandtl number of the fluid. These groups will be discussed more extensively in the following section. The Marangoni number is a measure of driving forces from surface tension gradients. Here ΔT and L should be chosen to lie along the free surface. Marangoni flows can be quite important in systems with a melt-gas free surface [39, 45, 46]. The Reynolds number provides a measure of the nonlinear inertial forces in the flow; generally speaking, the higher the Reynolds number, the more complicated the flow. A rotational Reynolds number is often used to measure the importance of imposed rotation of crystal or crucible on flow intensity.

The use of dimensionless groups can yield great insight to dominant physical behavior. However, care must be taken that these scaling arguments are not used to oversimplify the behavior of real systems. For example, there is no universal Grashof number or Marangoni number which clearly marks the transition to more complicated flows (such as time-dependent or turbulent phenomena). Dimensionless numbers are relative measures only; the precise interpretation of dimensionless groups is possible only in well-defined problems with simple geometries and boundary conditions. In crystal growth, the real behavior is a strong function of the details of each specific system. This issue is also discussed with respect to understanding the nature of fluid flows in the following section.

3.3. Dominant Balances

Another powerful approach to understand a system after scaling of mathematical equations is the identification of the dominant terms of the equation and their relationships. Let's do one relatively simple example from buoyancy-driven flows to illustrate these ideas.

The single most important dimensionless group for understanding fluid flows is the Reynolds number, defined as $Re \equiv VL/\nu$, where V is a characteristic velocity, L is a characteristic length, and $\nu \equiv \mu/\rho$ is the kinematic viscosity of the fluid. This dimensionless group arises naturally when the momentum balance, equation (20), is re-written in dimensionless form using scalings of $\tilde{\mathbf{v}} \equiv \mathbf{v}/V$ to define a nondimensional velocity and $\tilde{\mathbf{x}} \equiv \mathbf{x}/L$ to define nondimensional spatial coordinates, where the tilde refers to the nondimensional variable.

The dimensionless form of the momentum balance is then given as,

$$\frac{\partial \tilde{\mathbf{v}}}{\partial \tilde{t}} + Re(\tilde{\mathbf{v}} \cdot \nabla \tilde{\mathbf{v}}) = -\nabla \tilde{\mathcal{P}} + \nabla^2 \tilde{\mathbf{v}} - Ra(\tilde{T}\mathbf{e}_g). \tag{30}$$

It is convenient to employ the *dynamic* pressure, $\mathcal{P} \equiv p - \rho g z$, that, via its definition, contains the hydrostatic term of the body force to simplify this equation. Note that the resultant scalings for time and pressure are $\tilde{t} \equiv t\nu/L^2$ and $\tilde{\mathcal{P}} \equiv \mathcal{P}L/\nu V$, respectively. Finally, we have also neglected the catch-all term for applied body forces, $\mathbf{F}(\mathbf{v}, \mathbf{x}, t)$, that was specified in equation (20).

We find that the last term, representing thermal buoyant forces, includes another dimensionless group, the Rayleigh number, defined as $Ra \equiv g\beta\Delta T L^3/\nu\alpha$, multiplying a dimensionless temperature difference, $\tilde{T} \equiv (T - T_0)/\Delta T$, and $\mathbf{e}_g$, a unit vector in the direction of gravity. In these definitions, the thermal diffusivity is defined as $\alpha \equiv \kappa/\rho C_p$, and we need to specify another scale, ΔT, a characteristic temperature difference across the fluid. Alternatively, one may encounter the Grashof number, $Gr \equiv g\beta\Delta T L^3/\nu^2$, in the buoyancy term of the dimensionless momentum equation. The Grashof number arises when one defines a characteristic time based on the thermal diffusion scaling of L^2/α rather than the viscous time scale of L^2/ν, as applied in equation (30). The Rayleigh number is related to the Grashof number by $Ra = PrGr$, where $Pr \equiv \nu/\alpha$ is the Prandtl number of the fluid.

When properly defined, these dimensionless numbers provide significant insight to the nature of the flow. The Reynolds number provides a measure of the ratio of inertial to viscous forces. The Reynolds number is always substantial for flows in large-scale crystal growth systems and represents the importance of the nonlinear effects of inertia. Systems with moderate Reynolds numbers, typically less than several thousands, usually exhibit laminar, time-independent flows. However, stronger flows bring more complicated behavior, and flows with Re larger than several thousands will almost always exhibit time-dependent behavior. As the Reynolds number increases further, the flow evolves toward turbulence and exhibits strong fluctuations in time and space.

Flows are driven by thermal buoyancy in melt crystal growth systems, and the Rayleigh and Grashof numbers are most useful for representing the strength

of buoyant driving forces and the intensity of the resulting flows. The Rayleigh and Grashof numbers are linearly proportional to ΔT, the temperature difference across the system, and scale with the cubed power of L, the characteristic dimension. This L^3 scaling indicates that buoyancy-driven flows grow geometrically with system size; convection is always much more intense in large-scale systems. The most appropriate measures for ΔT and L are those lying in the horizontal plane, perpendicular to the force of gravity.

For most melt crystal growth processes, both the Reynolds and Rayleigh numbers are large. For a steady-state flow in such a system, we can ignore all terms of dimensionless equation (30), except those representing the *dominant* forces of inertia and buoyancy to write,

$$Re(\tilde{\mathbf{v}} \cdot \nabla \tilde{\mathbf{v}}) \sim Ra\, \tilde{T}. \tag{31}$$

We argue that our scaling makes $\tilde{T} \approx 1$ and rearrange the balance to read,

$$\tilde{\mathbf{v}} \cdot \nabla \tilde{\mathbf{v}} \sim Re^{-1} Ra. \tag{32}$$

Now, let's put equation (32) back into dimensional terms,

$$\left(\frac{v}{V}\right)\left(\frac{L}{\Delta L}\frac{v}{V}\right) \sim \left(\frac{\nu}{VL}\right)\left(\frac{g\beta_T \Delta T L^3}{\alpha\nu}\right). \tag{33}$$

In the equation above, the dimensionless geometric ratio that arises from the approximation of ∇ in equation (32) can be approximated as , $L/\Delta L \approx 1$. Since thermal effects are driving this flow, we argue that the thermal diffusion time scale provides an appropriate characteristic value for velocity as $V \equiv \alpha/L$. We make these substitutions and do some canceling of terms to arrive at,

$$v \sim \sqrt{g\beta_T \Delta T L}. \tag{34}$$

Thus, when inertial forces dominate in a buoyancy-driven flow, equation (34) can be used to estimate the velocity. Simulations have shown this relationship to be valid for many melt crystal growth systems.

Forgive me for plunging in one more time, but if we now take equation (34) and multiply both sides of the equation by L/ν, we get an equation that is dimensionless,

$$\frac{vL}{\nu} \sim \sqrt{\frac{g\beta_T \Delta T L^3}{\nu^2}}, \tag{35}$$

which then gives us,

$$Re^* \sim Gr^{1/2}, \tag{36}$$

where Re^* is a Reynolds number based on a measure of the velocity and Gr is the Grashof number for the system. This relationship holds when inertia is important, $Re \gg 1$, in natural convection [47, 48] and has been demonstrated to be valid for buoyant flows in many melt crystal growth systems [49, 50, 124].

We desire to make one more point on the role and meaning of dimensionless

numbers. In search of simple answers, many come to the false conclusion that discrete transitions in behavior are marked by universal, critical values of dimensionless numbers. For example, it is well established that flow in a pipe will be steady and laminar when its Reynolds number is less than 2,300 and will be time-dependent and turbulent when the Reynolds number exceeds 4,000 or so [51]. Notwithstanding this profound observation, the critical Reynolds number for turbulence is *different for every geometry.* Similarly, the onset of natural convective flow in the Rayleigh–Bénard configuration [52, 53], consisting of a fluid heated from below, occurs at a critical Rayleigh number of $Ra_c = 1{,}708$. However, this analysis only holds for the case of a fluid layer between infinite, parallel plates that are isothermal and perfectly horizontal. Though referred to time and time again in crystal growth literature, this classical problem for natural convection, including its well-known Ra_c, has little relevance for real systems of finite extent with complicated heating. Thus, one must accept the more nuanced interpretation that dimensionless numbers are relative measures only; their precise interpretation is possible only in well-defined problems with simple geometries and boundary conditions. In crystal growth, the real behavior is strongly dependent upon the details of each system.

3.4. Numerical Methods

Unfortunately, the mathematical descriptions of bulk crystal growth processes are only sometimes amenable to analytical solution approaches, so numerical methods have become essential for their analysis. There are a wide variety of methods applied to solve crystal growth process models, ranging from general purpose commercial codes to highly specialized research codes. The topic is vast, and we make no attempt at an overview here. Rather, we point the interested reader toward many treatises already in print on this topic [1–5, 13, 37, 54–64].

4. Crystal growth examples

4.1. Interface position and shape during Bridgman crystal growth

The Bridgman or Bridgman-Stockbarger crystal growth method, shown schematically by the left image in Figure 2, is one of the oldest melt crystal growth techniques, pioneered by Bridgman in 1925 [65] and later significantly refined by Stockbarger [66]; see [7, 67] for a more extensive historical discussion. In this technique, the material to be grown is contained within a sealed crucible (sometimes referred to as an ampoule), which is placed within a furnace that is engineered to maintain a thermal gradient along the length of its inner bore. The crucible and contents are carefully melted (often while maintaining a single-crystal seed placed in a small well beneath the main portion of the crucible) then moved to the cooler region of the furnace to promote directional solidification or crystal growth.

Most commonly, the crucible and bore of the furnace are cylindrical in shape, and their axis is oriented in the vertical direction, with cooler temperatures

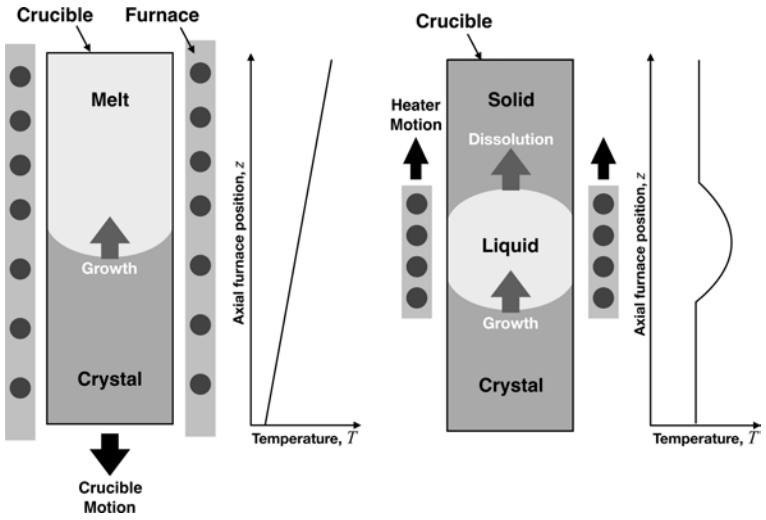


Figure 2: Left: A schematic of the vertical Bridgman-Stockbarger method. A crucible containing a charge is typically moved downward, through a temperature gradient in a furnace, to induce directional solidification. Right: A depiction of the traveling heater method (THM), where a heater locally melts a liquid zone that is enriched with an excess component to act as solvent. The heater is then typically moved upward, dissolving feed material above and growing a crystal below. This method is discussed in Section 4.4.

under warmer temperatures. This is known as the *vertically stabilizing* configuration and presents several advantages to other arrangements. First, the vertical alignment of furnace and crucible with gravity promotes two-dimensional, axisymmetric behavior, and all fields are expected to be independent of azimuthal angle. This is a much simpler behavior than would be obtained with the axis aligned horizontally, which would make buoyant flows in the melt three-dimensional. Second, with cooler temperatures underlying warmer, the melt is thermally stabilized, in that cooler, denser fluid lies beneath warmer, lighter fluid. Only radial forces, typically produced by smaller, radial temperature gradients, will drive flows; hence, the melt flows are much weaker in intensity compared to other orientations, which is usually desirable.

The gradient freeze method is functionally equivalent to the Bridgman method. Here, the axial thermal profile of the furnace is changed in a time-dependent manner to effectively translate the profile along the charge. This system has an advantage of no moving parts; the translation of the temperature field is accomplished by changing the heat input within the furnace over time. This is most easily accomplished by simply powering down the furnace over time.

While the Bridgman system appears to be quite simple, it exhibits surprisingly complicated behavior with respect to heat transfer and has been subject to many analyses [7, 68–87]. Let us start with some simple ideas, however. One of the first realizations is that heat transfer is essentially quasi-static in virtually every Bridgman crystal growth system. Namely, the time scale for conduction

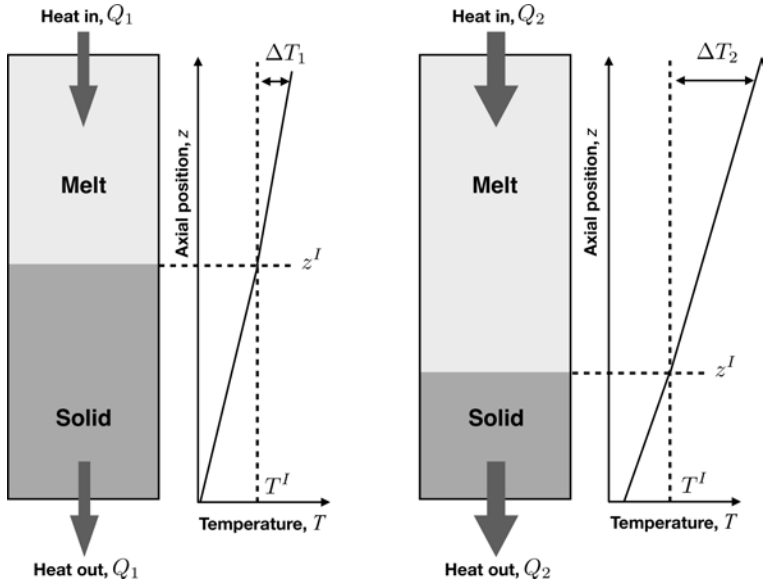


Figure 3: The amount of heat flowing through an idealized, one-dimensional, quasi-steady vertical Bridgman system will determine thermal gradients and the axial position of the melt-sold interface. Here, the melt has a higher thermal conductivity than the solid, $\kappa_m > \kappa_s$, and no latent heat is generated at the interface, $\Delta H_f = 0$.

is typically on the order of 10^2–10^3 seconds (and time scales for convective heat transport are typically orders of magnitude smaller), whereas growth typically occurs over a period of 10^4–10^6 seconds. Thus, heat transfer occurs over a time scale that is essentially instantaneous with respect to the time scale for changes in growth geometry. The temperature field is then considered to be steady over the snapshot in time for any position of the crucible in the furnace. In addition, we expect that heat flows near the interface will be relatively constant over time, so that the growth velocity will closely match the ampoule translation rate. Exceptions to this steady-growth scenario will occur due to thermal end effects, when the the melt-solid interface is on the order of an ampoule diameter away from the ends of the crucible during the first and last stages of growth.

Even under quasi-static heat transfer and constant growth rate conditions, it is important to realize that this system is *not* in a state of thermodynamic equilibrium. Indeed, there is always significant heat flowing through the system. Rather than thinking of a static situation, one should think of a stationary state that has arisen from a balance of steady heat flows. For example, consider an idealized Bridgman system where heat transfer occurs in only the axial direction, conduction is the only mode of heat transfer, and latent heat is not produced at the interface, as depicted by the schematic drawings of Figure 3.

The left image depicts the quasi-steady-state for a given heat flow, Q_1, into the system. Under our simple assumptions and with the quasi-steady nature of the heat flows, there must be exactly Q_1 units of heat per unit time flowing

out of the system, as shown along the bottom of the drawing. This flowing heat passes axially through both phases via the establishment of axial thermal gradients, as depicted by the accompanying plot to the right of the system. We have assumed that the thermal conductivity of the melt is higher than that of the solid, $\kappa_m > \kappa_s$. Consistent with Fourier's law, equation (9), the axial thermal gradient is steeper in the solid than in the melt, as indicated by the change in slope of the temperature profile at the melt-solid interface. For a flux of Q_1 into the system, the melt-solid interface is located roughly half-way up the crucible, as shown by the coordinate z^I that corresponds to the interface temperature, T^I.

If we reconfigure the furnace so that it puts more heat into the system, Q_2, as shown in the right drawing, the additional heat flowing through the system increases the temperature in the melt—compare the superheating above the interface temperature, where $\Delta T_2 > \Delta T_1$. To accommodate the increased flow of heat through melt and solid, the axial thermal gradients must increase compared to the prior case. The net result is that the melt-solid interface has been pushed downward. This shifting of the interface position is important, since it will significantly affect the nature of radial heat flows and, hence, the shape of the melt-solid interface.

Let us consider how two-dimension effects arise in our depiction of heat transfer through a Bridgman growth system. In reality, heat is flowing both in the axial and radial directions. In general, heat is flowing radially inward to the melt from the warmer parts of the furnace and is flowing radially outward from the solid to the cooler parts of the furnace. If there is any radial component of heat flow, the thermal conductivity ratio between melt and solid will tend to deflect the interface from being flat. When the solid is more conductive than the melt, $\kappa_s > \kappa_m$, the resistance to heat flow is smaller in the solid and the interface will deflect upward, producing a more convex interface shape with respect to the solid. This case is depicted by the schematic on the left of Figure 4. When the situation is reversed, namely when $\kappa_m > \kappa_s$, the resistance to heat flow is larger in the solid, thus deflecting the interface downward and producing a concave interface. A similar effect is produced when latent heat is generated along the solidifying interface, with $\Delta H_f \neq 0$. This additional heat must flow into the solid, since heat always flows "downhill," from higher to lower temperatures, and the interface is also made more convex by latent heat. This case is depicted by the schematic on the right of Figure 4.

Of great practical interest is how a Bridgman crystal growth system might be designed to promote a specific interface shape. It has been widely appreciated that the macroscopic shape of the solidification interface during growth is an important determinant of crystal quality [5, 68, 88–92], with a convex interface tending to produce fewer defects and favorable grain selection conditions. Wilcox and co-workers were among the first to analyze heat transfer and its effects in interface shape in Bridgman crystal growth [68–71]. Chang and Wilcox [68] considered the effect of heat flows on interface shape, leading to the understanding illustrated schematically in Figure 5. They reasoned that the isothermal melt-solid interface must be perpendicular to the heat flux lines,

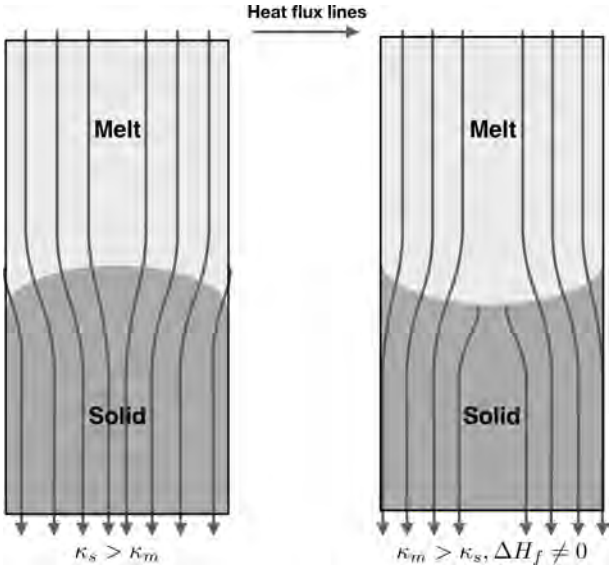


Figure 4: Effects of thermal conductivity ratio and latent heat on interface shape during vertical Bridgman crystal growth.

since Fourier's law for heat conduction requires that heat must flow in a direction normal the isotherms of the temperature field. This is a mathematical outcome of the requirement that the flow of heat, $\mathbf{q}$, is proportional to the gradient of the temperature field, ∇T.

As discussed above, heat in a Bridgman system generally flows axially from top (hot) to bottom (cold); however, heat also flows radially inward to the melt and outward from the solid. This is depicted by the curved heat flux lines in Figure 5. The turning of the heat flux lines, from radially inward to outward, so that the direction of heat flow is purely vertical, is indicated by the position of the dotted line across the figure. Here we have assumed that the thermal conductivities of both phases are equal and that no latent heat is generated at the melt-sold interface. Hence, the thermal field and heat flows will be unaffected by the position and shape of the melt-solid interface. Of critical importance to interface shape is where the melting-point isotherm lies with respect to these flux lines.

If the turning of the heat flux lines occurs at $T = T_m$, there is absolutely no radial heat flow at the interface and its shape will be flat, as indicated by the left schematic in Figure 5. However, as pointed out in the discussion associated with Figure 3, the furnace thermal profile can be rearranged so that the heat flux lines are shifted with respect to the melting temperature. When this is done to push the interface upward, the turning of the heat flux lines occurs at a temperature below the melting point, $T < T_m$. With this shift of heat flows and temperature, there is an inward radial component of heat flow along the interface and a convex shape will arise, as shown by the middle schematic. If

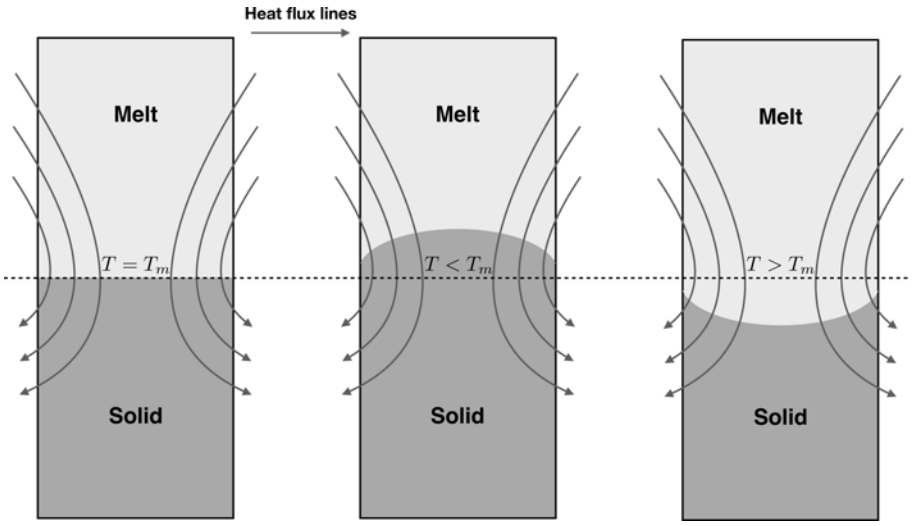


Figure 5: The shape of the melt-solid interface depends on the relative position of melting temperature with respect to the direction of the heat fluxes. The dotted horizontal line denotes the axial position where the flux lines are perfectly vertical and there is no radial component of heat flow. Left: A flat interface arises when the radial component of heat flows is zero near the interface. Middle: A convex interface will result from inward radial heat flows near the interface. Right: Outward heat flows near the interface will produce a concave interface. These images are drawn under the assumption of $\kappa_m = \kappa_s$ and $\Delta H_f = 0$.

the interface is pushed downward, then the heat fluxes are purely vertical at a temperature above the melting point, $T > T_m$. Heat flows radially outward near the interface, and its shape becomes concave, as depicted by the right schematic in Figure 5.

These ideas have led to several design recommendations, ranging from an "adiabatic" zone around the melting point of the material to flatten the interface [68, 70, 93] to the idea of a "booster" heater to be placed near the interface to make it more convex [76, 85]. Zhang *et al.* [86] recommended a "bell-curve" furnace temperature profile to induce inward radial heat flows near the melt-solid interface and promote convex interface shapes. More recently, Peterson and Derby [87] presented a unifying idea for the engineering of convex melt-solid interface shapes in Bridgman crystal growth systems. Building from prior ideas about interface shape and radial heat fluxes, they constructed arguments to relate these radial fluxes to the underlying axial heat flows as a function of position. They showed that a convex interface shape will naturally result when the interface is located in a region of the furnace where the axial thermal profile exhibits negative curvature, i.e., where $d^2T/dz^2 < 0$. This criterion explains prior literature results on interface control and promises new insight for future furnace designs. The interested reader is directed to [87] and [94] for more detailed discussions.

We finish this discussion on interface shape in Bridgman growth with a sober-

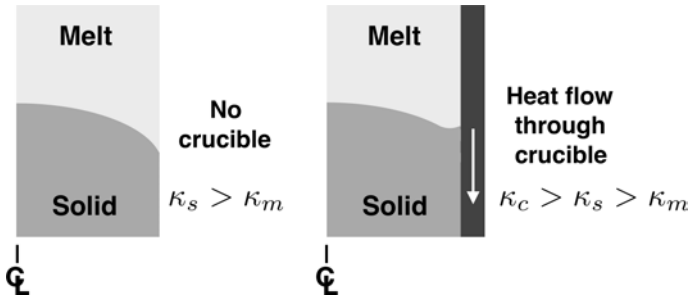


Figure 6: The shape of the interface can be affected by heat transfer through the crucible wall. Left: A convex interface shape will be promoted when $\kappa_s > \kappa_m$. Right: Heat flows through the crucible wall locally deflect the interface; see discussion in text. Here the additional heat flux through the crucible wall increases radial heat flow outward near the interface, thus changing its shape to concave as it approaches the wall. Note that only the the right side of an axisymmetric, cylindrical geometry is depicted in these images; CL denotes the system centerline.

ing reminder that nature cannot always be bent to our wills. This is exemplified by the effects of heat transfer through the ampoule on interface shape. In several insightful analyses, Jasinski, Rohsenow, and Witt [74–76] showed the significant influence of ampoule thermal mass on the thermal field and, most importantly, the "interface effect," where the thermal conductivity mismatch among melt, crystal, and ampoule results in significant interface deflection at the ampoule wall. This is illustrated schematically in Figure 6. The case of an initially convex interface shape is shown on the left, without any influence of a crucible. When this system is enclosed by a crucible with a thermal conductivity greater than that of the melt and solid, the resistance to heat flow through the crucible wall is much smaller than in the melt and solid. The downward heat flow through the crucible provides for additional heat removal near the interface, producing a small, radial flux outward that defects the interface upward as it approaches the crucible wall. Here, the predominantly convex interface that arises from $\kappa_s > \kappa_m$ is altered to being slightly concave around its periphery. This effect can be mitigated by changing the thermal conductivity of the crucible wall or by changing its thickness.

4.2. Classical analyses of segregation

An important measure of quality in a large, single crystal is its compositional uniformity, particularly when a desired species, often called a *dopant*, is added to a pure material. Transport and segregation will determine the composition of a crystal solidified from a liquid. The concept of segregation arises from the requirement of thermodynamic equilibrium at the growth interface, which dictates a discontinuity in concentration of such a chemical species between adjacent phases of solid and liquid. This effect was described briefly in Section 1, where the idea of a distribution coefficient was introduced in equation (4) and typical concentration profiles that result from growth are presented in the upper

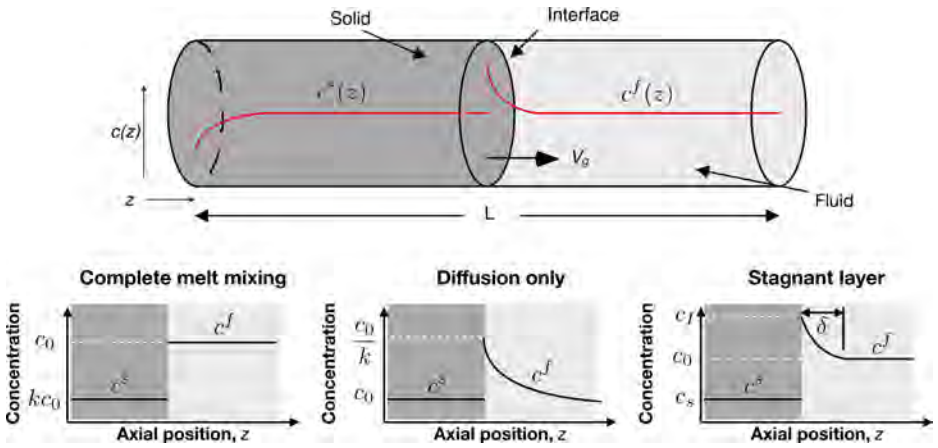


Figure 7: A chemical species, such as a dopant or impurity, will be segregated during the directional solidification of a melt. Here, a species with distribution coefficient less than unity, $k < 1$, is represented. Upper: Schematic depiction of axial dopant segregation that occurs during directional solidification. Bottom: Depictions of concentration profiles under different conditions of mixing in the fluid phase. Left: Complete mixing of the fluid makes the concentration uniform everywhere in the melt. Middle: Diffusion alone in the fluid results in a "pile-up" of rejected solute in front of the interface, with a dying exponential concentration profile into the melt. Right: A stagnant layer of width δ defines an inner region, where only diffusion occurs, and a perfectly mixed outer region.

right plot of Figure 1. The segregation of a dopant or impurity species will result in a changing compositional profile throughout the crystal during growth. We examine this behavior more quantitatively in the following discussion.

Let us consider a crystal that is undergoing directional solidification along the axis of a container, as depicted schematically as the upper image in Figure 7. We desire to obtain a mathematical description of the composition of a dopant, with a distribution coefficient less than unity, in the grown crystal. For $k < 1$, the growing crystal will incorporate the segregated species at a concentration lower than that in the fluid phase adjacent to the interface. As the crystal grows, dopant will be continually rejected into the melt, and we expect that the melt composition will change in time, giving rise, in turn, to a non-uniform axial concentration in the grown crystal.

Let's put together some mathematical models for the growth and subsequent redistribution of a dopant species in the crystal. Let us assume that growth and species transport are one-dimensional, so that the only variation of solute in a growing crystal is along its growth axis. Let us also assume that the melt is initially uniform in composition at c_0 and that the growth rate, V_g, is constant. As shown in Figure 7, we denote the axial concentration profiles in the solid and fluid phases as $c^s(z)$ and $c^f(z)$, respectively, with the axial coordinations z being located at the end of the container where growth is initiated, and we set the container length to L. Since solid-state diffusion is so much slower than diffusion through fluids, all of our models will assume that the dopant

concentration profile in the melt is "frozen in" and that no diffusion occurs in the solid.

In our first model, let us assume that vigorous mixing occurs in the melt, making its composition uniform throughout. This situation is depicted by the concentration profiles near the growth interface shown in the lower left plot of Figure 7. We may apply a simple conservation equation for the dopant. Let's imagine that the interface moves forward over a differential distance corresponding to dz and consider the change of the amount of dopant in the melt. We write the following balance,

$$(c^f - c^s)Adz = (L - z^I)Adc^f. \tag{37}$$

where the left-hand side represents the amount of dopant that has been rejected into the melt by segregation at the growth interface. This is simply the difference in melt and solid concentrations multiplied by the volume of the newly solidified disk, Adz, with A as the cross-sectional area of the container. The right-hand side is the resultant change of the amount of dopant in the melt, where $(L-z^I)A$ is the total volume of the melt, with L as the initial length of melt and z^I as the interface position. As solidification proceeds, the value of c^f, which we have presumed to be constant throughout the melt due to intense mixing, changes by the amount dc^f.

Dividing both sides by A, using the segregation condition at the interface, $c^s = kc^f$, to write the equation in terms of c^s, and rearranging, we get:

$$\frac{1-k}{L-z^I}dz = \frac{dc^s}{c^s}. \tag{38}$$

Let us now integrate this expression from the start of solidification until the interface has reached z^I;

$$\int_0^{z^I} \frac{1-k}{L-z}dz = \int_{kc_0}^{c^s} \frac{dc^s}{c^s}. \tag{39}$$

Evaluating this integral, rearranging, and substituting $f = z^I/L$ for the fraction of melt solidified, this solution is written as,

$$\frac{c^s}{c_0} = k(1-f)^{(k-1)}. \tag{40}$$

This model was originally derived by Scheil [95] and is sometimes called the the normal freezing expression or simply the *Scheil equation.* A depiction of the shape of this profile for $c^s(z)$ is shown in Figure 8. This is a simple model, and equation (40) provides a reasonably accurate description of solute segregation in many systems. However, it does not well represent cases where the mixing in the melt is not complete.

Tiller *et al.* [96, 97] took a special interest in a different model for segregation under situations where only diffusion occurs in the melt, essentially the opposite

limit of complete mixing as assumed in the Scheil equation. They first considered that the solute concentration in the melt under steady-state solidification must follow a simple differential equation,

$$\mathcal{D}\frac{d^2c^f}{dz^2} + V_g\frac{dc^f}{dz} = 0, \tag{41}$$

where $\mathcal{D}$ is the diffusion coefficient in the melt, c^f is the liquid-phase concentration, z is the axial distance in into the melt, with $z = 0$ denoting the melt-solid interface position, and V_g as the steady-state growth velocity. Note that this is identical to equation (16) for the case of steady-state, one-dimensional species transport. The second term in equation (41) represents convection, because our coordinate frame, with $z = 0$ attached to the interface, is moving with velocity V_g. In this frame of reference, fluid is moving toward the stationary interface and the solid phase is moving away from it.

Boundary conditions are applied at the growth interface that enforce solute conservation and segregation, like equation (18), re-written here as,

$$-\mathcal{D}\left.\frac{dc^f}{dz}\right|_{z=0} = V_g c^f(1-k), \tag{42}$$

and a far-field condition of $c^f \to c_0$ is applied as $z \to \infty$.

The solution of the above differential equation and boundary conditions yields the steady-state concentration profile for the solute in the melt,

$$c^f(z) = c_0\left(1 + \frac{1-k}{k}e^{-(V_g/\mathcal{D})z}\right). \tag{43}$$

This profile features a *diffusion boundary layer* of characteristic length $\mathcal{D}/V_g$ that is depicted in in the lower middle image of Figure 7. Physically, the rejected solute builds up in front of the interface until the rate of diffusion of dopant into the melt exactly balances that incorporated into the solid. If we evaluate the fluid concentration at the interface, by setting $z = 0$ in equation (43), we find that $c^f(0) = c_0/k$.

This model predicts that solidification can occur with no change in axial solute concentration, except for initial and final transients, as depicted in the diffusion-limited profile shown in Figure 8. In this ideal situation, there is no change in the axial composition over most of the length of the solidified charge. The form of the initial and final transients for $c^s(z)$ were elegantly, and painstakingly, also derived in analysis of Smith, Tiller, and Rutter [97]. From a historical perspective, Jackson [98] recounts that the prediction of such a diffusion layer was derived before the complete analysis of Smith, Tiller, and Rutter [97] found the solution represented by equation (43) above.

We now have two different models that predict the axial segregation of a dopant into a growing crystal. Depictions of the predictions of these models for the axial distribution of a dopant with a distribution coefficient less than

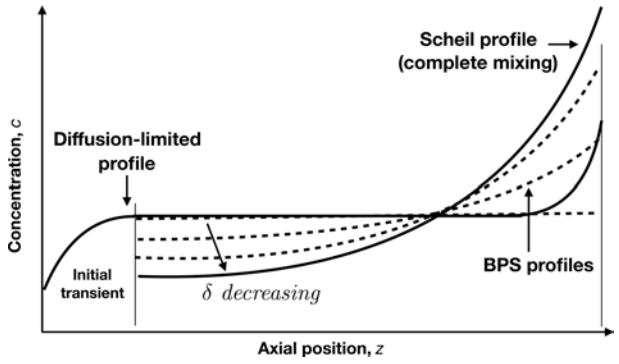


Figure 8: A depiction of the axial concentration profiles that result from different models of segregation during directional solidification. The BPS profiles continuously span the limiting cases of the Scheil profile for complete mixing and the constant-concentration outcome of the diffusion-limited profile.

unity are depicted by the solid curves in Figure 8. Neither of these predictions is entirely realistic; however, both represent limiting cases—the Scheil solution for the case of complete melt mixing and the Smith, Tiller, Rutter model for the case of only diffusion in the melt. Indeed, all measured segregation profiles fall between these two limiting cases, thus these models are meaningful for understanding axial segregation.

Let us discuss one more model for axial segregation during crystal growth. Realizing that both convection (mixing) and diffusion must both act during growth, Burton, Prim, and Schlicter [99] put forth a scenario that is depicted in the lower right image of Figure 7. Here, a stagnant film of thickness δ is postulated to exist in front of the interface. Transport is assumed to occur only by diffusion within the film and by perfect convective mixing beyond the film.

Under this scenario, the same differential equation as used by Smith, Tiller, and Rutter, namely equation (41), is posited to hold in the fluid phase. However, Burton, Prim, and Schlicter, posed the interfacial boundary condition as,

$$-\mathcal{D}\left.\frac{dc^f}{dz}\right|_{z=0} = V_g(c^f(0) - c^s(0)), \tag{44}$$

where $c^f(0)$ and $c^s(0)$ are the interfacial concentrations of the dopant in the fluid and solid phases, respectively, and the other boundary condition as $c^f = c_0$ at $z = \delta$.

Solving with these new boundary conditions, we obtain,

$$c^f(z) = (c^f(0) - c^s(0))e^{-(V_g/\mathcal{D})(z-\delta)} + c^s(0). \tag{45}$$

This equation can be evaluated at the growth interface, $z = 0$, and rearranged

using the equilibrium condition, $c^s(0) = kc^f(0)$, to show,

$$c^s(0) = \frac{kc^f(0)}{k + (1-k)\exp(-V_g\delta/\mathcal{D})}. \tag{46}$$

This equation can be interpreted as defining an "effective" distribution coefficient given by

$$k_{\text{eff}} = \frac{k}{k + (1-k)\exp(-V_g\delta/\mathcal{D})}, \tag{47}$$

where k is the equilibrium distribution coefficient, V_g is the growth velocity of the crystal, and $\mathcal{D}$ is the diffusion coefficient of the dopant in the melt.

Now, we can return to the logic behind the Scheil equation to calculate an axial concentration profile after growth. In fact, the mathematical analysis is identical if we use k_{eff} rather than k, and the axial distribution of a dopant in the crystal is given by

$$\frac{c_s}{c_0} = k_{\text{eff}}(1-f)^{(k_{\text{eff}}-1)}, \tag{48}$$

where c_s is the concentration of dopant in the crystal, c_0 is the initial concentration of solute in the melt, and f is the fraction of melt solidified.

In the Burton, Prim, Schlicter, or BPS, equation, if $\delta \to \infty$, the effective segregation coefficient approaches unity, $k_{\text{eff}} \to 1$. Then, equation (48) shows that $c^s = c_0$, and the constant axial concentration profile for diffusion-controlled growth is obtained (which, apart from the initial and final transients, is the Smith, Tiller, Rutter result [96, 97]). As $\delta \to 0$, complete mixing of the melt is implied, $k_{\text{eff}} \to k$, and the *Scheil equation* [95] for axial segregation is recovered. Thus BPS can predict a continuum of profiles that evolve from one limit to the other as the value of δ is changed; such profiles are depicted schematically in Figure 8. The BPS equation is often extremely effective for fitting experimental segregation data by suitable choice of the parameter δ. Indeed, Hurle and Rudolph [100] stated, "This famous BPS equation probably represents the single most useful piece of theory ever produced for practical crystal growers." For a more extensive discussion of axial segregation models, the reader is referred to the excellent book by Flemings [101].

The simplicity and elegance of the BPS expression is perhaps a bit misleading, since it has virtually no predictive capabilities. The underlying idea for this model is too simple; there is no precise physical meaning of the parameter δ, since flows in real systems are never completely stagnant nor intense enough to produce perfect mixing. Shortcomings of the stagnant layer concept and similar boundary layer models have been discussed by Wilcox [102] and Rosenberger and Müller [103]. Brown and Kim [84] provided an erudite discussion of the validity of the BPS model by comparison with results from detailed numerical simulations of Bridgman growth.

Before leaving the topic of segregation, let us consider two more important effects that are observed in real crystal growth systems. First, the above models presumed that the growth interface moved at a constant velocity. Interestingly,

Tiller *et al.* [96] also considered the effect of a changing growth rate on the axial solute distribution. They reasoned that a very fast change in growth rate would cause the diffusion layer in the melt to spatially rearrange and, in doing so, would result in "transverse bands [104] differing in concentration from the equilibrium value of c_0" [96]. This effect, a rapid change in growth rate, is now understood to produce locally enriched or depleted concentration bands, which are typically referred to as solute striations. Striations commonly occur during the melt growth of a doped material, when driving forces such as time-dependent flows or rotationally-driven changes in interface position result in fast changes of the growth velocity.

Second, segregation *across* the face of the crystal, in the *radial* or *lateral* direction, can be as important as segregation along its length; however, these effects are ignored in the one-dimensional solidification models presented above. Lateral segregation arises from the non-planar growth interface shapes and the effects of incomplete mixing by melt flows that are adjacent to it. While there are analyses that quantify the expected magnitude of lateral segregation for rather simple flows, see, e.g., [1, 105–108], the details of interface shape and flow structure and their impact on lateral segregation are very difficult to predict without detailed knowledge provide by a complete simulation of the growth process.

Here, we choose to illustrate combined axial and radial segregation via experimental measurements and numerical simulations of zinc segregation during the Bridgman growth of cadmium zinc telluride (CZT); details are reported by Zhang *et al.* [109]. The upper graph shown in Figure 9 plots the zinc composition along the centerline as a function of axial distance for both model and experiment. The profile is clearly not constant, indicating some amount of mixing within the melt. Note also that the concentration of zinc decreases steadily along the growth axis due to its segregation coefficient being larger than unity, specifically $k = 1.35$. Here, a *depletion layer* forms in front of the growth interface, since zinc is preferentially incorporated into the growing crystal. The agreement between the experimentally measured profile and that predicted by the numerical model is excellent. Significantly, only the initial composition of zinc in the first-to-freeze region of the crystal was used to set the unknown initial composition of the melt for the simulation; all other parameters were set according to known experimental parameters and previously measured physical properties.

The lower plots of Figure 9 show zinc composition color maps across the axial cross-section of the grown ingot. The experimental results are shown on the left, while the model predictions are featured on the right. The color scale of the calculation was chosen to approximately match the output of the photoluminescence (PL) mapping. Clearly, there is substantial axial and radial segregation of zinc across the grown crystal. Both data and model show the same upward bowing of the zinc compositional field in the middle of the crystal, with a decrease in zinc concentration as the ampoule walls are approached. Towards the end of growth, both data and model show a radial flattening of the radial zinc profile. We believe that the extent of agreement between this experiment and compu-

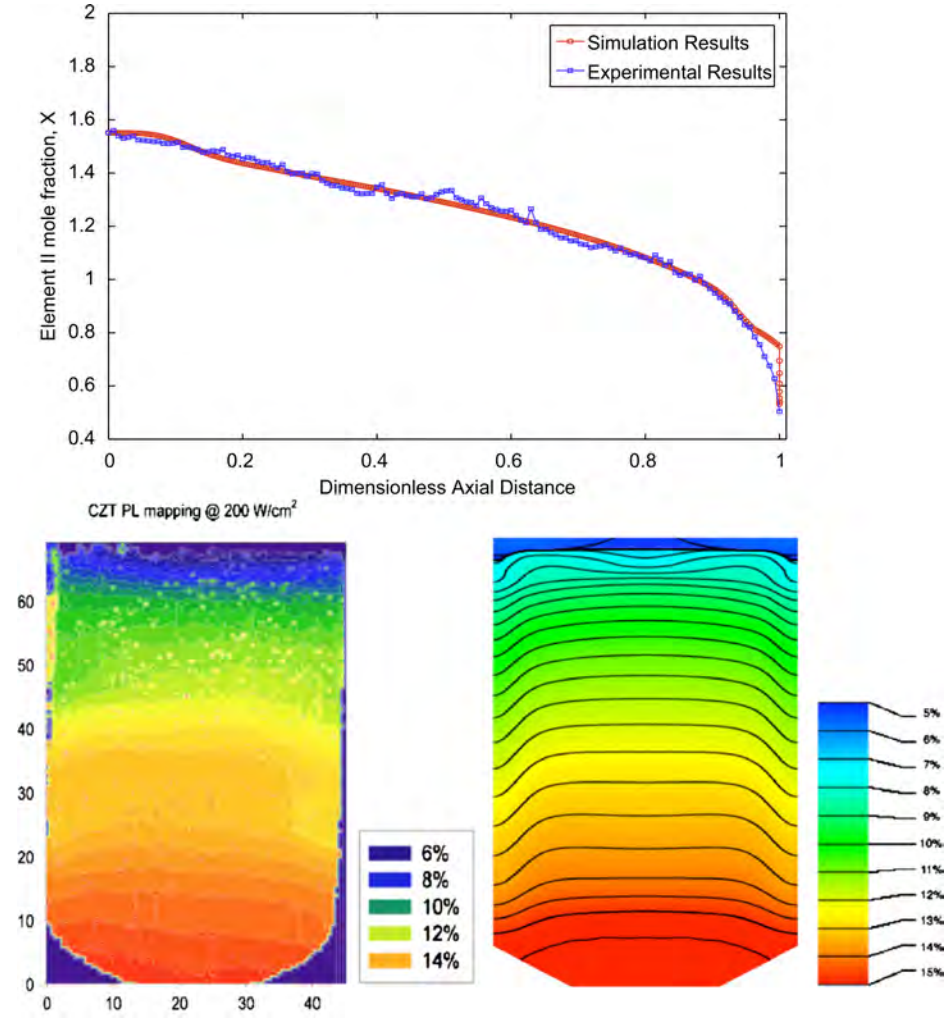


Figure 9: The segregation of zinc during the growth of cadmium zinc telluride is measured and compared to predictions from a simulation of transport, segregation, and growth. Upper: Comparison of axial concentration of zinc along the centerline. Lower: zinc composition along a length-wise axial cut of the crystal is indicated for the experiment using PL mapping (left) and by color and contours in the model computation (right). Adapted from [109].

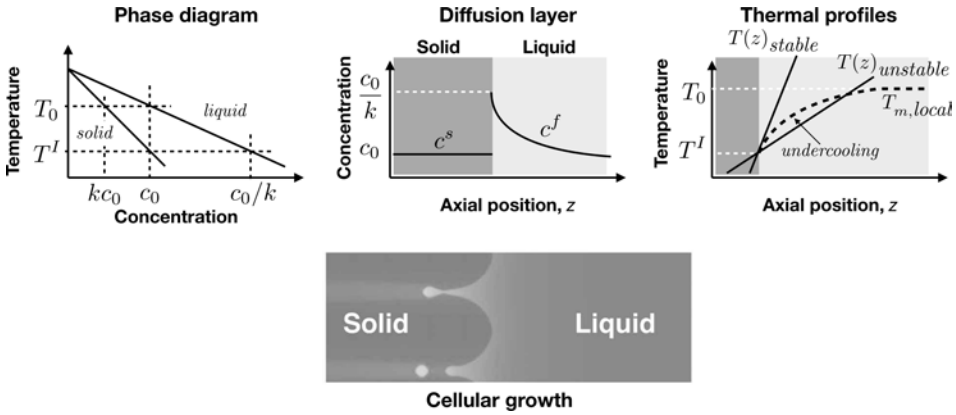


Figure 10: Above: Unstable solidification can arise due to segregation and constitutional supercooling. Refer to text for explanation. Below: Cellular growth instability is computed by Bi [110, 111] using a two-dimensional, phase field model for directional solidification of a binary alloy. The lighter regions show a melt enriched with one component due to solute segregation.

tation argues convincingly that continuum transport models for segregation are valid and that predictions represent physically faithful outcomes.

4.3. Morphological stability

The continuous growth of a large single crystal is aided by the establishment of a relatively constant growth rate and thermal gradients at the interface. However, under certain conditions, the phase-change interface can be destabilized, particularly under conditions of fast growth or low gradients. One-dimensional directional solidification models, like those presented in the prior section, proved to be crucial to understanding the *morphological stability* of a crystal interface during growth. The situation leading to instability is depicted in the top plots of Figure 10.

A simple representation of a phase diagram at constant pressure is presented in the upper left image of Figure 10. This diagram indicates the thermodynamically stable state, solid or liquid, under different conditions of temperature and composition, here interpreted to be the concentration of an additional species in the system, like a dopant or an impurity. The system exists as a liquid for conditions above the upper line on the plot, known as the liquids curve. By indicating the limit of stability for the liquid phase, the liquidus curve thereby defines the freezing or melting temperature of a melt at a certain composition.

Conditions below the lower curve, named the solidus curve, represent states that are solid. When a liquid of certain composition solidifies, the composition of the solid in equilibrium with this liquid is given by this curve. Referring to the upper left image of Figure 10, a liquid of concentration c_0 will solidify at temperature T_0, and the solid that forms in equilibrium with this liquid has composition kc_0, where k is the distribution coefficient.

The concentration profile of a species rejected at the growth interface is depicted in the center upper plot of Figure 10. This corresponds to the case of diffusion only in the melt, and its form is described by equation (43), which was derived in the previous section.

We now desire to consider how the concentration profile through the diffusion layer in the melt affects the local equilibrium phase-change temperature. Note that we will always refer to the equilibrium phase-change temperature as the melting temperature, even though it also represents the temperature at which freezing occurs. Equilibrium melting temperatures are provided by the liquidus curve of the phase diagram, shown in the upper left image of Figure 10. Thus, with a liquid composition of c_0/k at the interface, the equilibrium melting temperature is T^I. As the diffusion layer approaches the concentration of c_0 far in front of the interface, the melting temperature goes to T_0. If we take each local concentration value and determine its corresponding melting point, we can plot a local melting point profile, $T_{m,local}$, as a function of axial position and indicated by the dashed curve in the upper right image of Figure 10.

The two solid lines in the upper right image of Figure 10 represent possible axial temperature profiles in the crystal growth system (which would be determined by the design of the furnace and growth system). The curve labeled $T(z)_{stable}$ represents solidification conditions that lead to a stable growth interface. Under these conditions, a disturbance that pushes the interface forward into the melt will encounter liquid that is always above the equilibrium melting temperature, and we expect the disturbance to melt back. Unstable solidification occurs when the actual temperature profile in front of the interface, as depicted by the curve labeled $T(z)_{unstable}$, falls below the the local thermodynamic melting profile, $T_{m,local}$. Under such a scenario, the melt in front of the interface is below its freezing point, and a perturbation to the interface will grow rapidly into the supercooled region, resulting in an unstable growth interface.

This situation is known as *constitutional supercooling,* since it is driven by compositional, or constitutional, effects, and the criterion for it to arise is,

$$\frac{dT^f}{dz} < \frac{mc_0(1-k)V_g}{k\mathcal{D}}, \tag{49}$$

where dT^f/dz denotes the axial temperature gradient in the melt at the interface and m is the slope of the liquidus curve on the phase diagram. The original derivation of this condition was given by Tiller *et al.* [96] using the mathematical form of the diffusion layer, represented by equation (43), coupled with physical reasoning similar to that presented above. A much more comprehensive analysis was later derived by Mullins and Sekerka [112, 113], using linear stability theory; hence, this phenomenon is often referred to as the *Mullins–Sekerka instability.* Mullins and Sekerka pointed out that many additional factors can affect interface stability during solidification; however, their results took on the form of equation (49) in the limit of the conditions of melt crystal growth considered by Tiller *et al.*

Under unstable conditions, an initially planar interface typically evolves to

a wavy interface, which, under larger driving forces, becomes successively more unstable in the form of cells and, eventually, dendrites. A modern, phase-field computation of such an unstable interface by Bi and Sekerka [110, 111] is also shown in the lower image of Figure 10.

4.4. Growth rate limitations in the traveling heater method

Most of the examples discussed in the previous sections were simple enough to allow for analytical solution of the underlying governing equations. Here, we wish to present an example that is complicated enough to require numerical solution but which also is understandable using the basic concepts discussed above. In the following example, we demonstrate how surprising results can arise due to the combined effects of of segregation, transport, and fluid mechanics [7].

Specifically, we desire to analyze the workings of the traveling heater method (THM), which is an important technique for producing compound semiconductor crystals, particularly detector-grade cadmium zinc telluride (CZT) [114–116]. The traveling heater method is depicted schematically in the right image of Figure 3. Unlike the Bridgman method, the THM employs a liquid zone that is enriched in one component of the compound (tellurium, for the growth of CZT), which acts as a solvent. As the heater travels past the ampoule, it forms and moves this liquid zone to steadily dissolve a solid feed above while simultaneously growing a crystal of a similar composition at the opposite end of the zone. Since the crystal grows from a liquid flux, the THM allows for operation at much lower temperatures than the Bridgman process. Currently, the traveling heater method provides the best-quality CZT for high-performance gamma radiation detectors.

Despite the attractiveness of the THM, it is hampered by growth rates that are typically an order of magnitude slower than those routinely employed by Bridgman methods for the growth of CZT [114–120]. While prior models for this process suggested that morphological instability could readily arise in THM [121, 122], these past works did not identify the mechanisms that are responsible. Peterson *et al.* [123, 124] used the classical constitutional supercooling criterion, defined by equation (49), to estimate instability conditions for the THM growth of CZT but found that the theoretically predicted maximum growth rate far exceeded that experienced in practice. This motivated a series of studies to more clearly understand growth limitations in this system [123, 124].

For such a small liquid zone, typically of several centimeters in size, its fluid flows are surprisingly complicated. Interestingly, the fluid flow within the liquid zone features a structure known as "lee waves," which are associated with atmospheric flows that oscillate within a vertically stratified fluid [125]. Such waves, depicted in Figure 11, typically arise in the lee of a mountain range, where there is a vertically stabilized density field that arises from a cool mesa or valley below. These structures are readily identified by cloud formations that form in the upper portion of the waves, which often result in spectacular, lenticular clouds.

Lee waves come into being from an oscillatory response of the fluid after the flow has been vertically perturbed by a mountain. Consider a parcel of fluid



Figure 11: Left: A schematic diagram illustrating the formation of atmospheric lee waves. Adapted from the COMET Website, http://meted.ucar.edu. Right: Lenticular clouds that have resulted from lee waves. From Bill Randel, http://acd.ucar.edu/∼randel/clouds.html. Adapted from [7].

and the vertical body forces acting upon it. Via Newton's second law, we can write a simple balance,

$$\frac{\partial^2 z'}{\partial t^2} = \frac{g}{\rho_0}\frac{\partial \rho}{\partial z} z', \tag{50}$$

where z' is the with mean elevation of the fluid parcel, z denotes vertical elevation, g is the gravitational constant, and ρ is the fluid density.

In a vertically stabilized density field, denser fluid lies under lighter fluid, so $\partial\rho/\partial z < 0$. If we assume this value to be constant, we can obtain a solution to the above equation as,

$$z' = A\cos\omega t + B\sin\omega t, \tag{51}$$

where A and B are integration constants, indicating that the fluid parcel is oscillating vertically while traveling horizontally. This leads to waves with a frequency given by,

$$\omega \equiv N = \sqrt{-\frac{g}{\rho_0}\frac{\partial \rho}{\partial z}} = \sqrt{g\beta_T \frac{\partial T}{\partial z}}, \tag{52}$$

where N is known as the classical Brunt–Väisälä frequency [126] . The expression on the far right is written in terms of the vertical temperature gradient, $\partial T/\partial z$, and the Boussinesq approximation, with β_T representing the thermal expansion coefficient of the fluid. Thus, the frequency of oscillation and the wavelength of the resulting flow structure depend on the magnitude of the vertical temperature gradient.

Let us now turn from the atmosphere to the liquid zone of the THM system. Figure 12 shows simulations for the steady-state growth of a 3.2 cm diameter CdTe crystal via THM, where flow streamlines are plotted on the left and the temperature field is depicted on the right via isotherms. Adjacent streamlines and isotherms are plotted in constant increments. The CdTe solid feed is above and dissolving into the Te-enriched liquid zone, and a single crystal of CdTe grows downward at a rate of 1.24 mm/day from the zone. Simultaneous dissolution and growth are driven by the upward motion of the traveling heater

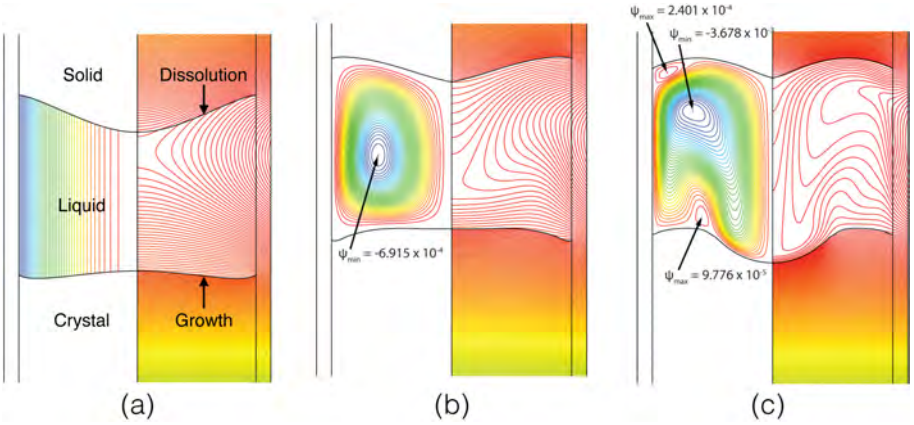


Figure 12: Model for steady-state THM crystal growth of CdTe, showing streamlines on the left and temperature contours on the right. (a) Without gravity. (b) With gravity set to 1% of earth. (c) With terrestrial gravity forces; note the formation of a lee wave structure with vortex adjacent to the growth interface. Adapted from [124].

(which is not shown in the figure). We consider how the flow in the zone evolves by changing the magnitude of the gravitational force in these cases.

Figure 12(a) shows a calculation without gravity, namely with $g = 0$. The streamlines on the left show a constant downward flow through the liquid zone caused by the change in density from solid to liquid; the spacing of the streamlines indicates the changing cross sectional area with radial position in the cylindrical zone. The zone is established by the surrounding heater, as reflected by the temperature isotherms on the right, showing hotter temperatures along the outer ampoule wall and heat diffusing into the liquid zone. The strongly coupled nature of this system is evident by the changing temperature across the interfaces, most readily seen along the upper, dissolution interface, which results from the composition-dependent melting temperature from the phase diagram.

The middle image, Figure 12(b), is a calculation for gravity set to 1% of its terrestrial value. Here, a single, torroidal vortex is driven by buoyancy and occupies the liquid zone. Warmer, lighter fluid near the ampoule wall rises, while the cooler, denser fluid sinks along the centerline. This recirculating flow is fairly weak but still strong enough to slightly deflect the temperature isotherms, due to the fairly large Prandtl number for the liquid in the zone; $Pr \approx 0.4$ is assumed for the liquid.

Under the effects of full gravity on earth, depicted in Figure 12(c), the flow is quite strong, with $Gr \approx 1.5 \times 10^6$ and $Re \approx 400$. The primary vortex spins in the same direction as the prior case, directing a strong flow downward along the system centerline. As the liquid in the hot zone plunges toward the cooler growth interface, it feels a resistance from the stable vertical stratification of density. As the liquid turns to flow outward along the growth interface, the situation is analogous to the perturbed flow over the cool mountain valley, as depicted in Figure 11, and a single lee wave forms with an accompanying, counter-rotating

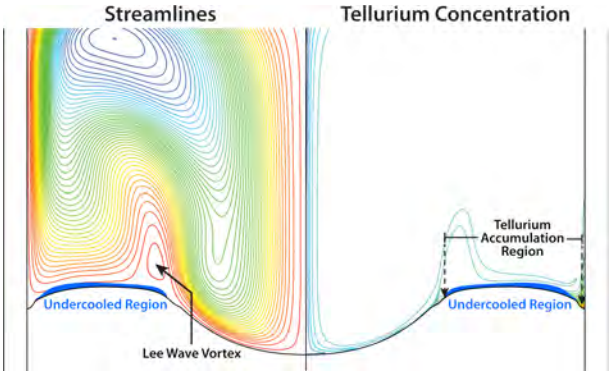


Figure 13: The formation of a lee wave vortex promotes the accumulation of excess tellurium in the liquid zone adjacent to the growth interface during the THM growth of CdTe. This accumulation leads to thermodynamically undercooled regions in the liquid adjacent to the growth interface, resulting in morphological instability and growth rate limitations. Adapted from [123].

vortex.

The effect of this lee wave and vortex on growth is shown in Figure 13, where flow streamlines are shown on the left and the tellurium iso-concentration contours are depicted on the right. The vigorous flows in the liquid promote mixing, and the Te concentration is nearly uniform in the bulk, with thin boundary layers exhibited along the centerline and growth interface. Due to segregation, excess tellurium is rejected from the growing solid and is subsequently swept outward along the interface and into the bulk as the flow turns upward along the inner ampoule wall. However, the counter-rotating vortex nested under the lee wave reverses the flow over a portion of the interface, creating a resistance to mass transport and promoting the local accumulation of tellurium. This accumulation leads to large concentration gradients within the solutal boundary layer. When these gradients are large enough, the composition-dependent melting point increases faster than the temperature field extending into the liquid. This results in an substantial region of supercooled liquid immediately in front of the growth interface, as shown in Figure 13, leading to constitutional supercooling and an unstable growth situation.

Significantly, the fluid dynamics in the THM liquid zone are the primary cause of the supercooling in this system, and this is quite different than the classical scenario of constitutional supercooling during melt crystal growth discussed in the prior section. In fact, due to the lee wave in the liquid zone, supercooling in this system occurs at growth rates more than an order of magnitude smaller than expected from such classical arguments. Paradoxically, the traditional strategy to alleviate constitutional supercooling during crystal growth, namely increasing the axial temperature gradient at the interface, is expected to strengthen the lee-wave vortex and accentuate the onset of instability. Thus, different strategies, that somehow lessen the impact of this fluid

dynamical instability, will be needed to overcome growth limits in the traveling heater method.

While this example represents a very complicated interplay among fluid flow, species transport, segregation, and thermodynamic stability, everything we need to understand it is supplied by the basic notions presented in previous sections.

5. Final remarks

We hope that the above discussion has provided some background to understand transport phenomena in crystal growth systems. Such systems present a rich collection of complex behaviors, particularly when transport is coupled to thermodynamic phenomena and the kinetics of phase transformations. Nevertheless, these systems can be understood and quantified via analysis and modeling. In particular, modern tools of computational modeling will be increasingly employed to better understand transport effects in crystal growth processes and to provide a powerful means to improve them.

Acknowledgments

The author would like to acknowledge prior and current support of many organizations including the Alexander von Humboldt Foundation, the Graduate School of the University of Minnesota, the Israeli-US Binational Science Foundation, the McKnight Foundation, the Petroleum Research Fund, and the United States DHS, DOD, DOE, NASA, and NSF. The results presented on zinc segregation during the Bridgman growth of cadmium zinc telluride were supported in part by the Department of Energy, National Nuclear Security Administration, under Awards DE-FG52-06NA27498 and DE-FG52-08NA28768. This results on the traveling heater method were supported in part by the U.S. National Science Foundation NSF DMR-10007885. The content of this paper does not necessarily reflect the position or policy of the United States Government, and no official endorsement should be inferred. The author would also like to acknowledge all of his graduate students and research colleagues who have provided stimulus for expanding his understanding of crystal growth; however, all opinions and biases expressed in this chapter are his own.

References

[1] R. A. Brown, Theory of transport processes in single crystal growth from the melt, AIChE Journal 34 (6) (1988) 881–911.

[2] J. J. Derby, Macroscopic transport processes during the growth of single crystals from the melt, in: J. van der Eerden, O. Bruinsma (Eds.), Science and Technology of Crystal Growth, Kluwer Academic Publishers, Dordecht, The Netherlands, 1995, pp. 97–110.

[3] A. Yeckel, J. J. Derby, Computational simulations of the growth of crystals from liquids, in: H. Scheel, T. Fukuda (Eds.), Crystal Growth Technology, John Wiley & Sons, West Sussex, UK, 2003, Ch. 6, pp. 115–137.

[4] A. Yeckel, J. J. Derby, Computer modelling of bulk crystal growth, in: P. Capper, A. Willougby, S. Kasap (Eds.), Bulk Crystal Growth of Electronic, Optical, and Optoelectronic Materials, John Wiley & Sons, West Sussex, UK, 2005, pp. 73–119.

[5] C. W. Lan, Recent progress of crystal growth modeling and growth control, Chem. Eng. Sci. 59 (2004) 1437–1457.

[6] J. J. Derby, A. Yeckel, Heat transfer analysis and design for bulk crystal growth: Perspectives on the Bridgman method, in: T. Nishinaga, P. Rudolph (Eds.), Handbook of Crystal Growth, 2nd Edition, Elsevier, 2015, pp. 793–843.

[7] J. J. Derby, Fluid dynamics in crystal growth: The good, the bad, and the ugly, Progress in Crystal Growth and Characterization of Materials 62 (2016) 286–301.

[8] R. Talalaev, Transport phenomena in vapor phase epitaxy reactors, in: T. F. Kuech (Ed.), Handbook of Crystal Growth, 2nd Edition, North-Holland, Boston, 2015, pp. 909–942.

[9] M. E. Glicksman, Diffusion in Solids, John Wiley & Sons, Inc., 2000.

[10] K. A. Jackson, Mechanism of growth, in: Liquid Metals and Solidification, Am. Soc. Metals, 1958, pp. 174–186.

[11] W. K. Burton, N. Cabrera, Crystal growth and surface structure: Part I, Discussions Faraday Soc. 5 (1949) 33.

[12] W. K. Burton, N. Cabrera, F. C. Frank, The growth of crystals and the equilibrium structure of their surfaces, Phil. Trans. Roy. Soc. London 243 (R-2) (1951) 299–358.

[13] Y. I. Kwon, B. Dai, J. J. Derby, Assessing the dynamics of liquid-phase solution growth via step growth models: From BCF to FEM, Prog. Crystal Growth and Charact. 53 (2007) 167–206.

[14] M. Uwaha, Introduction to the BCF theory, Progress in Crystal Growth and Characterization of Materials 62 (2) (2016) 58 – 68, special Issue: Recent Progress on Fundamentals and Applications of Crystal Growth; Proceedings of the 16th International Summer School on Crystal Growth (ISSCG-16).

[15] K. M. Beatty, K. A. Jackson, Monte Carlo modeling of silicon crystal growth, Journal of Crystal Growth 211 (1) (2000) 13–17.

[16] A. A. Chernov, How does the flow within the boundary layer influence morphological stability of a vicinal face?, J. Crystal Growth 118 (1992) 333–347.

[17] A. A. Chernov, S. R. Coriell, B. T. Murray, Morphological stability of a vicinal face induced by step flow, J. Crystal Growth 132 (1993) 405–413.

[18] S. R. Coriell, B. T. Murray, A. A. Chernov, G. B. McFadden, Step bunching on a vicinal face of a crystal growing in a flowing solution, J. Crystal Growth 169 (1996) 773–785.

[19] S. R. Coriell, A. A. Chernov, B. T. Murray, G. B. McFadden, Step bunching: generalized kinetics, J. Crystal Growth 183 (1998) 669–682.

[20] W. M. Deen, Analysis of Transport Phenomena, 2nd Edition, Topics in Chemical Engineering, Oxford University Press, 2012.

[21] S. Brandon, J. J. Derby, Internal radiative transport in the vertical Bridgman growth of semitransparent crystals, J. Crystal Growth 110 (1991) 481–500.

[22] S. Brandon, J. J. Derby, Heat transfer in vertical Bridgman growth of oxides: Effects of conduction, convection, and internal radiation, J. Crystal Growth 121 (1992) 473–494.

[23] S. Brandon, D. Gazit, A. Horowitz, Interface shapes and thermal fields during the gradient solidification method growth of sapphire single crystals, J. Crystal Growth 167 (1996) 190–207.

[24] A. Virozub, S. Brandon, Radiative heat transport during the vertical Bridgman growth of oxide single crystals: slabs versus cylinders, J. Crystal Growth 193 (4) (1998) 592–596.

[25] V. S. Yuferev, O. N. Budenkova, M. G. Vasiliev, S. A. Rukolaine, V. N. Shlegel, Y. V. Vasiliev, A. I. Zhmakin, Variations of solid–liquid interface in the BGO low thermal gradients Cz growth for diffuse and specular crystal side surface, J. Crystal Growth 253 (1–4) (2003) 383–397.

[26] O. Budenkova, M. Vasiliev, V. Yuferev, V. Kalaev, Effect of internal radiation on the solid–liquid interface shape in low and high thermal gradient Czochralski oxide growth, J. Crystal Growth 303 (1) (2007) 156–160.

[27] R. B. Bird, W. E. Stewart, E. N. Lightfoot, Transport Phenomena, John Wiley & Sons, New York, 1960.

[28] E. L. Cussler, Diffusion — Mass Transfer in Fluid Systems, Cambridge University Press, 1997.

[29] M. Boussinesq, Theory Analytique de la Chaleur, Vol. 2, Gauthier-Villars, 1903.

[30] G. K. Batchelor, An Introduction to Fluid Dynamics, Cambridge University Press, 1967.

[31] D. T. J. Hurle, Temperature oscillations in molten metals and their relationship to growth striae in melt-grown crystals, Philosophical Magazine 13 (122) (1966) 305–310.

[32] P. A. Davidson, Magnetohydrodynamics in materials processing, Annu. Rev. Fluid Mech. 31 (1999) 273.

[33] A. Yeckel, J. J. Derby, Dynamics of three-dimensional convection in microgravity crystal growth: g-jitter with steady magnetic fields, J. Crystal Growth 263 (2004) 40–52.

[34] A. Yeckel, J. J. Derby, The prospects for traveling magnetic fields to affect interface shape in the vertical gradient freeze growth of cadmium zinc telluride, J. Crystal Growth 364 (2013) 133–144.

[35] V. Galindo, K. Niemietz, O. Pätzold, G. Gerbeth, Numerical and experimental modeling of VGF-type buoyant flow under the influence of traveling and rotating magnetic fields, J. Crystal Growth 360 (2012) 30–34.

[36] D. Vizman, Flow control by magnetic fields during crystal growth from melt, in: T. Nishinaga, P. Rudolph (Eds.), Handbook of Crystal Growth, 2nd Edition, Elsevier, Boston, 2015, pp. 909–950.

[37] J. J. Derby, Modeling and bulk crystal growth processes: What is to be learned?, in: M. Wang, K. Tsukamoto, D. Wu (Eds.), Selected Topics on Crystal Growth: 14th International Summer School on Crystal Growth, Vol. 1270 of AIP Conference Proceedings, Melville, New York, 2010, pp. 221–246.

[38] K. Kakimoto, B. Gao, Fluid dynamics: Modeling and analysis, in: T. Nishinaga, P. Rudolph (Eds.), Handbook of Crystal Growth, 2nd Edition, Elsevier, Boston, 2015, pp. 845–870.

[39] T. Tsukada, The role of Marangoni convection in crystal growth, in: T. Nishinaga, P. Rudolph (Eds.), Handbook of Crystal Growth, 2nd Edition, Elsevier, Boston, 2015, pp. 871–907.

[40] P. Capper, E. Zharikov, Oscillatory-driven fluid flow control during crystal growth from the melt, in: T. Nishinaga, P. Rudolph (Eds.), Handbook of Crystal Growth, 2nd Edition, Elsevier, Boston, 2015, pp. 951–993.

[41] L. Onsager, Reciprocal realtions in irreversible processes. II., Phys. Rev. 38 (12) (1931) 2265–2279.

[42] R. W. Balluffi, S. M. Allen, W. C. Carter, Kinetics of Materials, Wiley-Interscience, 2005.

[43] J. J. Derby, N. Ponde, V. F. de Almeida, A. Yeckel, Modeling segregation and convection during the growth of ternary alloys under terrestrial and microgravity conditions, in: A. Roósz, M. Rettenmayr, D. Watring (Eds.), Solidification and Gravity 2000, Vol. 329–330 of Material Science Forum, Trans Tech Publications Ltd, Zurich, 2000, p. 93.

[44] J. J. Derby, Y. Tao, C. Reimann, J. Friedrich, T. Jauß, T. Sorgenfrei, A. Croell, A quantitative model with new scaling for silicon carbide particle engulfment during silicon crystal growth, Journal of Crystal Growth 463 (2017) 100–109.

[45] D. Schwabe, Surface-tension-driven flow in crystal growth melts, in: Superhard Materials, Convection, and Optical Devices, Vol. 11 of Crystals, Springer, 1988, pp. 75–112.

[46] H. C. Kuhlmann, Thermocapillary Convection in Models of Crystal Growth, Springer, 1999.

[47] A. Acrivos, On the combined effect of forced and free convection heat transfer in laminar boundary layer flows, Chem. Eng. Sci. 21 (1966) 343–352.

[48] A. E. Gill, The boundary-layer regime for convection in a rectangular cavity, J . Fluid Mech. 26(3) (1966) 515–536.

[49] P.A. Sackinger, R.A. Brown, and J.J. Derby, A finite element method for analysis of fluid flow, heat transfer and free interfaces in Czochralski crystal growth, Intern. J. Numer. Meth. Fluids 9(4) (1989) 453–492.

[50] Q. Xiao and J.J. Derby, Bulk flow versus thermal-capillary models for Czochralski growth of semiconductors, J. Crystal Growth 129 (1993) 593–609.

[51] O. Reynolds, An experimental investigation of the circumstances which determine whether the motion of water shall be direct or sinuous, and of the law of resistance in parallel channels, Phil. Trans. R. Soc. Lond. 174 (1883) 935–982.

[52] L. Rayleigh, On convective currents in a horizontal layer of fluid when the higher temperature is on the under side, Philos. Mag. 32 (1916) 475–480.

[53] H. Bénard, Les tourbillons cellulaires dans une nappe liquide transportant de la chaleur par convection en régime permanent, Annales de Chimie et de Physique 23 (1901) 62–144.

[54] J. J. Derby, R. A. Brown, On the quasi-steady-state assumption in modeling Czochralski crystal growth, J. Crystal Growth 87 (1988) 251–260.

[55] G. Müller, A. Ostrogorsky, Convection in melt growth, in: D. T. J. Hurle (Ed.), Handbook of Crystal Growth Vol. 2b: Bulk Crystal Growth, Growth Mechanisms and Dynamics, North-Holland, Amsterdam, 1994, pp. 711–814.

[56] K. Kakimoto, Heat and mass transfer under magnetic fields, in: H. Scheel, T. Fukuda (Eds.), Crystal Growth Technology, John Wiley & Sons, West Sussex, UK, 2003, Ch. 7, pp. 139–153.

[57] J. J. Derby, A. Yeckel, Modeling of crystal growth processes, in: G. Müller, J.-J. Métois, P. Rudolph (Eds.), Crystal Growth — From Fundamentals to Technology, Elsevier, Amsterdam, 2004, pp. 143–167.

[58] J. J. Derby, Crystal growth: Crystal growth, bulk (theory and models), in: F. Bassani, J. Liedl, P. Wyder (Eds.), Encyclopedia of Condensed Matter Physics, Academic Press, Amsterdam, 2005, pp. 274–282.

[59] J. J. Derby, Y.-I. Kwon, A. Pandy, P. Sonda, A. Yeckel, T. Jung, G. Müller, Developing quantitative, multiscale models for microgravity crystal growth, Ann. N.Y. Acad. Sci. 1077 (2006) 124–145.

[60] Proceedings of the second international workshop on modelling in crystal growth, in: F. Dupret, J. J. Derby, K. Kakimoto, G. Müller, N. V. D. Bogaert, A. Wheeler (Eds.), J. Crystal Growth, Vol. 180, 1997.

[61] Proceedings of the third international workshop on modelling in crystal growth, in: A. Yeckel, V. Prasad, J. J. Derby (Eds.), J. Crystal Growth, Vol. 230, 2000.

[62] Proceedings of the fourth international workshop on modelling in crystal growth, in: C. Lan, N. Imaishi, K. Kakimoto (Eds.), J. Crystal Growth, Vol. 226, 2004.

[63] Proceedings of the fifth international workshop on modelling in crystal growth, in: J. Friedrich, G. Meuller (Eds.), J. Crystal Growth, Vol. 303, 2007.

[64] Proceedings of the sixth international workshop on modelling in crystal growth, in: C. Lynch, J. J. Derby, R. Bhatt, C. Caneau, S. Dost, A. Yeckel (Eds.), J. Crystal Growth, Vol. 312, 2010.

[65] P. W. Bridgman, Certain physical properties of single crystals of tungsten, antimony, bismuth, tellurium, cadmium, zinc, and tin, Proceedings of the American Academy of Arts and Sciences 60 (6) (1925) 305–383.

[66] D. C. Stockbarger, The production of large single crystals of lithium fluoride, Rev. Sci. Instrum. 7 (1936) 133.

[67] R. S. Feigelson, Crystal growth through the ages: A historical perspective, in: T. Nishinaga (Ed.), Handbook of Crystal Growth, 2nd Edition, Vol. VOLUME I, Part A, Elsevier, 2015, pp. 1–84.

[68] C. E. Chang, W. R. Wilcox, Control of interface shape in the vertical Bridgman-Stockbarger technique, J. Crystal Growth 21 (1) (1974) 135–140.

[69] S. Sen, W. R. Wilcox, Infuence of crucible on interface shape, position and sensitivity in the vertical Bridgman-Stockbarger technique, J. Crystal Growth 28 (1975) 26–40.

[70] T.-W. Fu, W. R. Wilcox, Influence of insulation on stability of interface shape and position in the vertical Bridgman-Stockbarger technique, J. Crystal Growth 48 (1980) 416–424.

[71] T.-W. Fu, W. R. Wilcox, Rate of change of transients in Bridgman-Stockbarger growth, J. Crystal Growth 51 (1981) 557–567.

[72] R. J. Naumann, An analytical approach to thermal modeling of Bridgman-type crystal growth: I. one-dimensional analysis, J. Crystal Growth 58 (3) (1982) 554–568.

[73] R. J. Naumann, An analytical approach to the thermal modeling of Bridgman-type crystal growth II. Two-dimensional analysis, J. Crystal Growth 58 (1982) 569–584.

[74] T. Jasinski, W. M. Rohsenow, A. F. Witt, Heat transfer analysis of the Bridgman-Stockbarger configuration for crystal growth : I. Analytical treatment of the axial temperature profile, J. Crystal Growth 61 (1983) 339–354.

[75] T. Jasinski, W. M. Rohsenow, A. F. Witt, Heat transfer analysis of the Bridgman-Stockbarger configuration for crystal growth : II. Analytical treatment of radial temperature variations, J. Crystal Growth 67 (1984) 173–184.

[76] T. Jasinski, A. F. Witt, On control of the crystal melt interface shape during growth in a vertical Bridgman configuration, J. Crystal Growth 71 (1985) 295–304.

[77] C. J. Chang, R. A. Brown, Radial segregation induced by natural convection and melt/solid interface shape in vertical Bridgman growth, J. Crystal Growth 63 (1983) 343.

[78] P. M. Adornato, R. A. Brown, Convection and segregation in directional solidification of dilute and non-dilute binary alloys: Effects of ampoule and furnace design, J. Crystal Growth 80 (1987) 155–190.

[79] P. M. Adornato, R. A. Brown, Petrov-Galerkin methods for natural convection in directional solidification of binary alloys, Int. J. Num. Meth. Fluids 7 (1987) 761.

[80] D. H. Kim, P. M. Adornato, R. A. Brown, Effect of vertical magnetic field on convection and segregation in vertical Bridgman crystal growth, J. Crystal Growth 89 (1988) 339.

[81] D. H. Kim, R. A. Brown, Models for convection and segregation in the growth of HgCdTe by the vertical Bridgman method, J. Crystal Growth 96 (1989) 609.

[82] M. J. Crochet, F. Dupret, Y. Ryckmans, F. T. Geyling, E. M. Monberg, Numerical simulation of crystal growth in a vertical Bridgman furnace, J. Crystal Growth 97 (1989) 173.

[83] D. H. Kim, R. A. Brown, Modelling of the dynamics of HgCdTe growth by the vertical Bridgman method, J. Crystal Growth 114 (1991) 441–434.

[84] R. A. Brown, D. H. Kim, Modeling of directional solidification: From Scheil to detailed numerical simulation, J. Crystal Growth 109 (1991) 50–65.

[85] M. Volz, K. Mazuruk, M. Aggarwal, A. Cröll, Interface shape control using localized heating during Bridgman growth, Journal of Crystal Growth 311 (8) (2009) 2321 – 2326.

[86] N. Zhang, A. Yeckel, J. J. Derby, Maintaining convex interface shapes during electrodynamic gradient freeze growth of cadmium zinc telluride using a dynamic, bell-curve furnace profile, J. Crystal Growth 355 (2012) 113–121.

[87] J. H. Peterson, J. J. Derby, An axial temperature profile curvature criterion for the engineering of convex crystal growth interfaces in Bridgman systems, J. Crystal Growth 468 (2017) 899–904.

[88] J. C. Brice, Crystal Growth Processes, Halsted Press, New York, 1986.

[89] W. A. Tiller, Principles of solidification, in: J. J. Gilman (Ed.), The Art and Science of Growing Crystals, John Wiley & Sons, Inc., 1963, p. 276.

[90] D. T. J. Hurle, A mechanism for twin formation during Czochralski and encapsulated vertical Bridgman growth of III–V compound semiconductors, J. Crystal Growth 147 (1995) 239–250.

[91] H. Chung, M. Dudley, D. J. Larson, D. T. J. Hurle, D. F. Bliss, V. Prasad, The mechanism of growth-twin formation in zincblende crystals: New insights from a study of magnetic liquid encapsulated Czochralski-grown InP single crystals, J. Crystal Growth 187 (1998) 9.

[92] J. Amon, F. Dumke, G. Müller, Influence of the crucible shape on the formation of facets and twins in the growth of GaAs by the vertical gradient freeze technique, J. Crystal Growth 187 (1) (1998) 1–8.

[93] C. A. Wang, Crystal growth and segregation in verical Bridgman configuration, Ph.D. thesis, Massachusetts Institute of Technology (1984).

[94] J. H. Peterson, Understanding growth rate limitations in production of single-crystal cadmium zinc telluride (CZT) by the travelling heater method (THM), Ph.D. thesis, University of Minnesota (March 2017).

[95] E. Scheil, Bemerkungen zur schichtkristallbildung, Z. Mettalk. 34 (1942) 70.

[96] W. A. Tiller, K. A. Jackson, J. W. Rutter, B. Chalmers, The redistribution of solute atoms during the solidification of metals, Acta Metallurgica 1 (1953) 428.

[97] V. G. Smith, W. A. Tiller, J. W. Rutter, A mathematical analysis of solute redistribution during solidification, Canadian J. Phys. 33 (1955) 723–745.

[98] K. A. Jackson, Constitutional supercooling surface roughening, J. Crystal Growth 264 (2004) 519–529.

[99] J. A. Burton, R. C. Prim, W. P. Slichter, The distribution of solute in crystals grown from the melt. part I. Theoretical, J. Chem. Phys. 21 (1953) 1987–1991.

[100] D. T. J. Hurle, P. Rudolph, A brief history of defect formation, segregation, faceting, and twinning in melt-grown semiconductors, J. Crystal Growth 264 (4) (2004) 550–564.

[101] M. C. Flemings, Solidification Processes, McGraw-Hill, Inc., New York, 1974.

[102] W. R. Wilcox, Validity of the stagnant film approximation for mass transfer in crystal growth and dissolution, Mat. Res. Bull. 4 (1969) 265–274.

[103] F. Rosenberger, G. Müller, Interfacial transport in crystal growth, a parametric comparison of convective effects, J. Crystal Growth 65 (1983) 91–104.

[104] M. T. Stewart, R. Thomas, K. Wauchope, W. C. Winegard, B. Chalmers, New segregation phenomena in metals, Phys. Rev. 83 (1951) 657–657.

[105] D. Camel and J. J. Favier, Scaling analysis of convective solute transport and segregation in Bridgman crystal growth from the doped melt, J. Phys. France 47(6) (1986) 1001–1014.

[106] J. Garandet, On the problem of radial segregation in an idealized horizontal Bridgman configuration: scaling and numerical approaches, Journal of Crystal Growth 114 (4) (1991) 593 – 602.

[107] J. Garandet, Microsegregation in crystal growth from the melt: an analytical approach, Journal of Crystal Growth 131 (3) (1993) 431 – 438.

[108] S. Kaddeche, J. Garandet, D. Henry, H. B. Hadid, A. Mojtabi, On the effect of natural convection on solute segregation in the horizontal Bridgman configuration: Convergence of a theoretical model with numerical and experimental data, Journal of Crystal Growth 409 (2015) 89 – 94.

[109] N. Zhang, A. Yeckel, A. Burger, Y. Cui, K. Lynn, J. J. Derby, Anomalous segregation during electrodynamic gradient freeze growth of cadmium zinc telluride, J. Crystal Growth 325 (2011) 10–19.

[110] Z. Bi, Directional solidification of a binary alloy using the phase field model, Ph.D. thesis, Carnegie Mellon University, Pittsburgh, PA (2001).

[111] Z. Bi, R. Sekerka, Phase field modeling of shallow cells during directional solidification of a binary alloy, J. Crystal Growth 237–239 (2002) 138–143.

[112] W. W. Mullins, R. F. Sekerka, Stability of a planar interface during solidification of a dilute binary alloy, J. Appl. Phys. 35 (1964) 444–451.

[113] R. F. Sekerka, Morphological stability, J. Crystal Growth 3 (1968) 71.

[114] M. Funaki, T. Ozaki, K. Satoh, R. Ohno, Growth and characterization of CdTe single crystals for radiation detectors, Nuclear Instruments and Methods in Physics Research Section A: Accelerators, Spectrometers, Detectors and Associated Equipment 436 (1999) 120–126.

[115] H. Chen, S. Awadalla, J. Mackenzie, R. Redden, G. Bindley, A. Bolotnikov, G. Camarda, G. Carini, R. James, Characterization of traveling heater method (THM) grown $Cd_{0.9}Zn_{0.1}Te$ crystals, IEEE Transactions on Nuclear Science 54 (4) (2007) 811–816.

[116] S. Awadalla, J. Mackenzie, H. Chen, B. Redden, G. Bindley, M. Duff, A. Burger, M. Groza, V. Buliga, J. Bradley, Z. Dai, N. Teslich, D. Black, Characterization of detector-grade CdZnTe crystals grown by traveling heater method (THM), Journal of Crystal Growth 312 (4) (2010) 507–513.

[117] P. Rudolph, M. Mühlberg, Basic problems of vertical Bridgman growth of CdTe, Mater. Sci. Eng. B 16 (1993) 8–16.

[118] P. Rudolph, Fundamental studies on Bridgman growth of CdTe, Progress in Crystal Growth and Characterization of Materials 29 (1994) 275–281.

[119] A. El Mokri, R. Triboulet, A. Lusson, A. Tromson-Carli, G. Didier, Growth of large, high purity, low cost, uniform CdZnTe crystals by the "cold travelling heater method", J. Crystal Growth 138 (4) (1994) 168–174.

[120] Y. Wang, K. Kudo, Y. Inatomi, R. Ji, T. Motegi, Growth interface of CdZnTe grown from Te solution with THM technique under static magnetic field, Journal of Crystal Growth 284 (2005) 406–411.

[121] C. W. Lan, D. T. Yang, A computer simulation of crystal growth by the traveling-solvent method (TSM): Pseudo-steady-state calculations, Modelling and Simulation in Materials Science and Engineering 3 (1) (1995) 71–92.

[122] C. Stelian, T. Duffar, Numerical modeling of CdTe crystallization from Te solution under terrestrial and microgravity conditions, Journal of Crystal Growth 400 (2014) 67–75.

[123] J. H. Peterson, A. Yeckel, J. J. Derby, A fundamental limitation on growth rates in the traveling heater method, J. Crystal Growth 452 (2016) 12–16.

[124] J. H. Peterson, A. Yeckel, M. Fiederle, J. J. Derby, Analysis of the traveling heater method for the growth of cadmium telluride, J. Crystal Growth 454 (2016) 45–58.

[125] T. H. Bell, Lee waves in stratified flows with simple harmonic time dependence, Journal of Fluid Mechanics 67 (1975) 705–722.

[126] C. J. Nappo, Fundamentals, in: C. J. Nappo (Ed.), An Introduction to Atmospheric Gravity Waves, Vol. 102 of International Geophysics, Academic Press, 2012, pp. 29–56.

4. Nucleation and Growth Kinetics

Nucleation and Growth Mechanisms

Elias Vlieg and Willem J.P. van Enckevort

Radboud University, Institute for Molecules and Materials,
Heyendaalseweg 135, 6525 AJ Nijmegen, The Netherlands

Contents

1. Introduction 2
2. 3D Nucleation 2
   2.1. Homogeneous nucleation 2
   2.2. Heterogeneous nucleation 5
   2.3. Primary and secondary nucleation 6
   2.4. Spinoidal decomposition 7
   2.5. Non-classical nucleation 8
3. Growth mechanisms 9
   3.1. Morphology of a crystal 9
   3.2. Flat and rough surfaces 11
   3.3. 2D nucleation 14
   3.4. Kinetic roughening 16
   3.5. Steps 16
   3.6. Intermezzo: kinks and microscopic reversibility 18
   3.7. Step growth 18
   3.8. Spiral growth 22
   3.9. Additives and impurities 24
4. Summary 27
References 28

1. Introduction

The growth of crystals is a complicated process, involving many aspects and length scales going from the atomic to the metre scale. The bridging of length scales is typical for crystal shape and crystal growth: the structure and processes at the atomic/molecular length scale are directly reflected in the shape and growth rate at the macroscopic scale. Here we therefore focus on the elementary processes of nucleation and growth in order to understand the growth and shape of crystals at larger length scales.

Fully understanding crystal growth requires many more facets, including knowledge of the phase behaviour (phase diagrams) of the materials involved, the role of mass transport, the role of the crystallographic structure and the growth equipment and method used. These important aspects are hardly discussed here, but can be found elsewhere.

2. 3D Nucleation

2.1. Homogeneous nucleation

Thermodynamics tells us that when there is a positive driving force, a crystal should form. The driving force for crystallisation can be written as:

$$\Delta\mu = \mu_f - \mu_{c,} \tag{1}$$

with μ_f and μ_c the chemical potential of the fluid and crystal phase, respectively. (We use here the term fluid phase to denote the medium from which the crystal is grown, this can for example be a solution, melt or vapour). The way the driving force is controlled depends on the type of growth, e.g. undercooling in the case of growth from the melt and concentration for solution growth. In the latter case, the driving force is often expressed in terms of the relative supersaturation σ:

$$\frac{\Delta\mu}{kT} = \ln\left(\frac{c}{c_{eq}}\right) \cong \frac{c-c_{eq}}{c_{eq}} \equiv \sigma, \tag{2}$$

where c is the actual concentration, c_{eq} the concentration at equilibrium and k is Boltzmann's constant.

A positive $\Delta\mu$ is not enough, however, because crystals only form when the driving force is sufficiently large. This is caused by the nucleation barrier. Figure 1 illustrates the situation for the formation of a (small) spherical crystal with radius r. There is a gain in free energy owing to the formation of the bulk crystal, but at the same time an interface is formed between the fluid and crystal phase that costs surface energy σ_{cf} (which we assume for simplicity to be uniform). The change in free energy due to the formation of the spherical nucleus is thus:

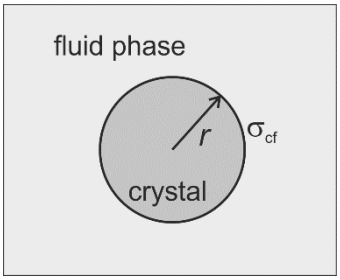


Figure 1. A spherical crystal with radius r embedded in a fluid phase and with an interfacial energy σ_{cf}.

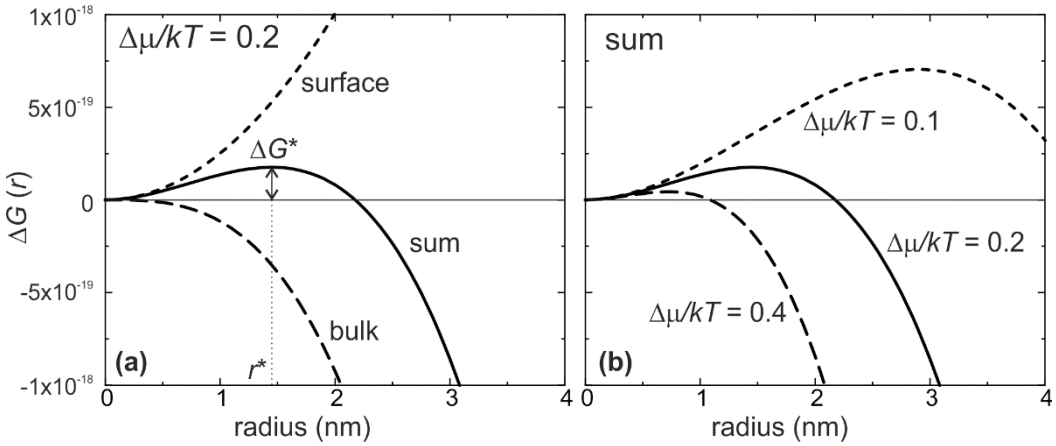


Figure 2. The change in free energy during the formation of a spherical nucleus as a function of its radius r. The summation of the bulk and surface terms leads to a maximum, the nucleation barrier. The calculations assume an interfacial energy of 20 mJ/m^2 and a volume of 0.03 nm^3 for a growth unit.

$$\Delta G = \Delta G_{bulk} + \Delta G_{surf} = \frac{-4\pi r^3}{3\Omega}\Delta\mu + 4\pi r^2\sigma_{cf}, \tag{3}$$

where Ω is the volume of one growth unit (atom, molecule). Figure 2a shows the two free energy contributions as a function of r. The bulk term is always favourable for positive $\Delta\mu$, but is initially overruled by the energy costs due to surface formation. The surface cost scales with r^2 and is eventually overcome by the bulk term that scales with r^3. This leads to a maximum, called *nucleation barrier* ΔG^*, that occurs at the *critical radius* r^*. According to this model, nuclei with a radius $r < r^*$ will dissolve, while those with $r > r^*$ will grow. From the derivative of ΔG, it is straightforward to compute:

$$\Delta G^* = \frac{16\pi\sigma_{cf}^3\Omega^2}{3(\Delta\mu)^2}, \tag{4}$$

and

$$r^* = \frac{2\sigma_{cf}\Omega}{\Delta\mu}. \tag{5}$$

A nucleus with size r^* is called a *critical nucleus*. Starting from a clean fluid phase with a driving force $\Delta\mu$, a crystal can form by spontaneous fluctuations in which growth units attach and detach from a nucleus. Most of these tiny crystals will dissolve before reaching the critical radius, and only for a sufficiently large driving force crystals will actually form. Figure 2b shows that the nucleation barrier and critical radius depend strongly on $\Delta\mu/kT$. For small values of $\Delta\mu/kT$, the probability of crystal formation is extremely small. The model described above is the *classical nucleation model*. It can be refined, e.g. by adding anisotropy or non-spherical nuclei, but the essential features remain the same.

The number of nuclei per second and volume that grow out into crystals is called the nucleation rate J. This rate can be estimated using the following assumptions:

1. the concentration of nuclei with $r \leq r^*$ follows Boltzmann statistics
2. if one additional particle attaches to a critical nucleus, it will grow out and form a crystal.

From the first assumption, the concentration of critical nuclei is:

$$C^* = C_0 e^{-\Delta G^*/kT}. \tag{6}$$

C_0 is roughly the density of locations where a nucleus could potentially form, e.g. the concentration of molecules. If we call the frequency for the addition of one growth unit to a critical nucleus f^*, we find for the nucleation rate:

$$J = f^* C_0 e^{-\Delta G^*/kT}. \tag{7}$$

f^* is the product of the area $4\pi(r^*)^2$ of the critical nucleus and the attachment frequency per unit area:

$$\beta c_{eq} e^{\Delta\mu/kT}, \tag{8}$$

with β a kinetic coefficient. Thus

$$f^* = 4\pi(r^*)^2 \beta c_{eq} e^{\Delta\mu/kT} = \frac{8\pi\sigma\Omega}{(\Delta\mu)^2} \beta c_{eq} e^{\Delta\mu/kT}. \tag{9}$$

This shows that f^* depends strongly on $\Delta\mu$, even when this is often not explicitly included in the expression for J. It turns out that the assumptions used here to derive J are too crude, in particular the density of critical nuclei is less than our estimate, because such nuclei rapidly grow out to larger crystals. This situation was analysed in more detail by Zeldovich, and the expression that is commonly used to estimate the nucleation rate contains a dimensionless correction term z called the *Zeldovich factor.* We then obtain:

$$J = z f^* C_0 e^{-\Delta G^*/kT} = z f^* C_0 e^{-A/(\Delta\mu)^2}, \tag{10}$$

with

$$A = \frac{16\pi\sigma_{cf}^3\Omega^2}{3kT}. \tag{11}$$

The Zeldovich factor typically has values between 0.01 and 1. While it is difficult to calculate the precise value of J, the equation clearly shows its very strong dependence on $\Delta\mu$ and σ_{cf}. For low values of $\Delta\mu$ it can take weeks or years for a nucleus to form; at high driving force f^* determines the rate and nucleation can occur everywhere and within milliseconds.

The nucleation barrier explains the *metastable zone* that is usually identified in a phase diagram: the range of driving force values in which growth is possible, but in which nucleation does not occur at a practical rate. The width of the metastable zone depends on how long one is willing to wait; from a thermodynamical point of view a crystal will eventually form for any positive driving force. The metastable zone allows controlled crystal growth: since no new crystals will nucleate, only existing crystals will grow. An example of this is the addition of seeds to a slightly saturated solution.

A compound often can crystallize in different crystal forms, a phenomenon that is called *polymorphism.* One form will be the most stable one, the others are metastable or unstable. Experimentally, it regularly happens that at sufficiently high driving force, first a metastable polymorph nucleates, which subsequently transforms into the stable one. This is called *Ostwald's rule of stages*, and it is indeed a rule, not a law. The driving force for a metastable polymorph is always lower than for the stable crystal form (it has by definition a higher chemical potential), but nucleation can still be more favourable because this also depends on the surface energy. A system can thus follow the rule of stages if the surface energy of the metastable phase is significantly lower than that of the stable phase. Figure 3 shows an example of a system that follows Ostwald's rule.

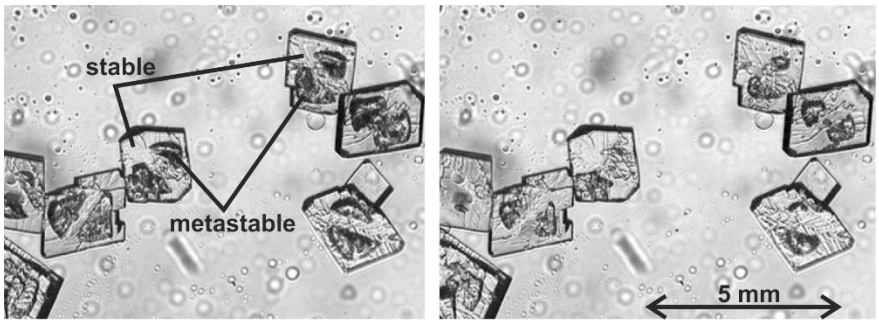


Figure 3. Ostwald's rule of stages as exhibited in a pharmaceutical compound that nucleates in a metastable form and subsequently transforms to the stable form. In this case the stable form nucleates heterogeneously on the metastable one. As a function of time (from left to right) the metastable crystals disappear. Adapted from [3].

2.2. Heterogeneous nucleation

The nucleation process we described is called homogeneous nucleation, because it involves only the compound itself (plus a solvent, in case of solution growth). In practise, homogeneous nucleation rarely occurs, except at very high supersaturations. Often nuclei are formed on a foreign surface, e.g. dust, the wall of a container or an intentionally inserted surface (template). This is called *heterogeneous nucleation*. Figure 4 sketches the situation, again for a spherical particle that is now truncated because of its contact with the foreign solid. The particle has a contact angle θ with the surface, and the relation between this and the interfacial energies is given by Young's equation:

$$\sigma_{cs} + \sigma_{cf} cos\theta = \sigma_{sf}. \tag{12}$$

The angle is only < 180° if:

$$\sigma_{cs} \leq \sigma_{cf} + \sigma_{sf}. \tag{13}$$

In that case (partial) *wetting* occurs and nucleation is facilitated. The total change in free energy now contains a term from the crystal-solid interface. The fact that the sphere is truncated also needs to be taken into account and this gives:

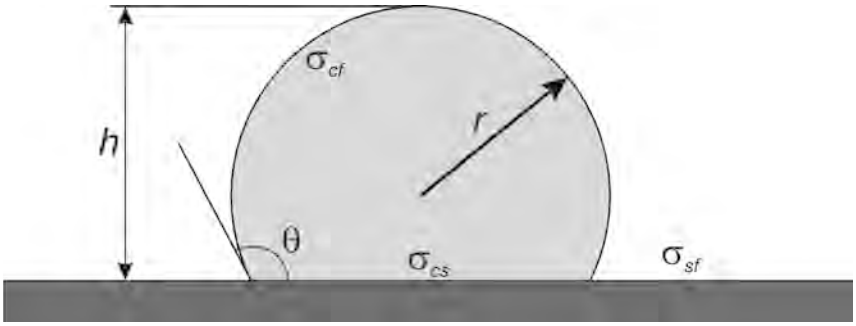


Figure 4. Heterogeneous nucleation of a crystal that partially wets a solid substrate. σ_{cs}, σ_{cf} and σ_{sf} are the interfacial energies of the crystal-substrate, crystal-fluid and substrate-fluid interfaces, respectively.

$$\Delta G_{het} = \Delta G_{bulk} + \Delta G_{cf} + \Delta G_{cs} = \frac{-\pi h^2(3r-h)}{3\Omega}\Delta\mu + 2\pi r h\sigma_{cf} + \pi h(2r-h)\left(\sigma_{cs} - \sigma_{cf}\right), \quad (14)$$

with h the height of the spherical segment. This leads to a similar behaviour as a function of r as for the homogeneous case. Some elaborate mathematics show that the values for the critical radius and barrier are now:

$$r^* = \frac{2\sigma_{cf}\Omega}{\Delta\mu} \quad (15)$$

and

$$\Delta G^*_{het} = \Delta G^*\left(\tfrac{1}{2} - \tfrac{3}{4}\cos\theta + \tfrac{1}{4}\cos^3\theta\right), \quad (16)$$

with ΔG^* the barrier for homogeneous nucleation. The radius is thus the same as for the homogeneous case, but the barrier can be significantly reduced, depending on the value of θ. For $\theta = 0$, i.e. complete wetting, the barrier disappears completely. For $\theta = 180°$, i.e. non-wetting, the barrier is the same as for homogeneous nucleation and the substrate plays no role.

For low driving force, the heterogeneous nucleation rate is typically much higher than the homogeneous one and thus dominates crystal formation. The number of sites, however, for heterogeneous nucleation is much less than for homogeneous nucleation, because the latter can occur anywhere in the bulk fluid. Therefore, at high driving force homogeneous nucleation outpaces heterogeneous nucleation.

A special case of heterogeneous nucleation is *epitaxy*, which is the oriented growth of crystals on a foreign crystalline substrate. Whether such growth is possible and how perfect the layers grow depends on the mismatch between the crystal lattice parameters. When the match is nearly perfect (case of complete wetting), thick and perfect layers can be grown. This *Frank-Van der Merwe* growth mode is for example used in the growth of AlGaAs layers on GaAs in solar cell devices. When there is a larger mismatch and only partial wetting occurs, no closed layer, but separate, 3D islands are formed. When growth is continued, the islands may merge into a continuous film, but with imperfections. This is called *Volmer-Weber* growth. The intermediate case is called *Stranski-Krastanov* growth, where first a thin, flat layer forms. However, because of the mismatch between substrate and film, strain is building up and above a critical thickness, the growth switches to 3D islands.

2.3. Primary and secondary nucleation

We discussed the case where new crystals form from the fluid phase. This is called *primary nucleation*. The number of crystals present can also increase by breaking existing crystals in several pieces. This can occur, for example, when a crystal is hit by a stirring propeller or by other crystals in a crystallisation vessel. This is called *secondary nucleation*. When primary nucleation is slow, all the crystals that are formed may in fact originate from one crystal: this first crystal that is formed through primary nucleation leads to many crystals through secondary nucleation. The growth of these secondary crystals reduces the supersaturation, making additional primary nucleation events very unlikely [5].

A nice demonstration of this is provided by the crystallisation of $NaClO_3$. From its achiral building blocks, this salt forms a chiral structure and left or right-handed crystals grow with equal probability. However, when performing a slow crystallisation experiment under gentle stirring, one can generate a vessel full of crystals that all originate from the same starting crystal and that thus all have the same handedness [6]. This is a nice example of chiral symmetry breaking induced by crystallisation. The

overall symmetry is not broken, because repeating the experiment will result in a left or right handed outcome with equal probability.

2.4. Spinoidal decomposition

The classical nucleation model predicts that the nucleation barrier becomes very small for increasing driving force. In some situations, this barrier disappears completely and this is called *spinoidal decomposition*. This describes the situation where a (binary) mixture of compounds is suddenly transformed into crystals of its separate compounds. The driving force at which this barrier-less decomposition starts is called the spinoidal. The kinetics of this process is determined by mass transport, as nucleation does not play a role.

A statistical thermodynamics model that is often used in crystal growth, the *Jackson mean-field model*, can illustrate how spinoidal decomposition works. The details of the model are not important here, we restrict ourselves to the essential results. The model assumes a binary mixture (e.g. two

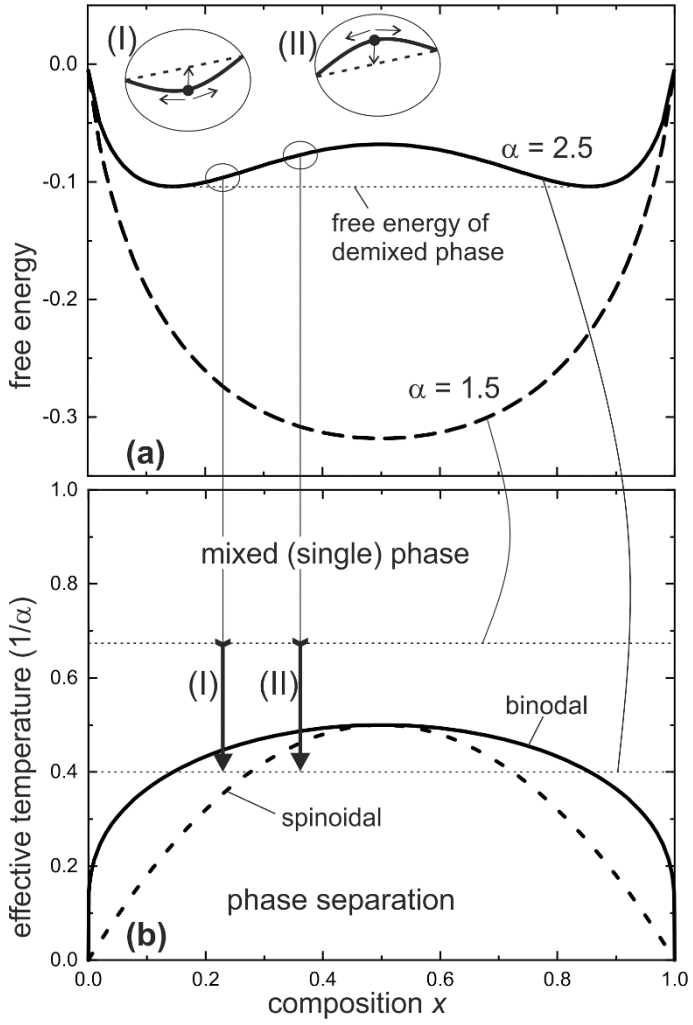


Figure 5. Mean-field model with (a) two free energy curves and (b) the corresponding phase diagram. The arrow (I) represents a case where a nucleation barrier is present, while for arrow (II) it is not. The driving force for demixing is the difference with the free energy of the demixed phase, see (a).

metals A and B or an occupied versus an empty site), in which the fraction of the second component is called *x.* The value of *x* ranges from 0 to 1. The effective interaction between the components is denoted by the parameter $\alpha = n\varphi/2kT$, where *n* is the number of nearest neighbours and φ is the bond strength. The normalized free energy for this model is:

$$g = \alpha x(1-x) + x\ln x + (1-x)\ln(1-x). \qquad (17)$$

The first term is the enthalpy; the last two terms denote the entropy. The model predicts complete mixing for $\alpha < 2$ and phase separation otherwise. The phase diagram of this model is shown in figure 5 together with the corresponding values of the free energy for two representative values of α. The curve in the phase diagram that separates the mixed region from the two-phase region is called the binodal. The free energy curves clearly show that it costs energy to demix for $\alpha = 1.5$, but separation in two phases with $x \approx 0.15$ and 0.85 is favourable for $\alpha = 2.5$ when *x* is in the range between 0.15 and 0.85.

For any composition *x* in that range, phase separation (e.g. in the form of crystallisation) should occur if the temperature is lowered (e.g. α changes from 1.5 to 2.5). When this is done for $x = 0.25$, see arrow (I) in the figure, the free energy locally has a convex shape, and this means that the phase separation initially increases the free energy (see insert). This corresponds to a nucleation barrier. If the composition equals 0.35 instead, arrow (II), the local shape is concave, and free energy is gained immediately. In that case there is no barrier and spinoidal decomposition will occur. The phase diagram shows the spinoidal as a dashed curve: in this model, spinoidal decomposition always occurs for large enough driving force. On the other hand, the model also shows that for $x = 0.5$ the nucleation barrier is absent even for very small driving force. In terms of the classical nucleation model, this corresponds to a situation with very small interfacial energy.

2.5. Non-classical nucleation

The nucleation process we discussed assumes that the crystalline phase directly forms in its final structure from the fluid phase. This simple path may not always be followed in real systems. The crystal phase is always different from the fluid phase because of its order, but will typically also differ in its density. It is therefore also possible that an intermediate step occurs, e.g. first the fluid becomes denser and subsequently ordering occurs. Such a two-step mechanism likely plays a role in the nucleation of protein crystals [7]. Similarly, in biomineralization an amorphous solid phase is first formed from which the crystals grow [8].

A second assumption in classical nucleation theory is that the nucleus grows by the addition of single growth units. This also does not have to be the case, and many examples have been found where larger particles (oligomers, droplets, amorphous and crystalline nanoparticles) interact and form larger objects [9]. This particle attachment, like the two-step process, gives a very different free-energy landscape and thus a path for nucleation with a different (lower) barrier. Growth though particles is stimulated when specific sizes of nanoparticles have a favourable configuration (lower energy). Such 'magic clusters' will therefore have a much higher concentration than expected from classical models.

3. Growth mechanisms

3.1. Morphology of a crystal

Once a 3D nucleus is formed, it will continue to grow as long as there is a sufficient driving force. Typically, crystals will not grow equally fast along all directions, and this means that a crystal will normally have a non-isotropic shape in the form of the faceted morphology characteristic of many crystals. The growth shape of a crystal is determined by the faces with the *slowest* growth rates. This is illustrated in figure 6. Faces that grow very fast grow out of the morphology and one is left with the slowest ones.

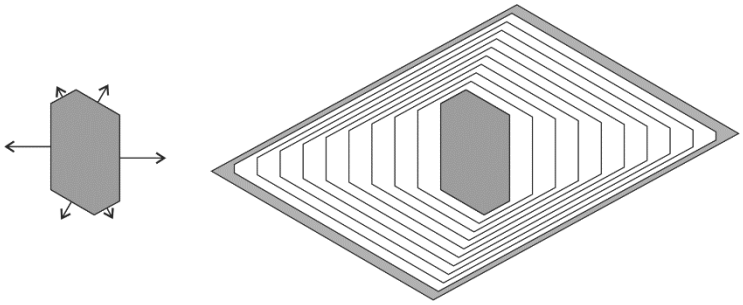


Figure 6. The growth morphology contains the facets with the slowest growth velocity; the fast directions grow out of the crystal shape. In the example, the smallest facet evolves to become the largest.

Thermodynamically, the shape of a crystal should correspond to the equilibrium shape, i.e. the shape with the minimal surface energy. However, mass transport limitations and small energy gains when acquiring the equilibrium shape mean that the crystal morphology is determined by the growth kinetics for all but the smallest crystals (< 10 μm, depending of course on the time scale). The equilibrium shape can be derived if the surface energy is known as a function of orientation, $\sigma(\theta,\varphi)$, with θ and φ the polar angles. A plot of this energy is called a *Wulff plot* and figure 7a gives a 2D example. The cusps in such a plot correspond to directions without steps, thus flat planes. The minimal surface energy shape can be determined from the Wulff plot using the *Gibbs-Wulff construction*, in which for each point $\sigma(\theta,\varphi)$ a plane is drawn perpendicular to the direction vector $\mathbf{n}(\theta,\varphi)$. The figure enclosed by all planes is the equilibrium shape, see figure 7b. The example shows that the local minima give very large facets and that directions with large surface energy are completely absent from the equilibrium shape.

However, as already stated, under most circumstances the shape of a crystal is not determined by thermodynamics, but by growth kinetics, i.e. the growth rate. The expected morphology can then be derived by a similar method as for the equilibrium shape. Now one plots the growth rate $R(\theta,\varphi)$ as a function of the orientation. This is called a *dynamic Wulff plot*. We already saw that the growth morphology is determined by the directions with the slowest growth rates, and this means that the growth morphology can be constructed in the same way as for the equilibrium shape, thus using the Gibbs-Wulff construction. Figure 7 can again serve as an example, now showing that the orientations with the lowest growth rate (the cusps in the plot) are dominant in the final growth morphology.

The Gibbs-Wulff construction gives the ideal growth morphology. When the starting crystal, e.g. a seed, has a different shape, the morphology will slowly evolve toward this ideal, as already

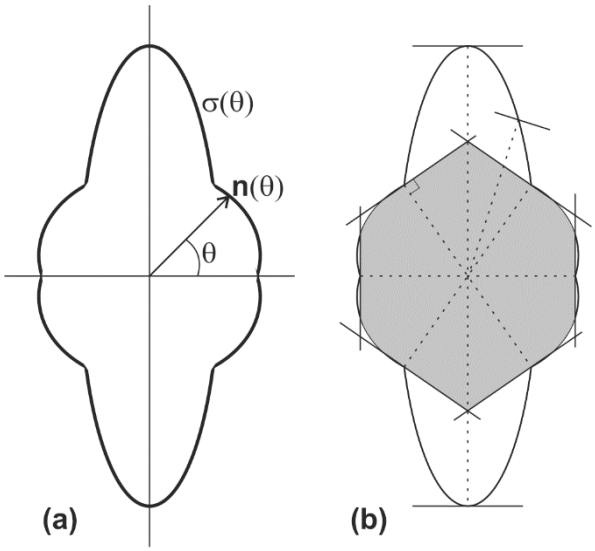


Figure 7. (a) A 2D Wulff plot, showing the surface energy as a function of the orientation. In 'flat' directions, the surface energy has a local minimum, leading to cusps in the plot. (b) The corresponding equilibrium shape, generated using the Gibbs-Wulff construction.

illustrated in figure 6 [10]. Moreover, the morphology will also depend on mass transport and the local growth conditions like the presence of a vessel wall or the driving force.

The fact that orientations with steps grow faster is the basis of a classic and simple method to predict the growth morphology, the Bravais-Friedel-Donnay-Harker (BFDH) method. In a crystal structure, the slowly growing orientations without steps normally correspond to large lattice plane spacings. Conversely, small lattice spacings correspond to fast growing directions with many steps. The *BFDH-morphology* is derived by assuming that the growth rate is inversely proportional to the lattice spacing d_{hkl}. This means that the growth rate is proportional to the associated reciprocal lattice vector $\mathbf{H}_{hkl}$:

$$R_{hkl} \propto \frac{1}{d_{hkl}} \Rightarrow R_{hkl} \propto \mathbf{H}_{hkl}. \tag{18}$$

A Gibbs-Wulff-like construction in reciprocal space therefore yields the BFDH morphology (the morphology is in fact identical to the first Brillouin zone in reciprocal space). In this construction the

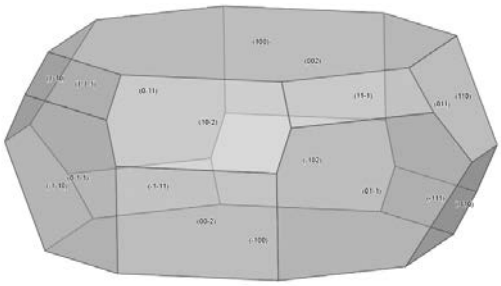


Figure 8. The BFDH morphology of paracetamol, calculated and plotted using the Mercury software from the CCDC.

effect of non-primitive Bravais lattices and other translations (screw axes and glide planes) on the possible lattice spacings needs to be taken into account. Figure 8 shown an example.

The BFDH morphology is easily derived and therefore often used. It ignores many of the important aspects of crystal growth and several more advanced methods for morphology prediction exist to estimate the growth velocity as a function of orientation and for different crystal structures [11-14]. Once $R(\theta,\varphi)$ is known (or R_{hkl} if only lattice orientations are included), the Gibbs-Wulff construction yields the corresponding morphology.

3.2. Flat and rough surfaces

How fast a crystal grows in a specific direction depends on many factors, but the surface structure and morphology are the most important ones. In general, the rougher the crystal surface, the faster it will grow. We will now take an atomic-scale look at how crystal growth depends on the structure of the crystal-fluid interface. In order to understand growth at such a scale, it is useful to apply a very simple model, the Kossel crystal, which assumes simple cubic building blocks with six bonds to their neighbours. Figure 9 shows a schematic of a Kossel crystal and the three main types of surfaces one can distinguish: *Flat, Stepped* and *Kinked* faces. This classification was introduced by Hartman and

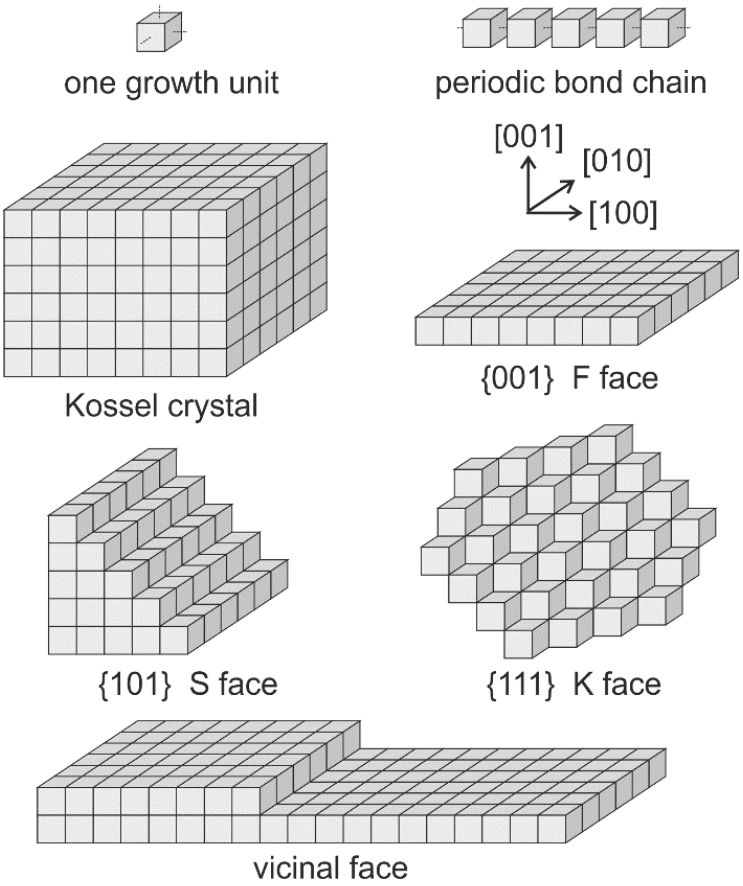


Figure 9. (a) The Kossel crystal is a very simple model for a crystal structure that is often used in crystal growth. It considers a cubic crystal built from cubic growth units with six bonds in total. Depending on the orientation of the crystal planes, facets can either be Flat, Stepped or Kinked. Faces that are nearly flat are called vicinal faces.

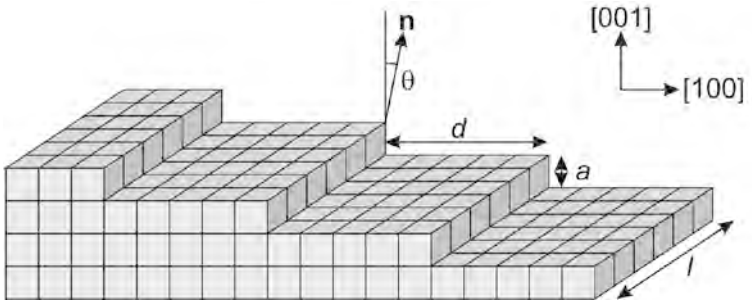


Figure 10. A schematic of a Kossel surface with angle θ with respect to the [001] direction. The additional steps with respect to a flat surface leads to additional surface energy.

Perdok in the 1950's [15] and uses the concept of a *period bond chain* (PBC). This is a chain of bonds within one crystal plane that connects the different growth units. An *F* face has at least two PBC's and thus all growth units are directly interconnected. This is also called a *connected net*. An *S* face has only one PBC, has many dangling bonds and the face has thus a higher energy than an *F* face. A *K* face, finally, has no PBCs and is the least stable. Because they are much rougher, *S* and *K* faces grow much faster than *F* faces and (following the Gibbs-Wulff construction) *S* and *K* directions are usually not present on the final crystal morphology. Orientations that have only a small misorientation (up to a few degrees) with respect to an *F* face are called *vicinal faces*; these have a somewhat higher growth rate than true *F* faces and are often part of the crystal morphology.

The surface energy for the Kossel crystal can be derived quite easily. The size of a growth unit is a (volume a^3) and the strength of one bond φ. The bond is divided over two growth units, so it's effective strength is ½φ per growth unit (when the growth is not in vacuum the effective bond strength needs additional corrections). The surface energy of the flat {100} face is thus $\sigma_{\{100\}} = ½\varphi/a^2 = \sigma_0$. For the {110} (stepped) and {111} (kinked) faces, these are $\sigma_{\{110\}} = ½\sqrt{2}\varphi/a^2$ and $\sigma_{\{111\}} = ½\sqrt{3}\varphi/a^2$. For other directions the calculations are a bit more elaborate, but still simple. Consider for example all planes parallel to the [010] direction, the {$h0l$} planes, as schematically drawn in figure 10. The surface energy is:

$$\sigma(\theta) = \frac{\varphi l(d+a)}{2la^2\sqrt{d^2+a^2}} = \sqrt{2}\sigma_0 \sin(\theta + 45°), \qquad (19)$$

where we used $\tan(\theta) = a/d$ (note that this reproduces the special cases $\sigma_{\{100\}}$ and $\sigma_{\{110\}}$). The Wulff plot of this is shown in figure 11a, together with the square equilibrium shape predicted for this case.

A crystal surface orientation corresponding to an *F*-face ideally contains no steps. However, at any finite temperature excursions from the flat surface may occur in the form of adatoms and steps because of the gain in entropy. For every *F*-face a critical temperature exists above which the free energy for step formation becomes zero and the flat orientation is lost. This effect is called *thermal roughening* and the temperature at which this phase transition occurs is called the *roughening temperature* T_R [16]. Above its roughening temperature, a facet will contain so many steps and kinks that its growth rate increases significantly and it will therefore tend to disappear from the crystal morphology. In real cases, the T_R may be higher than the melting point and then such roughening will not occur.

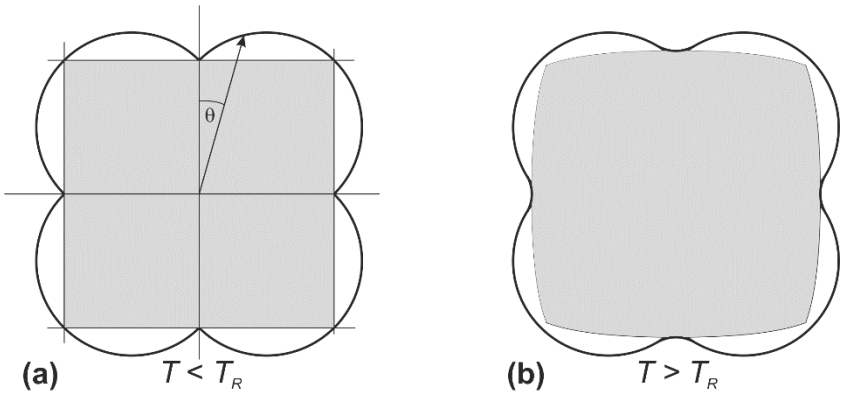


Figure 11. (a) The Wulff plot of the Kossel {$h0l$} planes and the equilibrium shape derived from this. (b) Above the thermal roughening transition, the cusps in the Wulff plot disappear, and the equilibrium morphology becomes rounded.

Figure 11b shows the effect of thermal roughening for the Kossel crystal. The cusps (corresponding to the flat faces) in the Wulff plot below the roughening temperature are replaced by rounded minima above the roughening transition. This happens because the presence of numerous steps at the exact {100} faces above T_R means that the extra steps at slightly tilted orientations have only a small effect on the surface energy. This lead to a disappearance of the cusps, which means that the large facets disappear and are replaced by rounded surfaces. This occurs for the equilibrium shape, but since the growth velocity depends on the step density, a similar change in growth morphology happens above the roughening transition. Figure 12 shows an example of a paraffin crystal below and above the roughening transition.

The roughening transition is a very smooth (high order) transition, i.e., the step density changes only slowly as a function of temperature when going through the transition. The roughening temperature is nevertheless accurately defined as the temperature at which the free energy cost for step formation becomes zero [17]. For the Kossel {100} surface this occurs at $\varphi/kT_R = 0.78$.

We have thus identified (so far) three cases in which a surface contains many steps and kinks (is rough): S and K faces, and F faces above the roughening temperature. The growth rate of such a surface is found to be (approximately) proportional to the driving force. This can be understood as

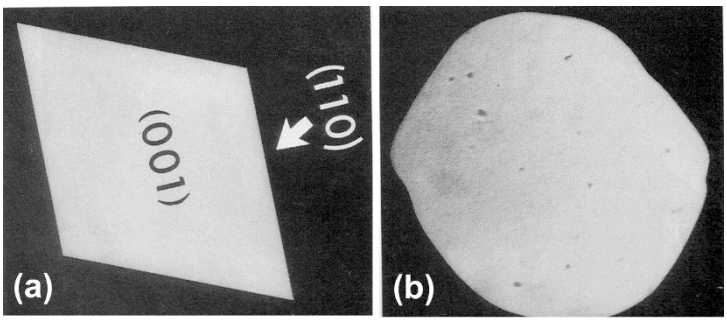


Figure 12. The morphology of n-$C_{23}H_{48}$ paraffin crystal grown (a) below and (b) above the thermal roughening transition of the {110} side facets. Note that the top (001) facet is still flat. The size of the crystal is around 0.5 mm. Adapted from [4].

follows. When a crystal is in equilibrium, the number of growth units added per second equals that of the growth units removed. The flux is made up of a wide variety of processes at many different sites, but the net sums over addition and removal have to be exactly equal at equilibrium:

$$J_{eq}^{+} = J_{eq}^{-}. \tag{20}$$

When a driving force Δμ is applied, the probability for adding growth units increases by a factor $\exp(\Delta\mu/kT)$ for each site. For a surface that is rough, we may assume that the frequency of occurrence of the different sites does not change significantly. In that case the sum over all sites increases by the factor $\exp(\Delta\mu/kT)$ and the number of growth units attaching to the step becomes:

$$J^{+} = J_{eq}^{+} e^{\Delta\mu/kT}. \tag{21}$$

The growth rate of the surface now becomes:

$$R \propto J^{+} - J_{eq}^{-} = J_{eq}^{+}\left(e^{\Delta\mu/kT} - 1\right) \cong J_{eq}^{+}\frac{\Delta\mu}{kT}, \tag{22}$$

where we assumed relatively small driving forces. The growth rate of a rough surface thus depends linearly on Δμ. This is known as the *Wilson-Frenkel growth law* and this type of growth is also called *normal growth*. We will show later that for flat surfaces the growth rate does not follow this law and thus an observation of Wilson-Frenkel behaviour points to a rough surface. Note that the growth law does not state that all rough orientations have the same growth rate, only that their rate is proportional to the driving force.

3.3. 2D nucleation

We now turn our attention to the remaining case of a (really) flat surface (*F* face). This is a very important case, because the growth morphology of typical crystals is determined by these slow growing faces. If we start with a completely flat surface, a new layer has to start from scratch and we again encounter a nucleation barrier as in the 3D case. Also here there is a balance between the enthalpy gain by the addition of growth units to the bulk crystal and the loss due to the formation of an edge (or step). The step is the 1D analogue of the 2D surface cost in the case of 3D nucleation. The barrier can be calculated by considering the free energy of a 2D nucleus. For simplicity, we will only consider a circular nucleus with radius *r* and an isotropic step energy γ_{st}, see figure 13. The change in free energy in this case is:

$$\Delta G_{2D} = \Delta G_{bulk} + \Delta G_{step} = \frac{-\pi r^2 h_{st}}{\Omega}\Delta\mu + 2\pi r\gamma_{st}, \tag{23}$$

where h_{st} is the step height. Analogous to the 3D case, also here a maximum in ΔG is found, corresponding to the 2D nucleation barrier ΔG_{2D}^{*} at a critical radius r_{2D}^{*}:

$$\Delta G_{2D}^{*} = \frac{\pi\Omega\gamma_{st}^{2}}{h_{st}\Delta\mu} \tag{24}$$

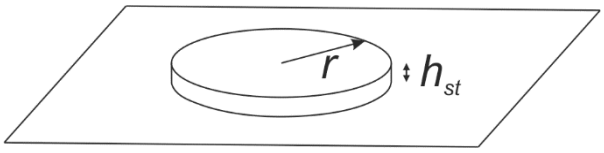


Figure 13. A circular 2D nucleus on a perfect crystal surface.

and

$$r_{2D}^{*} = \frac{\Omega\gamma_{st}}{h_{st}\Delta\mu}. \tag{25}$$

Both ΔG_{2D}^{*} and r_{2D}^{*} decrease with increasing driving force, so the formation of 2D nuclei will become more likely as a function of Δμ.

In order for a flat surface to grow, first one or more nuclei need to form and grow out. The 2D nucleation rate can be estimated in an analogous manner as for 3D nucleation, and is the product of the concentration of critical nuclei C_{2D}^{*} with the frequency f_{2D}^{*} of the addition of one growth unit to these nuclei:

$$C_{2D}^{*} = \mathrm{C}_{0,2D} e^{-\Delta G_{2D}^{*}/kT} \tag{26}$$

with $C_{0,2D}$ the density of available nucleation sites and

$$f_{2D}^{*} = 2\pi r_{2D}^{*}\beta c_{eq} e^{\Delta\mu/kT} = \frac{2\pi\Omega\gamma_{st}}{h_{st}\Delta\mu}\beta c_{eq} e^{\Delta\mu/kT}, \tag{27}$$

with $2\pi r_{2D}^{*}$ the circumference of the critical nucleus and β a kinetic coefficient. Here we ignored surface and volume diffusion and simply assumed that the growth units are directly incorporated into the step. Also here a Zeldovich correction factor *z* is required, leading to the following nucleation rate:

$$J_{2D} = \mathrm{z} f_{2D}^{*} C_{0,2D} e^{-\Delta G_{2D}^{*}/kT}. \tag{28}$$

While less extreme than in the 3D case, also for 2D nucleation there is a strong dependence on Δμ and the rate of nucleation is very small for low values of the driving force. When the crystal surface and Δμ are small, the nuclei will thus appear one after the other, a situation called *mononuclear growth*. This occurs, for example, during the growth of nanowires via the VLS (Vapour-Liquid-Solid) mechanism. In that case the droplet is so small (typically < 100 nm) that during the growth phase that follows nucleation, the supersaturation decreases significantly, further reducing the chance of another nucleation event. For mononuclear growth the growth rate equals:

$$R_{mononuclear} = J_{2D} A h_{st}, \tag{29}$$

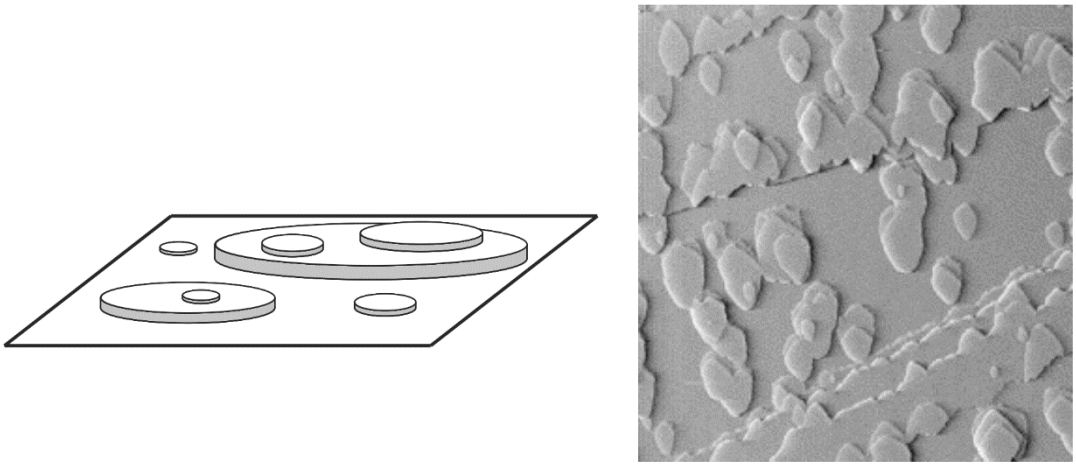


Figure 14. During Birth and Spread growth, several 2D nuclei form at different locations and merge into a single layer. The right picture is an AFM graph showing the early stages this type of growth on a $BaCrO_4$ surface.

with A the surface area.

If the nucleation rate is higher and the relevant surface area large enough, several nuclei form and grow in parallel, see figure 14. This is called *Birth and Spread* growth and this mode is far more common than mononuclear growth. The computation of the growth rate now involves estimating the time required to complete a full layer by all the different growing nuclei. The derivation will not be shown here, but leads to the following growth rate:

$$R_{Birth\ \&\ Spread} = Ce^{\Delta\mu/3kT}(\Delta\mu)^{5/6}e^{-\Delta G^*_{2D}/3kT}. \quad (30)$$

3.4. Kinetic roughening

Above we derived the critical radius for 2D nucleation r^*_{2D}. At high values of Δμ, the critical radius will equal the size of a single growth unit. In that case there is no longer a nucleation barrier; each single growth unit arriving at the surface is a critical nucleus and will in principle grow out. This leads to a rough surface and this phenomenon is called *kinetic roughening*. Figure 15 shows a computer simulation of the surface morphology for increasing driving force. Unlike the well-developed theory for thermal roughening, there is no fully accepted criterion for kinetic roughening [18], but choosing the value of Δμ for which the critical radius corresponds to a single growth unit is often used. Thus for $\Delta\mu \geq \Delta\mu_{crit}$ the surface will be kinetically rough and will grow much faster than at low driving force. Kinetic roughening will therefore, like its thermal counterpart, lead to the disappearance or rounding of the corresponding facet from the crystal morphology. For driving forces larger than $\Delta\mu_{crit}$ a facet that is initially flat will become rough. This also means that the strong non-linear dependence on driving force as found for 2D nucleation, will be replaced by a linear dependence at high Δμ.

We have thus found a fourth way in which a surface can be rough. In addition to the intrinsically rough *S* and *K* faces, also *F* faces can become rough both as a function of temperature and/or driving force.

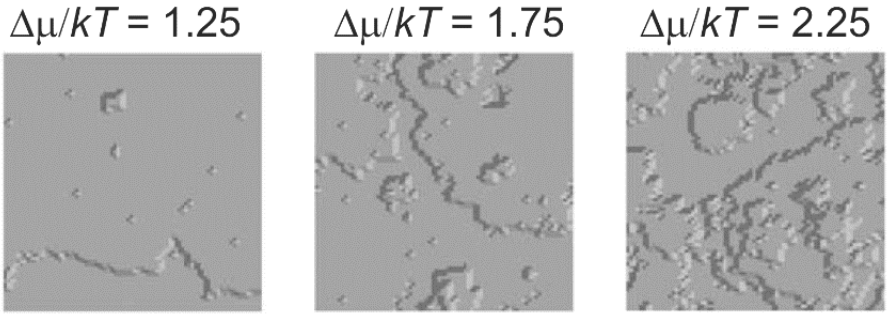


Figure 15. The kinetic roughening of a surface that occurs for increasing driving force. The example is for a Kossel {100} surface with a bond strength $\varphi/kT = 2$. (Adapted from [2]).

3.5. Steps

The growth rate predicted based on 2D nucleation is very low at low driving forces. At about 1% supersaturation essentially no growth should occur for facetted crystals, while experimentally it does. The difference between theory and experiment can be as large as a factor 10^{10}! This huge discrepancy was resolved by Charles Frank in 1949, who realized that crystals and their surfaces are rarely perfect, but contain many defects. In particular, screw dislocations ending at a surface form an eternal

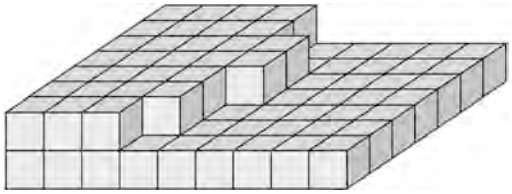


Figure 16. A step with three kinks on a Kossel (001) surface.

step source and allow growth without a 2D nucleation barrier. Burton, Cabrera and Frank developped an extensive model for such crystal growth and other behaviour of surfaces in the most famous article in the field, the BCF paper from 1951 [16].

Before discussing the effect of screw dislocations, we first need to look at steps in general. Figure 16 shows a single step on a Kossel crystal, drawn with three kinks. This is clearly not the state of the step with the lowest enthalpy, because each kink will cost energy. Of course in thermodynamics it's the free energy, including entropy, that determines the equilibrium configuration. We can obtain an estimate of the kink density at such a step by using the tools of statistical thermodynamics. We here use a simple model of a straight step along the [010] direction in a Kossel model and allow only kinks with a single height (up or down). With respect to a straight step, the energy cost of a single kink is the kink energy φ_k. Using Boltzmann statistics, the relative weights of the three possible configurations are:

no kink	1,
kink up or down	$e^{-\varphi_k/kT}$.

The sum over all (three) configurations is the partition function that normalizes the probabilities for the configurations. The probability for a kink is thus:

$$n = n^+ + n^- = \frac{2e^{-\varphi_k/kT}}{1+2e^{-\varphi_k/kT}}. \qquad (31)$$

Even if we assume a relatively high kink energy and low temperature ($\varphi_k \approx 0.1$ eV, $kT \approx 0.025$ eV; thus $\varphi_k/kT = 4$), the expression shows that a kink occurs with a probability of 3%, thus one every 30 growth units. This probability increases rapidly for higher temperatures and/or weaker bonds. This leads to an important conclusion: steps typically have many kinks. From a thermodynamic point of view, the *steps are rough*. This remains true if kinks with larger than a single height are included [19].

When a step is not along a [010] (or similar) direction, it will contain even more kinks and will grow faster, despite the fact that steps are rough to begin with. At moderate temperatures (high values for φ_k/kT), there will thus be significant anisotropy in the step velocity, with minima in the 'straight' directions. Analogous to the case of flat crystal orientations that lead to growth facets, this leads to 1D faceting of steps in the directions of minimum growth speed: virtually straight steps along major crystallographic directions. For increasing temperatures, the kink density will become more equal for the different directions, and thus the step velocity will become more uniform and steps become curved.

Even when there is a reasonably high kink density, a growth unit may still arrive at a location where there is no kink. At such a straight step location, a growth unit encounters in principle a 1D nucleation barrier. Consider therefore a 1D nucleus, i.e., a string of N growth units, attached to a straight step. The change in free energy with respect to the fluid phase in this case is:

$$\Delta G_{1D} = \Delta G_{bulk} + \Delta G_{kink} = -N\Delta\mu + 2\varphi_k. \quad (32)$$

This is similar to the 2D and 3D cases we discussed earlier, except that now the maximum in ΔG_{1D} occurs for $N = 1$. The critical nucleus is thus one growth unit for any value of $\Delta\mu$, corresponding to 1D kinetic roughening, and the probability for growth is very high. There is thus no effective 1D nucleation barrier [20].

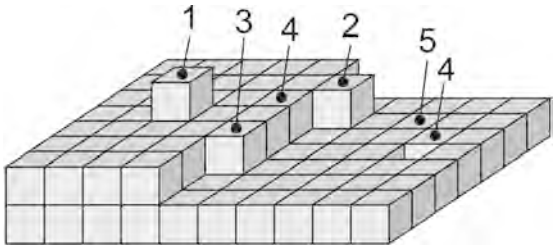


Figure 17. Growth units at the surface of a Kossel crystal with different number of bonds to their neighbours. In the bulk, each growth unit has six bonds.

3.6. Intermezzo: kinks and microscopic reversibility

An excellent way to obtain an understanding of the atomic processes occurring during crystal growth is to perform Monte Carlo (MC) computer simulations. (The MC aspect arises from the fact that the probability of atomic-scale moves is determined by random numbers: throwing dice). The Kossel crystal is again an ideal model for this. As figure 17 shows, at the surface growth units with a different number of bonds occur, from 1 to 5 (in the bulk there are 6 bonds). The probability of removing an atom depends on the number of bonds j: P_j^-. There is also a probability for adding a growth unit: P_j^+. The concept of *microscopic reversibility* states that there is a relation between the removal and addition of growth units in a specific configuration that depends on the free energy difference of the configuration with respect to the fluid phase:

$$\frac{P_j^+}{P_j^-} = e^{-(\Delta G+\Delta\mu)/kT}. \quad (33)$$

In equilibrium, $\Delta\mu = 0$. For the Kossel crystal, the different surface configurations depend on the number of horizontal bonds i, each with effective energy φ (which in vacuum equals $\frac{1}{2}\varphi_{ss}$). For this case, the condition of microscopic reversibility becomes:

$$\frac{P_i^+}{P_i^-} = e^{2(i-2)\varphi+\Delta\mu/kT}. \quad (34)$$

This shows that a kink position, where $i = 2$, is special, because under equilibrium conditions, an atom at a kink has the same free energy as in the fluid phase.

3.7. Step growth

As we have seen, on flat surfaces, steps (with a height as small a one unit cell) are well-defined and growth proceeds by the incorporation of growth units at the steps in general and kinks in particular. This growth behaviour is called *layer-by-layer growth* or *step-flow* and figure 18 illustrates this behaviour. To promote this type of growth, sometimes crystals are intentionally cut at an angle

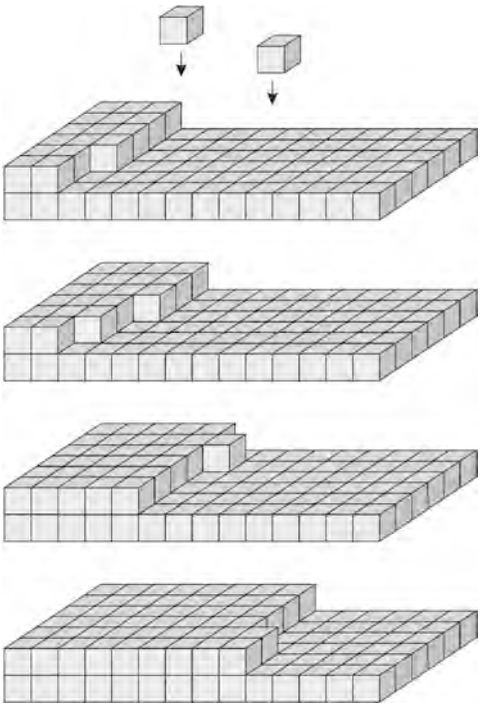


Figure 18. When a surface has well-defined steps, i.e. on flat surfaces, growth proceeds layer-by-layer. Individual growth units attach to the step and the step appears to flow across the surface.

with respect to a flat orientation: this will produce a high density of (regularly spaced) steps and thus faster and better controlled growth.

When a crystal is in equilibrium, the number of growth units added per second equals that of the growth units removed. This is also true locally at a step:

$$J^{+}_{step,eq} = J^{-}_{step,eq}. \tag{35}$$

Earlier, we derived the Wilson-Frenkel growth law for a rough surface. A similar argument holds for a step, because it is also rough. If a step has many kinks, we may assume that the occurrence of the different sites does not change significantly during growth and the step velocity will depend linearly on the driving force:

$$v_{step} = b\,\frac{\Delta\mu}{kT}. \tag{36}$$

The proportionality constant b is the called the *step kinetic coefficient* and it varies with step orientation.

In principle there are two routes for a growth unit to a step, see figure 19:

1. directly from the fluid phase through volume diffusion to the step,
2. volume diffusion to a terrace, followed by surface diffusion to the step.

Route 1 is typical for growth from a liquid phase, route 2 for growth from a gas or vapour. When route 1 is dominant, the growth rate is determined by incorporation in the step, following equation (36). In

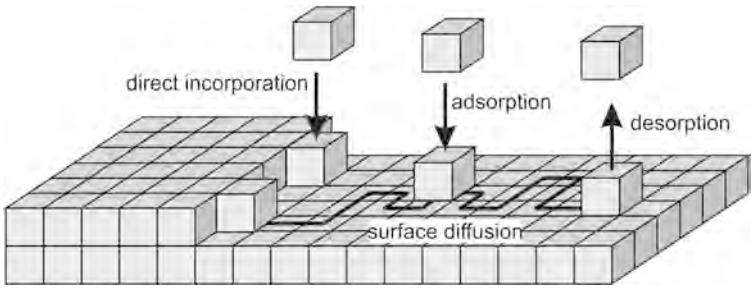


Figure 19. Growth units can either be directly incorporated into a step, or first adsorb and diffuse over a terrace, if desorption does not occur first.

this case the structure, and in particular the kink density, of a step determines the growth rate and steps tend to follow crystallographic orientations.

Now consider the case when surface diffusion is dominant. Growth units that adsorb on a terrace have only a limited bonding (in the Kossel model a single bond with the underlying growth unit), and thus they can desorb quite easily. The probability for this depends on the bond strength, φ_{ss}. The residence time τ of an adsorbed growth unit is the inverse of the desorption probability and equals:

$$\tau^{-1} = \frac{kT}{h} e^{-|\varphi_{ss}|/kT}, \tag{37}$$

with h Planck's constant. During this time, the growth unit can jump to neighbouring sites with a probability:

$$P_D = \frac{kT}{h} e^{-\varphi_D/kT}, \tag{38}$$

with φ_D the diffusion barrier. The surface diffusion constant is then:

$$D_S = a^2 P_D, \tag{39}$$

with a the length of each jump (typically a single lattice constant). The various jumps are uncorrelated, and the growth unit performs a random walk. The average distance a growth unit travels, the diffusion length l_{diff}, scales in this case with the square root of the number of jumps:

$$l_{diff} = a\sqrt{\tau P_D} = \sqrt{\tau D_S}. \tag{40}$$

If a growth unit encounters a step during diffusion, it will be incorporated (most of the time at least) and growth occurs. On average, this only happens when the growth unit is adsorbed within a distance l_{diff} from a step.

From the expressions used above, we can estimate the diffusion length:

$$l_{diff} = a e^{(|\varphi_{ss}| - \varphi_D)/2kT}. \tag{41}$$

For growth from the gas phase, $|\varphi_{ss}|/kT \simeq 8$, while φ_D is typically much smaller, $\varphi_D \simeq \frac{1}{4}|\varphi_{ss}|$. Using these values, the residence time equals $\tau = 5 \times 10^{-10}$ s, and $l_{diff} = 20a$. Despite the small residence time, the step thus collects material from quite a large area. For growth from a liquid phase the situation is different, because surface diffusion now requires the displacement of the solvent molecules. This leads to a much larger value for φ_D, roughly equal to $|\varphi_{ss}|$. In that case, l_{diff} is only a single lattice spacing and surface diffusion hardly plays a role.

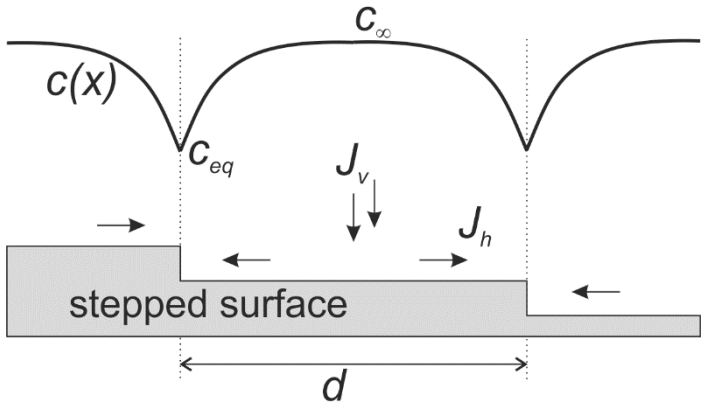


Figure 20. The concentration profile of adsorbed growth units during step growth via surface diffusion.

In the case of growth from a liquid, steps have little influence on each other, but for vapour growth steps that are separated by $2l_{diff}$ or less, interact because they consume each other's diffusing growth units. A simple, one-dimensional model to describe this was developed by Burton, Cabrera and Frank [16]. Assume a surface with equidistant steps, separated by a distance d, see figure 20. The surface is exposed to a constant flux from the vapour and in the horizontal direction diffusion takes place. The concentration at a specific location is given by the combination of the nett (vertical) influx J_v and horizontal diffusion:

$$\frac{\partial c(x,t)}{\partial t} = \frac{\partial J_h(x,t)}{\partial x} + J_v(x,t). \tag{42}$$

We may assume that the step velocity is small compared to the diffusivity, and thus the concentration is constant (steady-state condition):

$$\frac{dJ_h(x)}{dx} + J_v(x) = 0. \tag{43}$$

For the horizontal flux, Fick's first law for mass transport holds:

$$J_h(x) = -D_s \frac{dc(x)}{dx}. \tag{44}$$

J_v is the difference between the vertical supply J_v^+ and removal J_v^-. The supply is constant everywhere (and depends on the applied supersaturation), while the removal depends on the local concentration $c(x)$. Far away from a step, a constant concentration c_∞ will be established and $J_{v,\infty}^+ = J_{v,\infty}^- = c_\infty/\tau$. We can now rewrite the equation for the flux in terms of the concentration:

$$-D_s \frac{d^2c(x)}{dx^2} + \frac{c_\infty - c(x)}{\tau} = 0. \tag{45}$$

This is (written in a slightly different form) the well-known BCF equation for step growth through surface diffusion. In order to solve it, we have to apply boundary conditions at the steps (located at $x = \pm 0.5d$) that act as sinks for the arriving growth units. For simplicity, we here assume these are perfect sinks, and then the concentration at the steps will be the equilibrium concentration c_{eq}. Solving the BCF equation requires a number of additional mathematical steps, and then yields for the concentration profile:

$$c(x) = c_\infty - \frac{\Delta\mu}{kT} c_{eq} \frac{\cosh(x/l_{diff})}{\cosh(d/2l_{diff})}. \tag{46}$$

The profile is shown in figure 20.

The step velocity is subsequently found by computing the horizontal flux to the step:

$$J_h(0.5d) = -D_s \frac{dc}{dx}\Big|_{x=0.5}. \quad (47)$$

This flux arrives from two sides, and each growth unit corresponds to a growth area of a^2. Then:

$$v_{st} = -2a^2 J_h = \frac{2a^2 D_s c_{eq}}{l_{diff} kT} \tanh\left(\frac{d}{2l_{diff}}\right) \Delta\mu. \quad (48)$$

From this equation, we see that under the applied assumptions the step velocity is again proportional to the supersaturation (i.e. driving force). In this case we have obtained a detailed expression for the step kinetic coefficient. The step velocity decreases rapidly when the step spacing is less than $2l_{diff}$. For the smallest step spacings, v_{st} is proportional to the spacing d; for very large spacings, v_{st} becomes independent from the spacing.

Note that in many cases the flux to the steps will not be equal from both sides, because the diffusion over the step is hampered by an additional diffusion barrier at the edge, the Ehrlich-Schwoebel barrier. This is caused by the fact that the growth unit has to go through a low-coordination transition state [21]. If that barrier is very high, flux would only arrive from the lower terrace in front of the step.

In the derivation, we assumed that step incorporation is very fast and thus that growth is limited by surface diffusion. The kink density, and thus the step orientation, then doesn't play a role and steps tend to be circular. Diffusion does not have to be isotropic on a crystalline surface, thus in general the step patterns are elliptical in case of diffusion-limited growth.

3.8. Spiral growth

We now return to the topic of growth on a flat face. We have seen that on a perfectly flat surface, without any steps, growth requires the formation of 2D nuclei, and this is so rare at low driving force that essentially zero growth is predicted. Experimentally, however, growth does occur and in 1949 Frank realized that this is owing to screw dislocations. A screw dislocation is a line defect in a crystal that creates a step on the crystal surface that ends at the dislocation line. When a driving force is

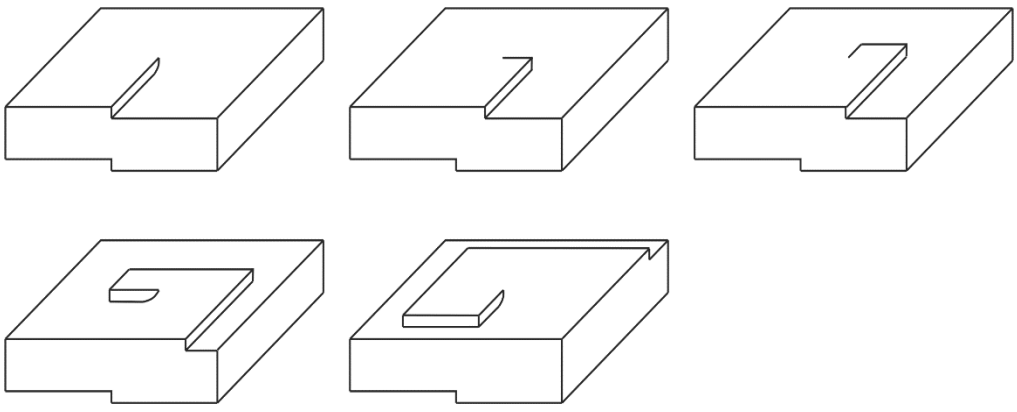


Figure 21. The half-step at the surface caused by a screw dislocation leads to a growth spiral, because growth units keep attaching to the exposed step. The height of the step depends on the size of the Burgers vector of the dislocation and can be several monolayers.

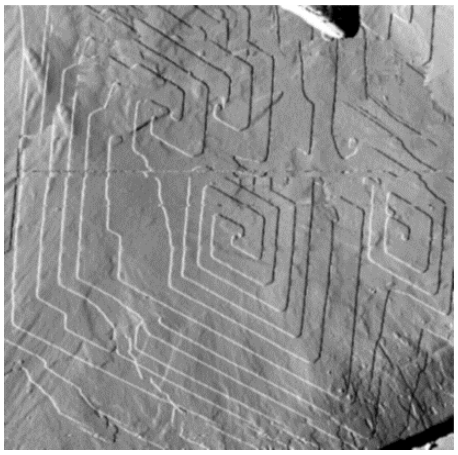


Figure 22. AFM picture of several growth spirals on the surface of n-$C_{40}H_{82}$ paraffin crystals. The scanned area is 18 x 18 μm^2. (Adapted from [1]).

applied, the step will grow. As figure 21 illustrates, this leads to a growth spiral, with its centre anchored at the dislocation line. The step never disappears, so growth will continue as long as there is a driving force. Figure 22 shows an atomic-force microscopy (AFM) image of growth spirals on a paraffin crystal surface.

The growth rate of a crystal through spiral growth can be estimated by using a simple model for the spiral: the Archimedean spiral, defined by

$$r(\theta) = \frac{d}{2\pi}\theta, \tag{49}$$

with r the radius, d the spacing between the spiral arms and θ the polar angle, see figure 23. In one revolution, each step moves over a distance d with a velocity v_{st}, and the crystal grows by the height h_{st} of one step. The growth rate is thus:

$$R_{spiral} = \frac{h_{st}}{d} v_{st}. \tag{50}$$

The curvature of the spiral (which leads to excess step energy with respect to a straight step) decreases the effective driving force according to:

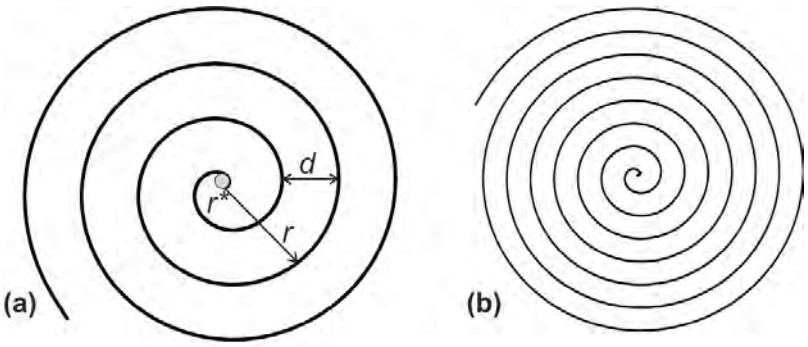


Figure 23. A schematic of an Archimedean growth spiral at (a) low and (b) high driving force.

$$\Delta\mu_{curv} = \Delta\mu\left(1 - \frac{r_{2D}^*}{r}\right), \tag{51}$$

with r the local radius of curvature and r_{2D}^* the critical radius for 2D nucleation derived in eq. (25). Since r_{2D}^* decreases with increasing Δμ, a higher driving force allows a higher curvature of the spiral. At the centre of the spiral the curvature is maximal and in a steady state, this is the location where the growth is zero. The radius of curvature at the origin of the Archimedean spiral equals $d/4\pi$ and thus:

$$d = 4\pi r_{2D}^* = \frac{4\pi\gamma_{st}\Omega}{h_{st}\Delta\mu}. \tag{52}$$

The step distance is thus proportional to the step free energy and inversely proportional to the driving force. In practise the slope of spirals is low, ranging from 0.01 to 1 degrees. If the driving force is known, the expression allows an estimate of the step free energy by measuring the step spacing. A more general analysis, not assuming an Archimedean spiral, leads to an improved estimate for d:

$$d = 19r_{2D}^*, \tag{53}$$

and this yields the following growth rate:

$$R_{spiral} = \frac{h_{st}}{19r_{2D}^*}v_{st} = \frac{h_{st}^2}{19\gamma_{st}\Omega}\Delta\mu v_{st}. \tag{54}$$

We have discussed several cases for v_{st}. When step incorporation is rate limiting (typical for growth from the liquid), we find, using eq. (36):

$$R_{spiral,step\ inc.} = \frac{h_{st}^2 b}{19\gamma_{st}\Omega}(\Delta\mu)^2, \tag{55}$$

a parabolic dependence on the supersaturation. For growth determined by surface diffusion, we found for the step velocity, eq. (48):

$$v_{st} = \frac{2a^2 D_S c_{eq}}{l_{diff}kT}\tanh\left(\frac{d}{2l_{diff}}\right)\Delta\mu = \frac{2a^2 D_S c_{eq}}{l_{diff}kT}\tanh\left(\frac{19\gamma_{st}\Omega}{2l_{diff}h_{st}\Delta\mu}\right)\Delta\mu. \tag{56}$$

The growth rate then becomes:

$$R_{spiral,surf.diff.} = \frac{h_{st}^2}{19\gamma_{st}\Omega}\frac{2a^2 D_S c_{eq}}{l_{diff}kT}\tanh\left(\frac{19\gamma_{st}\Omega}{2l_{diff}h_{st}\Delta\mu}\right)(\Delta\mu)^2. \tag{57}$$

For small Δμ, we find in this case $R \propto (\Delta\mu)^2$, while for large Δμ, $R \propto \Delta\mu$. For spiral growth limited by surface diffusion, there is thus a transition from a parabolic to a linear dependence on the supersaturation. In the parabolic regime, the diffusion fields around adjacent steps do not overlap, in the linear regime they do. At low driving force, spiral growth is thus always characterized by a parabolic dependence on Δμ, irrespective of whether growth is limited by step incorporation or by surface diffusion. This behaviour is a macroscopic signature of spiral growth and distinguishes it from rough growth with a linear dependence on Δμ.

3.9. Additives and impurities

So far we discussed clean systems, but crystal growth can be strongly influenced by other compounds. Depending on whether these are intentional or not, they are called additives or impurities. The additives can have a number of effects, and most often decrease the growth rate. An increase is possible as well, either through heterogeneous 2D nucleation (analogous to the case of heterogeneous 3D nucleation) or by lowering the surface free energy (following the Gibbs isotherm equation). A lower surface free energy means a lower step energy and this results in faster growth as follows from all equations we presented. In the most extreme case, the step free energy can go to zero and the surface becomes rough. This is called *chemical roughening.*

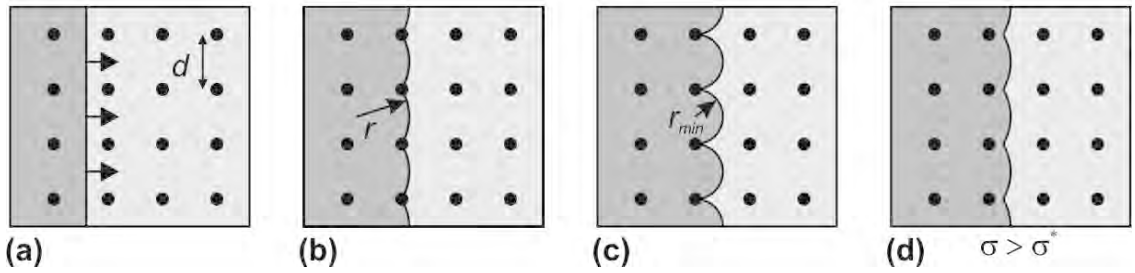


Figure 24. The model of Cabrera and Vermilyea for step pinning by impurities. The impurities from a square array on the surface and the step has to bend around and pass the impurities. This is only possible for a sufficiently high driving force.

A more typical effect is the deceleration of growth. If the surface has a significant concentration of additives, many growth sites are blocked and this will reduce growth. The most important effect of impurities, however, is blocking the movement of steps. As we have seen, on flat surfaces growth proceeds by the movement of steps and hampering this will have a large effect. A simple model for this *pinning of steps* was developed by Cabrera and Vermilyea [22]. It assumes that the additives are completely immobile and form a square lattice with spacing *d*. Steps cannot pass through the additives directly, but have to move around them, while the impurities are then incorporated into the crystal. Figure 24 illustrates this. When the step passes the impurities, the step will curve and this decreases the effective driving force as already shown in equation (51). The maximum curvature occurs when the step has almost passed the impurities, figure 24c. In that case $r_{min} = \frac{1}{2}d$. The step can only pass through this phase if the driving force is large enough, and this means $r_{min} > r_{2D}^*$. Thus:

$$\frac{d}{2} > \frac{\Omega\gamma_{st}}{h_{st}\Delta\mu} \Rightarrow \Delta\mu > \Delta\mu^* \text{ with } \Delta\mu^* = \frac{2\Omega\gamma_{st}}{dh_{st}}. \qquad (58)$$

In the model of Cabrera and Vermilyea it is assumed that growth completely stops if $\Delta\mu < \Delta\mu^*$. The step would then be fixed in a position as in figure 24b. For $\Delta\mu \geq \Delta\mu^*$ the model takes a geometrical average of the step velocities during the various phases, leading to:

$$\langle v_{st} \rangle = \frac{b\Delta\mu}{kT}\sqrt{1 - \frac{\Delta\mu^*}{\Delta\mu}} \text{ for } \Delta\mu > \Delta\mu^*. \qquad (59)$$

A plot of the predicted growth rate is shown in figure 25. A *dead zone* is predicted for low values of Δμ. This is impurity poisoning of growth. At higher Δμ, the step velocity catches up with the rate for a pure system. The model makes rather crude assumptions, but the overall result is correct [23].

An example of the use of additives is as anticaking agents in rock salt (NaCl). Under conditions of varying humidity, rock salt crystals tend to lump together, and this is caused by crystal growth at the locations where they touch. The additive $Fe(CN)_6$ is widely used to prevent this caking and the anticaking mechanism is the prevention of growth by the step pinning just described [24].

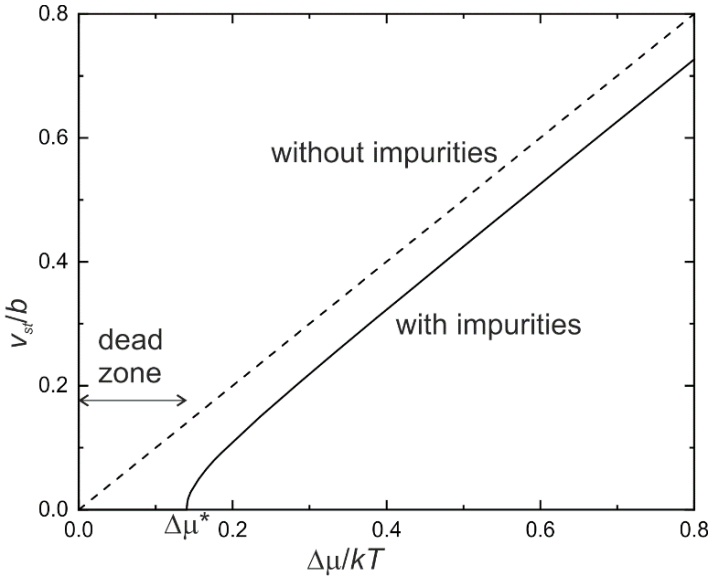


Figure 25. The step velocity (normalized on the kinetic coefficient *b*) as a function of the supersaturation. The calculation assumes a step energy of 2 x 10^{-11} J/m and a impurity coverage of 0.1%. This gives a critical supersaturation of 0.14.

Additives may have a stronger affinity for one crystal surface orientation over another and in that case the growth rate will be modified in an anisotropic way. Then the additives are *habit modifiers*, which may be applied to change the growth morphology of a crystal. As early as 1783, Romé de I'Isle found experimentally that adding urea to an aqueous solution of NaCl will change the morphology from cubes with {100} facets to octahedrons with {111} facets [25].

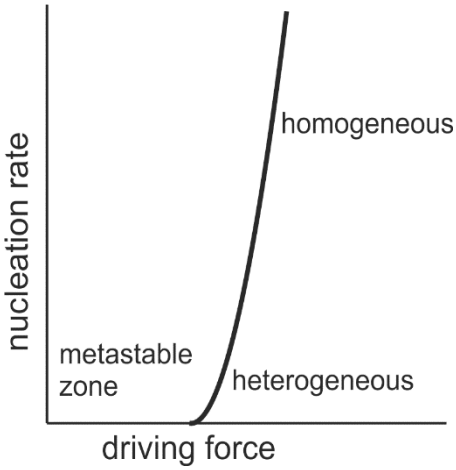


Figure 26. The nucleation rate depends very strongly on the driving force. For low driving force, there is essentially zero nucleation, but above a certain threshold, the nucleation rate becomes very large.

4. Summary

We have discussed the genesis of crystals, i.e. the nucleation of new crystals from the fluid phase. Figure 26 summarizes the main phenomena. The nucleation barrier, both in 3D and 2D, has a large effect on the kinetics of crystal formation, because the barrier makes crystal formation very unlikely at low driving force. In the case of 3D crystals, heterogeneous nucleation can help and at low driving force this is the typical mechanism for crystal formation. At high driving force homogeneous nucleation takes over, as this involves far more sites where it can take place. The lack of spontaneous nucleation at low driving force can be exploited to control crystal formation and growth by seeding in the metastable zone. Classical nucleation theory provides a good framework for understanding nucleation, but it is now well-known that other routes to crystal formation can be important as well, e.g. using intermediate phases or the agglomeration of nanoparticles. In the 2D case at low driving force, the nucleation barrier is often avoided through spiral growth.

The growth mechanism of a surface is completely different for the two main types of surfaces: flat or rough, see figure 27. On flat surfaces, growth proceeds through the flow of steps that either originate from screw dislocations or are generated by 2D island formation at higher driving force. There are many ways in which a surface can be rough: (1) because its crystallographic orientation contains many steps and/or kinks (*S* and *K* faces), (2) because the temperature of flat (*F*) faces is above roughening transition (thermal roughening) or (3) because the driving force for these *F* faces is too high (kinetic roughening). The facets that are characteristic of many crystals are *F* faces that correspond to crystallographic orientations with a clear local minimum in the growth rate.

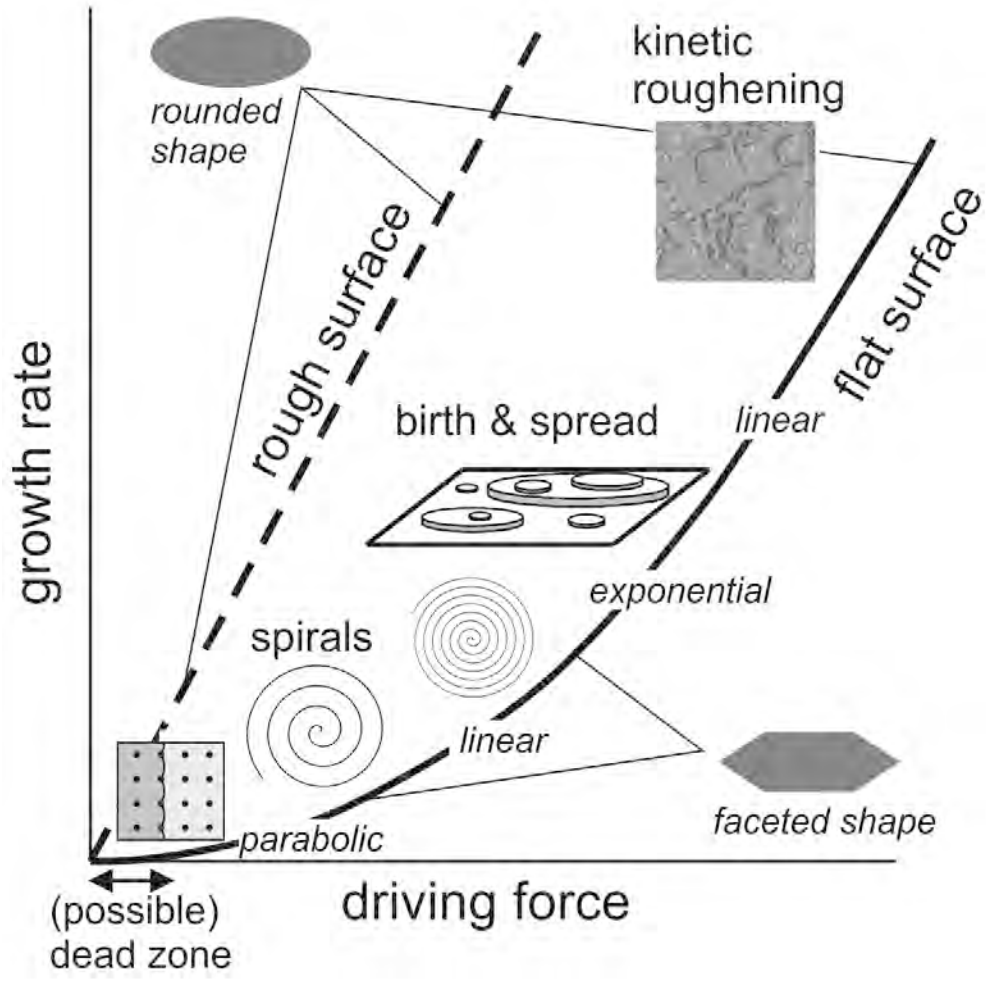


Figure 27. An overview of the most important crystal growth mechanisms. For rough surfaces, the rate depends linearly on the driving force, but for a flat surface there is a transition through different growth modes. Mass transport will also have a large effect on the actual growth rate. The faceted shape characteristic of many crystals will only occur if the corresponding orientations are not rough.

References

[1] M. Plomp, W.J.P. van Enckevort, P. van Hoof, C.J. van de Streek, Morphology of and dislocation movement in n-C40H82 paraffin crystals grown from solution, J. Cryst. Growth, 249 (2003) 600-613.

[2] H.M. Cuppen, H. Meekes, W.J.P. van Enckevort, E. Vlieg, Kink incorporation and step propagation in a non-Kossel model, Surf. Sci., 571 (2004) 41-62.

[3] C. Stoica, P. Tinnemans, H. Meekes, E. Vlieg, P.J.C.M. van Hoof, F.M. Kaspersen, Epitaxial 2D nucleation of metastable polymorphs: a 2D version of Ostwald's rule of stages, Cryst. Growth Des., 5 (2005) 975-981.

[4] X.Y. Liu, P. Bennema, Observations on the roughening transtions and the influence on morphology of crystals, J. Cryst. Growth, 139 (1994) 179-189.

[5] S.S. Kadam, H.J.M. Kramer, J.H. ter Horst, Combination of a Single Primary Nucleation Event and Secondary Nucleation in Crystallization Processes, Cryst. Growth Des., 11 (2011) 1271-1277.

[6] D.K. Kondepudi, R.J. Kaufman, N. Singh, Chiral symmetry breaking in sodium chlorate crystallization, Science, 250 (1990) 975-976.
[7] P. Vekilov, Dense liquid precursor for the nucleation of ordered solid phases from solution, Cryst. Growth Des., 4 (2004) 671-685.
[8] L. Addadi, S. Raz, S. Weiner, Taking advantage of disorder: Amorphous calcium carbonate and its roles in biomineralization, Advanced Materials, 15 (2003) 959-970.
[9] J.J. De Yoreo, P. Gilbert, N. Sommerdijk, R.L. Penn, S. Whitelam, D. Joester, H.Z. Zhang, J.D. Rimer, A. Navrotsky, J.F. Banfield, A.F. Wallace, F.M. Michel, F.C. Meldrum, H. Colfen, P.M. Dove, Crystallization by particle attachment in synthetic, biogenic, and geologic environments, Science, 349 (2015) 10.
[10] Y. Zhang, J.P. Sizemore, M.F. Doherty, Shape evolution of 3-dimensional faceted crystals, AIChE Journal, 52 (2006) 1906-1915.
[11] P. Bennema, H. Meekes, S.X.M. Boerrigter, H.M. Cuppen, M.A. Deij, J. van Eupen, P. Verwer, E. Vlieg, Crystal growth and morphology: new developments in an integrated Hartman-Perdok-connected net-roughening transition theory, supported by computer simulations, Cryst. Growth Des., 4 (2004) 905-913.
[12] P. Hartman, P. Bennema, The attachment energy as a habit controlling factor, J. Cryst. Growth, 49 (1980) 145-156.
[13] D. Winn, M.F. Doherty, Modeling crystal shapes of organic materials grown from solution, AIChE Journal, 46 (2000) 1348-1367.
[14] M.A. Deij, H. Meekes, E. Vlieg, The step energy as a habit controlling factor. Application to the morphology prediction of aspartame, venlafaxine and a yellow isoxazolone dye., Cryst. Growth Des., 7 (2007) 1949-1957.
[15] P. Hartman, W.G. Perdok, On the relations between structure and morphology of crystals I, Acta Cryst., 8 (1955) 49-52.
[16] W.K. Burton, N. Cabrera, F.C. Frank, The growth of crystals and the equilibrium structure of their surfaces, Philosophical Transactions of the Royal Society of London, Series A: Physical Sciences and Engineering, 243 (1951) 299-358.
[17] H.J. Leamy, G.H. Gilmer, Equilibrium properties of crystal-surface steps, J. Cryst. Growth, 24 (1974) 499-502.
[18] H.M. Cuppen, H. Meekes, W.J.P. van Enckevort, E. Vlieg, H.J.F. Knops, Nonequilibrium free energy and kinetic roughening of steps on the Kossel (001) surface, Phys. Rev. B, 69 (2004) 245404.
[19] H.M. Cuppen, H. Meekes, E. van Veenendaal, W.J.P. van Enckevort, P. Bennema, M.F. Reedijk, J. Arsic, E. Vlieg, Kink density and propagation velocity of the 010 step on the Kossel (100) surface, Surf. Sci., 506 (2002) 183-195.
[20] M.N. Joswiak, M.F. Doherty, B. Peters, Critical length of a one-dimensional nucleus, J Chem Phys, 145 (2016) 6.
[21] M.D. Johnson, C. Orme, A.W. Hunt, D. Graff, J. Sudijono, L.M. Sander, B.G. Orr, Stable and unstable growth in molecular beam epitaxy, Phys. Rev. Lett., 72 (1994) 116-119.
[22] N. Cabrera, D.A. Vermilyea, The growth of crystals from solution, in: R.H. Doremus, B.W. Roberts, D. Turnbull (Eds.) Growth and Perfection of Crystals, Wiley & Sons Inc., New York, 1958, pp. 393-408.
[23] W.J.P. van Enckevort, A. van den Berg, Impurity blocking of crystal growth: a Monte Carlo study, J. Cryst. Growth, 183 (1998) 441-455.
[24] A.A.C. Bode, S.F. Jiang, J.A.M. Meijer, W.J.P. van Enckevort, E. Vlieg, Growth inhibition of sodium chloride crystals by anticaking agents: in–situ observation of step pinning, Cryst. Growth Des., 12 (2012) 5889-5896.
[25] J.B. Romé de l'Isle, Cristallographie, Imprimerie de Monsieur, Paris, 1783, pp. 379.

5. Bulk Crystal Growth from the Melt

Bulk Crystal Growth from the Melt

C.W. Lan,

Department of Chemical Engineering, National Taiwan University

Taipei, Taiwan 10617, ROC

Tel (Fax): 886-2-2363-3917

cwlan@ntu.edu.tw

Keywords: crystal growth; thermodynamics, kinetics; segregation; melt growth. Czochralski method; Kyropoulos (KY) method; Bridgman method; floating zone method; flow control; defect control

OUTLINE

1. INTRODUCTION
    1.1 Brief history of crystal growth methods
    1.2 Crystal applications and their market
2. FUNDAMENTALS
    2.1 Driving force
    2.2 Surface smoothness
    2.3 Growth mechanisms
    2.4 Segregation
    2.5 Morphological instability
3. MELT GROWTH TECHNOLOGY
    3.1 Czochralski (CZ)/Kyropoulos (KY) method
    3.3 Bridgman/vertical Gradient Freeze (VGF) methods
    3.2 Floating-zone (FZ)/ZM method
4. FLOW AND SEGREGATION CONTROL
    4.1 Flow control by magnetic fields
    4.2 Flow and segregation control through rotation
5. DEFECT FORMATION AND CONTROL
    5.1 Point defects
    5.2 Defect clusters and oxygen precipitates
    5.3 Twinning
    5.4 Dislocations
6. CONCLUSIONS

1. INTRODUCTION

Crystals are solids in which molecules are arranged in a regular, repetitive three-dimensional pattern. Because of the repetitive nature, crystals can take on characteristic and interesting forms, for examples, the colorful and beautiful shine of various gem stones like diamond, ruby, and sapphire. Although such bulk crystals grown by the mother earth have fascinated men for thousands of years, the industrial growth of synthetic bulk crystals did not start until the invention of the flame-fusion method by A. Verneuil in 1902 (Scheel, 1994; 2000; Feigelson, 2015). Interestingly, most of the growth techniques, such as the Czochralski (CZ) method (Czochralski, 2018), Kyropoulos (KY) (Kyropoulos, 1926), Bridgman (Bridgman, 1923), and vertical gradient freeze (VGF) methods (Ramsberger and Malvin, 1927), we are familiar today were invented before World War II, but they were mainly used for scientific purposes. With the rapid development of microelectronic industry in the second half of the twentieth century, the demand of large and perfect single crystals, used as the substrates or components for devices, has increased rapidly. This becomes the key driving force for the research and technology development of bulk crystal growth and processing. The efforts by Teal and Little in the development of Ge crystal pulling (Teal and Little, 1950) and by Dash in the necking technique for dislocation-free crystals (Dash, 1959) were the foundations for the industrial CZ crystal growth. Teal and Little started to use a seed crystal to define the crystal orientation, and they introduced the concepts of diameter control and dopant distribution by controlling temperature and crystal/crucible rotation. Moreover, the techniques for refining, such as the zone-melting (ZM) method (Pfann, 1952) and the floating-zone (FZ) method (Theurer, 1952), later on became popular growth methods used in industry. Without the ZM method for materials refining, high purity materials

would not be possible. Detailed review and discussion of the crystal growth history could be found elsewhere (Scheel, 1994; 2000; 2003; Feigelson, 2015).

Nowadays, bulk crystals have been widely used in the industry. Scheel estimated the global annual production of bulk crystals to be about 20,000 t in 1999 (Scheel, 2000), which was double his estimated in 1975 (Elwell and Scheel, 1975). However, for the past nearly 20 years, the grown ingot size of electronic silicon has been increased from 8 to 12 in. The annual production of silicon crystals for semiconductors has increase to more than 20,000 t within the past ten years or so (TECHCET Report, 2018); the consumption of polysilicon was about 25,000 t. Meanwhile, due to the booming of the photovoltaic (PV) market, the installation of solar panels was increased from several hundred MW in 2000 to nearly 100 GW in 2017, 93% of which were silicon based solar cells. As a result, the annual production of PV silicon, both mono- and multi-crystalline silicon (mc-Si), was over 250,000 t (Fraunhofer, 2018). Meanwhile, the light emitting diode (LED) industry, especially in the area of GaN blue LEDs for lighting, which uses single crystal sapphire substrates, was growing rapidly for the past 20 years as well. The sapphire ingot size was increased from 60 kg in 2000 to over 400 kg this year. The estimated production of sapphire single crystals is at least 2000 t, which is about the market size of all optical crystals in 1999. Even scintillation crystals, known to be used in large particle physics experiments and medical imaging, experienced market growth over 300 million US dollars in 2016. Their applications in nuclear power plants, homeland security and defense have increased rapidly. More recently isotopic imaging, such as positron emission tomography (PET), has had a spectacular development because of its very high sensitivity at the picomolar level for precision diagnostics. Moreover, acoustic crystals, such as $LiNbO_3$, $LiTaO_3$, and langasite ($La_3Ga_5SiO_{14}$), having high

piezoelectric constants and electromechanical coupling factors, are used for surface acoustic wave (SAW) filters which are widely used in smart phones today. In addition, III-V compound semiconductors, such as GaAs and InAs, beside their applications in LEDs are widely used in microwave transistors for wireless communication. The major crystals and their estimated market share based on weight, applications, and growth methods are listed in Table 1 for reference. The importance of crystal growth technology for mankind in a few areas including renewable energy, energy saving, health, water, etc., has been reviewed by Schell (2005) and Bruni and Scheel (2013). Besides crystal growth from the melt, crystals could be grown from liquid solutions or vapor phase. However, they are beyond the scope of this chapter.

In this chapter, I will give an introductory overview of bulk crystal growth from the melt. The material is used for a two-hour lecture in the 2019 International Summer School for Crystal Growth. Besides the growth methods and their applications, the fundamentals, interesting research topics, and how to improve the ingot quality in practice are also reviewed and discussed. It is far away from extensive, and the selection of topics is based on my personal preference. For more details, interested readers can find them in the provided references, especially in the classic books on crystal growth (Laudise, 1970; Brice, 1986) and the handbooks for crystal growth and related topics (Dhanarai et al., 2010; Rudolph, 2015; Sasap and Casper, 2017).

2. FUNDAMENTALS

2.1 Driving force for melt growth

The growth of bulk single crystals requires a carefully control of the first-order phase transition from a "seed" crystal. It begins with the nucleation of a thermodynamically stable phase, followed by the construction (growth) of surfaces and morphologies. The melt growth is carried out by solidification from a melt. The seed crystal acts as a substrate providing a given crystallographic orientation with a good lattice match to the growing crystal. For most of applications, dopants are often needed, which are impurities purposefully added to tailor the properties of the growing crystal. To grow the crystal, the molecules in the melt require a driving force to transport, through convection and diffusion, from the fluid phase to the crystal surface. Thermodynamically, the crystal should be stable at the growth condition and the driving force for nucleation and crystal growth is the excess Gibbs free energy generated by supercooling. To grow a single bulk crystal, the growth environment needs to be carefully controlled, so that the driving force exists only around the seed crystal, without the parasitic nucleation from elsewhere.

From the thermodynamic point of view, the first-order transition from a fluid phase into a solid phase requires an excess Gibbs free energy $\Delta G_{L\text{-}S}$, which could be written as the following:

$$\Delta G_{LS} \approx -\Delta H \sigma = -\Delta H \Delta T / T_m , \qquad (1)$$

where ΔH is the latent heat per volume and $\sigma = \Delta T / T_m$ the dimensionless supercooling. To grow a bulk single crystal, an oriented seed is often used. Self-seeding is possible, but the control of growth orientation is more difficult. For example, in the growth of nickel-based superalloy single crystal turbine blades (Kubiak et al., 2015), a spiral grain selector is often used to select the fast-growing grain, [001] for nickel. Furthermore, the growth environment should be carefully controlled, so that the supercooling is kept small and exists only around the growing crystal. With a given

driving force, the growth speed depends on the growth mechanisms and the properties of the growing interface. As a result, the crystal morphology is determined by the interfacial energies and growth kinetics. However, in melt growth, the driving force is usually set in a specific direction, i.e., directional solidification. In such a case, the growth proceeds along a given direction. If the heat flux is uniform, the interface could be nearly flat; however, it is also affected by the crucible materials due to different thermal conductivities.

Depending on the magnitude of the driving force, the amount of impurities, and the growth environment, the growing crystal surface can either be smooth or rough, and the overall morphology could be quite different. Meanwhile, the buoyancy convections generated by temperature and concentration gradients in the system also play an important role in both crystal quality and growth rate. All these reasons make crystal growth more as an art than as a science in early days. Today, a well controlled growth technique requires a global optimization of the transport processes, as well as a feedback control to ensure the stability of the growth environment. For melt growth, the energy balance at the growth interface can be described as follows:

$$V\Delta H = k_S G_S - k_L G_L \,, \qquad (2)$$

where V is the growth rate, k_S and G_S are the thermal conductivity and gradient of solid, respectively, while k_L and G_L are the thermal conductivity and gradient of the melt, respectively. As shown in Eq. (2), the growth rate depends on the thermal gradients. As will be discussed shortly, to pull the crystal faster, higher temperature gradient in the crystal, as well as the lower thermal gradient in the melt, would be necessary. On the other hand, the high thermal gradient in the crystal could generate thermal stresses that induce dislocations. Therefore, a trade-off between production throughput and crystal quality exists. Moreover, the transport and incorporation rates

of different species during phase transformation are different, resulting in segregation during crystal growth. Consequently, to grow a bulk single crystal with a uniform composition that meets the electrical and optical needs of substrates, the control of segregation is also important.

2.2 Surface smoothness

As crystal growth proceeds through the transport of the molecules to the crystal surface, the newly formed surface could be smooth or rough depending on the growth condition and the crystallographic orientations. At absolute zero temperature, a surface at equilibrium should contain no growth steps, i.e., perfectly flat. At higher temperature T, there are adatoms on the surface due to thermal energy, and the adatom density ρ_a can be described by the Gibbs formula as (Markov, 1995; Pimpinelli and Villain, 1998):

$$\rho_a = \exp(-\Delta G_a / k_B T), \tag{3}$$

where ΔG_a is the Gibbs free energy needed to extract an atom from a step to make it an adatom and k_B the Boltzmann constant. Detailed calculations of the energy involved are required to estimate the roughening transition temperature, which provides a thermodynamic criterion for a smooth surface. Jackson took a rather different approach to estimate the transition. He formulated an α factor (Jackson, 1958) that takes into account the contact nature of the solution and the surface. The α factor is defined as

$$\alpha = (\Delta H / kT) f_{hkl}, \tag{4}$$

where ΔH is the latent heat of the phase change and f_{hkl} (<1) is a crystallographic factor representing the fraction of all first neighbors lying in a plane parallel to the crystal surface. For a large α factor (α>>2), the surface is almost smooth due to the

strong bonding energy as compared to the thermal fluctuation. This is typical for organic crystals. For most of the metallic materials, the α factors are low, so that their surfaces are rough and they are less prone to faceting. On the other hand, usually rough faces grow so fast that they disappear from the growth form in the case of free growth. There are also other advanced theories and computational approaches to predict the surface roughness. However, the Jackson's α factor provides a first estimate of the surface quality. For silicon, (111) is the only orientation that forms facets. For compound semiconductors, facets often appear on (111) as well (Jurisch et al., 2015).

2.3 Growth mechanisms

When the surface is rough, the growth kinetic is usually simple because the growth sites are randomly distributed. For such a case, the growth rate is in general proportional to the local driving force, and the local supercooling is also small. However, for facets the crystal surface is consisted of steps, with terraces and kinks, as well as adatoms and vacancies. The preferred growth sites are the kinks due to more bonding to grape the adatoms. The growth requires adsorption of atoms and then surface diffusion to the growth sites. The simple step model with surface diffusion could lead to a simple linear law for the growth, i.e., the growth rate is linearly proportional to the undercooling σ, similar to the one in the rough surface formed by kinks. However, when the surface is smooth, the kinetics depends on the growth mechanisms. For example, as soon as step growth completes, the smooth surface requires a new two-dimensional (2D) nucleation for the next layer growth. For example, in a dislocation-free crystal, the new steps on (111) require 2D nucleation, and the supercooling ΔT is about 3.7 K at a normal pulling velocity (~ 1 mm/min) (Voronkov, 1973). However, with dislocations, the undercooling could become trivial

according to Voronkov's estimate for Si (Voronkov et al., 2015). As discussed by Voronkov et al. (2015) using a Si facet with steps shown in Fig. 1(a), the facets often appear near the periphery of CZ Si growth having a concave interface. For the maximum undercooling of 3.7 K observed during CZ Si growth, the step velocity $v = \beta \Delta T = 185$ cm/s for $\beta = 50$ cm/s K, which is very fast. The pulling rate could be related to the step velocity by $V = h v / l = v \theta$, where h is the step height, l the distance between steps, and θ the tilt angle of the growth facet. As a screw dislocation appears, such as the case in Fig. 1(b) for screw dislocation, l is small and the tilt angle θ is not trivial. If $\theta = 1^{o}$ at $V = 1$ mm/min, $\Delta T = 0.001$K. This indicates that the supercooling almost disappears on the facet, and the facet becomes very small. In other words, for Si pulling the disappearance of the facets is a good indicator in practice for the structure loss, i.e., having dislocations. Figure 1(c) shows the disappearance of the growth facet during the growth of the top crown of a heavily As-doped CZ Si crystal (Stockmeier et al., (2017)). For a facet in a dislocated crystal, the growth rate V is determined by the source points having the highest supercooling that creates the largest lateral flux of steps. It could be shown that $V \sim \Delta T_{\max}^{2}$ (Voronkov et al, 2015).

The facets are also important in twining, which is quite common in the growth III-V compound semiconductors (Hurle, 1995; Chung et al., 1995; Amon et al., 1998; Jurisch et al., 2015). Even in the casting of mc-Si or quasi-mono Si ingot, twining is a crucial mechanism for the formation of new grains and Σ3 grain boundaries (Duffar and Nadri, 2012; Lin and Lan, 2017; Jhang et al., 2018).

2.4 Segregation

In most of industrial applications, dopants are added into the crystals for tailoring their electrical or optoelectronic properties. However, because of the different dopant

solubility in the crystal and in the melt, dopant segregation (inhomogeneity) during growth is inevitable. This is a problem particularly for a batch growth process, such as the CZ and Bridgman methods. Let's take the normal freezing as an example. The crystal growth starts from one end to the other by solidification. With an initial dopant concentration in the melt at C_0 and no solid-state diffusion, the axial dopant segregation with complete dopant mixing can be described by the Schiel equation (Flemming, 1974):

$$C_s = C_0(1-f)^{k-1}, \tag{5}$$

where f is the fraction of solidification and k the segregation coefficient. The segregation coefficient k is the ratio of the dopant solubility in the solid and that in the melt. The schematic dopant distributions for $k<1$ having complete dopant mixing and no mixing (diffusive growth) in the melt after solidification are illustrated in Fig. 2. However, in practice the dopant mixing in the melt is in between. During crystal growth, the dopant boundary layer is established in front of the interface, which is governed by the dopant flux balance as follows:

$$-D\frac{dC}{dz} + VC = VC_0, \tag{6}$$

where D the dopant diffusivity in the melt, C the dopant concentration and C_0 the dopant concentration in the bulk melt. The Schiel equation is often used to fit the dopant profile in the crystal by using the segregation coefficient as a parameter, even when the dopant is not well-mixed. The fitting value is often referred to as the effective segregation coefficient k_{eff}. Burton et al. (1953) further proposed a simple model, the so-called BPS theory, to correlate the effective segregation coefficient with the convection, which is characterized by a boundary layer thickness δ, as:

$$k_{eff} = \frac{k}{k + (1-k)e^{-V\delta/D}}. \tag{7}$$

Although the BPS theory is not quite correct for the closed system, it still gives a nice physical insight for understanding dopant segregation with convection. Apparently, from Eq. (7), to improve axial dopant uniformity, one can increase the solidification speed or reduce dopant mixing (having a thicker boundary thickness), so that k_{eff} can be closer to unity. In other words, if the solidification distance is long enough, the axial dopant distribution can be more uniform. Hence, reducing mixing of the growth in the diffusive environment, such as crystal growth in space, has been an active research topic in crystal growth. Suppressing the flow by magnetic fields, and thus reducing axial segregation, has also been extensively adopted in practice (Rudolph and K. Kakimoto, 2009). With the evaporation of dopants, such as As and Sb dopants in silicon growth, k_{eff} could be modified by considering the evaporation coefficient γ_e (Flemming, 1974). Further reading on the effective segregation coefficient could be found in a nice review by Ostrogorsky and Glicksman (2015).

Despite the segregation in the axial direction, segregation can also occur in the lateral (or radial) direction due to the non-uniform dopant boundary layer. The control of lateral segregation is extremely important in industry to ensure the wafers cut from the ingot have a good uniformity, such as the radial resistance variation (RRV) in silicon wafers. The interface shape and the convection in the bulk phase are the key factors affecting the lateral segregation. Flow instability, time-dependent flow, or rotation, also affect growth rate and the dopant boundary layer which eventually causes microsegregation. This microsegregation could be visualized as the so-called “growth striation”, an indication of dopant inhomogeneity. Morphological instability, as will be discussed shortly, could also cause microsegregation. A nice discussion on microsegregation could be found in Hurle’s book (1993). Extensive research efforts through computer modeling have been paid to control the transport processes and the

interface shape for improving crystal uniformity (Brown, 1988; Lan, 2005; Derby and Yeckel, 2015). More discussion on this topic will be given in Sec. 4.

2.5 Morphological instability

Because of dopant segregation, the dopant boundary layer affects the solidification temperature, i.e., the liquidus temperature T_L, in front of the growth interface, as shown in Fig. 3(a). If the thermal gradient G_L is smaller than the gradient of the solidification temperature at the growth front, constitutional supercooling (CS), i.e., the shaded area in Fig. 3(a), could occur (Rutter and Chalmers, 1953; Tiller et al., 1953). The criterion for CS is described by:

$$G_L \le mdC / dz, \tag{8}$$

where m is the slope of the liquidus temperature in the phase diagram; for a dilute solution, $T_L=T_m+mC$. By substituting Eq. (6), and replacing C by C_0/k at the growth front, we could get critical growth velocity V_c as the following:

$$V_c = \frac{G_L D k}{m C_0 (1-k)}. \tag{9}$$

Once the supercooling is large enough to overcome the interfacial energy, the microscopically planar interface can break down into cellular cells or dendrites. The basic concept of CS was first formulated by Rutter and Chalmers (1953), and the theory was elucidated by Tiller et al. (1953). The top photograph of Fig. 3(b) shows an in-situ observed faceted interface during directional solidification of Si wafer as the growth speed exceeded V_c. The lower one in Fig. 3(b) is the image of the etched wafer in the longitudinal direction from a heavily B-doped CZ Si ingot (Taishi et al., (2000)). The (111) facets on the sawtooth morphology could be clearly seen as well. The faceted growth striation was due to the CS. After severe CS, a polycrystalline

structure was observed.

Mullins and Sekerka (MS) (1964) gave an excellent analysis on the morphological instability, which predicts the onset wavelength forming a steady cellular array. The MS loop, a stability diagram of velocity (V) vs wavelength (λ), is often adopted for predicting the onset wavelength of the unstable cellular structure. Their linear stability analysis gives the first insight into this problem, by assuming that the interface instability occurs from steady-state temperature/solute profiles. By inducing a small sinusoidal perturbation on the interface of a dilute alloy system, they calculated the variation of the wave with time, and if the perturbation grows with time, the interface is unstable. The derived relationship between the concentration, pulling speed, thermal gradients, and the sinusoidal wavelength for morphological instability is as the following:

$$C_{0c} > \frac{k}{(1-k)}\frac{D}{V}\frac{\left[2T_m\Gamma\omega^2 + (g_S + g_L)\right]\left[\omega^* - \frac{V}{D}(1-k)\right]}{2m\left(\omega^* - \frac{V}{D}\right)}, \qquad (10)$$

where $g_S = \frac{\alpha_S}{\overline{\alpha}}G_S$, $g_L = \frac{\alpha_L}{\overline{\alpha}}G_L$, $\overline{\alpha} = \frac{\alpha_S + \alpha_L}{2}$, where α_S and α_L are the thermal diffusivity of solid and melt, respectively, $\omega^* = \frac{V}{2D} + \left[\left(\frac{V}{2D}\right)^2 + \omega^2\right]^{1/2}$, $\omega = 2\pi/\lambda$, λ is the sinusoidal wavelength, and $\Gamma = \sigma T_m / \Delta H$, which is known as Gibbs-Thompson coefficient. Equation (10) is equivalent to Eq. (8) if the interfacial effect is neglected.

In Sekerka's analysis (1965), he found that the behavior of V is very interesting at fixed G and C_0. The interface becomes unstable by increasing V; however, if V is large enough, i.e., the upper limit (V_a) of the MS loop, the interface becomes planar again. In other word, inside the MS loop, the interface is not stable. The MS loop for a vertical Bridgman (VB) growth of 0.01 mol% acetone-doped SCN using Eq. (10) is

plotted in Fig. 3(c); some observed interface morphologies are shown as well (Shih et al., 2005). In the MS theory, a steady state is assumed. If transient solute diffusion is involved, the more rigorous theory was developed by Warren and Langer (1993). For both theories, although the onset of the morphological instability could be estimated, the development of nonlinear dynamic morphologies, such as the observed ones in Fig. 3(c), requires numerical simulation. Phase field modeling has been developed as a powerful tool for simulating the morphological development, and some simulated morphologies are also shown in Fig. 3(c) for the comparison with experiments (Lan, 2004; Shih et al., 2005).

As the CS occurs, the dopant inhomogeneity could lead to growth striations, as just mentioned in Fig. 3(b). Microsegregation due to time-dependent flow and unstable growth rate, as mentioned previously, could also induce similar growth striations.

3. MELT GROWTH TECHNOLOGY

3.1 CZ/KY method

Among the crystal growth techniques, the CZ method, as depicted in Fig. 4(a), is the most widely used one for both semiconductors and oxide/halide materials. The KY method, as shown in Fig. 4(b), is a very similar method, but the crystal is usually not pulled upward, while the diameter of the grown crystal is near the inner diameter of the crucible. For semiconductor silicon, 12-in dislocation-free ingots through Dash necking technique have been grown routinely by the CZ method for semiconductor industry. Although this method is named after J. Czochralski (1918), who established a technique for crystallization study of metals, the pulling method widely used today was mainly developed by Teal and Little (1950). In 1950, they successfully grew germanium single crystals, but only 0.75 inches in diameter. Nowadays, the CZ puller

has been designed sophisticatedly, and large-diameter silicon single-crystals up to 400 mm in diameter with a nearly perfect structure have been grown (Shiraishi et al., 2001). Figure 5(a) shows a CZ puller with a cusp magnetic field used in production. The recharge talk filled with granular silicon is used for multiple charging that allows several crystals pulled from one crucible without shutting down the power. Such a puller, originally designed for 8-in ingots with a 27-in hot zone, is just enough for pulling 12-in Si ingots. Nowadays, the 32-in hot zone is more popular for growing longer ingots. A grown 12-in Si ingot is shown in Fig. 5(b); the ingot weight is about 200 kg. The growth pressure in silicon growth is about 20 to 80 torr, and argon flow rate about 60 slpm. The CZ method is normally applicable to those materials that melt congruently or nearly congruently. For the crystal without congruent composition, a solvent or flux is often used. To such a technique, people often refer to it as the top seeded solution method or simply the flux method.

For silicon growth, a graphite heater is used, and the growth atmosphere is argon. The crucible made of silica is consisted of two layers; the outer layer is the bubble layer for better insulation and the inner layer is a glass layer, which is denser, for a longer lifetime. To avoid the nonuniform erosion forming crystoballite particles, which often cause structure loss, a special coating on the inner crucible surface is necessary, sometimes also applied to outer surface as well for better mechanical strength. Typically, a dense barium silicate coated layer is used as reported in a US patent (Hansen et al., 1999). In this GE patent, barium oxide is used as a devitrification promoter that helps forming a uniform crystoballite layer on the crucible inner surface during crystal growth. Hence, the particle generation is reduced. Adding Ba or Sr before or during melting down is also useful to form the devitrification layer on the inner surface of the crucible.

The growth rate for silicon is around 6 cm/h, and the power consumption is

around 70 kW for the growth of 8 to 12-in ingot. However, for PV applications which mostly uses 6-in diameter ingot reduce the cost, the hot zone design for higher pulling speeds and lower power consumption is important (Huang et al., 2004). Besides the thermal shield, an additional cooling ring could be added to enhance the growth rate for solar silicon, as shown in Fig. 6(a); the average growth speed could be increased to be more than 10 cm/h. The thermal fields are shown in Fig. 6(b). As indicated by Eq. (2), to pull the crystal faster, higher thermal gradients in the solid would be necessary. For silicon growth, multiple charging is rather matured. Normally 5 crystals could be pulled from one silicon crucible. Recently, to further improve the throughput and dopant uniformity, the continuous CZ (CCZ) method had also been proposed (Wang et al., 2003; Hu, 2015). However, the key challenge is the lifetime of the silica crucible.

The diameter control during CZ silicon growth is carried out by monitoring the optical ring around the meniscus. If the crystal size is bigger than the setting point, the pulling rate is increased. On the other hand, one could also control the pulling rate by adjusting the heater power or temperature. The traditional CZ pullers usually have two PID controllers for crystal diameter and the pulling speed. Advance pullers could use heater power to control crystal diameter for a given speed. Such a control is often necessary for the growth of perfect silicon, which needs to control a precise V/G ratio near the critical value. The perfect silicon will be discussed more shortly in Sec. 4.

The CZ method is also popular for the growth of III-V semiconductors, such as GaAs and InP. To control the stoichiometry of the grown crystal, liquid-encapsulation (LEC) (Mullin et al., 1965), pressure balancing or vapor pressure–controlled (VCZ) (Rudolph and Kiessling, 2006) techniques would be necessary. The LEC was pioneered by Mullin (1998) used for the growth of GaAs and GaP crystals, where the

suppression of the volatile As and P was crucial. This technique uses an inert B_2O_3 layer floating upon the melt surface as a liquid seal. The B_2O_3 layer adheres to the grown ingot and significantly reduces the dislocation on the crystal surface. Pyrolytic boron nitride (pBN) crucibles are now often used. The heating could be either resistance or induction heating, but in the original design by Mullin et al. (1965), induction heating was adopted, while the susceptor was graphite crucible. Unlike Si, which has an optical ring around the meniscus, diameter control in III-V growth is often carried by crystal weight. For III-V, reducing dislocation density is crucial to crystal quality because their critical resolved shear stress (CRSS) is rather low, 0.3-0.5 MPa for GaAs and 0.6 MPa for InP near the melting point. Silicon is one order larger in CRSS (6-9 MPa). Moreover, the thermal conductivity of silicon is significantly larger as well, so that for the same heat flux, the temperature gradient in silicon would be smaller. On the other hand, to keep the compound from dissociation, high pressure would be needed. Especially for the growth of InP and GaP, their dissociation pressures are 27.5 and 32 atm, respectively, at their respective melting points of 1062 and 1465^{o}C. Moreover, for semi-insulation (SI) GaAs, due to the requirement of excess As, high pressure up to 100-200 atm is often adopted, the so-called high pressure LEC, so that elemental Ga and As can be used as the starting materials. Due to the excess As, the anti-site defects and their complexes lead to Fermi level pinning, so that the resistivity of the un-doped boule could have very high resistivity (10^8 ohm-cm) similar to SI materials. It is widely believed that the most dominant EL2 defect is related to As_{Ga} defects. The EL2 defect basically controls the electrical and optical properties of GaAs, and its existence makes it possible to achieve thermally stable SI GaAs, the key material in IC technology. Because high-resistivity substrates partially replace the function of the oxide in silicon devices to isolate discrete devices or layers within ICs. The SI materials could also be grown by transition metal doping,

such as Cr-doped GaAs and Fe-doped InP. Detailed discussion of the CZ growth of III-V compound crystal could be found elsewhere (Mullin, 1998; 2015).

The CZ method is also popular in the growth of oxide or halide crystals. However, for oxide growth induction heating is often adopted using radio frequency (RF). The RF is around 10 kH, and the crucible materials need to be electrically conductive. The most widely used crucible materials are precious metals, such as Pt and Ir, depending on the melting temperature. The growth rate for oxides is a about one order of magnitude lower than that for silicon being about several mm/h. Due to the high thermal gradients in the oxide crystals, to avoid the grown crystal from cracking, reduction of thermal gradients by proper thermal insulation is crucial. Similar to silicon growth, necking is also necessary for oxide growth, but getting a dislocation free crystal is not possible. For most oxide growth, the growth atmosphere is air or N_2 atmosphere. Single crystal sapphire crystals (T_m= 2050 ^oC) could also be grown by the CZ method, although nowadays the KY method is the major growth method used in the industry. Large diameter crystals up to 10 inches for blue LED substrates have been demonstrated for various growth directions, a-axis, c-axis, or even r-axis (Sarukura et al., 2015).

However, for fluoride growth, such as CaF_2, vacuum up to 10^{-4} Pa in the growth furnace is necessary; beside Ar, CF_4 is also used to control the vacancy defects. Also, the hot zone and raw material need to be dry prior to the melting process, so that CaF2 would not react with the moisture at high temperature. High performance vacuum pumps, such as a cryosorption pump, are recommended (Sarukura et al., 2015). To meet the lithography lens material applications, the grown ingot size of CaF_2 is up to 300 mm. The growth period is very long, which requires 4 days in purification and 6 days in growth and cooling. The annealing process could also take several weeks. For

optical applications, the reduction of light scattering centers is crucial, but it is particularly challenging for large crystals.

The CZ method is also widely used for the growth of $LiNbO_3$ (LN) and $LiTaO_3$ (LT) crystals for SAW filters used in smart phones. The typical boule size is about 4 inches. Furthermore, with the advance of healthcare, the X-ray computed tomography (X-ray CT) and PET have been widely used, and they use a lot of dense scintillator oxide crystals, such as bismuth germinate (BGO), cadmium tungstate (CWO), lead tungstate (PWO), cerium-doped gadolinium silicate (Ce:GSO), and cerium-doped lutetium silicate (Ce:LSO) (Melcher, 1990). It should be pointed out that Ce-doped LSO is one of the most popular crystals used in high energy physics and medical imaging societies because of its high density (7.41 g/cm^3), fast decay (40 ns), and high light output (four times as that of BGO). The melting point of LSO crystal, 2150 ^oC, is very close to the meltdown temperature of iridium crucible. By adding yttrium oxide, the melting point is reduced, which makes the crystal growth slightly easier, but the grown crystal (LYSO) has a lower energy output (Chai et al., 2003; Mao et al., 2013).

Moreover, besides silicon all the diameter control in the CZ method uses the crystal weight. Weighting the crucible is also possible, but it would be more complicated because the levitation force due to the induction and the capillary force due to the meniscus need to be taken into account (Hurle, 1993).

The KY method is named for Spyro Kyropoulos, who proposed the technique in 1926 as a method to grow brittle alkali halide and alkali earth metal crystals for optical applications (Bliss, 2005). In recent years, the KY method has become a popular technique for the growth of large sapphire crystals used for the substrates of blue GaN LEDs. As compared with the CZ method, the equipment cost for KY is much lower, and the ingot quality is better due to the much lower thermal gradients.

As shown in Fig. 4(b), because the grown crystal remains inside the crucible during crystal growth, the thermal gradient could be very small, which reduces thermal stress and thus the dislocation density. The dislocation density of the KY grown crystals is usually one or two orders in magnitude smaller than that grown by the CZ method. The use of W or Mo for the crucible, as well as the heater and thermal shields is also quit economical, especially the crucible thickness needs to be thick, more than 25 mm, for the melt of more than 500 kg. This would be too costly for Ir used by the CZ method. The photographs of a KY growth station used today and a 400 kg sapphire boule grown from the station are shown in Figs. 7(a) and (b), respectively. This technique is suitable for growing large crystals whose density is higher than the melt density. Hence, the melt level decreases with growth. Also, the resulting crystal normally has a diameter near the crucible diameter. Because the free surface is too small for gas bubbles to escape, the KY grown boules often have bubble inclusions. Although crystal pulling and rotation are not required, in practice both functions remain for industrial KY furnaces. Because of the booming of solid-state lighting, to increase the substrate size and to reduce the processing cost, the sapphire boule weight was increased rapidly from 30 kg in early 2000 to 400 kg in 2018. The bigger the crystal, the more the material could be drilled from the crystal. Because the c-axis substrates are needed for GaN LEDs, the a-axis ingots are drilled horizontally. The undrilled volume and the place containing bubbles significantly reduce the growth yield. It has been proposed to grow the c-axis by the CZ method to effectively increase the growth yield. Unfortunately, the facets on the c-axis make the CZ growth difficult and slow growth is necessary. Apparently over years of competition, the KY method seems to have won the Holy Grail in the biggest market for sapphire.

For the growth of non-congruent crystals, such as the stoichiometric LN or LT, the double-crucible (Furukawa et al., 1999) or zone-leveling CZ (Tsai et al., 2005)

method could be considered. The idea for both methods is rather simple by using a suitable non-congruent melt with continuous feeding. Moreover, for a variety of technically important materials, such as $Sr_{1-x}Ba_xNb_2O_6$ (SBN), $Pb_{1-x}Ba_xNb_2O_6$ (PBN), $BaTiO_3$, β-BaB_2O_4 (BBO), $K_2Be_2BO_3F$ (KBBF), etc., the so-called top-seeded solution growth method (TSSG) is often used. TSSG could be considered as a variant of the CZ method. The major difference is that a solution is used in TSSG instead of the melt. Extensive discussion could be found in the classic book written by Elwell and Schell (1975) for high temperature solution growth.

3.2 The Bridgman and VGF methods

The Bridgman method is one of the simplest melt growth method for bulk crystals. The schematic is shown in Fig. 8(a) for the vertical Bridgman (VB) method, where the crucible containing the molten material moves downward in a vertical two-zone furnace, having an adiabatic zone in the middle. This setup allows the material to solidify progressively from the seed end to the other. Either the crucible or the furnace can be moved to grow the crystal. The horizontal orientation is also feasible. The VGF is a variant of the VB method. As shown in Fig. 8(b), instead of moving the crucible downward, the temperature profile could be adjusted dynamically to facilitate the growth. Because of no moving parts, the growth furnace could be more compact. Nevertheless, in practice the economic design for VGF considers only for several heats, typically 4, to control the thermal gradients efficiently, mixing the crucible downward for VGF is often considered.

The crucible material is very important to the quality of the grown crystal. Besides the contamination issues, sometimes the grown crystal could stick the crucible, and this induces significant defects on the surface, even cracking. To

such a situation, suitable lining or coating would be necessary. For example, in the growth of mc-Si crystals using a silica crucible, the spray coated Si_3N_4 is used as the releasing layer. Using liquid lining, such as B_2O_3 in GaAs and InP or $CaCl_2$ in Si, could be a useful way to mitigate the sticking problem. The material having layer structures, such as pBN, could also be used for crucibles. Because the inner layer often peels off after growth, the grown crystal is protected. For III-V compound semiconductors, pBN crucibles are widely used. The pBN crucible could be used many times because only a thin layer peels from the inside wall of the crucible and seed well after each run (Moore, 1990). Pretreated fused silica crucibles, such as carbon coating, could be used for the growth of GaSb, InSb and tellurides. Glassy graphite could be considered as well.

Because the thermal gradients could be small, the thermal stress and thus the dislocation density could be reduced. As a result, the VG or VGF grown crystals usually have lower defects than those grown by the CZ methods. For 6" GaAs, the dislocation density of the VGF grown crystals is about $10^3/cm^2$, which is one order smaller than that of the CZ grown crystals. Nowadays, the VB or VGF method is widely used for the production of compound semiconductors, such as GaAs and InP single crystals for the LED substrates, wireless communication devices as well, and CdTe crystal for infrared detectors. Large CaF_2 crystals used for deep UV window have also been produced by the VB method in the industry.

The directional solidification (DS) or casting of mc-Si used in PV industry could be considered as a variant of the VG method. With the booming of the PV market, more than 4000 DS stations have been installed worldwide. especially in China. In 2017, more than 150,000 t mc-Si were produced, and this makes the mc-Si the biggest commodity in the crystal growth industry. The schematic of a normal DS silicon ingot growth is shown in Fig. 9(a). The hot zone in the DS, with

the moving insulation basket and the heat exchange graphite block, is designed to melt silicon and to control its solidification in the upward direction with a planar growth front. Meanwhile, the growth is at a reduced pressure (~0.6 atm) flushed with argon to protect the hot zone, mainly made of graphite, from oxidation. The crucible spray-coated with Si_3N_4 is placed upon a graphite block, which is cooled by thermal radiation as the insulation basket, made of graphite felt, moves upwards; the growth rate in industry is at around 1 cm/h. In a typical production procedure, solar-grade polysilicon as well as the doping material is loaded in the quartz crucible, and then covered with a graphite plate. The cover plate, as shown in Fig. 9(a), having argon flushing is important in the control of impurities, particularly carbon. During crystal growth, flushing argon, through the hole of the cover plate, is to carry away SiO evaporated from the melt; SiO is due to the reaction of silicon melt and the silica crucible. Nowadays, a normal silicon charge per run for a G6 furnace used in production is around 800 kg; a G6 ingot could be cut into 6×6 bricks for wafer slicing (156mm×156mm in size for a standard solar cell). Recently, a charge of 2 t for G8 furnaces has also been adopted in production. Fig. 9(b) is a photograph showing the comparison of G5 and G8 ingots. The whole growth cycle for a G6 ingot takes about 70 h including the meltdown, crystal growth (30– 40 h), annealing, and cooling down procedures. Up to now, pretty much all the mc-Si wafers available in the market are boron-doped, i.e., p-type. The resistivity of the wafers ranges from 1.2 (top) to 1.8 Ω-cm (bottom). For a G6 ingot, the growth yield is around 70%, after cutting off the red zone, i.e., the area in the edges having low minority lifetime due to the contamination from the coating/crucible, as well as the area near the top surface due to the segregation of impurities. About 30,000 wafers, 180 μm thick, could be sliced from a G6 ingot. In other words, a G6 furnace could produce more than

3-million wafers per year, which corresponds to about 13 MW in terms of solar cell power output. The high throughput, 8 times higher than a normal CZ growth, and the nearly automatic growth give the DS technology a cost effective solution for PV silicon. In practice, using the lager furnace has several advantages. In addition to the higher throughput, the contact area per volume decreases linearly with the ingot width. As a result, the total impurities from the crucible/coating materials and thus the red zone also decrease. Moreover, most of silicon cut off from the ingot, except a small portion near the top surface, could be recycled (Lan et al., 2015; 2017).

Over the years, three major growth techniques have been developed for Si casting, namely the mono-like (Stoddard et al., 2008), the dendritc casting (Fujiwara et al., 2006), and the high-performance (HP) mc-Si (Yang et al., 2015), as summarized in Fig. 10. The mono-like method uses split mono-crystalline seeds. With a careful control of the seeding and the growth interface, more than 90% of the ingot could be mono-crystalline. The dendritic casting method imposes high undercooling during initial nucleation. The large thin dendritic crystals could be induced, so that large grains with electrically inactive $\Sigma 3$ grain boundaries could dominate for the rest of the growth. Although high-quality ingots have been demonstrated for both mono-like and dendritic casting techniques, the multiplication and propagation of dislocation clusters due to thermal stress are still very difficult to control during crystal growth, especially for industrial-scale production. As a result, the solar cells fabricated from the materials grown by both techniques have a very wide distribution in the conversion efficiency, and the low-efficiency tail in the distribution causes significant yield loss in the cell production. Surprisingly, if the growth started with small grains having a lot of random grain boundaries, the grown ingot

turned out to have a much better uniformity, and quality as well (Yang et al., 2015). The defect multiplication and propagation were significantly mitigated. Figure 11 shows the lifetime mappings from the G5 ingots grown by the conventional mc-Si, mono-like, and HP mc-Si casting, respectively. As shown, the lifetime mapping from the HP mc-Si is very uniform. For the others, lifetime is deteriorated due to the multiplication of dislocation clusters. Even for mono-like ingot, the defects from the seed junctions multiplies quickly, and the average lifetime turns out to be the worst among the three ingots. For HP mc-Si casting, to get the small grains at the beginning, one could use silicon particles as seeds or use nucleation agents to induce small-grain nucleation. This approach has been widely adopted by industry since its invention in 2011 (Lan et al, 2011).

The control of the growth interface to be slightly convex to prevent the parasitic nucleation from the crucible is crucial to the VB/VGF method. It is the same for mono-like Si casting. For most cases, pushing the growth interface toward the hot zone, either by reducing the hot zone or cold zone temperature, is the easiest way to get the desired interface shape. However, in some cases due to the high crucible thermal conductivity, convection, or solutal effect, such as in the case of $Zn_xCd_{1-x}Te$, as well as the conical part during seeding, the situations could be more complicated (Derby and Yeckel, 2015). Twinning is a common phenomenon that causes significant yield loss for III-V (Amon et al., 1998) and mono-like Si growth (Trempa et al., 2012) . It will be discussed more shortly in Section 5.

3.3 FZ/ZM method

In the FZ technique, a molten zone is maintained by the surface tension between two solid rods, as illustrated in Fig. 12(a). By moving the heater upward

or down ward, the crystal could grow. A single crystal seed is often necessary. Depending on the materials, various heating approaches, such as e-beam, laser, focused lamp, and induction, could be considered. For oxides, the optical heating is a convenient one, as shown in Fig. 12 (b) for the growth of a rutile crystal using an ellipsoid mirror furnace. Because it is a crucible-free process, the contamination from the crucible could be removed. Moreover, because the molten zone is small, a steady-state growth, as well as an axial composition uniformity, could be reached quickly. The FZ method could also be applied for the growth of incongruently melting materials by replacing the molten zone with a solvent material, i.e., the so-called traveling solvent floating zone (TSFZ) technique. In this technique, the chosen of solvent materials is from the corresponding phase diagram. Besides silicon, the FZ grown crystals are small, and the grown diameter is usually less than 1 cm because it is difficult to maintain a large stable molten zone. The laser heated pedestal growth (LHPG) method is also a variant of the FZ method. The LHPG method is suitable for fiber crystals. Because of the high thermal gradients, the CS could be reduced making the method suitable for searching new crystals having complicated compositions. Interestingly, although the molten zone is small, due to the Marangoni flow the convection or mixing inside the small zone is quite intense (Lan and Kou, 1991). Detailed review of the FZ growth of oxides and metallic alloys could be found elsewhere (Dabkowska et al., 2015). The ZM technique with crucible, either vertical or horizontal, was originally proposed by Pfann (1952) for materials refining. The method could also be used for growing single crystals, and more discussion could be found elsewhere (Pfann, 1958).

For silicon, the needle-eye configuration using RF induction heating with a

frequency of 2-3 MHz is used, as shown in Fig, 12(c). In the needle-eye technique, the shape of the molten zone is stabilized by the electromagnetic forces generated by the specially shaped induction coil (Keller and Mühlbauer, 1982). The silicon crystals produced by this FZ technique could have a diameter of up to 200 mm having extremely low oxygen content (less than 1 ppma). Such pure silicon substrates are suitable for power devices. The low-oxygen wafers are also particularly favored for high efficiency solar cells because the light-reduced degradation (LID) caused by the B-O pairs is greatly reduced. On the other hand, because of not enough oxygen to strengthen the ingot, nitrogen doping is often necessary. Moreover, due to the high thermal gradient, the pulling speed of FZ is the highest among all growth methods, up to 180-300 mm/h, but the power consumption is the highest as well. More skillful operation would be needed. Although the consumables for FZ are less, the feed rod for FZ is costly. Dold (2015) have recently proposed a new feed rod obtained from fast-pulled CZ ingots, and the technology seems to be promising for PV applications. More discussion could be found elsewhere (Keller and Mühlbauer, 1982; Dold, 2015; Muiznieks et al., 2015).

4. FLOW AND SEGREGATION CONTROL

4.1 Magnetic fields

In mass production, as the melt mass increases, the buoyancy force increases. Even the natural convection induced by the buoyancy force could lead to turbulent flow that causes growth striations, as a result of compositional micro-inhomogeneities. For CZ Si growth, this is particularly important, and the most effective way to suppress the turbulent flow is through magnetic fields, which apply only for electrically conductive materials. In the CZ growth of 400-mm silicon crystals during the Japanese “Super Silicon” project, the strong

turbulent flows, arising within melt volumes of more than 400 kg, could be suppressed by a superconducting magnet having field strengths above 0.35 T (Shiraishi et al., 2001). Three typical configurations, namely axial, transversal, and cusp fields, have been used. The cusp configuration was proposed by Series (1989) and Hirata and Hoshikawa (1989) independently. This magnetic field provides an essential radial field near the crystal-melt interface but an axial one deep in the melt. The axisymmetry of the system is preserved. Such a configuration is realized by using a pair of Helmholtz coils operated in the opposed current mode.

The transversal or horizontal magnetic field has been widely used for the growth of low oxygen silicon, down to several ppma. Although the horizontal field gives non-axisymmetric temperature and velocity fields, but still remains two-fold symmetry. Interestingly, the convection on the plane parallel to the magnetic field is suppressed, but not on the perpendicular plane due to the non-conducting silica crucible. As shown in Fig. 13(a), the downward Lorentz force, i.e., $\mathbf{J}\times\mathbf{v}$, where $\mathbf{J}$ is the current density vector, damps the upward buoyancy force on the parallel plane, but $\mathbf{J}$ vanishes near the crucible on the perpendicular plane. As a result, two flow loops on the x-z plane remain. Because of the asymmetric heat flow, crystal rotation is necessary to keep an axisymmetric growth interface. Three-dimensional simulation of the transversal magnetic CZ Si growth has also been carried out for 12-in CZ Si growth (Tokotama et al., 2017), and the simulated flow fields are shown in Fig. 13(b) for the case of no rotation. As shown, the flow structure is consistent with the theoretical analysis. In addition, because the convection near the silica crucible on the parallel plane is damped by the magnetic fields, the oxygen dissolution becomes rather sensitive to crucible rotation. Therefore, as the magnetic field is applied, the crucible

rotation speed needs to be as low as possible for low oxygen silicon. Detailed discussion of using magnetic fields in crystal growth could be found elsewhere (Series and Hurle, 1991; Rudolph and Kakimoto, 2009; Kakimoto and Gao, 2015; Vizman, 2015).

Besides the static magnetic field, time-dependent magnetic fields are also useful in flow control. A few configurations have been proposed for crystal growth, such as the rotating magnetic fields, alternating (pulsing) magnetic fields, or traveling magnetic fields (TMFs), etc. Recently, the combined internal heater magnet modules for simultaneous generation of heat and TMFs have been developed and have been tested successfully for LEC and VGF growth of GaAs and Ge crystals (Rudolph, 2008). The schematics are shown in Fig. 14(a) (Rudolph and Kakimoto, 2009). The amplitude, frequency, and phase shift of the three-phase current are all adjustable and combined with a direct current component to control the crystal growth. In the VGF growth of 4-in Ge crystals, as shown in Fig. 14(b), nearly microstriation-free structures were obtained. The unfavorable concave interface shape, known from the standard VGF process without the magnetic field, could be made flat or even slightly convex with the TMF module (Rudolph and Kakimoto, 2009). A nice review of TMF and its applications was given by Peter Rudolph (2008).

4.2 Segregation control through rotation

Besides the magnetic fields, rotation could also be used for flow and segregation control. For VB/VGF growth, because of a lack of control over mixing conditions, the use of external forces is often necessary, and rotation could be a simple approach. Friedrich et al. (1996) and Wilcox et al. (1998) used the Coriolis force, in a free-swing centrifuge, to suppress the natural convection. A

magic-g level was reported at a certain rotation speed having the weakest melt convection. This was ever an active research topic for crystal growth under high gravity. However, in a later study by Lan and Tu (2001a, b), the rotation about the growth axis was found much more effective than the free-swing configuration. Figure 15(a) shows the comparison of both configurations on the flow suppression. The flow and dopant fields at the least convection condition for both configurations are shown on the right. The VB growth experiments of SCN doped with 0.07wt% acetone on a rotating table also verified this view point (Lan et al., 2002), as shown in Fig. 15(b). As shown, with a sufficient rotation speed at 200 rpm, the acetone was pushed outward to the outer edge of the interface, and the growth interface remained smooth. No morphological breakdown was observed. More detailed discussion could be found in my review article (Lan, 2004).

Beside steady rotation, time-dependent rotation is also a useful technique for flow and segregation control. Scheel and Schulz-DuBois (1971) proposed an accelerated crucible rotation technique (ACRT) to control the melt mixing. By controlling the acceleration cycle, it is possible to control the melt mixing at either an enhanced mixing or diffusion-limited mode. The effects of ACRT also depend on the ratio of the melt depth to the size of Ekman cells, on the buoyancy convection, and on the vortices that sometimes form due to the Taylor–Gortler instability near the ampoule wall (Brice, 1986; Capper et al., 1984). Figure 16(a) shows the flow pattern during spin up (left) and spin down; the Taylor–Gortler cells near the ampoule wall during spin down are shown (Capper et al., 1984). Particularly, ACRT is believed to be useful for the VB growth of ZnCdTe and has attracted extensive discussion (Capper et al., 1984; 1988; Coates et al., 1989).

Both the rotation cycle pattern and the period are critical to the flow control. Again, let's take VB SCN as an example again. The ACRT cycle pattern is shown in Fig. 16(b) (top), and some instantaneous flow patterns and acetone concentrations corresponding to the stages A, B, and C in the ACRT pattern are shown in Fig. 16(b). The spin-up flows at A and B near the interface are counterclockwise in direction. The spin-down flow at C is in the opposite flow direction. The acetone fields are significantly affected by the instantaneous flow as well. Similarly, the isotherms (not shown here) near the interface are found to be distorted toward the center of the interface. As a result, the interface becomes significantly concave at 60 rpm (Liu et al., 2007). Although the interface is rather concave, no morphological breakdown was observed; pit formation and morphological breakdown without ACRT are shown the left photograph of Fig. 16(b). The ACRT pattern could also be modified for better flow and interface control. Figure 17 shows the flow and acetone concentration fields, as well as the growth interface for two different ACRT cycle patterns; the amplitude is 60 RPM and period 24 s (Liu et al., 2007b). As shown, the triangular pulse pattern (Fig. 17(b)) gives a flatter interface than that by the trapezoidal pattern. Again, no morphological breakdown was observed for both cases. The simulated results predicted well the observed interface shapes.

The ACRT mentioned previously usually requires a rotation cycle having a period long enough to develop Ekman flows. The Ekman time scale can be estimated by $R_c / \sqrt{\Omega \nu}$, where R_c is the crystal radius, Ω is the rotation speed, and ν is the kinematic viscosity of the melt. For the growth of SCN in small to medium VB systems, the Ekman time scale is up to a few seconds. An alternative approach to applying ACRT is to use a cycle time that is much shorter than the

Ekman time constant. This method is known as the angular vibration technique (AVT) (Yu et al., 2004). In this technique the ampoule is vibrated at a frequency greater than 1 Hz in the rotational direction to generate a radial outward Schlichting flow near the growth front. In addition to SCN, the technique was also applied to Ga-doped Ge growth and showed better control on the radial dopant segregation without enhancing the global mixing. Moreover, a problem due to ACRT is the oscillatory growth speed. Sometimes, remelting could occur when ACRT is applied during crystal growth, and this could induce growth striations. On the contrary, due to the much shorter period, angular vibration significantly mitigates this issue.

The vibrating submerged disk could also be used to control the segregation and the interface shape (Fedyushkin et al., 2005). The frequency is usually high at 50 Hz or more. Ultrasonic vibration in the range from kHz to MHz has also been used for the CZ growth of semiconductors, such as GaAs, BiSb, InSb and GaAs (Kozhemyakin, 1992; 2016).

5. DEFECT FORMATION AND CONTROL

5.1 Point defects

Imperfections in the grown crystal include point defects, impurity, dislocations, grain boundaries, second-phase and foreign particles, twins, and so on. Dopant, oxygen, and structure inhomogeneities due to interface concavity, convection, segregation, or constitutional supercooling are also detrimental to applications, but they are usually not considered as the intrinsic structure defects. Nevertheless, both should be minimized during crystal growth.

Some defect types, such as point defects, are due to thermodynamic equilibrium and they cannot be removed. For silicon, the type of point defects,

either vacancies or interstitials, and their clusters are crucial. The defect type depends on V/G as explained in the famous Voronkov theory (Voronkov, 1982), where V is the growth speed and G the thermal gradient at the interface. There exists a critical value $(V/G)_c$ at 1.34x10^{-3} cm^2 K^{-1}min^{-1}. If V/G is greater than this value, the grown crystal is vacancy rich. Otherwise, it is interstitial rich. During cooling down of the growing crystal, the aggregation and incorporation of excess vacancies form voids or the so-called D defects, while A- and B-swirl defects are the clusters of interstitials. It needs to be pointed out that the interstitial aggregates first form stacking faults (SFs). If the SFs reach a critical size, the strain exerted on the crystal lattice is relaxed by the generation of dislocation loops of several micrometers in size around the SF. The dislocation loops are the A-swirl or L-pit. The B-swirl defects are also self-interstitial clusters but with a smaller size. The A-swirl/L-pit defects are extremely stable and cannot be destroyed by high-temperature processes, while B-swirl defects can be dissolved during annealing at temperatures above 1000 ^{o}C. The voids, or the so-called COPs (crystal originated pits), are bounded by (111) planes and usually exhibit an octahedral shape. Compared to A-swirl/L-pit defects, they are considerably smaller (70-150 nm). Nevertheless, in the device design rules well below 100 nm, the voids could affect the device performance (Ammon, 2004; Friedrich et al., 2015). In fact, the design rule nowadays has down to 10 nm, the number of COPs greater than 50 nm needs to be strictly controlled.

Indeed, silicon shows a very peculiar behavior, which is due to the coexistence of both types of intrinsic point defects at the crystallization temperature, and due to the relative values of their equilibrium concentrations ($C_{Ve} > C_{Ie}$) and the diffusivities ($D_I > D_V$); $D_I C_{Ie} > D_V C_{Ve}$. At high pulling rates, the convective transport (VC_V) dominates, so that vacancies become richer. On the

other hand, the diffusion flux favors the self-interstitial transport, because $D_I > D_V$. Also, this flux is inversely proportional to the characteristic recombination length L, which is inversely proportional to the thermal gradient G. Therefore, the diffusion flux is proportional to G, so that the higher G favors the transport of self-interstitials. As a result, the type and concentration of defects incorporated into the growing crystals are control by the ratio V/G, i.e,., high (V/G) prefers vacancies (Voronkov et al., 2011).

Moreover, because the axial and radial variation of V and G, the wafer sliced from a crystal may contain both V- and I-type regions, having a well-defined defect-free boundary (V/I boundary) in between. The V-type region contains D defects, while the I-region contains A/B defects. The featureless gap in between has insufficient point defects to form the detectable aggregates. An example is shown in Figure 18(a). This pattern was revealed by copper decoration followed by etching; the V core is seen as the milky region surrounded by a black ring. The A/B defects are dislocation loops and are detrimental for the devices, especially since they cause dislocations during epitaxy. The voids are of much smaller in size down to nanometers, and they are either more tolerated or could be mitigated by annealing (~1200 ^{o}C for 2 h). Through epitaxy growth of a thin layer silicon on the fast pulled nitrogen-doped void-rich wafer, the so-called “flash! wafer”, is a low-cost approach for the perfect silicon, i.e., about 10 μm in depth for the defect free region. On the other hand, bulk micro defects (BMDs) of about $10^9/cm^3$ would be necessary for internal gettering of metallic impurities and the mechanical strength for high temperature processing (Donberger et al., 2001).

The growth of a perfect silicon at the condition near $(V/G)_c$ is rather challenging. In order to have a sufficient growth speed for throughput, a high thermal gradient would be necessary. Using a thermal shield with a cooling tube

has been adopted in industry. However, in such a process, the pulling rate needs to be kept at a certain value, and the diameter control is carried out through heater power. For 12-in silicon growth, the time lag of more than 20 min caused by the large thermal mass, makes the diameter control through the heater power very difficult. Nevertheless, this has been conquered in mass production.

For the growth of compound semiconductor materials, in situ control of stoichiometry is crucial to control anti-site defects. The melt composition needs to be controlled by partial pressure of the volatile element. For example, the in situ control of stoichiometry could be achieved in GaAs by the VCZ technique (Neubert and Rudolph, 2001; Neubert et al., 2008). The SI GaAs grown by the excess of As is a good example.

5.2 Voids and oxide precipitates

As the vacancies are excess, during cooling of the growing crystal, the supersaturated vacancy solution forms small vacancy clusters (or aggregates) of the lowest energy in the form of octahedral voids. There exists a temperature front for nucleation, around 1100 ^{o}C, as shown in Fig. 18(b). In CZ silicon, there is also a competing aggregation path through the joint aggregation of vacancies and oxygen atoms into small silicon dioxide particles (Voronkov et al., 2012). Because silicon dioxide is about twice as large as silicon, oxide particles cannot be formed without absorbing vacancies. In the presence of vacancies, the volume misfit is accommodated by adding vacancies to the growing oxide particles. At the same time, a reduction in the free energy is achieved due to removal of vacancies from the supersaturated solid solution. Thus, the oxide particles produced during crystal growth can be seen as a type of V aggregates.

The nucleation rate of voids is controlled by vacancy supersaturation, while

the nucleation rate of oxide particles is controlled by both vacancy supersaturation and oxygen supersaturation. At a higher C_V, the void nucleation dominates, and the microdefects are almost exclusively voids; the nucleation temperature is around 1100 ^oC, i.e., the nucleation front in Fig. 18(b). At a lower C_V, however, the oxide nucleation becomes dominant, since it requires oxygen supersaturation. As a result, most vacancies are consumed on the production of oxide particles there. Voids coexist with oxide particles at an intermediate C_V., termed the H band, as shown in Fig. 18(a). This competition between two types of vacancy clusters, voids and oxide particles, leads to a peculiar microdefect pattern within a V region of a crystal. Inside this region (corresponding to a high pre-aggregation C_V), voids are present, while at the edge of the V region (corresponding to a low pre-aggregation C_V), there is a narrow band populate with oxide particles, termed the P band. At still lower pre-aggregation C_V, a specific band of smaller, but much more numerous, oxide particles resides; this one is termed the L band, or the V perfect band, since the local oxide particles are too small to be harmful. The residual vacancies in the P band are the least, as compared with the H and L bands; the P band is in between. A peculiarity of the L band is that after annealing at a not too high temperature, say 800^oC (to prevent dissolution of small oxide particles), it exhibits a heavier oxygen precipitation compared to the neighboring P band containing larger but less numerous oxide particles. The wafer after Cu decoration in Fig. 18(a) shows the distribution of different regions, where the P and L (V perfect) bands are between the H band and I perfect band (Voronkov et al., 2012).

The existence of a P band, having large oxide particles, leads to a well-known phenomenon of the formation of a narrow ring of SFs in oxidized wafers, the so-called oxidation-induced stacking fault (OSF) ring (Dornberger and von

Ammon, 1996). The reason for the OSF ring appears in the P band is because relatively large oxide particles of the P band serve as heterogeneous sites for the precipitation of oxidation-induced self-interstitials in the form of SFs. In this way, the marginal P band of a vacancy region is decorated by SFs, and it is clearly revealed. The OSF ring, when located well inside a wafer, marks the V/I boundary; but it is only an approximate marking, since the true V/I boundary is separated from the OSF ring (P band) by a marginal L band that may be quite wide (Voronkov et al., 2012).

In addition, oxygen can form the so-called thermal donors during crystal growth in the temperature range of 300–500 ^{o}C (most pronounced near 450 ^{o}C). Depending on the oxygen content, the concentration of these donors can reach more than $10^{16}/cm^{3}$, which corresponds to a resistivity of 0.5 Ω-cm (Zulehner and Huber, 1982). Near the seed end as compared to the tail end, the thermal donors are more profound because the seed end has higher oxygen content and the longer exposure time to 450 ^{o}C The thermal donors can be easily destroyed by annealing above 500 ^{o}C and subsequent rapid cooling to temperatures below 300 ^{o}C (Friedrich et al., 2015). New donors could also form in the presence of carbon.

5.3 Twinning

Twinning is often observed in the CZ and VGF growth of zincblende crystals through its nucleation from (111) facets adjacent to the three-phase boundary (TPB) of melt, crystal, and ambient (Hurle, 1995). As shown in Fig. 19(a), the twins, the bands on the left ingot, could be easily seen from the appearance of the grown crystal. By controlling the crucible shape, twinning might be mitigated. As pointed out by Hurle (1995), there exists a certain orientation relationship that the free energy of

formation is reduced by forming a twin nucleus at the TPB. In other words, twinning only occurs at the TPB under certain conditions. Identifying the angle ν between the facet and the crystal surface, as shown in Fig. 19(b) for the growth of (100) InP, there is a range of $\nu_{min} < \nu < \nu_{max}$ for twinning, where ν_{min} and ν_{max} are material dependent values. For example, for GaAs and InP, ν_{min} = 30 and 31^o and ν_{max} = 104 and 112^o, respectively (Chung et al., 1998).

Inside $\nu_{min} < \nu < \nu_{max}$, the facet nucleus attaching to the TPB is energetically favorable, but it still requires a certain degree of undercooling. This is the reason that the faceted interface deviates from the rough growth interface at the freezing temperature. For twinning, the formation free energy of a truncated twin nucleus on the facet would be slightly higher by the amount of the twin energy (near SF energy) compared to a facet nucleus. As a result, the critical supercooling for twining would be higher. The twinning probability is proportional to $\exp(-\Delta G_T^* / kT)$, where ΔG_T^* is the energy barrier for twinning. For InP growth shown in Fig. 19(b), the twin happens to be a twist one, i.e., through 180^o rotation on the facet plane. For the $(1\bar{1}1)$ facet, the rotation matrix or *T* matrix could be calculated as the following (Jhang et al., 2018):

$$T_{\langle 1\bar{1}1\rangle,180^o} = \frac{1}{3}\begin{bmatrix} \bar{1} & \bar{2} & 2 \\ \bar{2} & \bar{1} & \bar{2} \\ 2 & \bar{2} & \bar{1} \end{bmatrix}.$$

Therefore, for the growth in <100> direction, the twin grain has the orientation of $\langle \bar{1}\bar{2}2 \rangle$. In fact, there are 5 possible twinning operations for the cubic system (Jhang et al., 2018), but the 180^o twist twinning seems to be a common one. Amon et al. (1998) tried to control the cone angle to avoid twinning for the VGF growth of GaAs crystals. They used an angle of ν=107^o, which is greater than ν_{max}=104^o, but no $\{111\}_{Ga}$ facets

were found. In the (110) oriented cut, $\{111\}_{As}$ facets existed; however they detached from the TPB in accordance with the model, and they were replaced by $\{111\}_{Ga}$ facets at the edge of the crystal. Therefore, they concluded that twinning would still be possible. Nevertheless, the patch twins grew out and were less harmful to the yield loss. Interestingly, even so, the length of the facets decreased with the increasing cone angle. Based on Hurle's theory, using a flat bottom crucible having a seed with the same diameter would be effective to prevent twinning; the grown crystal is shown on the right of Fig. 19(a). Reducing temperature fluctuation using magnetic fields was found useful as well (Chung et al., 1998).

Twinning is also quite common in the growth of quasi-mono silicon ingot (Trempa et al., 2012). Again, the twinning occurs at the crucible wall and causes the yield loss. Based on Hurle's model, Duffar and Nadri (2010) proposed a similar model for twinning at the faceted groove during solidification of mc-Si. This model was revised by Lin and Lan (2017). Jain et al. (2018) and Jhang et al. (2019) further extended the model to three-grain tri-junctions and the tri-junction in contact with wall or gases, respectively. For mc-Si growth, the twinning may not be harmful, but the coherent grain boundaries are not useful in the reduction of thermal stress. Therefore, for HP mc-Si growth, the more the random grain boundaries at the beginning, the lower the dislocation clusters in the grown ingot.

5.4 Dislocations

For melt growth, due to the requirement of thermal gradients for solidification and avoiding the CS, thermal stress is inevitable. As the thermal stress is greater than the critical resolved shear stress (CRSS), dislocations appear. The dislocation density is commonly determined by the etch pit density (epd) after a dislocation sensitive

etching. Nowadays, the epd of 6” VGF grown GaAs is in the order of $10^3/cm^2$, which is an order in magnitude smaller than that in the CZ grown crystals due to the much smaller thermal gradients. Similarly, the epd in sapphire is also lower in KY growth compared to CZ growth. Therefore, reducing the thermal stress is the most effective way in reducing the dislocation density. On the other hand, doping, such as in Si/B- or In-doped GaAs (Birkmann et al., 2000), would also be useful due to solution hardening. Reducing native defects through in situ stoichiometric control, such as in the VCZ GaAs growth, was found useful in reducing dislocation density as well (Rudolph et al., 2005).

In the mc-Si casting for solar cells, the control of dislocation clusters is particularly important. Extensive efforts in the hot-zone design and process optimization for reducing thermal stress have been carried out (Chen el al., 2010; Fang et al., 2012; 2013). However, the progress in ingot quality was slow until the invention of HP mc-Si. The idea of the HP mc-Si technique is to initiate the growth from small and uniform grains having a high fraction of random grain boundaries. This could be achieved by either seeding with silicon particles or controlled nucleation, e.g., using nucleation agents (Yang et al., 2015; Lan et al., 2017). The grains developed from such small grain structures significantly relax thermal stress and suppress the massive generation and propagation of dislocation clusters. The gettering efficacy of HP mc-Si is also superior to the conventional one. Nowadays, most of commercial mc-Si is grown by using this approach. Further reading in defect control is referred to the review chapters by Rudolph (2010) and Klapper and Rudolph (2015).

CONCLUSIONS

In this article, we give an overall view of bulk crystal growth from the melt. We start from the short history of growth techniques and the market and applications of crystals. For better understanding of the growth techniques, some fundamentals, such as the related thermodynamics and kinetics, as well as the CS and morphological instability, are given first. Then, the three major crystal growth techniques are introduced. To better grow the crystals, the control of flow and segregations would be necessary. A few examples using magnetic fields and rotation are given. Finally, the defect generation and their control during crystal growth are further discussed. Bulk crystal growth from the melt is a big topic, and it is not possible to cover all the topics in a two-hour lecture. Therefore, the topics that I discuss here are on my personal preferences. Nevertheless, further readings are given in the references. Particularly, the Elsevier handbook of crystal growth (Nishinaga, 2015; Rudolph, 2015) pretty much provides the materials needed to understand crystal growth in general including bulk crystal growth from the melt.

REFERENCES

1. Ammon W.v., Silicon crystal growth, in Crystal Growth - from Fundamentals to Technology, G. Müller, J.-J. Métois and P. Rudolph, Eds. (2004) 239-270.

2. Amon J., Dumke F., Muller G., Influence of the crucible shape on the formation of facets and twins in the growth of GaAs by the vertical gradient freeze technique, J. Cryst Growth 187 (1998) 1-8.

3. Birkmann B., Stenzenberger J., Jurisch M., Hartwig M.J., Alex V., Muller G., Investigation of residual dislocations in VGF-grown Si-doped GaAs, Journal of Crystal Growth 276 (2005) 335–346.

4. Bliss D.F., Evolution and Application of the Kyropoulos Crystal Growth Method, in 50 Years of Progress in Crystal Growth: A Reprint Collection, Ed. R. Feigelson, Elsevier, 2005.

5. Brice J.C., Crystal Growth Processes, Wiley, New York, 1986.

6. Bridgman P.W. : Proc. Am. Acad. Arts Sci. **58**, 165 (1923)

7. Brown R.A., Theory of transport processes in single crystal growth from the melt. *AIChE J.* 1988, 34, 881-911.

8. Bruni F.J., Scheel H.J., The technology of single crystals and epitaxial layers: The case for energy, water, health, education, and security, A White Paper, 15 April 2013.

9. Burton J.A., Prim R.C., Slichter W.P. The distribution of solute in crystals grown from the melt. Part I. Theoretical. *J. Chem. Phys.*, 1953, **21** (1953) 1987-1991.

10. Capper P., Gosney J.J.G., Jones C.L., Application of the accelerated crucible rotation technique to the Bridgman growth of $Cd_xHg_{1-x}Te$: Simulations and crystal growth, J. Crystal Growth 70 (1984) 356.

11. Capper P., Brice J.C., Jones C.L., Coates W.G., Gosney J.J.G., Ard C., Kenworthy I., Interfaces and flow regimes in ACRT grown $Cd_xHg_{1-x}Te$ crystals, J. Crystal Growth 89 (1988) 171.

12. Chen X., Nakano S., Kakimoto K., Three-dimensional global analysis of thermal

stress and dislocations in a silicon ingot during a unidirectional solidification process with a square crucible, J. Crystal Growth 312 (2010) 3261-3266.

13. Chung H., Dudley M., Larson D.J., Hurle D.T.J., Bliss D.F., Prasad V., The mechanism of growth-twin formation in zincblende crystals: new insights from a study of magnetic liquid encapsulated Czochralski-grown InP single crystals, Journal of Crystal Growth 187 (1998) 9-17.

14. Coates W.G., Capper P., Jones C.L., Gosney J.J.G, Ard C.K., Kenworthy I., Clark A., Effect of ACRT rotation parameters on Bridgman grown CdxHg1−xTe crystals. J. Crystal Growth 94 (1989) 959.

15. Czochralski J., A new method for the measurement of crystallization rate of metals, Z. phys. Chem., **1918**, 92, 219-221.

16. Chai B.H.T., Yanyan Ji, Lutetium–Yttrium Orthosilicate Single Crystal Scintillator Detector, U.S. Patent No. 6,624,420 B1, 2003.

17. Dash W.C., The growth of silicon crystals free from dislocations. In R. H. Doremus, B. W. Roberts, and David Turnbull, Eds., Growth and Perfection of Crystals, John Wiley and Sons, Inc., New York, 1958, 361-385.

18. Dabkowska H.A., Dabkowski A.B., Hermann R., Priede J., Gerbeth G., Floating Zone Growth of Oxides and Metallic Alloys, in: 2nd Ed. Handbook of Crystal Growth 2A: Bulk Crystal Growth: Basic Techniques, P. Rudolph, ed., North-Holland, Amsterdam (2015), 281-330.

19. Derby J.J., Yeckel A., Heat Transfer Analysis and Design for Bulk Crystal Growth: Perspectives on the Bridgman Method, in: 2nd Ed. Handbook of Crystal Growth 2B: Bulk Crystal Growth: Growth Mechanisms and Kinetics, P. Rudolph, ed., North-Holland, Amsterdam (2015), 793-843.

20. Dold P., Chapter One - Silicon Crystallization Technologies, Semiconduct. Semimet. 92 (2015) 1-61.

21. Dornberger E., von Ammon W., The dependence of ring-like distributed stacking faults on the axial temperature gradient of growing Czochralski silicon crystals. Journal of the Electrochemical Society 143 (1996) 1648–1653.

22. Donberger E., Temmler D., von Ammon W., Defects in silicon crystals and their impact on device characteristics, Electrochemical Society Proceedings Vol. 2001-29, 35-49.

23. Duffar T., Nadri A., On the twinning occurrence in bulk semiconductor crystal growth, Scripta Mater 62 (2010) 955-960.

24. Elwell D., Scheel H.J. Crystal Growth from High Temperature Solutions, Academic Press: London, 1975.

25. Fang H.S., Wang S., Zhou L., Zhou N.G., Lin M.H., Influence of furnace design on the thermal stress during directional solidification of multicrystalline silicon, J. Crystal Growth 346 (2012) 5-11.

26. Fang H.S., Zhang Q., Pan Y., Wang S., Zhou N., Zhou L., Lin M.H., Characteristics of Thermal Stress Evolution During the Cooling Stage of Multicrystalline Silicon, Journal of Thermal Stresses, 36 (2013) 947–961.

27. Fedyushkin A., Bourago N., Polezhaev V., Zharikov E., The influence of vibration on hydrodynamics and heat-mass transfer during crystal growth, Journal of Crystal Growth 275 (2005) 1557-1563.

28. Feigelson R.S., Crystal Growth through the Ages: A Historical Perspective, in: 2nd Ed. *Handbook of Crystal Growth 1A: Fundamentals: Thermodynamics and kinetics*, T. Nishinaga, ed., North-Holland, Amsterdam (2015), 1-83.

29. Flemings M.C., *Solidification Processing*, McGraw-Hill, New York, 1974.

30. Frank-Rotsch Ch., Rudolph P., Vertical gradient freeze of 4 inch Ge crystals in a heater-magnet module, J. Cryst. Growth, 311 (2009) 2294–2299.

31. Fornari R., Comprehensive Semiconductor Science and Technology Vol. III: Materials, Preparation, and Properties, P. Bhattacharya, R. Fornari and H. Kamimura Eds., 2011.

32. Fraunhofer Photovoltaics Report, www.ise.fraunhofer.de, August 27, 2018.

33. Friedrich J., Baumgartl J., Leister J.-J., Muller G., Experimental and theoretical analysis of convection and segregation in vertical Bridgman growth under high gravity on a centrifuge, Journal of Crystal Growth 167 (1996) 45-63.

34. Friedrich J., Ammon W.v., Müller G., Czochralski Growth of Silicon Crystals, in: 2nd Ed. Handbook of Crystal Growth 2B: Bulk Crystal Growth: Basic Techniques, P. Rudolph, ed., North-Holland, Amsterdam (2015), p. 45-104.

35. Fujiwara K., Pan W., Sawada K., Tokairin M., Usami N., Nose Y., Nomura A., Shishido T., Nakajima K., Directional growth method to obtain high quality polycrystalline silicon from its melt, J. Cryst. Growth 292 (2006) 282-285.

36. Furukawa Y., Kitamura K., Suzuki E., Niwa K., Stoichiometric $LiTaO_3$ single crystal growth by double crucible Czochralski method using automatic powder supply system, Journal of Crystal Growth 197 (1999) 889—895.

37. Hansen R.L., Drafall L.E., McCutchan R.M., Holder J.D., Allen L.A., Shelley R.D., Surface-Treated Crucibles for Improved Zero Dislocation Performance, US Patent No. 5,976,247, November 1999.

38. Hirata H., Hoshikawa K., Silicon crystal growth in a cusp magnetic field, Journal of Crystal Growth 96 (1989) 747-755.

39. Huang L.I., Lee P.C., Hsieh C.K., Hsu W.C., Lan C.W. On the hot-zone design of Czochralski silicon growth for photovoltaic applications. *J. Crystal Growth*, 2004, 261 (2004) 433-443.

40. Hurle D.T.J. *Crystal Pulling from the Melt*; Springer-Verlag: Berlin, 1993.

41. Hurle D.T.J., A Mechanism for Twin Formation during Czochralski and Encapsulated Vertical Bridgman Growth of III-V Compound Semiconductors, Journal of Crystal Growth 147 (1995) 239-250.

42. Jackson K.A. Mechanism of Growth, in Liquid Metals and Solidification; American Society for Metals: Cleveland, 1958; 174.

43. Jain T., Lin H.K., Lan C.W., Twinning mechanism at three-grain tri-junction during directional solidification of multi-crystalline silicon, Acta Mater. 144 (Supplement C) (2018) 41-50.

44. Jhang J.W., Jain T., Lin H.K., Lan C.W., Possible Twinning Operations during Directional Solidification of Multicrystalline Silicon, Cryst. Growth Des. 18 (2018) 2518−2524.

45. Jhang J.W., Regula G., Reinhart G., Mangelinck-Noël N., Lan C.W., Heterogeneous Twinning during directional solidification of multi-crystalline silicon, J. Cryst. Growth, in press.

46. Jurisch M., Eichler St., Weinert B., Scheffer-Czygan M., Crystal growth by a modified vapor pressure-controlled Czochralski (VCz) technique, Journal of Crystal Growth 310 (2008) 2120-2125.

47. Jurisch M., Eichler S., Bruder M., Vertical Bridgman Growth of Binary Compound Semiconductors, in: 2nd Ed. Handbook of Crystal Growth 2A: Bulk Crystal Growth: Basic Techniques, P. Rudolph, ed., North-Holland, Amsterdam (2015), p. 331.

48. Kakimoto K., Liu L., Flow instability of silicon melt in magnetic fields, FDMP, vol.2, no.3 (2006) 167-173.

49. Kakimoto K., Gao B., Fluid dynamics: modeling and analysis, in: 2nd Ed. Handbook of Crystal Growth 2B: Bulk Crystal Growth: Growth Mechanisms and Kinetics, P. Rudolph, ed., North-Holland, Amsterdam (2015), 845-870.

50. Kasap S., Capper P. (Eds.), Springer Handbook of Electronic and Photonic Materials, Springer, 2017.

51. Keller W., Mühlbauer A. *Floating-Zone Silicon*, New York: Marcel Dekker, 1982.

52. Klapper H., Rudolphl P., Defect generation and interaction during crystal growth, in: 2nd Ed. Handbook of Crystal Growth 2B: Bulk Crystal Growth: Growth Mechanisms and Dynamics, P. Rudolph, ed., North-Holland, Amsterdam (2015) 1093-1141.

53. Kozhemyakin G.N., Kosushkin V.G., Kurochkin S.Y., Growth of GaAs crystals pulled under the presence of ultrasonic vibrations, J. Cryst. Growth 121, 240 (1992).

54. Kozhemyakin G.N., Crystal growth of BixSb1−x solid solutions with an ultrasound presence in two orthogonal directions, Cryst. Growth Des. 2016, 16, 6269−6274.

55. Kubiak K., Szeliga D., Sieniawski J., Onyszko A., The unidirectional crystallization of metals and alloys (turbine blades), in: 2nd Ed. Handbook of Crystal Growth 2B: Bulk Crystal Growth: Basic Techniques, P. Rudolph, ed., North-Holland, Amsterdam (2015) 413-457.

56. Kyropoulos S. : Z. Anorg. Chem. **154** (1926) 308.

57. Lan C.W., Kou Sindo, Heat transfer, fluid flow and interface shapes in floating-zone crystal growth, J. Cryst. Growth 108 (1991) 351-366.

58. Lan C.W., Tu C.Y., Three-dimensional analysis of heat flow, segregation, and interface shape of gradient-freeze growth in a centrifuge. Journal of Crystal Growth 226 (2001a) 406-418.

59. Lan C.W., Tu C.W., Morphological instability due to double diffusive convection in directional solidi cation: the pit formation. Journal of Crystal Growth 220 (2001b) 619-630.

60. Lan C.W., Yang Y.W., Chen H.Z., Lee I.F., Segregation and morphological instability due to double diffusive convection in rotational directional solidi cation. Metallurgy and Material Transactions A 33A (2002) 3011-3017.

61. Lan C.W., Recent progress in crystal growth modeling and growth control, Chem. Eng. Sci., 59 (2004) 1437-1457.

62. Lan C.W., Yu W.H., Yang Y.M., Chou H.S., Hsu C.L., Hsu W.C., Crystalline Silicon Ingot and Silicon Wafer Therefrom, ROC Patent TWI452185B.

63. Laudise R.A., *The Growth of Single Crystals*; Prentice-Hall; Englewood Cliffs, New Jersey, 1970.

64. Lin H.K., Lan C.W., Revisiting the twinning mechanism in directional solidification of multi-crystalline silicon sheet, Acta Mater. 131 (2017) 1-10.

65. Lin H.K., Lan C.W., A multilayer nucleation model for twinning during directional solidification of multi-crystalline silicon, J. Cryst. Growth 478 (2017) 47-51.

66. Liu X., Jie W., Zhou Y., Numerical analysis of $Cd_{1-x}Zn_xTe$ crystal growth by the vertical Bridgman method using the accelerated crucible rotation technique, J.

Crystal Growth 219 (2000) 22.

67. Liu X., Jie W., Zhou Y., Numerical analysis on Hg1−xCdxTe growth by ACRT-VBM, J. Cryst. Growth 209 (2000) 751.

68. Liu Y.C., Roux B., Lan C.W., Effects of accelerated crucible rotation on segregation and interface morphology for vertical Bridgman crystal growth: Visualization and simulation, Journal of Cryst. Growth 304 (2007a) 236–243.

69. Liu, Y.C., Roux B., Lan C.W., Effects of cycle patterns of accelerated crucible rotation technique (ACRT) on the flows, interface, and segregation in vertical Bridgman crystal growth, International Journal of Heat and Mass Transfer 50 (2007b) 5031–5040.

70. Mao R., Wu C., Dai L.N., Lu S., Crystal growth and scintillation properties of LSO and LYSO crystals, Journal of Cryst. Growth 368 (2013) 97–100.

71. Markov, I.V., *Crystal Growth for Beginners: Fundamentals of Nucleation, Crystal Growth and Epitaxy*; World Scientific: Singapore, 1995.

72. Melcher C.L., Lutetium Orthosilicate Single Crystal Scintillator Detector, U.S. Patent No. 4,958,080, 1990.

73. Moore A.W., Characterization of pyrolytic boron nitride for semiconductor materials processing, Journal of Crystal Growth 106 (1990) 6-15.

74. Muiznieks A., Virbulis J., Lüdge A., Riemann H., Werner N., Floating Zone Growth of Silicon, in: 2nd Ed. Handbook of Crystal Growth 2A: Bulk Crystal Growth: Basic Techniques, P. Rudolph, ed., North-Holland, Amsterdam (2015) 241-280.

75. Mullin, J.B., Straughan B.W., Brickell W.S., Liquid encapsulation techniques: The use of an inert liquid in suppressing dissociation during the melt-growth of InAs and GaAs, J. Phys. Chem. Solids 26 (1965) :782–784.

76. Mullin J.B.: Compound semiconductor processing. In: *Compound Semiconductor Devices: Structures and Processing*, ed. by K.A. Jackson (Wiley, Weinheim 1998) p. 1.

77. Mullin J.B., Liquid Encapsulation and Related Technologies for the Czochralski

Growth of Semiconductor Compounds, in: 2nd Ed. Handbook of Crystal Growth 2A: Bulk Crystal Growth: Basic Techniques, P. Rudolph, ed., North-Holland, Amsterdam (2015), 105-130.

78. Mullin W.L., Sekerka R.F., Stability of a Planar Interface During Solidification of a Dilute Binary Alloy J. Appl. Phys. 35 (1964) 444-451.

79. Nishinaga T. (Ed.), *Handbook of Crystal Growth 1A: Fundamentals: Thermodynamics and kinetics*, North-Holland, Amsterdam (2015).

80. Neubert M., Rudolph P., Progress in crystal growth and characterization; 2001. p. 119–185.

81. Neubert M., Rudolph P., Frank-Rotsch Ch., Czupalla M., Trompa K., Pietsch M., Ostrogorsky A.G., Glicksman M.E., Segregation and Component Distribution, in: 2nd Ed. Handbook of Crystal Growth 2B: Bulk Crystal Growth: Growth Mechanisms and Dynamics, P. Rudolph, ed., North-Holland, Amsterdam (2015), p. 995-1047.

82. Pfann, W.G.: Trans. AIME **194**, 747 (1952).

83. Pfann, W.G., Zone melting, Wiley 1958.

84. Pimpinelli A.; Villain, *J. Physics of Crystal Growth*; Cambridge Univ. Press: Cambridge, 1998.

85. Ramsberger H.C., Malvin E.H.: J. Opt. Soc. Am. 15 (1927) 359.

86. Rudolph, P., Jurisch M., Bulk growth of GaAs: an overview. *J. Crystal Growth*, 198/199 (1999) 325–335.

87. Rudolph P., Frank-Rotsch Ch., Juda U., Kiessling F.-M., Scaling of dislocation cells in GaAs crystals by global numeric simulation and their restraint by in situ control of stoichiometry, Materials Science and Engineering A 400–401 (2005) 170–174.

88. Rudolph P., Kiessling F.-M., Growth and characterization of GaAs crystals produced by the VCz method without boric oxide encapsulation, Journal of Cryst. Growth 292 (2006) 532–537.

89. Rudolph P., Travelling magnetic fields applied to bulk crystal growth from the melt: The step from basic research to industrial scale, Journal of Crystal Growth 310 (2008) 1298–1306.

90. Rudolph P., Kakimoto K., Crystal Growth from the Melt under External Force Fields, MRS Bulletin, 34 (2009) 251-258.

91. Rudolph P. (Ed), *Handbook of Crystal Growth 2A: Bulk Crystal Growth: Basic Techniques*, P. Rudolph, ed., North-Holland, Amsterdam (2015).

92. Rutter J.W., Chalmers B. A prismatic substructure formed during solidification of metals, Canad. J. Phys., 31 (1953) 15.

93. Sarukura N., Nawata T., Ishibashi H., Ishii M., Fukuda T., Czochralski Growth of Oxides and Fluorides, in: 2nd Ed. *Handbook of Crystal Growth 2A: Bulk Crystal Growth: Basic Techniques*, P. Rudolph, ed., North-Holland, Amsterdam (2015), p. 373.

94. Kasap S., Capper, P. Eds., Springer Handbook of Electronic and Photonic Materials, 2nd Ed., Springer, 2017.

95. Scheel H.J., Schulz-Dubois E.O., Flux growth of large crystals by accelerated crucible rotation technique, J. Crystal Growth 8 (1971) 304.

96. Scheel, H.J. Chapter 1: Historical Introduction, In *Handbook of Crystal Growth 1a: Thermodynamics and Kinetics*; Hurle, D.T.J. Eds.; North-Holland: Amsterdam, 1994; 1-42.

97. Scheel H.J., Historical aspects of crystal growth technology, J. Crystal Growth 275 (2000) 1-12.

98. Scheel H.J. Chapter 1: The development of crystal growth technology, In *Crystal Growth Technology*; Scheel H.J; Fukuda, T. Eds.; John Wiley & Sons: New York, 2003.

99. Scheel H.J., Crystal growth technology CGT for energy: saving energy and renewable energy, J. Crystal Growth 275 (2005) 331-337.

100. Sekerka R.F., A Stability Function for Explicit Evaluation of the Mullins-Sekerka Interface Stability Criterion, Journal of Applied Physics 36

(1965) 264-267.

101. Series R.W., Effect of a shaped magnetic field on Czochralski silicon growth, Journal of Crystal Growth 97 (1989) 92-98.

102. Series R.W., Hurle D.T.J., The use of magnetic fields in semiconductor crystal growth, Journal of Crystal Growth 113(1991) 305-328.

103. Shih C.J., Hsu W.T., Lan C.W., Morphological transitions of shallow cells during thin-film solidification of an alloy: phase field modeling & experimental observation, J. of Chinese Institute of Chemical Engineers 36 (2005) 311-320.

104. Shiraishi Y., Takano K., Matsubara J., Iida T., Takase N., Machida N., Kuramoto M., Yamagishi H., Growth of silicon crystal with a diameter of 400 mm and weight of 400 kg, J. Cryst. Growth 229 (2001) 17-21.

105. Stockmeier L., Kranert C., Raming G., Miller A., Reimann C., Rudolph P., Friedrich J., Edge facet dynamics during the growth of heavily doped n-type silicon by the Czochralski method, Journal of Crystal Growth 491 (2018) 57–65.

106. Stoddard N., Wu B., Witting I., Wagener M., Park Y., Rozgonyi G., Clark R., Casting single crystal silicon: novel defect profiles from BP Solar′s Mono 2 wafers, Solid State Phenom. 1 (2008) 131-133.

107. Teal G..K., Little J.B., Growth of germanium single crystals, Phys. Rev. 78 (1950) 647.

108. TECHCET Critical Materials Report, “Silicon Wafers Market & Supply-Chain, 2018.

109. Theurer H.C.: Method of Processing Semiconductor Materials, US Patent (Application) 3 060 123 (1952)

110. Tiller W.A., Jackson K.A., Rutter J.W., Chalmers B., The redistribution of solute atoms during the solidification of metals. *Acta Metall*., 1 (1953) 428-437.

111. Trempa M., Reimann C., Friedrich J., Muller G., Oriwol D. Mono-crystalline growth in directional solidification of silicon with different orientation and splitting of seed crystals. J. Cryst. Growth 351 (2012) 131-140.

112. Tsai C.B., Hsia Y.T., Shih M.D., Tai C.Y., Hsieh C.K., Lan C.W., Zone-levelling Czochralski growth of MgO-doped near-stoichiometric lithium niobate single crystals, Journal of Crystal Growth 275 (2005) 504–511.

113. Verneuil A.V. L.: Compt. Rend. 135, 791 (1902).

114. Vizman D., Flow control by magnetic fields during crystal growth from melt, in: 2nd Ed. Handbook of Crystal Growth 2B: Bulk Crystal Growth: Growth Mechanisms and Kinetics, P. Rudolph, ed., North-Holland, Amsterdam (2015), 909-950.

115. Voronkov V.V., Supercooling at a facet located at a curved crystal–melt interface. Soviet Physics: Crystallography 17 (1973) 807–814.

116. Voronkov V.V., The mechanism of swirl defects formation in silicon, Journal of Crystal Growth 59 (1982) 625-643.

117. Voronkov V.V., Dai B., Kulkarni M.S., Fundamentals and Engineering of the Czochralski Growth of Semiconductor Silicon Crystals, In book: Comprehensive Semiconductor Science and Technology, Vol. III, pp.81-169.

118. Wang C., Zhang H., Wang T.H., Ciszek T.F., A continuous Czochralski silicon crystal growth system, J. Cryst. Growth 250 (2003) 209–214.

119. Warren J.A., Langer J.S. Prediction of dendritic spacings in a directional-solidification experiment. *Phys. Rev. E,* 1993, 47, 2702-2712.

120. Wilcox W.R., Regel L.L., Arnold W.A., Convection and segregation during vertical Bridgman growth with centrifugation, Journal of Crystal Growth 187 (1998) 543-558.

121. Xu H., Characterization of n-type mono-crystalline silicon ingots produced by continuous Czochralski (Cz) Technology, Energy Procedia 77 (2015) 658 – 664.

122. Yokoyama R., Nakamura T., Fujiwara T., Hamaogi K., Takatani K., Fully three dimensional numerical analysis of industrial scale silicon Czochralski growth with a transverse magnetic field, Journal of Crystal Growth 468 (2017) 905-908.

123. Yu W.C., Chen Z.B., Hsu W.T., Roux B., Lyubimova T.P., Lan C.W., Reversing radial segregation and suppressing morphological instability during Bridgman

crystal growth by angular vibration, Journal of Crystal Growth 271 (2004) 474–480.

124. Zulehner W, Huber D., Czochralski-Grown Silicon, Crystals, vol. 8. Berlin: Springer; 1982. 1.

Table 1 Typical commercial crystals: their market share, applications, and growth methods.

Crystals (Market share %)	Examples (size)	Applications	Growth methods
Semiconductor and photovoltaics (94%)	**mc-Si (850 kg)**, Si (12 in), Ge(3 in), GaAs (8 in), InP (6 in), GaSb(2 in), GaInSb (2 in), InSb (3 in), CdTe, ZnCdTe (5 in), etc.	Integrated circuits (ICs), Transistors, Solar cells, LEDs, etc.	CZ, VG/VGF, FZ
Scintillation Crystals (2%)	$Bi_4Ge_3O_{12}$ (5.5 in), Lu_2SiO_5 (LSO), BaF_2, CaF_2, $PbWO_4$ Tl:CsI, Na:CsI, NaI, CdTe, ZnCdTe	Radiation detectors, Positron emission tomography (PET)	Cz, VB/VGF
Optical Crystals (2%)	**Sapphire (400 kg)**, CaF_2 (15 in), BaF_2, MgF_2, MgO, Quartz, Si, Ge, ZnSe, ZnS, $CaCO_3$, YVO_4, $LiNbO_3$, β-BaB_2O_4 (BBO), $Y_3Al_5O_{12}$(YAG)	Substrates, Lenses, Mirror, Prisms, Wave plate, Polarizer, etc.	KY, CZ, VG
Acoustic Crystals (1%)	$LiNbO_3$ (4 in), $LiTaO_3$(4 in), $La_3Ga_5SiO_{14}$ (4 in)	SAW filter, Sensor, etc.	CZ, VB
Nonlinear Optics & Laser Crystals (1%)	YAG, KH_2PO_4(KDP), $Bi_{12}SiO_{20}$(BSO), $KTiOAsO_4$ (KTA), β-BBO, LiB_3O_5 (LBO), $KTiOPO_4$(KTP), $AgGaS_2$, $ZnGeP_2$, Mg:$LiNbO_3$, Nd:YVO_4 Nd:YAG, Nd:$GdVO_4$ Ti:Sapphire	Laser applications, Optical communication, etc.	CZ, Solution growth
Jewelry (<1%)	Sapphire, Ruby (8 in), Amber, $MgAl_2O_4$, $CaCO_3$	Decoration, watch window.	CZ, Vernuil method

FIGURE CAPTIONS

Fig. 1 (a) Schematic of the step growth on a (111) facet having steps; (b) step growth from a screw dislocation (D); (c) photograph of a growth ridge loss which occurred during the growth of the top cone of a heavily As-doped CZ Si crystal. Reprinted from Stockmeier et al., (2017) with permission from Wiley-VCH.

Fig. 2 Axial dopant segregations, diffusive vs complete-mixing, in normal freezing.

Fig. 3 (a) Schematic of constitutional supercooling (CS); (b) an optical micrograph of the vertical wafer where cellular growth occurred due to the CS. The wafer was cut from a heavily B-doped ($5.4x10^{20}$ at/cm^3) Si CZ crystal; (c) the MS loop of 0.01 mol% acetone-doped succinonitrile (SCN); some simulated results and experimental observations are attached. The lower figure of (b) is reprinted from Taishi et al., (2000) with permission from Japan Applied Physics Society, while (c) is reprinted from Shih and Lan (2005) with permission from Elsevier.

Fig. 4 (a) Schematic of CZ crystal growth using a resistance heater; (b) Schematic of KY crystal growth.

Fig. 5 (a) The CZ puller for 8- to 12-in silicon crystal growth with a recharge tank and a cusp magnetic field; (b) a grown 12-in silicon ingot. Courtesy of Global Wafer Inc.

Fig. 6 (a) The cooling ring in a CZ puller for solar silicon; (b) simulated thermal field with the cooling ring. Courtesy of Dalian Linton NC Machine Co.

Fig. 7 (a) The KY crystal growth station for 400 kg sapphire crystals; (b) as grown 400 kg sapphire boule. Courtesy of TDG Holding Co.

Fig. 8 Schematics of (a) VB and (b) VGF crystal growth methods; the dynamic thermal profiles are shown on the right.

Fig. 9 (a) Schematic of DS growth of Si ingot; (b) photograph of G5 (left) and G8 (1340 mm×1340 mm×500 mm) ingots; courtesy of Aton Solar Technology Inc. Reprint from Lan et al. (2017) with permission from Elsevier.

Fig. 10 Schematic of different DS technologies: (a) mono-like casting using splitting seeds; (b) dendritic casting; (c) HP mc-Si. Reprint from Lan et al. (2017) with permission from Elsevier.

Fig. 11 Lifetime mappings of the G5 mc-Si ingots grown from conventional (top), mono-like, and HP mc-Si casting. Courtesy of Prof. X. Huang.

Fig. 12 (a) Schematic of the FZ method; (b) FZ rutile growth using a double-ellipsoid mirror furnace; (c) FZ Si growth using a needle-eye configuration; courtesy of Topsil Inc.

Fig. 13 (a) Schematic of the magnetic field, electric current, and forces in the CZ growth using a static horizontal magnetic field; reprint from Kakimoto and Liu (2006) with permission from Tech Science Press; (b) simulated flow field on the z-x plane (top) and the x-y planes; reprint from Yokoyama et al. (2017) with permission from

Elsevier.

Fig. 14 (a) Traveling magnetic fields in CZ (left) and VGF (right) crystal growth systems generated by heater-magnet modules; (b) 4-inch vertical gradient freeze Ge single crystal grown within a combined heater-magnet module (left), etched longitudinal crystal cuts showing nearly no striations at growth in TMF (top right) but marked inhomogeneities when conventional growth without magnetic fields. Reprint from Rudolph and Kakimoto (2009) with permission from Cambridge University Press.

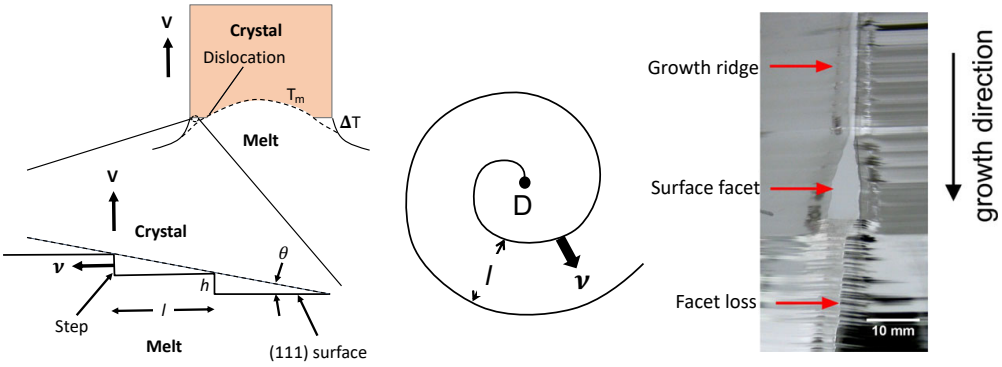
Fig. 15 (a) Effects of rotation rate on the maximum melt velocity for 2 cm? Ga-doped germanium growth in a graphite ampoule. The flow and the dopant fields at 80 rpm rotation for the free-swing (a) and rotation-about-growth-axis (b) are shown on the right; θ is the angle between the rotation axis and ampoule axis; Reprint from Lan (2004) with permission of Elsevier.

Fig. 16 (a) Schematic of Ekman flow and Taylor–Gortler cells during spin down (left) and spin up of ACRT; (b) The ACRT pattern (top) and the simulated flow and acetone fields in VB growth of SCN containing 0.064wt% acetone; reprint from Liu et al. (2007a) with permission from Elsevier.

Fig. 17 Effect of ACRT cycle pattern on the simulated flow and acetone fields and the growth interface (left) during VB growth of SCN containing 0.064wt% acetone: (a) trapezoidal pattern; (b) triangular pulse pattern; the photographs are the observed interface. Reprint from Liu et al. (2007b) with permission from Elsevier.

Fig. 18 (a) Microdefect bands revealed by the copper decoration and etching in a quarter of a wafer produced from a CZ Si crystal of a mixed type. The sequential bands, moving from the center to the edge, are the inner void core (with a marginal H band showing the heaviest decoration), the I-type perfect ring, the ring of interstitial A/B swirl defects, and the I-type perfect ring adjacent to the crystal surface; (b) schematic of the nucleation front in a growing V-type crystal. The higher-T region (below the front) is populated only with vacancies and a lower-T region (above the front) contains voids formed by vacancy nucleation. The U-shape of the nucleation front is due to a reduction in the incorporated vacancy concentration along the radial coordinate. Reprint from Voronkov et al. (2001) with permission form Elsevier.

Fig. 19 (a) Heavily twinned 4-inch liquid encapsulation VGF InP crystal and twin-free crystals grown in a standard and a flat bottom crucible, respectively; (b) schematic representation of the orientation relationship between matrix (M) and twin (T) at the three-phase boundary (TPB). Reprint from Jurisch et al., (2015) with permission from Elsevier.



(a) (b) (b)

Fig. 1

1

Fig. 1 (a) Schematic of the step growth on a (111) facet having steps; (b) step growth from a screw dislocation (D); (c) photograph of a growth ridge loss which occurred during the growth of the top cone of a heavily As-doped CZ Si crystal. Reprinted from Stockmeier et al., (2017) with permission from Wiley-VCH.

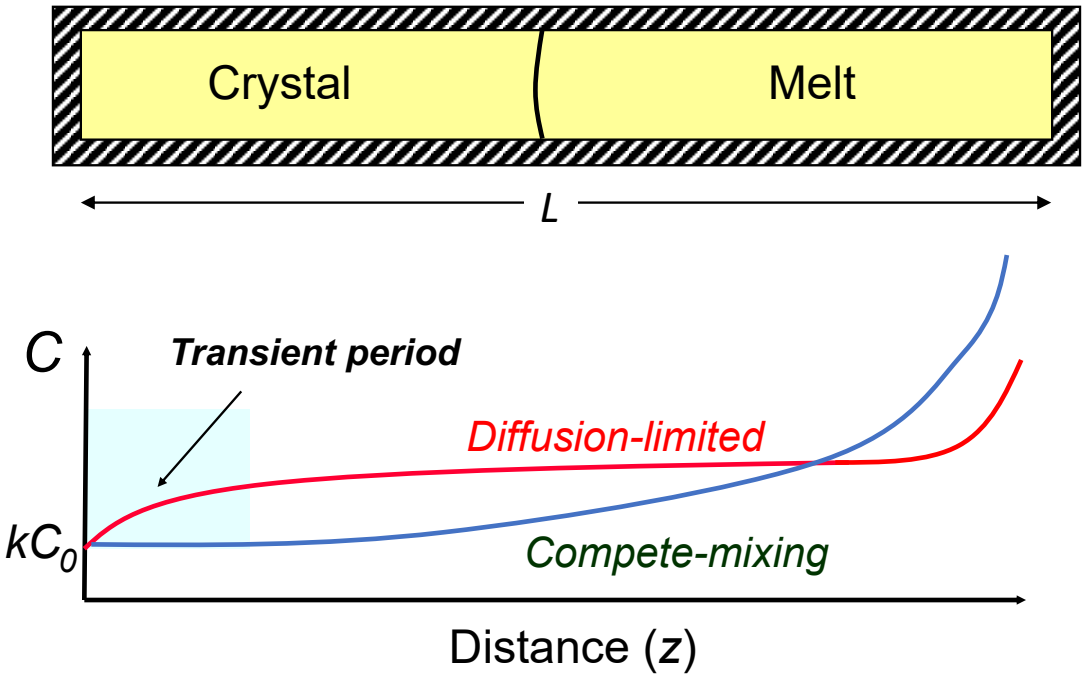


Fig. 2 Axial dopant segregations, diffusive vs complete-mixing, in normal freezing.

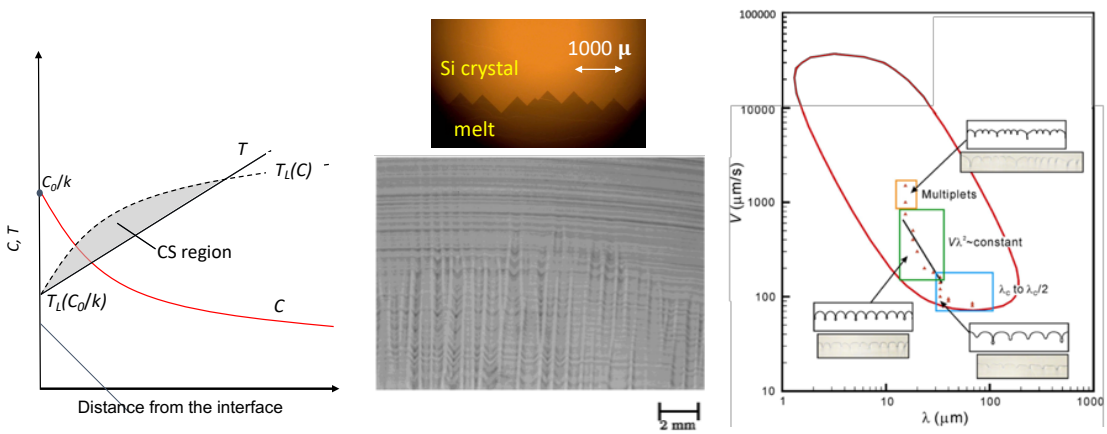


Fig. 3 (a) Schematic of constitutional supercooling (CS); (b) an optical micrograph of the vertical wafer where cellular growth occurred due to the CS. The wafer was cut from a heavily B-doped ($5.4x10^{20}$ at/cm^3) Si CZ crystal; (c) the MS loop of 0.01 mol% acetone-doped SCN; some simulated results and experimental observations are attached. The lower figure of (b) is reprinted from Taishi et al., (2000) with permission from Japan Applied Physics Society, while (c) is reprinted from Shih and Lan (2005) with permission from Elsevier.

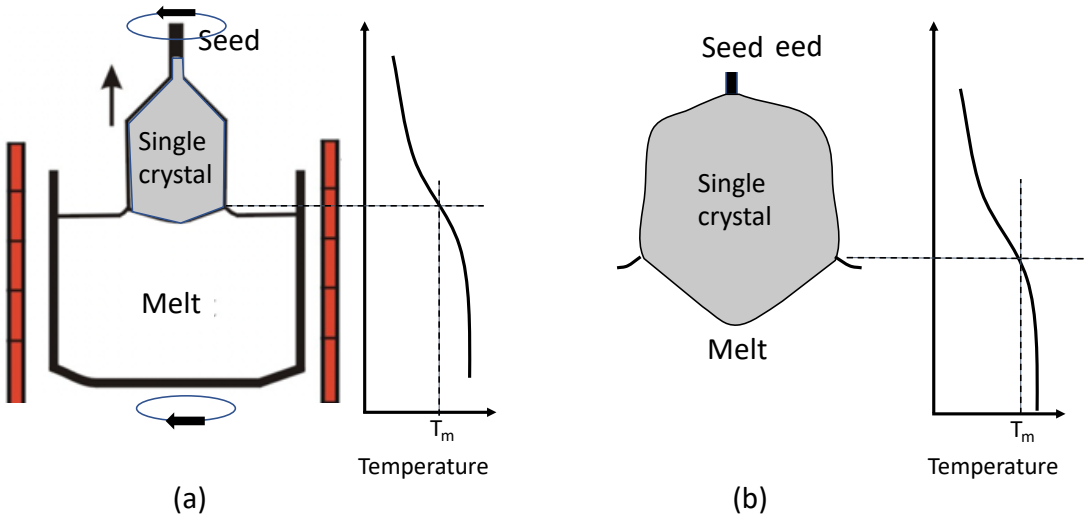
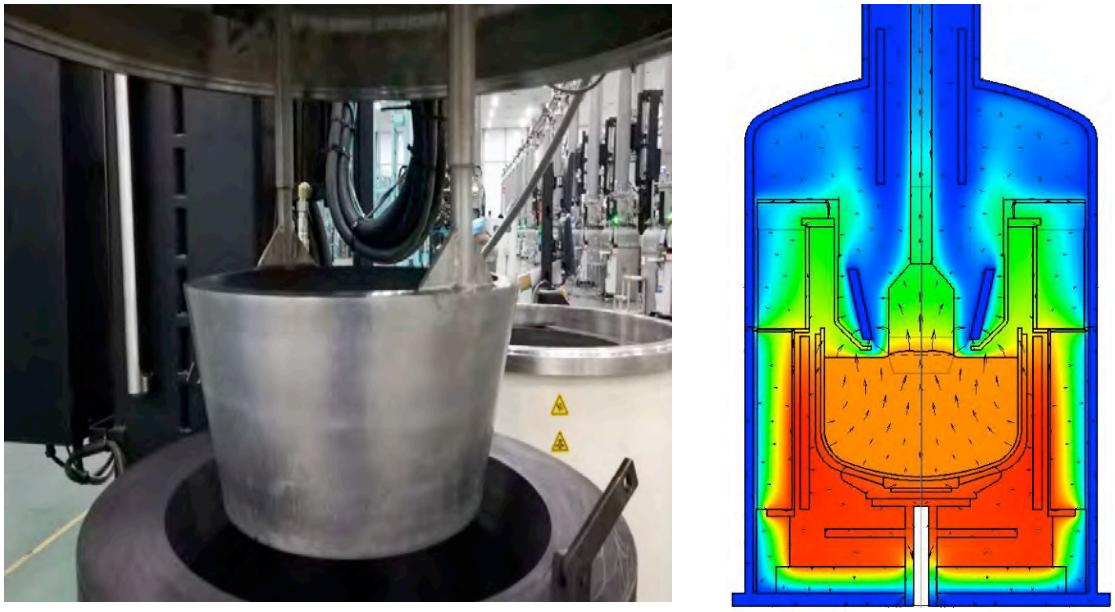


Fig. 4 (a) Schematic of CZ crystal growth using a resistance heater; (b) Schematic of KY crystal growth.



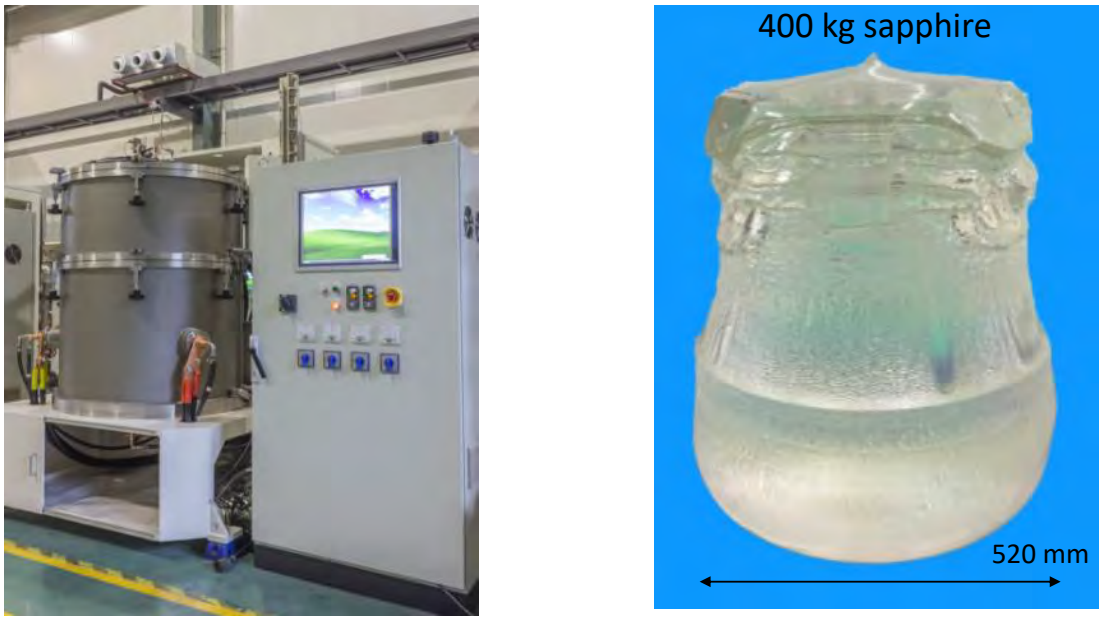
(a) (b)

Fig. 5 (a) The CZ puller for 8- to 12-in silicon crystal growth with a recharge tank and a cusp magnetic field; (b) a grown 12-in silicon ingot. Courtesy of Global Wafer Inc.



(a) (b)

Fig. 6 (a) The cooling ring in a CZ puller for solar silicon; (b) simulated thermal field with the cooling ring. Courtesy of Dalian Linton NC Machine Co.



(a) (b)

Fig. 7 (a) The KY crystal growth station for 400 kg sapphire crystals; (b) as grown 400 kg sapphire boule. Courtesy of TDG Holding Co.

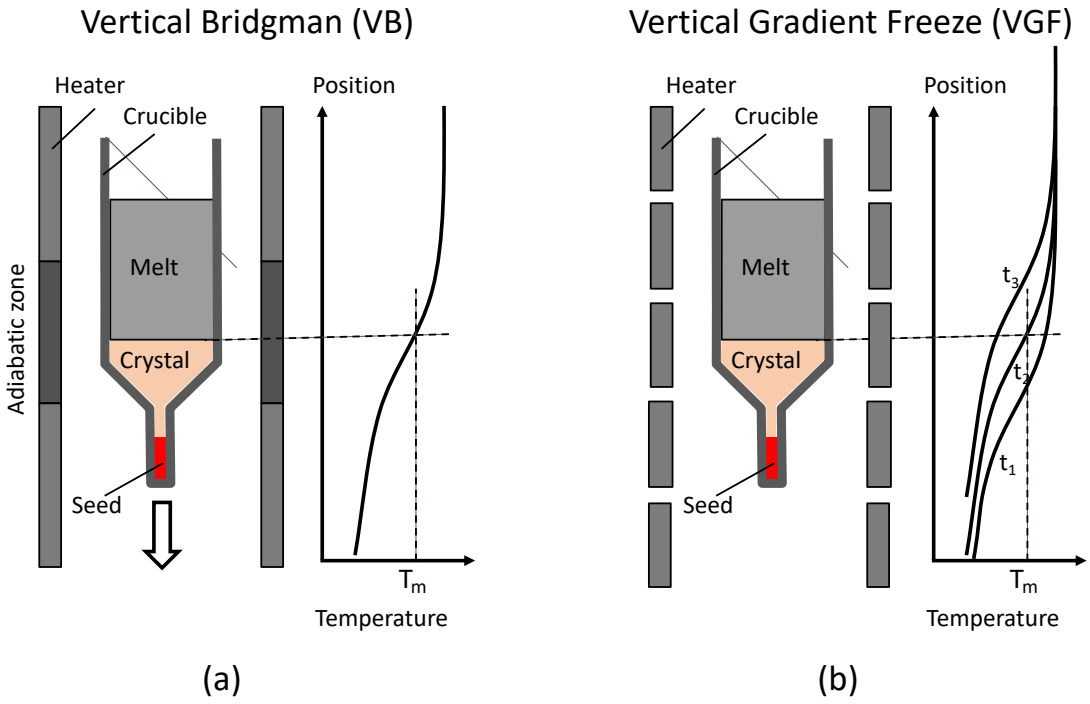


Fig. 8 Schematics of (a) VB and (b) VGF crystal growth methods; the dynamic thermal profiles are shown on the right.

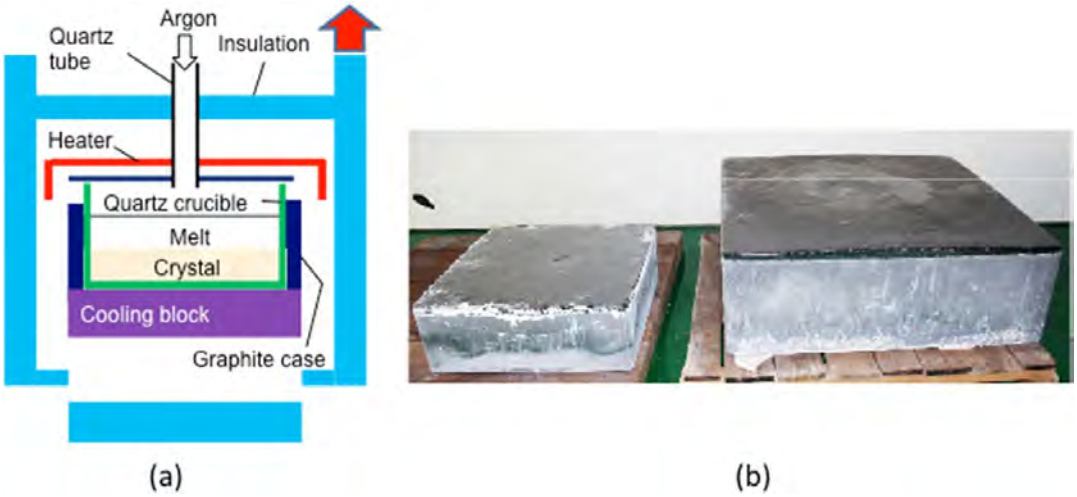


Fig. 9 (a) Schematic of DS growth of Si ingot; (b) photograph of G5 (left) and G8 (1340 mm×1340 mm×500 mm) ingots; courtesy of Aton Solar Technology Inc. Reprint from Lan et al. (2017) with permission from Elsevier.

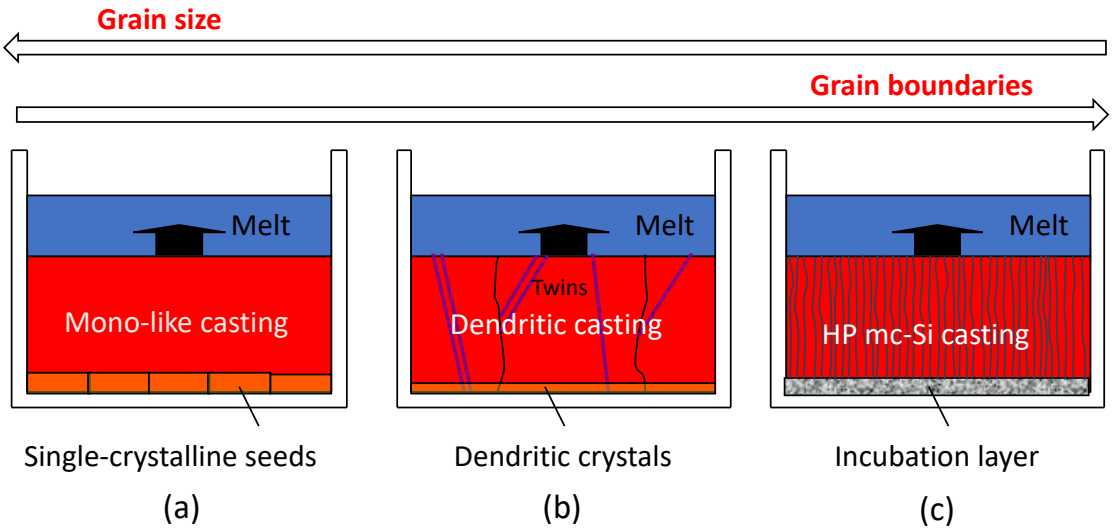


Fig. 10 Schematic of different DS technologies: (a) mono-like casting using splitting seeds; (b) dendritic casting; (c) HP mc-Si. Reprint from Lan et al. (2017) with permission from Elsevier.

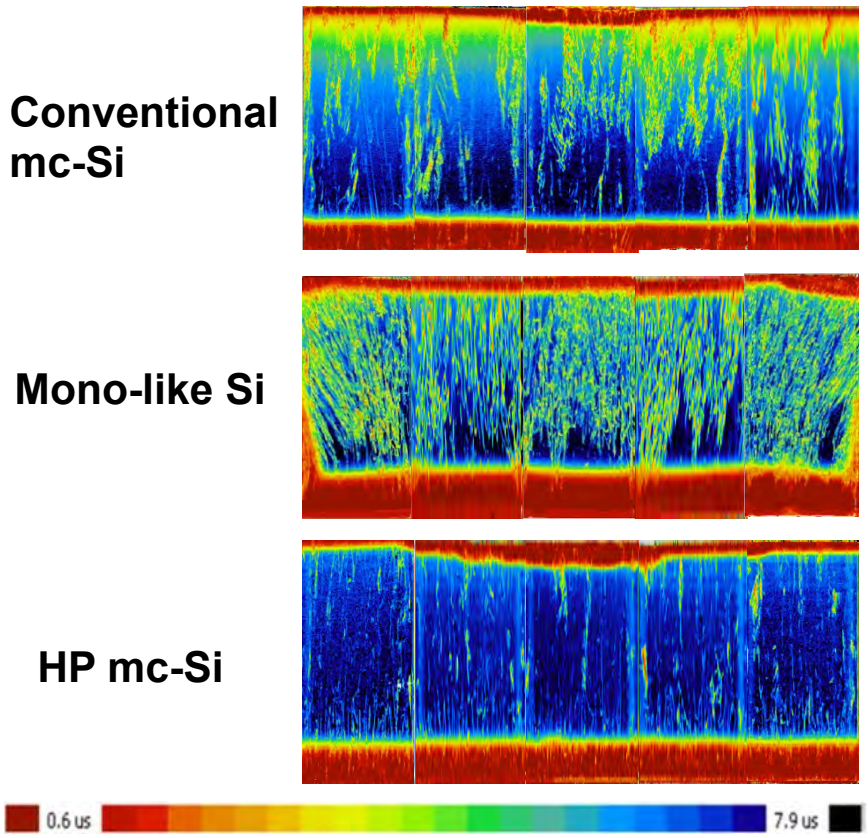


Fig. 11 Lifetime mappings of the G5 mc-Si ingots grown from conventional (top), mono-like, and HP mc-Si casting. Courtesy of Prof. X. Huang.

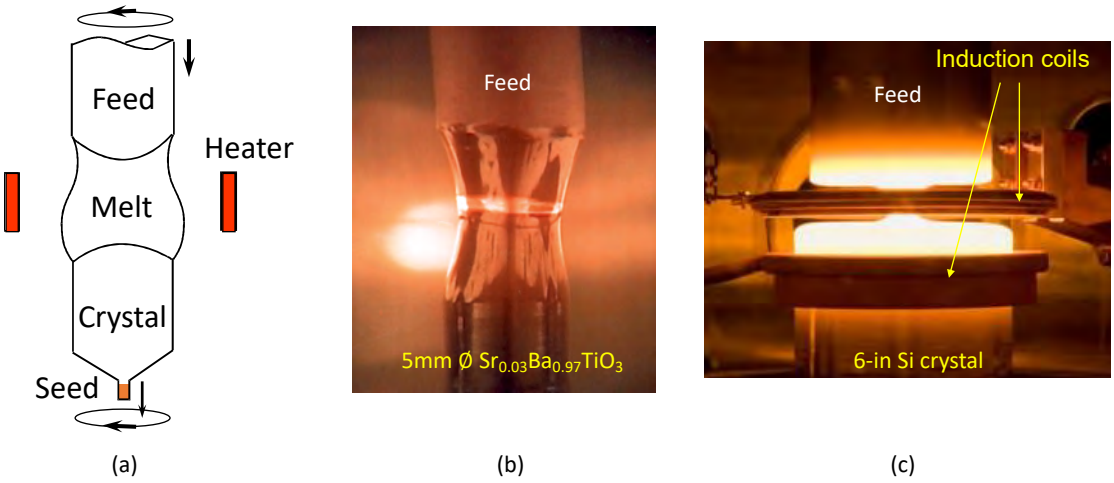
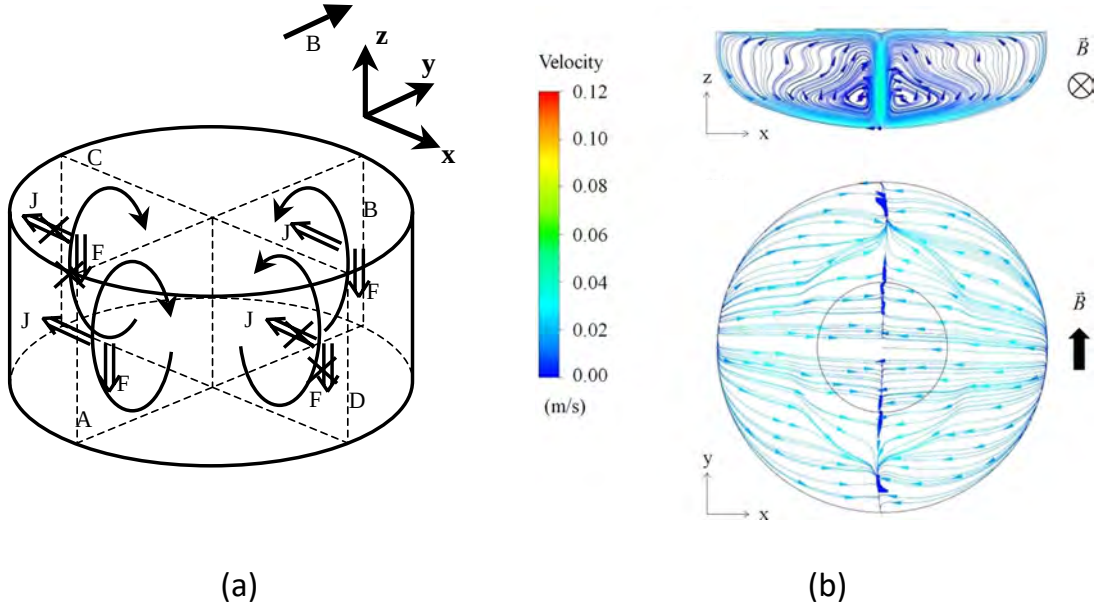
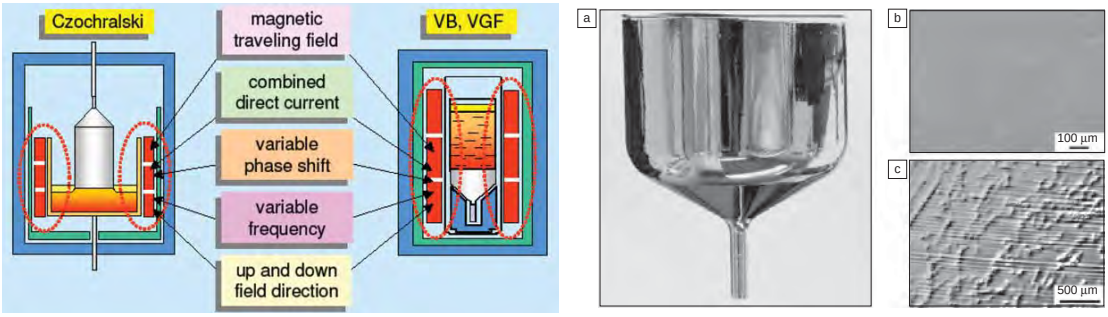


Fig. 12 (a) Schematic of the FZ method; (b) FZ rutile growth using a double-ellipsoid mirror furnace; (c) FZ Si growth using a needle-eye configuration; curtesy of Topsil Inc.



(a) (b)

Fig. 13 (a) Schematic of the magnetic field, electric current, and forces in the CZ growth using a static horizontal magnetic field; reprint from Kakimoto and Liu (2006) with permission from Tech Science Press; (b) simulated flow field on the z-x plane (top) and the x-y planes; reprint from Yokoyama et al. (2017) with permission from Elsevier.



(a) (b)

Fig. 14 (a) Traveling magnetic fields in CZ (left) and VGF (right) crystal growth systems generated by heater-magnet modules; (b) 4-inch vertical gradient freeze Ge single crystal grown within a combined heater-magnet module (left), etched longitudinal crystal cuts showing nearly no striations at growth in TMF (top right) but marked inhomogeneities when conventional growth without magnetic fields. Reprint from Rudolph and Kakimoto (2009) with permission from Cambridge University Press.

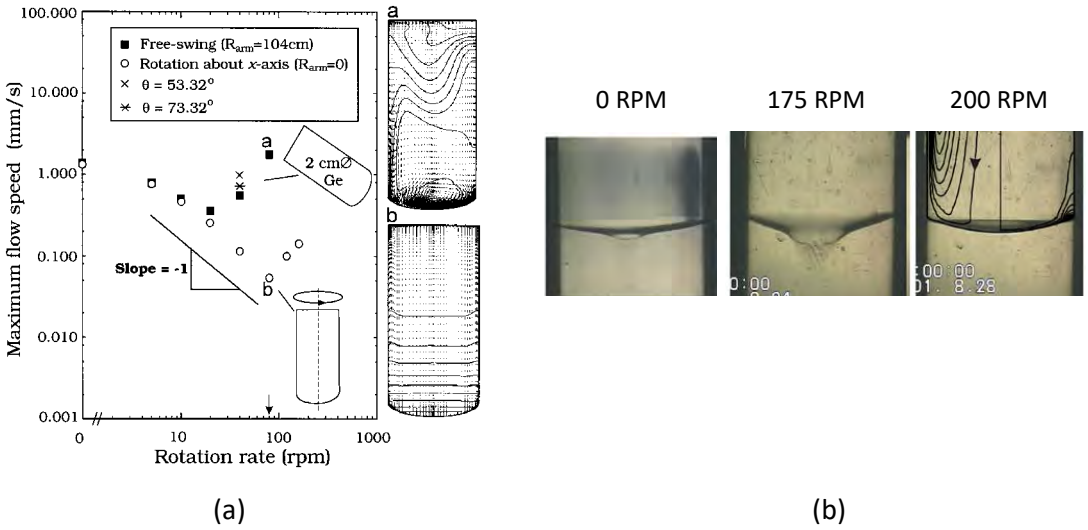


Fig. 15 (a) Effects of rotation rate on the maximum melt velocity for 2 cm? Ga-doped germanium growth in a graphite ampoule. The flow and the dopant fields at 80 rpm rotation for the free-swing (a) and rotation-about-growth-axis (b) are shown on the right; θ is the angle between the rotation axis and ampoule axis; Reprint from Lan (2004) with permission of Elsevier.

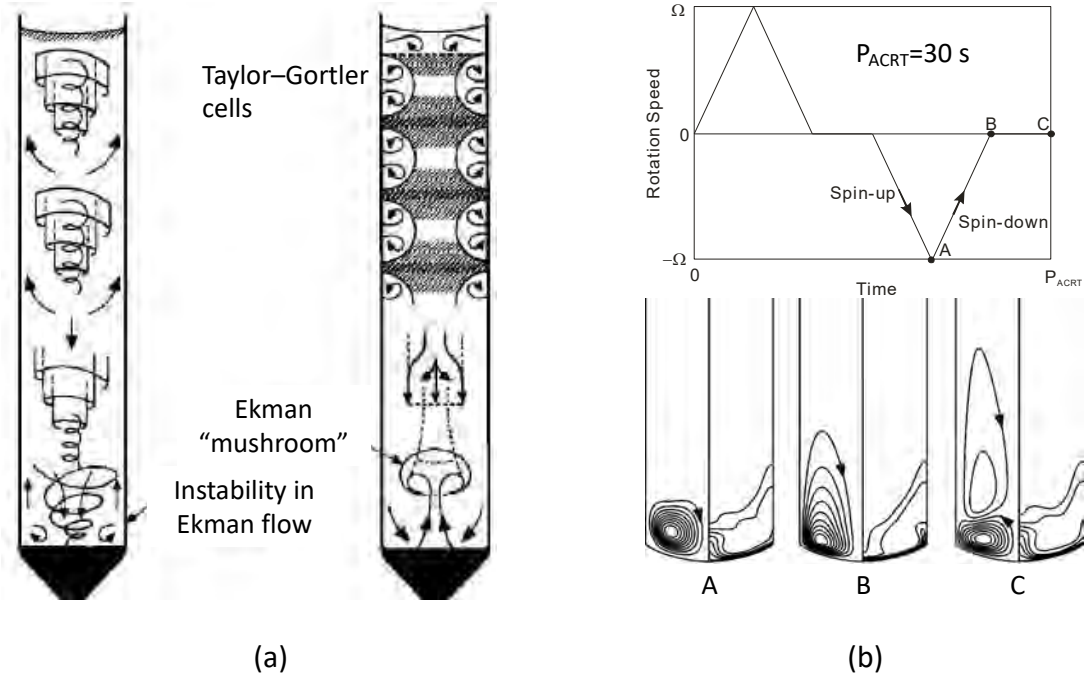


Fig. 16 (a) Schematic of Ekman flow and Taylor–Gortler cells during spin down (left) and spin up of ACRT; (b) The ACRT pattern (top) and the simulated flow and acetone fields in VB growth of SCN containing 0.064wt% acetone; reprint from Liu et al. (2007a) with permission from Elsevier.

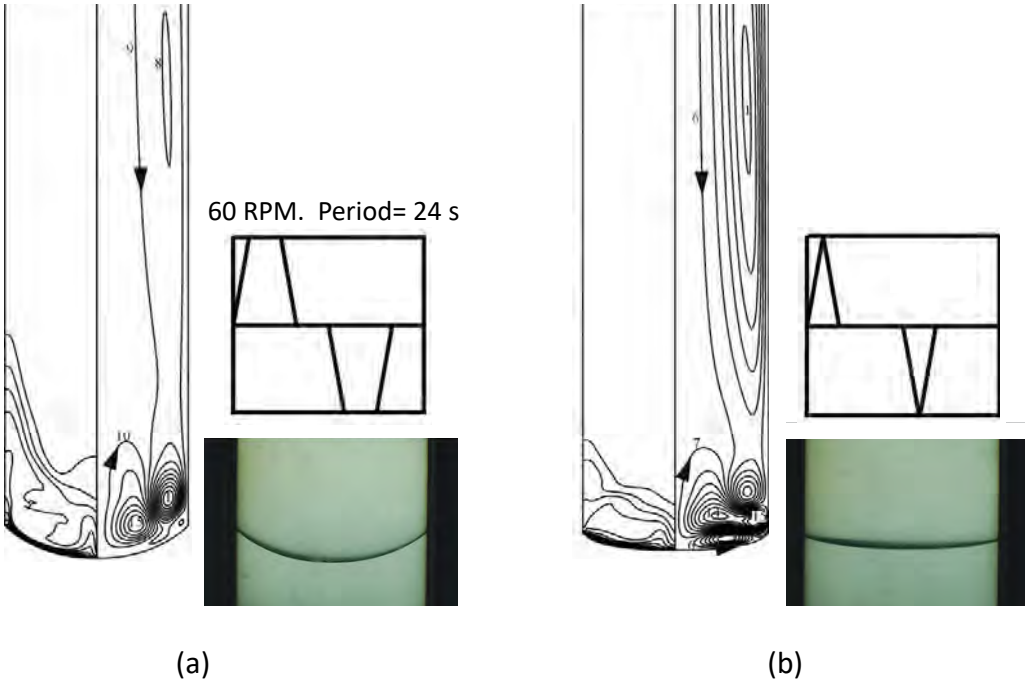


Fig. 17 Effect of ACRT cycle pattern on the simulated flow and acetone fields and the growth interface (left) during VB growth of SCN containing 0.064wt% acetone: (a) trapezoidal pattern; (b) triangular pulse pattern; the photographs are the observed interface. Reprint from Liu et al. (2007b) with permission from Elsevier.

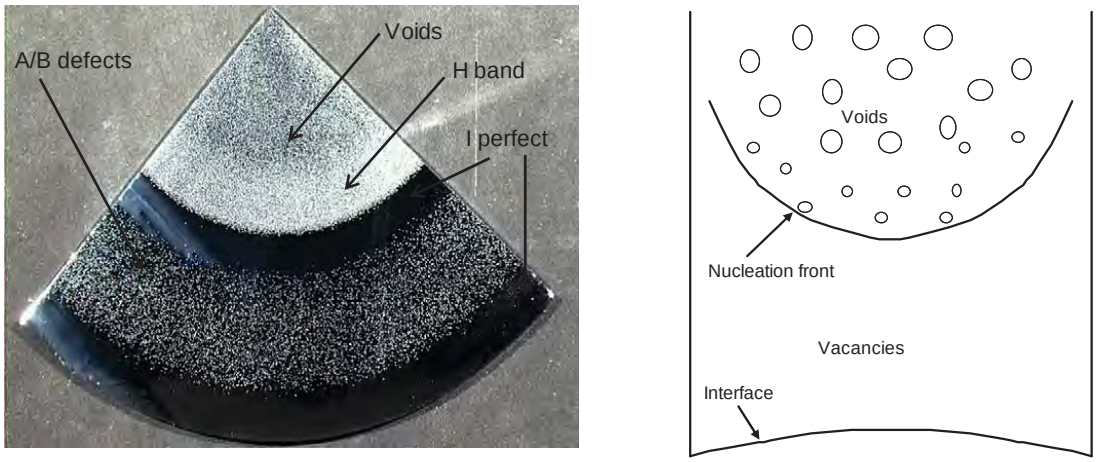


Fig. 18 (a) Microdefect bands revealed by the copper decoration and etching in a quarter of a wafer produced from a CZ Si crystal of a mixed type. The sequential bands, moving from the center to the edge, are the inner void core (with a marginal H band showing the heaviest decoration), the I-type perfect ring, the ring of interstitial A/B swirl defects, and the I-type perfect ring adjacent to the crystal surface; (b) schematic of the nucleation front in a growing V-type crystal. The higher-T region (below the front) is populated only with vacancies and a lower-T region (above the front) contains voids formed by vacancy nucleation. The U-shape of the nucleation front is due to a reduction in the incorporated vacancy concentration along the radial coordinate. Reprint from Voronkov et al. (2001) with permission form Elsevier.

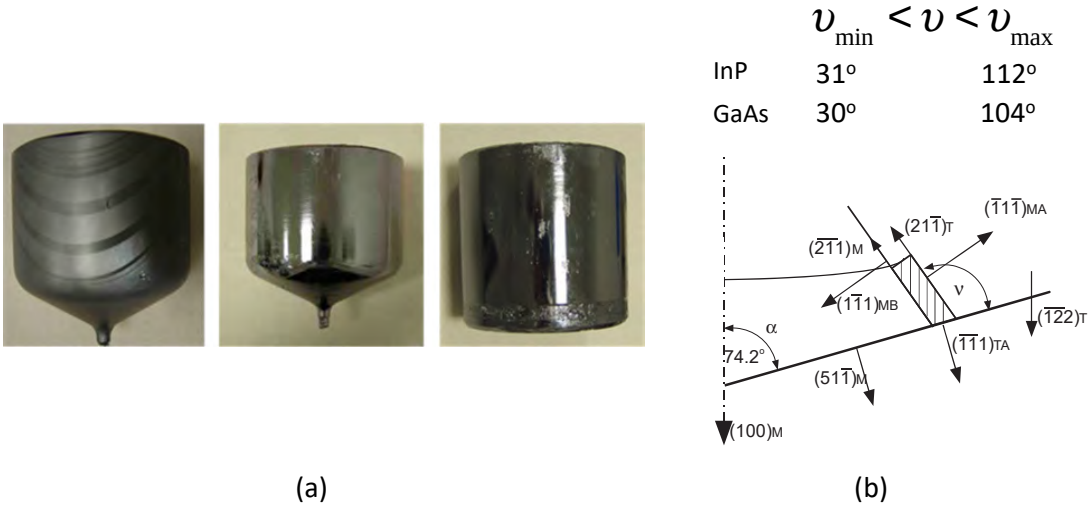


Fig. 19 (a) Heavily twinned 4-inch liquid encapsulation VGF InP crystal and twin-free crystals grown in a standard and a flat bottom crucible, respectively; (b) schematic representation of the orientation relationship between matrix (M) and twin (T) at the three-phase boundary (TPB). Reprint from Jurisch et al., (2015) with permission from Elsevier.

6. Defects and Impurities in Crystal Growth

Defects and Impurities in Crystal Growth

Mark S. Goorsky
Dept. Materials Science and Engineering
University of California of Los Angeles
Los Angeles, CA 90095-1595

Defects and Impurities

Introduction

This chapter focuses on defects and impurities in electronic and optical materials, with a significant focus on semiconductors. Defects, including impurities, are important to the crystal growth community because a wide range of materials properties depend on their presence and concentration as is noted in other chapters. Both plays roles in the electronic, thermal, optical and structural properties of bulk and epitaxial materials. In addition, an understanding of the defects – how they form and their electronic, mechanical, or other properties – can lead to defect engineering such that the defects can be controlled and utilized to improve the material or device performance. This chapter is organized with initial definitions and schematics and then presents specific materials applications.

Point Defects and Impurities

Defects can be classified based on their dimensionality with respect to a crystalline lattice. Point defects are zero dimensional defects which are perturbations to a perfect crystal – these primarily include isolated lattice vacancies as well as interstitial atoms of the host crystal as shown in Figure 1. In addition, isolated impurity species are point defects and these can occupy lattice sites or interstitial sites. Interstitial type defects – while not as common in close-packed metals – are prevalent in many types of electronic materials. Semiconductors possess relatively open lattices (the packing factor for a silicon unit cell is approximately 0.34 compared to 0.74 for an ideal, close-packed metal). For many crystalline oxides, the typically smaller cations can occupy interstitial positions so interstitial species are present in those systems as well. Other configurations that are typically included in the classification of point defects are anti-site defects and defect complexes. Anti-site defects are present in compound semiconductors and complex oxides where an atom of one type is present on a lattice site of another species, as in Figure 2. Defect pairs or complexes are typically included in this classification as well – and typically involve two or more species with a specific configuration. Schematics of these defects are shown below in Figures 3 and 4. Note that the pictures in the figure show two-dimensional square lattices (as is typically the case) with approximate distortions around the different defects whereas defects in three dimensional solids exhibit much more complex configurations. Presently the advances in theory, simulations, and modelling of such solid state defects have led to three-dimensional configurations that can be used to better understand experimental results of defects in different materials systems.

A standard nomenclature to describe point defects includes the identification of a host element coupled with the location of that species in relationship to a lattice site. For example, consider an elemental material "A". The presence of an A atom on an A lattice site is A_A. A vacancy at an A lattice site is V_A and an interstitial A atom is A_I. An impurity element 'E' on a lattice site would be represented by E_A while E_I represents an impurity in an interstitial position.

In a compound AB, one has vacancies of both types, for example V_A and V_B, as well as interstitial species, but in addition, also has anti-site defects such as B species on an A site (B_A – or an A species on a B site A_B). A defect pair or a complex can be represented by, for example, $V_A - A_I$ which would be a vacancy-interstitial pair.

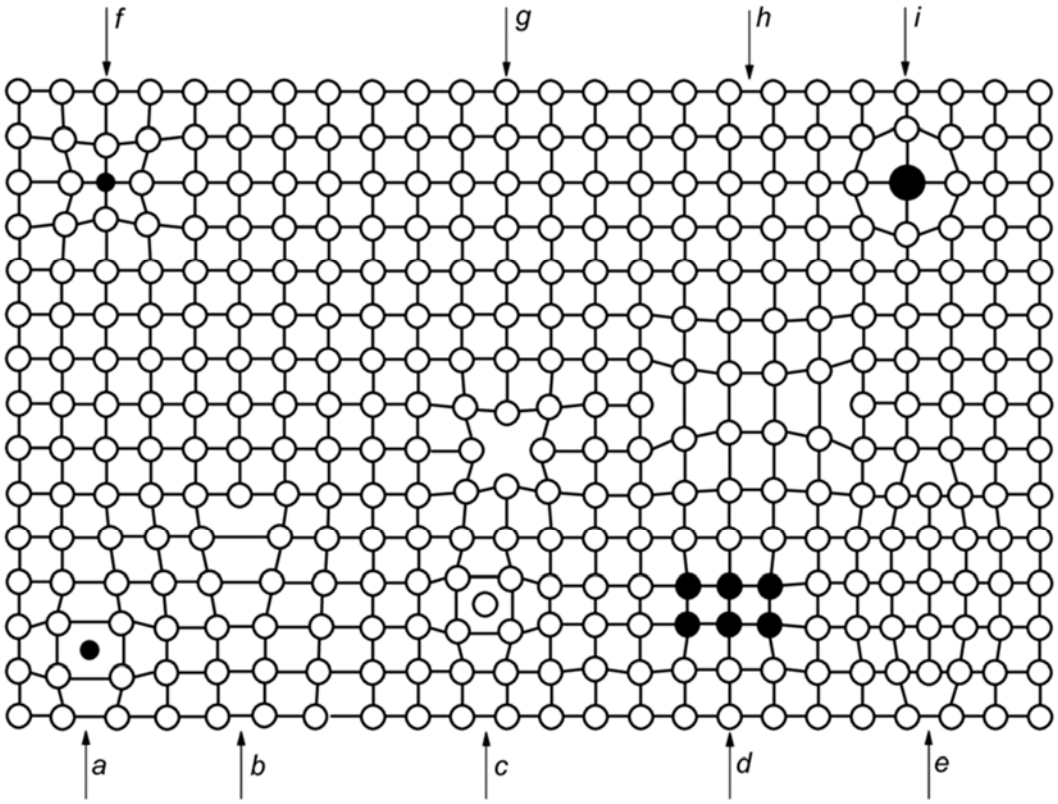


Figure 1. Two-dimensional lattice with defects. a) Interstitial impurity atom, b) Edge dislocation, c) Self interstitial atom, d) Vacancy, e) Precipitate of impurity atoms, f) Vacancy type dislocation loop, g) Interstitial type dislocation loop, h) Substitutional impurity atom (Föll, https://www.tf.uni-kiel.de/matwis/amat/def_en/index.html).

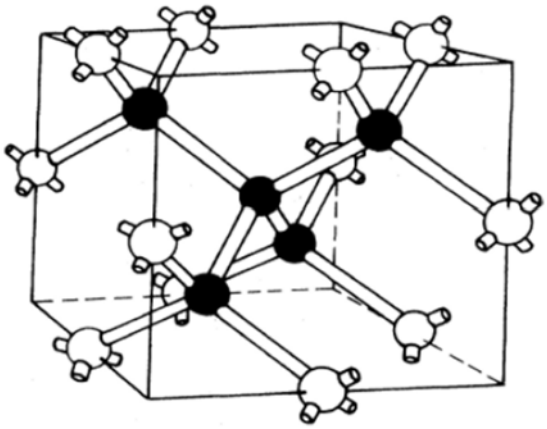


Figure 2. An anti-site defect in a zincblende lattice. In a perfect unit cell, each solid atom should be surrounded by four open atoms. Thesolid atom in the center is an anti-site defect [Dabrowski (1989)].

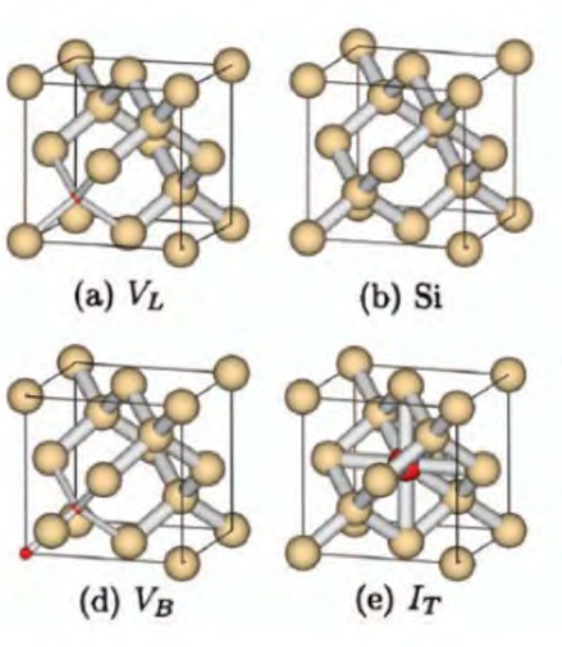


Figure 3. Three-dimensional diamond cubic defects. (a) A vacant atom (red dot) at ¼ ¼ ¼ atom position. (b) Diamond lattice. (c) A divacancy with a silicon interstitial (d) A silicon interstitial in the unit cell center ½ ½ ½ . [Centoni (2005)]

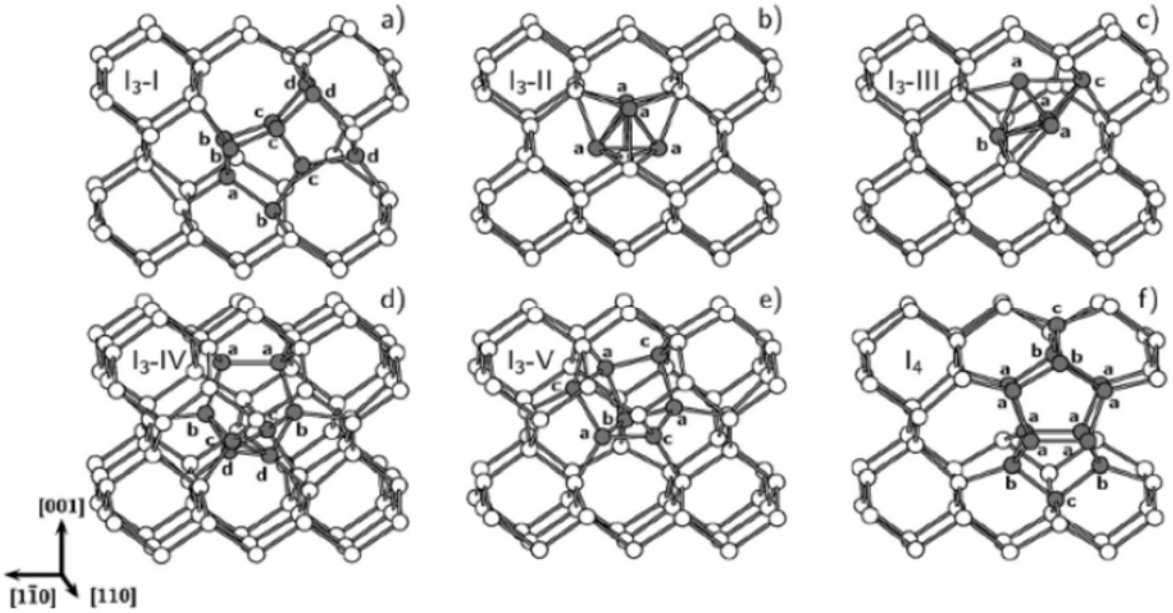


Figure 4. Different complex defect configurations. See Carvalho (2005) for details.

In any materials system, the ability to control a property by an order of magnitude or so is a key aspect of materials engineering. For semiconductors, the electrical conductivity can be

changed by several orders of magnitude through the introduction of certain species and is referred to as doping. Doping is achieved by the controlled introduction of impurities.

Isolated point defects and small complexes play extremely important roles in semiconductors and other electronic materials. Impurities, in particular, determine the electronic properties of semiconductors as well as the optical properties of optical materials. The association between a particular defect and the host material for semiconductors is best described through an approach that utilizes the electronic band diagram, while the relation between a defect and optical properties can be understood at a simple but effective level by considering the crystal field effect of the lattice on the defect.

In the band diagram approach, the properties of an intrinsic (basically the absence of impurities or defects) semiconductor with a three-dimensional periodic structure are described. Band structure calculations can determine the bandgap of a material (energy difference between the highest valence band energy level and the lowest conduction band energy level), including whether a semiconductor has an indirect or a direct bandgap as well as the densities of state of the valence and conduction bands and the effective masses of electrons and holes. While a more extensive discussion of band structure is not within the topic of this discussion, examples are shown below in Figure 5(a) for the band structure of silicon with a simplified explanation. Valence electrons associated with an atom possess discrete energy levels. When the atoms are arranged into a lattice, these individual states merge into energy bands. In an intrinsic semiconductor at 0 K, all of the valance states are filled. The energy level of the next higher (empty) state is referred to as the conduction band and all of those states are empty. Here, the energy is plotted against the wave vector, with inverse length units, and shows directions within a crystal unit cell (Ioffe references). For many purposes, at the expense of a significant amount of information, the band structure can be simplified as shown in Figure 5(b). At 0 K all of the electrons are in the valence band states and all of the conduction band states are empty. At higher temperatures, some of the charge carriers (electrons) can move into the conduction band as is illustrated in Figure 5(b). Simultaneously, the state with the absent electron is described as a hole. Holes possess the opposite charge as electrons and also conduct electricity.

In intrinsic semiconductors, the electron concentration, n, and the hole concentration, p, are therefore the same and designated as n_i. In general, the electron concentration can be approximated by

$$n = N_c \cdot \exp\left[-\frac{E_c - E_F}{kT}\right] \qquad \text{Equation 1}$$

where N_c is the effective conduction band density of states, E_c is the minimum conduction band energy level and E_F is the Fermi Energy. For holes, N_v is the effective valence band density of states and E_v is the valence band maximum energy. Typically, E_v is taken as zero and the exponential term is simply the energy difference between the Fermi level and either the valence or conduction band.

$$p = N_v \cdot \exp\left[-\frac{E_F - E_v}{kT}\right] \qquad \text{Equation 2}$$

Therefore, the product of the electron and hole concentrations is simply

$$n \cdot p = N_c N_v \cdot \exp\left[-\frac{E_g}{kT}\right] \qquad \text{Equation3}$$

For an intrinsic semiconductor,

$$n = p = n_i = [N_c N_v]^{0.5} \cdot \exp\left[-\frac{E_g}{2kT}\right] \qquad \text{Equation 4}$$

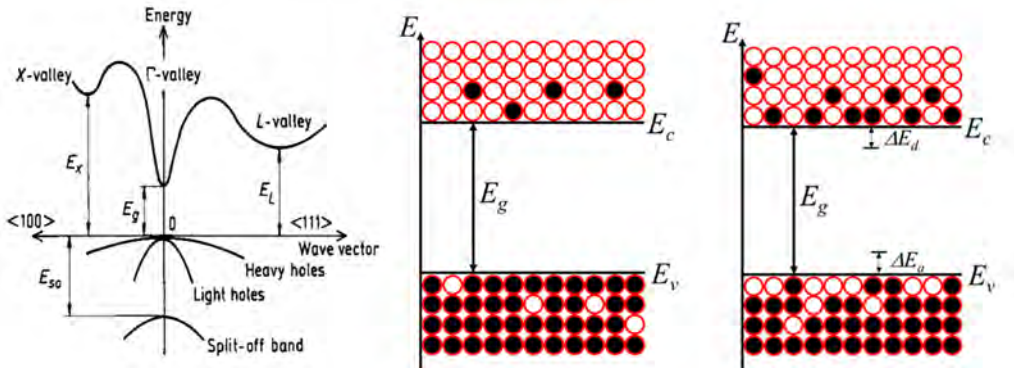


Figure 5. (a) The band structure of silicon. (b) Simplified band structure for intrinsic silicon at T> 0 K. Some carriers are in the conduction band. (c) Simplified band structure for extrinsic (doped silicon). ΔE_d and ΔE_a represent the donor and acceptor energy levels with reference to the conduction and valence band, respectively.

When point defects and impurities are present into the lattice, energy states within the bandgap can be introduced. Dopants are those impurities that are intentionally introduced to contribute to electrical conductivity. The states for dopants are typically referred to as 'shallow' levels. These are near the conduction band (to readily introduce excess electrons to make the materials n-type) or valence band (holes to make the material p-type). Dopant species are typically those elements that are in adjacent columns of the periodic table to the host species. Dopants are typically substitutional impurities and do not perturb the local lattice arrangements significantly. For example, phosphorus atoms on silicon lattice sites in silicon contribute electrons (n-type) and thus act as donors in a silicon lattice and boron atoms contribute holes (p-type) as thus act as acceptors.

Figure 5(c) superimposes an example of a dopant with a shallow energy level that introduces electrons (donors) with an energy ΔE_d (the distance from the conduction band edge to the shallow energy level) and also shows an example of a shallow energy level that introduces acceptors with an energy ΔE_a (distance from the valence band edge to that shallow energy level).

Other defects and impurities are associated with 'deep' energy levels. Defects whose configuration is very different from the local bonding are associated with deep energy levels. An example in III-V semiconductors is the anti-site defect in GaAs, As_{Ga}. Impurities whose valence structure is not similar to the host species are also associated with deep energy levels. Transition metals are good examples of species that introduce deep energy levels in the bandgap. Figure 6

shows examples from the literature of different deep levels and the corresponding metallic impurities or complexes for silicon. Note that these values should be treated with some caution as, over time, some of the deep levels have been shown to be associated with different defects or contaminants. Complexes of vacancies and dopants ($As_{Si} – V_{Si}$) or transition metals and dopant species ($Fe_I – B_{Si}$) also introduce deep levels into the lattice. In some cases, these complexes prevent the dopant species from acting as dopants and thus reduce the carrier concentration (as well as carrier lifetime and other important device parameters).

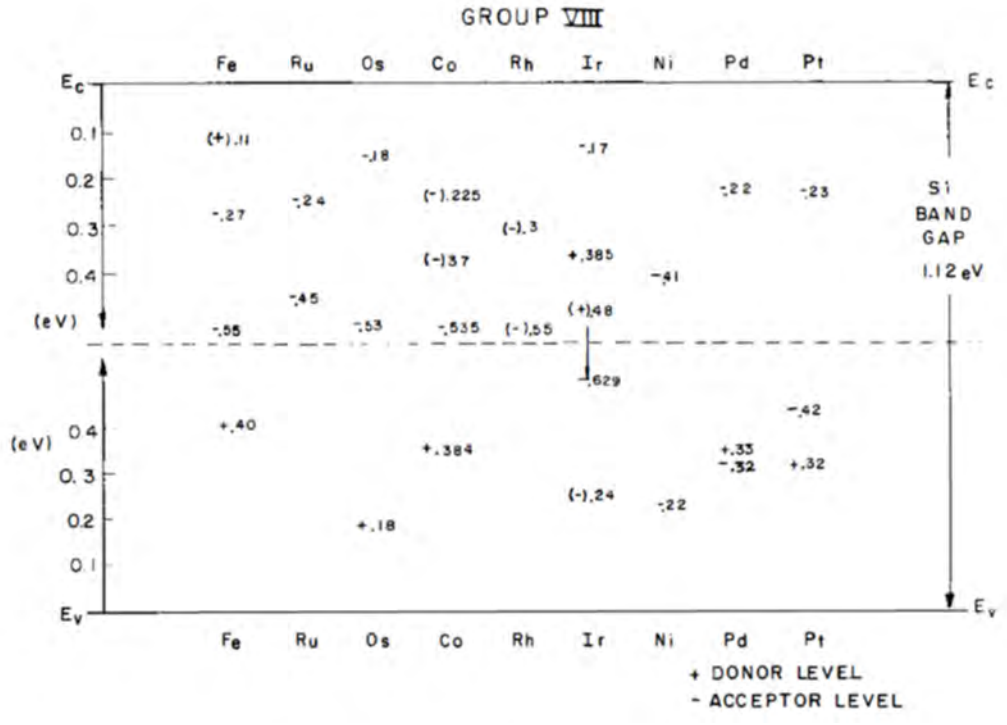


Figure 6. Fig. 6 from Chen (1980) showing deep energy levels in silicon for transition metal impurities.

The defect and impurity-related electronic properties of a semiconductor can be understood by considering the concept of charge balance. In these systems, the concentration of negatively charged species (electrons and ionized acceptors) and positively charged species (holes and ionized donors) are equal at equilibrium.

$$n + \sum N_a^- = p + \sum N_d^+ \qquad \text{Equation 5}$$

The concentration of a species of ionized acceptors or donors is also related to the Fermi level such that:

$$N_a^- = \frac{N_a}{1+g_a \cdot exp\left[-\frac{E_v+\Delta E_a-E_F}{kT}\right]} \qquad \text{Equation 6a}$$

$$N_d^+ = \frac{N_d}{1+g_d \cdot exp\left[-\frac{E_c-\Delta E_d-E_F}{kT}\right]} \qquad \text{Equation 6b}$$

where g_d and g_a are the spin degeneracy values for each level (typically $g_d = 2$ and $g_a = 4$). Note that these equations are valid at higher temperatures (e.g., above 100K).

The concentration of negatively ionized species and positively ionized species are graphically represented using a so-called Shockley diagram in Figure 7 below. Examples are shown below for intrinsic silicon at room temperature and also n-type silicon with a dopant concentration of 10^{16} cm^{-3}. In this case, a donor ionization energy of $\Delta E_d = 0.05$ eV is used.

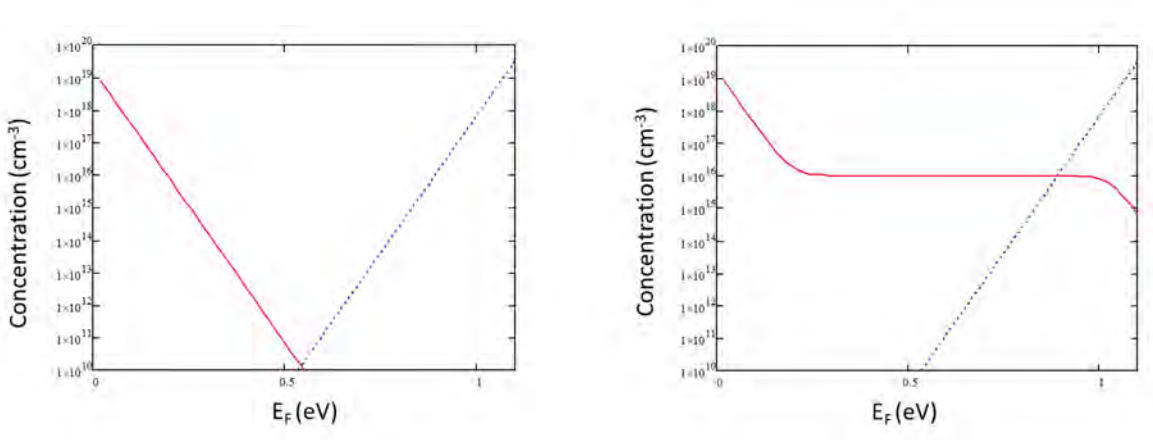


Figure 7. (left) The hole and electron concentrations at different Fermi levels. For intrinsic material, the Fermi level is approximately at mid-gap (0.545 eV in this case and it depends on N_c and N_v which, in turn depend on the effective masses for the electrons, and holes, respectively). The intrinsic carrier concentration is at 1.4×10^{10} cm^{-3} at room temperature. (right) With a donor concentration of 1×10^{16} cm^{-3} and a donor ionization energy of 0.05 eV, the Fermi level shifts to ~ 0.891 eV and the ionized donor concentration is 9.96×10^{15} cm^{-3} (effectively complete ionization).

For complex oxides and other predominantly ionic systems, charged impurities and defects tend to dominate electronic and optical properties. Thus, one typically considers charge balance among the different species, including impurities. For an ionic compound, AX, a cation A vacancy (V_A) would exist with an anion vacancy (V_X) to maintain charge balance in the lattice. This pair of defects is referred to as a Schottky defect. Alternately, a cation could occupy an interstitial position and thus would be a cation vacancy – cation interstitial pair. This is referred to as a Frenkel defect. Anion vacancy-anion interstitial pairs are less likely due to the – typically – much larger size of the anion species compared to the cation species. Impurities that possess a different charge state than the host species would also have to include charge compensation, either by an interstitial of the opposite type, or a vacancy-impurity pair. Complex oxides possess two cation (metal) species and oxygen as the anion, for example, $SrTiO_3$. Alternately, a single metal species that is in two different charge (oxidation) states with oxygen as the anion can be considered a complex oxide. An example is a spinel, Fe_3O_4, for example with two Fe^{3+} and one Fe^{2+}.

Extended Defects

Higher dimension defects can also exist and these can also impact the properties of crystals. The impact of these defects – unlike intentional dopant impurities – are detrimental to performance and are typically minimized.

Dislocations are linear defects that consist of a half-plane of atoms or group of atoms in a crystal. Dislocations are produced due to an applied stress to a material or to instabilities during growth. There are two basic types of dislocations that can be envisioned in a cubic lattice. They are the edge and screw dislocations as shown below in Figure 8. An important parameter for dislocations is the Burgers vector, **b**. Figure 8 (a) shows how such a Burgers vector is determined. As shown in the figure below, the Burgers vector is a circuit around the region of distorted atoms. Starting at the atom (or row of atoms) at the bottom of the extra half plane (the starting point is arbitrary), one moves right by one atomic placement (1), down by one atomic place (2), left by one (3), and finally up one (4). In a perfect crystal, one would be back at the starting point, but around the dislocation, one needs an extra step (labeled **b**) to get back to the origin. This is the Burgers vector. The dislocation line (end of the half plane) is perpendicular to the Burgers vector and which is one characteristic of an edge dislocation whereas the right side of Figure 8 shows a dislocation in which the dislocation line is vertical as is the Burgers vector and is referred to as a screw dislocation. There are many instances of crystal growth occuring from a screw dislocation with an example in Figure 8. In many materials – semiconductors and complex oxides included – the dislocations can have partial edge character and partial screw character and are referred to as mixed dislocations. For example, face-centered cubic (fcc) group IV, III-V and II-VI compounds tend to possess 60° dislocations, which have both edge and screw components. As with fcc metals, these dislocations are of the type {111}<1$\underline{1}$0> meaning they are on (111) planes – the close packed planes – and along [110] directions – close packed directions.

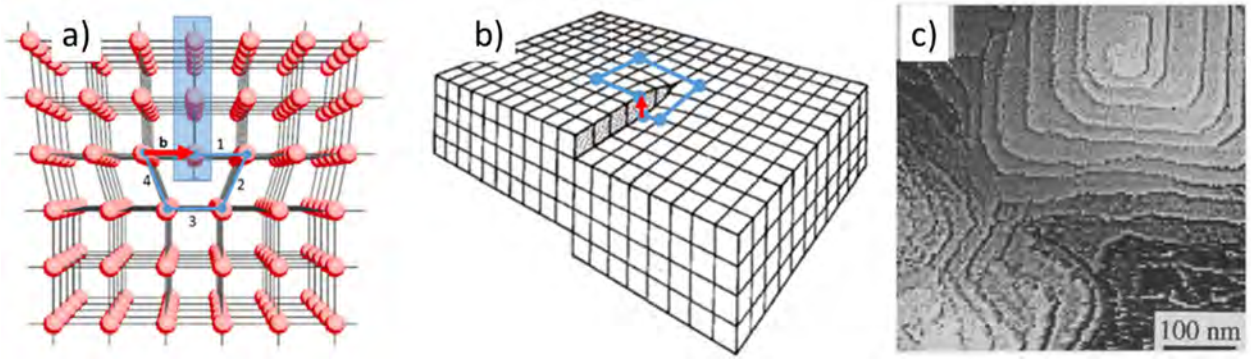


Figure 8. (a) Edge dislocation with extra half-plane of atoms highlighted as well as the Burgers vector circuit. The dislocation line is coming out of the page so the Burgers vector is orthogonal to the line direction. (b) Screw dislocation with Burgers vector circuit highlighted. The dislocation line is vertical and is parallel to the Burgers vector. (c) An example of crystal growth via a screw dislocation [N. Savvides (1994)]

Dislocations in crystals are commonly associated with bulk crystals and epitaxial films. For bulk crystals, the dislocation form during bulk growth as stresses are introduced due to thermal gradients. The magnitude of the stress depends on the thermal conductivity and the

coefficient of thermal expansion of the material. Whether dislocations form depends on the magnitude of the stress at a given temperature compared to the critical resolved shear stress, which typically decreases significantly with temperature such that materials that are rigid at room temperature can readily deform plastically at higher temperatures.

In epitaxial structures, the primary origin of stress is related to the lattice parameter difference between the substrate and the epitaxial layer. For blanket films, this situation represents the case for an applied bi-axial stress. For a given crystal structure and with the substrate being much thicker than the layer, the atoms in the layer will maintain a commensurate interface and follow the template of substrate surface atoms. The substrate constrains the layer to its lattice parameter. If the substrate lattice parameter is smaller than the lattice parameter of the epitaxial layer, the layer will contract to match the substrate in-plane lattice parameter but will then expand out-of-plane, with the magnitude of that expansion due to the layer's Poisson ratio in that direction and produces a pseudomorphic distortion. For example, the epitaxial cubic unit cell will be distorted to form a tetragonal unit cell. However, the layer distortion can be relieved by the formation of misfit dislocations at the interface as shown below in Figure 9.

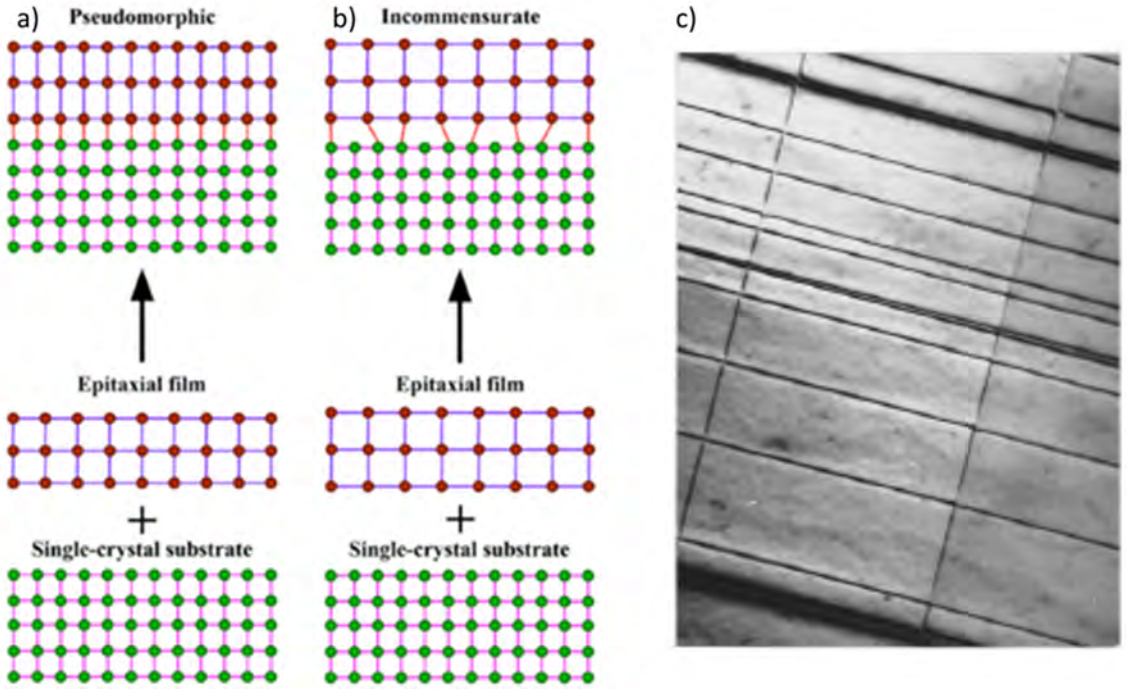


Figure 9. The deposition of an epitaxial film can produce a (a) pseudomorphic structure or (b) can include misfit dislocations at the interface; (c) plan view transmission electron microscopy image of orthogonal misfit dislocations at the interface between a layer of $In_{0.2}Ga_{0.8}As$ and a GaAs substrate. [Meshkinpour (1997)]

Whether the pseudomorphic strained layer or the layer with the incommensurate interface is formed can be assessed with the concept of a critical thickness, h_c [Matthews (1974)] An expression for this critical thickness [Tsao (1993)] is derived by balancing the coherency energy – the energy associated with distorting the layer to maintain its lattice coherency with the substrate – and the energy associated with the introduction of dislocations.

Here, for a single strained layer on a thick substrate:

$$f_c = \frac{b}{8\pi h \cos\lambda}\left(\frac{1-\nu\cos^2\beta}{1+\nu}\right)\ln\left(\frac{4h}{b}\right)$$

$$h_c = \frac{b}{8\pi f \cos\lambda}\left(\frac{1-\nu\cos^2\beta}{1+\nu}\right)\ln\left(\frac{4h_c}{b}\right)$$

Equation 7

The top equation describes a critical misfit strain f_c, below which the pseudomorphic structure is energetically favorable and above which the presence of misfit dislocations is energetically favorable.

For the case of 60° mixed dislocations, the angle β is the angle between the dislocation line and its Burgers vector (60°) and λ is the angle between the slip direction and that direction in the film plane which is perpendicular to the line of intersection of the slip plane and the interface (also 60°). The Burgers vector b and the Poisson ratio υ, are properties of the layer and the critical strain is dependent on the thickness, h, of the layer.

The bottom equation describes the critical thickness as a function of the misfit strain. The misfit strain is

$$f = \frac{a_l - a_s}{a_l}$$ Equation 8

Where a_l is the lattice parameter of the unstrained layer and a_s is the lattice parameter of the substrate. Figure 10 below shows the plot of misfit strain vs. thickness for a cubic (diamond or zincblende) semiconductor with ν = 0.3, b = 0.4 nm and 60° dislocations. In the lower left section, the pseudomorphic state is energetically stable. To the upper right, the introduction of misfit dislocations represents the more energetically stable condition. Note, however, that this is a thermodynamic argument – the dislocations must nucleate and extend across the interface. Therefore, if the kinetics are not favorable for dislocation movement (high activation energy to extend along the interface and / or low deposition temperature), the layer can remain in a pseudomorphic state.

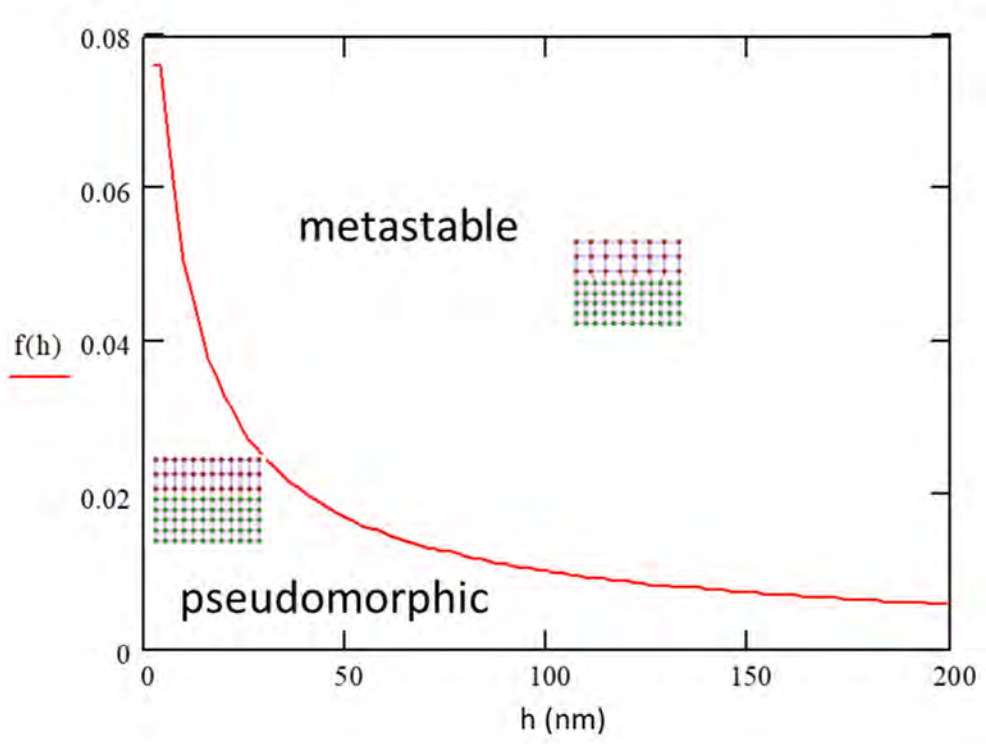


Figure 10. The critical thickness plot which shows the misfit strain and the thickness for which a strained layer is stable as a pseudomorphic layer or where interfacial misfit dislocations are energetically favorable to be present.

Stacking faults and polymorphic structures represent another important aspect of crystal defects. A stacking fault is simply a change in the stacking sequence of planes of atoms. For example, an fcc lattice exhibits an ABCABC stacking sequence of atoms on (111) planes. Layer B is offset from layer A and layer C is offset from both as shown in Figure 11 below.

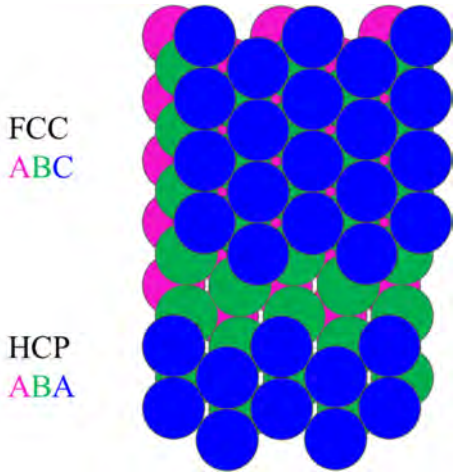


Figure 11. Stacking sequence for fcc and hcp cells.

However, if the 'C' atoms lie directly above the 'A' atoms, this becomes a hexagonal close packed structure. Compound semiconductors and many complex oxides exhibit this type

of behavior in which there is – energetically – only a small difference is the stability of one arrangement compared to another. When the sequence shifts from one pattern (e.g. ABCABC) to another (ABABAB) and back the pattern becomes ABCAB|ABABAB|ABCABC and the crystal exhibits both structures. For compound semiconductors, those with greater ionicity will more likely exhibit stacking faults (have a lower stacking fault energy). Ionicity represents the bond character between the species. In group IV, the identical atoms possess fully covalent bonds but zincblende structures have partial ionic character and II-VI compounds will generally have more ionic character than III-Vs and will thus possess lower stacking fault energies than III-V compounds. Even for the class of III-V compounds, InP has an ionicity of 0.42 and a stacking fault energy (zincblende vs. wurtzite structure) of 17 meV/atom whereas GaAs has a lower ionicity (0.31) and a higher stacking fault energy (47 meV/atom) [Gottschalk (1978)].

Polymorphism is a related condition in which a certain material can be stable with different crystal structures – typically at different temperatures but also when constrained as in epitaxial growth on a specific substrate template. Thus, a compound could take on a different crystal structure in an epitaxial thin film than its lowest energy bulk state.

Examples

Point defects and Czochralski Si growth

Intrinsic point defects have been widely studied in silicon and advances in crystal growth, modelling, and analysis have led to a deep understanding of point defects and how they impact crystalline perfection. [Voronkov (1982), Voronkov, (2008) Válek (2012)]. At the melt-solid interface, high concentrations of Frenkel defects (V_{Si} and Si_I) are created. As that part of the crystal is pulled away from the interface, most of the now supersaturated point defects recombine. However, there can be an imbalance in the vacancy and interstitial concentrations because of differences in their diffusion coefficients and alternate pathways to removal. These parameters depend on the ratio of the growth rate *V* and the thermal gradient *G*. If the ratio *V/G* is greater than a certain value, there will be an excess of Si_I and these will eventually recombine into dislocation loops – the extra half planes of Si atoms and have been observed as ‘A-defects’ or ‘swirl defects’. These defects appear (Figure 12) when as-grown silicon wafers are sliced, polished and preferentially etched. These swirl defects degraded device performance and so, with the understanding of how they were formed, the growth rate was decreased to reduce *V/G* and the swirl defects disappeared. Subsequently, another defect was observed in the 1990s and referred to as ‘crystal originated particle’ (COP). In fact, these defects were octahedral voids caused by the agglomeration of excess vacancies. Subsequently, it was determined that well controlled growth parameters could lead to silicon that did not have an excess of either interstitials or vacancies at the expense of slow growth rates. [R. Falster (1999)].

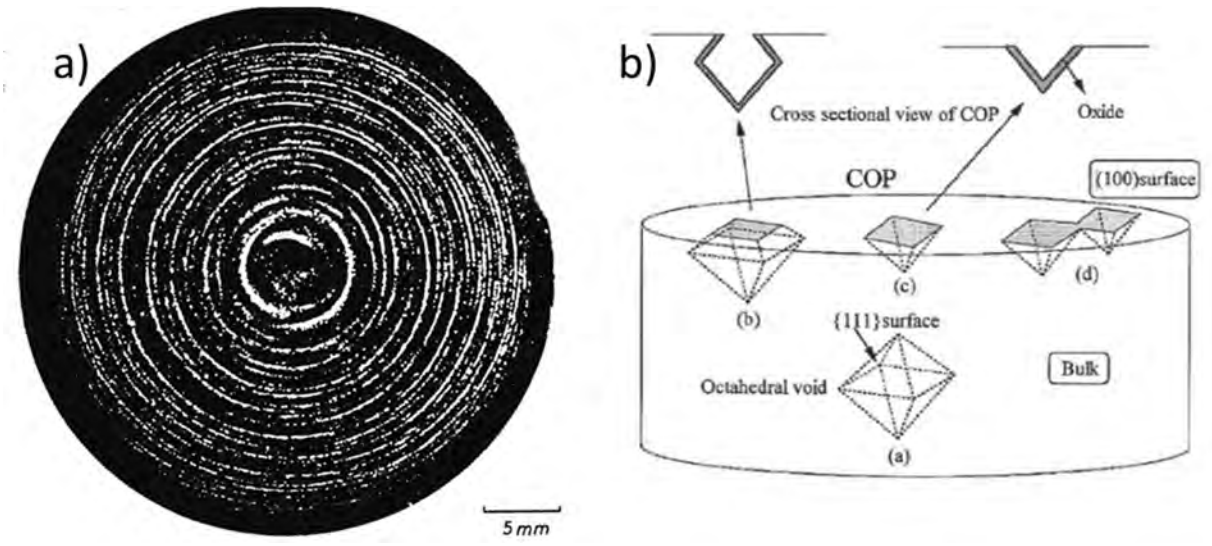


Figure 12. a) Swirl defects observed after preferential etching. [https://www.tf.uni-kiel.de/matwis/amat/def_en/kap_6/illustr/i6_1_1.html#_dum_2]. b) COP vacancy defects [H. Shimizu (2017)]

Oxygen and Transition Metals in Silicon

Although silicon is an extremely pure material, impurities such as oxygen [F. Shimura (1994)] and transition metal species can be present. Oxygen is present in Czochralski silicon because the silicon melt dissolves the silica crucible; oxygen gets incorporated into the melt and thus into the growing crystal at concentrations of $10^{17} – 10^{18}$ cm^{-3}. The oxygen occupies an interstitial position in the lattice and is electrically inactive. During annealing in the 400 – 500 °C range, however, oxygen reconfigures and acts as a donor with concentrations in the 10^{16} cm^{-3} range. This suggests that oxygen would not be desirable in a silicon crystal but other studies showed that Czochralski silicon showed better resistance to plastic deformation during wafer processing. [Yonenaga (1984)].

Another phenomenon associated with oxygen in silicon is that of intrinsic gettering. First, however, is to assess the role of transition metals in silicon. Unlike dopant species, transition metals in silicon do not reside on silicon lattice sites, but rather at interstitial positions within the open silicon lattice. The diffusivity and solubility of the 3d transition metals as a function of temperature are shown in Figure 13. Note that the diffusivity of these species is (i) orders of magnitude greater than silicon self-diffusion or dopant diffusion and (ii) does not decrease rapidly with decreasing temperature. On the other hand, the solubility of most of those species is orders of magnitude lower than dopant solubility and exhibits a very strong decrease of solubility with decreasing temperature. Consider that during standard processing, transition metal contamination is possible – furnace winding, sputtering from stainless steel chambers during ion implantation, etc. During any subsequent annealing, most of these species can diffuse through the entire wafer. As such, they introduce deep levels (see Fig. 6) if they remain in solution and if they precipitate (typically as a silicide), they will preferentially precipitate at the surface or in strained regions such as p-n junctions. To mitigate this potential problem, schemes

have been developed to getter or remove these transition metal contaminants from the devices on the front side of the wafer.

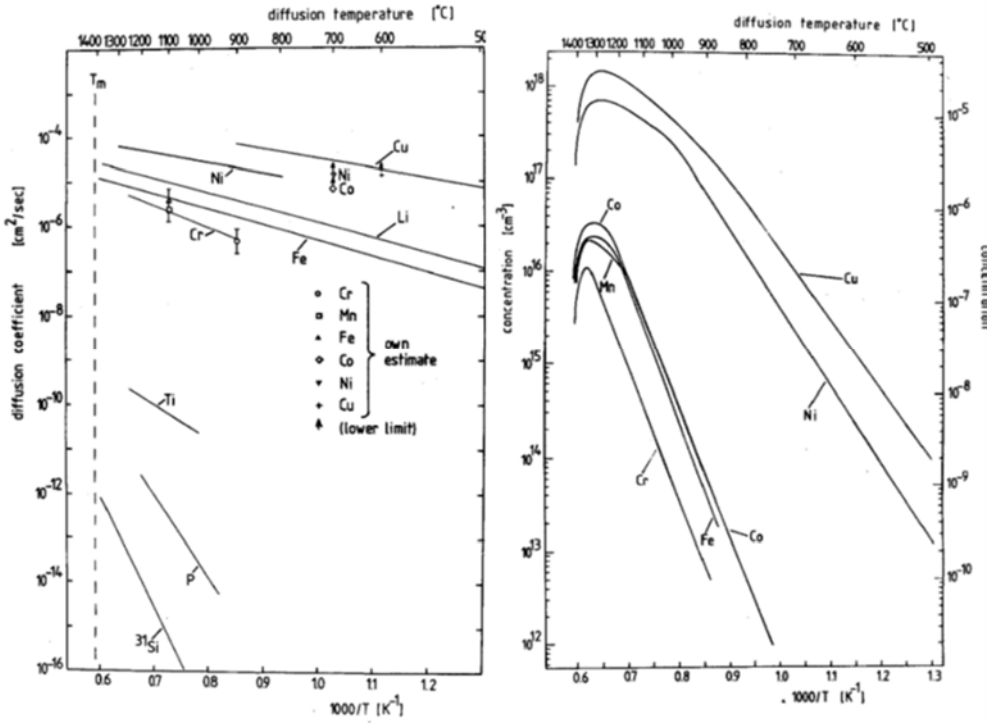


Figure 13. The diffusivity and solubility of transition metals in silicon. [E. R. Weber (1983)]

The oxygen present in silicon was defect engineered to provide a means to do this. In the 1970s [Hu (1998)] it was noted that devices processed on wafers from the seed end of a crystal tended to exhibit greater yields. The oxygen content from seed-end wafers was higher, establishing a connection between the oxygen content and yield. During processing, the driving force was for oxygen to precipitate as SiO_2. The oxide precipitate formation also introduced stress (the oxide possessed a greater volume than the silicon and interstitial oxygen) and produced dislocations around the precipitates. The precipitates and dislocations, in turn, acted as very effective nucleation sites for the precipitation of the metal silicides. A thermal treatment based on certain device processing steps was developed in order to form oxide precipitates in the bulk but not near the surface to getter the metals deep in the wafer and to produce a denuded zone of (oxide precipitates as well as transition metals) in the device active regions. This denuded zone was typically on the order of tens of microns. A typical annealing sequence, shown in Figure 14 starts with a high temperature (~ 1150 °C, a few hrs.) step to outdiffuse oxygen from the wafer surface. This is followed by a low temperature step (700-800 °C, a few hrs.) to nucleate the oxide precipitates in the bulk of the wafer where the oxygen content remained high and the final step was an intermediate temperature (~1000-1050 °C, several hrs.) to grow the oxide precipitates.

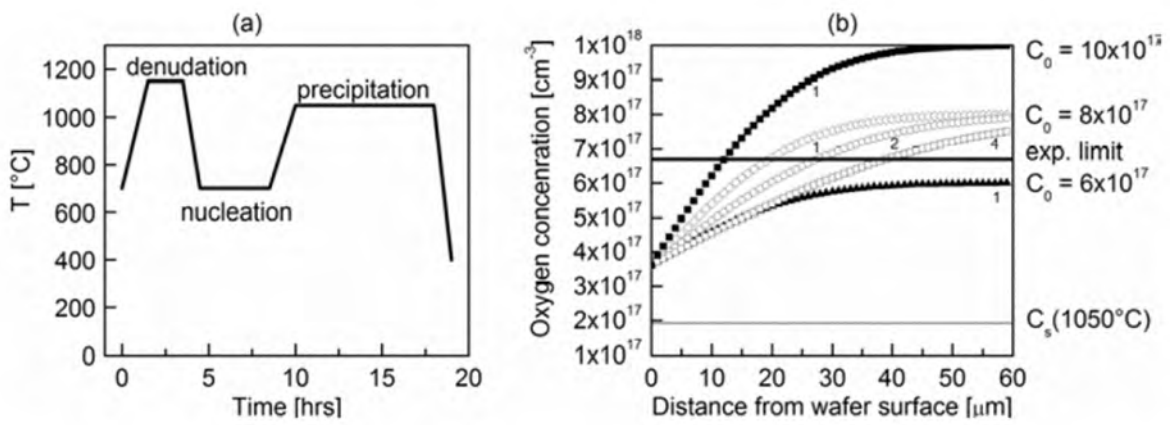


Figure 14. (a) An example of a thermal cycle for formation of the denuded zone and effective intrinsic gettering. (b) The concentration of oxygen in the wafer with initial oxygen concentration C_o denuded at 1150°C. Denuding duration in hours is noted in the plot below the curves. The thin horizontal line in (b) represents the equilibrium concentration of oxygen at the temperature of the precipitation step (1050°C); the thick solid line represents the experimental limit of oxygen precipitation. [Válek (2012)]

Compensation in III-V materials

III-V semiconductors exhibit many superior electronic properties compared to silicon. GaAs and InP are two such materials that are relatively widely used for high speed transistors. An important requirement for circuits built using such devices is a very high resistivity – often referred to as semi-insulating – substrate. GaAs with a bandgap of 1.42 eV at room temperature has an intrinsic carrier concentration of $2x10^6$ cm^{-3} (resistivity of $3.3x10^8$ Ω·cm) and InP with a bandgap of 1.35 eV has an intrinsic carrier concentration of $1.3x10^7$ cm^{-3} (resistivity of $8.6x10^7$ Ω·cm), which are in the range for semi-insulating behavior. However, it is not possible to purify either of these materials (or any other semiconductor) to those levels; the background dopant concentrations are at best $10^{14} – 10^{15}$ cm^{-3}. However, one can employ the principle of dopant compensation to offset the carrier concentrations so as to produce material that has high resistivity. Briefly, if there are 10^{16} cm^{-3} shallow donors and also 10^{16} cm^{-3} shallow acceptors, the electrons and holes introduced by these dopants will cancel and only the intrinsic concentrations will remain. However, this is an unrealistic task as even a slight imbalance in the dopant levels ($1.001x10^{16}$ cm^{-3} donors vs $1.000x10^{16}$ cm^{-3} acceptors) would have a residual carrier concentration ($1x10^{13}$ cm^{-3} donors in this case; several orders of magnitude above the intrinsic case). The carrier concentration can be reduced to near the intrinsic values, however, by compensation of residual shallow donors (acceptors) with deep acceptors (donors). As noted above for silicon, transition metal species introduce deep levels in the bandgap of III-V materials [Clerjaud (1985); Langer (1988)] as shown in Figure 15 and both GaAs and InP have utilized transition metal dopants to provide semi-insulating material.

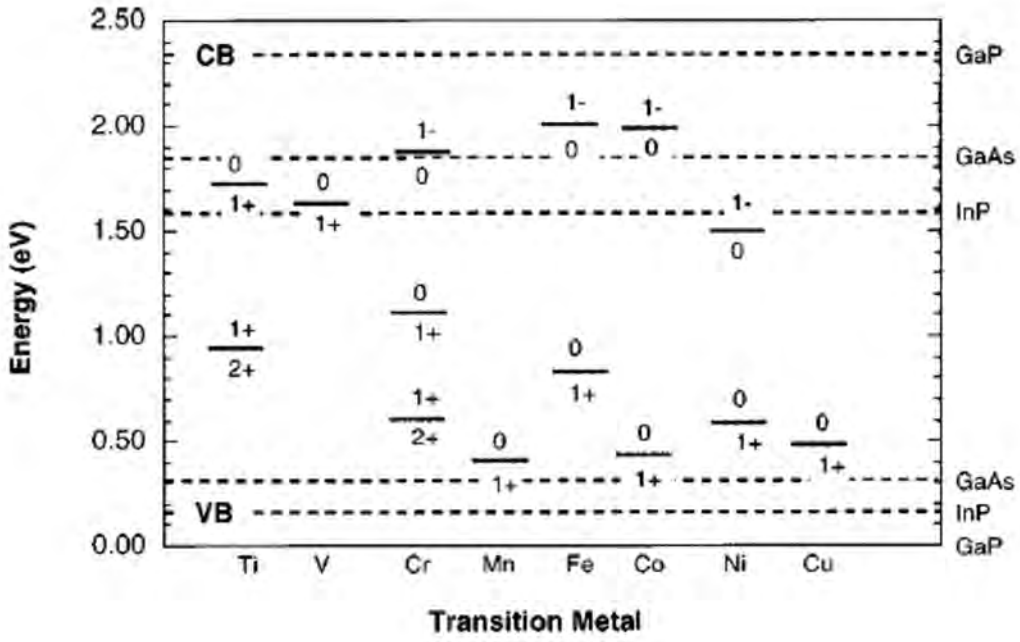


Figure 15. Transition–metal energy levels in the III–V semiconductors GaP, GaAs, and InP. [Nolte (1999)]

The strategy is to overcompensate the shallow level dopant with a higher concentration of a deep level impurity. For GaAs, Cr introduces a deep acceptor (0/1+ as in Figure 15) at approximately 0.78 eV above the valence band. A typical shallow residual dopant is Si in GaAs (Si_{Ga}) at a concentration of $3x10^{15}$ cm^{-3}. Using a deep acceptor Cr with a concentration of $1x10^{16}$ cm^{-3}, the Shockley diagram (at room temperature) is shown in Figure 16 below.

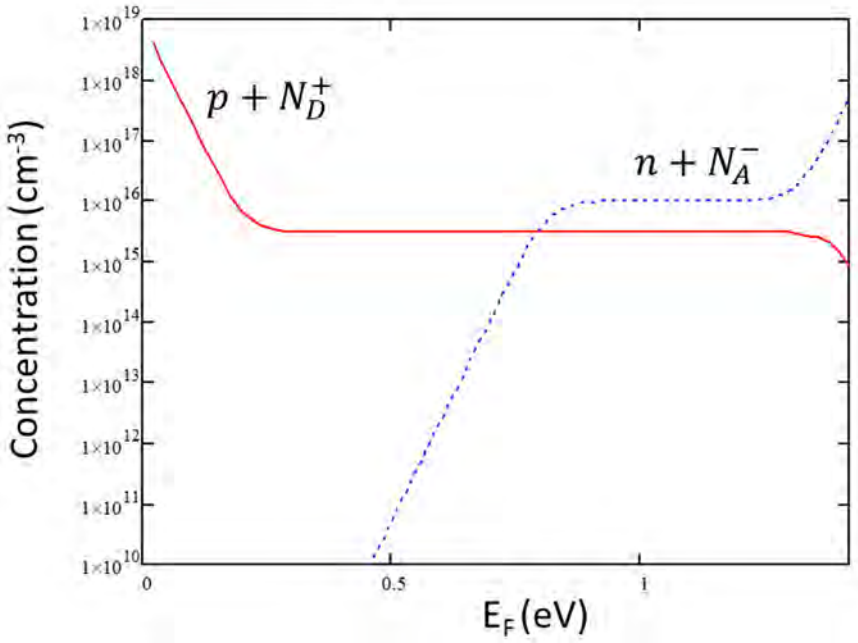


Figure 16. Shockley diagram for GaAs with Si shallow donors ($3x10^{15}$ cm^{-3}) and Cr deep acceptors ($1x10^{16}$ cm^{-3}).

Under these conditions, the Fermi level is at 0.794 eV, the electron concentration is $1.4x10^{7}$ cm^{-3}, and the hole concentration is at $4.2x10^{5}$ cm^{-3}. Using an electron mobility (μ_e) of $8x10^{3}$ $cm^2/(V\cdot s)$ and a hole mobility (μ_h) of 400 $cm^2/(V\cdot s)$, the resistivity is $9.8x10^{7}$ $\Omega\cdot cm$; therefore, the material can be considered semi-insulating. Note that the Fermi level is at approximately the same energy level as the deep acceptor level. This is referred to as 'Fermi level pinning' as ~2X changes to the shallow doping concentration or the deep level concentration do not alter the Fermi level position significantly.

Although GaAs:Cr is an effective means by which to produce semi-insulating material, transition metals also diffuse rapidly in III-V materials and also are supersaturated. This was an issue for metal-semiconductor field effect transistor (MESFET) applications which relied on ion implantation and subsequent annealing. During the annealing, the Cr out-diffused or precipitated and the material near the surface became conducting (n-type). It was known, however, that a deep donor (EL2, E_c- 0.75 eV) was also present in GaAs bulk substrates as well. EL2 has been attributed to the arsenic anti-site defect As_{Ga} [Hoinkis (1989)] although a significant debate was established as to other aspects of the defect. The As-antisite was much more stable during processing and, up to the present, is responsible for the semi-insulating behavior in GaAs and is readily introduced into GaAs through an excess of As during bulk crystal growth. As a deep donor, EL2 compensates shallow acceptors, typically carbon. In practice, shallow acceptors are introduced to compensate for residual shallow donors and growth conditions are established to produce a greater EL2 concentration than the shallow acceptor concentration.

InP, unfortunately, does not have an anti-site defect that acts as a deep level for compensation purposes. However, InP technology was developed later than GaAs technology and epitaxy (with lower temperatures than associated with ion implantation) had become widely used to produce device structures. Therefore, a transition metal – in this case iron (see Fig. 15) – provided effective compensation such that semi-insulating material could be achieved. Other wide bandgap semiconductors also utilize transition metal species to provide semi-insulating behavior. SiC has several polymorphic phases, typically referred to as polytypes. A common one is 6H, a hexagonal phase. In 6H SiC, with a bandgap of 3.0 eV, vanadium acts as a deep level, with both a deep donor level at E_c- 1.42 eV and a deep acceptor level at E_v+2.4 eV [Mitchel (1998)]. Hexagonal GaN, with a bandgap of 3.4 eV can be made semi-insulating using iron as a deep acceptor, as well. [Vaudo (2003)]

Dislocations in bulk crystal growth

The growth of single crystal substrates with low defect densities is important for many different applications. As noted above, the formation of dislocations involves both materials and growth properties. For crystal growth from a liquid, as a segment of the grown crystal moves

away from the melt, stress will develop due to the thermal gradients both axially (from the melt to the seed) and radially (from the center of the boule to the outer surface). While the temperature distribution may be radially symmetric [Jordan (1984)], with respect to the growing crystal, the stress depends on the thermal conductivity and the coefficient of thermal expansion; whether dislocations will form will depend on whether the stress exceeds the critical resolved shear stress, σ_c. Figure 17 shows the results of modelling crystal growth of Si, GaAs, and InP from (001) oriented boules. There are two main points of interest here. First, the contours show the expected dislocation densities. These dislocations are 60° dislocations and it is noted that unlike the symmetric thermal gradient used in the model, the dislocation distribution is different along different crystallographic directions. This is a result of the fact that these single crystals have anisotropic mechanical strength (greater along <110> than <100>, for example). Second, it can be seen that the silicon crystal is expected to have large regions free of dislocations, whereas the InP and GaAs have higher dislocation densities (with GaAs higher than InP). These differences are due to the superior mechanical properties of silicon. The thermal properties (thermal conductivity and thermal diffusivity) of silicon are approximately a factor of 2-3 better than GaAs or InP and the σ_c is greater by about a factor of 3-5 under these conditions. At present, 300 mm silicon wafers with dislocation densities < 1 cm^{-2} are typical and 100 mm GaAs and InP substrates are available with dislocation densities ~10^3 – 10^4 cm^{-2}.

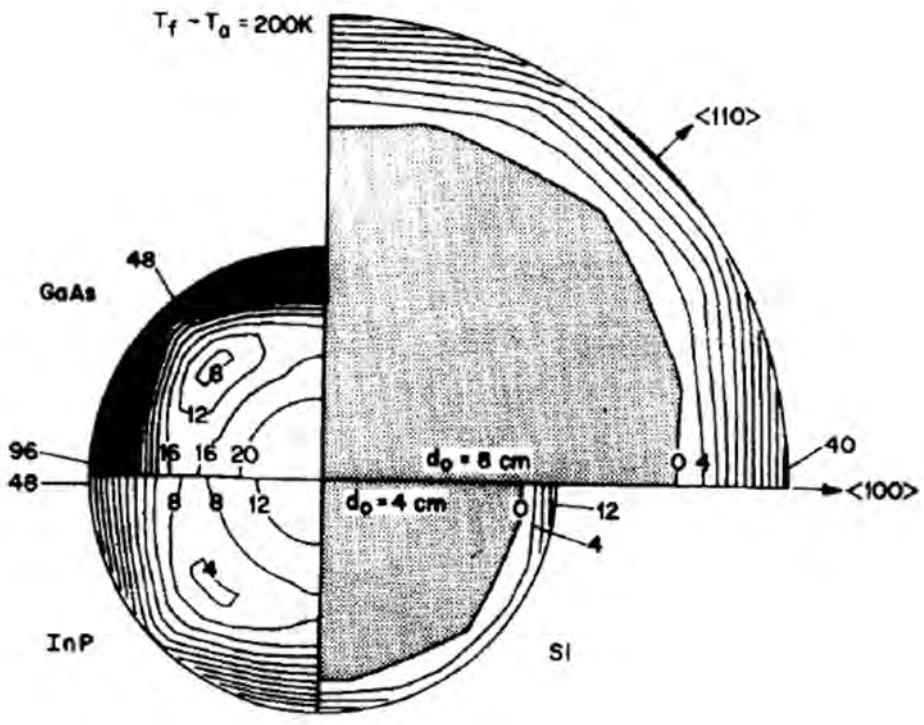


Figure 17. Dependence of the dislocation density distribution on diameter at the top end of pulled < 100> GaAs, InP, and Si boules when the average ambient temperature is 200 K below the respective melting points. (Figure 4 from Jordan (1984)).

SiC single crystal substrates possess additional complications. SiC cannot be grown from the melt but rather from the vapor phase. As noted above, SiC has several polytypes with similar thermodynamic stability. Therefore, it requires even greater care to prevent polytype formation in SiC crystals. 6H and 4H SiC are the most common hexagonal crystal structures and 3C SiC is a common cubic crystal structure. Figure 18 [Wellmann (2018)] shows the stacking sequences for these and other common polytypes. Screw dislocations are often observed in SiC. In some cases, these dislocations can possess extremely large Burgers vectors (~ 10 nm) and are referred to as micropipes. These are open-core screw dislocations that are known to degrade device performance. With more advanced growth techniques, both polytype inclusions and micropipe defects have become much more rare.

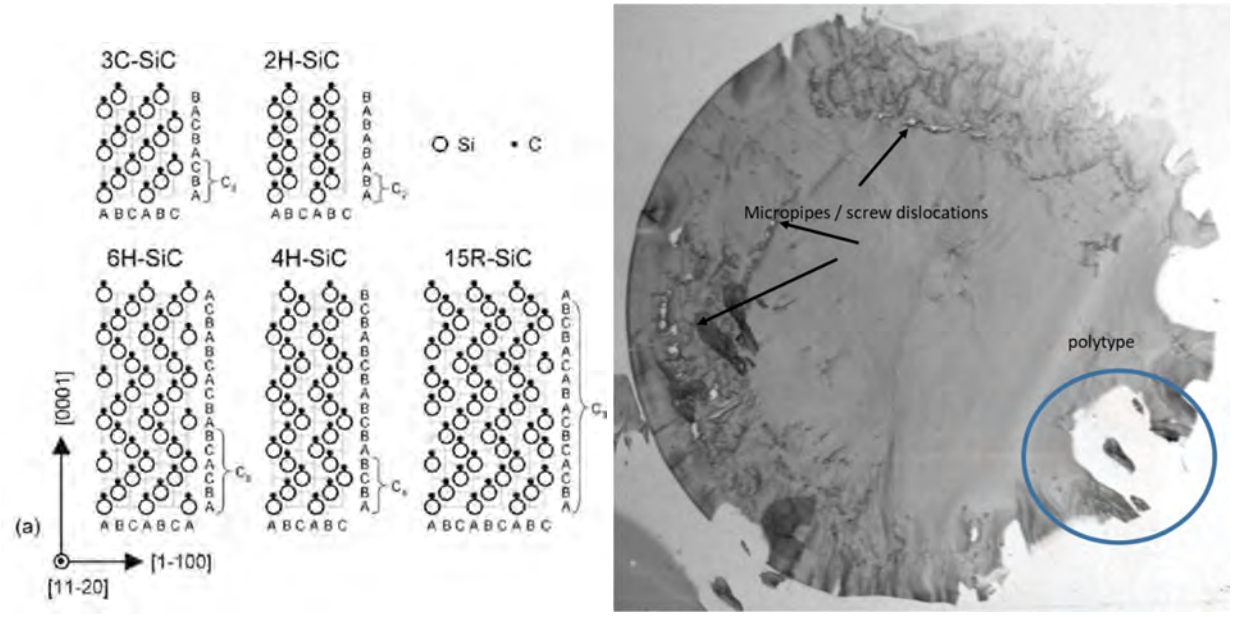


Figure 18. (left) Common polytypes of SiC showing the different stacking sequences of the Si-C double layers and [Wellman 2018] and (right) X-ray topography image showing a 2 in. diameter 4H crystal with inclusions and dislocations / micropipes.

$SrTiO_3$, with the perovskite crystal structure, is a common substrate for many complex oxide applications. $SrTiO_3$ is commercially grown using the Verneuil process. The Verneuil process also has high thermal gradients and the boule can possess high thermal stresses. Dislocations are present in relatively high concentrations (10^6 cm^{-2}) in commercial substrates, and because of the ionic character of the bonds, they play an important role in the electronic, magnetic, and optical properties of these materials [Szot (2018)] and there is evidence that the dislocation core is deficient in Sr. [Fitting (2006)] . Figure 19 shows edge dislocation models for $SrTiO_3$]. Experimentally, b<100> screw dislocations have also been observed in commercial $SrTiO_3$ wafers [Kamaladasa (2011)].

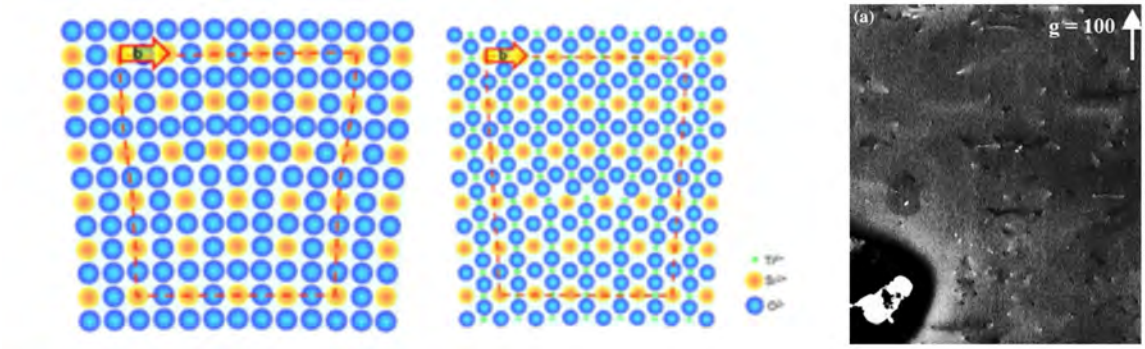


Figure 19. (left) Dislocations in $SrTiO_3$ for <100>{010} and <100>{110} systems. **b** = <100>, [Szot (2018)] and (right) dislocation images near the surface of a commercial $SrTiO_3$ substrate. [Kamaladasa 2011]

Dislocations in Epitaxial Films

For both semiconductors and epitaxial oxides, strain in the deposited films is a key issue. First, there are a limited number of choices for bulk, single crystal substrates. These available substrates may not match the lattice parameter for the deposited layer, introducing strain between the substrate and the layer. Figure 20(a) plots the bandgap vs. lattice parameter for a wide range of semiconductors and Figure 20(b) [Martin (2012)] shows a range of oxide substrate lattice parameters for deposition of a variety of thin films.

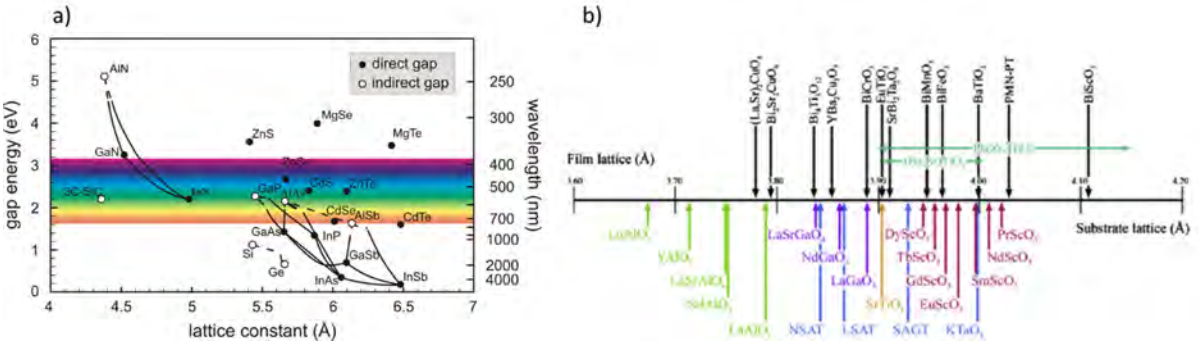


Figure 20. (a) The bandgap vs. lattice constant for Group IV, III-V, and II-VI semiconductors; (b) The lattice parameter of common oxide substrates as well as film compositions of technological interest [Martin (2012)].

Second, in many cases, this strain is utilized or engineered to modify the electronic, optical or magnetic properties of the film. Understanding the limits of the amount of strain or the thickness of the strained film is important to best utilize these layers. The critical thickness concept discussed earlier is relevant here. The mechanism of the formation of misfit dislocations can have a significant impact on the film properties.

Misfit dislocations are nucleated at some sort of existing defect. The most obvious of these is the dislocation that propagates from the substrate. Figure 21 below demonstrate how a substrate dislocation extends through the epitaxial layer and then can form a misfit segment to relieve the strain. The term 'threading dislocation' only means that it 'threads' though the substrate and layer; it does not signify whether the dislocations is an edge, screw or mixed dislocation.

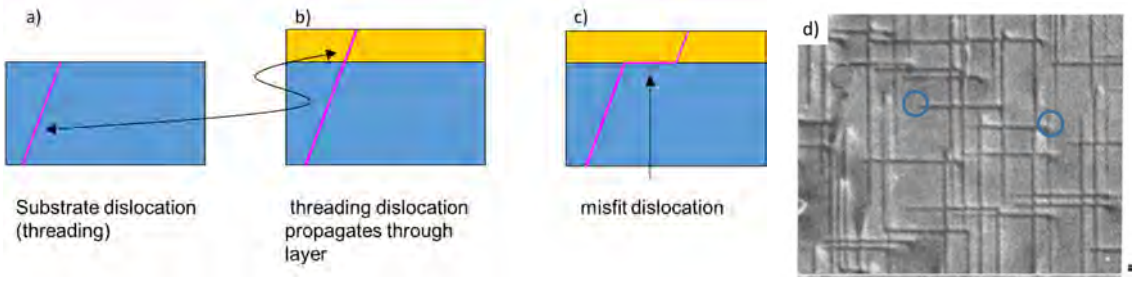


Figure 21. (a) – (c) The formation and propagation of a misfit dislocation segment from an existing substrate threading dislocation. (d) X-ray topograph showing that dislocations originate from threading dislocations [Jenichen (1985)] for (001) $Al_xGa_{1-x}As$ on GaAs.

There is extensive evidence that threading dislocations are the source for misfits but in some cases, there must be other origins to misfits. For example, silicon wafers have a very low density of threading dislocations so the strain relaxation must initiate at some other defect. Figure 22 below shows that misfit dislocations nucleate at the wafer edge or from scratches on the wafer surface. In this example, a lightly doped p-type layer is deposited on a (001) p+ (boron doped) substrate. The high boron concentration (>10^{20} cm^{-3}) shrinks the lattice so this structure represents a larger lattice parameter layer deposited on a smaller lattice parameter substrate, as is shown in Fig. 9 so the layer is under in-plane compressive stress. With reference to Fig.10, the structure is in the metastable regime as the critical thickness is 1.25 μm and the layer is 6 μm thick. The growth temperature is 1100 °C so dislocation motion is sufficient to produce misfit segments. The constraint is whether there are sources for misfit dislocation nucleation. A high density of misfit dislocations is present if wafers with standard edge grinding are used, but the density of misfit dislocations is much lower for wafers with the edge treated with a caustic etch to remove some damage, and misfit dislocations are completely absent if the edge is subjected to caustic etch plus chemical mechanical polishing of the edge.

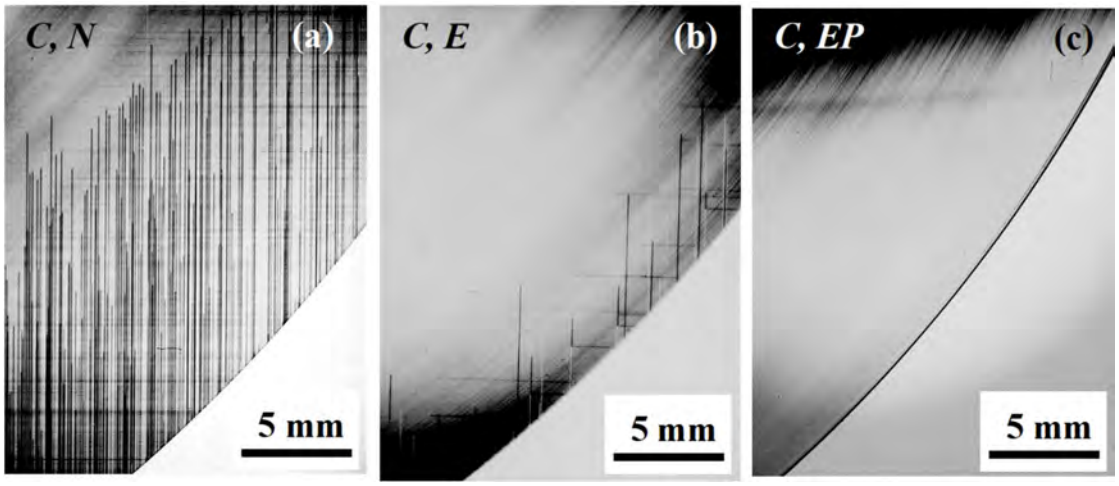


Figure 22. (224) X-ray topographs of silicon p/p+ epitaxy demonstrating the role of edge damage on misfit dislocation nucleation. (a) standard edge grind step; (b) wafer edges treated to a caustic acid etch to remove some grinding damage; (c) caustic etch and chemical mechanical edge polish to remove all grinding damage.

Particles and scratches can also initiate misfit nucleation formation. Figure 23 shows the same structure with a scratch introduced on the surface after growth. During subsequent annealing, misfit dislocations are observed to emanate from the scratch. Likewise, growth of a strained $In_{0.2}Ga_{0.8}As$ layer on a GaAs substrate by molecular beam epitaxy shows that particles present near the wafer periphery produce a high density of dislocations.

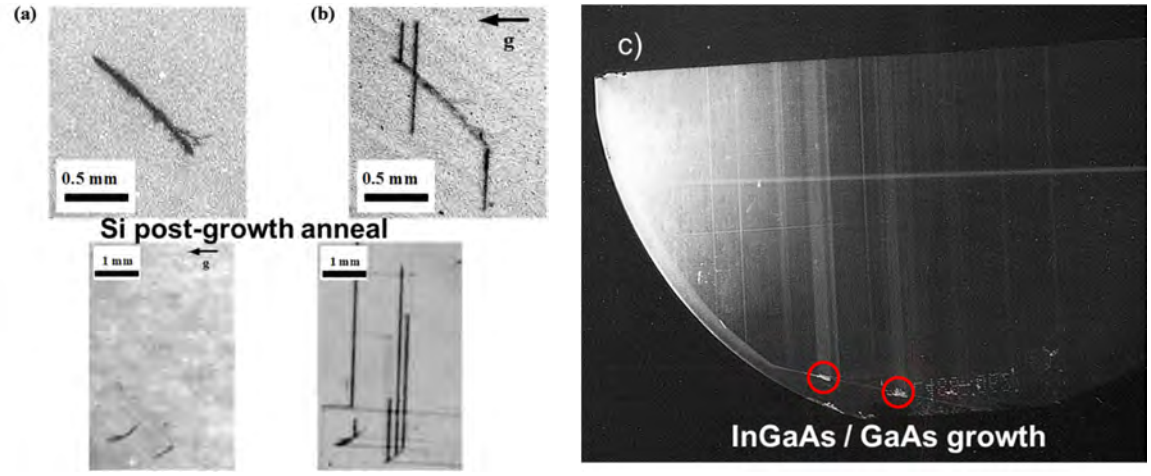


Figure 23. (a) (224) X-ray topographs of (001) silicon p/p+ epitaxy shows that scratches introduced after growth can produce misfit segments (b) after subsequent high temperature (1100 °C). (c) shows (115) topograph from an $In_{0.2}Ga_{0.8}As$ layer grown on 75 mm diameter (001) GaAs. In the lower left are two particles present during growth that produce a high density (white streaks) of misfit segments.

In semiconductors, the presence of misfit dislocations relieves the stress and can have an impact on device performance, especially if there are nucleation sites that help produce multiple defects. For epitaxial oxides, the situation is somewhat more complicated as polymorphs are much more common in complex oxides. For $BaTiO_3$ on $SrTiO_3$, for example, the strain relaxation follows that observed with semiconductors [Sun (2004)]. For a given strain due to the lattice parameter difference between the two materials, thin layers remain pseudomorphic. As the thickness increases, the layer relaxes through the formation of misfit dislocations as shown in Figure 24. The crystal structure (simple cubic perovskite) is different than for semiconductors discussed previously, so the Burgers vectors will also be different – in this case, the misfit dislocations are **b** = a<100> and **b** = a<010>. However, the surface orientation is (001), as in the case for the semiconductor systems above, so the misfits form an orthogonal array. Misfit dislocations are first observed at thicknesses below 4 nm and this corresponds to the expected critical thickness. The cross section image of the interface clearly shows the dislocation circuit.

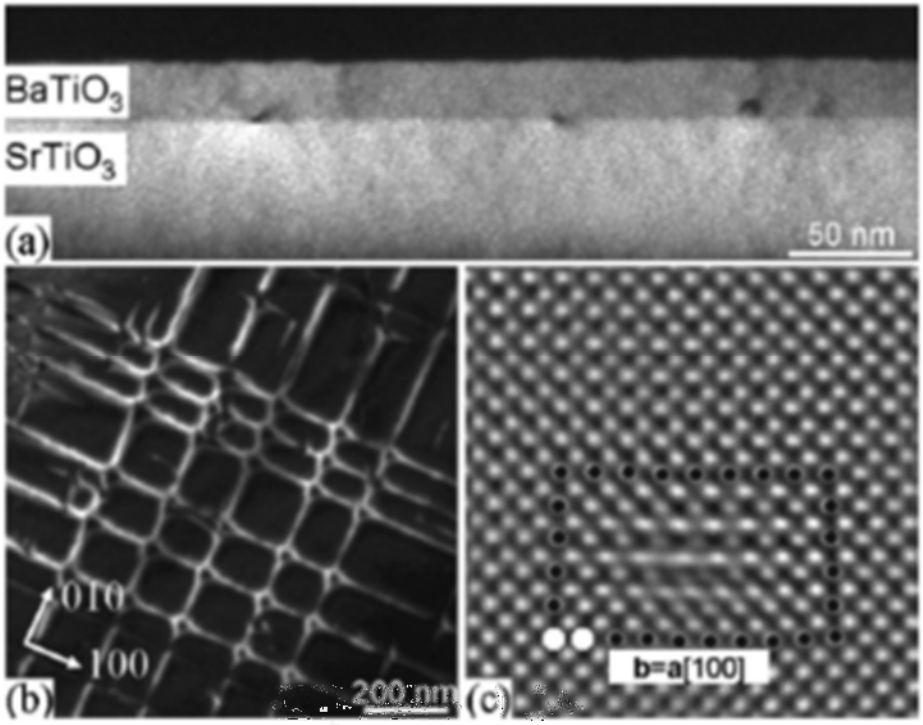


Figure 24. (Figure 1 in Sun (2004)) Cross-sectional dark-field image of a 20 nm $BaTiO_3$ /$SrTiO_3$ film showing the dislocation cores at the interface. (b) Plane-view dark-field image of the same $BaTiO_3$ /$SrTiO_3$ film displaying a dislocation array. (c)HRTEM image of a dislocation core at the film/substrate interface.

In another system, $BiFeO_3$ deposited on $LaAlO_3$, misfit strain is not the only issue. [Damodaran (2012)] Bulk $BiFeO_3$ is rhombohedral at room temperature, but tetragonal $BiFeO_3$ has been observed in films under a few percent strain. Figure 25 shows a stability phase diagram of $BiFeO_3$ as a function of strain. On the $LaAlO_3$ substrate, the monoclinic phase M_{II} is stabilized when the fil remains highly strained. As the layer thickness increases, strain-relieving misfit dislocations form. This drives the spinodal decomposition of the structure to two different monoclinic phases M_I and M_{II}. At even greater thickness, the layer reverts back to the relaxed rhombobedral phase.

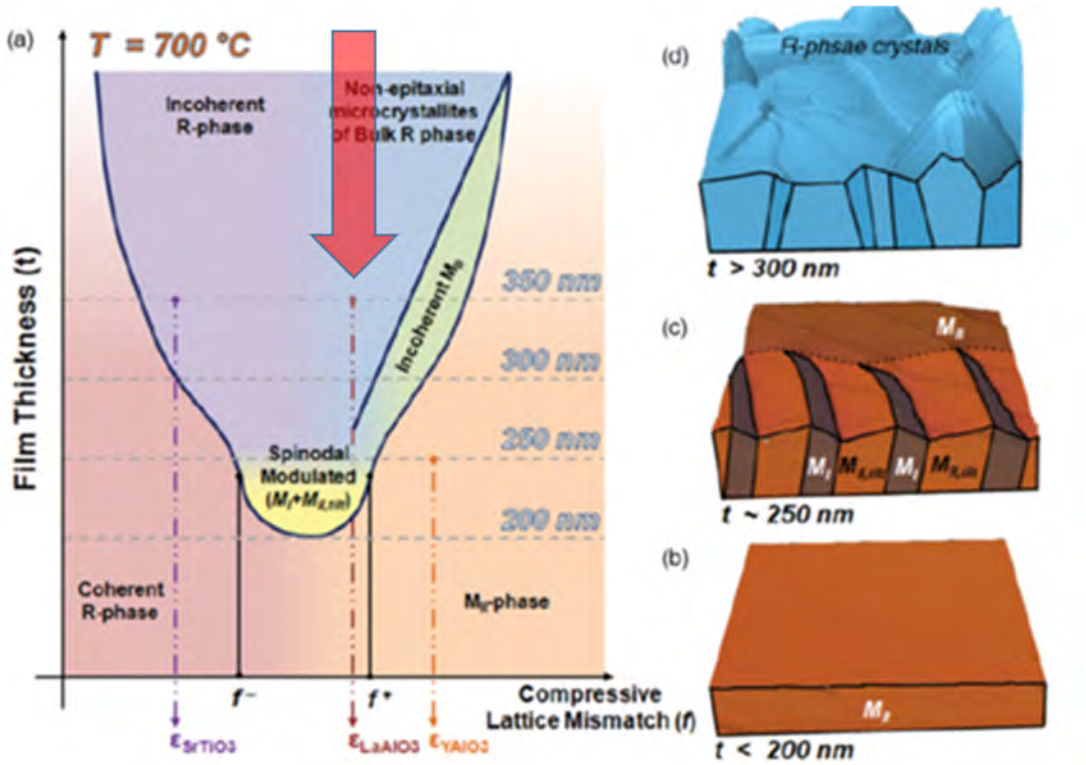


Figure 25. (From Fig. 7 [Damodaran (2012)]) (a) Schematic phase diagram showing the evolution of the microstructure as a function of epitaxial lattice mismatch (f) and film thickness (t) at a growth temperature of 700 °C. At the lattice mismatch expected between $BiFeO_3$ and $LaAlO_3$, we expect three different stages of growth: (b) coherent growth of the highly distorted M_{II} phase in thin films, (c) relaxation by formation of spinodal modulated structure of the M_I and $M_{II,tilt}$ phases at intermediate thicknesses, and (d) eventual relaxation and transformation to nonepitaxial microcrystals of bulk R phase.

Conclusion

Defects and impurities play key roles in the growth, processing, and use of crystals. The study of defects in well-developed materials such as silicon remains an important issue and lessons learned here readily apply to more complex and less well developed systems. An understanding of native point defects and impurities is key for all crystal materials systems as in the nature of dislocations and how to control them. Polymorph phases occur for many materials systems – in some, the phenomenon leads to novel oxide (or other) crystal structures which in turn leads to improvements in device structures as well.

References

Carvalho A, Jones R, Coutinho J et al. (2005) Phys Rev B: Condens Matter 72 (2005) 155208

Centoni SA, Sadigh B, Gilmer GH et al. (2005) Phys Rev B: Condens Matter 72 (2005) 195206.

Chen, J.-W. and A.G. Milnes, Ann. Rev. Mater. Sci. 1980. 10: 157-228 (1980)

Clerjaud, B., Journal of Physics C: Solid State Physics, Vol. 18, No. 19 (1985) p.3615.

Dabrowski, Jaroslaw, and Matthias Scheffler. Physical Review B 40, no. 15 (1989): 10391.

Damodaran, A.R., S. Lee, J. Karthik, S. MacLaren, and L.W. Martin. " Physical Review B 85, no. 2 (2012): 024113.

Falster, R.: Proc. Silicon Wafer Symp., Portland (1999) p. E13.

Fitting, L., S. Thiel, A. Schmehl, J. Mannhart, and D. A. Muller. Ultramicroscopy 106, no. 11-12 (2006): 1053-1061.

Föll, H., https://www.tf.uni-kiel.de/matwis/amat/def_en/index.html

Gottschalk, H., G. Patzer, and H. Alexander, phys. stat. sol. (a) 46, (1978) 207.

Hoinkis, M., E. R. Weber, W. Walukiewicz, J. Lagowski, M. Matsui, H. C. Gatos, B. K. Meyer, and J. M. Spaeth. Physical Review B 39, no. 8 (1989): 5538.

Hu, S.M., "Proceedings of the Eighth International Symposium on Silicon Materials Science and Technology, H.R. Huff, H. Tsuya, and U. Goesele, eds., Electrochemical Society (1998) p.220-256.

Jenichen, B., B. Köhler, and W. Möhling, physica status solidi (a) 89, no. 1 (1985): 79-87

Jordan, A.S., A.R. Von Neida and R. Caruso, J. Crystal Growth 70 (1984) 555-573.

Kamaladasa, R., J., W. Jiang., and Y. N. Picard. Journal of Electronic Materials 40, no. 11 (2011): 2222

Langer, J. M., C. Delerue, M. Lannoo, and H. Heinrich, Phys. Rev. B 38, (1988) 7723.

Martin, L.W., and D.G. Schlom. Current Opinion in Solid State and Materials Science 16, no. 5 (2012): 199-215

Matthews, J.W. &A.E.Blakeslee., Journal of Crystal Growth, Vol27, 1974, 118-125.

Meshkinpour, M., and M. S. Goorsky, B. Jenichen, D. C. Streit and T. R. Block, Journal of Applied Physics 81, (1997) 3124.

Mitchel, W.C., Perrin, R., Goldstein, J., Roth, M., Ahoujja, M., Smith, S.R., Evwaraye, A.O., Solomon, J.S., Landis, G., Jenny, J. and Hobgood, H.M.,In *Materials Science Forum* (Vol. 264, pp. 545-548). Trans Tech Publications (1998).

Nolte, D. , J. Appl. Phys., Vol. 85, No. 9, (1999) 6259-6289.

Savvides N., and A.Katsaros, Physica C: Superconductivity Volume 226, Issues 1–2, (1994), Pages 23-36,; *also see D.G. Schlom, D. Anselmetti, J.G. Bednorz, Ch. Gerber, J. Mannhart, and K.A. Müller, Physica C 185-189 (1991) 2007-2008.]*

Shimura, F. editor, Oxygen in Silicon, Semiconductors and Semimetals Vol. 42 (Academic, London), 1994.

Shimuzu, H. and T. Inoue, J. Coll. Eng. Nihon Univ. 59 (1) (2017)

Sun, H. P., Wei Tian, X. Q. Pan, Jeffery H. Haeni, and Darrell G. Schlom. Applied Physics Letters 84, no. 17 (2004): 3298-3300.

Szot, K., C. Rodenbücher, G. Bihlmayer, W. Speier, R. Ishikawa, N. Shibata, and Y. Ikuhara., Crystals 8, no. 6 (2018): 241

Tsao, J. "Materials Fundamentals of Molecular Beam Epitaxy" Chapter 5, 1993, Elsevier Inc.

Weber, E. R. Applied Physics A, Vol.30,(1) (1983) pp 1–22.

Válek, Lukáš, and Jan Šik. "Modern Aspects of Bulk Crystal and Thin Film Preparation". IntechOpen, 2012]

Vaudo, R. P., X. Xu, A. Salant, J. Malcarne, and G. R. Brandes. physica status solidi (a) 200, no. 1 (2003): 18-21.

Voronkov, V.V., Journal of Crystal Growth. Vol. 59, No. 3, (1982), pp. 625- 643,

Voronkov, V.V. Journal of Crystal Growth, Vol. 310, No. 7-9, (2008), pp. 1307-1314

Wellmann, P. J, Semiconductor Science and Technology, Vol 33, No. 10, (2018) p.1

Yonenaga, I. K. Sumino, and K. Hoshi, Journal of Applied Physics 56, (1984) 2346

7. Characterization and in situ Observation

From
CHARACTERIZATION IN COMPOUND SEMICONDUCTOR PROCESSING

Editors:
Yale Strausser and Gary E. McGuire

BUTTERWORTH-HEINEMANN ,
copyright 1997

Chapter 2 by Thomas F Kuech

2

III–V Compound Semiconductor Films for Optical Applications

THOMAS F. KUECH

Contents

2.1 Introduction
2.2 Growth Rate/Layer Thickness
2.3 Composition Analysis
2.4 Impurity and Dopant Analysis
2.5 Electrical Properties in Optical Structures
2.6 Optical Properties in Single and Multilayer Structures
2.7 Interface Properties in Multilayer Structures
2.8 Summary

2.1 Introduction

Optical devices have become an important part of our technology. The light emitting diode (LED) is an integral component of many displays. The solid state laser is used in communication systems, connecting our phones and data processing equipment through fiber-optic cables. Consumer products, such as the compact disk player, have benefited from the availability of inexpensive, compact, and reliable solid state light emitters and detectors. Other optical components required in an optical system are now available in solid state form. Detectors, modulators, and waveguides can be formed through the application of modern epitaxial growth and semiconductor-processing techniques. Compound semiconductors, such as GaAs, $Al_xGa_{1-x}As$, InP, and $In_xGa_{1-x}As_yP_{1-y}$, are all direct bandgap materials suitable for such optical device structures. The availability of multicomponent semiconductor alloy systems provides independent control of both bandgap and lattice parameter. The bandgap controls the wavelength regime over which the material interacts

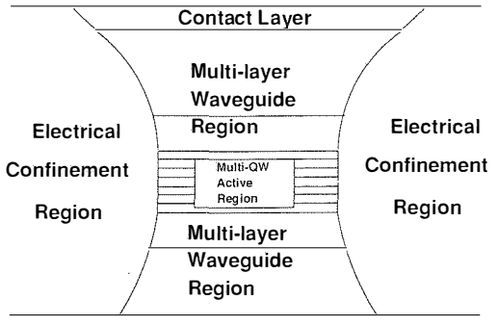


Figure 2.1 **A double heterostructure laser is typical of many of the advanced multilayer optical devices being developed and manufactured. This structure contains separate layers for the optical waveguiding and electrical current confinement required for efficient lasing. Multiple epitaxial steps are often employed to regrow specialized regions onto an existing etched and patterned structure.**

strongly with light. The choice of lattice parameter is important in the growth of high-quality material on readily available substrates.

A distinguishing feature of compound semiconductor devices, in general, over Si-based technology lies in the formation of the active device region. In Si-based devices, the active region is formed through the modification of the near-surface region of a single-crystal Si wafer. Advanced compound semiconductor devices are formed, however, through the process of epitaxial crystal growth. Thin regions of semiconductors are deposited onto an existing substrate, typically GaAs or InP. Through controlled deposition onto this substrate, multiple semiconductor layers differing in composition and doping are deposited on the substrate in sequence such that the crystallographic orientation is maintained. This process of epitaxial growth is central to forming the complex multilayered structures needed in laser fabrication. A laser structure, shown schematically in Figure 2.1, contains many individual layers and can possibly entail multiple growth steps. All the individual layers and their interfaces must work properly to produce a high-efficiency laser. The deposited film must have a lattice parameter close to that of the substrate to prevent disregistry of the atoms as the film grows. Such disregistry eventually leads to the formation of strain-relieving defects, such as dislocations, which can strongly degrade the device performance. Pseudomorphic growth, shown schematically in Figure 2.2, allows for the strained epitaxial growth of thin lattice-mismatched layers. This growth continues up to a "critical" thickness beyond which defects are formed to relieve the built-in strain.[1] In either lattice-matched or -mismatched growth, materials properties are largely determined by alloy composition and growth conditions. These materials properties are dependent on the structural characteristics of the film, such as thickness and morphology, which must be monitored and controlled.

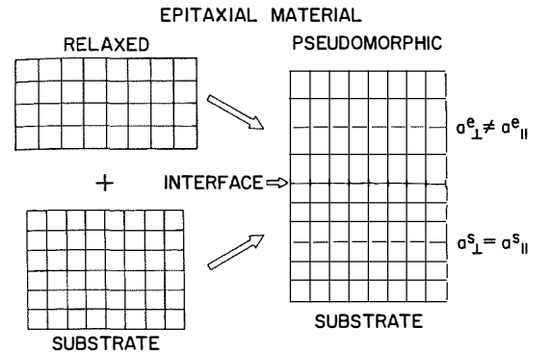


Figure 2.2 **The growth of pseudomorphic layers expands the range of possible materials useful in optical device structures. The lattice mismatch is accommodated by increasing the strain in the overgrown layer. This type of growth will continue up to a "critical" thickness after which strain-relieving defects such as dislocations are formed.**

Several forms of crystal growth are used in the formation of these multilayer structures: liquid phase epitaxy (LPE), vapor phase epitaxy (VPE), metal-organic vapor phase epitaxy (MOVPE), and molecular beam epitaxy (MBE). Most LED structures have been formed using LPE and VPE. New material structures, such as quantum well lasers, are being primarily grown by MOVPE and MBE. All these growth techniques, generally, do not directly monitor the film formation during the actual growth process. As a result, the formation of a multilayered structure involves an iterative process of growth, measurement, and then growth based on the refined parameters. This process places a heavy burden on the characterization of single-layer structures as well as multilayer structures of increasing complexity.

Most optical devices utilize the standard semiconductor device fabrication techniques—ion implantation, diffusion, and dielectric deposition—to form the epitaxial structure into a working device. The unique feature of modern devices is the reliance on the epitaxial formation of the material's structure. While several device formation techniques are discussed elsewhere in this volume, this chapter will concentrate on the evaluation of the epitaxial structures used in optical devices. The pre–device fabrication characterization of the epitaxial wafer is an essential part of this technology. The device performance in many ways is set at the moment of growth of the structure.

This chapter presents these characterization techniques in the context of the important film properties required in these structures. The techniques and procedures are not unique to any specific crystal growth technique and are generally used by all crystal growers and device engineers. The structural aspects and optical and electrical characterization of individual layers and multilayer structures are addressed. The correct physical structure alone is not sufficient for ensuring the formation of

high-performance devices. These layers and structures must also possess the proper electrical and optical characteristics. The essential information required for the interpretation of device characteristics are (1) the physical properties of the film, such as composition and thickness of the individual layers, (2) doping and unintentional impurity incorporation, (3) optical properties such as luminescence and wavelength dependence, (4) interface structure and properties, and (5) the strain induced in an individual layer due to a lattice mismatch. The uniformity of these properties is critical to achieving a high yield from the fabricated devices and has received a great deal of attention in the pre–device fabrication characterization.

There are many complementary techniques which have become standard in the characterization of these structures. Typically, no one technique can unambiguously yield the desired information. Data from a variety of techniques must be correlated, and a self-consistent description should arise. The range of common techniques are given in Figure 2.3. The acronyms pictured in this figure are discussed in the following text. This figure indicates the multifaceted approach to materials and device characterization necessary in the development of optical device structures. These techniques are discussed below in the context of the information required from the device structure.

2.2 Growth Rate/Layer Thickness

In Situ Growth Monitors

The development of the epitaxial growth process for optical devices starts with the simple determination of the growth rate, composition, and morphology of a film. The growth rate within the epitaxial system, as well as the thickness of the individual layers, is required for one to interpret results obtained from device measurements. The thickness of specific layers is crucial in most device structures. Ideally, the growth rate would be measured during the actual layer growth or the real-time thickness of the growing layer monitored. Such "in situ" monitoring techniques are currently being developed. In the case of MBE, the growth temperature is typically monitored by an optical pyrometer. The pyrometer signal, however, oscillates during the growth of a heteroepitaxial layer due to optical interference of the infrared light passing through the sample.[2] As the heteroepitaxial layer grows, it forms an "anti-reflection" coating on the substrate, resulting in the oscillations of the measurement signal. Knowledge of the optical constants of the growing material combined with the oscillation period of the pyrometer signal can yield the growth rate or corresponding layer thickness.

The development of in situ probes applicable to both MOVPE and MBE growth systems is ongoing. These are generally optically based, such as with optical laser reflectivity at the visible or near-visible wavelengths. Oscillations in the reflected light intensity can again develop, as in the case of the optical pyrometer. Such reflectivity techniques can be implemented for real-time measurements of growth thickness while the device structure is being fabricated. The analysis of the intensity

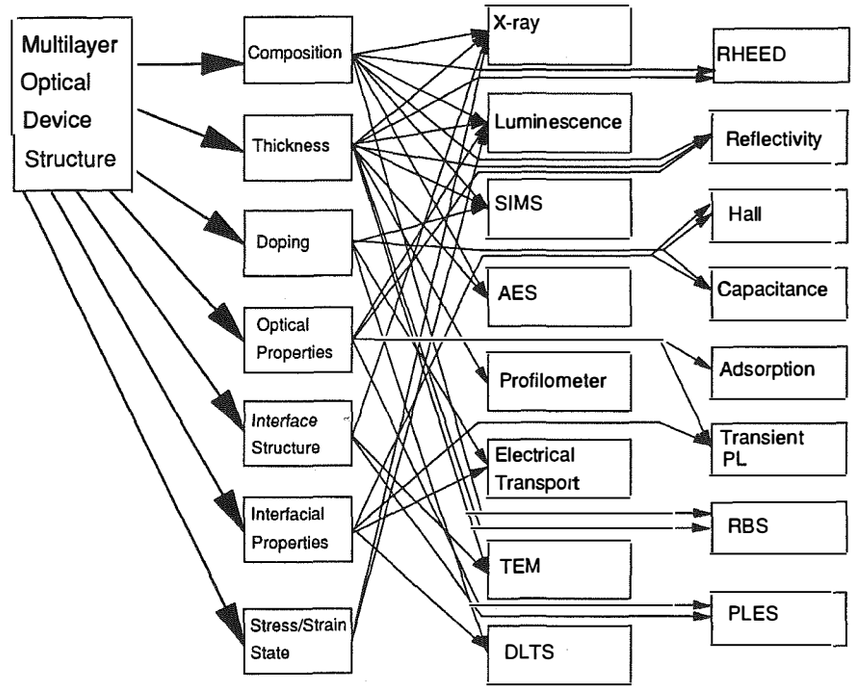


Figure 2.3 The characterization of the epitaxial wafer used in optical device fabrication requires a multifaceted approach to develop a full understanding of the materials structure. A particular measurement can yield information on several materials properties, increasing the value of that technique.

and variation of the reflected light is easily modeled using standard geometrical optics.[3] Control of the composition of a growing film can be accomplished by the real-time calculation of the reflectivity, comparison to the experimentally determined value, and the subsequent adjustment of the growth controlled parameters. Post-growth measurement of the layer thickness can also be determined optically through ellipsometry.

Newer optical probes, such as reflection difference spectroscopy (RDS) and spectral ellipsometry, are currently being developed as real-time in situ growth monitors. The RDS spectrum exhibits oscillations, under suitable conditions, that can be related to the growth of a single atomic layer of material. Spectral ellipsometry can be used to determine both composition and thickness, provided the optical constants of the growing materials are approximately known. Both these measurements,[4] as well as those described above, require direct line-of-sight access to the growth environment. Growth-related changes in the optical path, such as fogging of the optical ports by extraneous deposited material, must be controlled or taken into account during the measurement, limiting the applicability of these measurements.

Specific to the MBE-based growth techniques is reflected high energy electron diffraction (RHEED). RHEED is usually used to monitor the surface stoichiometry and structure of the growth surface.[5] RHEED has also been used as a tool for monitoring growth at the atomic level. During the layer-by-layer growth of the semiconductor, the intensity of the main Bragg reflection of the RHEED pattern oscillates in intensity. The period of oscillation has been shown to correspond to the growth of a single monolayer of the semiconductor. The physical origins of these oscillations are still a matter of discussion; however, RHEED oscillations provide an accurate, rapid means of obtaining growth-rate data. This technique is used to calibrate the growth rate when employing a specific source Knudsen cell. Its application to real-time analysis is limited, due to degradation of the materials properties under electron-beam exposure, damping of the oscillation with layer thickness during continuous growth, and the somewhat specialized growth conditions required to obtain the oscillations. Despite these limitations, RHEED oscillations can be used to rapidly calibrate growth rates just prior to growth of the actual device wafer.

Post-Growth Structural Analysis

The post-growth determination of the layer thickness is more commonly made by one of several usually destructive techniques. For thicker layers, the substrate–epilayer combination can be cleaved and the layers chemically stained. The chemical stain darkens or highlights layers, with the degree of staining dependent on the specific composition or doping. The cleaved sample edge is later inspected after staining by optical microscopy, typically using a technique such as Nomarski phase contrast, in order to determine the layer thickness. The thickness of very thin layers can also be determined through the inspection of the cleaved and stained edge by scanning electron microscopy (SEM).[6] In all these cases, the accuracy of the thickness measurement is dependent on a determination of the magnification of the instrument. Very thin layers can only be imaged by the time-consuming and expensive process of cross-sectional transmission electron microscopy (TEM). The TEM micrograph seen in Figure 2.4 was taken from an $Al_{0.3}Ga_{0.7}As/GaAs$ multilayer structure. The individual layers are clearly seen in the micrograph, allowing for the determination of the various layer thicknesses. The high magnification achievable in TEM[6] allows for almost atomic resolution on the TEM image. This process, while yielding detailed information, is not amenable to routine structure determination. The determination of the actual interface abruptness, that is, the spatial variation in composition, is very difficult to obtain from these micrographs, since the actual change in contrast is due to a variety of instrumental and sample-dependent factors.

A profilometer can also be used to mechanically measure the thickness of a layer. Stylus profilometers can accurately and rapidly determine physical step heights etched into a sample surface. Many profilometers can measure step edges with a resolution of a few nanometers. Wet and plasma-based etches are available for most

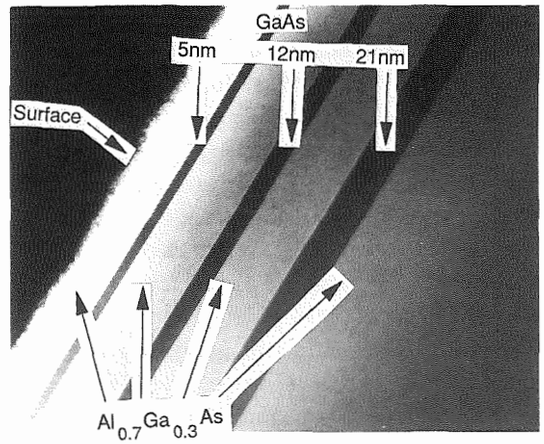


Figure 2.4 **Transmission electron micrograph of an $Al_{0.7}Ga_{0.3}As/GaAs$ multilayer structure. The dark bands in the micrograph are thin layers of GaAs (5, 12, and 21 nm in thickness) between thicker layers of $Al_{0.7}Ga_{0.3}As$. The contrast in these types of micrographs allows for the determination of the thickness of the individual layers but does not yield exact compositional information.**

alloy semiconductor systems which are highly compositionally selective. For example, $Al_xGa_{1-x}As$, with $x > 0.50$, can be rapidly etched in HCL or HF solutions, while GaAs is relatively untouched. A wide variety of selective etches have been developed for all the standard ternary and quaternary optical materials. An overlying epitaxial layer can be selectively removed down to an underlying layer by masking an overlayer with photoresist or another etch-resistant material. The profilometer can be used to find the thickness of the overlayer once the etch mask is removed. The ease and convenience of this technique combined with the general availability of profilometers is responsible for its widespread use, despite the destruction of some of the sample area.

2.3 Composition Analysis

The composition of the material, in addition to layer thickness, determines a laser optical emission wavelength, the cutoff wavelength of a detector, and any property which is dependent on bandgap. The direct band edge of $Al_xGa_{1-x}As$ increases, for example, ~14 meV for $\Delta x = 0.01$. This change in composition corresponds to a wavelength shift of ~7 nm in the light emission for compositions near GaAs. In the lattice-matched ternary alloy systems, such as the $Al_xGa_{1-x}As/GaAs$ system, the band edge is determined only by the relative ratio of the two constituent binaries in the material, such as the AlAs/GaAs ratio in $Al_xGa_{1-x}As$. More complex structures involving quaternary materials, such as $In_xGa_{1-x}As_yP_{1-y}$, require control of

multiple species. This implies that two ratios must be controlled in quaternary materials; for example, both the In/Ga and As/P ratios must be controlled in the growth of $In_xGa_{1-x}As_yP_{1-y}$. In non-lattice-matched systems, the bandgap is a function of the strain state of the layer. The strain state must be determined from other physical measurements. Composition control is required to maintain a desired lattice match between the epilayer and the underlying substrate. In epilayers which must be lattice-matched to a substrate, the degree of lattice match required is usually better than $\Delta a/a \leq 10^{-3}$, where a is the substrate lattice parameter and Δa is the difference in lattice between the epilayer and substrate parameters.

Layer composition can be determined by a variety of physical and optical techniques. The choice of techniques depends on the accuracy required. Auger electron spectroscopy[6] (AES) is a high-vacuum technique compatible with the MBE growth system. AES is based on the emission of Auger electrons under electron bombardment. Since the energy of an Auger electron is specific to a given element, the energy distribution of the Auger electrons can yield the composition of the sample.[7] The sensitivity of AES is usually on the order of ~0.5% which is insufficient for many applications. The addition of an ion gun, which removes the surface region by sputter erosion, to the AES system does allow for the depth profiling of the elemental composition in a multilayer sample. A related physical analysis technique is electron microprobe analysis. In this case, an incident electron beam generates X-ray emission from the constituent elements comprising the sample. The volume sampled by the electron probe is large. The electron beam penetrates into the sample, generating X rays over a depth of 0.5 to 1 μm, which limits this technique to the analysis of thick epitaxial layers. Electron microprobe characterization of thin layers demands extensive data analysis, typically requiring additional information concerning the sample geometry or composition.

High-resolution X-ray diffraction is a convenient, quantitative means of determining the structural properties of a multilayer structure. Commercial, user-friendly, double crystal X-ray diffractometers (DCXRD) along with diffraction simulation programs allow for the acquisition of an X-ray spectrum and its direct modeling. As a result, DCXRD has been developed into the premier technique for determining the composition of multicomponent semiconductors.[6] The measurement technique, when used on samples containing nearly or actually lattice-matched layers, is referred to as a rocking curve measurement or spectrum. Examples of a rocking curve from two separate single $Al_xGa_{1-x}As$ layers grown on GaAs are shown in Figure 2.5.[6] These spectra contain information concerning layer thickness and composition. The position of the Bragg reflection peaks from the epitaxial layer, $\Delta\Theta$, relative to the substrate peaks allows the determination in the difference in lattice parameter from the substrate. Since the substrate lattice parameter is known, the epilayer lattice parameter is determined and the composition deduced from known lattice constants. The data analysis for thick layers is well understood and simple to carry out. In Figure 2.5, the angular splitting between the substrate and $Al_xGa_{1-x}As$ peaks is small, less than 300", indicating a close lattice match

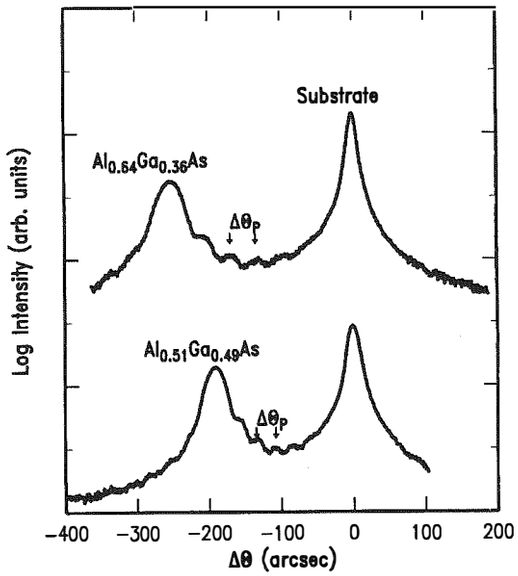


Figure 2.5 **The double crystal X-ray rocking curve taken from two separate samples of $Al_{0.64}Ga_{0.36}As$ and $Al_{0.51}Ga_{0.49}As$ grown on GaAs. The close lattice match between the $Al_xGa_{1-x}As$ layers and GaAs results in pseudomorphic growth. The separation of the two principal narrow Bragg peaks yields compositional information while the additional oscillatory structure, $\Delta\Theta_p$, is related to the film thickness.**

between GaAs and $Al_xGa_{1-x}As$. The analysis of the data for such pseudomorphic layers also requires knowledge of the Poisson's ratio of the material, typically possessing a value of about 0.3. The determination of whether or not a layer is pseudomorphic can be ascertained, generally, from the width of the epilayer Bragg peak. Large peak widths for epitaxial layers are sometimes a strong indication of the appearance of extended defects arising from the relaxation of the pseudomorphic growth. In these single-overlayer structures, the DCXRD spectrum yields an oscillating intensity between the two principal Bragg reflections, one from the substrate and one from the overlayer, also shown in Figure 2.5. These oscillations, known as Pendelossing oscillations, have a period, $\Delta\Theta_p$, that is related to the single-layer thickness.[6] The DCXRD spectrum from superlattice structures can determine the period of the repeating unit and the average thickness of the individual layers, such as the $Al_xGa_{1-x}As$ or GaAs thickness in an alternating structure. As indicated, the DCXRD measurements on ternary materials can yield composition directly, since only the simple mixture of two binary compounds needs to be considered (e.g., InAs/GaAs in $In_xGa_{1-x}As$). Additionally, all ternary and quaternary materials follow Vegard's law, simplifying the analysis. The determination of the exact composition of a quaternary material is more complex, requiring additional data such as

the bandgap. The combined data of lattice parameter and bandgap allows the determination of the composition in closely lattice-matched systems.

DCXRD measurements and analysis can also be performed on multilayer structures in order to determine the details of the final structure. The DCXRD spectrum from a multilayer structure contains a great deal of fine structure, due to complex interference effects between X rays reflected from many layers, which can be compared to calculated spectra based on test or hypothetical structures. A typical DCXRD rocking curve from an $Al_xGa_{1-x}As$/GaAs multilayer structure is shown in Figure 2.6, along with the result of a dynamic simulation of the rocking curve.[8] The structure is composed of a GaAs substrate, 445 nm layer of $Al_{0.33}Ga_{0.67}As$, 183 nm layer of GaAs, and a 460 nm surface layer of $Al_{0.33}Ga_{0.67}As$. The dynamic simulation, often performed using commercial software, can accurately model this multilayer sample and predict the many fine-structure features in the DCXRD spectrum. A comparison of the experimentally determined rocking curve to the calculated curve offers a means of characterizing a multilayered sample in a fairly accurate fashion, depending on the precision of the data and the details of the calculation. This nondestructive measurement can be performed over the surface of the wafer, determining uniformity in thickness and composition.

The composition of multicomponent materials can also be accurately obtained from photoluminescence (PL) measurements.[6] PL from an alloy, typically obtained at low temperatures of 77 K or below, can be obtained rapidly in a nondestructive

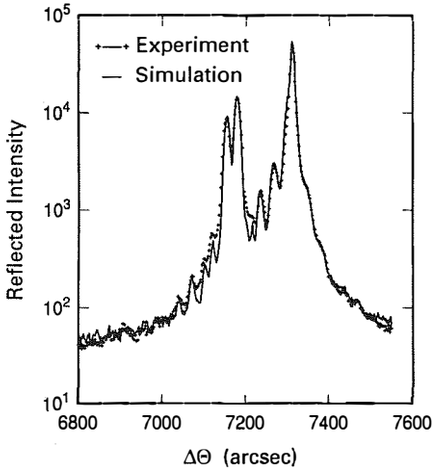


Figure 2.6 **The DCXRD rocking curve obtained from a structure composed of a GaAs substrate, 445 nm layer of $Al_{0.33}Ga_{0.67}As$, 183 nm layer of GaAs, and 460 nm surface layer of $Al_{0.33}Ga_{0.67}As$ is modeled using a dynamic simulation of the X-ray scattering from a multilayer structure. A comparison between the experimental data and the stimulation can be used to determine the composition and thickness from multilayer structures.**

fashion. The band-edge luminescence spectra has well-defined features for most ternary and quaternary materials. PL spectra from $Al_xGa_{1-x}As$ layers grown on GaAs substrates is shown in Figure 2.7.[9] The highest energy peak is associated with either a band-to-band radiative transition (at higher measurement temperatures) or various excitonic and impurity-related transitions (at very low temperatures). The energy of these transitions are related to the band structure and bandgap of the material. The lower Al mole fraction $Al_xGa_{1-x}As$ samples shown in Figure 2.7 are direct bandgap materials, while the higher composition sample is an indirect gap semiconductor. The change from direct to indirect band structure is accompanied by a shift in the structure of the luminescence spectrum. Once identified, the band structure can be used to derive the sample composition. The composition is related to the bandgap provided the strain states of the materials are known. PL from pseudomorphic layers, particularly under a high degree of strain, exhibit predictable shifts in the bandgap from the relaxed or nonstrained case. The strain must be determined from other measurements, DCXRD in particular. The composition in nonstrained ternary alloy layers can be obtained from PL measurements through a comparison to known bandgap-versus-energy curves. Both DCXRD and luminescence maps of the composition over the wafer surface can be obtained. These combined measurements can yield an accurate view of the compositional uniformity over the substrate surface.

2.4 Impurity and Dopant Analysis

The concentration of impurity atoms within a layer is difficult to quantitatively determine due to the high sensitivity required in the depth profiling of trace atoms. Secondary ion mass spectrometry (SIMS) measurements can be a quantitative profiling technique with an extremely large dynamic range.[6, 10, 11] The sample surface

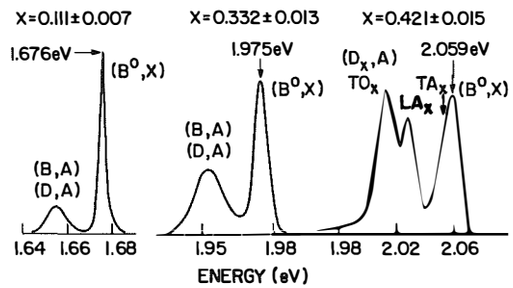


Figure 2.7 **The PL spectrum from an alloy compound semiconductor can be used to determine the composition of the sample. The spectra shown here are obtained from high-purity $Al_xGa_{1-x}As$ samples grown by the MOVPE technique. The change in the spectral signature from the sample between $x = 0.33$ and $x = 0.42$ indicates the shift from a direct to indirect band structure, which occurs at a composition of about $Al_{0.37}Ga_{0.63}As$.**

in the SIMS technique is sputtered, and those sputtered atoms which leave the surface as ions, referred to as secondary ions, are collected in a high-resolution mass spectrometer. The intensity of the signal is related to the composition of the sample. The mass spectrometer has a very wide dynamic range, which allows for the measurement of major constituents as well as trace impurities. The SIMS spectra in Figure 2.8 contain depth profiles of both ^{12}C and ^{13}C as impurities in GaAs.[12] The carbon incorporation was stepwise altered during growth, yielding a steplike profile to the impurity concentration. A dynamic range of about 4 decades was obtained in the ^{13}C spectrum in this figure. The limits to the overall dynamic range of the SIMS measurement extend all the way to the pure elements, yielding an overall range of $\sim 10^8$. The absolute sensitivity limits are set by the instrument and the sample, but sensitivities on the order of 1 ppm or less can be achieved for impurities in most semiconductors. Despite this seemingly straightforward procedure, quantitative SIMS measurements can be difficult to obtain due to experimental complications which must be keep in mind. The yield of secondary ions is dependent on the host matrix containing the impurity. These "matrix" effects necessitate the use of an internal calibration standard for the quantitative measurement of impurity levels. This is most easily achieved through the use of an ion implant of the sought impurity into the surface of the sample of interest. The measured signal from the implanted region can be compared to the known dose of the implant, affording a ready calibration standard free of matrix effects. A peak from ion-implanted ^{13}C superimposed with the ^{12}C peak is seen in the near-surface region of Figure 2.8, providing an internal calibration of the carbon concentration. The wide dynamic range and quantitative nature of the SIMS technique has expanded its role in the characterization of semiconductor materials.

SIMS is limited in the depth resolution that can be typically achieved due to sputter-induced mixing in the sample. Typically, for a large step change in an impurity concentration in depth in the sample, the SIMS measurement is limited to a decade drop in measured concentration for about a 10 nm sputter depth change. This places a limit on the ability of SIMS to determine very rapid changes in composition and impurity concentration.

2.5 Electrical Properties in Optical Structures

The electrical properties carrier concentration mobility and resistivity are generally controlled by intentional impurities or dopants introduced during growth. In most optical devices, highly controlled doping of the device structure is not required. This is in sharp contrast to the high degree of doping control and uniformity required in electronic charge control devices such as field effect transistors (FETs). There are two standard techniques used in the measurement of doping and resistivity: Hall and capacitance–voltage (C–V) measurements. Hall measurements are used to obtain the free carrier concentration and mobility. This measurement is generally destructive, requiring test structure formation and metallization. The Hall

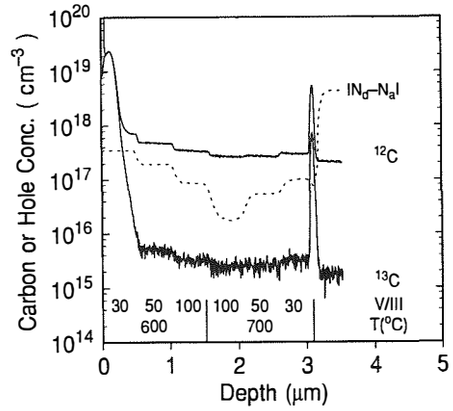


Figure 2.8 **The SIMS profiles of intentionally carbon-doped GaAs reveal the sensitivity and wide dynamic range of this technique which is necessary in the analysis of very minor constituents such as dopants. The near-surface region contains an ion-implanted carbon peak used as an internal calibration for the SIMS measurement.**

coefficient determined from the measurements on uniformly doped samples can be directly related to the depth of integrated carrier concentration, or the sheet concentration of carriers on single-layer samples. The conversion to a volumetric concentration requires a knowledge of the surface depletion region formed by the pinning of the Fermi level due to the high density of surface states found at most compound semiconductor surfaces and many interfaces. For example, the surface depletion width is ~0.1 μm for GaAs doped to an electron concentration of 10^{17} cm^{-3}. The electrical thickness used in calculating the bulk carrier concentration would therefore be smaller than the metallurgical thickness by these depletion regions; that is, the electrically active thickness of a 1 μm layer of GaAs:$n = 10^{17}$ cm^{-3} would be 0.8 μm, accounting for surface and interface depletion regions. Hall measurements taken from multilayer structures, where several layers are conductive, are difficult to interpret, since an aggregate sheet carrier concentration is obtained as a result of the coupled and parallel conduction between the multilayers.

Hall measurements also yield the mobility of the layer. The purity of undoped or lightly doped materials used in the active regions of lasers or that are required in photodetectors can be evaluated by noting the 77 K mobility. The purity of undoped materials is often cited in these terms. The loss of doping control, particularly at low doping concentration, can be analyzed by the low-temperature mobility. The mobility value at 77 K is dominated by scattering from ionized impurities. The presence of a low mobility value, for a given carrier concentration, indicates the presence of compensating impurities or defects. The higher the concentration of such impurities, such as unintentional carbon in *n*-type GaAs, the lower the mobility. Tabulated values of mobility versus carrier concentration at various levels of

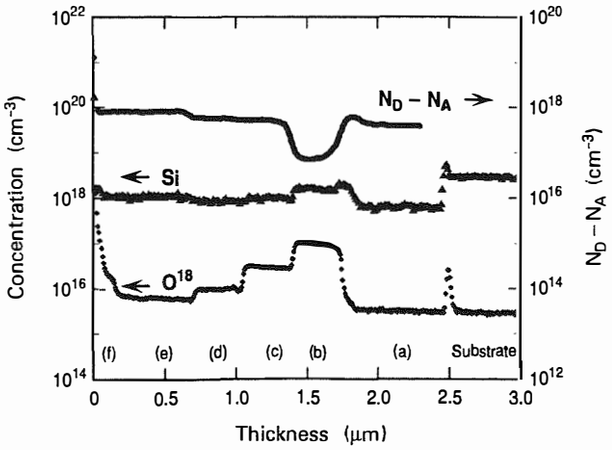


Figure 2.9 **The electrochemical capacitance profile of a GaAs sample co-doped with Si and ^{18}O. A comparison of the carrier concentration, N_d–N_a, to the SIMS profiles of Si and ^{18}O indicates that the carrier concentration attributed to the Si doping is compensated by the oxygen deep level. The carrier concentration is roughly equal to the difference between the Si and ^{18}O. Such combined SIMS and capacitance measurements allow for the diagnosis of contamination-related doping problems.**

compensating impurities allow for the quantitative evaluation of the concentration of these defects,[13] at least in higher-purity films (e.g., $<10^{16}$ cm^{-3} in GaAs).

Capacitance measurements can be readily performed on the exposed surface region of the semiconductor. The differential C–V characteristic can yield the carrier concentration profile of the near-surface region. These measurements can be combined with electrochemical etching, which allows for the profiling of the carrier concentration through a complex multilayer structure. The changes in carrier concentration in the depth of the sample can be easily obtained through such an electrochemical profiling technique. Figure 2.9 has an electrochemically derived carrier profile of GaAs co-doped with Si and ^{18}O. The oxygen compensates the Si dopant, leading to a reduction in the carrier concentration from the expected value, which would be that of the Si concentration. The Si and ^{18}O profiles were determined by a SIMS measurement. The combination of Hall, capacitance, and some physical profiling measurements can yield the complete electrical profile of the structure, as well as point to any anomalous features.

Hall and C–V measurements should, in principle, agree in the case where there are only simple donors or acceptors in the materials. Infrared lasers and other optical devices rely, however, on ternary materials in which the typical donors, such as Si and $Al_xGa_{1-x}As$, form several levels. These donors form so-called DX centers. DX centers are associated with persistent photoconductivity effects and carrier freeze-out for alloys within certain composition regions. Since DX centers are an

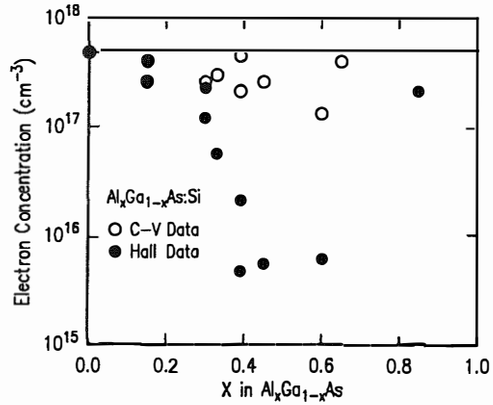


Figure 2.10 **The free electron concentration determined by Hall effect measurements and the net donor concentration determined by capacitance measurements differ considerably within the immediate composition range of $Al_xGa_{1-x}As$:Si.[13] This behavior is due to DX centers formed by the donors in the $Al_xGa_{1-x}As$ layer.**

inherent property of donors in many alloys, they must be understood in order to develop an understanding of many doping processes. A recent review of these donors has been published describing their properties.[14] These centers can lead to a large discrepancy between C–V and Hall measurements. Room temperature C–V measurements in these DX center-dominated materials yield carrier concentrations indicative of the net active donor concentration. The Hall measurement, however, can yield a carrier concentration orders of magnitude lower than the C–V derived value. The Hall measurements yield the concentration of carriers ionized from the donors, while C–V measurements yield the total donor concentration. This is shown for the case of $Al_xGa_{1-x}As$:Si as a function of alloy composition in Figure 2.10.[15] In practical terms, the carrier concentration in several layers can be quite low, yielding high resistivity values for those layers, despite the large concentration of electrically active dopants. Since the DX state is an intrinsic property of the donors in these materials, there is no available means of altering this persistent and troublesome behavior. Knowledge of the electrical behavior of these states is necessary for the correct interpretation of the electrical measurements and for proper device design.

Deep electrically active levels within the bandgap of the active region of a laser structure or LED can prevent the efficient generation of light. Oxygen and transition metals, for example, are known to kill or greatly diminish radiative lifetimes in semiconductors, strongly reducing their luminescence efficiency. The presence, concentration, and properties of such deep levels can be determined within actual device structures, in addition to simple single layers, through deep level transient spectroscopy[16] (DLTS). DLTS is a time-resolved capacitance measurement which

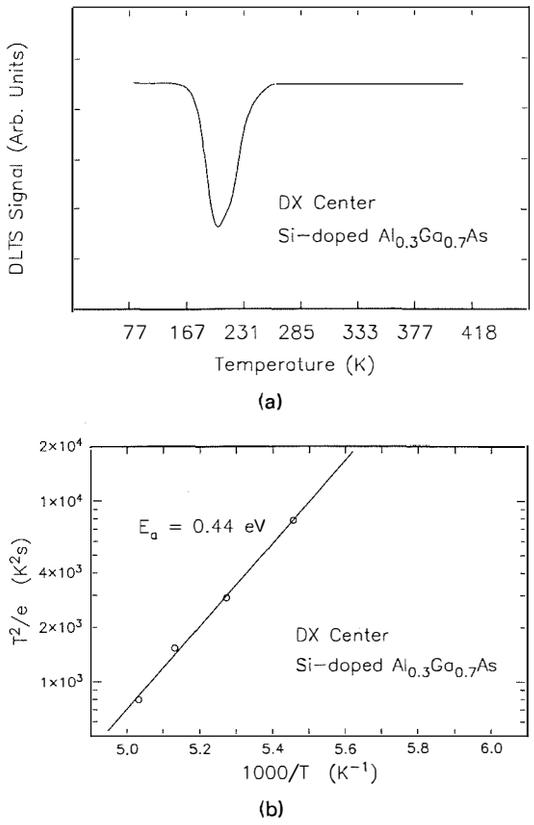


Figure 2.11 **DLTS can yield the energy position of a deep state within the bandgap of the semiconductor. (*a*) The DLTS signal is related to a transient change in capacitance within the structure in response to a voltage pulse, shown here for Si DX-related centers in $Al_{0.3}Ga_{0.7}As$. (*b*) This signal is then related through an Arrhenius plot to the emission energy of the deep state, which can lead to the identification of a deleterious impurity or defect.**

can reveal the presence of electrically active deep states. The simple structures required for a DLTS measurement, often only a Schottky diode, receive a short voltage pulse over a set dc bias. The traps can capture (emit) carriers during this pulse, and the relaxation of the capacitance to its quiescent value is monitored. Since emission (capture) is a thermally activated process, the rate of this process can be monitored—that is, the change in capacitance with time—as a function of measurement temperature, as shown in Figure 2.11*a*. The Arrhenius plot of the maximum emission rate, approximately given by the maximum change in capacitance, as a function of temperature under a given set of experimental parameters can yield the emission energy, as given in Figure 2.11*b*. This emission energy is

associated with the position of the deep state within the bandgap, and the concentration of a deep state is deduced from the amplitude of the DLTS signal. Many of these emission energies have been related to a specific chemical or structural impurity, allowing for the identification of a particular deleterious defect. It is not always clear, however, that the detected deep level is solely responsible for the decreased luminescence. Correlations between the concentration of deep levels, their energy position in the bandgap, and luminescence measurements can identify a key defect as the problem within a material.

2.6 Optical Properties in Single and Multilayer Structures

Light-emitting structures require both a high luminescence efficiency and a low concentration of below-bandgap states. Nonradiative deep states provide a competing recombination pathway, diminishing the quantum efficiency of the optical structure. The optical properties can be qualitatively evaluated from photoluminescence, as mentioned above, and cathodoluminescence (CL) measurements. The difference between these measurement techniques is in the source of excess carriers: PL derives carriers from the illumination of the sample with above-bandgap (direct edge for efficient generation) light, while CL utilizes electron-beam excitation.[6] CL does allow for the local excitation of individual parts of a multilayer structure through the selective exposure of the layers to a finely focused and directed electron beam. These measurements are typically incorporated into a scanning electron microscope (SEM), allowing for surface imaging as well as luminescence measurements.

PL or CL spectra yield a variety of data useful in the compositional and physical analysis of optical device structures. The luminescence spectra obtained from single-layer structures possess several spectral features which typically can be easily interpreted, providing structural, purity, and compositional information. Compositional information can be obtained from the band-edge energy, if the luminescence feature can be identified, as discussed in a previous section. The ease of performing PL measurements, particularly at room temperature, enables the rapid acquisition of band-edge energy as a function of position over the wafer surface. The PL mapping of a wafer surface can effectively display the compositional uniformity of the epitaxial layer. These PL maps provide a means of studying irregularities within the growth system, which result in unexpected variations in compositional uniformity over the surface. PL maps of the luminescence intensity can also be used to identify regions containing extended or point defects, which result in diminished PL intensity. Strain relaxation in pseudomorphic layers can often be identified in this way.

Luminescence measurements have been applied to determining the thickness in quantum-sized (<20 nm) layers in multilayer heterostructures. These luminescence measurements are often the easiest means to determine the quality and physical properties of thin layer structures. The quantum confinement induced by the diminished layer thickness causes a blue-shift in the emitted light from the structure,

as indicated in Figure 2.12.[17] The lowest energy level in the smaller bandgap or well material (GaAs) is shifted to the blue by an amount approximately dependent on layer thickness, $\Delta E_{blue} \propto 1/a^2$. The specific amount of blue shift can be calculated using an envelop function approximation for a given materials system. Figure 2.12 contains both a TEM micrograph of the physical structure as well as a schematic of the band structure through the multilayer $Al_xGa_{1-x}As/GaAs$ structure. This figure indicates the increasing shift of the radiation with diminishing well thickness. The luminescence spectral position can yield layer thickness information, provided assumptions such as abrupt compositional profiles are met within the structure. The luminescence linewidth can also provide information on the uniformity of the thin layer structure, as well as the purity level. The linewidth is often cited as a figure of merit in the formation of quantum structures, with narrower linewidths generally indicating higher purity and enhanced, smoother, or more uniform heterointerfaces. The luminescence linewidth is affected by a variety of factors. The linewidth is broadened by elevated levels of impurities in the well and the barrier materials. Thickness variations also can lead to line broadening, as indicated schematically in Figure 2.13. Thickness variation on a length scale greater than the exciton diameter (about 20 nm in GaAs) will result in light emission from wells of varying thickness, as described in the figure caption. Since these adjacent well regions usually differ by only a few atomic layers, the energy separation between such peaks, close in energy, is not well resolved, and a broadened luminescence line results. The analysis of luminescence position and linewidth is therefore used to study the structure of the thin layer sample and can be used to diagnose difficulties in impurity incorporation, junction placement (through the appearance of impurities in the well material), and interfacial structure.

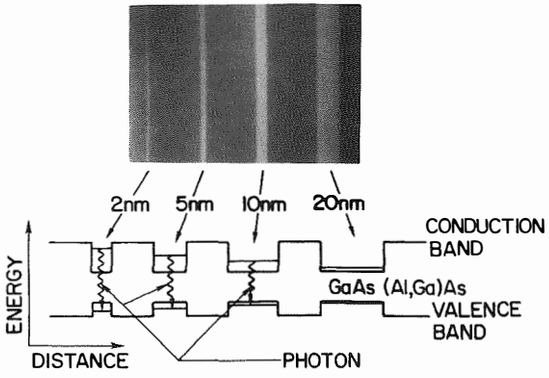


Figure 2.12 **The electronic structure of a multi-quantum well structure is schematically shown compared to its physical structure given by the TEM micrograph.[15] The thin layer structures yield a shift in the energy or wavelength of the emitted light. The luminescence spectrum of the multilayer structure can be used to ascertain the physical dimension of the quantum-well layer.**

2.7 Interface Properties in Multilayer Structures

The controlled formation of doping and compositional interfaces is crucial to the fabrication of high-performance light-emitting devices. As indicated above, several structural probes serve to determine the physical structure of the multilayer film. The performance of a device can be determined by factors other than the physical structure alone. Interface properties lie in three main areas: junction placement, compositional grading, and electrical behavior of the interface.

Junction placement is affected by a variety of growth and post-growth processing-related factors. The accurate placement of the dopant atoms within the device structure can be complicated by the appearance of dopant transients within the structure. This is shown in Figure 2.14 for the case of GaAs:Mg grown by MOVPE using $(C_5H_5)_2Mg$ or Cp_2Mg as the dopant source. The dopant source was abruptly turned on at a depth of about 1.3 μm and turned off at a depth of 0.9 μm. While the injection of the source into the growth reactor was a step function, the incorporation of dopant forms long transients related to the interaction of the dopant with the internal surfaces of the reactor. Cp_2Mg exhibits particularly long transients in the growth profile, with other dopant sources forming greatly reduced or no transients. These transients place dopant atoms far from the expected depth within the structure and may lead to the misplacement of the electrical junction. MBE growth often exhibits similar doping transients, particularly with Be and Sn dopants. Be and Sn tend to segregate to the growing surface, riding on the growth front and slowly incorporating into the layer. These transients are often identified through SIMS profiling or from unexpected electrical characteristics

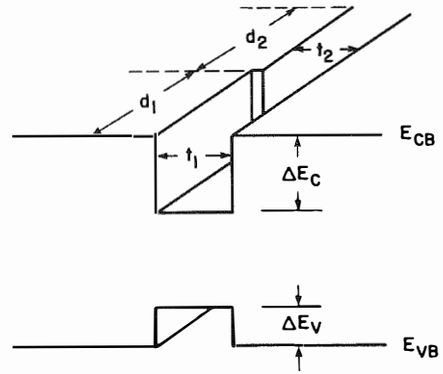


Figure 2.13 **The luminescence linewidth is broadened by a variety of factors, including elevated impurity levels and well-thickness variations. The quantum confinement is created by the band edge offsets, ΔE_C and ΔE_V. If the exciton diameter, d_{ex}, is smaller than the typical lateral dimension of the thickness variation, d_1 or d_2, the luminescence peak will be composed of superimposed light emitted from wells of differing thickness, t_1 and t_2.**

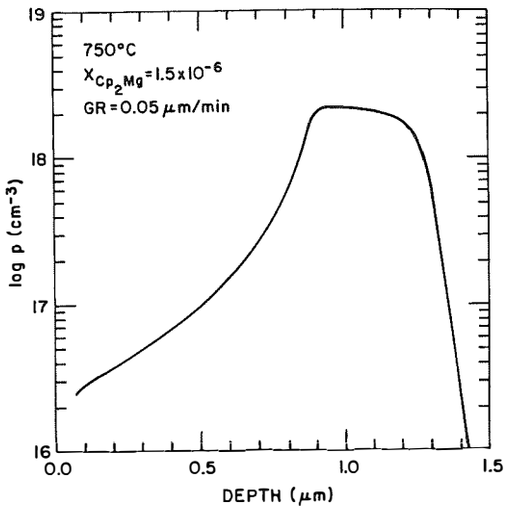


Figure 2.14 **The growth of doped structures is complicated by a variety of growth-related factors. Junction placement, critical in heterojunction devices, depends on the details of the doping process. The interaction of the dopant with the growth system can lead to a slow "turn on" and "turn off" of the dopant profile, despite abrupt changes in the introduction of the dopant into the system. This is shown here for Cp_2Mg-based Mg doping of GaAs by MOVPE. The dopant profile decreases slowly over several hundred nanometers, limiting the utility of this particular dopant.**

of the device, such as an anomalous turn-on voltage to a *p–n* junction within the structure.

The motion of dopants also occurs in post-growth thermal processing, as in the formation of ohmic contacts or ion-implantation annealing. At low concentrations, dopant impurities are often characterized by a concentration-independent diffusion coefficient. Many of the common impurities used in III–V device formation, however, display a very pronounced concentration dependence to the dopant diffusion. Si, Zn, Be, Sn, and other dopant elements exhibit a strong concentration-dependent diffusion at the dopant levels typically found within many device structures. High dopant concentrations can therefore lead to the rapid formation of a sharp diffusion front.[18] The final diffusion profile is dependent on the composition and placement of the dopants within the structure. Sn and Zn are particularly fast diffusers, especially when placed in the near-surface region of the structure where there is a ready source of vacant lattice sites. The microscopic diffusion mechanism has been extensively studied, as discussed by Tuck.[17] Fast diffusion is used to advantage in several applications, as in the impurity-induced disordering of superlattice structures.[19] Analysis of such profiles is accomplished through SIMS measurements and, in the case of impurity-induced disordering, by TEM micrographs.

Compositional grading at heterointerfaces is difficult to quantitatively assess. Grading on the scale of a few nanometers can detract from the performance of a quantum-based device structure. Typically, TEM micrographs have been employed to determine the compositional grading. Sharp contrast between two layers in the TEM image is often used to assign a measure of interfacial abruptness to a heterointerface. TEM images, however, can be difficult to unambiguously interpret due to the effects of the imaging conditions on the image formation. High-precision DCXRD measurements can be used on suitable structures to determine the appearance of appreciable interface grading. These physical measurements, when used in conjunction with luminescence measurements, can provide a more accurate picture of the compositional profile on the scale of a few nanometers. In particular, photoluminescence excitation spectroscopy (PLES), adsorption measurements, and modulation spectroscopies, such as photoreflectance and electroreflectance, can yield information on the position of the higher-lying quantum states within quantum-confined structures. Comparison of these states to calculated levels based on a model compositional profile within the well can be used to estimate the compositional profile across the interface.

The electrical and optical properties of the heterointerface are directly accessible to measurement. The optical properties of the interface are affected by the presence of mid-gap recombination centers which increase the interfacial recombination velocity. A high interfacial recombination velocity serves as a sink for minority carriers, for example, injected into a quantum-well light emitter, reducing the light emission efficiency. The presence of such states can be probed by DLTS on suitable structures. Time-resolved luminescence measurements can be interpreted to yield an interfacial recombination velocity in heterostructure measurements.

2.8 Summary

The primary determinate of the performance of an optical device is the detailed characteristics of the initial epitaxial structure. This chapter summarizes the chief properties of the epitaxial structure in terms of its structural, compositional, electrical, and optical behavior. The means of determining these properties within single and multilayer structures are introduced and discussed. These characterization techniques are not particular to a specific growth technology, but are generally applicable to all epitaxial structures.

Acknowledgments

The author wishes to thank P. Mooney for providing Figure 2.11 and for discussions associated with the DX center. Joan Redwing is also acknowledged for her careful reading of the manuscript. The author would also like to acknowledge discussions with R. Potemski, M. A. Tischler, T. N. Theis, and G. Scilla.

References

1 *Semiconductors and Semimetals,* Vols. 32 and 33. (T. P. Pearsall, Vol. Ed., and R. K. Williardson and A. C. Beer, Series Eds.) Academic Press, San Diego, 1991. A general review of strained layer materials.

2 A. J. Springthrope and A. Majeed. *J. Vac. Sci. Technol.* **8**, 266, 1990.

3 O. S. Heavens. *Optical Properties of Thin Films.* Dover, New York, 1965.

4 D. E. Aspnes, R. Bhat, E. Colas, L. T. Florez, S. Gregory, J. P. Harbison, I. Kamiya, W. E. Quinn, S. A. Schwartz, H. Tanaka, and M. Wassermeier. In "Atomic Layer Deposition and Processing." (T. F. Kuech, P. D. Dapkus, and Y. Aoyagi, Eds.) *Proceedings.* Materials Research Society, Pittsburgh, 1991.

5 *Reflection High-Energy Electron Diffraction and Reflection Imaging of Surfaces.* (P. K. Larsen and P. J. Dobson, Eds.) Plenum, New York, 1988. For recent reviews and complete listing of references.

6 *Encyclopedia of Materials Characterization.* (C. R. Brundle, C. A. Evans, Jr., and S. Wilson) Butterworth-Heinermann, Boston, 1992.

7 *Methods of Surface Analysis.* (J. M. Walls, Ed.) Cambridge University Press, New York, 1988, chapt. 4.

8 M. S. Goorsky and T. F. Kuech. *Proceedings.* (T. C. Huang, P. J. Cohen, and D. J. Eaglesham, Eds.) Symposium on Advances in Surface and Thin Film Diffraction, Materials Research Society, Pittsburgh, 1991, p. 237.

9 T. F. Kuech, D. J. Wolford, R. Potemski, J. A. Bradley, K. H. Kelleher, D. Yan, J. P. Farrell, P. M. S. Lesser, and F. H. Pollak. *Appl. Phys. Lett.* **51**, 505, 1987.

10 *Reflection High-Energy Electron Diffraction and Reflection Imaging of Surfaces.* (P. K. Larsen and P. J. Dobson, Eds.) Plenum, New York, 1988, chapt. 7.

11 *Methods of Surface Analysis.* (A. W. Czanderna, Ed.) Elsevier Scientific, Amsterdam, 1975, chapts. 6 and 7.

12 N. I. Buchan, T. F. Kuech, G. Scilla, F. Cardone, and R. M. Potemski. *J. Crystal Growth.* **110**, 405, 1991.

13 D. A. Anderson and N. Apsley. *Semicond. Sci. Technol.* **1**, 187, 1986.

14 P. M. Mooney. *J. Appl. Phys.* **67**, R1, 1990.

15 T. F. Kuech, E. Veuhoff, and B. S. Meyerson. *J. Crystal Growth.* **68**, 48, 1984.

16 G. L. Miller, D. V. Lang, and L. C. Kimerling. *Ann. Rev. Mater. Sci.* **7**, 377, 1977.

17 T. F. Kuech and K. F. Jensen. In *Thin Film Processes II.* (J. L.Vossen and W. Kern, Eds.) Academic Press, Orlando, 1991, chapt. III-2.

18 B. Tuck. *Atomic Diffusion in III-V Semiconductors.* Adam Hilger, Bristol, 1988.

19 J. W. Lee and W. D. Laidig. *J. Electron. Mater.* **13**, 147, 1984.

8. Solution Growth

Fundamentals of Crystal Growth from Solutions

Igor Pritula[1], Keshra Sangwal[2]
[1]Institute of Single Crystals, National Academy of Sciences of Ukraine, Lenin Avenue 60, 61001 Kharkov, Ukraine
[2]Department of Applied Physics, Lublin University of Technology, ul. Nadbystrzycka 38, 20-618 Lublin, Poland

CONTENTS

Abstract
Introduction
1. Low-Temperature Solution Growth
    1.1. Basic Concepts of Low-Temperature Crystallization
        1.1.1. Driving Force for Crystallization
        1.1.2. Metastable Zone Width
        1.1.3. Temperature Dependence of Solubility
    1.2. Selection of Solvents
    1.3. Crystal Growth Techniques
        1.3.1. Temperature Changing Technique
        1.3.2. Solvent Evaporation Technique
        1.3.3. Temperature Gradient Techniques
        1.3.4. Growth from Boiling Solutions
    1.4. Different Factors Affecting Crystal Growth
    1.5. Crystal Growth Rates and Dead Supersaturation Zone
        1.5.1. Basic Concepts of Impurity Effects
        1.5.2. Effect of Organic Additives on Crystal Growth
    1.6. Effect of Mechanical Impurities on Crystal Growth
        1.6.1. Growth of Water Soluble Crystals with Embedded Organic Molecules
        1.6.2. Growth of Water Soluble Crystals with Embedded Nanoparticles
2. High-Temperature Solution Growth
        2.1. Principle of the Method
        2.2. Composition of Fluxes and Their Selection
        2.3. Some Properties of High-Temperature Solvents
    2.4. Crystal Growth Techniques
        2.4.1. Slow Cooling Method
        2.4.2. Solvent Evaporation Method
        2.4.3. Temperature Gradient Methods
        2.4.4. Other Methods
    2.5. Growth Instability and Facet Formation
Summary and outlook
References

Authors' original manuscreipt associated with the publication in the Handbook of Crystal Growth, Vol. II.B Elsevier; 2015. pp.1185–227

ABSTRACT

Fundamental aspects of the growth of single crystals from low- and high-temperature solutions are reviewed. Different modern methods for growing bulk single crystals from low- and high temperature solutions are described. The topics like new approaches to explain the dependence of metastable zone width on various factors, effects of impurities on growth rates and growth morphology of crystals, determination of growth mechanisms from experimental data on growth kinetics are discussed. The nature of supersaturation barriers observed during the growth of single crystals from aqueous solutions containing impurities are briefly described. Analysis of the effects of organic molecules and inorganic nanoparticles on the crystallization behavior of some inorganic and semiorganic salts is also presented. For the growth of crystals from high-temperature solutions, an overview of suitable solvents for growth, properties of high-temperature solvents and methods for the growth and characterization of single crystals is given.

KEYWORDS: crystal growth; metastable zone; supersaturation; growth kinetics; growth mechanisms; impurity; growth from solutions; crystal growth techniques.

Fundamentals of Crystal Growth from Solutions

Introduction

Crystallization of substances from supersaturated solutions at normal pressure conditions in suitable nonreactive solvents in which they are fairly soluble is usually referred to as crystal growth from solutions.The solvents used for crystallization of different substances are usually water, various organic liquids and their mixtures, and melts of some chemical compounds and/or their mixtures. Water and organic liquids and their mixtures are in the liquid state under the usual laboratory pressure and temperature conditions whereas chemical compounds and/or their mixtures are in the liquid state at elevated temperatures. From a consideration of the growth temperature when the solvent used is in the liquid state, one differentiates between crystal growth from low- and high-temperature solutions. In growth from low-temperature solutions the crystallization temperatures generally do not exceed 70–80 ºC, whereas in growth from high-temperature solutions the crystallization temperatures rarely exceed 1200–1300 ºC. In both low- and high-temperature growths, the highest possible growth temperature is the boiling point of the solvent used.

Crystallization from supersaturated solutions devoid of foreign particles and deliberately introduced seeds in them always occurs in two stages: formation of three-dimensional (3D) microscopic nuclei and development of these 3D nuclei into large entities visible to the naked eye. These two stages are called homogeneous 3D nucleation and crystal growth, respectively. Foreign particles, usually called impurities, present in solutions facilitate the formation of 3D nuclei (heterogeneous nucleation) and can change their subsequent growth, whereas seeds introduced in solutions eliminate the nucleation stage and enable to grow crystals without the necessity of occurrence of 3D nucleation. However, it should be mentioned that crystallization is usually understood as nucleation and devopment of crystalline product but the term growth is used for large-sized crystals with or without the nucleation stage. A necessary condition for the

crystallization of a solid mass dissolved in a pure or mixed solvent is the creation of supersaturation in the solution.

In this chapter the principles and experimental techniques for the growth of crystals from low- and high-temperature solutions are described. The contents of this chapter are an extended and revised version based on a review published before [1].

1. Low-Temperature Solution Growth

Crystal growth from low-temperature solutions is well suited for materials which decompose in the melt or in the solid at high temperatures and which undergo structural transformations while cooling from the melting point. It also allows to grow crystals of the same substance in a variety of morphologies and polymorphic forms by variations of growth conditions or of the solvent. Consequently, materials ranging from micrometer-sized crystalline organic pharmaceutical chemicals to large-sized inorganic nonlinear optical crystals are grown from low-temperature solutions. The method is widely used because: (i) the growth apparatus is relatively simple and cheap, (ii) in contrast to other methods involving melts, low growth temperature introduces small thermal stresses (and hence low concentration of equilibrium defects and dislocations) in the crystals, and (iii) the crystals obtained usually have well developed faces (growth habit), that make it possible to investigate crystal growth processes including in situ observations of the surfaces and capture of impurities.

Crystal growth from low-temperature solutions has been reviewed in several monographs and reviews [1-9]. The list of compounds grown from low-temperature solutions can be found in the monographs [3,6,7].

1.1. Basic Concepts of Low-Temperature Crystallization

1.1.1. Driving Force for Crystallization

Crystallization of a compound always occurs from its supersaturated solutions in the metastastable zone. Metastable zone is the region between curves representing solubility (solid curve) and supersolubility (dashed curve) shown schematically in Figure 1. Supersolubility curve indicates the limiting value of solute concentration when instantaneous 3D nucleation (i.e. precipitation) occurs in the solution.

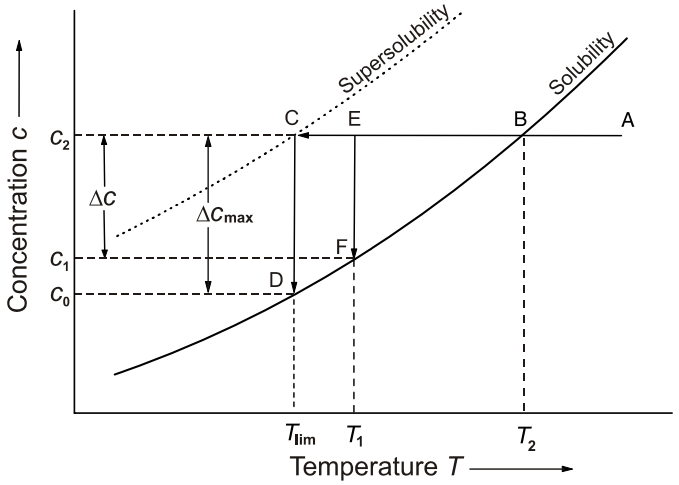


Figure 1. Schematic illustration of the dependence of solute concentration in a solute–solvent system on solution temperature. Solid and dashed curves represent solubility and supersolubility curves, respectively. See text for details. Adapted from ref. [12].

From Figure 1 three areas can be distinguished: (i) stable undersaturated zone, (ii) metastable zone, and (iii) unstable supersaturated area. In area (i) which lies below the solubility curve, the actual concentration c of a solute in the solution at a given temperature, say T_{lim}, is lower than the corresponding equilibrium concentration c_0 represented by the solubility for the solute–solvent system. In an undersaturated solution, more solute will dissolve. In areas (ii) and (iii) lying above the solubility curve, the actual solute concentration c at the temperature T_{lim} is higher than its solubility c_0. In these areas the solution is supersaturated. However, the processes of 3D spontaneous nucleation and crystal growth occur in the region lying between the solubility and supersolubility curves i.e. in the metastable zone. Obviously, the supersolubility curve represents the concentration when 3D spontaneous nucleation ceases to occur.

Deviation in the concentration of a dissolved salt from its equilibrium value at a given temperature or deviation in the temperature of the solute–solvent system of a given equilibrium concentration from a saturation temperature is a measure of the driving force for crystallization. In Figure 1, it is the concentration difference $\Delta c = c_2 - c_1$ corresponding to the saturation concentration c_1 at temperature T_1 or the temperature difference $\Delta T = T_2 - T_1$ corresponding to the saturation concentration c_2 at temperature T_2. In terms of solute concentrations in the solution the driving force for crystallization is the dimensionless supersaturation ratio $S = c_2/c_1$, and the degree of supersaturation or simply supersaturation $\sigma = \ln S \approx \Delta c/c_1$. Obviously, $S < 1$, $S > 1$ and $S = 1$ for undersaturated, supersaturated and saturated solutions, respectively. In terms of the solubility of a solute, when 3D nucleation of the new phase occurs instantaneously, as shown schematically by the dashed curve in Figure 1, the driving force for crystallization is the limiting value of metastable zone.

The metastable zone width can be described by polythermal or by isothermal method. In the polythermal (also called non-isothermal) method, the metastable zone width is measured as the maximum supercooling $\Delta T_{max} = (T_2 - T_{lim})$, with reference to a constant concentration c_0 corresponding to the saturation temperature T_{lim} (Point D), by cooling the solution at a constant cooling rate R from a temperature somewhat above T_2 (Point A in Figure 1) to a temperature T_{lim}

at which first crystals are detected in the solution (Point D). With reference to the temperature T_{lim} corresponding to the maximum solute concentration c_2, this metastable zone width is the maximum concentration difference $\Delta c_{max} = (c_2 - c_0)$. The isothermal method, on the other hand, consists of attaining solution supersaturation as fast as possible, followed by the measurement of time period for the appearance of first detectable nuclei in the solution. When the appearance of detectable nuclei occurs immediately after attaining the predefined supersaturation corresponding to the limiting temperature T_{lim}, one defines the maximum supersaturation ratio $S_{max} = (c_2/c_0)$ and the maximum supersaturation $\ln S_{max} = \ln(c_2/c_0)$ as the width of the metastable zone width with reference to T_{lim}.

When c_{max} is the solute concentration corresponding to the saturation temperature T in Figure 1, one obtains the traditional relations for maximum supersaturation ratio $S_{max} = c_{max}/c_0$ and maximum supersaturation $\sigma_{max} = (c_{max} - c_0)/c_0$. Then with reference to the saturation temperature T in Figure 1, the temperature difference $\Delta T_{max} = (T - T_{lim})$ is the maximum undercooling. Alternatively, with reference to the limiting temperature T_{lim}, $\Delta T_{max} = (T - T_{lim})$ is the maximum supercooling and defines the metastable zone width.

1.1.2. Metastable Zone Width

Polythermal technique is the most widely used method for determining the metastable zone width. In fact, investigation of solubility and metastable zone width of various solute–solvent systems has been a field of intensive research activity for over four decades [10]. However, since 2008 several papers have been devoted to the understanding of the effect of various experimental factors on the metastable zone width. The developments in the understanding of metastable zone width of solute–solvent systems have recently been reviewed [11].

According to the self-consistent Nývlt-like approach [12], the relationship between the maximum supercooling ratio $\Delta T_{max}/T$ and cooling rate R may be given by

$$\ln(\Delta T_{max}/T) = \Phi + \beta \ln R, \tag{1}$$

where Φ is the extrapolated value of $\ln(\Delta T_{max}/T)$ when $\ln R \to 0$, and $\beta = 1/m$ (m as the nucleation order). However, according to the approach based on the three-dimensional nucleation theory [13], the relationship between $\Delta T_{max}/T$ and R is of the form

$$\left(\frac{T}{\Delta T_{max}}\right)^2 = F(1 - Z \ln R), \tag{2}$$

where F is the extrapolated value of $(T/\Delta T_{max})^2$ when $\ln R \to 0$, and the constant Z is characteracteric for a solute–solvent system. Both Eqs. (1) and (2) predict that, at a given saturation temperature T, the quantities $\ln(\Delta T_{max}/T)$ and $(\Delta T_{max}/T)^{-2}$ decrease linearly with an increase in $\ln R$.

The parameters Φ and $\ln(F^{1/2})$ as a function of saturation temperature T may be described by an Arrhenius-type relation, written in the form [12, 13]

$$\ln y = \ln y_0 - E_{sat}/R_G T, \tag{3}$$

where ln$y$ denotes – Φ and ln($F^{1/2}$), the factor lny_0, associated with the pre-exponential factor y_0 of the Arrhenius-type relation, denotes the extrapolated values of –Φ and [ln($F^{1/2}$)] when $1/T \rightarrow 0$, R_G is the gas constant, and E_{sat} is the activation energy associated with the diffusion of solute molecules in the solution.

Irrespective of the cooling rate R, with an increase in saturation temperature T, the value of maximum supercooling $\Delta T_{max} = T - T_{lim}$ decreases for some solute-solvent systems, it remains practically constant for some others, whereas it increases for the remaining solute–solvent systems. Typical examples showing such trends are shown in Figure 2. This means that the supercooling ratio $\Delta T_{max}/T$ decreases, increases or remains constant with increasing saturation temperature T. Analysis of the experimental data revealed [11,14,15] that the nature of solute-solvent system is related to the activation energy E_{sat} for diffusion of nucleating species in the solution. When the value of E_{sat} is comparable with the value of activation energy E_D for diffusion of ideal species, the supersolubility curves are roughly parallel to the solubility curves (i.e. $\Delta T_{max}/T$ is independent of T). When $E_{sat} > E_D$, $\Delta T_{max}/T$ decreases with an increase in T_0. However, when $E_{sat} < E_D$, $\Delta T_{max}/T$ increases with an increase in T.

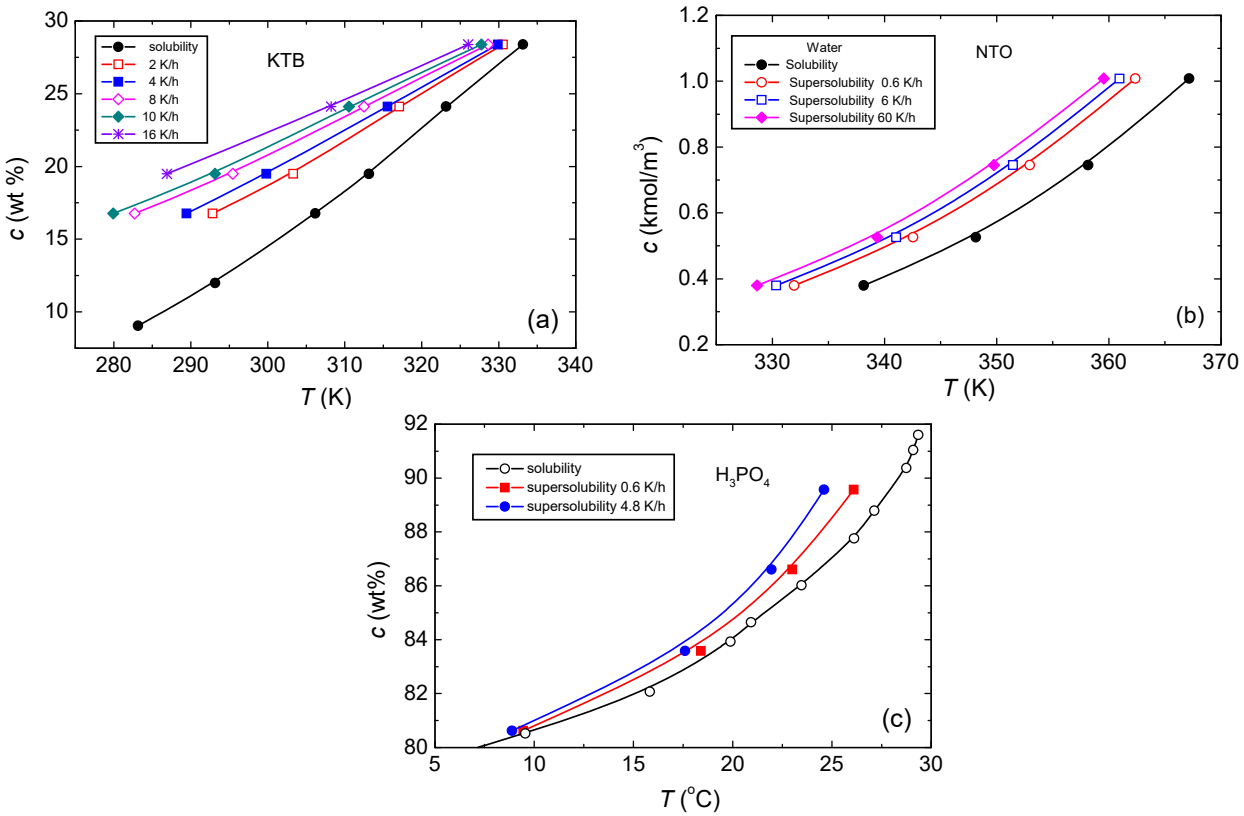


Figure 2. Typical examples of solubility and supersolubility curves for different systems: (a) KTB (potassium tetraborate tetrahydrate)–water [11], (b) NTO (3-nitro- 1,2,4-triazol-5-one)–water [11], (c) H_3PO_4–water. Supersolubility curves are for various cooling rates [15]. Reproduced with permission of (a) Royal Chemical Society and (b) Elsevier.

In the polythermal method the rate of creation of supersaturation in a solute–solvent system and its metastable zone width are determined by controlling the rate of cooling of the solution at a constant rate. However, this method can be used only for substances whose solubility increases with temperature (i.e. for substances which have a positive temperature coefficient of solubility). Irrespective of the temperature coefficient of solubility, supersaturation in the saturated solution of a solute in a solvent can also be generated by mixing another miscible solvent, usually called antisolvent or nonsolvent in which the solute is insoluble or poorly soluble. This is associated with the fact that, at a given temperature, the solubility of a solute in different solvents is different. The rate of creation of supersaturation in the solution and its metastable zone width are associated here with the rate of addition of miscible antisolvent. In recent years there is a steady interest in understanding the metastable zone width in antisolvent crystallization [16].

1.1.3. Temperature Dependence of Solubility

The experimental data of the solubility c of a compound in a solvent as a function of temperature T is described satisfactorily according to the empirical relation [16,17]

$$c = C_0 + C_1 T + C_2 T^2, \tag{4}$$

where the solubility c is expressed as mass of solute per given mass of solvent or solution, the temperature T is expressed in ºC or K, and C_0, C_1 and C_2 are empirical fitting parameters. The data of the temperature dependence of solubility, such as those shown in Figure 2, can be represented by Eq. (4) in the entire investigated range of temperature. Another relation, based on the theory of regular solutions, which can equally be used to describe the above data, is of the form [16,17]

$$\ln c = A - \frac{\Delta H_s}{R_G T}, \tag{5}$$

where solubility c is expressed in mole fraction, A is a constant, R_G is the gas constant and ΔH_s is the enthalpy of dissolution of the solute in the solvent. For ideal solutions, the constant $A = \Delta H_m / R_G T_m$, where T_m is the melting point of the solute and the enthalpy of melting $\Delta H_m = \Delta H_s$. However, for regular solutions, $A \neq \Delta H_m / R_G T_m$ and $\Delta H_m \neq \Delta H_s$.

Although Eqs. (4) and (5) are commonly used to describe the temperature dependence of solubility they are not satified in the entire range of the investigated temperature. Figure 3 illustrates typical examples of the temperature dependence of solubility c for some common inorganic compounds in water in the temperature interval 0–100 ºC. As seen from the figure, in certain temperature intervals the solubility of different compounds either increases or decreases with an increase in temperature.

The increasing or decreasing trends of the dependence of solubility c on temperature T are usually discussed in terms of positive or negative temperature coefficient of solubility (i.e. $\partial c/\partial T$) in a particular temperature range. Depending on the nature of solute–solvent system, the solubility coefficient can be high or low and can vary in different temperature intervals.

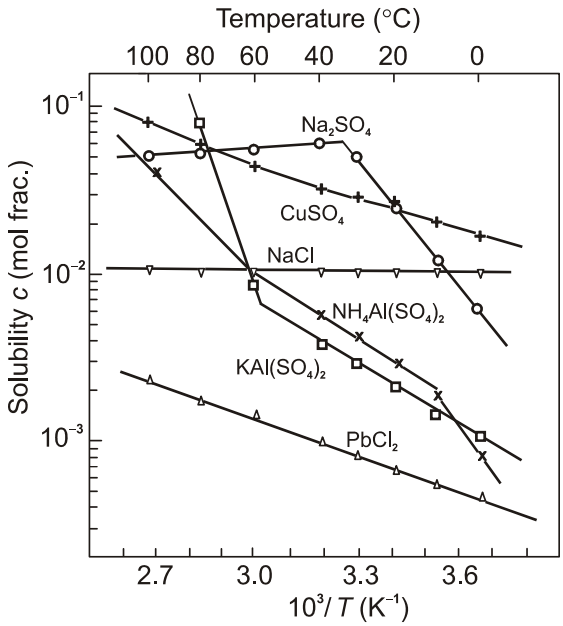


Figure 3. Examples of the temperature dependence of solubility *c* for some common inorganic compounds in water. Adapted from ref. [9].

1.2. Selection of Solvents

The first step for crystallization is the choice of solvent. Solution is a homogeneous mixture of a solute in a solvent. Solute is a component which is usually present in a smaller quantity than the solvent in the solution. For a given solution, there may be different solvents. At the growth temperature an ideal solvent should ensure a sufficient solubility and a good temperature gradient of solubility in it; it should have low vapor pressure, low toxity, low flammability and low viscosity; it should not corrode growth apparatus; and should be cheap.

The most commonly solvent used in low-temperature gowth is water because at least 90% of the crystals produced by low-temperature solution methods are soluble in water. It is not toxic and is less volatile than organic solvents which are, in general, toxic, volatile and flammable. Morever, in comparison with most organic solvents, it is easily available in the pure state and is cheap. Since its boiling point is higher than that of most of the organic solvents commonly used for the growth, it provides a reasonably wide range for the selection of the growth temperature. However, water is not a reversible solvent for some materials. It hydrolyzes some materials and introduces water of crystallization to other compounds which may be desired in the anhydrous form or in the hydrated form of particular composition.

A simple rule of thumb for the proper selection of a solvent is chemical similarity between the solvent and the compound to be grown. For example, crystals of nonpolar organic compounds can be grown easily from nonpolar organic solvents. Chemical similarity also defines solute solubility in the solvent.

The solvent from which a material is crystallized influences the crystal morphology and growth rate. These effects of the solvent on the morphology and growth rates of crystals from solutions

are related to the solubility of the crystallizing compound in the solvent and to the nature of crystal–solution interface. High solubility of the solute leads to high viscosity of the solution, which hinders mass transfer at the crystal–solution interface. The crystal–solution interface for a solute–solvent system can be rough at a given temperature as a result of high solubility of the solute in the solvent (thermodynamic roughening) and high supersaturation of the solution (kinetic roughening). Both of these yield high growth rates of crystals and high density of defects. Therefore, to ensure good crystal growth of a substance it is necessary to use: (1) a solvent in which the substance is moderately soluble, (2) medium solution supersaturation, and (3) non-turbulent stirring conditions.

Most crystallized inorganic materials are ionic. This means that dissociation reactions, ionic interactions and solution acidity (pH) determine the solubility of inorganic compounds in aqueous solutions. In the case of organic compounds and inorganic compounds in nonaqueous solvents, a wide variety of solvents and solvent mixtures are usually employed. The differences in the solubility of different compounds in various solvents are associated with solute–solvent interactions, which are determined by solute concentration in the solution, solution temperature, composition of the solvent, and impurities present in the solution.

Experiments suggest that a solvent in which the compound has a solubility between 10 and 60% at a given temperature is economically suitable for crystal growth. These growth rates from solutions fall in the range of 0.1 to 1 mm/day. Very low and very high solute solubilities provide low growth rates due to low solute concentration and increased viscosity, respectively. Therefore, in both cases it is desirable to use additives to change the solute solubility in a solvent or solution viscosity. Additives not only change the properties of solutions, but also lead to changes in crystal growth habits.

1.3. Crystal Growth Techniques

Crystal growth methods differ in the way the supersaturation is generated and maintained constant during a growth run, and 3D nucleation is initiated. In general, the selection of a method for the growth of a compound can be made from a consideration of temperature coefficient of its solubility (see Figure 3). If a compound has a reasonable temperature coefficient of solubility in a certain temperature interval and does not undergo phase changes, it can be grown by changing the temperature, with simultaneously maintaining the required supersaturation for growth (temperature changing method). In principle, substances with both positive as well as negative temperature coefficient of solubility can be grown by this technique (by decreasing and increasing temperature, respectively), but usually substances having positive temperature coefficients of solubility are grown by it. These subtances can also be grown by maintaining a temperature gradient between zones of crystal growth and solute supply (temperature gradient methods). If a compound undergoes phase transition at a particular temperature, the above methods cannot be used. Instead, one can use a method in which both temperature and supersaturation are maintained constant (constant temperature and supersaturation method). However, when the solubility remains practically constant with a change in temperature, the supersaturation can be created by evaporating the solvent (solvent evaporation method).

The importance of selecting an appropriate method lies in the fact that the same crystallization performed under different conditions can yield crystals of different properties (size, morphology, chemical purity, polymorphic form, etc.). However, the design of a cost-effective crystallization process requires many types of data, including mass transfer and equilibrium solubility as a function of the solvent, temperature and pH. However, surface and bulk supersaturation should be made as close as possible to the kinetic regime by suitably stirring solutions so that diffusion processes of supply of solute to the growing crystal do not limit the growth rate (see Sec. 2.4).

1.3.1. Temperature Changing Technique

In this method the value of supersaturation necessary for the growth of crystals is achieved due to slow temperature reduction which, as a rule, is controlled by a special program. The mass of the substance Δm depositing during the reduction of temperature by ΔT may be calculated from the relation

$$\Delta m = \frac{\mathrm{d}c}{\mathrm{d}T} V_0 \Delta T \,, \tag{6}$$

where c is the concentration of the substance in the solution, $\mathrm{d}c/\mathrm{d}T$ is the solubility coefficient, and V_0 is the solution volume. This relation follows from Eq. (4) and holds in a small temperature interval.

Typical vessels for crystal growth by the temperature changing method involve large glass containers with several seeds suspended in the supersaturated solution. For growth, a solution saturated at a temperature T is poured into the crystallizer and heated a few degrees above the saturation temperature to avoid spurious nucleation due to the cooling of its walls during its transfer to the outer water bath. When the solution temperature is slightly above the saturation temperature, the seeds are suspended in the solution and the crystallizer is hermetically sealed. Then the temperature is lowered to the growth temperature in the metastable zone and solution cooling is commenced at a preassigned rate such that the growing crystals remain the supersaturated solution. After the completion of growth with the temperature steadily decreasing to a terminal temperature, 10-15 ^{o}C above the room temperature, the crystals are gently taken out of the crystallizer, wiped and stored.

The temperature decreasing method is widely used for commercial crystal growth [3,18]. However, its inherent drawback is variation in the temperature during a growth run, which results in considerable changes in growth rate, adsorption of the impurity on the faces, and capture of the impurities by the growing crystal.

The possibility of obtaining large high-quality single crystals by the temperature reduction method using “point seeds” has been reported [19-21]. In this case the final size of the crystal does not depend on the size of the seed.

1.3.2. Solvent Evaporation Technique

In this technique, the supersaturation required for the growth is produced by evaporating the solvent at a constant temperature [3]. Therefore, the growth rate is regulated by controlling the evaporation rate. Excess mass of the substance for crystallization is created from a consideration of the solubility of the compound in the solvent and the evaporation rate of the solvent. In most cases the pressure of the solvent vapor over the solutions is higher than that of the solute. This enables to evaporate solvent vapor into the atmosphere or withdraw it as condensate using water-cooled coils. Therefore, the supersaturation necessary for crystal growth can be maintained by controlled evaporation of the solvent. For nontoxic solvents such as water, solvent evaporation into the atmosphere is permissible but for toxic and flammable solvents precautions are taken to avoid the leakage of solvent vapor into the atmosphere.

The mass of the deposited substance Δm is proportional to the volume ΔV of the solvent removed from the solution, and to the concentration c of the substance in the solution. Therefore, crystal growth rate is controlled by changing the rate of evaporation of the solvent. During growth by this method the solution always contains a reserve of the crystallized substance. However, as the amount of the solvent diminishes and the crystal grows, concentration of impurities increases in the solution. Consequently, as growth proceeds, impurity concentration also increases in the crystal. To reduce such an effect it is necessary to use large volumes of the solvents. However, in this method it is difficult to maintain constant supersaturation during a long growth run. As the solution volume decreases, the value of supersaturation available in the solution increases when the evaporation is maintained constant. High evaporation rates lead to spurious nucleation followed by mass crystallization in the solution. Spurious nucleation usually occurs on the solution miniscus where regions of high supersaturation may be formed locally by evaporation of the solvent.

1.3.3. Temperature Gradient Techniques

Temperature gradient techniques are based on the creation of two zones of different temperatures. In one of these zones at a lower temperature T_2 the crystal is grown onto an introduced seed whereas in the other zone at higher temperature T_1 the solute is dissolved to obtain saturated solution. The solution supersaturation can be controlled by changing the temperature difference $\Delta T = T_1 - T_2$. Material transport may be ensured by natural, thermal or forced convection. In growth involving natural convection, the saturation region of temperature T_1 is at the top whereas the growth region at temperature T_2 is at the bottom of the growth setup such as a cylinderical crystallizer. When the growth zone at T_2 is at the top and the nutrient zone of T_1 is at the bottom, material transport occurs by thermal convection. In two-tank crystallizers based on forced convection, solution is pumped between separate tanks for solutions kept at different temperatures. The solution is forced to circulate from one tank to the other through connecting pipes.

The common difficulty with two-tank crystallizers is the occurrence of parasitic nucleation in the connecting pipes and this may result in the cessation of solution circulation. This necessitates to run the tubes and pumps at relatively high temperatures. This difficulty is overcome by inserting an additional tank at a temperature $T_3 > T_1$ between the nutrient tank at temperature T_1 and the growth tank at temperature T_2. The additional tank serves as a reservoir of a subsaturated solution, which is pumped to the growth tank and again back to the nutrient tank to be reheated and

resaturated. The first well-known three-tank system for crystal growth is due to Walker and Kohman [2]. Nowadays three-tank crystallizers are widely used for crystal growth from low-temperature solutions [19].

The main advantages of the above method involve economy of solvent and growth of crystals of good quality. However, since growth rate depends on the temperature difference between the nutrient and the crystal growth zones, temperature changes have to be kept to the minimum. Moreover, the entire solute in the nutrient tank is not grown as crystals. Recently, a method has been introduced [22] which entables to achieve a 100% solute–crystal conversion efficiency. The experimental setup for crystal growth by this method consists of a growth ampoule made of glass with seed mounting pad at its base and a ring heater located at the top of the growth ampoule facilitates solvent evaporation, The main advantages of the above method are: (i) the experimental setup is simple, (ii) crystal growth occurs essentially at room temperature, (iii) it enables to grow bulk single crystals along specific orientations, and (iv) it prevents microbial. Since the temperatures in the top and bottom zones essentially remain stable during a growth run and the crystal grows at room temperature, growth occurs at controlled supersaturation and there are minimum thermal stresses in the crystals, resulting in their good quality.

1.3.4. Growth from Boiling Solutions

To grow a substance in a given phase and/or composition and at a reasonable rate, the choice of an optimum temperature interval is an important factor in low-temperature solution growth. As in other processes, the growth at elevated temperatures takes place faster. However, at elevated temperatures, smooth growth necessitates better temperature control, while increased vapor pressure creates problems connected with the control of supersaturation and spurious nucleation. These difficulties may be overcome during crystal growth from boiling solutions.

Crystal growth from boiling solutions has features of temperature changing, evaporation and temperature gradient methods. Constant supersaturation is developed by withdrawing a known amount of the solvent evaporated from the solution saturated at the boiling point that is constant during growth. Stirring is ensured by bubbles generated in the volume of the solution.

The greatest advantages of the method are constant temperature of boiling and stirring provided by bubbles nucleating at the walls of a reactor without an additional mechanical device. Moreover, the crystals grown from boiling solutions are less defective than those grown at low temperatures. The main drawback of the method stems from the relatively high temperature which gives rise to problems of leakage of solvent vapor at the joints of the growth assembly. Another difficulty is nonuniform temperature in the growth vessel owing to uncontrolled sourses of bubbling, because each bubble origin gives a temperature gradient along the direction of its movement. The principle of the technique, experimental apparatus for growth and applicability of the method are described in a review [8].

1.4. Different Factors Affecting Crystal Growth

Among the important parameters affecting the growth rate and quality of crystals are: pH, temperature and supersaturation of the solution. Change in the composition and, consequently, in

the solution pH is one of the parameters which enables to control the process of crystal growth. In particular, by choosing the acidity of a saturated solution one can control the growth rate either of one of the crystal faces or of the whole crystal, thereby changing the external shape (also called habit or morphology), and can regulate the incorporation of impurities in the crystal.

There are several explanations of the effect of pH on crystallization. For example, it has been suggested [2] that the presence of free acids or bases modifies the nature and concentration of ions in the solution. The effect of pH on the growth of potassium chloride crystals has been explained in terms of the structure of aqueous solutions involving hydration of ions [23].

Growth rates of different morphologically important faces at temperature T_g usually increase with increasing supersaturation σ at a given pH of the solution of saturation temperature T or supercooling defined in terms of temperature difference $\Delta T = T - T_g$. For instance, it has been observed [24] that the growth rates R of both prismatic and pyramidal faces of KDP crystals increase with increasing supercooling ΔT at different pH of solutions but for different values of supercooling the highest growth rates for these faces occur at pH of 4.2. The results also indicate that the growth of prismatic faces always occurs above a minimum supercooling for all values of pH and the lowest value of this critical supercooling for growth for the solution of pH of about 4. However, the growth of pyramidal faces occurs practically without the appearance of this minimum supercooling. The region of supersaturation or supercooling where no growth occurs is usually called dead supersaturation zone and the threshold supersupersaturation and threshold supercooling are denoted by σ_d and ΔT_d, respectively. The higher value of supersaturation or supercooling for the growth of prismatic face of KDP crystals is associated with the fact that this face is very sensitive to the adsorption of the growth sites by impurities.

Investigation of the effect of temperature on the growth of crystals from solutions has always been of interest. It is well known that the growth temperature has pronounced effect on the quality and morphology of crystals even in the same solvent. In fact, it is a general observation that the crystals grown at relatively high temperatures usually have a better quality than those grown at a low temperature. The effect of temperature is associated with the process of integration of growth species into the surface of a growing crystal. This process becomes favorable at increased temperature.

Crystallization can be regarded as a two-stage process: (1) supply of solute from solution to the crystal surface through a diffusion boundary layer of thickness δ between the growing crystal and the solution by molecular and convective diffusion, and (2) integration of solute ions/molecules into the crystal. The former is rate-limiting if the supersaturation at the crystallization surface is lower compared with the bulk supersaturation. In this case, the growth is said to proceed in the diffusion regime. The second stage is rate-limiting if the bulk supersaturation and crystal surface supersaturation are similar. In this case, the growth regime is said to be kinetic. Crystals are generally considered to grow in a mixed diffusion–kinetic regime. Following Chernov [5], the basic ideas of kinetic and diffusion regimes are given below.

Assuming that a spherical crystal of radius r_x grows in an isotropic environment such that its growth is determined by kinetic coefficient β and the solute concentration in the bulk solution phase and at the crystal surface, separated by distance x, is c and c_0, respectively, the relationship

between the resultant growth rate R of the crystal, the concentration difference $(c-c_0)$ across the diffusion layer and the effective kinetic coefficient β_{eff} for the growth of crystal surface and the rate D/r_x of solution diffusion is given by [5]

$$R = \beta_{\text{eff}}\Omega(c - c_0), \tag{7}$$

where the effective kinetic coefficient β_{eff} of growth of crystal surface is defined in terms of the sum of resistances due to the two contributions β and D/r as

$$\frac{1}{\beta_{\text{eff}}} = \frac{1}{\beta} + \frac{r_x}{D} = \frac{1}{\beta}\left(1 + \frac{\beta r_x}{D}\right), \tag{8}$$

where D is the solute diffusion coefficient in the solution and Ω is the solute molecular volume ($\Omega = 1/\rho$; ρ is the solute density).

Crystal and environment interact through the medium of the boundary layer, the thickness of which may vary from the minimum (e.g. in stirred solutions) virtually to infinity in unstirred solutions under certain conditions. From Eq. (7) the following two extreme cases may be distinguished.

1. Kinetic regime. When $\beta r_x/D << 1$, the contribution due to diffusion can be neglected. In this case, the rate $R = \Omega\beta(c-c_0)$ does not depend on crystal size which increases as $r_x = \Omega\beta(c-c_0)t$. Since the kinetic coefficient β depends on supersaturation, it reflects the reaction of the growing surface to the deviations from equilibrium. The specific response, in turn, depends primarily on the interface roughness and defect structure of the surface which define its growth mechanism: layered (by screw dislocations or two-dimensional nucleation) or continuous (normal).

2. Diffusion mode. When $\beta r_x/D >> 1$, the rate-limiting step is solute diffusion transfer across the boundary layer $\delta \approx r_x$. In this case, the crystal size increases as $r_x = [2\Omega(c-c_0)D]^{1/2}t^{1/2}$ and the rate decelerates as $R = \Omega(c-c_0)D/r_x$. Steady state is never reached in this regime. The main feature here is that, after exceeding a certain critical size which decreases with increasing supersaturation, the crystal loses morphological stability and the starving surface disintegrates into separate sinks for the insufficient nutrient. Morphologically, the event is marked by the onset of hopper and dendritic growth.

In recent years, numerous investigations of surface morphological evolution have been carried out on crystals grown from solutions. [25-27]. The results of these studies have been analyzed within the formalism of BCF theory [28] and its subsequent modifications [29], and have led to a broad uderstanding of the mechanics of dislocation-controlled crystal growth. For example, the growth rate of KDP crystals depends on many parameters, such as growth temperature, supersaturation of growth solution, impurities. Typically these KDP crystals grow on vicinal hillocks formed by dislocations. The normal growth rate R of a crystal face growing by the screw dislocation mechanism is given by the geometrical relation

$$R = pv \tag{9}$$

where p is the slope of dislocation hillock and v is the tangential velocity of the elementary steps. According to Eq. (9) , there are two ways to increase the growth rate: either increase the step velocity v or the slope p of the dislocation hillock.

We consider a composite hillock composed of m equally-spaced dislocations of Burgers vector h, arranged along a line of length L. The slope p of the hillock in this case is given by [28,29]

$$p = \frac{mh}{y + 2L}, \tag{10}$$

where the interstep distance $y = 19r_{2D}^*$, with the radius of the critically-sized two-dimensional given by

$$r_{2D}^* = \frac{\gamma\Omega}{k_B T\sigma} \tag{11}$$

where γ is the solute–solvent interfacial energy which is related to the linear edge free energy γ by the relation: $\gamma = \gamma a^2$ (the growth unit dimension $a \approx \Omega^{1/3}$) and σ is the supersaturation.

As seen from Eq. (10), the hillock slope p (and hence R) can be increased by increasing either σ or T or by changing the number m of dislocations in the growth source. In the kinetic regime, the step velocity v is given by [27,29]

$$v = b\beta\sigma \tag{12}$$

with the constant b related to the solubility c_0 and the kinetic coefficient

$$\beta = \beta_0 \exp(-E_A/k_B T), \tag{13}$$

where β_0 is a constant, E_A is the activation barrier of the slowest stage of growth and T is the temperature. Thus, the step velocity (and hence R) can equally increased either by increasing T or σ.

It should be mentioned that direct control of the growth rate by changing the dislocation structure is difficult because of the complicated relationship between the structure of a dislocation source σ and T. However, as was shown by De Yoreo et al. [30], in contradiction to the predictions of simple BCF models, for $\sigma > 5\%$ the activity of a growth hillock is dominated by the presence of strain-induced dislocation cores and is nearly independent of σ.

1.5. Crystal Growth Rates and Dead Supersaturation Zone

1.5.1. Basic Concepts of Impurity Effects

Growth of crystals occurs by the attachment and detachment of adatoms at kinks in the steps (ledges) present on their flat faces (F faces). Under ideal conditions, growth on a vicinal F face proceeds by step flow, with steady motion of a uniform train of steps. However, addition of small concentrations of impurities can greatly change the properties, morphology and kinetics of the growing crystal, with important consequences in materials applications. Consequently, the effects of impurities on the growth kinetics of crystals have been studied intensively both theoretically and experimentally. Here the kinetic effects of impurities are briefly described. For more details the reader is referred to ref. [31].

Impurities are usually more effective at low supersaturations due to the favorable competition of impurity species with low concentration of solute particles for the adsorption and occupation of same growth sites available on the growing face. This results in a threshold supersaturation σ_d below which no growth takes place, which is usually revealed in the dependence of the displacement rate v of steps on the F faces and face growth rate R of crystals growing from solutions containing a certain amount of impurity on supersaturation σ. The value of the threshold supersaturation σ_d increases with increasing impurity concentration c_i in the solution. The occurrence of a dead supersaturation zone induced by impurities has been reported for many crystals growing from solutions. Typical examples are: KH_2PO_4, paraffin, $K_2Cr_2O_7$, ammonium oxalate monohydrate [$(NH_4)_2C_2O_4 \cdot H_2O$; AO] and KCl.

Bredikhin et al. [32] reported extensive data on the existence of dead zone in the case of the supersaturation dependence of the linear growth rate R of the (100) face of KDP crystals grown from aqueous solutions containing different concentrations of Al^{3+} and Fe^{3+} ions under the conditions of free convection. These authors observed two different supersaturation barriers σ_d and σ^* for these impurities, such that for $\sigma < \sigma_d$ there is no growth, for $\sigma_d < \sigma < \sigma^*$ the growth rate slowly increases following the classical Burton–Cabrera–Frank (BCF) parabolic law: $R = b(\sigma-\sigma_d)^n$, where b is an empirical constant and the exponent $n = 1$ or 2, while for $\sigma > \sigma^*$ the growth rate rapidly increases following an $R[(\sigma-\sigma^*)^{5/4}]$ dependence.

Rashkovich and Kronsky [33] studied the effect of trivalent cations on the supersaturation dependence of displacement velocity v of steps on the (100) and (101) faces of KDP crystals and made observations similar to those described above. These authors found three regions of $v(\sigma)$ dependence: (1) there is no growth for $\sigma < \sigma_d$, (2) the velocity v increases slowly with σ for $\sigma_d < \sigma < \sigma^*$, and (3) for $\sigma^* < \sigma < \sigma^{**}$, v steeply increases with σ above σ^*. In the region $\sigma > \sigma^{**}$ the $v(\sigma)$ curve becomes a straight line passing through the origin, as expected from the theoretical linear dependence, and the step velocity v in the presence of attains a value equal to the velocity v_0 for the system without impurities occurs at a threshold supersaturation σ^{**}. These authors attributed the behaviour of the $v(\sigma)$ curves to the effect of impurities at low values of σ. The appearance of these different threshold supersaturations is illustrated schematically in Figure 4.

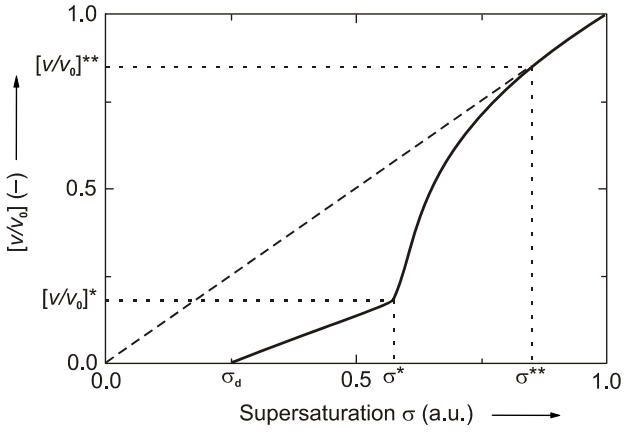


Figure 4. Schematic presentation of the above $v(\sigma)$ data illustrating the appearance of different threshold supersaturations at a hypothetical concentration c_i of an impurity. Adapted from ref. [15].

The origin of the appearance of the above threshold superaturations σ_d, σ and σ^* may be explained in terms of adsorption of impurity particles at kinks in step ledges (Kubota–Mullin model) and on the surface terrace between successive ledges (Cabrera–Vermilyea model). These two models differ in the way impurity particles arriving from the bulk medium at the terraces between the ledges on an F face are adsorbed. Once they are adsorbed, they physically block the motion of advancing step ledges (pinning mechanism), as illustrated in Figure 5. This figure shows two steps from an array of steps, moving from left to the right, with an average distance y_0 and an average distance x_0 betweeen the kinks in a step.

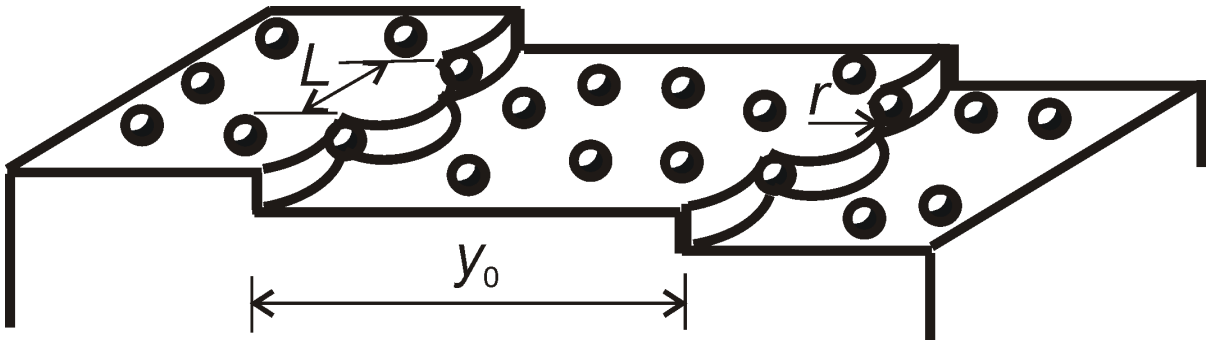


Figure 5. Illustration of blocking of movement of step ledge by two firmly attached impurity particles. Adapted from ref. [31].

There are two extreme cases for the impurity particles to block the motion of steps. When the adsorbed impurities are sufficiently mobile on the surface, they can reach some of the kinks in the step ledges instantaneously (mobile impurities). These adsorbed impurity particles not only block the integration of solute molecules in the advancing step ledges but also physically block their movement by the pinning mechanism. However, the impurity particles can also be firmly adsorbed onto the surface terrace as soon as they reach there (immobile impurities). When the advancing step contacts an impurity particle, it tends to curl around it. The step will stop when the average distance between the adsorbed particles $L < 2r_{2D}^*$, while it will squeeze between a pair of neighboring particles when $L > 2r^*$. The critically sized two-dimensional nucleus radius r_{2D}^* on the surface is given by expression (11). The configuration of the advancing steps is thus changed by the adsorbed impurity particles and their average velocity v in the presence of the impurity become smaller than the velocity v_0 in the absence of the impurity. The mechanism of blocking of the movement of a step ledge by two firmly adsorbed particles is shown in Figure 5.

Using the relationship between the advancement velocity v_r of a curved step and the radius r of the curvature of the step given by [34]

$$v_r / v_0 = 1 - r_{2D}^* / r, \tag{14}$$

one obtains the minimum velocity v_{min} corresponding to the curvature $r = L/2$ in the form

$$v_{min} / v_0 = 1 - 2r_{2D}^* / L. \tag{15}$$

In the absence of impurity when $L \to \infty$, $v_{max} = v_0$. In Eq. (15) when v is taken as the arithmetic mean velocity $v = (v_{min}+v_0)/2$ and the geometric mean velocity $v = (v_{min}v_0)^{1/2}$, one obtains [28,31,35]

$$v/v_0 = 1 - r_{2D}^*/L = 1 - \sigma_{dl}/\sigma, \qquad \text{Kubota–Mullin model;} \qquad (16)$$

$$v/v_0 = (1 - r_{2D}^*/L)^{1/2} = (1 - 2\sigma_{ds}/\sigma)^{1/2}, \qquad \text{Cabrera–Vermilyea model.} \qquad (17)$$

In Eqs. (16) and (17) σ_{dl} and σ_{ds} are the threshold supersaturation barriers by Kubota–Mullin and Cabrera–Vermilyea models, respectively, given by

$$\sigma_{dl} = \frac{\gamma_l a}{k_B T L} = \left(\frac{\gamma_l a}{k_B T x_0}\right)\theta_l, \qquad (18)$$

$$\sigma_{ds} = \frac{\gamma_l a}{k_B T L} = \left(\frac{\gamma_l a}{k_B T \lambda}\right)\theta_s^{1/2}, \qquad (19)$$

where x_0 is the average distance between kinks in a step, λ is average distance between possible adsorption sites on the surface terrace, the fractional linear coverage $\theta_l = x_0/L$ and fractional surface coverage $\theta_s = (\lambda/L)^2$, and the terms given in the brackets are measures of impurity effectiveness. Since x_0 is much larger than $\lambda \approx a$, for a solute–impurity system the impurity effectiveness and the threshold supersaturation σ_{dl} according to the Kubota–Mullin mechanism is always much lower than σ_{ds} predicted by the Cabrera–Vermilyea mechanism.

According to the above concept, growth proceeds according to the usual growth mechanism after the occurrence of the threshold supersaturation barrier σ_d upto a particular value of supersaturation σ^* when impurity adsorption on the growing surface becomes time dependent. However, in the case of time-dependent impurity adsorption at kinks, there is a time constant τ characterizing the upper limit when impurity adsorption ceases to be time dependent [28, 35-37]. This upper limit corresponds to a third threshold supersaturation σ^{**} when the step velocity v approaches the value v_0.

The theoretical interpretation of effect of impurities and threshold supersaturations σ_d and σ^* relates step velocity v with supersaturation σ for crystal growth, but no theoretical relationship between face growth R and supersaturation σ has been reported. However, in comparison with the $v(\sigma)$ data, there is a large amount of published data on face growth R as a function of supersaturation σ, where threshold supersaturations have been observed.

The $\sigma_d(c_i)$, $\sigma^*(c_i)$ and $\sigma^*(c_i)$ data for different impurities used during the growth of crystals may be described by the following dependences [28,31,37]:

$$\frac{1}{\sigma_c^{1/\rho}} = Q^{1/\rho}\left(1 + \frac{1}{K_L c_i}\right), \qquad (20)$$

$$\sigma_c^{1/\rho} = B_0 + B_1 c_i, \qquad (21)$$

which are derived by using Langmuir and Freundlich adsorption isotherms, respectively. In these equations, K_L is the Langmuir constant, the constants B_0 and B_1 are related to the parameters of

Freundlich isotherm, and Q is a parameter related to the value of step velocity v corresponding to the type of threshold supersaturation. Figure 6 presents the plots of σ_d, σ^* and σ^{**} for the (100) face of KDP crystals against the concentration c_i of different trivalent impurities according to Eq. (21).

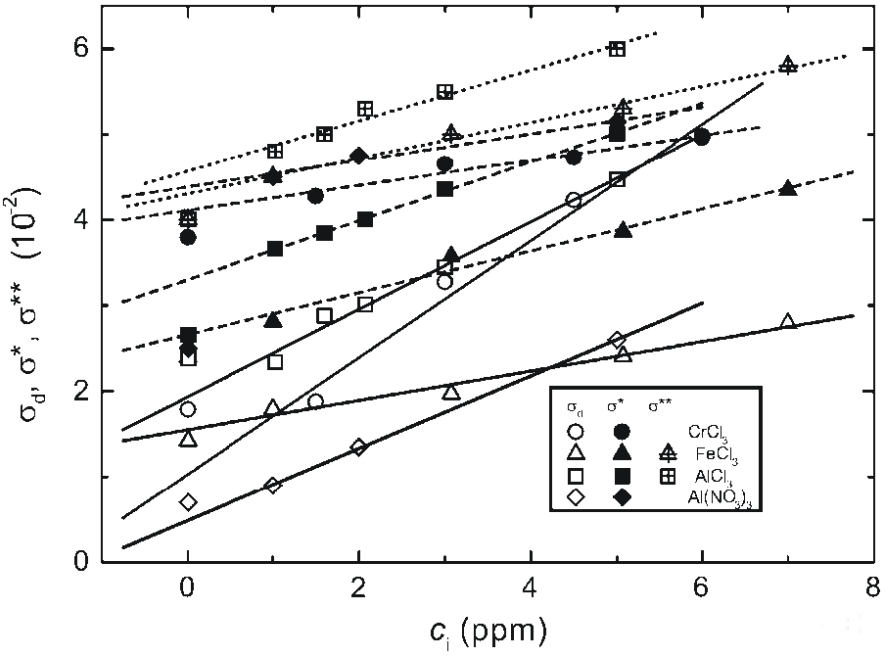


Figure 6. Example the plots of σ_d, σ^* and σ^{**} for the (100) face of KDP crystals against the concentration c_i of different trivalent impurities according to Eq. (21). From [37], reproduced with permission of Wiley-VCH.

Analysis of the data according to Eq. (21) revealed [36] that the average interkink distance x_0 corresponding to the three three threshold supersaturations σ_d, σ^* and σ^{**} follows the trend: $x_0(\sigma_d) > x_0(\sigma^*) > x_0(\sigma^{**})$. These distances correspond to three different values of supersaturation representing three average distances $y_0 = 19r_{2D}^*$ between successive steps (cf. Eq. (13)): (1) when the steps are completely stopped, $y_0 \geq l_d$, (2) when the steps squeeze out through the fence of adsorbed impurity particles as a result of decreasing r_{2D}^* until $y_0 = l^*$, and (3) when the steps essentially become straight and impurity adsorption no longer takes place on the steps. Steady-state (or instantaneous) and unsteady-state (or time-dependent) impurity adsorption occur in the supersaturation regions $\sigma < \sigma^*$ and $\sigma > \sigma^*$, respectively. Finally, impurity adsorption becomes time independent at $\sigma > \sigma^{**}$.

The above conclusion of three distances corresponding to the three threshold supersaturations is consistent with the concept advanced by Rashkovich and Kronsky [33]. According to these authors, the barrier σ_d occurs at $2r_{2D}^* = l_d$ when the steps are completely blocked, while the origin of σ^* is associated with the burial of adsorbed imprity particles as a result of curling of advancing steps around them when the depth of the bent steps reaches a depth δ. The burial of impurity particles occurs when the critical nucleus diameter $2r_{2D}^* \propto \sigma^{-1}$ (see Eq. (13)) becomes equal to l^* between the adsorbed impurity particles. The threshold supersaturation σ^{**} corresponds to l^{**}

when the burial of impurity particles is complete and the successive steps are parallel to each other.

It should be mentioned that more than fifty years ago Frank [38], and Cabrera and Vermilyea [39] used the concept of time-dependent impurity adsorption to explain the origin of kinematic waves and step bunching in terms of relationships between flux of steps passing across a point and the density of steps on the surface. According to this concept, at given concentration of an impurity its adsorption is time-dependent at low density of steps but the impurity adsorption becomes time independent at high density of steps (i.e. low interstep distance y_0). Later van der Putte et al. [40] suggested that adsorption of an impurity remains time-independent at high concentrations of the impurity.

In a study of the effect of Fe(III), Cr(III) and Al(III) ions on the growth of KDP Land et al. [41] proposed that recovery of crystal growth beyond the dead supersaturation zone in KDP is accompanied by the propagation of macrosteps (bunches of monolayer steps) in contrast to the growth of elementary steps considered in the Cabrera–Vermilyea model. Weaver et al. [42] suggested an improved model for describing impurity effects on crystal growth by synergizing the Langmuir model of adsorption dynamics along with the Cabrera–Vermilyea model.

Extensive studies on the growth kinetics of AO crystals from pure aqueous solutions and from aqueous solutions containing various impurities revealed that the appearance of different threshold supersaturations is associated with the nature of solute–additive–solvent system [36, 43-47]. It was found that, for a given impurity concentrations, the face growth rate R approaches a value corresponding to pure solutions for supersaturation $\sigma > \sigma^{**}$, a behavior similar to that for KDP crystals [33]. Analysis of the experimental data on the kinetics of growth of different faces of the crystals in solutions containing Cr(III) impurity suggested that the appearance of threshold supersaturations at $\sigma > \sigma_d$ occurs when there is a transition in the mechanism of adsorption of an impurity from Cabrera–Vermilyea to Kubota–Mullin mechanism.

1.5.2. Effect of Organic Additives on Crystal Growth

Foreign substances inherently present in a growth medium or deliberately added to it affect growth rates in different ways. They can change the properties of the growth medium, whereby the equilibrium saturation concentration (i.e. solubility) of the solute and, hence, the supersaturation available for the formation of 3D nuclei and their subsequent growth in the medium are altered. The affect of foreign substances on the growth of crystals is associated with kinetic and thermodynamic terms involved in the growth models. The kinetic parameters involved in the growth models are connected with the density of kinks and obstructions provided by impurity particles in the movement of step ledges on the surface, whereas the thermodynamic parameter in these models is the crystal–medium interfacial energy γ. The kinetic effects of impurities were discussed in the preceding section, where no attention was paid to the thermodynamic parameters on growth kinetics. In fact, the above treatment holds when the interfacial energy γ remains unchanged during growth.

It is well known that the solubility c_0 of various substances in aqueous solutions is related to their interfacial energy γ [10]. The higher the solubility c of a substance in a solvent, the lower is its

interfacial energy γ, and, consequently, the higher is the step velocity v and the face growth rate R of its crystals. Following this line of argument it can be concluded that the usual retardation of step velocity v or face growth rate R by an impurity leads to an increase in the solute–solvent interfacial energy γ. However, consideration of the adsorption process in terms of adsorption isotherms and reversible adsorption equilibrium shows that adsorption of foreign substances decreases the value of γ [48,49]. This decrease in γ will, consequently, leads to an increase in v and R. Impurity particles firmly adsorbed at step ledge and onto the surface terrace can also serve as sources of additional kinks for the integration of solute molecules, thereby leading to an increase in v and R [31].

The above considerations show that, at relatively low concentrations of an impurity, one expects opposite effects of kinetic and thermodynamic parameters on growth kinetics. The kinetic parameter tends to decrease v and R whereas the thermodynamic parameter tends to increase them. Thus, at low supersaturations which ensure a low density of kinks in the step ledges, the rates increase for small impurity concentrations and decrease as the impurity concentration is increased. However, at relatively high supersaturations when a high density of kinks is available in the step ledges, impurity adsorption always decreases v and R for all values of impurity concentrations c_i. With an increase in impurity concentration c_i, an initial increase and then a decrease in R passing through a maximum at a particular impurity concentration c_i were first observed by Bliznakov and Kirkova [50] for the growth rates of the (100) and (111) faces of $Pb(NO_3)_2$ crystals grown from aqueous solutions in the presence of methyl blue.

For many crystals the ionic surface structure of different faces is fundamentally different. Therefore, organic additives interact differently with different crystal faces [51]. For example, in the case of KDP crystals, the {101} faces are terminated by a layer of K^+ ions whereas the {100} faces by a layer of both K^+ ions and $H_2PO_4^-$ groups. Consequently, since alcohols contain hydroxyl groups, adsorption of alcohols onto the {100} faces through the formation of H-bonds between the alcohols and $H_2PO_4^-$ groups is more favorable than that onto the {101} faces. Similarly, the effect of urea is less pronounced on the growth rate than that of alcohol. Enqvist et al. [52] showed that the negative charge on O atoms of alcohols containing the hydroxyl group is about 1.6 times higher than that of urea containing the carbonyl group. Therefore, the adsorption of alcohols on the {101} faces is more favorable than that of urea. Consequently, alcohols inhibit the growth of the {101} faces more than that of urea.

Small amounts of organic impurities can also cause a growth promoting effect. The positive effects of organic additives on crystal growth and quality have been reported by several authors [53-56]. For example, during ADP and KDP crystal growth, the addition of ethylene glycol, glycerol and ethylenediamine tetra-acetic acid (EDTA) significantly increases the width of the metastable zone and the crystal growth rate in comparison with those from pure solutions [55,56]. These observations are usually explained by the ability of formation of complexes of additive molecules with multivalent ions inherently present in growth solutions.

1.6. Effect of Mechanical Impurities on Crystal Growth

Nonlinear optical (NLO) materials capable of second harmonic generation (SHG) have received a great deal of attention due to their commercial importance in optical communication, signal processing, sensing and instrumentation. Systematic investigations of NLO materials are devoted to inorganic and semiorganic crystals such as KDP, K_2SO_4, KAP and LAP with embedded organic molecules and inorganic nanoparticles. These impurities offer mechanical obstruction during growth. These studies were aimed at correlating structural properties to the nonlinear responses with the ultimate goal being the possibility of "tuning" the structure to enhance the nonlinear properties. Therefore, crystallization of some inorganic and semiorganic salts in the presence of organic molecules and inorganic nanoparticles is an important process still under careful examination by several research groups.

1.6.1. Growth of Water Soluble Crystals with Embedded Organic Molecules

Gliko et al. [57] studied the morphology and growth kinetics of the pyramidal face of KDP crystals in the presence of dye Chicago Sky Blue. The crystals were grown in crystallizers of about 10 L volume at the initial temperature of about 60 °C and impurity concentration c_i = 1.4 ppm ($1.4 \cdot 10^{-6}$ mole/mole KDP). It was found that staining of the crystal begins only at temperatures below 35 °C when the crystal already reaches a sufficiently large size. This observation is a consequence of a sharp increase in dye adsorption with decreasing temperature.

Figure 7 shows the dependence of normal growth rate R of dislocation hillocks on supersaturation σ of aqueous solutions containing different dye concentration c_i. It may be seen from the figure that the measured values of normal growth rate R in the pure solution and in the presence of the dye are close. The minor difference between them can be attributed to the difference in the activity of dislocation sources and influence of temperature. The experimentally derived dependence of velocity v of movement of steps on supersaturation σ, shown in Figure 8, has a character unusual for pyramidal faces. The $v(\sigma)$ dependence is sublinear for the shallow sector below $\sigma \approx 0.035$ (top curve), whereas v is nearly proportional to σ for steep sectors in the whole region of supersaturation (bottom curves). From the figure it may also be seen that the dye concentration does not effect noticeably the velocity of the growth layers movement.

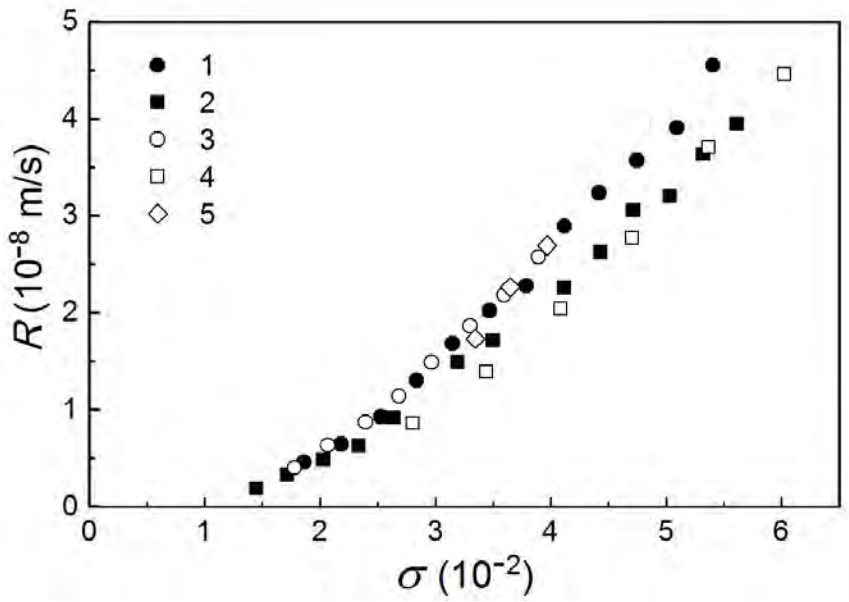


Figure 7. Dependence of normal growth rate R of dislocation hillocks on supersaturation σ of aqueous solutions containing different dye concentration c_i: (1,2) no additive, (3) 1 ppm, (4) 1.5 ppm, and (5) 2 ppm. Saturation temperature: (1,3) ca. 33 °C, and (2,4,5) ca. 37.5 °C. After [57], reproduced with permission of Materials Research Society.

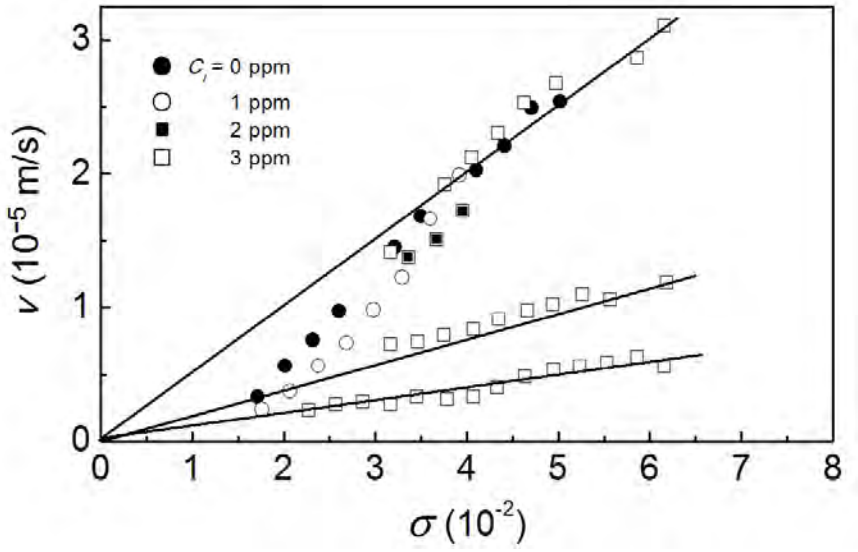


Figure 8. Dependence of velocity v of moving growth layers in three vicinal sectors on supersaturation σ. Saturation temperature about 37.5 °C. After [57], reproduced with permission of Materials Research Society.

The fact that the capturing of a dye starts only at a sufficiently high velocity of the step in the case of the shallow sector composed of array of parallel steps with large interstep distance y_0 but

is not captured by the steepest vicinal sectors comprised of arrays of parallel steps with small y_0 is an evidence for a short lifetime of dye molecules on the surface. Another observation in support of this argument is the occurrence of capturing of impurity particles only at its sufficiently high concentration in the solution. Gliko et al. [57] explained the observation of capture of dye particles in the framework of a model, proposed before in [58], describing the movement of a step and its morphological stability in the presence of mobile impurity stoppers.

In an *in situ* atomic force microscopy (AFM) study of potassium sulfate (K_2SO_4) crystal growth in the presence of acid fuchsin and pyranine, Moret [59] found that these polysulfonated dyes adsorb onto the {110} and {010} faces producing strong habit modification and changes in the surface micromorphology of the crystals. The main observations of this study were the following:

(1) Presence of dye molecules at concentrations as low as about $2 \cdot 10^{-6}$ and $4 \cdot 10^{-4}$ M for pyranine and acid fuchsin, respectively, to produce significant changes in the step morphology and growth rates.
(2) Bunching of steps occurs as a result of absorption of impurities binding to the crystal surface.
(3) Additive molecules attach to the terraces pinning the growing front and lead to the roughening of edges of the growing steps.
(4) At a given supersaturation there exists a critical value of dye concentration above which crystal growth is stopped along particular crystallographic directions (i.e. dead supersaturation zone).
(5) At low supersaturations layers grow by step flow at preexisting steps by the addition of growth units at the step edges.

The former 4 observations may be explained by the Caberera–Vermilyea mechanism whereas the last obsevation suggests that growth is controlled by volume diffusion.

The validity of Cabrera–Vermilyea mechanism in the above study is associated with the adsorption behavior of acid fuchsin and sulfonated pyrene molecules on the two faces of K_2SO_4 crystals. Acid fuchsin and sulfonated pyrene are strong polyelectrolytes which can adsorb on terraces thanks to a high number of simultaneous attaching points on a molecule (three/four sulfonated groups) strongly interacting with the surface via long distance electrostatic forces. This class of molecules should remain practically immobile once adsorbed onto the surface due to the strong interactions with the host surface, provided that sulfonate–sulfonate distances reasonably match the distance between the sulfate ions on the surface host lattice and with sulfonate groups substituting for surface anions. This should particularly hold for pyranine due to its conformational rigidity, and its effects on K_2SO_4 are indeed significantly stronger than those produced by acid fuchsin.

A major goal in crystal growth studies is to ascertain whether the additives adsorb onto the surface terraces between steps or at kink sites on the steps. For example, correlation of distribution of foreign molecules inside the host crystal with surface microtopography can shed light on the relationships between surface structure, growth mechanism and additive incorporation. For layer growth, specific affinity for dye incorporation into a growing surface is associated with its detailed structural features (i.e. density of kinks and ledges). Since non-equivalent crystallographic directions have different structural properties, they differ in their affinities toward the capture of an additive.

1.6.2. Growth of Water Soluble Crystals with Embedded Nanoparticles

The methods of growth of single crystals with inclusions of the second fine-crystalline phase (of nanometric dimensions) are of great interest for designing new composite crystalline materials with new valuable properties. Examples of such materials are the so-called combined nonlinear–optical media based on inorganic matrix (single crystal) with incorporated nanoparticles [60-62]. In the case of KDP crystals, SiO_2 and CdTe nanoparticles of size up to 250 nm were found to be captured [60,63].

Rudneva et al. [60] carried out an interesting study devoted to the nature of interaction of nanocrystals and crystalline SiO_2 particles with the growing face and the mechanism of their incorporation into KDP crystal. This study showed that in unstirred solutions the capture of nanocrystals and crystalline SiO_2 particles by a growing crystal face takes place at a growth rate exceeding a certain critical value which depends on particle size. The smaller the particles, the higher is the growth rate. Crystal growth from stirred solutions in the presence of solid particles showed that capture of particles by a growing crystal is also possible. As in the case of growth from unstirred solutions, the probability of capture of particles depends mainly on particle size and decreases with decreasing particle size. The specific feature of the experiments on crystal growth under the conditions of solution stirring was the formation of long channels during the capturing of particles. Such channels are not observed from unstirred solutions. It was found that at the growth rates exceeding the critical values the influence of supersaturation and growth rate of a crystal on the probability of the particle capture is insignificant.

Pritula et al. [61] carried out a similar study on the growth of KDP crystals from aqueous solution in the presence of TiO_2 nanoparticles by the temperature reduction method onto a point seed. The authors found that, under the conditions of intense stirring, TiO_2 nanoparticles are captured predominantly by the pyramidal growth sector, and to a considerably lesser extent, by the prismatic sector. Difference in the nature of interaction of the nanoparticles with the {100} and {101} growth faces is obviously caused by differences in the structure of the two faces and the nature of adsorption of impurity particles onto them. These differences are responsible for the threshold value of supersaturation necessary for the growth of the faces.

Capture of mechanical impurities in crystal growth from solutions may be explained from a consideration of two forces [5]: (1) force pressing impurity (e.g. SiO_2 particles) at the crystallization front against the crystal surface, and (2) repulsive force of disjoining pressure arising in a thin (10^{-5}–10^{-7} cm) solution layer between a particle and a crystal. The pressing force, in addition to the hydrodynamic component, also has a component related to the effect of the particle entrainment by a diffusion flow. The disjoining pressure arises mainly because of the molecular (van der Waals) and electrostatic (Debye) forces and the structural component of the disjoining pressure due to partial ordering of the liquid in the vicinity of solid surfaces. According to this concept [5], if the distance between a particle of radius r and a crystal surface becomes less than a certain critical distance ca. $0.1r$, the particle screens the surface of a growing face from the diffusion flow. This decreases solution supersaturation under the particle, which, in turn, leads to the formation of a V-like depressions on the growing face. At certain critical growth rate, the conditions for capture of a foreign particle by the crystal are created and a channel filled with mother solution is formed.

Pritula et al. [62] showed the possibility of creating a composite material on the basis of KDP crystal with incorporated $Al_2O_3 \cdot nH_2O$ (NAO) nanoparticles. These authors investigated the effect of NAO nanoparticles on the growth kinetics of KDP crystal faces and showed predominant interaction of the nanoparticles with the {100} crystal faces. KDP:NAO crystals were grown from aqueous solutions containing 1–100 ppm NAO impurity (with respect to KH_2PO_4 by the temperature reduction method. It was found that the nature of the $R(\sigma, \Delta T)$ curves for the {101} and {100} faces of KDP in the presence of NAO nanoparticles and their incorporation in different sectors is similar to that observed in the case of TiO_2 nanoparticles discussed above and trivalent cationic impurities [32,33].

2. High-Temperature Solution Growth

Complex multicomponent compounds usually have high melting points, high vapor pressure, or decompose incongruently before melting. It is difficult to grow such substances from conventional methods such as growth from their melts. Crystallization of these compounds is carried out from high-temperature solution where temperature for their growth is much lower than their melting points.

High-temperature solution growth has features similar to those of growth of substances from low-temperature solutions. The compound to be crystallized, or components reacting to form it, is first dissolved in a solvent at high temperature. Then a supersaturation in the solution is attained by slow cooling of the solution or evaporation of the solvent such that crystals nucleate and grow in the supersaturated solution. Supersaturation can also be attained by creating a temperature difference between the locations of growing crystal and nutrient. Growth is carried out either in the air or in any other suitable atmosphere. The growth temperature is usually between 300 and 1800 ^oC, and the concentration of the solute in the high-temperature solution is between 1 and 30 wt%.

The main advantage of the method is that practically any material can be grown in some solvent whose composition may be found from a knowledge of the composition of solvents used for the crystallization of chemically similar compounds. Since the growth temperature in this method is lower than that in melt growth, technically the control of growth temperature is easier and the quality of the crystals is better in terms of dislocation densities and point defects. The main disadvantage of the method is that the solvent provides a variety of impurities which can be incorporated into the grown crystals either substitutionally as solvent ions or as solvent inclusions.

Crystallization from high-temperature solutions has been described before in excellent books [3,64,65] and reviews [66-69]. The reader is referred to these excellent literature sources for more information on experimental procedures for growth, characterization methods, and the materials crystallized before 1998.

2.1. Principle of the Method

High-temperature solution growth method employs the fact that complex compounds with high melting points have high solubilities in appropriate molten salts and oxides used as solvents. Once appropriate solvents are found for substances to be grown, crystal growth is carried out on seeds spontaneously nucleated in the bulk molten solution or on seeds introduced into the solution, using some procedures to achieve supersaturation,

The range of substances grown as single crystals from high-temperature solutions extends from elements like diamond and metals, semiconducting compounds such as GaP, GaN and AlGaAs, borates and various oxides. Table 1 lists some examples of substances grown from high-temperature solutions. This table contains examples of fluxes published in the literature during the last two decades.

A usual growth experiment consists of weighing and mixing of required consituent materials, their loading into a crucible, tightly closing the crucible to avoid solvent losses by evaporation, placing the crucible in a furnace initially heated to the maximum temperature, holding the crucible for several hours of soaking time to dissolve and homogenize the solution, slow cooling of the furnace to the desired temperature to create supersaturation for nucleation and growth of crystals, fast cooling down of the furnace to room temperature, and finally leaching out the crystals. The crystals obtained after growth can also be separated from the solution by decanting it. Typical procedure used for crystal growth from high-temperature solutions is summarized in Figure 9.

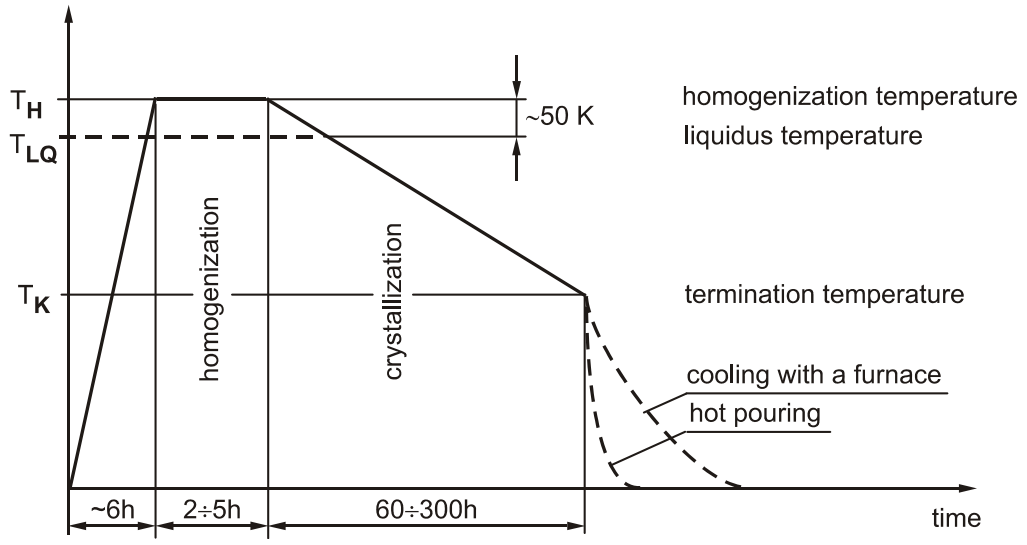


Figure 9. Typical procedure for crystal growth from high-temperature solutions. Adapted from [68].

Table 1. Some examples of single crystals grown by different high-temperature methods*

Crystal	Solvent/solution	Method	Ref.
KTP	$K_8P_6O_{19}$–BaF_2	Top-seeded solution growth; Pt crucible, homogenization at 1100 °C, cooled at 40 °C/h to about 900 °C, seed introduced at about 10 °C above saturation temperature, temperature decreased at 0.2–1 °C/day until end of growth; rotation rate 60–120 rpm with rotation direction reversed every 120 s with interval pause of 5 s; after growth crystal withdrawn from solution and furnace cooled to room temperature at 20 °C	[70]
KTP:Zr	K_2O–P_2O_5–TiO_2–ZrF_4	Slow cooling method; Pt crucibles, homogenization at 1100 °C for 10 h, cooled to 750 °C at 3 K/h	[71]
NdP_5O_{14}	$H_2P_4O_7$	Slow solvent evaporation; platinum crucible, growth temp. 500 °C	[72]
$KNbO_3$	K_2CO_3–NbO_5	Micro-pulling down; Pt crucible, cooling rate 30 °C/min, pulling rate 0.5 mm/min	[73]
$LaMn_{1-x}Co_xO_3$	Cs_2MoO_4–MoO_3	Electrochemical growth; Pt crucible, anode current density 5–10 mA/cm^2, 80–100 h	[74]
LiNbO3	(Li_2O:Nb_2O_5)–K_2O	Czochralski method; pulling rate 2 mm/h, rotation rate 20 rpm	[75]
β-$FeSi_2$	Sn	Temperature gradient solution growth; quartz ampoule, T_G = 880 °C, T_S = 920–960 °C, temperature gradient 40 K/cm	[76]
PZN–PT (6–10mol% PT)	1.7–3.0 mol% TiO_2 +(ZnO:Nb_2O_5:PbO = 19:11:68)	Temperature gradient method; Pt crucible, homogenization at 1160 °C for 8 h, self-nucleation, cooling at 0.5–0.75 °C/h to 890 °C, crucible cooling in 70 h	[77]
3C-SiC	Si	Top-seeded dipping method (LPE); graphite crucible, growth on dipping 6H-SiC(0001) seed mounted at the end of graphite rod at 1300 °C for 50 h	[78]
$BaAlBO_3F_2$	LiF:B_2O_3:NaF = 5:2:0.6	Middle-seeded solution growth; Pt crucible, homogenization at 950 °C for 24 h, slowly cooled to temperature 10 K above melting, insertion of seed mounted on Pt rod, temperature decrease at 0.6–2.6 K/day, rotation rate 20–40 rpm with inversion; grown crystal withdrawn from solution surface by 10 mm, cooled down to RT at 10 K/h	[79]
$KBi(WO_4)_2$	80% $K_2W_2O_7$	Top-seeded solution growth; Pt crucible, homogenization at about 800 °C for 24 h; b-oriented seed, crucible rotated slow cooling at 10 rpm; after ten days of growth at 730 to 720 °C, crystal cooled to room temperature at rate 10 K/h	[80]
$Y_{1-x}Ca_xBa_2Cu_3O_{7-\delta}$	Y:Ba:Cu	Top-seeded solution growth; mixtures of Y_2O_3, $BaCO_3$, $CaCO_3$ and CuO homogenized in air in alumina crucible at 880 °C for 2 days; growth in ZrO_2 crucible on MgO seed, temperature gradient 15 K/cm above melt in air or oxygen; soaking temperature ca. 1050 °C; seed and crucible rotated at 40 rpm in opposite directions	[81]
$La_2CaB_{10}O_{19}$ (LCB)	LCB:CaO:Li_2O:B_2O_3	Top-seeded solution growth; solution homogenization at 1000 °C for 48 h, seed introduced into solution 10 °C above T_S, after initiation of growth temperature decreased between 0.24 and 0.5 °C/day, crystal rotation rate 15–45 rpm	[82]
NBT–KBT (5% KBT)	Na_2CO_3–K_2CO_3–Bi_2O_3 (20% excess flux)	Top-seeded solution growth; Pt crucible, homogenization at 1360 oC, growth on seed mounted on a rod, pulling rate 1.0–1.5 mm/day, rotation rate 5–10 rpm, crystal withdrawn from melt, furnace cooled down to room temperature at 30–50 °C	[83]
$CsLiB_6O_{10}$	Cs_2CO_3:Li_2CO_3:H_3BO_3: NaF (1:1:12:0.5)	Top-seeded solution growth; Pt crucible, homogenization at 850 °C for 24 h, z-oriented seed introduced in melt, for	[84]

	growth cooling rate 0.1–0.6 °C/h, rotation rate 20–40 rpm, crystal withdrawn from melt, furnace cooled to room temperature at 10–15 °C/h

*Abbreviation: T_S – saturation temperature.

2.2. Composition of Fluxes and Their Selection

Selection of a suitable solvent for the material to be grown from high-temperature solutions is also a critical step in this method. In the selection of a solvent both its physical and chemical properties are important. At the growth temperature a solvent should ensure a sufficient solubility of the compound and its components, and the solubility should show sufficient change with temperature. The compound to be crystallized should also be stable in the solvent. The solvent should have low melting point, low vapor pressure (low volatility), low viscosity, and low toxicity. It should also not corrode the growth apparatus (crucible and furnace) and should be cheaply available in the pure state.

There is no universal high-temperature solvent that satisfies all of the conditions mentioned above. Most of the solvents used for crystal growth are various individual chemical compounds or their mixtures, and up to about 1990 they were selected by trial and error method. However, in later years the composition of solvents for the growth of different materials have been established from knowledge of solvents proposed before for the crystal growth of similar compounds.

For the growth of oxides from high-temperature solutions, the following fluxes are commonly used: (i) compounds containing lead and bismuth, (ii) borates, (iii) vanadates, molybdates and tungstates, and (iv) various chlorides and fluorides. Fluxes from the first group are very effective for growth. They are volatile, toxic, and relatively active with platinum crucibles. They dissolve in hot aqueous HNO_3 solutions. Fluxes from the group of borates have relatively low melting points but they are very viscous (see Figure 11) and have a strong tendency to creep out of the crucible. They also dissolve in hot dilute HNO_3 whereas some of them also dissolve in water. Vanadium, molybdenum, and tungsten oxides are good solvents but they are very volatile at high temperatures. Consequently, their salts (i.e. vanadates, molybdates, and tungstates) are usually used. They all dissolve in aqueous solutions of acids and alkalies. Chlorides and fluorides are good solvents with low viscosity but they are volatile (see Figure 10). Fluorides dissolve in acids whereas chlorides in hot water.

Oxide superconductors usually have complex composition and have two or more oxide components. As the complexity of composition of oxide superconductors increases, they become increasing less stable. It is known that practically all high temperature T_c oxide superconductors decompose before melting. Consequently, these materials are usually grown from high temperature solutions. Three types of fluxes are used for their growth [69]: (i) self-fluxes, (ii) partial self-fluxes, and (iii) other fluxes. When components of the composition of an oxide superconductor serve as a solvent for growth, they are said to be the self-fluxes. When one of the components of the oxide superconductor is a part of its chemical structure while the other is partially or entirely related to its structure, one talks of partial self-flux. However, when the solvent is completely unrelated to the chemical composition of the superconductor, it is

categorized as other flux. For the growth of $YBa_2Cu_3O_{7-\delta}$ (YBCO) for example, CuO, CuO–BaO, and In_2O_3 are self-flux, partial self-flux and other flux, respectively.

For the growth of crystals of complex phosphates such as potassium titanyl phosphate ($KTiOPO_4$; KTP), potassium polyphosphates ($K_6P_4O_{13}$ and $K_8P_6O_{19}$, popularly abbreviated as K_6 and K_8 solvents, respectively) are known as good fluxes. A common problem with these fluxes is that they have high viscosity. Introduction of additives such as alkali and alkaline-earth fluorides are well known to reduce solution viscosity and increase solute solubility. However, these addives lead to an increase their volatility, which strongly increases with the additive content in the solvent (see Figure 10). The increase in the flux volatility is enormously high in the fluorides of alkali metals.

2.3. Some Properties of High-Temperature Solvents

The solubility of a substance in a given flux and the width of the metastable zone width are associated with the formation of ions and complexes [67,85,86]. Consequently, composition of the components of the original flux and addition of impurities, usually known as additives, determine the solubility curve and metastable zone width in it for a given compound.

Garnets ($A_3B_5O_{12}$), spinels (AB_2O_4) and perovskites (ABO_3) are usually grown at high temperatures from solvents composed of oxides and fluorides (see Table 1). These solvents are characterized by the dissociation of oxide supplying O^{2-} ions to the solution (basic behavior) and association of O^{2-} ions to the second component (acidic behavior) [87]. Successful growth of the compounds takes place in a wide range of composition of the solvents and the ratio of the garnet-forming oxides, and there is a correlation between oxygen ion concentration (OIC) and the range of crystallization of primary phases of a garnet, spinel or perovskite.

Volatility of a flux used for growth of a compound has an adverse effect on the quality of crystals grown from solutions and causes problems associated with spurious nucleation on the solution miniscus, decomposition of seed crystals and unstable growth. Therefore, while selecting the composition of a flux suitable for the growth of a compound knowledge of the volatility of the flux is very important.

Volatilization of the solution may be determined from the weight loss of the charged crucible during each crystal growth experiment [70]. Figure 10 shows an example of the volatility of four fluxes used for the growth of KTP ($KTiOPO_4$) crystals as a function of the content x of K_8 ($K_8P_6O_{19}$), and three fluoride additives (BaF_2, NaF and KF) in the starting high-temperature solution for volatility experiments. The parameter x defines the weight fraction of K_8 (curve 1) or fluoride additive (curves 2-4) in the K_8–KNT–additive solution. As seen from this figure, the volatility of different solutions increases practically linearly with increasing x of K_8 as well as of all fluoride additives. As indicated by the slope of the the plots of the volatility of different substances against their initial content x, above about 3 wt% the volatility of NaF and KF additives increases very rapidly with an increase in their content, and the volatility of NaF is much higher than that of KF. However, as in the case of K_8 solvent, the volatility of BaF_2 increases poorly with its content in the solution.

In the above study, the authors [70] used working seeds mounted on a platinum seed-rod for crystal growth. They observed deposition of volatilized mass on seed-rod in the case of NaF and KF additives, but no such deposition was found on the seed-rod in BaF_2 additive. These results suggest that pure K_8 solvent and BaF_2 additive contained in K_8 are favorable for the growth of KTP crystals.

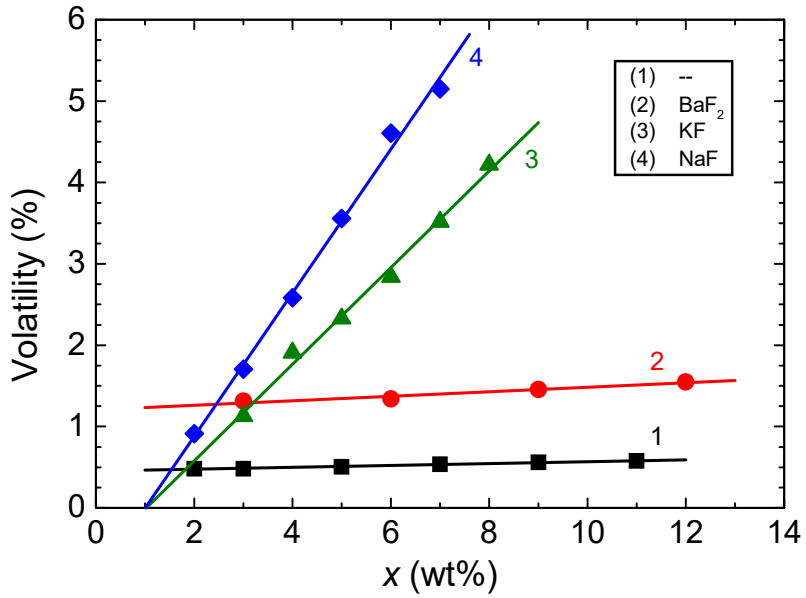


Figure 10. Volatility of KTP in four fluxes as a function of additive content x: (1) K_8 ($K_8P_6O_{19}$), (2) K_8–BaF_2, (3) K_8–KF, and (4) K_8–NaF. Additives to the pure solvent K_8 are given in the inset. Adapted from [70].

As in the case of different low-temperature solutions and solvents, the viscosity of high-temperature solutions decreases with an increase in temperature. The viscosity of high-temperature solution strongly depends on solution composition. For example, the viscosity of halide-free solutions used for the growth of KTP and CLBO crystals differs by a factor of about 5, and solutions of the CLBO system are more viscous than those of the KTP system. Moreover, fluoride additives, as a rule, decrease the viscosity of different systems and the relative decrease in the viscosity of the solution usually increases with increasing concentration of the fluoride additive.

The viscosity of different liquids usually follows the Arrhenious relation

$$\eta = \eta_0 \exp(E_a/R_G T), \qquad (22)$$

where η_0 is a constant and E_a is the activation energy for viscous flow. Figure 11a and b shows the viscosity of solutions of solute KTP in solvent K_8 or K_8–BaF_2 in the weight ratios between 0.4 and 0.5 and of flux composition used for the growth of $CsLiB_6O_{11}$ (CLBO) crystals, respectively, in the form of plots of $\ln\eta$ against $1/T$ according to Eq. (22). The calculated values of the preexponential factor η_0 and the activation energy for E_a viscous flow are given in Table 2. Obviously, the activation energy for viscous flow for solvents of different composition varies in a wide range. The highest activation energy is encountered for multicomponent solvents and its value is decreased by the alkali fluoride additives and their concentration.

Table 2. Calculated values of parameters A and E_a for growth solutions for KTP and CLBO

Crystal	Solution	$\ln\eta_0$	η_0 (mPa·s)	E_a (kJ·mol^{-1})
KTP	K_8	–3.65±0.35	$2.6\cdot10^{-2}$	82.2±3.5
	K_8+BaF_2	–4.28±0.25	$1.4\cdot10^{-2}$	86.0±2.5
CLBO	Cs_2CO_3:Li_2CO_3:H_3BO_3 (1:1:11)	–11.77±1.11	$7.7\cdot10^{-6}$	176.3±10.5
	Cs_2CO_3:Li_2CO_3:H_3BO_3 (1:1:12)	–10.40±0.90	$3.0\cdot10^{-5}$	162.0±8.5
	Cs_2CO_3:Li_2CO_3:H_3BO_3:NaF (1:1:12:0.5)	–9.22±0.73	$9.9\cdot10^{-5}$	147.9±6.9
	Cs_2CO_3:Li_2CO_3:H_3BO_3:NaF (1:1:12:0.67)	–9.69±0.84	$6.2\cdot10^{-5}$	151.5±7.9
	Cs_2CO_3:Li_2CO_3:H_3BO_3:NaF (1:1:12:2)	–9.07±0.47	$1.2\cdot10^{-4}$	138.3±4.4
$KLu(WO_4)_2$	$KLu(WO_4)_2$:$K_2W_2O_7$ (12:88)	0.68±0.38	1.96	28.0±4.0

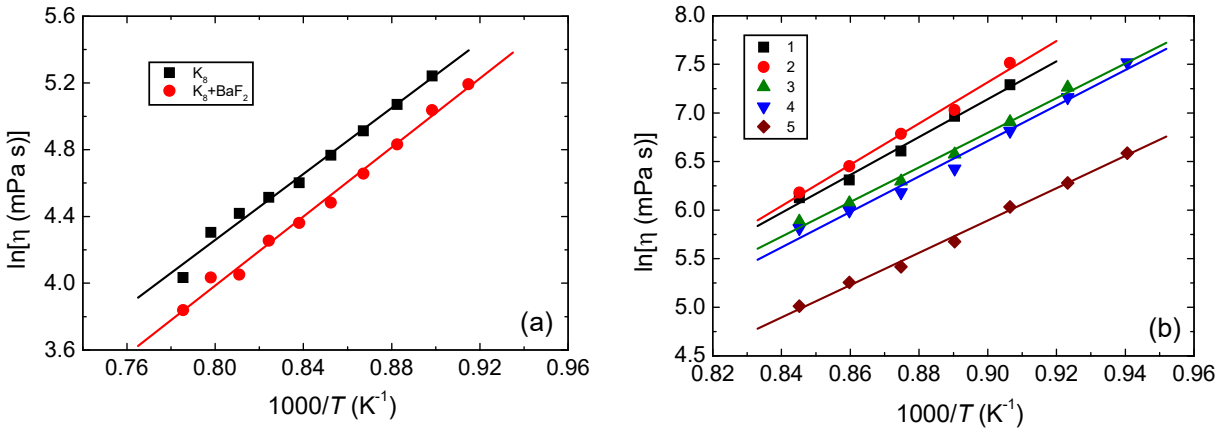


Figure 11. Plots of $\ln\eta$ on $1/T$ according to Eq. (16) for the data of viscosity η of two different solutions of (a) KTP in K_8 and K_8–BaF_2 solvents and (b) $CsLiB_6O_{11}$ (CLBO): (1) Cs_2CO_3:Li_2CO_3:H_3BO_3 = 1:1:12, (2) Cs_2CO_3:Li_2CO_3:H_3BO_3 = 1:1:11, (3) Cs_2CO_3:Li_2CO_3:H_3BO_3:NaF = 1:1:12:0.5, (4) Cs_2CO_3:Li_2CO_3:H_3BO_3:NaF = 1:1:12:0.667, and (5) Cs_2CO_3:Li_2CO_3:H_3BO_3:NaF = 1:1:12:2. Original data from: (a) [70] and (b) [88].

Figure 12 shows the dependence of solubility c of KTP in KTP–$K_8P_6O_{19}$ and KTP–$K_8P_6O_{19}$–BaF_2 solutions on temperature. In the study, the solubility of the solute KTP was determined from its known weights dissolved in the solution at different temperatures by using the traditional method of introducing trial seeds and changing the solution temperature. The saturation temperature of the solution was identified when the seed size remained unchanged. In the figure, open and filled squares represent solubility data from two different studies and are somewhat different from each other. They are represented by a single curve drawn for the data shown by open squares. The other two curves are for KTP solubility in solutions prepared from solid-reacted and solution-reacted materials. Solid-reacted solutions were prepared by homogenizing KTP solute with K_8 or K_8–BaF_2 solvents in weight ratio between 0.27 and 0.42 (filled squares and circles) and between 0.30 and 0.42 (open squares) at a temperature of about 50 °C above the saturation temperature for 24 h [70,88]. However, solution-reacted materials were prepared by reacting a solution of tetrabutyl titanate dissolved in ethanol with appropriate amounts of KH_2PO_4 and K_2CO_3 dissolved in water, which gave a white precipitate [88]. The excess amount of water was evaporated by heating the precipitate and finally the material was dried at 50 °C for 24 h and grinded into powder in an agate mortar (filled diamonds).

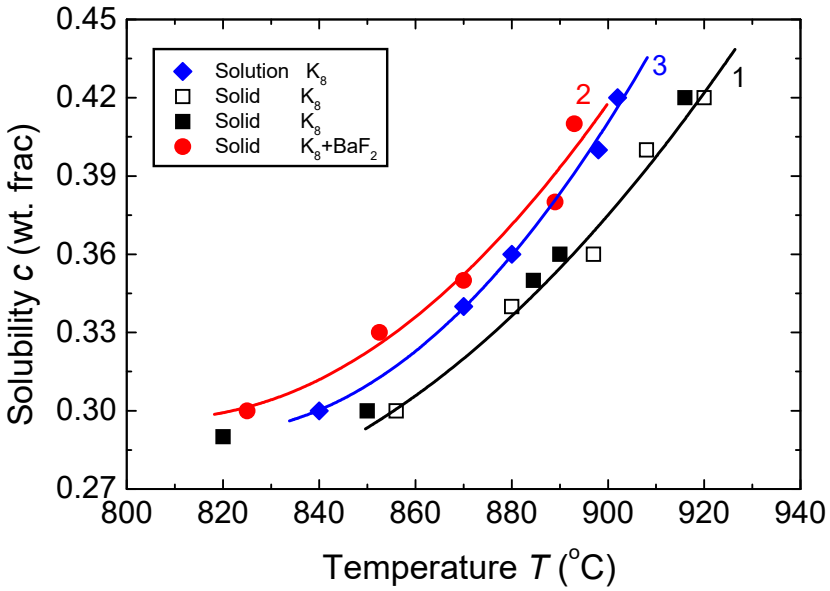


Figure 12. Temperature dependence of solubility c of KTP in (1,3) KTP–$K_8P_6O_{19}$, and (2) KTP–$K_8P_6O_{19}$–BaF_2 solutions. Curves (1,2) and (3) are for KTP solubility in solutions prepared from solid-reacted and solution-reacted materials, respectively. Data represented by filled squares and circles are from ref. [70], whereas those shown by filled diamonds and open squares are from ref. [88].

From Figure 12 one notes differences in the solubility c of KTP obtained not only from solid- and solution-reacted materials (compare data of filled diamonds with those of open and filled squares) but also from two different solid-reacted solutions (compare open and filled squares). Moreover, the solubility of KTP is increased by BaF_2 additive (compare data of filled and open squares with those of filled circles). It may be seen that the solubility of KTP in solution-reacted materials is higher than that in the solid-reacted materials, whereas it is somewhat different in the two different solid-reacted materials. The former observation is due to small amounts of TiO_2 insoluble in high temperature solutions [88], whereas the latter observation is associated with the difference in the initial composition of the solutions. BaF_2 additive increases the solubility of KTP at all temperatures. Using relation (5) these solubility differences can be analyzed from the plots of ln$c$ against $1/T$, as shown in Figure 13. The values of the preexponential factor A and the enthalpy of dissolution ΔH_s obtained from the plots are given in Table 3. Obviously, the differences in the solubility for the three systems are reflected by the values of A and ΔH_s. Since for ideal solutions $A = \Delta H_s / R_G T_m$, from the values of A and ΔH_s listed in Table 3 one finds $T_m \approx$ 700 K. Since this temperature is much lower than the saturation temperature T_s for the above systems, one may conclude that high-temperature solutions are regular.

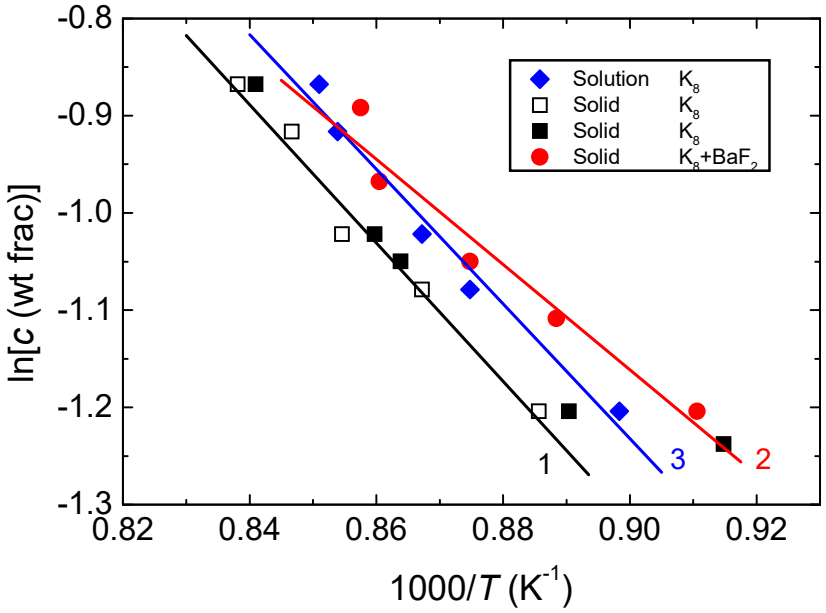


Figure 13. Plots of ln*c* against 1/*T* for KTP in different solvents according to Eq. (5). Data from Figure 12.

Table 3. Parameters *A* and ΔH_s for solubility of KTP prepared from solution and solid in K_8 and K_8+BaF_2 solvents

Solute origin	Solvent	*A*	ΔH_s (kJ mol^{-1})	T_m (K)
Solution	K_8	5.0±0.54	57.6±5.1	722±78
Solid	K_8	5.09±0.49	59.1±4.8	715±68
--	K_8+BaF_2	3.71±0.63	45.0±5.9	685±116

Dependence of the solubility of a solute on the composition of flux is intimately connected with the complexing properties of solute and solvent molecules/atoms. In the case of temperature dependence of solubility of a solute in different solvents the solubility difference is reflected by the enthalpy of dissolution ΔH_s. For example, the increase in the solubility of KTP due to the addition of BaF_2 to K_8 solvent leads to a decrease in ΔH_s. The relationship between ΔH_s and solvent composition is associated with solute–solvent interactions. The increase in the solubility of a solute with an increase in one of the components of high-temperature solvents is also associated with these solute–solvent interactions.

2.4. Crystal Growth Techniques

Depending on the method of achieving supersaturation in the solution, the techniques of growing crystals from high-temperature solutions may be grouped into three types. These are temperature reduction (i.e. slow cooling of the solution), solvent evaporation, and temperature gradient methods. In these methods the driving force (i.e. supersaturation) for growth is ensured by the values of the cooling rate of the solvent, the solvent evaporation rate, and the temperature

difference between saturated and growth zones, respectively. In the slow cooling method the cooling rate is typically around 1 $K \cdot h^{-1}$.

Crystal growth in high-temperature solutions may be carried out on spontaneously nucleated seeds as well as on seeds grown and prepared independently. Growth involving spontaneously nucleated seeds is usually carried out in slow cooling and solvent evaporation methods, but the crystals obtained by these methods are relatively small. These small crystals developed on self-nucleated seeds are subsequently used as seeds to grow large samples by temperature gradient methods.

2.4.1. Slow Cooling Method

Crystal growth by slow cooling is commonly used for producing small specimens. The method has the advantage that the apparatus is simple (a furnace, a crucible, and a temperature programmer) and a growth run requires poor attention after the beginning of the growth process. Conventional horizontal muffle furnaces and small crucibles are usually sufficient for crystal growth by this method.

The main difficulties of growth by slow cooling are that the flux introduces strain in the crystals due to its different thermal expansion coefficient than that of the crystal, and the high nucleation density results in small size of crystals. The former difficulty is overcome by draining away the flux before starting fast cooling. The latter difficulty may be solved by using small temperature oscillations at the nucleation stage or by initiating nucleation in a small region by localized cooling by blowing a stream of cold air (cold finger technique).

A silicon carbide heating element furnace, with a recrystallized alumina tube lining, in a vertical configuration ensures the growth of large single crystals of high melting-point materials [89]. The main components of this growth arrangement are: silicon carbide heating element, crucible support, and double crucible system. For the growth of crystals of relatively low melting-point materials, kanthal-wire bound furnace operating up to about 1200 ºC can be used instead of silicon carbide heating element.

The furnace arrangement enables to grow crystals of different materials and composition by changing the muffle and crucible support. The double crucible system involves an inner, smaller crucible containing crystal growing mixture and a bigger crucible placed inverted over the smaller one. After the completion of growth when this system is inverted, the solution left over in the inner crucible is drained out into the outer bigger crucible and the cooling program is commenced to cool the crucible to room temperature. This procedure enables to obtain big crystals free of flux adhering to them.

It should be mentioned that horizontal muffle furnaces have traditionally been used for the growth of different materials by the slow cooling method. After the completion of a growth run, the grown crystals are extracted from the unused flux by dissolving in water or in some acid or alkali.

2.4.2. Solvent Evaporation Method

Solvent evaporation method is usually used to grow single crystals of substances that are stable over a narrow temperature range. A simple horizontal muffle furnace to maintain a constant temperature and a crucible containing the chemicals are sufficient for crystal growth experiments. Unlike in the case of slow cooling method, even a temperature programmer is not required because growth occurs at a constant temperature. Since growth occurs at a constant temperature, the concentration of equilibrium defects and the incorporation of solvent ions as impurities remains constant in a growing crystal. The main problem is of control of the rate of evaporation of the solvent (and hence the growth rate), and the poisonous and/or corrosive nature of the solvent vapor released when an open growth system without provision of collection of solvent vapor is used.

The above problem is overcome in closed systems (Figure 14) in which the evaporation rate is controlled by varying the temperature T_2 at which solvent condensation takes place. In these closed systems a crystal is made to grow in the lower part of the crucible where the temperature $T_1 < T_2$. Consequently, mass transport to the growing crucible is possible mainly by solutal convection. Therefore, growth is solutal diffusion controlled unless stirring is applied. For closed systems this can be achieved by the accelerated crucible rotation technique (ACRT). In this arrangement the evaporation rate is determined by the dimensions r_1 and r_2 and by the temperatures T_1 and T_2.

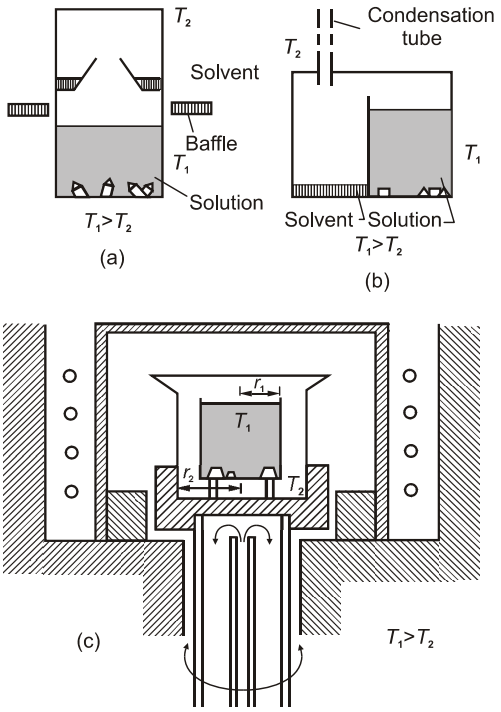


Figure 14. Arrangement for growth by flux evaporation: (a) system with collection of condensed solvent, (b) condensation of solvent in a tube, and (c) flux evaporation–condensation system with ACRT stirring. From Elwell and Scheel [64], reproduced with permission of Elsevier.

2.4.3. Temperature Gradient Methods

In the temperature gradient methods, nutrient (solute) is held at a temperature T_1 whereas a growing crystal is held at a temperature T_2 such that $T_1 > T_2$. Due to the temperature difference the solution is supersaturated and growth takes place on self-nucleated seeds or on an appropriately mounted seed surface in the supersaturated solution. Solute transport to the seed is ensured by natural or forced convection. Depending on the direction of the temperature gradient, crystal growth may be carried out either at the bottom of the crucible/ampoule or in the top part of the solution.

In the temperature gradient methods, introduction of the seed in the top part of the solution is popular. This method is known as the top-seeded solution growth (TSSG) method. An example of the apparatus used for such a growth is presented schematically in Figure 15 [90]. It consists of a vertical muffle furnace heated by a resistance heater, a platinum crucible and a seed rotating system. The platinum crucible is placed on an alumina support and the furnace top is covered by an alumina lid with observation holes. Instead of large alumina support (10), crucible support bases on a long rods passing through the furnace bottom have also been proposed [79,84].

In some cases the mounted seed has also be allowed to grow in the interior of the solution instead of keeping it in the top layer. This type of growth technique has been called the dipping solution technique [91]. The high growth yield in this arrangement of the seed in the solution is due to the a high temperature gradient in the lower part of the solution.

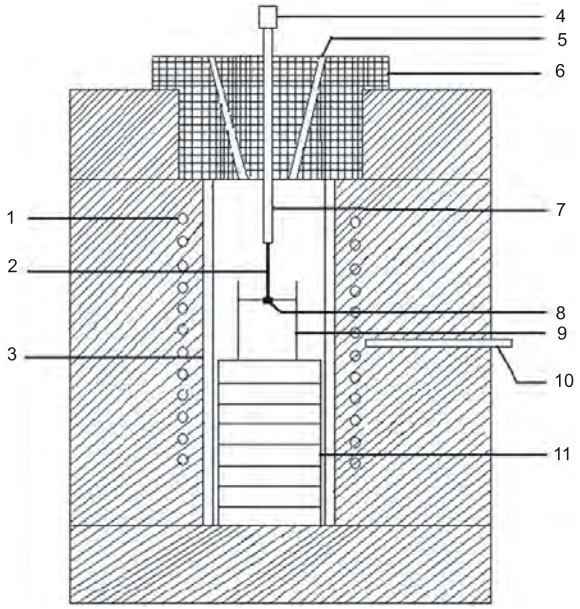


Figure 15. Schematic diagram of apparatus used for top-seeded solution growth: (1) resistance heater, (2) platinum rod, (3) alumina tube, (4) seed rotator, (5) observation hole, (6) alumina lid, (7) seed holding rod, (8) mounted seed, (9) platinum crucible, and (10) alumina support. From [90], reproduced with permission of Elsevier.

2.4.4. Other Methods

Among the other methods of crystal growth from high-temperature solutions are electrocrystallization and micropulling-down method. The principle of electrolytic crystallization from high-temperature solutions is essentially the same as used in conventional electrocrystallization from low-temperature solutions. The most difficult step is the selection of a solvent for growth. However, once a solution composition is known, crystallization can be carried out at constant current, constant potential difference between cathod and anode, or at a constant overpotential. Materials as diverse as bronzes, elemental and compound semiconductors, high T_c oxide superconductors, borides, CeS, ThS, MoS_2, Mo_2C, and lanthanum manganates have been grown by this method. However, the method has been poorly explored. For further details the reader is referred to the literature [69,92-98].

Micropulling-down method from molten solutions has been proposed for the growth of high-quality fiber crystals [73,99]. The principle of the method is similar to crystal pulling. Crystalline fibre of the desired material nucleated at the tip of a platinum pipe is pulled down from the central part of the bottom of a crucible containing molten solution of appropriate composition. Growth of $KNbO_3$ fibre crystals has been reported by this method.

2.5. Growth Instability and Facet Formation

It is usually observed that crystals grown by top-seeded solution growth show tendency to develop faceting at the crystal–liquid interface. The faceting planes are usually the slowest growing, low-index planes. Faceting leads to deterioratation of the quality of the growing crystal as a result of trapping of inclusions of solution and bubbles and release of internal stresses related to facet formation. Therefore, knowledge of optimum experimental parameters ensuring facet-free growth from high-temperature solution is useful.

An interesting study devoted to origin of facet formation was recently carried out by Szaller et al. [100], who grew stoichiometric lithium niobate (sLN) along the *z*-direction from 12.3 mol% K_2O and $Li_2O/Nb_2O_5 = 1$ in the starting liquid. Growth was carried out with pulling rate 0.2 mm/h and constant rotation rate in the range 8–28 rpm as well as gradually decreasing rotation rate starting from 30–45 rpm at the shoulder down to 26 rpm at the end. In the experiments cone angle of 120 and 75º maintained the crystal-to-crucible diameter ratio about 1:2 at the cylindrical part, whereas height-to-diameter of the crucible was 40/50 mm. Evolution of crystal quality was studied on the (0001) slices cut perpendicular to the growth direction.

The above study showed that the degree of structural perfection in the crystals is strongly affected by the necking process and that growth ridges on the shoulder surface and facets on the growth front are the main sources of crystal defects. After the introducion of seed, crystal grows with conically increasing diameter on a strongly convex growth front until the desired diameter is attained. Increase in the crystal diameter and ridge formation depend on the cone angle, whereas stresses associated with large ridges favor both cracking and mechanical twinning of the as-grown crystal during its final cooling down.

It was found [100] that growth of high-quality, facet-free stoichiometric lithium niobate crystals was possible by applying gradually variable rotation rate. Optimal conditions for the growth of good-quality crystals was achieved for $Gr/Re^2 > 1$, where the dimensionless Grashof number $Gr = g\beta\Delta TR^3/\nu^2$ is characteristic for buoyancy and the Reynolds number $Re = \omega r^2/\nu$ is characteristic for forced convection. In these relations, R is the crucible radius, r is the crystal radius, β is the volume expansion coefficient of the crystal, g is the acceleration due to gravity, ΔT is the radial temperature difference at the melt surface, ν is the kinematic viscosity of the melt, and ω is the crystal rotation speed.

Summary and Outlook

Studies of the processes of crystalization from solutions started in the nineteen sixties, with simultaneous rapid development in the techniques of growing single crystals due the increasing demand of materials for technological applications. Growth of single crystals and their characterization towards device fabrication have also undergone great impetus due to the importance of crystals for both academic as well as applied research. Knowledge of regularities in the processes of crystallization from solutions helps us in understanding and explaining biocrystallization processes which find wide application in medicine. Moreover, growth of crystals from solutions is the only method for the crystallization of substances which undegro decomposition before melting. A short overview of the fundamentals aspects of the crystals growth from low- and high-temperature solutions, including key techniques, is presented in this chapter.

Acknowledgement

The authors express their gratitude to Dr K. Wójcik for prepaing several figures presented in this contribution.

References

[1] K. Sangwal, In: Encyclopedia of Materials Science: Science and Technology, Elsevier, Amsterdam (2001), p. 3670.
[2] H.E. Buckley, Crystal Growth, Wiley, New York (1951).
[3] J.C. Brice, The Crystal Growth from Liquids, North-Holland, Amsterdam (1973).
[4] T.G. Petrov, E.B. Treivus, Yu.O. Punin, A. P. Kasatkin, Vyrashchivanie Kristallov iz Rastvorov [Crystal Growth from Solutions], Nedra, Leningrad, Russia (1983).
[5] A.A. Chernov, Modem crystallography III, Crystal growth, Springer-Verlag, Berlin (1984).
[6] K.-Th. Wilke, J. Bohm, Kristallzüchtung. VEB Deutscher Verlag der Wissenschaften, Berlin (1988).
[7] H.K. Henisch, Crystals in gels and liesegang rings, Cambridge University Press, Cambridge (1988).
[8] R. Rodriguez-Clemente, S. Veintemillas-Verdaguer, F. Rull-Perez, K. Sangwal, Prog. Cryst. Growth Charact. 17 (1988) 1-40.
[9] K. Sangwal, T. Sokołowski, B. Wiktorowska, In: K.Sangwal (Ed.), Elementary Crystal Growth, Saan Publishers, Lublin (1994), chap. 8, p. 255.

[10] J. Nývlt, O. Söhnel, M. Matuchova, M. Broul, The Kinetics of Industrial Crystallization. Academia, Prague (1985).
[11] K. Sangwal, CrystEngComm. 13 (2011) 489.
[12] K. Sangwal, Cryst. Res. Technol. 44 (2009) 231.
[13] K. Sangwal, Cryst. Growth Des. 9 (2009) 942.
[14] K. Sangwal, J. Cryst. Growth 318 (2011) 103.
[15] K. Sangwal, J. Cryst. Growth 312 (2010) 3316.
[16] K. Sangwal, E. Mielniczek-Brzóska, S. Barylska, Chem. Eng. Res. Des, (2014) http://dx.doi.org/10.1016/j.cherd.2013.08.031.
[17] J.W. Mullin, Crystallization. 4th Ed., Butterworth-Heinemann, Oxford (2001), chap. 5, pp. 181-215.
[18] A. Yokotani, H. Koide, K. Yomanuro, T. Sasaki, T. Yamanaka, C. Yamanaka, Rev. Laser. Eng. 11 (1983) 162.
[19] T. Sasaki, A. Yokotani, J. Cryst. Growth 99 (1990) 820.
[20] N.P. Zaitseva, L.N. Rashkovich, S.V. Bogatyreva, J. Cryst. Growth 148 (1995) 276.
[21] N.P. Zaitseva, J.J. DeYoreo, M.R. Dehaven, R.L. Vital, K.E. Montgomery, M. Richardson, L.J. Atherton, J. Cryst. Growth 180 (1997) 255.
[22] K. Sankaranarayanan, P. Ramasamy, J. Cryst. Growth 280 (2005) 467.
[23] H.A. Mohameed, J. Ulrich, Cryst. Res. Technol. 31 (1996) 27.
[24] S.K. Sharma, S. Verma, B.B. Shrivastava, V.K. Wadhawan, J. Cryst. Growth 244 (2002) 342.
[25] 26] L.N. Rashkovich, A.A. Mkrtchyan, A.A. Chernov, Sov. Phys. Crystallogr. 30 (1985) 219.
[26] K. Maiwa, K. Tsukamoto, I. Sunagawa, J. Crystal Growth 102 (1990) 43.
[27] P.G. Vekilov, Yu.G. Kuznetsov, A.A. Chernov, J. Crystal Growth 121 (1992) 643.
[28] W.K. Burton, N. Cabrera, F.C. Frank, Phil. Trans. Roy. Soc. London A 243 (1951) 299.
[29] A.A. Chernov, Sov. Phys. Uspekhi 4 (1961) 116.
[30] J.J. De Yoreo, T.A. Land, L.N. Rashkovich, T.A. Onischenko, J.D. Lee, O.V. Monovskii, .P. Zaitseva, J. Cryst. Growth 182 (1997) 442.
[31] K. Sangwal, Additives and Crystallization Processes: From Fundamentals to Applications, Wiley, Chichester (2007).
[32] V.I. Bredikhin, V.I. Ershov, V.V. Korolikhin, V.N. Lizyakina, S.Yu. Potapenko, N.V. Khlyunev, J. Cryst. Growth 84 (1987) 509.
[33] L.N. Rashkovich, N.V. Kronsky, J. Cryst. Growth 182 (1997) 434.
[34] K. Sangwal, J. Cryst. Growth 242 (2002) 215.
[35] N. Kubota, M. Yokota, J.W. Mullin, J. Cryst. Growth 212 (2000) 480.
[36] K. Sangwal, E.Mielniczek-Brzóska, J. Cryst. Growth 242 (2002) 421.
[37] K. Sangwal, Cryst. Res. Technol., 40 (2005) 635.
[38] F.C. Frank, In: R.H. Doremus, B.W. Roberts, D. Turnbull (Eds.), Growth and Perfection of Crystals, Wiley, New York (1958), p. 411.
[39] N. Cabrera, D.A. Vermilyea, In: R.H. Doremus, B.W. Roberts, D. Turnbull (Eds.), Growth and Perfection of Crystals, Wiley, New York (1958) p. 393.
[40] P. van der Putte, W.J.P. van Enckevort,; L.J. Giling, J. Bloem, J. Cryst. Growth 43 (1978) 659.
[41] T.A. Land, T.L. Martin, S. Potapenko, G.T. Palmore, J.J. DeYoreo, Nature 399 (1999) 442.
[42] M.L. Weaver, S. R. Qiu, J.R. Hoyer, W.H. Casey, G.H. Nancollas, J.J. DeYoreo, ChemPhysChem 7 (2006) 2081.

[43] E. Mielniczek-Brzóska, K.Giełzak-Koćwin, K. Sangwal, J. Cryst. Growth 212 (2000) 532.
[44] K. Sangwal, E. Mielniczek-Brzóska, Cryst. Res. Technol. 36(2001) 837.
[45] K. Sangwal, E. Mielniczek-Brzóska, J. Crystal Growth 233 (2001) 43.
[46] K. Sangwal, E. Mielniczek-Brzóska, J. Borc, Cryst. Res. Technol. 38 (2003) 103.
[47] E. Mielniczek-Brzóska, K. Sangwal, Cryst. Res. Technol. 11 (2004) 993.
[48] R.Kern, In: N.N. Sheftal (Ed.), Rost Kristallov (Growth of Crystals), vol. 8, Nauka, Moscow (1967), p. 5.
[49] [R.J. Davey, In: E.J. de Jong and S.J. Jancic (Eds), Industrial Crystallization, North-Holland, New York (1979).
[50] G.M. Bliznakov, E.K. Kirkova, Z. Phys. Chem. 206 (1957) 271.
[51] S.A. De Vries, P. Goedtkindt, S.L. Bennett, W.J. Huisman, M.J. Zwanenburg, D.-M. Smilgies, J.J. DeYoreo, W.J.P. Van Enckevort, P. Bennema, E. Vlieg, Phys. Rev. Lett. 80 (1998) 2229.
[52] Y. Enqvist, J. Partanen, M. Louhi-Kultanen, J. Kallas, Trans IChemE 81 (2003) 1354.
[53] R. Kern, R. Dassonville, J. Cryst. Growth, 116 (1992), 191.
[54] W.J. Kim, S.D. Kim, H.S. Jung, D.T. Hayhurst, MicroporMesopor Mater. 56 (2002) 89.
[55] V. Kuznetsov, T. Okhrimenko, M. Rak, J. Cryst. Growth 193 (1998) 164.
[56] K. Srinivasan, K.Meera, P. Ramasamy, J. Cryst. Growth 205 (1999) 457.
[57] O. Gliko, N. Zaitseva, L.N. Rashkovich, Res. Soc. Symp. Proc. 620 (2001) M9.9.1.
[58] V.V. Voronkov, L.N. Rashkovich, J. Cryst. Growth 144 (1994) 107.
[59] M. Moret, Mater. Chem. Phys. 66 (2000) 177.
[60] E.B. Rudneva, V.L. Manomenova, A. É. Voloshin, A.A. Kaminskiĭ, A.B. Vasil'ev, B.V. Mchedlishvili, Crystallogr. Rep. 51 (2006) 142.
[61] I. Pritula, V. Gayvoronsky, M. Kolybaeva, V. Puzikov, M. Brodyn, V. Tkachenko, A. Kosinova, M. Kopylovsky, V. Tsurikov, O. Bezkrovnaya, Opt. Mater. 33 (2011) 623.
[62] I.M. Pritula, A.V. Kosinova, D.A. Vorontsov, M.I. Kolybaeva, O.N. Bezkrovnaya, V.F. Tkachenko,; O.M. Vovk, E.V. Grishina, J. Cryst. Growth 355 (2012) 26.
[63] A.Bensouici, J.L. Plaza, O. Halimi, B. Boudine, M.Sebais, E. Dieguez, J. Optoelectron. Adv. Mater. 10 (2008) 3051.
[64] D. Elwell, H.J. Scheel, Crystal Growth from High-Temperature Solutions, Academic Press, London (1975).
[65] V.A. Timofeeva, Rost Kristallov iz Raztvorov-Razplavov (Crystal Growth from the Flux). Nauka, Moscow (1978).
[66] B.M. Wanklyn, In: Pamplin BR (Ed.) Crystal Growth, Pergamon, Oxford (1975), p. 217.
[67] P. Görnert, F. Voigt, In: Kaldis E (Ed.). Current Topics in Materials Science, Vol. 11, North-Holland, Amsterdam (1984), p. 1.
[68] H.A. Dąbkowska, In: Sangwal K (Ed.), Elementary Crystal Growth. Saan, Lublin, Poland (1994), chap. 9, p. 303.
[69] C.-K. Chen, Prog. Cryst. Growth Charact. Mater., 36 (1998) 1.
[70] J. Hu, Z.-G. Hu, J. Cryst. Growth 311 (2009) 4235.
[71] V.I. Ivanenko, I.V. Zatovsky, N.S. Slobodyanik, P.G. Nadgornyi, N.V. Baumer, Cryst. Res. Technol. 43 (2008) 355.
[72] K. Watanabe, Cryst. Res. Technol. 34 (1999) 47.
[73] V.I. Chani, K. Shimamura, T. Fukuda, Cryst. Res. Technol. 34 (1999) 519.
[74] D.D. Khalyavin, S.V. Shiryaev, G.L. Bychkov, S.N. Barilo, S.N. Istinovich, H. Szymczak, R. Szymczak, P. Allenspach, Cryst. Res. Technol. 38 (2003) 748.

[75] D.L. Sun, Y. Hang, L.H. Zhang, G.Z. Luo, S.N. Zhu, P.K. Lim, W.W. Hung, Cryst. Res. Technol. 39 (2004), 511.
[76] H. Udono, K. Matsumura, I.J. Osugi, I. Kikuma, J. Cryst. Growth 275 (2005) e1967.
[77] A. Dąbkowski, H.A. Dąbkowska, J.E. Greedan, W. Ren, B.K. Mukherjee, J. Cryst. Growth 265 (2004) 2004.
[78] T. Ujihara, K. Seki, R. Tanaka, S. Kozawa, Alexander, K. Morimoto, K. Sasaki, Y. Takeda, J. Cryst. Growth 318 (2011) 389.
[79] T. Yue, Z. Hu, C.Chen, J. Cryst. Growth 310 (2008) 1264.
[80] H.D. Xie, D.Z. Shen, C.Z. Xie, X.Q. Wang, G.Q. Shen, Cryst. Res. Technol. 41 (2006) 961.
[81] C.T. Lin, B. Liang, H.C. Chen, J. Cryst. Growth 237 (2002) 778.
[82] F. Jing, Y. Wu, P. Fu, J. Cryst. Growth 292 (2006) 454.
[83] R. Sun, X. Li, Q. Zhang, B. Fang, H. Zhang, D. Lin, S. Wang, X. Zhao, H. Luo, J. Cryst. Growth 341 (2012) 34.
[84] X. Yu, Z.-G. Hu, J. Cryst. Growth 312 (2010) 2415.
[85] B.Wanklyn, J. Cryst. Growth 65 (1983) 533.
[86] P. Görnert, E. Sinn, In: E. Kaldis (Ed.). Crystal Growth of Electronic Materials, Elsevier, Amsterdam (1985), p. 23.
[87] E. Sinn, D. Linzen, K. Fischer, Cryst. Res. Technol. 20 (1985) 965.
[88] Y. Lu, W. Jie, T. Wang, X. Zheng, Y. Xu, L. Luan, J. Cryst. Growth 355 (2012) 33.
[89] S.M. Rao, M.K. Wu, J.K. Srivastava, B.H. Monk, N.Y. Yen, H.Y. Lin, H.Y. Tang, M.C. Ling, H.L. Liu, Cryst. Res. Technol. 41 (2006) 859.
[90] X. Yu, Y. Yue, J. Yao, Z.-G. Hu, J. Cryst. Growth 312 (2010) 3029.
[91] T. Ujihara, R. Maekawa, R. Tanaka, K. Sasaki, K. Kuroda, Y. Taeda, J. Cryst. Growth 310 (2008) 1438.
[92] D. Elwell, In: E. Kaldis, H.J. Scheel (Eds.). Current Topics in Materials Science, Vol. 2, Elsevier, Amsterdam (1977), p. 605.
[93] D. Elwell, J. Cryst. Growth 52 (1981) 741.
[94] R.S. Feigelson, Adv. Chem. 186 (1980) 243.
[95] D. Elwell, R.S. Feigelson, Solar Ener. Mater. 6 (1982) 123.
[96] D. Elwell, G.M. Rao, J. Appl. Electrochem. 18 (1988) 15.
[97] W.H. McCarroll, K.V. Ramanujachary, M. Greenblatt, F. Cosandey, J. Solid State Chem. 136 (1998) 322.
[98] W.H. McCarroll, I.D. Fewcett, M. Greenblatt, K.V. Ramanujachary, J. Solid State Chem. 146 (1999) 88.
[99] D.H. Yoon, I. Yonenaga, T. Fukuda, N. Ohnishi, J. Cryst. Growth 142 (1994) 339.
[100] Zs. Szaller, A. Peter, K. Polgar, Gy. Szabo, J. Cryst. Growth 360 (2012) 181.

Reprinted with permission from (Crystal Growth and Design, 2007, Vol. 2796–2810. Copyright 2007 American Chemical Society.

CRYSTAL GROWTH & DESIGN
2007
VOL. 7, NO. 12
2796–2810

Reviews

What Determines the Rate of Growth of Crystals from Solution?

Peter G. Vekilov

Department of Chemical and Biomolecular Engineering, and Department of Chemistry, University of Houston, Houston, Texas 77204-4004

Received May 8, 2007; Revised Manuscript Received August 27, 2007

ABSTRACT: Crystallization from solution underlies numerous laboratory, industrial, geological, and biological processes. The interface between a crystal and the solution is smooth and comprised of singular crystal faces. On such smooth interfaces, the locations at which a molecule from the solution can associate to the crystal, the kinks, are few and located along the edges of unfinished crystalline layers, the steps. The rate of step propagation, and through it, the rate of growth of a crystal from solution, is determined by the kink density and by the kinetics of incorporation into the kinks. In turn, the latter depends on the free energy barriers for incorporation. Here, three mechanisms of generation of kinks are discussed: by thermal fluctuations of the steps, by one-dimensional nucleation of new crystalline rows, and by association to the steps of two-dimensional clusters, preformed on the terraces between the steps. The latter two mechanisms only operate in the cases where the kink density, determined by the thermal fluctuations, is low. The rate of incorporation into kinks follows Kramers-type kinetics, in which the transition over the free energy barrier is governed by diffusion in the solution, in contrast to the Eyring-type transition state, which decays due to the vibrations of the activated complex. Finally, the barrier is not due to stretched bonds between the incoming molecules and the kink but rather corresponds to the destruction of the shell of structured water around both the kink and the incoming molecule. The latter two insights allow rationalization of the effects of additives on crystallization kinetics, especially those employed in biological regulation in living organisms.

Introduction

Crystallization from solution underlies a large variety of technological and laboratory procedures, and physiological and pathophysiological processes. Single solution-grown crystals of inorganic salts or mixed organic–inorganic materials are used in nonlinear optics elements[1] and for other electronic and optical–electronic applications, chemical products and production intermediates are precipitated as crystals in thousands-of-tons amounts, and organic and protein pharmaceuticals are prepared in crystalline form to ensure slower and sustained rates of release upon administering into the patient,[2] etc. Insulin crystals form in the β-cells in mammalian pancreases and serve as storage for this hormone.[3,4] Crystals of a mutant hemoglobin, C, form in the erythrocytes of patients with an inherited disorder and cause hemolytic anemia.[5–8] Molecular-level understanding of the crystallization processes provides the capability to quantitatively model the respective crystallization processes, to prevent or control them, and to direct them toward desired outcomes in terms of crystal size, crystal quality, size uniformity between numerous crystals growing in the same environment, etc.

The elementary act of growth of a crystal is the attachment of building blocks: atoms, molecules, assemblies, or particles, from the growth medium: vapor, melt, solution, gel, plasma, or other. This attachment occurs at sites called kinks, in which an incoming building block, which we will call "molecule" from here on, has half of the number of neighbors that it would have in the crystal bulk[9,10] (Figure 1). The kinks were defined as special sites for growth because of two specificities of attachment there: the kinks are retained after the attachment, and the attachment does not alter the surface free energy of the crystal.[10] The rate constant of growth of a crystal is determined by two factors: the density of kinks on the interface with the growth medium, and the barriers, both entropic and enthalpic, for incorporation of a molecule into a kink.

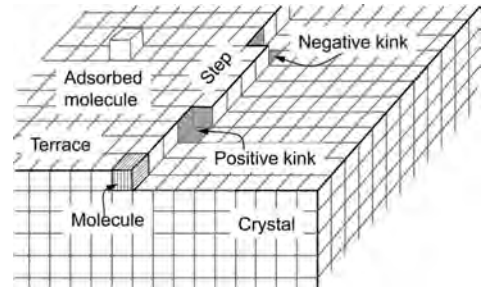


Figure 1. Schematic illustration of the structure of the surface of a faceted crystal.

10.1021/cg070427i CCC: $37.00 © 2007 American Chemical Society
Published on Web 12/05/2007

Crystals growing from solution typically exhibit smooth interfaces because, roughly, of high surface free energy between the crystal and the growth medium. The correlation between the surface free energy and the step roughness can be established in two steps: First, the Jackson[11] and Temkin[12] criteria link the step roughness with the latent heat of crystallization so that high latent heat leads to smooth interfaces. Second, a correlation by Nielsen and Söhnel[13] demonstrates that high latent heat of crystallization corresponds to high surface free energy. At the solution crystal interface, high surface free energy is partially due to the dramatically different density of the two phases, which leads to significant surface enthalpy. The surface entropy is also significant: it is due to the large difference in rotational and translational degrees of freedom between the solution and the crystal.[14] On smooth interfaces, the kinks are located along the edges of the unfinished crystal layers and the generation of kinks is a major rate-determining step of the mechanism of crystal growth. The presence of solvent leads to significant barriers for incorporation of the solute molecules into the kinks. Thus, if one strives toward understanding of the elementary act of crystallization from solution at the molecular level, one should understand both kink generation and the nature of the incorporation barriers.

Below, we discuss mechanisms of kink generation during growth of crystals from solution, the mechanisms of incorporation of molecules into the kinks, and the nature of the free energy barrier for this incorporation. We deliberately avoid several very significant features of the mechanism or crystallization from solution. We do not discuss the mechanisms of layer generation and only briefly summarize them at the start. We do not discuss the pathway by which molecules reach the kinks: directly from the solution, or after adsorption on the terraces and surface diffusion toward the steps. The latter issue has been the subject of significant controversy: it was initially assumed that direct incorporation was favored in solution growth;[15–19] however, further investigations revealed for all tested cases that the "surface diffusion" mechanism[20–22] operated.[23–30] We do not discuss step–step interactions or impurity effects on step kinetics;[31–33] experiential evidence for these at the molecular level has been reviewed elsewhere.[34–40] We do not discuss complex kinks consisting of chemically or symmetrically different molecules.[41–43] We do not discuss instabilities of step motion and step configuration[44,45] and the effects that they may have on the overall kinetics.[46–50]

The objectives of the review limit the considerations to molecular-level experimental data. Of all solution growth systems, the most abundant set of molecular-level data is available for proteins and is obtained by in-situ monitoring of the crystallization processes by atomic force microscopy (AFM);[34–36,38,51–62] results at the mesoscopic lengthscales, dealing with step generation and motion for protein and inorganic crystals and obtained by a variety of techniques,[24,63–71] are not considered here.

Proteins are particularly attractive for studies of fundamental crystal growth mechanisms. This is because the size of the protein molecules (a few nanometers) and the time-scales for growth (up to a few seconds between sequential discrete growth events) are within the reach of the current advanced experimental techniques. On the other hand, the molecular masses typical of most protein molecules still leave the thermal equilibration times relatively short. Thus, conclusions drawn from studies of protein model systems may still be meaningful for small molecule crystallization. In this regard, proteins could be a better model than, for instance, colloid crystals.[72,73] To ensure that the conclusions drawn from experimental results obtained with proteins are relevant to the numerous nonprotein crystals grown from solution, these experimental observations are placed in their respective theoretical context. In several cases, the specificity or generality of concrete results is addressed in the text.

Relationships between Growth Rate, Kink Density, and Molecular Flux into Kinks

The smooth interfaces between crystals and solution are usually crystal planes with a high density of molecules, designated with low Miller indexes. Faceted crystals in contact with solution typically follow the layer growth mode. In this mode, a new layer, typically one lattice spacing high, is deposited on the smooth surface of the previous lattice layer (Figure 1). The edges of the incomplete layers are called steps. The flat terraces between the steps are singular crystal planes. The kinks on faceted crystals are located at the steps (Figure 1).

Thus, faceted crystals grow by the generation and spreading of layers. New layers are generated only in supersaturated solutions by several mechanisms. A common layer generation mechanism is by screw dislocations, piercing the growing facet. The dislocation produces a step on the facet, which terminates and is pinned at the point where the dislocation outcrops on the surface. The step grows in a supersaturated solution and because of the pinned end, twists into a spiral around the dislocation. This mechanism was postulated by F. C. Frank in 1948[74,75] and is illustrated by an image from insulin crystallization in Figure 2a.[26,49]

Another common layer generation mechanism is by two-dimensional (2D) nucleation of islands of new layers. This is the original layer generation mechanism, put forth by Stranski and Kaischew in the 1930s.[76,77] This mechanism operates at high supersaturations and is illustrated in Figure 2b on the example of an apoferritin crystal.

Recently, a new mechanism of layer generation was discovered during crystallizations of the enzyme lumazine synthase. In a certain supersaturation range, below the threshold needed for 2D nucleation, droplets of dense liquid of the protein,[78] several hundred nanometers in size, land on the crystal facet and transform into a crystalline matter, which is in perfect registry with the underlying lattice.[79,80] The island of layers, several lattice parameters thick, spreads sideways generating several new steps (Figure 2c). Since such clusters are common in protein,[78,79,81] and, importantly, also in small-molecule solutions,[82] this mechanism is likely to operate in a wide range of systems.[83]

Other modes of layer generation discussed in literature mostly involve gross defects in the crystals: occlusions of solution, or the imperfect incorporation of microcrystals into larger growing crystals.[38–40,84,85]

The growth rate R of a faceted crystal, measured in a direction perpendicular to the growing facet, is related to the step velocity v via the mean step density, h/l, where l is the characteristic spacing between the steps and h is the step height

$$R = (h/l)v \tag{1}$$

If the steps are generated by a screw dislocation, the spiral around its outcrop point forms a hillock. Since the spacing l between the steps in this spiral is constant,[15,75] this hillock has constant slope $p = h/l$ and

$$R = pv \tag{2}$$

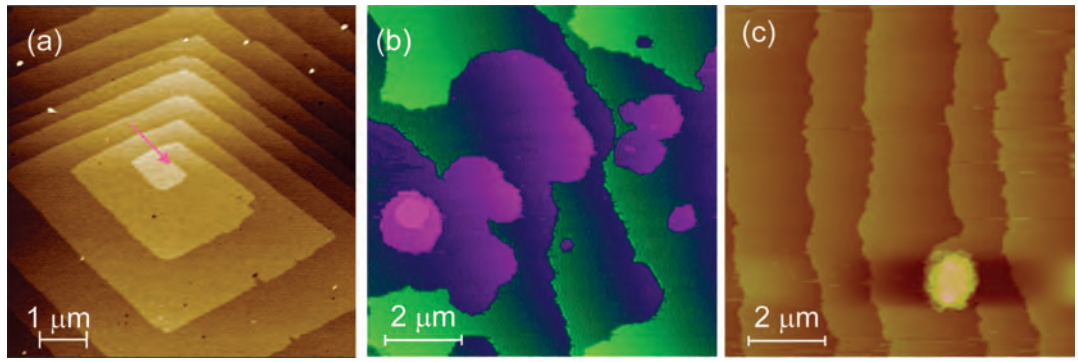


Figure 2. Three mechanisms of generations of crystalline layers. (a) By a screw dislocation outcropping on the face: a (100) insulin face is shown (reproduced by permission from ref 26. Copyright 2003 American Chemical Society. (b) By 2D nucleation; a (111) ferritin face. (c) By the landing and subsequent crystallization of metastable clusters of dense liquid, as the one indicated with an arrow; a (001) face of a lumazine synthase crystal (reproduced by permission from ref 79. Copyright 2005 American Chemical Society).

If the step contains kinks with a mean spacing $y_0 = a\bar{n}_k$, where a is the molecular size or more accurately, the lattice parameter, and $\bar{n}_k$ is the mean number of molecules between two kinks, then[86]

$$v = a/\bar{n}_k(j_+ - j_-) \tag{3}$$

In this relation, $(j_+ - j_-)$ is the net flux of molecule into a kink, the difference between the number incoming j_+ and departing j_- molecules per unit time, and $a(j_+ - j_-)$ is the rate of kink propagation along the step. The kink density $\bar{n}_k^{-1}$ relates the one-dimensional (1D) growth of a kink to the 2D growth of a step in the same way that the slope p relates the step propagation to the three-dimensional (3D) growth of the crystal.

Since the incorporation of molecules into steps is a monomolecular process and follows first-order chemical kinetics, v is proportional to $[\exp(\Delta\mu/k_BT) - 1]$,[87,88] where $\Delta\mu = \mu_{solution} - \mu_{crystal}$ is the difference in chemical potential of the crystallizing species, k_B is the Boltzmann constant, and T is absolute temperature. Note that according to the general physico-chemical convention, Δ = final – initial; however, since $\mu_{crystal} = \mu_{solution,equilibrium}$, in studies of phase transitions, the above definition of $\Delta\mu$ is accepted. This leads to a change of sign of the underexponential expression in the above formula for the driving force. In the case of crystallization of ionic, or other binary, ternary, etc., compounds, the expression in the exponent is more complex.[30] Since

$$\mu_{solution} = \mu^0_{solution} + k_BT \ln \hat{a} \quad \text{and} \quad \mu_{crystal} = \mu^{eq}_{solution} = \mu^0_{solution} + k_BT \ln \hat{a}_e \tag{4}$$

where $\hat{a}$ and $\hat{a}_e$ are the activities of the crystallizing substance in, respectively, the growth solution and in equilibrium with the crystal. Since $\hat{a} = \gamma C$, where γ is the activity coefficient and C is the concentration of the crystallizing substance, it is often assumed that $\gamma/\gamma_e \approx 1$ and $C/C_e = 1$ is often designated with σ. In some cases, the activity coefficient has been evaluated from data on the second osmotic virial coefficient.[89] In the case of the formation of polymers of sickle cell hemoglobin, which may be viewed as 1D crystals, up to six virial coefficients have been employed to adequately account for the solution nonideality in γ.[90] This is because the hemoglobin concentration in the solution is up to 35 g/100 mL. The correction increases the value of $\Delta\mu$ by about 2-fold.[91]

It has always been assumed that the incorporation of molecules from the solution into kinks follows first-order rate law.[15,75] Chernov was the first to view the incorporation into kinks as a chemical reaction and suggest that a barrier for the incorporation exists, which is likely related to the solvation shell around the incoming solute molecules.[15] Chernov introduced the step kinetic coefficient β to correlate the step velocity to the driving force $[\exp(\Delta\mu/k_BT]$. Since the molecular concentration of the crystallizing species in the solution is significantly lower than in the crystal, the coefficient of proportionality between v and $C/C_e - 1$ is divided into two, and v is written as

$$v = \beta\Omega C_e(C/C_e - 1) \tag{5}$$

where Ω is the crystal volume per molecule, so that the dimensionless product ΩC_e accounts for the change in number density between the solution and the crystal. Derivations of eq 5 have been offered, which however imply a mechanism of incorporation of molecules from the solution into the crystal.[86] Thus, it is better justified to use eq 5 as a definition of β. This provides uniformity and the ability to compare kinetic coefficients of different systems regardless of their concrete mechanism. On the other hand, the physical meanings of β should be judged on the basis of additional data on the mechanism of attachment of molecules from the solution into kinks.[25]

The kinetic coefficient β has units of length per time and is related to the first-order kinetic constant for incorporation into a kink k as $\beta = ak$. β is also related to the free energy barrier $\Delta G^{\ddagger}$ for incorporation into a kink as

$$\beta = a\bar{n}_k^{-1}\nu_+ \exp(-\Delta G^{\ddagger}/k_BT) = a\bar{n}_k^{-1}\nu_+ \exp(\Delta S^{\ddagger}/k_B) \exp(-\Delta H^{\ddagger}/k_BT) \tag{6}$$

where υ_+ is an effective frequency of attempts by a solute molecule to enter a kink by overcoming the barrier $\Delta G^{\ddagger}$.

Equation 6 shows that the kinetic coefficient β and thus the step velocity v and, to a large extent, the crystal growth rate R, are determined by the kink density $\bar{n}_k^{-1}$ and the incorporation barrier $\Delta G^{\ddagger}$. The kink density $\bar{n}_k^{-1}$ is determined by the mechanism of generation of kinks, while $\Delta G^{\ddagger}$ is determined by the mechanism of incorporation of molecules into kinks and the chemical interactions between solute and solvent and crystal surface and solvent. Below we discuss these issues.

Generation of Kinks by Thermal Fluctuations at Equilibrium and in Supersaturated Solutions

The suggestion that the edges of the unfinished layers, the steps, fluctuate and in this way create kinks was put forth by J. W. Gibbs.[92,93] Considering the equilibrium between a crystal and its medium, he wrote in a footnote to the second of his two

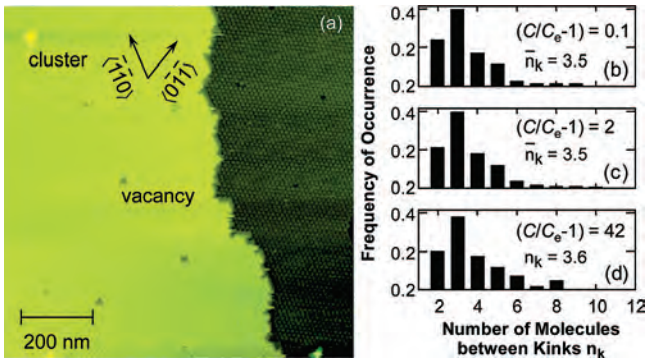


Figure 3. (a) Molecular structure of a growth step on an apoferritin crystal at protein concentration of 70 μg/mL, corresponding to supersaturation $(C/C_e - 1) = 2.0$. Dark color: lower layer; light color: advancing upper layer. Adsorbed impurity clusters and surface vacancies are indicated. (b–d) Distribution of number of molecules between kinks on steps located >0.5 μm apart, obtained from images similar to (a) at the three supersaturations indicated in the plots; the mean values of the distributions for each case are also shown. Reproduced by permission from ref 99. Copyright 2000 American Physical Society.

papers "On the Equilibrium of Heterogeneous Substances",[92,93] p. 325 "... several of the outermost layers of molecules on each side of the crystal are incomplete towards the edges. The boundaries of these imperfect layers probably fluctuate as molecules join them and depart from them." Burton, Cabrera, and Frank hypothesized that the same mechanism would apply in supersaturated solutions, and it would determine the kink density during growth of a step.[75] They derived a relation between the mean kink density $\bar{n}_k^{-1}$ and the free energy of kinks ω. On a step segment of length L oriented along a dense singular crystallographic direction, the number of positive n_+ and negative n_- kinks should be equal, $n_+ = n_- = n$ (see Figure 1). If the number of lattice sites without kinks along the step segment is n_0, then

$$n_+ + n_- + n_0 = 2n + n_0 = L/a \tag{7}$$

On the other hand,

$$n_+/n_0 = n_-/n_0 = n/n_0 = \eta = \exp(-\omega/k_BT) \tag{8}$$

Solving for the mean number of molecules between kinks $\bar{n}_k$, we get

$$\bar{n}_k = L/2na = 1 + 1/2\eta = \tfrac{1}{2}\exp(\omega/k_BT) + 1 \tag{9}$$

To justify their hypothesis that the equilibrium kink density is maintained in supersaturated environments during growth, Burton, Cabrera, and Frank estimated the kink energy from the expected energy of the bond between molecules in the crystal. These estimates suggested that the equilibrium $\bar{n}_k^{-1}$ is sufficiently high so that its further increases with supersaturations would not occur. According to eq 9, the validity of this conclusion crucially depends on the kink energy ω.

A test of the applicability of the equilibrium kink density to the kinetics of steps in supersaturated solution was carried out with the proteins ferritin and apoferritin. In the presence of Cd^{2+}, ferritin and apoferritin crystallize in the cubic $F432$ group.[94,95] The molecular structures of a {111} apoferritin face and of a growth step are shown in Figure 3a. A molecule at a kink in the f.c.c. lattice of ferritin and apoferritin has six neighbors, which is half of the total number of adjacent molecules in this lattice. Out of the six neighbors in a kink, three molecules belong to the underlying layer, and three molecules are from the step.

From Figure 3a and other similar images, the distribution of the number of molecules between two kinks, n_k, is determined and is plotted in Figure 3b–d for apoferritin. The mean $\bar{n}_k = 3.5$ was obtained for both proteins.[96] Comparing Figure 3, panels b, c, and d, we see that the n_k distributions are nearly the same near equilibrium, as well as at very high supersaturations. The lack of dependence of the kink density on the thermodynamic supersaturation suggests that additional kinks are not created at higher supersaturation. Hence, the observed kink density $\bar{n}_k^{-1}$ is an equilibrium property of this surface, which is retained during growth in a supersaturated environment. In this case, the number of molecules between the kinks n_k is solely determined by the balance of molecular interactions and thermal fluctuations in the top crystal layer and should be a function of the energy ω needed to create a kink.

From the value of $\bar{n}_k$ in Figure 3 and eq 9, we get $\omega = 1.6\ k_BT$. Quite surprisingly, this value of ω is only slightly lower than the energy of kinks on Si crystals:[97] one would expect the strong covalent bonds in the Si crystal lattice to lead to significantly higher kink energies.

If we assume first-neighbor interactions only, we can evaluate the intermolecular bond energy, φ. When a molecule is moved from within the step on a (111) face of a f.c.c. crystal to a location at the step, four kinks are created. For this, seven bonds (four in the top layer and three with molecules from the underlying layer) are broken, and five are formed. Then, $\omega = \varphi/2$ and $\varphi = 3.2\ k_BT \cong 7.8$ kJ/mol.

The intermolecular bonds in ferritin and apoferritin crystals involve two chains of bonds Asp – Cd^{2+} – Glu between each pair of adjacent molecules.[95,98] The above value of φ seems significantly lower than the typical coordination bond energies. This lowering may stem from the need to balance Cd^{2+} coordination with the amino acid residues and with the water species (H_2O and OH^-) or from free energy loss due to spatially and energetically unfavorable contacts by the other amino acid residues involved in the intermolecular contacts. This type of bond makes the ferritin and apoferritin systems more akin to inorganic crystallization systems than to proteins.

To judge whether the equilibrium kink density indeed scales the step velocity, as suggested by Burton, Cabrera, and Frank, one needs to determine the net flux of molecules into a step site $(j_+ - j_-)$ and test whether eq 3 is obeyed. To monitor the fast kinetics of incorporation, the slow scanning axis of the AFM was disabled, and the fast direction was oriented perpendicular to a step. The advance of the monitored step site is shown in Figure 4a.[99] Despite the relatively high solution supersaturation $(C/C_e - 1) = 2$, the time trace in Figure 4a reveals not only 25 arrivals to but also 22 departures of molecules from the monitored site. All arrivals and departures of molecules to and from the monitored site involve single molecules.

Molecules may enter the line of observation due either to molecular diffusion along the step or to exchange with either the terrace between the steps or the adjacent solution. While the latter results in step propagation and growth, the former is a process that only involves rearrangement of molecules already belonging to the crystal and may not be associated with growth. The distinction between the two scenarios was carried out using the time correlation function of the step position (Figure 4b). Analyses of the resulting correlation, following theories from refs 100 and 101, revealed that the trace in Figure 4 likely reflects exchange of molecules between the step and interstep terraces.[25,99,102] This conclusion allows us to extract from Figure 4a the net frequencies of attachment of molecules to kinks. For apoferritin at $(C/C_e - 1) = 2$, from the net attachment of three

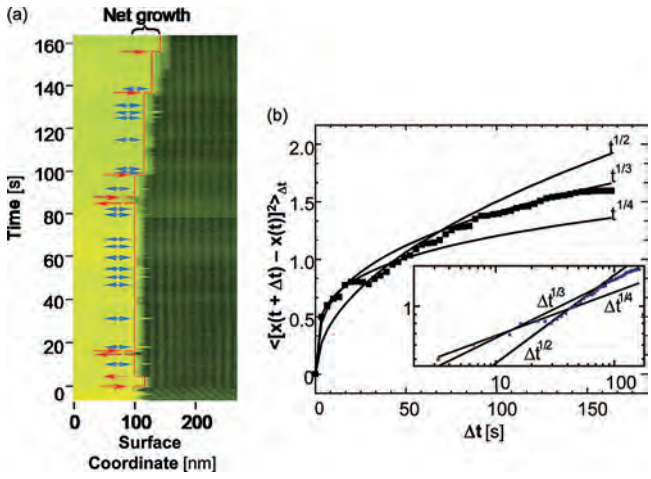


Figure 4. Incorporation of molecules into steps at apoferritin concentration of 70 μg/mL, $(C/C_e - 1) = 2.0$. (a) Pseudoimage recorded the Y scan axis disabled at time = 0 shows displacement of one step site. Contour traces step position. Red arrows indicate attachment and detachment events with residence time >1 s, blue double-sided arrows - with residence time <1 s, for details, see text. Appearance of 1/2 molecule attachments at times >80 s, highlighted in green, is due to events at a neighboring site that enters the image due to scanner drift. (b) Time correlation curve, characterizing mean square displacement of a location at a step for a time interval Δt as a function of this Δt, corresponding to the trace of step location in (a); inset: logarithmic plot. Solid squares - data; lines - fits with exponential dependencies of time as indicated in plot. Reprinted with permission from ref 99. Copyright 2000 American Physical Society.

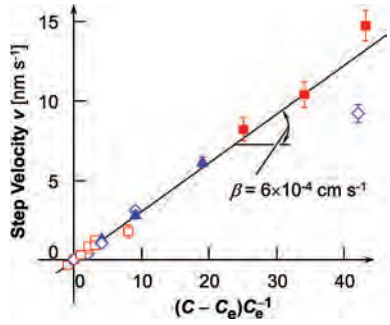


Figure 5. Dependencies of the step velocity v on the crystallization driving force $(C/C_e - 1)$ for ferritin and apoferritin. Red boxes and blue diamonds denote v values for, respectively, ferritin and apoferritin, from sequences of molecular resolution in situ AFM images of the advancing steps. Blue solid triangles are data for apoferritin extracted from disabled y-axis scans. Red solid squares are data for ferritin from time traces of the step growth rate using laser interferometry. Straight line corresponds to the step kinetic coefficient $\beta = 6 \times 10^{-4}$ cm s^{-1}. (Used by permission from ref 127. Copyright 2003 National Academy of Sciences).

molecules for 162 s and the probability of viewing a kink of $\bar{n}_k^{-1} = 1/3.5$, we get $(j_+ - j_-) = 0.065$ s^{-1}, or one molecule per ~15 s. For ferritin at $(C/C_e - 1) = 1$, the net growth is two molecules for 128 s, leading to an average net flux $(j_+ - j_-) = 0.054$ s^{-1} into the growth sites.

The step velocities v for the two proteins are shown in Figure 5. The data fit well the proportionality in eq 5. Since there are no sources or sinks of molecules at the step other than the attachment sites, the step velocity v should be expressed by eq 3. At $(C/C_e - 1) = 1$, at which all data for ferritin were collected, the value of the step growth rate for ferritin from Figure 5 is $v = 0.20$ nm s^{-1}, equal to the product $a\bar{n}_k^{-1}(j_+ - j_-)$. For apoferritin,

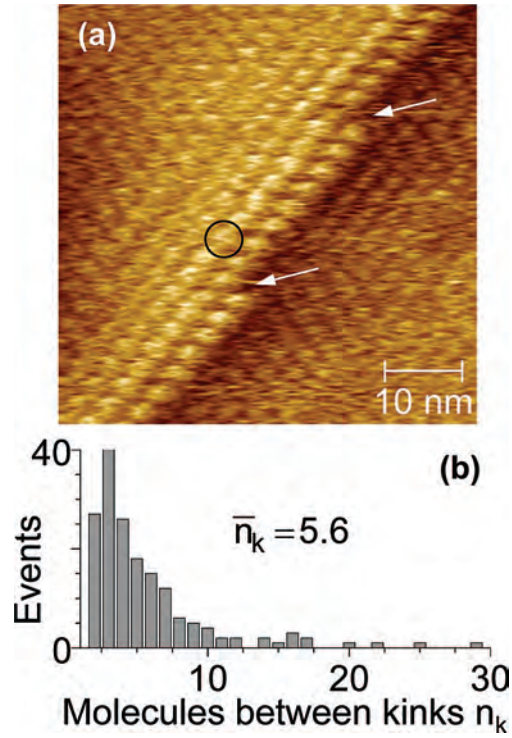


Figure 6. Structure of steps on {100} faces of insulin crystals at supersaturations $(C/C_e - 1) < 0.05$. (a) AFM image of typical structure of steps on a (100) face of insulin crystals. A step with two kinks, indicated with arrows, is shown. An insulin molecule is encircled in black. (b) Distribution of the number of molecules between kinks n_k determined from images similar to (a).

the average step velocity at $(C/C_e - 1) = 2$, is $v = 0.26$ nm/s. The product $a\bar{n}_k^{-1}(j_+ - j_-)$ determined at the same conditions is 0.24 nm/s.

The closeness of the values of the product $a\bar{n}_k^{-1}(j_+ - j_-)$ and measured v's indicates that the step propagation in ferritin crystallization occurs only due to incorporation of molecules into the kinks along the steps.[99,102] Furthermore, this equality shows that the kink density, determined by the thermal fluctuations of the steps and independent of supersaturation, is the factor scaling the step velocity.

1D Nucleation of New Molecular Rows

According to eq 9, on materials for which the energy of the bonds between the molecules is such that ω becomes higher than (1–2)k_BT, the distance between kinks exponentially increases. One example of such high kink energy is the crystallization of insulin, illustrated in Figure 6. At low supersaturations, near equilibrium, the step only contains single-molecule kinks. From Figure 6a and other similar images at low supersaturations, the number of molecules between kinks n_k on step segments along the densely packed <010> directions was found to have a Poissonian-like distribution with a mean $\bar{n}_k = 5.6$, Figure 6b, corresponding to a kink density $\bar{n}_k^{-1} = 0.18$. Assuming that the kinks at low supersaturations are generated by thermal fluctuations, a kink energy $\omega = 5.5$ kJ/mol and energy of the bond between an insulin molecule and the other molecules in the same layer $\phi_2 = 11.1$ kJ/mol were determined.[103] This value of ϕ_2 agrees with independent thermodynamic determinations of the enthalpy and entropy changes of the solvent and solute during crystallization.[104] This consistency confirms the applicability of the assumption of kink generation

by thermal fluctuations at low supersaturations. Note that an increase of the intermolecular bond energy from 7.8 in ferritin/apoferritin to 11.1 kJ/mol in insulin results in an almost 2-fold decrease in kink density and, as shown below, allows the action of another kink generation mechanism.

Several other cases of such steps have been studied, and it was found that instead of growing with correspondingly low velocity, the steps use additional mechanisms of kink generation. One of these mechanisms, by 1D nucleation of new molecular rows is discussed in this subsection; a second one, by the association to the steps of clusters preformed on the terraces, is the subject of the next subsection.

In contrast to 3D and 2D nuclei, 1D nucleus cannot be defined thermodynamically. A nucleus is a cluster for which the free energy gain due to the formation of the new phase stops the increase of free energy due to the formation of an interface between the old and new phases. For 2D and 3D nuclei, the surface free energy is proportional to the number of molecules on the surface or at the contour, while the gain is due to the total number of molecules in the nucleus, proportional to the nucleus volume. These dependencies provide for a unique size of the respective nucleus. For a growing row of molecules, the boundary consists of the two ends and is not a function of length of the row. These conditions cannot be used to thermodynamically define a 1D nucleus.[105,106]

However, as put forth by Voronkov,[107] a 1D nucleus can be defined kinetically, as a molecular row of length such that its probability to grow is equal to its probability to dissolve. At equilibrium, the incoming and departing fluxes into a row of molecules are equal, $j_+ = j_-$ and the end of a molecular row fluctuates with a diffusivity

$$D = a^2 j_- \tag{10}$$

In a supersaturated solution, the end of the row, the kink, moves with velocity

$$v_k = a(j_+ - j_-) = a j_-(C/C_e - 1) \tag{11}$$

where the second equality follows from eqs 3 and 5. During a time Δt, a molecular row would retract by a distance l

$$l = 2\sqrt{D\Delta t} - v_k \Delta t \tag{12}$$

The most likely shift backward for any Δt is

$$l_{max} = D/v_k = a(C/C_e - 1)^{-1} \tag{13}$$

If the thermodynamically determined kink density is such that a retraction of length l_{max} reaches a kink of opposite sign, the row would disappear. Thus, a molecular row with a length greater than $a(C/C_e - 1)^{-1}$ has a higher probability to grow than to dissolve, while molecular rows shorter than this length are more likely to dissolve. This quantity plays the role of a 1D nucleus. Remarkable, the length of the 1D nucleus is inversely proportional to $(C/C_e - 1)$, the "kinetic supersaturation", similar to the inverse proportionality between 2D and 3D nuclei and $\Delta\mu$, the "thermodynamic supersaturation". If we extend this analogy further, we note that the role of the surface free energy or the edge energy is played, in the case of 1D nuclei, by the end point energy, which is equal to the thermal energy $k_B T$. From here it follows that if $(C/C_e - 1)$ is greater than the thermodynamically determined kink density $\bar{n}_k^{-1}$, most newly formed molecular rows will grow and the step will move forward at a rate faster than suggested by the equilibrium kink density.[107]

Further analyses[107] yielded that if new rows are generated by 1D nucleation, the mean distance between kinks decreases with supersaturation from its equilibrium value $\bar{n}_{k,0}$

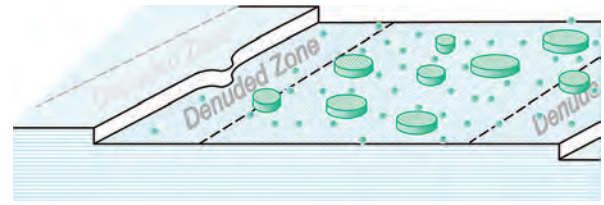


Figure 7. Illustration of 2D cluster association mechanism. Single molecules and 2D clusters exist and diffuse on terraces between steps. Clusters reaching the step create multiple kinks. Because of incorporation of molecules into steps, denuded zones of width ~ 50 nm,[16,17] in which the surface concentration of insulin is lower, exist along the steps. Because of the exchange between molecules and 2D clusters, the concentration of 2D clusters in the denuded zones is also lower. The association of an cluster to a step and the creation of a multiple kink promotes the step into the denuded zone, where the cluster concentration is higher, and this increases the probability of association of another cluster and the creation of even larger kink agglomeration.

$$\bar{n}_k = \bar{n}_{k,0}(C/C_e)^{-1/2} \tag{14}$$

and

$$v \propto a v_+ (C/C_e)^{1/2}(C/C_e - 1) \tag{15}$$

Equation 15 assumes that the kinks generated by 1D nucleation are still relatively few and the kink density does not reach its limit. However, the kink density is limited by geometry to 0.5, and, if one accounts for kink stabilization due to their mobility, reflected in eq 10 above, the upper bound of the kink density should be even lower. Thus, if upon supersaturation increase this maximum kink density is reached, v can only increase linearly with supersaturation. The total dependence of v on $(C/C_e - 1)$ then consists of a linear part at $(C/C_e - 1) < \bar{n}_k^{-1}$, accelerating part at $(C/C_e - 1) > \bar{n}_k^{-1}$, and a second linear part at $(C/C_e - 1) >> \bar{n}_k^{-1}$. Such dependencies have been observed for the very important case of calcite crystallization, both in pure solutions and in the presence of inhibitors.[29,108]

Another example of low kink density is the crystallization of the orthorhombic form of lysozyme, for which it was found that $\omega = 7.4\ k_B T$.[109] This high value leads to an extremely low kink density with $\bar{n}_k$ as high as 400–800, and step propagation limited by the rate of kink generation.[109]

Generation of Kinks by the Association of Preformed Clusters

A novel mechanism of kink generation was demonstrated for the crystallization of insulin: 2D clusters of several insulin molecules, preformed on the terraces between steps, Figure 7, associate to the steps. This mechanism operates at moderate and high supersaturations, while, as shown in Figure 6, at low supersaturations, only kinks generated by thermal fluctuations exist.

The action of this mechanism during the growth of insulin crystals is illustrated in Figure 8, which monitors the association of two 2D clusters to a step. The 2D clusters are only detected in the vicinity of a step: they are undetectable on the terraces because of their mobility and hydrodynamic interactions with the scanning tip.[96,110] The mobility of clusters of several molecules is not surprising (see discussion, theory, and experimental examples in refs 111 and 112). In the vicinity of a step, the cluster mobility is reduced. Still, their residual mobility prevents identification of their structure prior to their association. They might be ordered or disordered, akin to a 2D liquid formed

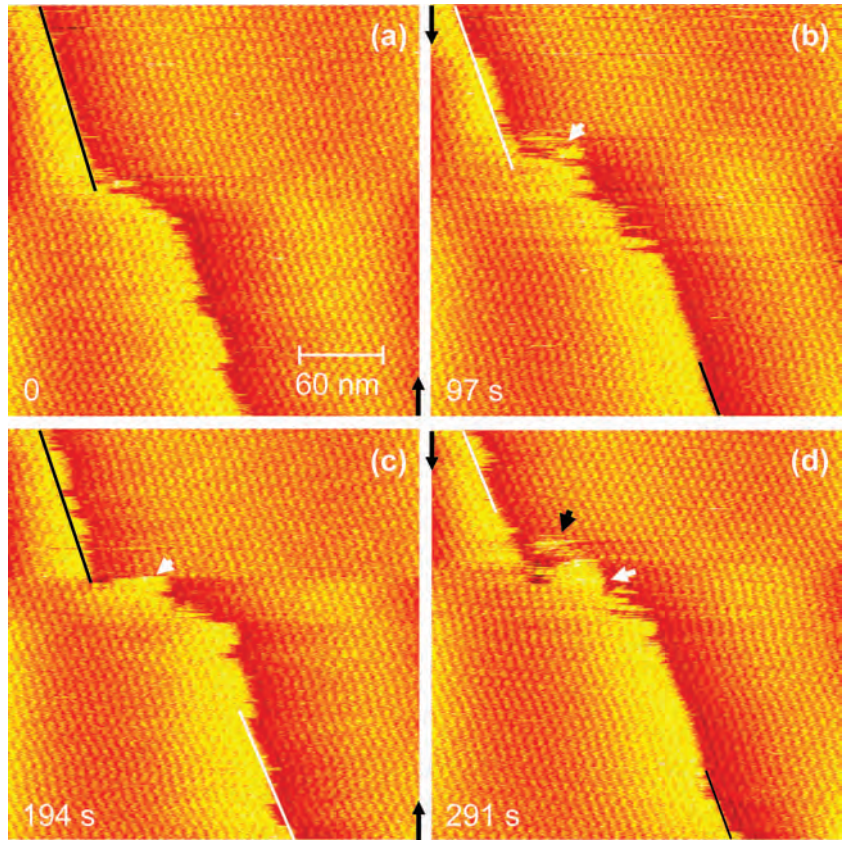


Figure 8. Attachment of two clusters to a multiple kink formation. (a) Starting configuration of a step with an advancing multiple kink. (b) A 2D cluster, indicated with a white arrowhead near a multiple kink. Image of cluster is fuzzy, likely due to cluster mobility. (b) Cluster joins step creating. (c) Another cluster indicated with a black arrowhead is seen near protruding mound. Black arrows indicate scan directions. Black lines mark step position in current image; white lines mark location of step in the preceding image. Reprinted with permission from ref 103. Copyright 2006 National Academy of Sciences.

in the pool of insulin hexamers adsorbed on the terraces: examples of liquid phases in 2D systems[113] have been discussed.[114] A 3D analogue of this process would be layer generation by the landing of dense liquid droplets on the surface of an existing crystal,[79] seen in Figure 2c.

The clusters form on the terraces between steps from the population of adsorbed mobile molecules.[25–27,47,49] Step propagation by multiple kinks leads to a several-fold increase in the step velocity v: the step kinetic coefficient β, defined in eq 5, is 2.2×10^{-3} cm s^{-1} at $(C/C_e - 1) = \sigma \leq 0.05$ and 6.3×10^{-3} cm s^{-1} at $\sigma \geq 0.1$.[103]

The association of 2D clusters affects step propagation in two ways: they lead to higher kink density $\bar{n}_k^{-1}$ and each cluster locally advances the step several molecules at a time, Figures 9 and 10. The statistics of single and double or greater kinks, and the times between single-molecule attachment events[103] revealed the existence and propagation mostly of single kinks. It was concluded that the main contribution of the cluster attachment to step kinetics is by generating abundant kinks. Because of the limitation on the kink-density increase, the cluster mechanism of nonlinear kinetic acceleration is limited, and a constant value of the step kinetic coefficient would ensue over a threshold supersaturation. Comparing $\beta = 6.3 \times 10^{-3}$ cm s^{-1} at $\sigma \approx 0.1$ to $\beta = 6.3 \times 10^{-3}$ cm s^{-1} at $\sigma > 0.2$,[115] we conclude that the threshold value of σ is 0.10–0.15. The nonlinear acceleration in step kinetics due to cluster attachment is schematically illustrated in Figures 11a,b and compared to experimental $v(\sigma)$ data in Figure 11b.

Some of the multiple kinks in Figures 9 and 10 are deeper than the observed clusters at the steps in Figures 8 and 10.

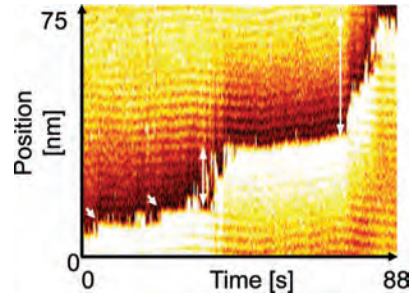


Figure 9. Step dynamics on (100) faces of insulin crystals at supersaturation $(C/C_e - 1) \approx 0.1$. A pseudoimage showing, in addition to one-molecular-diameter stepshifts, indicated with arrowheads, jumps of 5 and 11 molecular diameters, indicated with double-sided arrows, due to the propagation of multiple kinks. Reprinted with permission from ref 103. Copyright 2006 National Academy of Sciences.

This suggests that a mechanism of cooperative association of several clusters operates. Cooperative association of two clusters is illustrated in Figure 8. The sequence of processes that may lead to such cooperative association is schematically depicted in Figure 7: an associating cluster promotes the step to the area away from the step, where the concentration of molecules and clusters is higher, and this facilitates the association of further clusters. This is a mechanism of instability of the step shape, similar to the Mullins-Sekerka[116] or the Bales-Zangwill[117] models; however, the instability is due to the supply of clusters to the step, and correspondingly, the evolution of the instability is stopped by the depletion

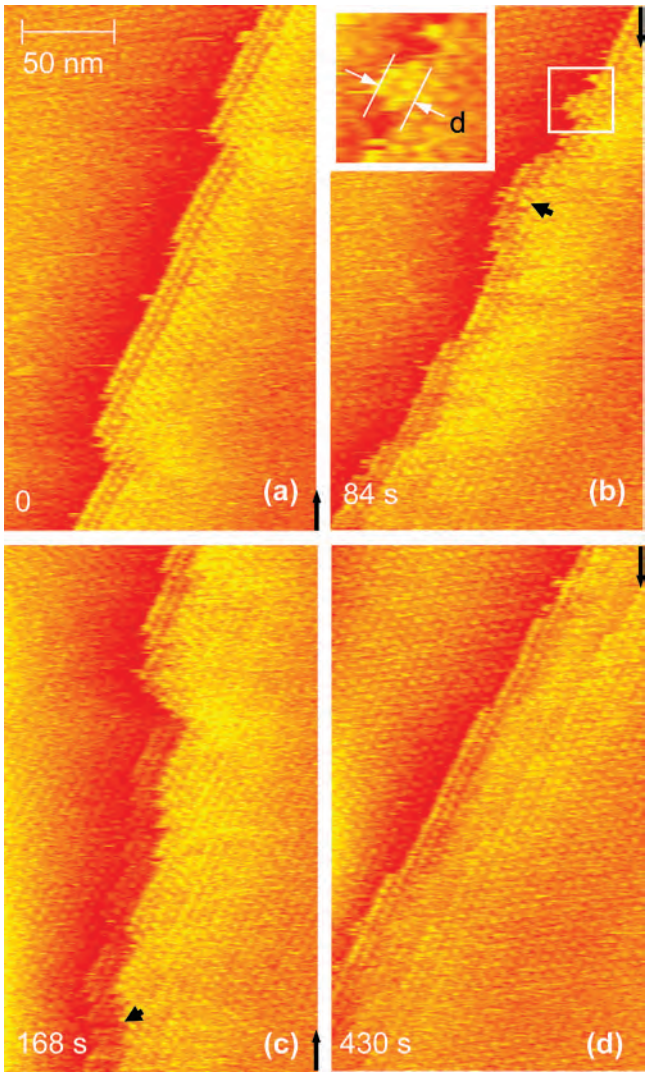


Figure 10. Evolution of step morphology at $(C/C_e - 1) \sim 0.1$. Two newly attached clusters, indicated with a black arrowhead and a white square (shown enlarged in inset) are seen in (b); cluster size d is defined in the inset. The lower cluster in (b) produces multiple kinks indicated with arrowhead in (c). Multiple kinks generated above the field of view cover molecular rows generated by clusters in (b). At 430 s in (d), the step straightens out again. Black arrows indicate scan directions. Times after first image are marked on frames.

of the clusters on the terraces. This mechanism explains the occurrences of 7- and 11-fold kinks initiated by clusters that are at most five molecules deep.

Rhombohedral crystals of insulin form in the islets of Langerhans in the pancreatic β-cells of mammals.[3,4,118,119] The likely biological function of insulin crystallization in vivo is to protect the insulin from further proteolysis (after conversion from proinsulin) while it is stored until regulated secretion into the blood serum.[4,118] Also, crystal formation increases the degree of conversion from soluble proinsulin.[4,120] Either of the two functions of crystallization requires that the rate of growth of the crystals be fast and readily responsive to inevitable fluctuations in the rate of conversion. The other two kink generation mechanisms, by thermal fluctuations,[75,92] and by 1D nucleation of new crystalline rows[30,107,109] lead to weak near-linear responses of the growth rate to variations of the Zn-insulin concentration.[30,75,99,109] Thus, they fail to provide an understanding of the expected fast growth rates and nonlinear acceleration of the rates of insulin crystallization.

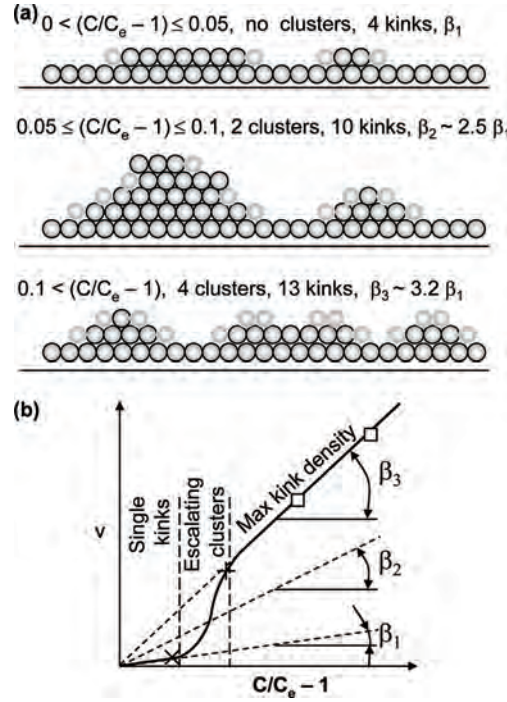


Figure 11. A schematic illustration of the effect of cluster association on kink density $\bar{n}_k^{-1}$, kinetic coefficient β, and step velocity v. (a) As the supersaturation $C/C_e - 1$ increases from top to bottom cartoons, the intensity of the cluster association increases. This leads to a higher $\bar{n}_k^{-1}$ and proportionally higher β and v, according to eq 3. In (a), kinks are indicated by light-color contour around molecules to left or right of them. In (b), $\times$ marks kinetics at $(C/C_e - 1) \approx 0.05$, $v \approx 0.10$ nm s^{-1}; + marks kinetics at $(C/C_e - 1) \approx 0.1$, $v \approx 0.6$ nm s^{-1}, and mark data from ref 26 for $(C/C_e - 1) > 0.2$. Vertical dashed lines delineate $(C/C_e - 1)$ ranges of three kink generation regimes illustrated in (a). Used by permission from 103. Copyright 2006 National Academy of Sciences.

In this context, the physiological significance of the nonlinear acceleration of step kinetics is related to the corresponding values of the kinetic coefficient for the face β_f defined as $R = \beta_f \Omega n_e \sigma$ so that $\beta_f = \beta p$; for insulin $p \approx 10^{-2}$ in broad supersaturation ranges.[26] The β_f values are 2.2×10^{-5} cm s^{-1} at $(C/C_e - 1) \leq 0.05$ and 6.3×10^{-5} cm s^{-1} at $(C/C_e - 1) \geq 0.1$. If these β_f values apply in vivo, crystal growth rates of $\sim$0.05 nm s^{-1} (that would allow $\sim$100 nm crystal to grow within 30 min)[4] require $C \approx 2C_e$ with the high β_f and significantly higher $C \approx 4C_e$ if kinks are only generated by thermal fluctuations and the lower β_f operates at all supersaturations.

The low supersaturations related to the higher density of cluster-generated kinks indicate that neither of the two steps in the proinsulin conversion/insulin crystallization reaction control its overall rate: if proinsulin conversion were the slow and controlling step, $C \approx C_e$ would ensue; if the crystallization step were slow, this would result in the accumulation of dissolved insulin and high σ values. Thus, proinsulin conversion and insulin crystallization are kinetically coupled.

Eyring or Kramers-type Kinetics of Incorporation into Kinks

Both Eyring's[87] and Kramers's[121,122] kinetic mechanisms evaluate the rate of an elementary chemical reaction from the rate of decay of a transition state or activated complex. The excess of free energy of the transition state over the reactants is the free energy barrier for the reaction. Eyring modeled

reactions in gases. In gases, the reactant molecules have kinetic energy, which is transformed into vibrational energy of the activated complex, when it is formed. Thus, the reaction rate is proportional to the frequency of oscillation of the activated complex. Because the vibrations of the activated complex stem from stored kinetic energy, the oscillation frequency depends on the mass of the molecules. In the case of crystallization, in which one of the reactants is the large crystal, the reduced mass of the activated complex is equal to the mass of the incoming molecule.

Kramers considered reactions in solution.[121] In viscous media, the kinetic energy of the solute molecules is completely dissipated to the solvent.[123] The solute molecules move only by Brownian motion, a sequence of random jumps in different directions. These jumps occur due to the misbalanced collisions by solvent molecules, and these misbalances are significant only for small solute molecules; for solutes with a diameter greater than a few microns, Brownian motion is negligible. Thus, the rate of Brownian motion does not depend on the solute mass but is inversely proportional to solute size. Furthermore, it is inversely proportional to solvent viscosity. The expression derived under Kramers' assumptions is similar to the one derived by Debye as an expansion of the Smoluchowski mechanism of diffusion limited aggregation for chemical reactions between molecules interacting in solution via midrange repulsion.[87,124] In Debye's derivation, the role of the barrier is played by the maximum in the repulsive potential between the reacting molecules.

From these considerations, it seems clear that the kinetics of crystallization from solution should follow a Kramers-type law. Historically, the transition state for crystallization from solution was introduced to distinguish it from crystallization from vapor,[15,16] where incorporation barriers are negligible.[75] Direct molecular observations of the elementary acts, which would be matched to theory, were not possible at that time, and an Eyring-type transition state, which decays due to its vibrations, was assumed. In the derived kinetics law, the kinetic coefficient was a decreasing function of the mass of the solute molecules. In further works, this apparent misconception was expanded, and the slow crystallization of large molecules, such as proteins, was explained through their large mass.

Critical tests to decide between Eyring and Kramers-types kinetics were carried out with ferritin/apoferritin, a unique pair of proteins, which share a near-spherical protein shell.[94,125] In addition to this shell, ferritin contains a ferrite core, which leads to its greater mass. The molecular mass of apoferritin has been determined by many techniques to be $M_w = 450\,000$ g mol^{-1},[94,125] with the mass of a molecule $m = 7.47 \times 10^{-19}$ g. M_w of ferritin in the samples used in these studies was determined by static light scattering[126] and was $M_w = 780\,000$ g mol^{-1}, $m = 1.30 \times 10^{-18}$ g.

The crystals of ferritin and apoferritin are faceted by [111] faces and grow by the lateral spreading of layers generated by 2D nucleation[25,99,102] (see Figures 2b and 3a). For both proteins, it was shown that the steps propagate by the incorporation of single protein molecules at the kinks, as discussed above.[25,99,102,127]

To quantify the crystallization kinetics of ferritin and apoferritin, the step velocities were measured using AFM[102] and interferometry.[128,129] Figure 5 shows that the proportionality between the step growth rate v and the crystallization driving force ($C/C_e - 1$) is valid in a broad range of concentrations of both proteins.

Figure 5 shows that at equal driving forces, the step velocities are equal for the two proteins. The kinetic coefficient defined

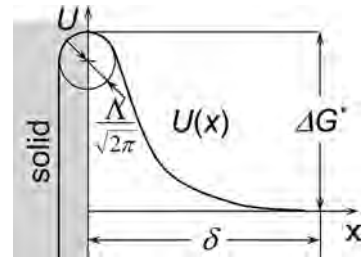


Figure 12. A schematic illustrating the potential energy relief in front of the growth interface.

is eq 5, with $\Omega = 1.56 \times 10^{-18}$ cm^3, and is for both proteins $\beta = (6.0 \pm 0.4) \times 10^{-4}$ cm s^{-1}. This accuracy in the determination of the two β values is due to the high accuracy of the determinations of the step velocities v, whose standard deviation < 7% for all of the data points in Figure 5.[127] If β were proportional to $m^{-1/2}$, the values of β for ferritin and apoferritin should differ by ~40% due to the ~2-fold difference in their masses. Since for both proteins step propagation occurs only due to incorporation of molecules into the kinks along the steps,[25,99,102] the equality of the kinetic coefficients suggests that β does not depend on the mass of the crystallizing molecules.

This observation is in apparent contradiction with Eyring-type kinetic laws, in which the vibrational components of the transition-state partition function lead to proportionality of β to $m^{-1/2}$. This leads to the conclusion that the kinetics of incorporation into the kinks follows Kramers–type kinetics, in which the decay of the transition state preceding the incorporation into kinks is driven by the collisions of the solvent molecules into the incoming molecule. Equivalently, one could say that rate of incorporation into kinks is determined by the slow diffusion over a repulsive maximum in the interaction potential between the incoming molecule and the kink, a statement from Debye's theory of diffusion-limited kinetics.

An expression for the kinetic coefficient of growth of crystals from solution as diffusion over a free-energy barrier ΔG^{μ}, followed by unimpeded incorporation was derived[127] following refs 87, 121, and 130. The assumed potential mean force $U(x)$ in the vicinity of the kink is schematically depicted in Figure 12, and its physical nature is discussed below. The potential reaches its maximum value $\Delta G^{\ddagger}$ at the crossing of the increasing branch, due to the repulsion between the incoming solute molecules and the crystal surface at medium separations, and the receding branch, which corresponds to the short-range attraction required if the molecules should enter the growth site. A finite curvature was assigned to $U(x)$ about $x = 0$ in analogy to previous solutions to similar problems.[131,132]

Since Brownian diffusion does not depend on the molecular mass, the above model yields a mass-independent kinetic coefficient.[127] Using eq 3 to link step velocity and the flux into the step, an expression for the step velocity v was obtained

$$v = \frac{a^3}{\bar{n}_k}\frac{D}{\Lambda}\exp\left(-\frac{\Delta G^{\ddagger}}{k_B T}\right)(C - C_e) \qquad (16)$$

where Λ contains the radius of curvature of $U(x)$ around its maximum.

With $a^3 = \Omega$, eq 16 can be rewritten in the typical form of eq 5 that is readily comparable to experimental data. This defines β as

$$\beta = \frac{1}{\bar{n}_k}\frac{D}{\Lambda}\exp\left(-\frac{\Delta G^{\ddagger}}{k_B T}\right) \qquad (17)$$

Equations 16 and 17 were derived assuming a Smoluchowski-Debye pathway of incorporation into the kink, that is, a molecule diffuses toward the kink and on its way overcomes a barrier. This is reflected in the presence of the diffusivity in the pre-exponential term. However, an analogous expression could be derived assuming Kramers-type incorporation pathway through a transition state of free energy $\Delta G^{\ddagger}$. Accordingly, since D is proportional to η^{-1}, β is inversely proportional to the solution viscosity η.

The parameters in this expression, $\bar{n}_k^{-1}$, D, Λ, and $\Delta G^{\ddagger}$ have a clear physical meaning. $\bar{n}_k^{-1}$and D can be independently measured. The evaluations of the enthalpy and entropy components of $\Delta G^{\ddagger} = \Delta H^{\ddagger} - T\Delta S^{\ddagger}$ and of Λ from crystallization kinetics data are illustrated below. An advantage of the definition of the kinetic coefficient β in eq 17 is that the found values can be compared to expectations stemming from the model for an initial validation.

Evidence for Kramers-type kinetics in other solution crystallization systems can be found in experiments on growth of protein crystals in gels, where the protein diffusivity is significantly lower than in a "free" solution. It was found with two proteins that the maximum value of the growth rate, recorded at the early stages of growth before solution depletion and transport control set in, is 1.5–3 times lower in gels than in free solutions.[133] Since in the viscous gel environment the diffusivity is lower than in free solutions, this suggests that the kinetic coefficient of growth is correlated to the diffusivity. In another work with the protein lysozyme, it was found that in gelled media the protein concentration at the growth interface is essentially equal to the one in free solutions, while the concentration gradient at the interface, proportional to the growth rate, is lower by ~1.5 times.[134] This is only possible if the kinetic coefficient in gels is lower, supporting the correlation between β and D derived above.

The Nature of the Barrier for Incorporation into Kinks

Numerous recent investigations have shown that a several-angstroms-thick solvent layer exists around molecules.[135–139] Within this hydration layer,[139,140] the water molecules are in either of two states, between which a dynamic equilibrium exists: directly attached to the protein surface and "free". Another equilibrium exits between the hydration layer and the bulk solution–water.[139] For protein molecules, this layer determines the thermodynamics and kinetics of enzyme–substrate and DNA–drug binding.[141,142] Below, we show that enthalpy and entropy contributions from the solvent layer largely determine the thermodynamics of crystallization. Furthermore, the dynamics of the water molecules within the hydration layer and of exchange between the layer and the bulk water determines the kinetics of incorporation into kinks.

The transfer of molecules from solution to an ordered solid phase, such as crystals, is governed by the reduction in the free energy $\Delta G^{\circ} = \Delta H^{\circ} - T\Delta S^{\circ}$. Intuitively, it appears that crystallization is prohibitively disfavored by a negative change in entropy. The entropy balance due to the ordering of the molecules into crystals consists of a loss of six translational and rotational degrees of freedom per molecule, only fractionally compensated by the newly created vibrational degrees of freedom.[143,144] It is estimated that for protein molecules, this results in an average loss of entropy $\Delta S^{\circ} \approx -(100–120)$ J mol^{-1} K^{-1},[143,145] although it may be as high as –280 J mol^{-1} K^{-1}.[144] Experimentally determined values reach –100 J/mol K.[7,102,104,146] Unless this entropy contribution to the free energy is compensated, no crystallization will occur.

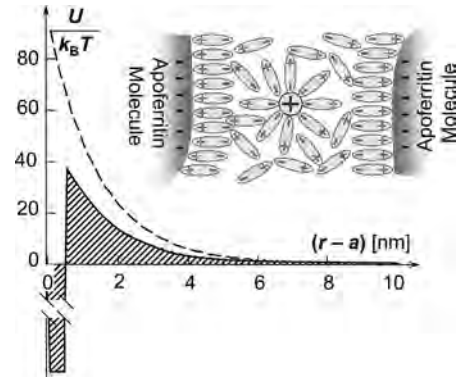


Figure 13. The potential of interaction between ferritin (and apoferritin) molecules in solution. Dashed line: in the presence of Na^+, the interactions are repulsive at all separations, due to hydration structuring of the water molecules with the help of the Na^+ ions, illustrated in the inset. In the presence of Cd^{2+}, short range attraction exists due to the ferritin–Cd^{2+}–ferritin bond, leading to potential depicted with the solid line.

Several analyses of protein crystallization have shown that the respective standard free energy change, ΔG°, is moderately negative. To understand the nature of the compensating factors, which make crystallization possible, we consider the crystallization enthalpy ΔH°. In several studied protein systems, ΔH° varied within a broad range, from –70 kJ/mol for lysozyme,[147] through ~0 for ferritin, apoferritin, and lumazine synthase,[80,102,148] to 155 kJ/mol for hemoglobin C.[7,146] This broad variation of crystallization enthalpy is similar to the situation with inorganic materials, where several examples of $\Delta H^{o} > 0$ exist. Thus, enthalpy effects cannot rationalize crystallization in general, and in many cases are unfavorable.

The answer to the above puzzle was found in recent experiments on the thermodynamics of crystallization of the proteins apoferritin, ferritin, hemoglobin C, lysozyme, insulin, and lumazine synthase. The enthalpy, entropy, and the standard free energy change for crystallization were evaluated as functions of the temperature and of the composition of the respective solutions.[7,102,104,146] Additional data derived from the investigations of the interactions between the dissolved protein molecules yielded intermolecular interaction potentials for these proteins.[126,148] This potential, illustrated in Figure 13, contains a repulsive maximum at intermediate separations of ~1 nm. However, interaction potentials with a repulsive maximum are by no means limited to the studied proteins. A summary of many biophysical data sets suggests that they are a general feature of interactions in protein solutions and between biological surfaces, where water is structured due to a combination of hydration and hydrophobic forces.[136,149]

The data on the intermolecular interactions are consistent with the evidence stemming from the thermodynamics of crystallization. Both data sets indicate that upon incorporation into a crystal lattice, some of the structured water/solvent molecules are released (Figure 14) or, conversely, additional water/solvent molecules may be trapped. Both phenomena would have a significant entropy effect, commensurate with the one of the transfer of water from clathrate, crystal hydrate, or other ice-like structures that leads to an entropy gain of ~22 J mol^{-1} K^{-1}.[124,145,150–152] Considering how important the entropy effects are, solvent and protein entropy changes were distinguished:

$$\Delta G^{\circ} = \Delta H^{\circ} - T\Delta S^{\circ}_{\text{protein}} - T\Delta S^{\circ}_{\text{solvent}} \qquad (18)$$

A negative value of the standard ΔG^{o} that would thermodynamically allow for crystallization to proceed is favored by a

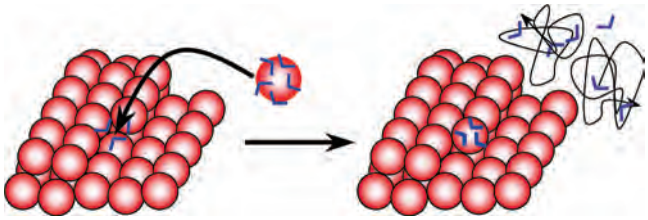


Figure 14. A schematic illustration of the increase in solvent entropy, $\Delta S_{solvent} > 0$, during incorporation of solute molecules from solution into kinks. The protein molecules in solution and the kink are coated with water molecules, which are released upon attachment of the protein molecules to the crystal. If, alternatively, additional water molecules are trapped upon attachment of a protein molecule, $\Delta S_{solvent} < 0$ would ensue.

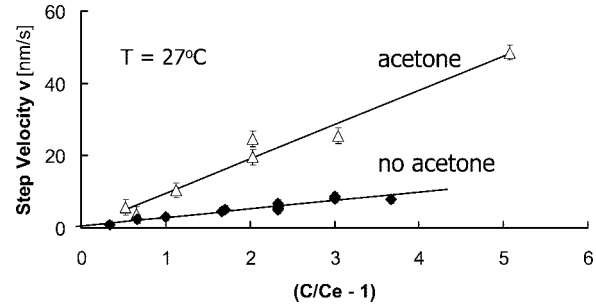


Figure 15. Step velocity on the (110) face of insulin as a function of supersaturation ($C/C_e - 1$), in the presence and in the absence of acetone. Lines are regression fits to the respective sets of data. (Used by permission from ref 26. Copyright 2003 American Chemical Society).

positive sum of ($\Delta S°_{protein} + \Delta S°_{solvent}$). Separating the two entropy factors, $\Delta S°_{protein}$, was determined as the difference between the macroscopically determined $\Delta G°$ and the one corresponding to the free energy of the bond in the crystal lattice, evaluated from the density of the growth sites, as discussed above.[34,102,146] It was found that $\Delta S°_{protein}$ is, as expected, in the range of –15 to –100 J/mol K. Thus, in many cases, the only factor in the above free energy expression that favors crystallization is $\Delta S°_{solvent}$.[34,35,153] The estimated values of $\Delta S°_{solvent}$ reach >600 J mol^{-1} K^{-1}, corresponding to the release of ~5 to 30 water or solvent molecules upon the incorporation of a protein molecule into a crystal. Thus, the structuring of the water around the protein molecules underlies the main thermodynamic driving force for crystallization.[146,153]

Given the crucial role of structured water in the thermodynamics of crystallization in solutions, it is natural to hypothesize that the water structuring plays a major role in crystal growth kinetics. This suggestion was first put forth by Chernov as a part of the first definition of a kinetic coefficient for crystallization from solution.[15,16,86] As discussed above, the rate of the elementary step of crystallization, the attachment of a molecule from the solution to an existing growth site on the crystal surface, is determined by the rate of diffusion over a repulsive barrier.[34–36,127] Within the hypothesis of the role of water structures in the kinetics of crystallization, this barrier would be the repulsive maximum depicted in Figure 13. There is no contradiction with the other interpretation of this barrier as excess free energy of a transition state in which the water shell of the kink and of the incoming molecule are partially destroyed: the repulsive maximum in the intermolecular interaction potential has the same origin. The two schematics highlight different features of the process of association of a molecule to a kink in solution.

Critical tests of this hypothesis were carried out with the protein insulin. In laboratory conditions, this protein crystallizes in the presence and in the absence of an organic cosolvent, acetone. Thermodynamic analyses revealed that acetone destroys the shell of structured water around the insulin molecules in solution.[104] Figure 15 shows that this leads to faster kinetics of crystallization and a 5× greater kinetic coefficient β.[26] When transport limitations were overcome by using the edges of larger crystals, around which buoyancy-driven convection is faster,[67,154] or by forced solution flow, [69] β in the presence of acetone reached 0.4 mm s^{-1}, comparable to those of small molecules compounds.[155] Thus, the destruction of the water shell correlates with faster kinetics, supporting the important role of structured water for the kinetics of incorporation.

The destruction of the water shell around solute molecules is likely the main component of the barrier for incorporation in kinks not only for protein but also for other materials. For evidence of this hypothesis, the enthalpy part $\Delta H^{\ddagger}$ of the barriers was determined for about 10 diverse substances and were found to fit into an unusually narrow range of 28 ± 7 kJ mol^{-1}.[156] The chemical nature of these substances ranges from inorganic salts, through organic molecular compounds, to proteins and viruses. Hence, the narrow range of the activation barriers is unexpected if they should reflect the chemical variety of the crystallizing compounds. On the other hand, if the barrier in all cases reflects a high-energy state of partial destruction of the water structures around the solute molecules and at the kinks, the consistency of the barrier is natural. This magnitude of the barrier corresponds to the energy of one or two hydrogen bonds; that is, one can think that the high-energy state is when these bonds have been broken and the new bonds that exist in the crystal have not formed. While the participation of one or two hydrogen bonds in the association of small molecules and ions to kinks is expected, one may wonder why the barriers are not higher for protein crystals, where a greater number of hydrogen bonds may be broken. The answer seems to be that the large protein molecules have relatively limited areas of intermolecular contact in the crystal lattice,[157] where only few hydrogen bonds exist.

Another piece of evidence for the applicability of a Kramers-type kinetics law, in which the barrier for incorporation is due to the structuring of the water molecules on the surface of the solute, comes from data on the kinetics of adsorption of solute ions on the surface of a growing ammonium-dihydrogen phosphate (ADP) crystal.[23,24] The data for the temperature range 29–67 °C were fitted to an equivalent of eq 17 with $\bar{n}_k^{-1} = 1$ to account for the suspected density of the adsorption sites.[23,24] The fit yielded $\Lambda \exp(\Delta S^{\ddagger}/k_B) = 13$ Å and $\Delta H^{\ddagger} = 27$ kJ/mol. $\Delta H^{\ddagger}$ is in the range found for all other studied systems, as expected for a barrier due to water structuring, demonstrating the applicability of insights, derived from experiments with proteins, to small-molecule materials. Assuming that the value of Λ is 13 Å, it would correspond to the thickness of a layer of several water molecules. The correspondence of the found values of Λ and $\Delta H^{\ddagger}$ to the expectations stemming from the water structuring model suggest that $\Delta S^{\ddagger}$ is essentially 0.

Clearly, the barrier for incorporation which is due to the water structuring contains a large entropy component, which, as the entropy of crystallization, splits into entropy due to solvent and entropy due to the solute molecules. The solvent component may be both positive and negative, depending on whether additional molecules of water are trapped in the transition state, or some of those associated with the solute molecules are released. The contribution of the solute molecules to the

Table 1. Kinetic Coefficient, β, Diffusivity, D, Effective Molecular Diameter a, Point Symmetry Group of Molecule G, Order of Symmetry Group Z, for Protein and Inorganic Systems

system	β, 10^{-4} [cm s^{-1}]	D, 10^{-6} [cm^2 s^{-1}]	a [nm]	G	Z	source
insulin			5.5	$\bar{3}$	6	26
no acetone	90	0.79				
~5% acetone	420					
apoferritin	6	0.32	13	432	24	102
ferritin	6	0.32	13			127
canavalin, R3 form	5.8–26	0.4	3.5–8	3	3	27
lumasine synthase	3.6	0.16	16	m5	60	79
catalase	0.32	n.a.	11.5	222	4	160
hemoglobin C	0.2	0.5	5.5	2	2	8
lysozyme {101}		0.73	3	1	1	
typical	2–3					161
no step bunching	22–45					69
lysozyme {110}	2–3					162
STMV	4–8	0.2	18	m5	60	51
thaumatin	2	0.6	4.0	1	1	163
various inorganic systems (ADP, KDP, alums, etc.)	~100–1000	~1–5	0.5	1, 2, $\bar{2}$, m, etc.	1, 2	34

activation entropy is due to the necessity to orient the molecule in a way suitable for association to the kink.[86,158] There have been estimates that the solute reorientation may slow crystallization kinetics of large molecules by as much as 1000× . The estimates of this contribution are based on the following line of thought: With the typical translational diffusivities of the protein molecules of order 10^{-7} cm^2 s^{-1}, see Table 1, a protein molecule spends ~10^{-7} s traveling through the last 10 Å prior to incorporation. During that time, with the typical rotational diffusivities of 10^6 s^{-1}, the molecule could rotate by ~0.3 rad. Since an incorrectly aligned molecule would not be able to form the necessary bonds with the kink and will be rejected, only $0.3/4\pi \approx 0.02$ of all attempts of incorporation will succeed, decreasing by 50× the kinetic coefficient. This factor corresponds to a contribution to $\Delta S^{\ddagger}$ of about –(30 to 40) J mol^{-1} K^{-1}. Since the rotational diffusivity scales as a^{-3} (ref 159) and the translational diffusivity scales as a^{-1}, (ref 123) the slowing down is significantly stronger for larger molecules. For small-molecule materials, this contribution is insignificant and may be completely compensated by the contribution from the release or trapping of the few, in this case, water molecules. This seems to be the case of discussed above, for which the total $\Delta S^{\ddagger} \approx 0$.

To evaluate the significance of the contribution from the loss of rotational entropy of the solute molecules upon incorporation into kinks, in Table 1 we compare the step kinetic coefficients β of about a dozen proteins, protein complexes and viruses, as well as some inorganic substances.[8,26,27,34,51,69,79,102,127,160–163] The β values for the large molecules fit in the range (0.2–420) × 10^{-4} cm s^{-1}. The molecular symmetry groups of these large molecules have orders ranging from 1, through 3, to 24 for ferritin and apoferritin, and 60 for the viruses and lumazine synthase. No correlation exists between higher molecular symmetry and higher kinetic coefficients.

This lack of correlation once again suggests that in the case of solution growth the activated state is not a classical one with stretched bonds, but rather is a state in which the water shell is slowly destroyed, while the molecule retains rotational freedom. The slow destruction of the water shell prolongs significantly, by a factor of $\exp(28\,000/RT) \approx 10^5$, the approach of the molecule to the kink from the above estimate based on uninhibited diffusion all the way to the kink. During this extended approach time, the incoming molecule tests different orientations and finds the "right" one. With some inaccuracy, it could be said that overcoming of the barrier due to the water shells is the rate limiting step in the association to a kink, while the selection of the proper orientation is significantly faster and does not affect the kinetics. Clearly, further theoretical and experimental developments are needed to fully understand the role of molecular symmetry for the crystallization, and more broadly, aggregation of proteins.

This insight about the nature of the barrier for incorporation into kinks was used to understand the effects of biomolecules on the growth of calcite ($CaCO_3$).[164] The step velocity of calcite was determined in the presence of 15 peptides and proteins, and it was found that while at micromolar and millimolar concentrations the biomolecules act as typical impurities and inhibit step propagation, at nanomolar concentrations they promote calcite growth by increasing the step kinetic coefficient. The growth enhancement was interpreted in terms of reduction of the magnitude of the activation barrier $\Delta G^{\ddagger}$ by the biomolecules, which displace water molecules around the solute. The reduction of $\Delta G^{\ddagger}$ varied from 12 to 2300 J mol^{-1} and was small, compared to the total barrier for incorporation of Ca^{2+} and CO_3^{2-} ions into calcite crystals of 32.8 kJ mol^{-1}. The degree of promotion of calcite growth was found to correlate with the molecular hydrophilicity, which can be independently evaluated.[165] From these results, the acceleration of step velocity can be estimated a priori from the composition of the additive and its hydrophilicity and net charge.[164] This is a first example in crystallization research and practice, in which the effects of a dopant on the crystallization kinetics can be quantitatively predicted. This prediction is based on the understanding of the nature of the activation barriers for incorporation into kinks.

Conclusions and Perspectives for Future Work

On the surfaces of crystals growing from solution, the density of kinks, the sites at which molecules from the solution can associate to the crystal, is low: only about 10^{-3} of all molecular sites on the surface are kinks. Thus, the availability of kinks is a major factor for the rate of growth of the crystals from solution. The surface kink density is determined by the density of steps and the density of kinks along the steps. The step density is typically on the order of 10^{-2} to 10^{-3}. The density of kinks along a step is bound from above by geometry to 0.5, and if one accounts for the entropy of the different kink configurations, to about 0.3 kinks per molecular site. If the free energy of the bonds between the pairs of molecules in the crystal is relatively low, this upper bound of the kink density along a step is reached

even in saturated solutions and the kink density does not increase in supersaturated solutions. If the free energy of the bond is high, the kink density is low in a saturated solution and may increase as supersaturation is increased. Two mechanism of generation of new kinks in supersaturated solutions have been put forth in literature: by "nucleation" of new molecular rows (1D nucleation) along the steps and by association of 2D clusters, preformed on the terraces between the steps. These two mechanisms yield increasing kink density as supersaturation is increased, leading to faster step motion and a superlinear dependence of the step velocity on supersaturation. The action of the 1D nucleation mechanism does not depend on any materials parameters, and it ensures that at supersaturations ($C/C_e - 1$) > 0.3 the limiting kink density along a step is reached so that the step velocity becomes a linear function of supersaturation. Potentially, the 2D cluster association mechanism could be used for control of the step velocity at supersaturations lower than 0.1. For this, further insight is needed into the parameters that govern the formations and stability of the 2D clusters and in particular their mobility.

The rate of step motion during crystallization from solution depends on the product of the kinks density along a step, the rate of attachment of molecules into the existing kinks, and the concentration of molecules in the vicinity of a kink. The latter concentration depends on the parameters of the pathway that a molecule uses to reach a kink starting from the solution. In most of the cases where this pathway has been probed, it was found that the solute molecules adsorb on the terraces between the steps and then diffuse towards the steps and kinks. Very little is known about the adsorption and surface diffusion rate constants for crystal surfaces in contact with solution. However, the available experimental evidence allows conclusions about the major factor in the kinetic barriers for adsorption on the surface and for incorporation into steps from the surface. It appears that these barriers are due to the structuring of the water on the surfaces of the solute molecules and the crystal. Furthermore, emerging experimental results indicate that the step velocity and the crystal growth rate can be significantly slowed down or accelerated by rearranging these water structures. Further progress in the regulation of crystal growth rate crucially depends on the understanding of how solution additives: ions, organic, and inorganic molecules, and others, affect the structures around the solute molecules and the surface of the crystal.

Acknowledgment. My deep gratitude goes to my colleagues to who took part in the original experiments, from which many of the insights reviewed here were gained: S.-T. Yau, O. Gliko, D. Georgiou, D. N. Petsev, I. Reviakine, and K. Chen. This work has benefited from in-depth discussions with J. J. De Yoreo, A. A. Chernov, Z. Derewenda and B. M. Pettitt. Support by the Welch Foundation (Grant E-1641) is gratefully acknowledged.

References

(1) De Yoreo, J. J; Burnham, A. K; Whitman, P. K. *Int. Mater. Rev.* **2002**, *47*, 113–152.
(2) Reichert, P.; McNemar, C.; Nagabhushan, N.; Nagabhushan, T. L.; Tindal, S.; Hruza, A. U.S. Patent 5,441,734, 1995.
(3) Howell, S.; Tyhurst, M. In *The Secretory Granule*; Poisner, Trifaro, Eds.; Elsevier: Amsterdam, 1982; pp 155–172.
(4) Dodson, G.; Steiner, D. *Curr. Opin. Struct. Biol.* **1998**, *8*, 189–194.
(5) Hirsch, R. E.; Raventos-Suarez, C.; Olson, J. A.; Nagel, R. L. *Blood* **1985**, *66*, 775–777.
(6) Hirsch, R. E.; Rybicki, A. C.; Fataliev, N. A.; Lin, M. J.; Friedman, J. M.; Nagel, R. L. *Br. J. Haematol.* **1997**, *98*, 583–588.
(7) Vekilov, P. G.; Feeling-Taylor, A. R.; Petsev, D. N.; Galkin, O.; Nagel, R. L.; Hirsch, R. E. *Biophys. J.* **2002**, *83*, 1147–1156.
(8) Feeling-Taylor, A. R.; Yau, S.-T.; Petsev, D. N.; Nagel, R. L.; Hirsch, R. E.; Vekilov, P. G. *Biophys. J.* **2004**, *87*, 2621–2629.
(9) Kossel, W. *Nachr. Ges. Wiss. Götingen* **1928**, *135*, 138.
(10) Stranski, I. N. *Z. Phys. Chem.* **1928**, *136*, 259–278.
(11) Jackson, K. A. In *Growth and Perfection of Crystals*; Doremus, R. H; Roberts, B. W.; Turnbull, D., Eds.; Chapman and Hill: London, 1958; pp 319–323.
(12) Temkin, D. *Mechanism and Kinetics of Crystallization*; Nauka i Technika: Kiev, 1964.
(13) Nielsen, A. E.; Sohnel, O. *J. Cryst. Growth* **1971**, *11*, 233–242.
(14) Spaepen, F. In *Solid State Physics*; Academic Press: Boston, 1994; Vol. 47, pp 1–32.
(15) Chernov, A. A. *Sov. Phys. Uspekhi* **1961**, *4*, 116–148.
(16) Chernov, A. A. *Modern Crystallography III, Crystal Growth*; Springer: Berlin, 1984.
(17) Chernov, A. A. *Contemp. Phys.* **1989**, *30*, 251–276.
(18) Chernov, A. A. *Prog. Cryst. Growth Charact.* **1993**, *26*, 121–151.
(19) Bostanov, V.; Staikov, G.; Roe, D. K. *J. Electrochem. Soc.* **1975**, *122*, 1301–1305.
(20) Bennema, P. *J. Cryst. Growth* **1967**, *1*, 278–286.
(21) Gilmer, G. H.; Ghez, R.; Cabrera, N. *J. Cryst. Growth* **1971**, *8*, 79–93.
(22) Van der Eerden, J. P. In *Handbook of Crystal Growth*: Hurle, D., Ed.; North Holland: Amsterdam, 1994; Vol. 1a, pp 307–476.
(23) Vekilov, P. G.; Kuznetsov, Y. G.; Chernov, A. A. *J. Cryst. Growth* **1992**, *121*, 643–655.
(24) Vekilov, P. G.; Kuznetsov, Y. G.; Chernov, A. A. *J. Cryst. Growth* **1992**, *121*, 44–52.
(25) Chen, K.; Vekilov, P. G. *Phys. Rev. E* **2002**, *66*, 021606.
(26) Reviakine, I.; Georgiou, D. K.; Vekilov, P. G. *J. Am. Chem. Soc.* **2003**, *125*, 11684–11693.
(27) Land, T. A.; DeYoreo, J. J.; Lee, J. D. *Surf. Sci.* **1997**, *384*, 136–155.
(28) De Yoreo, J. J.; Land, T. A.; Dair, B. *Phys. Rev. Lett.* **1994**, *73*, 838–841.
(29) Teng, H. H.; Dove, P. M.; De Yoreo, J. J. *Geochim. Cosmochim. Acta* **2000**, *64*, 2255–2266.
(30) Teng, H. H.; Dove, P. M.; Orme, C. A.; De Yoreo, J. J. *Science* **1998**, *282*, 724–727.
(31) Rubbo, M. *Eur. J. Mineral.* **2007**, *19*, 333–338.
(32) Rubbo, M. *J. Cryst. Growth* **2001**, *223*, 235–250.
(33) Rubbo, M. *J. Cryst. Growth* **2006**, *291*, 512–520.
(34) Vekilov, P. G.; Chernov, A. A. In *Solid State Physics*; Ehrenreich, H.; Spaepen, F., Eds.; Academic Press: New York, 2002; Vol. 57, pp 1–147.
(35) Vekilov, P. G. In *Nanoscale Structure and Assembly at Solid-fluid Interfaces. Vol. II: Assembly in Hybrid and Biological Systems*; De Yoreo, J. J.; Lui, X. Y. Eds.; Kluewer Academic Publishers: New York, 2004; pp 145–200.
(36) Vekilov, P. G. In *Methods in Molecular Biology, Vol. 300: Protein Nanotechnology, Protocols, Instrumentation, and Applications*; Vo-Dinh, T., Ed.; Humana Press: Totowa, NJ, 2005; pp 15–52.
(37) Vekilov, P. G. In *Methods in Enzymology*; Carter, C. W., Sweet R. M., Eds.; Academic Press: San Diego, 2003; *Vol. 368 Macromolecular Crystallography, Part C*; pp 170–188.
(38) Malkin, A. J.; Thorne, R. E. *Methods* **2004**, *34*, 273–299.
(39) Malkin, A. J.; Kuznetsov, Y. G.; McPherson, A. *Proteins: Struct. Funct. Genet.* **1996**, *24*, 247–252.
(40) Malkin, A. J.; Kuznetsov, Y. G.; McPherson, A. *J. Struct. Biol.* **1996**, *117*, 124–137.
(41) Chernov, A. A.; Rashkovich, L. N.; Vekilov, P. G. Proceedings of the 14th International Conference on Crystal Growth and the 12th International Conference on Vapor Growth and Epitaxy. *J. Cryst. Growth* **2005**, *275*, 1–18.
(42) Chernov, A. A.; Petrova, E. V.; Rashkovich, L. N. *J. Cryst. Growth* **2006**, *289*, 245–254.
(43) De Yoreo, J. J.; Chernov, A. A.; Zepeda-Ruiz, L. A.; Wasylenki, L. E.; Elhadj, S.; Orme, C. A.; Gilmer, G.; Dove, P. M. *Geochim. Cosmochim. Acta* **2005**, *69*, A481.
(44) Van der Eerden, J. P.; Mueller-Krumbhaar, H. *Phys. Rev. Lett.* **1986**, *57*, 2431–2433.
(45) Van der Eerden, J. P.; Mueller-Krumbhaar, H. *Electrochem. Acta* **1986**, *31*, 1007.
(46) Sunagawa, I.; Bennema, P. *J. Cryst. Growth* **1979**, *46*, 451–450.
(47) Vekilov, P. G.; Alexander, J. I. D. *Chem. Rev.* **2000**, *100*, 2061–2089.
(48) Gliko, O.; Booth, N. A.; Vekilov, P. G. *Acta Crystallogr.* **2002**, *D58*, 1622–1627.

(49) Gliko, O.; Reviakine, I.; Vekilov, P. G. *Phys. Rev. Lett.* **2003**, *90*, 225503.
(50) Lin, H.; Yau, S.-T.; Vekilov, P. G. *Phys. Rev. E* **2003**, *67*, 0031606.
(51) Malkin, A. J.; Land, T. A.; Kuznetsov, A.; McPherson, A.; DeYoreo, J. J. *Phys. Rev. Lett.* **1995**, *75*, 2778–2781.
(52) Malkin, A. J.; Kuznetsov, Y. G.; Glanz, W.; McPherson, A. *J. Phys. Chem.* **1996**, *100*, 11736–11743.
(53) Kuznetsov, Y. G.; Malkin, A. J.; Land, T. A.; DeYoreo, J. J.; Barba, A. P.; Konnert, J.; McPherson, A. *Biophys. J.* **1997**, *72*, 2357–2364.
(54) Malkin, A. J.; Kuznetsov, Y. G.; McPherson, A. *J. Cryst. Growth* **1999**, *196*, 471–488.
(55) McPherson, A.; Malkin, A. J.; Kuznetsov Yu, G. *Annu. Rev. Biophys. Biomol. Struct.* **2000**, *29*, 361–410.
(56) Malkin, A. J.; Kuznetsov, Y. G.; Lucas, R. W.; McPherson, A. *J. Struct. Biol.* **1999**, *127*, 35–43.
(57) Li, H.; Perozzo, M. A.; Konnert, J. H.; Nadarajah, A.; Pusey, M. L. *Acta. Crystallogr.* **1999**, *D55*, 1023–1035.
(58) Konnert, J. H.; D'Antonio, P.; Ward, K. B. *Acta Crystallogr.* **1994**, *D50*, 603–613.
(59) Durbin, S. D.; Carlson, W. E. *J. Cryst. Growth* **1992**, *122*, 71–79.
(60) Durbin, S. D.; Feher, G. *Annu. Rev. Phys. Chem.* **1996**, *47*, 171–204.
(61) Nakada, T.; Sazaki, G.; Miyashita, S.; Durbin, S. D.; Komatsu, H. *J. Cryst. Growth* **1999**, *196*, 503–510.
(62) De Yoreo, J. J.; Vekilov, P. G. *Biomineralization* **2003**, *54*, 57–93.
(63) Onuma, K.; Tsukamoto, K.; Sunagawa, I. *J. Cryst. Growth* **1988**, *89*, 177.
(64) Maiwa, K.; Tsukamoto, K.; Sunagawa, I. *J. Cryst. Growth* **1990**, *102*, 43–53.
(65) Onuma, K.; Tsukamoto, K.; Nakadate, S. *J. Cryst. Growth* **1993**, *123*, 706–718.
(66) Dold, P.; Ono, E.; Tsukamoto, K.; Sazaki, G. *J. Cryst. Growth* **2006**, *293*, 102–109.
(67) Lin, H.; Vekilov, P. G.; Rosenberger, F. *J. Cryst. Growth* **1996**, *158*, 552–559.
(68) Vekilov, P. G.; Lin, H.; Rosenberger, F. *Phys. Rev. E* **1997**, *55*, 3202–3214.
(69) Vekilov, P. G.; Thomas, B. R.; Rosenberger, F. *J. Phys. Chem. B* **1998**, *102*, 5208–5216.
(70) Vekilov, P. G.; Rosenberger, F. *J. Cryst. Growth* **1998**, *186*, 251–261.
(71) Kuznetsov, Y. G.; Malkin, A. J.; Geenwood, A.; McPherson, A. *J. Struct. Biol.* **1995**, *114*, 184–196.
(72) Pusey, P. N.; Van Megen, W. *Nature* **1986**, *320*, 340–343.
(73) Van Megen, W.; Underwood, S. M. *Nature* **1993**, *362*, 616–619.
(74) Frank, F. C. *Discuss. Faraday Soc.* **1949**, *5*, 48–186.
(75) Burton, W. K.; Cabrera, N.; Frank, F. C. *Phil. Trans. R. Soc. London Ser. A* **1951**, *243*, 299–360.
(76) Stranski, I. N; Kaischew, R. *Z. Phys. Chem.* **1934**, *B 26*, 100–113.
(77) Kaischew, R. *Z. Phys.* **1936**, *102*, 684–690.
(78) Gliko, O.; Pan, W.; Katsonis, P.; Neumaier, N.; Galkin, O.; Weinkauf, S.; Vekilov, P. G. *J. Phys. Chem. B* **2007**, *111*, 3106–3114.
(79) Gliko, O.; Neumaier, N.; Pan, W.; Haase, I.; Fischer, M.; Bacher, A.; Weinkauf, S.; Vekilov, P. G. *J. Am. Chem. Soc.* **2005**, *127*, 3433–3438.
(80) Gliko, O.; Neumaier, N.; Pan, W.; Haase, I.; Fischer, M.; Bacher, A.; Weinkauf, S.; Vekilov, P. G. *J. Cryst. Growth* **2005**, *275*, e1409–e1416.
(81) Pan, W.; Galkin, O.; Filobelo, L.; Nagel, R. L.; Vekilov, P. G *Biophys. J.* **2007**, *92*, 267–277.
(82) Jacob, J.; Anisimov, M. A.; Sengers, J. V.; Oleinikova, A.; Weingartner, H.; Kumar, A. *Phys. Chem. Chem. Phys.* **2001**, *3*, 829–831.
(83) Kuznetsov, Y. G.; Malkin, A. J.; McPherson, A. *Phys. Rev. B* **1998**, *58*, 6097–6103.
(84) Malkin, A. J.; Kuznetsov, Y. G.; Land, T. A.; DeYoreo, J. J.; McPherson, A. *Nat. Struct. Biol.* **1996**, *2*, 956–959.
(85) Malkin, A. J.; McPherson, A. In *From Fluid-Solid Interfaces To Nanostructural Engineering. Vol. 2. Assembly in Hybrid and Biological Systems*; De Yoreo, J. J., Lui, X. Y., Eds.; Plenum/Kluwer Academic: New York, 2004; pp 201–238.
(86) Chernov, A. A.; Komatsu, H. In *Science and Technology of Crystal Growth*; van der Eerden, J. P., Bruinsma, O. S. L.; Eds.; Kluwer Academic: Dordrecht, 1995; pp 67–80.
(87) Eyring, H.; Lin, S. H.; Lin, S. M. *Basic Chemical Kinetics*; John Wiley and Sons: New York, 1980.
(88) Houston, P. L. *Chemical Kinetics and Reaction Dynamics*; McGraw-Hill Higher Education: New York, 2001.
(89) Filobelo, L. F.; Galkin, O.; Vekilov, P. G. *J. Chem. Phys.* **2005**, *123*, 014904.
(90) Eaton, W. A.; Hofrichter, J. In *Advances in Protein Chemistry*; Anfinsen, C. B., Edsal, J. T., Richards, F. M, Eisenberg, D. S., Eds.; Academic Press: San Diego, 1990; Vol. 40, pp 63–279.
(91) Galkin, O.; Vekilov, P. G. *J. Mol. Biol.* **2004**, *336*, 43–59.
(92) Gibbs, J. W. *Trans. Connect. Acad. Sci.* **1878**, *16*, 343–524.
(93) Gibbs, J. W. *The Scientific Papers of J. W. Gibbs. Volume One Thermodynamics*; Oxbow Press: Woodbridge, Connecticut, 1993.
(94) Harrison, P. M.; Arosio, P. *Biochim. Biophys. Acta* **1996**, *1275*, 161–203.
(95) Hempstead, P. D.; Yewdall, S. J.; Fernie, A. R.; Lawson, D. M.; Artymiuk, P. J.; Rice, D. W.; Ford, G. C.; Harrison, P. M. J. *Mol. Biol* **1997**, *268*, 424–448.
(96) Yau, S.-T.; Thomas, B. R.; Galkin, O.; Gliko, O.; Vekilov, P. G. *Proteins: Struct. Funct., Genet.* **2001**, *43*, 343–352.
(97) Swartzentruber, B. S.; Mo, Y.-W.; Kariotis, R.; Lagally, M. G.; Webb, M. B. *Phys. Rev. Lett.* **1990**, *65*, 1913–1916.
(98) Lawson, D. M.; Artymiuk, P. J.; Yewdall, S. J.; Smith, J. M. A.; Livingstone, J. C.; Trefry, A.; Luzzago, A.; Levi, S.; Arosio, P.; Cesareni, G.; Thomas, C. D.; Shaw, W. V.; Harrison, P. M. *Nature* **1991**, *349*, 541–544.
(99) Yau, S.-T.; Thomas, B. R.; Vekilov, P. G. *Phys. Rev. Lett.* **2000**, *85*, 353–356.
(100) Ihle, T.; Misbah, C.; Pierre-Louis, O. *Phys. Rev. B* **1998**, *58*, 2289–2309.
(101) Pimpinelli, A.; Villain, J.; Wolf, D. E.; Metois, J. J.; Heyraud, J. C.; Elkinari, I.; Uimin, G. *Surf. Sci.* **1993**, *295*, 143–153.
(102) Yau, S.-T.; Petsev, D. N.; Thomas, B. R.; Vekilov, P. G. *J. Mol. Biol.* **2000**, *303*, 667–678.
(103) Georgiou, D. K.; Vekilov, P. G. *Proc. Natl. Acad. Sci. U. S. A.* **2006**, *103*, 1681–1686.
(104) Bergeron, L.; Filobelo, L.; Galkin, O.; Vekilov, P. G. *Biophys. J.* **2003**, *85*, 3935–3942.
(105) Markov, I. V. *Crystal Growth for Beginners. Foundations of Nucleation, Crystal Growth and Epitaxy*; World Scientific: Singapore, 1995.
(106) Markov, I. V. *Crystal Growth for Beginners. Foundations of Nucleation, Crystal Growth and Epitaxy*, 2nd ed.; World Scientific: Singapore, 2003.
(107) Voronkov, V. V. *Sov. Phys.-Crystallogr.* **1970**, *15*, 8–13.
(108) Davis, K. J.; Dove, P. M.; De Yoreo, J. J. *Science* **2000**, *290*, 1134–1137.
(109) Chernov, A. A.; Rashkovich, L. N.; Yamlinski, I. V.; Gvozdev, N. V. *J. Phys.: Condens. Matter* **1999**, *11*, 9969–9984.
(110) Hooks, D. E.; Yip, C. M.; Ward, M. D. *J. Phys. Chem. B* **1998**, *102*, 9958–9965.
(111) Kellogg, G. L. *Phys. Rev. Lett.* **1994**, *73*, 1833–1836.
(112) Sholl, D. S.; Skodje, R. T. *Phys. Rev. Lett.* **1995**, *75*, 3158–3161.
(113) Lyuksyutov, I.; Naumovets, A. G.; Pokrovsky, V. *Two-Dimensional Crystals*; Academic Press: Boston, 1992.
(114) Schwartz, D. K. *Annu. Rev. Phys. Chem.* **2001**, *52*, 107–137.
(115) Georgiou, D. K. Masters Thesis, University of Houston, 2003.
(116) Mullins, W. W.; Sekerka, R. F *J. Appl. Phys.* **1963**, *34*, 323–329.
(117) Bales, G. S.; Zangwill, A. *Phys. Rev. B* **1990**, *41*, 5500–5508.
(118) Halban, P.; Mutkoski, R.; Dodson, G.; Orci, L. *Diabetologia* **1987**, *30*, 348–353.
(119) Baker, E. N.; Blundell, T. L.; Cutfield, J. F.; Cutfield, S. M.; Dodson, E. J.; Dodson, G. G.; Crowfoot-Hodgkin, D. M.; Hubbard, R. E.; Isaacs, N. W.; Reynolds, C. D.; Sakabe, K.; Sakabe, N.; Vijayan, N. M. *Phil. Trans. R. Soc. London* **1988**, *B319*, 369–456.
(120) Carroll, R. J.; Hammer, R. E.; Chan, S. J.; Swift, H. H.; Rubenstein, A. H.; Steiner, D. F. *Proc. Natl. Acad. Sci. U. S. A.* **1988**, *85*, 8943–8947.
(121) Kramers, H. A. *Physica A* **1940**, *7*, 284–304.
(122) Hänggi, P.; Talkner, P.; Borkovec, M. *Rev. Mod. Phys.* **1990**, *62*, 251–341.
(123) Berry, P. S.; Rice, S. A.; Ross, J. *Physical Chemistry*; 2nd ed. Oxford University Press: New York, 2000.
(124) Eisenberg, D.; Crothers, D. *Physical Chemistry with Applications to Life Sciences*; The Benjamin/Cummins: Menlo Park, 1979.
(125) Massover, W. H. *Micron* **1993**, *24*, 389–437.
(126) Petsev, D. N.; Thomas, B. R.; Yau, S.-T.; Vekilov, P. G. *Biophys. J.* **2000**, *78*, 2060–2069.
(127) Petsev, D. N.; Chen, K.; Gliko, O.; Vekilov, P. G. *Proc. Natl. Acad. Sci. U. S. A.* **2003**, *100*, 792–796.
(128) Vekilov, P. G.; Monaco, L. A.; Rosenberger, F. *J. Cryst. Growth* **1995**, *146*, 289–296.
(129) Gliko, O.; Booth, N. A.; Rosenbach, E.; Vekilov, P. G. *Cryst. Growth Des.* **2002**, *2*, 381–385.
(130) Smoluchowski, M *Phys. Z.* **1916**, *17*, 557–585.

(131) von Smoluchowski, M. *Z. Phys. Chem.* **1918**, *92*, 129–135.
(132) Zel'dovich, Y. B. *Acta Physicochim. URSS* **1943**, *18*, 1–22.
(133) Garcia-Ruiz, J. M.; Moreno, A. *J. Cryst. Growth* **1997**, *178*, 393–401.
(134) Hou, W. B.; Kudryavtsev, A. B.; Bray, T. L.; DeLucas, L. J.; Wilson, W. W. *J. Cryst. Growth* **2001**, *232*, 265–272.
(135) Svergun, D. I.; Richard, S.; Koch, M. H.; Sayers, Z.; Kuprin, S.; Zaccai, G. *Proc. Natl. Acad. Sci. U. S. A.* **1998**, *95*, 2267–2272.
(136) Leckband, D.; Israelachvili, J. *Q. Rev. Biophys.* **2001**, *34*, 105–267.
(137) Raviv, U.; Klien, J. *Science* **2002**, *297*, 1540–1543.
(138) Ball, P. *Nature* **2003**, *423*, 25–26.
(139) Pal, S. K.; Zewail, A. H. *Chem. Rev.* **2004**, *104*, 2099–2124.
(140) Bhattacharyya, S. M.; Wang, Z.-G.; Zewail, A. H. *J. Phys. Chem. B* **2003**, *107*, 13218–13228.
(141) Chalikian, T. V.; Plum, G. E.; Sarvazyan, A. P.; Breslaver, K. J. *Biochemistry* **1994**, *33*, 8629–8640.
(142) Chalikian, T. V.; Völker, J.; Srinivasan, A. R.; Olson, W. K.; Breslauer, K. J. *Biopolymers* **1999**, *50*, 459–471.
(143) Finkelstein, A.; Janin, J. *Protein Eng.* **1989**, *3*, 1–10.
(144) Tidor, B.; Karplus, M. *J. Mol. Biol.* **1994**, *238*, 405–414.
(145) Fersht, A. *Structure and Mechanism in Protein Science*; W. H. Freeman: New York, 1999.
(146) Vekilov, P. G.; Feeling-Taylor, A. R.; Yau, S.-T.; Petsev, D. N. *Acta Crystallogr.* **2002**, *D58*, 1611–1616.
(147) Schall, C.; Arnold, E.; Wiencek, J. M. *J. Cryst. Growth* **1996**, *165*.
(148) Petsev, D. N.; Thomas, B. R.; Yau, S.-T.; Tsekova, D.; Nanev, C.; Wilson, W. W.; Vekilov, P. G. *J. Cryst. Growth* **2001**, *232*, 21–29.
(149) Israelachvili, J. N. *Intermolecular and Surface Forces*; Academic Press: New York, 1995.
(150) Tanford, C. *The Hydrophobic Effect: Formation of Micelles and Biological Membranes*; John Wiley & Sons: New York, 1980.
(151) Eisenberg, D.; Kauzmann, W. *The Structure and Properties of Water*; University Press: Oxford, 1969.
(152) Dunitz, J. D. *Science* **1994**, *264*, 670.
(153) Vekilov, P. G. In *Methods in Enzymology, Volume 368, Macromolecular Crystallography, Part C*; Carter, C. W., Sweet, R. M., Eds.; Academic Press: San Diego, 2003; pp 84–105.
(154) Lin, H.; Petsev, D. N.; Yau, S.-T.; Thomas, B. R.; Vekilov, P. G. *Cryst. Growth Des.* **2001**, *1*, 73–79.
(155) Georgiou, D. K. Phase transitions in insulin solutions and possible implications in living organisms, Ph.D. Dissertation, University of Houston, Houston, 2006.
(156) De Yoreo, J. J. In *13th International Conference on Crystal Growth*; Hibiya, T., Mullin, J. B., Uwaha, M., Eds.; Elsevier: Kyoto, Japan, 2001.
(157) Oki, H.; Matsuura, Y.; Komatsu, H.; Chernov, A. A. *Acta Crystallogr.* **1999**, *D55*, 114–121.
(158) Chernov, A. A.; Komatsu, H. In *Science and Technology of Crystal Growth*; van der Eerden, J. P., Bruinsma, O. S. L., Eds.; Kluwer Academic: Dordrecht, 1995; pp 329–353.
(159) Doi, M.; Edwards, S. F. *The Theory of Polymer Dynamics*; Clarendon Press: Oxford 1986.
(160) Malkin, A.; Kuznetsov, Y.; McPherson, A. *Surf. Sci.* **1997**, *393*, 95–107.
(161) Vekilov, P. G. In *Studies and Concepts in Crystal Growth*; Komatsu, H., Ed.; Pergamon: Oxford, 1993; pp 25–49.
(162) Vekilov, P. G.; Rosenberger, F. *J. Cryst. Growth* **1996**, *158*, 540–551.
(163) Kuznetsov, Y. G.; Konnert, J.; Malkin, A. J.; McPherson, A. *Surf. Sci.* **1999**, *440*, 69–80.
(164) Elhadj, S.; De Yoreo, J. J.; Hoyer, J. R.; Dove, P. M. *Proc. Natl. Acad. Sci. U. S. A.* **2006**, *103*, 19237–19242.
(165) Hopp, T. P.; Woods, K. R. *Proc. Natl. Acad. Sci. U. S. A.* **1981**, *78*, 3824–3828.

CG070427I

9. Epitaxial and Vapor Phase Growth

Reprinted from The Handbook of Crystal Growth, Vol 3B, 2nd Edition, Chapter 21, Thomas F Kuech, Metal Organic Vapor Phase Epitaxy Chemical Kinetics 869-907, Copyright 2015, with permission from Elsevier .

21 Metal Organic Vapor Phase Epitaxy Chemical Kinetics

Thomas F. Kuech

DEPARTMENT OF CHEMICAL AND BIOLOGICAL ENGINEERING, UNIVERSITY OF WISCONSIN–MADISON, MADISON, WI, USA

CHAPTER OUTLINE

21.1 Introduction to MOVPE 870
21.1.1 Phenomenological Description of the MOVPE 871
21.1.2 Organometallic Compounds Used in MOVPE 873
21.2 Thermochemical Aspects of the MOVPE Growth Process 876
21.3 Chemical Kinetic Processes within the MOVPE System 879
21.3.1 Simple Theory of Kinetic Rates and Processes 879
21.3.2 Homogeneous Gas Phase Kinetics 880
21.3.3 Heterogeneous Reactions 881
21.3.3.1 Nature of the Surface Structure 881
21.3.3.2 Heterogeneous Reactions 883
21.3.3.3 Surfactants 886
21.4 Reaction Kinetics of Organometallic Compounds 887
21.4.1 Determination of the Gas Phase and Surface Kinetic Processes 887
21.4.2 Gallium Sources 887
21.4.3 Aluminum Sources 890
21.4.4 Indium Sources 891
21.5 Reaction Kinetics of Group 15 Compounds 891
21.5.1 Arsenic and Phosphorus Sources 891
21.5.2 Nitrogen, Group 12, and Antimony Sources 892
21.5.3 Reactions between Precursors 893
21.6 Growth Reactions 896
21.6.1 Empirical Models 897
21.6.2 Large-Scale Computational Models 898
21.7 Conclusion 902
References 902

Handbook of Crystal Growth. http://dx.doi.org/10.1016/B978-0-444-63304-0.00021-4
Copyright © 2015 Elsevier B.V. All rights reserved.

21.1 Introduction to MOVPE

Chemical vapor deposition (CVD) is perhaps the most widely used thin-film deposition technique for the formation of advanced electronic and optoelectronic materials. It is used for commercial applications because of its ability to deposit over broad substrate areas at moderately high growth rates. It has moderately high efficiencies in terms of reactant utilization and uses lower temperatures than the bulk crystal growth techniques forming the same materials. CVD in its many embodiments has been used to deposit thin films, from nanometers to millimeters thick, of all classes of materials, including metals, oxides, insulators, and, of course, semiconductors. The versatility of CVD increases principally from two sources: use of low-pressure gas phase transport and the range of chemical precursors available. The gas phase transport of these source materials at a moderate pressure, typically less than 1 atm, can be rapid. The rapid transport of reactants at moderate gas phase temperatures minimizes the influence of chemical reactions within the gas phase. The elimination of extensive reaction and product formation in the gas phase allows for the reactants to reach the growth surface and provide for a higher reactant utilization. Reactant utilization is defined as the ratio of the reactants input into the reactor to the film produced. This gas phase transport can simplify the growth process and reduce the dependence of the growth rate and film properties on detailed parameters present over the substrate.

The reactor conditions can be chosen to simplify the growth process and improve process control, but it is the wide array of chemical sources that has allowed CVD to contribute to the formation of almost all classes of materials. Early embodiments of CVD initially focused on readily available reactants with sufficient purity. In the case of semiconductors, the earliest demonstrations of thin-film formation, particularly epitaxial films, relied on the use of volatile halides. These halides were generally formed in situ and were the high temperature forms of the room temperature compounds. For example, GeI_2 or GaCl could be formed through the high temperature reaction of the element, Ge or Ga, with the halide. Although the initial demonstrations of CVD were performed in closed tube reactors, open flow systems were used to improve control over the thin-film properties and increase reactor throughput. The range of inorganic reactants that provided sufficient volatility at moderate temperatures was, however, limited. The use of metal organic reactants greatly expands the range of potential sources that are available for CVD-based thin-film formation. The range of possible metal-organic compounds is large because of the versatility and synthetic capability of organic chemists. The attachment of organic ligands to a source atom can affect several critical properties when developing a source reagent. The volatility, or vapor pressure, of the source can be altered through the choice of organic ligand. Perhaps more importantly, organometallic compounds (alias metal organic compounds) greatly increase the range of possible reaction pathways that can be used to generate the film. The use of organometallic compounds in the CVD process has led to the development of a process known as metal organic chemical vapor deposition (MOCVD or OMCVD), and in the case where the

resulting film is grown epitaxially on the substrate, metal organic vapor phase epitaxy (MOVPE). There is a long-standing discussion on the appropriate descriptor for this process. The terms MOCVD/MOVPE were initially used by H. Manasevit [1,2] in a series of articles that are considered by most to have initiated the interest and tremendous growth in this process. The terms OMCVD/MOVPE are also commonly used in deference to the chemical class of precursors. These terms can be used interchangeably and, in this chapter, I will defer to the initial use of the term by Manasevit. MOVPE has become the dominant technology, at present, for the formation of electronic and optoelectronic devices made from compound semiconductors. Growth of Si, Ge, and associated alloys generally uses hydrides or halogenated source compounds, such as SiH_2Cl_2 or SiH_4.

The object of any crystal growth process is to create materials of controlled structure and composition, including the relevant optical electrical properties, at a controlled rate with high uniformity over large areas of interest. To control the rate, an understanding of those transport and reaction steps that comprise the crystal growth process is required. The transport environment and the chemical kinetics required in this process are linked. The film itself will be a function of those reactions occurring homogeneously in the gas phase that determine the distribution of chemical species arriving at the growth front. These reactions, if present, determine the chemical species that participate in the heterogeneous or surface reactions. These final steps at the growth front form the class of heterogeneous reaction pathways that lead to the final film composition and properties. Given the richness of chemical structure of organometallic compounds, there can be a wide variety of reaction pathways and kinetics operating during the growth process.

21.1.1 Phenomenological Description of the MOVPE

A detailed description of the CVD process, and specifically the MOCVD process, is given in other chapters within Volume 3. It is useful to briefly describe in phenomenological terms the CVD process to understand those steps within the process where chemical kinetics can play a dominant role. The reactants are introduced into the reactor diluted by a carrier gas. The gas phase temperature is generally at or near room temperature until the gas approaches the heated growth front. The growth front is typically a semiconductor substrate that resides on a heated platen or susceptor. Reactor walls are usually unheated or possibly even actively cooled to control the wall temperature. The walls of the reactor are heated by radiative heat transport, which can be from the hot substrate and its holder. Substrate temperatures are generally between 200 and 1100 °C, depending on the choice of material system. Low melting point materials, such as InSb, or materials where the film constituents require a high elemental vapor pressure in the gas phase (e.g., CdTe) are grown at lower temperatures. SiC and GaN and related compounds require elevated temperatures for control over structural material properties during growth. Control over the temperatures in the susceptor region of the reactor, in turn, dictates the temperature profile of the flowing gas environment. Once at temperature, the gas phase environment is generally considered to be at steady state. The heat

and mass transport present inside a typical reactor are described in Chapter 3 of Volume 3B. The thermal environment within the reactor is characterized by steep temperature gradients near the heated growth front and is a function of the fluid flow within the reactor. Source molecules, on entering the reactor, are transported to the growth front. Along this transport path, the source material can experience a rapidly changing thermal environment, going from near room temperature to the substrate temperature. While being transported, these growth reactants can undergo possible gas phase reactions. These gas phase reactions can lead to changes in the chemical composition of gas phase. Growth reactants can undergo partial unimolecular decomposition, react with the carrier gas, or react with other chemical species within this flowing and heated gas phase environment. The extent of these gas phase reactions will determine the chemical nature of the specific chemical species reaching the growth front and comprise the set of chemical reactions termed homogeneous gas phase reactions. Within an MOVPE reactor, the gas phase environment will have gradients of both temperature and the wide variety of chemical species that are serving both as reactants and byproducts. Although within a local environment the gas phase will appear homogeneous, on a larger scale the local chemical environment will be a function of position within the reactor.

The substrate surface, and perhaps the substrate holder, serve as the site of the reactions that result in film formation. These reactions are termed heterogeneous reactions because of their occurrence at the surface. As will be described in more detail, the nature of these heterogeneous reactions will depend on the flux to the surface, the nature of the surface itself in terms of its stoichiometry, crystallographic structure, coverage by various chemical species, and the temperature. This chemical environment is difficult to characterize except in well-controlled and defined experimental situations. The chemical species on the surface will consist of the parent source reactants, any fragments or daughter products, and reaction byproducts. The surface can also contain other chemical species that are either contaminants or perhaps part of the gas phase chemical environment that could lead to incorporation of additional species into the growing film.

The growth rate in the MOVPE technique typically exhibits three distinct temperature regimes as a function of substrate temperature. These three regimes correspond to regions where different kinetic or mass transport processes determine the specific realized growth rate. These regimes are somewhat dependent on reactor design and operating conditions but in general provide an overall picture of the growth process. In Figure 21.1, the growth rate as a function of temperature and substrate crystallographic orientation for the growth of GaAs, when using trimethyl gallium (TMGa, $(CH_3)_3Ga$) and arsine (AsH_3), exhibits these three temperature regimes, which shift slightly with crystallographic orientation [3]. At the lowest growth temperatures, the growth rate is considered to be limited by a heterogeneous surface reaction occurring at the substrate surface. At the highest growth temperatures, the growth rate decreases with increasing temperature with an apparent (negative) activation energy. This decrease in growth rate has been attributed to either re-evaporation of the growing material into the gas stream or

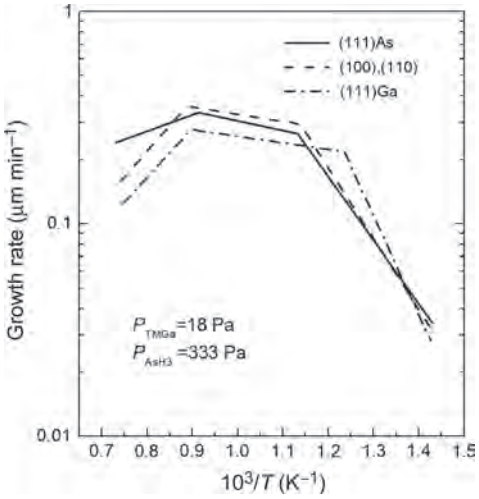


FIGURE 21.1 Growth rate versus reciprocal temperature for epitaxial layers on (100), (110), (111) Ga, and (111) As-oriented GaAs substrates when using $(CH_3)_3Ga$ and AsH_3. *Data obtained from reference, reprinted with permission from the Electrochemical Society [3].*

parasitic homogeneous gas phase reactions occurring because of the increased temperature of the flowing gas. The intermediate temperature regime shows little temperature dependence and is associated with a mass transport limitation to the growth rate. It is in this intermediate temperature regime that most MOVPE growth processes occur. The mass transport limitation is because of the rapid heterogeneous reactions occurring at the surface. The rate of consumption reactants at the surface exceeds their diffusional transport from the gas stream to the surface. This diffusional transport will be affected by factors such as the reactor pressure, gas phase boundary layer thickness, and growth temperature. A more detailed description of the MOVPE growth process can be found in many references, such as Volume 3A, Chapter 3, of this Handbook and Ref. [4]. A comprehensive reference on this process can be found in Stringfellow [5].

To fully describe this chemically rich environment, the detailed chemical kinetics of the reactants, carrier gas, and any reaction byproducts have to be characterized. The chemical kinetics can then be used in the development of reactor and growth models used to both design new CVD reactors and to characterize the growth process. Models generated using these chemical kinetics and the mass and thermal transport are also used to optimize a growth process and provide a means of process control.

21.1.2 Organometallic Compounds Used in MOVPE

Organometallic compounds span a wide range of chemical structures and composition. In general, there are favored classes of compounds for use in broad classes of CVD deposition. Because the chapter will be restricted to the epitaxial growth of compound semiconductors, those compounds used in the development of these thin

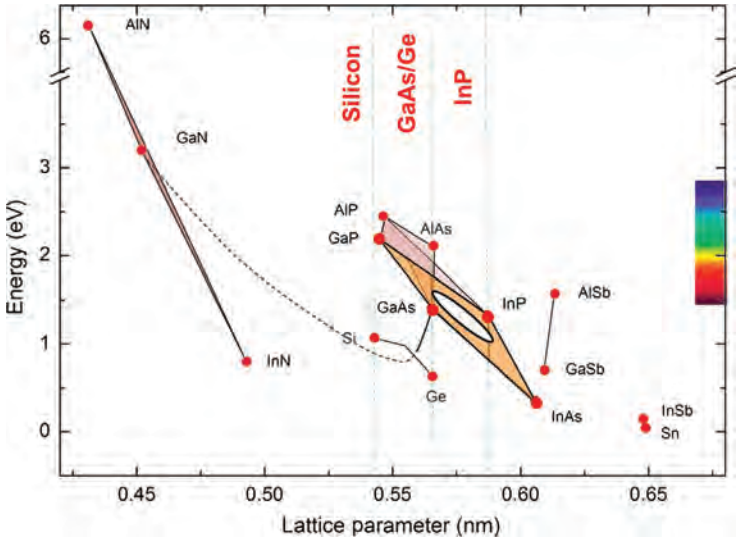


FIGURE 21.2 Energy band gap versus lattice parameter for the commonly used III–V and elemental semiconductors. Solid lines indicate the alloys that have been routinely synthesized by MOVPE. The shaded regions indicate regions of quaternary materials that have also been developed. Vertical lines indicate commercially available substrates that are most commonly used.

films will be highlighted. The range of compound semiconductors plotted is a function of the lattice parameter (Figure 21.2). The lines and shaded regions on this Figure correspond to those regions of composition that have been successfully produced. This is not an exhaustive range. The strength of the MOVPE technique is the ease by which multicomponent systems can be produced, leading to a large class of possible alloy systems.

The choice of source precursor depends on several practical considerations. The vapor pressure, controlled through the source temperature, must typically be greater than 0.1 Torr at or near room temperature. This provides for easy and sufficient mass transport into the reactor. Precursors should not interact with typical materials of construction, such as stainless steel or quartz, to allow unimpeded transport into the reactor. A consideration in the growth process is the specific reaction pathways and reaction products that result from thermal pyrolysis and reaction with the other supplied reactants. The final consideration is the ability to purify the source precursor to a high level, typically >99.999%, with respect to heavy metals and potential dopants. The synthetic routes used to create a source material need to be sufficiently developed to allow commercial availability. These considerations generally restrict the range of potential source molecules for compound semiconductor growth to relatively simple metal organic compounds and often to those that have use in other technology areas.

The additional constraints on the choice of precursor molecules lie in the reaction pathways available to the molecule both in the gas phase and on the growth surface. Required reaction pathways, facile at the growth temperatures used, should have minimal homogeneous gas phase reactions, and produce reaction byproducts with leaving groups that do not result in the incorporation of undesired impurities, which can alter the electrical properties of the film. The range of compounds has been generally restricted to simple alkyls, amines, and halogenated derivatives. In the case of the group 15 elements, such as As and P, the hydrides have been most commonly used: AsH_3 and PH_3. Organic compounds of these elements are also widely used and provide distinct advantages in terms of higher reactivity at lower temperatures and present a potentially lower safety hazard as a liquid source when compared with high-pressure compressed gas [6–8]. The most common nonhydride sources are t-butyl arsine ($C_4H_9AsH_2$) and t-butyl phosphine ($C_4H_9PH_2$), although other compounds have been used, such as trimethyl arsine [9,10] and dimethyl arsine [11,12]. The properties of these compounds can be found in common chemical handbooks or the literature from prominent chemical suppliers.

The metal, group 12 or 13, alkyls are either generally planar or linear molecules, as schematically shown in Figure 21.3. The deviation from linearity for these molecules depends on the specific ligand and metal atom. Trimethyl and triethyl aluminums are nearly associated in the dimeric form (the liquid and gas phases at room temperature) [13]. The dimeric form of trimethyl aluminum is schematically shown in Figure 21.3. These compounds do dissociate in the gas phase to the monomeric form at moderate, elevated temperatures [13]. The stoichiometry of the source compound must be taken into account when calculating the gas phase composition near the growth front during epitaxial growth. The group 12 metal alkyls tend to be linear molecules.

Group 15 metal organic compounds can have a variety of structures depending on the mix of ligands on the central atom. Most N, As, and P compounds used in MOVPE are trivalent. These molecules have three ligands with an additional lone pair orbital. This leads to a generally pyramidal structure with the angles dependent on the specific ligands. In the case of the hydride MH_3, the H–M–H bond angle decreases on this pyramidal structure from 107.8° → °93.6° → °91.8° → °91.3° when going from NH_3 to SbH_3. Stibine has not been used extensively in the growth of antimonide-based semiconductors [14–16] because of its low stability and tendency for decomposition before arrival at the growth front [17].

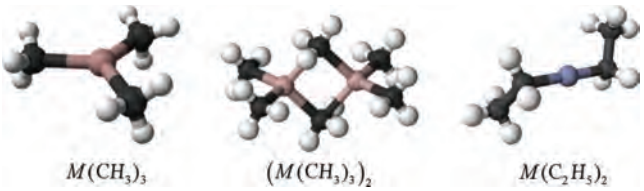


FIGURE 21.3 Commonly used precursors for metal organic vapor phase epitaxy exhibiting typical molecular forms.

21.2 Thermochemical Aspects of the MOVPE Growth Process

The starting point for the discussion of the chemical processes and reaction kinetics of the MOVPE growth process is the thermodynamic analysis of the overall growth process. Although the crystal growth process itself is not at equilibrium, the processes that take place in MOVPE under moderate growth temperatures are rapid. A local thermodynamic equilibrium can be considered to be established near the growth interface under many of the MOVPE growth conditions. The overall growth of the film occurs when there is a supersaturation in the gas phase that drives the system toward equilibrium. As an example, the growth of gallium arsenide from trimethyl gallium and arsine can be considered:

$$(CH_3)_3Ga + AsH_3 \Leftrightarrow 3CH_4 + GaAs; \quad \Delta G_{rxn}. \tag{21.1}$$

The free energy of reaction, ΔG_{rxn}, can be computed in the usual fashion from the free energy of formation, ΔG_f, of the constituent molecules:

$$\Delta G_{rxn} = \Delta G_f^{GaAs} + 3\Delta G_f^{CH_4} - \Delta G_f^{AsH_3} - \Delta G_f^{(CH_3)_3Ga}. \tag{21.2}$$

At thermodynamic equilibrium, considering only Eqn (21.1), the law of mass action would state at equilibrium:

$$K_{rxn} = e^{-\frac{\Delta G_{rxn}}{RT}} = \frac{a_{GaAs}P_{CH_4}^3}{P_{AsH_3}P_{(CH_3)_3Ga}P_T}. \tag{21.3}$$

where P_i is the partial pressure of the specific precursor, P_T is the total pressure, and a_{GaAs} is the activity of the solid GaAs, usually considered to be unity. In actuality, there are a wide number of possible reaction byproducts in this system at thermodynamic equilibrium. The availability of commercial programs to compute gas phase and solid equilibria among many species, with large databases, has allowed generation of the equilibrium composition for any set of chemical components. This has been performed for the expanded set of reactions beyond Eqn (21.1) associated with GaAs formation [18–20].

At the growth front, there is always some supersaturation, which serves as the driving force for growth. This supersaturation can be defined in terms of the partial pressures of the growth reactants related to that required by the law of mass action. The stability of the compound, such as GaAs, can also be described in terms of these mass action considerations. For the compound to be at thermodynamic equilibrium, the gas phase composition within the environment is restricted to values prescribed by:

$$\begin{gathered} Ga_v + \frac{1}{2}As_2 \Leftrightarrow GaAs; \quad \Delta G_f \\ K_{eq} = e^{-\frac{\Delta G_{rxn}}{RT}} = \frac{a_{GaAs}P_T^{3/2}}{P_{As_2\ eq}^{1/2}P_{Ga\ eq}} \end{gathered} \tag{21.4}$$

where P_{Ga} and P_{As_2} are the partial pressure of Ga and As at the growth front. As can exist as As_4 or As_2, as with most group 15 elements. There is a coupled range of values determined by Eqn (21.4) for $P_{Ga\ eq}$ and $P_{As_2\ eq}$. Within the range, the growing crystal will be stable, in that it will not decompose to create the necessary elemental activities in the gas phase. This is shown in Figure 21.4 [4,21]. For the crystal to grow, there must be sufficient supersaturation in the vapor phase. The degree of supersaturation, σ, is a measure of the deviation of the composition of the growth ambient from that indicated by Eqn (21.4).

$$\sigma = \frac{\Delta\mu}{RT}$$

$$\Delta\mu = \left[-RT \ln \left(\frac{a_{GaAs}P_T^{3/2}}{P_{As_2}^{1/2}P_{Ga}}\right)\right] - \left[-RT \ln \left(\frac{a_{GaAs}P_T^{3/2}}{P_{As_2\ eq}^{1/2}P_{Ga\ eq}}\right)\right] \tag{21.5}$$

$$\Delta\mu = RT \ln \left(\frac{P_{As_2}^{1/2}P_{Ga}}{P_{As_2\ eq}^{1/2}P_{Ga\ eq}}\right)$$

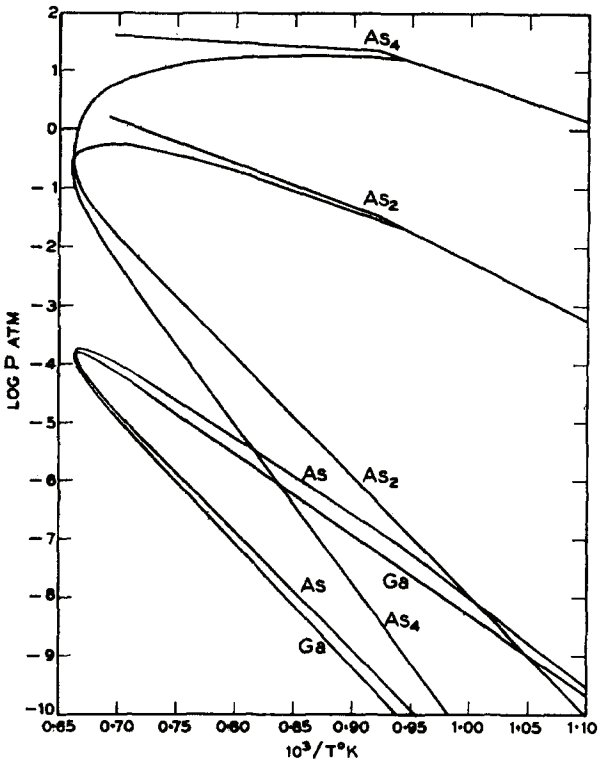


FIGURE 21.4 Equilibrium vapor pressures of As, As_2, As_4 and Ga defining the phase stability region for GaAs as a function of T^{-1}. *Taken from Ref. [21].*

For growth to occur, $\Delta\mu > 0$ or

$$P_{As_2}^{1/2} P_{Ga} > P_{As_2\ eq}^{1/2} P_{Ga\ eq} \tag{21.6}$$

and these partial pressures are developed by the decomposition of the growth precursors. Typically, the MOVPE of GaAs at atmospheric pressure takes place with a cation or $(CH_3)_3Ga$ mole fraction of $\sim 10^{-4}$ and a $AsH_3/(CH_3)_3Ga$ ratio of ~ 10. If all the precursors are decomposed to the elemental constituents, a comparison to Figure 21.4 indicates that the As_x pressure would always be in the range constrained to the regions of thermodynamic equilibrium, but the Ga pressure is several orders of magnitude over those in equilibrium, indicating a high supersaturation. This observation has often led to the conclusion that the MOVPE process is far from equilibrium for the process overall. Most MOVPE growth occurs in the nearly temperature-independent temperature regime of Figure 21.1, indicating a mass transport, rather than chemical kinetic limitation to the growth rate.

A typical growth rate in MOVPE under mass transport limited growth conditions is 3 μm h^{-1}, which corresponds to a $(CH_3)_3Ga$ mole fraction of $\sim 10^{-4}$ or a partial pressure of $\sim 10^{-4}$ atm. This is equal to a flux impinging on the surface, with unity sticking coefficient, of 2.3×10^{14} $cm^{-2}s^{-1}$. Such a flux corresponds to an equivalent partial pressure of 9.1×10^{-9} atm. The mass transport limitation reduces the arrival flux to the surface, hence limiting the growth rate. If there was no mass transport limitation and unity incorporation, the growth rate would be 33,000 μm h^{-1}! The equilibrium vapor pressure of Ga required for the phase stability of the GaAs at typical growth temperatures is less than $\sim 10^{-8}$–10^{-9} atm (Figure 21.4). These flux estimates indicate that the flux required to achieve the observed film growth rates is comparable with the vapor pressure present at the surface for stability of the GaAs surface and far less than the availability of growth precursor in the bulk of the gas phase. Stringfellow used a similar analysis in reaching the conclusion that the MOVPE growth surface is near thermodynamic equilibrium under typical mass transport limited growth conditions used for most materials [22]. A high supersaturation is, therefore, not present at the growth front and the MOVPE growth front is considered near equilibrium under typically used growth conditions. The overall supersaturation is, therefore, dropped across the precursor gradient through gas phase boundary layer above the growth surface, as shown schematically in Figure 21.5.

The deviation of the growth rate from this mass transport limited growth behavior, particularly at low growth temperatures, is because of the reduced rate of decomposition of the growth sources. In the mass transport limited regime, the rate of decomposition is much faster than the transport rate. At a GaAs growth rate of 0.05 μm min^{-1}, the time to complete one monolayer of GaAs is 340 ms or a characteristic time constant of 3 s^{-1}. If a characteristic time for any of the chemical reaction processes, such as decomposition or reaction product desorption, approaches these times, there will be a kinetic limitation to the growth process and a deviation from mass transport limited growth. In both the mass transport limited and kinetically limited regimes, the growth and surface chemistry can

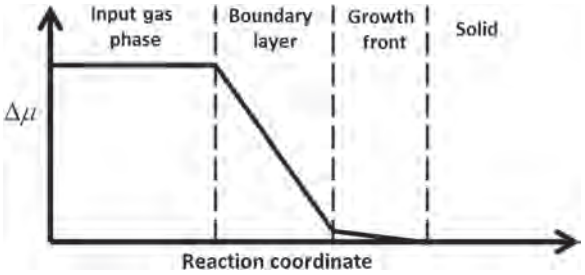


FIGURE 21.5 The chemical potential of the MOVPE system is dropped across the boundary layer under most typical growth conditions leaving the growth front near equilibrium. *Adapted from Ref. [23].*

be important in determining local morphology, impurity incorporation, and interface structure.

21.3 Chemical Kinetic Processes within the MOVPE System

21.3.1 Simple Theory of Kinetic Rates and Processes

Chemical reactions are typically presented in terms of a balanced mass action relationship, such as that shown in Eqn (21.4). The equilibrium coefficient is a function of temperature and can also be expressed in terms of the two rates corresponding to the forward and reverse reaction.

$$\begin{aligned} \mathrm{Ga}(v) + \frac{1}{2}\mathrm{As}_2(v) &\xrightarrow{k_f} \mathrm{GaAs}; \quad \frac{d[\mathrm{GaAs}]}{dt} = k_f[\mathrm{Ga}][\mathrm{As}_2]^{1/2} \\ \mathrm{GaAs} &\xrightarrow{k_r} \mathrm{Ga}(v) + \frac{1}{2}\mathrm{As}_2(v) \quad \frac{d[\mathrm{Ga}]}{dt} = k_r[\mathrm{GaAs}] \end{aligned} \tag{21.7}$$

At equilibrium, these rates are equal, which leads to the familiar mass action relationship:

$$\begin{aligned} k_f[\mathrm{Ga}][\mathrm{As}_2]^{1/2} &= k_r[\mathrm{GaAs}] \\ K_{eq} = \frac{k_r}{k_f} = \frac{[\mathrm{GaAs}]}{[\mathrm{Ga}][\mathrm{As}_2]^{1/2}} &= \frac{a_{\mathrm{GaAs}}}{\left(\frac{P_{\mathrm{Ga}}}{P_T}\right)\left(\frac{P_{\mathrm{As}_2}}{P_T}\right)^{1/2}} \end{aligned} \tag{21.8}$$

This relationship allows the determination of the forward (reverse) rate constant, k_i, once one of the rates and the equilibrium constant are known. The reaction rates do not have to follow the stoichiometry coefficients, as indicated in Eqns (21.7) and (21.8). In practice, the reaction rate is typically determined through experiment and is parameterized as follows:

$$aA + bB \rightarrow cC + dD; \quad Rate = k_f[A]^m[B]^n \tag{21.9}$$

where m and n are the reaction rate orders of the reaction and not necessarily equal to the stoichiometry coefficients, a–d. The reactants in the gas phase will exchange energy on collision with another reactant or the inert carrier gas. For a reaction to occur, the

source molecule goes through an intermediate or transition state that typically requires some additional energy. This transition state is characterized by a threshold energy, sometimes called an activation energy. In general, the reaction rate coefficient is a function of temperature:

$$k_i = k_{0i} e^{-\Delta G_i^{\dagger}/k_B T} \tag{21.10}$$

with $\Delta G_i^{\dagger}$ as the energy associated with the transition state of the ith process and k_{0i} is the pre-exponential constant [24]. This formalism is used for gas phase or homogeneous reactions as well as surface or heterogeneous reactions [25].

21.3.2 Homogeneous Gas Phase Kinetics

There are many reaction pathways through which the heated molecule will undergo unimolecular decomposition at elevated temperatures [26,27]. The rate constant for these reactions can also have a strong pressure, in addition to temperature, dependence. This pressure dependence is particularly pronounced at low pressure and when dealing with small molecules, such as NH_3. The theory of unimolecular gas phase reactions is well developed to account for the influence of pressure-based collisional energy transfer needed to provide the necessary energy to drive the decomposition reaction. A simplified analysis of the collisional activations leads to a pressure dependence to the rate constant and reduces to simpler forms at pressure extremes.

$$\begin{aligned} k_i(P,T) &= \frac{k_{i,1}k_{i,2}[M]}{k_{i,-1}[M] + k_{i,2}} \\ k_i(\infty,T) &= \frac{k_{i,1}k_{i,2}}{k_{i,-1}};\ \text{pressure independent at high pressures} \\ k_i(P,T) &= k_{i,1}[M];\ \text{proportional to pressure at low pressures} \end{aligned} \tag{21.11}$$

Expressing the rates associated with the generic unimolecular reaction of A decomposing homogeneously to B and C as reaction by products:

$$\begin{gathered} A \xrightarrow{k_i(P,T)} B + C \\ A + M \underset{k_{i,-1}}{\overset{k_{i,1}}{\rightleftharpoons}} A^* + M \\ A^* \xrightarrow{k_{i,2}} B + C \end{gathered} \tag{21.12}$$

in which M is an inert "bath gas," which provides the energy transfer through collisional processes. This dependence becomes important for small molecules that are more difficult to collisionally excite, such as AsH_3 and PH_3. This is seen in Figure 21.6, [26] which indicates that the rate constant for the unimolecular decomposition into the monohydride and H_2 is linear with pressure even at atmospheric pressure. This simple expression can be more fully developed through taking into account the vibrational mode structure of the reactant and the quantum mechanical aspects of the energy transfer process [28,29].

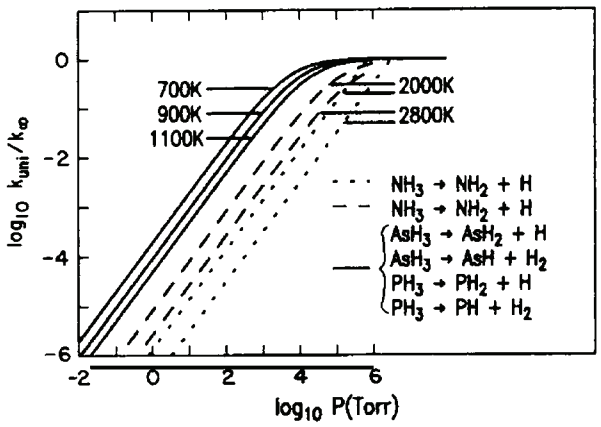


FIGURE 21.6 The unimolecular rate constant is a function of the temperature, and pressure for specific reactions and molecules [26].

The development of computational means, such as density function theory [30,31], has allowed for the direct calculation of these rate parameters to varying levels of accuracy, allowing some independence from experimental determination of these parameters. There have been many studies of the homogenous gas phase decomposition over a broad array of materials. Typical experimental studies have focused on sampling the gas phase environment within a well-defined flow geometry. A typical arrangement would be a simple tube often packed with additional materials to enhance the surface area. The reactor effluent is monitored by mass spectroscopic techniques or by optical spectroscopy. The change in surface area is used to determine whether there is strictly homogeneous gas phase decomposition or some measure of heterogeneous surface reactions taking place. The change in reaction products with time within the heated zone and with temperature and pressure are used to determine the decomposition reaction network and its thermal and time dependence. Examples of these techniques for the case of the homogeneous decomposition of arsine can be found in other studies [10,32,33]. Both the reaction network and the associated rate constants are needed to accurately determine the gas phase composition, in both concentration and identity, of the chemical species arriving at the growth front. Such information is needed to understand experimental growth behavior and develop a growth model. These growth models can be incorporated into more complex computational fluid, thermal, and chemical models of the reactor with predictions of the growth rate, composition, and often impurity content.

21.3.3 Heterogeneous Reactions

21.3.3.1 Nature of the Surface Structure

The growth surface of compound semiconductors and their alloys can be both structurally and chemically complex. The specific chemical composition of the growth surface depends on the crystallographic orientation of the substrate and is a strong function of the temperature and gas phase ambient, which can possess a wide variety of chemical

constituents. The growth of the film is because of the heterogeneous reaction of these chemical species arriving on the surface. The actual growth of the film is considered to consist of many elementary reaction steps, which themselves are a function of this complex environment.

In the absence and presence of chemical species other than the elements comprising the growing film, the surface will exhibit a specific structure referred to as a surface reconstruction. The surface crystallographic structure does not have to be the same as the bulk material generated by cleavage or termination of the bulk structure. Initially, the formation of a solid surface can be conceptually thought of as proceeding in two steps: (1) the solid is cleaved such that the new surface is exposed and the atoms are retained in their bulk positions, and (2) the atoms on the surface or at the near-surface regions are allowed to relax themselves to a new equilibrium position [34]. The relaxed arrangement would be affected further by any absorbed chemical species. Most epitaxial growth takes place on a single crystal substrate that has a well-defined overall orientation (e.g., (100) or (111)), within a certain accuracy. Often, the wafer will be specified to have a polished (100) surface with an intentional misorientation angle toward another major crystal direction (e.g., (100) tilted 2° toward the nearest $< 111 >$ direction). Such surfaces are often referred to as vicinal surfaces. This intentional or unintentional off-orientation of the wafer increases the structure on the wafer surface. The detailed surface structure is characterized by three separate, but related, features: terraces, kinks, and ledges along with surface vacancies, as schematically shown in Figure 21.7. These sites are both structurally and chemically distinct, offering different reaction pathways and rates to the adsorbed chemical reactants.

The advent of scanning tunneling microscopy (STM) has enabled the direct imaging of these surface structures under high vacuum condition. A prevalent GaAs reconstruction on the (001) surface is As-terminated (2×4) reconstruction characterized by the formation of As-dimers. This is shown in Figure 21.8. The surface reconstruction is often given in terms of Wood's notation, wherein the surface crystallography is described by the notation $(hkl)(n \times m)R\varphi$, where (hkl) and n and m describe the periodicity of the

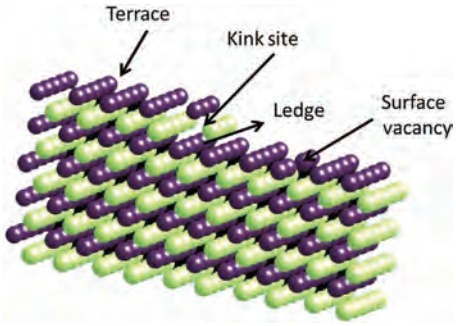


FIGURE 21.7 A schematic of a compound semiconductor surface indicating typical surface structures such as terraces, ledges (arrow drawn along ledge edge), kink sites and surface vacancies.

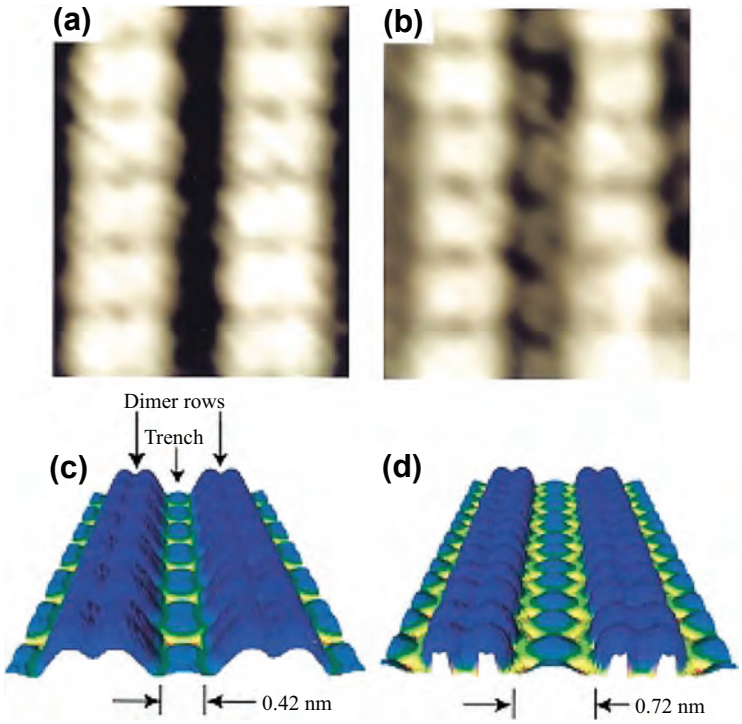


FIGURE 21.8 (a) and (b) 2.8 × 4.4 nm filled-state STM images of the same area acquired with sample biases of −3.0 and −2.1 V, respectively. (c) and (d) Simulated STM images using filled-state biases of 1.1 and 0.3 V below the valence band maximum, respectively. *The caption and image are directly taken from Ref. [35]. Copyright 1999 by The American Physical Society.*

surface unit cell in terms of the underlying, bulk, unit cell lengths. A (2×4) reconstruction would have the periodicity of twice and four times the underlying (001) unit cell aligned with the underlying bulk unit cell. The $R\varphi$ would indicate a rotation of the surface unit cell by an angle φ relative to the underlying bulk unit cell. Any chemical species must adsorb and react within the context of the surface geometry present, which can affect the reaction rates and products. GaAs itself can develop many different reconstructions, depending on the As and Ga activities present at the surface. These reconstructions are generally equilibrium structures and have been presented in the form of a phase diagram. One such phase diagram for GaAs (001) is presented in Figure 21.9 [36]. The presence of other chemical species can modify this surface structure substantially as in the case of Bi on the GaAs (001) surface, shown in Figure 21.10, where the nature of the structures and the range over which they appear change substantially [37].

21.3.3.2 Heterogeneous Reactions

The gas phase reactions determine the concentration and composition of the chemical species arriving at the growth front. Once arriving at the growth front, these species can

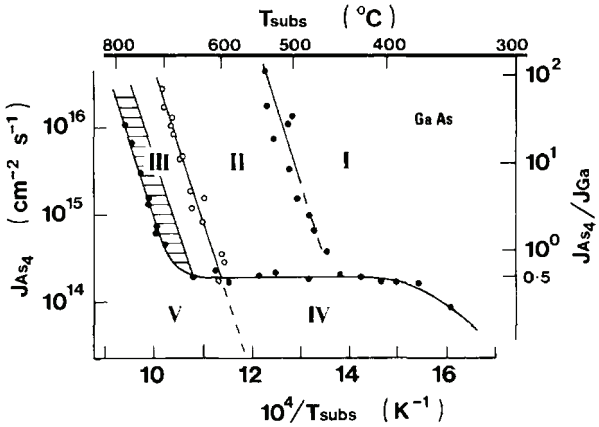


FIGURE 21.9 The surface reconstruction phase for (100) GaAs at fixed growth rate of 0.65 μm h^{-1} as a function of flux ration and total As flux impinging at the surface: Region I mixed (2 × 4)/c(4 × 4), Region II (2 × 4), Region III (1 × 1) bulk streaks, Region IV (4 × 2), Region V c(8 × 2) [36].

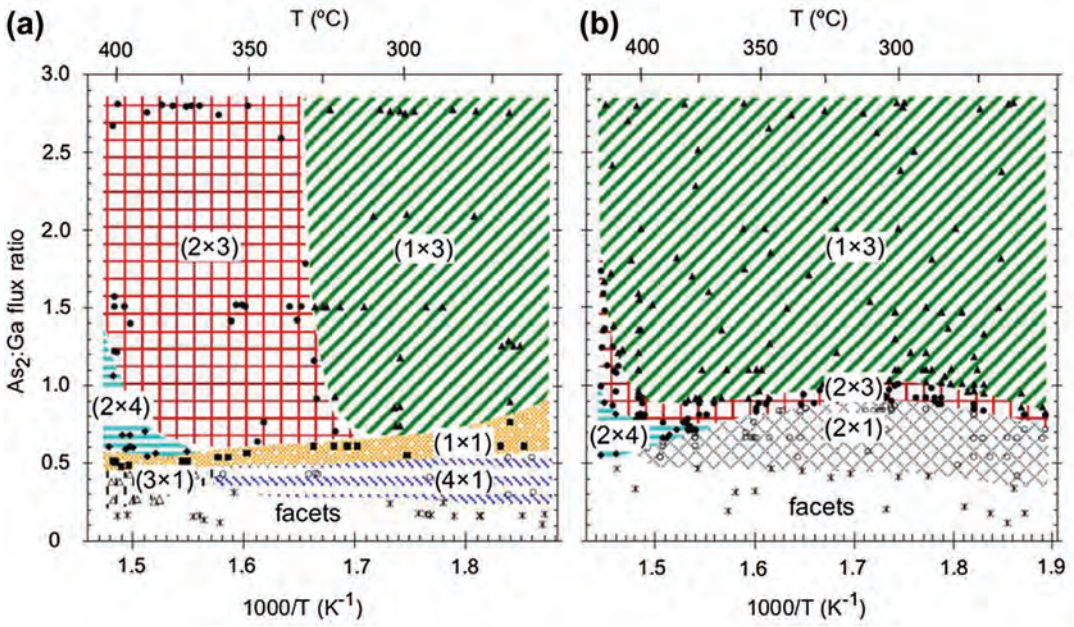


FIGURE 21.10 Surface reconstruction (a) GaAs (001) and (b) $GaAs_{1-y}Bi_y$ (001) over a substrate temperatures range of 250–425 °C and As_2:Ga flux ratio from 0 to 3 and in (b) a Bi beam equivalent pressure of 3×10^{-9} Torr [37].

undergo a variety of reactions that will lead to the growth of the film. In addition, depending on the nature of these reactions, such reactions can lead to incorporation of impurities originating in the source molecules, such as carbon, hydrogen, or oxygen. There are several elementary steps associated with the heterogeneous chemistry at the growth surface. After diffusion of the reactant to the surface, the reactant can undergo

adsorption onto the surface at an appropriate surface site, proceed with some elementary or series of elementary reactions of the adsorbate with other surface-absorbed species or gas phase molecules with the incorporation of the reaction product into the solid surface, and desorption of the reaction byproducts. These heterogeneous reactions are characterized by the same formalism used for gas phase or homogeneous reactions. There are often two states characterizing the process of adsorption: physical adsorption or physisorption and chemical adsorption or chemisorption. Physisorption is the weak interaction of a molecule with the surface because of weak electrostatic interaction, such as van der Waals forces. Chemisorption typically requires the formation of a new chemical bond to the surface, which entails bond breaking within the source molecule and the surface atoms. This is typically covalent bonding and is typically site specific on the surface.

The adsorption of a reactive species depends on several factors: the energy required for, or released by, the adsorption of reactants, the availability of an adsorption site, and the concentration of gas phase species that are competing for these sites. The concentration of reacting species on the surface will be the balance between the arriving species, c_i, interacting with suitable vacant surface sites, S_j. The adsorption of gas phase species is often modeled via simple Langmuir adsorption isotherms, which is a model also based on thermodynamic equilibrium. The fraction of available adsorption sites is represented in terms of the partial pressure of reactant [38]. This simple model assumes that the gas phase molecules behave ideally with the formation of only one monolayer, that all the sites on the surface, S_j, are equivalent, and that the absorbed molecules do not interact and are immobile once adsorbed. The fraction of available adsorption sites, θ_j, covered by given reactive species is given by the balance of adsorption of the species and its subsequent desorption [39]:

$$\begin{aligned} &A_i + S_i \Leftrightarrow A_{i,S}; \quad K_i^{ad} \\ &\frac{d\theta_i}{dt} = k_i^{s+} P_i S_T (1-\theta_i) \quad \text{adsorption} \\ &\frac{d\theta_i}{dt} = k_i^{s-} S_T \theta_i \quad \text{desorption} \end{aligned} \tag{21.13}$$

where P_i is partial pressure of the specific reactant species and S_T is the number of total competing surface sites. We assume that these become independent of time at steady state:

$$\begin{aligned} &k_i^{s+} P_i S_T (1-\theta_i) = k_i^{s-} S_T \theta_i \\ &\theta_i = \frac{k_i^{s+} P_i S_T}{k_i^{s+} P_i S_T + k_i^{s-} S_T} = \frac{b_i P_i}{1 + b_i P_i} \end{aligned} \tag{21.14}$$

where $b_i = \frac{k_i^{s+}}{k_i^{s-}}$ or the chemical equilibrium constant for adsorption of the ith species, K_i^{ad}. In the case of multiple competing chemical species, N, Eqn (21.14) is modified to be:

$$\theta_i = \frac{K_i^{ad} P_i}{1 + \sum_{j=1}^{N} K_j^{ad} P_j} \tag{21.15}$$

This is but one of the possible descriptions of competing adsorption on the surface and assumes a steady-state coverage. This is equivalent to assuming that changes due to the actual growth of the film are slow compared with the times required to set up equilibrium. The Langmuir isotherm has often been used to describe the coverage of the surface species during growth and has been included into many reaction schemes. Alternative descriptions could rely directly on the simultaneous solution of the kinetic relationships used to describe adsorption, reaction, and byproduct desorption with time.

21.3.3.3 Surfactants

The kinetic and thermodynamic factors of the growth of a specific system can lead to the preferential segregation of an element or species to the growth front. The segregation of an element leads to changes in the termination of the growth front, altering the surface reconstruction and altering the surface chemistry. These changes in surface chemistry can lead to a catalytic effect that enhances the reaction rate of the precursors as well as, perhaps, reducing the rate of reaction or even preventing reaction and growth. These elements, when affecting these primary steps during crystal growth, are often referred to as "surfactants." The term surfactant has a specific meaning in chemistry: "A substance which lowers the surface tension of the medium in which it is dissolved, and/or the interfacial tension with other phases, and accordingly is positively adsorbed at the liquid–vapor or other interfaces" [40]. It has been used in a much broader context within the crystal growth and epitaxy literature, as any species segregated to the growth front that affects the growth behavior, composition, or defect structure. There are numerous reports of surfactant behavior in MOVPE as affecting composition, atomic ordering, and impurity incorporation [41–49]. There are several review articles on various aspects of surfactant-mediated behavior [34,47,50–52]. In all cases, the surfactant preferentially resides on the surface and affects the surface properties, such as the surface energy or reconstruction and the surface kinetic processes of the growing surface. The segregation is generally because of the decrease in overall free energy. In the case of a highly segregated species, the surface rapidly can accumulate this element despite a low concentration in the growth ambient. As a result, a small amount of surfactant impurities can significantly alter the growth characteristics and change the resulting film structure without a high level of surfactant incorporation into the films. Hence, the choice of a specific surfactant lies in an understanding of the thermochemistry of the growing material. Any surfactant must have limited solubility within the growing film and possess a suitable vapor pressure, such that surface coverage of the surfactant is limited to a single monolayer, preventing second phase formation. Ideally, the segregating species would not have compound formation with the constituents of the growing film. These requirements have focused the choice of surfactants in MOVPE of compound semiconductors to the elements such as Sb [47,53], Te [45,54], and Bi [46,55–57]. These particular elements exhibit miscibility gaps in many of the ternary alloy systems containing them, [58–62] which can be modified by the presence of lattice mismatched strain [63–65].

21.4 Reaction Kinetics of Organometallic Compounds

The specific proposed reaction schemes for the wide variety of metal organic compounds form an extensive literature. The purpose herein is to outline features of many of the common metal organic systems.

21.4.1 Determination of the Gas Phase and Surface Kinetic Processes

There have been experimental and computational approaches to the determination of the homogeneous and heterogeneous chemical kinetics associated with the commonly used metal-organic compounds. These reaction pathways and rates are used in the development of reactor-scale models of the growth process and subsequently for reactor design. Experimentally, these reaction rates were obtained by allowing the source molecule of interest to pass under conditions of controlled temperature, gas environment, and pressure for a known period and the resulting gas phase or surface composition monitored. In a typical and well-used experimental arrangement, the reactants of interest pass through a tube of constant temperature, typically referred to as a "flow tube" and the effluent monitored. Gas is sampled from within the heated region to prevent unwanted reactions that could be present if the reacted gas mixture was allowed to cool to room temperature. The composition of the gas is often determined by mass spectroscopy [66,67] or optical means, such as Fourier transform infrared spectroscopy [68], or deduced by deposition rates [69]. There are many common features to the decomposition or reaction networks. The most studied of the commonly used precursors are trimethyl and triethyl gallium, which exhibit many of the characteristics common to many of the group 15 alkyls.

21.4.2 Gallium Sources

The most commonly used gallium source in MOVPE is trimethyl gallium. The initial studies of the pyrolysis of trimethyl gallium were conducted by Jacko and Price [70]. In those studies, the $(CH_3)_3Ga$ was heated in a toluene carrier gas. The toluene is a scavenger for methyl radicals through the formation of methane and C_7H_7, which would suppress the subsequent reaction of these radicals on the parent molecule [71]. This early study found that the homogeneous decomposition of $(CH_3)_3Ga$ occurred through the homolytic cleavage of methyl groups from the compound at elevated temperatures:

$$\begin{aligned} &Ga(CH_3)_3 \rightarrow Ga(CH_3)_2 + CH_3 \\ &Ga(CH_3)_2 \rightarrow Ga(CH_3) + CH_3 \\ &n(GaCH_3) \rightarrow (GaCH_3)_n \\ &CH_3 + CH_3 \rightarrow C_2H_6 \end{aligned} \tag{21.16}$$

with an activation energy of 59.4 and 35.4 kcal mol^{-1} for the first and second listed reaction, respectively. At a high enough concentration, the monomethyl Ga would polymerize and non-scavenged methyl radicals would be able to form ethane. These reactions have also been subsequently studied in greater detail. Larson and coworkers

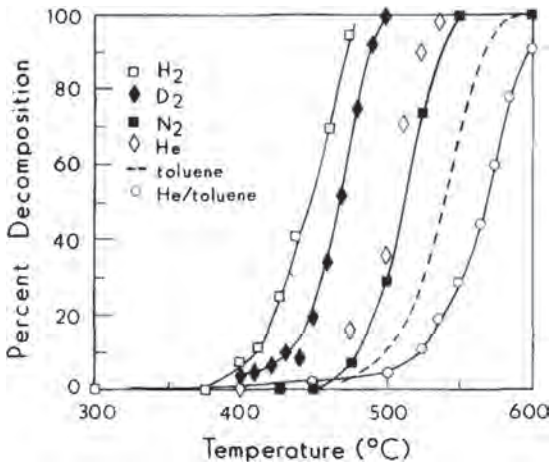


FIGURE 21.11 Decomposition rate with temperature of $(CH_3)_3Ga$ in He-toluene mixture, N_2, He, D_2 and H_2 [66]. The dashed line, calculated for pure toluene carrier. *From data of Ref. [70].*

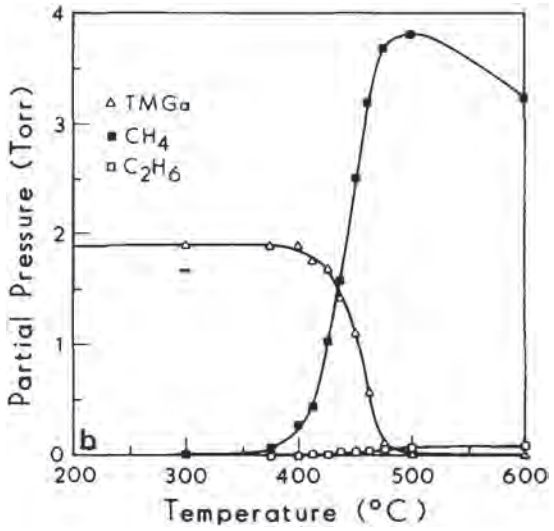


FIGURE 21.12 Decomposition products of $(CH_3)_3Ga$ in H_2 [32].

studied the decomposition of $(CH_3)_3Ga$ in a variety of carrier gasses: He, N_2, H_2, and D_2 in the presence and absence of toluene. The rate of decomposition and the distribution of measured reaction products are presented in Figures 21.11 and 21.12, respectively [66]. The change in decomposition rates with carrier gas indicates that there is an active role for hydrogen in scavenging methyl radicals resulting from decomposition. In addition to those reactions described by Eqn (21.16), in the case of a hydrogen carrier

gas, there is an active reaction between the methyl radicals and hydrogen which accelerates the decomposition rate [66]:

$$\begin{aligned} &Ga(CH_3)_3 \rightarrow Ga(CH_3)_2 + CH_3 \\ &CH_3 + H_2 \rightarrow CH_4 + H \\ &H + Ga(CH_3)_3 \rightarrow GaCH_3 + CH_4 + CH_3 \\ &CH_3 + CH_3 \rightarrow C_2H_6 \end{aligned} \tag{21.17}$$

The heterogeneous reaction of $(CH_3)_3Ga$ on a growth surface is equally complex and depends on the surface structure, surface orientation, and surface composition. For example, $(CH_3)_xGa$ resulting from the gas phase decomposition will react rapidly at an arsenic site on the GaAs (001) surface. It will also react, albeit at a much slower rate, on the Ga-terminated GaAs (001) [72]. As noted above, the relative populations of As and Ga on the growth front will depend on the gas phase ambient and temperature. $(CH_3)_3Ga$ will decompose more rapidly in the presence of AsH_3. High (V/III) ratios of AsH_3 to $(CH_3)_3Ga$ do lead to reduced carbon incorporation [73]. This is attributed to the reaction of surface-adsorbed methyl radicals with hydrogen arising from surface AsH_x species or AsH_3 in the gas phase. AsH_3 will, therefore, accelerate the decomposition of $(CH_3)_3Ga$ [32,74] through enhancing its decomposition.

Triethyl gallium, $(C_2H_5)_3Ga$, exhibits a different reaction behavior from $(CH_3)_3Ga$. There are two primary reactions accessible for the decomposition of $(C_2H_5)_3Ga$ in the gas phase, which have been noted: the homolytic cleavage of the ethyl radical and the β-elimination reaction.

$$\begin{aligned} &(C_2H_5)_3Ga \rightarrow (C_2H_5)_2Ga + C_2H_5 \\ &(C_2H_5)_3Ga \rightarrow (C_2H_5)_2HGa + C_2H_4 \end{aligned} \tag{21.18}$$

The β-elimination reaction has been experimentally shown to occur much more rapidly within the CVD gas phase environment [67,75]. This is shown in Figure 21.13, where the decomposition rate is relatively independent of the carrier gas unlike that seen for $(CH_3)_3Ga$ [67]. The β-elimination reaction leads to a reduced carbon incorporation because the C_2H_4 leaving group does not interact with the growth surface under typical MOVPE growth conditions [76]. The lower decomposition temperature also allows this gallium source to be used in applications where low growth temperatures are required, such as in the formation of low melting point materials and metastable alloys.

The heterogeneous reactions of $(C_2H_5)_3Ga$ have been studied in some detail because of its use in a high vacuum-based technology called chemical beam epitaxy [77] and in studies of atomic layer epitaxy [78]. The surface chemistry of all these organometallic compounds is complex. As with $(CH_3)_3Ga$, the adsorption and reaction of $(C_2H_5)_3Ga$ depends on a wide variety of factors and there is an extensive literature associated with it. $(C_2H_5)_3Ga$ rapidly adsorbs onto an arsenic site and appears to undergo dissociation to $(C_2H_5)_2Ga$, (C_2H_5) Ga, Ga adatoms, and ethyl radicals on the surface [79]. These surface ethyl radicals further desorb or decompose to ethylene or desorb.

Other gallium sources have been investigated, such as isopropyl gallium [80,81] and gallane (Ga_2H_6) based adduct compounds [82–84]. The adduct compounds stabilize the

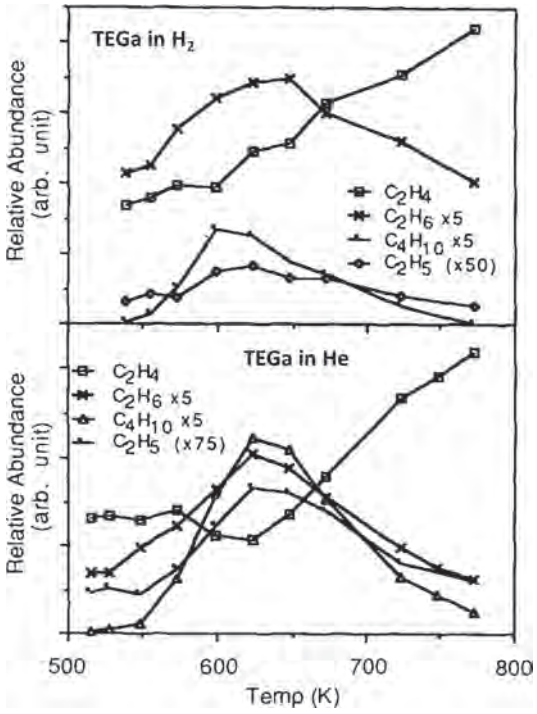


FIGURE 21.13 Decomposition products of $(C_2H_5)_3Ga$ in H_2 and He [67].

gallane from rapid decomposition at room temperature. These sources have not gained widespread use because of their difficulty in synthesis, purification, and storage.

21.4.3 Aluminum Sources

Trimethyl aluminum, $(CH_3)_3Al$, has been a primary growth source used in MOVPE, particularly in the growth of $Al_xGa_{1-x}As$, $Al_x(In,Ga)_{1-x}P$, and $Al_xGa_{1-x}N$. Unlike $(CH_3)_3Ga$, $(CH_3)_3Al$ is dimer in the liquid phase and in the gas phase at near-room temperature conditions. Unlike the analogous gallium source, the thermal pyrolysis of $(CH_3)_3Al$ leads to the formation of Al_2C_3 and not Al metal [85–87]. Overall, $(CH_3)_3Al$ appears to initially decompose through similar mechanism as $(CH_3)_3Ga$, with homolytic cleavage of the methyl radicals. Triethyl aluminum, $(C_2H_5)_3Al$, and triisobutyl aluminum, $((CH_3)_2CHCH_2)_3Al$, decompose through a β-elimination reaction [88] and can lead to the deposition of metallic Al [89]. Alane or AlH_3 has also been extensively used in the growth of aluminum-bearing alloys. In these studies, the alane forms an adduct with a primary amine, such as trimethyl amine, $(CH_3)_3N$ [90,91]. The adduct bond is relatively weak and is thought to dissociate at low temperatures within the reactor. The absence of a direct aluminum–carbon bond in alane has led to a strong decrease in the background carbon incorporated into a growing film relative to the other sources described.

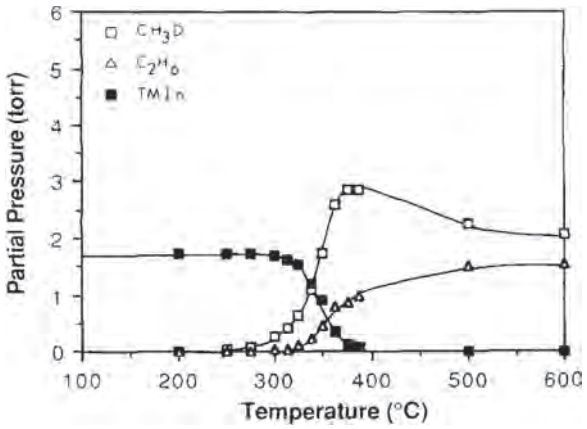


FIGURE 21.14 Decomposition products of $(CH_3)_3In$ in D_2 [92].

21.4.4 Indium Sources

The two most commonly used In sources are trimethyl indium, $(CH_3)_3In$, and triethyl indium, $(C_2H_5)_3In$, which are solid and liquid, respectively. As with the Ga and Al compounds, these sources have been studied through various pyrolysis experiments. The thermal pyrolysis of the In alkyls is thought to be similar to the Ga-based compounds. The weaker In–C bond leads to lower decomposition temperatures [92,93], well lower than the range of 450–500 °C which is characteristic of the Ga and Al compounds. A feature of $(CH_3)_3In$ decomposition is the subsequent formation of ethane as a reaction product in the absence of a group 15 source, as shown in Figure 21.14 [66]. This has been rationalized by the reaction [66]:

$$\begin{aligned} CH_3 + (CH_3)_3In &\rightarrow (CH_3)_2In + C_2H_6 \\ CH_3 + (CH_3)_3In &\rightarrow (CH_3)_2CH_2In + CH_4 \end{aligned} \tag{21.19}$$

Initial studies of the growth of In-base' semiconductors were plagued by surface and gas phase decomposition within the growth environment within the cold regions of the reactor. This was eventually attributed impurities remaining within the metal alkyl source and eliminated through the further purification of the trimethyl indium source material.

21.5 Reaction Kinetics of Group 15 Compounds

21.5.1 Arsenic and Phosphorus Sources

The group 15 elements also form compounds of the type XR_3, where R = H, CH_3, C_2H_5, C_4H_9, and so on. The most used sources of As and P have been the hydrides (R = H): AsH_3 and phosphine (PH_3). There are severe toxicity concerns with these P, As, and Sb compounds [65]. In addition, as gases stored in high-pressure gas cylinders, these sources present a high safety hazard which must be addressed through strict adherence to local safety standards for their use, storage and handling [94]. AsH_3 and PH_3 have been

used extensively in the MOVPE based growth of most arsenide and phosphide materials. The gas phase pyrolysis of these materials is slow at the low temperatures characteristic of the bulk of the reactor gas phase environment. Two reaction pathways have been proposed for the homogeneous gas phase reaction, both AsH_3 and PH_3:

$$\begin{array}{l}(a)AsH_3 \rightarrow AsH_2 + H \\ (b)AsH_3 \rightarrow AsH + H_2\end{array} \tag{21.20}$$

Previous calculations have indicated that the second reaction, Eqn (21.20b), has a much higher rate over a broad range of temperature and pressure should be favored for homogeneous gas phase decomposition [26]. There have been some experimental determinations of the homogeneous gas phase decomposition of these hydrides [95]. In one study, AsH_3 decomposition performed in a D_2 carrier gas did not lead to any formation of HD as would be expected if the reaction Eqn (21.20b) was present. In subsequent studies, the lack of the formation of HD led to the conclusion that the decomposition is dominated by the heterogeneous surface reaction wherein the hydride is adsorbed at the surface and decomposes by the loss of an H atom to the surface. Surface-absorbed H atoms then recombined to form H_2 [96]. In all cases, the gas phase decomposition rates are slow at typical gas phase temperatures within the reactor, except close to the growth front, and AsH_3 decomposition has been shown to be dominated by surface reactions. The dominance of the heterogeneous reaction in the MOVPE environment is further substantiated because the decomposition rate of AsH_3 [96–99] is greatly accelerated by the presence of a GaAs substrate, adsorbing and reacting on a Ga surface site. Phosphine may react in a similar manner to AsH_3, with the characteristic temperatures for decomposition being somewhat higher.

The group 15 alkyls have also been used in MOVPE growth systems. The most commonly used organo-As and organo-P sources are t-butyl arsine and phosphine, $(C_4H_9)AsH_2$ and $(C_4H_9)PH_2$. One study has indicated that the gas phase decomposition of these compounds can be rationalized by the existence of two major decomposition routes: (1) a low activation energy pathway producing isobutane and AsH, and (2) a higher activation energy, β-elimination pathway producing isobutene and AsH_3 [100,101]. These compounds are used as an alternative to gas sources, arsine and phosphine, and as liquid sources they present a reduced safety hazard. They decompose at substantially lower temperatures than the hydrides and are used in the low temperature growth of several compound semiconductors.

21.5.2 Nitrogen, Group 12, and Antimony Sources

Organometallic sources exist for the other common anions used in compound semiconductor alloy growth. There are many alkyl sources for antimony, selenium, and tellurium that were developed in response to the formation of $GaAs_{1-y}Sb_y$ and for II–VI materials, such as ZnSe or $Hg_xCd_{1-x}Te$. Commercially available sources are of the form, SbR_3 where $R = CH_3$, C_2H_5, C_3H_7,… or similar sources of Zn and Cd (e.g., $(CH_3)_3Zn$). These sources generally decompose and similar manner to that described for $(CH_3)_3Ga$

with homolytic fissure of the alkyl group [102]. The use of organometallic compounds as both the anion and cation sources in the growth of $GaAs_{1-y}Sb_y$ has led to the complex interaction of these species when combined with the complex strain-related phase diagrams associated with this alloy system [63,64,103,104]. The growth exhibits a complex dependence of the composition on the gas phase composition, which is dependent on the specific chemical sources, growth temperature, and strain state of the epitaxial film. In the case of selenium and sulfur, commercially available compressed gas hydrides do exist and are used along with organo-S and Se compounds. Ammonia, NH_3, is the most common source used in the growth of nitride-based semiconductors such as GaN or $In_xGa_{1-x}N$. The homogeneous gas phase reaction pathways of ammonia are well known [26,105]. Given the high temperature decomposition temperatures associated with ammonia, 1,1-dimethylhydrazine, $(CH_3)_2NNH_2$, has also been used [106], particularly in the growth of $In_xGa_{1-x}N$. $In_xGa_{1-x}N$ requires lower growth temperatures than used for AlN or GaN because of the evaporative loss of indium from the surface. A common feature of the decomposition of these sources is the generation of $^{\bullet}NH_2$ and $^{\bullet}NH$ radicals, which are considered to be a precursor to subsequent nitrogen incorporation [107,108]. The interaction of these radicals with the H_2 carrier gas and the other gas phase species could alter the nature and concentration of these initially radical species at the growth front. There have been other nitrogen sources that are based on the analogy to the decomposition kinetics of other group 3 and 5 sources, such as tertiary-butyl hydrazine, $t\text{-}C_4H_9NHNH_2$ [109], and tertiary-butyl amine, $t\text{-}C_4H_9NH_2$, but they have not been as extensively studied [110].

21.5.3 Reactions between Precursors

The previous section presented the reaction pathways associated with individual precursors used in the MOVPE technology. The growth of the film is not generally the superposition of the individual reactions. There are many reactions between these reactive compounds in the gas phase and at the surface. In the case of group 13 sources, the exchange of ligands within the gas phase has been previously noted [111–113]. For example, mixtures of $(CH_3)_3In$ and $(C_2H_5)_3Ga$ lead to the formation of mixed ligand alkyls within the reactor [111] (e.g., $(CH_3)_x(C_2H_5)_{3-x}In$). There are more substantial reactions between the group 13 and group 15 sources in the gas phase and at the growth surface.

The group 13 alkyls are Lewis acids, whereas the group 15 sources are Lewis bases. These compounds can form adducts or Lewis acid–base compounds. The bond energies associated with the native bonds are typically weaker than the covalent bonds within the source molecule [114]. As an example, the adduct between $(CH_3)_3Ga$ and ammonia, $(CH_3)_3Ga{:}NH_3$, is important in the growth of GaN given the high concentration of ammonia within the reactor for the growth of nitride materials. This adduct can rapidly form, particularly at low gas phase temperatures. This adduct bond has a measured bond strength of $\sim 18\ \text{kcal mol}^{-1}$ [115]. The initial $Ga\text{–}CH_3$ bond strength for comparison is

57.5 kcal mol^{-1} [70]. The lower bond strength of the adduct bond indicates that there can be an equilibrium set up at low temperatures between the adduct and its constituents, whereas high temperatures favor dissociation:

$$(CH_3)_3Ga + NH_3 \Leftrightarrow (CH_3)_3Ga : NH_3 \tag{21.21}$$

These compounds can and do form within the gas phase regions of the MOVPE system. For the $(CH_3)_3Ga{:}AsH_3$ adduct, the bond energy is only 4–5 kcal mol^{-1} [116]. This variation in bond energies indicates that the adduct reaction for the case of $(CH_3)_3Ga$ and AsH_3 is not important for the understanding of the growth behavior but for $(CH_3)_3Ga{:}NH_3$ it is a major reactant within the gas phase.

Adducts in the liquid phase have also been used to great effect in the purification of group 13 compounds. The adduct formation in the liquid phase between the MOVPE trialkyls and selected Lewis base solvents can be made extremely selective resulting in a solid adduct compound which can be removed from the solution. The nonadduct forming impurities remain in the solution and hence the material is purified. The trialkyl is reclaimed through a small increase in temperature. "Adduct-purified" organometallics have allowed for extreme levels of purity to be achieved, including the removal of alkoxide-based impurities, which often lead to oxygen incorporation into the growing semiconductor [117–120]. Oxygen serves as a nonradiative recombination center decreasing the photoluminescence and electroluminescence efficiency [121,122].

Adduct formation in the gas phase, as it affects the growth of semiconductors, has been studied in detail for several source compound combinations. When formed, the adduct compounds can possess a high molecular weight and often a correspondingly lower vapor pressure. If the adduct is formed in the reactor, a low vapor pressure could lead to condensation of the adduct compound and its removal from the growth process affecting uniformity and film composition [123]. The advent of higher purity metal alkyls have reduced or eliminated those reactions with AsH_3 and PH_3. Intentional adducts have been used to both prevent other adduct reactions within a reactor and stabilize desirable reactants [124]. Trimethyl amine-alane has been used in the formation of Al-based compounds at low temperatures or within a high vacuum environment [125–128]. These sources have found use in the formation of II–VI semiconductors, such as ZnSe or ZnS, or in the use of Zn-based alkyls [129–131].

The most important adduct reaction occurs in the growth nitride-based materials using ammonia or dimethyl hydrazine [106,132–134]. In the case of trimethyl gallium and ammonia, the adduct bond is approximately −18 kcal mol^{-1} [114]. The high growth temperatures used in the growth of nitrides would lead to the conclusion that this adduct would dissociate before some intramolecular reaction. The growth behavior of GaN from trimethyl gallium and ammonia indicates that there are substantial gas phase reactions resulting in the depletion of trimethyl gallium from the gas phase and a decrease in growth rate and degraded uniformity of deposition [135]. These reactions have driven the redesign of conventional MOVPE reactors to minimize these gas phase reactions [136–140]. Similar adduct reactions occur with trimethyl aluminum. These reactions

tend to be more severe than with trimethyl gallium and lead to a steep decrease in growth rate and in aluminum incorporation under certain reactor conditions. A typical adduct reaction that is presented in the literature is as follows:

$$\begin{aligned}&(CH_3)_3M + NH_3 \rightarrow (CH_3)_3M : NH_3\\&(CH_3)_3M : NH_3 \rightarrow (CH_3)_2M : NH_2 + CH_4\\&n\left[(CH_3)_3M : NH_3\right] \rightarrow \text{particle or polymer formation}\end{aligned} \tag{21.22}$$

where M can be Ga, Al, or In [133,141–143]. Similar reactions have been discussed for adducts formed using 1,1dimethylhydrazine, a source commonly used to reduce the growth temperature of $In_xGa_{1-x}N$ [107,144]. In all cases, there is a gas phase reaction that leads to the removal of the metal species from the gas phase. There is discussion in the literature on the nature of the ammonia-based adduct formation with Ga and In. Through experiment and density functional theory-based calculations [143,145], it is known that complex gas phase reactions can occur between these metal alkyls and amines. These reactions lead to deposition of adduct reaction byproducts and eventual formation of particles in the gas phase [142,146]. These reactions happen both at room temperature and continue to occur at elevated temperatures as shown in Figure 21.15 [133] where a comparison of $(CH_3)_3Ga$ decomposition in H_2 and ND_3/H_2 are compared.

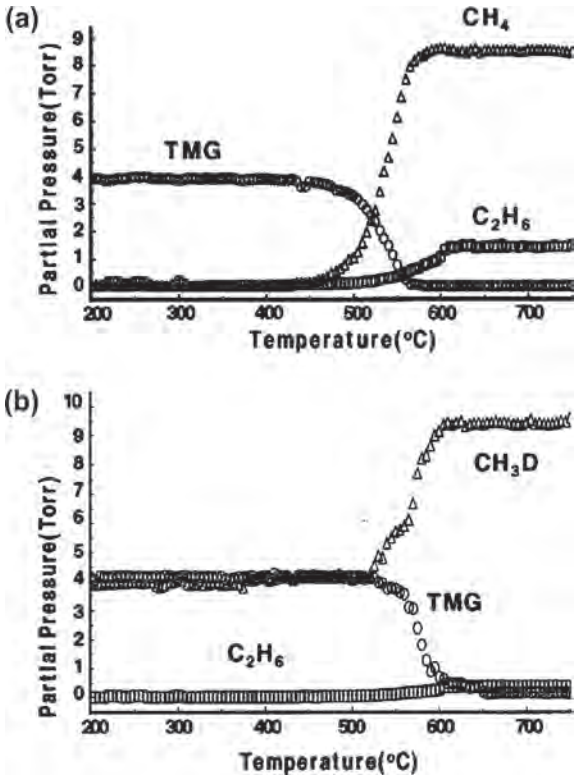


FIGURE 21.15 The temperature dependence of decomposition within the TMG/H_2 (a) and TMG/H_2/NO_3 (b) systems. Immediate reaction between TMG and ND_3, resulting in the elimination of a single CH_3D, is observed at higher temperature. Complete decomposition of TMG within the TMG/H_2/ND_3 system is achieved at about 50 °C higher than without TMG/H_2. *Figure and caption quoted from Ref. [133], Reprinted with permission from the Materials Research Society.*

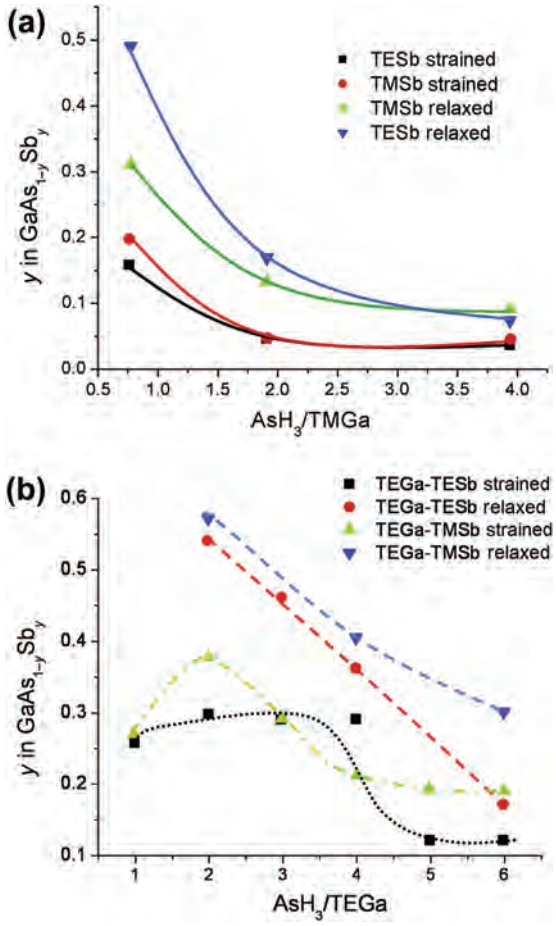


FIGURE 21.16 The Sb incorporation with gas-phase stoichiometry exhibits a dependence on both precursor and strain state for samples grown at 530 °C with a Ga precursor gas-phase mole fraction fixed at 4.3×10^{-5}; (a) TMGa-based growth at a constant Sb/TMGa-precursor ratio of 1.55 and (b) TEGa-based growth at a constant Sb/TEGa-precursor ratio of 4. *Caption and figures adapted from Refs [102,103].*

The rapid elimination of deuterated methane indicates a reaction attributable to an adduct intermediate species. The rate and extent of reaction will be a function of concentration of these reactants in the gas phase (Figure 21.16).

21.6 Growth Reactions

The formation of a predictive growth model requires an understanding of the species interacting with the surface, hence knowledge of the gas phase chemistry, their interaction with the surface when competing for adsorption sites, the reaction between adsorbed species, and the desorption of reaction byproducts. Although each one of these elementary reaction steps may be understood, the assembly of all pertinent reactions, both gas and surface, with their interaction with the growth surface and structure is a complicated and inherently incomplete task. The growth of several binary compound

semiconductors, such as GaAs, GaN (and other nitrides), and InP, have been modeled to a great extent and detailed, as well as consolidated or reduced order, models for the growth have been developed. These chemical models are typically embedded within a fluid-thermal model of the flowing gas within the reactor to predict growth rate, composition, and uniformity of growth [147–150].

21.6.1 Empirical Models

In an early study by Reep and Ghandhi [3], GaAs growth was modeled through a reaction scheme whereby the AsH_3 and $(CH_3)_3Ga$ adsorb on the surface and then react. This model has the virtue of a strong physical basis with a simplified chemical kinetic scheme. The growth rate, R, would be then a function of the rate of reaction between these two adsorbed species as a form of Langmuir–Hinshelwood model. The surface concentration of these two species would follow the Langmuir isotherm model:

$$\begin{aligned} R &= K_{LH}\theta_{AsH_3}\theta_{Ga(CH_3)_3} \\ \theta_{AsH_3} &= \frac{K^{ad}_{AsH_3}P_{AsH_3}}{1+K^{ad}_{AsH_3}P_{AsH_3}+K^{ad}_{Ga(CH_3)_3}P_{Ga(CH_3)_3}} \\ \theta_{Ga(CH_3)_3} &= \frac{K^{ad}_{Ga(CH_3)_3}P_{Ga(CH_3)_3}}{1+K^{ad}_{AsH_3}P_{AsH_3}+K^{ad}_{Ga(CH_3)_3}P_{Ga(CH_3)_3}} \end{aligned} \tag{21.23}$$

where K_{LH} is the rate constant for the growth reaction using the Langmuir–Hinshelwood model, and K_i^{ad} is the mass action constant related to the adsorption equilibrium. This model can be simplified by assuming that the surface species, assumed by Reep and Ghandhi to be AsH and $GaCH_3$, do not compete for surface sites:

$$R = K_{GR}\frac{P_{AsH_3}P_{Ga(CH_3)_3}}{1+K^{ad}_{AsH_3}P_{AsH_3}+K^{ad}_{Ga(CH_3)_3}} \tag{21.24}$$

where K_{GR} is the overall kinetic coefficient. In the case where the population of species on the surface is low, this is further reduced to:

$$R = K_{GR}P_{AsH_3}P_{Ga(CH_3)_3} \tag{21.25}$$

Because the AsH_3 is typically in great excess and assumed to be not rate limiting to the incorporation under most conditions, this reaction model could alternatively be simplified to the observed dependence on the metal alkyl alone at typical growth temperatures.

$$R = KP_{Ga(CH_3)_3} \tag{21.26}$$

In the case of alloy growth, the growth rate is then dependent only on the total metal alkyl gas phase partial pressure:

$$R = K'\sum_{i=1}^{N} P_i \tag{21.27}$$

This simple growth model captures much of what is observed empirically in MOVPE growth at low and moderate growth temperatures.

21.6.2 Large-Scale Computational Models

These simple models have been replaced by more complicated and comprehensive chemical reaction networks. The number of reactions, both in the gas phase and on the surface, can be expanded greatly to include a wide variety of major and minor reaction pathways. One such scheme of 17 gas phase and 28 surface reactions for the growth of GaAs on the (001) surface orientation using $(CH_3)_3Ga$ and AsH_3 are summarized in Tables 21.1 and 21.2 [151,152]. This model is embedded within a reactor-scale model of the thermal/fluid gas phase transport to describe the growth over a wide variety of growth parameters and predict materials properties. Growth rate, uniformity, gas phase, and surface distribution of various chemical species included in the model, and the gas phase thermal and fluid velocity profiles, are calculated for a given reactor geometry. To provide insight into the primary reactions determining the rate of deposition, a sensitivity analysis was also performed in this study that allows for the primary reactions to be identified [151,152]. This reduced set of "important" reactions can then be used in more complex reactor models.

This model was later expanded through the inclusion of additional gas phase and surface reactions to 28 gas phase and 54 surface reactions to determine the rate of carbon incorporation [153]. Carbon is an impurity that can typically range in atomic mole fraction within an MOVPE-grown materials from 10^{-9} to 10^{-3}, which corresponds to an atomic concentration on the order of 10^{14}–10^{20} cm^{-3}. The incorporation of carbon

Table 21.1 Gas–Phase Reaction Mechanisms and Forward Reaction Rate Parameters [152]

	Reaction: $k = k_0 T^{\beta} \exp(-E_a/RT)$	k_0^a	E_a (kcal mol^{-1})	β
[G1]	$Ga(CH_3)_3 \Rightarrow Ga(CH_3)_2 + CH_3^{\bullet}$	3.5×10^{15}	59.5	0
[G2]	$Ga(CH_3)_2 \Rightarrow GaCH_3 + CH_3^{\bullet}$	8.7×10^{7}	35.4	0
[G3]	$CH_3^{\bullet} + AsH_3 \Rightarrow AsH_2 + CH_4$	3.9×10^{10}	1.65	0
[G4]	$CH_3^{\bullet} + H_2 \Rightarrow CH_4 + H^{\bullet}$	2.9×10^{12}	8.71	3.1
[G5]	$H^{\bullet} + H^{\bullet} + M \Rightarrow H_2 + M$	1.0×10^{16}	0	0
[G6]	$CH_3^{\bullet} + H^{\bullet} + M \Rightarrow CH_4 + M$	2.4×10^{22}	0	−1
[G7]	$CH_3^{\bullet} + CH_3^{\bullet} + M \Rightarrow C_2H_6$	2.0×10^{13}	0	0
[G8]	$GaCH_3 + CH_3^{\bullet} \Rightarrow GaCH_2 + CH_4$	2.0×10^{11}	10	0
[G9]	$GaCH_2 + H^{\bullet} \Rightarrow GaCH_3$	1.0×10^{14}	0	0
[G10]	$Ga(CH_3)_3 + CH_3^{\bullet} \Rightarrow Ga(CH_3)_2CH_2 + CH_4$	2.0×10^{11}	10	0
[G11]	$Ga(CH_3)_2CH_2 + H^{\bullet} \Rightarrow Ga(CH_3)_3$	1.0×10^{14}	0	0
[G12]	$Ga(CH_3)_2CH_2 \Rightarrow Ga(CH_3)CH_2 + CH_3^{\bullet}$	3.5×10^{15}	59.5	0
[G13]	$Ga(CH_3)CH_2 \Rightarrow GaCH_2 + CH_3^{\bullet}$	8.7×10^{7}	35.4	0
[G14]	$Ga(CH_3)_3 + H^{\bullet} \Rightarrow Ga(CH_3)_2 + CH_4$	5.0×10^{13}	10	0
[G15]	$Ga(CH_3)_2 + H^{\bullet} \Rightarrow GaCH_3 + CH_4$	5.0×10^{13}	10	0
[G16]	$Ga(CH_3)_2 + CH_3^{\bullet} \Rightarrow Ga(CH_3)CH_2 + CH_4$	2.0×10^{11}	10	0
[G17]	$Ga(CH_3)CH_2 + H^{\bullet} \Rightarrow Ga(CH_3)_2$	1.0×10^{14}	0	0

Table 21.2 Surface Reaction Mechanism and Forward (+) and Reverse (−) Rate Parameters for the (001) GaAs Surface [151]

	Reaction: $k = k_0 \exp(-E_a/RT)$	k^a_{0+}	E_{a+}	k^a_{0-}	E_{a-}
[S1]	$H^{\cdot} + S_G \rightleftharpoons H^*_G$	$s = 1$	0	–	–
[S2]	$H^{\cdot} + S_A \rightleftharpoons H^*_A$	$s = 1$	0	–	–
[S3]	$CH^{\cdot}_3 + S_G \rightleftharpoons (CH_3)^*_G$	$s = 1$	0	1×10^{12}	20
[S4]	$CH^{\cdot}_3 + S_A \rightleftharpoons (CH_3)^*_A$	$s = 1$	0	1×10^{12}	20
[S5]	$GaCH_3 + 2S_G \rightleftharpoons GaCH^*_3$	$s = 1$	0	1×10^{14}	45
[S6]	$Ga(CH_3)_2 + 2S_G \rightleftharpoons GaCH^*_3 + CH^{\cdot}_3$	$s = 1$	0	–	–
[S7]	$Ga(CH_3)_3 + 2S_G \rightleftharpoons GaCH^*_3 + 2CH^{\cdot}_3$	$s = 1$	0	–	–
[S8]	$GaCH_2 + S_G + S_A \rightleftharpoons GaC + H_2$	$s = 1$	0	–	–
[S9]	$Ga(CH_3)CH_2 + S_G + S_A \rightleftharpoons GaC + CH^{\cdot}_3 + H_2$	$s = 1$	0	–	–
[S10]	$Ga(CH_3)_2CH_2 + S_G + S_A \rightleftharpoons GaC + 2CH^{\cdot}_3 + H_2$	$s = 1$	0	–	–
[S11]	$AsH + S_A \rightleftharpoons AsH^*$	$s = 1$	0	1×10^{14}	40
[S12]	$AsH_2 + S_A \rightleftharpoons AsH^* + H^*$	$s = 1$	0	–	–
[S13]	$AsH_3 + S_A \rightleftharpoons AsH^* + H_2$	$S = 1$	0	–	–
[S14]	$CH^{\cdot}_3 + H_G \rightleftharpoons CH_4 + S_G$	Collisional	0	–	–
[S15]	$CH^{\cdot}_3 + H_A \rightleftharpoons CH_4 + S_A$	Collisional	0	–	–
[S16]	$H^{\cdot} + (CH_3)^*_G \rightleftharpoons CH_4 + S_G$	Collisional	0	–	–
[S17]	$H^{\cdot} + (CH_3)^*_A \rightleftharpoons CH_4 + S_A$	Collisional	0	–	–
[S18]	$H^*_A + (CH_3)^*_A \rightleftharpoons CH_4 + 2S_A$	1×10^{17}	10	–	–
[S19]	$H^*_G + (CH_3)^*_G \rightleftharpoons CH_4 + 2S_G$	1×10^{17}	10	–	–
[S20]	$H^*_A + H^*_A \rightleftharpoons H_2 + 2S_A$	1.2×10^{17}	20	–	–
[S21]	$(CH_3)^*_A + (CH_3)^*_A \rightleftharpoons C_2H_6 + 2S_A$	1×10^{17}	16.8	–	–
[S22]	$GaCH^*_3 + AsH^* \rightleftharpoons GaAs + CH_4 + 2S_G + S_A$	4.5×10^{17}	24.4	–	–
[S23]	$AsH^* + AsH^* \rightleftharpoons As_2 + H_2 + 2S_A$	1×10^{17}	35	–	–
[S24]	$CH^*_3 + AsH^* \rightleftharpoons As^* + CH_4$	Collisional	20	–	–
[S25]	$As^* + As^* \rightleftharpoons As_2 + 2S_A$	1×10^{18}	30	–	–
[S26]	$GaCH^*_3 + As^* \rightleftharpoons GaAs + CH^*_3 + 2S_G + S_A$	4.5×10^{17}	20	–	–
[S27]	$H^*_G + H^*_G \rightleftharpoons H_2 + 2S_G$	1.2×10^{17}	29.9	–	–
[S28]	$(CH_3)^*_G + (CH_3)^*_G \rightleftharpoons C_2H_6 + 2S_G$	1×10^{17}	20	–	–

Surface reaction rates are in (mol cm^{-2}); $E_{a\pm}$ is in (kcal $mo1^{-1}$). (a) Assumed to occur with unity sticking coefficient, s, at zero coverage, actual collision rate computed from Eqn (21.1) in Ref. [151] and coverage-dependent sticking coefficient from Eqn (21.2) in Ref. [151]. (b) Collision rate, *collision*, computed from Eqn (21.5) in Ref. [151].

involves minority reactions that are difficult to accurately capture in a model. Such an expanded complex model can, however, capture many of the trends qualitatively, and often quantitatively, as a function of gas phase composition and temperature.

The growth of GaN and related compounds has been the focus of many large computational studies. Unlike the case for GaAs, the potential extensive gas phase reactions between ammonia and the metal alkyls complicates the growth and product uniformity. The need for large-scale multiwafer reactors for the commercial production of light-emitting diodes and power devices places stringent demands on the uniformity and precision of growth over all wafers within the growth run and from run to run. Current batch reactor can hold many wafers, such as approximately 20, 200-mm diameter wafers. The requirement for a uniform growth on these reactors has led to the development of growth models used

for the reactor design and control of the growth process. Initial models have evolved from the reduced order chemical reaction schemes wherein the complications due to loss of reactant were lumped into a single or a few parameterized reactions [135,154,155]. Later, more complicated reaction models used postulated reaction schemes and used experimentally determined, calculated, or estimated reaction rate parameters [136,146,156].

Computational numerical approaches are now used to determine the important thermochemistry and kinetic parameters, including the transition state $\Delta G_i^{\dagger}$ and the pre-exponential constant k_{0i} in Eqn (21.10). There have been several approaches to the calculation of these parameters, which have been both refined and made more accessible. There are many quantum mechanical approaches to the calculation of the electronic structure of a system [154]. Several approaches have been grouped under the general theory of density functional theory [157–159]. These techniques allow for the detailed atomic modeling of the atomic positions and energy levels primarily associated with the ground state of the system for both molecules and surfaces. The transition state can be obtained through the investigation of the change in atomic displacements and the energy associated with the transition state through exploration of the energy landscape and finding the saddle points marking the transition state energy. There are various approaches to this problem, such as the Nudged Elastic Band method to find the minimum energy path from reactants to products [155]. Once these numerical parameters are determined, they can be used in reactor models of the growth where experimental kinetic information is lacking. There have been gas phase reactions postulated via ab initio calculations, which are used to explain many of the observed complexities in the growth of several systems and which are difficult to determine experimentally, such as the gas phase reaction between $(CH_3)_3Ga$ and NH_3 [145,160]. Although such calculations can be used to interrogate the possible reactions schemes, it is still difficult to experimentally verify such pathways.

Many important reactions take place on surfaces. Detailed kinetic information about specific chemical species progressing through various chemical reactions is extremely difficult to experimentally acquire. The use of these computational methods, as applied to surfaces, has tremendously aided our understanding of the growth process. As mentioned, the surface structure of a solid which can be modified dramatically in its atomic arrangement by the adsorption of chemical species can be calculated. Once understood, there can be numerical investigations of various chemical pathways and reactions on the surface. These types of calculations have been extremely successful in the area of catalysis [157–159]. Density functional theory-based calculations have been used to explore various chemical reactions relevant for semiconductor growth. The reaction of alkyl sources and NH_3 on GaN and InN surfaces has been studied by several groups [161–165]. The complex interactions of nonincorporating surface atoms, such as Bi and Sb, have been used to modify the reactions and transport of atoms at the surface [34]. Such atoms, often referred to as surfactants, have altered the surface morphology, surface crystallographic structure, and defect structure of growing films [45,47,53,57,166–170]. These effects can also be explored through calculation. The surface crystallographic structure, or reconstruction, can be altered by the addition of heteroatoms on the surface. This is shown in Figure 21.17

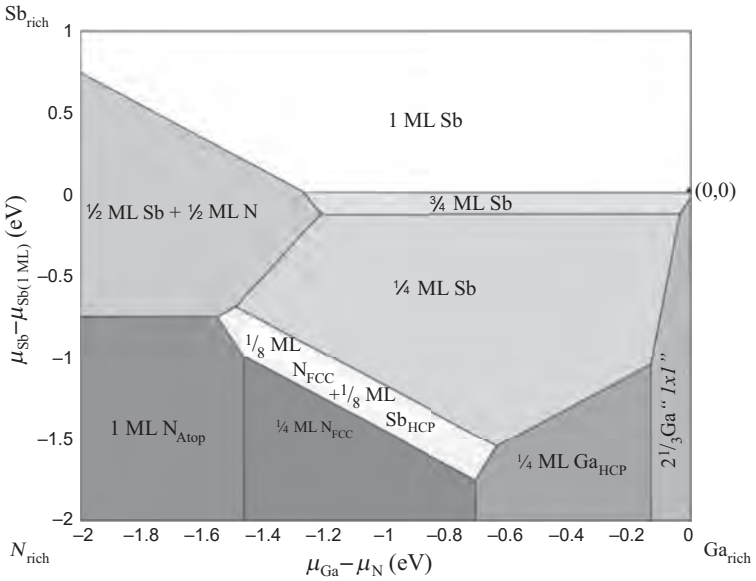


FIGURE 21.17 Stable reconstructions of various stoichiometries of Ga, Sb, and N on the Ga-terminated GaN (0001) surface for coverages ranging between 1/3 and $2\frac{1}{3}$ ML of these species. A Ga-rich environment with 1 ML Sb adsorbed is chosen as the origin (0,0). *Figure and caption taken from Ref. [171].*

for the case of Sb adsorption onto the GaN surface as a function of the activities of the principal components [171]. For example, the presence of Sb on the growing GaN surface during the MOVPE growth from $(CH_3)_3Ga$ and NH_3 can lead to a smoother surface morphology and reduced defect or dislocation density [47,172]. Through the use of ab initio–based calculations, these effects were explained by a proposed mechanism in which surface Sb forms a stable, highly mobile surface species serving to transport N on the surface [171,173], as shown in Figure 21.18. The formation of SbN* on the surface is favored

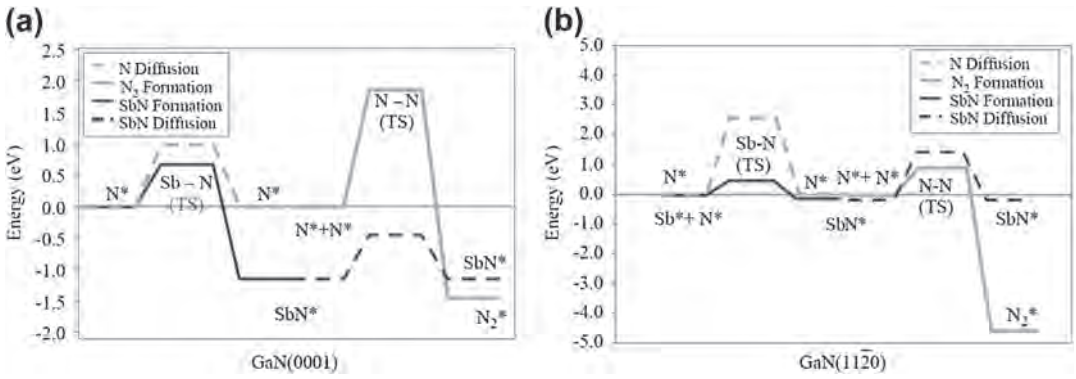


FIGURE 21.18 Potential energy surface for SbN and N_2 formation and diffusion of SbN and atomic N on (a) Ga-terminated GaN (0001) and (b) GaN $(11\bar{2}0)$ surfaces. * denotes a vacant site, X* denotes X adsorbed on the corresponding GaN surface, and TS signifies the transition state for the Sb–N and N–N bond-making steps. *Figure and caption taken from Ref. [171].*

over N_2. The surface N can then be transported to an appropriate surface site for incorporation, leading to improved morphology.

21.7 Conclusion

The gas and surface chemical kinetics associated with the growth of compound semiconductors using MOVPE is complex. Under most cases, the growth is dominated by fast surface reactions and a minimal extent of gas phase reactions. This leads to the familiar and highly advantageous mass transport limited growth characterizing the typical operating conditions of an MOVPE reactor. This behavior leads to a simplified control over the growth rate and the composition. Increasingly, gas phase and surface reactions must be controlled to produce materials with appropriate physical and electrical properties. The development of a deep understanding of these kinetic processes has allowed for the detailed modeling of these reactors, both in the gas phase and at the surface. These reactor models that incorporate the detailed chemical kinetics have led to improved understanding of the detailed atomic and molecular level processes impacting the final materials. Both experimental and computational approaches to determining the important kinetic processes and parameters are now being used to develop such models.

References

[1] Manasevit HM. J Cryst Growth 1972;13–14:306–14.
[2] Manasevit HM. J Cryst Growth 1974;22:125–48.
[3] Reep DH, Ghandi SK. J Electrochem Soc 1983;130:675–80.
[4] Kuech TF. Mater Sci Rep 1987;2:1–49.
[5] Stringfellow GB. Organometallic vapor-phase epitaxy: theory and practice. Elsevier Science; 1999.
[6] Fitzgerald M. Solid State Technol 1991;34:53–4.
[7] Lum RM, Klingert JK. J Cryst Growth 1991;107:290–6.
[8] Lum RM, Klingert JK, Lamont MG. J Cryst Growth 1987;89:137–42.
[9] Hoshino M. J Cryst Growth 1991;110:704–12.
[10] Li SH, Larsen CA, Stringfellow GB. J Cryst Growth 1990;102:117–25.
[11] Chen CH, Reihlen EH, Stringfellow GB. J Cryst Growth 1989;96:497–504.
[12] Li SH, Larsen CA, Chen CH, Stringfellow GB, Brown DW. J Electron Mater 1990;19:299–304.
[13] Smith MB. J Organomet Chem 1972;46:31–49.
[14] Clough RB, Tietjen JJ. Metal Soc Am Inst Min Metall Pet Eng Trans 1969;245:583–5.
[15] Foord JS, Howard FP, McGrady GS, Davies GJ. J Cryst Growth 1998;188:144–51.
[16] Sugiura O, Kameda H, Shiina K, Matsumura M. J Electron Mater 1988;17:11–4.
[17] Tamaru K. J Phys Chem 1955;59:1084–8.
[18] Abril EJ, Alonso A, Lopez M, Aguilar M. Jpn J Appl Phys Part 1 1992;31:1721–5.
[19] Leitner J, Mikulec J, Vonka P, Stejskal J, Hladina R, Klima P. J Cryst Growth 1991;112:437–44.

[20] Tirtowidjojo M, Pollard R. J Cryst Growth 1986;77:200–9.

[21] Arthur JR. J Phys Chem Solids 1967;28:2257–67.

[22] Stringfellow GB. J Cryst Growth 1983;62:225–9.

[23] Stringfellow GB. J Cryst Growth 1984;70:133–9.

[24] Laidler KJ, King MC. J Phys Chem 1983;87:2657–64.

[25] Baer T, Hase WL. Unimolecular reaction dynamics: theory and experiments. New York: Oxford University Press; 1996.

[26] Buchan NI, Jasinski JM. J Cryst Growth 1990;106:227–38.

[27] Jones AC, Hitchman ML. Chemical vapour deposition: precursors, processes and applications. Royal Society of Chemistry; 2009.

[28] Holbrook KA, Pilling MJ, Robertson SH. Unimolecular reactions. Wiley; 1996.

[29] Gilbert RG, Smith SC. Theory of unimolecular and recombination reactions. Blackwell Scientific Publications; 1990.

[30] Sholl DS, Steckel JA. Density functional theory a practical introduction. NJ: Wiley, Hoboken, 2009.

[31] Langenaeker W, De Proft F, Geerlings P, Vrije Universiteit B, Fonds voor Wetenschappelijk O-V. Density functional theory: a bridge between chemistry and Physics. Brussels: VUB University Press, 2001.

[32] Larsen CA, Li SH, Buchan NI, Stringfellow GB, Brown DW. J Cryst Growth 1990;102:126–36.

[33] Welz B, Schubert-Jacobs M, Sperling M, Styris DL, Redfield DA. Spectrochim Acta Part B 1990;45:1235–56.

[34] Kuech TF. AIP Conf Pro 2007;916:288–306.

[35] LaBella VP, Yang H, Bullock DW, Thibado PM. Phys Rev Lett 1999;83:2989–92.

[36] Newstead SM, Kubiak RAA, Parker EHC. J Cryst Growth 1986;81:49–54.

[37] Masnadi-Shirazi M, Beaton DA, Lewis RB, Lu X, Tiedje T. J Cryst Growth 2012;338:80–4.

[38] Pogge HB. Electronic materials chemistry. New York: Marcel Dekker, 1995.

[39] Adamson AW. Physical chemistry of surfaces. Wiley; 1990.

[40] Wilkinson A, McNaught AD. Compendium of chemical terminology: IUPAC recommendations. Oxford (Oxfordshire); Malden, MA: Blackwell Science; 1997.

[41] Howard AD, Chapman DC, Stringfellow GB. J Appl Phys 2006;100.

[42] Jun SW, Lee RT, Fetzer CM, Shurtleff JK, Stringfellow GB, Choi CJ, et al. J Appl Phys 2000;88:4429–33.

[43] Lee RT, Shurtleff JK, Fetzer CM, Stringfellow GB, Lee S, Seong TY. J Appl Phys 2000;87:3730–5.

[44] Massies J, Grandjean N, Etgens VH. Appl Phys Lett 1992;61:99–101.

[45] Newman FD, Stan MA, Murray SL, Murray CS. J Cryst Growth 2004;272:650–7.

[46] Wixom RR, Rieth LW, Stringfellow GB. J Cryst Growth 2004;265:367–74.

[47] Zhang L, Tang HF, Kuech TF. Appl Phys Lett 2001;79:3059–61.

[48] Kandel D, Kaxiras E. Phys Rev Lett 1995;75:2742–5.

[49] Kaxiras E, Kandel D. Appl Surf Sci 1996;102:3–5.

[50] Markov I. Phys Rev B 1996;53:4148–55.

[51] Markov I. Mater Chem Phys 1997;49:93–104.

[52] Tournie E, Grandjean N, Trampert A, Massies J, Ploog KH. J Cryst Growth 1995;150:460–6.

[53] Sato T, Mitsuhara M, Iga R, Kanazawa S, Inoue Y. J Cryst Growth 2011;315:64–7.
[54] Consorte CD, Fong CY, Watson MD, Yang LH, Ciraci S. Mater Sci Eng 2002;B96:141–4.
[55] Stringfellow GB, Fetzer CM, Lee RT, Jun SW, Shurtleff JK. Mater Res Soc Proc 2000;583:201–10.
[56] Zhang L, Tang HF, Schieke J, Mavrikakis M, Kuech TF. J Cryst Growth 2002;242:302–8.
[57] Zvonkov BN, Karpovich IA, Baidus NV, Filatov DO, Morozov SV, Gushina YY. Nanotechnology 2000;11:221–6.
[58] Stringfellow GB. J Appl Phys 1983;54:404–9.
[59] Stringfellow GB. J Cryst Growth 1989;98:108–17.
[60] Foster LM. J Electrochem Soc 1974;121:1662–5.
[61] Ishida K, Tokunaga H, Ohtani H, Nishizawa T. J Cryst Growth 1989;98:140–7.
[62] Onda T, Ito R. Jpn J Appl Phys Part 1 1991;30:1613–9.
[63] Mbaye AA, Wood DM, Zunger A. Phys Rev B Condens Matter 1988;37:3008–24.
[64] Wood DM, Zunger A. Phys Rev Lett 1988;61:1501–4.
[65] Jacobsen H, Puchala B, Kuech TF, Morgan D. Phys Rev B 2012;86:085207.
[66] Larsen CA, Buchan NI, Li SH, Stringfellow GB. J Cryst Growth 1990;102:103–16.
[67] Lee PW, Omstead TR, McKenna DR, Jensen KF. J Cryst Growth 1987;85:165–74.
[68] Salim S, Jensen KF, Driver RD. J Cryst Growth 1994;145:28–35.
[69] Omstead TR, Van Sickle PM, Lee PW, Jensen KF. J Cryst Growth 1988;93:20–8.
[70] Jacko MG, Price SJW. Can J Chem 1963;41:1560–7.
[71] Dunlop AN, Kominar RJ, Price SJW. Can J Chem 1970;48:1269–72.
[72] Maa BY, Dapkus PD. J Cryst Growth 1990;105:213–20.
[73] Kuech TF, Veuhoff E. J Cryst Growth 1984;68:148–56.
[74] Aspnes DE, Colas E, Studna AA, Bhat R, Koza MA, Keramidas VG. Vacuum 1990;41:978–81.
[75] Kuech TF, Potemski R. Appl Phys Lett 1985;47:821–3.
[76] Kuech TF, Scilla GJ, Cardone F. J Cryst Growth 1988;93:550–6.
[77] Foord JS, Davies GJ, Tsang WT. Chemical beam epitaxy and related techniques. Wiley; 1997.
[78] Suntola T. Atomic layer epitaxy. Blackie; 1990.
[79] Banse BA, Creighton JR. Surf Sci 1991;257:221–9.
[80] Freer RW, Martin T, Lane PA, Whitehouse CR, Hogan R, Foord JS, et al. J Cryst Growth 1993;127:152–7.
[81] Lane PA, Martin T, Freer RW, Calcott DJ, Whitehouse CR, Jones AC, et al. Appl Phys Lett 1992;61:285–7.
[82] Bohling DA, Muhr GT, Abernathy CR, Jordan AS, Pearton SJ, Hobson WS. J Cryst Growth 1991;107:1068–9.
[83] Ishikura K, Hayashi K-i, Ogawa T, Hasegawa F. Jpn J Appl Phys Part 2: Lett 1993;32:L1014–6.
[84] Lorberth J, Dorn R, Wocadlo S, Massa W, Gobel EO, Marschner T, et al. Adv Mater 1992;4:576–9.
[85] Squire DW, Dulcey CS, Lin MC. Proceedings of medicine and biology, proceedings of ICALEO'85. San Francisco, CA, USA: Laser Inst of America; 1985. p. 148–51.
[86] Suzuki N, Anayama C, Masu K, Tsubouchi K, Mikoshiba N. Jpn J Appl Phys Part 1: Regul Pap Short Notes 1986;25:1236–42.

[87] Itatani K, Hasegawa M, Aizawa M, Howell FS, Kishioka A, Kinoshita M. J Am Ceram Soc 1995;78:801–4.

[88] Kuech TF, Veuhoff E, Kuan TS, Deline V, Potemski R. J Cryst Growth 1986;77:257–71.

[89] Green ML, Levy RA, Nuzzo RG, Coleman E. Thin Solid Films 1984;114:367–77.

[90] Roberts JS, Button CC, David JPR, Jones AC, Rushworth SA. J Cryst Growth 1990;104:857–60.

[91] Gladfelter WL, Boyd DC, Jensen KF. Chem Mater 1989;1:339–43.

[92] Buchan NI, Larsen CA, Stringfellow GB. J Cryst Growth 1988;92:591–604.

[93] Larsen CA, Stringfellow GB. J Cryst Growth 1986;75:247–54.

[94] Braker W, Mossman AL, Siegel D. Effects of exposure to toxic gases: first aid and medical treatment. Matheson; 1977.

[95] Tamaru K. J Phys Chem 1955;59:777–80.

[96] Larsen CA, Buchan NI, Stringfellow GB. Appl Phys Lett 1988;52:480–2.

[97] Nishizawa J, Kurabayashi T. J Electrochem Soc 1982;130:413–7.

[98] Schlyer DJ, Ring MA. J Organomet Chem 1976;114:9–19.

[99] Leys MR, Veenvliet H. J Cryst Growth 1981;55:145–53.

[100] Safvi SA, Mountziaris TJ. Proc Mater Res Soc 1993;282:157–62.

[101] Larsen CA, Buchan NI, Li SH, Stringfellow GB. J Cryst Growth 1989;94:663–72.

[102] Kuech TF, Khandekar AA, Rathi M, Mawst LJ, Huang JYT, Song X, et al. J Cryst Growth 2008;310:4826–30.

[103] Khandekar AA, Yeh JY, Mawst LJ, Song X, Babcock SE, Kuech TF. J Cryst Growth 2007;303:456–65.

[104] Khandekar AA, Yeh JY, Mawst LJ, Song X, Babcock SE, Kuech TF. J Cryst Growth 2007;298:154–8.

[105] Manion REHJA, Levin RD, Burgess Jr DR, Orkin VL, Tsang W, McGivern WS, et al. NIST chemical kinetics database, NIST standard reference database 17, version 7.0 (Web version), release 1.4.3, data version 2008.12, National Institue of Standards and Technology, Gaithersburg, Maryland; 20899–8320.

[106] Bourret-Courchesne E, Ye Q, Peters DW, Arnold J, Ahmed M, Irvine SJC, et al. J Cryst Growth 2000;217:47–54.

[107] Lee RT, Stringfellow GB. J Electron Mater 1999;28:963–9.

[108] Sun YM, Sloan DW, McEllistrem M, Schwaner AL, White JM. J Vac Sci Technol A 1995;13:1455–60.

[109] Schmidtling T, Klein M, Pohl UW, Richter W. MRS Internet J Nitride Semicond Res 2000;5. art. no. W3.43.

[110] Liu Z, Lee RT, Stringfellow GB. J Cryst Growth 1998;191:1–7.

[111] Kappers MJ, Warddrip ML, Hicks RF. J Cryst Growth 1998;191:332–40.

[112] Williams KC, Brown TL. J Am Chem Soc 1966;88:5460–5.

[113] Henold KL, Soulati J, Oliver JP. J Am Chem Soc 1969;91:3171–4.

[114] Zaouk A, Salvetat E, Sakaya J, Maury F, Constant G. J Cryst Growth 1981;55:135–44.

[115] Leib A, Emerson MT, Oliver JP. Inorg Chem 1965;4:1825–6.

[116] Graves RM, Scuseria GE. J Chem Phys 1992;96:3723–31.

[117] Coward KM, Jones AC, Bickley JF, Steiner A, Smith LM, Ravetz MS, et al. J Cryst Growth 2000;221:81–5.

[118] Laube G, Kohler U, Weidlein J, Scholz F, Streubel K, Dieter RJ, et al. J Cryst Growth 1988;93:45–51.

[119] Coward KM, Jones AC, Pemble ME, Rushworth SA, Smith LM, Martin T. J Electron Mater 2000;29:151–5.

[120] Shatunov VV, Korlyukov AA, Lebedev AV, Sheludyakov VD, Kozyrkin BI, Orlov VY. J Organomet Chem 2011;696:2238–51.

[121] Kuech TF, Potemski R, Cardone F, Scilla G. J Electron Mater 1992;21:341–6.

[122] Ryan JM, Huang JW, Kuech TF, Bray KL. J Appl Phys 1994;76:1175–9.

[123] Benz KW, Renz H, Weidlein J, Pilkuhn MH. J Electron Mater 1981;10:185–92.

[124] Miyakoshi K, Fujii K, Hidaka T, Suemune I, Nakagawa M, Ogawa T. J Cryst Growth 1994;136:152–6.

[125] Abernathy CR, Bohling DA. J Cryst Growth 1992;120:195–9.

[126] Jones AC, Rushworth SA, Bohling DA, Muhr GT. J Cryst Growth 1990;106:246–52.

[127] Kohzen A, Tohmori Y, Akatsu Y, Kamada H. J Cryst Growth 1992;124:70–5.

[128] Sundaram VS, Fraas LM, Samuel CC. J Electron Mater 1992;21:1047–50.

[129] Jones AC, Wright PJ, Cockayne B. J Cryst Growth 1991;107:297–308.

[130] Jones AC, Rushworth SA, O'Brien P, Walsh JR, Meaton C. Adv Mater Opt Electron 1994;4:343–7.

[131] Lovergine N, Longo M, Gerardi C, Manno D, Mancini AM, Vasanelli L. J Cryst Growth 1995;156:45–51.

[132] Han J, Crawford MH. SPIE 1998;3419:46–50.

[133] Thon A, Safvi SA, Kuech TF. Proc Mater Res Soc 1996;423:445–50.

[134] Timoshkin AY, Bettingtt HF, Schaefer III HF. J Phys Chem A 2001;105:3240–8.

[135] Safvi SA, Redwing JM, Tischler MA, Kuech TF. J Electrochem Soc 1997;144:1789–96.

[136] Parikh RP, Adomaitis RA, Aumer ME, Partlow DP, Thomson DB, Rubloff GW. J Cryst Growth 2006;296:15–26.

[137] Walker R, Gurary AI, Yuan C, Zawadzki P, Moy K, Salagaj T, et al. Mater Sci Eng B 1995;B35:97–101.

[138] Wang HX, Wang T, Mahanty S, Komatsu F, Inaoka T, Nishino K, et al. J Cryst Growth 2000;218:148–54.

[139] Yang C-C, Huang C-K, Chi G-C, Wu M-C. J Cryst Growth 1999;200:39–44.

[140] Nishida K, Haneda S, Hara K, Munekata H, Kukimoto H. J Cryst Growth 1997;170:312–5.

[141] Creighton JR, Wang GT. J Phys Chem A 2005;109:10554–62.

[142] Creighton JR, Wang GT, Breiland WG, Coltrin ME. J Cryst Growth 2004;261:204–13.

[143] Wang GT, Randall Creighton J. J Phys Chem A 2006;110:1094–9.

[144] Lee RT, Stringfellow GB. J Cryst Growth 1999;204:247–55.

[145] Watwe RM, Dumesic JA, Kuech TF. J Cryst Growth 2000;221:751–7.

[146] Coltrin ME, Randall Creighton J, Mitchell CC. J Cryst Growth 2006;227:566–71.

[147] Brien D, Dauelsberg M, Christiansen K, Hofeldt J, Deufel M, Heuken M. J Cryst Growth 2007;303:330–3.

[148] Clayton AJ, Irvine SJC. J Cryst Growth 2007;300:277–83.

[149] Talalaev RA, Yakovlev EV, Karpov SY, Makarov YN. J Cryst Growth 2001;230:232–8.

[150] Tirtowidjojo M, Pollard R. J Cryst Growth 1989;98:420–38.

[151] Mountziaris TJ, Jensen KF. J Electrochem Soc 1991;138:2426–39.

[152] Jensen KF, Fotiadis DI, Mountziaris TJ, Einset EO, Kuech TF. Symposium on process physics and modeling in semiconductor technology. J Electrochem Soc 1991:142–60.

[153] Masi M, Simka H, Jensen KF, Kuech TF, Potemski R. J Cryst Growth 1992;124:483–92.

[154] Sun JX, Redwing JM, Kuech TF. Phys Stat Sol A 1999;176:693–8.

[155] Sun JX, Redwing JM, Kuech TF. J Electron Mater 2000;29:2–9.

[156] Pawlowski RP, Theodoropoulos C, Salinger AG, Mountziaris TJ, Moffat HK, Shadid JN, et al. J Cryst Growth 2000;221:622–8.

[157] Sholl D, Steckel JA. Density functional theory: a practical introduction. Wiley; 2011.

[158] Engel E, Dreizler RM. Density functional theory: an advanced course. Springer; 2011.

[159] Parr RG, Yang W. Density-functional theory of atoms and molecules. USA: Oxford University Press; 1989.

[160] Moscatelli D, Caccioppoli P, Cavallotti C. Appl Phys Lett 2005;86:1–3.

[161] Kempisty P, Strak P, Sakowski K, Krukowski S. J Cryst Growth 2014;390:71–9.

[162] Kempisty P, Strak P, Sakowski K, Krukowski S. J. Crystal Growth 2014;401:514–7.

[163] Krukowski S, Kempisty P, Jalbout AF. J Chem Phys 2008;129.

[164] Cardelino BH, Cardelino CA. J Phys Chem 2011;C115:9090–104.

[165] Suzuki H, Togashi R, Murakami H, Kumagai Y, Koukitu A. Phys Stat Sol C 2011;8:2267–9.

[166] Ben Naceur H, Mzoughi T, Moussa I, Nguyen L, Rebey A, El Jani B. Phys E 2010;43:106–10.

[167] Chapman DC, Howard AD, Rieth L, Wixom RR, Stringfellow GB. Mater Res Soc Symp 2003;794:291–6.

[168] Chapman DC, Stringfellow GB, Bell A, Ponce FA, Lee JW, Seong TY, et al. J Appl Phys 2004;96:7229–34.

[169] Wixom RR, Rieth LW, Stringfellow GB. J Cryst Growth 2004;269:276–83.

[170] Zhu JY, Liu F, Stringfellow GB. Phys Rev Lett 2008;101.

[171] Gokhale AA, Kuech TF, Mavrikakis M. J Cryst Growth 2005;285:146–55.

[172] Zhang L, Tang HF, Schieke J, Mavrikakis M, Kuech TF. J Appl Phys 2002;92:2304.

[173] Gokhale AA, Kuech TF, Mavrikakis M. J Cryst Growth 2007;303:493–9.

Reprinted from The Handbook of Crystal Growth, Vol 3B, 2nd Edition, Chapter 16, Matthias Bickermann and Tania Paskova, Vapor Transport Growth of Wide Bandgap Materials, 621-669, Copyright 2015, with permission from Elsevier .

16 Vapor Transport Growth of Wide Bandgap Materials

Matthias Bickermann[1,2], Tania Paskova[3]

[1]LEIBNIZ INSTITUTE FOR CRYSTAL GROWTH, BERLIN, GERMANY;
[2]INSTITUTE FOR CHEMISTRY, TECHNICAL UNIVERSITY BERLIN, BERLIN, GERMANY;
[3]DEPARTMENT OF ELECTRICAL AND COMPUTER ENGINEERING, NORTH CAROLINA STATE UNIVERSITY, RALEIGH, NC, USA

CHAPTER OUTLINE

16.1 Introduction 622
16.2 High Temperature Sublimation Growth of Wide Bandgap Materials (SiC and AlN) 623
16.2.1 Brief History and Applications of Bulk SiC and AlN Growth 623
16.2.2 Crystal Growth by High Temperature Dissociative Sublimation (PVT Method) 625
16.2.2.1 Growth Conditions 625
16.2.2.2 Considerations from Growth Theory 627
16.2.2.3 Dissociative Sublimation and Rate-Limiting Species 628
16.2.2.4 Crystal Habit and Anisotropic Growth 630
16.2.3 Technology of High Temperature Sublimation (PVT) Growth 631
16.2.3.1 Growth Setup and Process 631
16.2.3.2 Hot-Zone Materials 633
16.2.3.3 Seeded Growth and Crystal Enlargement 634
16.2.3.4 Doping 636
16.2.4 Structural Defects in PVT-Grown SiC and AlN Bulk Crystals 638
16.3 HVPE of Nitride Semiconductors (AlN, GaN, InN, and Ternary Alloys) 641
16.3.1 Thermodynamic Analysis of HVPE Growth of Compound and Ternary Nitride Growth 641
16.3.2 Growth Kinetics 645
16.3.3 Laboratory and Industrial Setups 647
16.3.4 Growth on Foreign Substrates 649
16.3.4.1 Substrates and Buffers 649
16.3.4.2 Template Growth 650
16.3.4.2 Quasi-Bulk Single-Wafer Growth 651
16.3.3.3 Bulk Growth 654

Handbook of Crystal Growth. http://dx.doi.org/10.1016/B978-0-444-63303-3.00016-X
Copyright © 2015 Elsevier B.V. All rights reserved.

16.3.5 Homoepitaxial Seeded Growth 654
16.3.6 Growth Related Properties 656
16.3.6.1 Residual Impurities and Native Defects 656
16.3.6.2 Doping 657
16.3.6.3 Structural Defects 659
16.4 Conclusion **661**
Acknowledgements **661**
References **661**

16.1 Introduction

Novel semiconductor materials show bandgap energies greater than 3 eV, which exceeds the classical definition of a semiconductor. Nevertheless, they can be doped (i.e., made *n*-type or *p*-type conducting) by introducing neighboring elements from the periodical table, in a way conventional semiconductors are. Out of these wide bandgap materials, gallium nitride (GaN) caused the solid state lighting revolution in optoelectronics and enabled the fabrication of blue laser diodes, silicon carbide (SiC) is about to take high shares in high power electronics, and aluminum nitride (AlN) is a promising material for UV optoelectronics. Other materials are also expected to find their applications, but are not in the scope of this work.

SiC, AlN, and GaN have in common that they crystallize in close-packed structures with strong, partly ionic bonding. As a consequence, these materials exhibit a very high thermal stability (e.g., melting point) and mechanical strength. The latter ensures their unique applicability for devices operating in a harsh environment, but also presents serious challenges to grow them as bulk single crystals. In the case of SiC, formation of different polytypes (modifications with different stacking sequences of the Si-C bilayers along the hexagonal *c*-axis direction) further complicates crystal growth. Providing conditions for melt growth is impossible or at least extremely difficult because the materials dissociate before they melt, and there is hardly any crucible material available that sustains against the molten compounds.

Unfortunately, most wide bandgap materials are not easily grown from solution either. For example, the solubility of nitrogen in liquid gallium is extremely low at atmospheric pressure and temperatures of GaN stability. It increases with pressure and temperature but is still limited to about 1 at.% even at pressures up to 2.0 GPa and temperatures of about 1600 °C. Thus, to overcome limitations of solubility and the challenges of melting conditions, alternative approaches have been developed, such as solvothermal growth, flux-mediated growth, or vapor transport growth. In fact, today vapor transport by sublimation or hydride vapor phase epitaxy (HVPE) is the common technique to produce bulk crystals of the most prominent and advanced wide bandgap semiconductor materials, SiC, AlN, and GaN.

16.2 High Temperature Sublimation Growth of Wide Bandgap Materials (SiC and AlN)

16.2.1 Brief History and Applications of Bulk SiC and AlN Growth

Today, bulk SiC and AlN crystals are almost exclusively grown by physical vapor transport (PVT). In this method, sublimation is used to facilitate the transport, mediated, e.g., by a concentration gradient that is induced by a temperature gradient, from the hotter source to the colder growth area, where the species recondense to form a crystal. While there are significant differences in growth technology, many common features allow for a unified discussion of growth of bulk SiC and AlN by PVT. Note that alternative growth methods like high temperature hot-wall chemical vapor deposition (HT-CVD) [1a,1b] and high temperature solution/flux growth [2], as well as PVT variations using a gas inlet [3], liquid precursors [4], or the sandwich sublimation method [5a,5b] are also investigated for bulk growth, but currently remain at a research level due to unresolved restrictions in crystal size, growth rate, or yield.

The first industrial synthesis of bulk SiC was performed around 1890 by E. G. Acheson [6] to utilize its hardness as an abrasive powder. In 1955, J. A. Lely [7] developed laboratory furnaces that replicated an isolated Acheson druse by heating a cave formed by SiC powder feedstock, either carefully arranged or stabilized by a porous graphite cylinder, within a graphite crucible (Figure 16.1(a)). At around 2600 °C in an argon atmosphere of about 1 bar, the SiC sublimates and SiC crystals nucleate and grow attached to the inner walls. The technological breakthrough was paved around 1976 when Yu. M. Tairov and V. F. Tsvetkov [11a,11b,12a,12b] modified the Lely-type growth process by separating the growth room into a (hotter) source and a (colder) growth area and mounting a SiC seed in the growth area. The seed crystal sets up the orientation, the initial diameter, and in most cases also the polytype of the growing crystal. The seeding also enables steady improvement of crystal quality and diameter by repeated growth on seeds prepared from previously grown crystals. Vodakov (1974) invented carburized Ta crucibles for SiC growth [13], and Ziegler (1983) employed an alternate

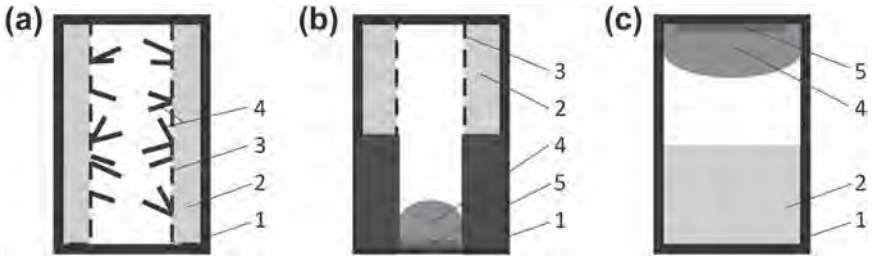


FIGURE 16.1 Schematic cross-section drawings of hot zone setups used for SiC bulk crystal growth. (a) Lely setup [7], (b) Ziegler setup [8a,8b,9], (c) modified PVT setup as typically used today [10], 1: graphite crucible, 2: SiC source material, 3: optional porous graphite cylinder, 4: growing SiC crystal(s), 5: SiC seed.

setup design with seed-down configuration [8a,8b], which was later used by Barrett et al. [9] (Figure 16.1(b)), but both were superseded during the 1990s by the design now commonly used [10] (Figure 16.1(c)).

In the 1980s, SiC substrates were first used to produce blue light emitting diodes (LEDs) [8], however, with low efficiency, as SiC is an indirect semiconductor. Later on, SiC was used as substrate material for InGaN/GaN LEDs. At the same time, SiC was successfully reconsidered as a promising material for high power electronics [14,15]. The crystal diameter steadily evolved, with 2-in, 4-in, and 6-in SiC substrates available commercially in 1999, 2005, and 2013, respectively [16]. While power electronics based on 4H-SiC is now established, and semi-insulating 4H-SiC substrates are used in GHz electronics, 6H-SiC as substrate for GaN-based optoelectronics was widely replaced by more cost-effective sapphire and silicon. Consequently, the focus in bulk SiC growth shifted from 6H-SiC to 4H-SiC. A part of SiC bulk production is used for gemstone manufacture [17].

The first serious attempts to grow bulk AlN single crystals dates to the 1960s [18,19]. AlN powder, sometimes also liquid Al, was used as source material in an atmosphere of nitrogen at temperatures exceeding 1700 °C. The experiments were conducted in carbon-containing setups (Figure 16.2(a)), which, however, led to highly contaminated crystals. In 1976, G. A. Slack and T. F. McNelly achieved mm-sized AlN single crystals with high purity [20,22a,22b] by using a type of Piper–Polich [23] growth technique, in which a sealed tungsten crucible was moved through a hot zone of an inductively heated furnace (Figure 16.2(b)). However, research on growth of large-area AlN bulk single crystals only started in the late 1990s with the advent of wide bandgap semiconductor research. Single-crystalline AlN is considered a preferential substrate material for UV optoelectronic applications (LEDs, lasers, and sensors), where devices contain epilayers of group III-nitride alloys with high Al content [24]. After some preliminary concepts [21] (Figure 16.2(c)), the successful SiC crucible design (Figure 16.1(c)) was widely adopted for AlN bulk growth, while using tungsten or tantalum carbide as hot-zone materials

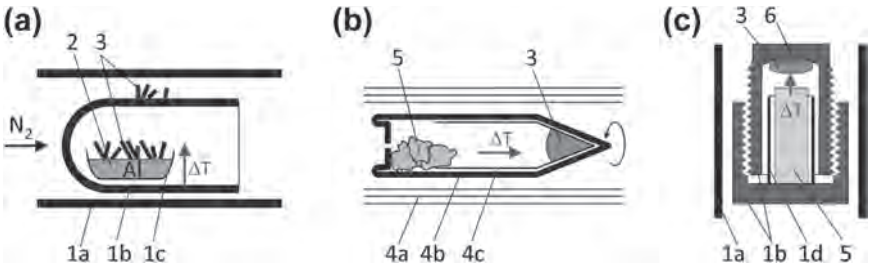


FIGURE 16.2 Schematic cross-sections of growth setups historically used for AlN bulk crystal growth. (a) graphite-based setup after Pastrnak et al. [19], (b) tungsten-based setup after Slack [20], (c) graphite-based setup for seeding on SiC after Balkas at el. [21]. 1: graphite parts (a heater, b tube/crucible, c boat, d sleeve); 2: liquid Al; 3: growing AlN crystal(s); 4: tungsten or rhenium parts (a heat shields, b rotating welded crucible with leak hole, c inner liner); 5: AlN source material; 6: SiC seed.

(see below). As of today, a few companies and research groups have demonstrated AlN single crystals of up to 2-in diameter. But worldwide AlN wafer production is still very small as compared to SiC.

16.2.2 Crystal Growth by High Temperature Dissociative Sublimation (PVT Method)

16.2.2.1 Growth Conditions

Several phase diagrams based on calculations and experimental data exist for the Si-C [25,26] and the Al-N [22a,22b,27] system; SiC (different polytypes are usually not accounted for [11a,11b,28].) and AlN are the only binary compounds in those systems. At about 2830 °C, SiC undergoes peritectic decomposition into solid C and a Si-based liquid containing about 13 at.% of carbon (Figure 16.3). In the interesting temperature range ($T > 660$ °C), AlN is in equilibrium with liquid Al or gaseous N_2. A liquid is expected to form at the decomposition point, whose composition however remains unclear. In any case, formation of a liquid at a given pressure represents the upper limit for crystal growth, as it will inevitably destroy the growing crystal or the setup.

Figure 16.4 shows calculated temperature-dependent partial pressures of gaseous species involved in the decomposition [22a,22b,29–31]; the occurrence of different species in the gas phase will be discussed later on. Assuming that the total partial pressure of growth species has to be at least 1 mbar to facilitate bulk growth by PVT, reasonable growth rates for SiC bulk growth can be achieved only at temperatures exceeding 2100 °C [28]. In contrast, the Al partial pressure over AlN provides sufficient evaporation for mass transport already at 1600 °C, but due to insufficient surface adatom

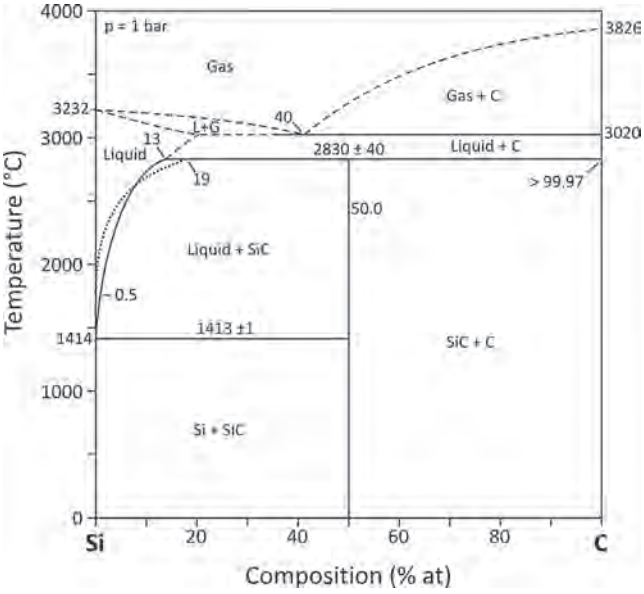


FIGURE 16.3 Phase diagram of the SiC-System (p = 1 bar) after Kleykamp et al. [26] (solid and slashed lines) and after Scace and Slack [25] (dotted line).

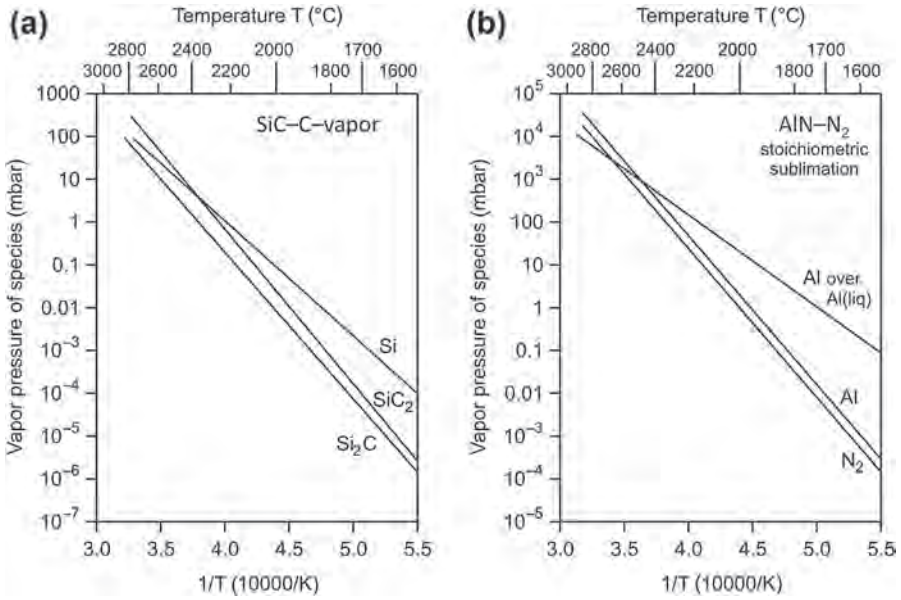


FIGURE 16.4 Calculated partial pressures for (a) SiC under C-rich conditions after Lilov [29], and (b) AlN under N-rich conditions after Slack and NcNelly [22a,22b] (note the different ordinate).

mobility and N_2 chemical activity, only very thin needles form [30]. Higher temperatures are beneficial for increasing both growth rate and surface kinetics, i.e., helping the atoms to properly arrange themselves at the surface.

Sublimation into vacuum is possible but leads to high deposition rates and polycrystalline growth due to lack of growth control. Transport and deposition during growth is regulated by buffering, i.e., using an additional "inert gas." For SiC, mostly argon is employed; AlN is grown with N_2 "in excess." To control and set p_{sys} during growth, the crucible has to be semi-open. The inert gas is introduced in the outer setup area at a controlled flow rate, and excess gas is pumped to exhaust. This implies that also a fraction of vapor species evades the crucible during growth, which influences the gas phase composition in the hot zone and may alter growth conditions.

The process windows for stable growth of SiC or AlN depend on the polytype and growth orientation (polarity). 4H-SiC single crystals are reported to grow at temperatures below 2300 °C. The temperature limit for 4H-SiC growth is associated with the stoichiometry in the gas phase [11a,11b,28]; reasonable growth rates can still be achieved by lowering the pressure to $p_{sys} = 5$ mbar [32]. In contrast, 6H-SiC boules are grown at 2300–2500 °C and $p_{sys} = 5$–50 mbar [33]. The reported growth temperatures vary, probably due to differences in pyrometer measurement. Formation of polytypes is also sensitive to stoichiometry and abundance of impurities in the gas phase [11a,11b], and to polarity of the growth surface. Growth of 4H-SiC is only stable on C-polar or non-polar planes, while it converts to 6H or 15R during growth on Si-polar SiC basal planes [33,34].

6H-SiC [35] and 15R-SiC [36] are grown with better structural quality and lower risk of polytype inclusions on the Si-polar basal plane. This is attributed to different surface energies of the crystal planes, leading to different surface kinetics and morphology (see below). AlN bulk growth is performed at temperatures ranging from 2000 to 2300 °C. Higher temperatures and supersaturations seem to stabilize N-polar growth [37], but influence of impurities is also under discussion. Typically, p_{sys} is chosen in the range of 300–900 mbar, while the dependence of pressure on growth rate is not as sensitive as in the case of SiC [31,38].

Understanding of sublimation growth of SiC and AlN remains limited due to unavoidable presence of impurities at the high temperatures employed for crystal growth. They may significantly change growth behavior via impurity-assisted transport of growth species [39,40], or by acting as surfactants, altering kinetic barriers at the growth surface [41,42]. As a consequence, preparation of highest purity starting materials is not only mandatory to control semiconductor properties of the grown crystals, but it is also necessary for stable and reproducible crystal growth.

16.2.2.2 Considerations from Growth Theory

Under thermodynamic equilibrium, the pressure, p, and the temperature, T, where a solid-to-gas phase transition of a single component occurs are linked by the Clausius–Clapeyron equation:

$$dp/dT = \Delta H/(T \cdot \Delta V), \tag{16.1}$$

where ΔH is the sublimation enthalpy (619 kJ/mol for SiC [43] and 630 kJ/mol for AlN [44]), $\Delta V = V_{gas} - V_{solid} \approx V_{gas} = RT/p$ is the ideal gas volume (as $V_{gas} >> V_{solid}$), and R is the universal gas constant. The equation can then be rewritten as [44]:

$$dp/dT = (\Delta H/R) \cdot (p/T^2). \tag{16.2}$$

Applying a temperature difference $\Delta T = T_{source} - T_{seed}$ between the hotter sublimation (source) and the colder recondensation (seed) area, a term describing the pressure ratio can be found by integration:

$$\sigma = \ln(p_{source}/p_{seed}) = (\Delta H/R) \cdot (1/T_{seed} - 1/T_{source}). \tag{16.3}$$

σ is called relative supersaturation, because the change in chemical potential $\Delta\mu = -RT_{seed} \cdot \ln\ (p_{source}/p_{seed})$ represents the driving force for transport and crystal growth. It can be approximated for small values by $\sigma \approx p_{source}/p_{seed} - 1$.

The sublimation of the source material is endothermic and depends on the surface area, in particular, on the form and grain size of the feedstock. The recondensation is accompanied by release of latent heat. The species flow, which is induced by a difference $\Delta p_v = |p_v^* - p_v|$ between the actual (supersaturated or supercooled) and the equilibrium partial pressure at the source or seed area, respectively, can be described by the Hertz–Knudsen equation:

$$J_v = \alpha_v \cdot (2\pi m R T_v)^{-1/2} \cdot \Delta p_v (v = \text{seed},\ \text{source}) \tag{16.4}$$

where $\alpha_v = 0\ldots1$ are the (effective) sublimation/condensation coefficients, which account for the surface reactions and kinetic barriers, and m is the molar mass of the transported species. Typically, $\alpha_{source} \leq \alpha_{seed}$ due to the source material properties [45]. Note that in a multicomponent system, it is sufficient to determine the flow of the rate-limiting species (see below) as it has the lowest supersaturation in the system, while all the other species are provided in excess. In SiC growth, α_{source} is often set to unity [46]. In AlN growth, $\alpha_{source} = 1$ for Al species, while the dissociation of N_2 at the growth interface is considered to yield values in the range of $\alpha_{seed} = 2\ldots5\cdot10^{-3}$ [47,48].

Natural convection is most probably absent in currently used growth geometries, as Grashof numbers are typically below 100 even in 4-in diameter growth cells [49,50]. Similarly, Stefan flow is not considered a significant transport mechanism for SiC and AlN sublimation growth as the inert gas concentration is several times higher than the concentration of growth species [46]. As a consequence, the mass transport in the gas phase is dominated by diffusion (Fick's law):

$$J_{transp} = -D \cdot (dc/dx) = D \cdot (dc/dT) \cdot (\Delta T/L) \approx D/RT \cdot (dp/dT) \cdot (\Delta T/L), \tag{16.5}$$

where $D \propto T^{1.8}/p_{sys}$ is the binary diffusion coefficient from kinetic gas theory, $c \approx RT \cdot p$ is the concentration, and $p = e^{-\Delta G/RT}$ (see Figure 16.4) is the partial pressure of the rate-limiting species, x is the coordinate between source and seed area, and L is the source-to-seed distance. The last expression is obtained assuming an ideal gas and neglecting higher-order terms [44]. With Eqn (16.2), one yields:

$$J_{transp} \propto (\Delta T/L) \cdot e^{-\Delta G/RT} \Big/ \left(T^{1.2} \cdot p_{sys}\right). \tag{16.6}$$

The parameters governing the mass transport are thus T, p_{sys}, and $\Delta T/L$. If the limiting step for bulk growth is indeed mass transport, i.e., sublimation or recondensation kinetics are considerably faster than diffusion in the vapor phase, the growth rate is $R_G = J_{transp}\, m/\rho$ where m is the mass and ρ the density of the growth-limiting vapor species. The experimentally achievable growth rate is lower due to volatile species leaving the semi-open crucible and reacting with the crucible materials. The growth rate increases with increasing temperature gradient and temperature (due to the exponential term), and with decreasing total pressure, as $R_G \propto 1/p_{sys}$ [44,46]. Note, however, that often only a relatively low growth rate (typically lower than 200 μm/h) will allow for single-crystalline growth without deterioration of structural quality. This is achieved by applying low axial gradients of 2–10 K/cm [51] in case of AlN growth and 5–30 K/cm [10] in case of SiC growth, which restricts the supersaturation to values in the range of 10–50%.

16.2.2.3 Dissociative Sublimation and Rate-Limiting Species

The sublimation of SiC and AlN is dissociative. Chemical reactions are involved in the dissociation of the feedstock and the reassembling of the gaseous species when they get attached to the crystal. The main species in the vapor phase, calculated or identified by high temperature mass spectrometry [22a,22b,47,52,53] are shown in Figure 16.4. Other

species appear at much lower concentrations, and their relevance for crystal growth is negligible. Neglecting any influence of impurities, sublimation and recondensation will occur according to the following simplified reactions [22a,22b,54]:

$$6\mathrm{SiC(s)} \rightleftharpoons 2\mathrm{SiC_2(g)} + \mathrm{Si_2C(g)} + 2\mathrm{Si(g)} + \mathrm{C(s)}, \quad \text{and} \tag{16.7}$$

$$2\mathrm{AlN(s)} \rightleftharpoons 2\mathrm{Al(g)} + \mathrm{N_2(g)}. \tag{16.8}$$

Note that Eqn (16.7) only formally obeys a quantitative relation. The growing crystal enforces stoichiometry, as the existence range of the solid compounds SiC or AlN is confined [10], but the composition in the gas phase clearly deviates from stoichiometry.

SiC dissociates incongruently, leaving solid carbon behind, which accumulates in the source zone. The gas phase is Si rich; it can be derived from Figure 16.4 that the relevant ratio of atoms [29a,29b,29c],

$$N_{Si}/N_C = \left(2 \cdot p_{Si_2C} + p_{SiC_2} + p_{Si}\right) \Big/ \left(p_{Si_2C} + 2 \cdot p_{SiC_2}\right), \tag{16.9}$$

is in the order of 5…10 at growth temperature. On the other hand, the volatile Si partly reacts with the graphite crucible to form SiC_2 and Si_2C, and some Si is lost due to evasion from the crucible. As a consequence, the Si excess in the vapor phase depends on the growth setup and conditions, including the temperature gradient. Growth of SiC in semi-open graphite crucibles is considered to eventually happen in a C-rich regime (SiC-C-vapor equilibrium) with the danger of decomposing/graphitizing the source and—in extreme cases—the growing crystal. In contrast, growth at low temperatures or in Ta crucibles might be better described in a Si-rich regime (SiC-Si-vapor equilibrium).

AlN is grown with N_2 in excess, and

$$N_{Al} \Big/ N_{N_2} = p_{Al} \Big/ 2 \cdot p_{N_2} \approx 0.1. \tag{16.10}$$

While excess N_2 doesn't necessarily lead to N-rich growth conditions, this is the commonly assumed growth regime for AlN growth (AlN-N_2 system). The chemical activity of N_2 is most probably governed by kinetics of the surface reaction [30]

$$\mathrm{Al(ads)} + \mathrm{N_2(ads)} \rightleftharpoons \mathrm{AlN(s)} + \mathrm{N(ads)}. \tag{16.11}$$

Additionally, nitrogen could be dissociated by reaction with impurities (e.g., cyanogen formation).

Consideration of a Si-rich and C-rich (or, in the case of AlN, Al-rich and N-rich) thermodynamic system leads to different border cases with different partial pressures of the species in the vapor phase. As a consequence, the rate-limiting species in a diffusion-limited regime depend on both temperature and the border case under review. In case of SiC-C-vapor equilibrium, according to Lilov [29a,29b,29c] the rate-limiting reactions and equilibrium constants are

$$\mathrm{SiC(s)} \rightleftharpoons \mathrm{Si(g)} + \mathrm{C(s)} \quad \text{with} \quad K_1 = p_{Si}, \text{ and} \tag{16.12}$$

$$2\mathrm{SiC(s)} \rightleftharpoons \mathrm{SiC_2(g)} + \mathrm{Si(g)} \quad \text{with} \quad K_2 = p_{Si} \cdot p_{SiC_2}. \tag{16.13}$$

The first reaction leads to carbon accumulation in the SiC source. It is calculated to become unfeasible at $T > 2270\ ^\circ\mathrm{C}$, but graphitization of the source appears also at higher

temperatures. The vapor pressure of silicon is larger than that of SiC_2 at $T < 2270\,^{\circ}C$, less than that of SiC_2 at $T > 2630\,^{\circ}C$, and equal in between [29a,29b,29c]. Thus, at $T < 2270\,^{\circ}C$, SiC_2 is the rate-limiting species with $\sigma = (p^*_{SiC_2} \cdot p^*_{Si})/K_2 - 1$. For $T > 2270\,^{\circ}C$, Si is considered as rate-limiting species with $\sigma = p^*_{Si}/K_1 - 1$. Above 2630 °C, SiC starts to dissociate in the condensed phase, accompanied by formation of liquid silicon, if no carbon source is available. For AlN growth, most recent reports see Al transport as the rate-limiting step [30], with $K = p_{Al} \cdot p_{N_2}^{0.5}$. As N_2 is provided in excess and thus $p_{sys} \approx p_{N_2}$, Eqn (16.6) changes to [44,55].

$$J_{transp} \propto (\Delta T/L) \cdot e^{-\Delta G/RT} \Big/ \left(T^{1.2} \cdot p_{sys}^{1.5}\right). \tag{16.14}$$

Detailed models have been elaborated for SiC and AlN bulk growth, including, e.g., release of latent heat, advective flows, growth kinetics, and possible reactions during dissociative sublimation [56]. During the last decade, numerical modeling has become a standard tool also in SiC and AlN sublimation growth. Even the evolution of the growth interface and the formation of dislocations can be predicted from the heat and mass transfer data [57]. However, different results are obtained from the models due to different assumptions on the material properties at growth temperature, the dissociative reactions, the rate-limiting step, mass and heat transfer mechanisms, and effective sublimation/condensation coefficients.

16.2.2.4 Crystal Habit and Anisotropic Growth

Growth rate and growth mode strongly depend on the crystallographic orientation of the growth interface. The differences are caused by different surface energies and kinetics. As an example, the surface energies of SiC are 2.2 J/m^2 and 0.3 J/m^2 for the Si-polar and the C-polar basal plane, respectively [58]. Impurities in the gas phase may act as surfactant on particular facets [42]. Also, faceted and non-faceted areas show significant differences. As shown in Figure 16.5, SiC generally forms platelets, thus growth is slowest on both basal plane facets [30]. Dual-seed experiments remained ambiguous about

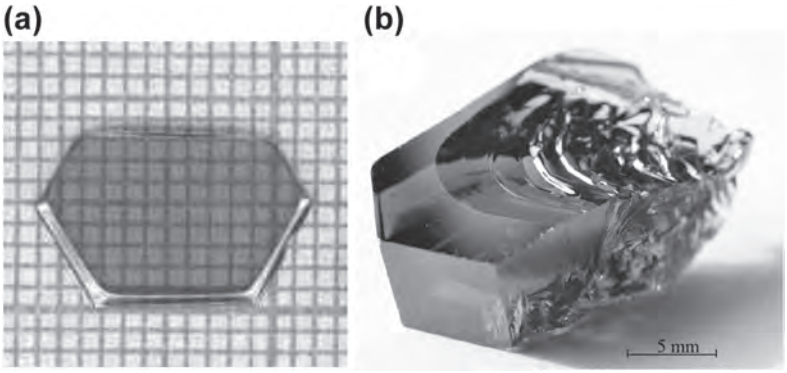


FIGURE 16.5 Spontaneously nucleated single crystals. (a) SiC platelet grown in a Lely furnace (on mm-sized grid), courtesy Heikki Helava/Nitride Crystals, Inc. [61]; (b) AlN crystal grown at T = 2200 °C [60].

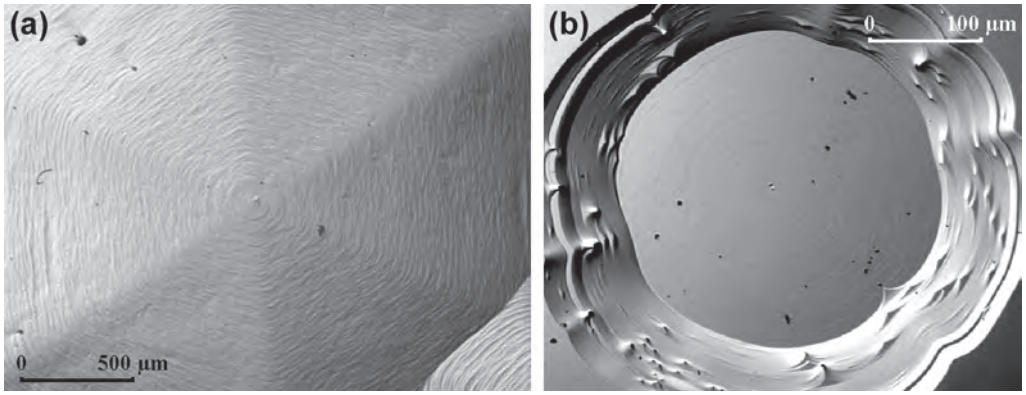


FIGURE 16.6 Spiral growth and step bunching on basal planes of SiC (optical microscopy images): (a) C-polar face, (b) Si-polar face.

growth rate dependence on polarity [33,62]. In contrast, the growth rate of AlN is slowest on the prismatic facets for all but the highest growth temperatures, thus the crystal habit changes from needles to almost equiaxed (isometric) crystals [30,60] with increasing temperature. Furthermore, AlN generally shows a stronger tendency to form pyramidal facets on the metal-polar side [59].

On the basal planes of SiC and AlN crystals, the dominant growth mechanism is in spiral growth, where a spiral originates from threading screw dislocations [63], thereby also preserving the SiC polytype during growth [64]. Step bunching is regularly observed on such surfaces, with the step height and terrace width depending on the supersaturation [65], surface inclination in respect to the basal plane [66], stoichiometry, impurities in the vapor phase, polytype, and polarity [37]. Due to the different surface energy, the spirals form hexagonal hillocks on the C-polar face and round plateaus on the Si-face of SiC [67], see Figure 16.6. Both types of morphologies have also been identified on basal plane AlN surfaces [68]. Crystals grown with an off-orientation or with very low density of dislocations are expected to grow in a step-flow mode.

16.2.3 Technology of High Temperature Sublimation (PVT) Growth

16.2.3.1 Growth Setup and Process

The hot zone of today's typically used vertical "modified PVT" setup consists of a cylindrical crucible with removable upper lid, surrounding susceptor, and thermal insulation (Figure 16.7). The crucible has to be porous or semi-open to allow for gas and pressure exchange with the environment, often provided already by the nonideal closure between the lid and the crucible. It is filled with source material—AlN or SiC as powder, sintered bodies, or lumps from previous growth experiments—to 50–80% of its total height.

Electrical power is used to heat the crucible either by induction (at 8–20 kHz frequency) or by resistive heating. The use of a susceptor is advantageous in that it remits

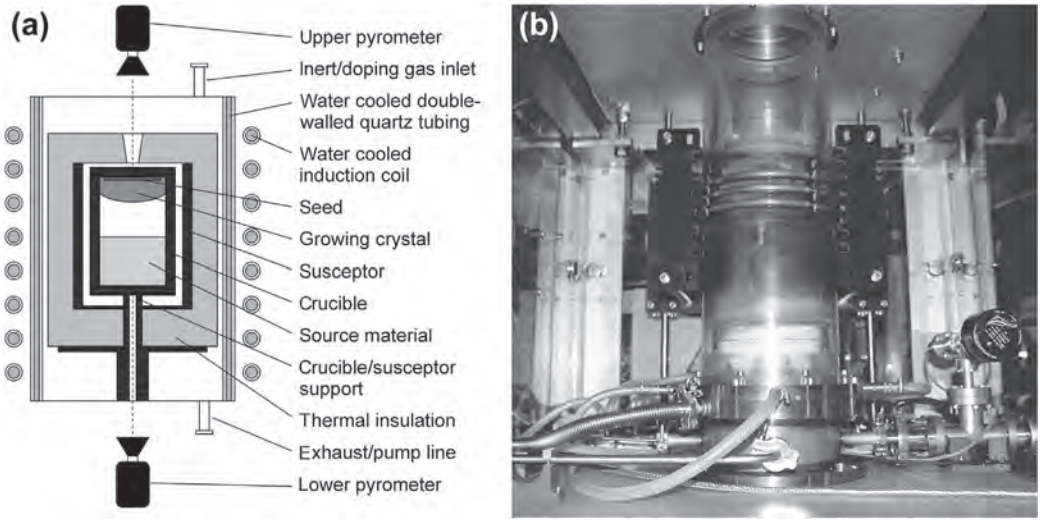


FIGURE 16.7 (a) Schematic and (b) photograph of a typical PVT growth setup.

the heat to the crucible via radiation, providing a more homogeneous temperature field in the growth cell. The setup is located inside a water-cooled growth vessel that provides the gas-tight enclosure, a loading port, and connections for pyrometer access and gas inlet/outlet as shown in Figure 16.7. The common vessel type consists of cylindrical double-walled quartz glass tubing with stainless steel flanges. As an alternative, the vessel can be made of stainless steel with the coil located inside the water-cooled vessel.

In order to provide the necessary purity, SiC or AlN source material is either synthesized directly from pure elements or prepared by purification of commercially available ceramic powder material. The latter can be achieved by high temperature processes, e.g., carbothermal reduction, sintering, or sublimation [22a,22b,71]. The knowledge of efficient purification is considered an important proprietary part of growth technology. After proper purification, the concentration of lightweight impurities (boron, carbon, oxygen, nitrogen) and trace metals should be clearly below 100 ppm and below 1 ppm, respectively.

The growth procedure typically includes the following steps: The hot zone is assembled and loaded into the reactor. Then the vessel is purged with inert gas. For high purity demands, a high vacuum ($<1\cdot10^{-5}$ mbar) preheating stage at moderate (1000–1200 °C) temperatures is used to remove moisture, adsorbed gases, and volatile impurities. The vessel is then filled with inert gas, and the growth cell is heated to growth temperature. During this stage, an elevated pressure may be chosen to suppress initial feedstock sublimation, as surface mobility of the species is still insufficient for single-crystal growth. Alternatively, the axial temperature gradient in the growth cell is

inverted, i.e., the seed is kept at a higher temperature than the source material to prevent early growth and to clean the seed surface. This is performed by moving the coil relative to the crucible [72]. If the growth temperature is reached, the gas flows are adjusted, gaseous dopants (e.g., nitrogen in SiC growth) are added, and a soft growth start is performed by reverting the temperature gradient or by slowly reducing the pressure to the finally desired value [11a,11b,12a,12b].

Maintaining the temperature gradients at the growth interface during growth is crucial in order to obtain crystals with high chemical and structural homogeneity. If the crystal length is small compared to the crucible dimensions, constant heating might be applied, but typically, a decrease of ΔT and thus R_G with growth time is observed [73]. Thus, the heater power is controlled by constant temperature monitoring. Corrections to the temperature field to account for the moving growth interface, the partial degradation of insulation materials, or the progressing feedstock consumption might also be achieved by a gradual change in heater position [74] or by separate control of several heaters. Considering the typical growth rates of 50–500 μm/h, it takes several days to grow 10–30 mm thick crystals. Mass transport yields exceeding 80% are possible if the evaporation losses through the semi-open crucible are kept at a low level [10]. Finally, the end of growth is initiated by decreasing the heater power, inverting the gradient again, or increasing the pressure. A controlled cooling is demanded to mitigate strain-induced defect formation.

16.2.3.2 Hot-Zone Materials

Due to their different chemical nature and materials compatibility, the choice of materials for the inner setup parts differs strongly for SiC and AlN bulk growth. In the case of SiC growth, all parts are made of high purity graphite/carbon, so no foreign chemical elements are introduced. The susceptor, the crucible support, and the crucible itself are machined from dense graphite parts (porosity 2–5% vol). Thermal insulation is provided by assembled parts of carbon-bonded carbon fiber (CBCF), carbon felt, or pressed exfoliated graphite. The porous nature of these materials effectively prevents generation of Joule's heat at induction frequencies of 8–20 kHz, chosen to match the intrusion depth of dense graphite to heat the susceptor homogeneously. The carbon purity is crucial; in former times, nominally undoped SiC crystals were *p*-type due to contamination with boron from the crucible and thermal insulation materials [33].

For AlN growth, requirements of refractory behavior and chemical inertness in regard to Al vapor strongly limits materials availability. A lot of work was dedicated to finding a chemically stable and suitable crucible material [75–78]. Graphite and boron nitride are stable up to temperatures of about 2000 °C, but lead to considerable contamination of the crystal with carbon or boron, respectively [42,77]. Coatings tend to crack and spall off due to differences in thermal expansion and chemical attack. Today, only tantalum carbide (TaC) and tungsten (W) are used as crucible materials in different combinations as described below. A few more materials have been evaluated (Re, TaN, HfN, TaB_2), but are not currently used.

Tungsten is long-term stable against Al vapor in the presence of excess N_2, and chemical erosion is negligible up to temperatures of about 2250 °C [20]. However, tungsten will react with oxygen, carbon, and silicon. The presence of SiC seeds as well as the use of a graphite susceptor or insulation parts is possible in such setups if not in direct contact, but the crucible lifetime will be seriously reduced. In contrast, TaC is chemically stable under AlN growth conditions at temperatures well exceeding 2300 °C. TaC elements are electrically conductive and compatible with graphite (for susceptor and insulation elements), tungsten (for an inner crucible), and SiC (as seeds), even if in direct contact. Long-term stability is generally limited by cracking due to internal grain growth [75] or decarburization. To prevent structural failure, they may be enclosed in graphite cylinders, which also act as a susceptor [79]. As a variant, carburized tantalum crucibles can be employed [80]. Such parts have no open porosity, and their mechanical stability under temperature cycling is excellent. However, especially if used in conjunction with graphite parts, such crucibles continue to carburize and finally become brittle, in particular at growth temperatures exceeding 2100 °C.

16.2.3.3 Seeded Growth and Crystal Enlargement

Both SiC and AlN growth are best performed on polar basal plane (c-plane) surfaces, because these planes possess isotropic in-plane properties. In SiC bulk growth, the demand of slightly offcut (2–8°) substrates for epitaxy [81] has led to optimized bulk growth using these offcut surface planes. On the other hand, growth in off orientations leads to formation of stacking faults [82]. Growth in other crystallographic directions is accompanied by an even higher density of structural defects, caused by propagation of basal plane dislocations and by crystal anisotropy, which leads to orientation-dependent growth mechanisms on the growth surface [83a,83b,84]. Thus, industrial production of boules remains focused on homoepitaxial seeds with basal plane surface. Wafers cut from the grown crystal are used as seeds in subsequent growth runs. A sample SiC crystal is shown in Figure 16.8(a).

In this regard, AlN growth is still in its infancy, and some groups still prepare their seeds out of freestanding single crystals that spontaneously nucleated on crucible parts in a Lely-type process, using conditions close to equilibrium and low nucleation density [59,85]. Such freestanding crystals, cf. Figure 16.5(b), are virtually unstrained and show the highest structural perfection, i.e., dislocation densities below 100/cm^2 without any micropipes or volume defects [60]. Single crystals with a size of up to $15 \times 15 \times 10$ mm^3 have been obtained. However, this process is not very reproducible; the yield of large and well-formed crystals is low and presumably depends on impurity contamination.

AlN crystals can also be grown on SiC seeds (Figure 16.8(b)), which are commercially available at industrial relevant sizes. AlN always grows Al-polar on polar SiC planes. However, the maximal crystal thickness is restricted to about 5 mm due to gradual deterioration of the structural quality. Still, the grown AlN layer can be separated from the SiC seed and used as a seed in subsequent AlN bulk growth [68,86]. The fundamental disadvantage is the partial decomposition of SiC in the presence of Al vapor already at

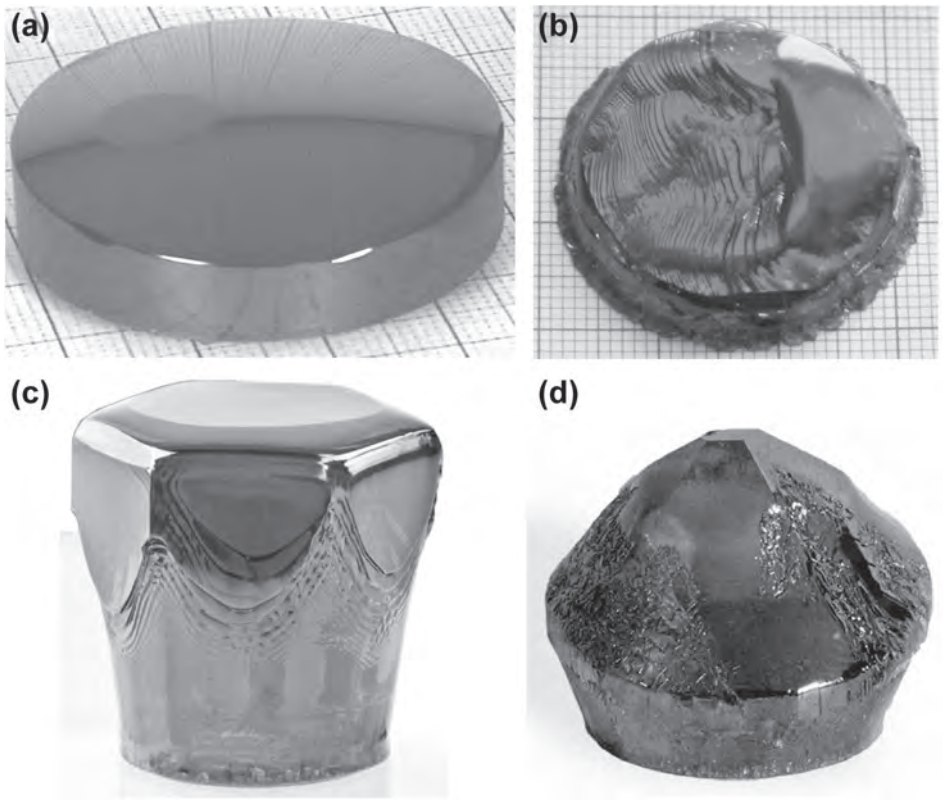


FIGURE 16.8 Bulk single crystals of SiC and AlN grown on seeds. (a) 4H-SiC bulk crystal (on mm grid) grown at the IKZ Berlin; (b) Al-polar AlN crystal grown on an SiC seed (on mm grid), courtesy R. R. Sumathi/LMU Munich [68]; (c) 1-in diameter AlN single crystal grown on the N-polar basal plane, courtesy Z. Sitar/Hexatech, Inc. [69]; (d) 1-in diameter AlN single crystal grown on the Al-polar basal plane, courtesy B. M. Epelbaum/CrystAl-N GmbH [70].

temperatures below 2000 °C. As a consequence, the AlN crystal is contaminated with up to several atomic percent of silicon [87]. Additionally, the mismatch of lattice parameters and thermal expansion coefficients between AlN and SiC lead to partial stress relaxation at the SiC/AlN interface, resulting in formation of tilted domains and the risk of crack formation.

Seed fixation is a critical issue in high temperature sublimation growth. Due to the differences in thermal expansion [78], a rigid interface between seed and crucible lid will cause strain and lead to crack formation or even seed separation during the heating-up stage. In contrast, pores or gaps between the seed and the lid lead to seed backside evaporation—material from the seed sublimes toward the colder crucible lid to close the pore or gap. As a consequence, voids travel through the seed and eventually through the growing crystal (negative crystal growth) and locally degrade the crystal quality [88,89]. Seed backside plating [90] is a possible means to mitigate both backside evaporation and cracking.

In case of SiC, chemical attachment to the lid is often performed using molten sugar [88]. During the heating-up stage in crystal growth, the glue decomposes into carbon and punctually bonds with the graphite lid. AlN seeds may be fixed in a similar way by AlN ceramic cement, which cures in air and also forms pores during sintering at growth temperatures. In the case of mechanical fixation, the seed is partially covered by a fixation rim. Finally, the seed can be fixed on the lid by heating the assembly in upside-down configuration until it is sublimated to the lid by sintering and surface sublimation.

A parasitic growth adjacent to the growing crystal leads to strain and crystal cracking during cooling due to anisotropic thermal expansion. Parasitic grains may induce structural defects, disturbance of structural quality, or even partial overgrowth of the main crystal [91]. In particular, a cylindrical or conical "growth channel" is proposed in order to close the space adjacent to the growing crystal and to provide for single-crystalline enlargement [92]. Another strategy is to facilitate freestanding growth by increasing the temperature adjacent to the seed area. Using tailored temperature fields, detached growth in a growth channel is possible [93].

The ideal interface shape in seeded sublimation growth is slightly convex, to allow the step flow from a single growth center (e.g., a screw dislocation to enable spiral growth) to spread across the whole surface area. The interface shape, and thus the local growth rate, during growth of SiC can be determined in situ by digital X-ray imaging [94]. Another method is to analyze colored striations in the crystal after growth. They are introduced by subjecting the growing crystal to periodic changes of dopant supply, e.g., introducing N_2 gas along with the Ar flow in SiC growth [95]. Finally, different facets feature a different incorporation of impurities and thus may show different optical properties (e.g., coloration, luminescence). The resulting crystal zones, i.e., volume parts that were grown on the respective facets, can be compared and analyzed after growth [60,95,96]. In the same way, polycrystalline areas can be reliably detected.

In sublimation growth, crystal enlargement is very challenging, and in order to grow a single crystal of a particular diameter, the seed must have roughly the same diameter. In principle, the ratio of normal and lateral growth rates can to some extent be influenced by the thermal gradients near the growth interface [95] or by the presence of impurities [42]. However, lateral growth is accompanied by formation of dislocations that may polygonize, form lineages and low-angle grain boundaries (LAGBs) [97–99]. Thus, the enlarged area typically shows a high defect density. Another problem in particular in regard to AlN bulk growth is that the enlargement decreases significantly as the crystal sides become faceted (Figure 16.8(c)). In the case of Al-polar AlN growth (e.g., on SiC seeds), the formation of pyramidal side facets even leads to an effective diameter decrease during growth (Figure 16.8(d)) [100]. As a rule of thumb for both SiC and AlN, the low-defect single-crystalline diameter can be increased by only about 1 mm in one growth run.

16.2.3.4 Doping

SiC bulk crystals are typically doped with nitrogen for *n*-type and with aluminum for *p*-type electrical behavior. Semi-insulating SiC crystals are obtained by doping with

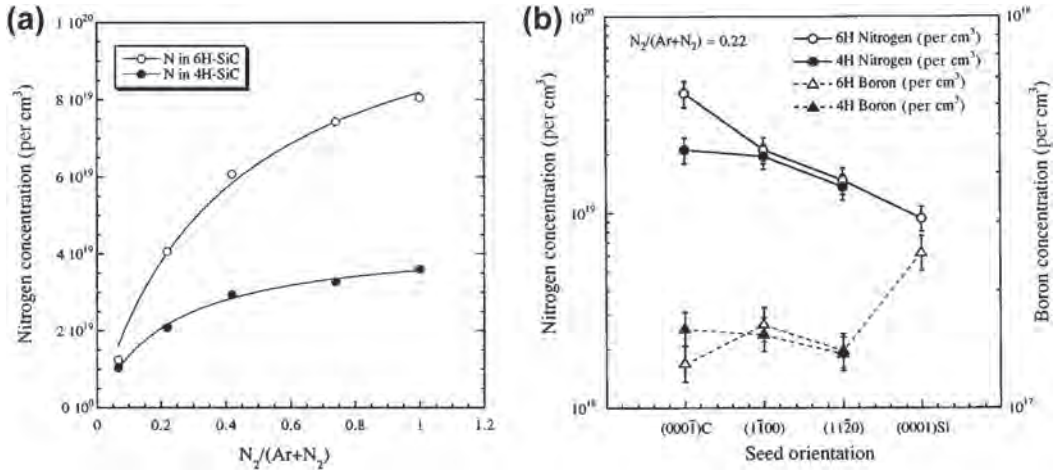


FIGURE 16.9 (a) N_2 partial pressure dependence of the nitrogen concentration in 6H- and 4H-SiC crystals grown on C-face basal planes of SiC. The solid lines are best-fitted theoretical curves using a Langmuir isotherm type equation. (b) Seed orientation dependence of the impurity incorporation during growth of 6H- and 4H-SiC crystals. *Reprinted with permission from [107]. Copyright 1998, American Institute of Physics.*

vanadium [101]; co-doping with boron or aluminum is used to compensate residual nitrogen, i.e., to pin the Fermi level to the more mid-gap $V^{4+/5+}$ transition energy instead of the $V^{3+/4+}$ level [102,103]. Semi-insulating SiC can also be prepared by providing high purity conditions where intrinsic defects with their deep levels in the bandgap govern the electrical behavior [104,105]. Note that for any dopant or impurity, the ionization levels in the bandgap, and thus the electrical and optical behavior of the crystals, depend on the polytype [106].

Nitrogen doping is provided by adding N_2 to the inert gas (argon) at ratios of N_2/Ar ranging from 0.01 to 1. As shown in Figure 16.9(a), the concentration of nitrogen in the crystal C_N at a given N_2 partial pressure p follows a Langmuir isotherm:

$$C_N \propto (K \cdot p)/(1 + K \cdot p), \tag{16.15}$$

where K is a kinetic coefficient [107]. While at low N_2/Ar ratios C_N goes linear with p, it saturates at higher N_2/Ar ratios at levels of high $10^{19}/cm^3$. C_N decreases with increasing growth temperature, because the partial pressure of species involved in SiC growth increases. Figure 16.9(b) shows that the nitrogen incorporation decreases from the C-polar to the Si-polar basal plane, with rhombohedral and prismatic planes in between. A gradual dependence of the polytype on the C-polar basal plane is attributed to a preferential incorporation of nitrogen on hexagonal lattice sites [107]. Unfaceted vicinal areas, which appear on the SiC crystals adjacent to the basal plane facet, feature different nitrogen incorporation with respect to the faceted area due to different step-flow conditions.

If added to the source material, aluminum, boron, and vanadium form carbides that are volatile at growth temperatures. Thus, their incorporation into the crystal strongly decreases during growth [108]. While the partial pressure of B_4C is sufficiently low to

provide for a virtually constant boron incorporation when added to the source material [109], vanadium should be better provided as a dense VC-SiC sublimation product whose vanadium supply is kinetically limited [102]. Constant aluminum incorporation can be facilitated by supply of gaseous trimethylaluminum (TMAl) or by a reservoir located at a colder place, from which Al-containing species are brought into the growth chamber by a carrier gas flow [110]. The effective segregation coefficient at the growth interface in the quasi-open system is about unity for nitrogen and boron, but only about 0.005 for vanadium [111]. The dependence of boron and aluminum incorporation on the facet orientation is reversed to that of nitrogen [107], cf. Figure 16.9(b). Also, incorporation increases with increasing growth temperature. Al and B doping is possible up to concentrations of several $10^{20}/\mathrm{cm}^3$, limited by deterioration of the structural quality of the crystals [109], while incorporation of vanadium is limited by its solubility to $3\cdot10^{17}/\mathrm{cm}^3$ [102].

Regarding AlN, incorporation of silicon is used to produce *n*-type epitaxial layers [112], but reports about doping during bulk growth are still rare [113]. At the time of writing, the efforts to influence electrical and optical properties of bulk AlN crystals are still focused on reducing contamination from both feedstock and setup materials, rather than on controlled doping.

16.2.4 Structural Defects in PVT-Grown SiC and AlN Bulk Crystals

Apart from structural defects being inherited from the seed or caused by backside evaporation due to improper seed fixation, a number of defects originate at the seed surface or form during initial stages of growth when the growth conditions are not yet stable [114]. Defect formation during further growth is caused by growth instabilities, such as local variations of the supersaturation at the growth interface, and promoted by high temperatures and gradients, low pressures, and high growth rates. In the seeded growth of SiC, continuous optimization of growth conditions have led to a formidable decrease of structural defects in the crystals, while size and wafer yield of the crystals have increased concurrently [115]. As of today, commercially available SiC wafer of production grade have at least 95% of useable surface area free of macroscopic defects such as micropipes, inclusions, and LAGBs. However, efforts to eliminate structural defects continue, in particular, in regard to the border areas of crystals during diameter enlargement. Again, seeded AlN growth is much less mature and the defect density in the crystals is considerably higher.

Dislocations in bulk crystals may form during growth by penetration from the seed crystal or adjacent parasitic grains into the bulk or by nucleation at other defects [115]. Due to annihilation processes, the dislocation density in the crystals generally decreases with increasing distance from the seed. Dislocations entering the crystal from the sides tend to polygonize and form lineages and LAGBs [98,99]. Thermal stress during cooling leads to formation of glide bands consisting of straight rows of basal plane dislocations [99].

Micropipes are considered as most detrimental defects in SiC crystals in regard to device applications, while they are hardly observed in nitride crystals. According to F. C. Frank [116], it is energetically profitable for dislocations with burgers vectors with their length exceeding about two unit cell heights [117] to form hollow cores, as the strain energy exceeds the necessary surface energy to form the core. While roughly running normal to the basal plane (i.e., in growth direction), they are also influenced by the thermal field and thus typically slightly bent outward in crystals grown with a convex growth interface. Their density is clearly lower on the faceted basal plane compared to vicinal unfaceted areas. Another type of hollow core is formed when voids originating from improper seed fixation travel through the seed and the crystal, leaving behind a deteriorated resublimated area that is not completely closed [73].

Generally, the polytype information of SiC crystals is inherited by spiral growth even on basal plane surfaces. However, areas with a different polytype in SiC crystals (polytype inclusions, Figure 16.10(a)) can nucleate at the crystal sides or at macrosteps on the

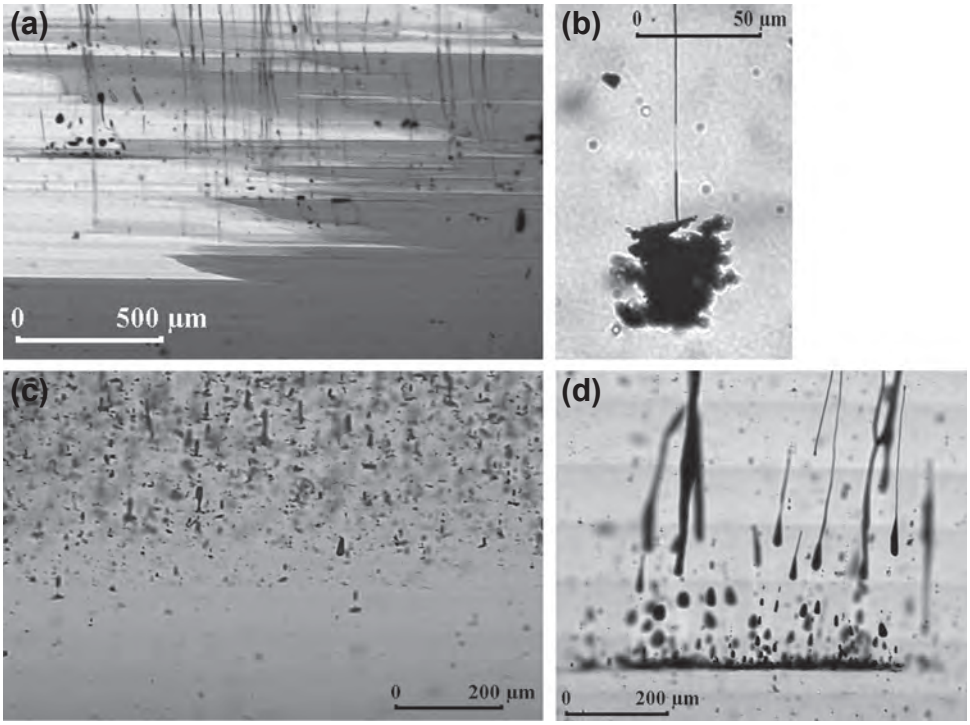


FIGURE 16.10 Structural defects in SiC observed in longitudinal cuts by optical transmission microscopy (growth direction is upward): (a) polytype instability with partial change from 4H-SiC (dark) to 15R-SiC (bright), many hollow defects and even silicon droplets nucleate at the polytype inclusion boundary. *(Reprinted from [118] with permission of ELSEVIER S.A.)*; (b) carbon precipitate with nucleating micropipe. *(Reprinted from [73] with permission of ELSEVIER BV.)*; (c) clusters of carbon inclusions form presumably after a gradual change of growth conditions; (d) "silicon droplet" formation. *(Reprinted from [118] with permission of ELSEVIER S.A.)*

surface. The former can be hindered to grow into the boule by providing a convex growth interface [32]. But growth of 4H-SiC without polytype inclusions remains a technological challenge due to the narrow growth window and the low stacking fault energy on the C-polar face [119]. The 4H polytype can be stabilized by providing more stoichiometric (carbon-rich) [11a,11b] or nitrogen-rich (highly doped) [41] conditions in the gas phase. Both carbon and nitrogen have been evidenced to change the step-flow properties and thus mitigate the formation of macrosteps [107]. On the other hand, several groups have reported that adding silicon to the source material might stabilize the 6H-SiC polytype [11,34] and mitigate formation of carbon inclusions [93], but excess silicon shortly evades from the crucible during growth.

Different types of carbon particles can appear in SiC crystals. Bigger inclusions are typically tens of microns in size and have an irregular surface (Figure 16.10(b)). They come as isolated defects or clustered in some volume fraction. Most probably they are graphitized feedstock particles, or particles that get detached from the crucible walls after attack by the silicon-rich vapor [73]. Smaller, more round carbon particles appear always in clusters (Figure 16.10(c)). They are generally attributed to local surface graphitization during growth, caused, e.g., by pressure reduction [120] or nonoptimized growth conditions [121]. It is assumed that local surface graphitization is correlated to the step flow and bunching. A more occasionally observed type of defect in SiC, which—from its form in longitudinal cuts—indicates that the growth interface was suddenly damaged in areas spanning over several 100 μm, is attributed to "silicon droplet" formation [73,118]. The defect is eventually overgrown, but the region above such a silicon droplet remains highly defective (Figure 16.10(d)).

Inclusions as well as macrosteps act as stress concentrators and may emit a number of dislocations or even micropipes that penetrate through the growing crystal [73,122]. As a consequence, the dislocation density in the crystals is typically inhomogeneous and their local density varies from $10^2/cm^2$ to $10^6/cm^2$. In SiC, basal plane dislocations can easily split into Shockley-type partial dislocations, which form stacking faults in between them [119]. Migration of these partial dislocations under high electric fields during SiC device operation is a serious problem for high power applications [123], but such dislocations can be converted into threading dislocations in subsequent SiC epitaxy [124].

A mosaic structure is often observed in AlN and SiC crystals. It consists of subgrains bound by LAGBs that are slightly tilted against each other and eventually form a cellular structure [125]. Several growth centers appearing at initial stages of growth may lead to tilted domains after coalescence [97]. A mosaic structure of the seed is inherited in the growing crystal. Additionally, lattice plane bending is observed in the crystals, as the lateral thermal gradient at the growth interface during growth leads to a continuous shift in crystallographic orientation after cooling down [126]. Finally, inversion domains can be observed in particular in nominally Al-polar AlN crystals grown on SiC seeds [89,127]. While their behavior during growth is similar to polytype inclusions in SiC, they are fenced by a dislocation wall.

16.3 HVPE of Nitride Semiconductors (AlN, GaN, InN, and Ternary Alloys)

In the 1990s, the need for nitride lattice-matched substrates had become apparent, and HVPE has attracted significant attention as a promising technique to produce thick nitride layers on foreign substrates that could be subsequently separated and used as quasi-bulk substrates. This became possible by the availability of high purity source materials, improved heteronucleation schemes, as well as by taking advantage of the high growth rate typical for this method and relatively inexpensive process [128–132].

16.3.1 Thermodynamic Analysis of HVPE Growth of Compound and Ternary Nitride Growth

The HVPE growth of epitaxial nitride-based materials is generally accomplished by reaction of a group-III metal chloride with NH_3. The general overall reaction for the HVPE growth of III-nitrides is given by [131]:

$$M^{III}Cl(g) + NH_3 \Leftrightarrow M^{III}N(s) + xHCl(g) + \frac{(3-x)}{2}H_2(g) \tag{16.16}$$

where M^{III} is the Ga, Al, or In species. An accurate thermodynamic analysis of the HVPE growth process requires a detailed understanding of the chemical reaction pathway. The HVPE reactors for growing III-nitrides consist of two main zones: source zone and growth zone. The chemistry of the both zones is quite complex, but generally the source zone enables the formation of chloride gas of group-III metals (Al, Ga, In) and the growth zone provides the necessary conditions for growth of the nitride (AlN, GaN, InN) binary material.

Thermodynamic analysis on the metal chloride formation can predict the preferred molecular form of the metal chlorides and identify a suitable carrier gas. The elemental metals Ga, Al, and In are liquids at the source zone temperature. When HCl flows over the liquid metal, there are several reactions that occur simultaneously, forming three gaseous metal chloride species: $M^{III}Cl$, $M^{III}Cl_2$, and $M^{III}Cl_3$ [132]:

$$M^{III}(l) + HCl(g) \Leftrightarrow M^{III}Cl(g) + {}^1\!/_2\, H_2(g) \tag{16.17}$$

$$M^{III}(l) + 2HCl(g) \Leftrightarrow M^{III}Cl_2(g) + H_2(g) \tag{16.18}$$

$$M^{III}(l) + 3HCl(g) \Leftrightarrow M^{III}Cl_3(g) + {}^3\!/_2\, H_2(g) \tag{16.19}$$

$$2M^{III}Cl_3(g) \Leftrightarrow \left(M^{III}Cl_3\right)_2(g) \tag{16.20}$$

where l = liquid, g = gas, s = solid. The equilibrium partial pressures of the gaseous species in the source zone versus temperature can be estimated by thermodynamic calculations [133–135]. Figure 16.11 shows in a comparative way the partial pressure for the gaseous species for Ga-, Al- and In-source zones as a function of temperature in inert N_2 atmosphere.

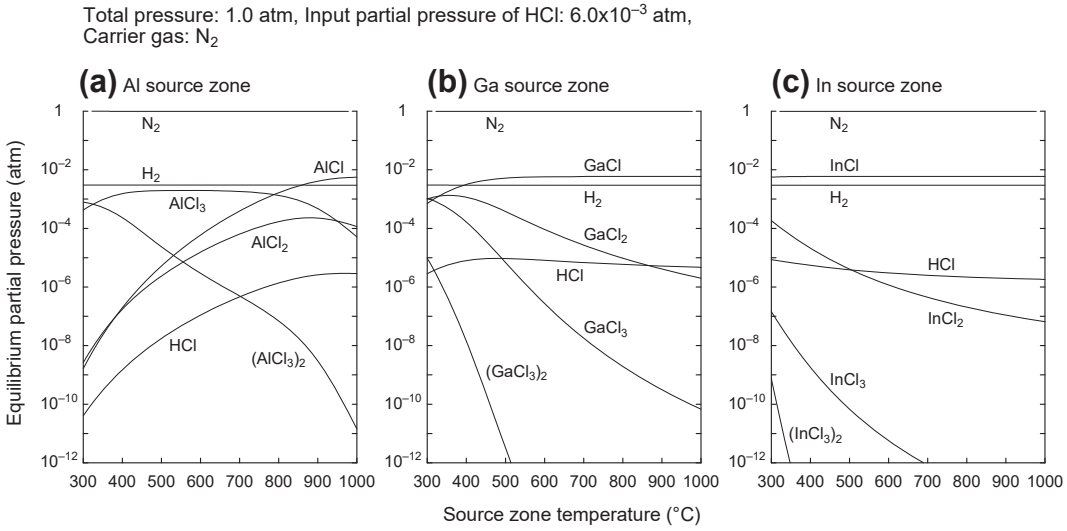


FIGURE 16.11 Equilibrium partial pressures of gaseous species over group-III metals placed in the source as a function of temperature calculated for: (a) Ga, (b) Al, (c) In source zones. *Courtesy of Yoshinao Kumagai.*

In case of AlN growth, when HCl reacts with Al liquid metal, three gaseous aluminum chloride species that may be formed: AlCl, $AlCl_2$, and $AlCl_3$. The dimer of $AlCl_3$, Al_2Cl_6, is not considered because at temperatures higher than 800 °C, the dimer molecule dissociates into two molecules of $AlCl_3$ [136]. Over the high temperature range typically used in the HVPE AlN growth, the equilibrium partial pressure of $AlCl_3$ is about eight and four orders of magnitude higher than the partial pressures of AlCl and $AlCl_2$, respectively. Several HVPE AlN growth experiments observed that $AlCl_3$ was the dominant aluminum chloride gaseous species [137–139].

$$\mathrm{Al(l) + 3HCl(g) \Leftrightarrow AlCl(g) + {}^{3}\!/_{2}\, H_2(g)} \tag{16.21}$$

$$\mathrm{Ga(l) + HCl(g) \Leftrightarrow GaCl(g) + {}^{1}\!/_{2}\, H_2(g)} \tag{16.22}$$

$$\mathrm{In(l) + HCl(g) \Leftrightarrow InCl(g) + {}^{1}\!/_{2}\, H_2(g)} \tag{16.23}$$

In case of GaN growth, the thermodynamic analysis predicts that the partial pressure of GaCl is about four and eight orders of magnitude higher than the partial pressures of $GaCl_2$ and $GaCl_3$, respectively, over the temperature range of 800–1000 °C, and experimental data confirmed the prediction that only gallium chloride species were formed at these high temperatures [140]. Furthermore, experiments in wide temperature ranges also confirmed that only GaCl was stable at temperatures above 600 °C [141–143].

In the case of InN growth, there are three gaseous indium chloride species that may be produced as well: InCl, $InCl_2$, and $InCl_3$. The thermodynamic study of the equilibrium between In metal and HCl shows that the partial pressure of InCl and $InCl_2$ is about four

to ten orders of magnitude higher than the partial pressures of $InCl_3$ [144], yet they are not involved in the growth of InN owing to their low reactivity with NH_3 [132], and thus leaving the only option of decreasing the source temperature below 500 °C to allow sufficient formation of $InCl_3$ species.

From the source zone, the metal chlorides flow to the deposition zone, and the dominating species react with NH_3 to synthesize GaN, AlN, and InN films, respectively:

$$AlCl_3(g) + NH_3(g) \Leftrightarrow AlN(s) + 3HCl(g) \tag{16.24}$$

$$GaCl(g) + NH_3(g) \Leftrightarrow GaN(s) + HCl(g) + H_2(g) \tag{16.25}$$

$$InCl_3(g) + NH_3(g) \Leftrightarrow InN(s) + 3HCl(g) \tag{16.26}$$

Thermodynamic analysis of the HVPE growth zones has been reported in multiple publications for GaN [145], AlN [146], and InN [144], analyzing the influence of different growth parameters. Among the three nitrides, AlN formation has the largest thermodynamic driving force. Experimental observations have shown severe gas phase reactions leading to the formation of AlN powder, such that the reactant gases become depleted of $AlCl_3$, resulting in a low growth rate [147,148]. The free energy dependence shows that GaN and InN formation reactions have a positive free energy of reaction; however, film growth is favored since the deposition zone is highly supersaturated by the metal chlorides and NH_3. The thermodynamic driving force for film growth, $\Delta G_{T,\text{driving force}}$, is given by [131]:

$$\Delta G_{T,\text{driving force}} = \Delta G_T^0 + RT\ln\left(\frac{(P_{HCl})^n (P_{H_2})^m}{P_{MCl} \cdot P_{NH_3}}\right) \tag{16.27}$$

where T is the growth temperature, ΔG_T^0 is the Gibbs free energy of layer formation at the growth temperature, R is the ideal gas constant, n is the stoichiometric coefficient of HCl (n = 1 for GaN, n = 3 for AlN and InN), m is the stoichiometric coefficient of H_2 (m = 1 for GaN, m = 0 for AlN and InN), and $M^{III}Cl$ is the metal chlorides (i.e., GaCl, $AlCl_3$, or $InCl_3$). When the deposition zone is highly supersaturated with the reactants, the second term on the right hand side of Eq (16.27) becomes a large negative number so that even though ΔG_T^0 is positive, the overall growth driving force is negative and, thus, thermodynamically favored.

The thermodynamic analysis also shows that InN formation is thermodynamically favored at higher temperatures, however, a rapid dissociation of InN film has been reported at temperatures above 500 °C [149]. In $In_xGa_{1-x}N$ alloy growth, experimental observations revealed a preferential incorporation of the GaN component into the alloy and that the epitaxial layer became GaN-rich with increasing growth temperature [144,150]. In fact, the InN mole fraction in the alloy was very low for films grown at higher temperatures. Changes in growth temperature lead to opposite trends in AlN and GaN growth. While the GaN formation reaction is exothermic and becomes more favored as the temperature decreases, the AlN formation reaction is endothermic and becomes more favored as the growth temperature increases. The difference in the

temperature dependence of the growth reaction is attributed to the greater stability of $AlCl_3$ over GaCl [139]. Thus, the optimum growth temperature of AlN should be higher than the optimum growth temperature of GaN. Experimental observations have indicated that the optimum growth temperature of AlN is around 1250 °C [151]. In fact, HVPE $Al_xGa_{1-x}N$ films have been grown over the entire alloy composition range [139,152,153], due to the fact that AlN is completely miscible in GaN over the entire composition range. The mole fraction of $AlCl_3$ molecules in the gas phase has been observed to be proportional to the mole fraction of AlN molecules in the film. The optimum growth temperature for $Al_xGa_{1-x}N$ is predicted to increase proportionally with AlN concentration. Melnik et al. reported that the quality of HVPE $Al_xGa_{1-x}N$ film decreased with increasing AlN concentration when the growths were performed at a single temperature [153].

The main formation mechanism of nitrides is given by Eqns (16.24–16.26) is accompanied by decomposition in the sense that the reactions may be reversed (etching of the growing crystal) and also thermal decomposition may take place:

$$M^{III}N(s) + HCl(g) \rightarrow M^{III}Cl(g) + \tfrac{1}{2}N_2(g) + \tfrac{1}{2}H_2(g) \tag{16.28}$$

$$M^{III}N(s) \rightarrow M^{III}(l) + \tfrac{1}{2}N_2(g) \tag{16.29}$$

However, in the temperature ranges typically used for the HVPE nitride growth (750–1200 °C) reactions 30 and 31 are practically negligible.

The main gaseous species involved in the HVPE growth of $M^{III}N$ are $M^{III}Cl$, $M^{III}Cl_2$, and $M^{III}Cl_3$, HCl, NH_3, H_2, and the carrier gas. Thermodynamic functions of the material, the enthalpy $H(T)$, entropy $S(T)$, and specific heat $C_p(T)$, of all the species involved in the growth have been theoretically calculated [154] for the standard pressure of 1 atm and arbitrary temperature using a polynomial approximation of the Gibbs free energy. Detailed thermodynamic calculations of HVPE growth of GaN have been published by several authors [140,155–157]. Based on their analysis, several important features can be pointed out, which make the GaN growth different from the growth of other III-V materials, and should be taken into account for successful HVPE $M^{III}N$ growth: (1) An inert ambient atmosphere is preferred and is more effective for the $M^{III}N$ growth than hydrogen atmosphere, the latter being widely used for other III-V systems, like GaAs; (2) In HVPE-GaN growth, NH_3 should be used as the source of the group V element rather than a nitrogen halide (NCl_3), which is highly explosive. Moreover, the thermal dissociation of NH_3 results in the formation of N_2 molecules, which are extremely stable and nonreactive at the temperatures used, while the thermal dissociation of $AsCl_3$, in GaAs growth, results in the formation of As_2 and As_4 molecules, which typically remain volatile and chemically reactive in the next step of the growth reaction; (3) Another problem comes from the fact that the $M^{III}N$ reaction tends to create huge amounts of byproducts such as NH_3Cl and $M^{III}Cl_3 \cdot NH_3$, leading to a massive condensation of these reaction species on the reactor walls. This fact makes the development of last-running process for very thick samples quite challenging.

16.3.2 Growth Kinetics

The kinetics of the HVPE nitride process and growth mechanisms occurring at the solid/vapor interface was predominantly studied for HVPE growth of GaN on sapphire substrate. The growth was simulated based on several models [157,158] for the surface process involving the following steps: (1) adsorption of NH_3 molecules, (2) adsorption of N atoms coming from ammonia decomposition, (3) adsorption of GaCl molecules on the N atoms forming NGaCl, and (4) decomposition of the NGaCl via different desorption mechanisms (Figure 16.12). Two of them were suggested in analogy with the GaAs model: desorption forming HCl and desorption forming $GaCl_3$ [158]. One more $GaCl_2$ desorption mechanism was suggested based on specific experimental observations for the GaN growth [159]. Statistical treatment of the dynamic equilibrium between the adsorbed and gas phase species allowed explicit expressions of the growth rates via the different pathways.

An optimum HVPE growth process requires a good selection of the reactor geometry and operating conditions, to ensure a minimization of undesired parasitic reactions and to provide a uniform reactant distribution across the substrate. Although, temperature distributions for specific reactor designs and geometry have been simulated using different software models [160], the optimization of HVPE growth is predominantly done by empirical studies of external parameters such as temperature, flow rates of active gases, and substrate orientation.

There are several detailed kinetics considerations published in the literature [161–165] even in the initial stages of development of the technique. The regularities established in the fundamental dependence of growth rate upon the temperature generally agree among different researchers, although the reported details are partly in contradiction to each other. These studies have identified regions with a different character, illustrated in Figure 16.13(a).

The *low-temperature region*: The exponential dependence of the growth rate in the low temperature region is a characteristic of kinetically controlled growth and may be attributed to the surface reaction, adsorption, and surface diffusion. The monotonic

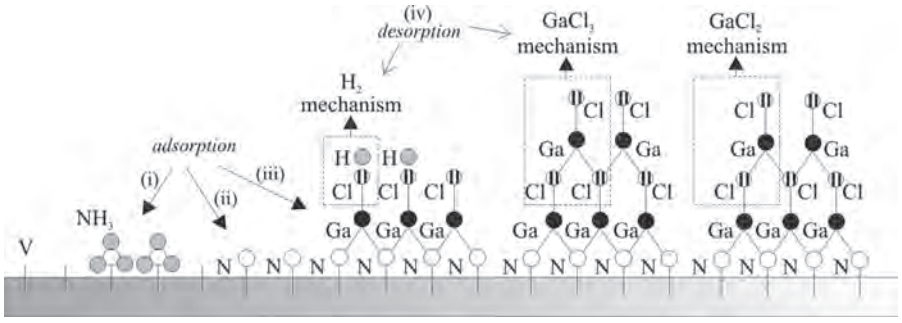


FIGURE 16.12 Schematic drawing of possible reaction steps: three possible adsorption (i – NH_3 adsorption, ii – N adsorption, iii– GaCl adsorption) and three possible desorption (H_2 desorption [158], $GaCl_3$ desorption [158], and $GaCl_2$ desorption [159]) mechanisms of the surface growth process of HVPE growth of GaN.

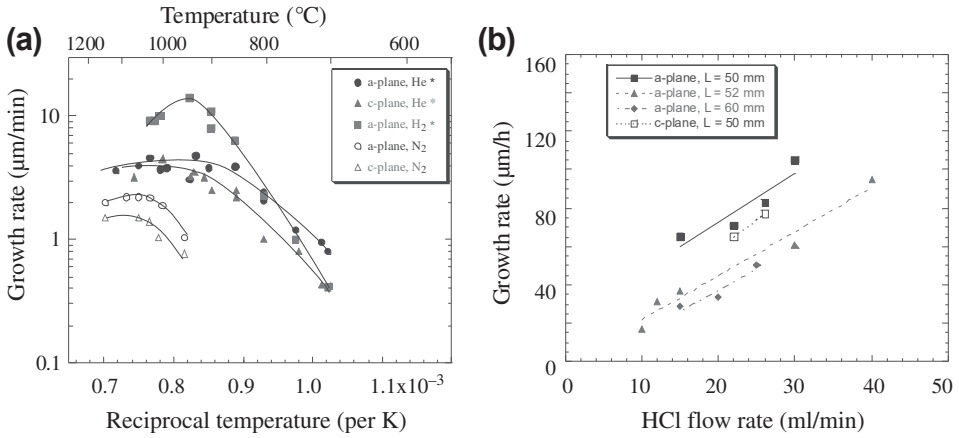


FIGURE 16.13 (a) Growth temperature dependence of the GaN growth rate. *Seifert et al. [155]. (b) The dependence of GaN growth rate on the HCl flow rate. The growth temperature was 1080 °C. The distance between the NH_3 outlet and the substrate is given in the inset, as well as the sapphire orientation.

increase of the growth rate with substrate temperature leads to a calculation of the activation energy of the epitaxial GaN growth from the Arrhenius plot. The reported values in the literature vary between 0.9 and 1.6 eV (21 and 37 kcal/mol), and the magnitude of the value suggests that the main rate-determining step in this low temperature region is related to the surface reaction [162,163]. A thermodynamic calculation of the equilibrium partial pressures in this region allowed speculations of a dominant mechanism for surface processes in different ambient [157,161].

The *high-temperature region* has been the subject of extensive experimental studies because of the larger practical interest and better material quality ensured. The growth rate reaches its maximum value at a temperature that varies in wide range of 950–1080 °C, according to different reports [162,163,166]. The difference in the temperature value for maximum growth rate may be attributed to differences in reactor design and growth conditions. At the temperature of 1080 °C, the dependence of GaN growth rate on HCl flow rate is shown in Figure 16.13(b). The growth rate increases linearly as a function of both HCl flow rate and GaCl partial pressure [163,164]. This fact combined with the weak temperature dependence of the growth rate in the higher growth temperature region indicates that the growth rate is limited by the transport of the gallium-containing species to the growth surface.

While the HCl flow rate appeared to be the key growth parameters, other parameters such as the NH_3 flow rate or the substrate orientation do not seem to affect the growth rate in a critical way, although they can affect the layer quality to a large extent. The weak growth rate dependence on NH_3 flow rate is reasonable since the concentration typically used in GaN HVPE is far larger than that of HCl, in order to suppress GaN dissociation. Also, the different carrier gases used were found to have noticeable effect in the range of low growth temperatures. Namely, the growth rate in case of using hydrogen was higher

than that in inert gas carrier gas for the temperature interval from 800 to 1050 °C. It was concluded that it was indicative of a growth rate–limiting surface reaction involving hydrogen [167]. The growth rate–determining steps in the high temperature region, which are typically thought to be related to enhanced gas-phase prereactions leading to a depletion of the chemical reactants at the substrate surface and/or enhanced etching of the growth surface, are likely to involve the hydrogen as a critical component controlling the process chemistry. There are also some experimental findings showing that additional HCl gas intentionally introduced downstream of the Ga boat can change the Cl/Ga ratio at the growth surface and thus enhance the lateral/vertical growth ratio, resulting in both a decrease of growth rate and an improvement of film quality.

16.3.3 Laboratory and Industrial Setups

The HVPE technique uses a hot-wall reactor due to the relatively low vapor pressure of the metal chloride at low temperature, aiming to avoid the condensation of the metal chloride molecules on unheated surfaces. Typically, the HVPE growth of the nitride layers is carried out in reactors based on the first concept reported over 30 years ago [128]. There are many different modifications, which can be summarized into two groups: horizontal and vertical reactor design [129–132].

In general, the HVPE reactor requires two temperature zones to enable the two chemical reactions in the standard HVPE growth of binary nitrides. However, most laboratory and all industrial reactors have more reactor zones, typically up to five temperature zones (Figure 16.14(a)). This allows larger flexibility, providing either more stable temperature control in the two main zones and/or allowing a doping or a second

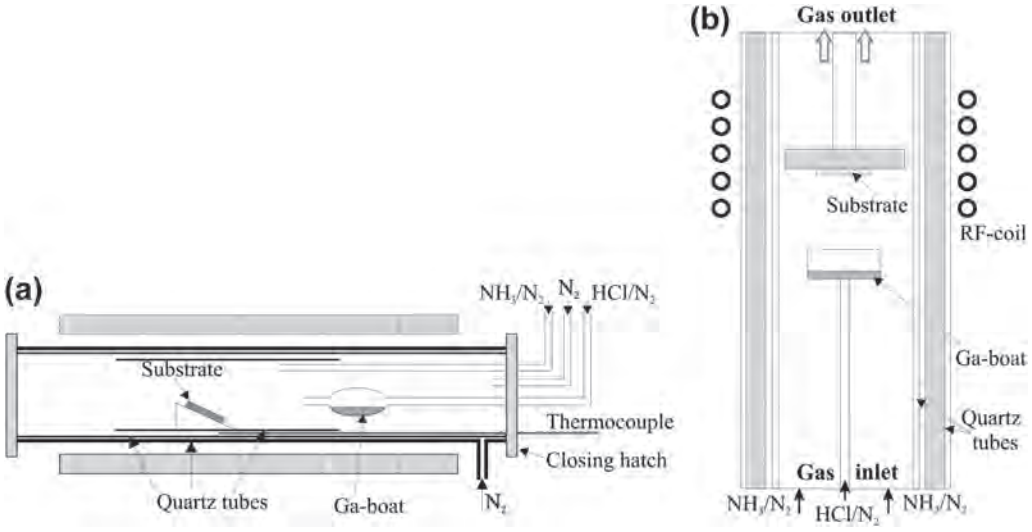


FIGURE 16.14 Schematic drawings of: (a) horizontal and (b) vertical HVPE reactors.

metal boat in case of growing nitride ternary alloys. The area of the liquid metal source is preferred to be as large as possible, depending on the reactor geometry, in order to achieve a large reactive surface area for efficient chloride production [168]. The second zone may be used for other metallic sources as In or Al, or for dopants when needed. In the third zone, kept at higher temperatures, the chloride and NH_3 are introduced and mixed. The substrate holder is placed in the fourth region of the reactor. We note that the reported substrate temperatures vary considerably, from 950 °C [169] up to 1150 °C [170], but some of the high quality GaN films, for example, were achieved at 1050–1080 °C [171]. The most common method of heating is a resistive one, although also RF heating is quite popular for some of the reactor zones. The horizontal reactors utilize a substrate holder that has a variety of designs and is situated either parallel or inclined or perpendicular to the gas flow direction. In most reported reactor designs, the active gases are delivered to the mixing point through separated parallel quartz liners. An alternative is the coaxial arrangement of the gas inlet tubes [161] to achieve a better mixing of the reaction gases prior the deposition and to improve the uniformity of the layers.

In the vertical design, the reactants are typically introduced through the top. The substrate is held flat on a susceptor that is perpendicular to the gas flow direction. The vertical reactor design usually facilitates easier substrate rotation during the growth to improve the film uniformity. An alternative modification is an inverted vertical reactor [130,132,171] where the process gases are supplied through the bottom inlet flange, while the top flange can be lifted for loading and unloading of substrates (Figure 16.14(b)). In this configuration the substrates are placed in the upper part where the gases are mixed. The inverted reactor keeps all advantages of the vertical design and also provides the possibility of raising the substrate holder, maintaining constant distance to the gas mixing point in case of long boule growth. An additional advantage of the inverted vertical reactor is the minimization of solid particle contamination of the growing surface.

The III-nitride HVPE growth is strongly thermodynamically favored, as compared to other III-V material systems grown using HVPE, which leads to undesirable homogeneous gas phase reactions and problems with extraneous wall deposition, especially in AlN growth [172]. This leads to severe gas phase depletion effects and difficulties in keeping constant growth rate over long growth runs and along consequent runs. The remaining portions of the NH_3 and HCl gases, which have not been consumed completely in the growth zone, proceed in the downstream of the reactor, where they react and form ammonium chloride (NH_4Cl), which leaves the process furnace in a vapor form but readily condenses to a heavy powder below ∼300 °C. Along with the $GaCl_3$ and the $GaCl_3$:NH_3 adduct, a large amount of NH_4Cl can eventually condense along the exhaust lines and complicate the system maintenance. Additional complications arise in AlN growth because $AlCl_3$ reacts with the quartz reactor wall at high temperatures [173]. The chemical reaction with the quartz wall can be mitigated by using a reactor liner and Al boat that are made from less reactive materials, such as alumina (Al_2O_3).

Most of the advanced laboratory and commercial reactors are reported with optimized laminar flow patterns in order to avoid the turbulence at the wafer edge and to achieve the necessary growth rate uniformity across a large wafer diameter and respectively uniform material properties [171–173]. The flow patterns are influenced by reactor geometry, the heat transfer, the flow boundary conditions, the choice of carrier gas, and all the gas velocities. A commercial software, for example, Hydride Epitaxial GaN Simulator (HEpiGANS) [174] is now developed, accounting for heat transfer by conduction, convection, and radiation, and species transport via convection, multicomponent diffusion, and thermodiffusion. The modeling of gas patterns is particularly useful to optimize the gas velocities in order to reduce the recirculation due to natural convection in vertical reactors and to avoid turbulent flows with vortex pattern in the middle of the wafer.

16.3.4 Growth on Foreign Substrates

16.3.4.1 Substrates and Buffers

In addition to the most commonly used sapphire substrates, several other substrates, such as sapphire (Al_2O_3), 6H-SiC, GaAs, Si, and some oxide substrates such as MgO, ZnO, TiO_2, $MgAl_2O_4$, and $LiGaO_2$ have been successfully used. Some characteristics are summarized in Table 16.1 [175], showing a significant lattice parameter and thermal expansion coefficient mismatch, for instance, of about 14% and 34%, respectively, for GaN on sapphire.

HVPE GaN, AlN, AlGaN, and AlInN layers grown directly on foreign substrates have varied from being highly transparent to brown. The surface morphology of thick layers is typically rough, consisting of hexagonal-shaped islands and often marked by hexagonal pits. The mosaicity and/or cracks are also typical in such layers. In order to mitigate the

Table 16.1 Characteristics of the Most Popular Substrates Used for HVPE Growth of GaN and AlN Substrates [175]

	Crystal Structure	Lattice Parameter a (A)	Lattice Parameter c (A)	TEC $\alpha \times 10^{-6}$/K	Substrate Separation
AlN	Wurtzite	0.31106	0.49795	$\alpha_a = 5.3$; $\alpha_c = 4.2$	
GaN	Wurtzite	0.31885	0.5185	$\alpha_a = 5.59$, $\alpha_c = 7.75$	
Sapphire	Rhombohedral	0.4765	1.2982	$\alpha_a = 5.0$; $\alpha_c = 9.03$	Laser liftoff self-separation
SiC	Wurtzite (6H)	0.30806	1.51173	$\alpha_a = 4.46$, $\alpha_c = 4.16$	Reactive ion etching
GaAs	Zincblende	0.56536		6.03	Chemical etching
Si	Diamond	0.543102		2.616	Chemical etching
MgO	Rock salt	0.421		8.0	
ZnO	Wurtzite	0.32496	0.5265	$\alpha_a = 6.5$; $\alpha_c = 3.0$	
$MgAl_2O_4$	Spinel	0.8083		7.45	
$\gamma LiAlO_2$	Tetragonal	0.5169	0.6267	$\alpha_{100} = 6.5$; $\alpha_{001} = 14.9$	Self-separation
$LiGaO_2$	Orthorhombic	0.5402/0.6372	0.5007	$\alpha_{100} = 6$; $\alpha_{010} = 9$	Chemical etching

large mismatch and some of the above drawbacks, specific pretreatments, buffers, and nucleation schemes have been developed. The most popular pretreatment was the so-called nitridation of the sapphire substrates, performed in 10–30% NH_3 atmosphere at the growth temperature for 5–30 min, which led to a noticeable improvement of the material properties [176,177]. Later on, alternative surface treatments of the foreign substrate were developed by GaCl gas [178] or a combination of the nitridation and the GaCl treatments [179].

Another widely used approach of growing nitrides by HVPE is by employing buffer layers. In contrast to the MOCVD nitride technology, the early work on low temperature GaN buffers in the same chamber was not successful in the HVPE technology, although some recent advances of the low temperature buffers resulted in good quality material [180]. Alternatively, buffers of different nature, deposited by different techniques, mostly reactive sputtering, have been proposed and demonstrated to ensure significant improvement of the crystal quality of the layers with thickness up to several tens of micrometers without cracks. The ZnO buffer was first suggested as a buffer for HVPE growth of thick GaN films [170]. Alternative buffers grown at high growth temperature were later suggested [181] and successfully employed in the HVPE growth to avoid the highly defective region at the interface containing columnar structures in case of direct growth on sapphire. Reactively sputtered thin AlN buffer with thickness of about 1 μm have been proven to ensure smooth epilayer surface and low defect density GaN material [182,183]. The use of MOCVD templates for GaN growth on sapphire has been firstly shown in MBE growth of thin GaN layers. Later on, it was successfully employed in the HVPE-GaN growth [184] and is currently used by many research groups.

It is important to note that the growth process (including nucleation scheme, the growth rate, and growth recipes), as well as the material properties resulting from using different foreign substrates and optimizations are very different for growth of thin films with thickness from 1 to 50 μm (often called templates), for thick films in the range of 100–2000 μm, and for boule growth with thickness more than several millimeters, the latter two being of interest for substrate applications after removing the foreign substrate.

16.3.4.2 Template Growth

Templates is the term typically used for layers deposited and remaining on foreign substrates (usually sapphire), with thickness in the range of 1–50 μm. This HVPE growth has been demonstrated practically for all binary and ternary nitrides, but it was particularly developed for GaN and AlN, which can be used for direct growth of device structures. The advantages of this approach in the device growth are based on the fact that these "template substrates" eliminate the need for the low temperature buffer growth step and, even more important, the dislocation density in these layers is noticeably reduced down to 10^8–$10^7/cm^2$, depending on the thickness. This ensures lower defect density and higher structural quality in the subsequently grown multilayer device structures.

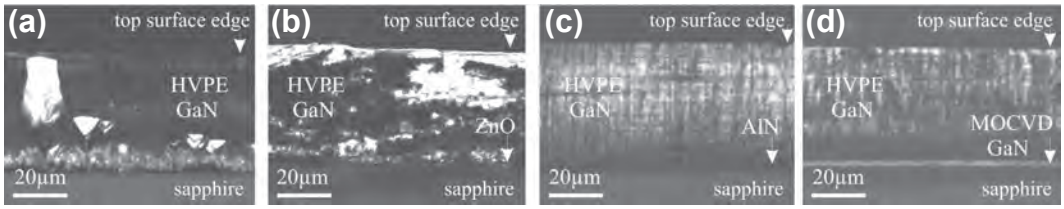


FIGURE 16.15 Panchromatic CL image in cross-section of thick HVPE-GaN layer grown (a) directly on sapphire, showing three specific growth zones—the highly disordered interface region, the columnar region, and the good quality region; (b) with ZnO buffer; (c) with reactive sputtered AlN buffer; and (d) with Si-doped MOVPE-GaN template.

The HVPE templates typically employ high temperature buffers deposited by other techniques, such as reactive sputtered ZnO and AlN or more often MOCVD-grown GaN. The ZnO is known to be one of the most effective buffers for growth of thick GaN layers of very good quality, but thick large-area crack-free layers suitable for quasi-substrate applications have not been demonstrated by using this buffer. Similar nucleation and layer quality improvements (Figure 16.15) have been observed by using reactive sputtered AlN and MOCVD-GaN templates with optimized ratio of the layer and buffer thicknesses [179,181–185].

Figure 16.15(a) shows panchromatic cathodoluminescence (CL) image of HVPE-GaN layers grown without buffer, revealing three distinctive regions [130]: (1) the interface region shows a greatly reduced radiative efficiency attributed to a very high degree of structural imperfections; (2) In the second zone clearly defined columns can be seen, often referred to as columnar defective region, with some of the columns protruding through the entire layer thickness, characterized with nonuniform emission attributed to nonuniform impurity incorporation; (3) the upper zone, extending over several tens of micrometers in thickness, is generally of good quality with more uniform radiative emission. Figure 16.15(b–d) show CL images of HVPE-grown GaN layers, employing reactive sputtered ZnO, AlN, and MOCVD-GaN buffers, respectively. The results show that the growth on these buffers helps to: (1) eliminate the large-scale structural defects at the sapphire/GaN interface; (2) reduce the concentration and nonuniform distribution of residual carriers; (3) partially relieve the compressive stress in the HVPE-GaN layers [130]. It is important to note that all the templates can provide good buffers for growth of thick HVPE-GaN layers with very good structural and optical characteristics, although it is difficult to grow films with sufficient thickness (larger than 50 μm) without cracks.

16.3.4.2 Quasi-Bulk Single-Wafer Growth

The growth of quasi-bulk single wafer for substrate applications needs to ensure layer thickness of at least a few hundreds of micrometers without cracks. A weak interface region between the substrate and nitride layer is also needed in order to allow easier delamination process for producing a freestanding nitride layer. This growth method is developed for GaN thick layers, while the AlN thick layer growth is still in its infancy. There are two main approaches for growth of single-wafer GaN substrate: the first one is

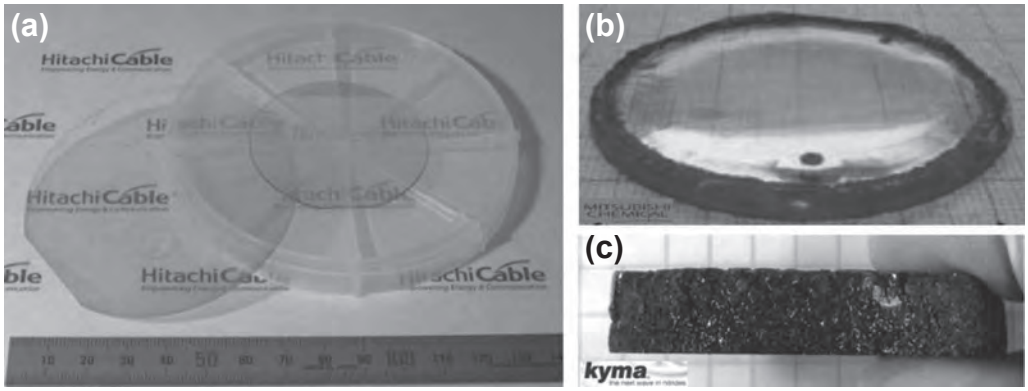


FIGURE 16.16 (a) Large 3″ GaN substrates announced by Hitachi Cable (CompoundSemiconductor.net) and currently the largest 2″ GaN boules reported by Mitsubishi Chemical (b) and Kyma Technologies (c). *After Ref. [190].*

producing GaN layers with a thickness in the range of 150–400 μm often with ELOG templates in order to achieve low defect density material in the lateral regions, and the second one is producing layers with thickness of 1–2 mm in order to achieve low defect density due to thickness increase. There are also several approaches for separation of the thick GaN layer from the substrate, depending on the thickness achieved and the buffer used. The most popular is the self-separation, which can be achieved by the so-called void-assisted separation, which in turn requires a special buffer. Such a buffer could be reactively sputtered TiN, as suggested by Japanese researchers in 2002 [186]. This approach was developed and successfully implemented for substrate manufacturing by Hitachi Cable, which announced production of crack-free 3-in freestanding GaN wafer (Figure 16.16(a)) [187,188]. Another high temperature reactively sputtered AlN buffer [189,190] was also found to be effective in suppressing defect formation in the GaN nucleation region, reducing tensile stress during GaN growth by forming a weak "pitted" interface that leads to optimized structural properties and allows self-separation of the films during cooldown.

Crack-free thick HVPE-GaN layers with thicknesses of about 300–500 μm have been demonstrated by using multiple-step technology processes such as epitaxial lateral overgrowth (ELOG) [191,192], two-step epitaxial lateral overgrowth (2S-ELOG) [193,194], or Pendeo epitaxy [194,195]. This growth procedure consists principally of an HVPE growth on a thin MOCVD-grown GaN layer. The MOCVD growth was performed using the conventional two-step procedure, consisting of a 20-nm-thick low temperature buffer layer and a high temperature main layer. A SiO_2 layer was then deposited by chemical vapor deposition and window stripes with a period of about 7 μm were opened using conventional photolithographic techniques. Alternatives of using W [196] and SiN [197] masks instead of SiO_2, or using GaAs [198], $LiGaO_2$ [199], or $LiAlO_2$ [200] substrates instead of sapphire have also been demonstrated. In addition, in order to further reduce the dislocation density, the ELOG approach can be performed by the so-called two-step



FIGURE 16.17 (a) A secondary electron image and (b) a panchromatic CL image in a cross-section of an HVPE-GaN layer grown on 2S-ELOG template.

approach (2S-ELOG), which can employ either a second layer of mask usually with shifted period with respect to the first mask, or it can employ a change of the growth parameters, usually a reduced growth temperature during the second stage [193]. In spite of complicated defect, strain, and emission distribution in the early stages of the growth, a more uniform main part of the film is followed (as shown in the panchromatic CL image in Figure 16.17(b)). A common feature for the growth on such templates is the formation of voids (Figure 16.17(a)) in the coalescence areas, found to partially release the strain. This allows an increase of the critical thickness for crack appearance, and in some cases leads to self-separation of the film.

These types of thick layers can be separated from the substrates by different methods, depending on the type of the substrate used and the nucleation scheme. The easiest substrate removal is through a chemical etching as is often done in the case of GaAs or $LiGaO_2$ substrate. This approach is now routinely used at Sumitomo Electric Industries Ltd for removing the initial GaAs substrate. In case of transparent sapphire substrates, a laser-induced liftoff process was developed in order to separate the GaN from the sapphire using pulsed UV laser beams. The process works by irradiating the sapphire/GaN interface with intense laser pulses just at the absorption edge of GaN. It leads to a fast and strong local heating, which causes thermal decomposition in the interface region of the film, yielding metallic Ga and nitrogen gas evaporation. This approach was particularly developed for 2S-ELOG buffer and successfully use in wafers production by Lumilog Ltd. [193].

16.3.3.3 Bulk Growth

The bulk growth is the most preferable and economical pathway to produce substrates with the necessary quality, size, and cost. At this time, however, GaN boule growth is still in early stages of development, and no mature technology is available yet due to several growth-related issues. The most critical challenges are related to maintaining stable growth conditions in the HVPE reactors during long growth runs. Wall deposition and secondary reaction products lead to reactor clocks, which can be handled by a proper pressure balance, or to a depletion of the growth efficiency, which can be mitigated by modulation epitaxy. Another issue is related to growth cracks, provoking lateral growth and polycrystalline inclusions, which limit the growth duration and the boule thickness. Mitsubishi Chemical Co. reported a successful growth of 2-in boules up to 6–10 mm thick (Figure 16.16(b)) [201]. Two-inch boule growth ranging from 2.5 mm up to 10 mm has been reported by ATMI Inc. [202], Ferdinand-Braun-Institute [203], and Kyma Technologies Inc. Figure 16.16(c) [187], respectively. Different buffers and high growth rates up to 300 μm/h are likely to be used by the different groups.

The boule growth approach is also the technique of choice for producing substrates with surface orientation different from the (0001) for growth of device structures on crystallographic planes that exhibit lower or no polarization (the so-called nonpolar and semipolar planes). This is so far accomplished by slicing nonpolar or semipolar substrates perpendicularly or inclined with respect to the as-grown c-plane surface of the boules.

16.3.5 Homoepitaxial Seeded Growth

Another approach that recently attracted significant attention is the so-called seeded growth by the HVPE process. This approach aims at combining the high growth rate and higher crystalline quality achievable by the homoepitaxial regrowth employing GaN seeds instead of using sapphire to avoid the initial highly defective interface region. Several alternatives of seeded growth have been elaborated recently by research from Unipress. Namely, seeds produced either by high pressure solution growth (HPSG), HVPE, or ammonothermal growth methods have been used for regrowth by HVPE. Figure 16.18(a–c) show optical images of the three types of seeds and the HVPE regrown wafers (Figure 16.18(d–f)), respectively.

The first type of seeded growth was reported first due to the early availability of high quality HPSG crystals, although of small form factor (Figure 16.18(a,d)). The main challenge of this seeded growth was the expansion of the seed crystal [204,205]. In HVPE growth of GaN, crystal expansion can be controlled through physical-chemical gradients and concentrations, which result in stabilization of crystal planes under the appropriate growth conditions. For in-plane expansion, size expansion will depend on the anisotropy of the growth rates for different crystallographic planes. Growth parameters, such as temperature, pressure, growth rate (source species flux), or the ratio between the nitrogen and the gallium species, can influence the stabilization of one crystal plane over another. Additionally, the geometric configuration of the seed in the system may

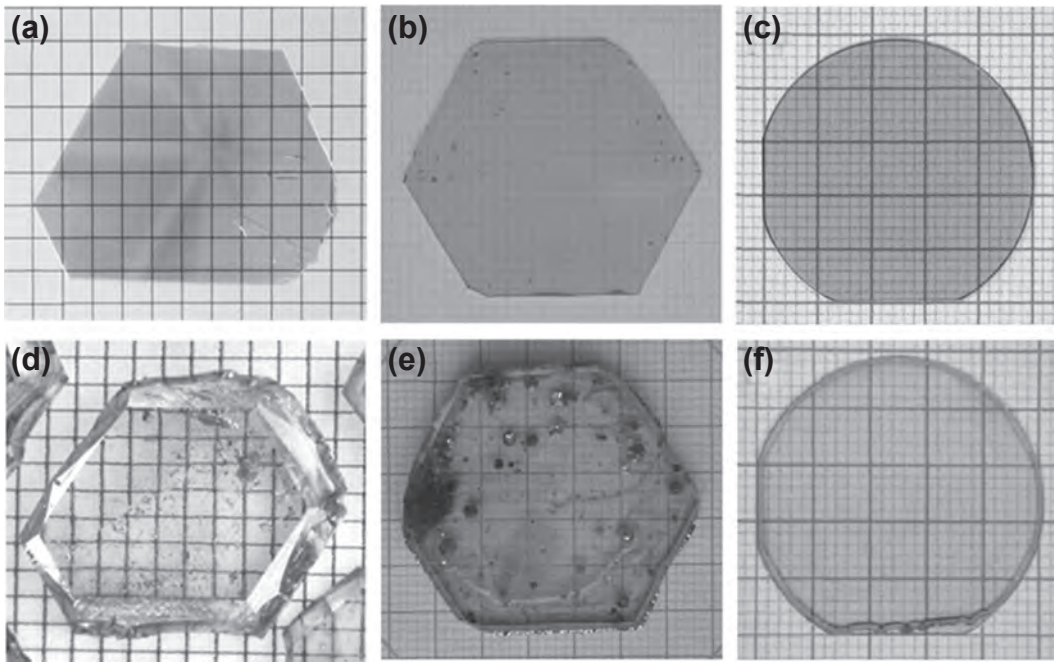


FIGURE 16.18 Optical images of GaN seeds grown by: (a) high pressure solution growth, (b) HVPE, (c) ammonothermal methods, and (D, E, F) HVPE-grown GaN on the respective seeds shown above. *Courtesy of Bolesław Łucznik.*

contribute to the flux of the growth species from additional sources, such as surface migration. As shown in the ELOG growth of GaN [197,198], inclined crystalline facets can be formed under certain growth conditions that give undesirable crystalline morphologies. An important part of the growth process development is to identify growth parameters that give a planar (as opposed to prismatic – Figure 16.18(d)) crystal, and then find the way to extend the growth in directions normal to those edge planes. One issue that has been observed with seed expansion is the variation in impurity content and carrier concentration. The physical and electrical properties of GaN grown by HVPE are very sensitive to the orientation of the crystallization front. This could present a challenge for bulk growth, particularly for undoped and semi-insulating material, where a low background concentration of shallow impurities, such as oxygen, is desired.

With the availability of larger wafers, produced by HVPE, the regrowth by HVPE was optimized and proven successful in maintaining the seed wafers' size during the HVPE-seeded growth, as shown in Figure 16.18(b,e) [206]. Even the very early HVPE regrowth on HVPE freestanding crystal showed that the material produced during regrowth possesses significantly improved structural characteristics. In particular, the dislocation density was found to be noticeably reduced. The analysis of the defect density in the regrown HVPE-GaN with different thicknesses has shown that the trend of decreasing the defect density with increasing thickness remains [207]. The high purity of

the crystals and the high optical quality have been proven reproducible. In particular, the low temperature photoluminescence (PL) spectra of the regrown GaN films showed comparable narrow (~2 meV) exciton peaks as in the PL spectrum of the seed. However, based on different studies performed by variety of techniques, such as X-ray diffraction, PL, Raman scattering spectroscopies [206,207], it is clear that both the residual strain and curvature (radius of about 10 m in the best case) of the seed was reproduced, which remains the main undesirable characteristic of these materials.

The most recent availability of low dislocation-density wafers grown by ammonothermal method open a new possibility for homoepitaxial seeded growth (Figure 16.18(c,f)). The HVPE-seeded growth on such seeds has also been proven successful in reproducing the seed characteristics in regard to very low curvature (radius close to 100 m) and low dislocation density (in the angle of $10^4/cm^2$) [208]. Moreover, in contrast to the ammonothermal seed characteristics, the HVPE-GaN wafer grown on ammonothermal seed possessed high purity and transparency, which are typical characteristics for the HVPE growth. Thus, the combination of the two methods seems to enable the advantages of both in the regrown material.

16.3.6 Growth Related Properties

16.3.6.1 Residual Impurities and Native Defects

The HVPE-grown nitrides, including GaN, AlN, and AlGaN, have generally been reported with high purity, low density of background impurity, vacancy and deep-level complexes, and with high transparency. The lowest unintentional free carrier concentration in bulk GaN material was reported in HVPE material to be in the range of 8×10^{15}–$2 \times 10^{16}/cm^3$ and was explained by the presence of oxygen and silicon impurities, being unavoidable in the nitride materials grown by HVPE. There are numerous reports about the origin of the residual impurities in HVPE-grown nitrides, as well as for their distribution. The interface region, close to the substrate, is typically characterized by high defect density of impurities, predominantly oxygen (Figure 16.19(a)) and vacancies (Figure 16.19(b)), which quickly decrease with increasing the layer thickness and overall leads to thickness improvement of material properties [210]. This trend, however, is typical for growth along the [0001] c-direction, and contradicts the flat thickness distribution of the V_{Ga}-O_N pair defects observed in the GaN growth along nonpolar directions, as seen in Figure 16.19(b) for a-plane GaN on sapphire [209]. This general trend of the point defects decreasing is more complicated, particularly in the interface region for material grown without buffers, possessing columnar interface structure, and in materials grown on ELOG-type of buffer. The material with columnar interface structure may dramatically affect the Hall effect results, indicating highly conductive or even degenerate materials in some cases, which was explained by the high concentration of the interface connected to the contacts via the columnar structure (Figure 16.15(a)) and thus bypassing the high quality low impurity concentration part of the layers. The impurity distribution in the ELOG part is even more complicated, as seen

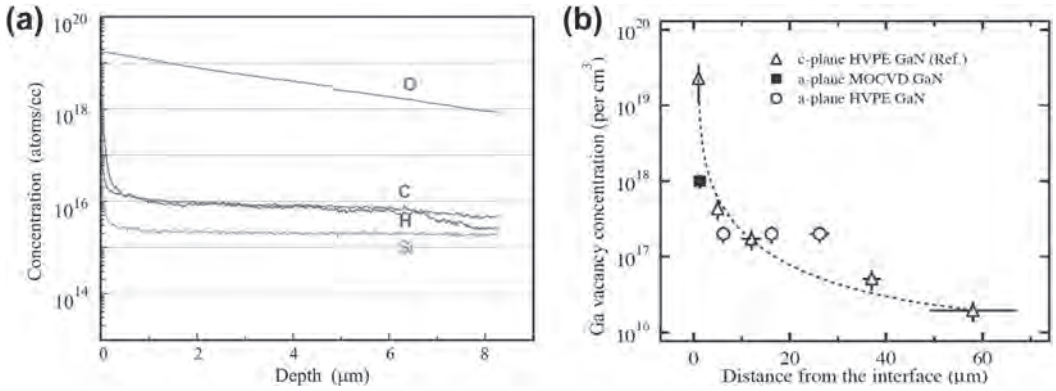


FIGURE 16.19 Ga vacancy defect distributions: (a) along the film thickness in polar and in nonpolar GaN heteroepitaxial layers grown by HVPE in the near interface region (60 μm) close to the substrate interface; (b) across a nonpolar bar sliced from a 2-in boule across the boule center—the experimental data depicted from the spots indicated in the inset. *After Ref. [209].*

in the CL images (Figure 16.17), although it is more regular and controllably distributed in the coalescent part, while the larger main part of the layer remains generally uniform and not affected by the interface impurities.

The presence of the interface layer with high density of point defects in most of the heteroepitaxial nitride and the near-surface accumulation layer often observed in InN layers provoked a need for using a two-layer model [211] for analysis of the Hall effect data in all cases of HVPE template layers. The bulk nitrides, however, do not require a consideration of this interface layer due to its self-separation removal or polishing away. The Hall effect data of bulk GaN grown by HVPE revealed high mobility, i.e., 1280/cm^2/Vs for free carrier concentration of 1.23×10^{16}/cm^3 at room temperature, close to the theoretical predictions [212].

16.3.6.2 Doping

Although all intentionally undoped GaN material grown by HVPE method possesses *n*-type conductivity, *p*-type and semi-insulating materials are also available by adding different impurities.

Intentional *n*-type doping can be achieved by O and Si doping introduced by gaseous or solid sources. Typical gaseous Si dopant precursors for HVPE growth include silane, disilane, and dichloresilane. Alternatively, Si doping can be achieved in HVPE by exposing Si to the HCl gas to form $SiCl_x$, which then transports to and reacts with the growing film. HVPE-grown bulk GaN doped with Si by using SiH_4 source was reported to result in material with carrier concentration in the range of 1.3×10^{16}–8.3×10^{18}/cm^3 while maintaining high crystalline and optical quality [213]. Alternative doping with oxygen, using gaseous source of high quality was also reported to achieve carrier concentration up to 8.5×10^{18}/cm^3. Temperature dependence of Hall carrier concentration and mobility of two such representative samples doped with Si ($n = 7.3 \times 10^{16}$/cm^3) and O ($n = 2 \times 10^{17}$/cm^3) are shown in

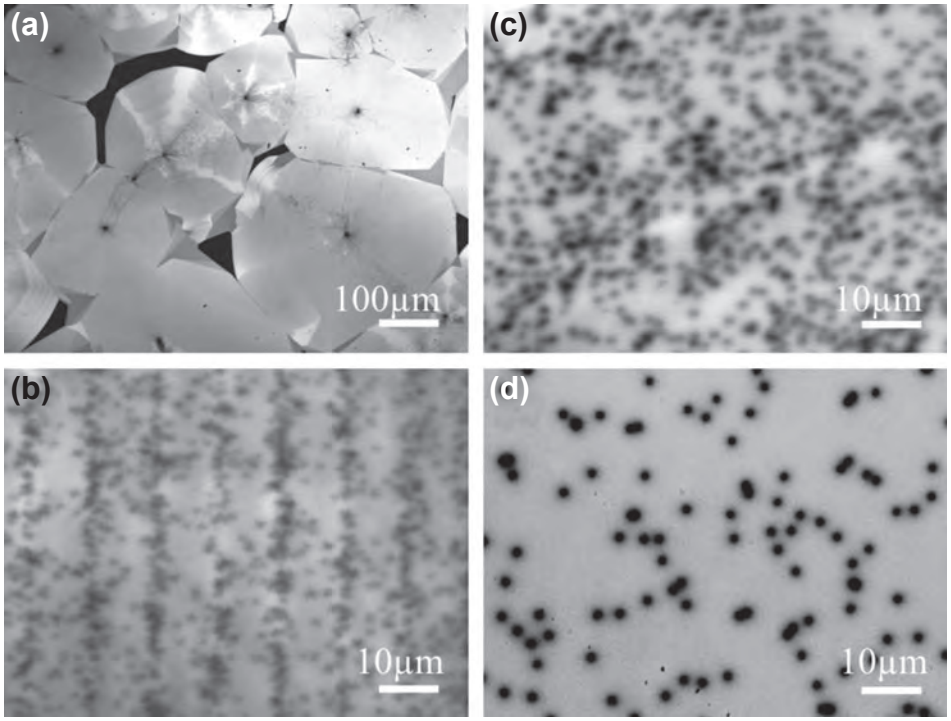


FIGURE 16.20 Panchromatic CL images visualizing in-plane dislocation distribution in GaN layer grown by HVPE on: (a) GaAs substrate using ELOG technique with hexagonal mask openings; (b) sapphire substrate using ELOG technique with striped mask; and on sapphire substrate using high temperature AlN buffer with thickness of about 150 μm (c) and 700 μm (d).

Figure 16.20(a,b), respectively, showing similar trends as the ones for undoped material with the offset related to the higher free carrier concentrations.

P-type doping of GaN bulk material was reported by HVPE techniques as well. Today Mg is the element proven to be the most efficient and controllable in achieving *p*-type conductivity. Despite that, high hole concentrations are challenging due to Mg high thermal activation energy of 150–200 meV [214], however, resulting in only a few percent of the Mg acceptor ionization at room temperature. Additionally, postgrowth annealing is required for removing the hydrogen passivation of the Mg dopant. Other elements such as Zn and Cd have also been used but with even less activation efficiency due to their larger thermal activation energy and much less activation achievable at room temperature. The doping with Mg in HVPE was done by either using a separate temperature zone and source bath or by mixing the Mg in the Ga source. The HCl gas, reacting with Mg can form MgCl, which is transported to the growth zone [215]. The role of H carrier gas was reported in a controversial way. Although one would expect that it is preferable to use inert carrier gas to avoid Mg-H passivation, the experimental results have shown preferable behavior of the passivation during growth to prevent the

incorporation of residual donor impurities [216]. Thus, despite the technological breakthroughs in growing *p*-type GaN by HVPE, the reports are very limited and the exact governing mechanisms remain unclear.

Semi-insulating GaN bulk substrates are currently only possible by doping with compensating elements. The most promising approach suggested so far in HVPE growth is doping with Fe using metalorganic source. The HVPE-growth GaN with varying Fe concentration for semi-insulating substrate application has been demonstrated, and such bulk wafers are available on the market. The material was reported with sufficiently high resistivity (larger than 10^6 Ωcm). Despite the fact that the reports on this topic are relatively limited, and the compensation mechanism is not yet fully understood, the growth of semi-insulating GaN with high quality was proven successful.

The doping of HVPE-grown bulk GaN technique was proven capable of maintaining good crystalline quality and excellent optical properties. The structural quality of non-intentionally doped (n−), Si-doped (n+), O-doped (n+), and Fe-doped (semi-insulating) GaN was studied by a variety of techniques, consistently revealing high crystalline quality, small lattice curvature, and low defect density [213]. The results are also suggestive of the relative independence of structural quality on the doping parameters within the moderate doping levels typically needed [217]. It is important to note that the doping has a noticeable effect on the lattice parameters, especially in the case of semi-insulating material doped with Fe. A precise analysis of the doping effect, however, requires a series of low defect density bulk material grown with controllable doping concentration and accounting for the background impurities and native point defects, such as Ga vacancies, despite the fact that the method produced the lowest density of native point defects as compared to all other bulk nitride techniques.

16.3.6.3 Structural Defects

The microstructure, particularly the dislocation density and distribution, represent especially important characteristics of HVPE-grown nitride template and substrates. There are two primary approaches toward decreasing the dislocation density in HVPE-GaN: ELOG-type approaches and greater GaN thickness (boule type), as mentioned earlier. The ELOG approaches can provide areas of very low defect density, where the lateral growth mode dominates. Depending on the mask geometry, these low-defect density areas could have different shape and size as visualized by panchromatic CL imaging in Figure 16.20(a,b) for hexagonal and stripe openings, respectively. Usually the devices have been placed on top of these areas.

Increasing thickness of the HVPE-GaN layer is another way of decreasing dislocation density. Panchromatic CL images (Figure 16.20(c,d)) visualize the dislocation density decrease down to 10^7–10^8/cm^2 in a ∼150-μm-thick film (Figure 16.20(c)) and 10^6–10^7/cm^2 in a ∼700-μm-thick film (Figure 16.20(d)). This effect was also visualized in transmission electron microscopy (TEM) cross-section image taken from the interface region of an HVPE-GaN layer grown on sapphire with reactive sputtered AlN buffer (Figure 16.21(a)). The AlN buffer comprises well-defined, slightly misoriented domains

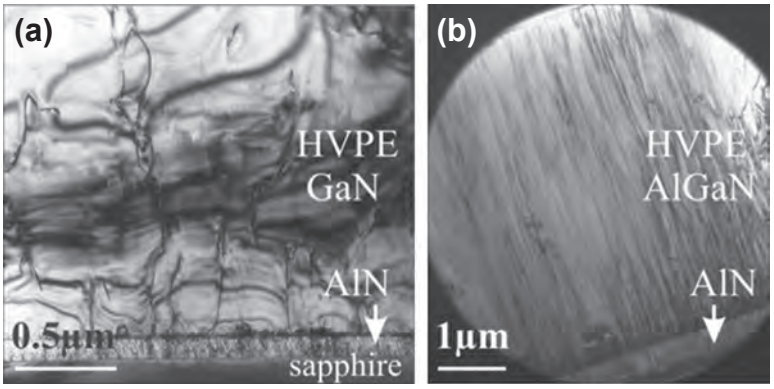


FIGURE 16.21 TEM images of: (a) HVPE-grown GaN and (b) HVPE-grown AlGaN *(Courtesy of Zuzanna Liliental-Weber)* layers, using reactive sputtered AlN buffers and showing similar decrease of dislocation density along the growth direction in both materials.

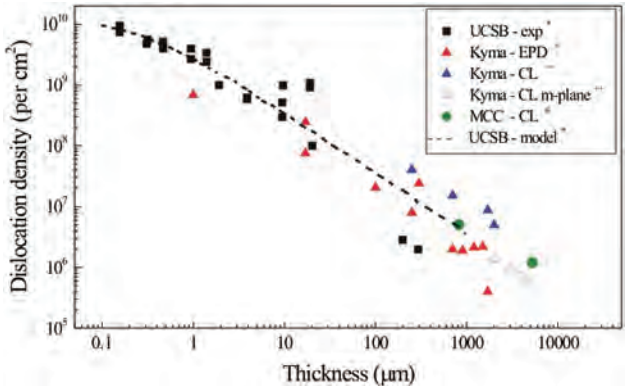


FIGURE 16.22 Combined graph of experimental data and theoretical expectations for dislocation density as a function of the GaN layer thickness. *Mathis et al. [218]; $^{+}$Hanser et al.[219]; $^{++}$Paskova et al. [187]; $^{\#}$Fujimori et al. [220].

[178] and accommodates most of the misfit defects usually generated in the interface region. One can see a reduction of the threading dislocation along the sample thickness, which was consistently shown in a number of publications. This effect is observed for all the nitrides heteroepitaxially grown by HVPE. For example, one representative TEM image of a ternary AlGaN layer grown by HVPE on sapphire substrate with reactive sputtered AlN buffer with a thickness of about 6 μm is shown in Figure 16.21(b), showing a similar trend of dislocation reduction with thickness down to $8 \times 10^8/\text{cm}^2$ in the near surface region.

The decrease of dislocation density with increasing film thickness was reported for all nitride materials and explained either by annihilation of mixed dislocations with opposite Burger's vectors [218] and/or by point defect–assisted dislocation climb. Figure 16.22 summarizes results obtained by different characterization techniques

[218–222]. TEM is the most reliable approach to differentiate and estimate the dislocation type and density, however, the technique approaches its sensitivity limit for densities around $10^5/cm^2$. Complementary studies by CL topography reveal [219,220] a different dark contrast usually interpreted as due to nonradiative recombination, with strong contrast for screw and mixed dislocations and a quite weak contrast for edge dislocations [216]. Alternative techniques used are atomic force microscopy and different etching procedures, revealing large pits related to dislocations of screw type and small pits related to edge type dislocations [222]. The graph shows a monotonic decrease of dislocation density with GaN layer thickness over several orders of magnitude, consistent with the theoretical model.

16.4 Conclusion

In this chapter the current status of vapor transport bulk growth of wide bandgap semiconductors, focusing on SiC, AlN, and GaN, was summarized. Remarkable development has been demonstrated during the last 10 years regarding understanding of the growth mechanisms and reactor optimizations. The crystal quality has been significantly improved, but much remains to be done, especially for the bulk nitrides. Growth-related defect density and doping control are the most critical current challenges that remain to be resolved in order to achieve the full potential of the bulk wide bandgap semiconductors.

Acknowledgements

T. Paskova acknowledges NSF support by DMR-1207075 and CBET-1336464 projects. M. Bickermann acknowledges DFG support by BI781/5-1, 6-1, and 8-1 projects, and BMBF support during Berlin WideBaSe project 03WKBT05A.

References

[1] [a] Kordina O, Hallin C, Ellison A, Bakin AS, Ivanov IG, Henry A, et al. Appl Phys Lett 1996;69:1456;
[b] Kordina O, Hallin C, Henry A, Bergman JP, Ivanov IG, Ellison A, et al. Phys Status Solidi B 1997;202:321.

[2] Hofmann DH, Müller MH. Mater Sci Eng B 1999;61–62:29.

[3] Wellmann P, Desperrier P, Mueller R, Straubinger T, Winnacker A, Baillet F, et al. J Cryst Growth 2005;275:e555.

[4] Schlesser R, Sitar Z. J Cryst Growth 2002;234:349.

[5] [a] Vodakov YuA, Mokhov EN, Ramm MG, . Roenkov AD. Krist Tech 1979;14:729;
[b] Mokhov EN, Shulpina IL, Tregubova AS, Vodakov YuA. Krist Tech 1981;16:879.

[6] [a] Acheson EG. Great Britain Patent 1890;17911;
[b] United States Patent 1893;492767.

[7] [a] Lely JA. Ber Dt Keram Ges 1955;8:229 [in German];
[b] United States Patent 1958;2854364.

[8] [a] Ziegler G, Lanig P, Theis D, Weyrich C. IEEE Trans Electron Devices 1983;ED-30:277;
[b] Ziegler G. German Patent 3230727 (1984).

[9] Barrett DL, Seidensticker RG, Gaida W, Hopkins RH, Choyke WJ. J Cryst Growth 1991;109:17.

[10] Tairov YuM. Mater Sci Eng B 1995;29:83.

[11] [a] Tairov YuM, Tsvetkov VF. Prog Cryst Growth Charact 1983;7:111;
[b] Tairov YuM, Tsvetkov VF. Cryst Growth Prop Appl 1984;10:1 [Springer].

[12] [a] Tairov YuM, Tsvetkov VF. J Cryst Growth 1978;43:209;
[b] Tairov YuM, Tsvetkov VF. J Cryst Growth 1981;52:146.

[13] Vodakov YuA, Roenkov AD, Ramm MG, Mokhov EN, Makarov YuN. Phys Status Solidi B 1997;202:177.

[14] Davis RF, Sitar Z, Williams BE, Kong HS, Kim HJ, Palmour JW, et al. Mater Sci Eng B 1988;1:77.

[15] Carter Jr CH, Tsvetkov VRF, Glass RC, Henshall D, Brady M, Müller StG, et al. Mater Sci Eng B 1999;61–62:1.

[16] Cree Inc., 4600 Silicon Drive, Durham, NC 27703–8475, USA, http://www.cree.com/.

[17] Charles & Colvard Ltd., 300 Perimeter Park Drive, Suite A, Morrisville, NC 27560, USA, http://www.charlesandcolvard.com/.

[18] Slack GA. MRS Symp Proc 1998;512:35.

[19] Pastrnak J, Roskovcova L. Phys Status Solidi 1964;7:331 [in German].

[20] Slack GA. Aluminum nitride crystal growth. U.S. Air Force Office of Scientific Research; 1979. DTIC document ADA085932, http://www.dtic.mil.

[21] Balkas CM, Sitar Z, Zheleva T, Bergman L, Nemanich R, Davis RF. J Cryst Growth 1997;179:363.

[22] [a] Slack GA, McNelly TF. J Cryst Growth 1976;34:263;
[b] Slack GA, McNelly TF. J Crystal Growth 1977;42:560.

[23] Piper WW, Polich SJ. J Appl Phys 1961;32:1278.

[24] Kneissl M, Kolbe T, Chua C, Kueller V, Lobo N, Stellmach J, et al. Semicond Sci Technol 2011;26:014036.

[25] Scace RI, Slack GA. J Chem Phys 1959;30:1551.

[26] Kleykamp H, Schumacher G. Ber Bunsenges Phys Chem 1993;97:799.

[27] Siang-Chung L. Mater Sci Lett 1997;16:759.

[28] Knippenberg WF. Philips Res Rep 1963;18:161.

[29] [a] Lilov SK. Cryst Res Technol 1993;28:503;
[b] Lilov SK. Diam Relat Mater 1995;4:1331;
[c] Lilov SK. Mater Sci Eng B 1993;21:65.

[30] Epelbaum BM, Bickermann M, Nagata S, Heimann P, Filip O, Winnacker A. J Cryst Growth 2007;305:317.

[31] Epelbaum BM, Bickermann M, Winnacker A. Mater Sci Forum 2004;457–460:1537.

[32] Straubinger TL, Bickermann M, Hofmann D, Weingärtner R, Wellmann PJ, Winnacker A. Mater Sci Forum 2001;353–356:25.

[33] Augustine G, Hobgood HMcD, Balakrishna V, Dunne G, Hopkins RH. Phys Status Solidi B 1997;202:137.

[34] Stein RA, Lanig P, Leibenzeder S. Mater Sci Eng B 1992;11:69.

[35] Snyder DW, Heydemann VD, Everson WJ, Barrett DL. Mater Sci Forum 2000;338–342:9.

[36] Schulze N, Barrett D, Weidner M, Pensl G. Mater Sci Forum 2000;338–342:111.

[37] Herro ZG, Zhuang D, Schlesser R, Collazo R, Sitar Z. J Cryst Growth 2006;286:205.

[38] Segal AS, Karpov SYu, Makarov YuN, Mokhov EN, Roenkov AD, Ramm MG, et al. J Cryst Growth 2000;211:68.

[39] Jacquier C, Ferro G, Cauwet F, Monteil Y. Mater Sci Forum 2002;389–393:307.

[40] Karpov SYu, Kulik AV, Przhevalskii IN, Ramm MS, Vodakov YuN. Phys Status Solidi C 2003;0:1989.

[41] Rost H-J, Doerschel J, Irmscher K, Roßberg M, Schulz D, Siche D. J Cryst Growth 2005;275:e451.

[42] Albrecht M, Wollweber J, Rossberg M, Schmidbauer M, Hartmann C, Fornari R. Appl Phys Lett 2006;88:211904.

[43] Kroko LJ. J Electrochem Soc 1966;113:801.

[44] Noveski V, Schlesser R, Mahajan S, Beaudoin S, Sitar Z. J Cryst Growth 2004;264:369.

[45] Schönherr E. Cryst Growth Prop Appl 1980;2:51 [Springer].

[46] Ma R, Zhang H, Prasad V, Dudley M. Cryst Growth Des 2002;2:213.

[47] Dreger LH, Dadape VV, Margrave JL. J Phys Chem 1962;66:1556.

[48] Hoch M, Ramakrishnan D. J Electrochem Soc 1971;118:1204.

[49] Chen Q-S, Zhang H, Prasad V, Balkas CM, Yushin NK. J Heat Transfer 2001;123:1098.

[50] Lilov SK, Yanchev IY. Cryst Res Technol 1993;28:495.

[51] Mokhov EN, Smirnov SN, Segal AS, Bazarevskiy D, Makarov YuN, Ramm MG, et al. Mater Sci Forum 2004;457–460:1545.

[52] Drowart J, De Maria G, Inghram MG. J Chem Phys 1958;29:1015.

[53] Sadowski H, Helbig R. J Electrochem Soc 1998;145:3556.

[54] Tairov YuM, Tsvetkov VF, Lilov SK, Safaraliev GK. J Cryst Growth 1976;36:147.

[55] Karpov SYu, Zimina DV, Makarov YuN, Mokhov EN, Roenkov AD, Ramm MG, et al. Phys Status Solidi A 1999;176:435.

[56] Chen Q-S, Prasad V, Zhang H, Dudley M. In: Byrappa K, Ohachi T, editors. Crystal growth technology. New York: William Andrew; 2003, ISBN 978-0-8155-1453-4 [chapter 7].

[57] Selder M, Kadinski L, Durst F, Hofmann D. J Cryst Growth 2001;226:501.

[58] Okamoto A, Sugiyama N, Tani T, Kamiya N. Mater Sci Forum 1998;264–267:21.

[59] Epelbaum BM, Seitz C, Magerl A, Bickermann M, Winnacker A. J Cryst Growth 2004;265:577–81.

[60] Hartmann C, Wollweber J, Dittmar A, Irmscher K, Kwasniewski A, Langhans F, et al. Jpn J Appl Phys 2013;52:08JA06.

[61] Nitride Crystals Inc., 181 E Industry Ct., Suite B, Deer Park, NY 11729, USA, http://www.nitride-crystals.com/.

[62] Heydemann VD, Schulze N, Barrett DL, Pensl G. Appl Phys Lett 1996;69:3728.

[63] Giocondi J, Rohrer GS, Skowronski M, Balakrishna V, Augustine G, et al. J Cryst Growth 1997;181:351.

[64] Frank FC. Philos Mag 1951;42:1014.

[65] Burton WK, Cabrera N, Frank FC. Philos Trans R Soc Lond Ser A 1951;243:299.

[66] Herro ZG, Epelbaum BM, Weingärtner R, Bickermann M, Masri P, Winnacker A. J Cryst Growth 2004;270:113.

[67] Ohtani N, Katsuno M, Aigo T, Fujimoto T, Tsuge H, Yashiro H, et al. J Cryst Growth 2000;210:613.

[68] Sumathi RR. CrystEngComm 2013;15:2232.

[69] Hexatech Inc., 991 Aviation Pkwy, Suite 800, Morrisville, NC 27560, USA, http://www.hexatechinc.com/.

[70] CrystAl-N GmbH, Dr.-Mack-Str. 77, 91762 Fürth, Germany, http://www.crystal-n.com/.

[71] Bickermann M, Epelbaum BM, Winnacker A. J Cryst Growth 2004;269:432.

[72] Madar R, Anikin M, Chourou K, Labeau M, Pons M, Blanquet E, et al. Diam Relat Mater 1997;6:1249.

[73] Hofmann D, Bickermann M, Eckstein R, Kölbl M, Müller StG, Schmitt E, et al. J Cryst Growth 1999;198/199:1005.

[74] Straubinger TL, Bickermann M, Grau M, Hofmann D, Kadinski L, Müller SG, et al. Mater Sci Forum 2000;338–342:39.

[75] Schlesser R, Dalmau R, Zhuang D, Collazo R, Sitar Z. J Cryst Growth 2005;281:75.

[76] Dalmau R, Raghothamachar B, Dudley M, Schlesser R, Sitar Z. MRS Symp Proc 2004;798:Y2.9.

[77] Liu B, Edgar JH, Gu Z, Zhuang D, Raghothamachar B, Dudley M, et al. MRS Internet J Nitride Semicond Res 2004;9:6.

[78] Slack GA, Whitlock J, Morgan K, Schowalter LJ. MRS Symp Proc 2004;798:Y10.74.

[79] Makarov YuN, Avdeev OV, Barash IS, Bazarevskiy DS, Chemekova TYu, Mokhov EN, et al. J Cryst Growth 2008;310:881.

[80] Hartmann C, Wollweber J, Albrecht M, Rasin I. Phys Status Solidi C 2006;3:1608.

[81] Matsunami H, Kimoto T. Mater Sci Eng R 1997;20:125.

[82] Siche D, Albrecht M, Rost H-J, Sendzik A. Mater Sci Forum 2007;556–557:21.

[83] [a] Takahashi J, Ohtani N. Phys Status Solidi B 1997;202:163;
[b] Takahashi J, Ohtani N, Katsuno N, Shinoyama S. J Cryst Growth 1997;181:229.

[84] Filip O, Epelbaum B, Li J, Bickermann M, Xu X, Winnacker A. Mater Sci Forum 2009;600–603:23.

[85] Raghothamachar B, Bai J, Dudley M, Dalmau R, Zhuang D, Herro Z, et al. J Cryst Growth 2006;287:349.

[86] Sumathi RR, Gille P. Jpn J Appl Phys 2013;52:08JA02.

[87] Bickermann M, Filip O, Epelbaum BM, Heimann P, Feneberg M, Neuschl B, et al. J Cryst Growth 2012;339:13.

[88] Sanchez EK, Kuhr T, Heydemann D, Snyder W, Rohrer S, Skowronski M. J Electron Mater 2000;29:347.

[89] Filip O, Epelbaum BM, Bickermann M, Heimann P, Winnacker A. J Cryst Growth 2011;318:427.

[90] Helava H, Mokhov EN, Avdeev OA, Ramm MG, Litvin DP, Vasiliev AV, et al. Mater Sci Forum 2013;740–742:85.

[91] Anikin M, Chourou K, Pons M, Bluet JM, Madar R, Grosse P, et al. Mater Sci Eng B 1999;61–62:73.

[92] Bahng W, Kitou Y, Nishizawa S, Yamaguchi H, Nasir Khan M, Oyanagi N, et al. J Cryst Growth 2000;209:767.

[93] Rost H-J, Siche D, Dolle J, Eiserbeck W, Müller T, Schulz D, et al. Mater Sci Eng B 1999;61–62:68.

[94] Wellmann PJ, Bickermann M, Hofmann D, Kadinski L, Selder M, Straubinger T, et al. J Cryst Growth 2000;216:263.

[95] Herro ZG, Epelbaum BM, Bickermann M, Masri P, Winnacker A. J Cryst Growth 2004;262:105.

[96] Bickermann M, Heimann P, Epelbaum BM. Phys Status Solidi C 2006;3:1902.

[97] Ha S, Nuhfer NT, De Graef M, Rohrer GS, Skowronski M. Mater Sci Forum 2000;469–472:477.

[98] Bondokov RT, Morgan KE, Shetty R, Liu W, Slack GA, Goorsky M, et al. MRS Symp Proc 2006;892: FF30-03.

[99] Dalmau R, Moody B, Xie J, Collazo R, Sitar Z. Phys Status Solidi A 2011;208:1545.

[100] Bickermann M, Epelbaum BM, Filip O, Tautz B, Heimann P, Winnacker A. Phys Status Solidi C 2012;9:449.

[101] Hobgood HMcD, Glass RC, Augustine G, Hopkins RH, Jenny J, Skrowonski M, et al. Appl Phys Lett 1995;66:1364.

[102] Bickermann M, Weingärtner R, Winnacker A. J Cryst Growth 2003;254:390.

[103] Rasp M, Straubinger ThL, Schmitt E, Bickermann M, Reshanov S, Sadowski H. Mater Sci Forum 2003;433–436:55.

[104] Mitchel WC, Saxler A, Perrin R, Goldstein J, Smith SR, Evwaraye AO, et al. Mater Sci Forum 2000; 338–342:21.

[105] Carter Jr. CH, Brady M, Tsvetkov VF, United States Patent 6218680 (2001).

[106] Pensl G, Choyke WJ. Physica B 1993;185:264.

[107] Ohtani N, Katsuno M, Takahashi J, Yashiro H, Kanaya M. J Appl Phys 1998;83:4487.

[108] Schulze N, Gajowski J, Semmelroth K, Laube M, Pensl G. Mater Sci Forum 2001;353–356:45.

[109] Bickermann M, Epelbaum BM, Hofmann D, Straubinger TL, Weingärtner R, Winnacker A. J Cryst Growth 2001;233:211.

[110] Straubinger TL, Bickermann M, Weingärtner R, Wellmann PJ, Winnacker A. J Cryst Growth 2002; 240:117.

[111] Glass RC, Augustine G, Balakrishna V, Hobgood HMcD, Hopkins RH, Jenny J, et al. Inst Phys Conf Ser 1996;142:37.

[112] Taniyasu Y, Kasu M, Makimoto T. Appl Phys Lett 2004;85:4672.

[113] Schulz T, Irmscher K, Albrecht M, Hartmann C, Wollweber J, Fornari R. Phys Status Solidi RRL 2007;1:147.

[114] Chen Y, Dhanaraj G, Vetter W, Ma R, Dudley M. Mater Sci Forum 2007;556–557:231.

[115] Schmitt E, Straubinger T, Rasp M, Weber A-D. Superlattices Microstruct 2006;40:320.

[116] Frank FC. Acta Crystallogr 1951;4:497.

[117] Si W, Dudley M, Glass R, Tsvetkov V, Carter Jr CH. Mater Sci Forum 1998;264–268:429.

[118] Hofmann D, Schmitt E, Bickermann M, Kölbl M, Wellmann PJ, Winnacker A. Mater Sci Eng B 1999; 61–62:48.

[119] Hong MH, Samant AV, Pirouz P. Mater Sci Forum 2000;338–243:513.

[120] Kitou Y, Bahng W, Nishizawa S, Nishino S, Arai K. Mater Sci Forum 2000;338–242:83.

[121] Rost H-J, Dolle J, Doerschel J, Siche D, Schulz D, Wollweber J. J Cryst Growth 2001;225:317.

[122] Dudley M, Huang XR, Huang W, Powell A, Wang S, Neudeck P, et al. Appl Phys Lett 1999;75:784.

[123] Lendenmann H, Dahlquist F, Bergman JP, Bleichner H, Hallin C. Mater Sci Forum 2002;389–393: 1259.

[124] Ha S, Mieszkowski P, Skowronski M, Rowland LB. J Cryst Growth 2002;244:257.

[125] Bickermann M, Schimmel S, Epelbaum BM, Filip O, Heimann P, Nagata S, et al. Phys Status Solidi C 2011;8:2235.

[126] Seitz C, Herro ZG, Epelbaum BM, Hock R, Magerl A. J Appl Cryst 2006;39:17.

[127] Dalmau R, Schlesser R, Sitar Z. Phys Status Solidi C 2005;2:2036.

[128] Maruska HP, Tjetjen JJ. Appl Phys Lett 1969;15:327.

[129] Molnar RG. In: Pankove J, Moustakas TD, editors. Galium nitride (GaN) II. Semiconductors and semimetals, vol. 57. London: Academic Press; 1999 [chapter 1].

[130] Paskova T, Monemar B. In: Manasreh O, editor. III-nitride semiconductors: growth. NY: Taylor & Francis Group; 2002. pp. 175–236 [chapter 10].

[131] Dwikusuma F, Kuech TF. In: Paskova T, Monemar B, editors. Nitrides as seen by technology. Research Signpost; 2002 [chapter 3].

[132] Hemmingsson C, Monemar B, Kumagai Y, Koukitu A. In: Dhanaraj G, Byrappa K, Prasad V, Dudley M, editors. Handbook of crystal growth. Berlin: Springer-Verlag; 2008.

[133] Cadoret R, Trasoidaine A. J Phys Condens Matter 2001;13:6893.

[134] Koukitu A, Hama S, Taki T, Seki H. Jpn J Appl Phys 1998;37:762.

[135] Kumagai Y, Yamane T, Miyaji T, Murakami H, Kangawa Y, Koukitu A. Phys Status Solidi C 2003;0: 2498.

[136] Nickel KG, Riedel R, Petzow G. J Am Ceram Soc 1989;72:1804.

[137] Efimov AN, Lebedev AO, Tsaregorodtsev AM. Tech Phys Lett 1998;24:810.

[138] Bugge F, Efimov AN, Pichugin IG, Tsaregorodtsev AM, Chernov MA. Cryst Res Technol 1987;22:65.

[139] Kumagai Y, Takemoto K, Kikuchi J, Hasegawa T, Murakami H, Koukitu A. Phys Status Solidi B 2006; 243:1431.

[140] Ban VS. J Electrochem Soc 1972;119:761.

[141] Ilegems M. J Cryst Growth 1972;13/14:360.

[142] Huang JS, Kuznetsov AV, Lee SS, Kim HS, Choi JG, Chong PJ. J Cryst Growth 1994;142:5.

[143] Tsuchiya H, Okahisa T, Hasegawa F, Okumura H, Yoshida S. Jpn J Appl Phys 1994;33:1747.

[144] Kumagai Y, Adachi H, Otake A, Higashikawa Y, Togashi R, Murakami H, et al. Phys Status Solidi C 2010;7:2022.

[145] Kumagai Y, Takemoto K, Hasegawa T, Koukitu A, Seki H. J Cryst Growth 2001;231:57.

[146] Kumagai Y, Yamane T, Koukitu A. J Cryst Growth 2005;281:62.

[147] Lebedev AO, Melnik YV, Tsaregorodtsev AM. Inst Phys Conf Ser 1994;137:405.

[148] Kumagai Y, Takemoto K, Koukitu A, Seki H. J Cryst Growth 2001;222:118.

[149] Trainor JW, Rose K. J Electron Mater 1974;3:821.

[150] Sato Y, Sato S. Jpn J Appl Phys 1997;36:4295.

[151] Noreika AJ, Ing DW. J Appl Phys 1968;39:5578.

[152] Tsaregorodtsev AM, Efimov AN, Pikhtin AN, Pichugin IG. Inst Phys Conf Ser 1997;155:243.

[153] Melnik Y, Nikolaev A, Stepanov S, Kikitina I, Vassilevski K, Ankudinov A, et al. Mater Sci Forum 1998;264–268:1121.

[154] Przhevalskii IN, Yu S, Karpov S, Makarov YN. MRS Internet J Nitride Semicond Res 1998;3. art 30.

[155] Seifert W, Franzheld R, Butter E, Sobotta H, Reide V. Cryst Res Technol 1983;18:383.

[156] Koukitu A, Hama S, Taki T, Seki H. Jpn J Appl Phys 1998;37:762.

[157] Aujol E, Napierala J, Trassoudain A, Gil-Lafon E, Cadoret R. J Cryst Growth 2001;222:538.

[158] Cadoret R. J Cryst Growth 1999;205:123.

[159] Trassaudaine A, Aujol E, Cadoret R, Paskova T, Monemar B. Mater Res Soc Symp Proc 2001:G.3.2.

[160] Segal AS, Kondratyev AV, Karpov S Yu, Martin D, Wagner V, Ilegems M. J Cryst Growth 2004;270:384.

[161] Safvi SR, Perkins NR, Horton MN, Thon A, Zhi D, Kuech TF. Mater Res Soc Symp Proc 1996;423:227.

[162] Shintani A, Minagawa S. J Cryst Growth 1974;22:1.

[163] Liu SS, Stevenson DA. J Electrochem Soc 1978;125:1161.

[164] Paskova T, Svedberg E, Henry A, Ivanov IG, Yakimova R, Monemar B. Phys Scr T 1999;79:67.

[165] Luzcnik B, Invited talk at the IW on Bulk Nitride Semiconductors VII (IWBNS-7), September 30–October 5, 2013, Kloster Seeon, Germany.

[166] Molnar RJ, Nichols KB, Maki P, Brown ER, Melngailis I. Mater Res Soc Symp Proc 1995;378:479.

[167] Dam CEC, Hageman PR, Larsen PK. J Cryst Growth 2006;205:123.

[168] Fremunt R, Cerny P, Kohout J, Rosicka V, Burger A. Cryst Res Technol 1981;16:1257.

[169] Ohki Y, Toyoda Y, Kobayasi H, Akasaki I. Inst Phys 1982:479.

[170] Molnar RJ, Gotz W, Romano LT, Johnson JM. J Cryst Growth 1997;178:147.

[171] Richter E, Henning C, Weyers M, Habel F, Tsay J-D, Liu W-D, et al. J Cryst Growth 2005;277:6.

[172] Kumagai Y, Takemoto K, Kikuchi Y, Hasegawa T, Murakami H, Koukitu A. Phys Status Solidi B 2006;243:1431.

[173] Wang WN, Stepanov SI, UK Patent GB 2 415 707, Vertical hydride vapor epitaxy deposition using a homogenising diaphragm.

[174] Semiconductor technology Research, http://www.str-soft.com/products/cvdsim/HVPE/, www.semitech.us.

[175] Liu L, Edgar J. Mater Sci Eng B 2002;37:61.

[176] Grandjean N, Leroux M, Laugt M, Massies J. Appl Phys Lett 1997;71:1240.

[177] Molnar RJ, Aggarwal R, Liau ZL, Brown ER, Melngailis I. Mater Res Soc Symp Proc 1996;395:189.

[178] Naniwae K, Itoh S, Amano H, Itoh K, Hiramatsu K. J. Crystal Growth 1990;99:381.

[179] Molnar RJ, Maki P, Aggarwal R, Liau ZL, Brown ER, Melngailis I, Götz W, Romano LT, Johnson NM. Mater. Res. Sos. Symp. Proc 1998;423:221.

[180] Hemmingsson C, Pozina G. Journal of Crystal Growth 2013;366:61.

[181] Paskova T, Birch J, Tungasmita S, Beccard R, Heuken M, Svedberg E, Runesson P, Goldys EM, Monemar B. Physica Status Solidi A 1999;176:415.

[182] Paskova T, Valcheva E, Birch J, Tungasmita S, Persson P, Paskov PP, Evtimova S, Abrashev M, Monemar B. Journal of Crystal Growth 2001;230:381.

[183] Valcheva E, Paskova T, Tungasmita S, Persson P, Birch J, Svedberg E, Hultman L, Monemar B. Applied Physics Letters 2002;76:1860.

[184] Paskova T, Tungasmita S, Valcheva E, Svedberg E, Arnaudov B, Evtimova S, Persson P, Henry A, Beccard R, Heuken M, Monemar B. Materials Research Society International Journal Nitride Semiconductor Research 2000;5S1:W3.14.

[185] Valcheva E, Paskova T, Birch J, Tungasmita S, Person POA, Hultman L, Monemar B. J Appl Phys 2001;90:6011.

[186] Oshima Y, Eri T, Sunakawa H, Usui A. Physica Status Solidi A 2002;194:554.

[187] [Online]. Available, http://www.hitachi-able.co.jp/en/products/news/20030213t.html; 2007.

[188] [Online]. Available, http://www.sei.co.jp/; 2007.

[189] Hanser D, Liu L, Preble EA, Thomas D, Williams M. Materials Research Society Symposium Proceedings 2004;798:Y2.1.1.

[190] Paskova T, Evans K. IEEE. J. Sel Topics Quantum Electronics 2009;15:1041.

[191] Kawaguchi Y, Nambu S, Sone H, Yamagichi M, Miyake H, Hiramatsu K, Sawaki N, Iyechika Y, Maeda T. Mater. Res. Sos. Symp. Proc. 1996;537:G.4.1.

[192] Usui A, Sunakawa H, Sakai A, Yamaguchi AA. Japanese Journal of Applied Physics 1997;36:L899.

[193] Gibart P, Beaumont B, Vennegues P. In: Ruterana P, Albrecht M, Neugebauer J, editors. Nitride Semiconductors, Handbook on Materials and Devices; 2003. ch. X, Wiley-VCH, Berlin.

[194] Paskova T, Valcheva E, Paskov PP, Monemar B, Rockowski AM, Davis RF, Beaumont B, Gibart P. Diamond and Related Materials 2004;13:1125.

[195] Zheleva Tz, Smith SA, Thomson DB, Linthicum KJ, Rajagopal P, Davis RP. J Electron Mater 1999;28:L5.

[196] Sone H, Nambu S, Kawaguchi Y, Yamaguchi M, Miyake H, Hiramatsu K, et al. Jpn J Appl Phys 1999;38:L356.

[197] Davis RF, Roskowski AM, Preble EA, Speck JS, Heying B, Freitas JA, et al. Proc IEEE 2002;90:993.

[198] Motoki K, Okahisa T, Nakahata S, Matsumoto N, Kimura H, Kasai H, et al. J Cryst Growth 2002;237–239:912.

[199] Kryliouk O, Reed M, Dann T, Anderson T, Chai B. Mater Sci Eng B 1999;66:26.

[200] Richter E, Hnnig C, Zeimer U, Weyers M, Tranke G, Reiche P, et al. Phys Status Solidi C 2006;3:1439.

[201] Fujito K, Kiyomi K, Mochizuki T, Oota H, Namita H, Nagao S, et al. Phys Status Solidi A 2008;5:1056.

[202] Vaudo RP, Xu X, Loria C, Salant AD, Flynn JS, Brandes JR. Phys Status Solidi A 2002;194:494.

[203] Weyers M, Richter E, Hennig C, Hagedorn S, Wernicke T, Trankle G. Proc SPIE 2008;6910:691001.1.

[204] Lucznik B, Pasturszka B, Grzegory I, Bockowski M, Kamler G, Litwin-Staszewska E, et al. J Cryst Growth 2005;281:38.

[205] Grzegory I, Łucznik B, Boćkowski M, Pastuszka B, Kryśko M, Kamler G, et al. Proc SPIE 2006;6121:612107.

[206] Lucznik B, Pasturszka B, Kamler G, Grzegory I, Porowski S. In: Ehrentraut D, Meissner E, Bockowski M, editors. Technology of gallium nitride crystal growth. Springer series in materials science, vol. 133. Springler; 2009 [chapter 3].

[207] Paskova T, Paskov PP, Birch J, Valcheva E, Abrashev M, Tungasmita S, et al. Proc IWN2000, Nagoya Jpn IPAP Conf Ser 2000;C1:19–22.

[208] Sochalski T, Bryan Z, Amilusik M, Collazo R, Lucznik B, Weyher JL, Nowak G, Sadovyi B, Kamler G, Kucharski R, Zajac M, Doradzinski R, Dwilinski R, Grzegory I, Bockowski M, Sitar Z. Appl Phys Express 2013:6:075504.

[209] Tuomisto F, Saarinen K, Paskova T, Monemar B, Bockowski M, Suski T. J Appl Phys 2006;99:066105.

[210] Oila J, Kivioja J, Ranki V, Saarinen K, Look DC, Molnar RJ, et al. Appl Phys Lett 2003;82:3433.

[211] Look DC, Reynolds DC, Hemsky JW, Sizelove JR, Jones RL, Molnar RJ. Phys Rev Lett 1997;79:2273.

[212] Look DC, Sicelove JR. Appl Phys Lett 2001;79:1133.

[213] Paskova T, Preble EA, Hanser AD, Evans KR, Kröger R, Paskov PP, et al. Phys Status Solidi C 2009;6:S344.

[214] Goetz W, Kern RS, Chen CH, Liu H, Steigerwald DA, Fletcher RM. Mater Sci Eng B 1999;59:211.

[215] Usikov A, Kovalenko O, Ivantsov V, Sukhoveev V, Dmitriev V, Shmidt N, et al. Mater Res Soc Symp Proc 2005;831:453.

[216] Neugebauer J, Van der Walle CG. Phys Rev Lett 1995;75:4452.

[217] Van der Walle CJ. Phys Rev B 2003;68:165209.

[218] Mathis SK, Romanov AE, Chen LF, Beltz GE, Pompe W, Speck JS. Phys Status Solidi A 2000;179:125.

[219] Hanser D, Liu L, Preble EA, Thomas D, Williams M. Mater Res Soc Symp Proc 2004;798:Y2.1.1.

[220] Fujimori T, Plenary talk at Int Workshop on nitride semiconductors, October 6–10, 2008, Montreux, Switzerland.

[221] Hino T, Tomiya S, Miyajima T, Yanashima K, Hashimoto S, Ikeda M. Appl Phys Lett 2000;76:3421.

[222] Weyher JL, Macht L, Kamber G, Borysiuk J, Grzegory I. Phys Status Solidi C 2003;0:821.

10. Bulk Growth of Oxide Materials

Bulk Growth of Oxide Materials

Satoshi Uda

Tohoku University, Sendia, Japan
uda@imr.tohoku.ac.jp

Abstract: This lecture discusses how to obtain compositional homogeneity and low defect formation in growing oxide crystals for optical use from both the fundamental and practical perspectives. The lecture covers conventional studies as well as new approaches to crystal growth, covering the basic thermodynamics.

First, the optical properties that characterize optical applications and their representative usable crystals are explained, including electro-optic (EO), magneto-optical (MO), acousto-optic (AO) and nonlinear-optical (NLO) effects. The growth methods appropriate for these optical crystals are briefly described with reference to the Czochralski (CZ), Bridgman (BR), floating zone (FZ), top-seeded solution growth (TSSG), hydrothermal and micro-pulling down (μ-PD) techniques. The growth fundamentals and practical techniques that support optical uniformity and low defect formation are discussed, particularly for the CZ method, which assures a uniform distribution of the refractive index, which is regarded as one of the optical uniformities, a lack of laser scattering and superior transparency with sharp absorption edges. With regard to compositional homogeneity, which is related to optical uniformity, a survey of congruent composition is discussed first. Doping is commonly employed to improve or modify the optical properties, and the dopant distribution should be homogeneous in the crystal. Solute partitioning between solid and liquid, and the resultant solute distribution in a crystal, are determined with the aid of conventional equations, i.e., a diffusion-controlled solute distribution, the BPS (Burton–Prime–Slichter) equation, the Scheil equation and the criteria equation for the occurrence of constitutional supercooling.

Next, defects ranging in size from macroscopic to nanoscopic are discussed in association with the growth conditions. These include cracks, cavities, subgrains, striations, cores, cellular structures, dislocations and vacancies. Their causes and methods of evaluation are also described. Conventional growth techniques and a growth mechanism to minimize defect generation are discussed. These deal with temperature gradients near the melt surface, crystal rotation and pulling rates, gas flow and temperature, crystallographic anisotropy, viscosity and thermal conductivity of the melt, which strongly influence the melt flow and interface shape. Suitable growth conditions are

desirable for adjusting the interface shape and avoiding defect formation.

In addition to the conventional growth methods, some new techniques are introduced. Mechanical stirring or laser beam irradiation into the melt modifies the physical properties and thermodynamic state of the melt, and evidently changes the growth temperature and growth rate, which is reflected in the crystal quality. The application of an external field to the growth system yields one more degree of freedom, which can be used to change the chemical potential of both the solid and liquid phases, and modifies the phase relationship, such as the conversion of incongruency to congruency. This could lead to the invention of a new growth method.

An optical oxide crystal typically has a complex structure, such as perovskite, ilmenite, garnet or langasite. One of the design factors of new optical oxide crystals is the allocation of a cation to an appropriate crystal site, i.e., tetrahedral, octahedral and decahedral sites. Many combinations are possible for such a site allocation. Examining the degrees of freedom in each site of a crystal, which is similar to the Gibbs phase rule, is an effective way to narrow down the possible combinations of site allocations for elements, and reduce the time and effort required to construct a complex crystal structure composed of several elements.

Melt constituents is an important subject of study with regard to its relationship to the compositional uniformity in a growing crystal. Most oxide melts exhibit ionic conductivity, and ionic species are present in the oxide melt via the release of an oxygen ion. A system that regards the oxygen as an independent component is required instead of pseudo-binary or pseudo-ternary systems where metal to oxygen stoichiometry is assumed to hold. By investigating the partitioning of ionic species, true congruent-melting growth is introduced that has no segregation of ionic species in the melt at the interface. Such a grown crystal has a peculiar characteristic in that its congruent point is coincident with the stoichiometric composition. The crystal can maintain a constant composition even if it experiences perturbation during growth due to non-equilibrium changes of the growth rate. This may be useful for future optical devices that require extremely small fluctuations of the refractive index, which is not possible by conventional congruent-melting growth, but is possible only by true congruent-melting growth.

Outline:

1. Oxide crystals as ferroelectric and piezoelectric materials

2. Solute partitioning during growth of bulk crystals of oxides

    2.1 'Bulk' crystal growth from the aspect of solute partitioning

    2.2 Equilibrium partitioning coefficient

    2.3 Solidification

        2.3.1 Equilibrium solidification

        2.3.2 Normal freezing I (complete mixing case)

        2.3.3 Normal freezing II (partial mixing case)

        2.3.4 Normal freezing III (no mixing case)

    2.4 Analytical approach for solute partitioning

        2.4.1 Coordination system

        2.4.2 Solute distribution in the diffusion boundary layer for the no-mixing case

    2.5 Constitutional supercooling and formation of cellular structure

    2.6 Compositional variation in a solid during normal freezing process (introduction of Scheil equation)

    2.7 Zone refining and floating zone method

    2.8 Equilibrium partition coefficient, k_0, and its thermodynamic interpretation

    2.9 Supercooling and driving force

3. Congruent-melting composition of oxide materials

    3.1 Congruent-melting composition

    3.2 Congruent-melting composition of a ferroelectric material

    3.3 Congruent-melting composition of a non-ferroelectric material

        3.3.1 Congruent-melting composition obtained via Czochralski method

        3.3.2 Congruent-melting composition obtained via Bridgeman method

    3.4 Evaluation of the homogeneity of a grown crystal

4. True congruent-melting composition

    4.1 Conventional congruent-melting and true congruent-melting

    4.2 Presence of ionic species in an oxide melt

    4.3 Oxygen independent system

    4.4 Extended concept of stoichiometry

        4.4.1 Conventional stoichiometric compositions and the law of multiple proportions

        4.4.2 Extended stoichiometric compositions including impurities and vacancies

4.5 Activities of constituent elements in a crystal

4.5.1 Degrees of freedom in a crystal site

4.5.2 Activity of the constituent elements in an extended stoichiometric crystal

4.5.3 Activities of constituent elements in the melt and solid state for an oxide crystal that is both stoichiometric and congruent

4.6 Oxide crystals having a stoichiometric composition coincident with the congruent point

4.6.1 MgO-doped $LiNbO_3$ and MgO-doped $LiTaO_3$

4.7 Bulk crystal growth of cs-MgO:$LiNbO_3$ and its nonlinear optical characterization

4.8 Thermodynamic requirements for impurity doping

4.9 True congruent-melting composition

1. Oxide crystals as ferroelectric and piezoelectric materials

In this lecture we mainly deal with oxide crystals from the viewpoint of their ferroelectric, non-ferroelectric and piezoelectric characteristics. Our discussion here is also applicable to magnetic materials, except for their applications. Regarding the recent progress of materials science, oxide bulk crystals play a number of important roles as substrates for the field of superconducting, strongly correlated system, oxide semiconducting and spintronics, but they are not dealt with here.

Ferroelectric oxides are often used as optical devices. They can be used for laser emission, second harmonic generation, light modulation, optical spatial modulation, light deflection, optical storage and light detection. A brief summary of the physical properties required for these devices are given and possible crystals for each of devices are listed.

(a) Solid-state laser element. Possible crystals: Nd:$Y_3Al_5O_{12}$ (YAG), Nd:YVO_4, Nd:$YLiF_4$ (YLF).
(b) Non-linear optical element. Used for second harmonic generation, sum-frequency generation or difference-frequency generation. Possible crystals: KH_2PO_4 (KDP), β-BaB_2O_4 (BBO), LiB_3O_5 (LBO), $Li_2B_4O_7$ (LB4), $K_3Li_2Nb_5O_{15}$ (KLN), $KNbO_3$ (KN), $LiNbO_3$ (LN), $LiTaO_3$ (LT).
(c) Electro-optic (EO) element. Applying an electric field to a crystal changes its refractive index, which leads to optical modulation and optical deflection of the transmitted beam in the crystal.
Possible crystals: $NH_4H_2PO_4$ (ADP), KDP, LN, LT, KTN, (Sr, Ba)Nb_2O_6 (SBN), $Bi_{12}SiO_{20}$ (BSO).
(d) Acousto-optic (AO) element. Applying an ultrasonic wave to a crystal leads to optical modulation and optical deflection due to its photo-elastic effect. Possible crystals: HIO_3, $PbMoO_4$, $Pb_5(GeO_4)(VO_4)_2$.
(e) Optical spatial modulation (OSM). An orthorhombic crystal provides an injected optical beam with spatial information that is electrically induced. There are two mechanisms: (1) Using the change of the anisotropy of the intrinsic refractive index caused by the polarization inversion. Possible crystals: $Gd_2(MoO_4)_3$ (GMO), $Bi_4Ti_3O_{12}$. (2) Using the inversion of the sign of the optical rotatory power due to the polarization inversion. Possible crystal: $Pb_5Ge_3O_{14}$ (5P3G).
(f) Optical memory element. The photorefractive effect (damage) of a crystal is caused by strong incident light. It is used in holographic memory. Possible crystals: $LiNbO_3$, Ce:SBN, $BaTiO_3$.
(g) Infrared detection element. Laser beams can be detected by using the pyroelectric effect of a crystal. Possible crystals: SBN, $LiNbO_3$, $PbTiO_3$.
(h) Scintillation element. A scintillation element converts γ- and particle-radiation into visible or UV light. Combined with a photo detector, it is mainly used as a medical device in PET and CT, and is also a key device for homeland security. Possible crystals: Ce:Gd_2SiO_5 (GSO), Pr:$Lu_3Al_5O_{12}$

(LuAG), Pr:Li_2SiO_5 (LSO).

2. Solute partitioning during growth of bulk crystals of oxides

2.1 'Bulk' crystal growth from the aspect of solute partitioning

'Bulk' crystals are ordinarily considered three-dimensional crystals with bulk body, in contrast to the form of a thin film crystal. The typical growth of a bulk crystal is from a melt, and compositional homogeneity is critical for the crystal to show stability in its physical properties, which guarantees reliable functionality when the crystal is used as a device or device substrate. Thus, the uniform distribution of the solute and/or impurities in a crystal is important in bulk crystal growth from both the scientific and technological perspectives. The solute or impurity partitioning during growth is based on the equilibrium partition coefficient, k_0, which represents the ratio of the solute concentration in the solid and that of the liquid at the interface, and is material dependent. Fluctuations in the solute concentration in the liquid at the interface has been thought to be a serious problem, resulting in nonuniformity in the solid. However, it is uncertain whether the solid composition is dominated by the interface stability. This chapter will consider whether the composition of bulk crystals and their uniformity is dominated by the bulk melt when assuming an infinite (or nearly infinite) amount of melt in the bulk melt, and a sufficiently rapid solute transportation via melt flow during growth, which enables sound communication between the interface and the bulk melt. In this sense, bulk growth means growth that it is dominated by the bulk melt rather than the interface melt. It is important to understand how the solute is partitioned from the melt into the crystal for various growth conditions. Here several partitioning models are demonstrated with analytical solutions, dealing first with the ideal case and moving on to more realistic cases.

2.2 Equilibrium partitioning coefficient

During growth from the melt, a local equilibrium holds at the interface, which is why the dopant or impurity is expected to be included in the crystal at the intended composition. The equilibrium relationship for the *j*th species between the solid and the liquid is given by the equilibrium partition coefficient, k_0^j, addressed by Eq. 2-1,

$$k_0^j = \frac{X_S^j}{X_L^j}, \tag{2-1}$$

where X_S^j and X_L^j are the mole fraction of the *j*th species in the solid and liquid, respectively. k_0^j is obtained by comparing the solidus composition with the liquidus composition at a certain temperature in the equilibrium phase diagram. An example of a phase diagram of Li_2O–Nb_2O_5 binary system is shown in Fig. 2.1. The congruent point of $LiNbO_3$ is presented as an intersecting point between the solidus and liquidus lines, and its composition is 48.5 mol% Li_2O. Thus, the amount of the bulk components, Li_2O and Nb_2O_5, are the same in the solid and liquid, and the equilibrium partition coefficients are $k_0^{Li_2O} = 1$ and $k_0^{Nb_2O_5} = 1$. This indicates the composition of the growing crystal remains equivalent to that of the melt during growth, which certainly yields a homogeneous crystal. On the other hand, $k_0^{Li_2O} > 1$ for a melt lower in Li_2O than the congruent, while for $k_0^{Li_2O} < 1$ the melt is richer in Li_2O. The constituent solutes in a melt with a composition that is not congruent (off-congruent) have non-unity k_0, and these solutes are segregated in a limited region of the melt at the interface, often called the diffusion boundary layer. Accordingly, the solid composition is not equal to that of the melt and its deviation becomes marked as the growth progresses. The solute distributions in the solid and melt during growth depend on k_0, the growth rate, the melt flow etc. The solute distributions in both the solid and liquid are classified in Table 2.1 (after Ref. 1) and they are demonstrated in the following for the case of $k_0 < 1$.

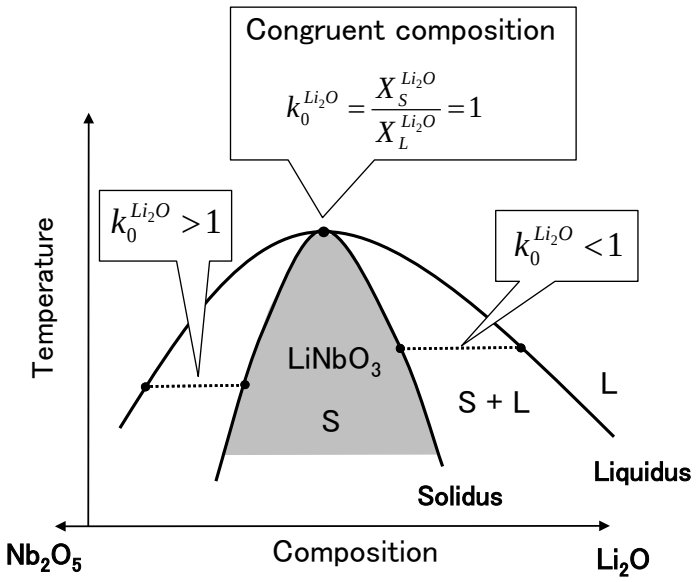


Fig. 2.1 Equilibrium phase diagram of $LiNbO_3$.

Table 2.1 Solute distribution models (after Ref. 1)

Solidification form	Solid	Liquid	Note
Equilibrium solidification	Complete diffusion	Complete diffusion	Infinitely slow cooling/infinitely slow growth
Normal freezing I	No diffusion	Complete mixing	Unidirectional solidification
Normal freezing II	No diffusion	Partial mixing	Czochralski or Bridgman technique
Normal freezing III	No diffusion	No mixing	μ-PD technique

2.3 Solidification

2.3.1 Equilibrium solidification

Equilibrium solidification is a growth process wherein an equilibrium relationship between the solid and liquid is maintained. The diffusion is complete and the solute is homogeneously distributed without gradients in both phases. The progress of the solute distribution in the solid and liquid during growth is illustrated in Fig. 2.2. The composition of the solid that first solidifies from the melt with the initial composition, C_0, is k_0C_0 (1 in Fig. 2.2). As the crystal grows, the solute

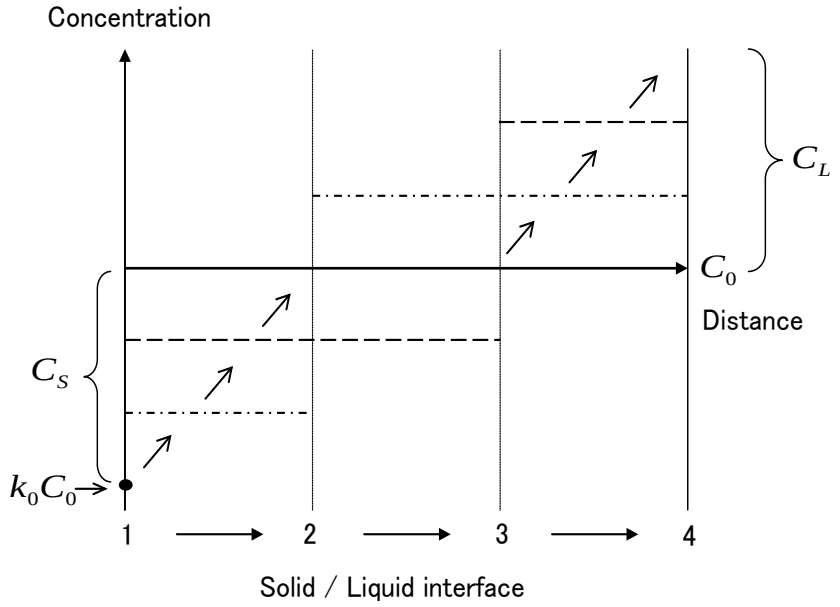


Fig. 2.2 Progress of solute distribution in the solid and liquid during equilibrium solidification.

concentration in the liquid increases due to the segregation, and accordingly the solute concentration in the solid increases as well (1→4 in Fig. 2.2). The final concentration of the solid after complete solidification is equal to C_0 (4 in Fig. 2.2). This equilibrium process requires a tremendous amount of time and such a process occurs only at infinitely slow growth, which does not occur in the real world.

2.3.2 Normal freezing I (complete mixing case)

The diffusion rate of the solute in the solid is smaller than the growth rate by several degrees of magnitude, and thus the solute transport in the solid is often ignored. The solidification process

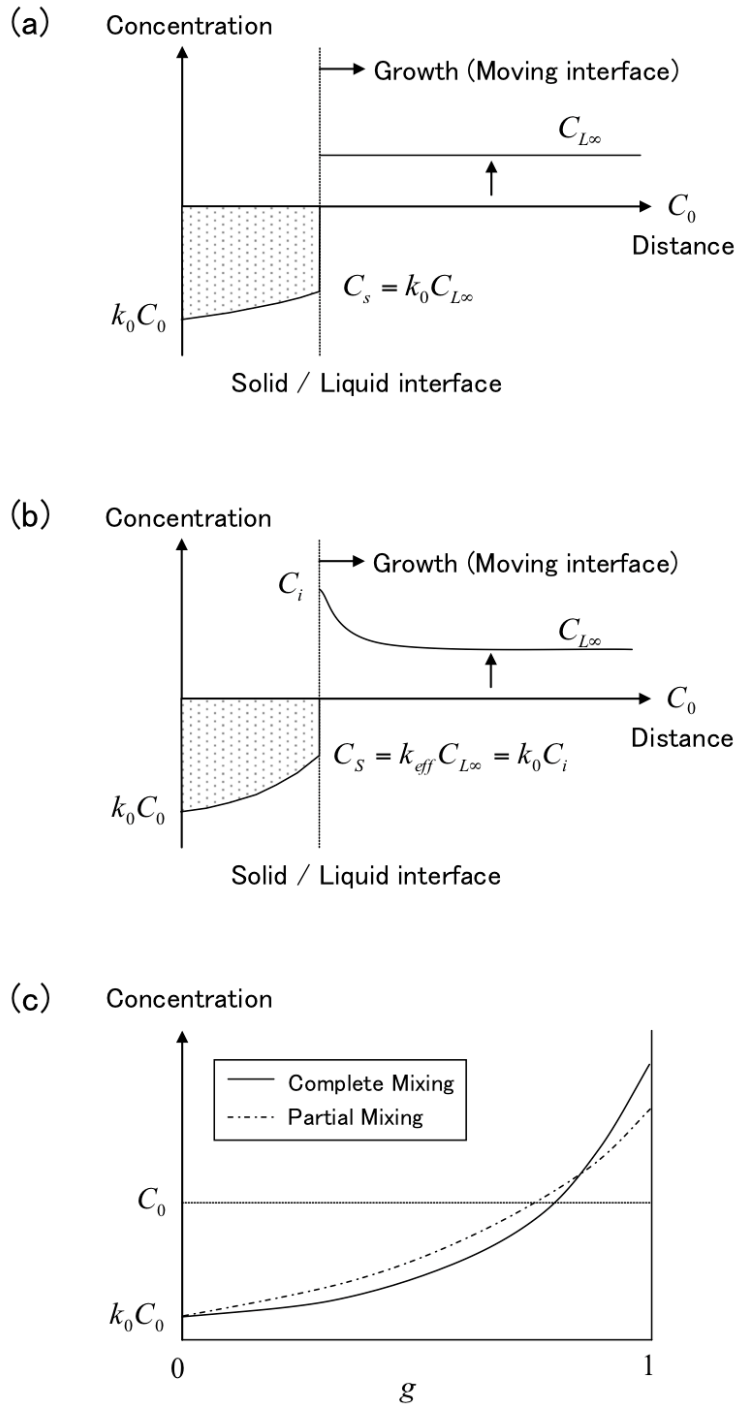


Fig. 2.3 Solute distribution in the solid and liquid for the normal freezing: (a) complete mixing case, (b) partial mixing case and (c) variation of the solute in the solid as a function of the solidified melt fraction, *g*.

assuming no diffusion in the solid and complete mixing in the liquid is often called normal freezing. The progress of solute distribution in the solid and liquid during growth is illustrated in Fig. 2.3. The solute distribution in the solid as a function of the solidified melt fraction, g, is also shown. Fig. 2.3 (a) illustrates the complete mixing case where the solute is distributed homogeneously in the liquid and increases as the crystal grows. Accordingly, the solute in the solid increases when $k_0 < 1$. The solute concentration is illustrated as a function of g in Fig. 2.3 (c), calculated by Scheil's equation, which is well known in the field of the metallurgy and will be later described in detail.

2.3.3 Normal freezing II (partial mixing case)

When the melt mixing is not complete during growth, a solute diffusion boundary layer forms in the liquid at the interface. This solidification process is referred to as normal freezing under partial mixing. Fig. 2.3 (b) illustrates the solute distribution in the solid and liquid during growth under partial mixing. The solute concentration in the bulk melt far from the interface is constant due to mixing by the melt convection, whereas the solute in the melt near the interface accumulates and forms the solute diffusion boundary layer where the solute is transported mainly by diffusion. This model is close to the solute distribution in real crystal growth via the Czochralski or Bridgeman methods, and their solute distributions are often analyzed based on this partial mixing case. The thickness of the diffusion boundary layer depends on the physical properties of the melt, growth conditions etc., where a typical value is about ~10^{-3} cm for good mixing and ~10^{-1} cm for insufficient mixing. The solute distribution in the solid is calculated by considering the mass balance at the interface by taking into account the presence of the diffusion boundary layer. It is then convenient to introduce the effective partition coefficient, k_{eff}, that relates the solute concentration in the solid, C_S, to that in the bulk melt, $C_{L\infty}$. The relationship between k_0 and k_{eff} is given by the BPS equation[2)], which will be described in detail later. C_S is obtained either from the bulk melt composition, $C_{L\infty}$, or the melt composition at the interface, C_i. Thus, Eq. 2-2 gives the relationship between k_0 and k_{eff},

$$C_S = k_0 C_i = k_{eff} C_{L\infty} \tag{2-2}$$

Fig. 2.3 (b) demonstrates that C_i is larger than $C_{L\infty}$ when $k_0 < 1$. Combined with Eq. (2-2) we have $k_{eff} > k_0$. Then, the solute concentration profile in the solid is illustrated by the broken line in Fig. 2.3 (c).

2.3.4 Normal freezing III (no mixing case)

This case deals with the solute distribution presuming no solute diffusion in the solid and no melt convection in the liquid and that the solute is transported in the liquid only by diffusion. Fig. 2.4 (a) illustrates the solute distribution in the solid and liquid during growth under no mixing. Fig. 2.4 (b) illustrates the solute distribution in the whole solid as a function of *g*. The composition of the first solidified portion is given by k_0C_0 and an amount of solute equal to $C_0 - k_0C_0$ is rejected by the

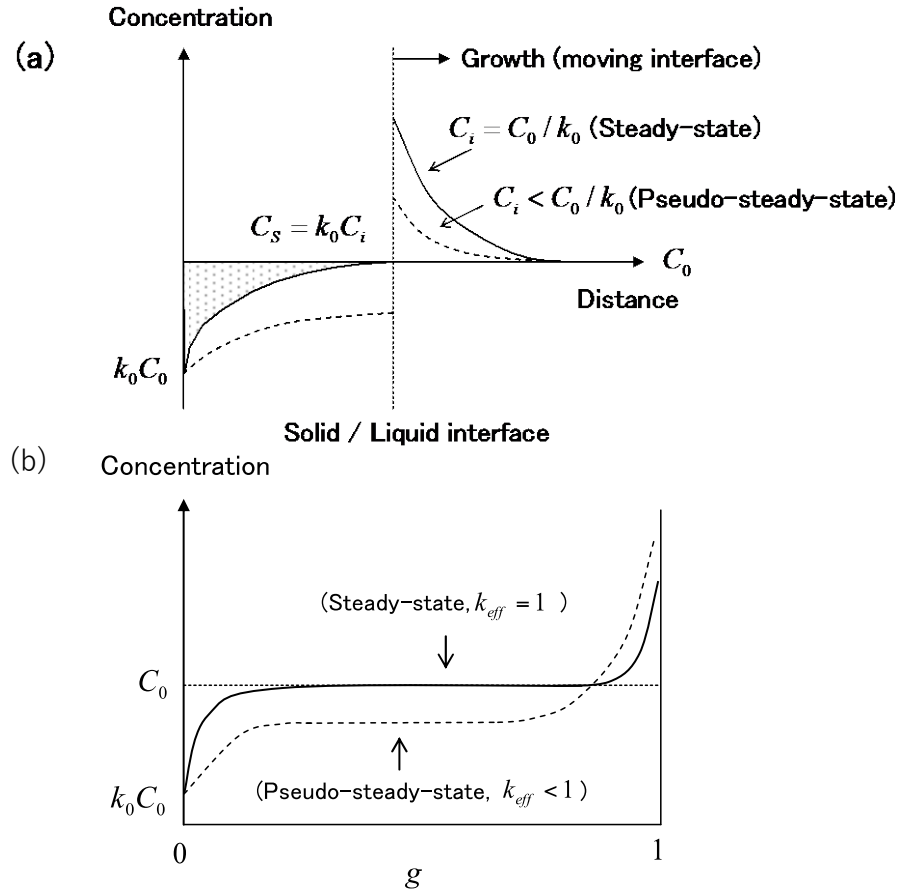


Fig. 2.4 Solute distribution in the solid and liquid under no mixing case: (a) solute distribution in the solid and liquid during growth, (b) variation of the solute in the solid as a function of *g*.

interface and goes back into the melt. The rejected solutes accumulate in the melt at the interface and form the solute diffusion boundary layer. They stay in the diffusion boundary layer and thus, the composition of the bulk melt is always kept at C_0, which differs from the normal freezing with partial mixing case. As the growth proceeds, C_i increases and so C_S also increases. C_i keeps increasing until it reaches C_0/k_0, which is the maximum quantity attainable. At this stage, a solid with composition C_0 crystallizes from the melt with composition C_0 and thus, the mass balance from C_0 to C_0 holds and only the solute boundary moves. This is a steady-state growth and k_{eff} becomes unity. Because the growth proceeds from a finite amount of melt, the melt composition at the end of the growth changes commensurate with the volume of the solute boundary layer, which is illustrated in Fig. 2.4 (b). In practical growth, a pseudo-steady-state is attained for small *g* even if

k_{eff} cannot reach unity. The growth process can be differentiated into (i) initial-transient, (ii) steady-state and (iii) terminal-transient by the mode of the concentration change. Such a no-mixing case is applicable to growth with little melt convection and/or with a very fast growth rate. Practically, the μ-PD method (micro-pulling-down method) or EFG method (edge-defined film-fed growth method) are employed to make the nearly no-mixing case possible. It is important to understand that the solute distribution or solute segregation is greatly affected by the growth conditions that determine the degree of mixing in the liquid and whether or not diffusion in the solid is considered. Thus, it is important to determine which normal freezing case is applicable to the obtained data, and then the solute distribution can be analyzed.

2.4 Analytical approach for solute partitioning

2.4.1 Coordination system

To simplify the analysis of the solute transport and partition during growth, a flat interface is assumed. The transport of the solute or impurities is dominated by diffusion, melt convection and any external forces, such as electric, magnetic or strain–stress. The magnitude of solute transport is called the flux, J (cm^{-2} s^{-1}), and an appropriate coordination system is selected for presenting J as a function of location. Fig. 2.5 shows a coordination system where the origin is tied with the moving interface with velocity V, and thus the interface is always at $x = 0$. Suppose that the location of an impurity (black solid circle) at $t = t_0$ is $x = x_1$. Although the impurity does not in fact move after Δt time passes, the impurity appears to move relative to the interface with $-V$ because the origin is tied to the moving interface. Then, the location of the impurity changes from $x = x_1$ to $x = x_1 - V\Delta t$ and the flux of the impurity in the liquid in this coordination system is $J_L = -VC_L$. The solute or impurity transport or partitioning is analytically considered in this system so that the time-dependent differential equation for the solute transport is readily handled.

2.4.2 Solute distribution in the diffusion boundary layer for the no-mixing case

First, the solute distribution in the diffusion boundary layer for the no-mixing case is discussed. The solute distribution is illustrated in Fig. 2.4 (a). The flux equation of the solute along the growth direction in the diffusion boundary is given by Eq. (2-3).

$$J_L = -D_L \frac{\partial C_L}{\partial x} - VC_L, \tag{2-3}$$

where D_L is the diffusion constant of the solute in the liquid. The solute concentration change with time, t, is given by applying Fick's second law to J_L:

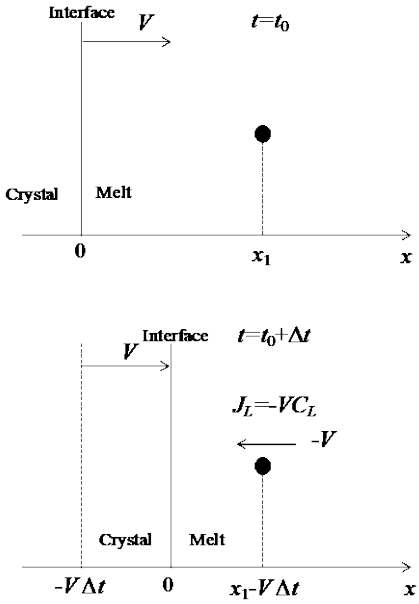


Fig. 2.5 Coordination system with the origin tied to the moving interface.

$$\frac{\partial J_L}{\partial x} = -\frac{\partial C_L}{\partial t}. \tag{2-4}$$

Inserting Eq. (2-3) into Eq. (2-4), we obtain

$$V\frac{\partial C_L}{\partial x} + D_L\frac{\partial^2 C_L}{\partial x^2} = \frac{\partial C_L}{\partial t}. \tag{2-5}$$

When sufficient time passes and the system reaches the steady state, only the solute diffusion boundary appears to move and there is no concentration variation with time in the liquid. Thus, the RHS of Eq. (2-5) becomes 0 and Eq. (2-5) becomes Eq. (2-6),

$$V\frac{\partial C_L}{\partial x} + D_L\frac{\partial^2 C_L}{\partial x^2} = 0. \tag{2-6}$$

The flux equations for the solid and liquid are written as Eqs. (2-7-1) and (2-7-2). Here, the diffusion constant of the solute in the solid, D_S, is smaller than D_L by several orders of magnitude and hence D_S can be neglected.

$$J_S = -D_S\frac{\partial C_S}{\partial x} - VC_S \approx -VC_S, \tag{2-7-1}$$

$$J_L = -D_L\frac{\partial C_L}{\partial x} - VC_L. \tag{2-7-2}$$

These fluxes are equal at the interface, i.e., $J_S = J_L$, which is one of the boundary conditions for solving the differential equation Eq. (2-6),

$$-VC_S = -D_L\frac{\partial C_L}{\partial x} - VC_L \quad \text{at } x=0, \tag{2-8-1}$$

where C_S is obtained from the product of C_L and k_0, and thus Eq. (2-8-1) can be rewritten into Eq. (2-8-2), which is a boundary condition,

$$C_L(1-k_0)V = -D_L \frac{\partial C_L}{\partial x} \quad \text{at } x=0. \tag{2-8-2}$$

Normally V denotes the velocity of the moving interface, however, strictly speaking, it is the relative velocity of a solute to the interface. When an electric field is applied to an ionic species, the overall relative velocity, V, of the ionic species is obtained by combining the velocity of the moving interface with the motion of the ionic species driven by the electric field. The equilibrium partition coefficient should be also converted to one that is influenced by the interface electric field[3].

Eq. (2-8) is the boundary condition at the interface. One more boundary condition is required to solve Eq. (2-6), namely that C_0 is constant in the bulk melt, which is written by Eq. (2-9),

$$C_L = C_0 \qquad \text{at } x = \infty. \tag{2-9}$$

Then, the solution to the differential equation Eq. (2-6) with the boundary conditions Eqs. (2-8) and (2-9) is given by Eq. (2-10),

$$C_{L(x)} = C_0\left(1+\frac{1-k_0}{k_0}\exp\left[-\frac{Vx}{D_L}\right]\right). \tag{2-10}$$

An alternative boundary condition at the interface in place of Eq. (2-8) is the concentration of the saturated solute at the interface. This stems from the fact that the solid composition eventually becomes $C_S = C_0$ when the solute is transported only by diffusion from the interface to the bulk melt for the no-mixing case. The saturated solute concentration at the interface is then

$$C_L = C_0 / k_0 \qquad \text{at } x=0. \tag{2-8-3}$$

Combining Eq. (2-8-3) with Eq. (2-9) gives the same solution, Eq. (2-10).

Constitutional supercooling, which will be discussed later, is a serious problem during growth from a melt. The criterion for its occurrence, given by Tiller et al.[4], presumes an impurity distribution in the melt denoted by Eq. (2-10), which demonstrates that the impurity concentration is saturated at the interface. However, such a saturation happens only in growth via the μ-PD method or EFG technique. In most growths, the solute is not saturated at the interface because the melt flow removes some of the accumulated solutes in the solute boundary layer and moves them to the bulk melt. The effect of the melt flow on the solute distribution was analyzed by Burton, Prim and Slichter[2], and they proposed an equation for the solute distribution in the diffusion boundary

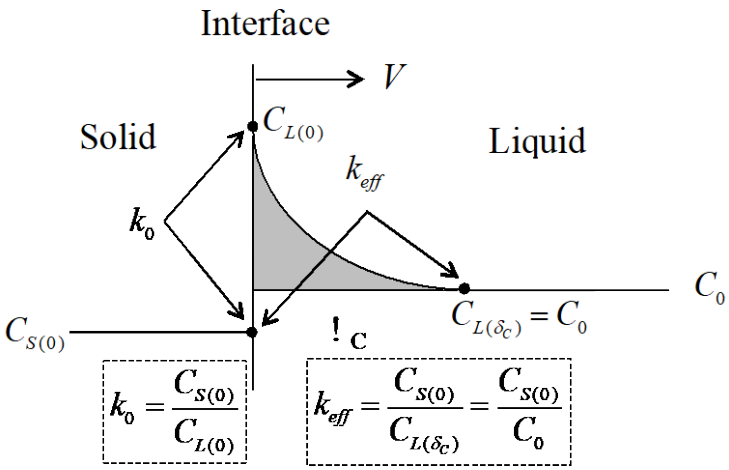


Fig. 2.6 Equilibrium partition coefficient, k_0 and effective partition coefficient, k_{eff}.

layer. They assume that the diffusion layer has a thickness of δ_C (Fig. 2.6) and that beyond the edge of the diffusion layer, the solute is well mixed by the melt convection and distributed at a constant concentration C_0, i.e., the bulk melt concentration. It should be noted that the thickness of the diffusion boundary layer is not confined in Eq. (2-10). The solution to Eq. (2-6) using the boundary condition Eq. (2-11) in place of Eq. (2-9), and combining with Eq. (2-8), is given by Eq. (2-12).

$$C_L = C_0 \quad \text{at } x = \delta_C. \tag{2-11}$$

$$C_{L(x)} = \frac{C_0 \exp\frac{V(\delta_C - x)}{D_L}\left(1 - k_0 + k_0 \exp\frac{Vx}{D_L}\right)}{1 - k_0 + k_0 \exp\frac{V\delta_C}{D_L}}. \tag{2-12}$$

Based on Eq. (2-12), the interface melt concentration $C_{L(0)}$(= C_i) is less than C_0 / k_0. Considering the solid concentration, $C_{S(0)}$, taken either from k_0 or k_{eff}, their relationship is obtained by Eq. (2-13), which is the same as Eq. (2-2),

$$C_{S(0)} = k_0 C_{L(0)} = k_{eff} C_{L(\infty)} = k_{eff} C_0. \tag{2-13, 2-2}$$

A schematic definition of k_0 and k_{eff} is illustrated in Fig. 2.6. Combining Eqs. (2-13) and (2-12) at $x = 0$, the BPS equation that relates k_{eff} with k_0 is obtained:

$$k_{eff} = \frac{k_0}{k_0 + (k_0 - 1)\exp\left[-\frac{V\,\delta_C}{D_L}\right]}. \tag{2-14-1}$$

Eq. (2-14-1) can be converted into Eq. (2-14-2), which is useful for experimentally obtaining k_0,

which is difficult to acquire by itself, by plotting a series of k_{eff} with varying V. This is the BPS plot (Fig. 2.7).

$$\ln\left(\frac{1}{k_{eff}}-1\right)=\ln\left(\frac{1}{k_0}-1\right)-\frac{V\delta_C}{D_L}. \tag{2-14-2}$$

The point at which the extrapolated line intersects the vertical axis gives the value of k_0, while the slope gives the diffusion coefficient of the solute in the liquid, D_L, if δ_C is known.

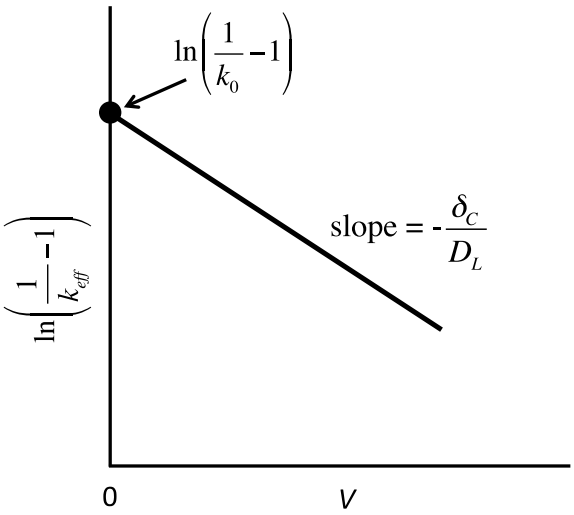


Fig. 2.7 BPS plot to obtain k_0.

Although the BPS equation is quite useful for expressing the solute distribution in practice and also determining the values of k_0 and D_L, the results sometime do not coincide with the experiment. This is partly because the BPS equation presumes that the solute is transported only by diffusion in the boundary layer and by convection outside the boundary layer, and that there is a discrete differentiation between them. However, it is not practically possible for the effect of the melt convection to suddenly disappear at the edge of the diffusion boundary layer (at $x = \delta_C$). Many modified BPS equations have been proposed around the 1970s to adjust for this discontinuity problem[5], but most of them are applicable only to specific cases and no universal model has yet been proposed.

A more serious problem is that the ordinary BPS equation, Eq. (2-14), is obtained by solving the one-dimensional differential equation, Eq. (2-6), so that only the effect of the vertical flow on the solute distribution is considered, leaving out the effect of the lateral flow. However, the effect of the lateral flow on the solute distribution is significant, which is why the diffusion constant of the solute is not correctly evaluated but is overestimated when using the one-dimensional BPS equation. This occurs because some amount of solute in the diffusion boundary layer is removed by the lateral melt flow as well and the solute concentration profile becomes less steep, which incorrectly leads to a larger diffusion constant than the true value. Kodera[6] obtained diffusion constants using a BPS plot for several dopants to Si, such as Ga, Sb and In. The work was very important and useful to those involved in the Si crystal growth industry. He assigned a value of 10^{-4} cm^2s^{-1} to most of the dopants, though it has turned out that they have an order of 10^{-5} cm^2s^{-1} when the horizontal analysis is taken into account[7-9].

It should be noted that Eq. (2-13) designates the meaning of bulk crystal growth. $C_{S(0)}$ at the interface is thought to be determined by partitioning of the solute of concentration, $C_{L(0)}$ at the interface with k_0. However, the bulk composition C_0 also governs $C_{S(0)}$ with k_{eff}. k_{eff} is uniquely determined since it consists of the material constants k_0 and D_L, as well as V and δ_c, which are fixed once the growth conditions are settled. Such a view of the bulk-melt-determined solid concentration presumes an infinite amount of melt and sound communication by melt convection between the bulk melt and the interface melt regarding mass transport. For instance, when a crystal grows from the congruent-melting point, there are zero degrees of freedom, which strongly constrains the composition to be constant. Some solutes may evaporate, e.g., the Li component during the growth of $LiNbO_3$ or $LiTaO_3$. If the mass transport is sufficient for the congruent bulk melt to compensate the deficiency, the melt beneath the interface can keep its composition even through the composition of the surface melt in contact with the gas phase may change. A solid bulk melt is required. Thus, it may not be necessary to add an extra component to the initial melt in anticipation of the evaporation loss. To recharge the source material to the residual, an amount of extra component equivalent to the amount of evaporation loss should be added.

2.5 Constitutional supercooling and formation of cellular structure

The interface is the boundary between the solid and liquid where the mass and heat are transferred from the melt to the crystal. Interface instability is one of the most important problems in crystal growth and there have been quite a few studies devoted to this problem since the historically significant study by Mullins and Sekerka[10]. One of the specific problems in melt growth regarding interface instability is the formation of a cellular structure caused by constitutional supercooling. Here the discussion is made for $k_0 < 1.0$, though it is also true for $k_0 > 1.0$. The growth conditions that are examined for bulk melt growth to avoid a cellular structure formation are the pulling and rotation rates of the crystal, the temperature gradient near the interface and the amount of impurities in the melt, which are associated with the occurrence of constitutional supercooling. Supercooling occurs when the temperature of the melt, T, is lower than the equilibrium melt temperature, T_E. The shaded area in Fig. 2.8 (a) is the supercooling zone. To minimize the occurrence of a cellular structure, the size of the supercooling zone needs to be reduced as much as possible. The temperature gradient of the melt, G_L, should be larger than the slope of the equilibrium melt temperature distribution line, (dT_E/dx), at the interface, to avoid the appearance of the supercooling zone, as illustrated in Fig. 2.8 (a). The T_E distribution line is given by Eq. (2-15), by combining Fig. 2.8 (b) with Eq. (2-10),

$$T_{E(x)} = T_0 - mC_{L(x)} = T_0 - mC_0\left(1 + \frac{1-k_0}{k_0}\exp\left[-\frac{Vx}{D_L}\right]\right). \tag{2-15}$$

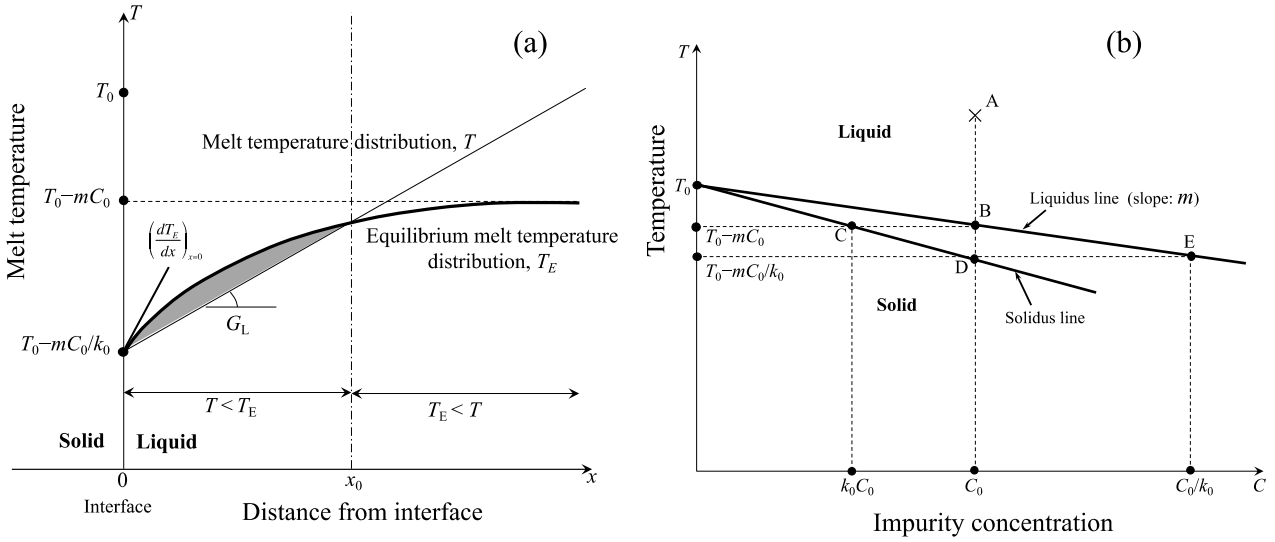


Fig. 2.8 (a) Occurrence of constitutional supercooling due to a difference in temperature between the real melt and the equilibrium melt. (b) Solidification temperature depression due to an impurity.

It is noted again that the criterion for avoiding the occurrence of constitutional supercooling is $G_L \geq (dT_E/dx)$ at the interface, which is represented by Eq. (2-16), proposed by Tiller et al.[4],

$$G_L \geq \left(\frac{dT_E}{dx}\right)_{x=0} \quad \Rightarrow \quad \frac{G_L}{V} \geq \frac{mC_0}{D_L}\frac{(1-k_0)}{k_0}. \tag{2-16}$$

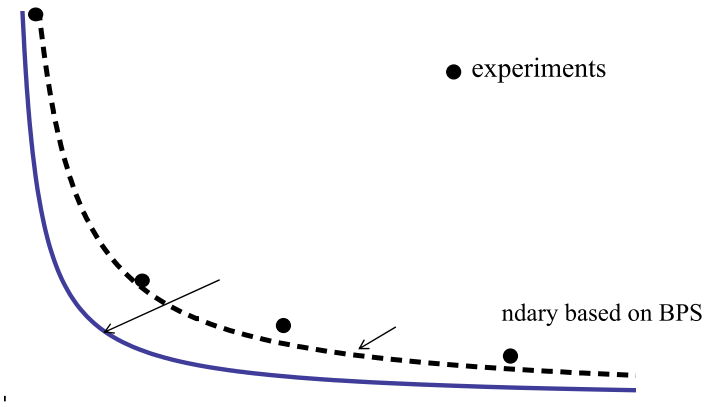


Fig. 2.9 Constitutional supercooling (C.S.C) boundaries for the growth of Ge-doped Si single crystal. The boundary based on BPS is closer to experimental data than that based on Tiller et al.'s criterion[4].

Eq. (2-16) is a very useful criterion since G_L, V and C_0 are all practically available. However, the criterion suggests much harder growth conditions than are practically recognized. This is because Eqs. (2-15) and Eq. (2-16) are deduced using Eq. (2-10), which assumes a saturated concentration of impurities at the interface, which almost never happens in normal Czochralski or Bridgeman growth.

On the other hand, using Eq. (2-12) based on the BPS model for $C_{L(x)}$ in place of Eq. (2-10) leads to a more practical criterion, which takes into account the effect of melt convection resulting in the non-saturated concentration at the interface. This is illustrated in Fig. 2.9. However, it is difficult to obtain a simple expression like Eq. (2-16). Though the threshold of occurrence of constitutional supercooling can be drawn in a V–C_0 diagram at a certain G_L by a straightforward numerical calculation.

It should be noted that different views are sometimes presented for the effect of stirring the melt on constitutional supercooling. One is the case of Czochralski or Bridgeman growth and the other is for the liquid-phase epitaxy (LPE) or traveling liquidus-zone (TLZ) method. In the former, stirring reduces the size of the diffusion layer and decreases the impurity concentration at the interface. Then, the slope of T_E at the interface becomes smaller. As indicated in Fig. 2.8 (a), the real melt temperature, T, is coincident with T_E at the interface for the former case. Thus, when the slope of T_E decreases after stirring, the supercooled region becomes smaller, which is beneficial for avoiding constitutional supercooling. In contrast, the latter case requires a constant melting temperature, T, at the interface to maintain the composition of the growing crystal. In such a case, when the slope of T_E decreases after stirring, T_E increases relative to T at the interface and the supercooled region becomes larger, which is detrimental to avoiding constitutional supercoiling.

2.6 Compositional variation in a solid during normal freezing process (introduction of Scheil equation)

Here, the compositional variation in a solid with the progress of growth is examined for unidirectional growth, which is well explained by the Scheil equation. First, unidirectional crystallization with complete mixing is examined, for which the solute or impurity distribution in the liquid is uniform. Fig. 2.10 illustrates that the melt solidifies with a small amount of dg at a certain solidified melt fraction, g ($0 \le g \le 1$), that is, the amount ratio of solid is g. The solute mass balance at the interface is an important consideration. With the solidification amount dg, the rejected solute at the interface is given by

$$\left(C_{L(g)} - C_{S(g)}\right)dg = C_{L(g)}(1 - k_0)dg, \tag{2-17}$$

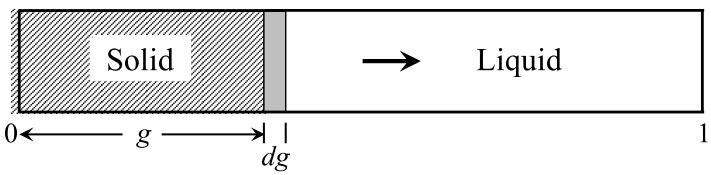


Fig. 2.10 Unidirectional solidification with an amount of *dg* at a melt solidified fraction, *g*.

where $C_{L(g)}$ and $C_{S(g)}$ are the solute concentration in the liquid and in the solid at g, respectively and k_0 is the equilibrium partition coefficient. The rejected solute goes back into the liquid whose amount is

(1 − g) and increases liquid concentration by dC. This solute mass balance is given by Eq. (2-18),

$$C_{L(g)}(1-k_0)dg = (1-g)dC_{L(g)}. \tag{2-18}$$

Employing the initial condition, $C_{L(0)} = C_0$, the solution to the differential equation, Eq. (2-18) is

$$C_{L(g)} / C_0 = (1-g)^{k_0-1},$$

and then the solid concentration as a function of g is (2-19-1)

$$C_{S(g)} = k_0 C_0 (1-g)^{k_0-1}. \tag{2-19-2}$$

Eqs. (2-19-1) and (2-19-2) are the Scheil equation. They are valid for the complete mixing case. However, the diffusion boundary layer is almost always present during growth via the Czochralski or Bridgeman method, so the solute concentration at the interface is not the same as in the bulk melt and it would appear that the Scheil equation is not applicable. In this case a virtual interface is set up at the edge of the diffusion boundary layer, at $x = \delta_C$, in place of the interface at x = 0, as illustrated in Fig. 2.11. The amount of solute in the diffusion boundary layer is small and can be neglected. Then, the solute concentration is constant from the virtual interface to the bulk melt and the Scheil equation is applicable using k_{eff} in place of k_0:

$$C_{S(g)} = k_{eff} C_0 (1-g)^{k_{eff}-1}. \tag{2-20}$$

In fact, applying the Scheil equation to the axial solute distribution in a crystal grown by the Czochralski method gives k_{eff} not k_0. Several growths with different growth rates, V, provide a variety of k_{eff}, which gives k_0 from the BPS plot.

2.7 Zone refining and floating zone method

In this section, the solute distribution in a crystal grown by the floating zone (FZ) method is surveyed. In contrast to growth from an infinite melt via the Czochralski or Bridgeman methods, in the FZ method the source material is constantly supplied to the melt, in the same quantity as the growing crystal. Fig. 2.12 illustrates the zone refining method, where a molten zone with length l moves rightward by the movement of a heater as the melting–solidification process continues. This is a useful way to remove the impurities in the solid and refine the solid. This method was invented by Pfann[11] at Bell Labs and has been applied to the FZ method. In Fig. 2.12 a unidirectional

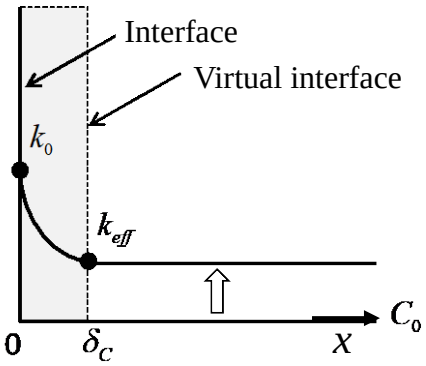


Fig. 2.11 Virtual interface.

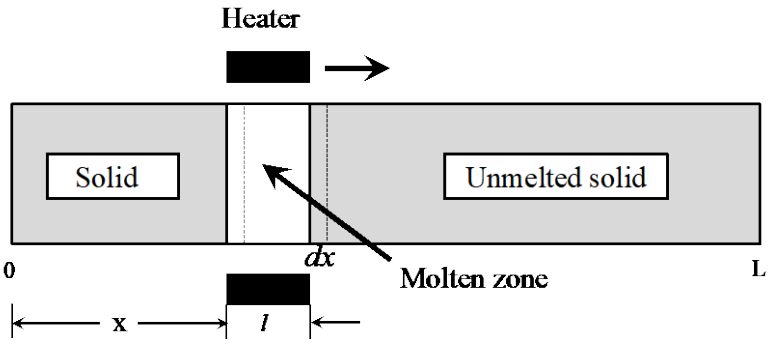


Fig. 2.12 Zone refining system (FZ method).

analysis along the *x*-axis, whose origin is the left end, is executed with an initial solute concentration in the melt of C_0. At the solid length *x*, an amount of source material *dx* melts while the same amount of melt solidifies. The solute concentration in the molten zone, $C_{L(x)}$, increases by an amount *dn*. The mass balance is represented by Eq. (2-21) when the solute concentration in the solid is $C_{S(x)}$,

$$dn(x) = C_0 dx - C_{S(x)} dx. \tag{2-21}$$

Since $C_{L(x)} = n(x)/l = C_{S(x)}/k_0$, Eq. (2-21) can be converted into Eq. (2-22),

$$l/k_0 \; dC_{S(x)} = dx \; (C_0 - C_{S(x)}). \tag{2-22}$$

Employing $C_{S(0)} = k_0 C_0$ as an initial condition, Eq. (2-22) is solved with respect to *x* as

$$C_{s(x)} = C_0\left(1-(1-k_0)\exp\left[-k_0 x/l\right]\right). \tag{2-23}$$

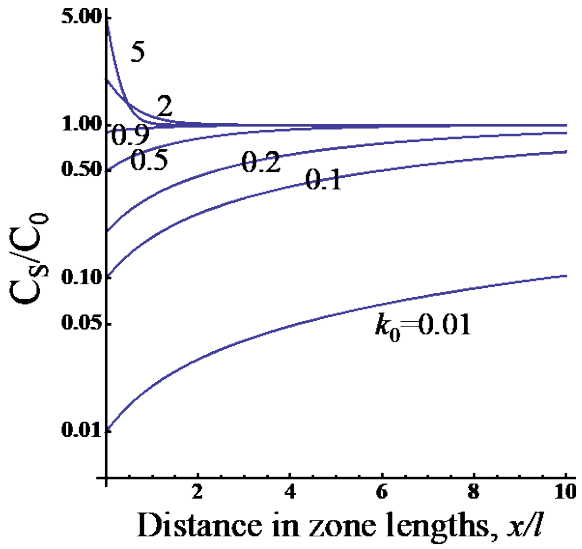


Fig. 2.13 Variation of solute concertation with growth via FZ method.

A calculation by Eq. (2-23) gives the variation of the solute concentration in the solid with the progress of growth via the FZ method in Fig. 2.13. It should be noted that the solute concentration converges to C_0 when $x \to \infty$. When k_0 is close to unity, such as $k_0 = 0.5$ or $k_0 = 2.0$, growth easily becomes steady-state and the solute concentration converges to C_0. However, it does not converge when k_0 is as small as 0.1, even after a crystal grows to a length 10 times the molten zone

length.

It should also be noted that k_0 in Eq. (2-23) can be replaced with k_{eff} for the incomplete mixing case, similar to the use of the Scheil equation, Eq. (2-20). For the case of $k_0 < 1.0$, k_{eff} is larger than k_0 and k_{eff} is closer to unity than k_0, and thus the length required for obtaining a steady state is somewhat shorter than the calculated value.

2.8 Equilibrium partition coefficient, k_0, and its thermodynamic interpretation

The equilibrium partition coefficient, k_0, of a solute or an impurity is derived from equating its chemical potential in the solid with that in the liquid, which is demonstrated by Eq. (2-24). Hereafter X_S and X_L are mole fractions of an impurity in the solid and liquid, respectively.

$$\mu_L = \mu_S. \tag{2-24}$$

The chemical potential of a solute in the solid can be differentiated into a standard-state chemical potential and a mixing term,

$$\mu_S = \mu_S^0 + RT \ln \gamma_S X_S. \tag{2-25}$$

Thurmond and Struthers[12] divided the mixing term into an enthalpy term, ΔH_S, and an entropy term, ΔS_S,

$$RT \ln \gamma_S X_S = \Delta H_S - T\Delta S_S \Rightarrow \Delta H_S = RT \ln \gamma_S,\ \Delta S_S = R \ln X_S. \tag{2-26}$$

The chemical potential of a solute in the liquid phase is handled in the same manner. However, the liquid is first treated here as an ideal solution and the enthalpy in the mixing term in the chemical potential in liquid is assumed to be 0. Combining Eqs. (2-24), (2-25) and (2-26), k_0 is given by Eq. (2-27),

$$\ln k_0 = \ln \frac{X_S}{X_L} = \frac{\Delta G^0 - \Delta H_S}{RT}, \tag{2-27}$$

where $\Delta G^0 = \mu_0^L - \mu_0^S \approx \Delta H_f - T\Delta S_f$ and ΔH_f and ΔS_f are the heat of fusion and entropy of fusion of the impurity at its melting temperature. Then, Eq. (2-27) can be converted into Eq. (2-28),

$$\ln k_0 = \frac{\Delta H_f - \Delta H_s}{RT} - \frac{\Delta S_f}{R}. \quad (2\text{-}28)$$

where ΔH_S is the mixing enthalpy, referred to as the differential heat of solution of the solute in the solid by Thurmond and Struthers[12], and the subscript '*f*' denotes 'fusion'. There are several points to note regarding the derivation of Eq. (2-27). ΔG^0 is the molar free energy change due to the phase transition from solid to liquid of an impurity at a certain temperature, *T*. This temperature, *T*, does not have to be the melting point of the impurity since the phase transition of the material can be thermodynamically considered at any temperature regardless of whether it is solid or liquid or in-between. ΔH_f and ΔS_f relate to the impurity at its melting temperature, T_f. They are used as fusion energies at the melting temperature of the host material, *T*. This may be allowed because the difference in heat capacity between the solid and the liquid is assumed to be very small and can be neglected in the region from T_f to *T*. On the other hand, the dominant energy in Eq. (2-28) is ΔH_S, which is the mixing enthalpy when the impurity enters the host crystal. ΔH_S consists of at least two kinds of energy. One is the elastic energy associated with the strain arising in both the host and impurity atoms due to the difference in their covalent or ionic radius. The other is the bond energy difference between them. This bonding energy difference is often referred to as the quasi-chemical approach for evaluating the mixing enthalpy.

As the melting–solidification process is regarded as a chemical reaction and both the solid and liquid are assumed to behave ideally, $\Delta H_S = 0$ and Eq. (2-28) is now equivalent to the Van't Hoff equation. Thurmond and Struthers started their discussion on k_0 with Eq. (2-28) and added non-ideality to the liquid and also considered the vibrational entropy, σ. They ultimately obtained Eq. (2-29) for k_0,

$$\ln k_0 = \frac{\Delta H_f - \Delta H_s}{RT} + \frac{\sigma - \Delta S_f}{R} + \ln \gamma_L, \quad (2\text{-}29)$$

where γ_L is the activity coefficient of the impurity in the liquid that represents the non-ideal mixing in the liquid. Weiser calculated k_0 for several dopants in Si and Ge by evaluating ΔH_S using reported thermodynamic data[13]. The calculated values of k_0 show good agreement with the experimentally determined values, although the valence of Si and Ge (group 14) is different from that of dopants of group 13 or group 15.

It may be valuable to consider the difference in k_0 between the cases where Ge is doped in Si crystal and Si is doped into Ge crystal (Fig. 2.14 (a)). Here Eq. (2-27) is used for a simple survey and $\Delta H_S > 0$ for both cases. When Ge is doped into Si crystal, ΔG^0 is the molar free energy change between the solid and liquid at the Si melting temperature. At the Si melting temperature, Ge is

present as a liquid phase so that $\Delta G^0 < 0$ (Fig. 2.14 (b)) and thus $k_0 < 1$. On the other hand, for Si doping into Ge crystal, Si is in a solid phase at the melting temperature of Ge and $\Delta G^0 > 0$ (Fig. 2.14 (b)). If ΔG_0 is larger than ΔH_S, $\Delta G^0 - \Delta H_S > 0$ and thus $k_0 > 1$.

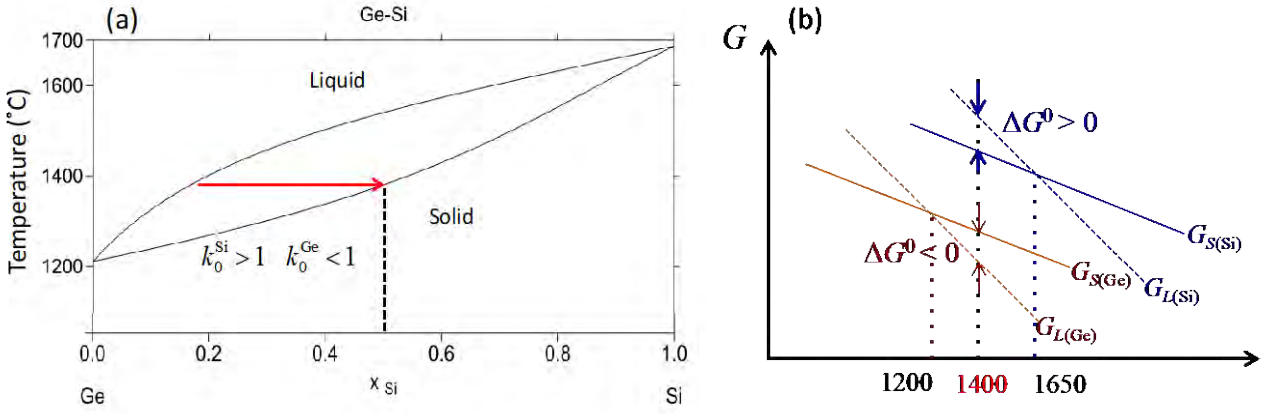


Fig. 2.14 (a) Phase diagram and equilibrium partition coefficients in the system of Ge-Si. (b) Free energy diagrams for liquid and solid phases of Si and Ge as a function of temperature.

2.9 Supercooling and driving force

It should be noted that the driving force for nucleation and growth is handled differently between a single component system such as Si, Ge etc., and multicomponent systems like SiGe, $LiNbO_3$ etc. For the case of a single component, the molar free energies of the solid, G_S, and the liquid, G_L, are functions of temperature (Fig. 2.15), as often given in textbooks. The intersection of these lines indicates the melting point, T_f, and the driving force by supercooling, ΔT, from T_f is given by Eq. (2-30),

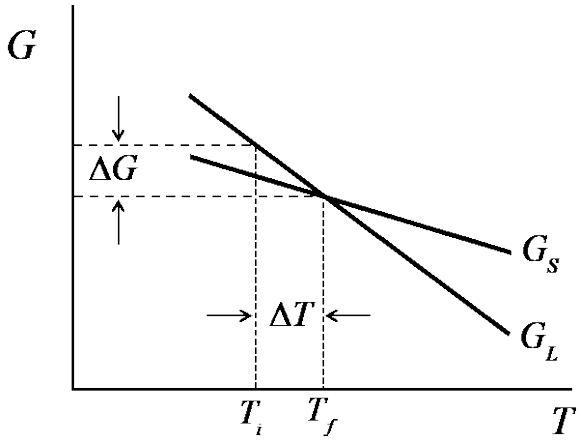


Fig. 2.15 Relationship between supercooling, ΔT and driving force, ΔG.

$$\Delta G \approx \frac{\Delta H_f \Delta T}{T_f}, \qquad (2\text{-}30).$$

where ΔH_f is the heat of fusion at the melting temperature. This approximation also assumes there is little difference in the heat capacity between the solid and liquid in the temperature region, $T_f - \Delta T$ to T_f.

In contrast, the equilibrium relationship between the solid and liquid phase in a multicomponent system is represented by the equality of their chemical potentials, and it is not possible to generate a μ-T (temperature) diagram or μ-C (composition) diagram resembling the G–T diagram since the equilibrium composition is not the same between the solid and the liquid, but varies with

temperature.

Fig. 2.16 (a) presents the equilibrium phase diagram of a continuous solid solution of a binary system, A–B. The equilibrium compositions of liquid and solid at the temperature T_∞ are C_L^* and C_S^*, respectively. At T_∞, the liquid with composition C_∞ has a supercooling degree of ΔT. Fig. 2.16 (b) illustrates that the chemical potential of component A in the liquid, μ_L^A, is obtained at the

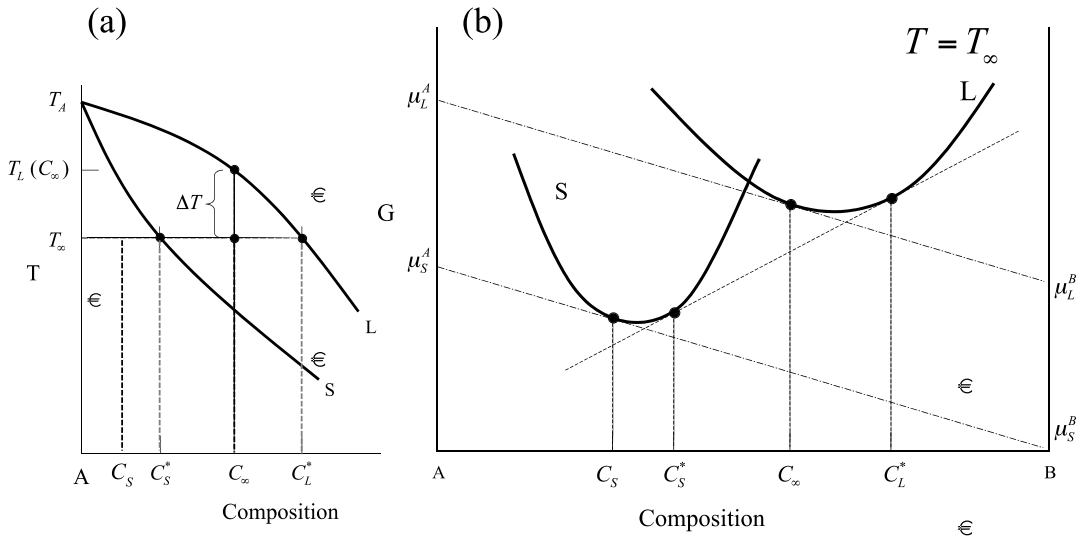


Fig. 2.16 Equilibrium phase diagram of continuous solid solution in a binary system, A–B. (a) Equilibrium compositions of solid and liquid and supercooling degree ΔT at temperature, T_∞. (b) Maximum driving force obtained by drawing parallel tangent lines to the molar free energies of the solid and liquid.

intersection of the vertical axis at pure A composition with the tangent line to the molar free energy of the liquid at C_∞. The chemical potential of the solid μ_S^A that gives the maximum driving force is obtained at the intersection of the vertical axis at pure A component with the tangent line to the molar free energy of the solid, drawn parallel to the tangent line to the molar free energy of the liquid. The maximum driving force is then $\mu_L^A - \mu_S^A$. The contact point indicates the composition, C_S, of the solid that precipitates from the liquid, C_∞.

3. Congruent-melting composition of oxide materials

3.1 Congruent-melting composition

One of the most important requirements for bulk crystal growth is growth with homogeneous composition. This is possible only once the congruent-melting composition has been determined. The congruent-melting composition is the composition that keeps the crystal composition coincident with the melt composition during the whole growth process. The congruent-melting point is the intersection of the solidus line and the liquidus line in the equilibrium phase diagram, which is an invariant point, so that k_0 is unity and the growing crystal is homogeneous in composition. However, this is valid only for steady-state growth. An oxide melt normally contains a variety of ionic species each with their own specific k_0, which is not normally unity, and these ionic species segregate in the solute diffusion boundary layer and charge neutrality does not hold there. This means that the oxygen to metal stoichiometry does not hold and thus oxygen should be regarded as an independent component during the growth of an oxide crystal. Such a segregation occurs even at the conventional congruent-melting point. In this chapter, several methods are introduced to obtain the conventional congruent-melting compositions that are effective only for steady-state growth. On the other hand, true congruent-melting composition is achieved where k_0 for all the ionic species is unity and no segregation occurs, which enables growth with homogeneous composition even for non-steady-state growth under a perturbation. The true congruent-melting composition will be introduced in the next section.

3.2 Congruent-melting composition of a ferroelectric material

The Curie temperature of a ferroelectric material can be used as an accurate indicator of its composition. $LiNbO_3$, for example, is a ferroelectric material. $LiNbO_3$ crystals exhibit 180-degree polarization structures (+*c* domain and −*c* domain). A useful way to determine the congruent-melting point of $LiNbO_3$ is to measure the Curie temperature, which is thought to be sensitive to the Li/Nb ratio of $LiNbO_3$. Carruthers et al.[14] investigated the Curie temperature of sintered $LiNbO_3$ with various Li/Nb ratios and that of crystal grown from these melts. The composition that gives the same Curie temperature between the

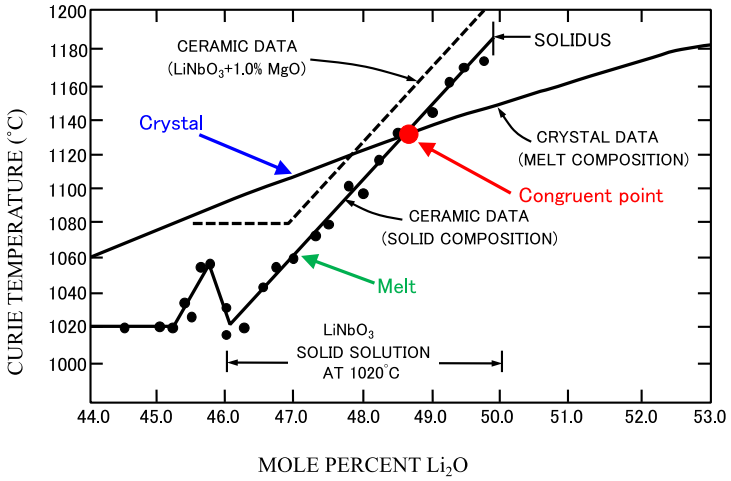


Fig. 3.1 Curie temperatures of solid and source materials of $LiNbO_3$ (after Ref.14).

melt and the crystal is 48.6 mol% Li_2O, which is found as the intersection of the Curie temperature lines of the source material and that of the grown crystal in Fig. 3.1. Bordui et al.[15] reported a slightly different value, 48.38 mol% Li_2O, by employing precise Curie temperature measurements. $LiNbO_3$ is used as a wavelength conversion element that converts a 1064-nm YAG laser to 532-nm green light. Bordui et al. found an interesting phenomenon in that a $LiNbO_3$ crystal with the exact congruent-melting composition exhibits no green emission upon being hit by a YAG laser since the quantity of $+c$ domain is the same as that of $-c$ domain, and hence complete compensation occurs.

3.3 Congruent-melting composition of a non-ferroelectric material

3.3.1 Congruent-melting composition obtained via Czochralski method

Langasite (LGS: $La_3Ga_5SiO_{14}$) is a non-ferroelectric material and with no phase transitions up to its melting point around 1500˚C. Thus, the Curie temperature cannot be used to determine the composition. In such a case, the observation of a compositional variation in a growing crystal from the top to the bottom, as well as in the residual melt, can be used. By growing crystals from melts with various compositions, it has been found that the composition that yields the least variation is the optimal composition. While this would seem to be tedious work, it does provide a practical composition when using pulling equipment. It should be noted that the optimal composition is a pseudo-congruent-melting composition since LGS is an incongruent-melting material and the direct growth of LGS from a melt is possible since the incongruent-melting point of LGS is close to the liquidus line of the primary phase.

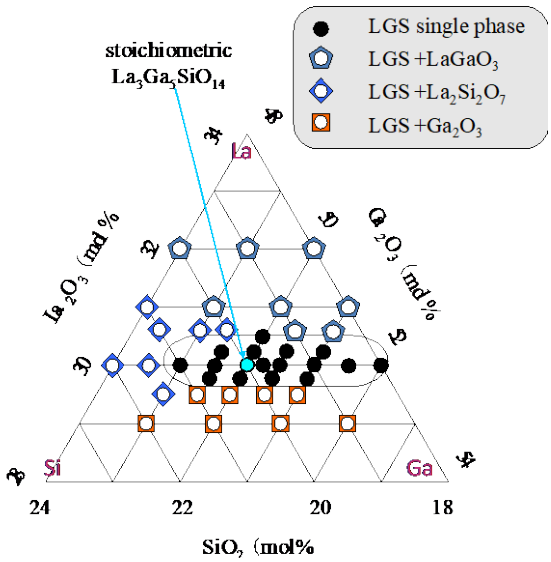


Fig. 3.2 Solid solution range of Langasite (LGS) at 1450˚C (after Ref. 16).

First, the solid solution region of LGS is investigated. About 50 different compositions were selected around stoichiometric LGS to investigate the solid solution range. Mixtures of La_2O_3, Ga_2O_3 and SiO_2 powders with 4N purity of these compositions were sintered at a temperature of 1450ºC. Fig. 3.2 illustrates the compositions chosen for the investigation of the solid solution range and the observed phases after sintering[16]. The solid solution range of LGS at a temperature of 1450ºC forms a narrow area around the stoichiometric composition. The boundary differentiates the single-phase region from the multi-phase region. The variable width of the La_2O_3 component of the solid solution range is much narrower than that of Ga_2O_3 and SiO_2. Coexisting phases are present outside this area. That is, $LaGaO_3$ is found in a La_2O_3 rich area, Ga_2O_3 in a Ga_2O_3 rich area and

$La_2Si_2O_7$ in a SiO_2 rich area. It should be noted that the optimal composition must lie within the solid solution region of LGS bounded by the solid line.

Because the congruent-melting composition exhibits the highest melting temperature, several compositions in the LGS solid solution region of high melting points are chosen, from which single crystals are grown via the Czochralski method with an index of melt solidified of about 80%. The compositions of the initial source materials, various parts of the crystals along the growth axis and the residual melt are analyzed using XFS. Fig. 3.3 illustrates variations in the compositions from the top of the crystal through the middle and the bottom to the residual melt for four different initial melts[16]. If the initial composition is not the exact congruent-melting composition, compositional variation arises from crystallization from an off-congruent melting composition. The compositional variation is large enough to draw a line connecting compositions of the crystal top, initial material, middle, bottom and residual melt in this order. These lines generally show an "S-type" curve[17] since each of the three major melt constituents, La_2O_3, Ga_2O_3 and SiO_2, change their concentration independently with their specific diffusion rates. The initial melt which is close enough to the optimal composition should vary its melt constituents in the same manner during growth, and their ratios become nearly constant, giving a straight connecting line. It is confirmed that a shorter line is straighter than a longer one in Fig. 3.3. The optimal composition should be found on the extrapolated line from the composition of the crystal top and it would be the intersecting point of four lines. As a result, a composition of La_2O_3 = 30.10±0.05 mol%, Ga_2O_3 = 50.60±0.05 mol% and SiO_2 = 19.3±0.05 mol%[16] shows an insignificant shift in the compositions of both the crystal and the residual melt. Thus, this is considered the optimal composition (pseudo-congruent-melting composition) for the growth of LGS via the Czochralski method.

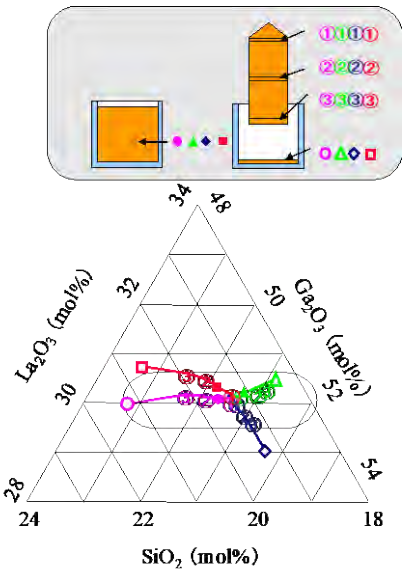


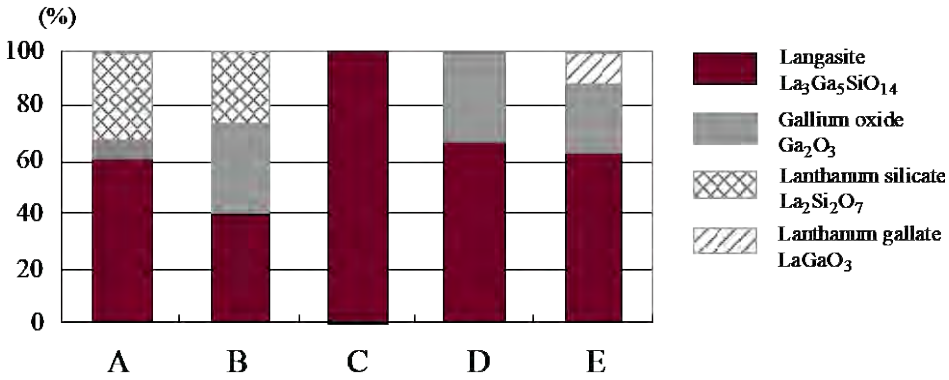
Fig. 3.3 Compositional variation of LGS during growth from four different initial melts (after Ref. 16).

3.3.2 Congruent-melting composition obtained via Bridgeman method

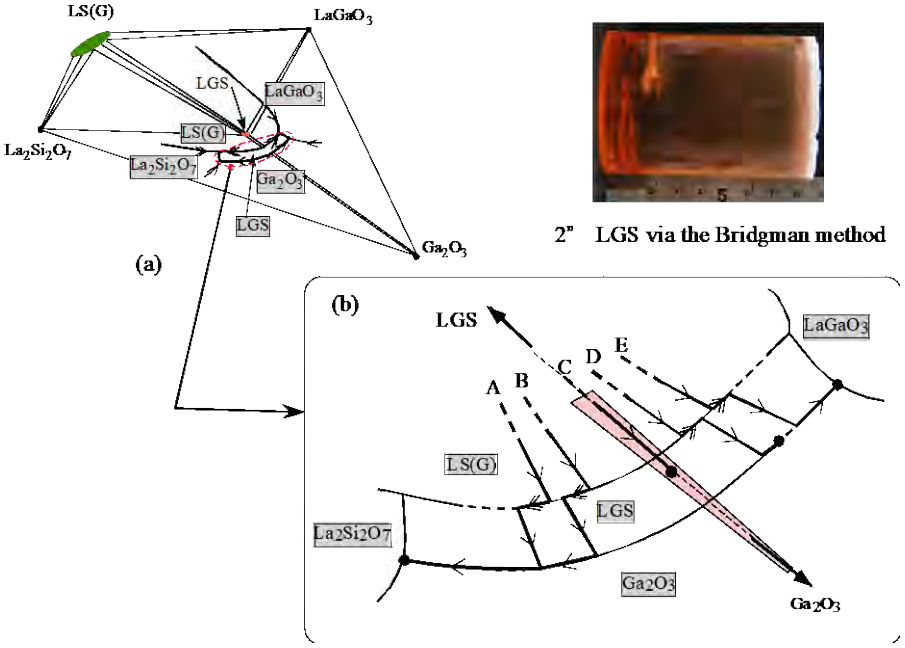
The Bridgman method using accelerated crucible rotation technique (ACRT) equipment provides an efficient way of determining the optimized composition since the growth consumes almost the entire melt, often yielding terminal transient products other than LGS, which reflects the deviation from the optimal source composition. Here five initial melt compositions are chosen: A (30.0L, 50.0G, 20.0S), B (30.0L, 50.1G, 19.9S), C (30.0L, 50.2G, 19.8S), D (30.0L, 50.3G, 19.7S) and E (30.0L, 50.6G, 19.4S), where L, G and S represent La_2O_3, Ga_2O_3 and SiO_2, respectively.

Composition A is stoichiometric. Terminal transient phases other than LGS appear when the composition diverges from the congruent-melting composition. The secondary products formed during the terminal transient are found to be either a mixture of gallium oxide (Ga_2O_3) and lanthanum gallium oxide ($LaGaO_3$) or a mixture of gallium oxide and lanthanum silicate ($La_2Si_2O_7$). A sample was taken from the non-transparent polycrystalline materials that precipitate as residual phases on the LGS crystal edge surface. Optical microscopic observations were made, combined with semi-quantitative analysis using X-ray diffraction. The composition of the source material and the resultant terminal transient phase are summarized in Table 3.1[18]. Growth from melts with compositions A and B yielded $La_2Si_2O_7$ and Ga_2O_3, composition D yielded Ga_2O_3 and E yielded Ga_2O_3 and $LaGaO_3$. Composition C did not yield any terminal secondary phases and is thought to

Table 3.1 Precipitates from the residual melt, after Ref. 18.



be optimal. This result reflects the position of the initial melt relative to the tie line connecting the LGS solid solution with Ga_2O_3 in the La_2O_3–Ga_2O_3–SiO_2 system assuming equilibrium and some fractional crystallization, and excluding deposited phases from the system. The terminal transient process is illustrated in Fig. 3.4. It should be noted that for all melts, $La_2Si_2O_7$ bearing a certain amount of Ga ($La_{14}Ga_xSi_{9-x}O_{39-x/2}$) (denoted as LS(G) in Fig. 3.4), which is the primary phase precipitating from the melt, is partially isolated from the melt or completely reacts with the melt to form LGS and



2" LGS via the Bridgman method

Fig. 3.4 Crystallization paths from LGS melts with different compositions[18].

extinguishes. Thus, the melts no longer stays on the reaction curve but moves on the liquidus surface of LGS down to the cotectic line with Ga_2O_3. Then, A and B trace the entire univariant line to the invariant point, where $La_2Si_2O_7$ joins. E moves to the opposite invariant point, at which $LaGaO_3$ joins, whereas D used up its melt somewhere on the univariant line before the invariant point. When the optimal melt composition (i.e., C) is selected, the path crosses the surface of the LGS primary phase field tracing the tie line of the LGS solid solution with Ga_2O_3 and stops before reaching the univariant line. To conclude, the optimum composition is C, that is, La_2O_3 = 30.0 mol%, Ga_2O_3 = 50.2 mol% and SiO_2 = 19.8 mol%[18], which is a little different from that obtained by the CZ method.

3.4 Evaluation of the homogeneity of a grown crystal

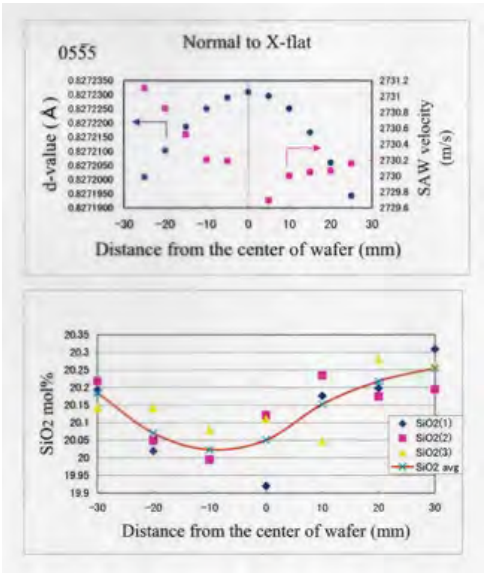


Fig. 3.5 Variation of SAW velocity and d-spacing of 05-55 in a wafer associated with SiO_2 composition (after Ref. 19).

As it is not possible to use the Curie temperature as a precise indicator of the composition for non-ferroelectric material, other physical properties are used to survey compositional variations in the crystal. Accurate measurements of lattice constants or the surface acoustic wave (SAW) velocity with high precision are sensitive to compositional variations in an LGS wafer. Fig. 3.5 illustrates variations of the SAW velocity and d-spacing of 05-55 in a wafer associated with SiO_2 composition[19]. The figure illustrates that they reflect well the compositional variation in the wafer.

More precise evaluation of homogeneity was performed by fabricating about 600 transversal SAW filters of 190-MHz central frequency on a wafer with 200 pairs of aluminum interdigital electrodes. Then, the distribution of SAW velocities was measured and the standard deviation was calculated. Fig. 3.6 illustrates the SAW velocity distribution on a wafer sliced from the top (Fig. 3.6(a)) and from the bottom (Fig. 3.6(b)) of the grown crystal[20]. The average SAW velocity is 2375.7 and 2375.9 m/s and the standard deviation is 108 and 118 ppm for the top wafer and bottom wafer, respectively, which is as good as the best SAW filter designed to date.

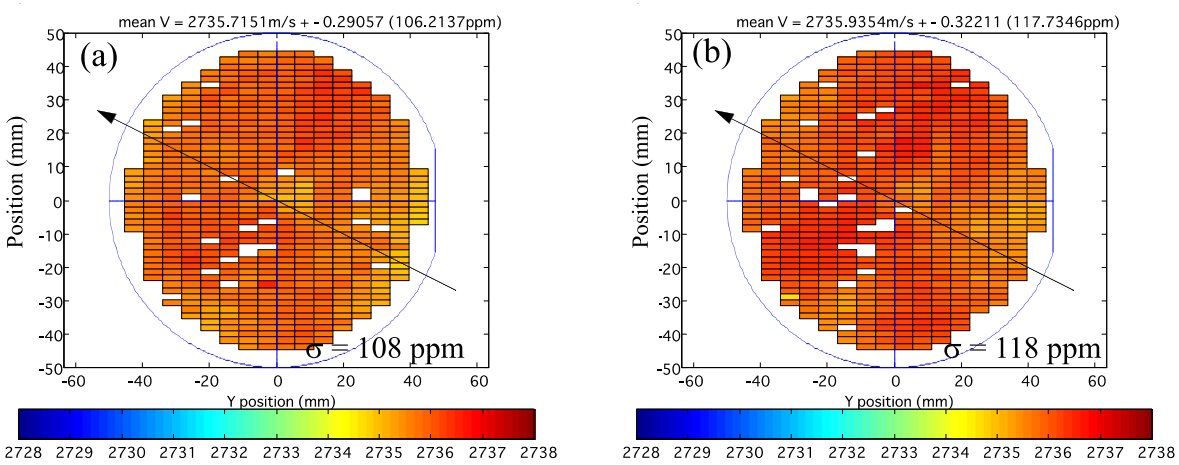


Fig. 3.6 Surface acoustic wave velocity distribution on 4-inch LGS wafers[20].

4. True congruent-melting composition

4.1 Conventional congruent-melting and true congruent-melting

As we learnt in the previous chapter, the initial bulk melt composition has to be congruent to grow a homogeneous crystal. The conventional congruent-melting point is located at the intersection of the solidus and liquidus lines in a pseudo-component system that assumes a stoichiometric ratio of metal to oxygen. 48.6 mol% Li_2O is the conventional congruent-melting composition for growing $LiNbO_3$. Congruence guarantees a homogeneous crystal during steady-state growth. However, this is not valid once the growth is out of equilibrium, which often arises from interface instability due to temperature fluctuations, melt flow turbulences or other disturbing factors. This is related to the fact that most oxide melts contain a variety of ionic species and their partition coefficients are not necessarily unity even for the congruent melt. Thus, an expected or unexpected disturbance during growth changes the growth rate and the ionic species can then become partitioned into crystals in a non-equilibrium manner. A compositional change then occurs. It should also be noted that oxygen should be dealt with as an independent component in the presence of ionic species in the melt and that the stoichiometric ratio of metal to oxygen does not hold in the diffusion boundary layer.

However, if k_0 for all ionic species is unity, every species is partitioned into the crystal without any compositional changes even if the growth rate suddenly changes in a non-equilibrium way since $k_{eff} = 1$ when $k_0 = 1$ regardless of the value of the growth rate, V (Eq. 2-14-1). Such a melt is true congruent-melting, which makes $k_0 = 1$ for all ionic species. This is obtained only when the congruent composition coincides with the 'stoichiometric' composition, in an extended concept in that stoichiometry is redefined such that *a material in which the activities of all the constituent elements can be unity is stoichiometric*[21,22]. In this section, we learn that oxide melts contain variable ionic species and a true congruent-melting composition guarantees crystal growth with a completely homogeneous composition even when the growth rate changes in a non-equilibrium way. The true congruent-melting composition is obtained only by the coincidence of being congruent and stoichiometric, in the extended concept.

4.2 Presence of ionic species in an oxide melt

Most oxide melts are electrically conductive[23-25] and therefore are considered to contain ionic constituent species in addition to neutral species, as illustrated in Fig. 4.1. The existence of ionic species in the oxide melt is easily demonstrated when one considers that molten salts are used as electrolyte solutions in electrochemical studies. The populations of these ionic species are dependent on the composition and temperature of the oxide melt. We have seen that pseudo-oxide

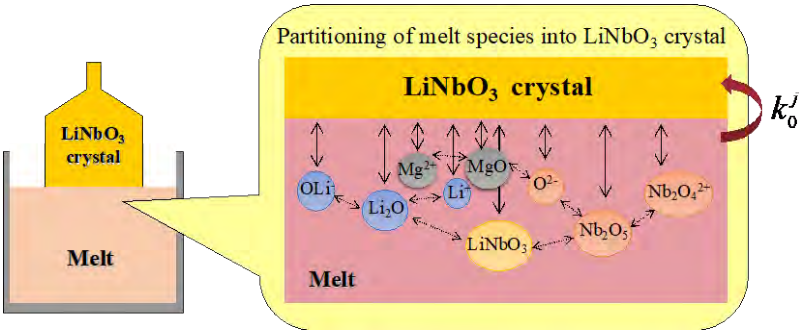


Fig. 4.1 Neutral and ionic chemical species possibly present in an $LiNbO_3$ melt. Each species is partitioned into the solid based on its own unique k_0 (after Ref. 26).

phase diagrams, in which stoichiometry between the metal and oxygen holds, only apply to oxide components in the material and do not provide any information concerning ionic species. It is generally believed that the partition coefficients are unity at the congruent composition since the solidus line coincides with the liquidus line at that point, meaning that the solid and liquid compositions are the same. However, this is true only for the oxide components appearing in the pseudo-phase diagram; it is not true considering that oxygen ions represent one of the ionic species present in the melt. As an example, the pseudo-binary diagram of Li_2O–Nb_2O_5 is not sufficient to explain the partitioning of ionic species in the $LiNbO_3$ melt. In this case, oxygen should be treated as an independent component, and the ternary Li–Nb–O diagram should be used instead of the pseudo-binary Li_2O–Nb_2O_5 diagram. Each of the constituent species, including ionic species, has its own equilibrium partition coefficient and it can be shown that k_0 of any element in the line-compound melt is unity, meaning that there is no segregation of ionic species near the interface during growth. This arises from the fact that the line compound is both stoichiometric and congruent. In contrast, even a congruent crystal that is not consistent with the stoichiometric point grows in such a manner that the ionic solutes have non-unity partition coefficients. Each ionic species, j, is partitioned based on its own equilibrium partitioning coefficient, k_0^j, and is accumulated or depleted at the growth interface due to solute segregation depending on the value of k_0^j, the diffusivity, D^j, and the growth rate, which results in differential segregation of ions of opposing valences, generating a net charge in the liquid boundary layer as well as a charge of the opposite sign in the crystal, thus producing a crystallization electromotive force (c-EMF)[27,22,28-30], $\Delta\phi_{EMF}$. This process is illustrated in Fig. 4.2. The $\Delta\phi$ term may be represented by Eq. 4-1[22,28,31],

$$\Delta\phi = \alpha_L(T_1 - T_i) + \alpha_S(T_i - T_2) + \Delta\phi_{EMF}. \quad (4\text{-}1)$$

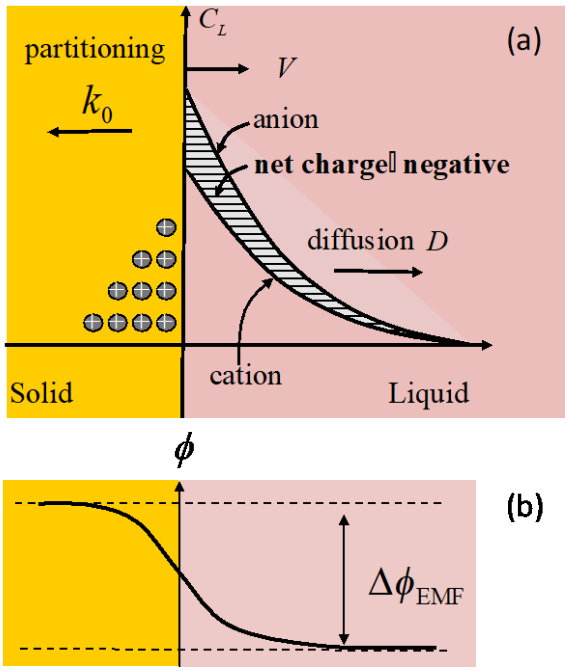


Fig. 4.2 (a) Schematic illustration of the segregation of ionic species in the liquid boundary layer. (b) Generation of crystallization electromotive force (c-EMF) during the growth of the $LiNbO_3$ crystal. (after Ref. 22.)

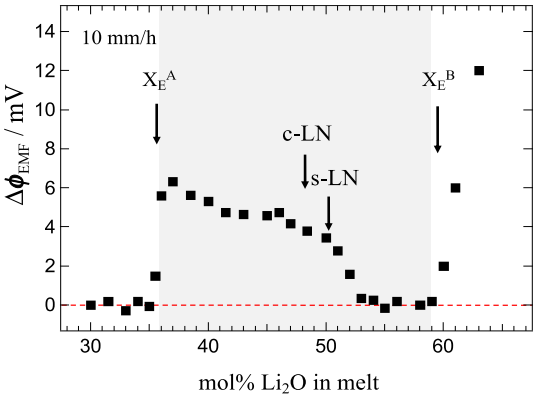


Fig. 4.3 c-EMF ($\Delta\phi_{EMF}$) values obtained during the growth of $LiNbO_3$ via a μ-PD measurement system plotted as a function of the Li_2O composition of the melt in the pseudo-binary Li_2O–Nb_2O_5 system at a growth rate of 10 mm/h. (after Ref. 29.) X_E^A and X_E^B are the eutectic points.

Here α_L and α_S are the Seebeck coefficients of the liquid and solid phases. The value of α_L is 0.27 mV/K, while α_S is −0.85 mV/K[22] for congruent-melting of $LiNbO_3$ (c-LN), both of which are nearly constant for all compositions. T_i is the temperature at the solid/liquid interface and $\Delta\phi_{EMF}$ is the c-EMF that is obtained from the hysteresis generated in the solid region during the solidification and melting process. The value of this term is normally in the range of several mV and can be measured with reasonable accuracy.

The generation of a c-EMF during the growth of $LiNbO_3$ from melts with various compositions demonstrates that the EMF has a non-zero value at the conventional stoichiometric point and even at the congruent point (Fig. 4.3)[29]. This EMF arises during growth as the result of the segregation of ionic solutes in the liquid boundary layer in a congruent melt in which the equilibrium partition coefficients are not unity, even though the coefficients of the net $\overline{Li_2O}$ and $\overline{Nb_2O_5}$ are unity, based on an interpretation of the conventional pseudo-phase diagram. In contrast, the c-EMF observed during the growth of $Li_2B_4O_7$ is zero at the congruent point but is non-zero during growth from the off-stoichiometric melt[29]. A zero-EMF exhibited by the stoichiometric-congruent composition will always occur during growth at various growth rates even though different growth rates will normally result for varying degrees of segregation of the ionic species at the interface if their partition coefficients are not unity. Therefore, no segregation of ionic species occurs at the stoichiometric-congruent point, meaning that every ionic species in the $Li_2B_4O_7$ melt has an equilibrium partition coefficient of unity[21]. On this basis, we may conclude that $\Delta\phi_{EMF}$ will be zero during growth when the crystal is simultaneously stoichiometric and congruent. In other words, the equilibrium partition coefficient

of any given constituent melt species will be unity when the crystal is stoichiometric and congruent. The converse is equally true; the crystal is stoichiometric and congruent if no segregation of any constituent species occurs ($\Delta\phi_{EMF} = 0$), or if, in other words, the equilibrium partition coefficient of any constituent species is unity.

4.3 Oxygen independent system

Solute partitioning behavior is generally investigated using an equilibrium phase diagram. However, most oxide phase diagrams are pseudo-phase diagrams where the stoichiometry of oxygen to metal always holds and the oxygen is not considered an independent component. For this reason, conventional oxide phase diagrams do not take into account the ionization of neutral species that actually occurs in oxide melts. Ionic species, which represent one of the major sources of point defects, are present in a melt[23] and are partitioned into the solid during crystallization[27,32-34]. Point defects, therefore, should be discussed together with crystallization, and the oxygen in the melt should be considered as an independent component in the phase diagram. The oxygen ions and metal ionic species behave independently, which has been experimentally demonstrated by observations of c-EMF generated by the segregation of ionic species at the solid–liquid interface, even in the case of c-$LiNbO_3$. Therefore, although the congruent $LiNbO_3$ point in the pseudo-binary diagram of Li_2O–Nb_2O_5 is invariant, it is not invariant in the ternary diagram of Li–Nb–O, and thus a variety of population ratios among the ionic species are allowed.

Since there are three components instead of two, one more degree of freedom is available in the melt, which enables the population ratio to vary among the ionic species even for a congruent melting composition. This population ratio will in turn depend on the growth conditions, such as growth velocity and temperature gradient. Although it initially seems strange that the ratio between ionic species changes with growth velocity while the congruent melt composition does not, this occurs because the congruent composition is defined based on the $Li_2ONb_2O_5$ pseudo-binary associated with $LiNbO_3$ and this is invariant regardless of the growth velocity. In contrast, the presence of ionic species requires the oxygen ion to be considered as an independent component, which adds one more degree of freedom to the ternary system and enables population change among the ionic species with growth velocity.

However, when these ionic species are partitioned into the solid, this one degree of freedom in the melt phase must be consumed in such a way that the partition coefficient for each ionic species is determined. Otherwise, the solid composition cannot be fixed in the pseudo-phase diagram. It should be noted that a physical phenomenon with a higher degree of freedom does not surpass one governed by a lower degree of freedom. Thus, the same number of constraints as that for the melt species is required to solve the partition coefficient for each species. The constraint that consumes

the one degree of freedom must then be determined. Because the composition of the solid phase is determined in the pseudo-phase diagram, the metal-to-oxygen stoichiometry in the solid must be known, which is the last constraint to achieve zero degrees of freedom.

4.4 Extended concept of stoichiometry

It would be beneficial, from both the scientific and technological perspectives, if stoichiometric compounds could be obtained over a wider compositional range. In the present chapter, by considering the essential concept of stoichiometry, we redefine 'stoichiometry' in such a way that a material in which the activities of all the constituent elements can be unity is stoichiometric[21,22]. The constituent elements in this definition include not only the primary constituent atoms but also the impurities and vacancies which replace these primary atoms. This revised concpet of stoichiometry expands the current definition of stoichiometric composition from a single point to a range described by a line.

One of the thermodynamic principles used for this purpose is 'activity,' a term that is associated with the standard-state chemical potential. The chemical potential of component *j*, termed μ^j, in a non-stoichiometric material is given by Eq. 4-2,

$$\mu^j = \mu_0^j + RT \ln a^j, \tag{4-2}$$

where μ_0^j is the standard-state chemical potential and a^j is the activity for *j* that indicates mixing with another solute. It should be noted that μ^j has a definite value while a^j is variable. Once μ_0^j is chosen, a^j is determined accordingly using the relationship

$$\ln a^j = \frac{\mu^j - \mu_0^j}{RT}. \tag{4-3}$$

The value of μ_0^j is essentially chosen based on one's preference although in most cases it represents the chemical potential of a pure substance at one atmosphere and 298.15 K. This is because the formation energy of pure substances is typically readily available, which is helpful for many thermodynamic calculations associated with practical applications.

The essence of 'stoichiometry' may be elucidated by comparing it with 'nonstoichiometry' from a thermodynamic perspective. A nonstoichiometric composition is created from a stoichiometric composition by the addition of impurities, which implies that the activity of the chemical species or element *j* is not unity, meaning that

$$a^j \neq 1. \tag{4-4}$$

In contrast the chemical potential of the stoichiometric composition has no mixing term, and thus

$$\mu^j = \mu_0^j, \tag{4-5}$$

which is equivalent to saying that the activity of species *j* is unity, or

$$a^j = 1. \tag{4-6}$$

It should be noted here that $a^j = 1$ also implies that the mole fraction is unity ($x^j = 1$), which means that the standard-state composition about *j* reflects the bulk composition of the material itself regardless of the quantity of *j* in the material. It should be noted again that the standard-state composition does not have to be purely *j*.

In order for the material to be stoichiometric, Eq. 4-6 must be valid for any component, *j*. That is, the activity of all constituent components in the stoichiometric material is unity. Conversely, if the activity of all constituent components is unity, the material can be considered to be 'stoichiometric'[21,22]. Below we will demonstrate the validity of the extended stoichiometry concept by comparing it with the conventional understanding of stoichiometry.

4.4.1 Conventional stoichiometric compositions and the law of multiple proportions

The composition of a conventional stoichiometric crystal is represented by a small integer that gives the ratio of constituent elements, representing the so-called law of multiple proportions[35]. Here we use two kinds of stoichiometric crystals to demonstrate different types of compositions: $Li_2B_4O_7$, which is a line-compound, and s-LN, which represents a solid solution with a wide compositional range.

$Li_2B_4O_7$ has a very limited solid solution range and so it can be considered to be a line compound (Fig. 4.4(a)). This solid solution range is determined by investigating the limits of the compositional shift from the stoichiometric composition[36], using XRD or DTA to determine whether or not the secondary phase is present in the residual melt after normal freezing under vigorous mixing of the melt. The solid solution was found to vary around the stoichiometric composition by a margin of ±0.3 mol% Li_2O[36]. However, the observation of zero c-EMF, which will be explained later, reveals that $Li_2B_4O_7$ is a line compound with an almost zero solid solution range. We should note here that there may still be some limited compositional variation in this material due to the presence of thermally activated vacancies. However, this small amount of

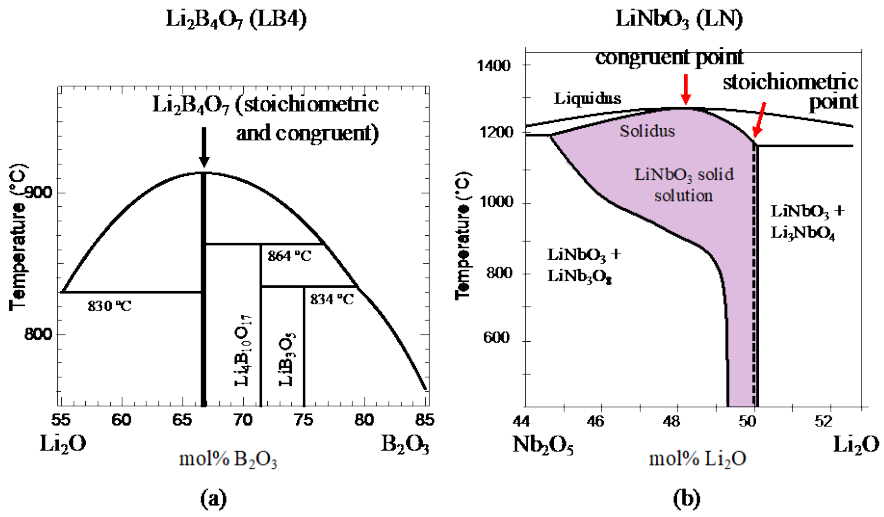


Fig. 4.4 Equilibrium phase diagrams of pseudo-binary systems. (a) Li_2O–B_2O_3 around $Li_2B_4O_7$ (after Ref. 36) and (b) Li_2O–Nb_2O_5 around $LiNbO_3$ (after Ref. 37). Note that the stoichiometric composition and the congruent point coincide in $Li_2B_4O_7$ but not in $LiNbO_3$.

compositional variation is neglected in the present discussion. The most important feature of this line-compound stoichiometric crystal is that it is coincident with the congruent point.

The phase diagram of the pseudo-binary system of Li_2O–Nb_2O_5 is presented[37] in Fig. 4.4 (b), in which conventional stoichiometric $LiNbO_3$ (s-LN) and conventional congruent-melting $LiNbO_3$ (c-LN) are indicated. In contrast to the stoichiometric line-compound $Li_2B_4O_7$, s-LN is separate from c-LN and is located at the far end of Li_2O composition in the $LiNbO_3$ solid solution. Although both $Li_2B_4O_7$ and s-LN are stoichiometric, $Li_2B_4O_7$ is coincident with the congruent point while s-LN is not, which reflects the different equilibrium partitioning of their constituent elements.

4.4.2 Extended stoichiometric compositions including impurities and vacancies

It should be noted again that a material in which the activity of each constituent element can be unity represents a stoichiometric material, by assigning each μ^j to μ_0^j. In other words, if we are allowed to assign μ^j to μ_0^j for any component *j*, such that $\mu_0^j = \mu^j$, the material can be considered stoichiometric. Stoichiometric materials by this definition may include impurities and vacancies and so may be more stable in terms of entropy than conventional stoichiometric substances. This raises an important objection, if an assignment such as this is possible in any material, then every material could potentially be considered stoichiometric, which is certainly not the case. The question is how we can know whether or not μ^j can be assigned to μ_0^j. To make such an assignment, we require a degree of freedom, since μ_0^j can have any value if one degree of freedom is present in the crystal site where the element *j* is present.

4.5 Activities of constituent elements in a crystal

4.5.1 Degrees of freedom in a crystal site

It is important to determine the element occupancy of each crystal site. These elements include

constituent cations, impurity ions, anti-site defects and vacancies. The possible element occupancy at a site is examined by considering the associated degrees of freedom, and the degrees of freedom of a crystal site can be explained by employing $LiNbO_3$ as an example. Here the vacancy is a defect that forms in order to compensate for the charge imbalance due to the difference between the valences of the impurity ions and that of the host ion present in a site. The oxygen sites are assumed to be saturated with oxygen.

The degrees of freedom are obtained by subtracting the number of constraints from the number of parameters[26]. In this case, the number of parameters at a site is the number of elements, based on the following three constraints[26].

(1) Mass conservation holds at each site. That is, the sum of the mole fractions of each constituent element, j (where j = 1 to C), is unity, as in Eq. 4-7.

$$X^1 + X^2 + \cdots + X^C = 1. \tag{4-7}$$

(2) If an element is present at multiple sites in a crystal, its chemical potentials at those sites are equal, thus

$$\mu^j_{\text{site 1}} = \mu^j_{\text{site 2}} = \cdots \ . \tag{4-8}$$

(3) The vacancy population is calculated in such a way that overall charge neutrality is maintained in the bulk crystal.

These three constraints are necessary conditions, although additional restrictions may be added to decrease the degree of freedom at a given site.

4.5.2 Activity of the constituent elements in an extended stoichiometric crystal

Based on our newly defined ‘stoichiometry,’ referring to a material in which the activity of all the constituent elements can be unity, the stoichiometric composition is extended from a single point to a linear series. Introducing impurities and vacancies is necessary in this case, which is not allowed in a conventional stoichiometric compound. As an example, MgO-doped $LiNbO_3$ in the pseudo-ternary system of Li_2O–Nb_2O_5–MgO is considered and shown in Fig. 4.5. The isoconcentration line at 50 mol% Nb_2O_5 is termed line *A* and the MgO-doped $LiNbO_3$ on line *A* is termed 50Nb-LN. The conventional stoichiometric compound $LiNbO_3$ (s-LN), the conventional congruent-melting $LiNbO_3$ (c-LN) on the pseudo-binary line of Li_2O-Nb_2O_5 and c-LN doped with 5

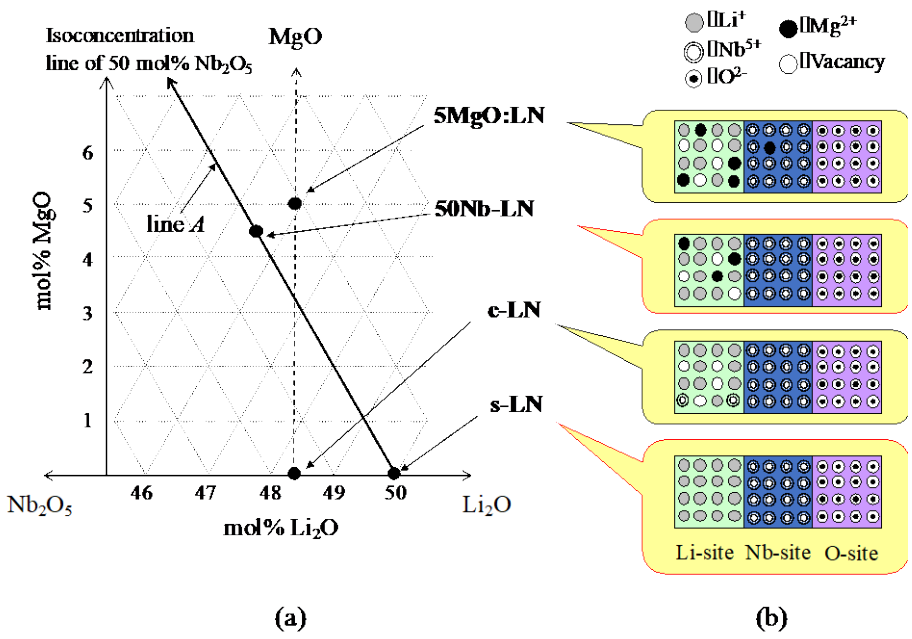


Fig. 4.5 (a) Composition diagram of various $LiNbO_3$ compositions in the pseudo-ternary system of Li_2O–Nb_2O_5–MgO. The isoconcentration line of 50 mol% Nb_2O_5 line is termed line *A* and represents an O to Nb ratio of exactly 3.0. (b) Crystal site structures for each of the various $LiNbO_3$ crystals. (after Ref. 26.)

mol% MgO (5MgO:LN) are also indicated.

The site structures of these crystals are presented in Fig. 4.5 (b). All the sites of conventional s-LN are filled with Li, Nb and O, without any excess atoms or deficiencies. Thus, it is readily understood that the activity of each site as well as the activity of the element at each site is unity. The site structures of c-LN and 50Nb-LN are similar in that both have fully occupied Nb and O sites and their Li sites are occupied with vacancies or cations other than Li, such as antisite Nb in c-LN and Mg in 50Nb-LN. Although the elements present in the Li sites are much the same, c-LN is not stoichiometric while 50Nb-LN is[22], a phenomenon which will be discussed subsequently. In 5MgO:LN, the Mg is located at both Li and Nb sites but no antisite Nb is present at the Li sites.

Whether a crystal is stoichiometric or not is determined by examining the possibility of each of the constituent elements in the crystal having an activity of unity. This question directly applies to the activities of the elements at Li sites in c-LN and 50Nb-LN.

Firstly, the degrees of freedom associated with the Li sites in c-LN can be examined. These sites have three parameters: Li, Nb and vacancies. The constraints on the Li site include conservation of mass, the exchange of equilibrium Nb between Li and Nb sites and the vacancy population required for charge compensation. Since the overall number of constraints is three, zero degrees of freedom are available for assigning μ^j to μ_0^j. Therefore, the activity of the elements at the Li sites cannot be unity and it has been proven on a thermodynamic basis that c-LN is not stoichiometric.

The degrees of freedom of the Li sites in 50Nb-LN can subsequently be examined using a similar process. Here the number of parameters is three while the number of constraints is two, since we are only concerned with conservation of mass and the vacancy population. As a consequence, the Li sites have one degree of freedom, which allows unrestricted choice of μ_0. It should be noted that, in the 50Nb-LN crystal, each element, including Mg and vacancies, belongs

only to one specific site. However, $\mu_0^j = \mu^j$ must be valid for all three of the elements which may be present at the Li sites (j = Li, Mg and vacancy) in order for the activities of these elements to be unity. Thus, it appears that three degrees of freedom are required and hence the challenge is to use one degree of freedom to assign μ to μ_0 for each of the three elements. To address this, one can consider the chemical potentials and activities of the crystal sites as well as the constituent elements in 50Nb-LN[26]. The Nb site is fully occupied by Nb and Nb does not enter into any other site, which is also the case for the O sites and O atoms. Hence the activities of the Nb and O sites is unity, and simultaneously the activity of Nb at the Nb sites and O at the O sites is unity. Since the Li sites preserve the overall charge neutrality with regard to the Nb and O sites, the Li site must also be neutral and the activity of the Li site must be unity. Thus

$$a_{\text{Li site}} = a_{\text{Nb site}} = a_{\text{O site}} = 1, \tag{4-9}$$

and

$$a_{\text{Nb site}}^{\text{Nb}} = a_{\text{O site}}^{\text{O}} = 1. \tag{4-10}$$

The chemical potential of the Li sites in 50Nb-LN is calculated by summing that of each element, as follows,

$$\mu^{\text{Li site}} = p\mu^{\text{Li}} + q\mu^{\text{Mg}} + r\mu^{\text{Va}}, \tag{4-11}$$

where Va denotes a vacancy and p, q and r are real numbers. By differentiating the chemical potential into the standard-state chemical potential and the mixing term, Eq. (4-11) may be rewritten as shown below.

$$\mu_0^{\text{Li site}} + RT\ln a_{\text{Li site}} = p(\mu_0^{\text{Li}} + \ln a_{\text{Li site}}^{\text{Li}}) + q(\mu_0^{\text{Mg}} + \ln a_{\text{Li site}}^{\text{Mg}}) + r(\mu_0^{\text{Va}} + \ln a_{\text{Li site}}^{\text{Va}}). \tag{4-12}$$

One degree of freedom allows the standard-state chemical relationship between the Li site and its constituent elements, which is shown in Eq. (4-13).

$$\mu_0^{\text{Li site}} = p\mu_0^{\text{Li}} + q\mu_0^{\text{Mg}} + r\mu_0^{\text{Va}}. \tag{4-13}$$

Subsequently, the activity relationship between the Li site and its constituent elements is obtained

by combining with Eq. (4-11) to give Eq. (4-14).

$$a_{\text{Li site}} = \left(a^{\text{Li}}_{\text{Li site}}\right)^{p}\left(a^{\text{Mg}}_{\text{Li site}}\right)^{q}\left(a^{\text{Va}}_{\text{Li site}}\right)^{r} = 1. \tag{4-14}$$

Eq. (4-14) is valid for any combination of *p*, *q* and *r* that lies on the iso-concentration line of 50 mol% Nb_2O_5 (line *A* in Fig. 4.5). Therefore, the activity of all three elements is unity[22], expressed as

$$a^{\text{Li}}_{\text{Li site}} = a^{\text{Mg}}_{\text{Li site}} = a^{\text{Va}}_{\text{Li site}} = 1. \tag{4-15}$$

Combining this equation with Eq. (4-10), the activity of all elements in 50Nb-LN can be shown to equal unity and so it is proven on a thermodynamic basis that 50Nb-LN, a Mg-doped LN on the iso-concentration line of 50 mol% Nb_2O_5, is stoichiometric.

4.5.3 Activities of constituent elements in the melt and solid state for an oxide crystal that is both stoichiometric and congruent

It is demonstrated on an empirical basis that a crystal presents zero c-EMF when it is simultaneously stoichiometric and congruent. The thermodynamic requirement for the coincidence of stoichiometry and congruency in the solid can be analyzed only when the activities of the constituent species in both the melt and the solid are unity, which also implies that k_0 is unity, that is, $k_0 = 1$, for any constituent species. The values obtained for activity, a^j (j = O, Nb, Li, Mg and vacancy) and equilibrium partition coefficient, k_0^j, are summarized in Table 4.1 for the growth of

Table 4.1 Activity, equilibrium partition coefficient, c-EMF associated with the growth of s-LN (stoichiometric), c-LN (congruent) and cs-MgO:LN (stoichiometric and congruent) crystals[26].

	Activity, a^j (j = Li, Nb, Mg, O, vacancy)	Equilibrium partition coefficient, k_0^j (j = Li, Nb, Mg, O, vacancy)	c-EMF, $\Delta\phi_{EMF}$
s-LN	$a_S^j = 1,\ a_L^j \neq 1$	$k_0^j \neq 1$	$\Delta\phi_{EMF} \neq 0$
c-LN	$a_S^j \neq 1,\ a_L^j \neq 1$	$k_0^j \neq 1$*	$\Delta\phi_{EMF} \neq 0$
cs-MgO:LN	$a_S^j = 1,\ a_L^j = 1$	$k_0^j = 1$	$\Delta\phi_{EMF} = 0$

*k_0^j is unity for the bulk components $\overline{Li_2O}$ and $\overline{Nb_2O_5}$ in the pseudo-binary system of $Li_2O - Nb_2O_5$.

s-LN (stoichiometric), c-LN (congruent), and cs-MgO:LN (stoichiometric and congruent) crystals.

In the next section, lithium niobite (LN) crystal and lithium tantalate (LT) crystal that are stoichiometric and congruent simultaneously are demonstrated.

4.6 Oxide crystals having a stoichiometric composition coincident with the congruent point

Note again when a compound has a stoichiometric structure at the congruent point, the equilibrium partitioning coefficients of all chemical species become unity and segregation does not occur. With regard to conventional c-LN or c-LT, the segregation of ionic species is observed during growth because these materials are not stoichiometric. A unique relationship between the unity of the partitioning coefficients of ionic species and the coincidence of stoichiometry and congruency is quite beneficial in terms of developing LN or LT crystals, which are superior to conventional LN and LT. The congruent compositions are found on the stoichiometric line of 50 mol% Nb_2O_5 (line *A* in Fig. 4.5) in the Li_2O–Nb_2O_5–MgO system and on the stoichiometric line of 50 mol% Ta_2O_5 in the Li_2O–Ta_2O_5–MgO system. Using Kröger–Vink notation, these materials may be written as $\left(Li_{Li}^{\times}\right)_{0.906}\left(Mg_{Li}^{\bullet}\right)_{0.047}\left(V_{Li}^{'}\right)_{0.047}\left(Nb_{Nb}^{\times}\right)\left(O_{O}^{\times}\right)_3$, termed cs-MgO:LN[22] and $\left(Li_{Li}^{\times}\right)_{0.816}\left(Mg_{Li}^{\bullet}\right)_{0.092}\left(V_{Li}^{'}\right)_{0.092}\left(Ta_{Ta}^{\times}\right)\left(O_{O}^{\times}\right)_3$, termed cs-MgO:LT[38], respectively. These compounds show no segregation of ionic species during growth, which demonstrates that k_0 are unity for all constituent chemical species in the melt, and thus cs-MgO:LN and cs-MgO:LT are congruent and stoichiometric simultaneously. Therefore, the conventional congruent materials $LiNbO_3$ and $LiTaO_3$, both of which are nonstoichiometric, are converted to congruent, stoichiometric crystals based on our extended concept of stoichiometry. Both materials, however, contain impurities and vacancies that are not allowed under the conventional definition of stoichiometry.

4.6.1 MgO-doped $LiNbO_3$ and MgO-doped $LiTaO_3$

In a conventional stoichiometric crystal, each element occupies only its own unique site in the crystal lattice and no defects arising from non-stoichiometry are allowed. Thus, a conventional stoichiometric crystal usually shows good optical properties. However, the stoichiometric composition often does not coincide with the congruent composition. In such a case, growth of the stoichiometric compound is difficult due to the compositional deviation caused by the segregation of constituent species in the melt during growth. $LiNbO_3$ (LN) is one such nonstoichiometric compound. As shown in Fig. 4.4 (b)[37], the stoichiometric composition (s-LN; Li_2O = 50 mol%) does not coincide with the congruent composition (c-LN; Li_2O = 48.38 mol%[39]). Although it can easily be grown from a melt, the optical properties of c-LN, such as conversion efficiency of secondary harmonic generation (SHG), photoconductivity and transparency in the short-wavelength region, are inferior to those of s-LN[40], and so impurity doping of c-LN is performed to improve its

optical properties. MgO is considered to be an effective impurity for LN, because MgO-doped s-LN exhibits high photoconductivity and has a high threshold for optical damage[40]. However, these crystals are no longer congruent nor are they stoichiometric. In the following section, the growth and characterization of cs-MgO:LN, a crystal that is simultaneously congruent and stoichiometric, is described.

cs-MgO:LN is obtained as follows. First, the distribution of the melting temperatures of sintered materials with various compositions is determined for the Li_2O–Nb_2O_5–MgO ternary system via DTA. The composition possessing the highest melting temperature is the congruent point of the MgO-doped LN. Next, this composition is confirmed to be the exact ternary congruent composition by confirming that no c-EMF is generated. Such a composition is found on the 50 mol% Nb_2O_5 stoichiometric line, where the congruent point meets the stoichiometric composition. The compound cs-MgO:LN (Li_2O:Nb_2O_5:MgO = 45.3:50:4.7) is such a compound as shown in Fig. 4.6 and is expected to be easily grown and to exhibit superior optical properties compared to those of conventional c-LN, MgO-doped c-LN and s-LN.

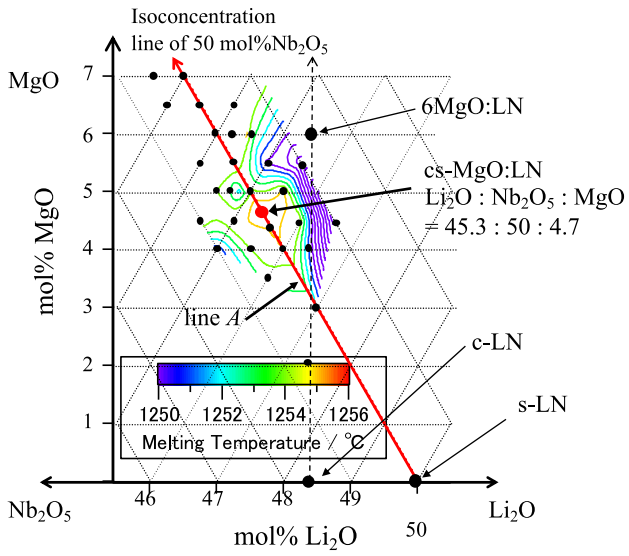


Fig. 4.6 Distribution of the melting temperatures of sintered compounds with various compositions around the isoconcentration line of 50mol% Nb_2O_5 (line *A*) in the pseudo-ternary system of Li_2O–Nb_2O_5–MgO (after Ref. 41).

Regarding lithium tantalate (LT), like LN, its congruent composition differs from its stoichiometric composition in the binary Li_2O–Ta_2O_5 system. By employing the extended concept of stoichiometry, cs-MgO:LT (Li_2O:Ta_2O_5:MgO = 40.8:50.0:9.2) is obtained[38] by the same way as cs-MgO:LN. As in the case of cs-MgO:LN, this material is stoichiometric and congruent. Because of this coincidence, cs-MgO:LT does not exhibit any c-EMF and does not show any segregation during growth, even for ionic species. A bulk crystal is grown from a cs-MgO:LT melt via the Czochralski method and shows excellent compositional homogeneity, as demonstrated by the constant distribution of the Curie temperature throughout the crystal.

4.7 Bulk crystal growth of cs-MgO:$LiNbO_3$ and its nonlinear optical characterization

A bulk single crystal of cs-MgO:LN was grown at a rate of 2 mm/h via the Czochralski method along the *Z*-axis in an air atmosphere. The resulting crystal was colorless and inclusion-free, as

shown in Fig. 4.7[41]. The crystal was about 22 mm in diameter and 40 mm long and its solidified melt fraction, *g*, was 0.25 after the completion of growth. c-LN, 5MgO:LN and s-LN were also grown by the Czochralski technique, although the s-LN was produced using the double-crucible method[42]. The superiority of cs-MgO:LN in both compositional homogeneity and nonlinear optical properties is demonstrated by comparing its second-harmonic-generation (SHG) properties with those of c-LN, s-LN and 5MgO:LN.

Since the phase-matching wavelength is sensitive to the crystal composition[43], its distribution in a crystal test plate is used to evaluate the compositional homogeneity of the crystal. Fig. 4.8 shows the in-plane distribution of the non-critical phase-matching wavelength on the *X*-plane for a 4 mm × 4 mm area on each crystal. The vertical direction in each test plate in Fig. 4.8 is parallel to the growth axis while the horizontal direction is parallel to the radial direction. The phase-matching wavelength of the cs-MgO:LN is almost constant over the whole test plate (Δg = 0.024–0.025)[41]. The variation of the phase-matching wavelength is less than 0.06 nm, which corresponds to the variation of the refractive index, $\Delta n < 10^{-5}$/cm. This homogeneity is surprisingly sustained during growth even with possible variations in the growth rate due to a changing crystal diameter, which is attributed to the complete unity of the partition coefficients of all the melt species. To confirm the compositional homogeneity over the entire length of the cs-MgO:LN crystal, its Curie temperature was measured via differential scanning calorimetry (DSC) at the top and the base. The Curie temperature difference between the top and bottom portions was 0.8°C, which corresponds to a 0.02



Fig. 4.7 A cs-MgO:LN single bulk crystal grown by the Czochralski method[41].

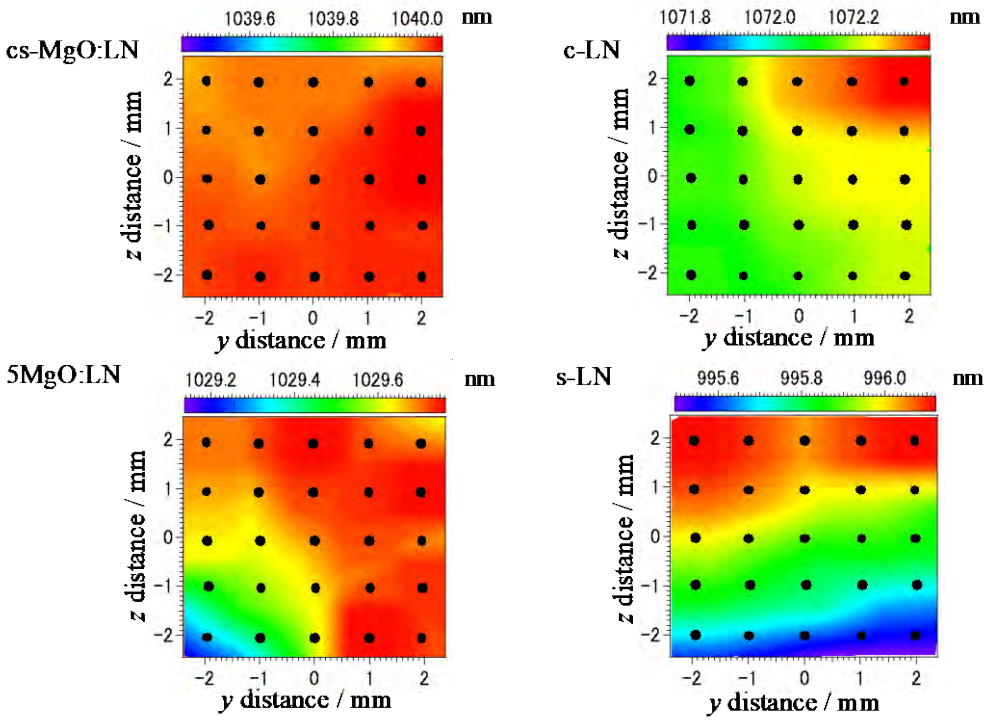


Fig. 4.8 In-plane distribution (4 mm × 4 mm) of the non-critical phase-matching wavelength[41]. The solid circles indicate the measured points.

mol% Li_2O variation[44] when neglecting the effect of MgO incorporation. This variation is sufficiently small to demonstrate the congruency of cs-MgO:LN. The c-LN crystal is slightly less homogeneous than the cs-MgO:LN, but is much more homogeneous than both the s-LN and 5MgO:LN materials. These results are consistent with the partitioning behavior of the solute components, since both c-LN and cs-MgO:LN have congruent-melting crystals and bulk components, such as Li_2O, Nb_2O_5 and/or MgO, that are not segregated but rather partitioned into the crystal with partition coefficients of unity. In the case of cs-MgO:LN, neither the bulk components nor the ionic species are segregated so that its composition would be expected to be more homogeneous than that of c-LN. In contrast, the phase-matching wavelengths of s-LN and 5MgO:LN varied drastically within the test plate since these compounds are not congruent. The maximum compositional deviations of s-LN and c-LN within the measured areas are estimated to be 0.0092 mol% Li_2O and 0.0042 mol% Li_2O, respectively. The observed variation in the phase-matching wavelength in s-LN might reflect the compositional variation along the growth axis during growth. This indicates the difficultly of growing homogeneous s-LN using the double-crucible method[42].

The SHG conversion efficiency is measured at the center of each test plate (*z*: 0 mm, *y*: 0 mm in Fig. 4.8) at a constant value of the fundamental beam power. As shown in Fig. 4.9, the conversion efficiency of cs-MgO:LN is slightly lower than those obtained with 5MgO:LN and s-LN[41], however, these values are almost equal in magnitude, while the value measured for the c-LN sample is considerably lower. These experiments demonstrated that cs-MgO:LN has been generated, based on the extended concept of stoichiometry, and that this material, due to its congruent state, is superior to conventional $LiNbO_3$ crystals having a highly homogeneous composition. This substance also exhibits a high conversion efficiency of secondary harmonic generation due to its stoichiometric structure.

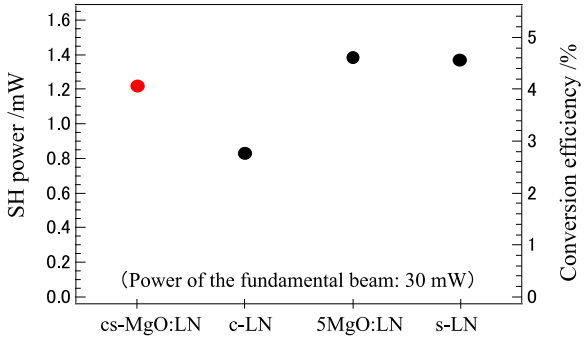


Fig. 4.9 Secondary harmonic generation conversion efficiency (after Ref. 26).

4.8 Thermodynamic requirements for impurity doping

MgO is a suitable doping oxide for the preparation of high-quality LN and LT crystals exhibiting the concurrent occurrence of stoichiometry and congruency in the ternary system. It is natural to inquire as to whether any other oxides produce a similar effect when added to LN or LT such that the resulting crystals become simultaneously stoichiometric and congruent and whether there are any specific requirements for an oxide to behave as an effective dopant.

In order to develop an LN or LT composition, the crystals must have zero c-EMF value. In other words, the activity of every constituent element in both the solid and liquid states is required to be unity. Suppose that a divalent oxide, AO, is doped into LN and subsequently is ionized in the melt according to the following equation.

$$AO \rightleftarrows A^{2+} + O^{2-}. \tag{4-16}$$

The congruent point is assumed to form at a certain composition in the ternary diagram of Li_2O–Nb_2O_5–AO. This composition must be found on the stoichiometric line of 50 mol% Nb_2O_5 and can be termed cs-AO:LN, since it is both congruent and stoichiometric. This scenario occurs in the case of MgO doping, which is understandable considering that MgO is an almost completely ionic oxide. In contrast, if AO is only partially ionized, both AO and A^{2+} will be partitioned into the crystal. As a result, even if $a^{AO} = 1$ (Eq. 4-16) is true, neither $a^{A^{2+}}$ nor $a^{O^{2-}}$ will necessarily equal unity and so the congruent point will not lie on the stoichiometric line for this material. In general, then, a dopant that is only partially ionized in the melt will not generate a compound LN in which stoichiometry and congruency are coincident. In contrast, when the oxide dopant AO is completely ionized, the congruent point can appear on the stoichiometric line[26].

4.9 True congruent-melting composition

Crystals like cs-MgO:LN or cs-MgO:LT are stoichiometric and congruent simultaneously and have k_0 of unity for all melt species including ionic species, so we can expect that they are partitioned into a crystal without any segregation even if a sudden change of growth velocity occurs due to the fluctuation of melt temperature and/or melt flow causing interface instability. In this view, these compositions could be true congruent-melting compositions that guarantee a homogeneous composition of the growing crystal under even non-steady state conditions. In contrast, a conventional congruent-melting composition like LN with 48.6 mol% Li_2O yields a homogeneous crystal during steady-state growth, though compositional fluctuation occurs when encountering a growth perturbation because k_0 is not unity for the ionic species and they segregate and are partitioned into the crystal in a non-equilibrium way. They are illustrated in Fig. 4.10.

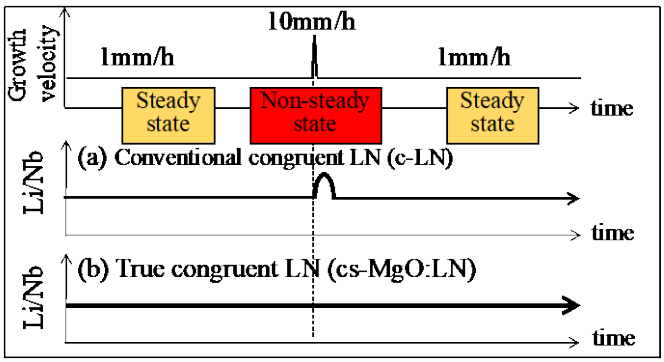


Fig. 4.10 Compositional stability in (a) c-LN and (b) cs-MgO:LN for non-steady-state growth.

References

1) S. Miyazawa, “Dynamics of melt growth”, Kyoritsu Publishing Co. 1992 (in Japanese).
2) J.A. Burton, R.C. Primm, W.P. Slichter, *J. Chem. Phys.*, **21** (1953) 1987.
3) S. Uda, T. Tsubota, *J. Cryst. Growth*, **312** (2010) 3650.
4) W. A. Tiller, K. A. Jackson, J. W. Rutter, B. Chalmers, *Acta Met.* **1** (1953) 428.
5) L.O. Wilson, *J. Cryst. Growth*, **44** (1978) 371.
6) H. Kodera, *Japan. J. Apple. Phys*., **2** (1963) 212.
7) C.T. Yen, W.A. Tiller, *J. Cryst. Growth*, **118** (1992) 259.
8) A.G. Ostrogorsky, G. Müller, *J. Cryst. Growth*, **130** (1993) 113.
9) A.G. Ostrogorsky, *J. Cryst. Growth*, **348** (2012) 97.
10) W.W. Mullins, R.F. Sekerka, *J. Appl. Phys*., **34** (1963) 323.
11) W.G. Pfann, *Metallurgical Reviews*, **2** (1957) 29.
12) C. D. Thurmond, J. D. Struthers, *J. Phys. Chem.* **57** (1953) 831.
13) K. Weiser, *J. Phys. Chem. Solids* **7** (1958) 118.
14) J. R. Carruthers, G. E. Peterson, and M. Grasso, P.M. Bridenbaugh, J. Appl. Phys. **42** (1971) 1846.
15) P. F. Bourdi, R. G. Norwood, C. D. Bird, and G. D. Calvert, J. Cryst. Growth **113** (1991) 61.
16) S.Q. Wang, J. Harada, S. Uda, J. Cryst. Growth, **219** (2000) 263.
17) L.S. Darken, *Trans.* AIME **180** (1949) 430.
18) S. Uda, H. Inaba, J. Harada, K. Hoshikawa, J. Cryst. Growth, **271** (2004) 229.
19) S. Uda, S.Q. Wang, N. Konishi, H. Inaba, J. Harada, J. Cryst. Growth, **237-239** (2002) 707.
20) S. Uda, S. Q. Wang, N. Konishi, H. Inaba, J. Harada, J. Cryst. Growth, **275** (2005) 251.
21) S. Uda, J. Cryst. Growth, 310 (2008) 3864.
22) H. Kimura, S. Uda, J. Cryst. Growth, 311 (2009) 4094.
23) S. Uda, W. A. Tiller, J. Cryst. Growth, 121 (1992) 155.
24) S. Uda, S. Koh, X. Huang, J. Cryst. Growth, 292 (2006) 1.
25) Y. Azuma, S. Uda, J. Cryst. Growth, 306 (2007) 217.
26) S. Uda, Ch. 4 in *Handbook of Crystal Growth*, Nishinaga, Rudolph, Kuech ed. Elsevier (2014).
27) S. Uda, W. A. Tiller, J. Cryst. Growth, 121 (1992) 93.
28) S. Koh, S. Uda, M. Nishida, X. Huang, J. Cryst. Growth, 297 (2006) 247.
29) S. Koh, S. Uda, X. Huang, J. Cryst. Growth, 306 (2007) 406.
30) H. Kimura, H. Koizumi, T. Uchida, S. Uda, J. Cryst. Growth, 311 (2009) 1553.
31) V. A. D’yakov, D. P. Shumov, L. N. Rashkovich, A. L. Aleksandrovskii, Bull. Acad. Sci. USSR, Phys. Ser., 49 (1985) 117.

32) S. Uda, J. Kon, J. Ichikawa, K. Inaba, K. Shimamura, T. Fukuda, J. Cryst. Growth, 179 (1997) 567.
33) S. Uda, J. Kon, K. Shimamura, J. Ichikawa, K. Inaba, T. Fukuda, J. Cryst. Growth, 182 (1997) 403.
34) Y. A. Boikov, B. M. Goltsman, V. K. Yarmarkin, V. V. Lemanov, Appl. Phys. Lett., 78 (2001) 3866.
35) J. Dalton, A New System of Chemical Philosophy Part 1, printed by S. Russell, Manchester, 1808.
36) S. Uda, R. Komatsu, K. Takayama, J. Cryst. Growth, 171 (1997) 458.
37) L. O. Svaasand, M. Eriksrud, G. Nakken, A. P. Grande, J. Cryst. Growth, 22 (1974) 179.
38) S. Fujii, S. Uda, K. Maeda, J. Nozawa, H. Koizumi, K. Fujiwara, T. Kajigaya, J. Cryst. Growth, 383 (2013) 63.
39) P. F. Bourdi, R. G. Norwood, C. D. Bird, G. D. Calvert, J. Cryst. Growth, 113 (1991) 61.
40) Y. Furukawa, K. Kitamura, S. Takekawa, Opt. Lett., 23 (1998) 1892.
41) H. Kimura, T. Taniuchi, S. Iida, S. Uda, J. Cryst. Growth, 312 (2010) 3425.
42) K. Kitamura, J. K. Yamamoto, N. Iyi, S. Kimura, J. Cryst. Growth, 116 (1992) 327.
43) D. H. Jundt, M. M. Fejer, R. L. Byer, IEEE J. Quant. Electron., 26 (1990) 135.
44) H. M. O'Bryan, P. K. Gallagher, C. D. Brandle, J. Am. Ceram. Soc., 68 (1985) 493.

11. Growth of Advanced Complex Oxides

Reprinted from Journal of the American Ceramic Society, Vol 91, Darrell G. Schlom, Long-Qing Chen, Xiaoqing Pan, Andreas Schmehl, and Mark A. Zurbuchen, A Thin Film Approach to Engineering Functionality into Oxides, 2429-2454, Copyright 2008, with permission from John Wiley and Sons .

journal

J. Am. Ceram. Soc., **91;** [8] 2429–2454 (2008)
DOI: 10.1111/j.1551-2916.2008.02556.x
© 2008 The American Ceramic Society

A Thin Film Approach to Engineering Functionality into Oxides

Darrell G. Schlom,[†,††,‡] Long-Qing Chen,[‡] Xiaoqing Pan,[§] Andreas Schmehl,[‡,¶] and Mark A. Zurbuchen[‖]

[‡]Department of Materials Science and Engineering, Pennsylvania State University, University Park, Pennsylvania 16802-5005

[§]Department of Materials Science and Engineering, University of Michigan, Ann Arbor, Michigan 48109-2136

[¶]Experimentalphysik VI, Elektronische Korrelationen und Magnetismus, Institut für Physik, Universität Augsburg, D-86159 Augsburg, Germany

[‖]The Aerospace Corporation, Microelectronics Technology Department, El Segundo, California 90245

The broad spectrum of electronic and optical properties exhibited by oxides offers tremendous opportunities for microelectronic devices, especially when a combination of properties in a single device is desired. Here we describe the use of reactive molecular-beam epitaxy and pulsed-laser deposition to synthesize functional oxides, including ferroelectrics, ferromagnets, and materials that are both at the same time. Owing to the dependence of properties on direction, it is often optimal to grow functional oxides in particular directions to maximize their properties for a specific application. But these thin film techniques offer more than orientation control; customization of the film structure down to the atomic-layer level is possible. Numerous examples of the controlled epitaxial growth of oxides with perovskite and perovskite-related structures, including superlattices and metastable phases, are shown. In addition to integrating functional oxides with conventional semiconductors, standard semiconductor practices involving epitaxial strain, confined thickness, and modulation doping can also be applied to oxide thin films. Results of fundamental scientific importance as well as results revealing the tremendous potential of utilizing functional oxide thin films to create devices with enhanced performance are described.

I. Oxides Beyond SiO_2

UNTIL recently, the word "oxide" could only mean one thing to anyone working in the semiconductor industry—SiO_2. But as every ceramist knows, oxides are an exciting class of electronic materials in their own right. Oxides exhibit the full spectrum of electronic, optical, and magnetic behavior: insulating, semiconducting, metallic, superconducting, ferroelectric, pyroelectric, piezoelectric, ferromagnetic, multiferroic, and nonlinear optical effects are all possessed by structurally compatible oxides. The unparalleled variety of physical properties of oxides holds tremendous promise for electronic applications. Analogous to today's semiconductor device structures, many device concepts utilizing oxides will likely use alternately layered structures where dimensions are minute enough to observe quantum size effects (nanometer-scale thicknesses).

The physical behavior of oxides confined to quantum size dimensions is not well established, and an understanding of the effect of such confinement (reduced dimensionality) on the physical properties of these structures cannot be achieved without the controlled preparation of well-ordered crystalline samples. Equally exciting are the new functionalities that can emerge at oxide interfaces. For instance, the interface between appropriate antiferromagnetic materials has been shown to be ferromagnetic.[1–7] Similarly, charge transfer at the interface between appropriate nonmagnetic insulators[8] can give rise to a magnetic[9] or superconducting[10] electron gas. These examples offer a glimpse of the new or enhanced functionalities that can be achieved by nanoengineering oxide heterostructures with atomic layer precision. As we show in this article, it is possible to structurally engineer crystalline oxides with a precision that rivals the structural control achieved in today's most advanced semiconductor structures.

Examples of the functional properties of specific oxides are listed in Table I. The oxides chosen were those with exceptional properties for each category. These include the oxide with the highest known electron mobility ($SrTiO_3$),[11] change in resistance at a metal–insulator transition (EuO),[12] superconducting transition temperature ($HgBa_2Ca_2Cu_3O_{8+x}$),[13] switchable spontaneous polarization ($PbZr_{0.2}Ti_{0.8}O_3$[14] and $BiFeO_3$[15–18]), piezoelectric coefficient ($PbZn_{1/3}Nb_{2/3}O_3$–$PbTiO_3$),[19] magnetization (EuO),[20] magnetoresistance ($Pr_{0.7}Sr_{0.04}Ca_{0.26}MnO_{3-\delta}$),[21] magnetostrictive coefficient ($Co_{0.8}Fe_{2.2}O_4$),[22] Verdet constant (EuO)[23]—a measure of the strength of the Faraday effect, spin polarization (CrO_2),[24,25]

D. Green—contributing editor

Manuscript No. 24429. Received March 17, 2008; approved June 1, 2008.
This work was financially supported by the National Science Foundation under grants DMR-0507146 and DMR-0213623, the Office of Naval Research under grant N00014-04-1-0426 monitored by Dr. Colin Wood, and the U.S. Department of Energy through grants DE-FG02-03ER46063 and DE-FG02-07ER46417. This work was supported by The Aerospace Corporation's Independent Research and Development Program.
[†]Author to whom correspondence should be addressed. e-mail: schlom@cornell.edu
[††]Current Address: Department of Materials Science and Engineering, Cornell University, Ithaca, NY 14853-1501

Feature

Table I. Examples of the Properties of Oxides

Property	Value	Oxide material	References
Mobility	$\mu = 22\,000\ cm^2 \cdot (V \cdot s)^{-1}$ (2 K)	$SrTiO_3$	Tufte and Chapman[11]
Metal–insulator transition	$\Delta R/R_{T_{low}} > 10^{13}$	EuO	Petrich *et al.*[12]
Superconductivity	$T_c = 135$ K	$HgBa_2Ca_2Cu_3O_{8+x}$	Schilling *et al.*[13]
Ferroelectricity	$P_s = 105\ \mu C/cm^2$	$PbZr_{0.2}Ti_{0.8}O_3$	Vrejoiu *et al.*[14]
	$P_s = 100\ \mu C/cm^2$	$BiFeO_3$	Wang *et al.*,[15] Li *et al.*[16] Das *et al.*,[17] Dho *et al.*[18]
Piezoelectricity	$d_{33} = 2500$ pC/N	$PbZn_{1/3}Nb_{2/3}O_3$–$PbTiO_3$	Park *et al.*[19]
Ferromagnetism	$M_s = 6.9\ \mu_B$/Eu	EuO	Matthias *et al.*[20]
Colossal magnetoresistance	$\Delta R/R_H > 10^{11}$ (5 T)	$Pr_{0.7}Sr_{0.04}Ca_{0.26}MnO_{3-\delta}$	Maignan *et al.*[21]
Magnetostriction	$\lambda_{100} = -590 \times 10^{-6}$	$Co_{0.8}Fe_{2.2}O_4$	Bozorth *et al.*[22]
Faraday effect	$\nu = 4 \times 10^{5\,\circ} \cdot (T \cdot cm)^{-1}$	EuO	Ahn and Shafer[23]
Spin polarization	$P > 98\%$	CrO_2	Soulen *et al.*,[24] Anguelouch *et al.*[25]
Ferromagnetic and ferroelectric simultaneously	$T_C = 105$ K	$BiMnO_3$	Hill and Rabe,[29] Moreira dos Santos *et al.*,[28] Sharan *et al.*,[30] Baettig *et al.*[31]
	$T_C = 250$ K	$LuFe_2O_4$, $FeTiO_3$	Ikeda *et al.*, Fennie[27]

and the ferromagnetic ferroelectric with the highest reported[26] ($LuFe_2O_4$) or predicted[27] ($FeTiO_3$) transition temperature. A challenge with materials that are simultaneously ferromagnetic and ferroelectric is that they are often too conductive for the fabrication of conventional ferroelectric switching devices. The ferromagnetic ferroelectric with the highest transition temperature on which a conventional polarization-electric field hysteresis measurement has been reported is $BiMnO_3$ ($TC \sim 105$ K).[28]

(1) Perovskites

The crystal structures of the oxides with the outstanding properties listed in Table I are shown in Fig. 1.[32] Half of the oxides belong to the same structural family—perovskite. The perovskite ABO_3 structure can accommodate with 100% substitution some 30 elements on the *A* site and over half the periodic table on the *B* site, as shown in Fig. 2.[33] Given the chemical and structural compatibility between many perovskites, this malleable structural host offers an opportunity to customize electronic, magnetic, and optical properties in thin films in ways not possible with conventional semiconductors.

The electroceramics industry currently utilizes the diverse electrical properties of oxides in separate components made primarily by bulk synthesis and thick-film methods for capacitors, sensors, actuators, night vision, and other applications. A significant opportunity exists, however, to combine these

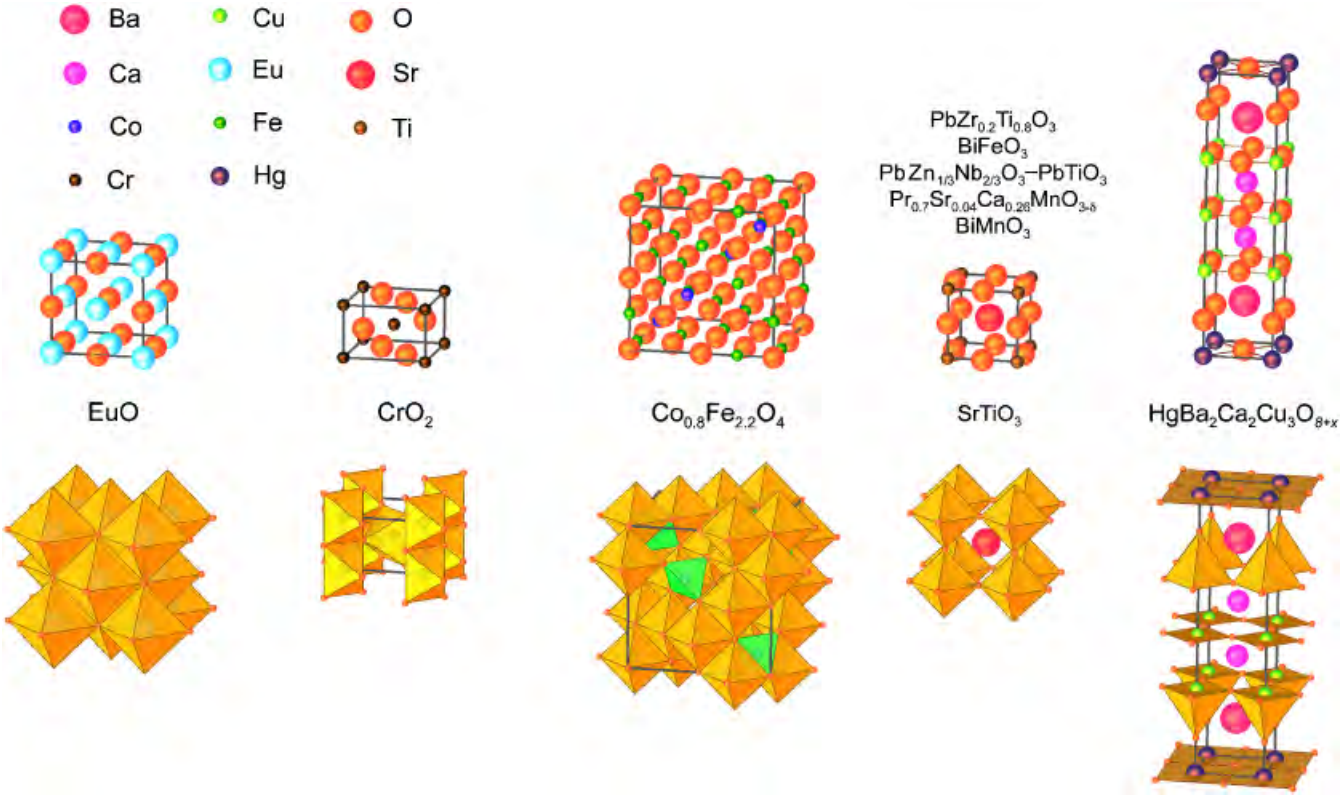


Fig. 1. The crystal structures of the oxides with the exceptional properties described in Table I. Two equivalent representations of these crystal structures are shown: the atomic positions (above) and the coordination polyhedra (below). The oxygen atoms occupy the vertices of the coordination polyhedra. Color is used to distinguish the two types of oxygen coordination polyhedra in $Co_{0.8}Fe_{2.2}O_4$, octahedra (orange), and tetrahedra (green). The pseudocubic subcell of the perovskites $PbZr_{0.2}Ti_{0.8}O_3$, $BiFeO_3$, $PbZn_{1/3}Nb_{2/3}O_3$–$PbTiO_3$, $Pr_{0.7}Sr_{0.04}Ca_{0.26}MnO_{3-\delta}$, and $BiMnO_3$ is shown for clarity. The relative sizes of the atoms reflect their relative ionic radii as given by Shannon.[32]

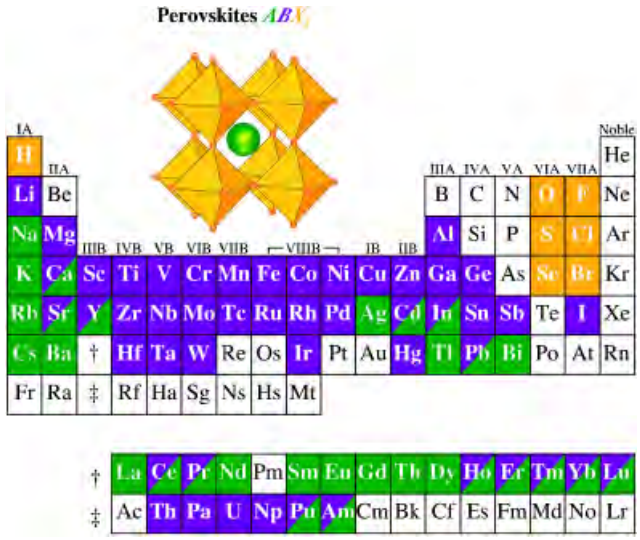


Fig. 2. A compilation of elements of the periodic table that can occupy the three sites (*A*, *B*, and *X*) of the perovskite crystal structure with 100% occupancy (based on the data in Landolt-Boernstein[33]).

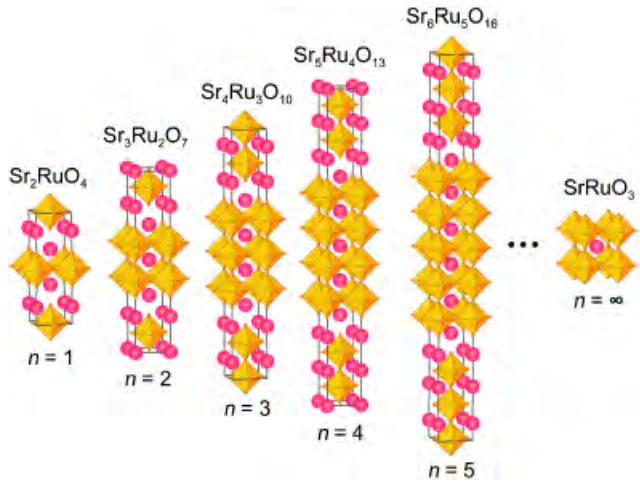


Fig. 3. The $n = 1$ (Sr_2RuO_4), $n = 2$ ($Sr_3Ru_2O_7$), $n = 3$ ($Sr_4Ru_3O_{10}$), $n = 4$ ($Sr_5Ru_4O_{13}$), $n = 5$ ($Sr_6Ru_5O_{16}$), and $n = \infty$ ($SrRuO_3$) members of the homologous Ruddlesden–Popper series of compounds $Sr_{n+1}Ru_nO_{3n+1}$. Ru^{4+} lie at the center of oxygen coordination polyhedra (octahedra). The filled circles represent Sr^{2+} ions (reprinted from Haeni *et al.*,[80] with permission; ©2001 American Institute of Physics).

properties together in oxide heterostructures where multiple properties can be utilized to yield functional integrated devices. Integration of epitaxial stacks of oxide crystals is motivated by the similarity in crystal structure (the perovskite oxides listed in Table I all have perovskite subcell dimensions in the 3.85–4.05 Å range), the chemical compatibility that exists between many oxides, and the directional dependence of properties that can be optimized for particular applications by controlling the orientation of a single crystalline film. In addition to synthesizing oxide heterostructures that integrate relatively thick layers of different oxides together, new oxides can be engineered at the atomic-layer level. Although now commonplace in the growth of semiconductors, such an ability is relatively new to oxides and makes possible the discovery/engineering of higher performance smart materials by exploiting the exceptional electrical, optical, and magnetic properties of oxides and building a coupling between these properties into oxide heterostructures.

(2) Perovskite-Related Phases

Structure–property relations have been studied for a great many oxides using solid-state synthesis methods. Many cases have been found where the property of a structurally related family of oxides (i.e., a homologous series) changes drastically from one end to the other of the series. Examples include the $Sr_{n+1}Ru_nO_{3n+1}$ Ruddlesden–Popper homologous series[34–36] shown in Fig. 3. In this series the positive integer n corresponds to the number of perovskite layers that are sandwiched between double SrO rock-salt layers. The $n = 1$ (Sr_2RuO_4) member of the series is paramagnetic and at very low temperature (<1.5 K) superconducting,[37] whereas the $n = \infty$ ($SrRuO_3$) member of the series is ferromagnetic.[38] The structural change accompanying this drastic change in properties involves going from a corner sharing RuO_6 octahedral network that is connected in all three dimensions for the $n = \infty$ member ($SrRuO_3$) to the $n = 1$ member (Sr_2RuO_4), where the RuO_6 octahedra are only connected in two dimensions and double SrO layers completely disrupt all corner sharing of the RuO_6 octahedra along the *c*-axis. Many other equally fascinating homologous series exist in perovskite-related oxide structures showing interesting variation in ferromagnetic, ferroelectric, superconducting, and metal–insulator behavior.

An example of an important ferroelectric homologous series is the Aurivillius homologous series with general formula $Bi_2O_2(A_{n-1}B_nO_{3n+1})$ shown in Fig. 4. Here again the positive integer n denotes the number of perovskite layers that in this case are sandwiched between Bi_2O_2 layers. The structures shown include the layered $n = 2$ Aurivillius compound $SrBi_2Ta_2O_9$ widely used in ferroelectric random access memories (FeRAM).[39] Over 500 million FeRAM chips containing either $SrBi_2Ta_2O_9$ or $Pb(Zr,Ti)O_3$ ferroelectrics have been made and worldwide production currently exceeds 70 million units per year.[40] Also included in Fig. 4 is an $n = 6$ Aurivillius compound $Bi_7(Mn,Ti)_6O_{21}$ into which the ferromagnetic perovskite $BiMnO_3$ has been inserted,[41] and at the end of the series is the $n = \infty$ three-dimensional perovskite structure.

When one desires to study the change in a property that occurs as n is varied in detail, however, solid-state synthesis methods often fall short. Invariably researchers have only been able to find conditions of temperature and pressure yielding single-phase products for low values of n and for $n = \infty$. Attempts to make intermediate n values result in uncontrolled intergrowths.[13,41–72] Calculation of the energy of formation of several homologous series of layered oxide phases indicates the reason for this difficulty—differences in formation energy become smaller and smaller as n increases.[73,74] Thus, apart from theoretical calculations, little is known about how the properties of a series of structures vary with n as the dimensionality of the structure changes. Because of correlated electron effects in many

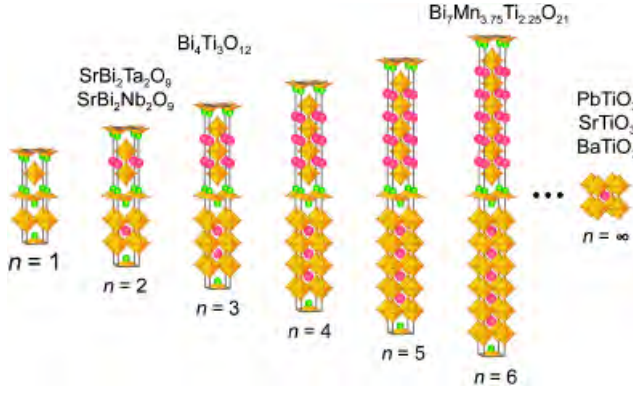


Fig. 4. Examples of the $n = 1$, $n = 2$ ($SrBi_2Ta_2O_9$, $SrBi_2Nb_2O_9$), $n = 3$ ($Bi_4Ti_3O_{12}$), $n = 4$, $n = 5$, and $n = \infty$ ($PbTiO_3$, $SrTiO_3$, and $BaTiO_3$) members of the Aurivillius homologous series of compounds with general formula $Bi_2O_2(A_{n-1}B_nO_{3n+1})$. *B* ions lie at the center of the oxygen coordination polyhedra (octahedra). The filled circles represent *A* ions. These structures consist of alternating sheets of Bi_2O_2 and $nABO_3$ perovskite layers.

homologous series of interest, experimental measurements are an important part of understanding the effect of dimensionality on these oxides.[75]

A key advantage of the use of thin film techniques for the preparation of oxide heterostructures is that single-phase epitaxial films with intermediate n values can often be synthesized even though nearby phases have similar formation energies.[76–80] This is made possible by the ability to supply incident species in any desired sequence with submonolayer composition control. A particular phase can often be grown by supplying the constituents in an ordered sequence corresponding to the atomic arrangement of these constituents in the desired phase.

II. Synthesis of Epitaxial Oxide Films by Pulsed-Laser Deposition (PLD) and Molecular-Beam Epitaxy (MBE)

Significant advances in deposition technologies and substrates over the past two decades have enabled the growth of oxide thin films with high structural perfection and the ability to customize oxide layering down to the atomic layer level. These advances were spurred by the discovery of high-temperature superconductivity over 20 years ago.[81,82] Existing thin film deposition techniques were rapidly adapted to the challenges of functional oxides, including PLD,[83–88] high-pressure[89–94] and off-axis sputtering,[95–102] reactive coevaporation,[103–105] and reactive MBE.[76,106–114] These physical vapor deposition techniques yielded high-quality oxide superconductor films just a few nanometers in thickness,[115–117] superlattices of superconducting oxides with atomic-scale thickness control and abrupt interfaces,[110,118–126] and the construction of new oxide superconducting phases with atomic layer precision.[76,127] Chemical techniques including metal-organic chemical vapor deposition (MOCVD)[128–143] and chemical solution deposition (CSD)[144–148] have also been adapted and applied to functional oxides, particularly ferroelectrics. In recent years, a growing cadre of researchers has applied these physical and chemical techniques with increasing precision to the growth of an ever-broadening set of functional oxide materials. Relevant achievements include the synthesis of oxide superlattices with atomic-scale thickness control and abrupt interfaces[79,113,117,149–157] and the synthesis of metastable oxides.[76,158–161] These advances in thin film deposition technology have made it possible to customize oxide heterostructures with subnanometer precision.

(1) PLD

The PLD technique is ideally suited to the rapid investigation of multicomponent functional oxides because it (1) allows them to be grown in a relatively compact and inexpensive chamber, (2) provides nearly stoichiometric composition transfer from the target to the sample if the growth conditions are optimized, (3) is compatible with oxidant pressures ranging from ultra-high vacuum (UHV) to atmospheric, (4) is amenable to the growth of superlattices with nanometer precision,[126,150,152–155] and (5) is capable of ablating a wide variety of materials.[86,162–165]

A schematic of a PLD system is shown in Fig. 5. The process amounts to flash evaporation of the surface of a multicomponent target. Its key elements are an UV laser capable of vaporizing the surface layer of the multicomponent target when suitably focused down to a high energy density (fluence) by a lens. The vaporized material, containing a variety of atomic, molecular, and excited species, is transported through the low vacuum environment (typically 100 mTorr of O_2) where it condenses on the substrate. If the substrate presents a suitable template for the depositing species, epitaxial growth can occur in which the deposited species follow the crystalline template of the substrate to extend the crystal.

A schematic showing how the presence of a substrate may influence the crystallization of a multicomponent mixture of depositing species is shown in Fig. 6.[166] In the example shown, the growth of $SrBi_2Nb_2O_9$ (or equivalently $SrBi_2Ta_2O_9$) on $SrTiO_3$, the film and substrate have different chemistries and crystal

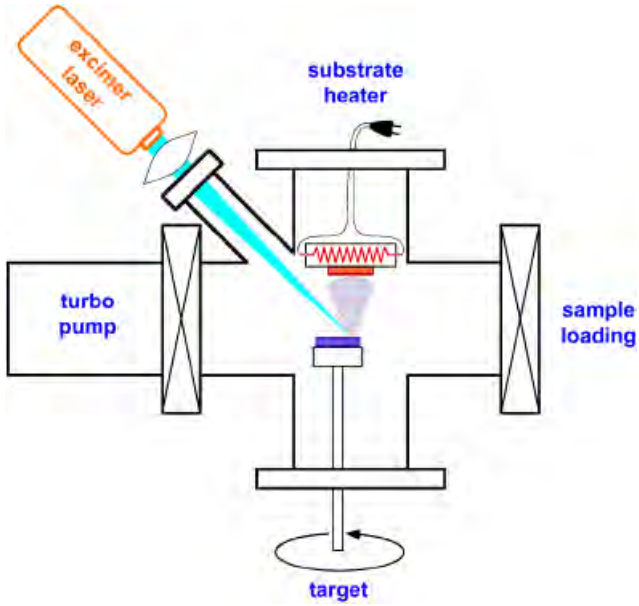


Fig. 5. A schematic diagram of a pulsed-laser deposition system dedicated to the controlled synthesis of oxide heterostructures. The key components are the UV laser whose output is focused by a lens to a sufficient fluence to vaporize the surface of the multicomponent oxide target. The vaporized material from the target is deposited on the heated substrate to form an epitaxial film. For the deposition of multilayers, a multiple-target carousel is used.

structures, yet just like the game Tetris™ the depositing atoms find low-energy configuration(s) to extend the single-crystal substrate into an epitaxial overlayer. In Fig. 6(a) the low-energy configuration is unique and the resulting epitaxial film is single crystalline with an orientation relationship (001) $SrBi_2Nb_2O_9 \| (001)$ $SrTiO_3$ and [100] $SrBi_2Nb_2O_9 \| [1\bar{1}0]$ $SrTiO_3$.[‡‡,167] In the other two cases, Figs. 6(b) and (c), several energetically degenerate low-energy configurations exist, leading to an epitaxial film with two or three types of domains related to each other via 180° or 120° rotational twinning, respectively. In Fig. 6(b) the (110) $SrTiO_3$ surface is shown faceted as has been observed to occur at the growth conditions for $SrBi_2Nb_2O_9$ films.[168] Thus, the epitaxy is actually occurring locally on the (100) and (010) faces of the faceted (110) $SrTiO_3$ substrate as has also been reported for the growth of epitaxial films of other perovskite-related phases on (110) $SrTiO_3$.[169–171] The orientation relationship for Fig. 6(b) is ~(116) $SrBi_2Nb_2O_9 \| (110)$ $SrTiO_3$ and (i) [001] $SrBi_2Nb_2O_9 \| [100]$ $SrTiO_3$ and (ii) [001] $SrBi_2Nb_2O_9 \| [010] SrTiO_3$ for the two growth twins.[‡‡,168] For Fig. 6(c) the orientation relationship is (103) $SrBi_2Nb_2O_9 \| (111)$ $SrTiO_3$ and approximately (i) [001] $SrBi_2Nb_2O_9 \| [100]$ $SrTiO_3$, (ii) [001] $SrBi_2Nb_2O_9 \| [010]$ $SrTiO_3$, and (iii) [001] $SrBi_2Nb_2O_9 \| [001]$ $SrTiO_3$ for the three growth twins.[‡‡,172,173] For clarity, another view of the threefold degenerate epitaxial relationship of the growth of $SrBi_2Nb_2O_9$ on (111) $SrTiO_3$ is shown in Fig. 6(d), where it can be more clearly seen that the three possibilities for the orientation of the c-axis of the $SrBi_2Nb_2O_9$ lie approximately parallel to the $\langle 100 \rangle$ axes of the $SrTiO_3$ substrate.

The chief advantages of PLD are its relatively modest cost and, after optimization of the growth conditions, the nearly faithful composition transfer from target to substrate, which allows a single multicomponent target with the same composition as the desired film to be used,[86,162–165] alleviating the need for accurate composition control. PLD offers an extremely

[‡‡]In addition to the *hkl* $SrBi_2Nb_2O_9$ indices given, *khl* $SrBi_2Nb_2O_9$ indices are also implied. The latter indices are omitted for clarity, but arise because of transformation twinning that occurs on cooling as the tetragonal $SrBi_2Nb_2O_9$ (the stable polymorph at growth temperature) goes through a phase transition where it becomes orthorhombic at room temperature with $a \approx b$ and a being the axis of the ferroelectric along which the spontaneous polarization exists.

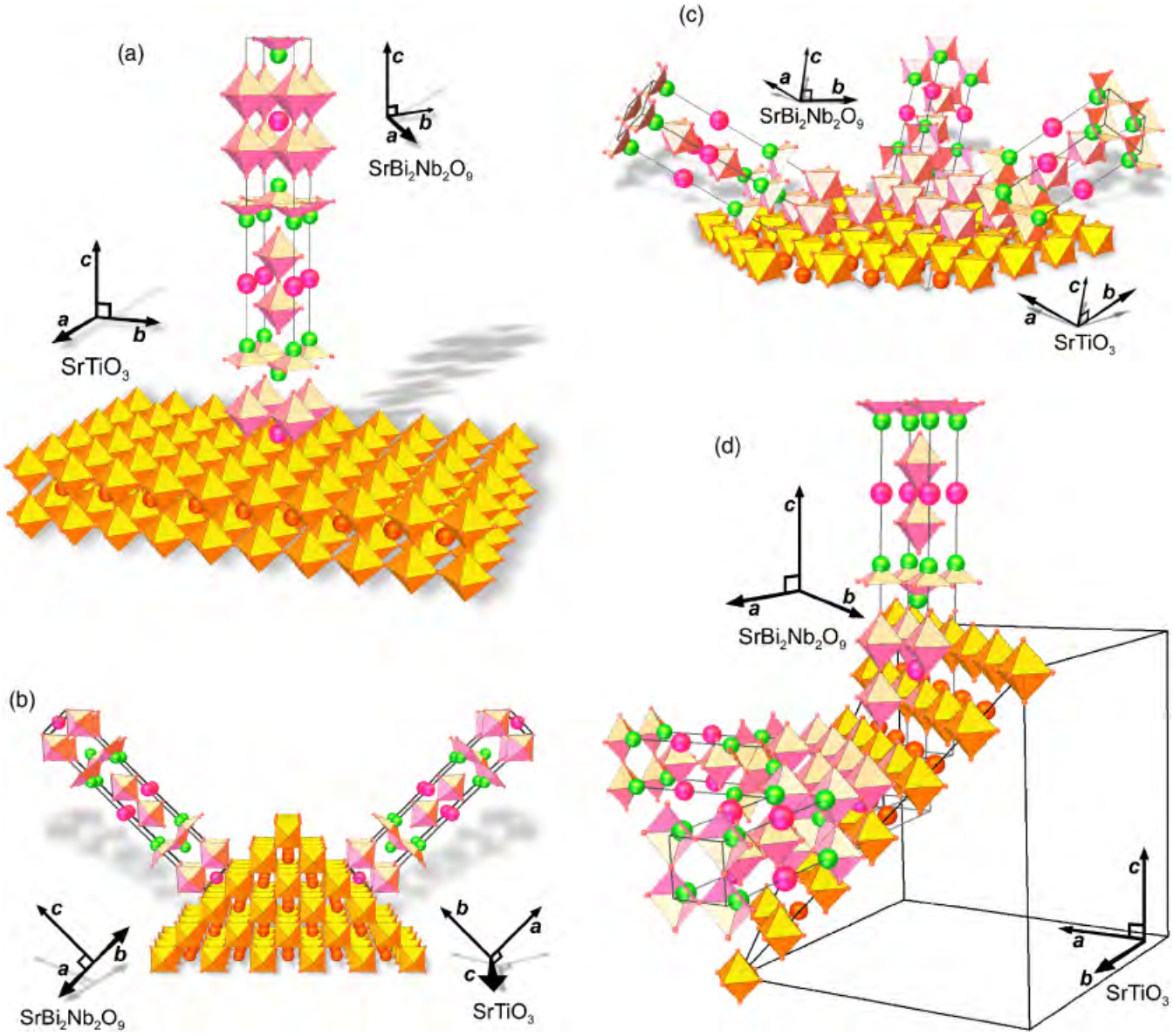


Fig. 6. The crystal structure and orientation of $SrBi_2Nb_2O_9$ (or equivalently $SrBi_2Ta_2O_9$) grown on (a) (001) $SrTiO_3$, (b) (110) $SrTiO_3$, and (c) (111) $SrTiO_3$, showing the low-energy epitaxial orientation relationship(s). Another view of the threefold degenerate epitaxial relationship of $SrBi_2Nb_2O_9$ on (111) $SrTiO_3$ is shown in (d) for clarity (reprinted from Lettieri *et al.*,[172] with permission; ©2000 American Institute of Physics). $SrBi_2Nb_2O_9$ and $SrBi_2Ta_2O_9$ grow epitaxially on (001) $SrTiO_3$ with the *c*-axis parallel to the substrate surface normal, on (110) $SrTiO_3$ in a twofold twin structure with the *c*-axes tilted by $\pm 45^\circ$ from the surface normal, and on (111) $SrTiO_3$ in a threefold twin structure with the *c* axes tilted by 57° away from the surface normal. The $SrBi_2Nb_2O_9$ is drawn and its unit cell is outlined in its tetragonal state above its Curie temperature ($\sim 430^\circ$C, Landolt-Boernstein[166]). Note that the growth temperature is well above the Curie temperature of $SrBi_2Nb_2O_9$, and so the crystallography shown is relevant during nucleation and growth of the epitaxial film. After cooling through the Curie temperature, each of the growth twins shown is twinned further due to *a–b* twinning, leading to a doubling of the expected twin states at room temperature. The orthorhombic axes of only one of the twin variants of the $SrBi_2Nb_2O_9$ films are drawn.

powerful means of scouting for materials with promising properties by enabling the rapid preparation of new materials in epitaxial form: thin single crystalline extensions of the underlying crystalline template provided by the substrate. Its key disadvantages are the micrometer-sized "boulders" common to PLD films[86,162–165] as well as the energetic species present, which can lead to interlayer mixing and extended lattice constants due to ion bombardment effects.[174–179] Stating that PLD provides stoichiometric composition transfer from target to substrate is an oversimplification. Careful studies have shown that only with careful tuning of deposition parameters (chamber pressure, laser fluence, target–substrate distance, etc.) can films with composition near to that of the target be attained.[178]

Techniques that can be used during film deposition to provide information on the nucleation and growth mechanisms in real time, rather than relying on "pathology" after the growth, are extremely useful for improving the quality of oxide thin films. Reflection high-energy electron diffraction (RHEED) is particularly useful in this context. Differential pumping has enabled RHEED to be used at the relatively high pressures of PLD[180,181] leading to tremendous improvements in the ability to tailor oxides at the atomic level. Because of the many possible phases and phase transitions in functional oxide systems, such *in situ* analytical tools that increase our understanding of the growth process and allow the growth conditions to be adjusted *during growth* are crucial to achieving improvements in the atomic layer engineering of oxides.

(2) Oxide MBE

The MBE method of thin film growth may be thought of as atomic spray painting, as shown in Fig. 7 in which an oxide

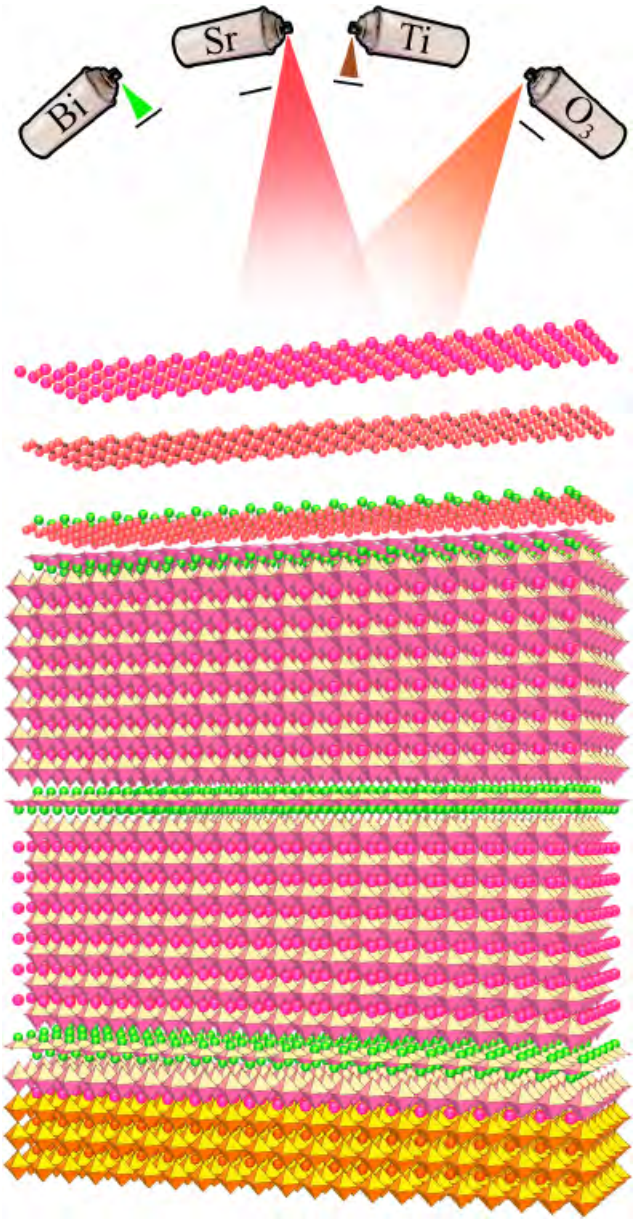


Fig. 7. A highly schematic representation of the molecular-beam epitaxy (MBE) growth of a (001) $Sr_4Bi_4Ti_7O_{24}$ film on a (001) $LaAlO_3$–Sr_2AlTaO_6 (LSAT) substrate by reactive MBE.

ferroelectric structure, e.g., $Sr_4Bi_4Ti_7O_{24}$ (an $n = 7$ Aurivillius phase) is schematically assembled layer by layer. The flux of spray from each atomic or molecular beam is controlled by the temperature (and thus vapor pressure) of the effusion cell in which each species is contained. The duration of spray is individually controlled for each beam by shutters, which control not only the open time (and thus dose), but also the sequence in which species reach the growth surface. By controlling the shutters and temperature of the evaporant (which control dose and flux, respectively), the layering sequence of the desired structure can be customized. This technique is capable of controlling the layering of oxides on a unit cell level.[76–80,110,113,117,119,124,157] A low growth temperature is frequently used to kinetically minimize subsequent bulk reordering and to minimize the loss of the customized (and often metastable) layered structures. The huge difference between surface and bulk diffusion rates in oxides[182,183] enables the growth of films with excellent structural order while at the same time preserving the potentially metastable layering of an oxide superlattice.

MBE is a vacuum deposition method in which well-defined thermal beams of atoms or molecules react at a crystalline surface to produce an epitaxial film. It was originally developed for the growth of GaAs and (Al,Ga)As,[184] but due to its unparalleled ability to control layering at the monolayer level and compatibility with surface-science techniques to monitor the growth process as it occurs, its use has expanded to other semiconductors as well as metals and insulators.[185,186] Epitaxial growth, a clean UHV deposition environment, *in situ* characterization during growth, and the notable absence of highly energetic species are characteristics that distinguish MBE from other thin film methods used to prepare functional oxide thin films. These capabilities are key to the precise customization of oxide heterostructures at the atomic layer level. MBE is traditionally performed in UHV chambers to avoid impurities. In addition to molecular beams emanating from heated crucibles containing individual elements, molecular beams of gases may also be introduced, for example to form oxides or nitrides. This variant of MBE is known as "reactive MBE"[187] in analogy to its similarity to "reactive evaporation," which takes place at higher pressures where well-defined molecular beams are absent. Reactive evaporation has also been extensively used to grow functional oxide films,[188] but here we limit our discussion to reactive MBE.

MBE has enjoyed significant success in the preparation of semiconductor microstructures with nanoscale thickness control and exceptional device characteristics. Examples of the thickness control achieved in semiconductors include interspersing layers as thin as one monolayer (0.28 nm) of AlAs at controlled locations into a GaAs film[189] and alternating monolayers of GaAs and AlAs to make a one-dimensional superlattice.[190] This nanoscale control has enabled tremendous flexibility in the design, optimization, and manufacturing of new devices, especially those making use of quantum effects.[191]

The use of MBE to grow functional oxides dates back to 1985, when it was used to grow $LiNbO_3$ films.[192,193] Since that time it has been used to grow the oxide superconductors $(Ba,K)BiO_3$, $(Ba,Rb)BiO_3$, $(La,Sr)_2CuO_4$, $YBa_2Cu_3O_{7-\delta}$, $NdBa_2Cu_3O_{7-\delta}$, $SmBa_2Cu_3O_{7-\delta}$, $DyBa_2Cu_3O_{7-\delta}$, and $Bi_2Sr_2Ca_{n-1}Cu_nO_{2n+4}$ for $n = 1$–11[76,110,117,119]; the oxide ferroelectrics $LiNbO_3$,[192–195] $LiTaO_3$,[194] $BaTiO_3$,[79,196–205] $PbTiO_3$,[79,112,206] and $Bi_4Ti_3O_{12}$[79,207,208]; the incipient ferroelectric $SrTiO_3$[79,114,197,198,204,209–218]; the ferromagnets $(La,Ca)MnO_3$,[219,220] $(La,Sr)MnO_3$,[219,221] and EuO[222–227]; the ferrimagnet Fe_3O_4[228]; the magnetoelectric Cr_2O_3[228]; the multiferroics $BiFeO_3$[229–231] and $YMnO_3$[232,233]; and superlattices of these phases.[4–7,76,79,110,119,124,157,199,234–237] Although the use of MBE to grow functional oxides is much less mature than its use for compound semiconductors, examples included in this article show how the layering capabilities of MBE can control the composition profile of multicomponent functional oxides along the growth direction with subnanometer precision. This capability is relevant to the fabrication of epitaxial device structures and to the nanoengineering of new functional materials.

The configuration of an MBE system for the growth of ferroelectric oxides differs in several important ways from today's more conventional MBE systems designed for the growth of semiconductors. The major differences are the required presence of an oxidant species, more stringent composition control, and to have adequate pumping to handle the oxidant gas load.

A schematic diagram of the growth chamber of an MBE system used in the growth of functional oxides is shown in Fig. 8. The particular example shown is a Veeco 930 (Veeco Compound Semiconductor Inc., MBE Operations, St. Paul, MN). A single-crystal substrate, heated to the desired growth temperature, is located near the center of the MBE growth chamber. Aimed at the substrate are molecular beams of the constituent elements of the functional oxide to be grown. Each molecular beam is created by a separate effusion cell, each at a different temperature to provide the desired flux of the particular element contained in a crucible within each effusion cell. Elements are used because multicomponent mixtures (especially oxides) rarely evaporate congruently.[238,239] In such

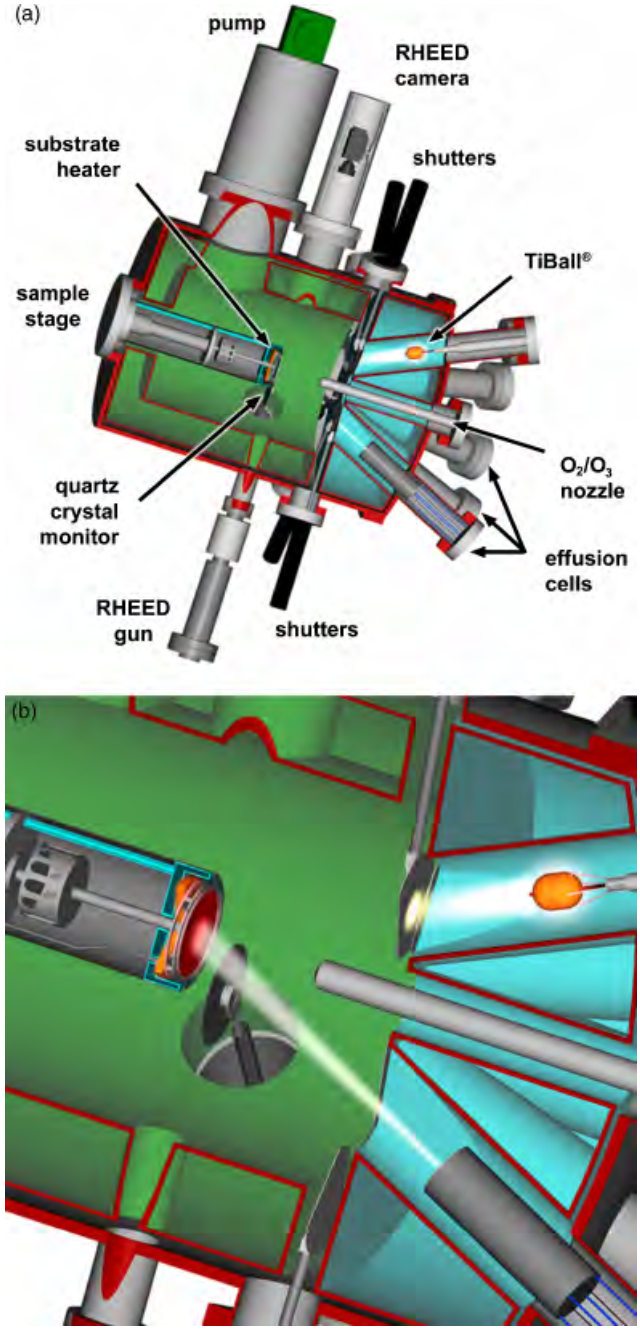


Fig. 8. A schematic diagram of the growth chamber of a molecular-beam epitaxy (MBE) system for the growth of multicomponent oxides. The growth chamber contains molecular beams (emanating from elemental sources), shutters, and ozone distillation and introduction, along with *in situ* characterization by reflection high-energy electron diffraction (RHEED), real-time spectroscopic ellipsometry (RTSE), mass spectrometry, quartz crystal microbalance (QCM), and atomic absorption spectroscopy (AA). The MBE geometry shown corresponds to a Veeco 930.

cases of incongruent evaporation, where the composition of the evaporant is not the same as its source, the composition of the source changes over time, resulting in a change in the absolute fluxes and relative concentrations of the species emitted from it. This would lead to serious composition-control issues. This problem is avoided by using elemental sources. An additional advantage of elemental sources is the completely independent control of the sequence in which the molecular beams of the elemental constituents are supplied to the substrate. The molecular beams impinge upon the substrate unless they are blocked by shutters. These shutters, which are positioned at the output end of each effusion cell, are controlled by a computer, which enables the elemental fluxes to be supplied to the substrate either at the same time (codeposition) or separately (sequential deposition). Because of the long mean free path inherent to MBE, the shutters do not need to seal tightly. Rather they only need to block the line-of-sight transfer of atoms or molecules from the source to the substrate. The chamber walls are kept cool to impede species that collide with the walls from ever reaching the substrate; ideally only the species in the molecular beams emanating from the sources with open shutters ever reach the substrate.

To oxidize the elemental species reaching the substrate to form the desired functional oxide, a molecular beam of oxidant is used. The tolerable pressure of this oxidant is limited so as not to destroy the long mean free path necessary for MBE. The maximum pressure depends on the MBE geometry, the element to be oxidized, and the oxidant species used, but oxidant pressures less than about 10^{-4} Torr are typically required for MBE.[76] While molecular oxygen has been used for the growth of oxides that are easily oxidized,[79,157,192,193,196–205,210–215,217,222–228,232,235–237] oxidants with higher activity are needed for the growth of ferroelectrics containing species that are more difficult to oxidize, e.g., bismuth-, lead-, or copper-containing oxides. For this purpose, purified ozone[4–7,76,79,110,112,114,117,119,203,206–209,216,218,230,231,234] or plasma sources[194,195,199,200,228,229,233] have been successfully used.

Inadequate composition control has been a major problem for previous oxide MBE work,[76] and the success and improvement of MBE for the controlled growth of multicomponent functional oxides is crucially dependent on accurate composition control. The use of atomic absorption spectroscopy (AA) for oxide MBE composition control has allowed fluxes to be measured with an accuracy of better than 1%.[240] The MBE system shown in Fig. 8 also contains a retractable quartz crystal microbalance to provide an absolute *in situ* flux measurement at the position of the wafer (before growth) for calibration of the fluxes before or after growth and calibration of the AA signals. The depositing fluxes of all the sources can be simultaneously monitored during growth by AA. The measured AA signal is fed into the MBE computer control system, which integrates the AA fluxes and closes the appropriate shutters after the desired dose has been delivered to the substrate. In addition, modern oxide MBE systems also contain features found in semiconductor MBE systems: *in situ* RHEED, mass spectrometry, load-locked wafer introduction, real-time spectroscopic ellipsometry,[241] substrate temperature measurement systems that utilize the temperature dependence of the bandgap of oxide substrates,[230,231,242,243] multibeam optical stress sensors (wafer curvature measurements to quantify film strain),[244,245] time-of-flight ion scattering and recoil spectroscopy,[246] and even low-energy electron microscopy.[246]

RHEED is widely used in MBE for the *in situ* characterization of the growing surface. The sensitivity of this grazing angle diffraction technique to surface structure is ideal for monitoring the evolution of growth from initial nucleation to the deposition of each subsequent layer. The formation of intermediate reaction products or impurity phases can be readily monitored and the growth conditions adjusted during growth accordingly.

The multielement deposition control, growth flexibility, and *in situ* monitoring advantages of MBE are well suited to the growth of multicomponent functional oxides that cannot be produced in single-phase form by bulk techniques, including the customized growth of new metastable materials, and heterostructures containing these phases. Other deposition techniques, in particular PLD, are, from an economic and process simplicity perspective, generally better suited than MBE to the synthesis of heterostructures made up of phases, each of which can be produced by bulk techniques in single-phase form (i.e., where the formation energy of each phase is sufficiently favored over other phases that could accommodate its composition).

III. Orientation Control

Except for the most trivial properties (e.g., density), functional properties depend in general on direction. Because of this there

exist in general optimal orientations for an epitaxial oxide film for any particular application. This might be the ones that align the spontaneous polarization of a ferroelectric material with the direction of the applied electric field from the electrodes that surround it to maximize the switchable polarization. Or it might be orientation that minimize the temperature variation of the resonant frequency of a piezoelectric oscillator. Whatever the application, the ability to control the orientation of the epitaxial film through the choice of substrate, its orientation (see, e.g., Fig. 6), and the growth conditions is a key advantage of epitaxial growth.[172,247–253] Orientation control is vital to the preparation of samples suitable for establishing the intrinsic properties of materials, especially those that cannot be prepared as bulk single crystals due to their metastability, high melting temperatures, or phase transitions that occur on cooling. When it comes to applications, techniques that can improve the functional properties of oxide films by controlling film texture through epitaxial growth on a grain-by-grain basis (local epitaxy) are also utilized, e.g., ion-beam-assisted deposition[254,255] and rolling-assisted biaxially textured substrates[256,257] for the growth of $YBa_2Cu_3O_7$ superconducting cables[258] as well as $Pb(Zr,Ti)O_3$ in FeRAMs.[259]

IV. Integration of Oxides

(1) Substrates and Substrate Preparation

The importance of the quality of the underlying crystalline template, on which an epitaxial film is grown, cannot be overemphasized. For conventional semiconductors (e.g., silicon and GaAs) highly perfect single crystals, chemical mechanical polishing, and chemical etching methods to prepare smooth and damage-free surfaces for epitaxial growth, and detailed knowledge of surface reconstructions all exist, and are a key to the success of semiconductor technology. For the growth of superlattices of functional oxides, tunneling heterostructures, etc., where the intrinsic properties of films with thickness in the nanometer range are desired, the availability of appropriate substrates and methods to prepare smooth and highly perfect surfaces on which epitaxial growth is initiated are also crucial.

For functional oxides with perovskite structures (e.g., $SrTiO_3$, $BiMnO_3$, $BiFeO_3$, $Pb(Zr,Ti)O_3$, and $PbZn_{1/3}Nb_{2/3}O_3$–$PbTiO_3$), chemically and structurally compatible perovskite substrate materials are needed. Intensive work on high-temperature superconductors stimulated the production of many perovskite single crystals[230–269] to diameters up to 4 in. as well as spawning a number of new perovskite and perovskite-related substrates.[270–273] These single-crystal perovskite and perovskite-related substrates include $YAlO_3$,[265] $LaSrAlO_4$,[270] $LaAlO_3$,[267,269] $LaSrGaO_4$,[271] $NdGaO_3$,[261,266] $(LaAlO_3)_{0.29}$–$(Sr_{1/2}Al_{1/2}TaO_3)_{0.71}$ (LSAT),[272,274] $LaGaO_3$,[260] $SrTiO_3$,[275–278] and $KTaO_3$[263]; many are produced with structural perfection rivaling that of conventional semiconductors. The pseudotetragonal or pseudocubic *a*-axis lattice spacings offered by these commercial substrates, together with the corresponding lattice spacings of several functional oxides with perovskite and perovskite-related structures, are shown in Fig. 9. As can be seen in Fig. 9, the lattice constants of the available perovskite substrates tend to be smaller than many of the ferroelectric and multiferroic[279] perovskites of current interest. This is because most of the commercially available perovskite substrates were developed for high-temperature superconductors, which typically have lattice constants in the 3.8–3.9 Å range. Rare-earth scandate ($REScO_3$) substrates have been recently developed with the larger lattice constants of ferroelectric and multiferroic perovskites in mind.[280–284]

In addition to appropriate substrate single crystals, a method to prepare substrates with a specific chemical termination of the surface is a prerequisite for atomic-layer-controlled thin film growth of epitaxial heterostructures. For example, chemical-mechanically polished (001) $SrTiO_3$ substrates display a mixture of SrO and TiO_2 terminated surfaces. Kawasaki *et al.*[285] showed that an NH_4F-buffered HF solution with controlled pH enables etching of the more basic SrO layer and leaves a completely TiO_2 terminated surface on the substrate.[285] This method of preparing a TiO_2-terminated (001) $SrTiO_3$ surface has been further perfected by Koster *et al.*[286] SrO-terminated (001) $SrTiO_3$ substrates can also be prepared.[287] A means to prepare low-defect surfaces with controlled termination has also been developed for $(001)_p$ $LaAlO_3$,[288,289] (110) $NdGaO_3$,[289] $(001)_p$ LSAT,[289] $KTaO_3$,[290] and (110) $DyScO_3$ substrates.[288] Here the *p* subscript refers to pseudocubic indices.

(2) Epitaxial Oxide Heterostructures

(A) Structural Quality of Epitaxial Films Versus Single Crystals: An example of the structural perfection possible in functional oxide films is shown in Fig. 10(a) where the rocking curve full-width at half-maximum (FWHM) of a strained $SrTiO_3$ film and typical commercial $SrTiO_3$ single crystals are compared. With rocking curve widths as narrow as 7 arc sec,[216,218,291] these epitaxial $SrTiO_3/DyScO_3$ films not only have the highest structural quality ever reported in heteroepitaxial films of any oxide grown by any technique, but they even have better structural perfection than $SrTiO_3$ single crystals.[277,278,292] Similarly, as shown in Fig. 10(b), the growth of $BaTiO_3$ films on $GdScO_3$ substrates has achieved films with narrower rocking curves than $BaTiO_3$ single crystals.[291] Epitaxial films of $BiFeO_3$,[293] $BiMnO_3$,[294] $EuTiO_3$, $(La,Sr)MnO_3$,[295] and $BaTiO_3/SrTiO_3$ superlattices[237] all with rocking curve FWHM $\leq$ 10 arc sec have been prepared by MBE on $REScO_3$ substrates. These narrow rocking curves are made possible by the excellent structural perfection of commercially available $REScO_3$ substrates[282,284]; they are grown by the Czochralski method, which is not applicable to either $SrTiO_3$ or $BaTiO_3$. The rocking curve widths of

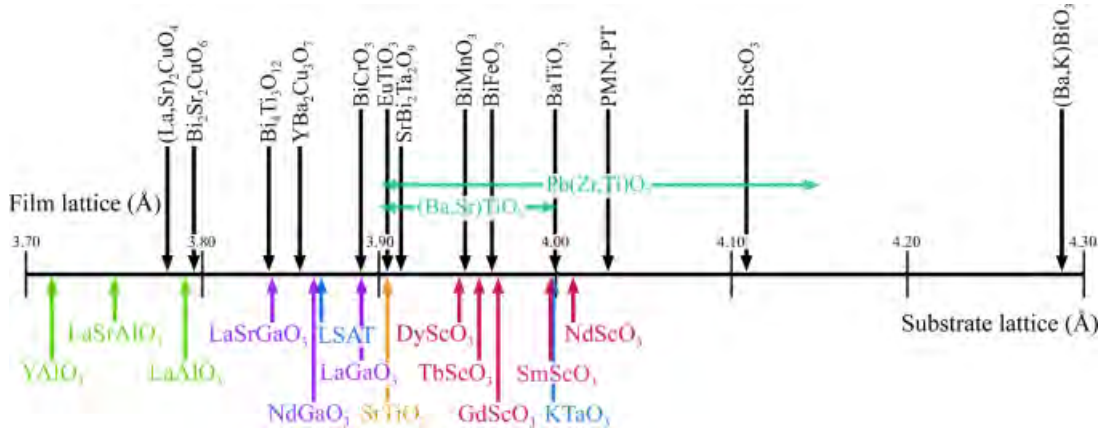


Fig. 9. A number line showing the pseudotetragonal or pseudocubic *a*-axis lattice constants in angstroms of some perovskites and perovskite-related phases of current interest (above the number line) and of some of the perovskite and perovskite-related substrates that are available commercially (below the number line). (Adapted from Schlom *et al.*[345])

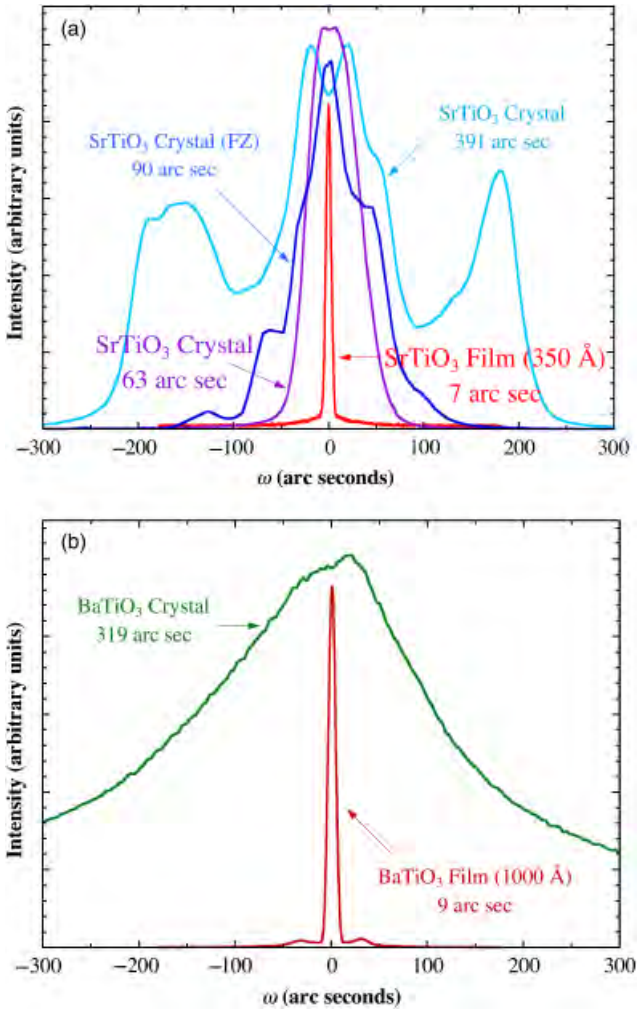


Fig. 10. (a) Rocking curves and full-width at half-maximum (FWHM) of three commercial $SrTiO_3$ single crystals (one grown by floating zone (FZ) and two by flame fusion) showing the variation in structural quality together with an epitaxial 350-Å-thick $SrTiO_3$ film grown on a (110) $DyScO_3$ substrate by molecular-beam epitaxy (MBE) at 650°C under biaxial tension of $\varepsilon_s = +1.1\%$. (b) Rocking curves and FWHM of a commercial $BaTiO_3$ single crystal and an epitaxial 1000-Å-thick $BaTiO_3$ film grown on a (110) $GdScO_3$ substrate by MBE at 650°C under biaxial compression of $\varepsilon_s = -1.0\%$. (From Schlom *et al.*[345])

these functional oxide films are within instrumental error identical to those of the substrates upon which they are grown.

(3) Epitaxial Integration of Oxides with Semiconductors

An important technological enabler is the ability to epitaxially integrate functional oxides with conventional semiconductors. Although the structural quality of films of functional oxides grown on semiconductor substrates is far from the quality of these materials grown on appropriate oxide substrates, significant improvements have been made over the last seven decades (and especially in the last two decades) because oxides were first epitaxially integrated with semiconductors.[296,297] Several routes now exist for the epitaxial integration of functional oxides with semiconductors including (001) Si,[196,204,205,210,212–215,225,226,298–306] (001) Ge,[198,204,307,308] (001) GaAs,[304,309,310] (001) InP,[311,312] and (0001) GaN.[226,313–315] Using these routes a multitude of functional oxides, with conducting top and bottom electrodes when desired, have been epitaxially integrated with semiconductor materials.[196,198,204,205,225,226,298,299,301,304,307–309,313,314,316–326] This capability could play a significant role in future hybrid devices.

Combining functional oxides with existing semiconductor technology greatly enhances the materials properties available for use in microelectronics, optoelectronics, and spintronics, by bringing new functionalities to conventional semiconductor platforms. Epitaxial integration with silicon is particularly important due to it being the backbone of modern semiconductor technology. Unfortunately, direct growth of functional oxides on silicon is frequently accompanied by extensive interdiffusion or chemical reactions that degrade the properties of the oxide, the underlying silicon, or both, and leads to electrically active defects at the semiconductor/oxide interface (D_{it}).[327–333] Such defects at the semiconductor/oxide interface preclude many potential applications, e.g., FeRAMs with a nondestructive readout based on the resistance of the semiconductor channel.[334–343] That $PbTiO_3$, $BaTiO_3$, and $SrTiO_3$ are all unstable in direct contact with silicon is evident from the chemical reactions below[344,345]:

$$3Si + PbTiO_3 \xrightarrow{\Delta G^\circ_{1000\,K} = -79.312 \frac{kJ}{mol}} PbSiO_3 + TiSi_2, \quad (1)$$

$$3Si + BaTiO_3 \xrightarrow{\Delta G^\circ_{1000\,K} = -101.802 \frac{kJ}{mol}} BaSiO_3 + TiSi_2, \quad (2)$$

and

$$3Si + SrTiO_3 \xrightarrow{\Delta G^\circ_{1000\,K} = -87.782 \frac{kJ}{mol}} SrSiO_3 + TiSi_2. \quad (3)$$

For each of these reactions $\Delta G^\circ_{1000\,K}$ is the free energy change of the system when the reaction between reactants and products, all taken to be in their standard state (the meaning of the $^\circ$ superscript), proceeds in the direction indicated at a temperature of 1000 K.[346] Note that all of the above reactions are energetically favorable ($\Delta G < 0$). This is true not only at 1000 K (a typical processing temperature), but at all temperatures between room temperature and the melting point of silicon. Consequently, the focus of a great deal of materials research has been devoted to overcoming this fundamental obstacle through the identification of compatible buffer layers for use between silicon and functional oxides.[234,344,347] Many factors must be considered in selecting materials for use as buffer layers between silicon and a particular oxide: chemical reactions, interdiffusion, crystal structure, and lattice match are some of the most important.[273,304,347,348]

The importance of avoiding interfacial chemical reactions, i.e., the need for a thermodynamically stable interface between the silicon substrate and the functional oxide or the buffer layer leading to the functional oxide is underscored by the observation that nearly all oxides that have been directly epitaxially integrated with silicon are either thermodynamically stable or possibly thermodynamically stable in contact with silicon. A periodic table depicting which elements have binary oxides that are stable or potentially stable in contact with silicon is shown in Fig. 11.[344,349] Also shown in Fig. 11 are those elements with binary oxides that have been epitaxially grown on silicon. BaO is the only binary oxide that thermodynamic data show to be unstable in contact with silicon, yet can be grown epitaxially on it at low temperatures (below ~200°C).[204,210,306] Nonetheless when BaO/Si films are heated or when growth is attempted at higher temperatures, reaction between BaO and silicon is observed as expected.[350–353]

The large difference in thermal expansion coefficient between silicon (which averages 3.8×10^{-6} K^{-1} between room temperature and 700°C)[354] and oxide ferroelectrics (typically 10×10^{-6} K^{-1}) remains a significant problem. Upon cooling after growth, the functional oxide films are in a state of biaxial tension, which can lead to cracking in thick films.[304,355]

V. Customizing Oxides at the Atomic Layer Level

(1) Metastable Phases

(A) $BiMnO_3$, Ba_2RuO_4, $LuScO_3$: Epitaxial growth can be used to create metastable phases by utilizing lattice misfit strain energies and interfacial energies to favor the

desired metastable phase over the equilibrium phase (epitaxial stabilization).[159,356–358] In contrast to bulk synthesis, in epitaxial growth, strain and interfacial energies play a significant role. Specifically, strain energies due to lattice mismatch are often sufficient to shift the energetics of phase stabilities. For sufficiently thin films, the interfacial free energy and strain free energy terms can overcome the volume free energy differences between polymorphs to make a desired metastable form have the lower total free energy (volume+interfacial+strain). Numerous examples of epitaxially stabilized phases exist in semiconductor, metal, and alkali halide systems.[182,356–359] Examples of metastable functional oxides grown by PLD and MBE include Ba_2RuO_4,[158] $BiMnO_3$,[160] and $LuScO_3$.[161] In these examples a substrate with a good lattice and structural match to the desired metastable phase is used to provide the interfacial+strain free energy bias that favors it over the equilibrium phase. Some of these metastable phases have been produced in bulk by high-pressure synthesis[158,160]; others are totally new.[161]

$BiMnO_3$ holds the record (Table I) as the material that is believed to be simultaneously ferromagnetic and ferroelectric at the highest temperature[28–30] on which a conventional polarization-electric field hysteresis loop has been reported.[28] Although it was the suggestion of possible simultaneous ferromagnetism and ferroelectricity in $BiMnO_3$ that started the recent renaissance of activity in multiferroics,[29] advances in computers and first principles methods have allowed these authors to perform more accurate calculations from which they conclude that $BiMnO_3$ is not ferroelectric.[30] At atmospheric pressure $BiMnO_3$ is unstable and phase separates to a mixture of Bi_2O_3 and $Bi_2Mn_4O_9$.[360] In bulk, $BiMnO_3$ is made in powder form at pressures of typically 60 000 atm and a temperature of 1100 K, where it is the stable phase.[361–363] But to establish the properties of $BiMnO_3$ and especially to determine whether or not it is truly ferroelectric, large single crystals or epitaxial films are desired. Using epitaxial stabilization, $BiMnO_3$ films have been prepared with several orientations.[30,160] Although the epitaxial films have the same symmetry as $BiMnO_3$ made at high pressure, they are too leaky (so far) for reliable ferroelectric measurements. Nonetheless, second harmonic generation (SHG) measurements made on metastable $BiMnO_3$ films are consistent with it being ferroelectric.[30]

Because of the unusual properties of the superconductor Sr_2RuO_4,[364] ruthenates with closely related structures are of great interest to help pin down the characteristics of Sr_2RuO_4 responsible for its unusual superconducting behavior. For example, in light of the observation that hydrostatic pressure reduces the superconducting transition temperature (T_c) of Sr_2RuO_4,[365] it is desirable to investigate the properties of Ba_2RuO_4 in which the larger Ba^{2+} ion is substituted for Sr^{2+}, expanding the structure. Utilizing such chemical substitutions to induce "chemical pressure" (negative pressure in this case) is common in superconducting research.[366] The only hitch to its use in this case is that Ba_2RuO_4 is not isostructural with Sr_2RuO_4 when synthesized at atmospheric pressure.[§§,¶¶ 367–373] In bulk, Ba_2RuO_4 powder isostructural with Sr_2RuO_4 has been synthesized using pressures of 65 000 atm.[371] As an alternative to the difficult task of growing extremely pure single crystals at 65 000 atm, epitaxial stabilization has been used to prepare the metastable K_2NiF_4-type polymorph of Ba_2RuO_4.[158]

$LuScO_3$ is another example of a new metastable phase prepared using epitaxial stabilization.[161] All attempts to prepare it using high-pressure synthesis techniques as a perovskite (isostructural to the available $REScO_3$ substrates), using pressures up to 60 000 atm, were unsuccessful.[374,375] But with an appropriate perovskite substrate, the perovskite polymorph of $LuScO_3$ was readily synthesized by epitaxial stabilization.[161]

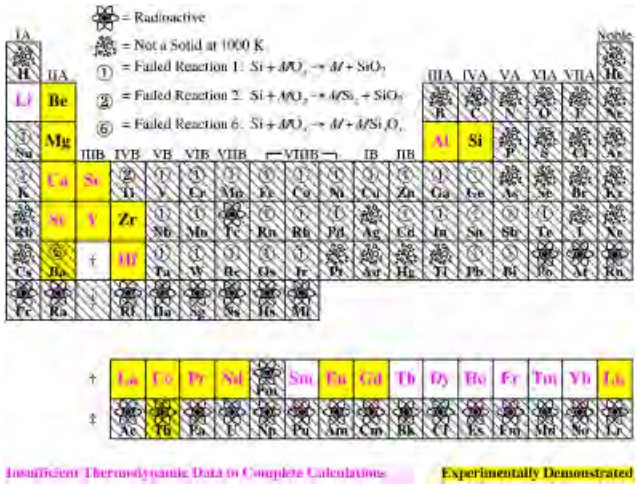


Fig. 11. Pictorial summary of which elements M have an oxide (MO_x) that may be thermodynamically stable in contact with silicon at 1000 K. Elements M having no thermodynamically stable or potentially thermodynamically stable oxide (MO_x) are shaded (hatched), and the reason for their elimination is given. Also shown are the elements M having an oxide (MO_x) that has been experimentally demonstrated to be stable in direct contact with silicon. Performing the thermodynamic analysis over the full range of temperatures for which relevant thermodynamic data are available (as much as 300–1600 K) does not alter the conclusions shown. (Adapted from Schlom and Haeni[349].)

These are just a few of many success stories in the preparation of metastable functional oxides by epitaxial stabilization.[159] An obvious approach to prepare the metastable ferroelectric ferromagnet with the highest predicted transition temperature, $FeTiO_3$ with the $LiNbO_3$ structure (see Table I) is epitaxial stabilization.[27]

(2) New Phases

(A) Ruddlesden–Popper Phases: In addition to preparing new metastable phases, MBE can be used to select a particular phase from among a homologous series of phases with nearly equal formation energies. An example is the creation of high-n Ruddlesden–Popper phases. These layered structures can be created by atomic-layer engineering using MBE. An example is the phase-pure growth of the $n = 1$–5 members of the $Sr_{n+1}Ti_nO_{3n+1}$ and $Sr_{n+1}Ru_nO_{3n+1}$ homologous series.[77–80] The crystal structures of the $n = 1$–5 members of this homologous series are shown in Fig. 3.

Complexities of the SrO–TiO_2 phase diagram have frustrated efforts to prepare bulk single crystals of any members of the $Sr_{n+1}Ti_nO_{3n+1}$ series other than the $n = \infty$ end member, $SrTiO_3$. The single-crystal growth of the $n = 1$ member of the series, Sr_2TiO_4, is complicated (if not prohibited) by a phase transition at 1550°C and a peritectic decomposition at 1860°C.[376] The $n = 2$ member, $Sr_3Ti_2O_7$, has a peritectoid decomposition at 1580°C,[376] which prohibits growth of single crystals of this phase from the melt.

Using reactive MBE the first five members of these Ruddlesden–Popper homologous series have been prepared.[77–80] X-ray diffraction (XRD) (Fig. 12) and high-resolution cross-sectional TEM images (Fig. 13) confirm that these films are epitaxially oriented and contain relatively few intergrowths. Detailed investigations using quantitative HRTEM methods reveal that the films have the expected $n = 1$–5 structures.[78] Among these films, the $n = 1$–3 thin films are nearly free of intergrowths, while the $n = 4$ and 5 thin films contain noticeably more antiphase boundaries in their perovskite sheets and intergrowth defects.[78] The $Sr_{n+1}Ru_nO_{3n+1}$ films contain fewer defects than their $Sr_{n+1}Ti_nO_{3n+1}$ counterparts and even the high-n $Sr_{n+1}Ru_nO_{3n+1}$ films are >98% phase pure.[80]

[§§]Although these authors did not determine the crystal structure of the stable form of Ba_2RuO_4 that they synthesized at atmospheric pressure and 1000°–1100°C, they did report the XRD pattern of the Ba_2RuO_4 that they made (which is completely different than the K_2NiF_4 form reported by Kafalas and Longo[367]) and described it as having "low symmetry."

[¶¶]There is one report in the literature of the synthesis of Ba_2RuO_4 with the K_2NiF_4 structure that does not mention the use of high-pressure methods: Prosychev and Shaplygin[370,371] and Gadzhiev and Shaplygin.[372,373] In addition to not stating the synthesis pressure, however, no X-ray or structural data are presented. As Kafalas and Longo[367] and Popova *et al.*[368,369] both contradict this claim and present X-ray data, their results are taken as evidence that Ba_2RuO_4 with the K_2NiF_4 structure is metastable at atmospheric (or lower) pressure and synthesis temperatures of 1000°–1100°C, as used in both Popova *et al.*[368,369] for bulk synthesis and Jia *et al.*[158] for epitaxial films.

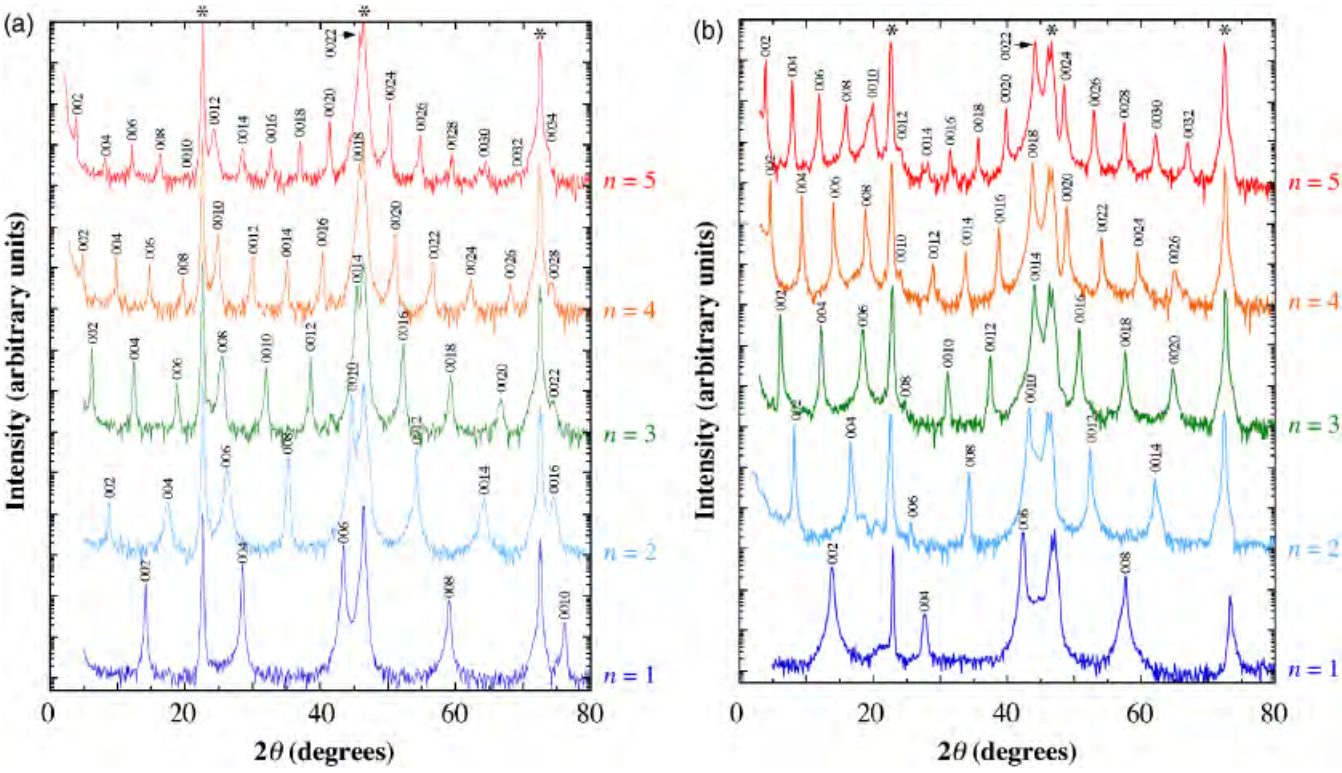


Fig. 12. θ–2θ X-ray diffraction scans of the first five members of the (a) $Sr_{n+1}Ti_nO_{3n+1}$ (reprinted from Haeni *et al.*,[77] with permission; ©2001 American Institute of Physics) and (b) $Sr_{n+1}Ru_nO_{3n+1}$ Ruddlesden–Popper homologous series (reprinted from Tian *et al.*,[80] with permission; ©2007 American Institute of Physics). Substrate peaks are labeled with an (*) and the plots are offset for clarity.

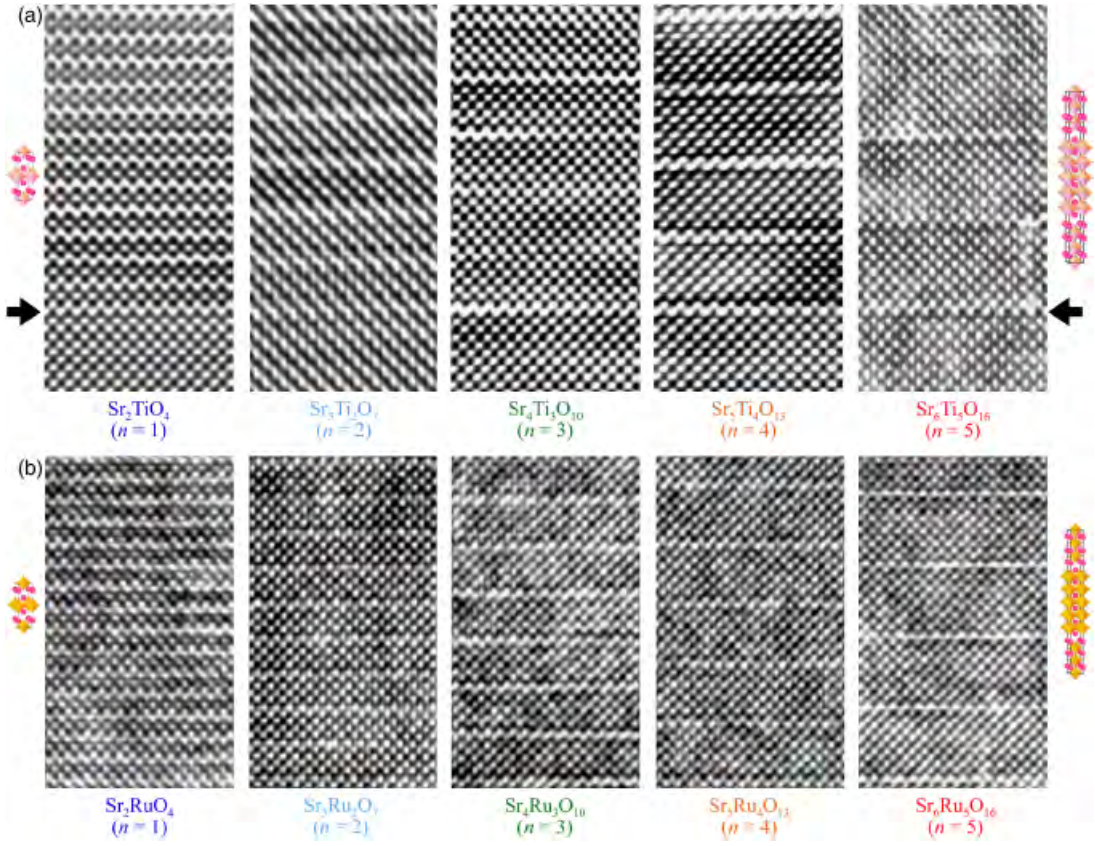


Fig. 13. High-resolution cross-sectional TEM images of the same five members of the (a) $Sr_{n+1}Ti_nO_{3n+1}$ (reprinted from Haeni *et al.*,[77] with permission; ©2001 American Institute of Physics) and (b) $Sr_{n+1}Ru_nO_{3n+1}$ Ruddlesden–Popper homologous series shown in Fig. 12 (reprinted from Tian *et al.*,[80] with permission; ©2007 American Institute of Physics). The two adjacent white rows in the images correspond to the [100] projections of the rock-salt SrO layers. Between the double SrO layers lies the [100] projection of the $SrTiO_3$ and $SrRuO_3$ perovskite sheets. The arrows in (a) indicate the position of the interface between the $Sr_{n+1}Ti_nO_{3n+1}$ films and (100) $SrTiO_3$ substrate on which they were grown.

The preparation of these materials as epitaxial films has allowed their properties to be explored. The full dielectric constant tensor of the $Sr_{n+1}Ti_nO_{3n+1}$ epitaxial films has been measured[377] as a function of frequency and temperature and compared with theory.[378] Preparation of the $n = 1$–5 $Sr_{n+1}Ru_nO_{3n+1}$ Ruddlesden–Popper phases has allowed the effects of dimensionality on the magnetic properties of these phases to be established. It is found that decreasing the dimensionality of this system, i.e., the effect of decreasing n on the magnetic properties of $Sr_{n+1}Ru_nO_{3n+1}$ phases, leads to a systematic reduction in ferromagnetism.[80] The minimum value of n for ferromagnetism is $n = 3$ ($Sr_4Ru_3O_{10}$). This corresponds to the case where at least one RuO_2 sheet in the structure is surrounded by RuO_2 sheets from above and below (see Fig. 3). For $n = 1$ and 2 $Sr_{n+1}Ru_nO_{3n+1}$ phases, no RuO_2 sheets are surrounded by RuO_2 sheets, resulting in the loss of ferromagnetism.

(B) Aurivillius Phases: Just as thin film techniques can be used to prepare and explore the properties of high-n Ruddlesden–Popper phases that cannot be realized by bulk synthesis, they can also be used to prepare high-n Aurivillius phases. An example is the $n = 7$ Aurivillius phase $Sr_4Bi_4Ti_7O_{24}$ whose XRD and cross-sectional TEM are shown in Fig. 14. This film was grown by PLD and is the highest-n Aurivillius phase ever reported.[379] As the schematic shows, this phase contains seven $SrTiO_3$ perovskite layers between Bi_2O_2 sheets.

In addition to increasing the number of perovskite layers between Bi_2O_2 layers in Aurivillius phases, different perovskite layers can be inserted between the Bi_2O_2 layers to alter the properties of the resulting phase as shown schematically in Fig. 4. This can be used, for example, as a composite approach on an atomic scale to the fabrication of a magnetic ferroelectric. Many Aurivillius phases are ferroelectric,[380] e.g., $Bi_4Ti_3O_{12}$, and one could imagine introducing a ferromagnetic perovskite, e.g., $BiMnO_3$, into $Bi_4Ti_3O_{12}$ to construct a ferromagnetic ferroelectric. Although in bulk, manganese has been found to have negligible solubility in $Bi_4Ti_3O_{12}$ itself,[381] this is not a constraint for thin film growth where the targeted phase is a superlattice composite of $BiMnO_3$ and $Bi_4Ti_3O_{12}$. A composite approach to fabricating two-phase ferroelectric–magnetic composite heterostructures[382–385] has been shown to be viable, and refining the scale of the composite down to the atomic scale is a useful goal in terms of both maximizing elastic coupling and exploring the spatial limits of this coupling. At the macroscale, 3–3 bulk composites[386] have mechanical stability issues and exhibit poor coupling.[387] At the microscale, tape-cast structures avoid mechanical issues and exhibit stronger coupling,[388] but granular orientation effects are likely to reduce mechanical coupling efficiency and to complicate analysis of strain within the crystalline lattice. At the nanoscale, thin film structures have been the most effective in producing multiferroic composite behavior. Although a 2–2 composite (stack of films on a substrate)[386] is convenient for electrical characterization, a nonferroic substrate will clamp the response.[389] A solution has been to use a ferroic substrate,[390] but the limited selection of substrate materials can be problematic, as can be domain effects in a noncentrosymmetric substrate crystal. Another solution has been to use a 1–3

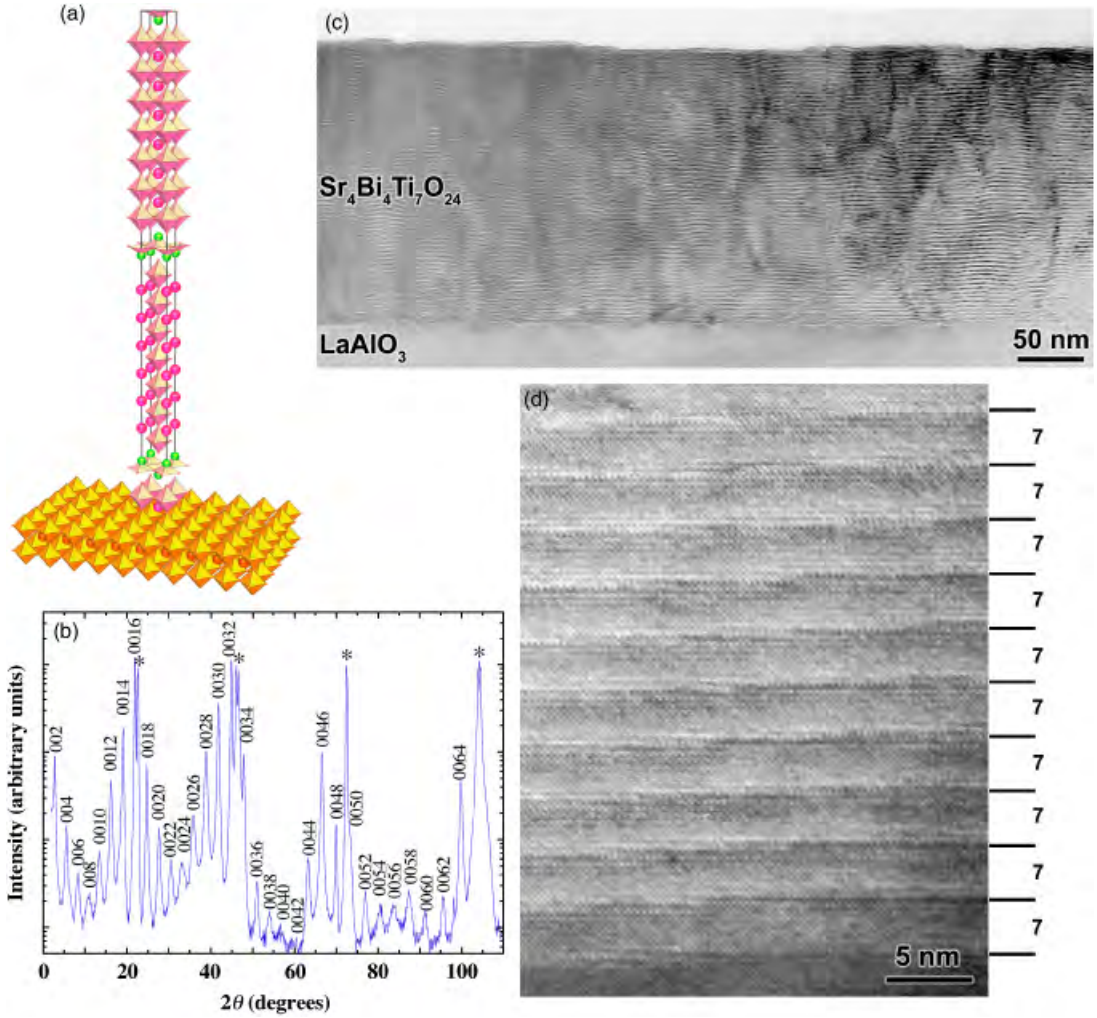


Fig. 14. An epitaxial film of the $n = 7$ Aurivillius phase $Sr_4Bi_4Ti_7O_{24}$. (a) Crystal structure showing the orientation relationship between the (001) $Sr_4Bi_4Ti_7O_{24}$ film and the (001) $LaAlO_3$ substrate, (b) θ–2θ X-ray diffraction scan in which the substrate peaks are labeled with an asterisk, and cross-sectional TEM images (c) showing the full film and (d) an HRTEM image showing the perfection of the layering.

composite system that maximizes out-of-plane mechanical coupling in a film, for example $BaTiO_3$–$CoFe_2O_4$.[391] The ultimate level for forming a composite is at the atomic or unit-cell scale. Most physical or phase separation approaches to composites are not feasible at this scale; hence, natural multiferroics, single-phase materials that can incorporate substructures of both types is a noteworthy approach. This composite strategy was recently applied using PLD to the $n = 6$ Aurivillius phase $Bi_7Mn_{3.75}Ti_{2.25}O_{21}$.[41]

VI. Thin Film Routes to Enhance the Properties of Oxides

(1) Epitaxial Strain

An advantage of using thin films as a platform to explore size effects in ferroelectrics is that they allow huge strains to be applied—strains far larger than where bulk ferroelectrics would crack.[392,393] These strains can be imparted through differences in lattice parameters and thermal expansion behavior between the film and the underlying substrate or arise from defects formed during film deposition.[393–396] Fully coherent, epitaxial films have the advantage that high densities of threading dislocations (e.g., the $\sim 10^{11}$ dislocations/cm^2 observed in partially relaxed $(Ba_xSr_{1-x})TiO_3$ films)[397,398] are avoided. Strain fields around dislocations locally alter the properties of a film, making its ferroelectric properties inhomogeneous and often degraded.[399–401] As the film is clamped to the substrate, but free in the out-of-plane direction, the effect of a biaxial strain state on properties can be dramatic.

The effects of biaxial strain and temperature on ferroelectric transitions and domain structures have been theoretically studied for a number of ferroelectrics.[291] These include $(001)_p$-oriented $PbTiO_3$,[402–406] $BaTiO_3$,[203,402,407,408] and $Pb(Zr_xTi_{1-x})O_3$,[409–411] where the subscript p refers to the pseudocubic index, and even $(001)_p$ $SrTiO_3$,[114,412–415] which is not normally ferroelectric, but can become ferroelectric when strained. Strain phase diagrams for these thin films, which graphically display the ferroelectric phase transition temperatures and domain structures as a function of strain, have been constructed using thermodynamic analysis and phase-field simulations.

The strain phase diagrams in Figs. 15 and 16, for $(001)_p$ $BaTiO_3$ and $(001)_p$ $SrTiO_3$, respectively, imply that ferroelectrics can be very sensitive to strain. These predictions imply that a biaxial tensile strain of order 1% will shift the T_C of $SrTiO_3$, a material that normally is not ferroelectric at any temperature, to the vicinity of room temperature (see Fig. 16).[114,291,412–415] Comparable shifts in transition temperature, roughly 300 K per percent biaxial strain, are expected for $BaTiO_3$ (Fig. 15)[203,291,402,407,408] and $PbTiO_3$.[291,402–406] These predictions have been borne out by experiments on strained $SrTiO_3$,[114,216,291,416–423] $PbTiO_3$,[291,424] and $BaTiO_3$ films[203,291]; large strain effects of comparable magnitude were observed earlier in $KTaO_3/KNbO_3$,[425] $SrTiO_3/SrZrO_3$,[426] and $SrTiO_3/BaZrO_3$ superlattices,[427] and strained $(Ba,Sr)TiO_3$ films.[428,429]

T_C has been determined on strained thin films using several experimental methods. The conventional method of measuring a hysteresis loop is problematic when the electrical leakage current is high, e.g., for extremely thin films where currents due to electron tunneling are high or at elevated temperatures where significant ionic conductivity can occur. It also requires electrodes, which alters the electrical boundary conditions and can impose experimental complications. Two methods that are applicable at high temperatures to extremely thin ferroelectric films have become popular. One method involves measuring the temperature dependence of the out-of-plane lattice parameter of the strained film. A kink in the out-of-plane lattice parameter occurs at T_C. Such kinks at T_C have been observed in a number of coherently strained ferroelectric films[203,424,425] and are expected from theory.[203,424,430] A second method is to use SHG. Only materials that lack inversion symmetry exhibit an SHG signal. All ferroelectrics must lack inversion symmetry, but there are many materials that lack inversion symmetry and are not ferroelectric. This makes SHG a necessary, but insufficient probe for ferroelectricity. A better test for ferroelectricity with SHG is to monitor changes in the symmetry of the SHG response that occur when external electric fields are applied; such changes imply the presence and rearrangement of ferroelectric domains.[431–435]

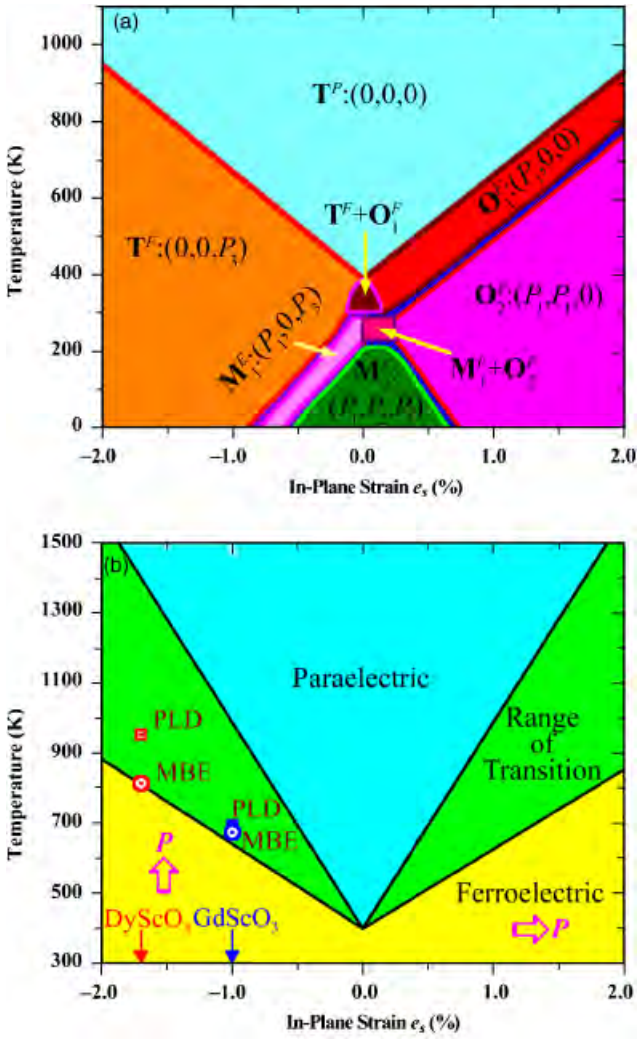


Fig. 15. (a) The strain phase diagram of $(001)_p$-oriented $BaTiO_3$ obtained from phase-field simulations. The letters **T**, **O**, and **M** used in the phase notations indicate tetragonal, orthorhombic, and monoclinic crystallographic symmetries, respectively, under a constraint. The paraelectric and ferroelectric natures of the phases are revealed by the superscript P and F, respectively. $\mathbf{M}_1^F + \mathbf{O}_2^F$ implies a mixture of $\mathbf{M}_1^F$ and $\mathbf{O}_2^F$ phases. The components of the polarization vector $\boldsymbol{P}$ corresponding to the phases (along the crystallographic directions of pseudocubic $BaTiO_3$) are indicated within the parentheses following the phase notation (reprinted from Li and Chen,[408] with permission; ©2006 American Institute of Physics). (b) A simplified strain phase diagram of $BaTiO_3$ showing the error bars of the prediction from thermodynamic analysis as well as the results on commensurately strained $BaTiO_3$ films grown on various substrates (From Choi *et al.*[203] Reprinted with permission from AAAS.)

(A) Strained $SrTiO_3$: Ferroelectricity in strained $SrTiO_3$ films has been inferred from dielectric constant versus temperature measurements,[114,216,291,421,422] the tunability of the dielectric constant through an applied electric field at temperatures just above T_C,[114,291] SHG measurements as a function of temperature and applied fields,[416,417,419,421] transmission IR measurements as a function of temperature showing changes in the soft modes,[423] piezo-force microscopy measurements as a function of temperature,[416] time-resolved confocal scanning optical microscopy,[114,418] electro-optic response measurements,[417,420] and conventional hysteresis loops as a function of

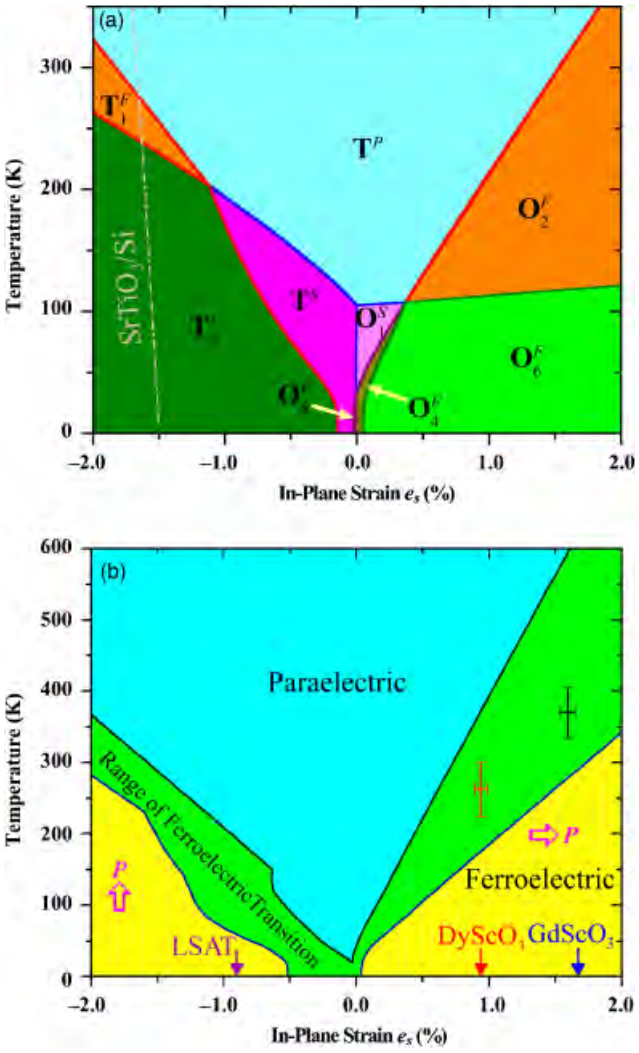


Fig. 16. (a) The strain phase diagram of $(001)_p$-oriented $SrTiO_3$ calculated assuming a single-domain state for all structural and ferroelectric phases (adapted from Li *et al.*[415]). Identical nomenclature as Fig. 15 is used to describe the crystallographic symmetry of the phases and order parameters. This diagram has only a minor difference from that presented in Pertsev *et al.*[412,413] (b) A simplified strain phase diagram of $SrTiO_3$ showing the error bars of the prediction from thermodynamic analysis as well as the results on commensurately strained $SrTiO_3$ films grown on various substrates. (Adapted from Haeni *et al.*[114])

temperature and orientation.[216,421,422] The combined experimental evidence from these methods is consistent with the predicted effect of strain on the ferroelectric transition and antiferrodistortive transition of $SrTiO_3$.[114,412–417,419,421] With strain, $SrTiO_3$ becomes a multiferroic.[416,419,421]

An overlay of the paraelectric-to-ferroelectric transition temperature found in commensurately strained $SrTiO_3$ films grown on different substrates is shown in Fig. 16(b) together with a simplified version of the prediction of strain on $SrTiO_3$ (Fig. 16(a)) that includes the error bars of the thermodynamic analysis. Thermodynamic analysis utilizes the electrostrictive coefficients and elastic constants of $SrTiO_3$. The strain phase diagram shown in Fig. 16(a) was made using a chosen set of these coefficients from the literature for measurements on $SrTiO_3$ single crystals. If instead of using a chosen set of these property coefficients, the range of reported values of the electrostrictive and elastic coefficients of $SrTiO_3$ single crystals are included in the thermodynamic analysis, the uncertainty of the predicted effect of strain on the ferroelectric transition of $SrTiO_3$ emerges. This range is explicitly shown in Fig. 16(b). As is evident, the observed effect of strain on the ferroelectric transition of $SrTiO_3$ is remarkably consistent with theory.

These strained $SrTiO_3$ films grown on (110) $DyScO_3$ substrates show a tunability of the dielectric constant at room temperature of 82% at 10 GHz and dielectric constant maxima near 20 000 at 500 Hz.[114,216,291] Strain enables room temperature access to the high and electric-field-tunable dielectric properties of $SrTiO_3$,[114,216] normally seen only at cryogenic temperatures.[436,437]

(B) Strained $BaTiO_3$: The ferroelectric properties of $BaTiO_3$ thin films have been dramatically enhanced using biaxial compressive strains up to 1.7% imposed by coherent epitaxial film growth on $REScO_3$ substrates.[203] In addition to significantly increasing the remanent polarization (P_r), T_C was increased by nearly 500°C.[203] To establish T_C, a combination of techniques was used because of the high temperatures involved and the electrical leakage of the thin $BaTiO_3$ films at high temperatures. The conventional test for ferroelectricity, hysteresis measurements, was used at room temperature to establish ferroelectricity. Then SHG and the temperature dependence of the out-of-plane lattice parameter was measured from the temperature of the hysteresis loops to where kinks were seen in the temperature-dependent XRD and SHG to establish T_C. The temperatures seen by both methods were in agreement with each other and with the predictions of thermodynamic analysis (Fig. 15).[203,291,402,407,408]

An overlay of the experimentally observed effect of strain on the ferroelectric transition of commensurately strained $BaTiO_3$ films grown on different substrates is shown in Fig. 15(b). Again the range in the theoretical predictions calculated using the range of relevant property coefficients reported for $BaTiO_3$ single crystals is shown and the agreement is again excellent. The epitaxial $BaTiO_3$ films for Fig. 15(b) were grown by both PLD and MBE. The similarity of the results by these two very different thin film preparation techniques is evidence that the observed strain effects represent the intrinsic effect of biaxial strain on $BaTiO_3$.

The first study of the effect of biaxial strain on the ferroelectric properties of $BaTiO_3$ dates more than 50 years when P. W. Forsbergh built a special fixture to biaxially strain a $BaTiO_3$ single crystal.[438] His observations of the effect of biaxial strain on $BaTiO_3$ single crystals are qualitatively similar to those observed in biaxially strained films: biaxial strain increases T_C. A notable difference, however, is that a T_C enhancement of only $\sim$10 K was observed for the strained $BaTiO_3$ single crystals before they broke.[438] A much larger strain effect can be seen in films because they can withstand far greater strains before fracture on account of their thinness,[392,393] which enables a plane stress condition to be controllably applied.

The resulting ferroelectric properties of strained $BaTiO_3$ films are comparable to those exhibited by unstrained $Pb(Zr_xTi_{1-x})O_3$, but in a more environmentally benign composition that is free of lead. These results demonstrate how strain can be used as a route to lead-free ferroelectrics for device applications, e.g., nonvolatile memories and electro-optic devices.

(C) Strained $EuTiO_3$: Strong coupling between the magnetic and ferroelectric order parameters via a spin–phonon interaction was recently predicted to occur in appropriately strained $EuTiO_3$.[439] Although unstrained $EuTiO_3$ is paraelectric and antiferromagnetic at low temperatures, first-principle calculations indicate that $(001)_p$ $EuTiO_3$ under a biaxial compressive strain of about 1% is on the verge of a transition to a ferroelectric and ferromagnetic state. For such strained $EuTiO_3$ films, the application of a modest electric field of order 10^5 V/cm is predicted to induce ferromagnetism with a magnetization of 7 μ_B per europium atom. Similarly, the application of a modest magnetic field of order 1 T is predicted to induce ferroelectricity with a spontaneous polarization of about 10 $\mu C/cm^2$.[439] The predicted coupling between the magnetic and ferroelectric order parameters in this strain-enabled material is orders of magnitude larger than any known multiferroic and a fantastic opportunity for strain tuning. Recent measurements of strained $EuTiO_3$ films show excellent agreement with theory on the dependence of the soft-mode frequencies on strain, and ferroelectricity at room

temperature has been observed in commensurately strained $EuTiO_3$ films.[423]

(2) Modulation Doping

Two-dimensional electron gases (2DEG) have been widely investigated in conventional semiconductors[440] and more recently in the II–VI semiconducting oxide ZnO.[441] But functional oxides have properties drastically different than conventional semiconductors. The perovskite $SrTiO_3$, for example, has an electron effective mass ($m_e^* = 5m_o$)[442,443] and dielectric constant ($\varepsilon_r = 20\,000$ at 4 K)[436] orders of magnitude higher than conventional semiconductors and the highest electron mobility ($\mu_n^{bulk} = 22\,000 cm^2/V\,s$ at 2 K)[11] of any known oxide. This completely different regime of semiconducting properties, coupled with the occurrence of superconductivity in appropriately electron-doped $SrTiO_3$,[444] makes the study of the behavior of a 2DEG in $SrTiO_3$ of great interest. The desire to study a 2DEG in $SrTiO_3$ was recognized long ago,[445] and was recently achieved experimentally using a $LaAlO_3/SrTiO_3$ heterostructure.[10]

Modulation doping, the dominant technique used to realize 2DEGs in conventional semiconductors,[446] is not foreign to oxides. Indeed it occurs naturally in layered functional oxides, e.g., oxide superconductors, as "charge reservoir" layers donate their carriers to surrounding CuO_2 layers.[447] In addition to the movement of charge (electronic compensation) relevant for the formation of a 2DEG, another way that an oxide may provide compensating charge is via charged defects (ionic compensation). Hence, to achieve modulation doping in oxides, one must overcome ionic compensation mechanisms. Modulation doping has begun to be applied artificially to oxides,[448] although information on the band offsets, a critical element of bandgap engineering, is generally lacking for oxide heterojunctions. This process can be engineered through the controlled growth of oxide heterostructures and due to the functional properties of oxides, the formation, study, and exploitation of 2DEGs in them is an area with tremendous potential. Exploration of the behavior of ferroelectric, magnetic, or even spin-polarized 2DEGs is within reach.

(3) Confined Thickness—Finite Size Effects in Superlattices

Thin film techniques offer powerful ways to assemble new materials, including metastable ones, that cannot be made by other methods. For single layer films, metastable materials may be accessed through epitaxial stabilization.[159,357–359] In multilayer films the tremendous difference between the diffusion coefficient at the surface of the growing thin film compared with the much lower diffusion coefficient within the bulk of the film, including buried interfaces, makes it possible to create two-phase mixtures of end member phases, even for materials that exhibit are fully miscible with each other in bulk form. This is used in the synthesis of many compound semiconductor device structures, e.g., AlAs/GaAs heterostructures, which are metastable heterostructures because their solid solution has a lower free energy over their entire composition range.[449] Similarly, heterostructures involving ferroelectrics such as $PbTiO_3/SrTiO_3$ or $BaTiO_3/SrTiO_3$ are metastable; it is energetically favorable for these oxides to dissolve into each other forming $(Pb,Sr)TiO_3$ and $(Ba,Sr)TiO_3$ solid solutions.[450,451] Although these superlattices are metastable, cation diffusion constants in oxides are sufficiently small that annealing at 1000°C for several hours is typically required before intermixing effects become discernable.[79] As can be seen in Fig. 17, the interface abruptness and layer thickness control of today's oxide superlattices involving functional oxides[79,110,113,117–126,149–157] are comparable to what has become commonplace for AlAs/GaAs superlattices grown by MBE[452] and MOCVD.[453]

Superlattices consisting of a periodic stacking of thin functional oxide layers have been predicted[454–459] or reported[113,155,235,426,427,460–462] to possess many improved physical properties over homogeneous thin films of the same compositions. Among the improved properties are reported enhancements of dielectric constants and remanent polarization in short-period two-component[235,460,461] and three-component[155] superlattices. While such reports need to be carefully evaluated considering that the movement of space charge in the superlattices can spuriously produce an apparent significant enhancement of dielectric constant,[463,464] the improved properties could result from the large lattice mismatch leading to huge strains for commensurate epitaxial growth.[155,235,460,461]

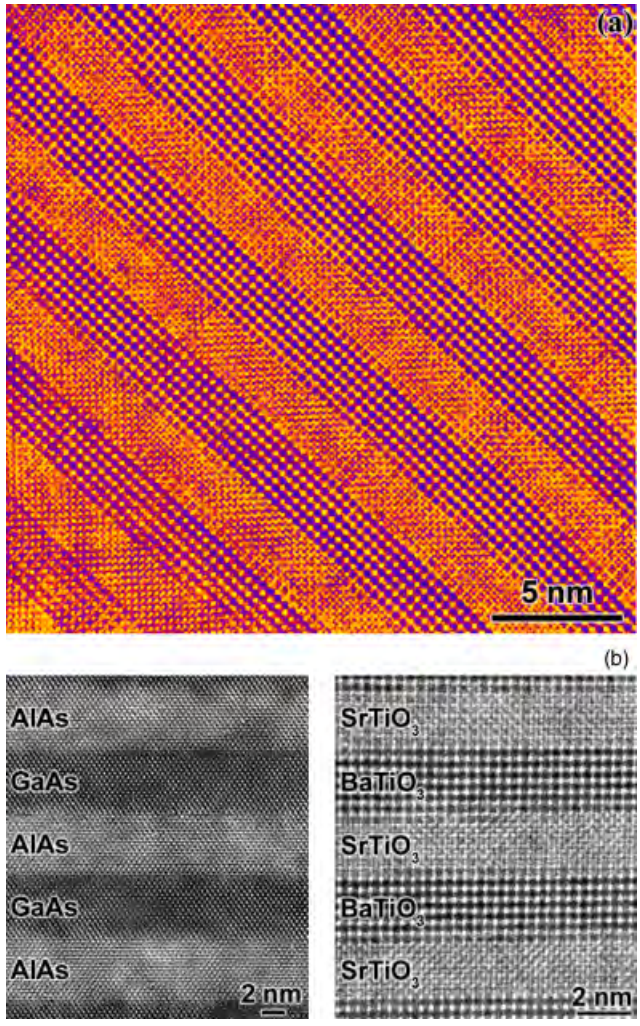


Fig. 17. (a) High-resolution TEM image of a $BaTiO_3/SrTiO_3$ superlattice grown by molecular-beam epitaxy (MBE). (b) A comparison between this same functional oxide superlattice is made with a GaAs/AlAs superlattice (reprinted from Gutakovskii *et al.*,[452] with permission; ©1995 Wiley-VCH). Both superlattices are grown by MBE.

Layered heterostructures including superlattices are just one type of epitaxial composite involving functional oxides. Epitaxial heterostructures that make use of phase separation to form connectivities beyond the 2–2 connectivity[386] of superlattices are also being explored by thin film techniques. These include 1–3 epitaxial nanocomposites involving pillars of magnetic oxides in a ferroelectric matrix[391] or pillars of ferroelectric oxides in a magnetic matrix.[465] These are being explored in ferroelectric systems to enhance the coupling between ferroelectric and magnetic oxides and thus form artificial magneto-electric heterostructures.

Artificially layered superlattices of functional oxides have enormous appeal from both a technological and a fundamental standpoint. With modern deposition techniques the degree of control that can be achieved is astounding and superlattices with essentially perfect interfaces and single-unit-cell constituent layers are well within our grasp. In terms of technology, superlattices of functional oxides with appropriate electrical and mechanical boundary conditions hold the potential of tailoring functional properties precisely for an application; there are some

indications that under certain circumstances the properties of a superlattice of two or more materials may be far superior to the parent materials from which they have been fabricated.

(A) $BaTiO_3/SrTiO_3$ Superlattices: Crucial to the enlightened (non-Edisonian) synthesis of superior materials is an understanding of how the properties of the resulting superlattice material are related to those of the parent materials used. In superlattices of ferroelectric functional oxides where the in-plane lattice parameter of all the constituents is constrained to that of the underlying substrate, the primary interaction that determines the overall properties of the superlattice seems to be electrostatic, with the principle consideration being the minimization of polarization mismatch between layers, any mismatch giving rise to very high electrostatic energy penalties.[456] This does not restrict the possibility of strain engineering, as the elastic constraint imposed by the substrate is an important factor in determining the orientation of the polarization in the superlattice layers and thus has a dramatic effect on the properties of the superlattice. Similarly, should a superlattice suffer relaxation due to misfit dislocations, changes in the orientation of the polarization can arise, as seen in the $SrTiO_3$ layers of relaxed $BaTiO_3/SrTiO_3$ superlattices.[466–468] Beyond the commercial appeal of precisely tailored exceptional materials, these systems also allow an extraordinary opportunity for the exploration of the fundamentals of ferroelectricity. In essence one can produce a system the physics of which is defined by ultra-thin components and interfaces, but with a larger total sample size allowing simple, precise characterization and a detailed exploration of the physics of ferroelectricity in ultra-thin systems.

$(001)_p$ $BaTiO_3/(001)_p$ $SrTiO_3$ superlattices have also been extensively studied to investigate size effects. In a recent study,[157] these superlattices were grown on (001) $SrTiO_3$ substrates and the $(001)_p$ $BaTiO_3$ layer in the superlattice was varied from 1 to 8 unit cells in thickness, while the $(001)_p$ $SrTiO_3$ spacer layer thickness was fixed to be either 4 unit cells or 13 unit cells thick. These superlattices can be denoted by $(BaTiO_3)_n/(SrTiO_3)_m$, where n and m refer to the thickness, in unit cells, of the $(001)_p$ $BaTiO_3$ and $(001)_p$ $SrTiO_3$ layers, respectively. The regularity of these superlattices grown by MBE is demonstrated by the presence and sharpness of all of the superlattice reflections in their XRD patterns. An example is shown in Fig. 18 of the XRD scans of $[(BaTiO_3)_n/(SrTiO_3)_m]_p$ superlattices for (a) $m = 4$ and (b) $m = 13$ $SrTiO_3$ layers separating the $BaTiO_3$ layers in the superlattices.[237] The presence of virtually all satellite peaks in these superlattices attests to their macroscopic structural perfection.

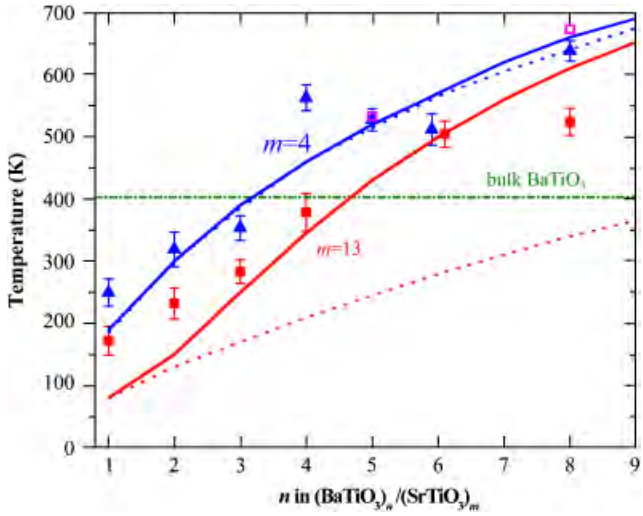


Fig. 19. The dependence of T_C on n and m in $(BaTiO_3)_n/(SrTiO_3)_m$ superlattices. The blue symbols are for $m = 4$ and red symbols are for $m = 13$. T_C was determined by UV Raman (closed symbols) and temperature-dependent X-ray diffraction (open symbols) measurements. A phase-field model with a single-domain assumption yields the dotted curves. The solid lines are from full three-dimensional phase-field calculations. The T_C of bulk unstrained $BaTiO_3$ is also shown (reprinted from Li *et al.*,[469] with permission; ©2007 American Institute of Physics).

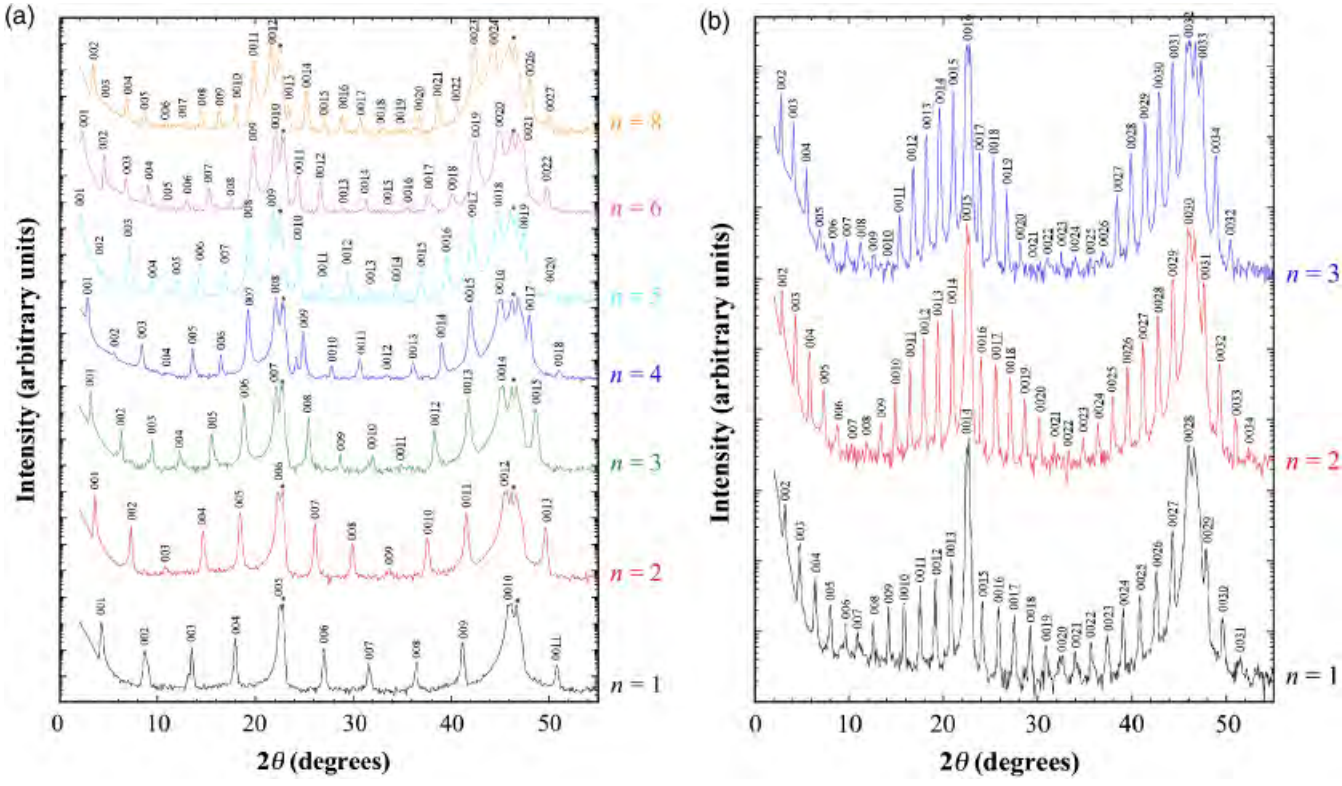


Fig. 18. θ–2θ X-ray diffraction scans of $[(BaTiO_3)_n/(SrTiO_3)_m]_p$ superlattices using CuK_α radiation for (a) $m = 4$ and $n = 1$, 2, 3, 4, 5, 6, and 8 and (b) $m = 13$ and $n = 1$, 2, and 3. Substrate peaks are marked with asterisks (*). (From Soukiassian *et al.*[237])

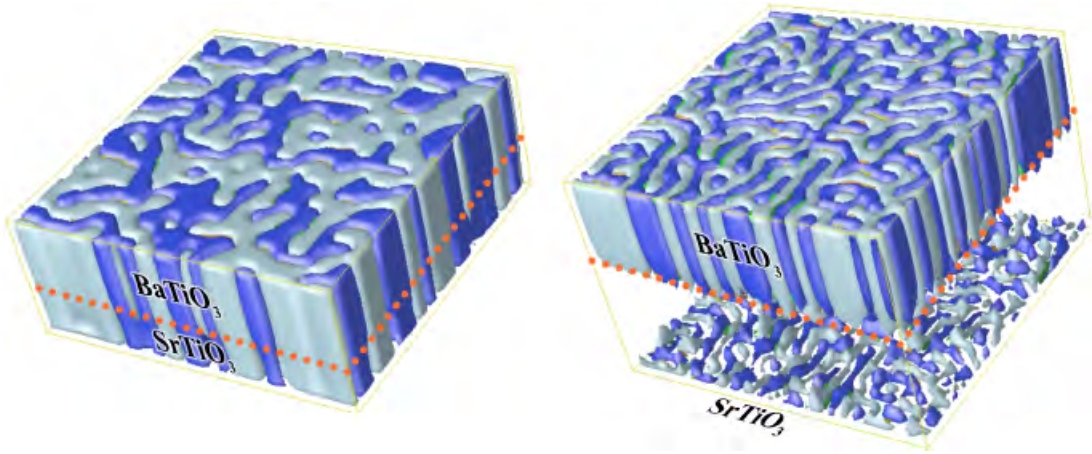


Fig. 20. Calculated multiple domain states of $[(BaTiO_3)_8/(SrTiO_3)_4]_p$ and $[(BaTiO_3)_8/(SrTiO_3)_{13}]_p$ superlattices. The blue and light-blue colors represent the two types of domains with out-of-plane polarization directions. The interfaces between them are 180° domain walls. The induced polarization domains are clearly shown in the $SrTiO_3$ layer of the $[(BaTiO_3)_8/(SrTiO_3)_4]_p$ superlattice with polarization values comparable to the $BaTiO_3$ layer. There is only a small induced polarization in the $SrTiO_3$ layer of the $[(BaTiO_3)_8/(SrTiO_3)_{13}]_p$ superlattice, and hence if we only count regions as domains if their polarization values are above a certain small threshold, there are no observed polarization domains in the $SrTiO_3$ layer for the $[(BaTiO_3)_8/(SrTiO_3)_{13}]_p$ superlattice.

Characterizing the resulting superlattices by UV Raman made it possible to confirm the prediction that the unstrained $SrTiO_3$ layer in these superlattices is polarized due to the electrostatic effect described above and also enabled the T_C of the ferroelectric superlattice to be established. T_C is shown as a function of n for $m = 4$ and $m = 13$ in Fig. 19 together with two different phase-field models of these superlattices. When the phase-field model is limited to a single-domain assumption (dashed lines in Fig. 19), the agreement between theory and experiment is good for $m = 4$, but poor for $m = 13$. Put another way, the $(001)_p$ $BaTiO_3/(001)_p$ $SrTiO_3$ superlattices show disagreement with theory when the $BaTiO_3$ layer is thinner than the $SrTiO_3$ layer, just as was seen for $(001)_p$ $PbTiO_3/(001)_p$ $SrTiO_3$ superlattices.[156] First principles calculations also operate under a single-domain assumption because of the limited number of atoms in the calculation. When a full three-dimensional phase-field simulation is performed (solid lines in Fig. 19), the agreement between theory and experiment becomes good for both $m = 4$ and $m = 13$ over the entire range. These calculations indicate that the low-energy configuration is a multiple-domain state, which allows the polarization in the $(001)_p$ $SrTiO_3$ layers to drop considerably when the $(001)_p$ $BaTiO_3$ layer is thinner than the $(001)_p$ $SrTiO_3$ layer, and results in a significant increase of T_C compared with the single-domain state.[157,469] The calculated multiple domain states of $[(BaTiO_3)_8/(SrTiO_3)_4]_p$ and $[(BaTiO_3)_8/(SrTiO_3)_{13}]_p$ superlattices are shown in Fig. 20. It is found that while the $SrTiO_3$ layer in $[(BaTiO_3)_8/(SrTiO_3)_4]_p$ is fully polarized with polarization values that are comparable to the $BaTiO_3$ layer, the polarization in $SrTiO_3$ for the $[(BaTiO_3)_8/(SrTiO_3)_{13}]_p$ superlattice is much smaller. The 180° walls between the blue domains and light-blue domains in $[(BaTiO_3)_8/(SrTiO_3)_4]_p$ display continuity from $BaTiO_3$ to $SrTiO_3$. Therefore, a single-domain assumption for the $[(BaTiO_3)_8/(SrTiO_3)_4]_p$ superlattice would be reasonable, whereas the same assumption would lead to a large error in the transition temperature for the $[(BaTiO_3)_8/(SrTiO_3)_{13}]_p$ superlattice.

VII. Outlook

The use of thin film techniques for the growth of functional oxides is still in its infancy and many hurdles remain to be overcome for these techniques to develop greater structural control at the atomic layer level, reproducibility, and ultimately precise control of electronic, optical, and spintronic properties. Nonetheless, PLD has become established as an extremely swift and nimble method for rapidly synthesizing epitaxial films and heterostructures of functional oxides. MBE is the premiere synthesis technique for the synthesis of layered oxides with customized layering control down to the atomic layer level. As the complexity and metastability of desired functional oxides and heterostructures involving functional oxides increases, the need to improve these atomic layer engineering techniques will become all the more important. Accurate composition control is key to the controlled growth of such structures and with improvements in composition control, further improvements in the perfection of the layering control attainable in the growth of functional oxides by MBE is expected.

Traditionally the search for new functional materials involves identifying bulk unstrained phases that exist within composition space. But the available configurational space for functional materials in thin films includes additional degrees of freedom: strain and dimensional confinement. Navigating this vastly increased dimensional space in search of functional materials with improved properties is a daunting task without guidance. Luckily today's multiscale modeling techniques are a tremendous aid in identifying likely locations for improved functional materials. This starts with first-principles methods[15,29,157,235,291,416,470–475] to elucidate the potential of new functional oxides including microstructures and strain states that are metastable. Continuum techniques may then be used to extend first-principles predictions to multidomain samples, finite temperatures, and include the dynamics of domain switching.[114,157,203,235,291,402,405,406,408,412,413,415,416,471] The resulting calculated phase diagrams including the effect of large strains are rich and depict how strain can greatly extend the range of functional behavior, performance, and utility beyond bulk compounds.[114,203,291,402,412,413,470,471,476] These modern theoretical methods can target specific compositions, strains, and dimensional confinement for improved functionality and have enjoyed considerable success, e.g., in the fields of ferroelectrics and multiferroics, for predicting the properties of new materials. Many of these new functional oxides are metastable and others attain their improved functionality via strain (strain-enabled). We firmly believe that a theory-driven intelligent approach is imperative for efficiently finding novel or greatly enhanced functional properties in oxides.

Acknowledgments

We gratefully acknowledge our colleagues and collaborators for sharing their insights and helping us to prepare, explore, and better understand the exciting area of functional oxide thin films. We especially thank C. Adamo, O. Auciello, M. D. Biegalski, D. H. A. Blank, I. Bozovic, C. D. Brandle, A. Bruchhausen, A. Cantarero, W. Chang, Y. B. Chen, K. J. Choi, S. Choudhury, H.-M. Christen, B.

Craigo, L. E. Cross, J. A. Eastman, J. N. Eckstein, C. B. Eom, A. Fainstein, C. J. Fennie, D. D. Fong, V. J. Fratello, P. H. Fuoss, V. Gopalan, J. H. Haeni, M. E. Hawley, T. Heeg, J. F. Ihlefeld, P. Irvin, Q. X. Jia, Y. Jia, J.C. Jiang, S. Kamba, R. S. Katiyar, X. Ke, D. M. Kim, S. W. Kirchoefer, H. Kohlstedt, A. Kumar, N. D. Lanzillotti-Kimura, J. H. Lee, J. Lettieri, J. Levy, Y. L. Li, F. Lichtenberg, Y. Liu, H. Z. Ma, J. Mannhart, L. Maritato, R. A. McKee, R. E. Newnham, K. M. Rabe, R. Ramesh, P. Reiche, J. Rodriguez-Contreras, P. Schiffer, J. Schubert, A. Sharan, V. Sherman, A. Soukiassian, N. A. Spaldin, G. B. Stephenson, S. K. Streiffer, H. P. Sun, A. K. Tagantsev, D. A. Tenne, C. D. Theis, C. Thompson, W. Tian, J.-M. Triscone, S. Trolier-McKinstry, R. Uecker, V. Vaithyanathan, A. Vasudevarao, F. J. Walker, M. Warusawithana, P. P. Wu, A. J. Ven Graitis, and X. X. Xi.

References

[1]P. A. Salvador, A.-M. Haghiri-Gosnet, B. Mercey, M. Hervieu, and B. Raveau, "Growth and Magnetoresistive Properties of $(LaMnO_3)_m(SrMnO_3)_n$ Superlattices," *Appl. Phys. Lett.*, **75** [17] 2638–40 (1999).

[2]T. Koida, M. Lippmaa, T. Fukumura, K. Itaka, Y. Matsumoto, M. Kawasaki, and H. Koinuma, "Effect of *A*-Site Cation Ordering on the Magnetoelectric Properties in $[(LaMnO_3)_m/(SrMnO_3)_m]_n$ Artificial Superlattices," *Phys. Rev. B*, **66** [14] 144418 (2002).

[3]H. Yamada, M. Kawasaki, T. Lottermoser, T. Arima, and Y. Tokura, "$LaMnO_3/SrMnO_3$ Interfaces with Coupled Charge-Spin-Orbital Modulation," *Appl. Phys. Lett.*, **89** [5] 052506 (2006).

[4]A. Bhattacharya, X. Zhai, M. Warusawithana, J. N. Eckstein, and S. D. Bader, "Signatures of Enhanced Ordering Temperatures in Digital Superlattices of $(LaMnO_3)_m/(SrMnO_3)_{2m}$," *Appl. Phys. Lett.*, **90** [22] 222503 (2007).

[5]S. J. May, A. B. Shah, S. G. E. te Velthuis, M. R. Fitzsimmons, J. M. Zuo, X. Zhai, J. N. Eckstein, S. D. Bader, and A. Bhattacharya, "Magnetically Asymmetric Interfaces in a $LaMnO_3/SrMnO_3$ Superlattice due to Structural Asymmetries," *Phys. Rev. B*, **77** [17] 174409 (2008).

[6]A. Bhattacharya, S. J. May, S. G. E. te Velthuis, M. Warusawithana, X. Zhai, B. Jiang, J.-M. Zuo, M. R. Fitzsimmons, S. D. Bader, and J. N. Eckstein, "Metal–Insulator Transition and Its Relation to Magnetic Structure in $(LaMnO_3)_{2n}/(SrMnO_3)_n$ Superlattices," *Phys. Rev. Lett.*, **100** [25] 257203 (2008).

[7]C. Adamo, X. Ke, P. Schiffer, A. Soukiassian, M. Warusawithana, L. Maritato, and D. G. Schlom, "Electrical and Magnetic Properties of $(SrMnO_3)_n/(LaMnO_3)_{2n}$ Superlattices," *Appl. Phys. Lett.*, **92** [11] 112508 (2008).

[8]A. Ohtomo and H. Y. Hwang, "A High-Mobility Electron Gas at the $LaAlO_3/SrTiO_3$ Heterointerface," *Nature*, **427** [6973] 423–6 (2004).

[9]A. Brinkman, M. Huijben, M. van Zalk, J. Huijben, U. Zeitler, J. C. Maan, W. G. van der Wiel, G. Rijnders, D. H. A. Blank, and H. Hilgenkamp, "Magnetic Effects at the Interface Between Non-Magnetic Oxides," *Nat. Mater.*, **6** [7] 493–6 (2007).

[10]N. Reyren, S. Thiel, A. D. Caviglia, L. Fitting Kourkoutis, G. Hammerl, C. Richter, C. W. Schneider, T. Kopp, A.-S. Rüetschi, D. Jaccard, M. Gabay, D. A. Muller, J.-M. Triscone, and J. Mannhart, "Superconducting Interfaces Between Insulating Oxides," *Science*, **317** [5842] 1196–9 (2007).

[11]O. N. Tufte and P. W. Chapman, "Electron Mobility in Semiconducting Strontium Titanate," *Phys. Rev.*, **155** [3] 796–802 (1967).

[12]G. Petrich, S. von Molnár, and T. Penney, "Exchange-Induced Autoionization in Eu-Rich EuO," *Phys. Rev. Lett.*, **26** [15] 885–8 (1971).

[13]A. Schilling, M. Cantoni, J. D. Guo, and H. R. Ott, "Superconductivity Above 130 K in the Hg–Ba–Ca–Cu–O System," *Nature*, **363** [6424] 56–8 (1993).

[14]I. Vrejoiu, G. Le Rhun, L. Pintilie, D. Hesse, M. Alexe, and U. Gösele, "Intrinsic Ferroelectric Properties of Strained Tetragonal $PbZr_{0.2}Ti_{0.8}O_3$ Obtained on Layer-by-Layer Grown, Defect-Free Single-Crystalline Films," *Adv. Mater.*, **18** [13] 1657–61 (2006).

[15]J. Wang, J. B. Neaton, H. Zheng, V. Nagarajan, S. B. Ogale, B. Liu, D. Viehland, V. Vaithyanathan, D. G. Schlom, U. V. Waghmare, N. A. Spaldin, K. M. Rabe, M. Wuttig, and R. Ramesh, "Epitaxial $BiFeO_3$ Multiferroic Thin Film Heterostructures," *Science*, **299** [5613] 1719–22 (2003).

[16]J. F. Li, J. Wang, M. Wuttig, R. Ramesh, N. Wang, B. Ruette, A. P. Pyatakov, A. K. Zvezdin, and D. Viehland, "Dramatically Enhanced Polarization in (001), (101), and (111) $BiFeO_3$ Thin Films due to Epitiaxial-Induced Transitions," *Appl. Phys. Lett.*, **84** [25] 5261–3 (2004).

[17]R. R. Das, D. M. Kim, S. H. Baek, C. B. Eom, F. Zavaliche, S. Y. Yang, R. Ramesh, Y. B. Chen, X. Q. Pan, X. Ke, M. S. Rzchowski, and S. K. Streiffer, "Synthesis and Ferroelectric Properties of Epitaxial $BiFeO_3$ Thin Films Grown by Sputtering," *Appl. Phys. Lett.*, **88** [24] 242904 (2006).

[18]J. Dho, X. Qi, H. Kim, J. L. MacManus-Driscoll, and M. G. Blamire, "Large Electric Polarization and Exchange Bias in Multiferroic $BiFeO_3$," *Adv. Mater.*, **18** [11] 1445–8 (2006).

[19]S. E. Park and T. R. Shrout, "Ultrahigh Strain and Piezoelectric Behavior in Relaxor Based Ferroelectric Single Crystals," *J. Appl. Phys.*, **82** [4] 1804–11 (1997).

[20]B. T. Matthias, R. M. Bozorth, and J. H. Van Fleck, "Ferromagnetic Interaction in EuO," *Phys. Rev. Lett.*, **7** [5] 160–1 (1961).

[21]A. Maignan, C. Simon, V. Caignaert, and B. Raveau, "Giant Magnetoresistance Ratios Superior to 10^{11} in Manganese Perovskites," *Solid State Commun.*, **96** [9] 623–5 (1995).

[22]R. M. Bozorth, E. F. Tilden, and A. J. Williams, "Anisotropy and Magnetostriction of Some Ferrites," *Phys. Rev.*, **99** [6] 1788–98 (1955).

[23]K. Y. Ahn and M. W. Shafer, "Relationship Between Stoichiometry and Properties of EuO Films," *J. Appl. Phys.*, **41** [3] 1260–2 (1970).

[24]R. J. Soulen Jr., J. M. Byers, M. S. Osofsky, B. Nadgorny, T. Ambrose, S. F. Cheng, P. R. Broussard, C. T. Tanaka, J. Nowak, J. S. Moodera, A. Barry, and J. M. D. Coey, "Measuring the Spin Polarization of a Metal with a Superconducting Point Contact," *Science*, **282** [5386] 85–8 (1998).

[25]A. Anguelouch, A. Gupta, G. Xiao, G. X. Miao, D. W. Abraham, S. Ingvarsson, Y. Ji, and C. L. Chien, "Properties of Epitaxial Chromium Dioxide Films Grown by Chemical Vapor Deposition Using a Liquid Precursor," *J. Appl. Phys.*, **91** [10] 7140–2 (2002).

[26]N. Ikeda, H. Ohsumi, K. Ohwada, K. Ishii, T. Inami, K. Kakurai, Y. Murakami, K. Yoshii, S. Mori, Y. Horibe, and H. Kito, "Ferroelectricity from Iron Valence Ordering in the Charge-Frustrated System $LuFe_2O_4$," *Nature*, **436** [4039] 1136–8 (2005).

[27]C. J. Fennie, "Ferroelectrically Induced Weak Ferromagnetism by Design," *Phys. Rev. Lett.*, **100** [16] 167203 (2008).

[28]A. Moreira dos Santos, S. Parashar, A. R. Raju, Y. S. Zhao, A. K. Cheetham, and C. N. R. Rao, "Evidence for the Likely Occurrence of Magnetoferroelectricity in the Simple Perovskite, $BiMnO_3$," *Solid State Commun.*, **122** [1–2] 49–52 (2002).

[29]N. A. Hill and K. M. Rabe, "First-Principles Investigation of Ferromagnetism and Ferroelectricity in Bismuth Manganite," *Phys. Rev. B*, **59** [13] 8759–69 (1999).

[30]A. Sharan, J. Lettieri, Y. Jia, W. Tian, X. Q. Pan, D. G. Schlom, and V. Gopalan, "Bismuth Manganite: A Multiferroic with a Large Nonlinear Optical Response," *Phys. Rev. B*, **69** [21] 214109 (2004).

[31]P. Baettig, R. Seshadri, and N. A. Spaldin, "Anti-Polarity in Ideal $BiMnO_3$," *J. Am. Chem. Soc.*, **129** [32] 9854–5 (2007).

[32]R. D. Shannon, "Revised Effective Ionic Radii and Systematic Studies of Interatomic Distances in Halides and Chalcogenides," *Acta Cryst. A*, **32** [5] 751–67 (1976).

[33]K.-H. Hellwege and A. M. Hellwege, *Landolt-Börnstein: Numerical Data and Functional Relationships in Science and Technology, Group III*, **Vol. 12a**, pp. 126–206. Springer-Verlag, Berlin, 1978.

[34]D. Balz and K. Plieth, "Die Struktur des Kaliumnickelfluorids, K_2NiF_4," *Z. Elektrochem.*, **59** [6] 545–51 (1955).

[35]S. N. Ruddlesden and P. Popper, "New Compounds of the K_2NiF_4 Type," *Acta Cryst.*, **10** [8] 538–9 (1957).

[36]S. N. Ruddlesden and P. Popper, "The Compound $Sr_3Ti_2O_7$ and Its Structure," *Acta Cryst.*, **11** [1] 54–5 (1958).

[37]Y. Maeno, H. Hashimoto, K. Yoshida, S. Nishizaki, T. Fujita, J. G. Bednorz, and F. Lichtenberg, "Superconductivity in a Layered Perovskite without Copper," *Nature*, **372** [6506] 532–4 (1994).

[38]A. Callaghan, C. W. Moeller, and R. Ward, "Magnetic Interactions in Ternary Ruthenium Oxides," *Inorg. Chem.*, **5** [9] 1572–6 (1966).

[39]O. Auciello, J. F. Scott, and R. Ramesh, "The Physics of Ferroelectric Memories," *Phys. Today*, **51** [7] 22–7 (1998).

[40]J. F. Scott, "Applications of Modern Ferroelectrics," *Science*, **315** [5814] 954–9 (2007).

[41]M. A. Zurbuchen, R. S. Freitas, M. J. Wilson, P. Schiffer, M. Roeckerath, J. Schubert, M. D. Biegalski, G. H. Mehta, D. J. Comstock, J. H. Lee, Y. Jia, and D. G. Schlom, "Synthesis and Characterization of an $n = 6$ Aurivillius Phase Incorporating Magnetically Active Manganese, $Bi_7(Mn,Ti)_6O_{21}$," *Appl. Phys. Lett.*, **91** [3] 033113 (2007).

[42]B. G. Hyde and S. Andersson, *Inorganic Crystal Structures*. Wiley-Interscience, New York, 1989.

[43]C. N. R. Rao and B. Raveau, *Transition Metal Oxides: Structure, Properties, and Synthesis of Ceramic Oxides*, 2nd edition, pp. 61–226. Wiley-VCH, New York, 1998.

[44]D. R. Veblen, "Polysomatism and Polysomatic Series: A Review and Applications," *Am. Mineral.*, **76** [5–6] 801–26 (1991).

[45]R. J. D. Tilley, "An Electron Microscope Study of Perovskite-Related Oxides in the Sr–Ti–O System," *J. Solid State Chem.*, **21** [4] 293–301 (1977).

[46]J. L. Hutchison, J. S. Anderson, and C. N. R. Rao, "Electron Microscopy of Ferroelectric Bismuth Oxides Containing Perovskite Layers," *Proc. R. Soc. London, Ser. A*, **355** [1682] 301–12 (1977).

[47]J. Drennan, C. P. Tavares, and B. C. H. Steele, "An Electron Microscope Investigation of Phases in the System La–Ni–O," *Mater. Res. Bull.*, **17** [5] 621–6 (1982).

[48]J. Gopalakrishnan, A. Ramanan, C. N. R. Rao, D. A. Jefferson, and D. J. Smith, "A Homologous Series of Recurrent Intergrowth Structures of the Type $Bi_4A_{m+n-2}B_{m+n}O_{3(m+n)+6}$ Formed by Oxides of the Aurivillius Family," *J. Solid State Chem.*, **55** [1] 101–5 (1984).

[49]D. A. Jefferson, M. K. Uppal, C. N. R. Rao, and D. J. Smith, "Elastic Strain at the Solid-Solid Interface in Intergrowth Structures: A Novel Example of Partial Structure Refinement by HREM," *Mater. Res. Bull.*, **19** [11] 1403–9 (1984).

[50]C. N. R. Rao and J. M. Thomas, "Intergrowth Structures: The Chemistry of Solid–Solid Interfaces," *Acc. Chem. Res.*, **18**, 113–9 (1985).

[51]R. A. Mohan Ram, L. Ganapathi, P. Ganguly, and C. N. R. Rao, "Evolution of Three-Dimensional Character across the $La_{n+1}Ni_nO_{3n+1}$ Homologous Series with Increase in *n*," *J. Solid State Chem.*, **63** [2] 139–47 (1986).

[52]J. M. Tarascon, W. R. McKinnon, P. Barboux, D. M. Hwang, B. G. Bagley, L. H. Greene, G. W. Hull, Y. LePage, N. Stoffel, and M. Giroud, "Preparation, Structure, and Properties of the Superconducting Compound Series $Bi_2Sr_2Ca_{n-1}Cu_nO_y$ with $n = 1$, 2, and 3," *Phys. Rev. B*, **38** [13] 8885–92 (1988).

[53]B. Raveau, C. Michel, and M. Hervieu, "Crystal Chemistry of Superconductive Bismuth and Thallium Cuprates"; pp. 151–7 in *Advances in Superconductivity: Proceedings of the 1st International Symposium on Superconductivity (ISS '88)*, Edited by K. Kitazawa, and T. Ishiguro. Springer-Verlag, Tokyo, 1989.

[54]W. T. Fu, H. W. Zandbergen, Q. Xu, J. M. van Ruitenbeek, L. J. de Jongh, and G. van Tendeloo, "Structural and Transport Properties of the Triple-Layer Compounds $Ba_4(Pb_{1-x}Bi_x)_3O_{10}$ $(0 \le x < 0.3)$," *Solid State Commun.*, **70** [12] 1117–21 (1989).

[55]O. Eibl, "Crystal Defects in $Bi_2Sr_2Ca_{n-1}Cu_nO_{4+2n+\delta}$ Ceramics," *Physica C*, **168** [1–2] 249–56 (1990).

[56]R. Ramesh, S. Jin, and P. Marsh, "Superconductor Defect Structure," *Nature*, **346**, 420 (1990).

[57]A. Nozaki, H. Yoshikawa, T. Wada, H. Yamauchi, and S. Tanaka, "Layered Perovskite Compounds $Sr_{n+1}V_nO_{3n+1}$ ($n = 1, 2, 3,$ and ∞)," *Phys. Rev. B*, **43** [1] 181–5 (1991).

[58]M. A. Señaris-Rodriguez, A. M. Chippindale, A. Várez, E. Morán, and M. A. Alario-Franco, "A Novel '126' Phase of the Family of $Y_2Ba_4Cu_{6+n}O_{14+n}$ High-Temperature Superconducting Materials," *Physica C*, **172** [5–6] 477–80 (1991).

[59]R. J. Cava, T. Siegrist, B. Hessen, J. J. Krajewski, W. F. Peck Jr., B. Batlogg, H. Takagi, J. V. Waszczak, L. F. Schneemeyer, and H. W. Zandbergen, "A New Homologous Series of Lanthanum Copper Oxides," *J. Solid State Chem.*, **94** [1] 170–84 (1991).

[60]K. Hawkins and T. J. White, "Defect Structure and Chemistry of $(Ca_xSr_{1-x})_{n+1}Ti_nO_{3n+1}$ Layer Perovskites," *Philos. Trans. R. Soc. London, Ser. A*, **336** [1644] 541–69 (1991).

[61]T. Williams, F. Lichtenberg, A. Reller, and G. Bednorz, "New Layered Perovskites in the Sr–Ru–O System: A Transmission Electron Microscope Study," *Mater. Res. Bull.*, **26** [8] 763–70 (1991).

[62]M. Čeh, V. Kraševec, and D. Kolar, "A Transmission Electron Microscope Study of SrO-Doped $CaTiO_3$," *J. Solid State Chem.*, **103** [1] 263–8 (1993).

[63]S. Adachi, H. Yamauchi, S. Tanaka, and N. Môri, "New Superconducting Cuprates in the Sr–Ca–Cu–O System," *Physica C*, **212** [1–2] 164–8 (1993).

[64]Z. Hiroi, M. Takano, M. Azuma, and Y. Takeda, "A New Family of Copper Oxide Superconductors $Sr_{n+1}Cu_nO_{2n+1+\delta}$ Stabilized at High Pressure," *Nature*, **364** [6435] 315–7 (1993).

[65]X.-J. Wu, S. Adachi, C.-Q. Jin, H. Yamauchi, and S. Tanaka, "Novel Homologous Series of Superconducting Copper Oxides, Cu-12(n−1)n," *Physica C*, **223** [3–4] 243–8 (1994).

[66]P. Laffez, G. Van Tendeloo, R. Seshadri, M. Hervieu, C. Martin, A. Maignan, and B. Raveau, "Microstructural and Physical Properties of Layered Manganites Oxides Related to the Magnetoresistive Perovskites," *J. Appl. Phys.*, **80** [10] 5850–6 (1996).

[67]M. A. McCoy, R. W. Grimes, and W. E. Lee, "Phase Stability and Interfacial Structures in the SrO–$SrTiO_3$ System," *Philos. Mag. A*, **75** [3] 833–46 (1997).

[68]R. Seshadri, M. Hervieu, C. Martin, A. Maignan, B. Domenges, B. Raveau, and A. N. Fitch, "Study of the Layered Magnetoresistive Perovskite $La_{1.2}Sr_{1.8}Mn_2O_7$ by High-Resolution Electron Microscopy and Synchrotron X-Ray Powder Diffraction," *Chem. Mater.*, **9** [8] 1778–87 (1997).

[69]S. D. Bader, R. M. Osgood III, D. J. Miller, J. F. Mitchell, and J. S. Jiang, "Role of Intergrowths in the Properties of Naturally Layered Manganite Single Crystals," *J. Appl. Phys.*, **83** [11] 6385–9 (1998).

[70]J. Sloan, P. D. Battle, M. A. Green, M. J. Rosseinsky, and J. F. Vente, "A HRTEM Study of the Ruddlesden-Popper Compositions $Sr_2LnMn_2O_7$ (Ln = Y, La, Nd, Eu, Ho)," *J. Solid State Chem.*, **138** [1] 135–40 (1998).

[71]K. Szot and W. Speier, "Surfaces of Reduced and Oxidized $SrTiO_3$ from Atomic Force Microscopy," *Phys. Rev. B*, **60** [8] 5909–26 (1999).

[72]G. Trolliard, N. Ténèze, P. Boullay, and D. Mercurio, "TEM Study of Cation-Deficient-Perovskite Related $A_nB_{n-1}O_{3n}$ Compounds: The Twin-Shift Option," *J. Solid State Chem.*, **177** [4–5] 1188–96 (2004).

[73]K. R. Udayakumar and A. N. Cormack, "Structural Aspects of Phase Equilibria in the Strontium-Titanium-Oxygen System," *J. Am. Ceram. Soc.*, **71**, C-469–71 (1988).

[74]K. R. Udayakumar and A. N. Cormack, "Non-Stoichiometry in Alkaline Earth Excess Alkaline Earth Titanates," *J. Phys. Chem. Solids*, **50** [1] 55–60 (1989).

[75]Y. Tokura, "Correlated-Electron Physics in Transition-Metal Oxides," *Phys. Today*, **56** [7] 50–5 (2003).

[76]D. G. Schlom and J. S. Harris Jr., "MBE Growth of High T_c Superconductors"; pp. 505–622 in *Molecular Beam Epitaxy: Applications to Key Materials*, Edited by R. F. C. Farrow. Park Ridge, Noyes, 1995.

[77]J. H. Haeni, C. D. Theis, D. G. Schlom, W. Tian, X. Q. Pan, H. Chang, I. Takeuchi, and X.-D. Xiang, "Epitaxial Growth of the First Five Members of the $Sr_{n+1}Ti_nO_{3n+1}$ Ruddlesden–Popper Homologous Series," *Appl. Phys. Lett.*, **78** [21] 3292–4 (2001).

[78]W. Tian, X. Q. Pan, J. H. Haeni, and D. G. Schlom, "Transmission Electron Microscopy Study of $n = 1$–5 $Sr_{n+1}Ti_nO_{3n+1}$ Epitaxial Thin Films," *J. Mater. Res.*, **16** [7] 2013–26 (2001).

[79]D. G. Schlom, J. H. Haeni, J. Lettieri, C. D. Theis, W. Tian, J. C. Jiang, and X. Q. Pan, "Oxide Nano-Engineering Using MBE," *Mater. Sci. Eng. B*, **87** [3] 282–91 (2001).

[80]W. Tian, J. H. Haeni, D. G. Schlom, E. Hutchinson, B. L. Sheu, M. M. Rosario, P. Schiffer, Y. Liu, M. A. Zurbuchen, and X. Q. Pan, "Epitaxial Growth and Magnetic Properties of the First Five Members of the Layered $Sr_{n+1}Ru_nO_{3n+1}$ Oxide Series," *Appl. Phys. Lett.*, **90** [2] 022507 (2007).

[81]J. G. Bednorz and K. A. Müller, "Possible High T_c Superconductivity in the Ba–La–Cu–O System," *Z. Phys. B*, **64** [2] 189–93 (1986).

[82]J. G. Bednorz, M. Takashige, and K. A. Müller, "Susceptibility Measurements Support High-T_c Superconductivity in the Ba–La–Cu–O System," *Europhys. Lett.*, **3** [3] 379–85 (1987).

[83]D. Dijkkamp, T. Venkatesan, X. D. Wu, S. A. Shaheen, N. Jisrawi, Y. H. Min-Lee, W. L. McLean, and M. Croft, "Preparation of Y–Ba–Cu Oxide Superconductor Thin Films using Pulsed Laser Evaporation from High T_c Bulk Material," *Appl. Phys. Lett.*, **51** [8] 619–21 (1987).

[84]X. D. Wu, A. Inam, T. Venkatesan, C. C. Chang, E. W. Chase, P. Barboux, J. M. Tarascon, and B. Wilkens, "Low-Temperature Preparation of High T_c Superconducting Thin Films," *Appl. Phys. Lett.*, **52** [9] 754–6 (1988).

[85]R. Ramesh, K. Luther, B. Wilkens, D. L. Hart, E. Wang, J. M. Tarascon, A. Inam, X. D. Wu, and T. Venkatesan, "Epitaxial Growth of Ferroelectric Bismuth Titanate Thin Films by Pulsed Laser Deposition," *Appl. Phys. Lett.*, **57** [15] 1505–7 (1990).

[86]D. B. Chrisey, and G. K. Hubler (ed), *Pulsed Laser Deposition of Thin Films*. Wiley, New York, 1994.

[87]T. Frey, C. C. Chi, C. C. Tsuei, T. Shaw, and F. Bozso, "Effect of Atomic Oxygen on the Initial Growth Mode in Thin Epitaxial Cuprate Films," *Phys. Rev. B*, **49** [5] 3483–91 (1994).

[88]G. Koster, G. J. H. M. Rijnders, D. H. A. Blank, and H. Rogalla, "Imposed Layer-by-Layer Growth by Pulsed Laser Interval Deposition," *Appl. Phys. Lett.*, **74** [24] 3729–31 (1999).

[89]U. Poppe, J. Schubert, R. R. Arons, W. Evers, C. H. Freiburg, W. Reichert, K. Schmidt, W. Sybertz, and K. Urban, "Direct Production of Crystalline Superconducting Thin Films of $YBa_2Cu_3O_7$ by High-Pressure Oxygen Sputtering," *Solid State Commun.*, **66** [6] 661–5 (1988).

[90]H. C. Li, G. Linker, F. Ratzel, R. Smithey, and J. Geerk, "*In Situ* Preparation of Y–Ba–Cu–O Superconducting Thin Films by Magnetron Sputtering," *Appl. Phys. Lett.*, **52** [13] 1098–100 (1988).

[91]B. Pachaly, R. Bruchhaus, D. Pitzer, H. Huber, W. Wersing, and F. Koch, "Pyroelectric Properties of Lead Titanate Thin Films deposited on Pt-Coated Si Wafers by Multi-Target Sputtering," *Integr. Ferroelectrics*, **5** [4] 333–8 (1994).

[92]P. Muralt, T. Maeder, L. Sagalowicz, S. Hiboux, S. Scalese, D. Naumovic, R. G. Agostino, N. Xanthopoulos, H. J. Mathieu, L. Patthey, and E. L. Bullock, "Texture Control of $PbTiO_3$ and $Pb(Zr,Ti)O_3$ Thin Films with TiO_2 Seeding," *J. Appl. Phys.*, **83** [7] 3835–41 (1998).

[93]T. Maeder, P. Muralt, and L. Sagalowicz, "Growth of (111)-Oriented PZT on RuO_2(100)/Pt(111) Electrodes by In-Situ Sputtering," *Thin Solid Films*, **345** [2] 300–6 (1999).

[94]N. K. Pervez, P. J. Hansen, and R. A. York, "High Tunability Barium Strontium Titanate Thin Films for RF Circuit Applications," *Appl. Phys. Lett.*, **85** [19] 4451–3 (2004).

[95]H. Koinuma, M. Kawasaki, M. Funabashi, T. Hasegawa, K. Kishio, K. Kitazawa, K. Fueki, and S. Nagata, "Preparation of Superconducting Thin Films of $(La_{1-x}Sr_x)_yCuO_{4-\delta}$ by Sputtering," *J. Appl. Phys.*, **62** [4] 1524–6 (1987).

[96]R. L. Sandstrom, W. J. Gallagher, T. R. Dinger, R. H. Koch, R. B. Laibowitz, A. W. Kleinsasser, R. J. Gambino, B. Bumble, and M. F. Chisholm, "Reliable Single-Target Sputtering Process for High-Temperature Superconducting Films and Devices," *Appl. Phys. Lett.*, **53** [5] 444–6 (1988).

[97]X. X. Xi, G. Linker, O. Meyer, E. Nold, B. Obst, F. Ratzel, R. Smithey, B. Strehlau, F. Weschenfelder, and J. Geerk, "Superconducting and Structural Properties of YBaCuO Thin Films Deposited by Inverted Cylindrical Magnetron Sputtering," *Z. Phys. B*, **74** [1] 13–9 (1989).

[98]C. B. Eom, J. Z. Sun, K. Yamamoto, A. F. Marshall, K. E. Luther, T. H. Geballe, and S. S. Laderman, "*In Situ* Grown $YBa_2Cu_3O_{7-d}$ Thin Films from Single-Target Magnetron Sputtering," *Appl. Phys. Lett.*, **55** [6] 595–7 (1989).

[99]C. B. Eom, R. B. Van Dover, J. M. Phillips, D. J. Werder, J. H. Marshall, C. H. Chen, R. J. Cava, R. M. Fleming, and D. K. Fork, "Fabrication and Properties of Epitaxial Ferroelectric Heterostructures with ($SrRuO_3$) Isotropic Metallic Oxide Electrodes," *Appl. Phys. Lett.*, **63** [18] 2570–2 (1993).

[100]C. H. Ahn, J.-M. Triscone, N. Archibald, M. Decroux, R. H. Hammond, T. H. Geballe, O. Fischer, and M. R. Beasley, "Ferroelectric Field Effect in Epitaxial Thin Film Oxide $SrCuO_2$/$Pb(Zr_{0.52}Ti_{0.48})O_3$ Heterostructures," *Science*, **269** [5222] 373–6 (1995).

[101]J.-M. Triscone, L. Frauchiger, M. Decroux, L. Mieville, O. Fischer, C. Beeli, P. Stadelmann, and G.-A. Racine, "Growth and Structural Properties of Epitaxial $Pb(Zr_xTi_{1-x})O_3$ Films and $Pb(Zr_xTi_{1-x})O_3$-Cuprate Heterostructures," *J. Appl. Phys.*, **79** [8] 4298–305 (1996).

[102]S. D. Bu, M. K. Lee, C. B. Eom, W. Tian, X. Q. Pan, S. K. Streiffer, and J. J. Krajewski, "Perovskite Phase Stabilization in Epitaxial $Pb(Mg_{1/3}Nb_{2/3})O_3$–$PbTiO_3$ Films by Deposition onto Vicinal (001) $SrTiO_3$ Substrates," *Appl. Phys. Lett.*, **79** [21] 3482–4 (2001).

[103]D. K. Lathrop, S. E. Russek, and R. A. Buhrman, "Production of $YBa_2Cu_3O_{7-y}$ Superconducting Thin Films *in Situ* by High-Pressure Reactive Evaporation and Rapid Thermal Annealing," *Appl. Phys. Lett.*, **51** [19] 1554–6 (1987).

[104]T. Terashima, K. Iijima, K. Yamamoto, Y. Bando, and H. Mazaki, "Single-Crystal $YBa_2Cu_3O_{7-x}$ Thin Films by Activated Reactive Evaporation," *Jpn. J. Appl. Phys., Part 2*, **27** [1] L91–3 (1988).

[105]P. Berberich, B. Utz, W. Prusseit, and H. Kinder, "Homogeneous High Quality $YBa_2Cu_3O_7$ Films on 3″ and 4″ Substrates," *Physica C*, **219** [3–4] 497–504 (1994).

[106]D. G. Schlom, J. N. Eckstein, E. S. Hellman, C. Webb, F. Turner, J. S. Harris Jr., M. R. Beasley, and T. H. Geballe, "Molecular Beam Epitaxy of Layered Dy–Ba–Cu–O Compounds"; pp. 197–200 in *Extended Abstracts, High-Temperature Superconductors II*, Edited by D. W. Capone II, W. H. Butler, B. Batlogg, and C. W. Chu. Materials Research Society, Pittsburgh, 1988.

[107]R. J. Spah, H. F. Hess, H. L. Stormer, A. E. White, and K. T. Short, "Parameters for *in Situ* Growth of High T_c Superconducting Thin Films Using an Oxygen Plasma Source," *Appl. Phys. Lett.*, **53** [5] 441–3 (1988).

[108]D. G. Schlom, J. N. Eckstein, E. S. Hellman, S. K. Streiffer, J. S. Harris Jr., M. R. Beasley, J. C. Bravman, T. H. Geballe, C. Webb, K. E. von Dessonneck, and F. Turner, "Molecular Beam Epitaxy of Layered Dy–Ba–Cu–O Compounds," *Appl. Phys. Lett.*, **53** [17] 1660–2 (1988).

[109]J. Kwo, M. Hong, D. J. Trevor, R. M. Fleming, A. E. White, R. C. Farrow, A. R. Kortan, and K. T. Short, "*In Situ* Epitaxial Growth of $Y_1Ba_2Cu_3O_{7-x}$ Films by Molecular Beam Epitaxy with an Activated Oxygen Source," *Appl. Phys. Lett.*, **53** [26] 2683–5 (1988).

[110]J. Eckstein and I. Bozovic, "High-Temperature Superconducting Multilayers and Heterostructures Grown by Atomic Layer-By-Layer Molecular Beam Epitaxy," *Annu. Rev. Mater. Sci.*, **25**, 679–709 (1995).

[111]I. Bozovic and D. G. Schlom, "Superconducting Thin Films: Materials, Preparation, and Properties"; pp. 8955–64 in *The Encyclopedia of Materials: Science and Technology*. Edited by K. H. J. Buschow, R. Cahn, M. C. Flemings, B.

Ilschner, E. J. Kramer, S. Mahajan, and P. Veyssiere. Pergamon, Amsterdam, 2001.
[112]C. D. Theis, J. Yeh, D. G. Schlom, M. E. Hawley, and G. W. Brown, "Adsorption-Controlled Growth of $PbTiO_3$ by Reactive Molecular Beam Epitaxy," *Thin Solid Films* **325** [1–2] 107–14 (1998).
[113]M. R. Warusawithana, E. V. Colla, J. N. Eckstein, with M. B. Weissman, "Artificial Dielectric Superlattices with Broken Inversion Symmetry," *Phys. Rev. Lett*., **90** [3] 036802 (2003).
[114]J. H. Haeni, P. Irvin, W. Chang, R. Uecker, P. Reiche, Y. L. Li, S. Choudhury, W. Tian, M. E. Hawley, B. Craigo, A. K. Tagantsev, X. Q. Pan, S. K. Streiffer, L. Q. Chen, S. W. Kirchoefer, J. Levy, and D. G. Schlom, "Room-Temperature Ferroelectricity in Strained $SrTiO_3$," *Nature*, **430** [7001] 758–61 (2004).
[115]T. Terashima, K. Shimura, Y. Bando, Y. Matsuda, A. Fujiyama, and S. Komiyama, "Superconductivity of One-Unit-Cell Thick $YBa_2Cu_3O_7$ Thin Film," *Phys. Rev. Lett*., **67** [10] 1362–5 (1991).
[116]A. Roelofs, T. Schneller, K. Szot, and R. Waser, "Piezoresponse Force Microscopy of Lead Titanate Nanograins Possibly Reaching the Limit of Ferroelectricity," *Appl. Phys. Lett*., **81** [27] 5231–3 (2002).
[117]I. Bozovic, G. Logvenov, M. A. J. Verhoeven, P. Caputo, E. Goldobin, and T. H. Geballe, "No Mixing of Superconductivity and Antiferromagnetism in a High-Temperature Superconductor," *Nature*, **422** [6934] 873–5 (2003).
[118]J.-M. Triscone, M. G. Karkut, L. Antognazza, O. Brunner, and Ø. Fischer, "Y–Ba–Cu–O/Dy–Ba–Cu–O Superlattices: A First Step Towards the Artificial Construction of High-T_c Superconductors," *Phys. Rev. Lett*., **63** [9] 1016–9 (1989).
[119]D. G. Schlom, J. N. Eckstein, I. Bozovic, Z. J. Chen, A. F. Marshall, K. E. von Dessonneck, and J. S. Harris Jr., "Molecular Beam Epitaxy—A Path to Novel High T_c Superconductors?"; pp. 234–47 in *Growth of Semiconductor Structures and High-T_c Thin Films on Semiconductors*, edited by A. Madhukar, *SPIE*, Vol. 1285. SPIE, Bellingham, 1990.
[120]D. H. Lowndes, D. P. Norton, and J. D. Budai, "Superconductivity in Nonsymmetric Epitaxial $YBa_2Cu_3O_{7-x}/PrBa_2Cu_3O_{7-x}$ Superlattices: The Superconducting Behavior of Cu–O Bilayers," *Phys. Rev. Lett*., **65** [9] 1160–3 (1990).
[121]S. J. Pennycook, M. F. Chisholm, D. E. Jesson, D. P. Norton, D. H. Lowndes, R. Feenstra, H. R. Kerchner, and J. O. Thomson, "Interdiffusion, Growth Mechanisms, and Critical Currents in $YBa_2Cu_3O_{7-x}/PrBa_2Cu_3O_{7-x}$ Superlattices," *Phys. Rev. Lett*., **67** [6] 765–8 (1991).
[122]K. Kamigaki, T. Terashima, K. Shimura, Y. Bando, and H. Terauchi, "Unit Cell-by-Unit Cell Grown $(YBa_2Cu_3O_{7-\delta})_1/(PrBa_2Cu_3O_{7-\delta})_1$ Superlattice," *Physica C*, **183** [4–6] 252–6 (1991).
[123]H. Tabata, T. Kawai, and S. Kawai, "Crystal Structure and Superconductivity of $(La,Sr)_2CuO_4/Sm_2CuO_4$ Superlattices Prepared by Excimer Laser Deposition," *Appl. Phys. Lett*., **58** [13] 1443–5 (1991).
[124]I. Bozovic and J. N. Eckstein, "Superconducting Superlattices"; pp. 99–207 in *Physical Properties of High Temperature Superconductors V*, Edited by D. M. Ginsberg. World Scientific, Singapore, 1996.
[125]J-M. Triscone and Ø. Fischer, "Superlattices of High-Temperature Superconductors: Synthetically Modulated Structures, Critical Temperatures and Vortex Dynamics," *Rep. Prog. Phys*., **60** [12] 1673–721 (1997).
[126]G. Koster, K. Verbist, G. Rijnders, H. Rogalla, G. van Tendeloo, and D. H. A. Blank, "Structure and Properties of $(Sr,Ca)CuO_2$–$BaCuO_2$ Superlattices Grown by Pulsed Laser Interval Deposition," *Physica C*, **353** [3–4] 167–83 (2001).
[127]H. Yamamoto, M. Naito, and H. Sato, "New Superconducting Cuprate Prepared by Low-Temperature Thin-Film Synthesis in a Ba–Cu–O System," *Jpn. J. Appl. Phys., Part 2*, **36** [3B] L341–4 (1997).
[128]B. S. Kwak, E. P. Boyd, and A. Erbil, "Metalorganic Chemical Vapor Deposition of $PbTiO_3$ Thin Films," *Appl. Phys. Lett*., **53** [18] 1702–4 (1988).
[129]M. Okada, S. Takai, M. Amemiya, and K. Tominaga, "Preparation of *c*-Axis-Oriented $PbTiO_3$ Thin Films by MOCVD Under Reduced Pressure," *Jpn. J. Appl. Phys., Part 1*, **28** [6] 1030–4 (1989).
[130]M. de Keijser, G. J. M. Dormans, J. F. M. Cillessen, D. M. de Leeuw, and H. W. Zandbergen, "Epitaxial $PbTiO_3$ Thin Films Grown by Organometallic Chemical Vapor Deposition," *Appl. Phys. Lett*., **58** [23] 2636–8 (1991).
[131]K. Fujii, H. Zama, and S. Oda, "Preparation of $YBa_2Cu_3O_x$ Thin Films by Layer-by-Layer Metalorganic Chemical Vapor Deposition," *Jpn. J. Appl. Phys., Part 2*, **31** [6B] L787–9 (1992).
[132]G. R. Bai, H. L. M. Chang, H. K. Kim, C. M. Foster, and D. J. Lam, "Epitaxy-Induced Phase of Near-Stoichiometry $PbTiO_3$ Films Prepared by Metalorganic Chemical Vapor Deposition," *Appl. Phys. Lett*., **61** [4] 408–10 (1992).
[133]G. J. M. Dormans, P. J. van Veldhoven, and M. de Keijser, "Composition-Controlled Growth of $PbTiO_3$ on $SrTiO_3$ by Organometallic Chemical Vapour Deposition," *J. Cryst. Growth*, **123** [3–4] 537–44 (1992).
[134]Z. Li, C. M. Foster, D. Guo, H. Zhang, G. R. Bai, P. M. Baldo, and L. E. Rehn, "Growth of High Quality Single-Domain Single-Crystal Films of $PbTiO_3$," *Appl. Phys. Lett*., **65** [9] 1106–8 (1994).
[135]M. de Keijser and G. J. M. Dormans, "Modelling of Organometallic Chemical Vapour Deposition of Lead Titanate," *J. Cryst. Growth*, **149** [3–4] 215–28 (1995).
[136]M. de Keijser and G. J. M. Dormans, "Chemical Vapor Deposition of Electroceramic Thin Films," *MRS Bull*., **21** [6] 37–43 (1996).
[137]C. M. Foster, "Chemical Vapor Deposition of Ferroelectric Thin Films;" pp. 167–97 in *Thin Film Ferroelectric Materials and Devices*, Edited by R. Ramesh. Kluwer, Boston, 1997.
[138]G.-R. Bai, I.-F. Tsu, A. Wang, C. M. Foster, C. E. Murray, and V. P. Dravid, "*In Situ* Growth of Highly Oriented $Pb(Zr_{0.5}Ti_{0.5})O_3$ Thin Films by Low-Temperature Metal-Organic Chemical Vapor Deposition," *Appl. Phys. Lett*., **72** [13] 1572–4 (1998).
[139]J. F. Roeder, T. H. Baum, S. M. Bilodeau, G. T. Stauf, C. Ragaglia, M. W. Russell, and P. C. Van Buskirk, "Liquid-Delivery MOCVD: Chemical and Process Perspectives on Ferroelectric Thin Film Growth," *Adv. Mater. Opt. Electron*., **10** [3–5] 145–54 (2000).
[140]M. V. Ramana Murty, S. K. Streiffer, G. B. Stephenson, J. A. Eastman, G.-R. Bai, A. Munkholm, O. Auciello, and C. Thompson, "*In Situ* X-Ray Scattering Study of $PbTiO_3$ Chemical-Vapor Deposition," *Appl. Phys. Lett*., **80** [10] 1809–11 (2002).
[141]K. Saito, I. Yamaji, T. Akai, M. Mitsuya, and H. Funakubo, "Quantitative Effects of Preferred Orientation and Impurity Phases on Ferroelectric Properties of $SrBi_2(Ta_{1-x}Nb_x)_2O_9$ Thin Films Measured by X-ray Diffraction Reciprocal Space Mapping," *Jpn. J. Appl. Phys., Part 1*, **42** [2A] 539–43 (2003).
[142]A. Nagai, H. Morioka, G. Asano, H. Funakubo, and A. Saiki, "Preparing $Pb(Zr,Ti)O_3$ Films Less than 100 nm Thick by Low-Temperature Metalorganic Chemical Vapor Deposition," *Appl. Phys. Lett*., **86** [14] 142906 (2005).
[143]Y. K. Kim, H. Morioka, R. Ueno, S. Yokoyama, and H. Funakubo, "Comparison of Electrical Properties of (100)/(001)-Oriented Epitaxial $Pb(Zr_{0.35},Ti_{0.65})O_3$ Thin Films with the same (001) Domain Fraction Grown on (100)Si and (100)$SrTiO_3$ Substrates," *Appl. Phys. Lett*., **86** [21] 212905 (2005).
[144]J. Fukushima, K. Kodaira, and T. Matsushita, "Preparation of Ferroelectric PZT Films by Thermal Decomposition of Organometallic Compounds," *J. Mater. Sci*., **19** [2] 595–8 (1984).
[145]K. D. Budd, S. K. Dey, and D. A. Payne, "Sol–Gel Processing of $PbTiO_3$, $PbZrO_3$, PZT, and PLZT Thin Films," *Br. Ceram. Proc*., **36**, 107–21 (1985).
[146]R. W. Schwartz, "Chemical Solution Deposition of Perovskite Thin Films," *Chem. Mater*., **9** [11] 2325–40 (1997).
[147]A. I. Kingon and S. Srinivasan, "Lead Zirconate Titanate Thin Films Directly on Copper Electrodes for Ferroelectric, Dielectric and Piezoelectric Applications," *Nat. Mater*., **4** [3] 233–7 (2005).
[148]M. D. Losego, L. H. Jimison, J. F. Ihlefeld, and J.-P. Maria, "Ferroelectric Response from Lead Zirconate Titanate Thin Films Prepared Directly on Low-Resistivity Copper Substrates," *Appl. Phys. Lett*., **86** [17] 172906 (2005).
[149]K. Iijima, T. Terashima, Y. Bando, K. Kamigaki, and H. Terauchi, "Atomic Layer Growth of Oxide Thin Films with Perovskite-Type Structure by Reactive Evaporation," *J. Appl. Phys*., **72** [7] 2840–5 (1992).
[150]H.-M. Christen, L. A. Boatner, J. D. Budai, M. F. Chisholm, L. A. Géa, P. J. Marrero, and D. P. Norton, "The Growth and Properties of Epitaxial $KNbO_3$ Thin Films and $KNbO_3/KTaO_3$ Superlattices," *Appl. Phys. Lett*., **68** [11] 1488–90 (1996).
[151]J. C. Jiang, X. Q. Pan, W. Tian, C. D. Theis, and D. G. Schlom, "Abrupt $PbTiO_3/SrTiO_3$ Superlattices Grown by Reactive Molecular Beam Epitaxy," *Appl. Phys. Lett*., **74** [19] 2851–3 (1999).
[152]A. Ohtomo, D. A. Muller, J. L. Grazul, and H. Y. Hwang, "Artificial Charge-Modulation in Atomic-Scale Perovskite Titanate Superlattices," *Nature*, **419** [6905] 378–80 (2002).
[153]D. A. Muller, N. Nakagawa, A. Ohtomo, J. L. Grazul, and H. Y. Hwang, "Atomic-Scale Imaging of Nanoengineered Oxygen Vacancy Profiles in $SrTiO_3$," *Nature*, **430** [7000] 657–61 (2004).
[154]C. H. Ahn, K. M. Rabe, and J.-M. Triscone, "Ferroelectricity at the Nanoscale: Local Polarization in Oxide Thin Films and Heterostructures," *Science*, **303** [5657] 488–91 (2004).
[155]H. N. Lee, H. M. Christen, M. F. Chisholm, C. M. Rouleau, and D. H. Lowndes, "Strong Polarization Enhancement in Asymmetric Three-Component Ferroelectric Superlattices," *Nature*, **433** [7024] 395–9 (2005).
[156]M. Dawber, C. Lichtensteiger, M. Cantoni, M. Veithen, P. Ghosez, K. Johnston, K. M. Rabe, and J.-M. Triscone, "Unusual Behavior of the Ferroelectric Polarization in $PbTiO_3/SrTiO_3$ Superlattices," *Phys. Rev. Lett*., **95** [17] 177601 (2005).
[157]D. A. Tenne, A. Bruchhausen, N. D. Lanzillotti-Kimura, A. Fainstein, R. S. Katiyar, A. Cantarero, A. Soukiassian, V. Vaithyanathan, J. H. Haeni, W. Tian, D. G. Schlom, K. J. Choi, D. M. Kim, C. B. Eom, H. P. Sun, X. Q. Pan, Y. L. Li, L. Q. Chen, Q. X. Jia, S. M. Nakhmanson, K. M. Rabe, and X. X. Xi, "Probing Nanoscale Ferroelectricity by Ultraviolet Raman Spectroscopy," *Science*, **313** [5793] 1614–6 (2006).
[158]Y. Jia, M. A. Zurbuchen, S. Wozniak, A. H. Carim, D. G. Schlom, L.-N. Zou, S. Briczinski, and Y. Liu, "Epitaxial Growth of Metastable Ba_2RuO_4 Films with the K_2NiF_4 Structure," *Appl. Phys. Lett*., **74** [25] 3830–2 (1999).
[159]O. Y. Gorbenko, S. V. Samoilenkov, I. E. Graboy, and A. R. Kaul, "Epitaxial Stabilization of Oxides in Thin Films," *Chem. Mater*., **14** [10] 4026–43 (2002).
[160]A. F. Moreira dos Santos, A. K. Cheetham, W. Tian, X. Q. Pan, Y. Jia, N. J. Murphy, J. Lettieri, and D. G. Schlom, "Epitaxial Growth and Properties of Metastable $BiMnO_3$ Thin Films," *Appl. Phys. Lett*., **84** [1] 91–3 (2004).
[161]T. Heeg, M. Roeckerath, J. Schubert, W. Zander, C. Buchal, H. Y. Chen, C. L. Jia, Y. Jia, C. Adamo, and D. G. Schlom, "Epitaxially Stabilized Growth of Orthorhombic $LuScO_3$ Thin Films," *Appl. Phys. Lett*., **90** [19] 192901 (2007).
[162]G. K. Hubler (ed), "Pulsed Laser Deposition," *MRS Bull*., **17** [2] 26–9 (1992).
[163]J. Cheung and J. Horwitz, "Pulsed Laser Deposition History and Laser–Target Interactions," *MRS Bull*., **17** [2] 30–6 (1992).
[164]D. B. Chrisey and A. Inam, "Pulsed Laser Deposition of High Tc Superconducting Thin Films for Electronic Device Applications," *MRS Bull*., **17** [2] 37–43 (1992).
[165]T. Venkatesan, X. D. Wu, R. Muenchausen, and A. Pique, "Pulsed Laser Deposition: Future Directions," *MRS Bull*., **17** [2] 54–8 (1992).
[166]K. -H. Hellwege, and A. M. Hellwege (eds), *Landolt-Börnstein: Numerical Data and Functional Relationships in Science and Technology, Part a*, **Vol. 16**, p. 233. Springer-Verlag, Berlin, 1981.
[167]J. Lettieri, Y. Jia, M. Urbanik, C. I. Weber, J-P. Maria, D. G. Schlom, H. Li, R. Ramesh, R. Uecker, and P. Reiche, "Epitaxial Growth of (001)-Oriented and (110)-Oriented $SrBi_2Ta_2O_9$ Thin Films," *Appl. Phys. Lett*., **73** [20] 2923–5 (1998).
[168]J. Lettieri, M. A. Zurbuchen, Y. Jia, D. G. Schlom, S. K. Streiffer, and M. E. Hawley, "Epitaxial Growth of $SrBi_2Nb_2O_9$ on (110) $SrTiO_3$ and the Establishment of a Lower Bound on the Spontaneous Polarization of $SrBi_2Nb_2O_9$," *Appl. Phys. Lett*., **77** [19] 3090–2 (2000).

[169]H. L. Kao, J. Kwo, R. M. Fleming, M. Hong, and J. P. Mannaerts, "*In Situ* Growth and Properties of Single-Crystalline-Like $La_{2-x}Sr_xCuO_4$ Epitaxial Films by Off-Axis Sputtering," *Appl. Phys. Lett*., **59** [21] 2748–50 (1991).
[170]O. Wada, K. Kuroda, J. Tanimura, M. Kataoka, K. Kojima, T. Takami, K. Hamanaka, and T. Ogama, "Defence of Crystal Orientation of BiSrCaCuO Thin Films on Off-Angles of Vicinal $SrTiO_3$ (110) Surfaces," *Jpn. J. Appl. Phys*., **30** [11A] L1881–3 (1991).
[171]J. Tanimura, K. Kuroda, M. Kataoka, O. Wada, T. Takami, K. Kojima, and T. Ogama, "(01*n*)-Oriented BiSrCaCuO Thin Films Formed on CeO_2 Buffer Layers," *Jpn. J. Appl. Phys*., **32** [2B] L254–6 (1993).
[172]J. Lettieri, M. A. Zurbuchen, Y. Jia, D. G. Schlom, S. K. Streiffer, and M. E. Hawley, "Epitaxial Growth of Non-*c*-Oriented $SrBi_2Nb_2O_9$ on (111) $SrTiO_3$," *Appl. Phys. Lett*., **76** [20] 2937–9 (2000).
[173]M. A. Zurbuchen, J. Lettieri, Y. Jia, D. G. Schlom, S. K. Streiffer, and M. E. Hawley, "Transmission Electron Microscopy Study of (103)-Oriented Epitaxial $SrBi_2Nb_2O_9$ Films Grown on (111) $SrTiO_3$ and (111) $SrRuO_3$/(111) $SrTiO_3$," *J. Mater. Res*., **16** [2] 489–502 (2001).
[174]M. Kitabatake, P. Fons, and J. E. Greene, "Molecular Dynamics Simulations of Low-Energy Particle Bombardment Effects During Vapor-Phase Crystal Growth: 10 eV Si Atoms Incident on Si(001)2×1 Surfaces," *J. Vac. Sci. Technol. A*, **8** [5] 3726–35 (1990).
[175]M. Kitabatake and J. E. Greene, "Molecular Dynamics and Quasidynamics Simulations of Low-Energy Particle Bombardment Effects During Vapor-Phase Crystal Growth: Production and Annihilation of Defects Due to 50 eV Si Incident on (2×1)-Terminated Si(001)," *J. Appl. Phys*., **73** [7] 3183–94 (1993).
[176]E. J. Tarsa, E. A. Hachfeld, F. T. Quinlan, J. S. Speck, and M. Eddy, "Growth-Related Stress and Surface Morphology in Homoepitaxial $SrTiO_3$ Films," *Appl. Phys. Lett*., **68** [4] 490–2 (1996).
[177]J.-P. Maria, S. Trolier-McKinstry, D. G. Schlom, M. E. Hawley, and G. W. Brown, "The Influence of Energetic Bombardment on the Structure and Properties of Epitaxial $SrRuO_3$ Thin Films Grown by Pulsed Laser Deposition," *J. Appl. Phys*., **83** [8] 4373–9 (1998).
[178]T. Ohnishi, M. Lippmaa, T. Yamamoto, S. Meguro, and H. Koinuma, "Improved Stoichiometry and Misfit Control in Perovskite Thin Film Formation at a Critical Fluence by Pulsed Laser Deposition," *Appl. Phys. Lett*., **87** [24] 2419191 (2005).
[179]T. Ohnishi, K. Shibuya, T. Yamamoto, and M. Lippmaa, "Defects and Transport in Complex Oxide Thin Films," *J. Appl. Phys*., **103** [10] 103703. (2008).
[180]H. Karl and B. Stritzker, "Reflection High-Energy Electron Diffraction Oscillations Modulated by Laser-Pulse Deposited $YBa_2Cu_3O_{7-x}$," *Phys. Rev. Lett*., **69** [20] 2939–42 (1992).
[181]G. J. H. M. Rijnders, A. G. Koster, D. H. A. Blank, and H. Rogalla, "*In Situ* Monitoring During Pulsed Laser Deposition of Complex Oxides Using Reflection High Energy Electron Diffraction Under High Oxygen Pressure," *Appl. Phys. Lett*., **70** [14] 1888–90 (1997).
[182]M. H. Yang and C. P. Flynn, "Growth of Alkali Halides from Molecular Beams: Global Growth Characteristics," *Phys. Rev. Lett*., **62** [21] 2476–9 (1989).
[183]S. Yadavalli, M. H. Yang, and C. P. Flynn, "Low-Temperature Growth of MgO by Molecular-Beam Epitaxy," *Phys. Rev. B*, **41** [11] 7961–3 (1990).
[184]A. Y. Cho and J. R. Arthur, "Molecular Beam Epitaxy," *Progress in Solid-State Chemistry*, **10** [3] 157–91 (1975).
[185]R. F. C. Farrow (ed), *Molecular Beam Epitaxy: Applications to Key Materials*. Noyes, Park Ridge, 1995.
[186]M. A. Herman and H. Sitter, *Molecular Beam Epitaxy: Fundamentals and Current Status*, 2nd edition, Springer-Verlag, Berlin, 1996.
[187]S. Yoshida, "Reactive Molecular Beam Epitaxy"; pp. 287–316 in *Critical Reviews™ in Solid State and Materials Sciences*, **Vol. 11**, Edited by D. E. Schuele, and R. W. Hoffman. CRC Press, Boca Raton, FL, 1984.
[188]K. Iijima, T. Terashima, K. Yamamoto, K. Hirata, and Y. Bando, "Preparation of Ferroelectric $BaTiO_3$ Thin Films by Activated Reactive Evaporation," *Appl. Phys. Lett*., **56** [6] 527–9 (1990).
[189]T. Sakamoto, H. Funabashi, K. Ohta, T. Nakagawa, N. J. Kawai, T. Kojima, and Y. Bando, "Well Defined Superlattice Structures Made by Phase-Locked Epitaxy Using RHEED Intensity Oscillations," *Superlattices Microstruct*., **1** [4] 347–52 (1985).
[190]A. C. Gossard, P. M. Petroff, W. Weigmann, R. Dingle, and A. Savage, "Epitaxial Structures with Alternate-Atomic-Layer Composition Modulation," *Appl. Phys. Lett*., **29** [6] 323–5 (1976).
[191]A. Y. Cho, "Molecular Beam Epitaxy from Research to Manufacturing," *MRS Bull*., **20** [4] 21–8 (1995).
[192]R. A. Betts and C. W. Pitt, "Growth of Thin-Film Lithium Niobate by Molecular Beam Epitaxy," *Electron. Lett*., **21** [21] 960–2 (1985).
[193]M. Petrucci, C. W. Pitt, and P. J. Dobson, "RHEED Studies on *z*-Cut $LiNbO_3$," *Electron. Lett*., **22** [18] 954–6 (1986).
[194]Z. Sitar, F. Gitmans, W. Liu, and P. Gunter, "Homo and Heteroepitaxial Growth of $LiTaO_3$ and $LiNbO_3$ by MBE"; pp. 255–60 in *Epitaxial Oxide Thin Films II*, **Vol. 401**, Edited by J. S. Speck, D. K. Fork, R. M. Wolf, and T. Shiosaki. Materials Research Society, Pittsburgh, 1996.
[195]W. A. Doolittle, A. G. Carver, and W. Henderson, "Molecular Beam Epitaxy of Complex Metal-Oxides: Where Have We Come, Where Are We Going, and How Are We Going to Get There," *J. Vac. Sci. Technol. B*, **23** [3] 1272–6 (2005).
[196]R. A. McKee, F. J. Walker, J. R. Conner, E. D. Specht, and D. E. Zelmon, "Molecular Beam Epitaxy Growth of Epitaxial Barium Silicide, Barium Oxide, and Barium Titanate on Silicon," *Appl. Phys. Lett*., **59** [7] 782–4 (1991).
[197]R. A. McKee, F. J. Walker, E. D. Specht, G. E. Jellison Jr., and L. A. Boatner, "Interface Stability and the Growth of Optical Quality Perovskites on MgO," *Phys. Rev. Lett*., **72** [17] 2741–4 (1994).
[198]R. A. McKee, F. J. Walker, and M. F. Chisholm, "Physical Structure and Inversion Charge at a Semiconductor Interface with a Crystalline Oxide," *Science*, **293** [5529] 468–71 (2001).
[199]T. Tsurumi, T. Suzuki, M. Yamane, and M. Daimon, "Fabrication of Barium Titanate/Strontium Titanate Artificial Superlattice by Atomic Layer Epitaxy," *Jpn. J. Appl. Phys., Part 1*, **33** [9B] 5192–5 (1994).
[200]H. Shigetani, K. Kobayashi, M. Fujimoto, W. Sugimura, Y. Matsui, and J. Tanaka, "$BaTiO_3$ Thin Films Grown on $SrTiO_3$ Substrates by a Molecular-Beam-Epitaxy Method Using Oxygen Radicals," *J. Appl. Phys*., **81** [2] 693–7 (1997).
[201]H. P. Sun, W. Tian, X. Q. Pan, J. H. Haeni, and D. G. Schlom, "Evolution of Dislocation Arrays in Epitaxial $BaTiO_3$ Thin Films Grown on (100) $SrTiO_3$," *Appl. Phys. Lett*., **84** [17] 3298–300 (2004).
[202]H. P. Sun, X. Q. Pan, J. H. Haeni, and D. G. Schlom, "Structural Evolution of Dislocation Half-Loops in Epitaxial $BaTiO_3$ Thin Films During High-Temperature Annealing," *Appl. Phys. Lett*., **85** [11] 1967–9 (2004).
[203]K. J. Choi, M. D. Biegalski, Y. L. Li, A. Sharan, J. Schubert, R. Uecker, P. Reiche, Y. B. Chen, X. Q. Pan, V. Gopalan, L.-Q. Chen, D. G. Schlom, and C. B. Eom, "Enhancement of Ferroelectricity in Strained $BaTiO_3$ Thin Films," *Science*, **306** [5698] 1005–9 (2004).
[204]F. J. Walker and R. A. McKee, "High-k Crystalline Gate Dielectrics: A Research Perspective"; pp. 607–37 in *High Dielectric Constant Materials: VLSI MOSFET Applications*, Edited by H. R. Huff, and D. C. Gilmer. Springer, Berlin, 2005.
[205]V. Vaithyanathan, J. Lettieri, W. Tian, A. Kochhar, H. Ma, A. Sharan, A. Vasudevarao, V. Gopalan, Y. Li, L. Q. Chen, P. Zschack, J. C. Woicik, J. Levy, and D. G. Schlom, "*c*-Axis Oriented Epitaxial $BaTiO_3$ Films on (001) Si," *J. Appl. Phys*., **100** [2] 024108 (2006).
[206]C. D. Theis and D. G. Schlom, "Epitaxial Lead Titanate Grown by MBE," *J. Cryst. Growth*, **174** [1–4] 473–9 (1997).
[207]C. D. Theis, J. Yeh, D. G. Schlom, M. E. Hawley, G. W. Brown, J. C. Jiang, and X. Q. Pan, "Adsorption-Controlled Growth of $Bi_4Ti_3O_{12}$ by Reactive MBE," *Appl. Phys. Lett*., **72** [22] 2817–9 (1998).
[208]S. Migita, H. Ota, H. Fujino, Y. Kasai, and S. Sakai, "Epitaxial $Bi_4Ti_3O_{12}$ Thin Film Growth using Bi Self-Limiting Function," *J. Cryst. Growth*, **200** [1–2] 161–8 (1999).
[209]I. Bozovic, J. N. Eckstein, and G. F. Virshup, "Superconducting Oxide Multilayers and Superlattices: Physics, Chemistry, and Nanoengineering," *Physica C*, **235–240** [1] 178–81 (1994).
[210]R. A. McKee, F. J. Walker, and M. F. Chisholm, "Crystalline Oxides on Silicon: The First Five Monolayers," *Phys. Rev. Lett*., **81** [14] 3014–7 (1998).
[211]J. H. Haeni, C. D. Theis, and D. G. Schlom, "RHEED Intensity Oscillations for the Stoichiometric Growth of $SrTiO_3$ Thin Films by Reactive Molecular Beam Epitaxy," *J. Electroceram*., **4** [2/3] 385–91 (2000).
[212]K. Eisenbeiser, J. M. Finder, Z. Yu, J. Ramdani, J. A. Curless, J. A. Hallmark, R. Droopad, W. J. Ooms, L. Salem, S. Bradshaw, and C. D. Overgaard, "Field Effect Transistors with $SrTiO_3$ Gate Dielectric on Si," *Appl. Phys. Lett*., **76** [10] 1324–6 (2000).
[213]Z. Yu, J. Ramdani, J. A. Curless, C. D. Overgaard, J. M. Finder, R. Droopad, K. W. Eisenbeiser, J. A. Hallmark, W. J. Ooms, and V. S. Kaushik, "Epitaxial Oxide Thin Films on Si(001)," *J. Vac. Sci. Technol. B*, **18** [4] 2139–45 (2000).
[214]J. Lettieri, "Critical Issues of Complex, Epitaxial Oxide Growth and Integration with Silicon by Molecular Beam Epitaxy"; Ph.D. Thesis, Pennsylvania State University, 2002. Available on-line at http://etda.libraries.psu.edu/theses/approved/WorldWideIndex/ETD-202/index.html
[215]H. Li, X. Hu, Y. Wei, Z. Yu, X. Zhang, R. Droopad, A. A. Demkov, J. Edwards Jr., K. Moore, W. Ooms, J. Kulik, and P. Fejes, "Two-Dimensional Growth of High-Quality Strontium Titanate Thin Films on Si," *J. Appl. Phys*., **93** [8] 4521–5 (2003).
[216]M. D. Biegalski, Y. Jia, D. G. Schlom, S. Trolier-McKinstry, S. K. Streiffer, V. Sherman, R. Uecker, and P. Reiche, "Relaxor Ferroelectricity in Strained Epitaxial $SrTiO_3$ Thin Films on $DyScO_3$ Substrates," *Appl. Phys. Lett*., **88** [19] 192907 (2006).
[217]L. Fitting Kourkoutis, C. S. Hellberg, V. Vaithyanathan, H. Li, M. K. Parker, K. E. Andersen, D. G. Schlom, and D. A. Muller, "Imaging the Phase Separation in Atomically Thin Buried $SrTiO_3$ Layers by Electron Channeling," *Phys. Rev. Lett*., **100** [3] 036101 (2008).
[218]M. D. Biegalski, S. Trolier-McKinstry, D. G. Schlom, D. D. Fong, J. A. Eastman, P. H. Fuoss, S. K. Streiffer, T. Heeg, J. Schubert, W. Tian, X. Q. Pan, M. E. Hawley, M. Bernhagen, P. Reiche, and R. Uecker, "Critical Thickness of High Structural Quality $SrTiO_3$ Films Grown on Orthorhombic (101) $DyScO_3$," *J. Appl. Phys*., in press.
[219]J. N. Eckstein, I. Bozovic, M. Rzchowski, J. O'Donnell, B. Hinaus, and M. Onellion, "Molecular Beam Epitaxy of Single Crystal Colossal Magneto-Resistive Material"; pp. 467–71 in *Epitaxial Oxide Thin Films II*, **Vol. 401**, Edited by J. S. Speck, D. K. Fork, R. M. Wolf, and T. Shiosaki. Materials Research Society, Pittsburgh, 1996.
[220]J. N. Eckstein, I. Bozovic, J. O'Donnell, M. Onellion, and M. S. Rzchowski, "Anisotropic Magnetoresistance in Tetragonal $La_{1-x}Ca_xMnO_\delta$ Thin Films," *Appl. Phys. Lett*., **69** [9] 1312–4 (1995).
[221]L. Maritato and A. Y. Petrov, "High Metal–Insulator Transition Temperature in $La_{1-x}Sr_xMnO_3$ Thin Films Grown in Low Oxygen Partial Pressure by Molecular Beam Epitaxy," *J. Magn. Magn. Mater*., **272–276** [2] 1135–6 (2004).
[222]G. M. Roesler Jr., M. E. Filipkowski, P. R. Broussard, Y. U. Idzerda, M. S. Osofsky, and R. J. Soulen Jr., "Epitaxial Multilayers of Ferromagnetic Insulators with Nonmagnetic Metals and Superconductors"; pp. 285–90 in *Superconducting Superlattices and Multilayers*, **Vol. 2157**, Edited by I. Bozovic. SPIE, Bellingham, 1994.
[223]N. Iwata, G. Pindoria, T. Morishita, and K. Kohn, "Preparation and Magnetic Properties of EuO Thin Films Epitaxially Grown on MgO and $SrTiO_3$ Substrates," *J. Phys. Soc. Jpn*., **69** [1] 230–6 (2000).

[224]P. G. Steeneken, "New Light on EuO Thin Films"; Ph.D. thesis, University of Groningen, 2002.
[225]J. Lettieri, V. Vaithyanathan, S. K. Eah, J. Stephens, V. Sih, D. D. Awschalom, J. Levy, and D. G. Schlom, "Epitaxial Growth and Magnetic Properties of EuO on (001) Si by Molecular-Beam Epitaxy," *Appl. Phys. Lett*., **83** [5] 975–7 (2003).
[226]A. Schmehl, V. Vaithyanathan, A. Herrnberger, S. Thiel, C. Richter, M. Liberati, T. Heeg, M. Röckerath, L. Fitting Kourkoutis, S. Mühlbaur, P. Böni, D. A. Muller, Y. Barash, J. Schubert, Y. Idzerda, J. Mannhart, and D. G. Schlom, "Epitaxial Integration of the Highly Spin-Polarized Ferromagnetic Semiconductor EuO with Silicon and GaN," *Nat. Mater*., **6** [11] 882–7 (2007).
[227]R. W. Ulbricht, T. Heeg, D. G. Schlom, A. Schmehl, and J. Schubert, "Adsorption-Controlled Growth of EuO by Molecular-Beam Epitaxy," *Appl. Phys. Lett*, submitted.
[228]S. A. Chambers, "Epitaxial Growth and Properties of Thin Film Oxides," *Surf. Sci. Rep*., **39** [5–6] 105–80 (2000).
[229]J. Kabelac, S. Ghosh, P. Dobal, and R. Katiyar, "rf Oxygen Plasma Assisted Molecular Beam Epitaxy Growth of $BiFeO_3$ Thin Films on $SrTiO_3$ (001)," *J. Vac. Sci. Technol. B*, **25** [3] 1049–52 (2007).
[230]J. F. Ihlefeld, A. Kumar, V. Gopalan, D. G. Schlom, Y. B. Chen, X. Q. Pan, T. Heeg, J. Schubert, X. Ke, P. Schiffer, J. Orenstein, L. W. Martin, Y. H. Chu, and R. Ramesh, "Adsorption-Controlled Molecular-Beam Epitaxial Growth of $BiFeO_3$," *Appl. Phys. Lett*., **91** [7] 071922 (2007).
[231]J. F. Ihlefeld, N. J. Podraza, Z. K. Liu, R. C. Rai, X. Xu, T. Heeg, Y. B. Chen, J. Li, R. W. Collins, J. L. Musfeldt, X. Q. Pan, J. Schubert, R. Ramesh, and D. G. Schlom, "Optical Band Gap of $BiFeO_3$ Grown by Molecular-Beam Epitaxy," *Appl. Phys. Lett*., **92** [14] 142908 (2008).
[232]S. Imada, S. Shouriki, E. Tokumitsu, and H. Ishiwara, "Epitaxial Growth of Ferroelectric $YMnO_3$ Thin Films on Si(111) Substrates by Molecular Beam Epitaxy," *Jpn. J. Appl. Phys., Part 1*, **37** [12A] 6497–501 (1998).
[233]Y. Chye, T. Liu, D. Li, K. Lee, D. Lederman, and T. H. Myers, "Molecular Beam Epitaxy of $YMnO_3$ on *c*-Plane GaN," *Appl. Phys. Lett*., **88** [13] 132903 (2006).
[234]J. C. Jiang, X. Q. Pan, W. Tian, C. D. Theis, and D. G. Schlom, "Abrupt $PbTiO_3/SrTiO_3$ Superlattices Grown by Reactive Molecular Beam Epitaxy," *Appl. Phys. Lett*., **74** [19] 2851–3 (1999).
[235]W. Tian, J. C. Jiang, X. Q. Pan, J. H. Haeni, Y. L. Li, L. Q. Chen, D. G. Schlom, J. B. Neaton, K. M. Rabe, and Q. X. Jia, "Structural Evidence for Enhanced Polarization in a Commensurate Short-Period $BaTiO_3/SrTiO_3$ Superlattice," *Appl. Phys. Lett*., **89** [9] 092905 (2006).
[236]A. Soukiassian, W. Tian, D. A. Tenne, X. X. Xi, D. G. Schlom, N. D. Lanzillotti-Kimura, A. Bruchhausen, A. Fainstein, H. P. Sun, X. Q. Pan, A. Cros, and A. Cantarero, "Acoustic Bragg Mirrors and Cavities Made Using Piezoelectric Oxides," *Appl. Phys. Lett*., **90** [4] 042909 (2007).
[237]A. Soukiassian, W. Tian, V. Vaithyanathan, J. H. Haeni, L. Q. Chen, X. X. Xi, D. G. Schlom, D. A. Tenne, H. P. Sun, X. Q. Pan, K. J. Choi, C. B. Eom, Y. L. Li, Q. X. Jia, C. Constantin, R. M. Feenstra, M. Bernhagen, P. Reiche, and R. Uecker, "Growth of Nanoscale $BaTiO_3/SrTiO_3$ Superlattices by Molecular-Beam Epitaxy," *J. Mater. Res*., **23** [5] 1417–32 (2008).
[238]R. H. Lamoreaux and D. L. Hildenbrand, "High Temperature Vaporization Behavior of Oxides I. Alkali Metal Binary Oxides," *J. Phys. Chem. Ref. Data*, **13** [1] 151–73 (1984).
[239]R. H. Lamoreaux and D. L. Hildenbrand, "High-Temperature Vaporization Behavior of Oxides II. Oxides of Be, Mg, Ca, Sr, Ba, B, Al, Ga, In, Tl, Si, Ge, Sn, Pb, Zn, Cd, and Hg," *J. Phys. Chem. Ref. Data*, **16** [3] 419–43 (1987).
[240]M. E. Klausmeier-Brown, J. N. Eckstein, I. Bozovic, and G. F. Virshup, "Accurate Measurement of Atomic Beam Flux by Pseudo-Double-Beam Atomic Absorption Spectroscopy for Growth of Thin-Film Oxide Superconductors," *Appl. Phys. Lett*., **60** [5] 657–9 (1992).
[241]B. J. Gibbons, M. E. Hawley, S. Trolier-McKinstry, and D. G. Schlom, "Real-Time Spectroscopic Ellipsometry as a Characterization Tool for Oxide Molecular Beam Epitaxy," *J. Vac. Sci. Technol. A*, **19** [2] 584–90 (2001).
[242]BandiT, k-Space Associates, Ann Arbor, MI.
[243]E. S. Hellman and J. S. Harris, "Infrared Transmission Spectroscopy of GaAs during Molecular Beam Epitaxy," *J. Cryst. Growth*, **81** [1–4] 38–42 (1987).
[244]MOSS, k-Space Associates, Ann Arbor, MI.
[245]C. Taylor, D. Barlett, E. Chason, and J. Floro, "Technology," *Ind. Phys*., **4** [1] 25 (1998).
[246]I. Bozovic and V. Matijasevic, "COMBE: A Powerful New Tool for Materials Science," *Mater. Sci. Forum*, **352**, 1–8 (2000).
[247]S. Y. Wu, W. J. Takei, M. H. Francombe, and S. E. Cummins, "Domain Structure and Polarization Reversal in Films of Ferroelectric Bismuth Titanate," *Ferroelectrics*, **3** [234] 217–24 (1972).
[248]W. J. Takei, S. Y. Wu, and M. H. Francombe, "Optimization of Epitaxial Quality in Sputtered Films of Ferroelectric Bismuth Titanate," *J. Cryst. Growth*, **28** [2] 188–98 (1975).
[249]J. Fujita, T. Yoshitake, A. Kamijo, T. Satoh, and H. Igarashi, "Preferentially Oriented Epitaxial Y–Ba–Cu–O Films Prepared by the Ion Beam Sputtering Method," *J. Appl. Phys*., **64** [3] 1292–5 (1988).
[250]C. B. Eom, A. F. Marshall, S. S. Laderman, R. D. Jacowitz, and T. H. Geballe, "Epitaxial and Smooth Films of *a*-Axis $YBa_2Cu_3O_7$," *Science*, **249** [4976] 1549–52 (1990).
[251]G. Asayama, J. Lettieri, M. A. Zurbuchen, Y. Jia, S. Trolier-McKinstry, D. G. Schlom, S. K. Streiffer, J-P. Maria, S. D. Bu, and C. B. Eom, "Growth of (103) Fiber-Textured $SrBi_2Nb_2O_9$ Films on Pt-Coated Silicon," *Appl. Phys. Lett*., **80** [13] 2371–3 (2002).
[252]R. Ramesh and D. G. Schlom, "Orienting Ferroelectric Films," *Science*, **296** [5575] 1975–6 (2002).
[253]H. N. Lee, D. Hesse, N. Zakharov, and U. Gosele, "Ferroelectric $Bi_{3.25}La_{0.75}Ti_3O_{12}$ Films of Uniform *a*-Axis Orientation on Silicon Substrates," *Science*, **296** [5575] 2006–9 (2002).
[254]Y. Iijima, N. Tanabe, O. Kohno, and Y. Ikeno, "Inplane Aligned $YBa_2Cu_3O_{7-x}$ Thin-Films Deposited on Polycrystalline Metallic Substrates," *Appl. Phys. Lett*., **60** [6] 769–71 (1992).
[255]C. P. Wang, K. B. Do, M. R. Beasley, T. H. Geballe, and R. H. Hammond, "Deposition of In-Plane Textured MgO on Amorphous Si_3N_4 Substrates by Ion-Beam-Assisted Deposition and Comparisons with Ion-Beam-Assisted Deposited Yttria-Stabilized-Zirconia," *Appl. Phys. Lett*., **71** [20] 2955–7 (1997).
[256]A. Goyal, D. P. Norton, J. D. Budai, M. Paranthaman, E. D. Specht, D. M. Kroeger, D. K. Christen, Q. He, B. Saffian, F. A. List, D. F. Lee, P. M. Martin, C. E. Klabunde, E. Hartfield, and V. K. Sikka, "High Critical Current Density Superconducting Tapes by Epitaxial Deposition of $YBa_2Cu_3O_x$ Thick Films on Biaxially Textured Metals," *Appl. Phys. Lett*., **69** [12] 1795–7 (1996).
[257]D. P. Norton, A. Goyal, J. D. Budai, D. K. Christen, D. M. Kroeger, E. D. Specht, Q. He, B. Saffian, M. Paranthaman, C. E. Klabunde, D. F. Lee, B. C. Sales, and F. A. List, "Epitaxial $YBa_2Cu_3O_7$ on Biaxially Textured Nickel (001): An Approach to Superconducting Tapes with High Critical Current Density," *Science*, **274** [5288] 755–7 (1996).
[258]A. P. Malozemoff, J. Mannhart, and D. Scalapino, "High-Temperature Cuprate Superconductors get to Work," *Phys. Today*, **58** [4] 41–6 (2005).
[259]J. Rodriguez, K. Remack, K. Boku, K. R. Udayakumar, S. Aggarwal, S. Summerfelt, T. Moise, H. McAdams, J. McPherson, R. Bailey, M. Depner, and G. Fox, "Reliability Properties of Low Voltage PZT Ferroelectric Capacitors and Arrays"; pp. 200–8 in *2004 IEEE International Reliability Physics Symposium*, Proceedings 42nd Annual IEEE, Piscataway, NJ, 2004.
[260]R. L. Sandstrom, E. A. Giess, W. J. Gallagher, A. Segmüller, E. I. Cooper, M. F. Chisholm, A. Gupta, S. Shinde, and R. B. Laibowitz, "Lanthanum Gallate Substrates for Epitaxial High-Temperature Superconducting Thin Films," *Appl. Phys. Lett*., **53** [19] 1874–6 (1988).
[261]R. W. Simon, C. E. Platt, A. E. Lee, G. S. Lee, K. P. Daly, M. S. Wire, J. A. Luine, and M. Urbanik, "Low-Loss Substrate for Epitaxial Growth of High-Temperature Superconductor Thin Films," *Appl. Phys. Lett*., **53** [26] 2677–9 (1988).
[262]G. Koren, A. Gupta, E. A. Giess, A. Segmüller, and R. B. Laibowitz, "Epitaxial Films of $YBa_2Cu_3O_{7-\delta}$ on $NdGaO_3$, $LaGaO_3$, and $SrTiO_3$ Substrates Deposited by Laser Ablation," *Appl. Phys. Lett*., **54** [11] 1054–6 (1989).
[263]R. Feenstra, L. A. Boatner, J. D. Budai, D. K. Christen, M. D. Galloway, and D. B. Poker, "Epitaxial Superconducting Thin Films of $YBa_2Cu_3O_{7-x}$ on $KTaO_3$ Single Crystals," *Appl. Phys. Lett*., **54** [11] 1063–5 (1989).
[264]E. A. Giess, R. L. Sandstrom, W. J. Gallagher, A. Gupta, S. L. Shinde, R. F. Cook, E. I. Cooper, E. J. M. O'Sullivan, J. M. Roldan, A. P. Segmüller, and J. Angilello, "Lanthanide Gallate Perovskite-Type Substrates for Epitaxial, High-T_c Superconducting $Ba_2YCu_3O_{7-\delta}$ Films," *IBM J. Res. Dev*., **34** [6] 916–26 (1990).
[265]H. Asano, S. Kubo, O. Michikami, M. Satoh, and T. Konaka, "Epitaxial Growth of $EuBa_2Cu_3O_{7-y}$ Films on $YAlO_3$ Single Crystals," *Jpn. J. Appl. Phys., Part 2*, **29** [8] L1452–4 (1990).
[266]G. W. Berkstresser, A. J. Valentino, and C. D. Brandle, "Growth of Single Crystals of Rare Earth Gallates," *J. Cryst. Growth*, **109** [1–4] 457–66 (1991).
[267]G. W. Berkstresser, A. J. Valentino, and C. D. Brandle, "Growth of Single Crystals of Lanthanum Aluminate," *J. Cryst. Growth*, **109** [1–4] 467–71 (1991).
[268]R. W. Ralston, M. A. Kastner, W. J. Gallagher, and B. Batlogg, "Cooperating on Superconductivity," *IEEE Spectrum*, **29** [8] 50–5 (1992).
[269]G. W. Berkstresser, A. J. Valentino, and C. D. Brandle, "Congruent Composition for Growth of Lanthanum Aluminate," *J. Cryst. Growth*, **128** [1–4] 684–8 (1993).
[270]R. Brown, V. Pendrick, D. Kalokitis, and B. H. T. Chai, "Low-Loss Substrate for Microwave Application of High-Temperature Superconductor Films," *Appl. Phys. Lett*., **57** [13] 1351–3 (1990).
[271]S. Hontsu, J. Ishii, T. Kawai, and S. Kawai, "$LaSrGaO_4$ Substrate Gives Oriented Crystalline $YBa_2Cu_3O_{7-y}$ Films," *Appl. Phys. Lett*., **59** [22] 2886–8 (1991).
[272]D. Mateika, H. Kohler, H. Laudan, and E. Volkel, "Mixed-Perovskite Substrates for High-T_c Superconductors," *J. Cryst. Growth*, **109** [1–4] 447–56 (1991).
[273]J. M. Phillips, "Substrate Selection for High-Temperature Superconducting Thin Films," *J. Appl. Phys*., **79** [4] 1829–48 (1996).
[274]B. C. Chakoumakos, D. G. Schlom, M. Urbanik, and J. Luine, "Thermal Expansion of $LaAlO_3$ and $(La,Sr)(Al,Ta)O_3$, Substrate Materials for Superconducting Thin-Film Device Applications," *J. Appl. Phys*., **83** [4] 1979–82 (1998).
[275]L. Merker, "Method of Prepration of Monocrystalline Strontium Titanate Composition of High Refractive Index"; US Patent No. 2,684,910, July 27, 1954.
[276]J. G. Bednorz and H. J. Scheel, "Flame-Fusion Growth of $SrTiO_3$," *J. Cryst. Growth*, **41** [1] 5–12 (1977).
[277]P. I. Nabokin, D. Souptel, and A. M. Balbashov, "Floating Zone Growth of High-Quality $SrTiO_3$ Single Crystals," *J. Cryst. Growth*, **250** [3–4] 397–404 (2003).
[278]H. J. Scheel, J. G. Bednorz, and P. Dill, "Crystal Growth of Strontium Titanate $SrTiO_3$," *Ferroelectrics*, **13** [1–4] 507–9 (1976).
[279]N. A. Spaldin and M. Fiebig, "The Renaissance of Manetoelectric Multiferroics," *Science*, **309** [5733] 391–2 (2005).
[280]J. Schubert, O. Trithaveesak, A. Petraru, C. L. Jia, R. Uecker, P. Reiche, and D. G. Schlom, "Structural and Optical Properties of Epitaxial $BaTiO_3$ Thin Films Grown on $GdScO_3(110)$," *Appl. Phys. Lett*., **82** [20] 3460–2 (2003).
[281]M. D. Biegalski, J. H. Haeni, S. Trolier-McKinstry, D. G. Schlom, C. D. Brandle, and A. J. Ven Graitis, "Thermal Expansion of the New Perovskite Substrates $DyScO_3$ and $GdScO_3$," *J. Mater. Res*., **20** [4] 952–8 (2005).
[282]R. Uecker, H. Wilke, D. G. Schlom, B. Velickov, P. Reiche, A. Polity, M. Bernhagen, and M. Rossberg, "Spiral Formation during Czochralski Growth of Rare-Earth Scandates," *J. Cryst. Growth*, **295** [1] 84–91 (2006).

[283]B. Veličkov, V. Kahlenberg, R. Bertram, and M. Bernhagen, "Crystal Chemistry of $GdScO_3$, $DyScO_3$, $SmScO_3$, and $NdScO_3$," *Z. Kristallogr.*, **222** [9] 466–73 (2007).

[284]R. Uecker, B. Velickov, D. Klimm, R. Bertram, M. Bernhagen, M. Rabe, M. Albrecht, R. Fornari, and D. G. Schlom, "Properties of Rare-Earth Scandate Single Crystals (Re = Nd–Dy)," *J. Cryst. Growth*, **310** [10] 2649–58 (2008).

[285]M. Kawasaki, K. Takahashi, T. Maeda, R. Tsuchiya, M. Shinohara, O. Ishiyama, T. Yonezawa, M. Yoshimoto, and H. Koinuma, "Atomic Control of the $SrTiO_3$ Crystal Surface," *Science*, **266** [5190] 1540–2 (1994).

[286]G. Koster, B. L. Kropman, G. J. H. M. Rijnders, D. H. A. Blank, and H. Rogalla, "Quasi-Ideal Strontium Titanate Crystal Surfaces Through Formation of Strontium Hydroxide," *Appl. Phys. Lett.*, **73** [20] 2920–2 (1998).

[287]A. G. Schrott, J. A. Misewich, M. Copel, D. W. Abraham, and Y. Zhang, "*A*-Site Surface Termination in Strontium Titanate Single Crystals," *Appl. Phys. Lett.*, **79** [12] 1786–8 (2001).

[288]. D. H. A. Blank (private communication).

[289]T. Ohnishi, K. Takahashi, M. Nakamura, M. Kawasaki, M. Yoshimoto, and H. Koinuma, "*A*-Site Layer Terminated Perovskite Substrate: $NdGaO_3$," *Appl. Phys. Lett.*, **74** [17] 2531–3 (1999).

[290]H-J. Bae, J. Sigman, D. P. Norton, and L. A. Boatner, "Surface Treatment for Forming Unit-Cell Steps on the (001) $KTaO_3$ Substrate Surface," *Appl. Surf. Sci.*, **241** [3–4] 271–8 (2005).

[291]D. G. Schlom, L. Q. Chen, C. B. Eom, K. M. Rabe, S. K. Streiffer, and J.-M. Triscone, "Strain Tuning of Ferroelectric Thin Films," *Annu. Rev. Mater. Res.*, **37**, 589–626 (2007).

[292]S. B. Qadri, J. S. Horwitz, D. B. Chrisey, R. C. Y. Auyeung, and K. S. Grabowski, "X-Ray Characterization of Extremely High Quality (Sr,Ba)TiO_3 Films Grown by Pulsed Laser Deposition," *Appl. Phys. Lett.*, **66** [13] 1605–7 (1995).

[293]J. F. Ihlefeld and D. G. Schlom (unpublished).

[294]J. H. Lee and D. G. Schlom (unpublished).

[295]C. Adamo, M. Warusawithana, D. G. Schlom, X. Ke, P. Schiffer, and L. Maritato (unpublished).

[296]T. Yamaguti, "Oxidation of a Crystal Surface Studied by Means of Cathode Ray Reflection," *Proc. Phys. Math. Soc. Jpn.*, **17** [11] 443–53 (1935).

[297]R. Sato, "Surface Oxidation of Zincblende Cleavage Face in the Roasting Atmosphere," *J. Phys. Soc. Jpn.*, **6**, 527–8 (1951).

[298]S. Matsubara, N. Shohata, and M. Mikami, "Epitaxial Growth of $PbTiO_3$ on $MgAl_2O_4$/Si Substrates," *Jpn. J. Appl. Phys.*, **24** [Suppl. 24-3] 10–2 (1985).

[299]S. Miura, T. Yoshitake, S. Matsubara, Y. Miyasaka, N. Shohata, and T. Satoh, "Epitaxial Y–Ba–Cu–O Films on Si with Intermediate Layer by RF Magnetron Sputtering," *Appl. Phys. Lett.*, **53** [20] 1967–9 (1988).

[300]H. Myoren, Y. Nishiyama, H. Fukumoto, H. Nasu, and Y. Osaka, "As-Grown Preparation of Superconducting Epitaxial $Ba_2YCu_3O_x$ Thin Films Sputtered on Epitaxially Grown ZrO_2/Si(100)," *Jpn. J. Appl. Phys., Part 1*, **28** [3] 351–5 (1989).

[301]D. K. Fork, F. A. Ponce, J. C. Tramontana, and T. H. Geballe, "Epitaxial MgO on Si(001) for Y–Ba–Cu–O Thin-Film Growth by Pulsed Laser Deposition," *Appl. Phys. Lett.*, **58** [20] 2294–6 (1991).

[302]H. Mori and H. Ishiwara, "Epitaxial Growth of $SrTiO_3$ Films on Si(100) Substrates Using a Focused Electron Beam Evaporation Method," *Jpn. J. Appl. Phys., Part 2*, **30** [8A] L1415–7 (1991).

[303]A. N. Tiwari, S. Blunier, H. Zogg, P. Lerch, F. Marcenat, and P. Martinoli, "Epitaxial Growth of Superconducting $YBa_2Cu_3O_{7-x}$ on Si(100) with CaF_2 as Intermediate Buffer," *J. Appl. Phys.*, **71** [10] 5095–8 (1992).

[304]D. K. Fork, "Epitaxial Oxides on Semiconductors"; pp. 393–415 in *Pulsed Laser Deposition of Thin Films*, Edited by D. B. Chrisey, and G. K. Hubler. Wiley, New York, 1994.

[305]M.-B. Lee, M. Kawasaki, M. Yoshimoto, and H. Koinuma, "Heteroepitaxial Growth of $BaTiO_3$ Films on Si by Pulsed Laser Deposition," *Appl. Phys. Lett.*, **66** [11] 1331–3 (1995).

[306]J. Lettieri, J. H. Haeni, and D. G. Schlom, "Critical Issues in the Heteroepitaxial Growth of Alkaline-Earth Oxides on Silicon," *J. Vac. Sci. Technol. A*, **20** [4] 1332–40 (2002).

[307]E. G. Jacobs, Y. G. Rho, R. F. Pinizzotto, S. R. Summerfelt, and B. E. Gnade, "Effect of a Ge Barrier on the Microstructure of $BaTiO_3$ Deposited on Silicon by Pulsed Laser Ablation"; pp. 379–84 in *Laser Ablation in Materials Processing: Fundamentals and Applications*, **Vol. 285**, Edited by B. Braren, J. J. Dubowski, and D. Norton. Materials Research Society, Pittsburgh, 1993.

[308]D. P. Norton, J. D. Budai, and M. F. Chisholm, "Hydrogen-Assisted Pulsed-Laser Deposition of (001) CeO_2 on (001) Ge," *Appl. Phys. Lett.*, **76** [13] 1677–9 (2000).

[309]K. Nashimoto, D. K. Fork, and T. H. Geballe, "Epitaxial Growth of MgO on GaAs(001) for Growing Epitaxial $BaTiO_3$ Thin Films by Pulsed Laser Deposition," *Appl. Phys. Lett.*, **60** [10] 1199–201 (1992).

[310]Y. Liang, J. Kulik, T. C. Eschrich, R. Droopad, Z. Yu, and P. Maniar, "Hetero-Epitaxy of Perovskite Oxides on GaAs(001) by Molecular Beam Epitaxy," *Appl. Phys. Lett.*, **85** [7] 1217–9 (2004).

[311]E. Vasco, L. Vazquez, M. Aguilo, and C. Zaldo, "Epitaxial Growth of Y-Stabilised Zirconia Films on (100) InP Substrates by Pulsed Laser Deposition," *J. Cryst. Growth*, **209** [4] 883–9 (2000).

[312]D. P. Norton, S. J. Pearton, H. M. Christen, and J. D. Budai, "Hydrogen-Assisted Pulsed-Laser Deposition of Epitaxial CeO_2 Films on (001) InP," *Appl. Phys. Lett.*, **80** [1] 106–8 (2002).

[313]C.-R. Cho, J.-Y. Hwang, J.-P. Kim, S.-Y. Jeong, S.-G. Yoon, and W.-J. Lee, "Growth and Characterization of $(Ba_{0.5}Sr_{0.5})TiO_3$ Films Epitaxially Grown on (002) GaN/(0006) Al_2O_3 Electrode," *Jpn. J. Appl. Phys., Part 2*, **43** [11A] L1425–8 (2004).

[314]H. S. Craft, J. F. Ihlefeld, M. D. Losego, R. Collazo, Z. Sitar, and J-P. Maria, "MgO Epitaxy on GaN (0002) Surfaces by Molecular Beam Epitaxy," *Appl. Phys. Lett.*, **88** [21] 212906 (2006).

[315]W. Tian, V. Vaithyanathan, D. G. Schlom, Q. Zhan, S. Y. Yang, Y. H. Chu, and R. Ramesh, "Epitaxial Integration of (0001) $BiFeO_3$ with (0001) GaN," *Appl. Phys. Lett.*, **90** [17] 172908 (2007).

[316]D. K. Fork, D. B. Fenner, R. W. Barton, J. M. Phillips, G. A. N. Connell, J. B. Boyce, and T. H. Geballe, "High Critical Currents in Strained Epitaxial $YBa_2Cu_3O_{7-\delta}$ on Si," *Appl. Phys. Lett.*, **57** [11] 1161–3 (1990).

[317]H. Ishiwara, N. Tsuji, H. Mori, and H. Nohira, "Preparation of $YbBa_2Cu_3O_{7x}$ Films on Si(100) Substrates Using $SrTiO_3$ Buffer Layers," *Appl. Phys. Lett.*, **61** [12] 1459–61 (1992).

[318]R. Ramesh, H. Gilchrist, T. Sands, V. G. Keramidas, R. Haakenaasen, and D. K. Fork, "Ferroelectric La–Sr–Co–O/Pb–Zr–Ti–O/La–Sr–Co–O Heterostructures on Silicon via Template Growth," *Appl. Phys. Lett.*, **63** [26] 3592–4 (1993).

[319]K. Nashimoto, D. K. Fork, F. A. Ponce, and J. C. Tramontana, "Epitaxial $BaTiO_3$/MgO Structure Grown on GaAs(100) by Pulsed Laser Deposition," *Jpn. J. Appl. Phys., Part 1*, **32** [9B] 4099–102 (1993).

[320]V. Srikant, E. J. Tarsa, D. R. Clarke, and J. S. Speck, "Crystallographic Orientation of Epitaxial $BaTiO_3$ Films: The Role of Thermal-Expansion Mismatch with the Substrate," *J. Appl. Phys.*, **77** [4] 1517–22 (1995).

[321]T. Maruyama, M. Saitoh, I. Sakai, T. Hidaka, Y. Yano, and T. Noguchi, "Growth and Characterization of 10-nm-Thick *c*-Axis Oriented Epitaxial $PbZr_{0.25}Ti_{0.75}O_3$ Thin Films on (100)Si Substrate," *Appl. Phys. Lett.*, **73** [24] 3524–6 (1998).

[322]A. Lin, X. Hong, V. Wood, A. Verevkin, C. H. Ahn, R. A. McKee, F. J. Walker, and E. D. Specht, "Epitaxial Growth of $Pb(Zr_{0.2}Ti_{0.8})O_3$ on Si and its Nanoscale Piezoelectric Properties," *Appl. Phys. Lett.*, **78** [14] 2034–6 (2001).

[323]B. T. Liu, K. Maki, Y. So, V. Nagarajan, R. Ramesh, J. Lettieri, J. H. Haeni, D. G. Schlom, W. Tian, X. Q. Pan, F. J. Walker, and R. A. McKee, "Epitaxial La-doped $SrTiO_3$ on Silicon: A Conductive Template for Epitaxial Ferroelectrics on Silicon," *Appl. Phys. Lett.*, **80** [25] 4801–3 (2002).

[324]Y. Liang, J. Kulik, Y. Wei, T. Eschrich, J. Curless, B. Craigo, and S. Smith, "Hetero-Epitaxy of Crystalline Perovskite Oxides on GaAs(001)"; pp. 379–84 in *Fundamentals of Novel Oxide/Semiconductor Interfaces*, Vol. 786, Edited by C. R. Abernathy, E. P. Gusev, D. Schlom, and S. Stemmer. Materials Research Society, Warrendale, 2004.

[325]S. Y. Yang, F. Zavaliche, L. Mohaddes-Ardabili, V. Vaithyanathan, D. G. Schlom, Y. J. Lee, Y. H. Chu, M. P. Cruz, Q. Zhan, T. Zhao, and R. Ramesh, "Metalorganic Chemical Vapor Deposition of Lead-Free Ferroelectric $BiFeO_3$ Films for Memory Applications," *Appl. Phys. Lett.*, **87** [10] 102903 (2005).

[326]A. Posadas, J.-B. Yau, C. H. Ahn, J. Han, S. Gariglio, K. Johnston, K. M. Rabe, and J. B. Neaton, "Epitaxial Growth of Multiferroic $YMnO_3$ on GaN," *Appl. Phys. Lett.*, **87** [17] 171915 (2005).

[327]J. K. G. Panitz and C. C. Hu, "Radio-Frequency-Sputtered Tetragonal Barium Titanate Films on Silicon," *J. Vac. Sci. Technol.*, **16** [2] 315–8 (1979).

[328]V. S. Dharmadhikari and W. W. Grannemann, "AES Study on the Chemical Composition of Ferroelectric $BaTiO_3$ Thin Films RF Sputter-Deposited on Silicon," *J. Vac. Sci. Technol. A*, **1** [2] 483–5 (1983).

[329]S. Matsubara, T. Sakuma, S. Yamamichi, H. Yamaguchi, and Y. Miyasaka, "Interface Structure and Dielectric Properties of $SrTiO_3$ Thin Film Sputter-Deposited onto Si Substrates"; pp. 243–53 in *Ferroelectric Thin Films, Materials Research Society Proceedings*, **Vol. 200**, Edited by E. R. Myers, and A. I. Kingon. Materials Research Society, Pittsburgh, PA, 1990.

[330]T. Sakuma, S. Yamamichi, S. Matsubara, H. Yamaguchi, and Y. Miyasaka, "Barrier Layers for Realization of High Capacitance Density in $SrTiO_3$ Thin-Film Capacitor on Silicon," *Appl. Phys. Lett.*, **57** [23] 2431–3 (1990).

[331]H. Yamaguchi, S. Matsubara, and Y. Miyasaka, "Reactive Coevaporation Synthesis and Characterization of $SrTiO_3$ Thin Films," *Jpn. J. Appl. Phys.*, **30** [9B] 2197–9 (1991).

[332]H. Nagata, T. Tsukahara, S. Gonda, M. Yoshimoto, and H. Koinuma, "Heteroepitaxial Growth of CeO_2(001) Films on Si(001) Substrates by Pulsed Laser Deposition in Ultrahigh Vacuum," *Jpn. J. Appl. Phys.*, **30** [6B] L1136–8 (1991).

[333]Y. Shichi, S. Tanimoto, T. Goto, K. Kuroiwa, and Y. Tarui, "Interaction of $PbTiO_3$ Films with Si Substrate," *Jpn. J. Appl. Phys.*, **33** [9B] 5172–7 (1994).

[334]D. H. Looney, "Semiconducting Translating Device"; US Patent No. 2,791,758, May 7, 1957.

[335]W. L. Brown, "Semiconductive Device"; US Patent No. 2,791,759, May 7, 1957.

[336]I. M. Ross, "Semiconducting Translating Device"; US Patent No. 2,791,760, May 7, 1957.

[337]J. A. Morton, "Electrical Switching and Storage"; US Patent No. 2,791,761, May 7, 1957.

[338]J. L. Moll and Y. Tarui, "A New Solid State Memory Resistor," *IEEE Trans. Electron Devices*, **10** [5] 338–9 (1963).

[339]P. M. Heyman and G. H. Heilmeier, "A Ferroelectric Field Effect Device," *Proc. IEEE*, **54** [6] 842–8 (1966).

[340]G. G. Teather and L. Young, "Non-Destructive Readout of Ferroelectrics by Field Effect Conductivity Modulation," *Solid State Electron.*, **11** [5] 527–33 (1968).

[341]S.-Y. Wu, "A New Ferroelectric Memory Device, Metal-Ferroelectric-Semiconductor Transistor," *IEEE Trans. Electron Devices*, **21** [8] 499–504 (1974).

[342]M. Suzuki, "Review on Future Ferroelectric Nonvolatile Memory: FeRAM—From the Point of View of Epitaxial Oxide Thin Films," *J. Ceram. Soc. Jpn.*, **103** [11] 1099–111 (1995).

[343]M. Suzuki, "Review on Future Ferroelectric Nonvolatile Memory: FeRAM - From the Point of View of Epitaxial Oxide Thin Films," *J. Ceram. Soc. Jpn. Int. Ed.*, **103** [11] 1088–99 (1995).

[344]K. J. Hubbard and D. G. Schlom, "Thermodynamic Stability of Binary Oxides in Contact with Silicon," *J. Mater. Res.*, **11** [11] 2757–76 (1996).

[345]D. G. Schlom, C. A. Billman, J. H. Haeni, J. Lettieri, P. H. Tan, R. R. M. Held, S. Völk, and K. J. Hubbard, "High-*K* Candidates for Use as the Gate Dielectric in Silicon MOSFETs"; pp. 31–78 in *Thin Films and Heterostructures for Oxide Electronics*, Edited by S. B. Ogale. Springer, New York, 2005.

[346]I. Barin, *Thermochemical Data of Pure Substances*, Vols. I and II, 3rd edition, VCH, Weinheim, 1995.
[347]E. J. Tarsa, K. L. McCormick, and J. S. Speck, "Common Themes in the Epitaxial Growth of Oxides on Semiconductors"; pp. 73–85 in *Epitaxial Oxide Thin Films and Heterostructures, Materials Research Society Proceedings*, Vol. 341, Edited by D. K. Fork, J. M. Phillips, R. Ramesh, and R. M. Wolf. Materials Research Society, Pittsburgh, PA, 1994.
[348]J. M. Phillips, "Substrate Selection for Thin-Film Growth," *MRS Bull.*, **20** [4] 35–9 (1995).
[349]D. G. Schlom and J. H. Haeni, "A Thermodynamic Approach to Selecting Alternative Gate Dielectrics," *MRS Bull.*, **27** [3] 198–204 (2002).
[350]V. V. Il'chenko, G. V. Kuznetsov, V. I. Strikha, and A. I. Tsyganova, "The Formation of a Barium Silicate Layer on Silicon," *Mikroelektron*, **27** [5] 340–5 (1998).
[351]V. V. Il'chenko, G. V. Kuznetsov, V. I. Strikha, and A. I. Tsyganova, "The Formation of a Barium Silicate Layer on Silicon," *Russ. Microelectron.*, **27** [5] 291–6 (1998).
[352]V. V. Il'chenko and G. V. Kuznetsov, "Effect of Oxygen on the Chemical Reactions and Electron Work Function in Ba–Si and BaO–Si Structures," *Pis'ma Zh. Tekh. Fiz.*, **27** [8] 58–63 (2001).
[353]V. V. Il'chenko and G. V. Kuznetsov, "Effect of Oxygen on the Chemical Reactions and Electron Work Function in Ba–Si and BaO–Si Structures," *Sov. Tech. Phys. Lett.*, **27** [4] 333–5 (2001).
[354]Y. S. Touloukian, R. K. Kirby, R. E. Taylor, and T. Y. R. Lee, *Thermal Expansion: Nonmetallic Solids, Vol. 13 of Thermophysical Properties of Matter*, p. 154. Plenum, New York, 1977.
[355]D. K. Fork, F. A. Ponce, J. C. Tramontana, N. Newman, J. M. Phillips, and T. H. Geballe, "High Critical Current Densities in Epitaxial $YBa_2Cu_3O_{7-\delta}$ Thin films on Silicon-on-Sapphire," *Appl. Phys. Lett.*, **58** [21] 2432–4 (1991).
[356]E. S. Machlin and P. Chaudhari, "Theory of 'Pseudomorphic Stabilization' of Metastable Phases in Thin Film Form"; pp. 11–29 in *Synthesis and Properties of Metastable Phases*, Edited by E. S. Machlin, and T. J. Rowland. The Metallurgical Society of AIME, Warrendale, 1980.
[357]C. P. Flynn, "Strain-Assisted Epitaxial Growth of New Ordered Compounds," *Phys. Rev. Lett.*, **57** [5] 599–602 (1986).
[358]R. Bruinsma and A. Zangwill, "Structural Transitions in Epitaxial Overlayers," *J. Phys. (Paris)*, **47** [12] 2055–73 (1986).
[359]R. F. C. Farrow (ed), *Molecular Beam Epitaxy: Applications to Key Materials*. Noyes, Park Ridge, 1995.
[360]E. M. Levin, C. R. Robbins, and H. F. McMurdie (eds), *Phase Diagrams for Ceramists*, **Vol. 1**, p. 127. American Ceramic Society, Columbus, 1964.
[361]F. Sugawara and S. Iida, "New Magnetic Perovskites $BiMnO_3$ and $BiCrO_3$," *J. Phys. Soc. Jpn.*, **20** [8] 1529 (1965).
[362]H. Faqir, H. Chiba, M. Kikuchi, Y. Syono, M. Mansori, P. Satre, and A. Sebaoun, "High-Temperature XRD and DTA Studies of $BiMnO_3$ Perovskite," *J. Solid State Chem.*, **142** [1] 113–9 (1999).
[363]T. Atou, H. Chiba, K. Ohoyama, Y. Yamaguchi, and Y. Syono, "Structure Determination of Ferromagnetic Perovskite $BiMnO_3$," *J. Solid State Chem.*, **145** [2] 639–42 (1999).
[364]Y. Maeno, T. M. Rice, and M. Sigrist, "The Intriguing Superconductivity of Strontium Ruthenate," *Phys. Today*, **54** [1] 42–7 (2001).
[365]N. Shirakawa, K. Murata, S. Nishizaki, Y. Maeno, and T. Fujita, "Pressure Dependence of Superconducting Critical Temperature of Sr_2RuO_4," *Phys. Rev. B*, **56** [13] 7890–3 (1997).
[366]C. W. Chu, P. H. Hor, R. L. Meng, L. Gao, Z. J. Huang, and Y. Q. Wang, "Evidence for Superconductivity above 40 K in the La–Ba–Cu–O Compound System," *Phys. Rev. Lett.*, **58** [4] 405–7 (1987).
[367]J. A. Kafalas and J. M. Longo, "High Pressure Synthesis of $(ABX_3)(AX)_n$ Compounds," *J. Solid State Chem.*, **4** [1] 55–9 (1972).
[368]I. I. Prosychev and I. S. Shaplygin, "Interaction in the BaO–RuO_2 System," *Zh. Neorg. Khim.*, **25**, 876–7 (1980).
[369]I. I. Prosychev and I. S. Shaplygin, *Russ. J. Inorg. Chem.*, **25** [3] 489 (1980).
[370]M. I. Gadzhiev and I. S. Shaplygin, "Reactions in the BaO–RuO_2 System," *Zh. Neorg. Khim.*, **29**, 2154–5 (1984).
[371]M. I. Gadzhiev and I. S. Shaplygin, "Reactions in the BaO–RuO_2 System," *Russ. J. Inorg. Chem.*, **29** [8] 1230–1 (1984).
[372]T. L. Popova, N. G. Kisel, V. I. Krivobok, and V. P. Karlov, "Interaction in the BaO–RuO_2 System," *Ukr. Khim. Zh.*, **48** [5] 457–60 (1982).
[373]T. L. Popova, N. G. Kisel, V. I. Krivobok, and V. P. Karlov, "Interaction in the BaO–RuO_2 System," *Sov. Prog. Chem.*, **48**, 8–10 (1982).
[374]J. B. Clark, P. W. Richter, and L. Du Toit, "High-Pressure Synthesis of $YScO_3$, $HoScO_3$, $ErScO_3$, and $TmScO_3$, and a Reevaluation of the Lattice Constants of the Rare Earth Scandates," *J. Solid State Chem.*, **23** [1–2] 129–34 (1978).
[375]R. P. Liferovich and R. H. Mitchell, "A Structural Study of Ternary Lanthanide Orthoscandate Perovskites," *J. Solid State Chem.*, **177** [6] 2188–97 (2004).
[376]E. M. Levin, C. R. Robbins, and H. F. McMurdie (eds), *Phase Diagrams for Ceramists*, **Vol. 2**, p. 93. American Ceramic Society, Columbus, 1969.
[377]N. Orloff, I. Takeuchi, J. C. Booth, D. Gu, A. Lewandoski, J. Mateu, C. J. Fennie, K. M. Rabe, W. Tian, and D. G. Schlom, "Broadband and Temperature Dependent Permittivity Measurements of Ruddlesden–Popper $Sr_{n+1}Ti_nO_{3n+1}$ ($n = 1,2,3$) Thin Films"; (unpublished).
[378]C. J. Fennie and K. M. Rabe, "Structural and Dielectric Properties of Sr_2TiO_4 from First Principles," *Phys. Rev. B*, **68** [18] 184111 (2003).
[379]M. A. Zurbuchen, J. Schubert, Y. Jia, W. Tian, V. Cherman, M. D. Biegalski, D. Fong, M. E. Hawley, A. K. Tagantsev, S. K. Streiffer, and D. G. Schlom, "Charge-Mediated Synthesis of $Sr_4Bi_4Ti_7O_{24}$"; (unpublished).
[380]E. C. Subbarao, "A Family of Ferroelectric Bismuth Compounds," *J. Phys. Chem. Solids*, **23**, 665–76 (1962).
[381]R. A. Armstrong and R. E. Newnham, "Bismuth Titanate Solid Solutions," *Mater. Res. Bull.*, **7** [10] 1025–34 (1972).
[382]J.van Suchtelen, "Product Properties: A New Application of Composite Materials," *Philips Res. Rep.*, **27** [1] 28–37 (1972).
[383]J. van den Boomgaard, D. R. Terrell, R. A. J. Born, and H. F. J. I. Giller, "An *in Situ* Grown Eutectic Magnetoelectric Composite Material: Part 1 Composition and Unidirectional Solidification," *J. Mater. Sci.*, **9** [10] 1705–9 (1974).
[384]A. M. J. G. van Run, D. R. Terrell, and J. H. Scholing, "An *in Situ* Grown Eutectic Magnetoelectric Composite Material: Part 2 Physical Properties," *J. Mater. Sci.*, **9** [10] 1710–4 (1974).
[385]L. P. M. Bracke and R. G. van Vliet, "A Broadband Magneto-Electric Transducer using a Composite Material," *Int. J. Electron.*, **51** [3] 255–62 (1981).
[386]R. E. Newnham, D. P. Skinner, and L. E. Cross, "Connectivity and Piezoelectric–Pyroelectric Composites," *Mater. Res. Bull.*, **13** [5] 525–36 (1978).
[387]J. van den Boomgaard and R. A. J. Born, "A Sintered Magnetoelectric Composite Material $BaTiO_3$–$Ni(Co,Mn)Fe_2O_4$," *J. Mater. Sci.*, **13** [7] 1538–48 (1978).
[388]G. Srinivasan, E. T. Rasmussen, A. A. Bush, K. E. Kamentsev, V. F. Meshcheryakov, and Y. K. Fetisov, "Structural and Magnetoelectric Properties of MFe_2O_4-PZT (M = Ni, Co) and $La_x(Ca, Sr)_{1-x}MnO_3$–PZT Multilayer Composites," *Appl. Phys. A*, **78** [5] 721–8 (2004).
[389]K. Lefki and G. J. M. Dormans, "Measurement of Piezoelectric Coefficients of Ferroelectric Thin Films," *J. Appl. Phys.*, **76** [3] 1764–7 (1994).
[390]M. A. Zurbuchen, S. Saha, T. Wu, J. Mitchell, and S. K. Streiffer, "Multiferroic Composite Ferroelectric–Ferromagnetic Films," *Appl. Phys. Lett.*, **87** [23] 232908 (2005).
[391]H. Zheng, J. Wang, S. E. Lofland, Z. Ma, L. Mohaddes-Ardabili, T. Zhao, L. Salamanca-Riba, S. R. Shinde, S. B. Ogale, F. Bai, D. Viehland, Y. Jia, D. G. Schlom, M. Wuttig, A. Roytburd, and R. Ramesh, "Multiferroic $BaTiO_3$–$CoFe_2O_4$ Nanostructures," *Science*, **303** [5658] 661–3 (2004).
[392]E. Klokholm, J. W. Matthews, A. F. Mayadas, and J. Angilello; pp. 105–9 in *Magnetism and Magnetic Materials*, Edited by C. D. Graham Jr., and J. J. Rhyne. American Institute of Physics, New York, 1972.
[393]L. B. Freund and S. Suresh, *Thin Film Materials: Stress, Defect Formation and Surface Evolution*, pp. 60–83, 283–90 Cambridge University Press, Cambridge, 2003.
[394]J. S. Speck, A. C. Daykin, A. Seifert, A. E. Romanov, and W. Pompe, "Domain Configurations due to Multiple Misfit Relaxation Mechanisms in Epitaxial Ferroelectric Thin Films. III. Interfacial Defects and Domain Misorientations," *J. Appl. Phys.*, **78** [3] 1696 (1995).
[395]W. D. Nix and B. M. Clemens, "Crystallite Coalescence: A Mechanism for Intrinsic Tensile Stresses in Thin Films," *J. Mater. Res.*, **14** [8] 3467–73 (1999).
[396]T. R. Taylor, P. J. Hansen, B. Acikel, N. Pervez, R. A. York, S. K. Streiffer, and J. S. Speck, "Impact of Thermal Strain on the Dielectric Constant of Sputtered Barium Strontium Titanate Thin Films," *Appl. Phys. Lett.*, **80** [11] 1978–80 (2002).
[397]C. L. Canedy, H. Li, S. P. Alpay, L. Salamanca-Riba, A. L. Roytburd, and R. Ramesh, "Dielectric Properties in Heteroepitaxial $Ba_{0.6}Sr_{0.4}TiO_3$ Thin Films: Effect of Internal Stresses and Dislocation-Type Defects," *Appl. Phys. Lett.*, **77** [11] 1695–7 (2000).
[398]I. B. Misirlioglu, A. L. Vasiliev, M. Aindow, S. P. Alpay, and R. Ramesh, "Threading Dislocation Generation in Epitaxial $(Ba,Sr)TiO_3$ Films Grown on (001) $LaAlO_3$ by Pulsed Laser Deposition," *Appl. Phys. Lett.*, **84** [10] 1742–4 (2004).
[399]M.-W. Chu, I. Szafraniak, R. Scholz, C. Harnagea, D. Hesse, M. Alexe, and U. Gösele, "Impact of Misfit Dislocations on the Polarization Instability of Epitaxial Nanostructured Ferroelectric Perovskites," *Nat. Mater.*, **3** [2] 87–90 (2004).
[400]S. P. Alpay, I. B. Misirlioglu, V. Nagarajan, and R. Ramesh, "Can Interface Dislocations Degrade Ferroelectric Properties," *Appl. Phys. Lett.*, **85** [11] 2044–6 (2004).
[401]V. Nagarajan, C. L. Jia, H. Kohlstedt, R. Waser, I. B. Misirlioglu, S. P. Alpay, and R. Ramesh, "Misfit Dislocations in Nanoscale Ferroelectric Heterostructures," *Appl. Phys. Lett.*, **86** [19] 192910 (2005).
[402]N. A. Pertsev, A. G. Zembilgotov, and A. K. Tagantsev, "Effect of Mechanical Boundary Conditions on Phase Diagrams of Epitaxial Ferroelectric Thin Films," *Phys. Rev. Lett.*, **80** [9] 1988–91 (1998).
[403]N. A. Pertsev and V. G. Koukhar, "Polarization Instability in Polydomain Ferroelectric Epitaxial Thin Films and the Formation of Heterophase Structures," *Phys. Rev. Lett.*, **84** [16] 3722–5 (2000).
[404]V. G. Koukhar, N. A. Pertsev, and R. Waser, "Thermodynamic Theory of Epitaxial Ferroelectric Thin Films with Dense Domain Structures," *Phys. Rev. B*, **64** [21] 214103 (2001).
[405]Y. L. Li, S. Y. Hu, Z. K. Liu, and L. Q. Chen, "Phase-Field Model of Domain Structures in Ferroelectric Thin Films," *Appl. Phys. Lett.*, **78** [24] 3878–80 (2001).
[406]Y. L. Li, S. Y. Hu, Z. K. Liu, and L. Q. Chen, "Effect of Substrate Constraint on the Stability and Evolution of Ferroelectric Domain Structures in Thin Films," *Acta Mater.*, **50** [2] 395–411 (2002).
[407]O. Diéguez, S. Tinte, A. Antons, C. Bungaro, J. B. Neaton, K. M. Rabe, and D. Vanderbilt, "Ab Initio Study of the Phase Diagram of Epitaxial $BaTiO_3$," *Phys. Rev B*, **69** [21] 212101 (2004).
[408]Y. L. Li and L. Q. Chen, "Temperature–Strain Phase Diagram for $BaTiO_3$ Thin Films," *Appl. Phys. Lett.*, **88** [7] 072905 (2006).
[409]N. A. Pertsev, V. G. Kukhar, H. Kohlstedt, and R. Waser, "Phase Diagrams and Physical Properties of Single-Domain Epitaxial $Pb(Zr_{1-x}Ti_x)O_3$ Thin Films," *Phys. Rev. B*, **67** [5] 54107 (2003).
[410]Y. L. Li, S. Choudhury, Z. K. Liu, and L. Q. Chen, "Effect of External Mechanical Constraints on the Phase Diagram of Epitaxial $PbZr_{1-x}Ti_xO_3$ Thin

Films-Thermodynamic Calculations and Phase-Field Simulations," *Appl. Phys. Lett*., **83** [8] 1608–10 (2003).
[411]S. Choudhury, Y. L. Li, and L. Q. Chen, "A Phase Diagram for Epitaxial $PbZr_{1-x}Ti_xO_3$ Thin Films at the Bulk Morphotropic Boundary Composition," *J. Am. Ceram. Soc*., **88** [6] 1669–72 (2005).
[412]N. A. Pertsev, A. K. Tagantsev, and N. Setter, "Phase Transitions and Strain-Induced Ferroelectricity in $SrTiO_3$ Epitaxial Thin Films," *Phys. Rev. B*, **61** [2] R825–9 (2000).
[413]N. A. Pertsev, A. K. Tagantsev, and N. Setter, "Erratum: Phase Transitions and Strain-Induced Ferroelectricity in $SrTiO_3$ Epitaxial Thin Films [Phys. Rev. B **61**, R825 (2000)]," *Phys. Rev. B*, **65** [21] 219901 (2002).
[414]A. Antons, J. B. Neaton, K. M. Rabe, and D. Vanderbilt, "Tunability of the Dielectric Response of Epitaxially Strained $SrTiO_3$ from First Principles," *Phys. Rev. B*, **71** [2] 024102 (2005).
[415]Y. L. Li, S. Choudhury, J. H. Haeni, M. D. Biegalski, A. Vasudevarao, A. Sharan, H. Z. Ma, J. Levy, V. Gopalan, S. Trolier-McKinstry, D. G. Schlom, Q. X. Jia, and L. Q. Chen, "Phase Transitions and Domain Structures in Strained Pseudocubic (100) $SrTiO_3$ Thin Films," *Phys. Rev. B*, **73** [18] 184112 (2006).
[416]A. Vasudevarao, A. Kumar, L. Tian, J. H. Haeni, Y. L. Li, C.-J. Eklund, Q. X. Jia, R. Uecker, P. Reiche, K. M. Rabe, L. Q. Chen, D. G. Schlom, and V. Gopalan, "Mutiferroic Domain Dynamics in Strained Strontium Titanate," *Phys. Rev. Lett*., **97** [25] 257602 (2006).
[417]Y. L. Li, S. Choudhury, J. H. Haeni, M. D. Biegalski, A. Vasudevarao, A. Sharan, H. Z. Ma, J. Levy, V. Gopalan, S. Trolier-McKinstry, D. G. Schlom, Q. X. Jia, and L. Q. Chen, "Phase Transitions and Domain Structures in Strained Pseudocubic (100) $SrTiO_3$ Thin Films," *Phys. Rev. B*, **73** [18] 184112 (2006).
[418]P. Irvin, J. Levy, J. H. Haeni, and D. G. Schlom, "Localized Microwave Resonances in Strained $SrTiO_3$ Thin Films," *Appl. Phys. Lett*., **88** [4] 042902 (2006).
[419]S. Denev, A. Kumar, M. D. Biegalski, H. W. Jang, C. M. Folkman, A. Vasudevarao, Y. Han, I. M. Reaney, S. Trolier-McKinstry, C. B. Eom, D. G. Schlom, and V. Gopalan, "Magnetic Color Symmetry of Lattice Rotations in a Diamagnetic Material," *Phys. Rev. Lett*., **100** [25] 257601 (2008).
[420]H. Z. Ma, J. Levy, M. D. Biegalski, D. G. Schlom, and S. Trolier-McKinstry, "Room-Temperature Electrooptic Properties of Strained $SrTiO_3$ Films Grown on $DyScO_3$," *J. Appl. Phys*., submitted.
[421]A. Vasudevarao, S. Denev, M. D. Biegalski, Y. L. Li, L. Q. Chen, S. Trolier-McKinstry, D. G. Schlom, and V. Gopalan, "Polarization Rotation Transitions in Anisotropically Strained $SrTiO_3$ Thin Films," *Appl. Phys. Lett*., **92** [19] 192902 (2008).
[422]M. D. Biegalski, S. Trolier-McKinstry, D. G. Schlom, S. K. Streiffer, M. Bernhagen, P. Reiche, and R. Uecker, "Asymmetric Dielectric Properties of $SrTiO_3$ Thin Films on $DyScO_3$ Substrates," *J. Appl. Phys*., submitted.
[423]S. Kamba, D. Nuzhnyy, V. Goian, S. Veljko, C. M. Brooks, J. H. Lee, D. G. Schlom, J.-H. Lee, J. Schubert, E. John, T. Katsufuji, and J. Petzelt, "Ferroelectricity in $SrTiO_3$ and $EuTiO_3$ Strained Thin Films: Polar Phonon Properties"; Presented at Fundamental Physics of Ferroelectrics, Williamsburg, Virginia, 2008.
[424]S. K. Streiffer, J. A. Eastman, D. D. Fong, C. Thompson, A. Munkholm, M. V. R. Murty, O. Auciello, G. R. Bai, and G. B. Stephenson, "Observation of Nanoscale 180° Stripe Domains in Ferroelectric $PbTiO_3$ Thin Films," *Phys. Rev. Lett*., **89** [6] 067601 (2002).
[425]E. D. Specht, H.-M. Christen, D. P. Norton, and L. A. Boatner, "X-Ray Diffraction Measurement of the Effect of Layer Thickness on the Ferroelectric Transition in Epitaxial $KTaO_3/KNbO_3$ Multilayers," *Phys. Rev. Lett*., **80** [19] 4317–20 (1998).
[426]H.-M. Christen, L. A. Knauss, and K. S. Harshavardhan, "Field-Dependent Dielectric Permittivity of Paraelectric Superlattice Structures," *Mater. Sci. Eng. B*, **56** [2–3] 200–3 (1998).
[427]H. M. Christen, E. D. Specht, S. S. Silliman, and K. S. Harshavardhan, "Ferroelectric and Antiferroelectric Coupling in Superlattices of Paraelectric Perovskites at Room Temperature," *Phys. Rev. B*, **68** [2] 20101 (2003).
[428]K. Abe, N. Yanase, K. Sano, M. Izuha, N. Fukushima, and T. Kawakubo, "Modification of Ferroelectricity in Heteroepitaxial $(Ba,Sr)TiO_3$ Films for Non-Volatile Memory Applications," *Integr. Ferroelectr*., **21** [1–4] 197–206 (1998).
[429]N. Yanase, K. Abe, N. Fukushima, and T. Kawakubo, "Thickness Dependence of Ferroelectricity in Heteroepitaxial $BaTiO_3$ Thin Film Capacitors," *Jpn. J. Appl. Phys., Part 1*, **38** [9B] 5305–8 (1999).
[430]M. Sepliarsky, S. R. Phillpot, M. G. Stachiotti, and R. L. Migoni, "Ferroelectric Phase Transitions and Dynamical Behavior in $KNbO_3/KTaO_3$ Superlattices by Molecular-Dynamics Simulation," *J. Appl. Phys*., **91** [5] 3165–71 (2002).
[431]V. Gopalan and R. Raj, "Domain Structure–Second Harmonic Generation Correlation in Potassium Niobate Thin Films Deposited on a Strontium Titanate Substrate," *J. Am. Ceram. Soc*., **79** [12] 3289–96 (1996).
[432]V. Gopalan and R. Raj, "Electric Field Induced Domain Rearrangement in Potassium Niobate Thin Films Studied by *in Situ* Second Harmonic Generation Measurements," *J. Appl. Phys*., **81** [2] 865–75 (1997).
[433]Y. Barad, J. Lettieri, C. D. Theis, D. G. Schlom, V. Gopalan, J. C. Jiang, and X. Q. Pan, "Probing Domain Microstructure in Ferroelectric $Bi_4Ti_3O_{12}$ Thin Films by Optical Second Harmonic Generation," *J. Appl. Phys*., **89** [2] 1387–92 (2001).
[434]Y. Barad, J. Lettieri, C. D. Theis, D. G. Schlom, V. Gopalan, J. C. Jiang, and X. Q. Pan, "Erratum: 'Probing Domain Microstructure in Ferroelectric $Bi_4Ti_3O_{12}$ Thin Films by Optical Second Harmonic Generation,' [J. Appl. Phys. **89**, 1387 (2001)]," *J. Appl. Phys*., **89** [9] 5230 (2001).
[435]M. Fiebig, D. Fröhlich, T. Lottermoser, and M. Maat, "Probing of Ferroelectric Surface and Bulk Domains in $RMnO_3$ (R = Y, Ho) by Second Harmonic Generation," *Phys. Rev. B*, **66** [14] 144102 (2002).
[436]K. A. Müller and H. Burkard, "$SrTiO_3$: An Intrinsic Quantum Paraelectric below 4K," *Phys. Rev. B*, **19** [7] 3593–602 (1979).
[437]R. C. Neville, B. Hoeneisen, and C. A. Mead, "Permittivity of Strontium Titanate," *J. Appl. Phys*., **43** [5] 2124–31 (1972).
[438]P. W. Forsbergh Jr., "Effect of a Two-Dimensional Pressure on the Curie Point of Barium Titanate," *Phys. Rev*., **93** [4] 686–92 (1954).
[439]C. J. Fennie and K. M. Rabe, "Magnetic and Electric Phase Control in Epitaxial $EuTiO_3$ from First Principles," *Phys. Rev. Lett*., **97** [26] 267602 (2006).
[440]T. Ando, A. B. Fowler, and F. Stern, "Electronic Properties of Two-Dimensional Systems," *Rev. Mod. Phys*., **54** [2] 437–672 (1982).
[441]A. Tsukazaki, A. Ohtomo, T. Kita, Y. Ohno, H. Ohno, and M. Kawasaki, "Quantum Hall Effect in Polar Oxide Heterostructures," *Science*, **315** [5817] 1388–91 (2007).
[442]H. P. R. Frederikse, W. R. Thurber, and W. R. Hosler, "Electronic Transport in Strontium Titanate," *Phys. Rev*., **134** [2A] A442–5 (1964).
[443]H. P. R. Frederikse and G. A. Candela, "Magnetic Susceptibility of Insulating and Semiconducting Strontium Titanate," *Phys. Rev*., **147** [2] 583–4 (1966).
[444]H. Suzuki, H. Bando, Y. Ootuka, I. H. Inoue, T. Yamamoto, K. Takahashi, and Y. Nishihara, "Superconductivity in Single-Crystalline $Sr_{1-x}La_xTiO_3$," *J. Phys. Soc. Jpn*., **65** [6] 1529–32 (1996).
[445]M. Gurvitch, H. L. Stormer, R. C. Dynes, J. M. Graybeal, and D. C. Jacobson, "Field Effect on Superconducting Surface Layers of $SrTiO_3$;" pp. 47–9, *Extended Abstracts Superconducting Materials*, **Vol. EA–9**, Edited by J. Bevk, and A. I. Braginski. Materials Research Society, Pittsburgh, 1986.
[446]R. Dingle, H. L. Störmer, A. C. Gossard, and W. Wiegmann, "Electron Mobilities in Modulation-Doped Semiconductor Heterojunction Superlattices," *Appl. Phys. Lett*., **33** [7] 665–7 (1978).
[447]R. J. Cava, "Structural Chemistry and the Local Charge Picture of Copper Oxide Superconductors," *Science*, **247** [4943] 656–62 (1990).
[448]J. H. Haeni, "Nanoengineering of Ruddlesden-Popper Phases using Molecular Beam Epitaxy"; Ph.D. Thesis, Pennsylvania State University, 2002. Available on-line at http://etda.libraries.psu.edu/theses/approved/WorldWideIndex/ETD-181/index.html
[449]G. B. Stringfellow (ed), *Phase Equilibria Diagrams*, **Vol. 9**, pp. 126, 130. American Ceramic Society, Westerville, 1992.
[450]T. Ikeda, "A Few Quarternary Systems of Perovskite Type $A^{2+}B^{4+}O_3$ Solid Solutions," *J. Phys. Soc. Jpn*., **14** [10] 1286–94 (1959).
[451]E. M. Levin, C. R. Robbins, and H. F. McMurdie (eds), *Phase Diagrams for Ceramists*, **Vol. 1**, p. 195. American Ceramic Society, Columbus, 1964.
[452]A. K. Gutakovskii, L. I. Fedina, and A. L. Aseev, "High Resolution Electron Microscopy of Semiconductor Interfaces," *Phys. Status Solidi A*, **150** [1] 127–40 (1995).
[453]S. Thoma and H. Cerva, "Comparison of the Information Content in 〈110〉- and 〈100〉-Projected High-Resolution Transmission Electron Microscope Images for the Quantitative Analysis of AlAs/GaAs Interfaces," *Ultramicroscopy*, **53** [1] 37–51 (1994).
[454]S. Li, J. A. Eastman, J. M. Vetrone, R. E. Newnham, and L. E. Cross, "Dielectric Response in Ferroelectric Superlattices," *Philos. Mag. B*, **76** [1] 47–57 (1997).
[455]N. Sai, B. Meyer, and D. Vanderbilt, "Compositional Inversion Symmetry Breaking in Ferroelectric Perovskites," *Phys. Rev. Lett*., **84** [24] 5636–9 (2000).
[456]J. B. Neaton and K. M. Rabe, "Theory of Polarization Enhancement in Epitaxial $BaTiO_3/SrTiO_3$ Superlattices," *Appl. Phys. Lett*., **82** [10] 1586–8 (2003).
[457]S. M. Nakhmanson, K. M. Rabe, and D. Vanderbilt, "Polarization Enhancement in Two- and Three-Component Ferroelectric Superlattices," *Appl. Phys. Lett*., **87** [10] 102906 (2005).
[458]S. M. Nakhmanson, K. M. Rabe, and D. Vanderbilt, "Predicting Polarization Enhancement in Multicomponent Ferroelectric Superlattices," *Phys. Rev. B*, **73** [6] 060101 (2006).
[459]J. Chaloupka and G. Khaliullin, "Orbital Order and Possible Superconductivity in $LaNiO_3/LaMO_3$ Superlattices," *Phys. Rev. Lett*., **100** [1] 016404 (2008).
[460]T. Shimuta, O. Nakagawara, T. Makino, S. Arai, H. Tabata, and T. Kawai, "Enhancement of Remanent Polarization in Epitaxial $BaTiO_3/SrTiO_3$ Superlattices with 'Asymmetric Structure'," *J. Appl. Phys*., **91** [4] 2290–4 (2002).
[461]M. H. Corbett, R. M. Bowman, J. M. Gregg, and D. T. Foord, "Enhancement of Dielectric Constant and Associated Coupling of Polarization Behavior in Thin Film Relaxor Superlattices," *Appl. Phys. Lett*., **79** [6] 815–7 (2001).
[462]L. Kim, D. Jung, J. Kim, J. S. Kim, and J. Lee, "Strain Manipulation in $BaTiO_3/SrTiO_3$ Artificial Lattice Toward High Dielectric Constant and its Nonlinearity," *Appl. Phys. Lett*., **82** [13] 2118–20 (2003).
[463]D. O'Neill, R. M. Bowman, and J. M. Gregg, "Dielectric Enhancement and Maxwell–Wagner Effects in Ferroelectric Superlattice Structures," *Appl. Phys. Lett*., **77** [10] 1520–2 (2000).
[464]G. Catalan, D. O'Neill, R. M. Bowman, and J. M. Gregg, "Relaxor Features in Ferroelectric Superlattices: A Maxwell–Wagner Approach," *Appl. Phys. Lett*., **77** [19] 3078–80 (2000).
[465]H. Zheng, Q. Zhan, F. Zavaliche, M. Sherburne, F. Straub, M. P. Cruz, L.-Q. Chen, U. Dahmen, and R. Ramesh, "Controlling Self-Assembled Perovskite-Spinel Nanostructures," *Nano Lett*., **6** [7] 1401–7 (2006).
[466]S. Ríos, A. Ruediger, A. Q. Jiang, J. F. Scott, H. Lu, and Z. Chen, "Orthorhombic Strontium Titanate in $BaTiO_3$–$SrTiO_3$ Superlattices," *J. Phys. Cond. Matter*, **15** [21] L305–9 (2003).
[467]K. Johnston, X. Y. Huang, J. B. Neaton, and K. M. Rabe, "First-Principles Study of Symmetry Lowering and Polarization in $BaTiO_3/SrTiO_3$ Superlattices with in-Plane Expansion," *Phys. Rev. B*, **71** [10] 100103(R) (2005).
[468]Y. L. Li, S. Y. Hu, D. Tenne, A. Soukiassian, D. G. Schlom, L. Q. Chen, X. X. Xi, K. J. Choi, C. B. Eom, A. Saxena, T. Lookman, and Q. X. Jia, "Interfacial

Coherency and Ferroelectricity of $BaTiO_3/SrTiO_3$ Superlattice Films," *Appl. Phys. Lett.*, **91** [25] 252904 (2007).
[469]Y. L. Li, S. Y. Hu, D. Tenne, A. Soukiassian, D. G. Schlom, X. X. Xi, K. J. Choi, C. B. Eom, A. Saxena, T. Lookman, Q. X. Jia, and L. Q. Chen, "Prediction of Ferroelectricity in $BaTiO_3/SrTiO_3$ Superlattices with Domains," *Appl. Phys. Lett.*, **91** [11] 112914 (2007).
[470]C. Ederer and N. A. Spaldin, "Effect of Epitaxial Strain on the Spontaneous Polarization of Thin Film Ferroelectrics," *Phys. Rev. Lett.*, **95** [25] 257601 (2005).
[471]K. M. Rabe, "Theoretical Investigations of Epitaxial Strain Effects in Ferroelectric Oxide Thin Films and Superlattices," *Curr. Opin. Solid State Mater. Sci.*, **9** [3] 122–7 (2006).
[472]C. Ederer and N. A. Spaldin, "Recent Progress in First-Principles Studies of Magnetoelectric Multiferroics," *Curr. Opin. Solid State Mater. Sci.*, **9** [3] 128–39 (2006).
[473]J. B. Neaton, C. Ederer, U. V. Waghmare, N. A. Spaldin, and K. M. Rabe, "First-Principles Study of Spontaneous Polarization in Multiferroic $BiFeO_3$," *Phys. Rev. B*, **71** [1] 014113 (2005).
[474]O. Dieguez, K. M. Rabe, and D. H. Vanderbilt, "First-Principles Study of Epitaxial Strain in Perovskites," *Phys. Rev. B*, **72** [14] 144101 (2005).
[475]M. Dawber, K. M. Rabe, and J. F. Scott, "Physics of Thin-Film Ferroelectric Oxides," *Rev. Mod. Phys.*, **77** [4] 1083–130 (2005).
[476]H. W. Jang, S. H. Beak, D. Ortiz, C. M. Folkman, R. R. Das, Y. H. Chu, P. Shafer, J. X. Zhang, S. Choudhury, V. Vaithyanathan, Y. B. Chen, X. Q. Pan, D. G. Schlom, L. Q. Chen, R. Ramesh, and C. B. Eom, "Strain-Induced Polarization Rotation in Epitaxial (001) $BiFeO_3$ Thin Films," *Phys. Rev. Lett.*, in press.



Long-Qing Chen is Professor of Materials Science and Engineering at Penn State University. He received a B.S. degree from Zhejiang University in China, a M.S. degree from State University of New York at Stony Brook, and a Ph.D. degree from MIT. After a 2-year post-doc appointment at Rutgers University, he joined the faculty at Penn State in 1992. His main research interest is in developing computational models for predicting mesoscale microstructure evolution in advanced materials. Prof. Chen is the author or co-author of more than 200 papers and has delivered more than 150 invited presentations. He received numerous awards including an ONR Young Investigator Award, a NSF special research creativity award, a Wilson Award for Excellence in Research from his college, a University Faculty Scholar Medal in Engineering at Penn State, a Outstanding Overseas Young Scholar by the Chinese Natural Science Foundation, a Changjiang Chair Professorship by the Chinese Ministry of Education, a Guggenheim Fellowship, a Royal Society Kan Tong Po Fellowship, and the 2006 ASM Materials Research Silver Medal.



Xiaoqing Pan is a Professor in the Department of Materials Science and Engineering at the University of Michigan, Ann Arbor. He received B.S. and M.S. degrees in condensed matter physics from Nanjing University in China and a Ph.D. degree from Universität des Saarlandes in Germany. After a post-doc at the Max-Planck Institute für Metallforschung in Stuttgart, he joined the faculty at the University of Michigan. His research interests involve the epitaxial growth and structural characterization of functional materials including catalysts, oxide semiconductors, dielectric, and ferroelectric oxides. He is particularly interested in the structure–property relationships of interfaces and defects at the atomic scale. He is best known for his atomic scale characterization of oxide materials using high-resolution transmission electron microscopy. He has published over 200 papers. He has received the National Science Foundation's CAREER Award and the Chinese Natural Science Foundation's Outstanding Young Investigator Award.



Darrell Schlom is a Professor in the Department of Materials Science and Engineering at Cornell University. He received a B.S. degree from Caltech, and M.S. and Ph.D. degrees from Stanford University. After a post-doc at IBM's research lab in Zurich, Switzerland, he joined the faculty at Penn State University where the work described in this paper was performed. His research interests involve the heteroepitaxial growth and characterization of oxide thin films, especially those with functional properties (ferroelectric, piezoelectric, ferromagnetic, or a combination of these properties), including their epitaxial integration with semiconductors. He is particularly interested in the preparation of high quality oxide heterostructures with electronic applications (e.g., superlattices and metastable phases of dielectric and ferroelectric oxides) by MBE. He has published over 300 papers and has seven patents. He has been awarded invention achievement awards by IBM and SRC; young investigator awards by ONR, NSF, and the American Association for Crystal Growth; an Alexander von Humboldt Research Fellowship, and the ASM International Bradley Stoughton Award for Young Teachers. He is a Fellow of the American Physical Society.



Andreas Schmehl is a researcher in the group of Prof. Jochen Mannhart at the Center for Electronic Correlations and Magnetism at the University of Augsburg, Germany. He received a physics diploma and a Ph.D. degree in physics from the University of Augsburg. As part of a Feodor Lynen research scholarship, awarded by the Alexander von Humboldt foundation, he spent 2 years as post-doc in the group of Prof. Darrell G. Schlom at Penn State University. His research interests involve the electronic properties of interfaces in materials with strong electronic correlations, electronics based on oxide thin films, and semiconductor-based spin electronics. His main focus is the preparation of high-quality metal-oxide thin films (spin polarized semiconductors, superconductors, ferromagnets) and their utilization for novel device concepts as well as for basic research. He has published over 30 papers and owns four patents. He is currently working on his habilitation.



Mark Zurbuchen is a senior member of the technical staff in the Microelectronics Technology Department at The Aerospace Corporation. He received a B.S. degree from U. Missouri, an M.S. from Rensselaer, and a Ph.D. from Penn State. He worked in R&D at a small tech firm and as a post-doc at Argonne. He was at NIST prior to joining the staff at Aerospace, and is owner of TAECO LLC (www.taecompany.com). His interest centers on synthesis and characterization of heteroepitaxial systems, particularly for the integration of heterogeneous materials and the formation of new compounds for microelectronic applications. His current work focuses on formation dynamics of epitaxial systems having differing anion chemistries (e.g., oxides, nitrides, fluorides, and sulfides), and on 3D analysis of nanoscale structures by TEM tomography. His main expertise are in TEM and X-ray diffraction methods, and film growth by pulsed-laser deposition. He has published 27 papers and has 10 patents awarded or pending. He has been awarded invention achievement awards by Aerospac e Corp., and an NRC Postdoctoral Fellowship award. □



Reprinted from the MRS Bulletin, Vol 39, Elastic strain engineering of ferroic oxides, Darrell G. Schlom, Long-Qing Che, Craig J. Fennie, Venkatraman Gopalan, David A. Muller, Xiaoqing Pan, Ramamoorthy Ramesh, and Reinhard Uecker, 118-130, Copyright 2014, with permission from Cambridge University Press.

Elastic strain engineering of ferroic oxides

Darrell G. Schlom, Long-Qing Chen, Craig J. Fennie, Venkatraman Gopalan, David A. Muller, Xiaoqing Pan, Ramamoorthy Ramesh, and Reinhard Uecker

Using epitaxy and the misfit strain imposed by an underlying substrate, it is possible to elastically strain oxide thin films to percent levels—far beyond where they would crack in bulk. Under such strains, the properties of oxides can be dramatically altered. In this article, we review the use of elastic strain to enhance ferroics, materials containing domains that can be moved through the application of an electric field (ferroelectric), a magnetic field (ferromagnetic), or stress (ferroelastic). We describe examples of transmuting oxides that are neither ferroelectric nor ferromagnetic in their unstrained state into ferroelectrics, ferromagnets, or materials that are both at the same time (multiferroics). Elastic strain can also be used to enhance the properties of known ferroic oxides or to create new tunable microwave dielectrics with performance that rivals that of existing materials. Results show that for thin films of ferroic oxides, elastic strain is a viable alternative to the traditional method of chemical substitution to lower the energy of a desired ground state relative to that of competing ground states to create materials with superior properties.

The strain game

For at least 400 years, humans have studied the effects of pressure (hydrostatic strain) on the properties of materials.[1] In the 1950s, it was shown that biaxial strain, where a film is clamped to a substrate but free in the out-of-plane direction, can alter the transition temperatures of superconductors[2] (T_c) and ferroelectrics (T_C).[3]

What has changed in recent years is the magnitude of the biaxial strain that can be imparted. Bulk ferroic oxides are brittle and will crack under moderate strains, typically 0.1%. One way around this limitation is the approach of bulk crystal chemists, to apply "chemical pressure" through isovalent cation substitution. A disadvantage of such a bulk approach, however, is the introduction of disorder and potentially unwanted local distortions. Epitaxial strain, the trick of the thin-film alchemist, provides a potentially disorder-free route to large biaxial strain and has been used to greatly enhance the mobility of transistors[4,5] (see the article by Bedell et al. in this issue), increase catalytic activity (see the article by Yildiz in this issue), alter band structure[6] (see the article by Yu et al. in this issue), and significantly increase superconducting,[7,8] ferromagnetic,[9–11] and ferroelectric[12–16] transition temperatures. This approach, which we refer to as the "strain game," is illustrated in **Figure 1** for elastically strained films of oxides with the perovskite structure.

Strains of about ±3% are common in epitaxial oxide films today,[17–20] with the record to date being a whopping 6.6% compressive strain achieved in thin $BiFeO_3$ films grown on (110) $YAlO_3$.[21–24] These strains are an order of magnitude higher than where these materials would crack in bulk.[25–27]

Strained $SrTiO_3$ and the importance of suitable substrates

The strain game for ferroics was ignited by the demonstration that an oxide that normally is not ferroelectric at any temperature can be made ferroelectric at room temperature through the application of biaxial strain.[12] Such a gigantic shift in properties and T_C had never before been clearly seen in any

Darrell G. Schlom, Department of Materials Science and Engineering, Cornell University and Kavli Institute at Cornell for Nanoscale Science; schlom@cornell.edu
Long-Qing Chen, Millennium Science Complex, Materials Research Institute, Penn State University; lqc3@psu.edu
Craig J. Fennie, School of Applied and Engineering Physics, Cornell University; fennie@cornell.edu
Venkatraman Gopalan, Materials Science and Engineering, Penn State University; vgopalan@psu.edu
David A. Muller, School of Applied and Engineering Physics, Cornell University and Kavli Institute at Cornell for Nanoscale Science, Cornell; dm24@cornell.edu
Xiaoqing Pan, Department of Materials Science and Engineering, University of Michigan; panx@umich.edu
Ramamoorthy Ramesh, Oak Ridge National Laboratory; rameshr@ornl.gov
Reinhard Uecker, Leibniz Institute for Crystal Growth, Berlin; reinhard.uecker@ikz-berlin.de
DOI: 10.1557/mrs.2014.1

© 2014 Materials Research Society

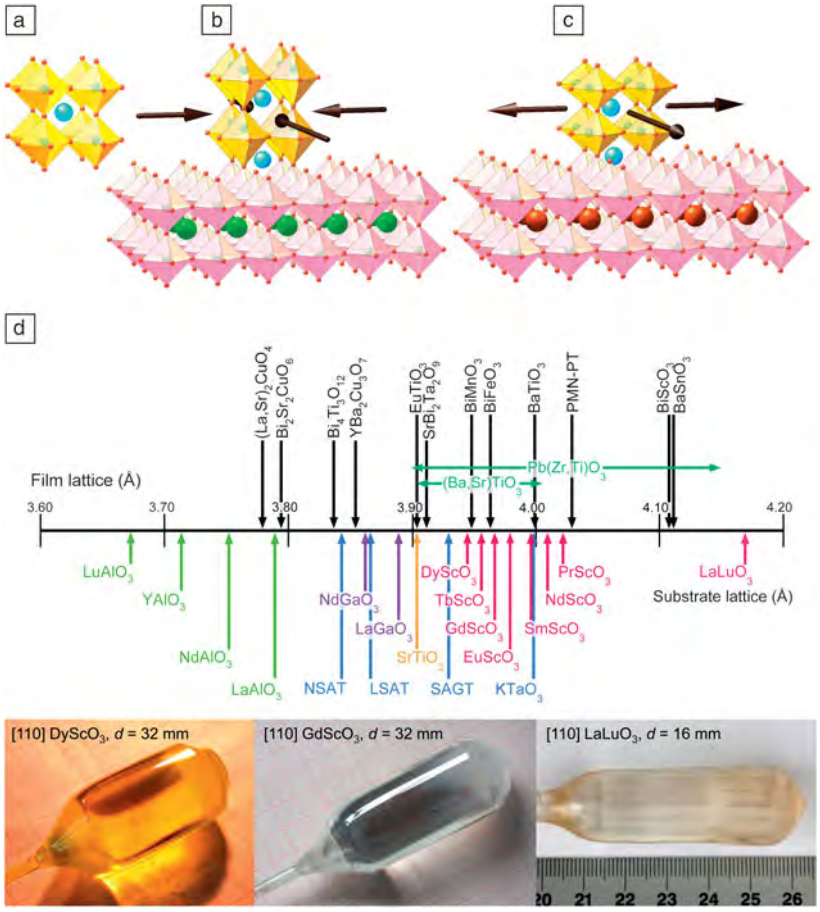


Figure 1. How the "strain game" is used to impart biaxial elastic strain on an oxide film via epitaxy. (a) The crystal structure of an unstrained oxide, in this case an oxide with the perovskite structure, in its unstrained state. When deposited on a substrate with a larger or smaller spacing, the energetic preference of the deposited atoms to follow the template of the underlying substrate (epitaxy) can result in the film beginning in either (b) biaxial compression or (c) biaxial tension. (d) A number line showing the pseudotetragonal or pseudocubic *a*-axis lattice constants in angstroms of some perovskites and perovskite-related phases of interest, including ferroics (above the number line) and of some of the perovskite substrates that are available commercially (below the number line). LSAT, $(LaAlO_3)_{0.29}$—$(SrAl_{1/2}Ta_{1/2}O_3)_{0.71}$; NSAT, $(NdAlO_3)_{0.39}$—$(SrAl_{1/2}Ta_{1/2}O_3)_{0.61}$; SAGT, $Sr_{1.04}Al_{0.12}Ga_{0.35}Ta_{0.50}O_3$. Photographs of exemplary single crystals used as substrates, each with diameter, *d*. (d) An updated version of the plot in Reference 24.

ferroic system; nonetheless, this achievement was the experimental realization of what had been predicted years earlier by theory.[28,29] **Figure 2** shows the strain phase diagram of $(001)_p$ $SrTiO_3$ calculated by thermodynamic analysis,[12,14,15,28–30] where the p subscript indicates pseudocubic Miller indices. These predictions imply that a biaxial tensile strain on the order of 1% will shift the T_C of $SrTiO_3$ to the vicinity of room temperature.[12,28–32] Although many researchers had grown $SrTiO_3$ films on substrates with different spacings, the lattice mismatches were so large and the films so thick that the films were no longer elastically strained.

Fully commensurate, elastically strained epitaxial films have the advantage that high densities of threading dislocations (e.g., the ~10^{11} dislocations cm^{-2} observed, for example, in partially relaxed $(Ba_xSr_{1-x})TiO_3$ films)[33,34] are avoided. Strain fields around dislocations locally alter the properties of a film, making its ferroelectric properties inhomogeneous and often degraded.[35–37] To achieve highly strained ferroic films and keep them free of such threading dislocations, one needs to keep them thin, typically not more than a factor of five beyond the Matthews-Blakeslee critical thickness, beyond which it becomes energetically favorable (though typically constrained by kinetics) for a film to relax by the introduction of dislocations.[27,38] Thickness-dependent studies, involving the growth of a ferroic on just one substrate material to study the effect of strain in partially relaxed films, are not as easy to interpret as experiments utilizing commensurate films grown on several different substrate materials covering a range of lattice spacings. In the former, the strains are inhomogeneous, and the high concentration of threading dislocations can obfuscate intrinsic strain effects.

Exploring the strain predictions in Figure 2a was greatly simplified by the development of new substrates with a broad range of spacings to impart a desired strain state into the overlying $SrTiO_3$ film. These substrates have the same structure as $SrTiO_3$—the perovskite structure—but different lattice spacings. The number of perovskite single crystals that are available commercially as large substrates (with surfaces at least 10 mm × 10 mm in size) has nearly doubled in the last decade due to the work of the present authors.[39–41] Today, various single crystal perovskite and perovskite-related substrates are commercially available (see Figure 1d), including $LuAlO_3$,[42,43] $YAlO_3$,[44] $LaSrAlO_4$,[45] $NdAlO_3$,[46] $LaAlO_3$,[47,48] $LaSrGaO_4$,[49] $(NdAlO_3)_{0.39}$—$(SrAl_{1/2}Ta_{1/2}O_3)_{0.61}$ (NSAT),[50] $NdGaO_3$,[51,52] $(LaAlO_3)_{0.29}$—$(SrAl_{1/2}Ta_{1/2}O_3)_{0.71}$ (LSAT),[50,53] $LaGaO_3$,[54] $SrTiO_3$,[55–58] $Sr_{1.04}Al_{0.12}Ga_{0.35}Ta_{0.50}O_3$ (SAGT), $DyScO_3$,[12,39] $TbScO_3$,[40] $GdScO_3$,[13,39,59] $EuScO_3$, $SmScO_3$,[39,60] $KTaO_3$,[61] $NdScO_3$,[39,62] $PrScO_3$,[63] and $LaLuO_3$;[64] many of these are produced with structural perfection rivaling that of conventional semiconductors. The perfection of the substrate, the best of which are grown by the Czochralski method (which is not applicable to most ferroic oxides because they do not melt congruently), can be passed on to the film via epitaxy. This has led to the growth of strained epitaxial films of the ferroics $SrTiO_3$,[38,65] $BaTiO_3$,[14] $BiFeO_3$,[66] $BiMnO_3$,[67] and $EuTiO_3$,[16] with rocking curve full width at half maximum values ≤11 arcsec (0.003°)—identical to those of the commercial substrates upon which they are grown and significantly narrower

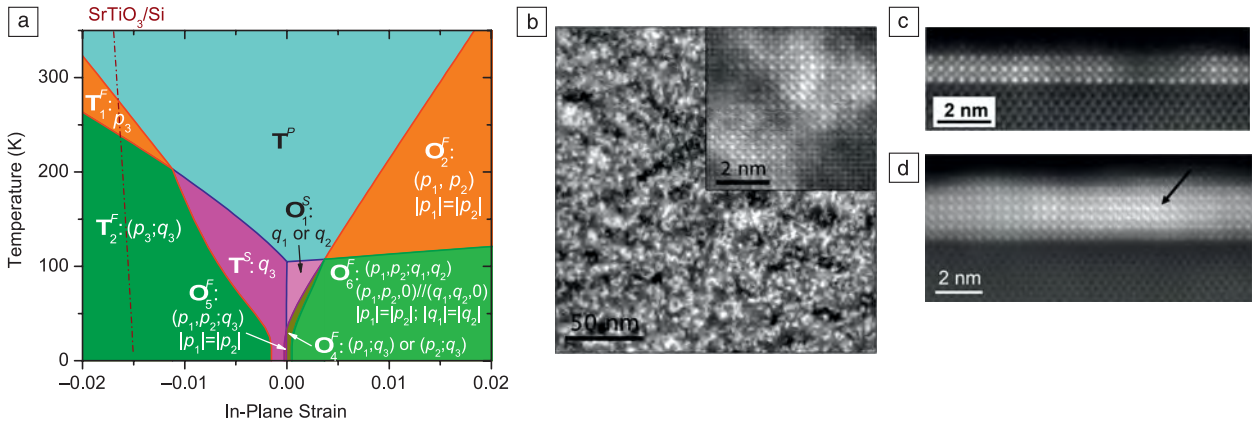


Figure 2. (a) The strain phase diagram of $(001)_p$-oriented $SrTiO_3$ calculated assuming a single-domain state for all structural and ferroelectric phases. The letters T and O used in the phase notations indicate tetragonal and orthorhombic crystallographic symmetries, respectively, under a constraint. The paraelectric, ferroelectric, and ferroelastic (or antiferrodistortive structural) natures of the phases are revealed by the superscripts *P*, *F*, and *S*, respectively. The components of the polarization vector **P** corresponding to the phases (along the crystallographic directions of pseudocubic $SrTiO_3$) are indicated within the parentheses following the phase notation. The dashed line corresponds to $(001)_p$ $SrTiO_3$ commensurately strained to (001) Si. At room temperature, it is strained in biaxial compression by ~1.7%. This strain decreases slightly with temperature due to the larger thermal expansion coefficient of $SrTiO_3$ than silicon. (b) Plan-view and (c) cross-sectional annular dark field (ADF) scanning transmission electron microscopy (STEM) images of a nominally 2 unit-cell-thick (0.8 nm) epitaxial $(001)_p$ $SrTiO_3$ film grown on (001) Si and capped with amorphous silicon. (d) Cross-sectional ADF-STEM images of a nominally 5 unit-cell-thick (2.0 nm) commensurate epitaxial $(001)_p$ $SrTiO_3$ film grown on (001) Si. The image shows an average film thickness of 6.5 unit cells, suggesting nonuniform $SrTiO_3$ coverage. In the area marked with an arrow, more than one $SrTiO_3$ grain is imaged in projection. (a) Adapted from References 14 and 15 and has only a minor difference from that presented in References 28 and 29. (b) and (c) Reprinted with permission from Reference 78. © 2008 American Physical Society. (d) Reprinted with permission from Reference 15. © 2009 AAAS.

(indicative of higher structural perfection) than the most perfect bulk single crystals of these same materials.

Using these new perovskite substrates, predictions of the $SrTiO_3$ strain phase diagram shown in Figure 2 were assessed. Not only was it found possible to transmute $SrTiO_3$ into a room temperature ferroic,[12,68,69] but the experimentally determined point group,[31,32,70–72] direction and magnitude of spontaneous polarization (P_S),[31,32,65,70–73] observed shifts in T_C [12,70,71] and soft mode frequency with biaxial strain,[74] and existence of a transition to a simultaneously ferroelectric and ferroelastic phase at lower temperatures[70–72,74] were all in accord with theory. Not all of the experimental observations, however, were in agreement with theory. For example, it was observed that strained $SrTiO_3$ films exhibit a significant frequency dependence to their dielectric response.[65,73] This relaxor ferroelectric behavior is due to defects. On account of the strain, the $SrTiO_3$ matrix is highly polarizable and can be easily polarized by defect dipoles that arise from non-stoichiometry in the $SrTiO_3$ film. Based on how the properties of strained $SrTiO_3$ films vary with non-stoichiometry, strained, perfectly stoichiometric $SrTiO_3$ films are not expected to show relaxor behavior.[75]

To make it possible for strain-enabled or strain-enhanced functionalities to be exploited in mainstream device architectures, it is desirable to play the strain game on substrates relevant to the semiconductor industry. One such example is the integration of commensurately strained $SrTiO_3$ films with silicon.[15] The lattice mismatch between $(001)_p$ $SrTiO_3$ and (001) Si is 1.7%, as indicated by the dashed line on the left side of the strain phase diagram in Figure 2a. From theory (Figure 2a), such a film would be expected to be ferroelectric with a T_C near room temperature. This integration is, however, rather challenging due to (1) the high reactivity of silicon with many elements and their oxides,[76,77] and (2) the thermodynamic driving force for a pristine silicon surface to oxidize and form an amorphous native oxide (SiO_2), which blocks epitaxy, under the oxidizing conditions typically used for the growth of oxide thin films. Despite these impediments, thin commensurate $SrTiO_3$ films have been grown directly on silicon without discernible intermediate layers and free of reaction, and are found to be ferroelectric at room temperature.[15]

Planar-view and cross-sectional annular dark field (ADF) scanning transmission electron micrographs (STEM) of epitaxial $(001)_p$ $SrTiO_3$ films grown on and commensurately strained to (001) Si are shown in Figure 2b–d. Although the interface between $SrTiO_3$ and silicon is seen to be abrupt and free of reaction, these images reveal additional challenges to the growth of $SrTiO_3$ on silicon. First is the propensity of $SrTiO_3$ to nucleate as islands and not wet the surface of the silicon substrate.[78] Even using kinetically limited growth conditions,[15,79] it takes multiple unit cells of growth before the $SrTiO_3$ islands coalesce.[78] Second are frequent out-of-phase boundaries in the $SrTiO_3$ film (see Figure 2d) resulting from the step height of (001) Si (0.14 nm) not matching the step height of $(001)_p$ $SrTiO_3$ (0.39 nm). Out-of-phase boundaries can form during the coalescence of $SrTiO_3$ islands that have nucleated on different (001) Si terraces. The arrow in Figure 2d marks an area where the $SrTiO_3$ islands are out-of-phase with each other.

For the growth of high-quality films of ferroic oxides with a desired strain state, not only are appropriate substrates of exceptionally high perfection needed, but also methods to prepare them with smooth, well-ordered surfaces with a specific chemical termination on which epitaxial growth can be reliably initiated. For example, chemical-mechanically polished (001) $SrTiO_3$ substrates display a mixture of SrO- and TiO_2-terminated surfaces. A combination of chemical etching and annealing has been shown to yield $SrTiO_3$ substrates with known surface termination. Kawasaki et al.[80] showed that an NH_4F-buffered HF solution with controlled pH enables etching of the more basic SrO layer and leaves a completely TiO_2 terminated surface on the substrate. This method of preparing a TiO_2-terminated (001) $SrTiO_3$ surface has been further perfected by Koster et al.[81] SrO-terminated (001) $SrTiO_3$ substrates can also be prepared.[82] A means to prepare low defect surfaces with controlled termination has since been developed for (110) $SrTiO_3$,[83] (111) $SrTiO_3$,[83,84] $(001)_p$ $LaAlO_3$,[85,86] $(111)_p$ $LaAlO_3$,[85] (110) $NdGaO_3$,[86] $(001)_p$ LSAT,[86,87] (110) $DyScO_3$,[88,89] (110) $TbScO_3$,[88] (110) $GdScO_3$,[88] (110) $EuScO_3$,[88] (110) $SmScO_3$,[88] (001) $KTaO_3$,[90] (110) $NdScO_3$,[88] and (110) $PrScO_3$[88] substrates.

The strain game is capable of enhancing the properties of a multitude of ferroelectric systems. Shifts in ferroelectric T_C of roughly 300 K per percent biaxial strain, quite comparable to those predicted[28–32] and observed[12,68–74] for $SrTiO_3$, were first predicted by theory and subsequently verified by experiments on biaxially strained $BaTiO_3$[13,14,91–94] and $PbTiO_3$[14,91,95–100] films. Strain effects of comparable magnitude have also been observed in strained (Ba,Sr)TiO_3 films[101,102] and in strained-layer superlattices: $KTaO_3/KNbO_3$,[103] $SrTiO_3/SrZrO_3$,[104] $SrTiO_3/BaZrO_3$,[105] $PbTiO_3/SrTiO_3$,[106,107] $BaTiO_3/SrTiO_3$,[108–111] and $CaTiO_3/SrTiO_3/BaTiO_3$.[112–114]

The success of theory in predicting the effect of strain on a multitude of ferroelectrics, together with advances in the ability to customize the structure and strain of oxide heterostructures at the atomic-layer level, has enabled a new era: ferroelectric oxides by design.[14] The appropriate theoretical methods to design strain-enhanced ferroelectrics depend on the material and whether or not domains need to be taken into account. First-principles methods are good for new materials where the coefficients of the Landau–Devonshire free energy expansion,[30] a Taylor expansion of the free energy of a material in powers of its order parameter (polarization for typical ferroelectrics), are unknown. Due to the relatively small number of atoms that can be included in such calculations, however, the calculations are limited to single-domain materials. Measurements on materials can yield the coefficients needed in Landau–Devonshire thermodynamic analysis to calculate the effect of strain in the absence of domains.[30]

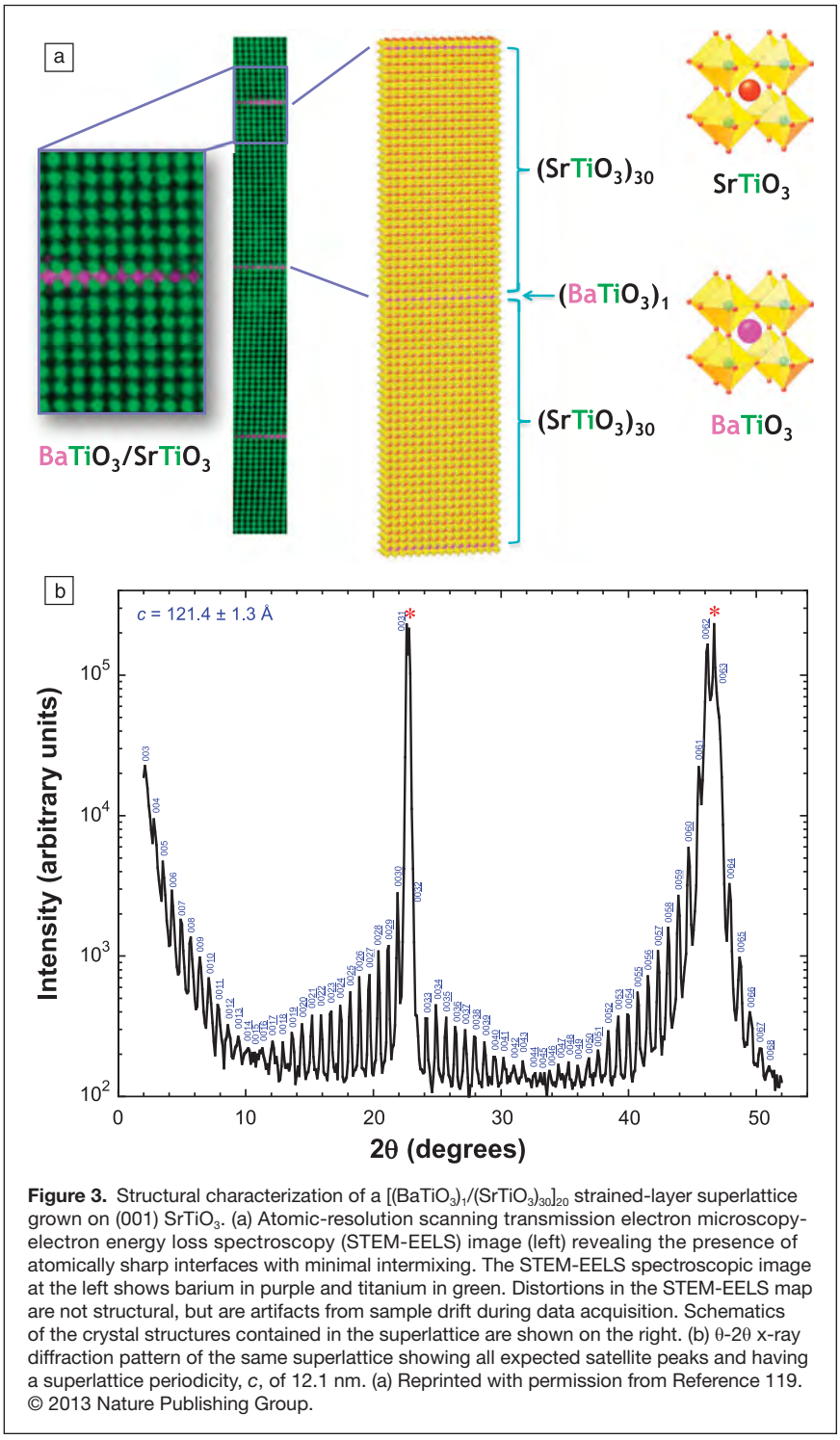


Figure 3. Structural characterization of a $[(BaTiO_3)_1/(SrTiO_3)_{30}]_{20}$ strained-layer superlattice grown on (001) $SrTiO_3$. (a) Atomic-resolution scanning transmission electron microscopy-electron energy loss spectroscopy (STEM-EELS) image (left) revealing the presence of atomically sharp interfaces with minimal intermixing. The STEM-EELS spectroscopic image at the left shows barium in purple and titanium in green. Distortions in the STEM-EELS map are not structural, but are artifacts from sample drift during data acquisition. Schematics of the crystal structures contained in the superlattice are shown on the right. (b) θ-2θ x-ray diffraction pattern of the same superlattice showing all expected satellite peaks and having a superlattice periodicity, *c*, of 12.1 nm. (a) Reprinted with permission from Reference 119. © 2013 Nature Publishing Group.

Phase-field simulations, which also require coefficients obtained from either experiment or first-principles calculations, can be used to take domains into account.[97,98] An example is $(BaTiO_3)_n/(SrTiO_3)_m$ strained-layer superlattices, where n and m refer to the thickness, in unit cells, of the $(001)_p$ $BaTiO_3$ and $(001)_p$ $SrTiO_3$ layers, respectively. Despite the 2.3% lattice mismatch between the $(001)_p$ $BaTiO_3$ and $(001)_p$ $SrTiO_3$ layers, such superlattices can be commensurately strained. In **Figure 3**, the structural characterization of a commensurate $(BaTiO_3)_n/(SrTiO_3)_m$ superlattice with $n = 1$ and $m = 30$ is shown. The macroscopic regularity of this superlattice, which was grown by molecular beam epitaxy (MBE), is demonstrated by the presence and sharpness of all of the superlattice reflections in its x-ray diffraction pattern (see Figure 3b).[60,119] Despite the $BaTiO_3$ layer being just a single unit cell thick (0.4 nm) and well-separated from neighboring $BaTiO_3$ layers, ultraviolet Raman measurements show that it is still ferroelectric.[60]

The ability to compare theory and experiment has motivated refinements in theory, including attention to not only mechanical (strain) and electrical boundary conditions (whether the ferroelectric is bounded by conducting electrodes or insulating layers), but also to unequal biaxial strain[115,116] and the ability of a ferroelectric film to break up into multiple domains.[97,98] For strained-layer superlattices of $BaTiO_3/SrTiO_3$, it was shown that quantitative agreement between the predicted and observed T_C for superlattices with a wide range of periodicities only occurred if calculations in which the possibility of multiple domains was considered.[109,110] For some $BaTiO_3/SrTiO_3$ superlattices, such three-dimensional phase-field calculations indicated that the low energy configuration was a multiple-domain state, which allowed the polarization in the $(001)_p$ $SrTiO_3$ layers to drop considerably when the $(001)_p$ $BaTiO_3$ layer was thinner than the $(001)_p$ $SrTiO_3$ layer, resulting in a significant increase in T_C compared to the single-domain state.[109,110] The domains anticipated to be present by theory, in order to quantitatively explain the observed T_C values, have recently been observed in $BaTiO_3/SrTiO_3$ strained-layer superlattices.[117,118]

Strain engineering of multiferroics

Emboldened by these successes, the strain game has more recently turned to enhancing materials containing multiple ferroic order parameters (i.e., multiferroics such as $BiFeO_3$) or to create new multiferroics from materials that are on the verge of being ferroic (e.g., $EuTiO_3$). Illustrative examples are described in the sections that follow.

Strained $BiFeO_3$—Morphing a room-temperature multiferroic

Bismuth ferrite, $BiFeO_3$, is one of the few materials that is simultaneously ferroelectric and magnetically ordered (antiferromagnetically in the case of $BiFeO_3$) at room temperature.[120–124] All of the other room-temperature multiferroics are, however, metastable. These include the high-pressure phase $BiCoO_3$,[122] strain-stabilized $ScFeO_3$ with the corundum structure,[123] and the hexagonal polymorph of $LuFeO_3$ that has been stabilized via epitaxy.[124] In its unstrained state, $BiFeO_3$ has the highest remnant polarization of any known ferroelectric.[120,121,125–127] $BiFeO_3$ also exhibits several polymorphs that are relatively close in energy to each other. Further, in $BiFeO_3$, the four fundamental degrees of freedom—electronic

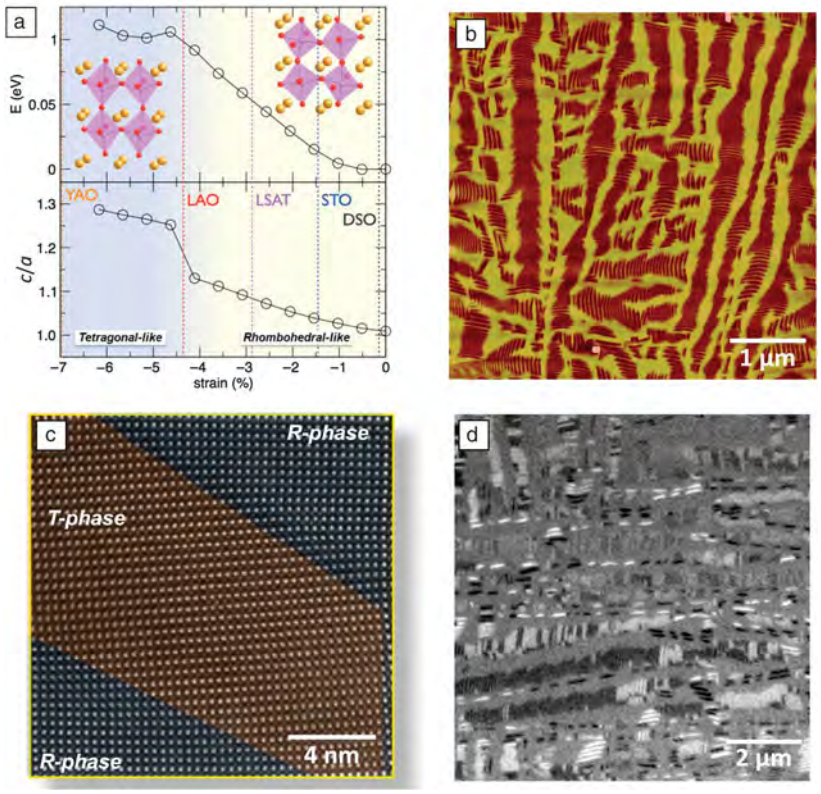


Figure 4. (a) *Ab initio* calculations of the energy and structure (ratio of pseudotetragonal lattice constants *c*/*a*) of the ground state of $BiFeO_3$ as a function of bi-axial, in-plane compressive strain on various substrates: YAO, $YAlO_3$; LAO, $LaAlO_3$; STO, $SrTiO_3$; LSAT, $(LaAlO_3)_{0.29}—(SrAl_{1/2}Ta_{1/2}O_3)_{0.71}$; DSO, $DyScO_3$. (b) Atomic force microscopy image of a partially relaxed, ~70-nm-thick $BiFeO_3$ film grown on a $LaAlO_3$ substrate that exhibits a characteristic tetragonal and rhombohedral (T+R) mixed phase nanostructure. (c) High-resolution transmission electron microscopy image of the T+R mixed phase that illustrates the commensurate nature of the interface, with the complete absence of misfit dislocations. (d) X-ray magnetic circular dichroism photoemission electron microscopy (XMCD-PEEM) image obtained using the iron absorption edge showing that the highly constrained R-phase shows enhanced ferromagnetism compared to the bulk or the T-phase. Enhanced magnetic contrast is given from the ratio of PEEM images taken with left and right circularly polarized x-rays at the same location. Black and white contrasts indicate magnetic moments pointing parallel and antiparallel to the incident x-rays. (a) Reprinted with permission from Reference 21. © 2009 AAAS. (b) Adapted from Reference 21. (c) Reprinted with permission from Reference 21. © 2009 AAAS. (d) Reprinted with permission from Reference 134. © 2011 Nature Publishing Group.

spin, charge, orbital, and lattice—are highly interactive. As a consequence, its ground state exhibits a strong sensitivity to temperature, pressure, electric fields, and magnetic fields. These qualities make $BiFeO_3$ unique and a natural candidate to tweak using the strain game.

Elastic strain, imparted via epitaxy, is able to distort and eventually change the structure and energy of the ground state of $BiFeO_3$. In its unstrained state, $BiFeO_3$ is rhombohedral.[128] The evolution of the structure of $BiFeO_3$ can be understood from *ab initio* calculations, **Figure 4**a. As an in-plane biaxial compressive strain is imposed via the substrate, the rhombohedral (R) structure becomes progressively monoclinic (and perhaps even triclinic) until a critical strain of ~4.5% is reached. For substrates that impose a larger strain (such as (110) $YAlO_3$, which imposes a hefty 6.6% biaxial compressive strain on commensurate $BiFeO_3$ thin films grown upon it[21–24]), the structure changes into a "super-tetragonal" (T) state (or a monoclinic derivative thereof) with a distinct jump in the ratio of its pseudotetragonal lattice constants c/a.[21] Such an isostructural monoclinic-to-monoclinic phase transition—in which the symmetry does not change, but the coordination chemistry changes dramatically—has also been observed in other materials.[129–132] The overlapping, roughly parabolic free energy versus strain curves of the R- and T-phases can be seen in Figure 4a. It is the change in ground state with strain from the R phase to the T phase that enables the huge (6.6%) biaxial strains to be achieved in $BiFeO_3$ films. In more typical oxide systems, the free energy versus strain landscape limits the growth of epitaxial perovskite films under common growth conditions to about 3% strain.

Partial relaxation of the epitaxial constraint by increasing the film thickness leads to the formation of a mixed-phase nanostructure that exhibits the coexistence of both the R- and T-phases, as illustrated in the atomic force microscope (AFM) image in Figure 4b. This mixed-phase nanostructure is fascinating from many perspectives. First, high-resolution electron microscopy shows that the interface between these two phases is essentially commensurate, Figure 4c. This is important because it means that movement of this interface should be possible simply by the application of an electric field, as is indeed the case.[133] Second, and perhaps more importantly, the highly distorted R-phase in this ensemble, shows significantly enhanced ferromagnetism. This can be discerned from the x-ray magnetic circular dichroism-photoemission electron microscopy (XMCD-PEEM) image in Figure 4d. The R-phase appears in either bright or dark stripe-like contrast in such PEEM images, corresponding to the thin slivers being magnetized either along the x-ray polarization direction or anti-parallel to it.

A rough estimate of the magnetic moment of this highly strained R-phase (from the PEEM images as well as from superconducting quantum interference device magnetometry measurements) gives a local moment of the order of 25–35 emu/cc.[134] It is noteworthy that the canted moment of the R-phase (~6–8 emu/cc) is not observable by the XMCD technique due to the small magnitude of the moment. This enhanced magnetic moment in the highly strained R-phase disappears around 150°C.[134] Application of an electric field converts this mixed (R+T) phase into the T-phase, and the enhanced magnetic moment disappears; reversal of the electric field brings the mixed phase back accompanied by the magnetic moment in the distorted R-phase.[134]

There has been limited work on the tensile side of the $BiFeO_3$ strain phase diagram. It was, however, predicted, using phase-field calculations, that an orthorhombic (O) phase of $BiFeO_3$ should exist under sufficient tensile strain,[21] and recent work has shown that an O-phase can indeed be stabilized.[135] These observations on biaxially strained $BiFeO_3$ films raise several questions. First, what is the magnetic ground state of the various strained $BiFeO_3$ phases (e.g., do they have enhanced canting or exhibit spin glass behavior?). Second, given that spin-orbit coupling is the source of the canted moment in the bulk of $BiFeO_3$, can this enhanced moment be explained based on the strain and confinement imposed on the R-phase? Finally, what is the state of the Dzyaloshinskii–Moriya vector, the antisymmetric microscopic coupling between two localized magnetic moments, in such a strained system?

Strained $EuTiO_3$—Transforming a boring dielectric into the world's strongest ferroelectric ferromagnet

The strain game involving $EuTiO_3$ is another tale in which theory led the way to a remarkable strain-enabled discovery. The idea behind this new route to ferroelectric ferromagnets is that appropriate magnetically ordered insulators that are neither ferroelectric nor ferromagnetic, of which there are many, can be transmuted into ferroelectric ferromagnets. Fennie and Rabe predicted[136] that $EuTiO_3$, a normally boring paraelectric and antiferromagnetic insulator (in its unstrained bulk state), could be transformed using strain into the strongest known multiferroic with a spontaneous polarization and spontaneous magnetization each 100× superior to the reigning multiferroic it displaced, $Ni_3B_7O_{13}I$.[137,138]

The physics behind this discovery makes use of spin-lattice coupling as an additional parameter to influence the soft mode of an insulator on the verge of a ferroelectric transition.[139] The soft mode is the lowest frequency transverse optical phonon, which as it goes to zero results in the phase transition from a paraelectric to a ferroelectric. Appropriate materials for this (1) have a ground state that in the absence of strain is antiferromagnetic and paraelectric, (2) are on the brink of a ferroelectric transition, and (3) exhibit large spin-lattice coupling manifested by a significant decrease in permittivity as the material is cooled through its Néel temperature.[136] $EuTiO_3$ meets these criteria and has much in common with $SrTiO_3$ except that $EuTiO_3$ magnetically orders at 5 K due to the existence of localized 4*f* moments on the Eu^{2+} site.[140,141] Similar to $SrTiO_3$, strain can be used to soften the soft mode and drive it to a ferroelectric instability. In contrast to $SrTiO_3$, which is diamagnetic, the permittivity of bulk $EuTiO_3$ is strongly coupled with its magnetism, showing an abrupt decrease in permittivity at the onset of the antiferromagnetic Eu^{2+} ordering.[142] This indicates that the

soft mode frequency hardens when the spins order antiferromagnetically; conversely, it will soften if the spins order ferromagnetically. This extra interaction provides the coupling favoring a simultaneously ferroelectric and ferromagnetic ground state under sufficient strain in $EuTiO_3$.

Although testing this prediction seems straightforward, the groups who first tested it ran into an unforeseen complication: no matter what substrate they deposited $EuTiO_3$ on, it was ferromagnetic. With its identical lattice constant (both are 3.905 Å at room temperature), $SrTiO_3$ is an obvious substrate for the growth of unstrained epitaxial $EuTiO_3$ films. Surprisingly, as-grown $EuTiO_{3-\delta}$ thin films synthesized by pulsed-laser deposition (PLD) on (001) $SrTiO_3$ substrates exhibit expanded out-of-plane spacings (0.4% to 2% longer than bulk $EuTiO_3$)[143–146] and are ferromagnetic with a Curie temperature of about 5 K.[144,145]

Could the observed expanded lattice spacings in $EuTiO_{3-\delta}$ thin films be due to oxygen vacancies? The effect of oxygen deficiency on lattice constant has been studied in $EuTiO_{3-\delta}$ bulk samples down to the $EuTiO_{2.5}$ limit of the perovskite $EuTiO_{3-\delta}$ structure, and negligible (<0.5%) variation in the cubic lattice constant was found.[147,148] Oxygen vacancies alone are thus insufficient to explain the 2% variation in out-of-plane lattice spacings observed in epitaxial $EuTiO_{3-\delta}$ films grown on (001) $SrTiO_3$ by PLD.[144–146]

One possible explanation is that the ferromagnetism observed in epitaxial $EuTiO_3$ films prepared by PLD on $SrTiO_3$ arises from extrinsic effects, masking the intrinsic properties of $EuTiO_3$ thin films. Extrinsic effects are known to occur in thin films, particularly for deposition methods involving energetic species, which can induce defects. Another factor favoring defect introduction is the relatively low growth temperatures common for oxide thin-film growth, enabling defects to be frozen in. For example, some epitaxial $SrTiO_3$ films grown on $SrTiO_3$ substrates by PLD have been reported to be ferroelectric,[149] in striking contrast to the intrinsic nature of unstrained $SrTiO_3$, which is not ferroelectric at any temperature.[150] Homoepitaxial $SrTiO_3$ films grown by PLD are also known to exhibit lattice spacings that deviate significantly from the $SrTiO_3$ substrates they are grown on,[151–153] although bulk $SrTiO_{3-\delta}$ (in either single crystal or polycrystalline form) exhibits negligible variation in its cubic lattice constant up to the $SrTiO_{2.5}$ limit[154,155] of the perovskite $SrTiO_{3-\delta}$ structure. The sensitivity of $EuTiO_3$ that made it an appropriate material to transmute via strain into a multiferroic also makes it quite sensitive to defects. To overcome this issue and examine the intrinsic effect of strain on $EuTiO_3$, a more delicate deposition technique was needed.

In contrast to PLD, homoepitaxial $SrTiO_3$ films grown by MBE[156] show bulk behavior and none of the unusual effects reported in homoepitaxial $SrTiO_3$ films grown by PLD.[149,151–153] Indeed unstrained, stoichiometric $EuTiO_3$ thin films grown by MBE on (001) $SrTiO_3$ have the same lattice constant as bulk $EuTiO_3$ and are antiferromagnetic.[157] Seeing that MBE can produce $EuTiO_3$ films with intrinsic properties in their unstrained state, MBE was used to test Fennie and Rabe's strained $EuTiO_3$ predictions.[136] Commensurate $EuTiO_3$ films were grown on three substrates: (001) LSAT, (001) $SrTiO_3$, and (110) $DyScO_3$ to impart –0.9%, 0%, and +1.1% biaxial

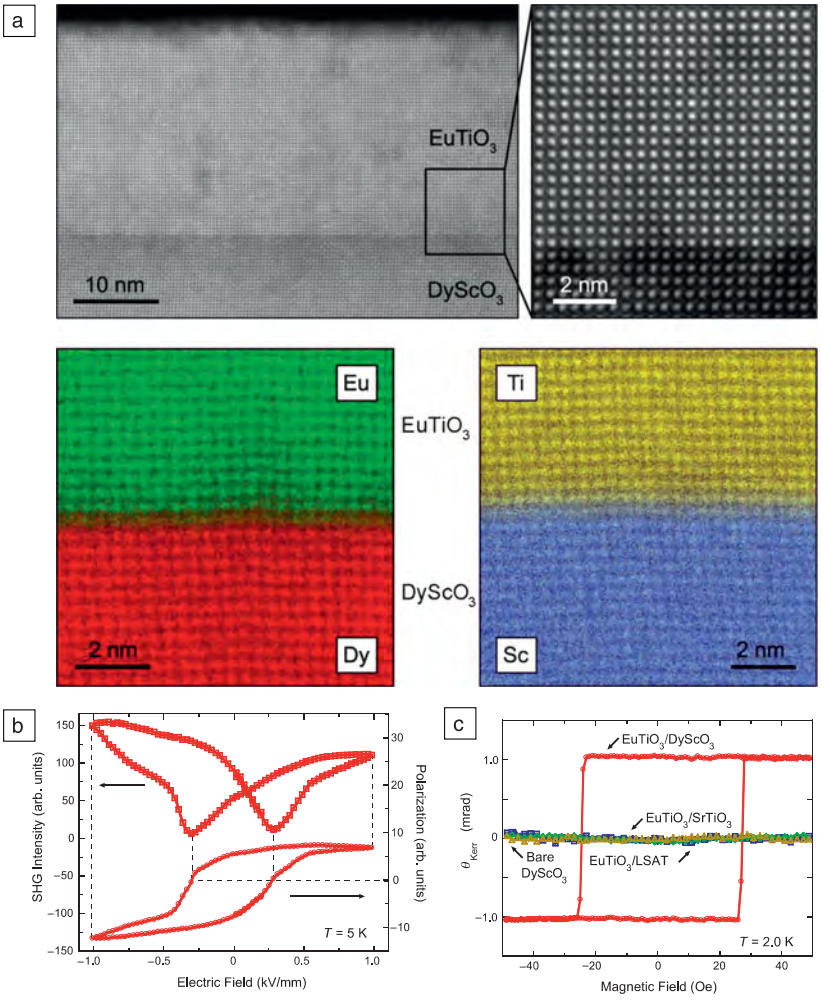


Figure 5. (a) Elemental maps of europium and dysprosium observed by scanning transmission electron microscopy-electron energy loss spectroscopy on a 22-nm-thick commensurate $EuTiO_3/DyScO_3$ film, confirming an abrupt $EuTiO_3/DyScO_3$ interface with the correct oxidation states. Observation of (b) ferroelectricity by second harmonic generation and (c) ferromagnetism by magneto-optical Kerr effect in this same strained $EuTiO_3$ grown on (110) $DyScO_3$, confirming predictions that under sufficient biaxial strain, $EuTiO_3$ becomes multiferroic. Control samples with zero ($EuTiO_3/SrTiO_3$) or opposite ($EuTiO_3/LSAT$)) strain are consistent with the theoretically predicted strain phase diagram for $EuTiO_3$. LSAT, $(LaAlO_3)_{0.29}-(SrAl_{1/2}Ta_{1/2}O_3)_{0.71}$. Reprinted with permission from Reference 16. © 2010 Nature Publishing Group.

strain, respectively. Using scanning transmission electron microscopy with electron energy loss spectroscopy (STEM-EELS), the oxidation state of the film constituents and the abruptness of the interface between the film and substrate was checked with atomic resolution and chemical specificity (**Figure 5**a). Experimental measurements utilizing second harmonic generation (SHG) and magneto-optic Kerr effect (MOKE) confirmed that the $EuTiO_3$ grown on (110) $DyScO_3$ was simultaneously ferroelectric (Figure 5b) and ferromagnetic (Figure 5c), while on the other substrates it was not, in agreement with theory[136] and resulting in the strongest multiferroic material known today.[16]

There are many other exciting predictions that remain to be verified of even stronger and higher temperature ferroelectric ferromagnets in strained $SrMnO_3$,[158] and EuO,[159] as well as the prediction that an electric field on the order of 10^5 V cm^{-1} can be used to turn on ferromagnetism in $EuTiO_3$ when it is poised on the verge of such a phase transition via strain.[136] It was recently shown that through the application of an electric field, the antiferromagnetic ground state of $EuTiO_3$, strained to be close to where it would have a ferromagnetic ground state (but still on the antiferromagnetic side), can be electrically tuned to the verge of the ferromagnetic state.[160] Turning on magnetism in a material by applying an electric field to it remains an open challenge. Such an important milestone would be a key advance to the field of ferroics, both scientifically and technologically.

Electronics has flourished because of the ability to route voltages with ease and on extremely small scales. If magnetism could be similarly controlled and routed, it would impact memory devices, spin valves, and many other spintronics devices and make numerous hybrid devices possible.

Strained $Sr_{n+1}Ti_nO_{3n+1}$—Creating a tunable dielectric with record performance

Strain has also been used to create a new family of tunable microwave dielectrics, which due to their low dielectric loss have a figure of merit at room temperature that rivals those of all such known materials.[161] In contrast to standard (textbook) dielectrics, whose dielectric displacement (**D**) as a function of applied electric field (**E**) can be described by the linear equation

$$\mathbf{D} = \varepsilon_0 \boldsymbol{K} \mathbf{E}, \qquad (1)$$

where ε_0 is the permittivity of free space and $\boldsymbol{K}$ is the dielectric constant of the material, a tunable dielectric has a highly nonlinear relationship between **D** and **E**. The nonlinearity results in the effective dielectric constant of the material ($\mathbf{D}/\varepsilon_0\mathbf{E}$) behaving not as a constant, but changing greatly with **E**; changes of tens of percent in the dielectric "constant" are common in tunable dielectrics at high **E**. This nonlinearity can be described by adding higher order terms to Equation 1. In tensor form, this more general relationship is

$$D_i = \varepsilon_0 K_{ij} E_j + \varepsilon_{ijk} E_j E_k + \varepsilon_{ijk\ell} E_j E_k E_\ell + \ldots, \qquad (2)$$

where ε_{ijk} and $\varepsilon_{ijk\ell}$ are higher order permittivity coefficients.

Highly nonlinear dielectrics, including the most extensively studied material with such properties, $Ba_xSr_{1-x}TiO_3$,[162–165] are found in displacive ferroelectric systems at temperatures just above the paraelectric-to-ferroelectric transition temperature.[162,165] These tunable dielectrics are normally used in their paraelectric state to avoid the dielectric losses that would occur in the ferroelectric state due to the motion of domain walls. Although thin films provide an excellent geometry for the application of high **E** at low applied voltages, $Ba_xSr_{1-x}TiO_3$ films unfortunately suffer significant dielectric losses arising from defects; the dielectric loss in today's best $Ba_xSr_{1-x}TiO_3$ tunable dielectrics films at GHz frequencies is about an order of magnitude worse than the best $Ba_xSr_{1-x}TiO_3$ in bulk form.[165]

A new approach to tunable microwave dielectrics is to take a system with exceptionally low loss and introduce a ferroelectric instability into it using strain. The appeal of this approach is that it can be applied to systems that are known to have exceptionally low dielectric loss, particularly in thin-film form. Such systems do not need to have a ferroelectric instability in their unstrained form; strain can be used to help impart the ferroelectric instability. This relaxed design constraint greatly increases the number of eligible systems that could yield improved performance over the best of today's known tunable dielectrics.

This approach has been applied to $Sr_{n+1}Ti_nO_{3n+1}$ phases—where $(SrO)_2$ crystallographic shear[166,167] planes provide an alternative to point-defect formation for accommodating nonstoichiometry.[168,169] These phases are known to have low dielectric loss,[170,171] even in thin-film form.[172] In their unstrained state, these phases are centrosymmetric, and thus lack a ferroelectric instability.

The strain game in combination with control of the distance between the $(SrO)_2$ planes in $Sr_{n+1}Ti_nO_{3n+1}$ phases can, however, induce a ferroelectric instability.[161,173] The emergence of this ferroelectric instability in $Sr_{n+1}Ti_nO_{3n+1}$ phases commensurately strained in biaxial tension to (110) $DyScO_3$ substrates (about 1% biaxial tension) can be seen in **Figure 6**a. For $n \geq 3$, a ferroelectric instability is evident from the double-well energy potential of the ion displacements, and this double-well becomes deeper with increasing n. A deeper well corresponds to the ferroelectric instability occurring at higher temperature until, by $n = 6$, it is just below room temperature.[161]

The low loss of this tunable dielectric at high frequencies is evident from Figure 6b, where both the real and imaginary parts of the in-plane dielectric constant K_{11} are shown over a frequency range spanning more than eight orders of magnitude and up to 125 GHz.[161] Only at these highest frequencies can the dielectric loss be seen. This low loss yields unparalleled performance at room temperature for these new tunable dielectrics.[164] The reason for the low dielectric loss, far lower than today's best $Ba_xSr_{1-x}TiO_3$ tunable dielectrics at GHz frequencies, is believed to be related to the propensity of $Sr_{n+1}Ti_nO_{3n+1}$ phases to form $(SrO)_2$ planar defects in response to

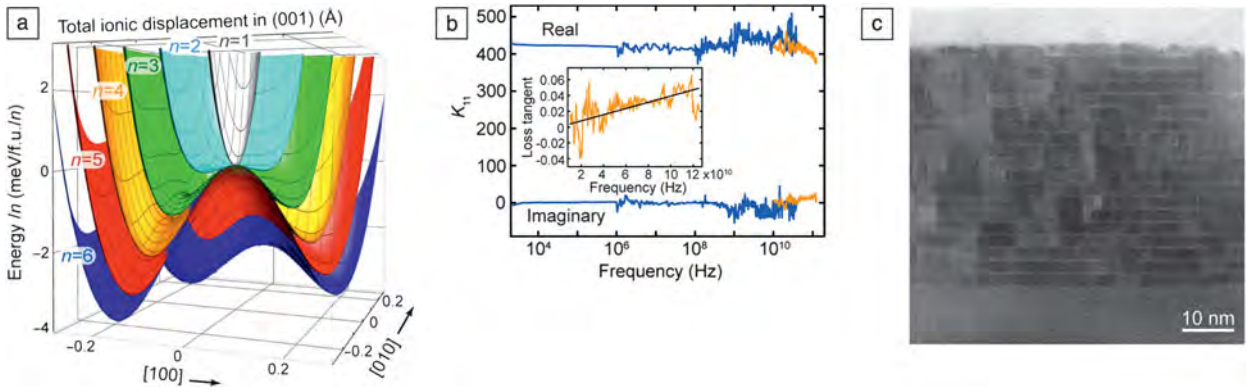


Figure 6. (a) First-principles calculations showing how the index n of $Sr_{n+1}Ti_nO_{3n+1}$ phases strained commensurately to (110) $DyScO_3$ substrates can be used to control the local ferroelectric instability. Plotted is the energy (per n) with respect to the nonpolar state of $Sr_{n+1}Ti_nO_{3n+1}$ phases for polar distortions in the (001) plane. (b) The real and imaginary parts of the in-plane dielectric constant (K_{11}) of an n = 6 $Sr_{n+1}Ti_nO_{3n+1}$ film grown on (110) $DyScO_3$ as a function of frequency. The inset shows the film loss tangent on a linear frequency scale in the gigahertz frequency regime along with a linear fit. (c) Bright-field scanning transmission electron microscopy image of an n = 6 $Sr_{n+1}Ti_nO_{3n+1}$ film grown on (110) $DyScO_3$. $Sr_{n+1}Ti_nO_{3n+1}$ phases can readily accommodate nonstoichiometry by the formation of $(SrO)_2$ double layers, the bright horizontal and vertical running layers in this image. Reprinted with permission from Reference 161. © 2013 Nature Publishing Group.

local stoichiometry deviations rather than point defects.[168,169] These $(SrO)_2$ double layers show up as bright layers in the STEM image of an n = 6 $Sr_{n+1}Ti_nO_{3n+1}$ film in Figure 6c. This is in contrast to the high point-defect concentrations that perovskite films like $SrTiO_3$ can incorporate in thin-film form;[75,156] such point defects could be the reason that $Ba_xSr_{1-x}TiO_3$ tunable dielectric films have significantly higher dielectric losses than bulk $Ba_xSr_{1-x}TiO_3$.[165]

Other ways oxides can react to strain

As the examples described in this article show, the strain game can be a powerful control parameter for enhancing the properties of ferroic oxides. It is important to consider, however, other ways in which a complex oxide might react to strain. Should there be an energetically more favorable route to accommodate the imposed strain, the system might take it. Examples include the possibility that the imposed strain will lead to changes in film composition, microstructure, or crystal structure (e.g., ordering [or disordering] of cations, anions, or their vacancies,[174,175] atom clustering, the stabilization of other polymorphs, or rotations of the oxygen coordination polyhedra[176–178]) rather than simply dilating or compressing the spacings between the atoms in the unstrained structure equally. Octahedral rotation patterns from underlying layers and substrates can be imparted into films over distances of several nanometers and can thus complicate a simple biaxial strain picture. An example is the creation of T-phase $BiFeO_3$ at relatively low biaxial strain (–1.4%, where the $BiFeO_3$ should be monoclinic), due to the competition between different octahedral rotation patterns in the film and in the substrate.[179] Such chemical and structural changes may also cause dramatic changes in properties, for better or worse, but it is important to distinguish the underlying causes of the changes in properties.

Advances in electron microscopy have been particularly beneficial in identifying these underlying causes (see the Hÿtch and Minor article in this issue). With respect to ferroics, recent advances enabling polarization mapping on the atomic scale,[180–183] octahedral rotation imaging,[184] and improved STEM-EELS analysis[185] are invaluable in separating true strain effects from changes in composition, structure, and microstructure that can occur to mitigate against a strain effect. These techniques have the potential to visualize closure domains in ferroelectrics,[182,183] usual domain walls with mixed Bloch–Néel–Ising character in strained ferroelectric superlattices,[186] and the exciting possibility of a dipole-dipole coupling analog of exchange-spring magnets[187,188] recently predicted to occur in strained ferroelectric systems.[189]

Other intriguing predictions, including using strain to poise a material (e.g., $SrCoO_3$[190]) on the brink of a metal-insulator transition, which could then be turned on or off through the application of an electric or magnetic field or even a small additional strain, are relevant to emerging piezotronic devices.[191,192]

Outlook

Elastic strain engineering of ferroics with the perovskite structure has been the most pursued to date. Yet there are many other fascinating oxides that either have a ferroic ground state or are borderline ferroic materials that might be enticed into a ferroic ground state with strain. Such non-perovskite structural families that are relevant include chrysoberyl Cr_2BeO_4,[193] pyrochlore $Ho_2Ti_2O_7$,[194] $YMnO_3$,[195,196] $MnWO_4$,[197] delafossite $CuFeO_2$,[198] CuO,[199] and hexaferrite $Sr_3Co_2Fe_{24}O_{41}$.[200] These systems are generally ignored by the thin-film community and have been the focus of the single crystal ferroic community. We believe the issue is the lack of suitable substrates for these latter structures; removing this roadblock would unleash a

huge opportunity in strain engineering for the future. Thin films also have the technological advantage of lower switching voltages and the ability to integrate them into more sophisticated heterostructures, as are relevant for devices.

Imagine the opportunities for strain engineering that substrates for the non-perovskite systems would bring. Substrates for $YMnO_3$ would enable more variants of hexagonal manganite ferroics to be constructed. These variants include not only known materials, but metastable polymorphs (e.g., $LuFeO_3$ that is isostructural to $YMnO_3$ rather than its stable centrosymmetric perovskite form)[124,201,202] by utilizing lattice misfit strain energies and interfacial energies to favor the desired metastable phase over the equilibrium phase (epitaxial stabilization),[203–206] or the prospect of interfacial multiferroicity that has been predicted to emerge in superlattices between centrosymmetric components.[207,208]

Similarly, substrates with the $LiNbO_3$ structure would enable the growth of the $LiNbO_3$-polymorph of $FeTiO_3$ and related multiferroics.[209,210] A range of appropriate substrates, like the range of substrates available for perovskites shown in Figure 1d, for each ferroic system of interest would allow the thin-film tricks of strain engineering,[12–16] epitaxial stabilization,[203–206] dimensional confinement,[161,173] polarization engineering,[112,211] and superlattice formation[60,103–114,117–119,207,208] to be freely applied to a much larger set of ferroic building blocks. Strain engineering of ferroic oxides is in its infancy and considering its brief, but vibrant past, a brilliant future awaits.

Acknowledgments

We gratefully acknowledge our colleagues and collaborators for sharing their insights and helping us to explore and better understand the exciting area of elastically strained ferroic oxide films. We especially thank the groups of E. Arenholz, M. Bedzyk, M.D. Biegalski, D.H.A. Blank, D.A. Bonnell, J.C. Booth, J.D. Brock, L.E. Cross, C.B. Eom, J.W. Freeland, P. Ghosez, P.C. Hammel, M.E. Hawley, E. Johnston-Halperin, S. Kamba, S.W. Kirchoefer, J. Levy, Yulan Li, T.E. Mallouk, J. Mannhart, L.W. Martin, K. Peters, K.M. Rabe, J.M. Rondinelli, P.J. Ryan, P. Schiffer, J. Schubert, N.A. Spaldin, S.K. Streiffer, A.K. Tagantsev, I. Takeuchi, D.A. Tenne, J.-M. Triscone, S. Trolier-McKinstry, D. Vanderbilt, J.C. Woicik, and X.X. Xi. L.Q.C., C.J.F., V.G., X.Q.P., D.G.S., and R.R. gratefully acknowledge financial support from the National Science Foundation (NSF) under Grant No. DMR-0820404. D.G.S. also acknowledges NSF Grant DMR-0948036. R.R. acknowledges sustained support from the US Department of Energy under Contract No. DE-AC0205CH11231.

References

1. A.E. Lindh, in *Nobel Lectures in Physics 1942–1962* (World Scientific, Singapore, 1998), pp. 49–52.
2. J.M. Lock, *Philos. Trans. R. Soc. London, Ser. A* **208**, 391 (1951).
3. P.W. Forsbergh Jr., *Phys. Rev.* **93**, 686 (1954).
4. L.D. Nguyen, A.S. Brown, M.A. Thompson, L.M. Jelloian, *IEEE Trans. Electron Devices* **39**, 2007 (1992).
5. J. Welser, J.L. Hoyt, J.F. Gibbons, *IEEE Electron Device Lett.* **15**, 100 (1994).
6. W. Shockley, J. Bardeen, *Phys. Rev.* **77**, 407 (1950).
7. H. Sato, M. Naito, *Physica C* **274**, 221 (1997).
8. I. Bozovic, G. Logvenov, I. Belca, B. Narimbetov, I. Sveklo, *Phys. Rev. Lett.* **89**, 107001 (2002).
9. R.S. Beach, J.A. Borchers, A. Matheny, R.W. Erwin, M.B. Salamon, B. Everitt, K. Pettit, J.J. Rhyne, C.P. Flynn, *Phys. Rev. Lett.* **70**, 3502 (1993).
10. Q. Gan, R.A. Rao, C.B. Eom, J.L. Garrett, M. Lee, *Appl. Phys. Lett.* **72**, 978 (1998).
11. D. Fuchs, E. Arac, C. Pinta, S. Schuppler, R. Schneider, H.v. Löhneysen, *Phys. Rev. B.* **77**, 014434 (2008).
12. J.H. Haeni, P. Irvin, W. Chang, R. Uecker, P. Reiche, Y.L. Li, S. Choudhury, W. Tian, M.E. Hawley, B. Craigo, A.K. Tagantsev, X.Q. Pan, S.K. Streiffer, L.Q. Chen, S.W. Kirchoefer, J. Levy, D.G. Schlom, *Nature* **430**, 758 (2004).
13. K.J. Choi, M.D. Biegalski, Y.L. Li, A. Sharan, J. Schubert, R. Uecker, P. Reiche, Y.B. Chen, X.Q. Pan, V. Gopalan, L.-Q. Chen, D.G. Schlom, C.B. Eom, *Science* **306**, 1005 (2004).
14. D.G. Schlom, L.Q. Chen, C.B. Eom, K.M. Rabe, S.K. Streiffer, J.-M. Triscone, *Annu. Rev. Mater. Res.* **37**, 589 (2007).
15. M.P. Warusawithana, C. Cen, C.R. Sleasman, J.C. Woicik, Y.L. Li, L.F. Kourkoutis, J.A. Klug, H. Li, P. Ryan, L.-P. Wang, M. Bedzyk, D.A. Muller, L.Q. Chen, J. Levy, D.G. Schlom, *Science* **324**, 367 (2009).
16. J.H. Lee, L. Fang, E. Vlahos, X. Ke, Y.W. Jung, L.F. Kourkoutis, J.-W. Kim, P.J. Ryan, T. Heeg, M. Roeckerath, V. Goian, M. Bernhagen, R. Uecker, P.C. Hammel, K.M. Rabe, S. Kamba, J. Schubert, J.W. Freeland, D.A. Muller, C.J. Fennie, P. Schiffer, V. Gopalan, E. Johnston-Halperin, D.G. Schlom, *Nature* **466**, 954 (2010).
17. C. Adamo, X. Ke, H.Q. Wang, H.L. Xin, T. Heeg, M.E. Hawley, W. Zander, J. Schubert, P. Schiffer, D.A. Muller, L. Maritato, D.G. Schlom, *Appl. Phys. Lett.* **95**, 112504 (2009).
18. H. Béa, B. Dupé, S. Fusil, R. Mattana, E. Jacquet, B. Warot-Fonrose, F. Wilhelm, A. Rogalev, S. Petit, V. Cros, A. Anane, F. Petroff, K. Bouzehouane, G. Geneste, B. Dkhil, S. Lisenkov, I. Ponomareva, L. Bellaiche, M. Bibes, A. Barthélémy, *Phys. Rev. Lett.* **102**, 217603 (2009).
19. I.C. Infante, S. Lisenkov, B. Dupé, M. Bibes, S. Fusil, E. Jacquet, G. Geneste, S. Petit, A. Courtial, J. Juraszek, L. Bellaiche, A. Barthélémy, B. Dkhil, *Phys. Rev. Lett.* **105**, 057601 (2010).
20. Z. Chen, Z. Luo, C. Huang, Y. Qi, P. Yang, L. You, C. Hu, T. Wu, J. Wang, C. Gao, T. Sritharan, L. Chen, *Adv. Funct. Mater.* **21**, 133 (2011).
21. R.J. Zeches, M.D. Rossell, J.X. Zhang, A.J. Hatt, Q. He, C.-H. Yang, A. Kumar, C.H. Wang, A. Melville, C. Adamo, G. Sheng, Y.-H. Chu, J.F. Ihlefeld, R. Erni, C. Ederer, V. Gopalan, L.Q. Chen, D.G. Schlom, N.A. Spaldin, L.W. Martin, R. Ramesh, *Science* **326**, 977 (2009).
22. P. Chen, N.J. Podraza, X.S. Xu, A. Melville, E. Vlahos, V. Gopalan, R. Ramesh, D.G. Schlom, J.L. Musfeldt, *Appl. Phys. Lett.* **96**, 131907 (2010).
23. H.M. Christen, J.H. Nam, H.S. Kim, A.J. Hatt, N.A. Spaldin, *Phys. Rev. B* **83**, 144107 (2011).
24. L.W. Martin, D.G. Schlom, *Curr. Opin. Solid State Mater. Sci.* **16**, 199 (2012).
25. A.A. Griffith, *Philos. Trans. R. Soc. London, Ser. A* **221**, 163 (1920).
26. E. Klokholm, J.W. Matthews, A.F. Mayadas, J. Angilello, in *Magnetism and Magnetic Materials*, C.D. Graham Jr., J.J. Rhyne, Eds. (American Institute of Physics, New York, 1972), pp. 105–109.
27. L.B. Freund, S. Suresh, *Thin Film Materials: Stress, Defect Formation and Surface Evolution* (Cambridge University Press, Cambridge, 2003), pp. 60–83, 283–290, 396–416.
28. N.A. Pertsev, A.K. Tagantsev, N. Setter, *Phys. Rev. B* **61**, R825 (2000).
29. N.A. Pertsev, A.K. Tagantsev, N. Setter, *Phys. Rev. B* **65**, 219901 (2002).
30. A.F. Devonshire, *Philos. Mag.* **3** (Suppl.), 85 (1954).
31. A. Antons, J.B. Neaton, K.M. Rabe, D. Vanderbilt, *Phys. Rev. B* **71**, 024102 (2005).
32. Y.L. Li, S. Choudhury, J.H. Haeni, M.D. Biegalski, A. Vasudevarao, A. Sharan, H.Z. Ma, J. Levy, V. Gopalan, S. Trolier-McKinstry, D.G. Schlom, Q.X. Jia, L.Q. Chen, *Phys. Rev. B* **73**, 184112 (2006).
33. C.L. Canedy, H. Li, S.P. Alpay, L. Salamanca-Riba, A.L. Roytburd, R. Ramesh, *Appl. Phys. Lett.* **77**, 1695 (2000).
34. I.B. Misirlioglu, A.L. Vasiliev, M. Aindow, S.P. Alpay, R. Ramesh, *Appl. Phys. Lett.* **84**, 1742 (2004).
35. M.-W. Chu, I. Szafraniak, R. Scholz, C. Harnagea, D. Hesse, M. Alexe, U. Gösele, *Nature Mater.* **3**, 87 (2004).
36. S.P. Alpay, I.B. Misirlioglu, V. Nagarajan, R. Ramesh, *Appl. Phys. Lett.* **85**, 2044 (2004).
37. V. Nagarajan, C.L. Jia, H. Kohlstedt, R. Waser, I.B. Misirlioglu, S.P. Alpay, R. Ramesh, *Appl. Phys. Lett.* **86**, 192910 (2005).
38. M.D. Biegalski, D.D. Fong, J.A. Eastman, P.H. Fuoss, S.K. Streiffer, T. Heeg, J. Schubert, W. Tian, C.T. Nelson, X.Q. Pan, M.E. Hawley, M. Bernhagen, P. Reiche, R. Uecker, S. Trolier-McKinstry, D.G. Schlom, *J. Appl. Phys.* **104**, 114109 (2008).
39. R. Uecker, H. Wilke, D.G. Schlom, B. Velickov, P. Reiche, A. Polity, M. Bernhagen, M. Rossberg, *J. Cryst. Growth* **295**, 84 (2006).

40. R. Uecker, B. Velickov, D. Klimm, R. Bertram, M. Bernhagen, M. Rabe, M. Albrecht, R. Fornari, D.G. Schlom, *J. Cryst. Growth* **310**, 2649 (2008).
41. R. Uecker, D. Klimm, R. Bertram, M. Bernhagen, I. Schulze-Jonack, M. Brützam, A. Kwasniewski, T.M. Gesing, D.G. Schlom, *Acta Phys. Pol. A* **124**, 295 (2013).
42. A. Lempicki, M.H. Randles, D. Wisniewski, M. Balcerzyk, C. Brecher, A.J. Wojtowicz, *IEEE Trans. Nucl. Sci.* **42**, 280 (1995).
43. A.G. Petrosyan, G.O. Shirinyan, C. Pedrini, C. Durjardin, K.L. Ovanesyan, R.G. Manucharyan, T.I. Butaeva, M.V. Derzyan, *Cryst. Res. Technol.* **33**, 241 (1998).
44. H. Asano, S. Kubo, O. Michikami, M. Satoh, T. Konaka, *Jpn. J. Appl. Phys., Part 2* **29**, L1452 (1990).
45. R. Brown, V. Pendrick, D. Kalokitis, B.H.T. Chai, *Appl. Phys. Lett.* **57**, 1351 (1990).
46. Y. Miyazawa, H. Toshima, S. Morita, *J. Cryst. Growth* **128**, 668 (1993).
47. G.W. Berkstresser, A.J. Valentino, C.D. Brandle, *J. Cryst. Growth* **109**, 467 (1991).
48. G.W. Berkstresser, A.J. Valentino, C.D. Brandle, *J. Cryst. Growth* **128**, 684 (1993).
49. S. Hontsu, J. Ishii, T. Kawai, S. Kawai, *Appl. Phys. Lett.* **59**, 2886 (1991).
50. D. Mateika, H. Kohler, H. Laudan, E. Volkel, *J. Cryst. Growth* **109**, 447 (1991).
51. R.W. Simon, C.E. Platt, A.E. Lee, G.S. Lee, K.P. Daly, M.S. Wire, J.A. Luine, M. Urbanik, *Appl. Phys. Lett.* **53**, 2677 (1988).
52. G.W. Berkstresser, A.J. Valentino, C.D. Brandle, *J. Cryst. Growth* **109**, 457 (1991).
53. B.C. Chakoumakos, D.G. Schlom, M. Urbanik, J. Luine, *J. Appl. Phys.* **83**, 1979 (1998).
54. R.L. Sandstrom, E.A. Giess, W.J. Gallagher, A. Segmüller, E.I. Cooper, M.F. Chisholm, A. Gupta, S. Shinde, R.B. Laibowitz, *Appl. Phys. Lett.* **53**, 1874 (1988).
55. L. Merker, US Patent No. 2,684,910 (27 July 1954).
56. J.G. Bednorz, H.J. Scheel, *J. Cryst. Growth* **41**, 5 (1977).
57. P.I. Nabokin, D. Souptel, A.M. Balbashov, *J. Cryst. Growth* **250**, 397 (2003).
58. H.J. Scheel, J.G. Bednorz, P. Dill, *Ferroelectrics* **13**, 507 (1976).
59. S.-G. Lim, S. Kriventsov, T.N. Jackson, J.H. Haeni, D.G. Schlom, A.M. Balbashov, R. Uecker, P. Reiche, J.L. Freeouf, G. Lucovsky, *J. Appl. Phys.* **91**, 4500 (2002).
60. A. Soukiassian, W. Tian, V. Vaithyanathan, J.H. Haeni, L.Q. Chen, X.X. Xi, D.G. Schlom, D.A. Tenne, H.P. Sun, X.Q. Pan, K.J. Choi, C.B. Eom, Y.L. Li, Q.X. Jia, C. Constantin, R.M. Feenstra, M. Bernhagen, P. Reiche, R. Uecker, *J. Mater. Res.* **23**, 1417 (2008).
61. R. Feenstra, L.A. Boatner, J.D. Budai, D.K. Christen, M.D. Galloway, D.B. Poker, *Appl. Phys. Lett.* **54**, 1063 (1989).
62. J.C. Yang, Q. He, S.J. Suresha, C.Y. Kuo, C.Y. Peng, R.C. Haislmaier, M.A. Motyka, G. Sheng, C. Adamo, H.J. Lin, Z. Hu, L. Chang, L.H. Tjeng, E. Arenholz, N.J. Podraza, M. Bernhagen, R. Uecker, D.G. Schlom, V. Gopalan, L.Q. Chen, C.T. Chen, R. Ramesh, Y.H. Chu, *Phys. Rev. Lett.* **109**, 247606 (2012).
63. S. Coh, T. Heeg, J.H. Haeni, M.D. Biegalski, J. Lettieri, L.F. Edge, K.E. O'Brien, M. Bernhagen, P. Reiche, R. Uecker, S. Trolier-McKinstry, D.G. Schlom, D. Vanderbilt, *Phys. Rev. B* **82**, 064101 (2010).
64. K.L. Ovanesyan, A.G. Petrosyan, G.O. Shirinyan, C. Pedrini, L. Zhang, *J. Cryst. Growth* **198**, 497 (1999).
65. M.D. Biegalski, Y. Jia, D.G. Schlom, S. Trolier-McKinstry, S.K. Streiffer, V. Sherman, R. Uecker, P. Reiche, *Appl. Phys. Lett.* **88**, 192907 (2006).
66. J.F. Ihlefeld, W. Tian, Z.-K. Liu, W.A. Doolittle, M. Bernhagen, P. Reiche, R. Uecker, R. Ramesh, D.G. Schlom, *IEEE Trans. Ultrason. Ferroelectr. Freq. Control* **56**, 1528 (2009).
67. J.H. Lee, X. Ke, R. Misra, J.F. Ihlefeld, X.S. Xu, Z.G. Mei, T. Heeg, M. Roeckerath, J. Schubert, Z.K. Liu, J.L. Musfeldt, P. Schiffer, D.G. Schlom, *Appl. Phys. Lett.* **96**, 262905 (2010).
68. P. Irvin, J. Levy, J.H. Haeni, D.G. Schlom, *Appl. Phys. Lett.* **88**, 042902 (2006).
69. H.Z. Ma, J. Levy, M.D. Biegalski, S. Trolier-McKinstry, D.G. Schlom, *J. Appl. Phys.* **105**, 014102 (2009).
70. A. Vasudevarao, A. Kumar, L. Tian, J.H. Haeni, Y.L. Li, C.-J. Eklund, Q.X. Jia, R. Uecker, P. Reiche, K.M. Rabe, L.Q. Chen, D.G. Schlom, V. Gopalan, *Phys. Rev. Lett.* **97**, 257602 (2006).
71. A. Vasudevarao, S. Denev, M.D. Biegalski, Y.L. Li, L.Q. Chen, S. Trolier-McKinstry, D.G. Schlom, V. Gopalan, *Appl. Phys. Lett.* **92**, 192902 (2008).
72. S. Denev, A. Kumar, M.D. Biegalski, H.W. Jang, C.M. Folkman, A. Vasudevarao, Y. Han, I.M. Reaney, S. Trolier-McKinstry, C.B. Eom, D.G. Schlom, V. Gopalan, *Phys. Rev. Lett.* **100**, 257601 (2008).
73. M.D. Biegalski, E. Vlahos, G. Sheng, Y.L. Li, M. Bernhagen, P. Reiche, R. Uecker, S.K. Streiffer, L.Q. Chen, V. Gopalan, D.G. Schlom, S. Trolier-McKinstry, *Phys. Rev. B* **79**, 224117 (2009).
74. D. Nuzhnyy, J. Petzelt, S. Kamba, P. Kužel, C. Kadlec, V. Bovtun, M. Kempa, J. Schubert, C.M. Brooks, D.G. Schlom, *Appl. Phys. Lett.* **95**, 232902 (2009).
75. C.H. Lee, V. Skoromets, M.D. Biegalski, S. Lei, R. Haislmaier, M. Bernhagen, R. Uecker, X.X. Xi, V. Gopalan, X. Martí, S. Kamba, P. Kužel, D.G. Schlom, *Appl. Phys. Lett.* **102**, 082905 (2013).
76. K.J. Hubbard, D.G. Schlom, *J. Mater. Res.* **11**, 2757 (1996).
77. D.G. Schlom, S. Guha, S. Datta, *MRS Bull.* **33**, 1017 (2008).
78. L.F. Kourkoutis, C.S. Hellberg, V. Vaithyanathan, H. Li, M.K. Parker, K.E. Andersen, D.G. Schlom, D.A. Muller, *Phys. Rev. Lett.* **100**, 036101 (2008).
79. H. Li, X. Hu, Y. Wei, Z. Yu, X. Zhang, R. Droopad, A.A. Demkov, J. Edwards, K. Moore, W. Ooms, J. Kulik, P. Fejes, *J. Appl. Phys.* **93**, 4521 (2003).
80. M. Kawasaki, K. Takahashi, T. Maeda, R. Tsuchiya, M. Shinohara, O. Ishiyama, T. Yonezawa, M. Yoshimoto, H. Koinuma, *Science* **266**, 1540 (1994).
81. G. Koster, B.L. Kropman, G.J.H.M. Rijnders, D.H.A. Blank, H. Rogalla, *Appl. Phys. Lett.* **73**, 2920 (1998).
82. A.G. Schrott, J.A. Misewich, M. Copel, D.W. Abraham, Y. Zhang, *Appl. Phys. Lett.* **79**, 1786 (2001).
83. A. Biswas, P.B. Rossen, C.H. Yang, W. Siemons, M.H. Jung, I.K. Yang, R. Ramesh, Y.H. Jeong, *Appl. Phys. Lett.* **98**, 051904 (2011).
84. J. Chang, Y.-S. Park, S.-K. Kim, *Appl. Phys. Lett.* **92**, 152910 (2008).
85. J.L. Blok, X. Wan, G. Koster, D.H.A. Blank, G. Rijnders, *Appl. Phys. Lett.* **99**, 151917 (2011).
86. T. Ohnishi, K. Takahashi, M. Nakamura, M. Kawasaki, M. Yoshimoto, H. Koinuma, *Appl. Phys. Lett.* **74**, 2531 (1999).
87. J.H. Ngai, T.C. Schwendemann, A.E. Walker, Y. Segal, F.J. Walker, E.I. Altman, C.H. Ahn, *Adv. Mater.* **22**, 2945 (2010).
88. J.E. Kleibeuker, G. Koster, W. Siemons, D. Dubbink, B. Kuiper, J.L. Blok, C.-H. Yang, J. Ravichandran, R. Ramesh, J.E. ten Elshof, D.H.A. Blank, G. Rijnders, *Adv. Funct. Mater.* **20**, 3490 (2010).
89. J.E. Kleibeuker, B. Kuiper, S. Harkema, D.H.A. Blank, G. Koster, G. Rijnders, P. Tinnemans, E. Vlieg, P.B. Rossen, W. Siemons, G. Portale, J. Ravichandran, J.M. Szepieniec, R. Ramesh, *Phys. Rev. B* **85**, 165413 (2012).
90. H.-J. Bae, J. Sigman, D.P. Norton, L.A. Boatner, *Appl. Surf. Sci.* **241**, 271 (2005).
91. N.A. Pertsev, A.G. Zembilgotov, A.K. Tagantsev, *Phys. Rev. Lett.* **80**, 1988 (1998).
92. O. Diéguez, S. Tinte, A. Antons, C. Bungaro, J.B. Neaton, K.M. Rabe, D. Vanderbilt, *Phys. Rev B* **69**, 212101 (2004).
93. Y.L. Li, L.Q. Chen, *Appl. Phys. Lett.* **88**, 072905 (2006).
94. D.A. Tenne, P. Turner, J.D. Schmidt, M. Biegalski, Y.L. Li, L.Q. Chen, A. Soukiassian, S. Trolier-McKinstry, D.G. Schlom, X.X. Xi, D.D. Fong, P.H. Fuoss, J.A. Eastman, G.B. Stephenson, C. Thompson, S.K. Streiffer, *Phys. Rev. Lett.* **103**, 177601 (2009).
95. A. Pertsev, V.G. Koukhar, *Phys. Rev. Lett.* **84**, 3722 (2000).
96. V.G. Koukhar, N.A. Pertsev, R. Waser, *Phys. Rev. B* **64**, 214103 (2001).
97. Y.L. Li, S.Y. Hu, Z.K. Liu, L.Q. Chen, *Appl. Phys. Lett.* **78**, 3878 (2001).
98. Y.L. Li, S.Y. Hu, Z.K. Liu, L.Q. Chen, *Acta Mater.* **50**, 395 (2002).
99. S.K. Streiffer, J.A. Eastman, D.D. Fong, C. Thompson, A. Munkholm, M.V.R. Murty, O. Auciello, G.R. Bai, G.B. Stephenson, *Phys. Rev. Lett.* **89**, 067601 (2002).
100. D.D. Fong, G.B. Stephenson, S.K. Streiffer, J.A. Eastman, O. Auciello, P.H. Fuoss, C. Thompson, *Science* **304**, 1650 (2004).
101. K. Abe, N. Yanase, K. Sano, M. Izuha, N. Fukushima, T. Kawakubo, *Integr. Ferroelectr.* **21**, 197 (1998).
102. N. Yanase, K. Abe, N. Fukushima, T. Kawakubo, *Jpn. J. Appl. Phys., Part 1* **38**, 5305 (1999).
103. E.D. Specht, H.-M. Christen, D.P. Norton, L.A. Boatner, *Phys. Rev. Lett.* **80**, 4317 (1998).
104. H.-M. Christen, L.A. Knauss, K.S. Harshavardhan, *Mater. Sci. Eng., B* **56**, 200 (1998).
105. H.M. Christen, E.D. Specht, S.S. Silliman, K.S. Harshavardhan, *Phys. Rev. B* **68**, 20101 (2003).
106. M. Dawber, C. Lichtensteiger, M. Cantoni, M. Veithen, P. Ghosez, K. Johnston, K.M. Rabe, J.-M. Triscone, *Phys. Rev. Lett.* **95**, 177601 (2005).
107. E. Bousquet, M. Dawber, N. Stucki, C. Lichtensteiger, P. Hermet, S. Gariglio, J.M. Triscone, P. Ghosez, *Nature* **452**, 732 (2008).
108. J.B. Neaton, K.M. Rabe, *Appl. Phys. Lett.* **82**, 1586 (2003).
109. D.A. Tenne, A. Bruchhausen, N.D. Lanzillotti-Kimura, A. Fainstein, R.S. Katiyar, A. Cantarero, A. Soukiassian, V. Vaithyanathan, J.H. Haeni, W. Tian, D.G. Schlom, K.J. Choi, D.M. Kim, C.B. Eom, H.P. Sun, X.Q. Pan, Y.L. Li, L.Q. Chen, Q.X. Jia, S.M. Nakhmanson, K.M. Rabe, X.X. Xi, *Science* **313**, 1614 (2006).
110. Y.L. Li, S.Y. Hu, D. Tenne, A. Soukiassian, D.G. Schlom, X.X. Xi, K.J. Choi, C.B. Eom, A. Saxena, T. Lookman, Q.X. Jia, L.Q. Chen, *Appl. Phys. Lett.* **91**, 112914 (2007).
111. Y.L. Li, S.Y. Hu, D. Tenne, A. Soukiassian, D.G. Schlom, L.Q. Chen, X.X. Xi, K.J. Choi, C.B. Eom, A. Saxena, T. Lookman, Q.X. Jia, *Appl. Phys. Lett.* **91**, 252904 (2007).
112. N. Sai, B. Meyer, D. Vanderbilt, *Phys. Rev. Lett.* **84**, 5636 (2000).
113. M.R. Warusawithana, E.V. Colla, J.N. Eckstein, M.B. Weissman, *Phys. Rev. Lett.* **90**, 036802 (2003).
114. H.N. Lee, H.M. Christen, M.F. Chisholm, C.M. Rouleau, D.H. Lowndes, *Nature* **433**, 395 (2005).
115. A.G. Zembilgotov, N.A. Pertsev, U. Böttger, R. Waser, *Appl. Phys. Lett.* **86**, 052903 (2005).

116. G. Sheng, Y.L. Li, J.X. Zhang, S. Choudhury, Q.X. Jia, V. Gopalan, D.G. Schlom, Z.K. Liu, L.Q. Chen, *J. Appl. Phys.* **108**, 084113 (2010).
117. K. Kathan-Galipeau, P.P. Wu, Y.L. Li, L.Q. Chen, A. Soukiassian, X.X. Xi, D.G. Schlom, D.A. Bonnell, *ACS Nano* **5**, 640 (2011).
118. K. Kathan-Galipeau, P.P. Wu, Y.L. Li, L.Q. Chen, A. Soukiassian, Y. Zhu, D.A. Muller, X.X. Xi, D.G. Schlom, D.A. Bonnell, *J. Appl. Phys.* **112**, 052011 (2012).
119. J. Ravichandran, A.K. Yadav, R. Cheaito, P.B. Rossen, A. Soukiassian, S.J. Suresha, J.C. Duda, B.M. Foley, C.H. Lee, Y. Zhu, A.W. Lichtenberger, J.E. Moore, D.A. Muller, D.G. Schlom, P.E. Hopkins, A. Majumdar, R. Ramesh, M.A. Zurbuchen, *Nat. Mater.* (2013), in press, doi: 10.1038/nmat3826.
120. J. Wang, J.B. Neaton, H. Zheng, V. Nagarajan, S.B. Ogale, B. Liu, D. Viehland, V. Vaithyanathan, D.G. Schlom, U.V. Waghmare, N.A. Spaldin, K.M. Rabe, M. Wuttig, R. Ramesh, *Science* **299**, 1719 (2003).
121. R. Ramesh, N.A. Spaldin, *Nat. Mater.* **6**, 21 (2007).
122. A.A. Belik, S. Iikubo, K. Kodama, N. Igawa, S.-I. Shamoto, S. Niitaka, M. Azuma, Y. Shimakawa, M. Takano, F. Izumi, E. Takayama-Muromachi, *Chem. Mater.* **18**, 798 (2006).
123. M.-R. Li, U. Adem, S.R.C. McMitchell, Z. Xu, C.I. Thomas, J.E. Warren, D.V. Giap, H. Niu, X. Wan, R.G. Palgrave, F. Schiffmann, F. Cora, B. Slater, T.L. Burnett, M.G. Cain, A.M. Abakumov, G. van Tendeloo, M.F. Thomas, M.J. Rosseinsky, J.B. Claridge, *J. Am. Chem. Soc.* **134**, 3737 (2012).
124. W. Wang, J. Zhao, W. Wang, Z. Gai, N. Balke, M. Chi, H.N. Lee, W. Tian, L. Zhu, X. Cheng, D.J. Keavney, J. Yi, T.Z. Ward, P.C. Snijders, H.M. Christen, W. Wu, J. Shen, X. Xu, *Phys. Rev. Lett.* **110**, 237601 (2013).
125. J.F. Li, J. Wang, M. Wuttig, R. Ramesh, N. Wang, B. Ruette, A.P. Pyatakov, A.K. Zvezdin, D. Viehland, *Appl. Phys. Lett.* **84**, 5261 (2004).
126. R.R. Das, D.M. Kim, S.H. Baek, C.B. Eom, F. Zavaliche, S.Y. Yang, R. Ramesh, Y.B. Chen, X.Q. Pan, X. Ke, M.S. Rzchowski, S.K. Streiffer, *Appl. Phys. Lett.* **88**, 242904 (2006).
127. J. Dho, X. Qi, H. Kim, J.L. MacManus-Driscoll, M.G. Blamire, *Adv. Mater.* **18**, 1445 (2006).
128. F. Kubel, H. Schmid, *Acta Crystallogr., Sect. B: Struct. Sci.* **46**, 698 (1990).
129. A.J. Hatt, N.A. Spaldin, C. Ederer, *Phys. Rev. B* **81**, 054109 (2010).
130. A.G. Christy, *Acta Crystallogr. Sect. B: Struct. Sci.* **51**, 753 (1995).
131. L. Ehm, K. Knorr, L. Peters, S. Rath, W. Depmeier, *J. Alloys Compd.* **429**, 82 (2007).
132. J. Haines, J.M. Léger, O. Schulte, *Phys. Rev. B* **57**, 7551 (1998).
133. J.X. Zhang, B. Xiang, Q. He, J. Seidel, R.J. Zeches, P. Yu, S.Y. Yang, C.H. Wang, Y.H. Chu, L.W. Martin, A.M. Minor, R. Ramesh, *Nat. Nanotechnol.* **6**, 98 (2011).
134. Q. He, Y.H. Chu, J.T. Heron, S.Y. Yang, W.I. Liang, C.Y. Kuo, H.J. Lin, P. Yu, C.W. Liang, R.J. Zeches, W.C. Kuo, J.Y. Juang, C.T. Chen, E. Arenholz, A. Scholl, R. Ramesh, *Nat. Commun.* **2**, 225 (2011).
135. J.C. Yang, Q. He, S.J. Suresha, C.Y. Kuo, C.Y. Peng, R.C. HaisImaier, M.A. Motyka, G. Sheng, C. Adamo, H.J. Lin, Z. Hu, L. Chang, L.H. Tjeng, E. Arenholz, N.J. Podraza, M. Bernhagen, R. Uecker, D.G. Schlom, V. Gopalan, L.Q. Chen, C.T. Chen, R. Ramesh, Y.H. Chu, *Phys. Rev. Lett.* **109**, 247606 (2012).
136. C.J. Fennie, K.M. Rabe, *Phys. Rev. Lett.* **97**, 267602 (2006).
137. J.P. Rivera, H. Schmid, *Ferroelectrics* **36**, 447 (1981).
138. W. von Wartburg, *Phys. Status Solidi A* **21**, 557 (1974).
139. T. Birol, C.J. Fennie, *Phys. Rev. B 88*, **094103** (2013).
140. T.R. McGuire, M.W. Shafer, R.J. Joenk, H.A. Alperin, S.J. Pickart, *J. Appl. Phys.* **37**, 981 (1966).
141. C.-L. Chien, S. DeBenedetti, F. De S. Barros, *Phys. Rev. B* **10** 3913 (1974).
142. T. Katsufuji, H. Takagi, *Phys. Rev. B* **64**, 054415 (2001).
143. H.-H. Wang, A. Fleet, J.D. Brock, D. Dale, Y. Suzuki, *J. Appl. Phys.* **96**, 5324 (2004).
144. K. Kugimiya, K. Fujita, K. Tanaka, K. Hirao, *J. Magn. Magn. Mater.* **310**, 2268 (2007).
145. S.C. Chae, Y.J. Chang, D.-W. Kim, B.W. Lee, I. Choi, C.U. Jung, *J. Electroceram.* **22**, 216 (2009).
146. K. Fujita, N. Wakasugi, S. Murai, Y. Zong, K. Tanaka, *Appl. Phys. Lett.* **94**, 062512 (2009).
147. M.W. Schafer, *J. Appl. Phys.* **36**, 1145 (1965).
148. G.J. McCarthy, W.B. White, R. Roy, *J. Inorg. Nucl. Chem.* **31**, 329 (1969).
149. Y.S. Kim, D.J. Kim, T.H. Kim, T.W. Noh, J.S. Choi, B.H. Park, J.-G. Yoon, *Appl. Phys. Lett.* **91**, 042908 (2007).
150. K.A. Müller, H. Burkard, *Phys. Rev. B* **19**, 3593 (1979).
151. E.J. Tarsa, E.A. Hachfeld, F.T. Quinlan, J.S. Speck, M. Eddy, *Appl. Phys. Lett.* **68**, 490 (1996).
152. T. Ohnishi, M. Lippmaa, T. Yamamoto, S. Meguro, H. Koinuma, *Appl. Phys. Lett.* **87**, 2419191 (2005).
153. T. Ohnishi, K. Shibuya, T. Yamamoto, M. Lippmaa, *J. Appl. Phys.* **103**, 103703 (2008).
154. M. Kestigian, J.G. Dickinson, R. Ward, *J. Am. Chem. Soc.* **79**, 5598 (1957).
155. D.A. Tenne, I.E. Gonenli, A. Soukiassian, D.G. Schlom, S.M. Nakhmanson, K.M. Rabe, X.X. Xi, *Phys. Rev. B* **76**, 024303 (2007).
156. C.M. Brooks, L. Fitting Kourkoutis, T. Heeg, J. Schubert, D.A. Muller, D.G. Schlom, *Appl. Phys. Lett.* **94**, 162905 (2009).
157. J.H. Lee, X. Ke, N.J. Podraza, L. Fitting Kourkoutis, T. Heeg, M. Roeckerath, J.W. Freeland, C.J. Fennie, J. Schubert, D.A. Muller, P. Schiffer, D.G. Schlom, *Appl. Phys. Lett.* **94**, 212509 (2009).
158. J.H. Lee, K.M. Rabe, *Phys. Rev. Lett.* **104**, 207204 (2010).
159. E. Bousquet, N.A. Spaldin, P. Ghosez, *Phys. Rev. Lett.* **104**, 037601 (2010).
160. P.J. Ryan, J.-W. Kim, T. Birol, P. Thompson, J.-H. Lee, X. Ke, P.S. Normile, E. Karapetrova, P. Schiffer, S.D. Brown, C.J. Fennie, D.G. Schlom, *Nat. Commun.* **4**, 1334 (2013).
161. C.H. Lee, N.D. Orloff, T. Birol, Y. Zhu, V. Goian, E. Rocas, R. HaisImaier, E. Vlahos, J.A. Mundy, L.F. Kourkoutis, Y. Nie, M.D. Biegalski, J. Zhang, M. Bernhagen, N.A. Benedek, Y. Kim, J.D. Brock, R. Uecker, X.X. Xi, V. Gopalan, D. Nuzhnyy, S. Kamba, D.A. Muller, I. Takeuchi, J.C. Booth, C.J. Fennie, D.G. Schlom, *Nature* **502**, 532 (2013).
162. O.G. Vendik, *Ferroelectrics* **12**, 85 (1976).
163. S.W. Kirchoefer, J.M. Pond, A.C. Carter, W. Chang, K.K. Agarwal, J.S. Horwitz, D.B. Chrisey, *Microwave Opt. Technol. Lett.* **18**, 168 (1998).
164. S.S. Gevorgian, E.L. Kollberg, *IEEE Trans. Microwave Theory Tech.* **49**, 2117 (2001).
165. A.K. Tagantsev, V.O. Sherman, K.F. Astafiev, J. Venkatesh, N. Setter, *J. Electroceram.* **11**, 5 (2003).
166. S. Andersson, A.D. Wadsley, *Nature* **211**, 581 (1966).
167. J.S Anderson, J.M. Browne, A.K. Cheetham, R. Vondreel, J.L. Hutchison, F.J. Lincoln, D.J.M. Bevan, J. Straehle, *Nature* **243**, 81 (1973).
168. R.J.D. Tilley, *Nature* **269**, 229 (1977).
169. R.J.D. Tilley, *J. Solid State Chem.* **21**, 293 (1977).
170. T. Nakamura, P.H. Sun, Y.J. Shan, Y. Inaguma, M. Itoh, I.S. Kim, J.H. Sohn, M. Ikeda, T. Kitamura, H. Konagaya, *Ferroelectrics* **196**, 205 (1997).
171. P.L. Wise, I.M. Reaney, W.E. Lee, T.J. Price, D.M. Iddles, D.S. Cannell, *J. Eur. Ceram. Soc.* **21**, 1723 (2001).
172. N.D. Orloff, W. Tian, C.J. Fennie, C.H. Lee, D. Gu, J. Mateu, X.X. Xi, K.M. Rabe, D.G. Schlom, I. Takeuchi, J.C. Booth, *Appl. Phys. Lett.* **94**, 042908 (2009).
173. T. Birol, N.A. Benedek, C.J. Fennie, *Phys. Rev. Lett.* **107**, 257602 (2011).
174. D.O. Klenov, W. Donner, B. Foran, S. Stemmer, *Appl. Phys. Lett.* **82**, 3427 (2003).
175. W. Donner, C. Chen, M. Liu, A.J. Jacobson, Y.-L. Lee, M. Gadre, D. Morgan, *Chem. Mater.* **23**, 984 (2011).
176. J.M. Rondinelli, N.A. Spaldin, *Adv. Mater.* **23**, 3363 (2011).
177. J.M. Rondinelli, S.J. May, J.W. Freeland, *MRS Bull.* **37**, 261 (2012).
178. W.S. Choi, J.-H. Kwon, H. Jeen, J.E. Hamann-Borrero, A. Radi, S. Macke, R. Sutarto, F. He, G.A. Sawatzky, V. Hinkov, M. Kim, H.N. Lee, *Nano Lett.* **12**, 4966 (2012).
179. Y. Yang, C.M. Schlepütz, C. Adamo, D.G. Schlom, R. Clarke, *APL Mater.* **1**, 052102 (2013).
180. C.-L. Jia, V. Nagarajan, J.-Q. He, L. Houben, T. Zhao, R. Ramesh, K. Urban, R. Waser, *Nat. Mater.* **6**, 64 (2006).
181. C.-L. Jia, S.-B. Mi, K. Urban, I. Vrejoiu, M. Alexe, D. Hesse, *Nat. Mater.* **7**, 57 (2008).
182. C.T. Nelson, B. Winchester, Y. Zhang, S.-J. Kim, A. Melville, C. Adamo, C.M. Folkman, S.-H. Baek, C.-B. Eom, D.G. Schlom, L.-Q. Chen, X. Pan, *Nano Lett.* **11**, 828 (2011).
183. C.L. Jia, K.W. Urban, M. Alexe, D. Hesse, I. Vrejoiu, *Science* **331**, 1420 (2011).
184. A.Y. Borisevich, H.J. Chang, M. Huijben, M.P. Oxley, S. Okamoto, M.K. Niranjan, J.D. Burton, E.Y. Tsymbal, Y.H. Chu, P. Yu, R. Ramesh, S.V. Kalinin, S.J. Pennycook, *Phys. Rev. Lett.* **105**, 087204 (2010).
185. D.A. Muller, L.F. Kourkoutis, M. Murfitt, J.H. Song, H.Y. Hwang, J. Silcox, N. Dellby, O.L. Krivanek, *Science* **319**, 1073 (2008).
186. D. Lee, R. Behera, P. Wu, H. Xu, Y.L. Li, S.B. Sinnott, S. Phillpot, L. Chen, V. Gopalan, *Phys. Rev. B* **80**, 060102 (2009).
187. E.F. Kneller, R. Hawig, *Magnetics, IEEE Trans. Magn.* **27**, 3588 (1991).
188. E.E. Fullerton, J.S. Jiang, S.D. Bader, *J. Magn. Magn. Mater.* **200**, 392 (1999).
189. P. Wu, X. Ma, Y. Li, V. Gopalan, L.Q. Chen, *Appl. Phys. Lett.* **100**, 092905 (2012).
190. J.H. Lee, K.M. Rabe, *Phys. Rev. Lett.* **107**, 067601 (2011).
191. D.M. Newns, B.G. Elmegreen, X.-H. Liu, G.J. Martyna, *Adv. Mater.* **24**, 3672 (2012).
192. D. Newns, B. Elmegreen, X. Hu Liu, G. Martyna, *J. Appl. Phys.* **111**, 084509 (2012).
193. R.E. Newnham, J.J. Kramer, W.A. Schulze, L.E. Cross, *J. Appl. Phys.* **49**, 6088 (1978).
194. M.J. Harris, S.T. Bramwell, D.F. McMorrow, T. Zeiske, K.W. Godfrey, *Phys. Rev. Lett.* **79**, 2554 (1997).

195. C. Fennie, K. Rabe, *Phys. Rev. B* **72**, 100103 (2005).
196. T. Choi, Y. Horibe, H.T. Yi, Y.J. Choi, W. Wu, S.W. Cheong, *Nat. Mater.* **9**, 253 (2010).
197. A. Arkenbout, T. Palstra, T. Siegrist, T. Kimura, *Phys. Rev. B* **74**, 184431 (2006).
198. F. Ye, Y. Ren, Q. Huang, J. Fernandez-Baca, P. Dai, J. Lynn, T. Kimura, *Phys. Rev. B* **73**, 220404 (2006).
199. T. Kimura, Y. Sekio, H. Nakamura, T. Siegrist, A.P. Ramirez, *Nat. Mater.* **7**, 291 (2008).
200. Y. Kitagawa, Y. Hiraoka, T. Honda, T. Ishikura, H. Nakamura, T. Kimura, *Nat. Mater.* **9**, 797 (2010).
201. A.A. Bossak, I.E. Graboy, O.Y. Gorbenko, A.R. Kaul, M.S. Kartavtseva, V.L. Svetchnikov, H.W. Zandbergen, *Chem. Mater.* **16**, 1751 (2004).
202. W. Wang, J. Zhao, W. Wang, Z. Gai, N. Balke, M. Chi, H.N. Lee, W. Tian, L. Zhu, X. Cheng, D.J. Keavney, J. Yi, T.Z. Ward, P.C. Snijders, H.M. Christen, W. Wu, J. Shen, X. Xu, *Phys. Rev. Lett.* **110**, 237601 (2013).
203. E.S. Machlin, P. Chaudhari, in *Synthesis and Properties of Metastable Phases*, E.S. Machlin, T.J. Rowland, Eds. (The Metallurgical Society of AIME, Warrendale, 1980), pp. 11–29.
204. C.P. Flynn, *Phys. Rev. Lett.* **57**, 599 (1986).
205. R. Bruinsma, A. Zangwill, *J. Phys. (Paris)* **47**, 2055 (1986).
206. O.Y. Gorbenko, S.V. Samoilenkov, I.E. Graboy, A.R. Kaul, *Chem. Mater.* **14**, 4026 (2002).
207. J.M. Rondinelli, C.J. Fennie, *Adv. Mater.* **24**, 1961 (2012).
208. A.T. Mulder, N.A. Benedek, J.M. Rondinelli, C.J. Fennie, *Adv. Funct. Mater.* **23**, 4810 (2013).
209. C.J. Fennie, *Phys. Rev. Lett.* **100**, 167203 (2008).
210. T. Varga, A. Kumar, E. Vlahos, S. Denev, M. Park, S. Hong, T. Sanehira, Y. Wang, C. Fennie, S. Streiffer, X. Ke, P. Schiffer, V. Gopalan, J. Mitchell, *Phys. Rev. Lett.* **103**, 047601 (2009).
211. G. Singh-Bhalla, C. Bell, J. Ravichandran, W. Siemons, Y. Hikita, S. Salahuddin, A.F. Hebard, H.Y. Hwang, R. Ramesh, *Nat. Phys.* **7**, 80 (2010). □

Career Center

JOB SEEKERS MEET YOUR NEXT EMPLOYER!

We'll show off your talents to the world's most prestigious high-tech firms, universities and laboratories. At the 2014 MRS Spring Meeting Career Center, you can access many interesting job postings, visit recruitment booths and interview with prospective employers. Please bring extra copies of your resume for your own use.

The Career Center is FREE to all MRS members and those registered to attend the 2014 MRS Spring Meeting.

ON-SITE REGISTRATION HOURS
Monday, April 21.....1:00 pm – 4:00 pm
(Candidate Registration Only)

CAREER CENTER HOURS
Tuesday, April 22 .....10:00 am – 5:00 pm
Wednesday, April 23.....10:00 am – 5:00 pm

Register and submit your resume today!
www.mrs.org/spring-2014-career-center



Rigaku
Better measurements. Better confidence. Better world.

www.Rigaku.com/products/xrd/smartlab



Powder Diffraction • Thin Film Diffraction • SAXS • In-Plane Grazing Incidence

Rigaku's SmartLab® is the most versatile diffractometer in the world. You can start using all XRD applications from the very first day because of the unique knowledge-based Guidance control software. The available 9 kW line focus X-ray source provides ultimate power for the most demanding applications. Automatic self-alignment ensures that you always collect the best data possible and beam path selection can be made without touching a multilayer optic.

for Material Scientists

The SmartLab combined with a novel two-dimensional detector enables one to measure a large-area reciprocal space map in minutes rather than days.

Rigaku Corporation and its Global Subsidiaries | www.Rigaku.com | info@Rigaku.com

Reprinted from Nature Reviews Materials, Vol 4, Ramamoorthy Ramesh and Darrell G. Schlom, Creating emergent phenomena in oxide superlattices, 257-268, Copyright 2019, with permission from Springer Nature.

Creating emergent phenomena in oxide superlattices

Ramamoorthy Ramesh[1]* *and Darrell G. Schlom*[2]*

Abstract | Complex oxides are record holder materials for many phenomena, including ferroelectricity, piezoelectricity, superconductivity and multiferroicity. Complex oxides often have competing ground states with energies slightly higher than that of the true ground state. This competition is fortuitous because thermodynamic variables (for example, temperature, electric field, magnetic field, stress and chemical potentials) can access these metastable phases that are usually hidden but emerge as the energetic landscape is reshaped by adjusting the thermodynamic variables. Epitaxial superlattices are a platform for imposing thermodynamic boundary conditions to unleash the properties of hidden phases by altering the delicate balance between competing spin, charge, orbital and lattice degrees of freedom. Additionally, a feature of complex oxides with large responses (large property coefficients) is the coexistence of phases on the nanoscale. New phases can emerge at the heterointerfaces of oxide superlattices, and X-ray, electron, neutron and proximal probes as well as ab initio theoretical studies can provide insights into these emergent phenomena.

Complex oxides and superlattices containing complex oxides have a broad range of functionalities, including the hottest high-temperature superconductor[1], largest metal–insulator transition[2], highest spin polarization[3], greatest colossal magnetoresistance[4] and strongest ferroelectric[5,6], piezoelectric[7] and multiferroic[8] properties. The desire to use and enhance these functionalities for applications has triggered studies to understand the fundamental nature of existing systems. As a consequence, research dedicated to complex oxides has intensified over the past decades, particularly in the condensed matter physics and materials science communities.

The complexity of complex oxides arises from the interplay between the fundamental degrees of freedom, namely, the electronic spin, charge and orbital and the effect of the lattice. New states of matter have emerged as a consequence of the competition between these degrees of freedom. Another feature that underpins large physical responses is nanoscale complexity, in the form of chemical, ionic or electronic inhomogeneities. Examples include piezoelectric and dielectric responses in relaxor ferroelectrics[9] such as $PbMg_{1/3}Nb_{2/3}O_3$–$PbTiO_3$ (REF.[7]), colossal magnetoresistance in doped manganites[10,11] and high-temperature superconductivity in cuprates[11–13].

Broadly speaking, the ability to precisely synthesize materials has enhanced our understanding of many physical phenomena. Although the classical approach of synthesizing single crystals is to use bulk crystal growth techniques[14], heteroepitaxial growth has emerged as a pathway to create model systems and to manipulate their ground states using thermodynamic variables, such as the electric field, magnetic field and stress[15–18]. Perhaps the most interesting attribute of complex oxides is the complex interplay of several fundamental effects, each with different energy scales[19] (FIG. 1). This interplay leads to competing ground states that consequently lead to large susceptibilities with respect to external stimuli. For example, the electronic correlations arising from on-site Coulombic repulsion and spin–orbit interactions are powerful ways to create new ground states. When we superimpose on this the power of epitaxy and the ability to artificially engineer the long-range order of the material, a plethora of physical phenomena arise.

An advantage of oxides (akin to compound semiconductors) is that the oxygen sublattice is an excellent structural and chemical framework for the construction of superlattices. Within the framework, cations are inserted mainly into interstitial sites. The most widely studied complex oxide superlattices have a perovskite structure with the general formula ABO_3 (FIG. 1a,b). The oxygen coordination polyhedral around the B sites are BO_6 octahedra, and the larger A-site cations occupy body-centred positions within the corner-sharing network of BO_6 octahedra (FIG. 1a,b). In the perovskite superlattice, the cationic species occupying the A sites and B sites are systematically swapped out to impose gradients in the thermodynamic responses. Superlattices of other complex oxides, including rocksalt[20], garnet[21] and rutile[22] structures, have also been constructed, indicating the generality of this superlattice approach. The use of

[1]*Department of Materials Science & Engineering and Department of Physics, University of California, Berkeley, CA, USA.*

[2]*Department of Materials Science and Engineering and Kavli Institute at Cornell for Nanoscale Science, Cornell University, Ithaca, NY, USA.*

**e-mail:* *rramesh@berkeley.edu; schlom@cornell.edu*

https://doi.org/10.1038/s41578-019-0095-2

thin-film deposition tools such as reflection high-energy electron diffraction (RHEED)-assisted pulsed-laser deposition (also known as laser molecular-beam epitaxy (MBE)), conventional MBE and chemical vapour deposition has enabled the synthesis of atomically sharp, artificial heterostructures that show novel physical phenomena, especially at heterointerfaces.

Epitaxial growth provides a pathway to manipulate new states of matter that arise as a consequence of the interactions between the spin, charge, orbital and lattice degrees of freedom. Vacuum deposition methods coupled with epitaxial growth can be used to self-assemble materials with atomic-layer precision and controllable properties (FIG. 2). The synthetic approaches include strain engineering[23–29] (FIG. 2a), interface engineering[30–38] (FIG. 2b), epitaxial nanocomposites[38–42] (FIG. 2c), epitaxial stabilization[43–47] (FIG. 2d), dimensional confinement[48] (FIG. 2e), modulation doping[49–51], polarization doping[34,35,52–56] (FIG. 2f) and symmetry breaking[57] (FIG. 2g).

Strain engineering (FIG. 2a) uses a substrate with a lattice constant different from that of the thin film grown upon it. As a result, a homogeneous biaxial strain is imposed on the thin film — within the limits of strain and film thickness so that strain-relaxing defects[58] (for example, dislocations, cracks or point defects[59–61]) are minimized. Although strain engineering has been used to improve the performance of the materials in semiconductor devices[62,63], if applied to oxides, strain engineering can more than simply enhance an existing property. In oxides, strain engineering can perturb the energetic landscape to such an extent that a metastable polymorph (or hidden ground state) becomes the ground state. The resultant phase may have properties that are absent in the bulk form of the material. Thus, hidden ground states with unparalleled properties can be unleashed[8,23,26,28].

Interface engineering (FIG. 2b) is the ability to create interfaces with atomic-layer precision. This ability is a prerequisite to the formation of many proof-of-principle oxide electronic devices in which termination-specific interfaces, the absence of reaction layers and minimizing interdiffusion are important for device function. Early examples of the precise interface engineering of oxides have been demonstrated by reactive evaporation[30], sputtering[37], pulsed-laser deposition (PLD)[32,34] and MBE[31,33,35,36]. Though most examples of interface engineering involve the epitaxial integration of perovskites, the interface engineering of rocksalt[20], garnet[21] and rutile[22] structures have also been achieved.

An epitaxial nanocomposite (FIG. 2c) is a self-assembled nanocomposite in which one phase forms 1D rods in a matrix of the other phase (a 1–3 composite[64]) and both phases are epitaxially oriented with respect to the substrate. For this approach, epitaxy occurs not only in the in-plane direction (on the substrate) but also in the out-of-plane direction between the constituents of the nanocomposite. As a consequence, it is possible to impose large strains on films that are thicker than the films within a conventional strained bilayer[65] (FIG. 2a).

Epitaxial stabilization (FIG. 2d) is the process by which lattice misfit strain energies and interfacial energies are exploited to favour a desired metastable phase over the equilibrium phase[43–47]. The ideal substrate is isostructural with and well lattice-matched to the metastable polymorph[43]; this approach is a direct route to stabilizing a hidden ground state and is applicable to a wide range of oxides. The propensity of competing ground states in many oxide systems and the ability of epitaxial stabilization to stabilize a targeted ground state chosen from among the competing ground states are manifest

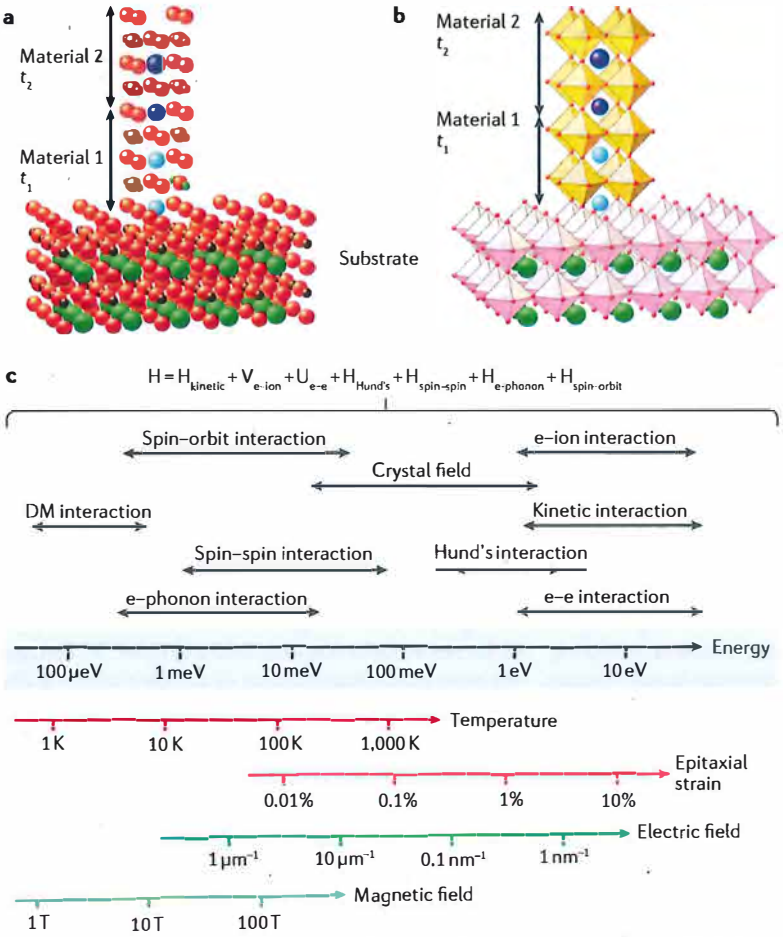


Fig. 1 | **A comparison of the energy scales of various thermodynamic constraints in oxide superlattices. a,b** | A schematic of an oxide superlattice epitaxially grown on an underlying substrate. The superlattice is formed by the repeated growth of material 1 (of thickness t_1) on material 2 (of thickness t_2), where t_1 and t_2 range from a few ångströms to micrometres. The example shown is for a superlattice in which the layers and substrate all have the perovskite structure. In panel **a**, the oxygen ions are shown in red, and the ions (A, B and O) are depicted with their full atomic radii. In panel **b**, the sizes of the oxygen ions are drastically reduced from their atomic radii, and the coordination polyhedral around the B cations are filled in, revealing the ordered arrangement. **c** | The range of energies for various interactions present in complex oxides. The equation at the top presents the various energy terms that go into the general Hamiltonian for such complex oxides. A comparison of the energy scales in various thermodynamic constraints, namely, temperature, magnetic field, electric field and mechanical strain from epitaxy, is shown at the bottom. Note that for thin films, electric field and epitaxial strain are powerful variables that can be used to control a broad range of physical phenomena. DM, Dzyaloshinskii–Moriya; e, electron. Panel **c** is adapted with permission of IOP Publishing, from Yi, D. et al. Engineering magnetism at functional oxide interfaces: manganites and beyond. *J. Phys. Condens. Matter.* **29**, 2017 (REF.[19]); permission conveyed through Copyright Clearance Center, Inc.

in studies that have selectively stabilized five different ground states of $ScFeO_3$ (REF.[66]) or three different ground states of VO_2 (REF.[67]) by depositing thin films of these materials on to different substrates. Key to the implementation of strain engineering and epitaxial stabilization is the existence of appropriate substrates. Indeed, though the potential of epitaxial stabilization was realized nearly 40 years ago[43], it is the development of appropriate substrates that has led to expanded use of this approach in complex oxides.

Dimensional confinement (FIG. 2e) is achieved by the insertion of layers that restrict the spatial extent of an order parameter, for example, a superlattice in which conducting layers alternate with insulating layers that confine

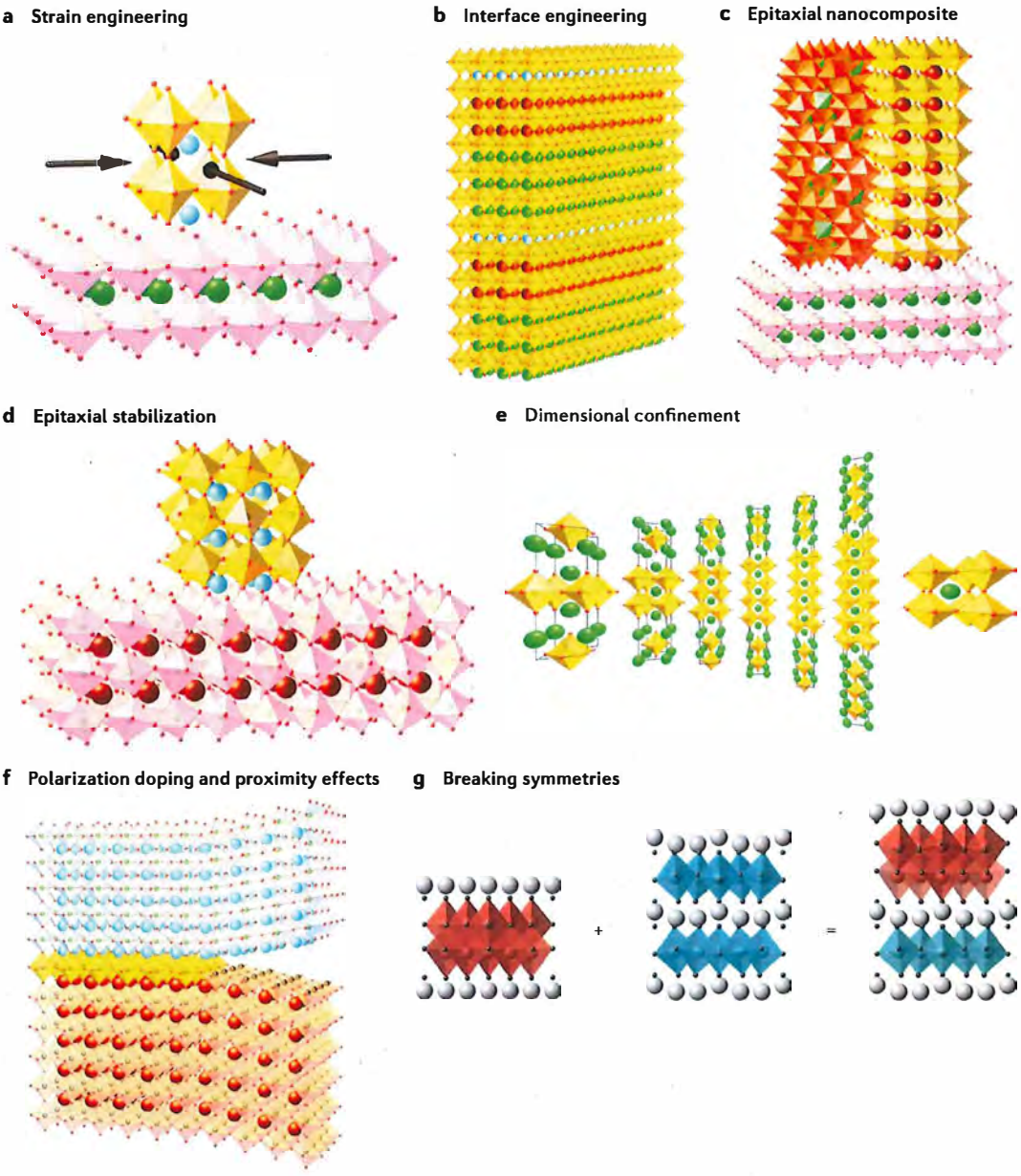


Fig. 2 | **A schematic of the approaches used in vacuum thin-film deposition techniques to create epitaxial heterostructures. a** | Strain engineering through lattice mismatch. **b** | Interface engineering to integrate different materials in an atomically abrupt manner and create interfacial phenomena. **c** | An epitaxial nanocomposite created using the principles of epitaxy along the out-of-plane direction as well as the in-plane direction. **d** | Epitaxial stabilization of new phases. **e** | Dimensional confinement uses epitaxy to reduce the dimensionality of a normally 3D material by confining a thin layer of it between barrier materials. **f** | Polarization doping and proximity effects in which the spontaneous polarization in one layer is used to modulate carrier concentrations, mobilities or spins in the adjacent layer. **g** | Breaking symmetry at interfaces, for example, by breaking mirror symmetry. Panel **a** is adapted with permission from Schlom, D. G. et al. Elastic strain engineering ferroic oxides. *MRS Bull.* **39**, 118–130 (REF.[29]). Panels **b** and **c** are adapted with permission from Ramesh, R et al. Whither oxide electronics. *MRS Bull.* **33**, 1066–1011 (REF.[38]). Panel **e** is adapted from REF.[48], Springer Nature Limited. Panel **f** is adapted from REF.[56], Springer Nature Limited.

the mobile electrons. Modulation doping is the dominant technique to realize 2D electron gases in conventional semiconductors by locating dopants remotely from an interface and using the energetics of band alignment to cause the carriers released by the remotely located dopants to spill over into the undoped material. In the undoped material, these carriers form a 2D electron gas with minimal ionized impurity scattering[49].

Polarization doping (FIG. 2f) occurs naturally in a range of oxides and materials, for example, in cuprate superconductors in which charge reservoir layers donate their carriers to surrounding CuO_2 layers[68], but analogous electronic reconstruction can also occur at epitaxially engineered oxide interfaces, such as the $LaAlO_3$/$SrTiO_3$ system[54,55]. Interfaces offer the opportunity to harness proximity effects from juxtaposed competing ground states (FIG. 2f).

Interfaces can also be used to break symmetries by stacking layers in a particular sequence. The ability to precisely control the sequence and the kind of atomic layers that are grown using advanced vacuum deposition techniques makes it possible to break symmetry. For example, the stacking sequence of alternating layers (A–B–A–B) contains mirror symmetry (at the positions of the A planes and the B planes) if the individual A layers and B layers possess mirror symmetry. By contrast, by the controlled addition of C layers to the aforementioned superlattice, the stacking sequence A–B–C–A–B–C breaks this symmetry[35,69]. This approach was first used to break symmetry with A = $BaTiO_3$, B = $SrTiO_3$ and C = $CaTiO_3$ (REFS[35,69]). Another way to break mirror symmetry in stacked layers is to use layers that themselves lack mirror symmetry, such as those in a geometric ferroelectric[70] (FIG. 2g).

Although several physical mechanisms can break the symmetry of the overgrown layer, for example, strain engineering can stabilize a hidden ground state of a material with a different symmetry, a geometric ferroelectric structure (FIG. 2g) does not involve macroscopic strain. Instead, this approach involves the atomic corrugation or rumpling of an overlying layer. If the overlayer follows the atomic corrugation, then the mirror symmetry that it would typically possess is lost, and with the loss of symmetry, new properties can emerge[16]. The rumpled template imposes local distortions but not macroscopic strain. The symmetry that is lost by following the rumpling of the template could be mirror symmetry (FIG. 2g) or another symmetry.

The ability of an underlying material (a substrate or just another film layer) to distort an overlying material and cause symmetry reduction occurs in many materials. For example, Sr_2TiO_4, which has a perovskite-related structure (FIG. 2e), can be considered a $SrTiO_3$/SrO superlattice with alternating formula units of these structures along its *c* axis. Although SrO planes are typically flat, when alternated with $SrTiO_3$ to form Sr_2TiO_4, the SrO planes become puckered. This puckering is slight (approximately ±0.07 Å) but is observed experimentally[71] and in first-principles calculations[72]. Puckering has been predicted for other superlattices, including $BaTiO_3$/BaO (REFS[73,74]) and $SrTiO_3$/$SrRuO_3$ (REF.[75]).

Nexus of theory and experiment

In parallel with the developments in synthetic tools, there has been dramatic progress in theoretical methods. For example, second-principles predictions of the ground state through the use of model Hamiltonians to increase the size of the building blocks from hundreds of atoms to several tens of thousands of atoms have enhanced our ability to predict emergent ground states such as vortices and polar skyrmions[76]. Such theoretical investigations have enabled the predictions of new states of matter, oftentimes well before their experimental counterparts. The emergence of a variety of electron, photon and neutron probes in conjunction with proximal sensing probes completes the synthesis–theory–characterization triad that is enabling these discoveries in condensed matter science. Given the rapid pace of the development, it is impossible to review all the progress in the past two decades. Instead, we use two examples to illustrate the power of such heteroepitaxial constructs in enabling the discovery of new states of matter: one example showing the combination of four of the approaches shown in FIG. 2 and another example focusing on how the fundamental boundary conditions at heterointerfaces control phase evolution in a specific subset of artificially constructed oxide superlattices.

Designed multiferroics. An example of an artificial multiferroic heterostructure made using a combination of the epitaxial integration approaches discussed above is $(LuFeO_3)_m/(LuFe_2O_4)_1$, which is a room-temperature magnetoelectric multiferroic[57]. Materials that exhibit simultaneous order in their electric and magnetic ground states are promising to enable the electrical control of magnetism. Such materials are, however, rare as a consequence of the competing requirements for ferroelectricity and magnetism, and until recently $BiFeO_3$ was the only material with this functionality at room temperature[77–80]. Oxide superlattices are a way to overcome these competing requirements, as was recently demonstrated for $(LuFeO_3)_m/(LuFe_2O_4)_1$ superlattices[57]. This example is described in detail below.

$(LuFeO_3)_m/(LuFe_2O_4)_1$ superlattices involve the hierarchical construction of a single-phase multiferroic in which ferroelectricity and strong magnetic ordering are coupled near room temperature[57]. Constructing this artificial multiferroic heterostructure involves a combination of interface engineering, epitaxial stabilization, polarization doping and symmetry breaking (FIG. 2b,d,f,g). Starting with hexagonal $LuFeO_3$, a metastable geometric ferroelectric[70] with the greatest known planar rumpling, individual extra monolayers of FeO were introduced during growth to construct formula-unit-thick layers of ferrimagnetic $LuFe_2O_4$ within the $LuFeO_3$ matrix, more specifically, $(LuFeO_3)_m/(LuFe_2O_4)_1$ superlattices. Note that the stable polymorph of $LuFeO_3$ has a centrosymmetric perovskite structure in which the iron coordination polyhedron is an octahedron. As $\bar{1}$ symmetry precludes ferroelectric behaviour, the stable polymorph of $LuFeO_3$ is unwanted. Epitaxial stabilization is used to achieve the desired hexagonal ferroelectric polymorph of $LuFeO_3$, in which the iron coordination polyhedron is a trigonal bipyramid, by growing

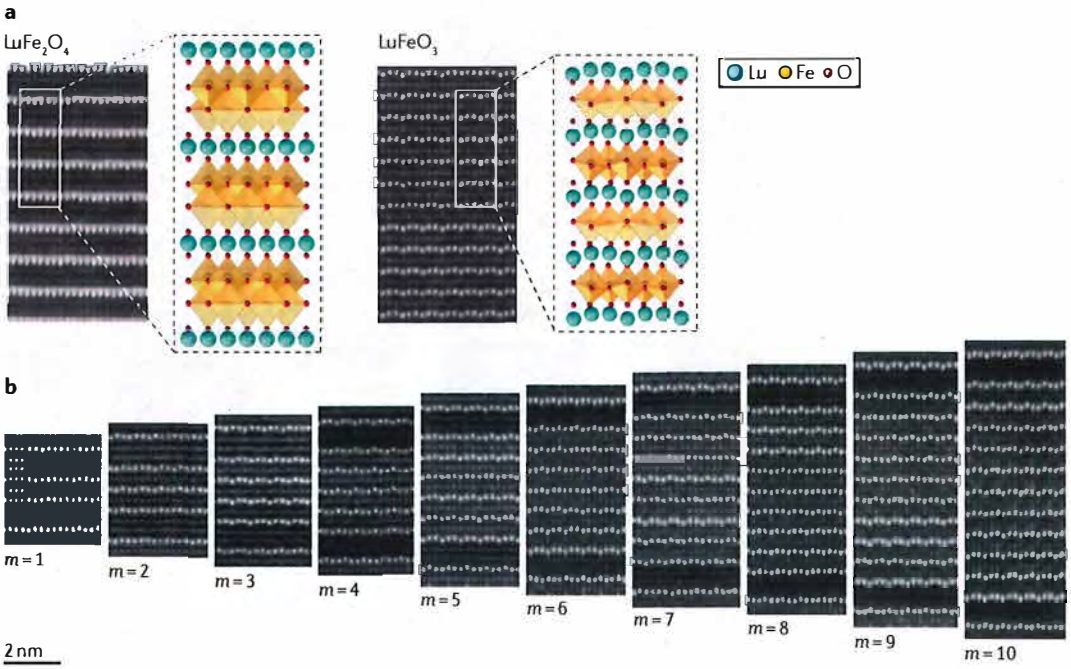


Fig. 3 | **An atomic-level composite comprising a ferrimagnet and a geometric ferroelectric. a** | High-angle annular dark-field scanning transmission electron microscopy (HAADF-STEM) images and crystal structures of the $LuFe_2O_4$ (a ferrimagnet) and the $LuFeO_3$ (a geometric ferroelectric) endmembers. **b** | Alternating layers of $LuFe_2O_4$ and $LuFeO_3$ are created using molecular-beam epitaxy. Cross-sectional HAADF-STEM images of $(LuFeO_3)_m/(LuFe_2O_4)_1$ superlattices with $m = 1$–10. The severe rumpling imposed by the $LuFeO_3$ drives the ferrimagnetic $LuFe_2O_4$ into a simultaneously ferroelectric state while also reducing the spin frustration of $LuFe_2O_4$. This rumpling increases the magnetic transition temperature to 281 K for $(LuFeO_3)_9/(LuFe_2O_4)_1$. Lu, Fe and O atoms are turquoise, yellow and red, respectively, in the crystal structures. Adapted from REF.[57], Springer Nature Limited.

it on (111) yttria-stabilized zirconia (YSZ)[81]. The fabrication of $(LuFeO_3)_m/(LuFe_2O_4)_1$ superlattices involves interface engineering. Cross-sectional transmission electron microscopy (TEM) images of these superlattices (FIG. 3) show that the severe rumpling imposed by neighbouring $LuFeO_3$ drives the ferrimagnetic $LuFe_2O_4$ into a ferroelectric state while simultaneously reducing the $LuFe_2O_4$ spin frustration. This rumpling increases the magnetic transition temperature significantly — from 240 K for $LuFe_2O_4$ to 281 K for $(LuFeO_3)_9/(LuFe_2O_4)_1$ — because it reduces the geometric frustration among the magnetic spins. Note that the rumpling from the $LuFeO_3$ imposes a local distortion on the neighbouring $LuFe_2O_4$ — a distortion that removes the mirror symmetry that the $LuFe_2O_4$ layers would otherwise have. This breaking of symmetry (FIG. 2g) enables the $LuFe_2O_4$ to become simultaneously ferrimagnetic and ferroelectric. This rumpling is distinct from strain engineering because no macroscopic strain is involved. Importantly, in these superlattices, the ferroelectric order couples to the ferrimagnetism, enabling electrical control of magnetism at 200 K (REF.[57]).

This result demonstrates a design methodology for creating higher-temperature magnetoelectric multiferroics (FIG. 4). The key aspect of this design is the combination of a geometrically frustrated ferrimagnet ($LuFe_2O_4$ in this example) with a geometric ferroelectric ($LuFeO_3$ in this example) that rumples it. When brought into atomic contact, the geometric ferroelectric distorts the ferrimagnet, reducing its frustration. This reduced frustration leads to a higher magnetic ordering temperature of the ferrimagnet and is an example of how ferroelectricity can enhance magnetism. Though rare, the strengthening of magnetism by ferroelectricity has been seen in other systems[8] and is desired for producing superior multiferroics. Ongoing work (D.G.S. and R.R., unpublished observations) has shown that other related superlattices can be prepared, with the possibility to enhance the magnetic ordering temperature through the introduction of ferrimagnetic spinels (for example, $CoFe_2O_4$) while seeking to maintain the ferroelectric coupling.

In addition to this design methodology, it is important to consider the role of electrostatics in these superlattices comprising alternate layers of ferroelectrics and non-ferroelectrics (in this case, ferrimagnets). The spontaneous polarization of the ferroelectric layers polarizes the non-ferroelectric layers, but polarizing a non-ferroelectric material costs energy[82]. The thicker the non-ferroelectric layer or the lower the dielectric constant of this layer, the higher the energy required to polarize it[82]. Thus, to achieve the desired multiferroic superlattice, it is favourable to use extremely thin layers of ferrimagnets (roughly <1 nm) with high dielectric constants and ensure that the ferroelectric layers are thick (roughly >3 nm). Conversely, if thicknesses of the ferroelectric and non-ferroelectric layers are used that do not follow this design methodology, a typically ferroelectric constituent can be driven into an antiferroelectric

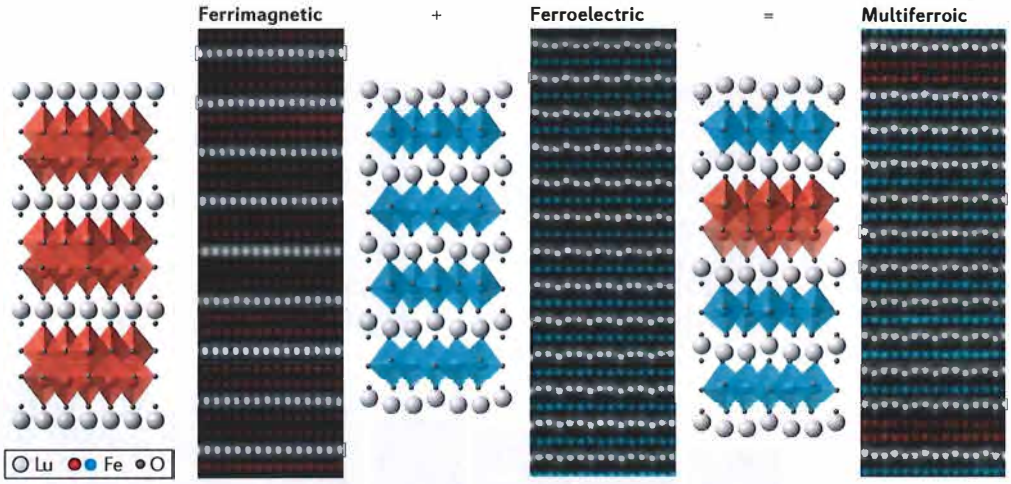


Fig. 4 | **A design methodology for creating higher-temperature magnetoelectric multiferroics in oxide superlattices.** Transmission electron microscopy (TEM) images of the superlattice constituents, $LuFe_2O_4$ and $LuFeO_3$, as well as an atomically precise layered combination of these constituents to form the multiferroic superlattice $(LuFeO_3)_9/(LuFe_2O_4)_1$. Lu and Fe atoms are white and dark grey, respectively, and O atoms are red or blue (depending on whether the layer is ferrimagnetic or ferroelectric, respectively), in the crystal structures and colourized TEM images. Images courtesy of Charles Brooks, Harvard University, USA, and Megan Holtz, Cornell University, USA.

state in a superlattice. This change in ground state has been predicted to occur in $BaTiO_3/BaO$ superlattices[74] (which has eluded fabrication owing to the extreme stability of the competing Ba_2TiO_4 phase[83]) and recently achieved in $BiFeO_3$-based superlattices[84].

$(LuFeO_3)_m/(LuFe_2O_4)_1$ superlattices are one example of artificial materials in which targeted functionality is incorporated within the material at the level of atomic layers. Such atomic-scale construction of materials, particularly those in which the electric and magnetic properties as well as the coupling between these two properties can be controlled is an immensely fertile area of research. It is fuelled by methods such as RHEED-assisted PLD and MBE, which enable control of the synthesis of matter at the atomic scale, and advances in theory that help superior manifestations to be identified and tested with ever improving accuracy via computation. The powerful combination of theory, synthesis and characterization to accelerate the discovery of superior materials lies at the heart of what is now commonly termed materials-by-design.

Some aspects of these materials that are designed and prepared with atomic-layer precision are not understood. For example, the pathway by which the rumpling in the $LuFeO_3$ layer (that causes broken inversion symmetry) couples to the magnetism in the $LuFe_2O_4$ layer is not established. Furthermore, the switching mechanism that enables deterministic switching of magnetization using an electric field in $(LuFeO_3)_9/(LuFe_2O_4)_1$ superlattices requires a deeper understanding. More generally, it is possible that superior and more broadly applicable manifestations of this methodology can be discovered by expanding the classes of materials that can be paired across a heterointerface.

Emergent phenomena in ferroelectric superlattices. Our second example is based on perovskite ferroelectric-based superlattices, which have been studied extensively over the past 20 years[85], with significant early work coming from ab initio theory[86,87]. The model system has been and continues to be superlattices constructed from the prototypical ferroelectric lead titanate ($PbTiO_3$), which is ep-itaxially partnered with strontium titanate ($SrTiO_3$). Early experimental work[37,82,85] on this system investigated short-period superlattices (composed of $(PbTiO_3)_n/(SrTiO_3)_m$) as a model system for interface engineering[85] (FIG. 2b) and focused on the role of the octahedral tilts in the $SrTiO_3$ layer and the consequent emergence of an improper ferroelectric order in this layer[37]. Meanwhile, theoretical work[86,87] focused on a different aspect of confined layers of $PbTiO_3$ in $SrTiO_3$, namely, the possibility for the existence of non-uniform polarization states (such as vortices) in confined nanoscale elements of $PbTiO_3$. It is intriguing to note that these theoretical predictions of the formation of vortex-like polar textures were not followed up with experimental manifestations until years later[88].

Using a combination of experimental measurements[82] and theory[89], the emergence of improper ferroelectricity in very-short-period (a few unit cells) $(PbTiO_3)_n/(SrTiO_3)_m$ superlattices was demonstrated[37]. Understanding this behaviour in more detail led to the discovery of a form of ferroelectricity, namely, hybrid improper ferroelectricity[90], and the synthesis of the first new bulk single-crystal ferroelectric in 50 years[91]. More recently, the possibility for phonon localization and a transition from incoherent to coherent thermal transport was explored[92] in a related $(BaTiO_3)_n/(SrTiO_3)_m$ superlattice system, triggered by prior theoretical predictions[93] that suggested the possibility of probing the wave nature (coherent transport) in appropriately tailored superlattices. Although there were indications of a wave-like behaviour (for example, a minimum in thermal conductance as a function of superlattice periodicity, which changed with temperature[92]), the results were not conclusive. Inspired by this work, we explored

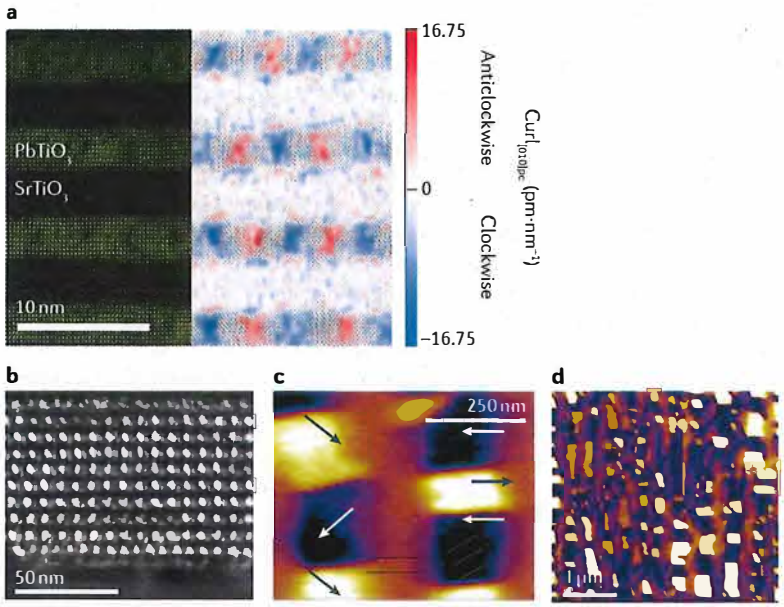


Fig. 5 | **Hierarchical structures in oxide superlattices. a** | A vector map of an atomic-resolution, cross-sectional scanning transmission electron microscopy (STEM) image showing the formation of vortex structures. The right side of panel **a** shows the alternating clockwise and anticlockwise curling of these vortices. **b** | A dark-field TEM image at a magnification that is ~10 times higher than that in panel **a**, which shows the ordered arrays of vortices. pc Refers to the pseudocubic axes. **c** | A scanning piezoforce microscopy image showing the bands (~200–300 nm wide) of the vortex phase alternating with the polar phase. The grey and white arrows denote the directions of the polarization. The lines in the dark-contrast region indicate the a_1 and a_2 ferroelectric twins, and the lines in the light brown area indicate the long axis of the vortices. **d** | A piezoforce microscopy image depicting the coexistence of the vortex arrays with regions of uniform polarization (in bright and dark contrast). Panel **a** is adapted from REF.[88], Springer Nature Limited.

$(PbTiO_3)_n/(SrTiO_3)_m$ superlattices[88] with the intention of enhancing the phonon contrast between the two layers by replacing Ba with Pb. The growth of superlattices with high structural quality in a layer-by-layer mode was, however, challenging. The growth of these structures was accomplished using a 20% Pb-enriched target (the source of the material that is volatized by a laser and transferred through the gas phase to the substrate in the PLD process) that enhanced surface diffusion — a growth protocol that has enabled the growth of atomically perfect superlattices, which is illustrated in the low-resolution and high-resolution electron microscope images (FIG. 5a,b). Analysis of the atomic-resolution images using a vector-mapping algorithm shows that the atomic displacements in the $PbTiO_3$ layer are not what would be expected in a tetragonal ferroelectric. Instead, the structural distortions map out a clockwise vortex-like pattern, paired with every other vortex with an anticlockwise rotation (FIG. 5a). Both experimental and theoretical calculations indicate that all the distortions are in the $PbTiO_3$ layer. Further work[94] has shown that these vortices are chiral. Such an emergent chirality is enabled by the existence of an axial component of the polarization vector that alternates in its direction from the clockwise and anticlockwise vortices. If these vortices are examined using dark-field imaging, a strong degree of order is observed in each $PbTiO_3$ layer as well as a significant degree of order vertically (FIG. 5b). Thus, it seems appropriate to look at such arrays of vortices like ferroelectric liquid crystals[95]. When samples are examined with a complementary surface probe such as scanning piezoforce microscopy, we observe features at the length scale of ~20–50 nm (FIG. 5c). Piezoforce microscopy images show that the superlattices with specific periodicities (in this case, a 16-unit-cell-thick layer of $PbTiO_3$ followed by a 16-unit-cell-thick layer of $SrTiO_3$, in which this bilayer is repeated 7 times, which we abbreviate as $[(PbTiO_3)_{16}/(SrTiO_3)_{16}]_7$) exhibit a mixed state, consisting of the ferroelectric phase (with the polarization vector in the plane of the sample) and the vortex phase[96]. Thermal studies show that the vortex phase emerges from the ferroelectric state below ~250 °C. At a larger scale (FIG. 5d), these regions of the ferroelectric phase and the vortex phase are seen as ordered stripes that extend throughout the sample.

We now summarize our understanding of the physical properties of such vortex structures. Anomalous dielectric behaviour was observed recently[97], leading to the conclusion that $(PbTiO_3)_n/(SrTiO_3)_m$ superlattices can show regions of negative capacitance[98,99]. This conclusion was validated using a combination of theory and direct imaging of the double-well structure through electron microscopy[61], which revealed that the fundamental origin of the negative capacitance is the core of the vortex[100]. This confirmation of negative capacitance is a significant development and has the potential to revolutionize semiconducting electronics by providing a pathway to overcome the Boltzmann tyranny[101], which sets the best possible output response of complementary metal–oxide–semiconductor (CMOS) transistors to a change in the controlling gate voltage (V_g) at 60 mV change in gate voltage per decade change in output current (I_d). A reduction in this slope of the I_d–V_g curve has ramifications for the power consumption of CMOS transistors. Early work[102] indicates that it may be possible to improve this response to lower than 60 mV per decade, but significant research is needed to validate these observations.

A pathway that has received less attention is the use of epitaxial constraints to change the crystal structure of a material. This pathway is illustrated in the case of the $BiFeO_3$ system (FIG. 6), wherein a large compressive strain of ~4.5% leads to an isosymmetric phase transition from a monoclinically distorted rhombohedral structure to a monoclinically distorted super-tetragonal structure (FIG. 6a). Partial relaxation of the epitaxial strain (through a systematic increase in the film thickness) leads to the formation of a nanoscale admixture of the rhombohedral and super-tetragonal phases (both monoclinically distorted; FIG. 6b), which are mutually epitaxial with respect to each other. The interface between these two phases is free of dislocations and instead shows a progressive rotation of the polar vector from the $[111]_p$-direction of the rhombohedral phase to the [001]-direction of the supertetragonal phase, where the p subscript indicates pseudocubic indices. Such an ensemble is also observed in atomic force microscopy images (FIG. 6c). The power of epitaxy is evident from the fact that the

tetragonal phase (which is the matrix phase) imposes a strong deformation of the rhombohedral phase, as a consequence of which the rhombohedral phase exhibits an enhanced canted moment.

Although progress has been made in terms of synthesis, theory and measurements, challenges remain in the field of oxide superlattices. From a synthetic point-of-view, interface roughening and intermixing are problematic. When the interfaces become smeared, the order parameters of each phase are generally diminished in the interfacial region, thus diminishing the potential for emergent phenomena that arise from the competition among order parameters. A vexing, though not insurmountable[103–106], example is the growth of an oxide superlattice in a direction that is not perpendicular to the low-energy surface of the oxide. Another challenge for some oxide systems is the inability to achieve desired interfacial strain because the system relaxes the strain by the formation of defects (for example, ordered arrays of vacancies[59–61]), changes in spin state[107] or octahedral tilting[108,109].

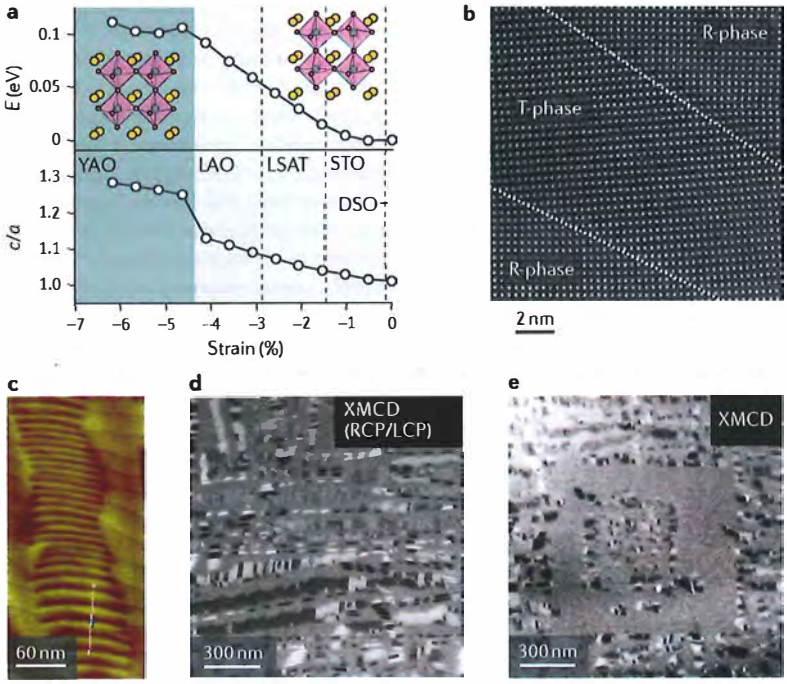


Fig. 6 | **Epitaxial constraints alter the crystal structure and the microstructure of $BiFeO_3$ to access hidden ground states, including an isostructural morphotropic phase transition. a** | Calculated phase diagram for the $BiFeO_3$ system as a function of in-plane biaxial strain. Note the phase transition to the super-tetragonal phase at ~4.5% compression. **b** | A high-resolution, cross-sectional transmission electron microscopy image of the tetragonal–rhombohedral (T–R) interface. **c** | A high-resolution atomic force microscopy image of the mixed T–R phase ensemble. **d** | An X-ray magnetic circular dichroism-photoemission electron microscope (XMCD-PEEM) image of the mixed phase, showing strong magnetic contrast in the nanoregions corresponding to the highly strained R-phase. The XMCD image is obtained as a ratio of the right circularly polarized (RCP) and left circularly polarized (LCP) light. **e** | XMCD-PEEM image of a region that has been electrically switched with +12 V and subsequently with −8 V. Switching with +12 V leads to a uniform T-phase with no XMCD, and reversing with −8 V leads to the return of the mixed phase. *a* and *c*, lattice constants; DSO, $DyScO_3$; LAO, $LaAlO_3$; LSAT, $(LaAlO_3)_{0.29}$–$(SrAl_{1/2}Ta_{1/2}O_3)_{0.71}$; STO, $SrTiO_3$; YAO, $YAlO_3$. Panels **a** and **b** are adapted with permission from REF.[27], AAAS. Panels **c**–**e** are adapted from REF.[28], Springer Nature Limited.

Achieving stoichiometric complex oxide films is also a challenge. When all the constituents have negligible vapour pressure at the growth conditions used, a growth technique that exactly transfers the composition of the target to the film is desired, as the composition of the bulk target can be precisely established. Sputtering and PLD are often said to provide such faithful transfer, but in reality, there is an angular dependence of the emitted composition that typically changes with time (as a racetrack is created on the target), resulting in films with spatial and temporal composition variation[110]. When one or more of the constituents has a high vapour pressure (for example, Pb in $PbTiO_3$ or Bi in $BiFeO_3$), the best known way to grow these oxide films is to provide an excess of the volatile constituent and exploit thermodynamics to provide automatic composition control[111], as is commonly used for the growth of compound semiconductors[112,113], a growth regime known as adsorption control. Adsorption control is an excellent composition control method for phases that are line compounds (that is, in a phase diagram, a compound with a specific stoichiometry and no solubility), resulting in compound semiconductor films that are extremely close to being stoichiometric even though the incident fluxes are greatly enriched in the volatile constituent. Unfortunately, when adsorption-controlled conditions are applied to materials that are far from being line compounds, as is the case for many complex oxides, the single-phase oxide samples grown can still have compositions deviating significantly from stoichiometric. For example, the composition range over which single-phase $PbTiO_3$ exists[114,115] is approximately 1,000 times wider than the composition range of single-phase GaAs (REF.[116]). Unfortunately, oxides are generally farther from being line compounds than compound semiconductors are. Indeed, growth by adsorption control is in general not synonymous with the growth of a perfectly stoichiometric material. Adsorption control accesses the single-phase region of the oxide[111], but depending on how wide that region is and from which side it is approached — things that change with temperature and chemical potentials — the stoichiometry of the resulting film will change, though it will always remain single phase.

As practitioners in the field, we are not satisfied with knowing chemical stoichiometry at the scale of Rutherford backscattering spectrometry or energy dispersive X-ray spectroscopy measurements (which is typically at the few per cent level). We urgently need higher-precision chemical tools that can be integrated into synthesis systems to dynamically provide more accurate compositional adjustment.

From a broader perspective, there needs to be more progress towards measuring and controlling point defects (particularly oxygen) and defect complexes in oxide films. Given that both anionic and cationic defects are active defects, it would be desirable to be able to precisely control them. In materials such as double perovskites, the problem of site ordering remains a key challenge. Many improved properties, for example, high-temperature ferrimagnets and multiferroics, would become accessible if such site ordering were to be achieved.

In terms of measurements, there is a need to probe physical phenomena at the sub-10 nm scale, such as in the polar vortices[100]. At the moment, TEM is the only way to directly probe the structure, and it would be immensely valuable to probe the emergent chirality (or other physical properties) at the scale of an individual vortex (~10 nm), without requiring complicated sample preparation that could perturb the phenomena. The intrinsically destructive nature of TEM sample preparation is, however, a detriment. Synchrotron-based approaches have immense power in terms of probing chirality using resonant techniques, but spatial resolution is lacking. Thus, near-field approaches that can probe dielectric, optical responses would be ideal.

Over the past decade, there has also been dramatic progress in theoretical studies, particularly the application of ab initio first-principles methods to oxide superlattices[69,117,118] and the development of second-principles approaches[119,120] (an extension of the effective-Hamiltonian method[121]). In second-principles approaches, potentials extracted from ab initio first-principles calculations enable calculations with computational sets approaching 50,000 atoms (compared with the 100–1,000 atoms in first-principles computations), yielding higher fidelity of the computation of ground states in oxide superlattices. Phase-field modelling has also toadied in the targeting of superlattice periodicities that yield desired emergent phenomena[122,123]. When coupled with high-quality, finite-temperature thermodynamic input (typically from experimental results, but increasingly from a combination of finite-temperature experimental results and 0 K density functional theory calculations), phase-field modelling can provide reliable predictions that are relevant at room temperature as well as include the subtle effects of unknown defects that affect the observed phenomena (for example, electrical leakage) but are difficult to include in first-principles or second-principles calculations. The role of correlations is being treated using empirical approaches (for example, the use of an empirical Hubbard parameter). Coupling of spin and charge degrees of freedom, which is central to oxides, needs to be pursued further.

Future perspectives

The field of oxide heteroepitaxy is, in many ways, following the path of compound semiconductors, in which dramatic phenomena (for example, the quantum Hall effect and the fractional quantum Hall effect) have been enabled by the synthesis of highly perfect Si-based or $Al_xGa_{1-x}As$-based heterostructures. In the field of oxide superlattices, there remains much to be understood about these phenomena, more specifically, regarding polar vortices, skyrmions, negative capacitance and colossal (or large) physical responses. The promise of oxides is that the breadth of physical phenomena is much larger than in compound semiconductors, within the framework of a common crystal structure (for example, the perovskite structure). We believe that the oxide field has emerged into a realm in which such artificially engineered superlattices can begin to claim the same degree of structural and chemical perfection as their semiconducting counterparts. The improved perfection of oxide systems is aided by the ability to reduce defect densities in these refractory oxide systems, at interfaces as well as in films, through growth at higher substrate temperatures[124,125] or in systems difficult to oxidize by higher oxidation activity during growth[126]. Perhaps this is one of the reasons why many physical phenomena (some of which were discussed here) are emerging. Although research has been aimed at phenomena occurring at higher energy scales (~1 eV), there are opportunities involving phenomena associated with lower energy excitations, such as magnons, polarons and excitons. Real-space topological textures such as polar skyrmions and vortices are being observed[88,94,97,100], and the field may be in the early stages of the exploration of a broader spectrum of such real-space textures. These topologies demonstrate chirality, which is an unexpected, emergent phenomenon, because neither $PbTiO_3$ nor $SrTiO_3$ are chiral. Unlike biological systems (for example, the human system can assimilate only D-glucose; similarly, only L-amino acids can be incorporated into the genetic sequence), the inorganic world has not fully taken advantage of chirality as an order parameter. If, for example, the chirality that is observed in the $PbTiO_3/SrTiO_3$ superlattices (or other such systems) can be manipulated by an external field (such as an electric field), then this would provide a powerful way to use the chirality as an externally controllable order parameter. An understanding of the origins of the chirality is required, which, in turn, requires new techniques to probe chirality with a spatial resolution of ~10 nm. Similarly, the dynamics of such vortices and skyrmion structures must be explored in detail. An aspect that is beginning to be addressed is the possibility for unconventional dielectric responses within such vortex structures. Recent work[100] has demonstrated the existence of regions of negative capacitance at the core of the vortices, which can be visualized in terms of the classical double-well structure that is used to describe the evolution of the polar state from the paraelectric state[55]. Within this double well, there are regions of negative curvature of the free energy (the second derivative of the free energy), which also correspond to regions of negative capacitance. Thus, the arrays of vortices represent a periodic array of negative capacitance, which is likely to have unique optical responses (akin to a negative refractive index material). Characterizing the local optical and dielectric properties of such topologies is an exciting area for future research. For example, the techniques used to probe the circular dichroism of a single vortex are of interest, and this will undoubtedly require either very-high-resolution near-field optical probes or high-resolution X-ray studies. As there are few details known regarding the spectroscopic nature of the optical responses in such vortices, these characterization tools will open up a valuable line of research.

We believe that the approach described in this Review will enable the discovery of other artificially engineered functional materials (such as multiferroics and magnetoelectrics), for example, the study of phase control and mixed phase coexistence, by the selection of suitable

constituent layers. For example, if superlattice stacking is used as a pathway to impose boundary conditions onto an active layer (similar to the polar vortices in FIGS 5,6), then it may be possible to create mixed phases that could be the precursors for large physical responses — such as dielectric or piezoelectric susceptibilities, magnetoelectric coupling, optical nonlinearities or electrically controllable chirality — within the layers.

Like in the case of semiconductor heterostructures[127] (as well as the $LaAlO_3/SrTiO_3$ oxide interface[128]), such oxide superlattices allow the investigation of quantum confinement effects, with the choice of appropriate model systems. In addition to electronic confinement, the tantalizing possibility for phonon confinement exists (which was our original motivation to investigate such superlattices). In the same vein, superlattices provide us with a pathway to control and manipulate the orbital degree of freedom in oxides (for example, orbital ordering). Considering the various pathways and control over physical phenomena detailed in FIG. 1, we believe that such superlattices could be fertile playgrounds to create confined quasi-particles, such as magnons and polarons, as well as providing pathways to manipulate them with appropriate thermodynamic fields[15–18].

Given the breadth of physical phenomena in oxide superlattices, their impact on technologies may be considerable. For example, a challenge for multiferroics is to reduce the operating voltage (and therefore energy per operation) required for the manipulation of the magnetic state. If it were possible to manipulate the magnetization direction with an electric voltage of just 100 mV (corresponding approximately to an energy of 1 aJ per operation for an ~10-nm-sized device), this could significantly change the computing landscape[129,130] Thus, there is significant interest from the electronics community to explore such pathways (for example, the MESO project from Intel[129,130]). If heterostructures and superlattices represent a means to accomplish this (through an interfacial exchange bias coupling between the ferromagnet and the multiferroic), then it is crucial that the ferromagnet–multiferroic interface is electronically robust; thus, there is a strong preference for an oxide-based ferromagnet that couples, in a robust fashion, with the multiferroic at room temperature. The circumvention of the Boltzmann tyranny (60 mV per decade of current) in the transistor performance using negative capacitance presents another opportunity for oxide superlattices to impact the field of microelectronics. In this context, the demonstration of polar textures in ferroelectric-based oxide superlattices[88], which also exhibit emergent chirality and dielectric responses, presents a tantalizing opportunity to use such exotic quasi-particles in real applications. Inspired by these examples, the broader oxide community could benefit from the active participation of device physicists and engineers to transfer these physical phenomena into applications to open up new technologies and markets.

Finally, as researchers immersed in the field of complex oxides for over three decades, we believe that the complex oxide materials with the most impact and influence remain to be unleashed. These new physical phenomena are on the verge of being exposed in oxide superlattices as we (the collective practitioners of oxide electronics) learn to navigate this relatively unexplored amalgamation of interfaces and competing order parameters in search of marvel.

Published online 19 March 2019

1. Schilling, A., Cantoni, M., Guo, J. D. & Ott, H. R. Superconductivity above 130 K in the Hg-Ba-Ca-Cu-O system. *Nature* **363**, 56–58 (1993).
2. Penney, T., Shafer, M. W. & Torrance, J. B. Insulator-metal transition and long-range magnetic order in EuO. *Phys. Rev. B* **5**, 3669–3674 (1972).
3. Anguelouch, A. et al. Properties of epitaxial chromium dioxide films grown by chemical vapor deposition using a liquid precursor. *J. Appl. Phys.* **91**, 7140–7142 (2002).
4. Tomioka, Y., Asamitsu, A., Moritomo, Y. & Tokura, Y. Anomalous magnetotransport properties of Pr1-xCaxMnO3. *J. Phys. Soc. Jpn* **64**, 3626–3630 (1995).
5. Li, J. et al. Dramatically enhanced polarization in (001), (101), and (111) BiFeO3 thin films due to epitiaxial-induced transitions. *Appl. Phys. Lett.* **84**, 5261–5263 (2004).
6. Vrejoiu, I. et al. Intrinsic ferroelectric properties of strained tetragonal PbZr0.2Ti0.8O3 obtained on layer–by–layer grown, defect–free single–crystalline films. *Adv. Mater.* **18**, 1657–1661 (2006).
7. Park, S.-E. & Shrout, T. R. Ultrahigh strain and piezoelectric behavior in relaxor based ferroelectric single crystals. *J. Appl. Phys.* **82**, 1804–1811 (1997).
8. Lee, J. H. et al. A strong ferroelectric ferromagnet created by means of spin–lattice coupling. *Nature* **466**, 954–958 (2010).
9. Cross, L. E. Relaxor ferroelectrics. *Ferroelectrics* **76**, 241–267 (1987).
10. Jin, S. et al. Thousandfold change in resistivity in magnetoresistive La-Ca-Mn-O films. *Science* **264**, 413–415 (1994).
11. Dagotto, E. Complexity in strongly correlated electronic systems. *Science* **309**, 257–262 (2005).
12. Bednorz, J. G. & Müller, K. A. Possible high Tc superconductivity in the Ba-La-Cu-O system. *Z. Phys. B* **64**, 189–193 (1986).
13. Bednorz, J. G., Takashige, M. & Müller, K. A. Susceptibility measurements support high-Tc superconductivity in the Ba-La-Cu-O system. *Europhys. Lett.* **3**, 379–386 (1987).
14. Rudolph, P. (ed.) *Handbook of Crystal Growth: Bulk Crystal Growth: Basic Techniques* 2nd edn Vol. 2 (Elsevier, Amsterdam, 2015).
15. Heckmann, G. Die Gittertheorie der festen Körper. *Ergeb. Exakten Naturwiss.* **4**, 100–153 (1925).
16. Nye, J. F. *Physical Properties of Crystals: Their Representation by Tensors and Matrices* (Oxford Univ. Press, 1985).
17. Spaldin, N. A. & Fiebig, M. The renaissance of magnetoelectric multiferroics. *Science* **309**, 391–392 (2005).
18. Kalinin, S. V. & Spaldin, N. A. Functional ion defects in transition metal oxides. *Science* **341**, 858–859 (2013).
19. Yi, D., Lu, N., Chen, X., Shen, S. & Yu, P. Engineering magnetism at functional oxides interfaces: manganites and beyond. *J. Phys. Condens. Matter* **29**, 443004 (2017).
20. Terashima, T. & Bando, Y. Formation of artificial superlattice composed of ultrathin layers of CoO and NiO by reactive evaporation. *J. Appl. Phys.* **56**, 3445–3447 (1984).
21. Ramesh, R., Simion, B. & Thomas, G. Epitaxial magnetic garnet heterostructures. *J. Phys. IV* **7**, C1-695–C1-698 (1997).
22. Kawasaki, J. K. et al. Rutile IrO2/TiO2 superlattices: a hyperconnected analog to the Ruddelsden-Popper structure. *Phys. Rev. Mater.* **2**, 054206 (2018).
23. Haeni, J. H. et al. Room-temperature ferroelectricity in strained SrTiO3. *Nature* **430**, 758–761 (2004).
24. Choi, K. J. et al. Enhancement of ferroelectricity in strained BaTiO3 thin films. *Science* **306**, 1005–1009 (2004).
25. Schlom, D. G. et al. Strain tuning of ferroelectric thin films. *Annu. Rev. Mater. Res.* **37**, 589–626 (2007).
26. Warusawithana, M. P. et al. A ferroelectric oxide made directly on silicon. *Science* **324**, 367–370 (2009).
27. Zeches, R. J. et al. A strain-driven morphotropic phase boundary in BiFeO3. *Science* **326**, 977–980 (2009).
28. He, Q. et al. Electrically controllable spontaneous magnetism in nanoscale mixed phase multiferroics. *Nat. Commun.* **2**, 225 (2011).
29. Schlom, D. G. et al. Elastic strain engineering of ferroic oxides. *MRS Bull.* **39**, 118–130 (2014).
30. Iijima, K., Terashima, T., Bando, Y., Kamigaki, K. & Terauchi, H. Atomic layer growth of oxide thin films with perovskite-type structure by reactive evaporation. *J. Appl. Phys.* **72**, 2840–2845 (1992).
31. Bozovic, I. et al. Atomic-layer engineering of cuprate superconductors. *J. Supercond.* **7**, 187–195 (1994).
32. Specht, E. D., Christen, H. M., Norton, D. P. & Boatner, L. A. X-ray diffraction measurement of the effect of layer thickness on the ferroelectric transition in epitaxial KTaO3/KNbO3 multilayers. *Phys. Rev. Lett.* 80, 4317–4320 (1998).
33. Schlom, D. G., Haeni, J. H., Lettieri, J. & Theis, C. D. Oxide nano-engineering using MBE. *Mater. Sci. Eng. B* **87**, 282–291 (2001).
34. Ohtomo, A., Muller, D. A., Grazul, J. L. & Hwang, H. Y. Artificial charge-modulation in atomic-scale perovskite titanate superlattices. *Nature* **419**, 378–380 (2002).
35. Warusawithana, M. P., Colla, E. V., Eckstein, J. N. & Weissman, M. B. Artificial dielectric superlattices with broken inversion symmetry. *Phys. Rev. Lett.* **90**, 036802 (2003).
36. Tenne, D. A. et al. Probing nanoscale ferroelectricity by ultraviolet Raman spectroscopy. *Science* **313**, 1614–1616 (2006).
37. Bousquet, E. et al. Improper ferroelectricity in perovskite oxide artificial superlattices. *Nature* **452**, 732–736 (2008).
38. Ramesh, R. & Schlom, D. G. Whither oxide electronics. *MRS Bull.* **33**, 1006–1011 (2008).

39. Zheng, H. et al. Multiferroic BaTiO3-CoFe2O4 nanostructures. *Science* **303**, 661–663 (2004).
40. Mohaddes-Ardabili, L. et al. Self-assembled single-crystal ferromagnetic iron nanowires formed by decomposition. *Nat. Mater.* **3**, 533–538 (2004).
41. Zheng, H. et al. Three-dimensional heteroepitaxy in selfassembled BaTiO3-CoFe2O4 nanostructures. *Appl. Phys. Lett.* **85**, 2035–2037 (2004).
42. MacManus-Driscoll, J. L. et al. Strain control and spontaneous phase ordering in vertical nanocomposite heteroepitaxial thin films. *Nat. Mater.* **7**, 314–320 (2008).
43. Machlin, E. S. & Chaudhari, P. (eds) *Synthesis and Properties of Metastable Phases* 11–29 (The Metallurgical Society, 1980).
44. Flynn, C. P. Strain-assisted epitaxial growth of new ordered compounds. *Phys. Rev. Lett.* **57**, 599–602 (1986).
45. Bruinsma, R. & Zangwill, A. Structural transitions in epitaxial overlayers, *J. Phys.* **47**, 2055–2073 (1986).
46. Zunger, A. & Wood, D. M. Structural phenomena in coherent epitaxial solids. *J. Cryst. Growth* **98**, 1–17 (1989).
47. Kaul, A. R., Gorbenko, O. Y. & Kamenev, A. A. The role of heteroepitaxy in the development of new thin-film oxide-based functional materials. *Russ. Chem. Rev.* **73**, 861–880 (2007).
48. Lee, C.-H. et al. Exploiting dimensionality and defect mitigation to create tunable microwave dielectrics. *Nature* **502**, 532–536 (2013).
49. Dingle, R., Stormer, H. L., Gossard, A. C. & Wiegmann, W. Electron mobilities in modulation-doped semiconductor heterojunction superlattices. *Appl. Phys. Lett.* **33**, 665–667 (1978).
50. Tsukazaki, A. et al. Quantum Hall effect in polar oxide heterostructures. *Science* **315**, 1388–1391 (2007).
51. Tsukazaki, A. et al. Observation of the fractional quantum Hall effect in an oxide. *Nat. Mater.* **9**, 889–893 (2010).
52. Harrison, W. A., Kraut, E. A., Waldrop, J. R. & Grant, R. W. Polar heterojunction interfaces. *Phys. Rev. B* **18**, 4402–4410 (1978).
53. Tasker, P. W. The stability of ionic crystal surfaces. *J. Phys. C* **12**, 4977–4984 (1979).
54. Ohtomo, A. & Hwang, H. Y. A high-mobility electron gas at the LaAlO3/SrTiO3 heterointerface. *Nature* **427**, 423–426 (2004).
55. Nakagawa, N., Hwang, H. Y. & Muller, D. A. Why some interfaces cannot be sharp. *Nat. Mater.* 5, 204–209 (2006).
56. Schlom, D. G. & Mannhart, J. Interface takes charge over Si. *Nat. Mater.* **10**, 168–169 (2011).
57. Mundy, J. A. et al. Atomically engineered ferroic layers yield a room-temperature magnetoelectric multiferroic. *Nature* **537**, 523–527 (2016).
58. Freund, L. B. & Suresh, S. in *Thin Film Materials: Stress, Defect Formation and Surface Evolution* 60–83; 283–290; 396–416 (Cambridge Univ. Press, 2003).
59. Klenov, D. O., Donner, W., Foran, B. & Stemmer, S. Impact of stress on oxygen vacancy ordering in epitaxial La0.5Sr0.5CoO3-δ thin films on (001) LaAlO3. *Appl. Phys. Lett.* **82**, 3427 (2003).
60. Donner, W. et al. Epitaxial strain-induced chemical ordering in La0.5Sr0.5CoO3-δ films on SrTiO3. *Chem. Mater.* **23**, 984–988 (2011).
61. Boullay, P. et al. Structure determination of a brownmillerite Ca2Co2O5 thin film by precession electron diffraction. *Phys. Rev. B* 79, 184108 (2009).
62. Nguyen, L. D., Brown, A. S., Thompson, M. A. & Jelloian, L. M. 50-nm self-aligned-gate pseudomorphic AlInAs/GaInAs high electron mobility transistors. *IEEE Trans. Electron Devices* **39**, 2007–2014 (1992).
63. Welser, J., Hoyt, J. L. & Gibbons, J. F. Electron mobility enhancement in strained-Si n-type metal-oxide-semiconductor field-effect transistors. *IEEE Electron Device Lett.* **15**, 100–102 (1994).
64. Newnham, R. E., Skinner, D. P. & Cross, L. E. Connectivity and piezoelectric-pyroelectric composites. *Mater. Res. Bull.* **13**, 525–536 (1978).
65. Huang, J., MacManus-Driscoll, J. L. & Wang, H. New epitaxy paradigm in epitaxial selfassembled oxide vertically aligned nanocomposite thin films. *J. Mater. Res.* **32**, 4054–4066 (2017).
66. Hamasaki, Y. et al. Crystal isomers of ScFeO3. *Cryst. Growth Des.* **16**, 5214–5222 (2016).
67. Lee, S., Ivanov, I. N., Keum, J. K. & Lee, H. N. Epitaxial stabilization and phase instability of VO2 polymorphs. *Sci. Rep.* **6**, 19621 (2016).
68. Cava, R. J. Structural chemistry and the local charge picture of copper oxide superconductors. *Science* **247**, 656–662 (1990).
69. Sai, N., Meyer, B. & Vanderbilt, D. Compositional inversion symmetry breaking in ferroelectric perovskites. *Phys. Rev. Lett.* **84**, 5636–5639 (2000).
70. Ederer, C. & Spaldin, N. A. Magnetoelectrics: a new route to magnetic ferroelectrics. *Nat. Mater.* **3**, 849–851 (2004).
71. Kawamura, K. et al. Structural origin of the anisotropic and isotropic thermal expansion of K2NiF4-type LaSrAlO4 and Sr2TiO4. *Inorg. Chem.* **54**, 3896–3904 (2015).
72. Birol, T., Benedek, N. A. & Fennie, C. J. Interface control of emergent ferroic order in Ruddlesden-Popper Srn+1TinO3n+1. *Phys. Rev. Lett.* **107**, 517–519 (2011).
73. Junquera, J., Zimmer, M., Ordejón, P. & Ghosez, P. First-principles calculation of the band offset at BaO/BaTiO3 and SrO/SrTiO3 interfaces. *Phys. Rev. B* **67**, 155327 (2003).
74. Bousquet, E., Junquera, J. & Ghosez, P. First-principles study of competing ferroelectric and antiferroelectric instabilities in BaTiO3/BaO superlattices. *Phys. Rev. B* **82**, 045426 (2010).
75. Verissimo-Alves, M., García-Fernández, P., Bilc, D. I., Ghosez, P. & Junquera, J. Highly confined spin-polarized two-dimensional electron gas in SrTiO3/SrRuO3 Superlattices. *Phys. Rev. Lett.* **108**, 107003 (2012).
76. Wojdeł, J. C. & Íñiguez, J. Ferroelectric transitions at ferroelectric domain walls found from first-principles. *Phys. Rev. Lett.* **112**, 247603 (2014).
77. Wang, J. et al. Epitaxial BiFeO3 multiferroic thin film heterostructures. *Science* **299**, 1719–1722 (2003).
78. Belik, A. A. et al. Neutron powder diffraction study on the crystal and magnetic structures of BiCoO3. *Chem. Mater.* **18**, 798–803 (2006).
79. Li, M.-R. et al. A polar corundum oxide displaying weak ferromagnetism at room temperature. *J. Am. Chem. Soc.* **134**, 3737–3747 (2012).
80. Pitcher, M. J. et al. Tilt engineering of spontaneous polarization and magnetization above 300 K in a bulk layered perovskite. *Science* **347**, 420–424 (2015).
81. Bossak, A. A. et al. XRD and HREM studies of epitaxially stabilized hexagonal orthoferrites RFeO3 (R = Eu–Lu). *Chem. Mater.* **16**, 1751–1755 (2004).
82. Dawber, M. et al. Unusual behavior of the ferroelectric polarization in PbTiO3/SrTiO3 superlattices. *Phys. Rev. Lett.* **95**, 177601 (2005).
83. Kwestroo, W. & Paping, H. A. M. The systems BaO-SrO-TiO_2, BaO-CaO-TiO_2, and SrO-CaO-TiO_2. *J. Am. Ceram. Soc.* **42**, 292–299 (1959).
84. Mundy, J. A. et al. A high-energy density antiferroelectric made by interfacial electrostatic engineering. Preprint at *arXiv* https://arxiv.org/abs/1812.09615 (2018).
85. Jiang, J. C., Pan, X. Q., Tian, W., Theis, C. D. & Schlom, D. G. Abrupt PbTiO3/SrTiO3 superlattices grown by reactive molecular beam epitaxy. *Appl. Phys. Lett.* **74**, 2851–2853 (1999).
86. Naumov, I. I., Bellaiche, L. & Fu, H. Unusual phase transitions in ferroelectric nanodisks and nanorods. *Nature* **432**, 737–740 (2004).
87. Prosandeev, S. & Bellaiche, L. Characteristics and signatures of dipole vortices in ferroelectric nanodots: first-principles-based simulations and analytical expressions. *Phys. Rev. B* **75**, 094102 (2007).
88. Yadav, A. K. et al. Observation of polar vortices in oxide superlattices. *Nature* **530**, 198–201 (2016).
89. Dawber, M. & Bousquet, E. New developments in artificially layered ferroelectric oxide superlattices. *MRS Bull.* **38**, 1048–1055 (2013).
90. Benedek, N. & Fennie, C. Hybrid improper ferroelectricity: A mechanism for controllable polarization-magnetization coupling. *Phys. Rev. Lett.* **106**, 107204 (2011).
91. Oh, Y. S., Luo, X., Huang, F.-T., Wang, Y. & Cheong, S.-W. Experimental demonstration of hybrid improper ferroelectricity and the presence of abundant charged walls in (Ca Sr)3Ti2O7 crystals. *Nat. Mater.* **14**, 407–413 (2015).
92. Ravichandran, J. et al. Crossover from incoherent to coherent phonon scattering in epitaxial oxide superlattices. *Nat. Mater.* **13**, 168–172 (2014).
93. Simkin, M. & Mahan, G. Minimum thermal conductivity of superlattices. *Phys. Rev. Lett.* **84**, 927–930 (2000).
94. Shafer, P. et al. Emergent chirality in the electric polarization texture of titanate superlattices. *Proc. Natl Acad. Sci. USA* **115**, 915–920 (2018).
95. Lagerwall, S. T. & Dahl, I. Ferroelectric liquid crystals. *Mol. Cryst. Liq. Cryst.* **114**, 151–187 (1984).
96. Damodaran, A. R. et al. Phase coexistence and electric-field control of toroidal order in oxide superlattices. *Nat. Mater.* **16**, 1003–1009 (2017).
97. Zubko, P. et al. Negative capacitance in multidomain ferroelectric superlattices. *Nature* **534**, 524–528 (2016).
98. Salahuddin, S. & Datta, S. Use of negative capacitance to provide voltage amplification for low power nanoscale devices. *Nano Lett.* **8**, 405–410 (2008).
99. Khan, A. I. et al. Negative capacitance in a ferroelectric capacitor. *Nat. Mater.* **14**, 182–186 (2015).
100. Yadav, A. K. et al. Spatially resolved steady-state negative capacitance. *Nature* **8**, 405 (2019).
101. Salahuddin, S., Ni, K. & Datta, S. The era of hyper-scaling in electronics. *Nat. Electron.* **1**, 442–450 (2018).
102. Kwon, D. et al. Response speed of negative capacitance FinFETs. Presented at the 2018 IEEE Symposium on VLSI Technology, Honolulu, HI (2018).
103. Shibuya, K., Kawasaki, M. & Tokura, Y. Metal-insulator transitions in TiO2/VO2 superlattices. *Phys. Rev. B* **82**, 205118 (2010).
104. Gibert, M., Zubko, P., Scherwitzl, R., Íñiguez, J. & Triscone, J.-M. Exchange bias in LaNiO3-LaMnO3 superlattices. *Nat. Mater.* **11**, 195–198 (2012).
105. Hirai, D., Matsuno, J. & Takagi, H. Fabrication of (111)-oriented Ca0.5Sr0.5IrO3/SrTiO3 superlattices—A designed playground for honeycomb physics. *APL Mater.* **3**, 041508 (2015).
106. Kim, T. H. et al. Polar metals by geometric design. *Nature* **533**, 68–72 (2016).
107. Choi, W. S. et al. Strain-induced spin states in atomically ordered cobaltites. *Nano Lett.* **12**, 4966–4970 (2012).
108. Rondinelli, J. M. & Spaldin, N. A. Structure and properties of functional oxide thin films: insights from electronic-structure calculations. *Adv. Mater.* **23**, 3363–3381 (2011).
109. Rondinelli, J. M., May, S. J. & Freeland, J. W. Control of octahedral connectivity in perovskite oxide heterostructures: An emerging route to multifunctional materials discovery. *MRS Bull.* **37**, 261–270 (2012).
110. Ohnishi, T., Shibuya, K., Yamamoto, T. & Lippmaa, M. Defects and transport in complex oxide thin films. *J. Appl. Phys.* **103**, 103703 (2008).
111. Smith, E. H. et al. Exploiting kinetics and thermodynamics to grow phase-pure complex oxides by molecular-beam epitaxy under continuous codeposition. *Phys. Rev. Mater.* **1**, 023403 (2017).
112. Günther, K. G. Aufdampfschichten aus halbleitenden III — V-Verbindungen. *Z. Naturforsch. A* **13**, 1081–1089 (1958).
113. Freller, H. & Günther, K. G. Three-temperature method as an origin of molecular beam epitaxy. *Thin Solid Films* **88**, 291–307 (1982).
114. Holman, R. L. & Fulrath, R. M. Intrinsic nonstoichiometry in the lead zirconate-lead titanate system determined by Knudsen effusion. *J. Appl. Phys.* **44**, 5227–5236 (1973).
115. Eisa, M. A., Abadir, M. F. & Gadalla, A. M. The system TiO2-Pb-O in air. *Trans. J. Br. Ceram. Soc.* **79**, 100–104 (1980).
116. Hurle, D. T. J. A thermodynamic analysis of native point defect and dopant solubilities in zinc-blende III–V semiconductors. *J. Appl. Phys.* **107**, 121301 (2010).
117. Sai, N., Rabe, K. M. & Vanderbilt, D. Theory of structural response to macroscopic electric fields in ferroelectric systems. *Phys. Rev. B* **66**, 104108 (2002).
118. Zhou, Y. & Rabe, K. M. Determination of ground-state and low-energy structures of perovskite superlattices from first principles. *Phys. Rev. B* **89**, 214108 (2014).
119. Wojdeł, J. C., Hermet, P., Ljungberg, M. P., Ghosez, P. & Íñiguez, J. First-principles model potentials for lattice-dynamical studies: general methodology and example of application to ferroic perovskite oxides. *J. Phys. Condens. Matter* **25**, 305401 (2013).
120. García-Fernández, P., Wojdeł, J. C., Íñiguez, J. & Junquera, J. Second-principles method for materials simulations including electron and lattice degrees of freedom. *Phys. Rev. B* **93**, 195137 (2016).

121. Rabe, K. M. & Joannopoulos, J. D. Ab initio determination of a structural phase transition temperature. *Phys. Rev. Lett.* **59**, 570–573 (1987).
122. Chen, L.-Q. Phase-field method of phase transitions/domain structures in ferroelectric thin films: A review. *J. Am. Ceram. Soc.* **91**, 1835–1844 (2008).
123. Hong, Z. et al. Stability of polar vortex lattice in ferroelectric superlattices. *Nano Lett.* **17**, 2246–2252 (2017).
124. Ohashi, S. et al. Compact laser molecular beam epitaxy system using laser heating of substrate for oxide film growth. *Rev. Sci. Instrum.* **70**, 178–183 (1999).
125. Jäger, M., Teker, A., Mannhart, J. & Braun, W. Independence of surface morphology and reconstruction during the thermal preparation of perovskite oxide surfaces. *Appl. Phys. Lett.* **112**, 111601 (2018).
126. King, P. D. C. et al. Atomic-scale control of competing electronic phases in ultrathin LaNiO3. *Nat. Nanotechnol.* **9**, 443–447 (2014).
127. Tsui, D. C., Stormer, H. L. & Gossard, A. C. Two-dimensional magnetotransport in the extreme quantum limit. *Phys. Rev. Lett.* **48**, 1559–1562 (1982).
128. Hwang, H. Y. et al. Emergent phenomena at oxide interfaces. *Nat. Mater.* **11**, 103–113 (2012).
129. Manipatruni, S., Nikonov, D. E. & Young, I. A. Beyond CMOS computing with spin and polarization. *Nat. Phys.* **14**, 338–343 (2018).
130. Manipatruni, S. et al. Scalable energy-efficient magnetoelectric spin–orbit logic. *Nature* **565**, 35–42 (2018).

Acknowledgements
For more than two decades, the authors have been extremely fortunate to have the pleasure to collaborate with outstanding colleagues within their home institutions and around the world. The authors are grateful to their past and current students and postdocs, who have made their learning experience much richer. The authors are also fortunate to have been funded from a variety of sources, enabling complementary aspects of their research activity, particularly the US National Science Foundation (NSF)-Materials Research Science and Engineering Centers (MRSEC), US Department of Energy, US Army Research Office (ARO)-Multidisciplinary University Research Initiative (MURI), US Office of Naval Research (ONR)-MURI, Semiconductor Research Corporation-Western Institute of Nanoelectronics (SRC-WIN), Nanoelectronics Research Initiative (NRI), Joint University Microelectronics Program (JUMP) and the NSF-Natural Sciences and Engineering Research Council of Canada (NSERC). The two examples discussed in detail in this Review were primarily supported by the US Department of Energy, Office of Basic Sciences, Division of Materials Sciences and Engineering, under award no. DE-SC0002334 (for the work at Cornell University) and by the ARO under grant W911NF-16-1-0315 and the Gordon and Betty Moore Foundation's EPiQS Initiative (for the work at University of California, Berkeley).

Author contributions
This Review was conceived, discussed and written by R.R. and D.G.S.

Competing interests
The authors declare no competing interests.

Publisher's note
Springer Nature remains neutral with regard to jurisdictional claims in published maps and institutional affiliations.

12. Crystal Growth of Energy Materials

CRYSTAL GROWTH OF ENERGY MATERIALS

Roberto Fornari

Dept. of Mathematical, Physical and Computer Sciences, University of Parma,

Area delle Scienze, 7/A

43124 Parma (Italy)

Abstract

The quest for reliable energy supply and reduced greenhouse gas emissions has triggered a lot of research aiming at developing new energy sources to replace fossil fuels, as well as new devices that may allow energy transportation and utilization with reduced losses. In both fields, crystal growth and epitaxy play a fundamental role.

This lecture will review some examples of advanced epitaxial technologies applied to fabrication of devices for energies conversion, namely high-efficiency multi-junction solar cells and thermo-photovoltaic devices. It will be shown that modern epitaxial methods can be tuned to provide epilayers with excellent properties, which allow the fabrication of PV devices with very high efficiencies. The structure and fabrication steps of advanced prototypes and the relevant epitaxial technology will be discussed.

The second part of the lecture will focus on the growth of semiconducting oxides. Because of their wide bandgap and high breakdown voltage, these oxides are good candidates for power electronics and high voltage switching applications. For example, Ga_2O_3 offers some advantages in comparison to the more studied SiC and GaN, including higher breakdown voltage and the availability of substrates prepared from melt grown single crystals. In this lecture, the physical characteristics of gallium oxide will be analysed and the growth technologies for high-quality epitaxial Ga_2O_3 will be presented.

The present text is adapted from two chapters, namely: *Epitaxy for Energy Materials*, in: Handbook of Crystal Growth, Vol. III, T. Nishinaga, T.F. Kuech eds., Elsevier 2015, pp. 1–49, ISBN: 9780444633040; and *Progress in MOVPE growth of* Ga_2O_3, in: Gallium Oxide -Technology, Devices and Applications, S. Pearton, Fan Ren, M. Mastro eds., Elsevier 2019, pp. 3-30, ISBN: 9780128145210 that the reader may like to consider for more details and the extended reference list.

1. Introduction

Epitaxial deposition has been a key factor for the development of novel devices based on advanced materials. One of the most impressive examples is provided by telecommunications, where all core devices are fabricated by epitaxy: light emitters and detectors for data transmission via optical fibres, high-frequency high-power transistors for broadcasting stations, high frequency amplifiers for cellular phones and wireless receivers in tablets and notebooks. This is just one out of many possible examples that demonstrate how crucial is the ability to produce thin layers and multilayers with high crystallographic quality, sharp interfaces and homogeneous doping. The access to miniaturization allows for design and achievement of materials with “artificial” properties, for instance with energy bandgaps which are not found in semiconductor single crystals. Thanks to the precise control over chemical composition, doping and crystal size, made possible by modern epitaxial methods, one can obtain entirely novel physical properties, often based on quantum phenomena arising from the confinement of charge carriers in very tiny volumes, comparable to their De Broglie wavelengths.

Epitaxy is nothing but a face of crystal growth, therefore in order to understand the epitaxial deposition, independently of the experimental set up, one has to know the relevant thermodynamic and kinetic conditions which make the transition from a disordered phase (gas or liquid) to an ordered crystalline phase possible. For epitaxial methods such as Liquid Phase Epitaxy (LPE) and Vapour Phase Epitaxy (VPE) both thermodynamics and kinetics are very important while in Molecular Beam Epitaxy (MBE) the kinetic effects dominate. Although epitaxy and deposition of thin layers are often used as synonyms, it should not be forgotten that in case of epitaxy we always get a crystallographic information from the crystalline substrate. This does not mean that the substrate and the layer have the same chemical composition and lattice parameter but, in any case, there is a regular arrangement of the layer building blocks on the homo- or hetero-substrate due to sensing of regular surface bonds.

On the contrary, deposition is a much more general term that simply implies the coverage of a substrate. One can choose among a large set of methods, like spray pyrolysis, deposition from supersaturated solutions, laser ablation, thermal evaporation, electron beam evaporation, sputtering, plasma-enhanced chemical vapour deposition, etc. depending on whether the main requirement is thickness uniformity, large coating areas or high deposition rate.

The fundamentals and experimental aspects of crystal growth as well as the different epitaxial methods are treated extensively elsewhere in this textbook therefore this chapter will rather provide an overview of epitaxial methods applied to deposition of energy materials.

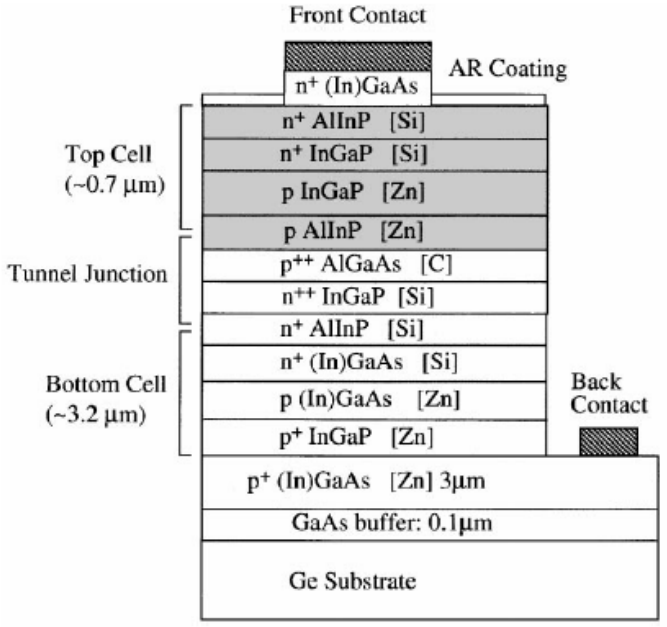
This survey will be limited to three examples:

- Epitaxial processes for high-efficiency III-V solar cells
- Epitaxy of low-bandgap semiconductors for thermo-photovoltaic applications
- Epitaxial growth of gallium oxide as wide bandgap material for power electronics

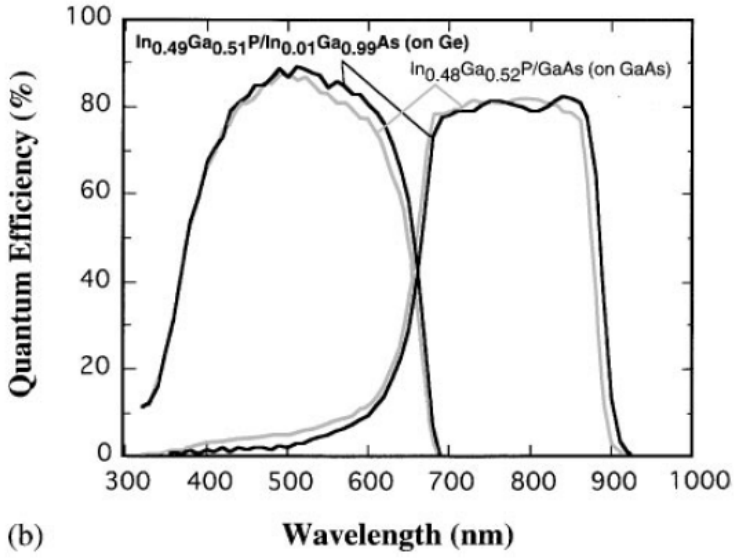
2. Epitaxial processes for high-efficiency III-V solar cells

The first report on application of MOVPE to fabrication of single-junction solar cells is about forty years old [1]. In that paper, a single 0.29 cm^2 AlGaAs/GaAs heterojunction device on GaAs substrate demonstrated the capability of the MOVPE technique to produce the high quality epitaxial semiconducting layers needed for photovoltaic devices. MOVPE and solar cells took another large step in 1985 with the development of the GaInP/GaAs dual-junction tandem device reaching 27.3%

efficiency [2, 3]. Today, III–V multi-junction devices dominate the world record efficiency tables for both one-sun and concentrated illumination. The availability of very high quality lattice matched and mis-matched alloys in the III–V alloy system enable many efficient device configurations. The triple-junction (3J) GaInP/GaAs/Ge based solar cell has become the standard in space applications and, more recently, it has also been adapted for high illumination concentrated photovoltaic (CPV) applications and applied in terrestrial power stations.



(a)



(b)

Fig. 1: (a) *Example of tandem cell with two p/n junctions fabricated on a Ge substrate; (b) corresponding internal quantum efficiency spectra; In (b) the spectra measured for the same device fabricated on a GaAs substrate is reported as a comparison (after [3]).*

Presently, triple-junction solar cells based on III-V compounds exhibit efficiency around 30% at one sun and over 40% in concentration systems. Unfortunately, multi-junction solar cells are still very expensive, which explains their almost exclusive use for satellites. However, with the further development of the concentration technology, the tandem cell technology will certainly play a role also in emerging terrestrial energy market.

The idea of tandem cell is quite old and it bases on a simple concept: harvesting a larger fraction of the solar spectrum by stacking cells made of semiconductors with different bandgap. The current flows through the device despite the presence of a reversely biased junction owing to carrier tunnelling across very thin and heavily-doped separation layers. A typical example of tandem cells is showed in Figure 1a, while the benefit in terms of internal quantum efficiency is well evidenced by the spectra of Figure 1b. The effective wavelength range over which carriers are photo-generated is practically doubled with respect to single junction cells. State-of-the-art high-efficiency III-V solar cells utilize a triple junction structure which consists of the Ge bottom sub-cell formed on the Ge substrate, a GaInAs middle sub-cell, and a GaInP top sub-cell. The multiple-junction III-V solar cells, when connected in series and designed in such a way that they generate the same photo-current, allows linear addition of the voltages from the individual subcell resulting in very high conversion efficiencies. The literature on multiple-junction cells is extremely rich and includes pseudomorphic and metamorphic structures based on III-V multilayers of different compositions deposited on Ge, Si or GaAs, see for example [4-7]. Extended reviews on the development of multi-junction solar cells and corresponding performance are provided by references [8-10]. Multi-junction solar cells from III-V compounds are indispensable for satellites with high power demand, owing to their high conversion efficiency and power-to-mass ratio. Very important is also the lifetime of cells under high-energy particle irradiation. The application of this technology for terrestrial energy production in photovoltaic concentrator systems is interesting but still very limited. Record solar cell efficiencies are exceeding 40 % under concentrated sunlight, making the overall cost of this technology competitive. This could be the starting point for a mass application of compound semiconductor materials to energy supplying.

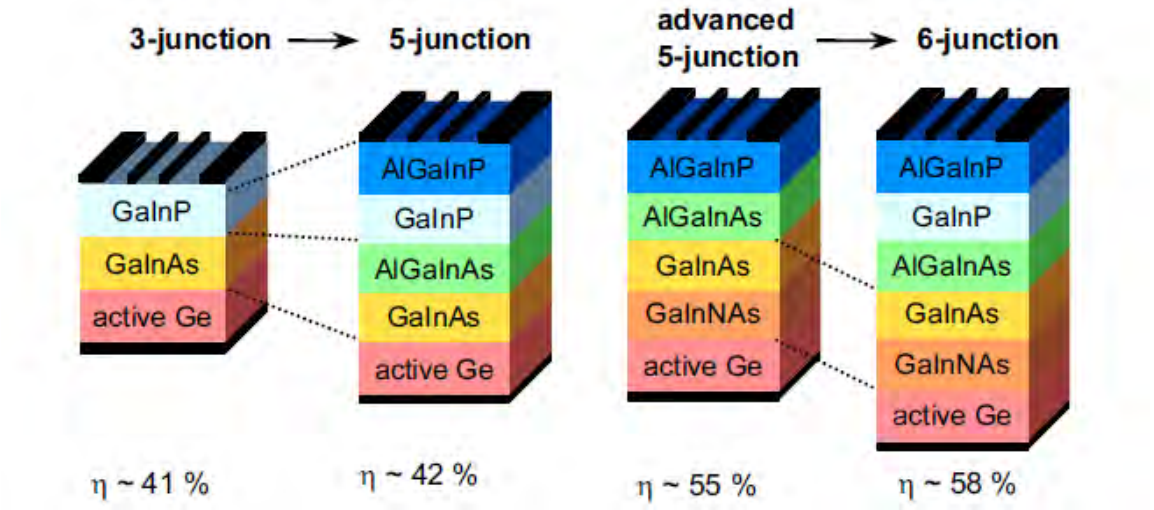


Fig. 2 *Roadmap of the development of high-efficiency multi-junction concentration solar cells (after ref. [10])*

The roadmap for the development of high-efficiency multiple-junction solar cells based on compound semiconductors is shown in Figure 2. The target is to reach an efficiency close to 60% in cells with six junctions, which poses formidable challenges to the relevant epitaxial technology.

2.1 Multi-junction III-V Solar Cells

There are four commercially available semiconductor substrates Ge, Si, GaAs and InP. This restricts the band-gap and lattice-constant selection when lattice-matched structure are desired, but those barriers can be overcome by growing thin pseudomorphic layers or by inserting in the structures layers of graded composition. In the following paragraphs, the characteristics of epitaxially-grown lattice-matched, metamorphic and pseudomorphic solar cell structures will be described.

2.1.1 III-V cells on germanium substrates

Currently available high-efficiency triple-junction solar cells consist of two III–V semiconductor junctions epitaxially grown lattice-matched on a Ge substrate, which, in addition to being a mechanical support, also provides the bottom junction. This highly mature lattice-matched design has achieved 40.1% efficiency at 135 suns concentration using $Ga_{0.5}In_{0.5}P$, $Ga_{0.98}In_{0.02}As$, and Ge junctions respectively with band gaps of 1.86, 1.39, and 0.67 eV. By growing alloy layers with the same crystal lattice constant as the substrate, most dislocations, which form dangerous recombination sites for the photocarriers, could be avoided.

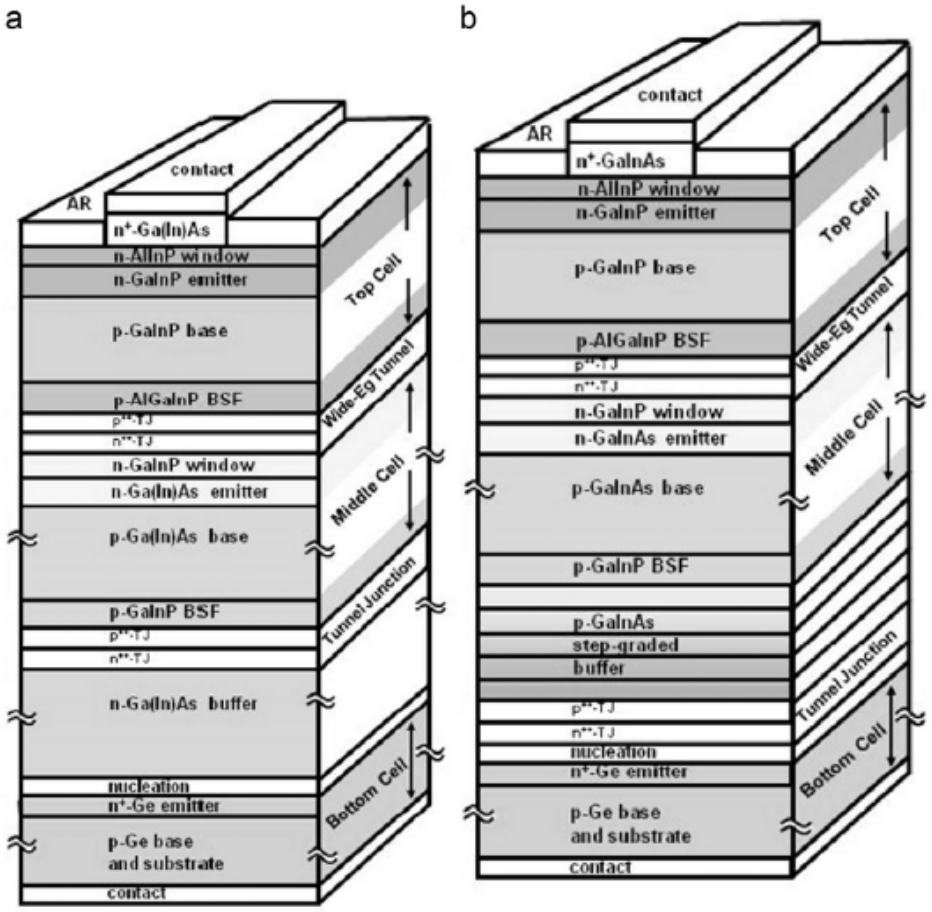


Fig. 3: *Schematic of lattice matched (a) and metamorphic (b) triple-junction GaInP/GaInAs/Ge solar cells. After [11].*

The growth of III–V layers on large diameter Ge has become very popular, however anti-phase domain formation and self-doping of the Ge in the III–V layers pose serious problems to this technology. Furthermore, commercial Ge wafers are usually thinner than GaAs or InP substrates of the same diameter; with typical 100 mm dia. Ge wafers ranging from 140 to 175 μm thickness. Such relatively thin wafers may result in wafer bowing during growth of lattice-mismatched layers. Any wafer bow translates into non-uniform temperature across the wafer growth surface. Therefore, the process scale-up to large diameter Ge wafers makes compositional uniformity a challenge in the case of alloys with temperature-sensitive composition.

As an example of state-of-art cells on germanium, two standard 3J device designs epitaxial cross-sections are shown in Fig. 3. A lattice-matched GaInP/GaAs/Ge triple junction in Fig. 3(a), which shows the details of the multiple GaInP and GaAs subcell layers interconnected with highly-doped thin tunnel junction. A second variant, an upright metamorphic GaInP/GaInAs/Ge device is reported in Fig. 3(b). The main difference between the two is the use of a GaInAs graded buffer layer to change lattice constant from the Ge substrate to a new compressive lattice constant. The reported structures were deposited on p-type, epi-ready vicinal (001) Ge substrates of either 100 mm or150 mm in diameter, and thickness between 175 μm and 235 μm.

2.1.2 III-V cells on GaAs

To grow a more efficient monolithic solar cell structure with improved band gap combination, lattice-mismatched alloys with low defect densities are required. Compositionally graded buffer layers may be used to accommodate the lattice-mismatch via formation of misfit dislocations within the buffer while inhibiting the propagation of these dislocations into the active junction. The resulting structure, incorporating active layers of different lattice constants separated by the graded layer, is commonly referred to as inverted metamorphic structure. An efficiency of 40.7% at 240 suns has been obtained in a metamorphic triple-junction device using a Ge bottom junction and two coupled metamorphic junctions that are both 0.5% misfit from the substrate with the band gaps 1.80, 1.29, and 0.67 eV. This design allows for an efficiency improvement with respect to lattice-matched devices, however its band gap combination is still far from optimized and some threading dislocations are introduced into the highest power producing top junction. Further decreasing the top two junction band gaps by this approach is very difficult because the performance is very sensitive to dislocations in the top GaInP junction. By inverting the direction of growth and then removing the substrate, a device with two high-quality lattice-matched top junctions, $Ga_{0.5}In_{0.5}P$ and GaAs, and highly lattice-mismatched (1.9% misfit) $Ga_{0.73}In_{0.27}As$ bottom junction with band gaps (1.84, 1.41, and 1.00 eV) can be grown on GaAs substrates, which further increases the efficiency by about 3 % relative to the lattice-matched design on Ge. This inverted design on GaAs containing a single metamorphic junction has several advantages over the conventional triple-junction designs that utilize a Ge bottom junction, but does not allow reaching the optimal band gap combination. A further step in that direction was made by utilizing an improved inverted triple-junction solar cell containing two independent metamorphic junctions (see Figure 4). The band gaps in this inverted design are 1.83, 1.34, and 0.89 eV, which more closely approach the theoretical global maximum. A performance of 40.8% efficiency at 326 suns was demonstrated for this design, but further development could potentially boost the efficiency by over 4% beyond that of the lattice-matched design.

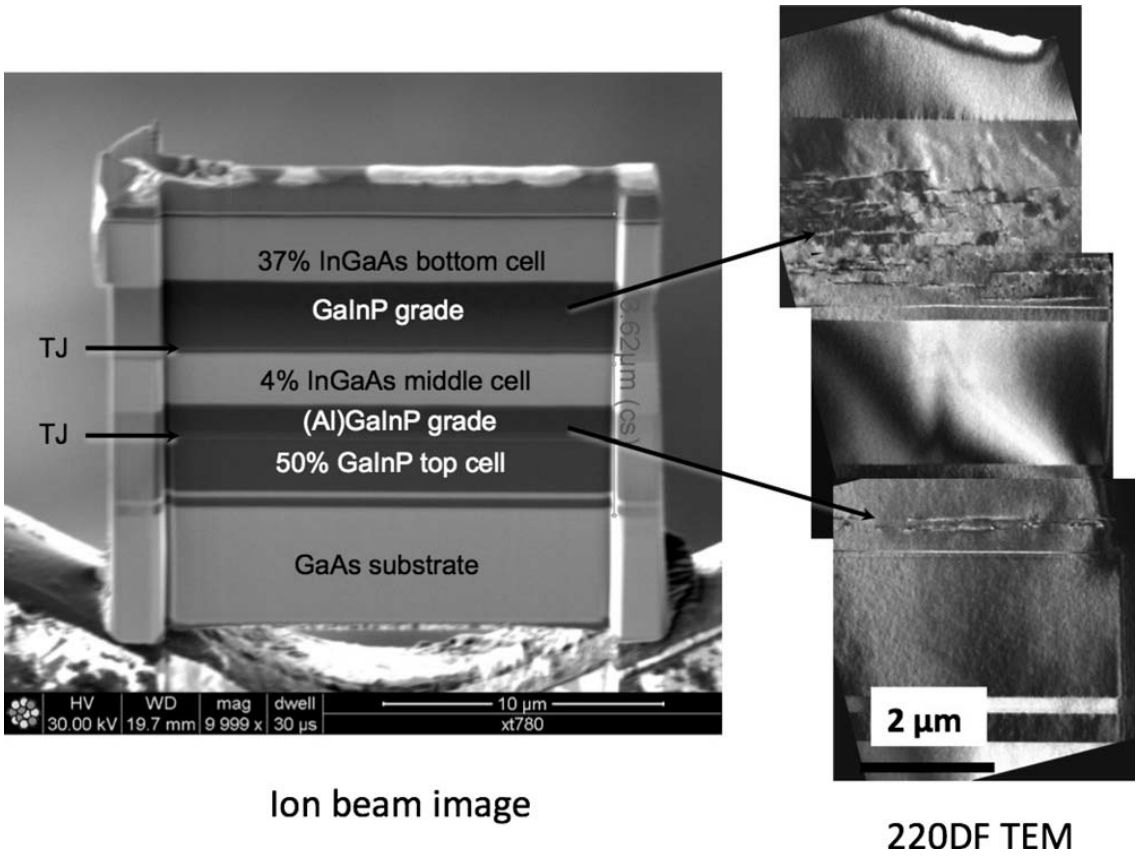


Figure 4: *Ion beam image and composite 220 dark-field TEM of a FIB cross-section of an inverted triple-junction solar cell structure (after [6]). Note the two tunnel junctions (TJ) and the graded buffer layers which separate the individual homo-junctions.*

This structure was grown by atmospheric-pressure MOVPE on a (001) GaAs substrate miscut 2° towards (111)B. The top 1.83 eV $Ga_{0.51}In_{0.49}P$ junction was grown first, lattice-matched to the GaAs substrate. The middle 1.34 eV $Ga_{0.96}In_{0.04}As$ junction was grown next after gradually increasing the lattice constant by 0.3% with an (Al)GaInP step-grade buffer. Finally, the bottom 0.89 eV $Ga_{0.63}In_{0.37}As$ junction (2.6% misfit) was grown after further increasing the lattice constant by inserting a GaInP step-grade. The thicknesses of the junctions were about 2.5–2.9 μm. As the band gaps were closed to optimum values, current-matching was achieved without the need to thin any junctions. The graded layers were realized to be transparent in the spectral range required by the junctions below them, and to produce a negligible strain within the active junctions. As clearly visible in Figure 4, each *n*-on-*p* homojunction was clad with passivating window and back-surface-field layers of an (Al)GaInP composition with higher band gap than the junction but identical lattice constant. Tunnel junctions were grown between each junction before the graded layers. The tunnel junction between the top and middle junction was thus lattice-matched to the top junction and the substrate, but the tunnel junction between the middle and bottom junction was grown on the metamorphic middle junction. This thin metamorphic junction consisted partly of $Ga_{0.96}In_{0.04}As$ doped with Se matching the metamorphic middle junction lattice constant on which it was grown, but also of $Ga_{0.70}Al_{0.30}As$ doped with C, that was grown in tension on the metamorphic middle junction. The doping of $Ga_{0.96}In_{0.04}As$ with C was avoided, as In-containing alloys are difficult to dope with carbon. While this tunnel junction design is not ideal because of the strained GaAlAs layer, it provided low-resistance Ohmic-like conduction in the device up to 826 suns concentration. X-ray diffraction investigations showed the metamorphic junctions to be in only

0.029% and 0.014% compressive strain. Plan-view, spectrally resolved cathodoluminescence images indicated approximately 1×10^{5} cm^{-2} and $2–3\times10^{6}$ cm^{-2} threading dislocations in the middle and bottom junctions, respectively, whereas the threading dislocations in the top junction were below the detection limit (5×10^{4} cm^{-2}). Additional investigations by TEM showed many dislocations within the two graded buffer layers, but almost none in the three active junction regions. The measured dislocation densities are believed to have just minor influence on recombination of photo-carriers.

2.1.3 III-V cells on Si Substrates

The viability of III-V InGaP/GaAs solar cells on Si depends on the ability to deposit high quality GaAs on Si thanks to careful lattice engineering and substrate treatment. The polar on non-polar epitaxy, the thermal mismatch and the 4% lattice-mismatch make the growth of high-quality GaAs on Si very challenging. The dislocations generated by the mismatch between GaAs and Si can propagate into the active region of the cell and significantly reduce the minority carrier lifetime and thus the overall cell performance. The thermal expansion coefficients of Si and GaAs are $2.6x10^{-6}$ K^{-1} and $5.7\ x10^{-6}$ K^{-1} at 300 K, respectively. Despite this large difference, the contribution of thermal mismatch strain plays a smaller role than the lattice mismatch strain during GaAs deposition on Si substrates and cooling from typical growth temperature of about 600°C down to room temperature. Hence, in a first approximation the dislocations due to thermal mismatch can be neglected compared to the dislocations generated by the lattice mismatch. Oh et al. investigated theoretically triple and dual junction solar cells on Si substrates and calculated the expected conversion efficiency as a function of TDD for two different hypothetical structures [12]. Based on these simulations, it appears that compound semiconductors on silicon can reach over 30% efficiency at 100 suns when TDD stays below 10^{6} cm^{-2}. The direct epitaxial growth of GaAs on Si substrates in fact results in dislocation densities in the films that reach values of $10^{9}–10^{10}$ cm^{-2}, and in addition other defects such as stacking faults and antiphase domains may appear. In the literature one can find several approaches to growth of GaAs with reduced defect density. For instance, Wilkins et al. [13] designed a multi-junction solar cell on silicon for 1 sun applications that includes diffusion of a p/n bottom junction in the Si substrate and the subsequent formation of a compliant porous layer on the Si surface prior to depositing the GaAs buffer layer and further sub-cells. Another popular way of reducing the consequences of lattice and thermal mismatches is to form a virtual substrate by growing a graded composition of the desired heteroepitaxial film on a defect-free Si substrate. A layer of constant composition, with the desired lattice parameter can then be grown on this buffer layer. Graded SiGe films have been demonstrated to be effective as they result in very low ($\sim10^{5}$-10^{6} cm^{-2}) defect densities. In principle, they can be used as good templates for the additional deposition of Ge and III-V epilayers. This approach presents, however, a major issue connected with the pronounced surface roughness.

A most promising approach is the epitaxial growth on patterned substrates. Mathews et al. [14] first proposed that limiting the lateral dimensions of the sample prior to growth could reduce the density of threading dislocations. That idea was later applied by Luan et al. [15] in order to obtain a consistent reduction in dislocation density using finite area growth on 10 μm x 10 μm mesas. Vanamu et al. performed hetero-epitaxy of $Ge/Si_{1-x}Ge_x/Si$ starting from differently patterned substrates [16]. The main aim of their study was to evaluate the role of the pattern size and depth on the quality of the heteroepitaxial layer while keeping other growth parameters fixed. The patterned substrates were fabricated on a 4” (0 0 1)-Si substrates, which were off-cut 4-5° in the 〈1 1 1〉 direction in order to prevent formation of anti-phase domains in the heteroepitaxial films. A wide

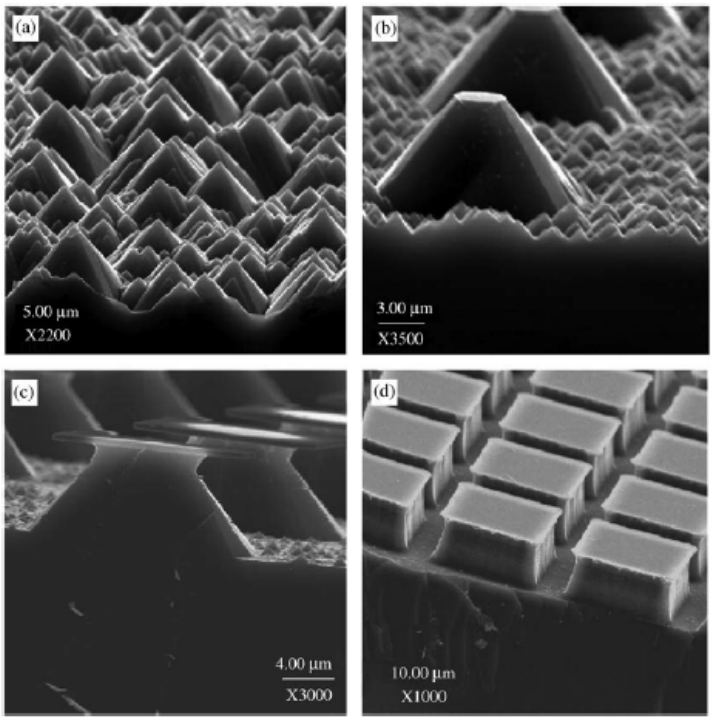


Figure 5: *SEM images of silicon substrate after different etching and patterning processes (after ref.[16]): a) planar KOH etching; b) masking and etching; c) small mesas; d) large mesas*

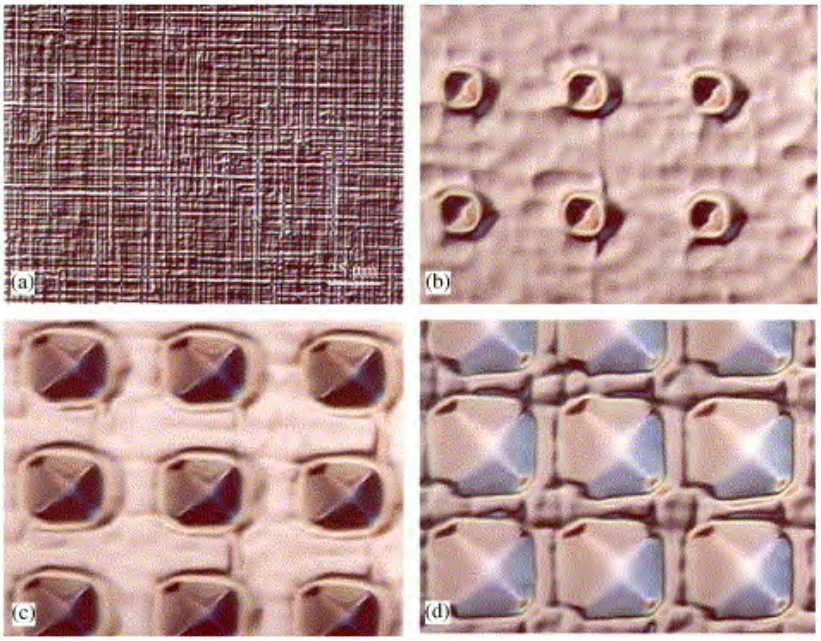
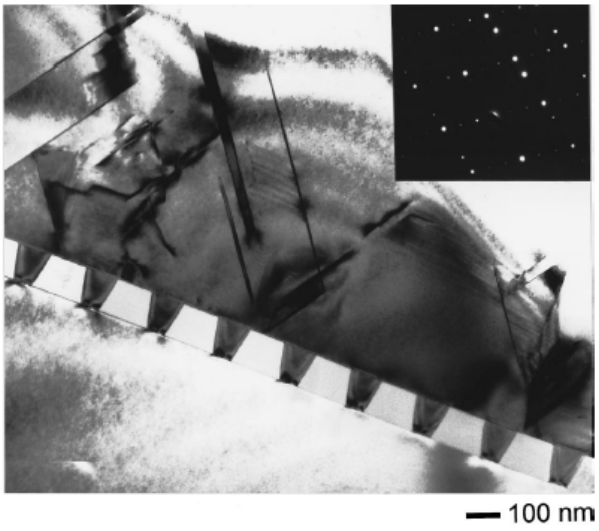


Figure 6: *Optical microscopy images of the surface (top view) of epitaxial layers deposited on the four patterned substrates of figure 9: a) planar etched surface; b) with smallest mesas; c) with intermediate mesas; d) with largest mesas. (After ref. [16]).*

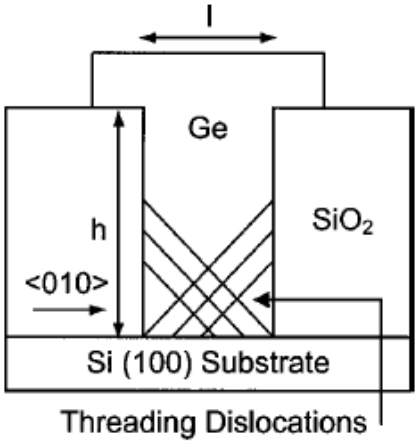
range of substrate patterns, with different dimensions and profiles were fabricated by optical lithography techniques combined with reactive ion and wet chemical etching. Figure 5 shows four different profiles while figure 6 gives the corresponding surfaces after having overgrown the mesas of different sizes and periodicity with 10 µm graded Si_xGe_{1-x} and final deposition of 6 µm of Ge. TEM and X-ray measurements confirmed that the defect density is reduced as the size of the mesas

decreased from 20 to 4 μm, while keeping the center-to-center distance between the posts constant at 25 μm. The dislocation density obtained for Ge/Si_xGe_{1-x} on the planar, the smallest patterned and the largest patterned structures were 6×10^8, 4×10^7 and 2×10^8 cm^{-2}, respectively.

Langdo et al. [17] and Li et al. [18] made use of another approach, namely the so-called selective area epitaxy, also called tunnel or micro-channel epitaxy, and grew low dislocation density Ge on silicon by exploiting the lateral overgrowth on SiO_2/Si substrates with 100 and 200 nm holes. The top surface of over-grown Ge has much higher crystallographic quality compared to conventional Ge lattice-mismatched growth on planar Si substrates. By using this ‘‘epitaxial necking’’ (see Figure 7) threading dislocations are blocked at oxide sidewalls, and effectively filtered, so that the major source of defects is not given by threading dislocations but rather by the stress at the merging of epitaxial lateral overgrowth fronts from neighbouring holes. This overgrowth technology is very often used for the epitaxial growth of dissimilar materials, specifically GaN on sapphire, GaAs on silicon, Ge on silicon.



a)



b)

Figure 7: *a) TEM image of highly-perfect laterally-overgrown germanium layer through 100 nm holes opened in the SiO_2 mask; b) schematic of the employed tunnel epitaxy (after ref. [17]).*

The highest efficiency reported for single-junction GaAs on Si is 21.3% at 200 suns under AM 1.5D [19], while the highest efficiency achieved for monolithic dual-junction 2J InGaP/GaAs solar cell on Si substrate is 18.6% at 1 sun under AM1.5G spectrum [20].

2.2 Use of multi-quantum wells (MQW) in solar cells technology

The availability of epitaxial technologies that offer superior control over interface abruptness, composition and doping of the thin films has given a great impulse to development of semiconductor heterostructures with quantum confinement effects. These effects can be obtained in bidimensional (2D) structures such as quantum wells, in unidimensional structures (1D) as quantum wires, and even in 0-dimensional structures like quantum dots.

As seen before, the triple-junction cell has many desirable characteristics; however, its full potential has not yet been realized. The highest efficiencies are achieved by reducing the thickness (and performance) of the top GaInP cell to below one micron, to favour higher photon flux towards the current-limited buried GaAs cell. Theory and simulation show that efficiencies above 30% would be reachable if one can substitute the GaAs cell by a cell that could efficiently convert photons with energies ranging from 1.2 to 1.3 eV and be still lattice-matched to commonly used Ge and GaAs substrates. On way to do so is introducing pseudomorphically strained thin (few nm) narrower bandgap wells of InGaAs in the intrinsic region of a conventional p-i-n subcells. When the thickness of the individual wells is chosen to be below the onset of lattice relaxation, the incorporation of narrow bandgap multi quantum well may result in a substantial increase of the cell photocurrent.

Many different MQW cell configurations have been proposed in the last years; however, they can be roughly divided in three categories: lattice-matched, strained, and strain-balanced MQW devices. The question of a fundamental efficiency enhancement using quantum well structures as photovoltaic power convertors is still an active area of research. Theoretically, if the QW cell behaves as a strictly two-level system, described by two continuous and constant quasi-Fermi levels separated by the applied bias, then no efficiency enhancement should be expected with respect to equivalent bulk cell. Recent experimental data indicate that quasi-Fermi level separation differ in the bulk and QW regions of the device. A quantum well solar cell may thus be better described by a multi-band model, allowing efficiency to exceed those of a bulk cell. The physical phenomena governing the recombination behaviour are beyond the scope of this chapter, and in the following we shall rather focus on lattice-matched GaInP/GaAs and strained InGaAs/GaAs epitaxial structures of quantum well material systems. Let us start with the strained GaAs/InGaAs quantum well solar cell, which represents the simplest configuration for an InGaAs-based p-i-n quantum well cell. The p and n regions are composed of GaAs and the i region accommodates the GaAs/InGaAs MQW, as shown in figure 8. The different lateral extension of wells and barriers in Figure 8a indicates that the InGaAs quantum well layers possess a larger lattice parameter than the surrounding GaAs, resulting in compressive strain. Figure 8b reports the electronic band-structure arising from such a device. Typically, there are 10 to 30 quantum wells of thickness around 80 Å and composition $In_{0.2}Ga_{0.8}As$ in real cell structures, which corresponds to an offset between QW conduction and valence band of about 0.64 eV. The quantum well energy levels serve to extend the spectral response, without degrading the bulk quantum efficiency, but at the same time the strain introduced by the InGaAs quantum wells has adverse effects upon the dark current of the quantum well cell. The dark-IV behaviour may be understood from the accumulation of strain energy as quantum wells are added to the i-region. It is convenient to define an average strain <f> across the i-region, considering quantum well composition x, thickness t_{qw}, barrier thickness t_b and number of

quantum wells N in one single parameter. The average strain may then be expressed by the relation (1), in which the lattice parameters are a_0 = 5.6533 Å for GaAs and a_x= 5.6533+0.4050 Å for the $In_xGa_{1-x}As$ alloy.

$$\langle f \rangle = \frac{(a_x - a_0) N t_{qw}}{a_0 (N t_{qw} + (N-1) t_b)} \qquad (1)$$

The average strain depends on the total MQW thickness ($Nt_{qw}+(N-1)t_b$). Cells remaining below the critical thickness remain strained, while cells above the critical thickness relax giving rise to a high misfit dislocation density at the top and bottom of the MQW region. The average strain therefore plays an important role in view of optimizing InGaAs/GaAs strained quantum well solar cells. To maximise the quantum well absorption, it is desirable to maximise the QW indium content, quantum well width and number of QWs. However, all three factors serve to increase the average strain and the cell will ultimately become limited by the critical thickness. The dark-IV degradation suffered by strained InGaAs/GaAs cells makes their performance inferior to that of good GaAs bulk cells in terms of AM0 conversion efficiency. This stimulated a further evolution of MQW cell technology, to include a strain-balance approach, which has successfully reduced the dark-IV of an InGaAs-based quantum well cell to that of the GaAs reference cell.

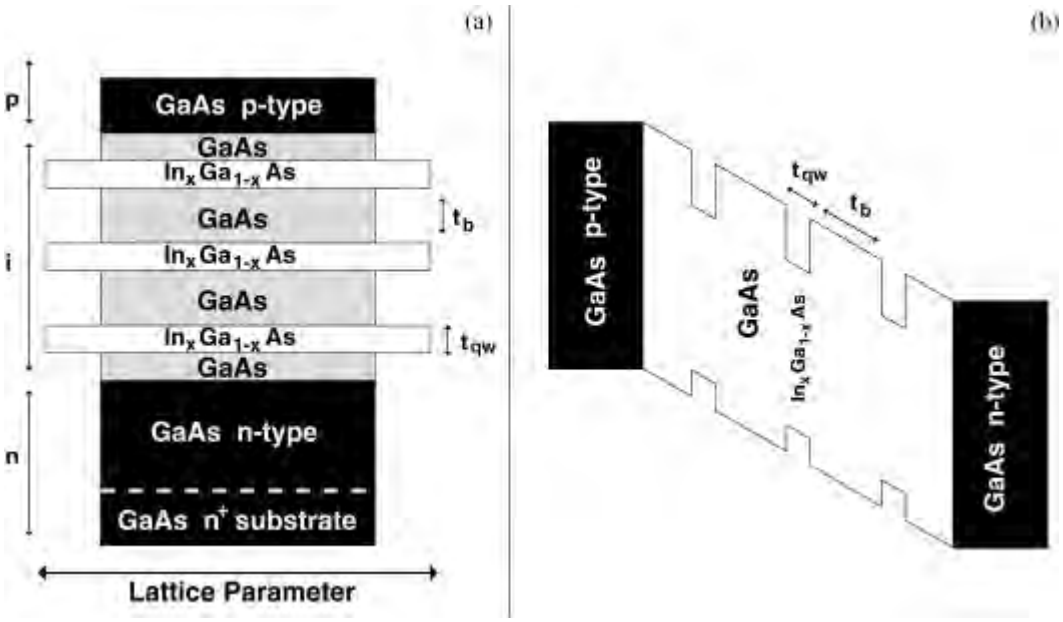


Figure 8: *Schematic of 3-period MQW InGaAs/GaAs-based solar cell (a) and corresponding band structure (b); t_b and t_{qw} are the barrier and well width, respectively. (After ref. [21])*

Strain-balance is a means for controlling the build-up of strain energy in a hetero-structure. The composition of the device layers must be specifically chosen so that each strained layer is compensated by the adjacent layer, realized with materials which result is exactly opposite strain. Therefore, it is possible to grow locally strained layers which are unstrained with respect to a given substrate. The modulated structure can be repeated, without relaxation, until the desired thickness is grown.

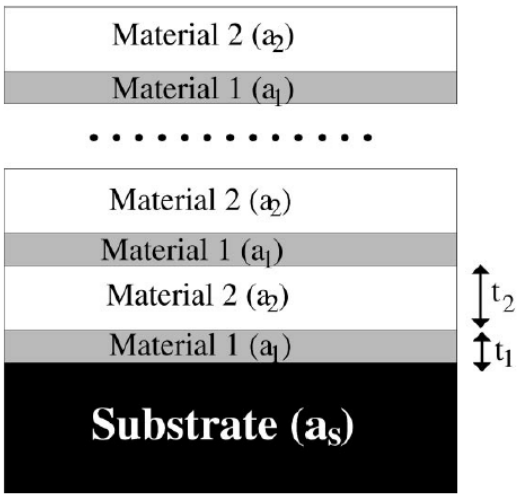


Figure 9: *Periodic structure composed of two materials 1 and 2, with different lattice parameters a_1 and a_2, deposited on a foreign substrate with lattice parameter a_s. (After ref. [21]).*

To clarify the concept let us take the structure reported in figure 9, where two lattice-mismatched materials 1 and 2 are grown on a substrate with lattice parameter different from that of materials 1 and 2. The strain-balance condition is satisfied when the average lattice parameter $\langle a \rangle$ across the modulated region defined by equation (2) equates to the substrate lattice parameter. Similarly, the average strain $\langle f \rangle$ between the MQW stack and neighbouring layers defined by equation (3) becomes zero when the structure is strain balanced.

$$\langle a \rangle = \frac{t_1 a_1 + t_2 a_2}{t_1 + t_2} = a_{\text{substrate}}, \tag{2}$$

$$\langle f \rangle = \frac{\langle a \rangle - a_{\text{substrate}}}{a_{\text{substrate}}}. \tag{3}$$

III–V semiconductors offer different combinations that can be used to achieve a strain-balanced structure. From the point of view of photovoltaic power conversion, there are two combinations particularly interesting: i) GaAsP/InGaAs strain-balance on a GaAs substrate and ii) GaAs/InGaAs strain-balance on a virtual substrate. In the first case, the compressive strain due to InGaAs quantum wells can be compensated by tensile $GaAs_{1-x}P_x$, leading to a structure which matches the GaAs lattice parameter. A p–i–n cell structure making use of this configuration is shown in figure 10, together with its corresponding band structure. The i-region is composed of a cyclic half-barrier/quantum well/half-barrier structure; each half-barrier GaAsP alloy provides half the strain compensation for the InGaAs quantum well. Thus, if t_b is the half-barrier thickness, t_{qw} is the well thickness, a_{GaAsP} and a_{InGaAs} are the well and barrier lattice constants, the average strain for this structure is given by equation (4)

$$\langle a \rangle = \frac{2t_b a_{GaAsP} + t_{qw} a_{InGaAs}}{2t_b + t_{qw}} \tag{4}$$

The well and barrier thicknesses are chosen to ensure that the average lattice parameter across the i-region $\langle a \rangle$ equates to that of the GaAs substrate. In this way, the average strain $\langle f \rangle$ of equation (3) is minimised.

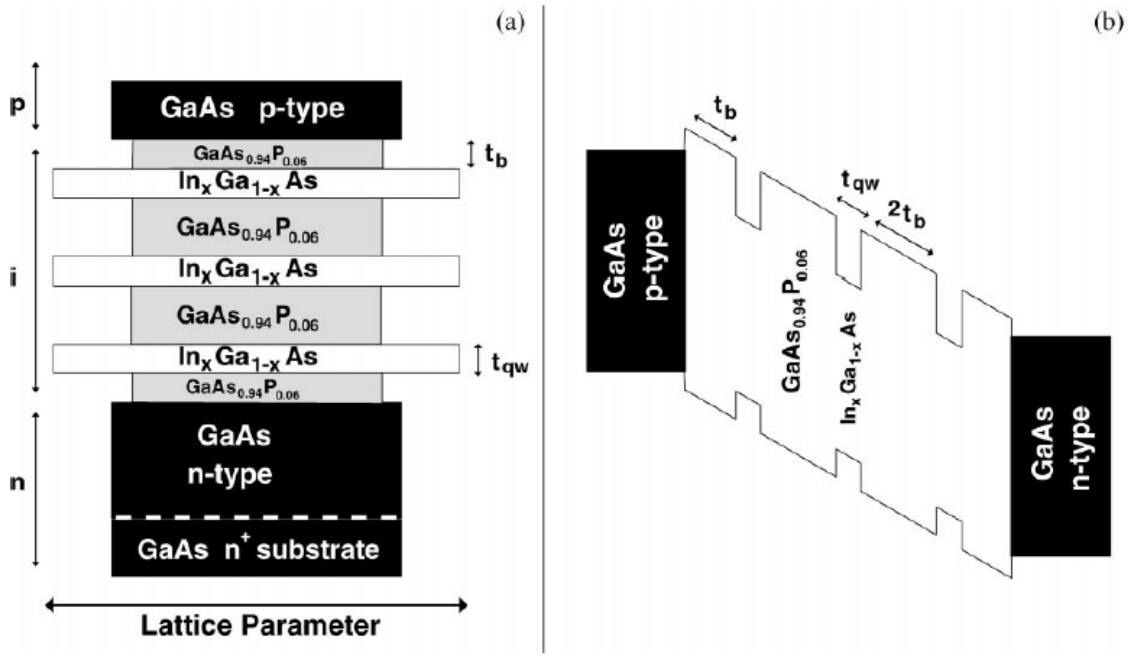


Figure 10: *(a) Example of strain-balance structure composed of three InGaAs quantum wells with thickness t_{qw} and three InGaP barriers with thickness t_b deposited on GaAs; the lateral extension of the layers gives an idea of the lattice parameters for the different alloy compositions; (b) Corresponding electronic band structure. After ref. [21].*

Let us see now the second way to balance strain in a MQW solar cell, namely by growing a certain number of InGaAs/GaAs periods on a virtual substrate. Conceptually a virtual substrate serves to alter the equilibrium lattice parameter determined by the substrate material. In principle, it involves the deposition of a doped buffer layer of strained material and allowing relaxation to take place so that the relaxed buffer layer possesses the desired lattice parameter. Once a virtual InGaAs substrate is established, an InGaAs alloy which is indium rich with respect to the virtual substrate will become compressively strained. Similarly, an indium poor InGaAs alloy will be under tensile stress. The In-rich and In-poor alloys may therefore be modulated to satisfy the strain-balance condition of equation (2) and remain lattice-matched overall to the virtual substrate. Figure 11 shows schematically this approach: a device employing this virtual substrate InGaAs alloy method of strain-balance is reported along with the corresponding band structure. In a real case, an $In_{0.05}Ga_{0.95}As$ virtual substrate and a 23-period MQW structure were grown on a n^+ GaAs substrate by molecular beam epitaxy (MBE) [21]. Relaxation has taken place at the GaAs/ $In_{0.05}Ga_{0.95}As$ interface and the lattice parameter designed to converge on that of bulk $In_{0.05}Ga_{0.95}As$. The MQW region is modulated between GaAs and $In_{0.24}Ga_{0.76}As$, such that the average lattice parameter is that of $In_{0.05}Ga_{0.95}As$. This device was again investigated and EBIC microscopy was used to probe the carrier diffusion length and dislocation density in the GaAs/InGaAs strain-balance cell. Threading dislocation were observed to emerge from the virtual substrate with a density of about 10^6 cm^{-2}. Some misfit dislocations were also observed.

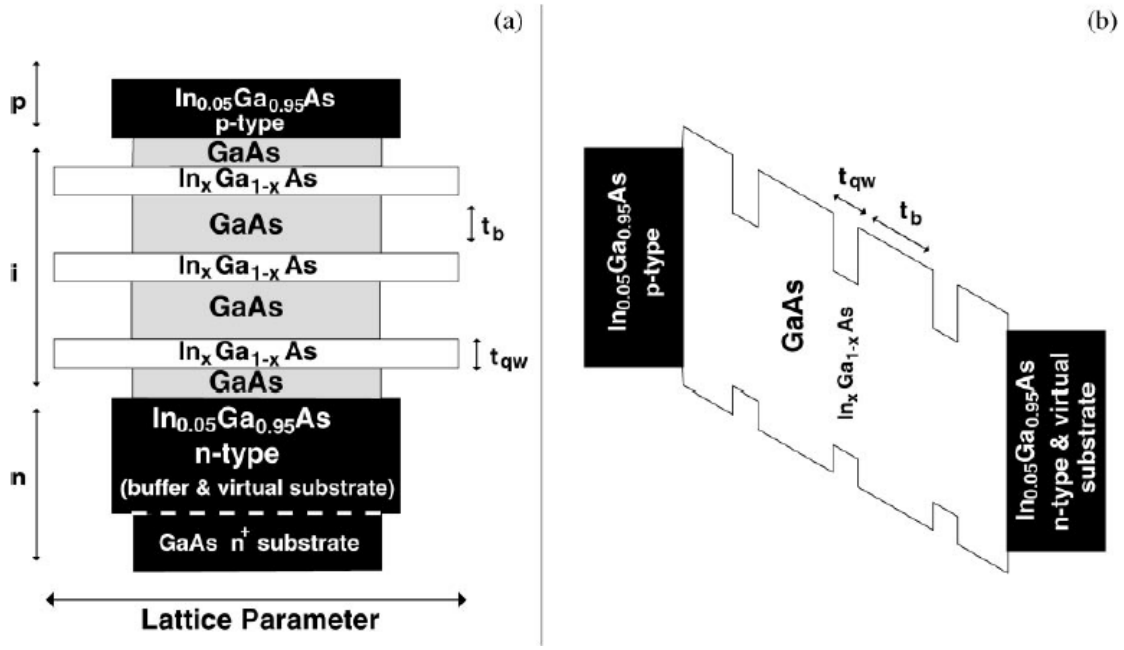


Figure 11: *(a) Schematic diagram of strain-balanced GaAs/InGaAs 3-period MQW device on an $In_{0.05}Ga_{0.95}As$ virtual substrate, t_b is the GaAs barrier thickness and t_{qw} is the $In_xGa_{1-x}As$ QW thickness, lateral extension of the layers corresponds to relaxed lattice parameter; (b) Electronic band-structure of this device. After ref. [21].*

The strain-balance approach is advantageous as it enables novel band-gap/lattice-constant combinations, giving rise to a rich array of 'new' material combinations for tandem and multi-junction cells

2.3 Use of nitride semiconductors in solar cells

In the last two decades, nitride semiconductors also found application in solar cell technology as top cell in tandem and multi-junction cells, thanks to the wide bandgap of InGaN alloys, or as bottom cell in four-junction solar cells. For the latter application, the materials of choice are the so-called diluted nitrides: GaAsN and InGaAsN. Typical structures of cells incorporating nitrides and diluted nitrides will be briefly discussed in the following sections.

2.3.1 Strain management by incorporation of diluted nitrides

Dilute nitride films with bandgap of 1 – 1.4 eV can be designed to be lattice-matched to gallium arsenide and germanium, and therefore may play a role as fundamental component in multi-junction solar cells, for example quaternary InGaAsN homo- and heterojunctions, which cover effectively the range between GaAs and Ge junctions. Quaternary dilute-nitride alloys, such as InGaAsN lattice-matched to GaAs, have been extensively studied for solar cell applications, but their device performance has been significantly limited due to short minority carrier diffusion lengths, narrow depletion widths, and high background carbon incorporation. The introduction of antimony during growth helped significantly to improve the efficiency. GaInNAs(Sb) indeed allowed the fabrication of cells with high quantum efficiency, almost 80% at maximum, mainly due to low background doping densities providing these devices with wide depletion widths. High-quality 1 eV quinternary InGaAsN(Sb) materials have been successfully grown lattice-matched to GaAs by both MBE [22] and MOVPE techniques [23, 24]. The growth of the five-component system however poses serious

challenges with regards to the epitaxial growth and the compositional uniformity. For example, it was reported that Sb plays a role as alloy constituent and simultaneously as a surfactant in the growth of the quinternary alloy, therefore the addition of Sb modifies the incorporation efficiency of the other components. This requires a corresponding modification of molecular fluxes (in case of MBE) or gas flows (for MOVPE).

2.3.2 Nitride-based top cell in tandem and multi-juntion cells

III-nitrides can be utilized in PV not only to produce, or relieve, a certain amount of strain, but also as active absorber. $In_xGa_{1-x}N$ alloys have a direct bandgap spanning nearly the entire solar spectrum (0.7 eV–3.4 eV). Furthermore, the InGaN alloys are characterized by high absorption coefficients (about 10^5 cm^{-1} at the band edge), which results in a large fraction of the incident light to be absorbed in a very thin active layer. Unfortunately, it is well known that growing high-indium content high-quality InGaN films is extremely complicated due to the large lattice mismatch between InN and GaN. Another complication arises from the lack of native substrates or conductive substrates with good thermal and lattice match. The most popular substrate is sapphire, which is highly resistive and impedes the usual front grid – back contact geometry. Both electrodes therefore must be fabricated on the same face of the devices (see figure 12).

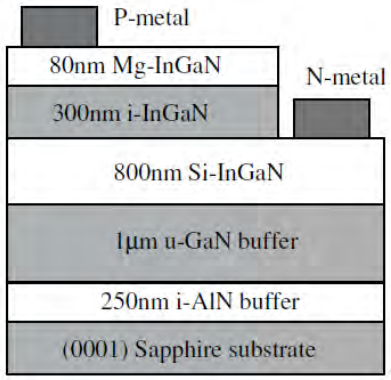


Figure 12: *Schematic of InGaN p-i-n solar cell (after ref. [25])*

3. Epitaxial processes for thermo-photovoltaic (TPV) devices

Thermo-photovoltaic systems allow the conversion of radiation from man-operated radiant sources into electricity using appropriate photovoltaic devices. These devices are required to convert longer wavelength radiation from radiators at 700 –1500 °C, i.e. much lower temperature compared to the sun (~6000 °C). This means that most of the radiation that can be utilized is in the infrared rather than the visible range. Consequently, the bandgap of TPV devices extends from 0.4 to 0.6 eV for cells to be used with grey body radiators operating in the temperature range 1200–1500 °C. Another major difference between solar PV and TPV is that in the latter the cells are very close (few centimetres) to the thermal source. The devices thus operate at high energy densities similar to those in solar concentrator systems. Various theoretical estimates of the maximum performance of TPV systems and devices have been made. These range from 85% for a solar TPV concentrator system with a two-junction cell, 13 - 22% overall system efficiencies (including combustion efficiency) for a combustion based system, to 35 - 40% for single and two bandgap cells converting blackbody-like radiation.

3.1 TVP devices fabricated from low-bandgap semiconductors

Certain III-V semiconductors possess small energy gap and may be applied conveniently in TPV devices. For example, GaSb (E_g = 0.72 eV), InGaAs lattice matched (0.75 eV) and mismatched (0.5–0.6 eV) to InP, InAsSbP and InGaAsSb (0.3–0.5 eV) and 0.52 eV InGaAs/InPAs cells. Sb-based heterostructures have been successfully grown by all of the major epitaxial techniques. While each of these technologies must contend with numerous challenges that are specific to the method of choice, several fundamental issues related to Sb-containing III–V alloys exist. These include: the low volatility of Sb compared to P- and As-based alloys, which necessitates stringent control of V/III ratio; the use of low growth temperatures (400–600 °C); the existence of a large solid-phase miscibility gap for many Sb-containing alloys; and the strong tendency of AlSb-based alloys to incorporate O and C. Consequently, MOVPE growth of Sb-based alloys differs significantly from the more conventional As- and P-based materials, and development of GaSb-based materials and devices has become a separated research field. Among the low-bandgap materials investigated for TPV energy conversion, InGaAs grown lattice-mismatched on InP substrates and InGaAsSb grown lattice-matched on GaSb substrates have demonstrated the highest performance for nominally 0.55 eV bandgaps. Figure 13 illustrates typical device architectures for these two material systems. In both cases, the p-type layer is utilized as absorption layer due to the higher minority carrier diffusion lengths with respect to n-type material. However, since shallow n-type ohmic contacts are difficult to realize in Sb-based devices, a thick p-type emitter is utilized for the InGaAsSb cell. For both devices, minimizing surface/interface recombination velocities is crucial for high-performance. In the case of n-on-p InGaAs devices, the back surface field is the critical layer, while for p-on-n InGaAsSb devices, the window is the critical layer. A major strength of MOVPE growth of III–V semiconductors has always been the use of precursors based on group III organometallics and group V hydrides. AsH_3 and PH_3 of electronic-grade purity have been readily available for years, which strongly contributed to the rapid development of arsenide- and phosphide-based devices. Unfortunately, this is not true for the equivalent Sb hydride SbH_3. This is unstable at room temperature, and was reported to boil at −18 °C and to have a half-life of just 2–4 h at room temperature. Therefore, only organometallic based Sb-precursors are being used in current practice. Unfortunately, their use does not provide free H radicals, which would help substrate oxide desorption and reduction of carbon incorporation (this is especially true for Al-containing alloys). Therefore, both in-situ substrate preparation prior to starting the deposition and C contamination result to be problematic.

Another major factor that differentiates the growth of Sb-based alloys from P- and As-based semiconductors is the greatly reduced volatility of Sb at the growth temperature compared to P or As. Because of the low-equilibrium vapour pressure, excess Sb does not evaporate. Above a critical V/III ratio, a Sb-rich secondary phase was observed for GaSb growth. On the other hand, Ga droplets tend to form below a critical V/III ratio. Thus, the V/III ratio must be very precisely adjusted around unity in order to avoid nonstoichiometric growth and phase separation. The parameter window required for acceptable morphology is definitely very narrow: it was found that metal droplets appear for GaSb growth with V/III=0.8, while the surface was featureless with V/III=0.9, but exhibited morphological defects with V/III=1.2. Furthermore, the low-equilibrium vapour pressure of Sb at the growth temperature results in a near unity sticking coefficient, which can impact the growth of ternary and quaternary alloys. In addition, Sb surface segregation can be problematic in the growth of heterostructures.

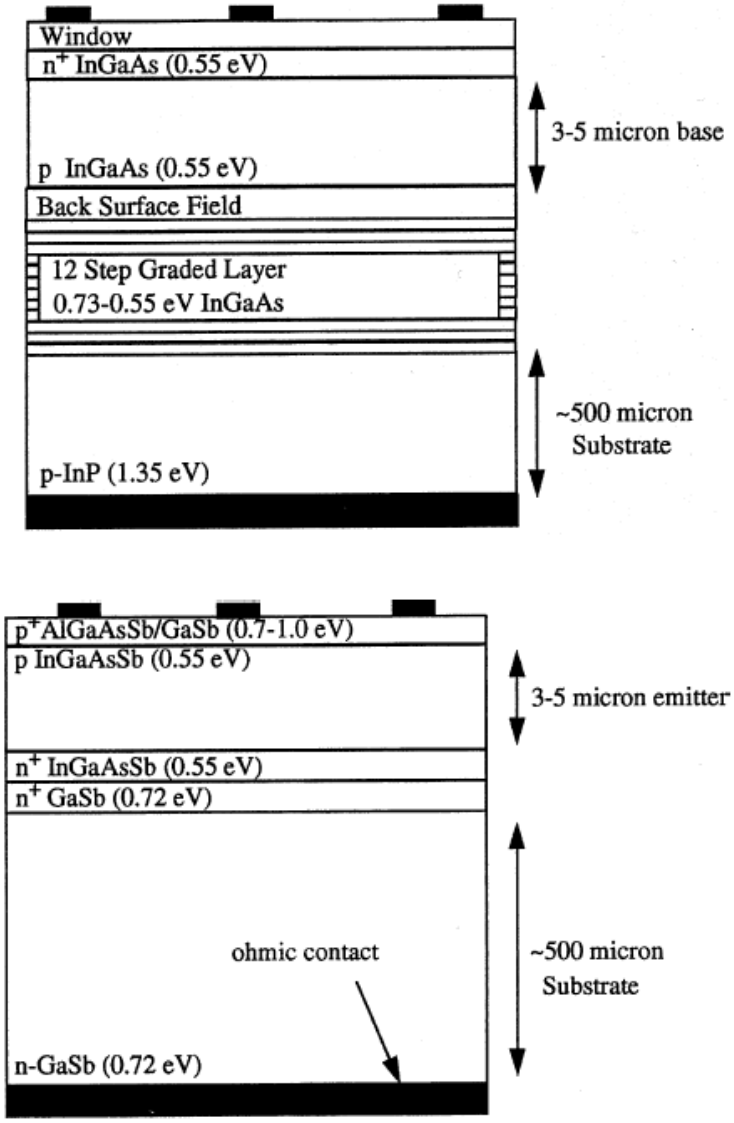


Figure 13: *Structure of 0.55 eV TPV devices based on InGaAs (upper picture) and InGaAsSb (lower picture). After ref. [26].*

While the above issues are significant, perhaps even more critical in determining the quality of Sb-containing III–V materials is the choice of starting precursors. Actually, MOVPE development of these alloys historically followed with some delay the MBE growth, primarily because of the lack of suitable group III and V precursors for Sb-based materials growth.

The low-bandgap GaSb-based alloys have low melting points and typically necessitate growth at temperatures below 600 °C, which is about 100 to 200 °C lower than the growth temperature of P- and As-based III–V semiconductors. At these low temperatures, growth of GaSb with conventional precursors such as trimethylgallium (TMGa) and trimethylantimony (TMSb) is kinetically limited since TMGa is incompletely pyrolized. On the other hand, when triethylgallium (TEGa) is used, growth is mass-transport limited. As temperature variations of just a few degrees can affect the extent of precursor decomposition, which in turn could result in non-uniform alloy composition and thickness, especially over large area substrates, TEGa is currently preferred for growth of GaSb as well as for GaSb-based ternary and quaternary alloys.

It is equally important for the group V precursor to decompose at the growth temperature. TMSb has a pyrolysis temperature of about 550 °C and is only partially decomposed under typical growth

conditions. Therefore, significant efforts were made to investigate alternative Sb precursors with lower pyrolysis temperatures, including: triethylantimony (TESb), triisopropylantimony, diisopropylantimonyhydride, tertiarybutyldimethylantimony, and trisdimethylaminoantimony (TDMASb). Many of these alternative Sb precursors were specifically developed for InSb, which is typically deposited below 450 °C. A benefit of these alternative precursors is that the decomposition does not produce methyl radicals, which helps to minimize carbon contamination. This is particularly important for Al-containing alloys.

Even if ideal precursors were available, another fundamental challenge is related to phase separation and atomic ordering of Sb-based III–V alloys. Atomic ordering is often observed in GaAsSb and InAsSb and can result in reduced energy gaps. Phase separation is a consequence of solution thermodynamics, which leads to existence of a large solid-phase miscibility gap for Sb-based alloys, as reported by Stringfellow [27]. The atomic size and electronegativity differences between the constituents result in a large positive enthalpy of mixing, and equilibrium growth of the solid solution can be achieved only above a critical temperature T_c, where the negative entropy of mixing exceeds the enthalpy. The values of T_c for $Al_xGa_{1-x}As_ySb_{1-y}$, $Ga_xIn_{1-x}As_ySb_{1-y}$, and $InP_xAs_ySb_{1-x-y}$ are 964, 1428, and 1319 K, respectively. These temperatures are considerably higher than typical growth temperatures. As a result, the deposited epilayers have a tendency towards phase separation into microscopic regions of non-uniform alloy composition. Systematic experiments have shown that phase separation in GaInAsSb epilayers can be significantly reduced by affecting growth kinetics so that adatom surface diffusion is limited. It was observed that growth temperature, growth rate, substrate miscut, and V/III ratio have a large impact on structural and optical quality.

3.2 Quantum cascade based TVP devices

The conversion efficiency of single-junction TPV devices is ultimately determined by two limiting factors: first, below-bandgap photons cannot be absorbed and therefore their energy cannot be harvested; secondly, while high-energy photons are efficiently absorbed, only a fraction of their energy is converted into electricity, with the rest is lost to the lattice as the resulting photocarriers relaxation via phonon emission. These limitations can be overcome with the use of cascaded multiple junctions of different bandgap energy, each providing efficient conversion of near-bandgap radiation over a different wavelength range. However, semiconductors of widely different bandgap energies also feature proportionally different lattice constants, so that the number of different p-n junctions that can be grown on top of one another is in practice limited by strain accumulation. In fact, tandem TPV devices have so far failed to improve on the performance of optimized single junction photodiodes [28]. An alternative approach to the development of infrared photovoltaic devices is the use of intersubband (ISB) transitions in suitably designed quantum-cascade (QC) structures [29-32]. Photodetectors based on this approach have already been demonstrated with a variety of quantum-well materials systems for thermal imaging applications, and typically involve a cascade of several so-called “stages”. One stage may contain ten or more well-barrier units, whereby the barriers have a constant thickness whereas the wells have variable thickness. For an extended description of the physics and device application of intersubband transitions in quantum wells the reader may consult reference [33].

The operation wavelength of QC devices can be tuned by design over a broad range using the same QW materials system, so that an arbitrary number of different stages absorbing at different wavelengths can be grown on top of one another without strain accumulation. Furthermore, each stage provides absorption over a relatively narrow spectral region, so that the energy of all absorbed

photons can be extracted efficiently. A key requirement for the development of multiple-junction ISB devices for TPV energy conversion is the use of QWs with sufficiently large conduction-band offset, to allow for ISB absorption of thermal radiation over a sufficiently broad spectral range. A possible QC structure is shown in figure 14 along with its bandgap diagramme.

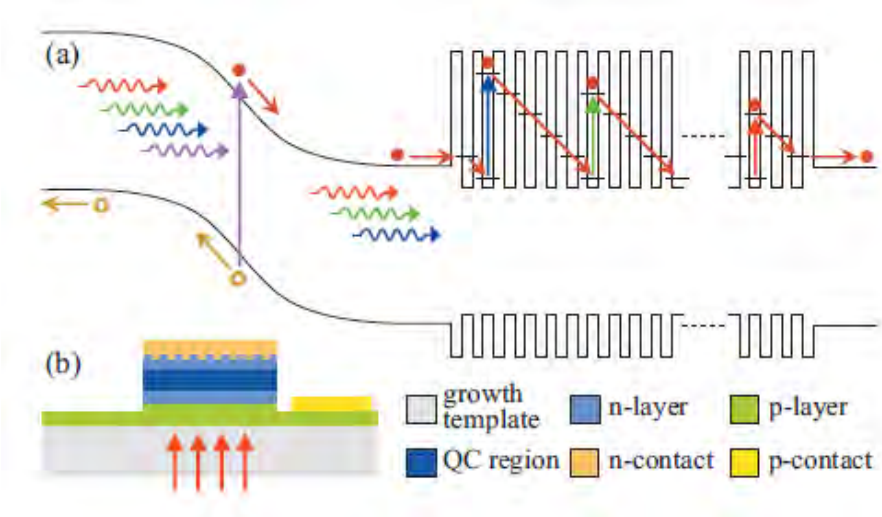


Figure 14: *(a) Schematic band diagramme for the device geometry (b). This structure sums up the advantages of band-band and intersubband absorption. The leftmost side of the band diagramme corresponds to the lower p-layer of the device. The IR radiation has a relatively broad spectrum and reaches the p-layer and the ISB periodical structure travelling across a transparent substrate. After [29].*

It could be fabricated with an $In_{0.67}Ga_{0.33}As$ p-n junction with E_g =0.6 eV, grown p-side down on a semi-insulating InPAs-buffer/InP-substrate, monolithically integrated with different QC stages based on large-conduction-band-offset $In_{0.83}Ga_{0.17}As/AlAs_{0.65}Sb_{0.35}$ QWs. With this choice of compositions, the average lattice constant of the QC active material is very close to that of the p-n junction so that the net strain across the device is practically null and there is no performance degradation due to lattice relaxation and defect formation. The p-n junction allows harvesting the high-energy incident thermal photons that cannot be absorbed later in the QC active material due to the finite conduction band offset ΔE_c of the QWs. At the same time, the individual QC stages are designed to be current-matched to one another and to the underlying interband absorber in order to maximize their combined output electrical power. The input thermal radiation is sent to the device perpendicular to the optically transparent substrate, so that the high-energy photons are immediately absorbed by the p-n junction. The resulting photoelectrons are swept by the junction built-in electric field towards the ISB absorption region where they are injected into the QC stages, while the photoholes are readily collected by the p-side contact. Due to the polarization selection rules of ISB transitions (which can only couple to TM-polarized light), the remaining lower-energy photons cannot be directly absorbed in the QC active material as they propagate towards the top contact. A two-dimensional reflection grating is therefore realized on the device top surface to scatter these photons into the TM guided modes supported by the epitaxial layer on InP. ISB photodetectors with near-unity quantum efficiency under non-polarized normal-incidence illumination were fabricated with this approach.

4. Epitaxial growth of Ga_2O_3 for power electronic applications

Semiconducting sesquioxides, especially Ga_2O_3, are known since decades however it is only in the past few years that they were massively investigated. This is essentially due to the development of suitable technologies for growth of large single crystals [34-36] and homo- and hetero-epitaxial layers [37-40]. The possibility of growing single crystals and films with relatively low defect density, opened the way to new application areas, in addition to the well-known TCO (transparent conducting oxides) electrodes, namely: i) substrates for GaN epilayers ii) high-power transistors, iii) UV detectors.

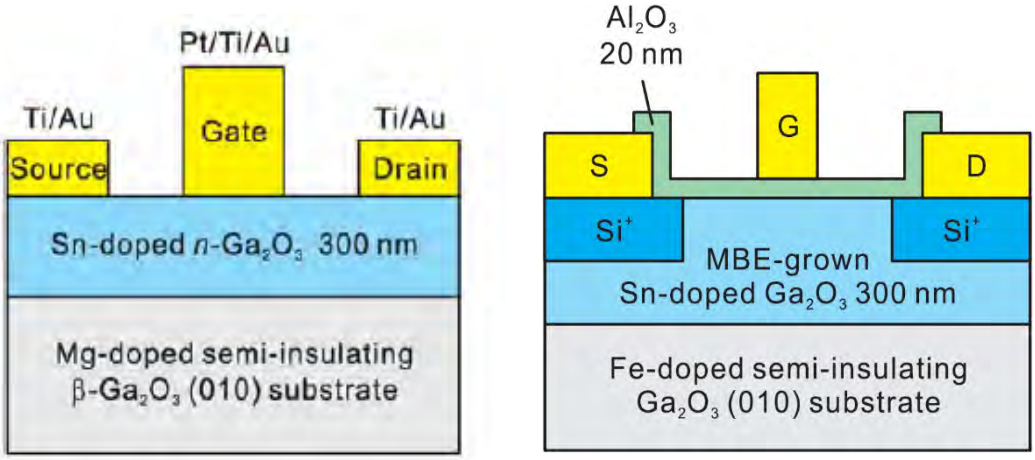


Figure 15: *Schematic structure of MESFET (left) and MOSFET (right) based on homoepitaxial Ga_2O_3 films (after [41]).*

Examples of FET transistors fabricated from homoepitaxial Ga_2O_3 films are shown in Fig. 15. Although the homo-epitaxial growth is supposed to provide layers of higher crystallographic perfection, the deposition of gallium oxide on hetero-substrates such as α-Al_2O_3 (sapphire) is still very popular. It has the advantage of directly providing electrical isolation of the film, which may turn out useful in view of the application of β-Ga_2O_3 to Field Effect Transistors (FETs) or UV photodetectors. Furthermore, sapphire wafers are commercially available with diameters of up to 6" and very cheap compared with the still expensive Ga_2O_3 substrates.

This section will review the recent advances in homo- and hetero-epitaxial deposition of β-Ga_2O_3 by Metal-Organic Vapour Phase Epitaxy (MOVPE). This includes: i) MOVPE deposition of β-Ga_2O_3 on differently-oriented β-Ga_2O_3 homo-substrates; ii) MOVPE deposition of β-Ga_2O_3 on hetero-substrates. It is worth mentioning that Ga2O3 presents five polymorphs (α, β, γ, δ, ε) with very different crystallographic structures and physical properties. Only the β phase is thermodynamically stable and therefore widely studied. In the following we shall concentrate on growth of this polymorph from the vapour phase.

4.1 Homoepitaxial deposition of β-Ga_2O_3

Most investigations on homoepitaxial β-Ga2O3 have been carried out by molecular beam epitaxy (MBE) and more rarely by MOVPE. The reason for this lies in the gap that for a long time existed between the relatively poor structural quality of β-Ga2O3 layers grown by MOVPE in comparison to

MBE materials. Indeed, the maximum electron mobility of MOVPE layers was limited to about 40 cm^2/Vs, while in layers grown by MBE on (010)-oriented homosubstrates it was >100 cm^2/Vs. However, as the MOVPE technology is more suitable for large-scale production of semiconductors, in the last times great efforts were made in order to improve the quality of homoepitaxial β-Ga_2O_3 by MOVPE. Different types of β-Ga_2O_3 wafers were tested as substrates and two orientations were generally used: (100) and (010). Of greatest importance is the wafer surface preparation before initiating the epitaxial growth: the (100) β-Ga_2O_3 substrates must be cleaned with organic solvents and then annealed in oxygen ambient at 1000°C for at least one hours. This is necessary to remove the subsurface polishing damage and get a regular step-and-terrace surface as shown in Figure 16. Of course, the terrace width is a function of the substrate disorientation. In the example of Figure 16 the surface deviated by about 0.2° from the perfect (100) and the corresponding width was about 70-100 nm.

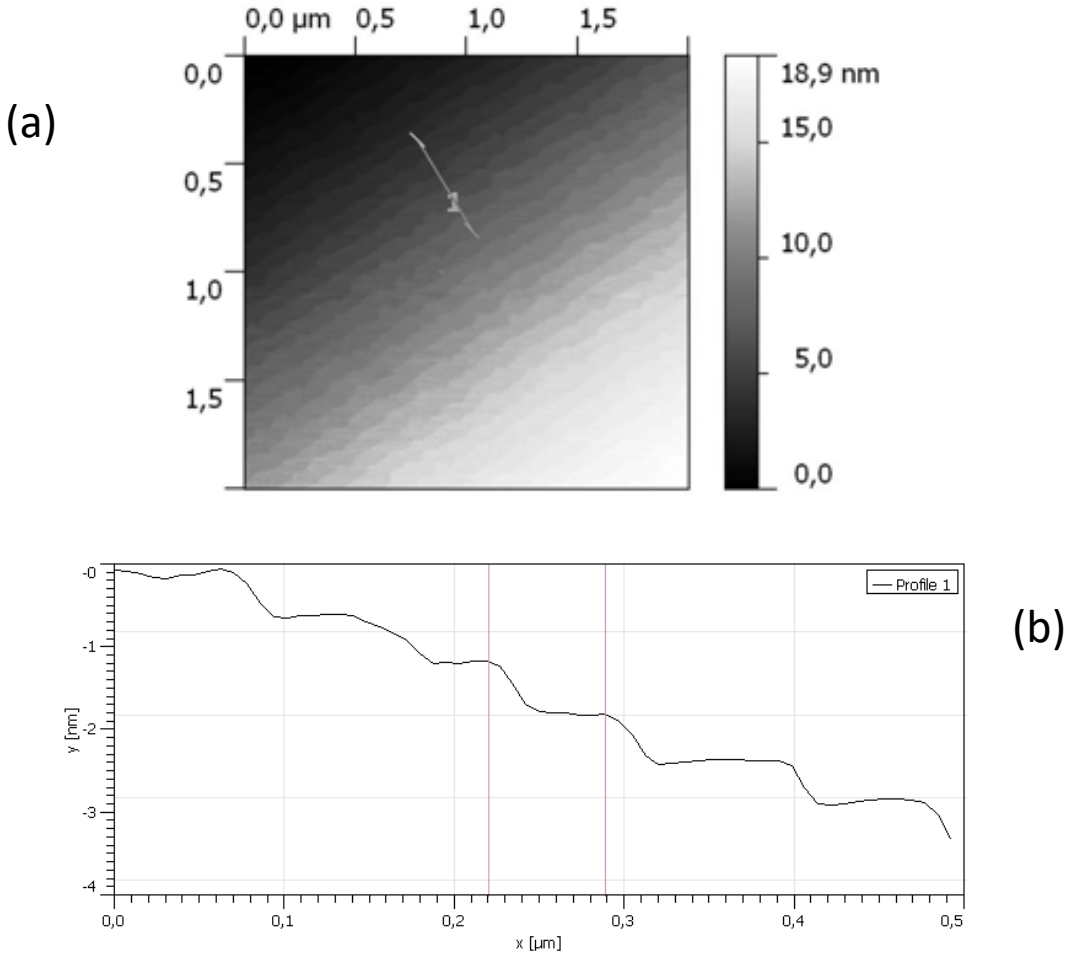


Fig. 16 *(a) AFM image of (100)-oriented β-Ga_2O_3 after thermal annealing at 1000 °C in oxygen ambient; (b) Corresponding surface scan. Note the formation of regular steps (0.6 nm high) and terraces (70-90 nm wide). After ref. [37].*

Trimethylgallium (TMG) is normally taken as Ga precursor while oxygen is supplied either as a pure gas (O_2) or via water dissociation in the growth reactor. Surprisingly, the initial MOVPE deposition on (100) substrates did not result in coherent layers, but rather in nanowire and nanoparticles deposition, when using oxygen gas as oxidation source. This happened for a wide range of epitaxial parameters: substrate temperature between 750 and 850 °C, reactor pressure in the range 5 to 100

mbar, oxygen-to-gallium ratios between 1000 and 9000. In the discussion on the influence of the oxygen precursor on the growth mode, authors of ref. [37] considered the different thermodynamic conditions connected with a large oxygen or hydrogen excess in the reaction chamber. From thermodynamic simulation, they concluded that when using pure oxygen the main reaction products are solid Ga_2O_3 and gaseous oxygen, water, and carbon dioxide, whereas if water is used then hydrogen molecules, H_2, are present in high concentration as compared with formed Ga_2O_3. O_2 molecules are not present at all, since they are fully consumed by reaction with the organic species. The influence of the oxygen precursor on the growth mode was hence qualitatively discussed as follows: when pure O_2 is employed, the formation energy of oxygen vacancies is substantially increased which in turn lowers their concentration. At the same time, H_2O and CO_2 are present in comparable concentrations, which promotes the formation of $Ga_2(CO_3)_3$ that may act as a mask through which whiskers grow. On the other hand, when H_2O is employed, the oxygen partial pressure is considerably low and oxygen vacancies are expected to form spontaneously. This time however H_2O is present at much higher concentrations than CO_2 so that the adsorption of CO_2, and related carbonate formation, is prevented. H_2O simply dissociates at oxygen vacancy sites thus promoting growth. An additional mechanism was also proposed, namely that hydrogen may occupy oxygen vacancy sites forming Ga-H bonds and thus reducing the surface state density. Therefore, this would change the surface potential and the kinetics at the substrate surface, promoting the layer-by-layer growth. The initial decomposition of the substrate, with formation of tiny Ga clusters, which catalyzes the nucleation and growth of nanostructures cannot however be ruled out. If that is the actual case, one is therefore led to conclude that atomic oxygen from water dissociation in the high-temperature reactor chamber is more effective in preventing dissociation of the (100) surface of β-Ga_2O_3. What is sure is that taking H_2O as atomic oxygen source leads to layer-by-layer growth and smooth layers.

The growth of homoepitaxial single-phase β-Ga_2O_3 on (010) substrates by low-pressure CVD was reported in ref. [40]. Authors investigated the surface morphology and crystal quality as a function of growth temperature dependences. The growth studies were carried out in a custom-designed CVD system on commercial (010) β-Ga_2O_3 substrates synthesized by the EFG growth method. The dislocation density of the substrate was estimated to be $< 10^7$ cm^{-2}. High purity gallium pellets and oxygen were used as the source materials and argon (Ar) was used as the carrier gas. A maximum growth rate of 1.3 μm/h was obtained at 850 °C while the best morphology was obtained at 950 °C, at the expenses of a lower growth rate. The smallest root-mean-square surface roughness was ~7 nm. The general trend indicates that the layers become more homogeneous with the increase of growth temperature. The crystal quality and interfacial structure of the β-Ga_2O_3 homoepitaxial layer grown at 850 °C were investigated with cross sectional TEM and HRTEM as well as selected area electron diffraction (SAED) pattern. They confirmed that the deposited crystal is monoclinic β-Ga_2O_3 and that the interface between the grown layer and the substrate is undifferentiable along the cross section, indicating that the layer is coherently grown on the substrate.

The HR-XRD characterisation of the epilayers again showed that the substrate temperature has a great influence on the final crystalline quality of the layers. At 950° the X-ray diffraction pattern of substrate and films were practically overlapping but the film grown and 900 °C was found to be under slight compressive strain, estimated to be of about 0.11%. The reason for such strain was not explained. The growth on (010) β-Ga_2O_3 substrates seems to be more favorable in terms of higher crystalline perfection than the growth on (100) substrates. Furthermore, if one considers that the thermal conductivity of bulk β-Ga_2O_3 is anisotropic, being higher along the [010] direction (27.0W/mK at RT) and substantially lower along the [100] direction (10.9 W/mK at RT), the (010)-oriented substrates become advantageous from the point of view of heat dissipation. Actually, in

power devices fabricated on (010) substrates the heat transfer is predicted to be almost three times more efficient than in other directions. This is an interesting finding, although the overall thermal conductivity of bulk β-Ga_2O_3 remains lower than the one of the competing materials SiC and GaN.

Further experiments on the homoepitaxial growth of β-Ga_2O_3 on (010) substrates by MOVPE clearly showed that (010)-oriented films generally possess higher structural quality and are easier to grow with respect to (100) orientation [42]. Authors used triethylgallitm (TEG) and O_2 as precursors under standard temperature and pressure conditions of 850 ◦C and 5 mbar. The layers exhibited a flat surface with a mean roughness (RMS) of ∼600 pm. The morphology being dominated by elongated islands oriented along the [001] direction. The growth rate, estimated from the resulting layer thickness and the growth time, was 2 nm/min, which was about 20% higher than that of layers grown on (100) substrates by the same group [11]. This result contrasted published data for MBE growth reporting that growth rates on (010) surfaces are more than ten times higher than those on (100) substrates because of a higher re-evaporation rate of the highly volatile Ga_2O species from the (100) plane [43]. Attempts to increase the growth rate by applying higher TEG and O_2 flow rates, while keeping a constant molar ratio between the two precursors, resulted in progressively increasing roughness up to RMS value of about 11 nm. The epitaxial growth on (010) Fe-doped semi-insulating β-Ga_2O_3 substrates proved to be very suitable from the point of view of n-type doping. Actually, by using tetraethylorthosilicate (TEOS) and tetraethyltin (TESn) as metallorganic precursors for Si and Sn, it was possible to achieve very high carrier concentrations. When the flow rates of TEOS and TESn were varied in the range $\sim 1 \times 10^{-11} - 1 \times 10^{-8}$ mol/min, the free carrier concentrations could be adjusted in the doping range 1×10^{17} and 8×10^{19} cm^{-3} [39]. It seems however that Si has to be preferred as donor, because of its higher incorporation rate and no memory effects in the MOVPE reactor.

In ref. [44], the electrical transport properties of Si-doped β-Ga_2O_3 (100) homoepitaxial layers were studied as a function of substrate misorientation: the layers perfectly (100) oriented, or with small off-orientation, exhibited low mobility values as well as low doping efficiency. Furthermore, the Hall mobility collapsed below a threshold electron concentration (about 10^{18} cm^{-3}), in that reproducing the behaviour already observed for Sn-doped layers. By using transmission electron microscopy (TEM), authors showed that these homoepitaxial layers contained a very high density of twin lamellae with two different atomic structures, namely coherent boundaries parallel to (100) and incoherent ones parallel to (001). While the former type of twins preserves the atomic coordination, in case of the incoherent twin boundaries (ITBs) one dangling bond per unit cell is present. The dangling bonds are arranged along the ITBs of thin twin lamellae and may act as acceptors. Thanks to this observation, it could be quantitatively confirmed that mobility reduction and collapse, as well as part of the compensation, are due to the presence of twin lamellae. Figure 17 shows the presence and distribution of such defects in layers homoepitaxially grown on substrates with different mis-cuts between 0.1 and 4 °. It is apparent that only substrates with relatively large mis-orientation yield layers free of laminar twins. On the other hand, one should remember that the terrace width changes with the mis-orientation, i.e. it is larger for small angles, which enhances the probability of 2D island nucleation, as schematically reported in Fig. 18. The way Ga atoms may stick to the surface is clearly twofold, therefore if they do not reach the step, due to large terraces or reduces diffusivity, the chance of laminar twinning becomes high.

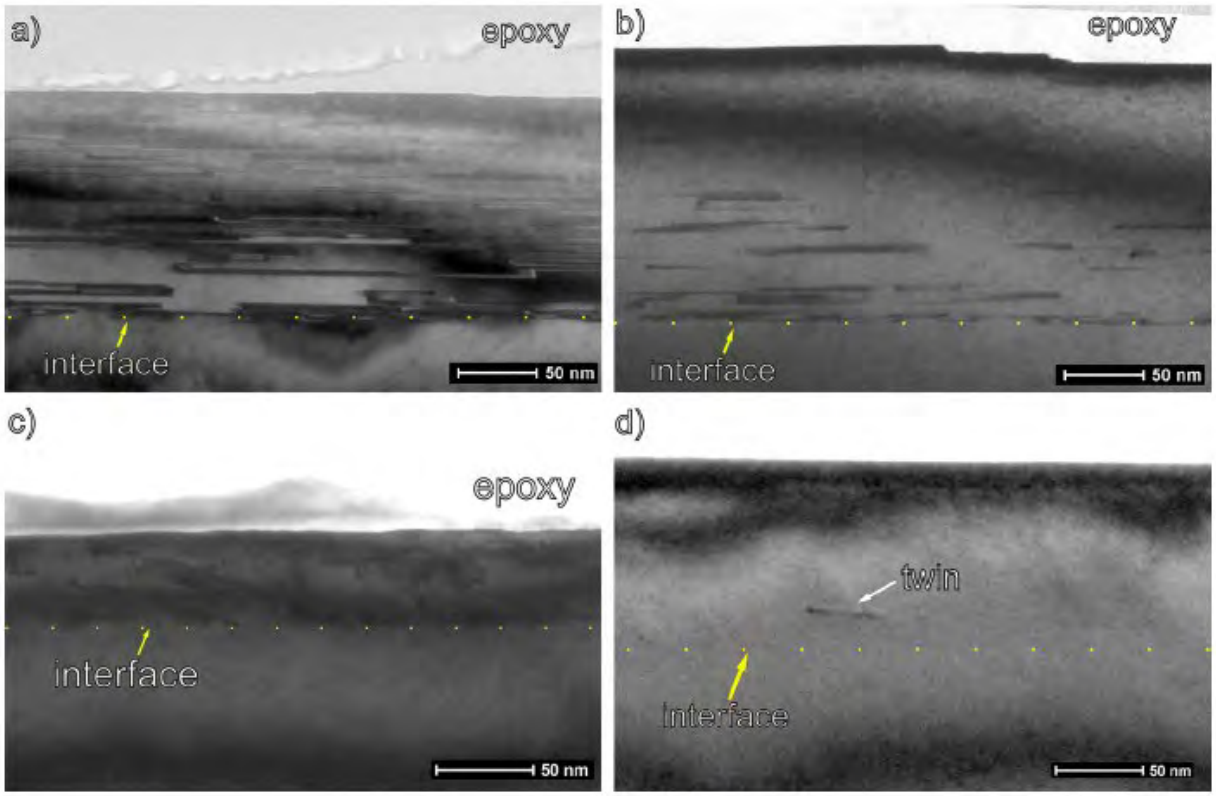


Fig. 17: *TEM study of twin lamellae in homoepitaxial (100) β-Ga_2O_3. A) Substrate with off-orientation of 0.1°; b) of 0.2 °; c) of 2.0° and d) of 4.0° (after ref. [44])*

The homoepitaxial growth by MOVPE on (100) β-Ga_2O_3 is therefore quite complicated. The stacking faults, in form of laminar twins, are characterized by a c/2 glide reflection as twin relation. Coalescence of twinned and epitaxial 2D islands results in the formation of incoherent twin boundaries that actually present electrically-active dangling bonds, and thus compensate and reduce the mobility of charge carriers. The limited surface diffusion of the Ga-adatoms and the small substrate miscut-angle are responsible for the high density of stacking-faults experimentally observed in homoepitaxial films. Therefore, one should look for growth conditions that yield step-flow. Possible approaches towards twin-free epilayers include: higher growth temperatures or application of surfactants to enhance the species diffusion on the surface or reduction of terrace width by adopting substrates with high miscut-angles of about 6°. The diffusion coefficient of Ga at the gas-solid interface at the growth temperature of 850 °C was estimated to be $7x10^{-9}$ cm^{-2} s^{-1}, i.e. two orders of magnitude lower than the one experimentally found in GaAs and even 6 orders of magnitude higher than for cubic GaN.

In another study on homo- and heteroepitaxial β-Ga_2O_3 is it was pointed out that in spite of a heavy Si-doping the films were found to be electrically insulating [45]. The positron annihilation study of these samples evidenced a relatively high Ga vacancy concentration (>$5x10^{17}$ cm^{-3}), higher than the silicon concentration of $10^{17}cm^{-3}$. Theoretical calculations predict that the V_{Ga} should be in a negative charge state when Fermi levels is located in the upper half of the band gap, hence compensating for n-type doping. The high resistivity of those Si-doped β-Ga_2O_3 epilayers was therefore attributed to the experimentally observed Ga vacancy concentrations in films.

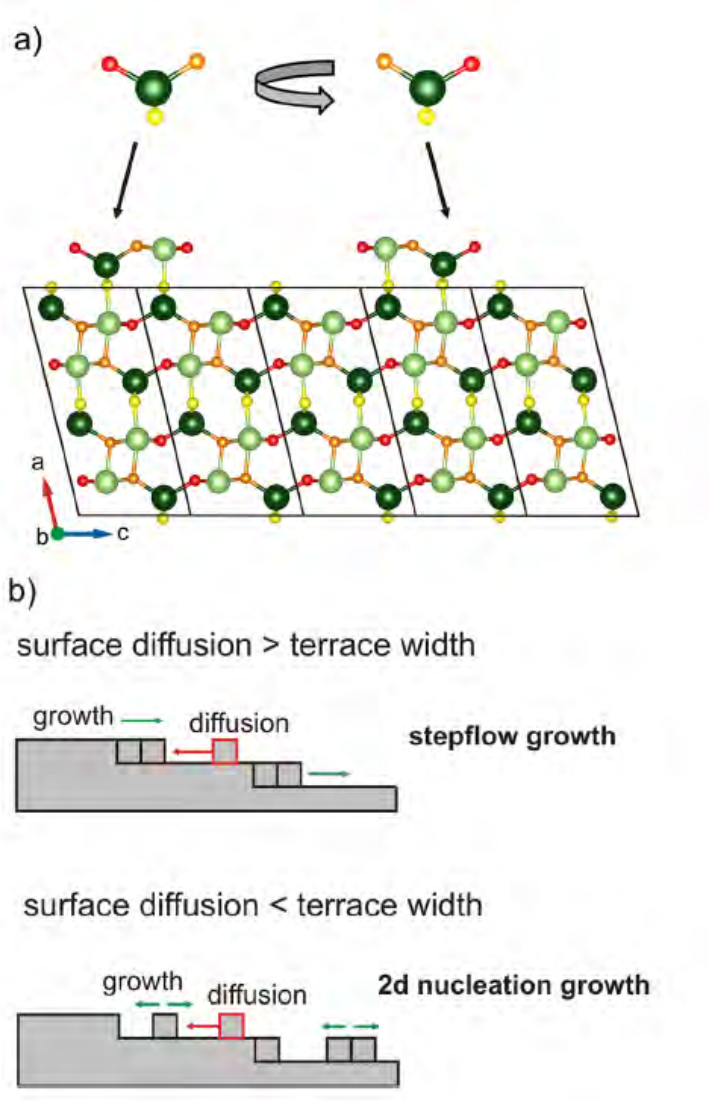


Fig. 18: *Schematic of monolayer growth on a terraced (100) surface of β-Ga_2O_3: a) Stick-and-ball model illustrating two possible positions of Ga on the (100); dark green and light green balls correspond to tetrahedral (Ga I) and octahedral (Ga II) bound Gallium atoms, respectively. The little red, orange, and yellow balls correspond to different oxygen sites OI, OII, and OIII. b) Schematic diffusion model showing step-flow growth or island nucleation in dependence of terrace width and/or atom surface diffusion coefficient. (after [44])*

4.2 Heteroepitaxial deposition of β-Ga_2O_3

So far, most work on Ga_2O_3 heteroepitaxy has been done with plasma-assisted MBE and relatively little with MOVPE. (0001)-oriented sapphire wafers were by far the most used hetero-substrates [40, 46-48], although attempts were made also on GaAs [49], $MgAl_2O_4$ [50], MgO [51] and SiC [52] substrates.

MOVPE heteroepitaxy of β-Ga_2O_3 was performed on both a-plane and c-plane sapphire substrates using a trimethylgallium (TMGa) precursor (22.5 lmol/min) and approximately 5:1 O_2/TMGa flow rate ratio. A pressure level of 6.67 kPa (0.066 atm, 50 Torr) at a temperature range of 600°C to 800°C was used to obtain crystalline films in the preferred phase. According to Raman investigation, the films were not phase-pure but probably contained some α-Ga_2O_3 inclusions as

well as other Ga-related phases. It is to be recalled here that small α-phase inclusions were usually detected in heteroepitaxial Ga_2O_3 by high-resolution TEM whichever the deposition technique. Clear X-ray diffraction peaks of β-Ga_2O_3 with (-201) orientation were observed for films grown on c-plane sapphire; while for growth on a-face sapphire other peaks with different orientations were also observed, suggesting a less oriented film. Least-squares refinement was performed to obtain the lattice constant values of the films grown on c-plane and a-plane substrates. For the c-plane sample, the lattice constants were a = 12.2648(20) Å, b = 3.0315(2) Å, and c = 5.8237(10) Å, and for the a-plane sample they were a = 12.2212(14) Å, b = 3.0384(7) Å, and c = 5.8315(6) Å. The full width at half-maximum (FWHM) from the rocking curve of the (-402) reflection was 2.42°, i.e. higher than typical FWHM values obtained for homoepitaxial β-Ga_2O_3. This result indicates that MOVPE on foreign substrates requires significant improvement effort to improve the Ga_2O_3 crystallographic quality.

In a study aiming at assessing the Sn doping in homo- and heteroepitaxial β-Ga_2O_3, Gogova et al. [39] reported that MOVPE deposition on (0001) sapphire always results in (-201)-oriented monoclinic films. The X-ray peaks positioned at 2θ = 18.9°, 37.8°, 58.7° and 80.7° were assigned to the –201, −402, −603 and −804 Bragg reflections of the β-phase. No additional Bragg peaks from the layer were observed proving evidence that the layers contained only β phase. It must however be noted that (−201)-oriented β-Ga_2O_3 layers indeed grow epitaxially on sapphire but are not single crystalline since there is an in-plane rotation of 60° between grains due to the difference in the crystal symmetry of the substrate (hexagonal) and the epilayer (monoclinic).

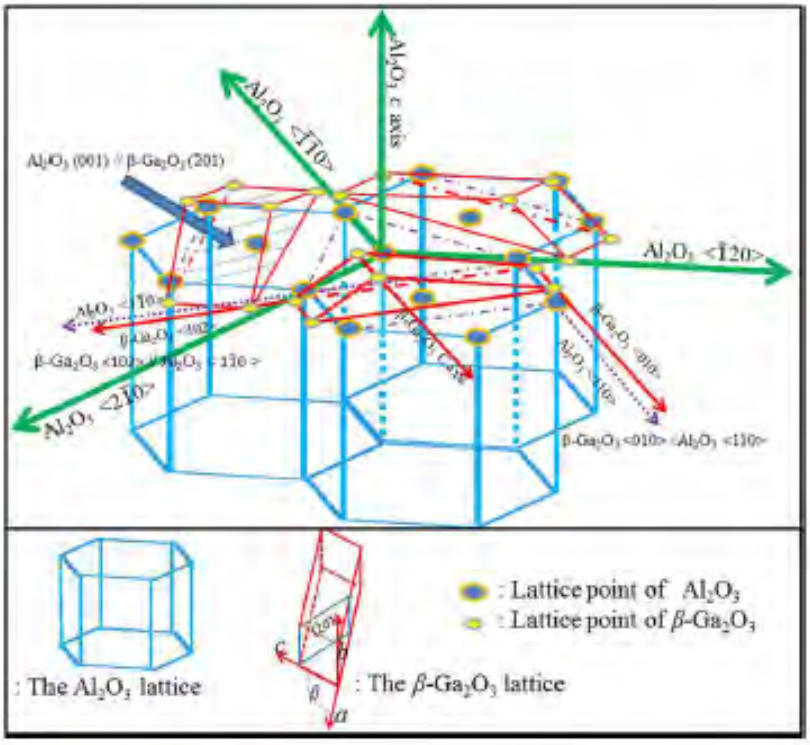


Fig. 18: *Origin of domains in heteroepitaxially-grown (−201)-oriented β-Ga_2O_3 layers on c-oriented sapphire according to ref. [46].*

Such grains were previously observed by Nakagomi et al. [53] and Chen et al. [46], and also detected by TEM investigation. The authors concluded that films on both (001) c-plane and (110) a-plane sapphire are (-201) oriented. β-Ga_2O_3 films formed on the (001) c-plane sapphire consist of

six types of β-Ga_2O_3 crystal rotated every 60° from the [110] direction. Similarly, β-Ga_2O_3 thin films on the (110) a-plane sapphire consist of six types of β-Ga_2O_3 crystals rotated by multiples of 60° from the [1-1 0] or [-110] direction. This crystal orientation of β-Ga_2O_3 formed on the c-plane or the a-plane sapphire depends on the arrangement of oxygen atoms on the substrate surface.

Using high resolution XRD, θ–2θ and Φ-scan measurements, the Bragg angles of β-Ga_2O_3 (-201), (-401), (111) and (-111) planes were measured in order to estimate the lattice constants a, b, c, and angle β of the monoclinic film. Comparing with the standard value reported for β-Ga_2O_3 single crystals, the values of a and c appear to be smaller, while the angle β becomes larger, only the value of b is practically unvaried. According to the epitaxial relationship between β-Ga_2O_3 film and c-plane sapphire substrate, one is led to conclude that β-Ga_2O_3 lattice would suffer compressive strain along [102] direction. The lattice mismatch and the six different types of β-Ga_2O_3 domains on c-oriented Al_2O_3 are therefore a major obstacle towards high-quality β-Ga_2O_3 films on sapphire. As shown in Fig. 18, indeed there are three different types of β-Ga_2O_3 crystal grains plus another three types that originate from the rotation of 180° of the scheme. The β-Ga_2O_3 (-201) plane is parallel to the (0001) sapphire surface, while the β-Ga_2O_3 [102] and [010] directions run parallel to the Al_2O_3 [1-10] and [110] directions, respectively. It is to be observed that both cited works assume that the (-201) plane of β-Ga_2O_3 lays parallel to the c-surface and that there are six in-plane domains resulting from 60°rotations about the [-201] axis of gallium oxide. However, the description of the gallium oxide-to-sapphire arrangement of sapphire differs by 60°. This may be due to the different deposition methods or to a misinterpretation of the X-ray diffraction data. Unfortunately, there are no additional comprehensive studies that can definitely clarify how the two lattices position with respect to each other.

In a recent report, Alema et al. [48] showed how to increase the β-Ga_2O_3 growth rate by applying a MOVPE close coupled showerhead reactor, where the substrate-to-showerhead separation was about 10 mm. The growth was carried out on (0001) sapphire (2 in.) substrates using solid $Ga(DPM)_3$ (DPM = Dipivaloylmethanate), and liquid Triethylgallium (TEGa) as well as Trimethylgallium (TMGa) metal organic precursors (MO) as the sources for Ga. The film growth was conducted from the respective sources by sublimating $Ga(DPM)_3$ at 155 °C or evaporating the TEGa and TMGa sources, respectively, at 22 °C and 5 °C. The vaporized Ga sources were carried into the reactor by Ar gas. A pure molecular oxygen (5 N) was separately injected into the reactor to mix with the TEGa, TMGa and $Ga(DPM)_3$ precursors in the proximity of the substrate for oxidation with oxygen flow rates of 300, 800 and 800 sccm, respectively. β-Ga_2O_3 thin film growth was performed at a chamber pressure of 30-120 Torr and substrate temperatures between 750 and 950°C. All Ga_2O_3 thin films grown from each MO sources were visibly smooth and transparent, but electrically highly resistive (sheet resistance $>10^9$ Ω /square), as no measurable conductivity was detected by the Hall effect technique. The deposited layers were (-201) oriented and exhibited good crystallographic characteristics as proved by narrow peaks in positions overlapping those of high-quality bulk Ga_2O_3. Unfortunately, authors did not perform a study about the actual epitaxial relationships between sapphire and β-Ga_2O_3 film, which would have confirmed one of the two options discussed above.

It is however remarkable that the close-coupled reactor allows for a very high deposition rate, which may reach 10 μm/h, that is about one order of magnitude higher than for standard horizontal or vertical reactors. This successful demonstration of high growth rate for β-Ga_2O_3 films using various Ga-precursors was achieved thanks to the separate injection of oxygen and MO precursors, as well as the close couple showerhead design of the MOVPE reactor which prevents the premature

oxidation of the MO precursors. These results are particularly interesting as they offer a solution to the long-standing challenge of realizing fast growth rate of Ga_2O_3 by MOVPE. Actually, so far only H-VPE provided monoclinic Ga_2O_3 films at a rate of several μm/h [54, 55].

REFERENCES

[1] R.D. Dupuis, P.D. Dapkus, R.D. Yingling, L.A. Moudy, Appl. Phys. Lett. 31 (1977) 201.

[2] J.M. Olson, S.R. Kurtz, A.E. Kibbler, P. Faine, Appl. Phys. Lett. 56 (1990) 624.

[3] T. Takamoto, T. Agui, E. Ikeda, H. Kurita, Sol. Energy Mater. Solar Cells 66 (2001) 511.

[4] M. Stan, D. Aiken, B. Cho, A. Cornfeld, J. Diaz, V. Ley, A. Korostyshevsky, P. Patel, P. Sharps, T. Varghese, J. Cryst. Growth 310 (2008) 5204.

[5] N.H. Karam, R.R. King, M. Haddad, J. H. Ermer, H. Yoon, H. L. Cotal, R. Sudharsanan, J. W. Eldredge, K. Edmondson, D. E. Joslin, D. D. Krut, M. Takahashi, W. Nishikawa, M. Gillanders, J. Granata, P. Hebert, B.T. Cavicchi, D. R. Lillington, Solar Energy Mater. and Solar Cells 66 (2001) 453.

[6] J. F. Geisz, D. J. Friedman, J. S. Ward, A. Duda, W. J. Olavarria, T. E. Moriarty, J. T. Kiehl, M. J. Romero, A. G. Norman, and K. M. Jones. (2008), Appl. Phys. Lett , Vol. 93, p. 123505 .

[7] W. Guter, R. Kern, , W. Köstler, T. Kubera, R. Löckenhoff, M. Meusel, M. Shirnow, G. Strobl. AIP Conf. Proc., Vol. 1407, (2011) p. 5.

[8] H. Cotal, C. Fetzer, J. Boisvert, G. Kinsey, R. King, P. Hebert, H. Yoon and N. Karam, Energy Environ. Sci. 2 (2009) 174.

[9] M. A. Green, K. Emery, Yoshihiro Hishikawa, W. Warta, E. D. Dunlop. Prog. Photovoltaics: Res. Appl. 21 (2013) 1.

[10] F. Dimroth, Phys. Stat. Sol. C 3 (2006) 373.

[11] C.M. Fetzer, X.Q.Liu, J.Chang, W.Hong, A.Palmer, D.Bhusari, B. Jun, M. Lau, H. Lee. J. Cryst. Growth 352 (2012) 181.

[12] S. Oh, D.H. Jun, C.I. Hye, E. Yoon, W.K. Park: AIP Conf. Proceedings, Vol. 1556, 2013, p. 101.

[13] M.M. Wilkins, A.Boucherif, R. Beal, J.E. Haysom, J. F. Wheeldon,V. Aimez, R. Ares, T. J. Hall, K. Hinzer, IEEE J. of Photovoltaics 3 (2013) 1125.

[14] J.W. Mathews, S. Mader, T.B. Light, J. Appl. Phys. 41 (1970) 3800.

[15] H.C. Luan, D.R. Lim, K.K. Lee, K.M. Chen, J.G. Sandland, K. Wada, L.C. Kimerling, Appl. Phys. Lett.75 (1999) 2909.

[16] G. Vanamu, A.K. Datye, S.H. Zaidi, J. Crystal Growth 280 (2005) 66.

[17] T.A. Langdo, C.W. Leitz, M.T. Currie, E.A. Fitzgerald, A. Lochtefeld, D.A. Antoniadi, Appl. Phys. Lett. 76 (2000) 3700.

[18] Q. Li, S.M. Han, S.R.J. Brueck, S. Hersee, Y.B. Jiang, H. Xu, Appl. Phys. Lett. 83 (2003) 5032.

[19] S.M. Vernon, S.P.Tobin, V.E.Haven, L. M. Geoffroy, M.M. Sanfacon, Proc. 22nd IEEE Photovoltaic Spec. Conf. 1991, p. 353.

[20] M. R. Lueck, C. L. Andre, A. J. Pitera, M. L. Lee, E. A. Fitzgerald, S. A. Ringel, IEEE Electr. Dev.Lett. 27 (2006) 142.

[21] N.J. Ekins-Daukes, J.M. Barnes, K.W.J. Barnham, J.P. Connolly, M. Mazzer, J.C. Clark, R. Grey, G. Hill, M.A. Pate, J.S. Roberts, Solar Energy Mat. and Solar Cells 68 (2001) 71.

[22] D. B. Jackrel, S. R. Bank, H. B. Yuen, M. A. Wistey, J. S. Harris Jr., A. J. Ptak, S. W. Johnston, D. J. Friedman, S. R. Kurtz, J. Appl. Phys. 101 (2007) 114916.

[23] T.J. Garrod, J. Kirch, P. Dudley, S. Kim, L.J. Mawst, T.F. Kuech, J. Crystal Growth 315 (2011) 67.

[24] T.W. Kim, K. Kim, J.J. Lee, T.F. Kuech, L.J. Mawst, N.P. Wells, S.D.LaLumondiere, Y.Sin, W.T. Lotshaw, S.C.Moss. 2013, Appl. Phys. Lett. 104 (2014) 051915

[25] X. Chen, K. D. Matthews, D. Hao, W. J. Schaff, L. F. Eastman, Phys. Stat. Sol. (a) 205 (2008) 1103.

[26] G.W. Charache J.L. Egley, D.M. Depoy, L.R. Danielson, M.J. Freeman, R.J. Diendzdiel, J.F. Moynihan, P.F. Baldasaro, B.C. Campbell, C.A. Wang, H.K. Choi, G.W. Turner, S.J. Wojtczuk, P. Colter, P. Sharps, M. Timmons, R.E. Fahey, K. Zhang, J. Electron. Mater. 27 (1998) 1038.

[27] G.B.Stringfellow, J. Crystal Growth 58 (1982) 144.

[28] R. R. Siergiej, S. Sinharoy, T. Valko, R. J. Wehrer, B. Wernsman, S. D.Link, R. W. Schultz, R. L. Messham, AIP Conf. Proc. Vol. 738 (2004) p. 480.

[29] J.Yin, R. Paiella, Appl. Phys. Lett. 98 (2011) 041103.

[30] D. Hofstetter, F. R. Giorgetta, E. Baumann,Q. Yang, Ch. Manz, K. Köhler, Appl. Phys. Lett. 93 (2008) 221106.

[31] L. Bhusal, A. Freundlich, J. Appl. Phys. 102 (2007) 074907.

[32] F. R. Giorgetta, E. Baumann, D. Hofstetter, C. Manz, Q. Yang, K. Köhler, M. Graf, Appl. Phys. Lett. 91 (2007) 111115.

[33] H.C.Liu, F. Capasso (Eds.), Intersubband transitions in quantum wells (Series Semiconductors and Semimetals Eds. R.K.Willardson and E.Weber, Vol.62), Academic Press, 2000.

[34] Y. Tomm, P. Reiche, D. Klimm, and T. Fukuda, J. Cryst. Growth 220 (2000) 510.

[35] A. Kuramata, K. Koshi, S. Watanabe, Y. Yamaoka, T. Masui, S. Yamakoshi, Jpn. J. Appl. Phys. 55 (2016) 1202A2.

[36] Z. Galazka, R. Uecker, K. Irmscher, M. Albrecht, D. Klimm, M. Pietsch, M. Brützam, R. Bertram, S. Ganschow, R. Fornari, Crystal Res. Technol. 45 (2010) 1229.

[37] G. Wagner, M. Baldini, D. Gogova, M. Schmidbauer, R. Schewski, M. Albrecht, Z. Galazka, D. Klimm, R. Fornari: Phys. Status Solidi A 211 (2014) 27.

[38] W. Mi, J. Ma, C. Luan, H. Xiao, J. Lumin. 146 (2014) 1.

[39] D. Gogova, M. Schmidbauer, A. Kwasniewski, CrystEngComm, 17 (2015) 6744.

[40] S. Rafique, L. Han, M. J. Tadjer, J. A. Freitas, N. A. Mahadik, H. Zhao, Appl. Phys. Lett. 108 (2016) 3.

[41] M. Higashiwaki, A. Kuramata, H. Murakami, Y. Kumagai, J. Physics D: Appl. Phys. 50 (2017) 333002.

[42] M. Baldini, M. Albrecht, A. Fiedler, K. Irmscher, D. Klimm, R. Schewski, G. Wagner, J. Mater. Sci. 51 (2016) 3650.

[43] K. Sasaki, A. Kuramata, T. Masui, E. G. Víllora, K. Shimamura, S. Yamakoshi, Appl. Phys. Express 5 (2012) 35502.

[44] A. Fiedler, R. Schewski, M. Baldini, Z. Galazka, G. Wagner, M. Albrecht, K. Irmscher, J. Appl. Phys.122 (2017) 165701.

[45] E. Korhonen, F. Tuomisto, D. Gogova, G. Wagner, M. Baldini, Z. Galazka, R. Schewski, M. Albrecht, Appl. Phys. Lett. 106 (2015) 242103.

[46] Y. Chen, H. Liang, X. Xia, P. Tao, R. Shen, Y. Liu, Y. Feng, Y. Zheng, X. Li, G. Du, J. Mater. Sci. Mater. Electron. 26 (2015) 3231.

[47] Y. Lv, J. Ma, W. Mi, C. Luan, Z. Zhu, H. Xiao, Vacuum 86 (2012) 1850.

[48] F. Alema, B. Hertog, A. Osinsky, P. Mukhopadhyay, M. Toporkov, W. V. Schoenfeld, J. Cryst. Growth 475 (2017) 77.

[49] V. Gottschalch, K. Mergenthaler, G. Wagner, J. Bauer, H. Paezelt, C. Sturm, U. Teschner, Phys. Status Solidi 206 (2009) 243.

[50] W. Mi, J. Ma, C. Luan, H. Xiao, J. Lumin. 146 (2014) 1.

[51] L. Kong, J. Ma, C. Luan, Z. Zhu, J. Solid State Chem. 184 (2011) 1946.

[52] S.A.O. Russell, A. Perez-Tomas, C. McConville, C.A. Fischer, D. P. Hamilton, P. A. Mawby, M. R. Jennings, J. Electron Dev, Soc. 5 (2017) 256.

[53] S. Nakagomi and Y. Kokubun, J. Cryst. Growth 349 (2012) 12.

[54] Q. T. Thieu, D. Wakimoto, Y. Koishikawa, K. Sasaki, K. Goto, K. Konishi, H. Murakami, A. Kuramata, Y. Kumagai, S. Yamakoshi, Jpn. J. Appl. Phys. 56 (2017) 110310.

[55] K. Nomura, K. Goto, R. Togashi, H. Murakami, Y. Kumagai, A. Kuramata, S. Yamakoshi, A. Koukitu, J. Cryst. Growth 405 (2014) 19.

13. Crystal Growth of 0, 1 and 2D Materials

Synthesis of Layered Transition Metal Dichalcogenides – from Bulk Crystals to Epitaxial Monolayers

Joan M. Redwing

2D Crystal Consortium – Materials Innovation Platform
Department of Materials Science and Engineering
The Pennsylvania State University, University Park, PA USA
E-mail: jmr31@psu.edu

Zakaria Y. Al Balushi

Department of Materials Science and Engineering
University of California, Berkeley, CA USA
E-mail: albalushi@berkeley.edu

Scope of the lecture

2D monolayers, surfaces and interfaces associated with layered metal chalcogenides have emerged as a compelling class of materials with transformative new science that can be harnessed for novel device technologies. Particular interest has focused on the properties of monolayer and few-layer transition metal dichalcogenide (TMD) films which can be formed by exfoliation of bulk crystals or vapor phase deposition methods. This lecture will review the structural and physiochemical properties of TMD crystals and fundamental issues associated with their synthesis in bulk and thin film form. Techniques for bulk crystal growth, vapor phase deposition and epitaxial growth of layered metal chalcogenides are highlighted along with methods for the formation of 2D heterostructures.

1. Introduction

Transition metal dichalcogenides (TMDs) form a compelling class of 2D materials with potential applications in optoelectronics, flexible electronics, chemical sensing and quantum technologies. At the monolayer limit, the semiconducting TMDs (*e.g.*, MX_2 where M = Mo/W and X = S/Se) exhibit direct band gaps within the visible range and large exciton binding energies.[1,2] The lack of out-of-plane bonding on the van der Waals surface of these materials enables heterostructure formation without the constraints of lattice matching.[3] Furthermore, the lack of inversion symmetry in the monolayer results in unique optical selection rules, enabling circularly polarized light to selectively populate degenerate valleys in the Brillouin zone which provides an additional degree-of-freedom for the realization of valleytronic devices.[4] There is also growing interest in the properties of metallic TMDs such as VS_2 and VSe_2 which exhibit ferromagnetism and 1T-$MoSe_2$ and Td-WTe_2 which are Weyl semimetals.[5]

1.1 Crystal structure and electronic properties of TMDs

TMDs crystallize as layered compounds comprised of metal atoms that are sandwiched between chalcogen atoms with stoichiometry of 1:2, respectively. The metal and chalcogens are bound by strong covalent bonds within a layer and the layers stack and are held together by weaker van der Waals bonds (Figure 1a).[6] As a result of the weak interaction between layers, a single layer (referred to as a monolayer) or stack of a few layers can be readily exfoliated from the bulk crystal. Approximately 40 different TMD compounds exist which are comprised of transition metals from Groups 4, 5, 6, 7, 9 and 10 of the period table along with S, Se and Te (Figure 1b).

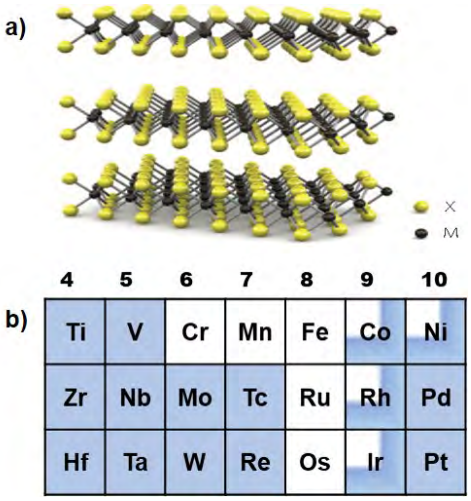


Figure 1. (a) Crystal structure of TMD designated as MX_2 where M=transition metal and X=chalcogen. (b) Transition metals that crystallize as layered dichalcogenides (solid blue). Co, Rh, Ir and Ni have dichalcogenide phases that are not layered (partial blue) (adapted from ref. 6).

The bonding arrangement or coordination of the metal and chalcogen atoms can be viewed as consisting of two tetrahedrons that are stacked in opposite directions to each other (Figure 2a).[5] The particular phases, which are designated as the H and T phases, are defined by the arrangement of the tetrahedra. In the H-phase, the upper and lower tetrahedra are arranged symmetrically to form a trigonal prismatic structure. In the T-phase the upper tetrahedron is rotated by 180° forming an octahedral structure which is typically distorted. As viewed from the top (inset in Figure 2a), the metal and chalcogen atoms exhibit hexagonal symmetry which is characteristic of TMDs.

In addition to the bonding arrangement of atoms, the stacking sequence of layers, also referred to as the polytype, impacts the electronic structure, vibrational modes and optical properties. The particular polymorph or polytype is designated using a number in the phase nomenclature. For example, the 2H phase consists of two layers with AB stacking while the 1-T phase has AA stacking (Figure 2b). The transition metals can also dimerize resulting in distortion of the chalcogen atoms out-of-plane which in turn changes the symmetry from 3-fold to 2-fold as exemplified by the 1T' phase. The distorted T phase (Td) is similar to the 1T' but exhibits a different c-axis angle. Additional phases include 3R (R refers to rhombohedral) and 4H.

The electronic properties of the TMD bulk crystal are dependent on the coordination and number of d-electrons in the transition metal.[7] For monolayer TMDs (1H and 1T phases), the non-bonding d-bands of the TMDs are located within the gap between the bonding and antibonding bands of M-X bonds (Figure 3a). The electronic properties of TMDs arise from the extent of filling of the non-bonding *d*-bands which determines whether the material is semiconducting or metallic and also whether it exhibits magnetic properties. When the orbitals are partially filled, as is the case for Group 5 and Group 7, the TMD exhibits metallic conductivity as is the case for 2H-$NbSe_2$ and 1T-ReS_2. When the orbitals are fully occupied, as is the case for Groups 4, 6 and 10, the TMD is a semiconductor as is the case for 1T-HfS_2, 2H-MoS_2 and 1T-PtS2. The chalcogen atom has

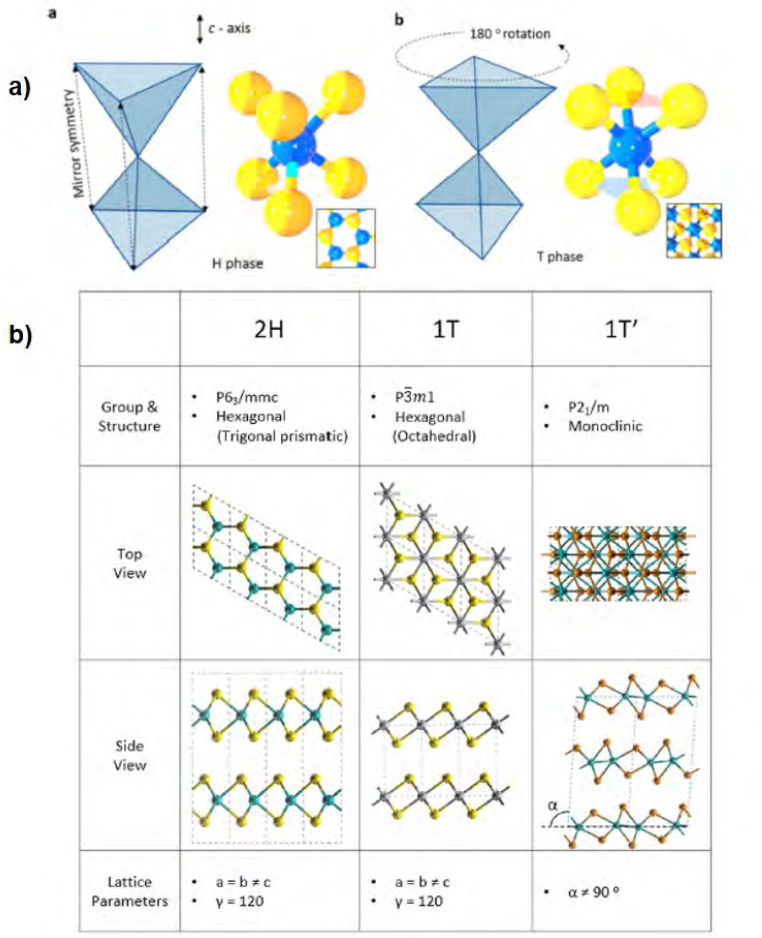


Figure 2. (a) Primary phases for 1:2 (metal:chalcogen) TMD: H phase and T phase. (b) Crystal structures (top and side view) of common TMD phases. (adapted from ref. 5)

less influence on the electronic properties compared to the transition metal, however, a general trend is toward a decreasing bandgap moving from S to Se to Te.

A reduction in the number of layers of the TMD results in a significant change in electronic properties which is particularly pronounced in semiconducting TMDs. These effects arise due to a combination of changes in crystal symmetry, dielectric environment and quantum confinement. Bulk 2H-MoS_2, for example, is an indirect-gap semiconductor while monolayer MoS_2 is direct gap with valence band maximum and conduction band minimum occurring at the K-point (Figure 3b). Furthermore, as a result of the lack of inversion symmetry, there are two inequivalent momentum valleys, K and K' within the first Brouillon zone of monolayer MoS_2 (Figure 3c). As a result of strong spin-orbit coupling, the valence band at these valleys splits with opposite spin splitting for K and K'. Electrons with a particular spin can be excited via circularly polarized light and will populate only one of the two valleys which is known as valley polarization. The control of valley polarization and its detection using light or electric fields offers an additional degree of freedom which may be exploited in the development of "valleytronic" switching devices.

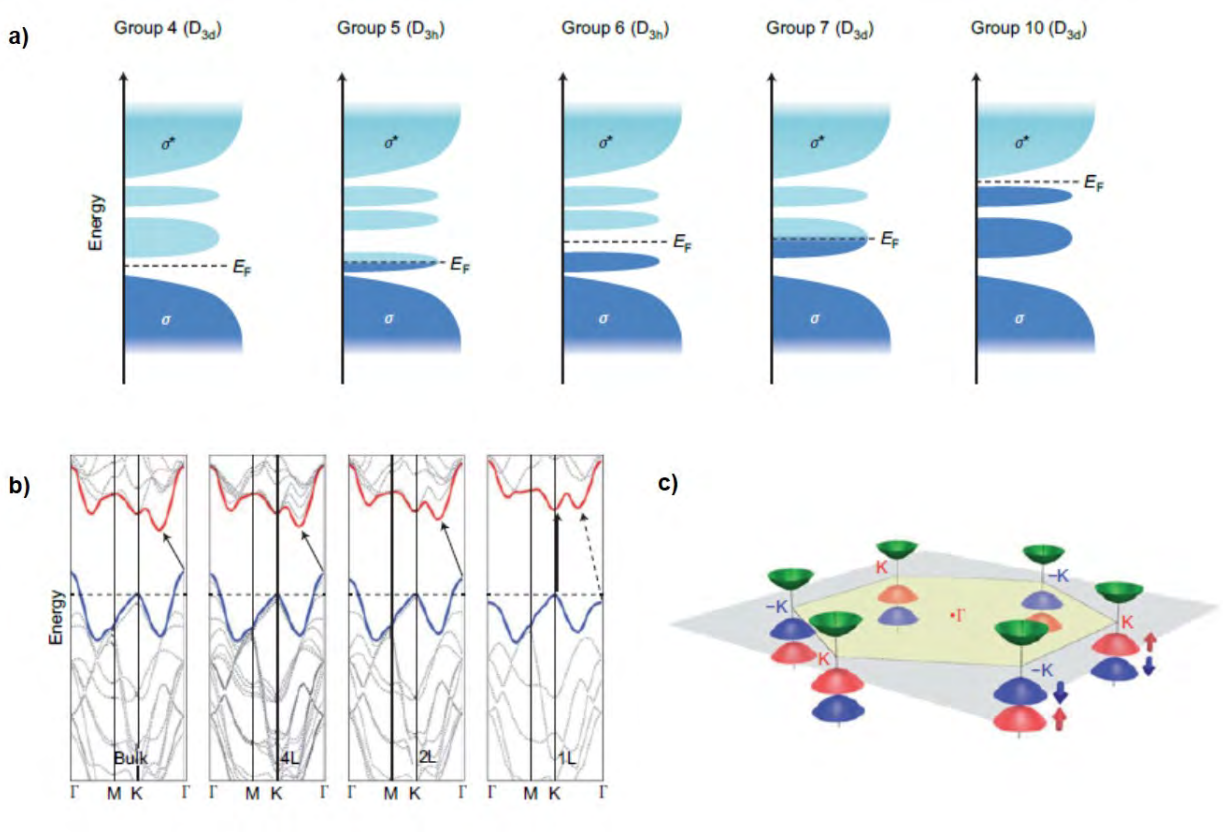


Figure 3. (a) Qualitative schematic showing the progessive filling of d orbitals that are located within the bonding and anti-bonding states in group 4, 5, 6, 7 and 10 TMDs and their corresponding point groups. (b) Energy dispersion of bulk, 4 layer (4L), bilayer (2L) and monolayer (1L) MoS2. (c) Band structure of MoS2 showing inequivalent valleys K and -K (K') within the first in MoS2 and spin splitting in the valence band. (from ref. 7)

1.2 General considerations for TMD synthesis

The transition metals and chalcogens, as pure elements, exhibit significantly different properties which has implications in the methods and conditions that can be used for synthesis of TMDs. Transition metals such as Mo, W and Nb, have high bond strength, correspondingly high melting temperatures (>2000°C) and negligible elemental vapor pressures even at temperatures as high as 1000°C (Figure 4a). In contrast, chalcogens such as S, Se and Te have much lower melting temperatures (< 500°C) and correspondingly higher elemental vapor pressures. Sulfur, for example, has a vapor pressure greater than atmospheric pressure at temperatures above 500°C.

These differences in elemental properties give rise to the characteristic phase diagrams of the binary TMD compounds. In the case of the Mo-S phase diagram, for example, stoichiometric MoS_2 melts at 1730°C forming a Mo-rich liquid phase that is in equilibrium with sulfur vapor (Figure 4b).[8] Consequently, it is not possible to synthesize MoS_2 via melt growth techniques such as Czochralski or Bridgman growth which rely on crystallization of the solid from a stoichiometric melt. Instead, MoS_2 is typically synthesized by vapor phase methods both for bulk crystals and

a)

Element	Melting Temp (°C)	Vapor Press (Torr) (@500°C)
W	3422	~0
Mo	2617	~0
Nb	2468	~0
S	115	>750
Se	221	49
Te	450	0.91

b)

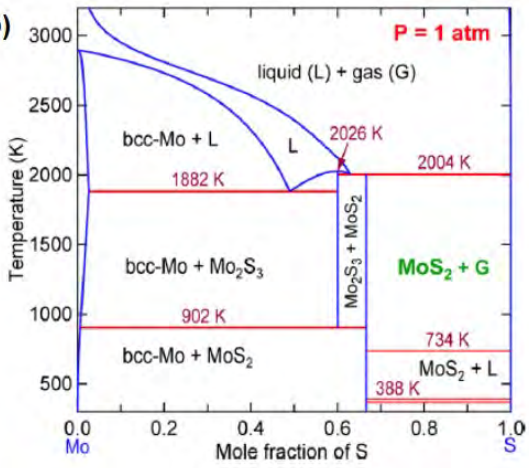


Figure 4. (a) Comparison of melting temperature and vapor pressure (at 500°C) for select transition metals and chalcogens. (b) Binary phase diagram of MoS_2. (from ref. 8)

thin (or monolayer) films, typically employing sulfur-rich growth conditions where, according to the phase diagram, MoS_2 is in equilibrium with sulfur vapor.

The synthesis of TMD bulk crystals and thin films is therefore dependent on the vapor phase supply of the chalcogen and transition metal to the growth front. As a result of the high vapor pressure of the chalcogens, and S and Se, in particular, this can be achieved in a straightforward manner via evaporation by heating elemental powders above their respective melting points. The transition metals, however, present a more significant challenge (Figure 5). Electron beam irradiation in a high vacuum environment is typically required for evaporation of Mo, W, etc. making this a suitable approach only for molecular beam epitaxy (MBE). As a result, chemical precursors such as MoO_3, $MoCl_5$ and $Mo(CO)_6$ are employed instead for vapor phase transport. MoO_3, used in combination with S powder, is a popular source for powder vapor transport growth of MoS_2, also referred to as powder source chemical vapor deposition. MoO_3 is air-stable and non-hazardous and therefore is safe to use directly in a tube furnace. However, it has a moderately high melting temperature (~795°C) and must be heated to >600°C to achieve an appreciable vapor pressure. In the PVT process, the MoO_3 powder is typically placed in close proximity to the substrate to ensure a sufficient vapor phase flux for growth. Transition metal halides such as $MoCl_x$ and $MoBr_x$ have higher volatilities and therefore are better suited for growth of bulk crystals using a chemical vapor transport (CVT) process. The transition metal halides can be formed *in situ* in CVT by heating MoS_2 or Mo powder in the presence of a transport agent such as Br_2, I_2 or Cl_2. Halide compounds such as $MoCl_5$, however, are air sensitive and will react readily with ambient H_2O to generate HCl, consequently, safety

Metal Source	T_M(°C)	T (°C) for 0.001 Torr	Pvap (Torr) at 25°C
Mo	2295	2533	$<10^{-4}$
MoO_3	795	583	$<10^{-4}$
$MoBr_3$	500	650	$<10^{-4}$
$MoCl_5$	194	-	1.75
$Mo(CO)_6$	150	-15.4	0.144

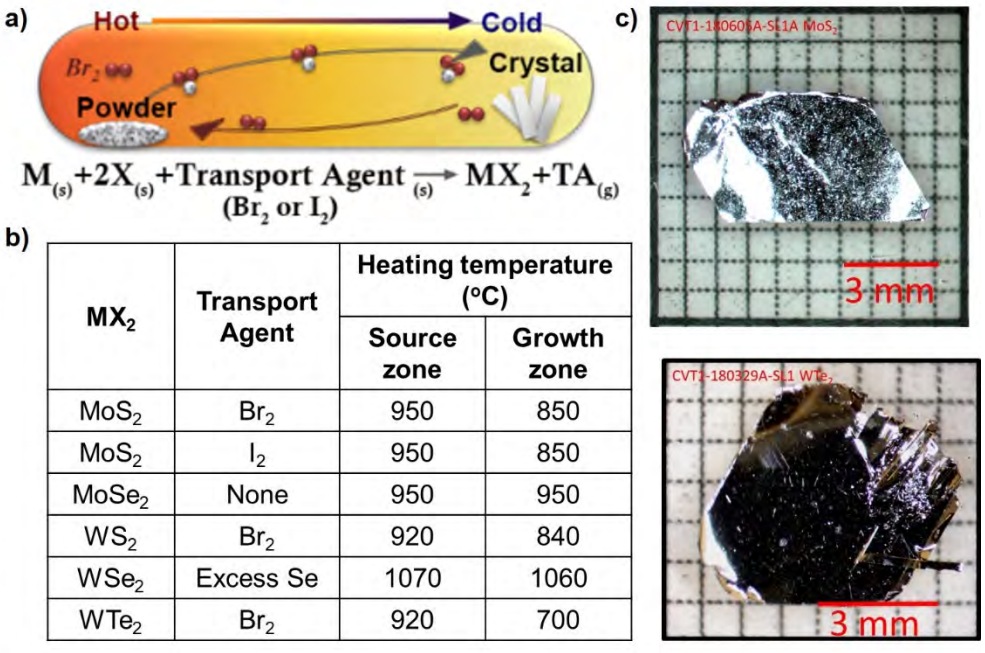
Figure 5. Comparison of melting temperature and vapor pressures of elemental Mo and candidate Mo precursors.

precautions are required when using these sources outside the sealed tube environment employed for CVT. Transition metal carbonyls such as $Mo(CO)_6$ have moderate vapor pressures at room temperature and therefore are suitable sources to use in epitaxial growth techniques such as metalorganic chemical vapor deposition (MOCVD) and metalorganic MBE (MOMBE), also referred to as hybrid MBE. However, these sources are toxic and will generate CO upon reaction and therefore are only suitable for use in a sealed source container.

2. Bulk crystal growth

2.1.1 Chemical vapor transport

Chemical vapor transport (CVT) is the most common method used for growth of TMD bulk crystals. CVT generally describes a process whereby a solid phase which has a low vapor pressure, is volatilized in the presence of a gaseous reactant referred to as the transport agent, and deposits elsewhere as a crystalline phase.[9] In the case of TMDs, the source material, typically pre-compounded MoS_2 powder, is placed on one end of an evacuated and sealed quartz ampoule along with a transport agent (I_2, Br_2 or Cl_2). The quartz ampoule is placed inside a multi-zone tube furnace and a temperature gradient (typically ΔT=100-200°C) is maintained between the source (hot) and crystallization (cold) zones (Figure 6a).[10] Typical transport agents and source and crystallization zone temperatures used for CVT of TMDs are given in Figure 6b.[11] Growth times range from one to a few weeks to obtain TMD crystals that are several millimeters in size (Figure



MX_2	Transport Agent	Heating temperature (°C)	
		Source zone	Growth zone
MoS_2	Br_2	950	850
MoS_2	I_2	950	850
$MoSe_2$	None	950	950
WS_2	Br_2	920	840
WSe_2	Excess Se	1070	1060
WTe_2	Br_2	920	700

Figure 6. (a) Schematic of CVT process in sealed quartz ampoule (adapted from ref. 10). (b) Typical transport agents and zone temperatures for CVT of TMDs (adapted from ref. 11). (c) MoS_2 (top) and WTe_2 (bottom) crystals grown by CVT.

6c).[12] In general, the transport efficiency, which determines the growth rate and ultimate size of the crystal, varies as Cl_2>Br_2>I_2. The use of Cl_2, however, which is a gas at room temperature, presents additional safety hazards due to its poisonous and corrosive nature compared to Br_2 and I_2 which are less volatile liquids. Care is also required when using sulfur as significant pressure can build up within the quartz ampoule when the sulfur powder vaporizes. For a 10 mm diameter quartz tube with 1mm thick tube walls, the sulfur pressure should be kept below 6 atm within the ampoule to avoid rupture. It is also recommended to slowly raise the temperature of the ampoule and dwell at ~450°C (boiling point of sulfur) for several hours to avoid cracking the ampoule.

3. Thin film growth

3.1 Substrates

Similar to thin film deposition of other materials, the substrate properties control the crystallinity of TMD films deposited by various vapor phase methods. Oxidized silicon with an amorphous SiO_2 top layer has been widely employed for PVT growth of MoS_2 and related TMDs. The amorphous nature of the SiO_2 leads to MoS_2 domains that are oriented in random directions on the surface. Often the objective is to grow large single crystal triangular domains of MoS_2 that are tens to hundreds of microns in size and spaced far apart for subsequent characterization or device fabrication, consequently, the random orientation of domains is not a concern. However, for wafer-scale films, coalescence of these misoriented domains will lead to polycrystalline monolayer films with high angle grain boundaries which can negatively impact the transport and optical properties of the films.

Epitaxial growth is therefore required to obtain wafer-scale single crystal TMD films. In this case, the substrate properties including crystal symmetry, lattice constant and surface energy are important factors to control the film orientation and surface coverage. There are a variety of candidate substrates with hexagonal symmetry that can be considered for TMD epitaxy (Figure 7a). Conventional substrates such as (0001) sapphire and (0001) SiC are suitable choices for epitaxial growth of TMDs given their hexagonal symmetry, size, availability and good thermal and chemical stability. In addition, commensurability between the MoS_2 and Al_2O_3 lattices such that (3x3)MoS_2/(2x2)Al_2O_3 reduces the effective lattice mismatch to -0.4% (Figure 7b). Van der Waals bonded materials such as graphene and hexagonal boron nitride (hBN) are also crystallographically compatible but are more difficult to obtain in large area. In addition, the low surface energy of graphene and hBN pose challenges to

a)

Substrate	In-plane lattice parameter, Å	Lattice mismatch to MoS_2, %
a-Al_2O_3	4.760	34
4H-, 6H-SiC	3.073-3.081	2.3 - 2.6
GaN	3.189	1.1
AlN	3.111	1.4
h-, r-BN	2.504	26
graphite	2.462	28

b)

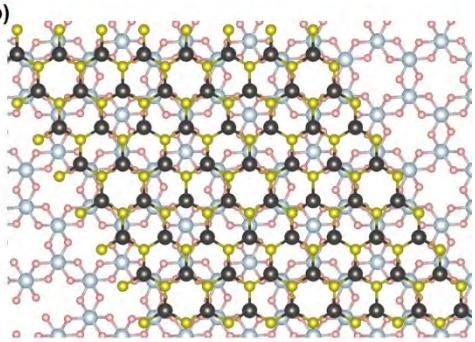


Figure 7. (a) Comparison of in-plane lattice parameters and lattice mismatch to MoS_2 for candidate substrates. (b) Schematic of (3x3)MoS_2/(2x2)Al_2O_3 epitaxial relationship. (courtesy of M. Chubarov)

adsorption and nucleation. Wurtzite GaN is also an interesting substrate choice given the near lattice match with MoS_2 and WS_2.

3.2 Powder vapor transport

Powder vapor transport (PVT), also referred to as powder source chemical vapor deposition (CVD), is a common method for thin film deposition of MoS_2 and related TMDs. A schematic of a typical PVT system for MoS_2 growth which employs a horizontal quartz flow tube configuration in a multi-zone or single zone tube furnace is shown in Figure 8a. Sulfur powder is placed in a boat which is positioned upstream in a region that is maintained at ~200°C. MoO_3 powder is placed downstream in a boat in a region that can be heated to 700-900°C. The substrates are placed upside down on top of the MoO_3. The reactor is initially heated to ~100°C under a flow of Ar carrier gas to remove air and residual moisture from the tube walls. The temperatures of the sulfur and MoO_3 regions are then increased to initiate vapor phase transport and growth.

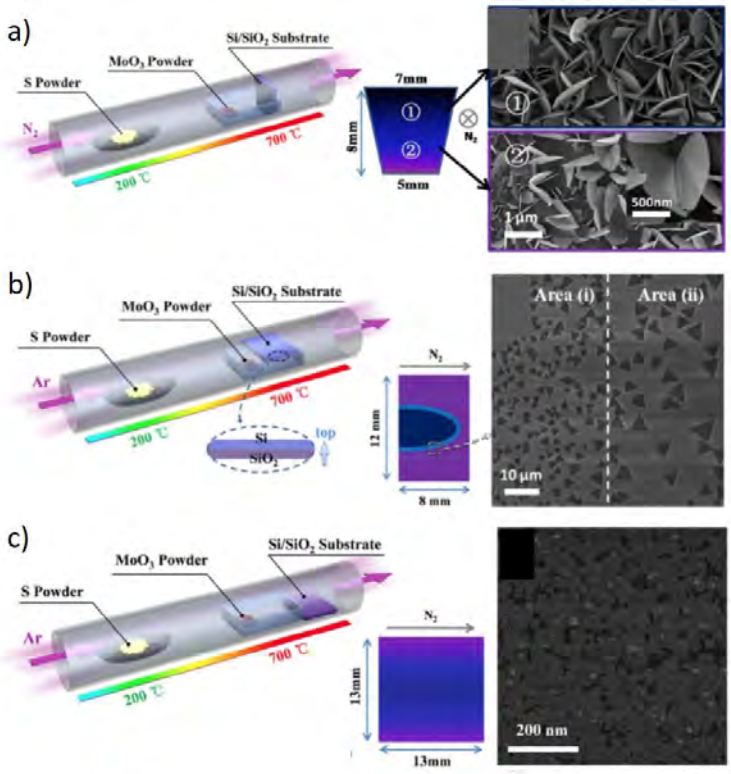


Figure 8. Comparison of MoS_2 uniformity and morphology as a function of substrate position relative to MoO_3 boat for (a) vertical substrate at back of boat; (b) horizontal substrate placed faced-down on boat and (c) horizontal substrate placed downstream of boat. (adapted from ref. 13).

In the PVT process, TMD growth is limited by the supply of the transition metal precursor to the substrate surface as the chalcogen is present in excess. As a result, the nucleation density, growth rate and morphology of the TMD film are strongly dependent on the position of the substrate relative to the transition metal powder source.[13] In the case of MoS_2 growth, for example, a high flux or impingement rate of MoO_3 is obtained in the direction of the substrate when the substrate is oriented vertically in the boat (Figure 8a). This results in a high nucleation density on the substrate surface and the perpendicular growth of MoS_2 platelets. Planar films consisting of isolated MoS_2 domains (Figure 8b) or coalesced polycrystalline films (Figure 8c) are obtained when the substrate is oriented horizontally. Likewise, the S/Mo vapor phase ratio varies as a function of position in the PVT tube which alters growth stoichiometry and the relative growth rate of metal versus chalcogen terminated edges (Figure 9a).[14] Under S-rich conditions (Mo:S<1:2), the growth rate of Mo-terminated edges is greater than that of S-terminated edges,

consequently, the equilibrium domain shape will be a triangle with S-terminated edges (Figure 9b). The opposite is true for growth under Mo-rich conditions. Hexagonal or truncated-triangular domain shapes are obtained when the growth chemistry approaches stoichiometric conditions. PVT growth chemistry can also be altered through the addition of NaCl or KCl in the growth chamber. The addition of NaCl to the MoO_3 source results in the formation of MoO_xCl_y species which have a higher volatility than MoO_3.[15] As a result, the flux of the Mo species is enhanced in the growth process resulting in the formation of large isolated domains that can be up to a millimeter in size.

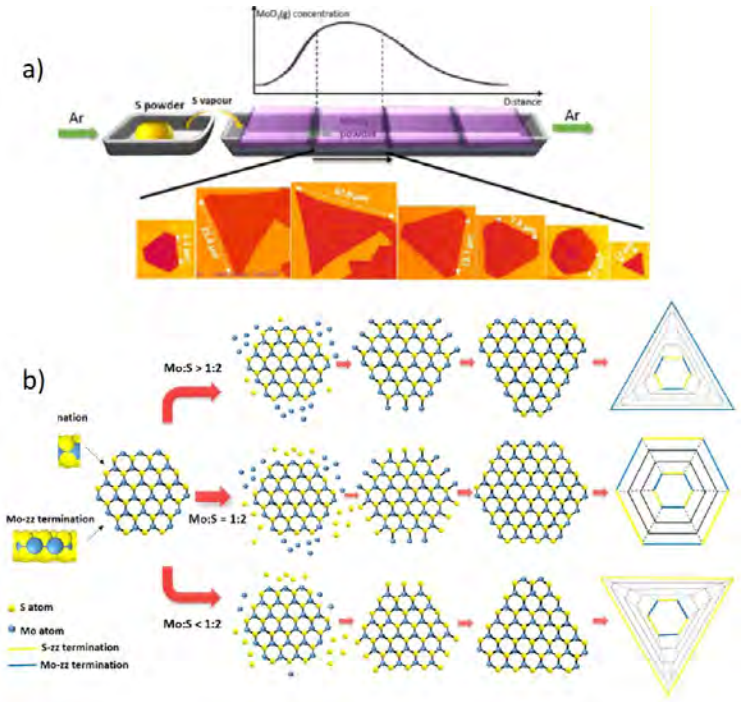


Figure 9. (a) Schematic showing variation of MoS2 domain shape as a function of position in PVT process. (b) Effect of growth stoichiometry on MoS_2 domain shape. (adapted from ref. 14).

Growth of vertical and lateral heterostructures using PVT is challenging since the vaporization rate of powder sources cannot easily be controlled or switched in this configuration. Nevertheless, there have been clever strategies employed to physically move the source boats within the reactor tube during growth or take advantage of the differences in vapor pressure of S and Se to synthesize MoS_2-$MoSe_2$ lateral heterostructures.[16]

3.3 Metalorganic Chemical Vapor Deposition

The PVT method, in which source powders and substrate are located in the same hot wall quartz reactor tube, is straightforward to implement and provides a high chalcogen partial pressure in the gas ambient which is particularly advantageous for TMD growth at elevated temperatures where the sticking coefficients of S and Se are low. The source concentrations cannot, however, be independently controlled and modulated in PVT growth, which limits its utility, and film uniformity over large areas is difficult to achieve. As a result, there has been growing interest in the use of conventional gas source-based CVD techniques such as metalorganic CVD (MOCVD) which offer improved process control and scalability to large substrate diameters. CVD methods of this type utilize volatile chemical precursors that are located outside of the deposition chamber and are controllably introduced as gases into the reactor inlet. In this case, growth can also be carried out in a cold-wall reactor chamber where only the substrate is heated which minimizes gas phase pre-reaction of sources and prevents upstream deposition on reactor surfaces which is essential for the growth of multi-layers and heterostructures.

MOCVD has previously been employed to synthesize a variety of TMD thin films.[17,18,19,20] In this case, the layers were relatively thick, consequently the films properties can be expected to be similar to that of bulk material. More recently, there has been renewed interest in MOCVD for the synthesis of monolayer and few-layer TMDs such as MoS_2,[21,22,23] and WSe_2.[24,25,26] A variety of precursors have been employed including metal carbonyls ($W(CO)_6$ and $Mo(CO)_6$), halides ($MoCl_5$, WCl_6, $NbCl_5$), organo-chalcogen compounds ($(CH_3)_2Se$, $(C_2H_5)_2Se$, $(C_4H_9)_2Se$, $(C_2H_5)_2S$, $(C_4H_9)_2S$, $(C_2H_5)_2Te$, $(C_3H_7)_2Te$), and hydrides (H_2S, H_2Se). In the case of the organo-chalcogens, carbon deposition can occur at high temperature and high chalcogen/metal precursor ratios along with the TMD film.[24,27] With the exception of the hydrides which are supplied as gases, the precursors are typically liquids or solids at room temperature with low to moderate vapor pressure. Precursor supply is controlled via the use of temperature and pressure-controlled bubbler manifolds which utilize a carrier gas such as H_2 or N_2 to transport controlled molar amounts of the volatile precursor to the deposition chamber (Figure 10b). The gas manifold may also include additional valves, mass flow controllers and pressure controllers to enable the precursor flow to be switched into and out of the deposition chamber without significant disruptions to the gas flow dynamics in the chamber.

Deposition chambers for MOCVD can be classified into two main categories: hot wall and cold wall. In a hot wall system (Figure 10a), a resistive tube furnace is typically used to heat both the chamber walls and the substrate while in a cold wall system (Figure 10c), the substrate is independently heated via induction, resistive or lamp heating and the walls are maintained at a lower temperature to minimize gas phase pre-heating.

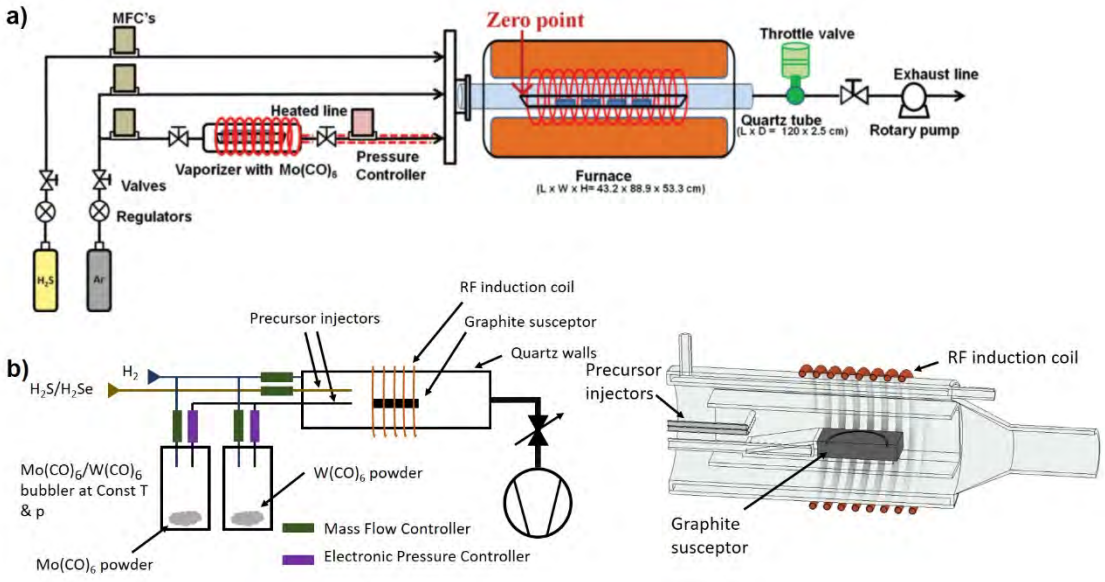


Figure 10. (a) Schematic of hot wall MOCVD system for TMD growth that includes a vaporizer for supply of $Mo(CO)_6$. (adapted from ref. 22). (b) Schematic of cold wall MOCVD system (left) and reactor (right) that includes bubbler manifolds for supply of $Mo(CO)_6$ and $W(CO)_6$. In both cases, the chalcogen precursor is a hydride gas including H_2S and H_2Se. (courtesy of M. Chubarov).

The ability to control and modulate the precursor concentration during growth provides flexibility to independently control the nucleation and lateral growth of TMDs on the substrate surface. For example, Zhang, et al. developed a three-step process for MOCVD growth of WSe_2 monolayers on c-plane sapphire at 800°C under a constant flow rate of H_2Se in an H_2 carrier gas.[28] A higher $W(CO)_6$ flow rate was initially employed to nucleate small clusters of WSe_x on the substrate surface. The $W(CO)_6$ was then switched out of the reactor and the clusters were allowed to diffuse and ripen under H_2Se eventually forming small triangular WSe_2 islands spaced further apart. The $W(CO)_6$ was then reintroduced at a lower flow rate to prevent additional nucleation and promote the lateral growth of the WSe_2 islands to form a coalesced film. Monolayer WSe_2 films with ~30% bilayer coverage were obtained over the temperature range from 700-900°C using a high Se/W ratio of ~26,000.

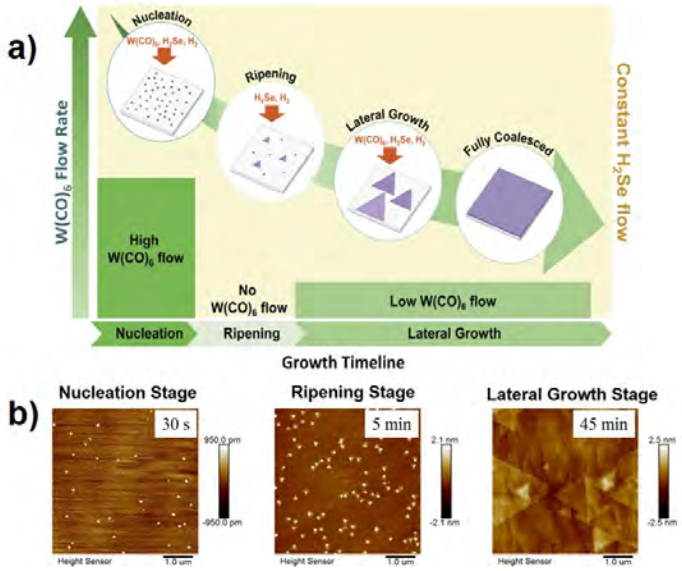


Figure 11. (a) Three-step process used for epitaxial growth of monolayer WSe_2 on sapphire. (b) AFM images showing surface during nucleation, ripening and lateral growth steps. (adapted from ref. 28)

This process has also been extended to the epitaxial growth of WS_2 monolayers on 2" sapphire using $W(CO)_6$ and H_2S (Figure 12a). The WS_2 exhibits a low surface roughness (Figure 12b) characterized by steps associated with the underlying sapphire substrate. A low density (~$8x10^7$ cm^{-2}) of small bilayer domains are present on the monolayer surface. In-plane XRD (Figure 10b) demonstrates that the films are epitaxially oriented with respect to the sapphire with narrow X-ray full-width-at-half-maximum (FWHM~360 arcsecs) indicating a low degree of rotational misorientation within the plane of the substrate. Post-growth TEM carried out on monolayers removed from the sapphire and transferred onto a TEM grid demonstrate that the films are nominally single crystal and include inversion domains that result from a merging of 0° and 60° oriented domains that initially form on

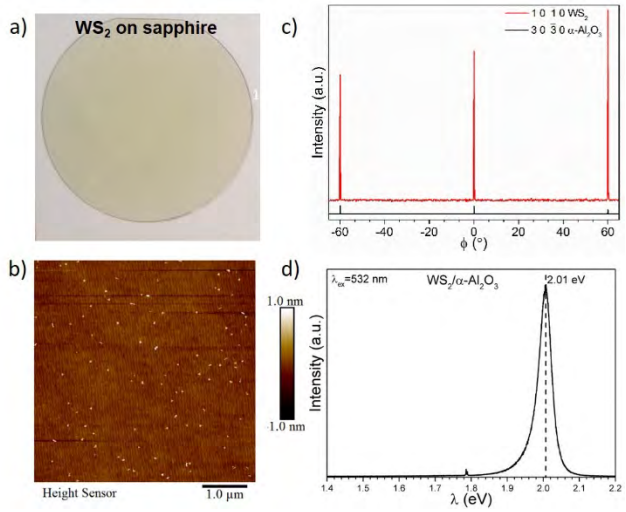


Figure 12. (a) WS_2 monolayer on 2" sapphire; (b) AFM showing uniform monolayer coverage with minimal bilayer islands; (c) in-plane XRD ϕ-scan showing epitaxial orientation, and (d) room temperature photoluminescence at ~2 eV. (courtesy of M. Chubarov)

sapphire (not shown). The monolayers exhibit room temperature photoluminescence at ~2.0 eV for the case of WS_2 (Figure 12d).

The ability to achieve uniform, wafer-scale epitaxial monolayer TMD films using MOCVD is advantageous for device applications. In addition, growth of strained WS_2/WSe_2 lateral heterostructures has also been demonstrated in MOCVD using sequential precursor pulsing.[29]

3.4 Molecular Beam Epitaxy

Molecular beam epitaxy (MBE) is traditionally well suited for epitaxial growth of ultra-thin films since it offers a high level of control in source flux and the use of *in situ* characterization methods such as reflection high energy electron diffraction (RHEED) and *in vacuo* characterization using methods such as x-ray photoelectron spectroscopy (XPS) and angle-resolved photoelectron spectroscopy (ARPES). However, the high vapor pressure of chalcogens and low vapor pressure of transition metals present special challenges for epitaxial growth of TMDs. In a typical solid source MBE system, effusion cells are used for evaporation of metals, however, the high melting temperature of transition metals such as Mo and W necessitates the use of electron-beam evaporation. In addition, the sticking coefficient of S (and Se to some extent) on the growth surface is low under ultra-high vacuum conditions impacting growth stoichiometry particularly at high growth temperatures which are beneficial to promote metal surface diffusion. As a result, TMD domain sizes are typically significantly smaller than those achieved using PVT or MOCVD. To alleviate this problem, MBE growth of TMDs is often carried out on van der Waals materials such as epitaxial graphene, HOPG and mica, which enable enhanced surface diffusion (Figure 13).[30] The growth of Te-based TMDs (e.g. $MoTe_2$ and WTe_2) which is typically carried out at lower temperatures than Se or S-based TMDs, is well suited for MBE growth. In addition, hybrid techniques such as metalorganic MBE (MOMBE), also referred to as hybrid MBE, can be used. In this case, the transition metal is supplied using a chemical precursor such as $Mo(CO)_6$ or $W(CO)_6$ which eliminates the need for e-beam evaporation.

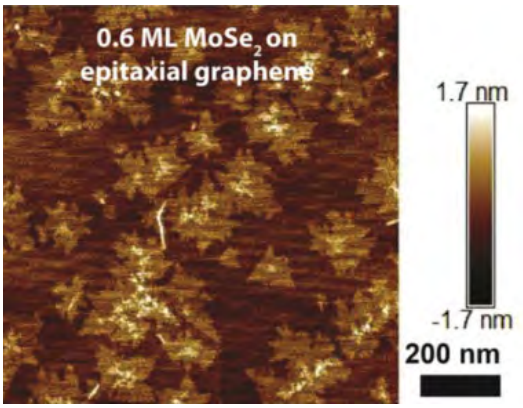


Figure 13. AFM image of a partial monolayer of $MoSe_2$ grown by MBE on epitaxial graphene showing a dendritic domain structure. (adapted from ref. 30)

Acknowledgements

The authors acknowledge the financial support of the National Science Foundation (NSF) through the Penn State 2D Crystal Consortium – Materials Innovation Platform (2DCC-MIP) under NSF cooperative agreement DMR-1539916.

References

[1] K.F. Mak, C. Lee, J. Hone, J. Shan, T.F. Heinz, "Atomically Thin MoS_2: A New Direct-Gap Semiconductor," Phys. Rev. Lett. vol. 105, p. 136805 (2010).

[2] A.T. Hanbicki, M. Currie, G. Kioseoglou, A.L. Friedman, B.T. Jonker, "Measurement of High Exciton Binding Energy in the Monolayer Transition-Metal Dichalcogenides WS_2 and WSe_2," Solid State Commun. vol. 203, pp. 16-20 (2015).

[3] K. S. Novoselov, A. Mishchenko, A. Caravalho and A.H. Castro Neto, Science 353, 461 (2016).

[4] J.R. Schaibley, P. Rivera, K.L. Seyler, J. Yan, D.G. Mandrus, T. Taniguchi, K. Watanabe, W. Yao, X. Xu, "Directional Interlayer Spin-Valley Transfer in Two-Dimensional Heterostructures," Nat. Commun. vol. 7, p. 13747 (2016).

[5] G.H. Han, D.L. Duong, D.H. Keum, S.J. Yun and Y.H. Lee, "van der Waals Metallic Transition Metal Dichalcogenides," Chem. Rev. 118, 6297 (2018).

[6] Q. H. Huang, K. Kalanter-Zadeh, A. Kis, J.N. Coleman and M.S. Strano, "Electronics and optoelectronics of two-dimensional transition metal dichalcogenides," Nature Nanotech. 7, 699 (2012).

[7] M. Chhowalla, H.S. Shin, G. Eda, L.J. Li, K.P. Loh and H. Zhang, "The chemistry of two-dimensional layered transition metal dichalcogenide nanosheets," Nature Chem. 5, 263 (2013).

[8] ASTM Phase Diagram Database.

[9] P. Schmidt, M. Binnewies, R. Glaum and M. Schmidt, InTech DOI:10.5772/55547.

[10] G.R. Bhimanapati, et al., "Recent advances in two-dimensional materials beyond graphene," ACS Nano 9, 1150-9 (2015).

[11] K. Ueno, "Introduction to the growth of bulk single crystals of two-dimensional transition metal dichalcogenides," J. Phys. Soc. Japan 84, 121015 (2015).

[12] Unpublished, Seng-Huat Lee, Penn State University.

[13] F. Zhang, K. Momeni, M. A. AlSaud, A. Azizi, M.F. Hainey Jr., J.M. Redwing, L.Q. Chen and N. Alem, "Controlled synthesis of 2D transition metal dichalcogenides: form vertical to planar MoS_2," 2D Mater. 4, 025029 (2017).

[14] S. Wang, Y. Rong, Y. Fan, M. Pacios, H. Bhaskaran, K. He and J.H. Warner, "Shape evolution of monolayer MoS2 crystals grown by chemical vapor deposition," Chem. Mater. 26, 6371 (2014).

[15] J. Zhou, et al. "A library of atomically thin metal chalcogenides," Nature 556, 355 (2018).

[16] X. Duan, C. Wang, J.C. Shaw, R. Cheng, Y. Chen, H. Li, X.P. Wu, Y. Tang, Q. Zhang, A. Pan, J. Jiang, R. Yu, Y. Huang and X.F. Duan,"Lateral epitaxial growth of two-dimensional layered semiconductor heterojunctions," Nature Nanotech. 9, 1024 (2014).

[17] N.D. Boscher, C.J. Carmalt and I.P. Parkin, "Atmospheric pressure chemical vapor deposition of WSe_2 thin films on glass—highly hydrophobic sticky surfaces," J. Mater. Chem. 16, 122 (2006).

[18] N.D. Boscher, C.J. Carmalt, R.G. Palgrave, J.J. Gil-Tomas and I.P. Parkin, "Atmospheric pressure CVD of molybdenum diselenide films on glass," Chem. Vap. Depos. 12, 692 (2006).

[19] C.J. Carmalt, E.S. Peters, I.P. Parkin, T.D. Manning and A.L. Hector, "Chemical vapor deposition of niobium disulfide thin films," Eur. J. Inorg. Chem. 4470 (2004).

[20] N.D. Boscher, C.J. Carmalt and I.P. Parkin, "Atmospheric pressure chemical vapour deposition of $NbSe_2$ thin films on glass," Eur. J. Inorg. Chem. 1255 (2006).

[21] K. Kang, et al. High-mobility three-atom-thick semiconducting films with wafer-scale homogeneity. Nature 520, 656 (2015).

[22] V. Kranthi Kumar, S. Dhar, T.H. Choudhury, S.A. Shivashankar and S.A. Raghavan, "A predictive approach to CVD of crystalline layers of TMDs: the case of MoS_2," Nanoscale **7,** 7802 (2015).

[23] M. Marx., S. Nordmann, J. Knoch, C. Franzen, C. Stampfer, D. Adrzejewski, T. Kummell, G. Bacher, M. Heuken, H. Kalisch and A. Vescan, "Large-area MoS_2 deposition via MOVPE," J. Cryst. Growth 464, 100–104 (2017).

[24] B. Nie, et al. "Uniform, large-area self-limiting layer synthesis of tungsten diselenide," J. Appl. Polym. Sci. 30**,** 0 (2011).

[25] S.M. Eichfeld, L. Hossain, Y.C. Lin, A.F. Piasecki, B. Kupp, A.G. Birdwell, R.A. Burke, N. Lu, X. Peng, J. Li, A. Azcatl, S. McDonnell, R.M. Wallace, M.J. Kim, T.S. Mayer, J.M. Redwing and J. A. Robinson, "Highly Scalable , Atomically Thin WSe_2 Grown via Metal À Organic Chemical Vapor Deposition," ACS Nano 9, 2080 (2015).

[26] X. Zhang, Z.Y. Al Balushi, F. Zhang, T.H. Choudhury, S.M. Eichfeld, N. Alem, T.N. Jackson, J.A. Robinson and J.M. Redwing, "Influence of Carbon in Metalorganic Chemical Vapor Deposition of Few-Layer WSe2 Thin Films," J. Electron. Mater. 45, 6273 (2016).

[27] T.H. Choudhury, H. Simchi, R. Boichot, M. Chubarov, S.E. Mohney and J.M. Redwing, "Chalcogen precursor effect on cold-wall gas-source chemical vapor deposition growth of WS_2," Cryst. Growth and Design 18, 4357 (2018).

[28] X. Zhang, T. Choudhury, M. Chubarov, Y. Xiang, B. Jariwala, F. Zhang, N. Alem, G.C. Wang, J.A. Robinson and J.M. Redwing, "Diffusion-controlled epitaxy of large area coalesced WSe2 monolayers on sapphire," Nano Lett. 18, 1049 (2018).

[29] S. Xie, L. Tu, Y. Han, L. Huang, K.B. Kang, P. Poddar, C.B. Park, D.A. Muller, R.A. DiStasio Jr. and J.W. Park, "Coherent, atomically thin transition-metal dichalcogenide superlattices with engineered strain," Science 359, 1131 (2018)

[30] Viswanath, X. Liu, S. Rouvimov, P.C. Mende, A. Azcatl, S. McDonnell, R.M. Wallace, R.M. Feenstra, J.K. Furdyna and D. Jena, "Comprehensive structural and optical characterization of MBE grown $MoSe_2$ on graphite, CaF_2 and graphene," 2D Mater 2, 024007 (2015).

14. Crystal Growth of Organic Materials

UNIVERSITY OF LEEDS

Crystal Growth of Organic Micro-Particulate Materials: A Molecular Perspective

Nornizar Anuar and Kevin J. Roberts

School of Chemical and Process Engineering, University of Leeds, Leeds, LS2 9JT, UK



Crystal Growth of Organic Micro-Particulate Materials: A Molecular Perspective

Nornizar Anuar[*] and Kevin J. Roberts[‡]

EPSRC Centre for Doctoral Training in Complex Particulate Products and Processes, School of Chemical and Process Engineering, University of Leeds, Leeds, LS2 9JT, UK.

Emails: [*] nornizar@uitm.edu.my; [‡] k.j.roberts@leeds.ac.uk

[*]On academic sabbatical leave from the Faculty of Chemical Engineering, Universiti Teknologi MARA, Shah Alam, 40450, MALAYSIA.

Scope of these Lectures

Time constraints will limit the scope of these lectures to the crystal growth of organic materials for application as micro-crystalline products with particular emphasis on the pharmaceutical and fine chemicals sectors. This focus reflects the fact that this area represents one of the major areas for industrial applications.

For the crystal growth of large (ca. cm^3) sized single crystals for fundamental study and/or electronic device applications readers are directed to a number of publications [1] – [3].

1. Introduction and Context

The crystal growth of organic materials represents an important unit-operation in the processing, separation and purification of a wide range of chemical products including bulk compounds; specialty chemicals and intermediates; high purity monomers for polymer production; pharmaceuticals and drugs; soaps and surfactants; fats and food products; and agrochemicals. The science, technology and engineering associated with such crystallisation processes is important in a wide range of technological areas. For example, in industrial-scale crystallisation, it is a much more energy-efficient (Table 1) process for product separation and isolation when compared to other techniques such as distillation.

Table 1. Comparison between crystallisation and distillation processes for the separation of benzene

	Temperature	Enthalpy Change
Melting	5.4°C	126 kJ/kg
Boiling	80°C	394 kJ/kg

In addition, the lower temperatures used for crystallisation reactions mean that it is particularly appropriate for the separation and processing of many heat-sensitive chemical products such as pharmaceutical products, food, agrochemicals etc.

Crystallisation also effects the purification of materials reflecting the ability through its molecular recognition properties to segregate impurities away from the growth interface. An example is the purification by melt crystallisation of caprolactam ($C_5H_{10}CONH$), an important intermediate in Nylon 6 polymer production in terms of removing trace amounts of the closely related molecule cyclohexanone ($C_5H_{10}C0$). The latter act as chain terminators thus lowering the product molecular weight and reducing product quality.

Control of the crystallisation process can be used to direct the formation of targeted crystal structures (polymorphic forms) and crystal morphologies which can be important as changes in such properties can result in processing difficulties (morphology) as well as changes to product behaviour, such as bio-availability (drugs), colour (dyes and pigments), reactivity (explosives) and taste (foods). For example, the production of chocolate in the UK involves the re-crystallisation of ca. 3M tons/year of cocoa butter fat with the taste of the resulting chocolate depending on crystal growth to produce a product with the desired crystal structure from the known 6 polymorphs of the fat.

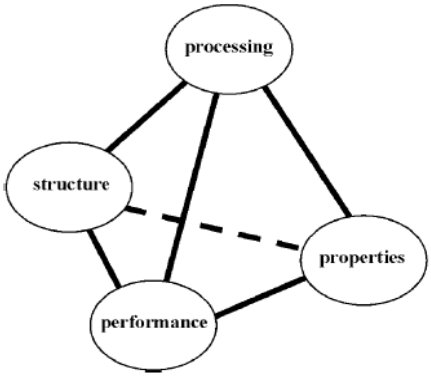


Figure 1. The material science tetrahedron, after Sun [5], (reproduced with the permission of Journal of Pharmaceutical Science)

Finally, the growth of crystals sometimes produces undesired outcomes; e.g. wax formation within hydrocarbon fuels in cold weather conditions causing fuel starvation and the formation of gallstones, gouty arthritis and kidney stones in human tissue.

Hence, understanding and controlling the growth of organic materials involves the need to understand, predict, manipulate and control the core processes involved in drug design, development and manufacture. The latter, perhaps, can be best understood through a consideration of integrated 5F materials transformation pathway [4] developed from the target molecule's molecular structure, which links and interrelates:

- Formulae (atomic and molecular structure),
- Formation (crystallisation, precipitation, spray drying, etc.),
- Form (crystal size, morphology, polymorphic form, etc.),
- Formulation (blending, granulation, compaction, etc.),
- Function (product purpose and performance).

This approach enables cross-correlation between the 5F and the material science tetrahedron (see Fig. 1) for a given crystalline material or formulated drug product and forms the basis for development of a new material. The material science tetrahedron consists of the following:

- Molecular and crystal structure
- Physical and chemical properties,
- Processing behaviour,
- Performance

Increased product performance is desired by every manufacturer and is reason for developing new materials. However, it is strongly affected by the properties of the material, and by its molecular and crystal structure. A product can be modified to meet its desired performance, by changing the way the material is processed, once the structure-properties relationship is understood.

2. Distinguishing Features Related to the Crystal Growth of Organic Materials

Whilst, in general, the overall features that characterise crystal growth theory and practice are broadly generic, there are distinct differences in the relative importance of these between the traditional area of the growth of large single crystals for electronic device purposes and the crystallisation of pharmaceutical materials for healthcare applications. These differences relate to a number of inter-related factors notably crystal structure and bonding, structure/properties inter-relationships, mode of crystal growth and multiplicities of structural types.

2.1 Crystal Structure and Bonding

Electronic materials are mostly inorganic whose solid-state structure mostly involves strong and directed ionic and/or covalent interactions, which takes place at the atomic and/or ionic levels giving rise, in turn, to higher and usually congruent melting points. In contrast, the solid-state structure of pharmaceutical materials is dominated by weak and undirected inter-molecular interactions, involving a balance between van der Waals interactions and hydrogen bonds. In terms of crystallography, the former mostly tend to crystallise in high symmetry crystal structures (cubic, trigonal, hexagonal and tetragonal) whereas the latter due to their anisotropic molecular shape mostly tend to crystallise in lower symmetry structures (orthorhombic, monoclinic and triclinic). A further complication is that the undirected nature of pharmaceutical materials gives rise to a multiplicity of potential solid-state structures (polymorphs).

2.2 Inter-Relationship between Structure and Properties

Because of the differences in crystal structure highlighted above, the physico-chemical properties of pharmaceutical crystals can be radically different from one crystal form to another and, indeed, in terms of their surface properties from habit plane (hkl) to another. Understanding such differences is critically important when developing a formulation process to transform an active pharmaceutical ingredient (API) through

blending with other ingredients (both crystalline and amorphous phases) into a practical drug product dosage form for delivery to patients.

2.3 Mode of Crystal Growth

Due to their strong structural bonding and high degree of stability, inorganic materials tend to be grown at higher temperatures either from the melt, from the vapour phase or from high temperature solutions. In contrast, organic materials usually have much lower melting points and stabilities. The latter is a reflection of the sensitivity of both the intra- and inter-molecular interactions to chemical and/or solid-state transformation. Hence, whilst melt growth is occasionally used for organic materials which have sufficient stability, in general and for most for practical applications the crystal growth of organic materials mostly takes place from low temperature solutions.

2.4 Multiplicities of Structural Types

Finally, many inorganic materials have been developed from concept to application through a continuous and incremental technological improvement in their performance. This has often taken place over many decades of R&D. As a result, the underpinning domain knowledge of such material's properties and processing behaviour tend to be very strong indeed, whilst the long-standing nature of the production of these materials provides an adequate source of material for further development. In contrast, every API tends to have quite different properties requiring a "fresh-start" approach for each new material.

Additionally, the selection of a suitable solid form [6] – [9] for a given drug is very much a variable in the R&D process with the key parameters being:

- API solubility and dissolution performance in relation its in-vivo bioavailability
- Chemical and physical state stability to changes that might impact drug product performance
- Downstream processing ability in terms of its formulation into a drug product.

Through such a selection process, a wide range of different forms encompassing free acids and bases, salts, hydrates and co-crystals, and any polymorphs thereof are typically prepared, characterised, screened and assessed against the key requirement that a drug product should be safe and efficacious regarding its eventual patient use. Such a multiplicity of options can place severe constraints on the R&D process. The latter requires a detailed investigation into the interrelationship between structure, properties, processing behaviour and API performance for each putative solid-form (see Fig. 1). A process can be made even more challenging, due to the limited quantities of materials that are available in the early stages of developing a drug formulation.

3. Crystal Chemistry

For a given molecular structure, there are two dominant factors, which can play an important role in terms of influencing what crystal structure a given material might adopt;

- Size and shape of molecules in a crystal;
- Nature of bonds between molecules.

These factors affect physical and crystallographic properties. Crystalline solids can be divided into five main groups, by the types of particles in them and the types of chemical bonding holding the particles together (see Fig. 2).

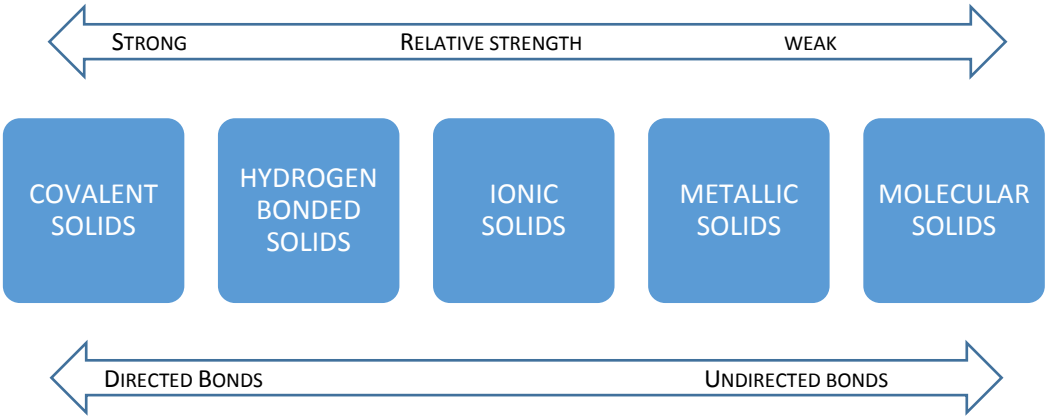


Figure 2. Schematic diagram showing the major types of inter-molecular bonding expected in the solid-state in relation to their relative strengths and their directional nature. Reproduced by consent of Springer & NATO Emerging Security Challenges Division from Ref. [4].

Directed bonds tend to stop or restrict close packing which, in turn, makes for a lower density solid when compared with similar materials which have undirected bonds. The size of a molecule is reflected in the magnitude of the unit cell lattice parameters; e.g. the molecular solid benzophenone [10] ($(C_6H_5C{=}O)_2$) has lattice parameters of a = 10.28, b = 12.12, c = 7.99 Å (orthorhombic), whilst much smaller atomic materials such as metal copper has a = 3.597 Å (cubic) [11]. The shape of a molecule reflects the crystal system:

- Elemental compounds, such as metals and semiconductors, crystallising in high symmetry crystal classes such as cubic and hexagonal.
- Irregularly shaped molecules, such as organic molecules and inorganic complexes, crystallising in the lower symmetry triclinic, monoclinic classes.

The nature of bonding in any solid is of considerable importance since it influences, either directly or indirectly, a wide range of properties, notably melting point, crystal structure and mechanical properties. In the case of organic solids, their structures reflect the nature of their intra- and inter-molecular bonding (see Table 2).

Hence, whilst the atoms within a molecule are held together by strong covalent bonds, the interatomic interactions there are mostly saturated and hence only weaker intermolecular forces exist between molecules. Some organic compounds are utilised in the form of their salts and therefore also exist as ionic species. In such cases, the role of strong ionic interactions must also be considered.

Drawing the above narrative together, it can be seen that there are three main factors of particular important in assessing the influence of intermolecular bonding on the properties of organic solids, notably:

- Strength of the interaction,
- Distance over which the interaction exerts an influence,
- Extent to which the bonding is directional.

Table 2. Types of bonding in organic solids. Reproduced by consent of Springer & NATO Emerging Security Challenges Division from Ref. [4].

Type	Occurrence	Strength of Interactions	Range	Directed Interactions?
van der Waals	All atoms and molecules	Weak (1 - 10 kJ/mol)	short	No
Dipole-dipole	Between polar molecules only	Weak (3 - 4 kJ/mol)	long	No
Hydrogen bonding	Molecules containing O, N or F and a hydrogen bonded to one of these electronegative atoms	Strong (10 – 40 kJ/mol)	short	Yes
Ionic	Monatomic and molecular ions	Strong (10 – 50 kJ/mol)	short	No
Covalent	Intramolecular interactions between atoms	Strong (50 – 1000 kJ/mol)	short	Yes

For organic compounds, their bond strength characteristics are:

- Strong intra-molecular bonds, consistent with fairly robust molecules albeit in the absence of double bonds and other steric hindrances - an ability to display a number of relatively stable molecular conformations.
- Weak and isotropic inter-molecular bonds consistent with somewhat soft solids which have quite low melting points.

The bonding directionality is largely un-directed except for crystals where there are H-bonds.

In summary, the main features that influence the organic solids are:

- Size of Molecules – large unit cells;
- Shape of Molecules – non-spherical shape;
- Nature of intermolecular forces – weak undirected;
- van der Waals bonds – close packed structures.

As a result, broadly speaking organic crystalline solids have the following key distinguishing properties:

- Low melting points
- Low symmetry crystal structures
- Strong tendencies for polymorphic behaviour
- Anisotropic physical and chemical properties.

4. Crystal Morphology and Surface Chemistry

The overall shape of the crystals prepared in crystallisation processes is important, as an inadequately defined crystal morphology may have a detrimental impact on particulate properties such as:

- Ease of separation, notably filtration;
- Particle caking;
- Packing density,
- Dissolution rate,
- Handling, packaging and storage.

In processing terms, this can have many economic ramifications, such as a product being difficult to filter which can result in a reduced efficiency for the separation of crystals after crystallisation.

The crystal morphology of a material and its inter-relationship with its surface chemistry can be understood by calculating the strength and directivity of the intermolecular interactions within the 3D crystallographic structure.

Table 3. Some typical atom-atom potential parameters [17].

Atom 1	Atom 2	A / kcal·Å·mol^{-1}	B / kcal·mol^{-1}	C / Å^{-1}
Hydrogen	Hydrogen	36.0	4000.0	3.74
Carbon	Carbon	535.0	74460.0	3.60
Carbon	Hydrogen	139.0	9411.0	3.67

4.1 Synthons and Lattice Energy

Intermolecular interactions or synthons can be sub-divided between those who are fully satisfied and coordinated within the bulk crystallographic structure (intrinsic synthons) and those which are broken due to surface termination and who hence are exposed at the crystal surfaces (extrinsic synthons).

The strength of an intermolecular synthon can be calculated using the atom-atom approximation through summation of the synthon's constituent atom-atom interactions using empirical force field modelling. For example, a Buckingham (6-exp) function (see the typical parameters given in Table 3) of the following form (including the coulombic contribution) can be used to calculate all the interatomic interactions (V_{ij}) associated with the interaction of two molecules:

$$V_{ij} = -\frac{A}{r^6} + Bexp^{-Cr} + \frac{qiqj}{Dr} \quad (1)$$

where r is the interatomic distance, A, B and C are atom-specific; q_i and q_j are the fractional charges on atoms i and j, and D is the dielectric constant.

Care is needed in selecting the atom specific parameters used in these potentials as the development of a genuinely *universal potential*, applicable to all atom types, remains rather elusive! Usually, the applicability of a chosen empirical potential is tested by first predicting the crystal lattice energy (E_{cr}) from a 3-D model of the crystal structure by summing the interactions between a central molecule and all the surrounding molecules in the crystal. In this, if there are n atoms in the central molecule and n' atoms in each of the N surrounding molecules, then E_{cr} can be expressed as:

$$E_{cr} = \frac{1}{2}\sum_{k=1}^{N}\sum_{i=1}^{n}\sum_{j=1}^{n'} V_{kij} \quad (2)$$

where V_{kij} is the interaction energy between atom i in the central molecule and atom j in the k_{th} surrounding molecule. The factor of ½ reflects the fact that such interactions take place between two molecules (see Figure 3).

Table 4. Comparison between calculated lattice energies and data calculated from experimental sublimation enthalpies for a range of organic materials.

Material	Lattice Energy (kcal/mol)	Experimental Lattice Energy (kcal/mol)
Biphenyl [13]	-21.6	-20.7
Naphthalene [12]	-19.4	-18.6
n-Octadecane [12]	-35.2	-37.8
Benzophenone [14]	-24.5	-23.9
Trinitrotoluene [14]	-25.1	-24.4
α-Glycine [14]	-33.0	-33.8
L-Alanine [14]	-33.3	-34.2
Benzoic acid [15]	-20.4	-23.0
Urea [15]	-22.7	-22.2
ß-Succinic acid [15]	-30.8	-30.1

The calculated value of E_{cr} can be confirmed, as shown in Table 4, with known thermodynamic data through an "experimental lattice energy" (V_{exp}), thus:

$$V_{exp} = -\Delta H_{sub} - 2RT \quad (3)$$

where ΔH_{sub} is the crystal sublimation enthalpy and 2RT is a correction factor representing the difference between the gas phase enthalpy and the vibrational contribution to the crystal enthalpy.

4.2 Crystal Morphology

The crystal morphology is governed by the relative growth rates of its constituent habit faces which are, in turn, related to the energetics on the binding of crystallising monomers at the various 2-D growth interfaces. Hence, by identifying those synthons that are “broken” through their termination on the external surfaces of a crystal, the surface attachment energy (E_{att}) for a given crystal habit plane (hkl) can be determined.

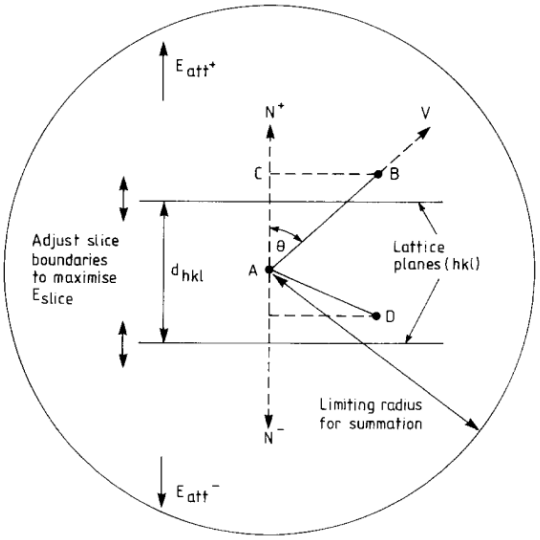


Figure 3. Basic approach for calculation of intermolecular interactions using atom-atom method showing how the lattice energy is partitioned between the slice and attachment energies within a limiting sphere. A is the central molecule, B is a molecule outside the slice, D is a molecule inside the slice, N^+ is the growth normal to the planes (hkl), N^- is the growth normal to the planes (`h`k`l), AB and AD are bonding vectors, d_{hkl} is the interplanar spacing, q is the angle between the growth normal and the bonding vector and AC is the component of the vector AB parallel to N the growth normal. Note that the slice-boundaries defined by d_{hkl} may be shifted along the growth normal to obtain the energetically most stable slice. Reproduced by consent of Journal of Crystal Growth from Ref. [16].

In this, E_{att} is defined by the extrinsic synthons as the energy released on the addition of a growth layer (slice) to the surface of a growing crystal. This is related to the lattice energy by:

$$E_{cr} = E_{sl} + E_{att} \quad (4)$$

where both E_{cr} and E_{sl} are defined by the intrinsic synthons with the slice energy being defined as the energy released upon the formation of a slice of thickness d_{hkl}.

Assembling all potential attachment energies into a 3D polar plot yields the expected crystal morphology.

4.3 Surface Chemistry

Superimposing the predicted crystal morphology onto the bulk crystallographic structure of the compound can be used to reveal surface chemistry of the crystal habit faces and, in particular, which functional groups are exposed at the surface and how these relate to the surface terminated extrinsic synthons.

Figure 4 shows the contracting surface chemistry for the {001} and {110} surfaces of the tetragon crystal form of urea ($O=C-(NH_2)_2$). Examination of this, reveals that the

- {001} surfaces display mixed polarity as defined by alternating orientations of this polar molecule with respect to the c-axis of the structure as related by inversion symmetry with growth promotion directed by synthon a.
- {110} surfaces, in contrast, are largely positively charged and protic in nature with growth promoted by synthon b.

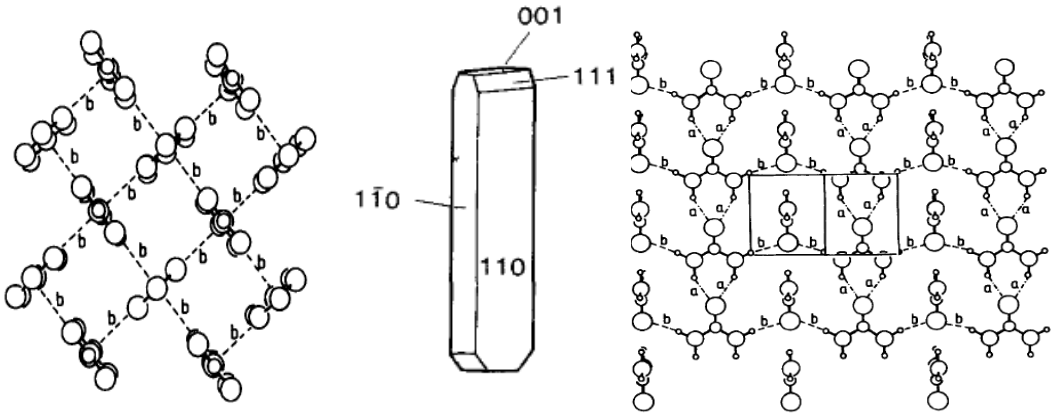


Figure 4. Intermolecular projections highlighting the anisotropic crystal structure of urea ($O=C-(NH_2)_2$) illustrated through the contrasting packing arrangements on the {001} (left) and {110} (right) surface planes together with the resultant crystal morphology (centre) – adapted from [17].

5. Crystallisation from Solution

Crystallisation involves the transformation of matter from one typically disordered phase to a highly ordered solid phase. For organic materials crystallisation from the solution phase is the most commonly applied technique, as most, though not all, solids exhibit an increase in solubility with increasing temperature. This can be exploited to induce crystallisation by cooling a solution, which has been saturated with solute at some higher temperature. Solubility or solute concentration changes can also be induced by evaporation of solvent from a solution or by addition of an anti-solvent. These also form the basis of several crystallisation techniques.

5.1 Particle Design via Crystallisation

The supersaturation driving force affects the kinetics of both the nucleation and growth stages and in turn, as shown in the schematic diagram in Figure 5, has a direct impact upon the properties of the resulting crystals with:

- Nucleation having an impact on the particles' size, crystallinity and the polymorphic form obtained;
- Crystal growth having an impact on the shape of the final crystals, their purity and their tendency to agglomerate with other crystals.

The driving force for solution phase crystallisation is supersaturation, which impacts on the two key stages of the process.

- Nucleation, which is three-dimensional (3D) (assembly of molecular clusters on nm size scale), and
- Growth, which is two-dimensional (2D) (on all atomically smooth particle surfaces).

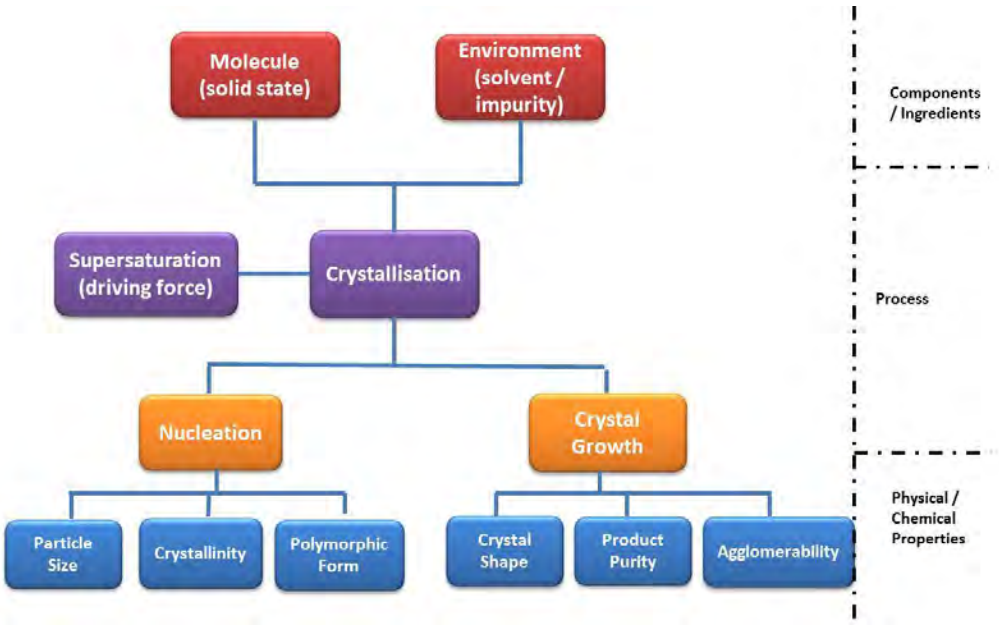


Figure 5. Schematic diagram, after Camacho Corzo et al. [18] showing the role played by the fundamental parameters of crystallisation (nucleation and growth) in directing the physical properties of the resulting solid forms. Prediction of the outcomes would allow greater control of the final product. Reproduced by consent of Springer & NATO Emerging Security Challenges Division.

Crystals resulting from stable growth process tend to exhibit a well-defined morphology as defined by low-indexed habit planes with each face having different surface chemistry and hence potentially different physical, chemical and processing properties. Overall, as shown in the schematic in Figure 6, a facetted crystal can be regarded developing from a 3D nucleation centre into the sum of n 2D growth processes where n = numbers of faces.

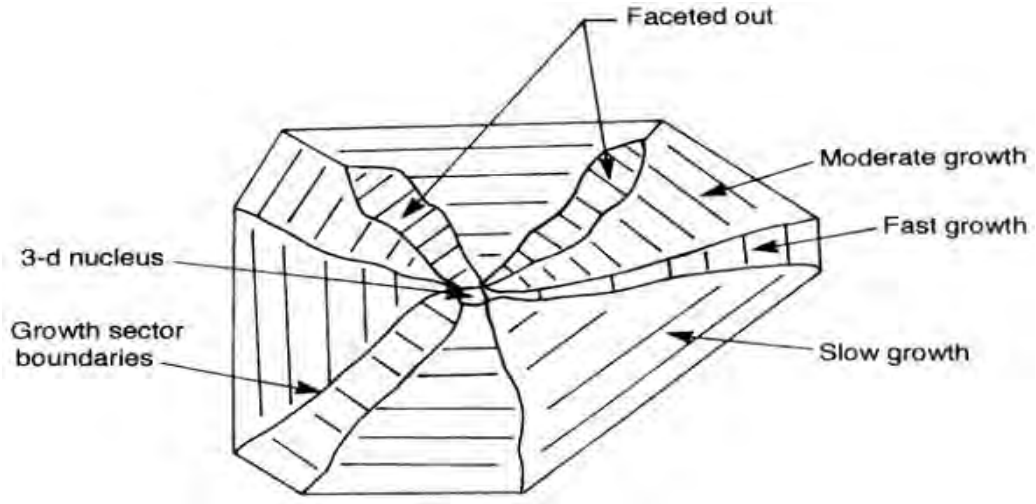


Figure 6. Schematic diagram showing a hypothetical 'cut' through a crystal particle showing the development of a fully facetted crystal from its initial 3D nucleation site. Reproduced by consent from J Phys D - Appl Phys, Ref. [19].

5.2 Solutions and Solubility

When excess solid is mixed with a solvent at constant temperature, the solid will dissolve until equilibrium is established. The resulting solution is said to be **saturated** and composition of the solution is the **equilibrium solubility** (or more commonly, simply the solubility) at that temperature.

Ideal solubility is solubility of solute in a solvent, without any energy penalty associated with the dissolution process, i.e. the energy of mixing is essentially zero. When the interaction between solute-solute in the solid is the same as the interaction between solute-solvent, then the only enthalpy change involved is heat of fusion, and can be represented by the Hildebrand equation:

$$\ln x = \frac{\Delta H_f}{R}\left[\frac{1}{T_f} - \frac{1}{T}\right] \quad (5)$$

Where ΔH_f is enthalpy of fusion of pure solute, T_f is melting temperature of pure solute, R is gas constant and T is the temperature. Enthalpy of fusion as a function of entropy of fusion is given by;

$$\Delta H_f = T_f \Delta S_f \quad (6)$$

where ΔS_f is the entropy of fusion. Thus, the Hildebrand equation becomes;

$$\ln x = \frac{\Delta H_f}{RT} + \frac{\Delta S_f}{R} \quad (7)$$

In the case of a non-ideal solution, the expressions of enthalpy and entropy of fusion can be replaced by enthalpy of dissolution (ΔH_{diss}) and entropy of dissolution (ΔS_{diss});

$$\ln x = \frac{\Delta H_{diss}}{RT} + \frac{\Delta S_{diss}}{R} \quad (8)$$

The difference between the ideal solubility and non-ideal solubility lines plotted on the graph of ln x(mol) and 1/T(K^{-1}) at saturation temperature, is called the activity

coefficient at saturation, γ. An ideal solution has γ =1 and can be defined as being where all the molecules, both solute and solvent, are homogeneously mixed. Most materials however do not display ideal behaviour and their solubility varies with solvent choice. Examination of solubility as a function of temperature through the van't Hoff relationship gives important information regarding molecular ordering within the solution, i.e.

- γ > 1 indicates the solution is less than ideal and solute/solute interactions are likely to be preferred. Such behaviour can be important to know when considering the mechanism by which a material can nucleate, see section 5.4.
- γ < 1 shows that the solution behaves in a more than ideal behaviour and that strong solute/solvent interaction can be expected. Such behaviour implies strong solvation which can impact upon a material's ease of crystallisation, see section 5.3.

Solubility, together with the manner in which it changes with environmental conditions, are the two most important influences on crystallisation behaviour. The amount of solute in solution obviously determines the ultimate yield from any crystallisation process.

5.3 Supersaturation, the Meta-Stable Zone and Crystallisability

Changes in solubility with environmental conditions provide the means of generating supersaturation – the driving force for crystallisation. The changes in these conditions may be, for example: decreasing the temperature of a saturated solution, changing the polarity or hydrogen bonding capability of the solution by addition of another solvent, or addition of a salt amongst many others. The nature and extent of these changes strongly influence crystallisation mechanisms and rates together with many physical properties of the resulting crystals, including particle size, shape, purity and polymorphic form.

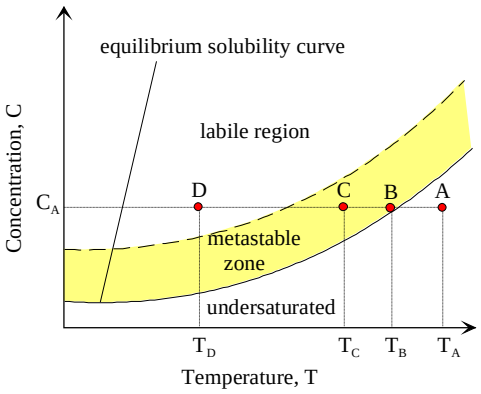


Figure 7. Schematic diagram of the interrelationship between solution temperature and solute concentration highlighting the metastable zone between the solubility and crystallisation (supersolubility) curves where crystallisation is not spontaneously taking place after an induction time. Reproduced by consent of Springer & NATO Emerging Security Challenges Division from Ref. [18].

Consider temperature T_A of a solution indicated by point A on the solubility curve in a typical solubility-temperature diagram shown in Figure 7. The concentration, C_A, of the solution is less than the equilibrium solubility at this temperature. Such a solution as referred to as **undersaturated,** and precipitation cannot occur. The solution at this point is in a stable region. If the solution is cooled, it remains undersaturated until point B at which temperature, T_B, the solution concentration is equal to the equilibrium concentration. At point B the solution is said to be **saturated**. By further cooling to T_C, the system is in a metastable zone, and leads to a metastable situation in which the solution concentration exceeds the equilibrium solubility (point C) and the solution is said to be **supersaturated**. The excess solute does not, however, precipitate immediately from solution. Indeed, supersaturated solutions may remain stable for hours or even months. This is because solute molecules must form stable nuclei before growth of the solid phase can proceed. This nucleation barrier is often the rate determining step of precipitation. The process of nucleation is considered in detail in Section 5.4. Finally, within the **labile** region, e.g., if the solution in Figure 7 is cooled further to point D at temperature T_D, precipitation occurs almost instantaneously. The width of the metastable zone depends upon a variety of factors, including agitation of the solution, impurity content and the method used to detect the onset of precipitation.

The extent to which a solution exceeds the equilibrium solubility is specified in terms of either relative supersaturation, σ or supersaturation ratio, S. These are defined by equations (9) and (10). As with all definitions of solution composition, it is essential to define carefully the units used in the calculation of either σ or S.

$$\sigma = \frac{c - c^*}{c^*} \tag{9}$$

$$S = \frac{c}{c^*} \tag{10}$$

where c is solution concentration and c* is equilibrium concentration of the solution at the given temperature.

A simple but very effective means of determining the metastable zone width as well as other aspects of nucleation behaviour is by measuring the turbidity of the crystallising solution. A simple turbidity probe comprises a light source, a solution gap and a detector. Fibre optics are typically the most convenient way of achieving such an arrangement in the minimum volume. As nuclei form and grow in an originally clear solution, the optical transmittance of the medium decreases.

Figure 8 shows the change in transmittance as a function of temperature for L-glutamic acid. It reveals both the onset of nucleation (decrease in transmittance) and the onset of dissolution (increase in transmittance) as the temperature is cycled above and below the saturation temperature of the solution. The difference between the temperature of dissolution and that of crystallisation is the metastable zone width (MZW). The measured MZW is strongly dependant upon cooling rate, agitation and process scale. These influences can be readily quantified using turbidity measurements. Since the measurements also indicate the dissolution temperatures, turbidity probes also allow automated determination of solubility curves as a function of temperature, composition, pH etc. It should be appreciated that all measurements of nucleation behaviour, including MZW, are strongly dependant on the sensitivity of the measurement technique. Nucleation undoubtedly starts to occur before the change

in optical transmittance detected by the turbidity probe. Despite this, the insight into nucleation behaviour afforded by this approach is still valid.

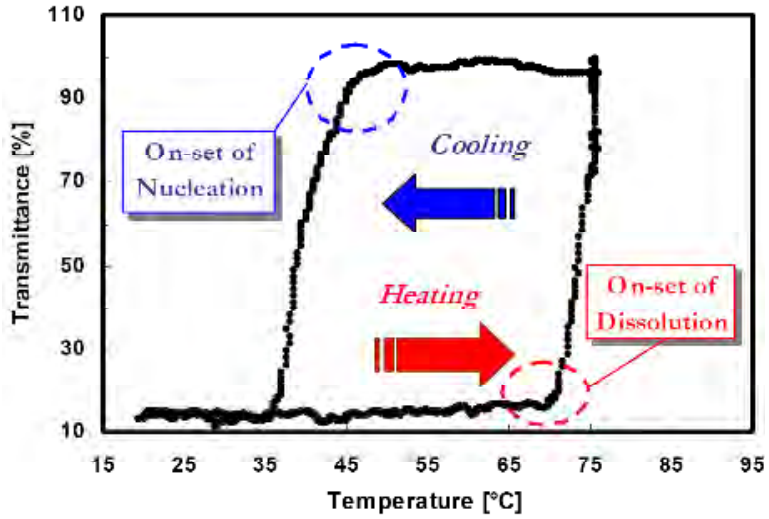


Figure 8. Optical transmittance of a bulk aqueous solution of L-glutamic acid, as measured using a turbidity probe, versus temperature for a cooling crystallising process showing both the onsets of nucleation and dissolution. Reproduced by consent of J. Cryst. Growth from Ref. [20].

5.4 Molecular Aggregation and Nucleation

The first stage in the precipitation of crystalline phase from a supersaturated solution is the formation and dissolution of small clusters of solute molecules. Some of these clusters may grow sufficiently to form stable nuclei and subsequently form crystals. This process is known as **nucleation**. Others fail to reach adequate dimensions before they dissolve again. Nucleation behaviour is best understood by examining the free energy change associated with nucleus formation. Two competing factors must be considered:

- The transfer of a molecule from a supersaturated solution to the solid phase results in a decrease in free energy per molecule.
- The surface of the new solid phase has an energy associated with it and this surface energy results in an increase in free energy per unit surface area of the cluster.

Figure 9 shows these two competing contributions to the free energy of a nucleus as a function of its radius.

Note that (a), being a volume effect and showing r^3 dependence, decreases more rapidly than the increase in (b) which varies as r^2. The sum of these two contributions yields a maximum in free energy at the critical radius, r_c. Nuclei smaller than the critical radius can achieve a decrease in free energy by reducing their size and dissolution is, therefore, favoured. If, through statistical fluctuations, a nucleus achieves the size greater than the critical radius, growth is favoured since an increase in size will lead to a decrease in free energy. Such nuclei are therefore stable and will grow into crystals.

Within the bulk of a solution, two types of nucleation can occur:

- Homogeneous nucleation, involving only solute molecules
- Heterogeneous nucleation in which nuclei form on a foreign particle or surface.

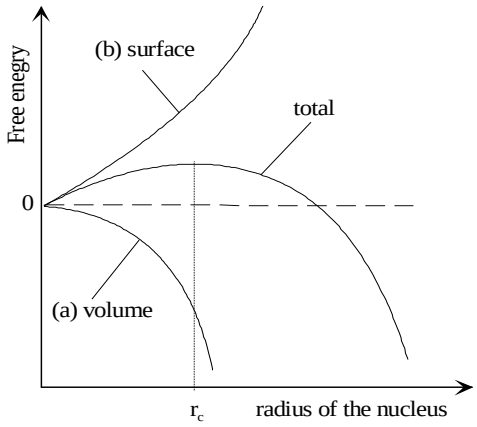


Figure 9. Schematic diagram showing how changes in the relative balance between the surface and bulk free energy leads to the formation of a critical nucleus for nucleation. Reproduced by consent of Springer & NATO Emerging Security Challenges Division from Ref. [18].

In practice, except at very high supersaturations, almost all nucleation is heterogeneous, since it is impossible to eliminate all foreign particulate material from solutions. The critical radius of a spherical three-dimensional nucleus is given by equation 11:

$$r_c = \frac{2\omega\gamma}{kT\ln(1+\sigma)} \qquad (11)$$

where γ is the surface energy, ω is the molecular volume, k is Boltzmann's constant, T is the temperature, and σ is the relative supersaturation. It can be seen from equation 11 that the critical radius decreases with increasing supersaturation. Thus, at high supersaturation, nucleation occurs readily due to the relatively small number of molecules required to form a nucleus of critical dimensions and promotes homogeneous nucleation.

6. Crystal Surface Morphology and the Growth Mechanism

6.1 Stages in Crystal Growth Process

There are a number of stages involved in the formation of a crystalline phase from a supersaturated solution (see Figure 10), and the relative importance of these in terms of both the thermodynamics and kinetics associated with the process can differ substantially depending upon the physical and chemical properties of the starting phase

Diffusion through bulk solution to the crystal surface: In order to form stable clusters and for subsequent growth to occur, molecules in solution must move through

the bulk solution. This process depends upon temperature, molecular size, solvation and solution properties such as viscosity (Figure 11).

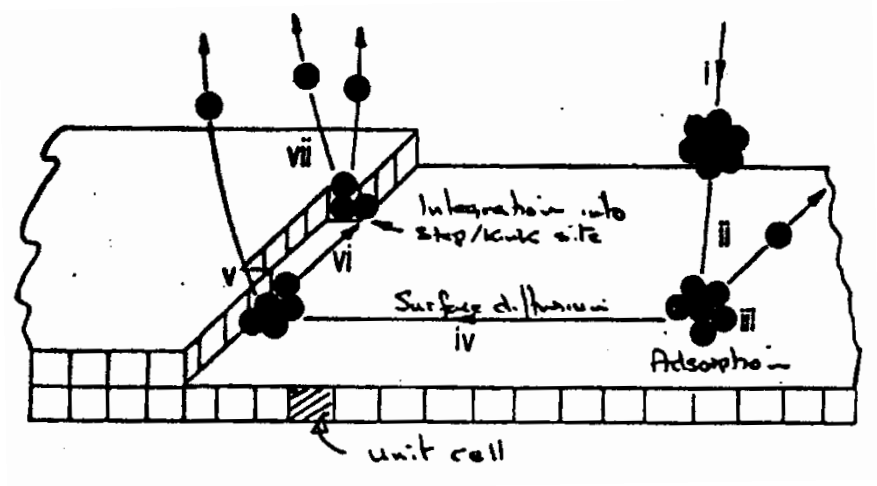


Figure 10. Schematic diagram showing the various crystal/solution interfacial stages that take place during the crystal growth process. Reproduced by consent of by Journal Phys. D: Appl. Phys., Ref. [21].

Surface diffusion: A molecule which is incident on a crystal face does not necessarily become part of the crystal immediately. If the surface is flat, surface diffusion of the molecule may be necessary for it to reach a suitable site where it can bind strongly with the surface and become a permanent part of the crystal.

Incorporation into surface sites: The ease with which a molecule is incorporated into the crystal depends upon the nature of the growing face. For a face which is rough at the molecular level, most or all molecules incident on the surface can be expected to be integrated into the crystal. For flat surfaces, solute molecules typically need to reach suitable sites on surface steps for this to happen.

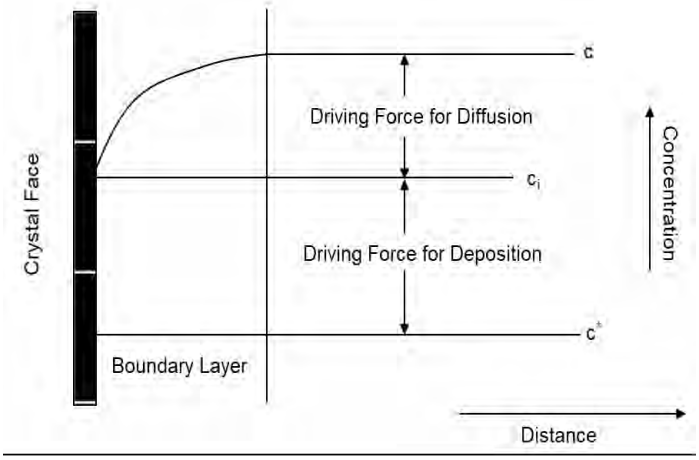


Figure 11. Schematic diagram highlighting the concentration boundary layer between the crystal surface and the bulk solution highlighting the depletion of solute concentration close to the crystal surface due to crystal growth.

Desolvation: Molecules in solution are typically surrounded by a cage of solvent molecules and are described as being solvated. The extent of solvation depends upon the specific intermolecular forces between solvent and solute molecules. Before a molecule or ion can be incorporated into a growing crystal, the solvent molecules must be shed. This occurs to different degrees from the solute molecule being adsorbed onto the crystal surface through to its final incorporation into the crystal lattice.

6.2 The Nature of Crystal Growth Surfaces.

Crystals grown from solution typically exhibit regular, planar facets. Although appearing flat to the naked eye, these crystalline surfaces are rarely so at the molecular level. The various features that make up the nanoscale surface topography of crystal face are intimately involved in the mechanisms by which crystals grow.

Figure 12 (a) is a schematic representation of crystal surface in which the molecules, or growth units, are represented by cubes. The principal features of interest are (i) steps; (ii) the terraces between them; (iii) kink sites on the steps; and (vi) terrace-adsorbed molecules. It is important to consider at what point a molecule from solution becomes truly part of the crystal. In this simplified model of a crystal surface, each cube can form a maximum of six bonds with surrounding cubes - one per face of the cube. Examining the various sites on the schematic crystal surface, we can see that each is capable of forming a different number of bonds with an incoming molecule from the solution. A molecule adsorbed onto a terrace can form only one bond with the crystal surface. A molecule in contact with a step can form two bonds while a molecule incorporated at a kink site can form three bonds. The kink site is of particular importance since a molecule placed in such a site does not increase the surface area or, therefore, the surface energy of the crystal. A molecule can, thus, be considered to be truly part of the crystal once it has reached a kink site. Though the nature of bonding for real molecules will be substantially more complex, this simple model reproduces the key differences between the various surface sites.

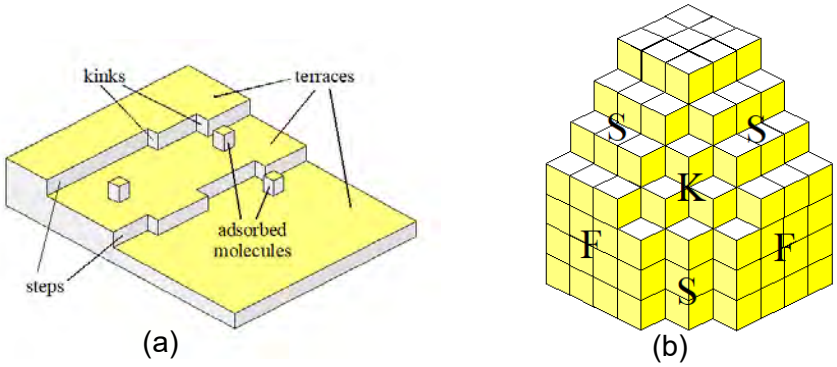


Figure 12. (a) Schematic diagram a representative surface morphology for a crystal surfaces undergoing growth highlighting the presence of steps, terraces, adsorbed molecules and kink sites on a crystal surface; (b) Schematic diagram of a hypothetical crystal built up from cubes 13(a) highlighting the differences between flat (F), stepped (S) and kinked (K) crystal habit faces. Reproduced by consent of Springer & NATO Emerging Security Challenges Division from Ref. [4].

When the cubes of Figure 12(a) are assembled to form a crystal, we find that three different types of crystal face occur: flat or F faces, stepped or S faces and kink or K

faces, as shown in Figure 12(b). In addition to having very different surface topography, the three types of face exhibit very different bonding within the surface. Recalling that, in this simplified model, bonds occur between the faces of the cubes, F faces therefore have continuous chains of bonds in two directions parallel to the face. Such chains of bonds are referred to as periodic bond chains (PBC). S faces have a PBC in only one direction parallel to the face while K faces have no PBCs parallel to the face.

Consider now the way in which each of these faces will behave during growth. Every molecule which is adsorbed on a K face is inevitably incorporated into a kink site and immediately becomes part of the crystal. The fate of molecules incident on an S face is rather more complex. Very few will be incorporated directly into kink sites. Most will be adsorbed onto steps and may diffuse to kink sites on such steps. Many, however, will be desorbed before being incorporated into kink sites. The rate of growth of S faces will, therefore, be substantially slower than that of K faces. Finally, an ideal F face has neither steps nor kink sites and, therefore, grows much more slowly than either K or S faces. As we will see, for F faces to grow at all steps must be introduced by some other mechanism.

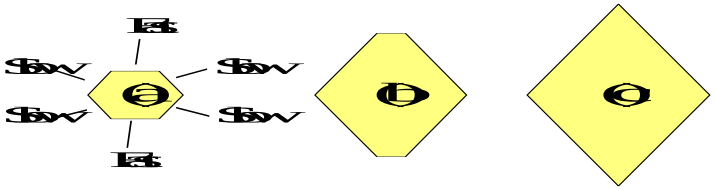


Figure 13. Schematic diagram showing the temporal evolution of crystal morphology showing “growing out” of the faster growing faces leading to a final morphology dominated by the slowest growing faces.

Figure 13(a) shows a schematic diagram of hypothetical crystal bounded by fast and slow growing faces. As the crystal grows, it can be seen that the fast-growing faces become smaller (b) and ultimately disappear (c). As a consequence of this behaviour and the differing growth rates of F, S and K faces, it becomes quite clear that faceted crystals are almost exclusively bounded by slow growing flat or F faces.

The crystal/solution interface relies on molecular recognition to effect high solute species-selectivity that to ensure the formation of a highly pure crystalline product. This in turn requires the maintenance of an appropriate solution supersaturation to ensure mechanistically stable crystal growth conditions.

6.3 Crystal Growth Mechanisms

How a specific crystal surface grows with time depends very much upon:

- Surface chemistry of the face and its interaction with solute and solvent molecules and the desolvation process;
- Crystallisation driving force reflecting both the solute concentration and solution supersaturation;

Depending upon the supersaturation, and as illustrated in Figure 14, there are three main mechanisms of growth at the crystal surface (hkl)/solution interface:

- Screw dislocation (BCF);
- Birth & spread (B&S);
- Rough interface growth (RIG).

It is important to note that the growth mechanism concerned is specific to a given crystal habit plane and that it can change with supersaturation. For example, at high supersaturation the growth interface can roughen leading to a loss of its inherent molecular selectivity resulting in a reduction in product purity.

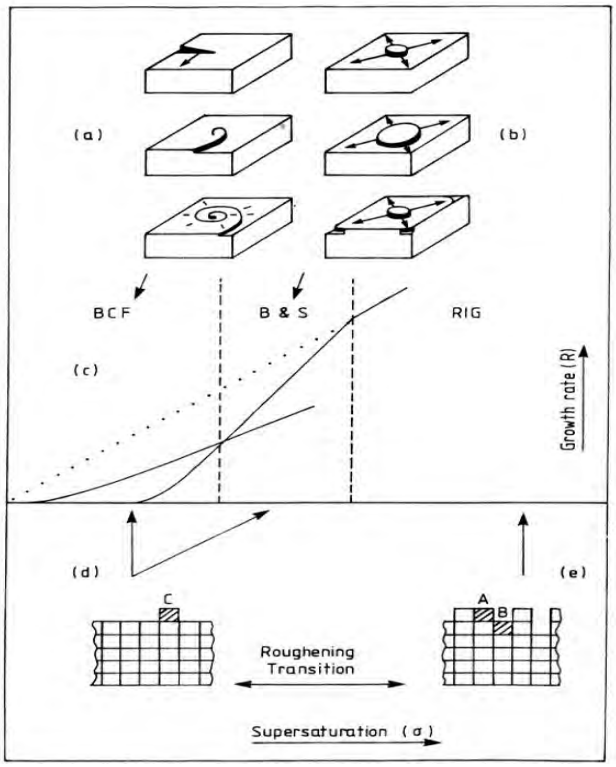


Figure 14. Schematic diagram illustrating the three main mechanisms which can take place at the crystal/solution interface: (a) BCF; (b) B&S; (c) RIG: together with the loss of step/terrace interface coherence through kinetic roughening associated with transformation from a molecularly smooth; (d) to a roughened and (e) interface as a function of supersaturation. Reproduced by consent of J. Phys. D: Appl. Phys., Ref. [22] [21].

Spiral growth: - Spiral crystal growth originates from screw dislocation. It follows from Equation 13 that, at low supersaturation, growth by two-dimensional nucleation is difficult since a very large number of molecules are required to form a stable nucleus of radius, r_c or larger. Detailed analysis reveals that at low supersaturation, the rate of growth by two-dimensional nucleation is negligibly small. Experimental studies show, however, that crystals do in fact grow at appreciable rates even at very low supersaturation. This apparent contradiction between theory and experiment was resolved by Sir Charles Frank who proposed that crystal imperfections known as

screw dislocations provide a surface step, thereby removing the need for two-dimensional nucleation as part of growth process.

Figure 15 shows a schematic diagram of a crystal with screw dislocation. This imperfection can be visualised by considering a block of crystal that has been cut half way through. The material either side of this cut is then displaced by one lattice spacing. The region surrounding the line at the end of the cut is distorted and strained while regions even a short distance from this line are effectively perfect crystal. The line itself is the screw dislocation. One of the most important consequences of the presence of the screw dislocation is the fact that it produces a step where it emerges onto the surface.

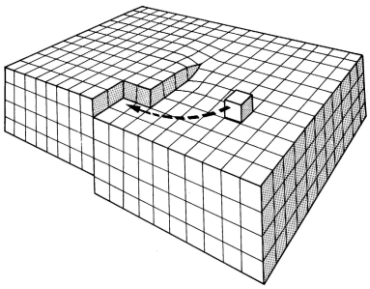
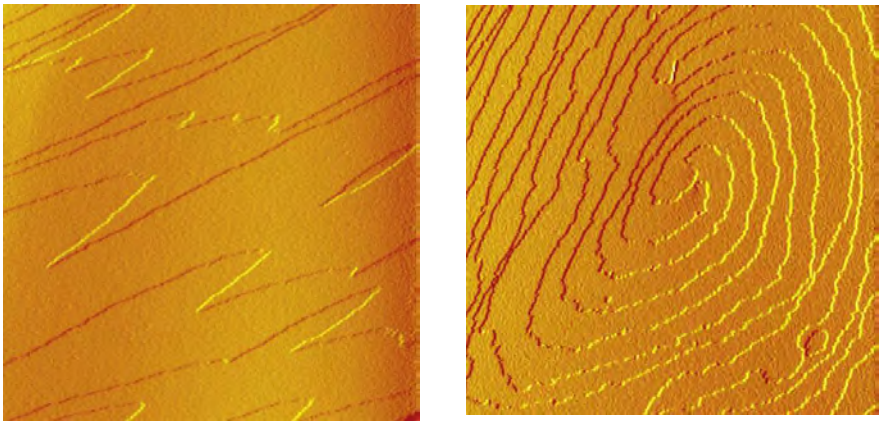


Figure 15. Schematic diagram of a crystal surface whose growth is mediated by the presence of a screw dislocation which creates a permanent step on the surface thus facilitating growth at lower solution supersaturations.

Like all other steps on crystal surfaces, it will contain a certain number of kink sites. Molecules from solution can be incorporated into the growing crystal at these sites either directly or by diffusing across the surface. The step, however, extends only part way across the surface. As the step grows by addition of molecules, it adopts the shape of the spiral and as a consequence, the screw dislocation acts as a continuous source of surface steps and two-dimensional nucleation is not required for the crystal to grow. Contrast this situation with the case of a step which extends across the full width of crystal face. Such a step would advance to the edge of the crystal but then leave a completely flat face only able to grow further by two-dimensional nucleation.



(a) (b)

Figure 16. In-situ AFM images of a {101} face of lysozyme grown at a) high supersaturation showing 2D nucleation, and (b) at low supersaturation where spiral growth dominates [22].

The BCF model follows a parabolic tendency with growth being mediated by the presence of screw dislocations on the crystal surface.

$$R_i = A_o \sigma^2 \tanh\left(\frac{B_o}{\sigma}\right) \quad (12)$$

where R_i is the rate of growth of a crystal face (m/s), σ is the relative supersaturation and A_o and B_o are system related constants.

Figure 16 (a) shows an in-situ AFM image of a {101} face of a lysozyme crystal during growth at high supersaturation. The surface is covered with islands 3.4nm in height which expand in successive images. The surface is, therefore, growing via two dimensional nucleation. The same crystal face though slightly different location is shown in Figure 16 (b) after reducing the supersaturation. The surface is now largely devoid of 2D nuclei and the dominant growth mechanism is spiral growth.

Two-dimensional nucleation: A molecule from solution which adsorbs onto an F face of a crystal is relatively weakly bound to the surface. In the case of a cube shaped molecule in the model discussed above (Figure 12), the cube is bound on only one side. There is, therefore, a high probability that the molecule will be desorbed again in a relatively short period of time. To remain on the flat surface, molecules must form stable clusters or nuclei. This process is the two-dimensional analogue of the nucleation process described in Section 6.2, where the formation of three-dimensional nuclei was considered. Two-dimensional nucleation, shown schematically in Figure 17, is again controlled by the competition between the free energy reduction produced by a molecule moving from solution to the crystal (volume component) and the increase in free energy due to the formation of a new surface - in this case the step surrounding the two-dimensional nucleus.

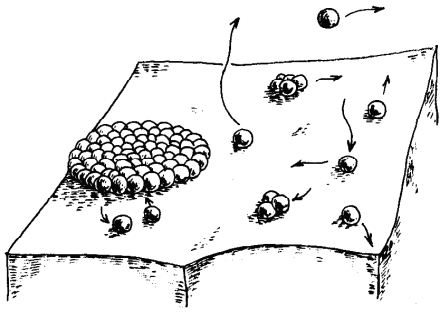


Figure 17. Schematic diagram showing the two dimensional nucleation - birth and spread (B&S) - process involving the aggregation of molecules on the crystal surface until a critical cluster size is formed. Reproduced by consent of Springer & NATO Emerging Security Challenges Division from Ref. [18].

The shape of the free energy-radius curve is essentially the same as that shown in Figure 9 for three-dimensional nucleation. As before, the sum of the volume and surface components for a two-dimensional nucleus exhibits a maximum at the critical radius, r_c. Two-dimensional nuclei larger than r_c are stable and continue to grow until they cover the entire crystal face. For the next layer to grow, nucleation must occur again. Equation 13 shows the relationship between the critical radius and supersaturation for a cylindrical two-dimensional nucleus. Again, high

supersaturations favour nucleation since a nucleus must achieve only relatively small dimensions in order to become stable.

$$r_c = \frac{\omega\alpha}{kT\ln(1+\sigma)} \quad (13)$$

where, α is the step edge free energy, ω is the molecular volume, k is Boltzmann's constant, T is temperature, and σ is relative supersaturation.

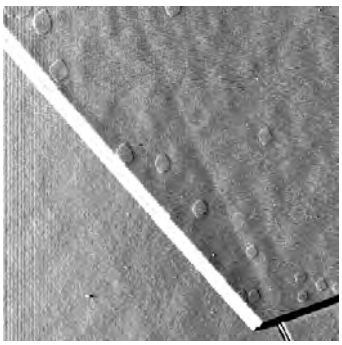


Figure 18. Ex-situ atomic force microscopy image showing the formation of two-dimensional nuclei on the (010) surface of a crystal of potassium hydrogen phthalate. Reproduced by consent of J. Cryst. Growth, from Ref. [23].

Figure 18 shows an atomic force microscope image of a crystal of potassium hydrogen phthalate grown from aqueous solution on a glass slide. The crystal is approximately 80μm in length and 230 nm thick. The edges of the crystal can be clearly seen in the AFM image. Imaging was carried out in air after rapid removal of the growth solution using a pulse of compressed nitrogen.

It can be seen that the crystal surface is mostly flat but with a few small islands, particularly near the crystal edges. The height of the islands corresponds to one lattice spacing (approximately 1nm). This face has grown by two-dimensional nucleation. The length to thickness ratio for potassium hydrogen phthalate crystals grown under similar conditions is typically much smaller.

The B&S model follows an exponential tendency with growth mediated by 2D nucleation:

$$R_i = A_o \sigma^{\frac{5}{6}} exp\left(\frac{B_o}{\sigma}\right) \quad (14)$$

where R_i is rate of growth of a crystal face (m/s), σ is relative supersaturation; and A_o and B_o are system related constants.

Rough Interfacial Growth (RIG): If a crystal surface is rough at the molecular level, as in the case of K faces above, every growth unit which impinges on the surface can be expected to be incorporated into the growing crystal. This is known as continuous or rough growth. Because a much larger proportion of incident growth units are incorporated compared to either 2D nucleation or spiral growth on flat faces, continuous growth is much more rapid.

This model follows a linear tendency as the growth occurs on a molecular roughened surface:

$$R_i = A_o \sigma \tag{15}$$

where R_i is the rate of growth of a crystal face (m/s), σ is relative supersaturation and A_o is a system related constant.

6.4 Growth Stability and Interfacial Roughening

The differences in surface roughness of crystal faces are not as clearly differentiated as suggested by the simple model on which the F, S and K faces of Figure 12 are based. Many factors combine to control the nature of a crystal face including: molecular shape, strength of intermolecular bonding, temperature, solvent and supersaturation.

The nature of a crystal face can be described by a quantity known as the alpha factor, α (also referred to as the surface entropy factor) where

$$\alpha = \xi \left(\frac{\Delta H_f}{RT} - \ln x_{seq} \right) \tag{16}$$

where ξ is the anisotropy factor, ΔH_f is the enthalpy of fusion, R is the gas constant, T is the temperature and x_{seq} is the mole fraction of the solute as calculated for the supersaturation for crystal growth.

The anisotropy factor is related to the number of nearest neighbour sites at the interface and in the bulk of the crystal. The alpha factor is simply the product of the anisotropy factor and the entropy change upon crystallisation. The latter is influenced in part by the shape and complexity of the crystallising species.

Based upon the magnitude of the alpha factor, it is possible to define several regions in which different surface structures and thus different growth modes exist.

- For $\alpha < 2$, the interface is expected to be rough at the molecular level, leading to a continuous growth mechanism, leading to rapid growth.
- At intermediate α values; $2 < \alpha < 5$, two-dimensional nucleation (B&S) is expected to dominate.
- For $\alpha > 5$, a molecularly flat interface is expected upon which 2-dimensional nucleation will be unfavourable, resulting in the dominance of a spiral growth mechanism (BCF) and much slower crystal growth.

An F face is only completely flat at absolute zero. At all other temperatures, molecules from the crystal may move to the surface to yield an adsorbed molecule and corresponding surface vacancy. Above some critical temperature a crystal face will become rough and exhibit a corresponding change in growth mechanism and rate. This roughening temperature depends in particular upon the strength of intermolecular bonding.

During growth a crystal face can become rough even below the roughening temperature. The critical radius of a 2-dimensional nucleus decreases as the supersaturation increases. Recall that nuclei larger than the critical radius are stable (Figure 9). At sufficiently high supersaturation, the critical radius can become equal to that of a single growth unit. Under such conditions any growth unit incident on the face

is stable and can be expected to remain there. Thus, the face will become rough at the molecular level. The phenomenon is known as kinetic roughening. Figure shows kinetic roughening of the {202} form of sodium dodecyl sulphate (SDS).

Under very high supersaturation conditions, quite unstable hopper and dendritic morphologies can be formed. The main characteristics of e.g. dendritic growth are shown in Figure 20 (a). In this, the main stem of the dendrite grows rapidly with additional, time-dependant, crystallisation producing branches growing significantly more slowly. In some cases, these primary branches may also exhibit smaller, secondary branches. Although such structure are well-known in the formation of e.g. metallic alloys and snowflakes, they can also be seen in organic materials under unstable crystallisation conditions. For example, Figure 20(b) shows the unwanted crystallisation of the drug Neupro within transdermal patches which reduced the amount of the drug dose delivered to a patient which led to product recall for re-formulation in 2008.

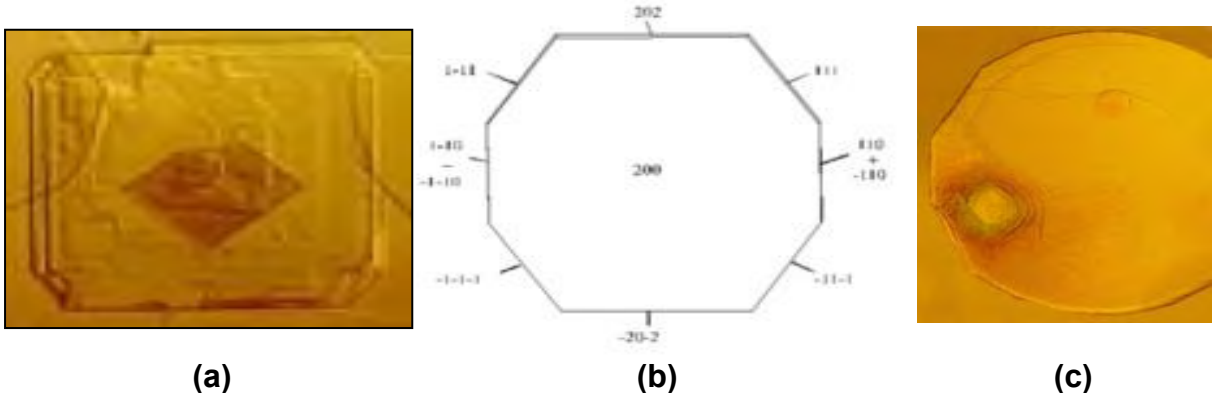


Figure 19. Sodium dodecyl sulphate (SDS): (a) optical micrograph of crystal grown at low supersaturation showing well-defined crystal morphology; (b) associated morphological sketch; (c) optical micrograph of crystal grown at higher supersaturation showing the kinetic roughening of the {202} surfaces. Reproduced by consent of J Cryst Growth, from Ref. [24].

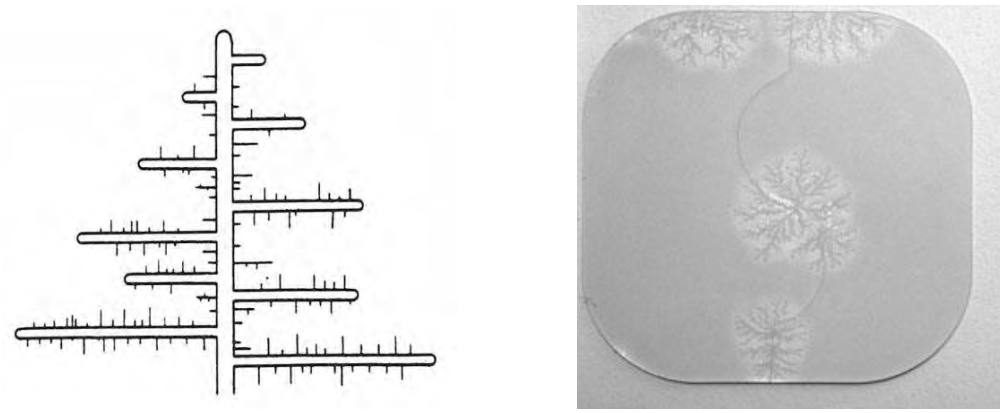


Figure 20. Unstable dendritic crystal growth: (a, left) schematic diagram showing the formation of one-dimensional crystal dendrites oriented along the strong intermolecular bonding; (b, right) micrograph showing the formation of dendritic crystals around the edges of a trans-dermal patch of the pharmaceutical product Neupro.

7. Case Study: Structure, Morphology, Growth Mechanism and Solvent Effects in Racemic (RS) Ibuprofen

This case study centres on the crystallisation of RS Ibuprofen, grown in different solvent type and supersaturation. The discussion will focus on the crystal growth assessment, growth mechanism and synthonic analysis affecting the growth, due to the solvents.

Racemic (RS) ibuprofen (2-(4-isobutyl-phenyl) propionic acid), $C_{13}H_{18}O_2$, molecular weight = 206.28 g mol^{-1}, melting point (77–78 °C) is a non-steroidal anti-inflammatory drug (NSAID) and widely used in the treatment of pain, cold, fever and inflammation. This material crystallizes in a monoclinic crystal structure with space group P21/c in a tetramolecular unit cell with unit cell dimensions of a = 14.667 Å, b = 7.886 Å, c = 10.730 Å, β = 99.3628°, Z = 4. An RS Ibuprofen molecule contains a carboxylic acid group at one end, an aliphatic chain at the other, and a phenyl ring group positioned in between them. It crystallizes in a centrosymmetric tetramolecular monoclinic unit cell, as shown in Figure 21.

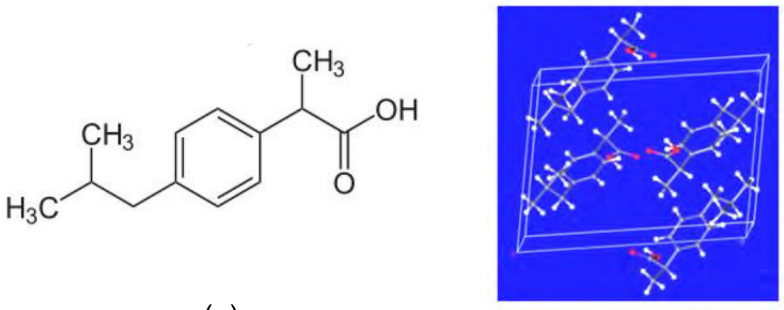


Figure 21. Molecular diagrams of RS Ibuprofen showing (a) the molecular structure, and (b) its crystal structure in a unit cell packing unit (Reproduced by consent of CrystEngComm from [25]).

The hexagonal plate-like morphology of RS Ibuprofen is dominated by a large {100} facet, followed by a smaller {001} and {011} side facets (see Figure 22) and it can have different crystal habits due to varying the crystallisation conditions, such as solvent selection.

7.1 Growth Rate Measurement and Mechanism

Measurements of growth rates for specific crystal faces (*hkl*) can be carried out using microscopy coupled with a growth cell set up [25]. Figure 22(a) shows the methodology used to measure the growth of individual faces of Ibuprofen crystals and Figure 22(b) an example of the corresponding growth rate values obtained experimentally. The growth rates of the individual faces R_i can be obtained by following the increase with time of the normal distance from the centre of the crystal to the faces.

The result in Figure 23 shows that the growth rates of {001} and {011} surfaces of RS Ibuprofen follow a constant growth model, which proposes that the faces underwent a constant relative growth rate during the growth period, even though each crystal experienced different growth rates. These crystals were grown in ethanol, and with different supersaturation.

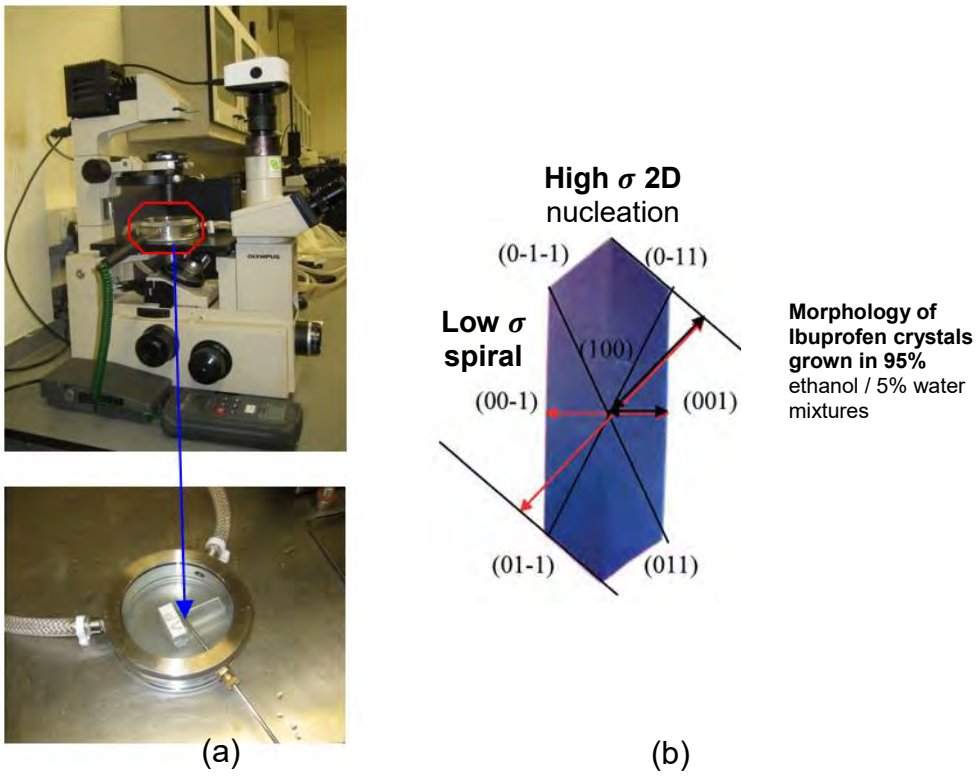


Figure 22. (a) Experimental set up and methodology for the measurement of growth rates of the {011} and {002} faces of Ibuprofen crystals: Olympus IMT-2 inverted optical polarising microscope integrated with Lumenera Infinity 3.3 megapixel CCD camera; enlarged picture of the crystal growth cell and example of measurement of normal distances from the centre of the crystal to the faces, (b) An image of ibuprofen crystal, with overlaid annotations highlighting the methodology for measuring the growth rate of the {001} and {011} surfaces. (Reproduced by consent of CrystEngComm from Ref. [25])

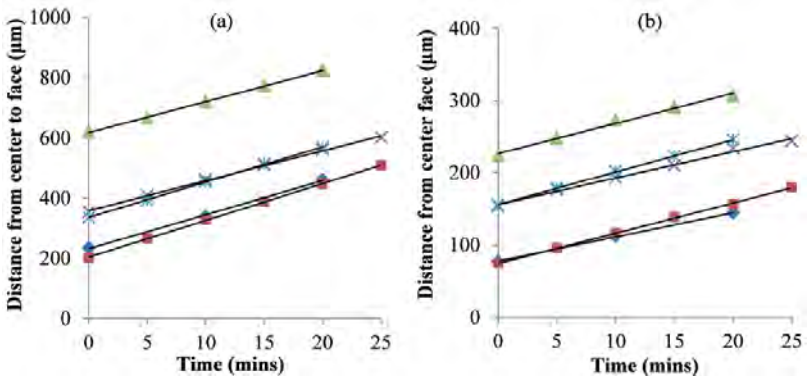


Figure 23. Example of normal distances from the centre of the crystals to the {011} and {001} faces as a function of time. Each line represents the growth rate of an individual crystal over time: (a) the {011} face in ethanol at σ = 0.66 and (b) the {001} face in ethanol at σ = 0.66. (Reproduced by consent of CrystEngComm from [25])

The mechanism of crystal growth of a specific crystal face can be assessed by fitting of measured growth rate data as a function of supersaturation to the models described. Figure 24 shows an example of this assessment for Ibuprofen crystals growing from different solvents.

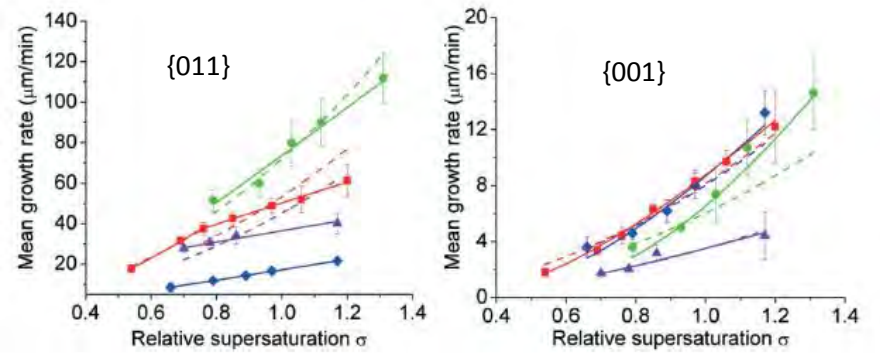


Figure 24. Growth rate versus relative supersaturation of ibuprofen crystals growing at 0.5 ml scale from ethanol (blue), ethyl acetate (red), acetonitrile (green) and toluene (purple) together with fitted B&S (solid lines) and BCF (dotted lines) mechanism models for the {011} (left) and {001} (right) surfaces. (Reproduced by consent of CrystEngComm from [25]).

The plots of the measured crystal growth data fitted against the growth mechanism model shows that the growth of both {001} and {011} surfaces is consistent with a two-dimensional nucleation (B&S). Crystals grown in various supersaturation (σ = 0.54 to 1.22) also show that both faces grow through a B&S mechanism, although for a few cases the BCF mechanism was also found to fit the data satisfactorily. The growth rates for both the {011} and {001} surfaces increase with increasing supersaturation, however the rate of growth is depending on the solvent type, which is due to the differences in the inter-molecular interactions between crystal surfaces and the solvents. This reflects on the crystal aspect ratios and causes the crystals to become more elongated (see Figure 25).

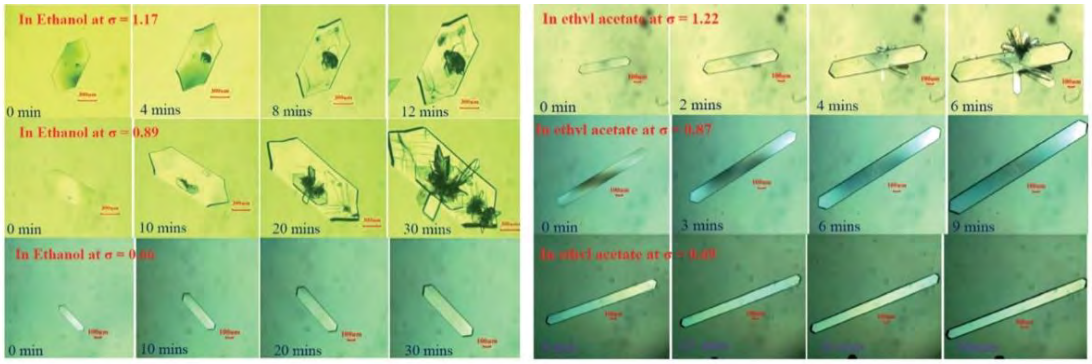


Figure 25. Series of optical micrograph images of ibuprofen crystals grown in (a) ethanol/water 95/5%, and (b) ethyl acetate. (Reproduced by consent of CrystEngComm from [25]).

7.2 Interfacial stability and inequivalent wetting on the crystal habit surface, in relation to its molecular and synthonic structure

The role of solvent in the change of morphology of RS ibuprofen was investigated, from the synthonic interactions point of view, involving surface interfacial stability, and surface chemistry to rationalise its growth behaviour as a function of crystal environment.

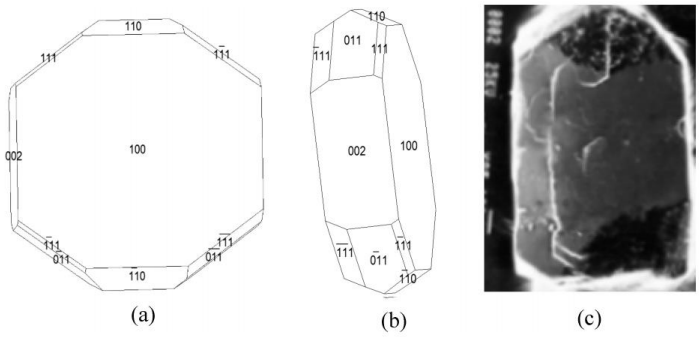


Figure 26. Comparison between predicted morphology of RS Ibuprofen and experimentally grown crystal: (a) morphology looking down the (100) face; (b) morphology looking down the {002}/or {001} surface; and (c) crystal grown in vapour [26].

The predicted crystal morphology using methods described in Section 4, can be seen in Figure 26. However, crystals grown from solution are found to have higher aspect ratios; i.e. less needle-like crystal morphology if grown in polar protic solvents (such as ethanol), than those prepared in aprotic solvents (such as ethyl acetate) (see Figure 25). This can be rationalised through an examination of chemistry for the {002} and {011} crystal habit surfaces, as shown in Figure 27.

This reveals that the termination of the {002} surface mainly involves weaker and less directed van der Waal's interactions whilst growth at the {011} capping surface involves stronger and more directed H-bond interactions. This contrasting surface chemistry suggests that protic polar solvents would be more likely to bind to the capping compared to the side surfaces hence inhibiting the growth of the long needle when compared to apolar or aprotic solvents [25].

This habit-modifying effect also reflects the molecular "roughness" or rugosity of the terminating surfaces with the {011} surfaces containing ridges and 'valleys' which acts as an energetically favourable docking for strong H-bonding site [28]. In contrast, the side faces such as {002} have smoother surfaces and involve only with weaker dispersive interactions with solute molecules. In the case of "hexagonal" RS Ibuprofen crystals grown in ethanol (see Figure 25), a strong interaction between the ethanol molecule and the {011} surface; and much weaker interaction with the {002} surface were identified through molecular modelling studies. These, indicate a lower growth rate of the {011} and higher growth rate of the {002} surfaces, compared to other solvents such as ethyl acetate. The H-bonds formed between ethanol and the capping {011} surface most likely inhibit the growth associated with the strong H-bonding that governs the growth along the needle axis [28].

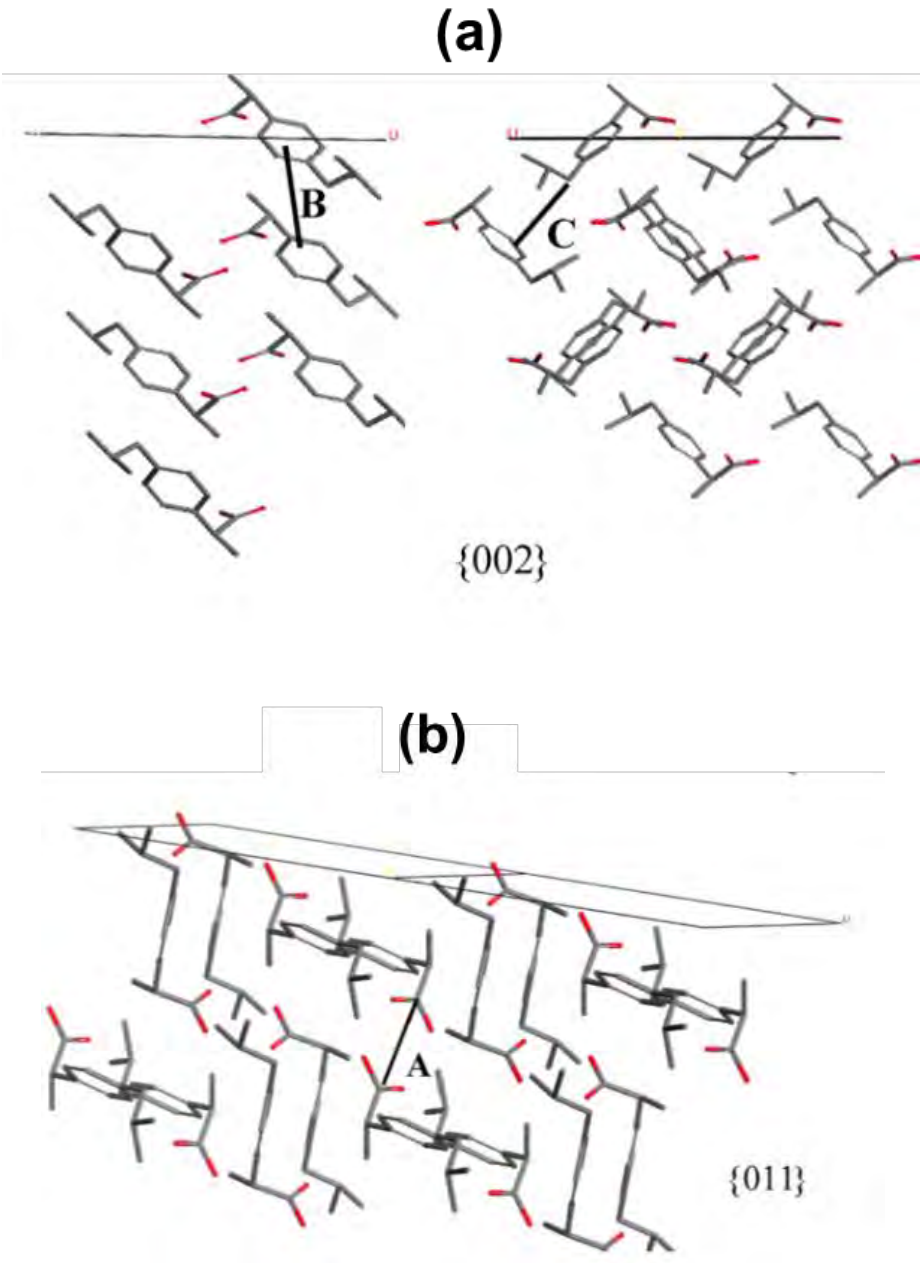


Figure 27. Intermolecular projections of the inbuprofen crystal structure highlighting the crystal surface chemistry for: (a) the side {002} faces and (b) the end-capping {011} habit surfaces. Noteworthy, is that growth of the {002} surface is dominated by van der Waals interactions (intermolecular synthons B and C) whilst that growth of the {011} surface is dominated by hydrogen bonds (intermolecular synthon A), after [28].

Investigation and analysis on the nature of crystal surface, based on the alpha factor, α (see Equation 16) suggests that the capping {011} will be the least smooth on the molecular level, with a higher degree of unsaturated extrinsic synthons when compared to the {002} surface [27]. This molecular-scale “roughness” of the {011} surfaces can also give rise to the formation of a re-entrant surface morphological instability on this capping surface [25].

8. Concluding Remarks

The objective of these lectures has been three-fold.

First, to highlight some of the distinguishing features of organic crystal growth when compared to other materials systems, notably their anisotropic crystal structures and bonding which impact on how their structures are intimately inter-related with their physico-chemical properties. These factors affect the mode of crystal growth, i.e. the selection mostly of the low temperature solution method. The importance for a crystal growth scientist to be able to assess, compare and then select a suitable candidate organic material from a multitude of different structures and structural types.

Secondly, the lectures have sought to provide a knowledge route map in terms of the basic crystallisation science and practice that underpins our understanding of how to prepare organic microcrystalline solids for industrial application. In this, the lectures have attempted to cover the solubility and solution ideality for crystallisation processes, supersaturation, nucleation and how these relate to the crystallisability of a compound, crystal growth rate and its measurement together with the characterisation of face-specific growth mechanisms.

Thirdly, the underpinning science described above is illustrated through a representative case study related to the interrelationship between the structure, morphology and crystal growth of a pharmaceutical compound, RS Ibuprofen.

Bibliography and Further Reading

1. G. Clydesdale, K. J. Roberts, E. M. Walker, “The crystal habit of molecular materials: A structural perspective,” in *Molecular Solid State: Synthesis, Structure, Reactions, Applications, Volume 2, Theoretical Aspects and Computer Modelling*, A. Gavezzotti, Ed. 1996, Chapter 7, pp. 203-232.
2. G. Clydesdale, K. J. Roberts, R. Docherty, “Computational studies of the morphology of molecular crystals through solid-state intermolecular force calculations using the atom-atom method,” in *Colloid and Surface Engineering: Controlled Particle, Droplet and Bubble Formation*, D. Wedlock, Ed. London: Butterworths Heineman, 1993, pp. 95-135.
3. G. J. Sloan, A. R. McGhie, *Techniques of Melt Crystallization*, 4th ed. New York: John Wiley & Sons, 1988.
4. J. P. van der Eerden, O. S. L. Bruinsma, Eds. *Science and Technology of Crystal Growth*, Netherland: Kluwer Academic Publishers, 1995.
5. N. Garti, K. Sato, Eds. *Crystallization Processes in Fats and Lipids Systems,* New York: Marcel Dekker Inc., 2001.
6. R. Ramanarayanan, W. Kern, M. Larson, S. Sikdar, Eds. *Particle Design Via Crystallization*, AIChE Symposium Series. New York: American Institute of Chemical Engineers, 1991, vol. 284, no 87.
7. Y. A. Abramov, Ed. *Computational Pharmaceutical Solid State Chemistry*, New Jersey: John Wiley & Sons, 2016.

Acknowledgements

These summer school notes draw down on final year MChem/MEng and MSc teaching courses on the structural aspects of crystal growth given over the past 30 years. I gratefully acknowledge my good friend and colleague Dr Peter J. Halfpenny (previously at the University of Bath) for his help in preparing some of the original course material presented here.

The involvement of the many researchers, co-investigators and graduate students who have been involved in crystallisation science and engineering research in this research group as highlighted through the papers cited here is also gratefully acknowledged.

Research funding from what is now RCUK and from a number of industrial companies over many years is also gratefully acknowledged, most recently through the Advanced Manufacturing Supply Chain Initiative 'Advanced Digital Design of Pharmaceutical Therapeutics' (ADDoPT) project (grant 14060) and EPSRC grants EP/I028293/1, EP/IO14446/1, EP/P006965/1 and EP/L015285/1 for the EPSRC Centre for Doctoral Training in Complex Particulate Products and Processes.

References

[1] P. J. Halfpenny, H. Morrison, R. I. Ristic, E. E. A. Shepherd, J. N. Sherwood, G. S. Simpson, C. S. Yoon, "The growth of large single crystals of the organic nonlinear optical material 2-(α-Methylbenzylamino)-5-Nitropyridine," *Proceedings of the Royal Society: Mathematical and Physical Sciences*, vol. 440, pp. 683-699, 1993.

[2] T. Ukachi, T. Shigemoto, H. Komatsu, T. Sugiyama, "Crystal growth, and characterization of a new organic nonlinear-optical material: l-N-(5-nitro-2-pyridyl) leucenol," *Journal of the Optical Society of America B*, vol. 10, pp. 1372-1378, 1993.

[3] M. Suresh, S. Asath Bahadur, S. Athimoolam, *"Crystal growth and characterization of a new NLO material: 4-Methoxyaniline,"* Advances in Applied Science Research, vol. 4, pp. 160-164, 2013.

[4] V. Ramachandran, P. J. Halfpenny, K. J. Roberts, *"Crystal Science Fundamentals,"* in Engineering Crystallography: From Molecule to Crystal to Functional Form, K. J. Roberts, R. Docherty, R. Tamura, Eds. Dordretch: Springer & NATO Emerging Security Challenges Division, pp. 3-19, 2017.

[5] C. C. Sun, "Materials science tetrahedron — a useful tool for pharmaceutical research and development," *Journal of Pharmaceutical Sciences,* vol. 98, pp. 1671–1687, 2009.

[6] A. Sarkar, D, Ragab, S. Rohani, "Polymorphism of progesterone: a new approach for the formation of form II and the relative stabilities of form I and form II," *Cryst. Growth Des.,* vol. 14, pp. 4574−4582, 2014.

[7] J-R. Wang, X. Wang, L. Lu, X. Mei, "Highly crystalline forms of valsartan with superior physicochemical stability," *Cryst. Growth Des.,* vol. 13, pp. 3261-3269, 2013.

[8] B. Zhu, Q. Zhang, J-R, Wang, X. Mei, "Cocrystals of baicalein with higher solubility and enhanced bioavailability," *Cryst. Growth Des*., vol. 17, pp.1893-1901, 2017.

[9] J-C. Monbaliu, T. Stelzer, E. Revalor, N. Weeranoppanant, K. F. Jensen, A. S. Myerson, “Compact and integrated approach for advanced end-to-end production, purification, and aqueous formulation of lidocaine hydrochloride,” *Org. Process Res. Dev.*, vol. 20, pp. 1347-1353, 2016.

[10] H. Kutzke, H. Klapper, R. B. Hammond, K. J. Roberts, “Meta-stable β-Phase of benzophenone independent structure determinations via X-ray powder diffraction and single crystal studies,” *Acta Crystallogr. B*, vol. 56, pp. 486 – 496, 2000.

[11] W. Davey, “Precision measurements of the lattice constants of twelve common metals,” *Physical Reviewer*, vol. 25, pp. 753 – 761, 1925.

[12] D. E. Williams, “Non-bonded potential parameters derived from crystalline aromatic hydrocarbons,” *J. Phys. Chem.*, vol. 45, pp. 3370 – 3378, 1966.

[13] A. I. Kataigorodskii, K. V. Mirskaya, A. B. Tovbis, “Lattice energy of crystalline benzene in the atom-atom approximation,” *Sov. Phys. Crystallogr.,* vol. 13, pp. 176 – 180, 1968.

[14] F. A. Momany, L. M. Carruthers, R. F. McGuire, H. A. Scheraga, “Intermolecular potentials from crystal data. III. Determination of empirical potentials and applications to the packing configurations and lattice energies in crystals of hydrocarbons, carboxylic acids, amines and amides,” *J. Phys. Chem.,* vol. 78, pp. 1595 – 1620, 1974.

[15] S. Lifson, A. T. Hagler, T. Dauber, “Consistent force field studies of intermolecular forces in hydrogen-bonded crystals. I. Carboxylic acids, amides, and the C=O···H hydrogen bonds,” *J. Am. Chem. Soc.,* vol. 101, pp. 5111 – 5121, 1979.

[16] G. Clydesdale, K. J. Roberts, R. Docherty, “Modelling the morphology of molecular crystals in the presence of disruptive tailor-made additives,” *J Cryst Growth*, vol. 135, pp. 331 - 340, 1993.

[17] R. Docherty, K. J. Roberts, V. Saunders, S. N. Black, R. J. Davey, “Theoretical – analysis of the polar morphology and absolute polarity of crystalline urea,” *Faraday Discussion*, vol. 95, pp.11-25, 1993.

[18] D. M. Camacho Corzo, C. Y. Ma, V. Ramachandran, T. Mahmud, K. J. Roberts, *“Crystallisation route map,”* in Engineering Crystallography: From Molecule to Crystal to Functional Form, K. J. Roberts, R. Docherty, R. Tamura, Eds. Dordretch: Springer & NATO Emerging Security Challenges Division, pp. 179-213, 2017.

[19] K. J. Roberts, R. Docherty, P. Bennema, L. Jetten, “The importance of considering growth-induced conformational change in predicting the morphology of benzophenone,” *J. Phys D-Appl Phys.,* vol. 26, pp. B7-B21, 1993.

[20] R. N. M. R. van Gelder, K. J. Roberts, J. Chambers, T. Instone, “Nucleation of single and mixed straight chain surfactants from dilute aqueous solutions,” *J. Cryst Growth*, vol. 166, pp. 189 – 194, 1996.

[21] Roberts, K., Docherty, R., Bennema, P., and Jetten, L. (1993) The importance of considering growth-induced conformational change in predicting the morphology of benzophenone. J. Phys. D: Appl. Phys., 26, B7 – B21.

[22] P. J. Halfpenny, Private communication / unpublished work, 2019.

[23] G. R. Ester, P. J. Halfpenny, “Observation of two-dimensional nucleation on the (010) face of potassium hydrogen phthalate (KAP) crystals using ex situ atomic force microscopy,” *J. of Cryst. Growth*, vol. 187, pp. 111 -118, 1998.

[24] L. A. Smith, A. Duncan, G. B. Thomson, K. J. Roberts, D. Machin, G. McLeod, “Crystallisation of sodium dodecyl sulphate from aqueous solution: phase identification, crystal morphology, surface chemistry and kinetic interface roughening,” *J. of Cryst. Growth*, vol. 263, pp. 480–490, 2004.

[25] T. T. H. Nguyen, R. B. Hammond, K. J. Roberts, I. Marziano, G. Nichols, “Precision measurement of the growth rate and mechanism of ibuprofen {001} and {011} as a function of crystallization environment,” *CrystEngComm.*, vol. 16, pp. 4568 – 4586, 2014.

[26] J. Bunyan, N. Shankland, D. Sheen, “In Solvent effects on the morphology of ibuprofen”, *AIChE Symposium Series*, pp. 44-54, 1991.

[27] T. T. H. Nguyen, I. Rosbottom, I. Marziano, R. B. Hammond, K. J. Roberts, “Crystal morphology and interfacial stability of RS-ibuprofen in relation to its molecular and synthonic structure,” *Cryst. Growth Des.,* vol. 17, pp. 3088-3099, 2017.

[28] I. Rosbottom, J. H. Pickering, B. Etbon, R. B. Hammond, K. J. Roberts, “Examination of inequivalent wetting on the crystal habit surfaces of RS-ibuprofen using grid-based molecular modelling,” *Phys.Chem.Chem.Phys.,* vol. 20, pp. 11622 – 11633, 2018.